Dov Bahat
Avinoam Rabinovitch
Vladimir Frid

Tensile Fracturing in Rocks

Tectonofractographic and Electromagnetic Radiation Methods

Springer

Dov Bahat
Avinoam Rabinovitch
Vladimir Frid

Tensile Fracturing in Rocks

Tectonofractographic and Electromagnetic Radiation Methods

Dov Bahat
Avinoam Rabinovitch
Vladimir Frid

Tensile Fracturing in Rocks

Tectonofractographic and Electromagnetic Radiation Methods

With 302 Figures

Springer

Authors

Prof. Dov Bahat

Department of Geological and Environmental Sciences
Ben Gurion University of the Negev, POB 653
Beer Sheva, 84105 Israel
Head, the Deichmann Rock Mechanics Laboratory of the Negev
e-mail: bahat@bgumail.bgu.ac.il, phone: +972-8-6472623, fax: +972-8-6472997

Prof. Avinoam Rabinovitch

Physics Department
Ben Gurion University of the Negev, POB 653
Beer Sheva, 84105 Israel
The Deichmann Rock Mechanics Laboratory of the Negev
e-mail: avinoam@bgumail.bgu.ac.il, phone: +972-8-6461172

Dr. Vladimir Frid

Department of Geological and Environmental Sciences
Ben Gurion University of the Negev, POB 653
Beer Sheva, 84105 Israel
The Deichmann Rock Mechanics Laboratory of the Negev
e-mail: vfrid@bgumail.bgu.ac.il, phone: +972-8-6461770

Library of Congress Control Number: 2004108439

ISBN 3-540-21456-9 **Springer Berlin Heidelberg New York**

Springer is a part of Springer Science+Business Media
springeronline.com

Printed in Germany

Cover design: Erich Kirchner, Heidelberg
Typesetting: Büro Stasch (stasch@stasch.com), Bayreuth
Production: Luisa Tonarelli
Printing: Mercedes-Druck, Berlin
Binding: Stein & Lehmann, Berlin

Printed on acid-free paper 32/3141/LT – 5 4 3 2 1 0

Preface

'Tensile Fracturing in Rocks' presents field observations on fracturing of sedimentary rocks and granite outcrops from various provinces in three continents. It also combines results of recent experiments conducted at different laboratories around the world with current theories on fracturing. In treating faults, this book limits itself to faults that are associated with joint sets produced by definable causes and occasionally to cases where interaction between the two types of fracture – faults and joints – is not clear. The book's subject matter is divided over six chapters, which are briefly described below.

Chapter 1 summarizes current key concepts in fracture physics. It starts with a presentation of the elastic theory of fracture, and concentrates on the results of linear elastic fracture mechanics. The chapter touches also upon other fracture properties, e.g., crack nucleation, dynamic fracturing and slow fracturing processes. Nucleation is addressed by statistical mechanics methods incorporating modern approaches of thermal and fiber bundle processes. The analyses of dynamic fracturing and slow fracturing focus on the differences, as compared to the linear elastic approach. The controversy in interpreting experimental dynamic results is highlighted, as are the surface morphology patterns that emerge in fracturing and the non-Griffith crack extension criterion in very slow fracturing processes.

Chapter 2 concentrates on basic topics in fracture geology. Fractography is applied to improve the understanding of some intricacies, such as nucleation and fracture growth in rocks. A review of fourteen lab experiments and a numerical experiment is followed by a discussion on the properties of mirror planes and fringes on joint surfaces. These are exemplified on sedimentary and granitic rocks. Concepts of conjugate hybrid joints and longitudinal splitting are re-evaluated in the light of recent experiments. Various aspects of joint classification are reviewed. The chapter's last section (2.4) relates to mutual relationships of primary and secondary fractures, such as wing cracks, pinnate joints and branching fractures.

Chapter 3 presents observations on sedimentary rocks in four fracture provinces: Two in the USA, one in south Britain and one in south Israel. Although not representing all types and styles of fracturing, the combined data allow a synthesis of joint formation in different tectonic settings.

Chapter 4 presents four fracture provinces in granites (in Germany, the Czech Republic and in California) that exhibit a wide spectrum of fracture settings. The syntectonic, uplift and post-uplift joint features resemble their equivalents in sedimentary rocks. However, granites also display unique fracture features that are associated with late cooling stages of the pluton.

Chapter 5 deals with a new method of investigating embryonic stages of rock failure by measuring high-frequency electromagnetic radiation (EMR) from micro-cracks. We review previous EMR investigations, present our new EMR model and show the extracted EMR 'fingerprints' in rocks and other materials when strained. EMR signals from laboratory tests as well as from quarry blasting are analyzed. Underground EMR preceding rock-bursts and gas outburst are studied, and some criteria for their forecasting based on the obtained parameters are derived. The EMR results described here are expected to lead to a novel forecasting method of earthquake nucleation.

Chapter 6 addresses some particular problems in fracture geology, including procedures for the study of joints. A discussion on previous paleostress studies in the Middle East, particularly in the Israeli Negev, leads to a model on regional jointing in the broad context of plate tectonics. This chapter contains a new approach in studying joint length and a brief account of the procedure of estimating the fracture paleostresses on a joint surface by a fractographic method. Also included is a detailed characterization of the unique fracture geometry of a fault termination zone. Additional topics are, the description of a variety of fault-joint geometric and genetic relationships and a characterization of a new joint category, termed 'surface joints'. We also take account of hydro-geological research that relies on fracture distribution data in the Beer Sheva syncline. Finally, we present here major features of a new mechanical model of *en echelon* segmentation that differs from the more conventional ideas.

This book is a sequel to a previous volume in this series, 'Tectonofractography' (1991), and many premises are not re-introduced here. Some terms are introduced in a special section on nomenclature.

Acknowledgements

The authors wish to thank all those who contributed to the writing of this book. Several persons contributed immensely to the field work and data collection. These include Peter and Elfriede Bankwitz who collaborated in the study of fracturing in granites in central Europe, particularly, the pre-uplift fracture during the cooling of the pluton. Jointing in sandstone (Zion National Park, Utah) and in granites (the Sierra Nevada Batholith, California) was studied in cooperation with Ken Grossenbacher and Kenzi Karasaki. Some of the initial observations that were made with them on post-uplift joints and oblique fractures during my (DB) Sabbatical year at LBNL matured during the years to concrete data, and they should share the credit for it. Section 4.12 was mostly contributed by Ken Grossenbacher. Important help was also given by Paul Witherspoon and Sally Benson. This book contains numerous citations from works by Terry Engelder and his associates that contributed greatly to the understanding of jointing. Working with Tsafrir Levi on his thesis has been a delight for one of us (DB). Julia Goldbaum enriched considerably our understanding of EMR phenomena. We also acknowledge the important contributions by Yoav Avni and Menachem Friedman, and instructive field trips with Yehuda Eyal and Ram Weinberger. Charles Howard contributed greatly to the writing of Sect. 6.8.

Special thanks are due to colleagues who critically reviewed chapters in draft: Chapter 2, Ram Weinberger; Chapter 3, Ithamar Perath; Chapter 4, Reginald Shagam; Chapter 6, Meir Abelson and Ronit Nativ.

Figures 2.35e and 3.35c were donated by Ran Kagan and Alon Raviv, respectively, and Fig. 2.69b and 3.10e were photographed during inspections of quarries with Peter and Elfriede Bankwitz.

Most of our experiments were conducted in the Ruth and Horst Deichmann Rock Mechanics Laboratory of the Negev, the Department of Geological and Environmental Sciences, the Ben Gurion University of the Negev.

For important technical help, we owe thanks to Vyacheslav Palchik, Dina, Isaak and Michael Frid, Julia and Boris Goldbaum, Avi Sharon, Leonid Baluashvili, Eli Shimshilashvili, Rivka Eini, Ran Novitsky, Hagit Lev, Ania Arbel, Daniela Vida, Michal Barima, Ronen Shavit from BGU, and Pascual Benito from LBNL. We also owe thanks to H. Hertrich from Solnhofer Bodenplatten-Industrie GmbH and Co KG for help in our experiments.

The help extended by members of the department of the Geological and Environmental Sciences was crucial to the completion of this book. Financial assistance was received from the Earth Sciences Administration (Ministry of Energy and Infrastruc-

ture), and thanks are due to Yosef Bartov for his interest and assistance. Support was also given by the Israel Science Foundation, the Ezvonot Committee of the Israeli Government Estate Distributions and by the Vatat and NRCN funds.

Many authors and publishers contributed valuable photographs and diagrams upon our request, enabling us to fundamentally upgrade our book. All readers are invited to write to us about errors that they find in the book.

The ideas presented in this book were beginning to crystallize when a sudden deterioration in my (DB) wife Hanna's health overshadowed all literary thinking. Dan and Merav, Zvi and Jonathan were with us during her last months of suffering. This book is dedicated to her memory.

Contents

Chapter 1

Fracture Physics

In this chapter we give a brief account of the theory of fracture, restricting ourselves to brittle fracture. The structure of this chapter is as follows. The first part describes the Griffith criterion of fracture initiation, since this criterion constituted the turning point in our understanding of the basics of fracture. We next consider the question of nucleation both of flaws and of fractures in a solid. This process has recently had a breakthrough and is related to the origin of fracture initiation. The general elastic theory of fracture is considered next – linear elastic fracture mechanics (LEFM) as the only complete theory and the rational extension of the Griffith approach. The analysis of two-dimensional problems, for some of which analytical solutions can be obtained, is emphasized. The last parts deal with two important topics that do not fall within and can not be dealt with by LEFM, namely, dynamic crack propagation and creep. In both of these topics, new advances have been made in recent years and both are therefore a subject matter for contemporary research.

A note of caution is in order. Although the Griffith criterion and the related linear elastic fracture mechanics methods have helped scientists in dealing with static cracks and engineers in building safer structures, the basic dynamics of the fracture problem are as of yet not well understood. This relative ignorance stems from the fact that on the one hand, fracturing is neither an equilibrium nor a near equilibrium process and is therefore not amenable to perturbation procedures, and on the other hand, fracturing, whose principle part occurs at a very restricted area and is highly nonlinear, influences the whole extension of the body in question, and it is therefore not easy to correlate between its different scales.

A full understanding of crack propagation would entail a quantum mechanical calculation of all atoms in a certain vicinity of the crack. Since each atom contains several electrons, a full "many-body" calculation (see, e.g., Fabrocini et al. 2002) should be made. Obviously, even numerically, this procedure is unachievable in the foreseeable future. A less presumptuous attempt would be to consider each atom as a point entity and to calculate fracture propagation by assuming a certain interaction among these entities. Even a classical (rather than a quantum mechanical) calculation would have to assume an approximation of only two or at most three body forces, and it would have to assume, moreover, that these two body forces (say of a Lennard Jones type; see, e.g., Ashcroft and Mermin 1981) can be extended to inter-atomic distances far greater (or smaller) than equilibrium ones. Even under such approximations, the number of atoms and the time period necessary for a useful calculation are as of yet beyond the scope of available computational means. Thus, the maximum number of atoms for which such numerical calculations have been tried is the boasted 10^9 (Abraham

et al. 2002). However, for a meaningful dynamical calculation a number about a thousand times higher is needed. As for the time periods needed, these should be scaled by atomic vibrations, which entail at least around 10^6 time steps even for such a short time as 1 μs, rendering this task unattainable at the present stage.

There are at present several groups of scientists around the world who try to "connect" the different scales that appear in fracture calculations. The idea is to use a quantum mechanical type of calculation in order to obtain the correct two-body atomic force even for large inter-atomic distances. These forces are to be used only for a relatively small number of atoms near the crack tip and the so called "process zone" to obtain an accurate microscopic (classical) calculation. The latter should yield inter alia the energy needed for crack advance, the stresses and strains near the tip and the appearance and motion of dislocations for non-brittle materials. The boundary conditions for this calculation would be the connection to the major part of the material, which is to be treated in a continuous manner (linear or non-linear fracture mechanics). This ambitious plan is still in its infancy but promises to become a real asset in understanding fracture dynamics in the future.

1.1 The Griffith Criterion

1.1.1 Stress and Strain

Consider the bar in Fig. 1.1 whose initial length and cross section are l_0 and $A = b \times b$, respectively. We apply a force in the x-direction, which causes the bar to elongate by x. We define $\sigma_{xx} = f/A$, as the *stress* operating inside the bar in the x-direction. Hence, stress has the units of force per area. It is assumed that the bar elongates with the continued application of the force in such a way as to preserve elasticity, namely that it operates like a spring, maintaining a linear relationship between the applied stress f/A and the elongation, x, $f = kx$ (Hook's law). This relationship together with Newton's law $f = ma$ are the basis of all of elasticity theory (see, e.g., Timoshenko and Goodier 1984). Defining the non-dimensional variable $\varepsilon_{xx} = x/l_0$ as the strain in the bar (the change in length divided by the initial length), one can write Hook's law as

$$\varepsilon_{xx} = \frac{\sigma_{xx}}{E} \tag{1.1}$$

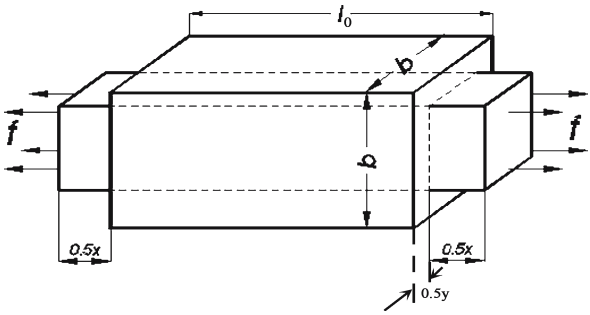

Fig. 1.1. Schematic stress-strain behavior of a bar ($l_0 \times b \times b$) under uniaxial force f

where E is Young modulus, related in the case of the bar, to the Hook's constant k through

$$k = \frac{f}{x} = \frac{\sigma_{xx} A}{\varepsilon_{xx} l_0} = \frac{AE}{l_0} \tag{1.2}$$

Under the same stress, there also occurs a (small) reduction of size of the bar in the lateral directions. Thus, if in the y-direction the decrease of width is denoted by $-y$ (the minus sign comes to denote a *reduction* of size), the strain in this direction is $\varepsilon_{yy} = -y / b$ and for elastic materials is given by

$$\varepsilon_{yy} = -\nu \varepsilon_{xx} = -\frac{\nu \sigma_{xx}}{E} \tag{1.3}$$

where ν is a non-dimensional constant called the Poisson ratio, which for different materials usually assumes values between 0.1 and 0.5. A similar reduction occurs in the z-direction (ε_{zz}).

An important issue to be used frequently in the following is the value of the elastic energy stored in the material. For the bar problem, suppose we apply the force quasi statically to avoid acceleration and kinetic energy and increase its magnitude from zero to a final value F. The elastic energy is given by the work needed to create the final state:

$$W = \int_0^{\Delta l} f(x)\mathrm{d}x = k \int_0^{\Delta l} x\mathrm{d}x = k\frac{\Delta l^2}{2} = \frac{l_0 A E \varepsilon_{\mathrm{f}}^2}{2} = \frac{V E \varepsilon_{\mathrm{f}}^2}{2} = V\frac{\varepsilon_{\mathrm{f}}\sigma_{\mathrm{f}}}{2} = V\frac{\sigma_{\mathrm{f}}^2}{2E} \tag{1.4}$$

where Δl is the final elongation of the bar, $\varepsilon_{\mathrm{f}} = \Delta l / l_0$ is the final strain, σ_{f} is the final stress ($= E\varepsilon_{\mathrm{f}}$) and V is the initial bar volume. We have therefore obtained the important result that the elastic energy per unit volume (W / V) stored in the sample is given by

$$\frac{W}{V} = \frac{1}{2}\sigma\varepsilon = \frac{1}{2}E\varepsilon^2 = \frac{1}{2}\frac{\sigma^2}{E} \tag{1.5}$$

Although this result was obtained for the specific case of a bar acted upon by a uniaxial force, this result is quite general and we will use it later, e.g., for the Griffith criterion.

In the general case, i.e., for a body of a general shape acted upon by a general distribution of forces and displacements, elasticity theory considers an infinitesimal cube inside the body and the force components per unit area on each side of the cube constitute the stress *tensor* σ_{ij}, where $i = 1, 2, 3$ and $j = 1, 2, 3$ denote the x-, y- and z-coordinates, respectively. Thus, for example $\sigma_{12} = \sigma_{xy}$ denotes the force (per unit area) component in the y-direction acting on the cube face, which is perpendicular to the x-direction. This tensor can in general depend both on the location of the cube within the body, $\mathbf{r}$, and on time. Therefore, σ is generally written as $\sigma_{ij}(r, t)$. It can be shown that σ is a symmetric tensor, namely

$$\sigma_{ij} = \sigma_{ji} \tag{1.6}$$

The force per unit area acting on a general surface perpendicular to a unit vector $\hat{n} = n_1\hat{x} + n_2\hat{y} + n_3\hat{z}$ ($\hat{x}, \hat{y}, \hat{z}$ are unit vectors in the x-, y- and z-directions respectively) is called the *traction* $\boldsymbol{t}$ and its components are given by

$$t_i = \sum_{j=1}^{3} \sigma_{ij} n_j \qquad (= \sigma_{i1} n_1 + \sigma_{i2} n_2 + \sigma_{i3} n_3) \tag{1.7}$$

Next, displacements from equilibrium position are defined such that under the action of forces, a point within the body initially (with no force) located at the position (x, y, z) is displaced to the position $(x + u_1, y + u_2, z + u_3)$ by the action of the forces. The displacement vector is thus denoted by $\mathbf{u} = u_1\hat{x} + u_2\hat{y} + u_3\hat{z}$. Newton's equation of motion (force = mass × acceleration) is transferred into the infinitesimal cube to yield (per unit volume)

$$\sum_j \frac{\partial \sigma_{ij}}{\partial x_j} + f_i = \rho \frac{\partial^2 u_i}{\partial t^2} \tag{1.8}$$

where the first term on the left denotes the effect of the surface forces (by measuring their difference in the i-direction between the two sides of the cube, while f_i is the i^{th} component of the so-called "body force" if such a force exists (e.g., gravity when it is relatively large compared with surface forces and can not be ignored) and ρ is the density (mass per unit volume) at the position (x, y, z). Equation 1.8 is the basic equation of motion of an elastic medium and all further linear elastic considerations are conducted in order to solve it. An important special case of Eq. 1.8 is static equilibrium, where all movements are zero. In that case,

$$\sum_j \frac{\partial \sigma_{ij}}{\partial x_j} + f_i = 0 \qquad \text{(static equilibrium)} \tag{1.9}$$

or, when no body forces exist,

$$\sum_j \frac{\partial \sigma_{ij}}{\partial x_j} = 0 \qquad \text{(static equilibrium, zero body force)} \tag{1.10}$$

In order to solve Eq. 1.8, one should have a way to connect σ with u. This is done via the generalized Hook's law in the following way. Firstly, a strain tensor ε_{ij} is defined as

$$\varepsilon_{ij} = \frac{1}{2}\left(\frac{\partial u_i}{\partial x_j} + \frac{\partial u_j}{\partial x_i} \right) \tag{1.11}$$

As can be seen, ε is also a symmetric tensor, i.e., $\varepsilon_{ij} = \varepsilon_{ji}$. The most general Hook's law can now be written as a linear relation between σ and ε,

$$\sigma_{ij} = \sum_{k,l} C_{ijkl} \varepsilon_{kl} \tag{1.12}$$

where C_{ijkl} is a constant tensor of the 4^{th} rank replacing the Young modulus of Eq. 1.1. It is a material property. For isotropic homogeneous materials, C_{ijkl} has only two components λ and μ (called the Lamé constants) different from zero and the law can be written as

$$\sigma_{ij} = 2\mu\varepsilon_{ij} + \lambda\delta_{ij}\sum_k \varepsilon_{kk} \tag{1.13}$$

where δ_{ij} is the Kronecker δ,

$$\delta_{ij} = \begin{cases} 1 & \text{if} \quad i = j \\ 0 & \text{if} \quad i \neq j \end{cases} \tag{1.14}$$

For example, $\sigma_{xz} = \sigma_{13}$ equals $2\mu\varepsilon_{13}$ while $\sigma_{zz} = \sigma_{33} = 2\mu\varepsilon_{33} + \lambda(\varepsilon_{11} + \varepsilon_{22} + \varepsilon_{33})$. The Lamé constants are connected to the Young modulus and the Poisson ratio ν through

$$\nu = \frac{\lambda}{2(\mu + \lambda)} \qquad \text{and} \qquad E = \frac{\mu(2\mu + 3\lambda)}{\mu + \lambda} \tag{1.15}$$

Now, the right hand side of Eq. 1.8 can be differentiated with respect to x_i and x_j to relate it through Eq. 1.11 with ε_{ij}, and the left-hand side of Eq. 1.8 in its turn can be transformed by Eq. 1.12 or 1.13 to be given in terms of ε_{ij} (as well). In this way, the ensuing equation will have similar variables on both sides. There is, however, a problem arising from the connection between the displacements and the strain (Eq. 1.11). Although the displacement **u** (a vector with three components) uniquely defines ε_{ij} (a symmetric tensor with six components), the ε_{ij} does not uniquely define the displacements. There is a redundancy. In order to insure a unique **u**, the strain components must satisfy an additional criterion (called the compatibility equations, see also Sect. 1.3.3.1)

$$\frac{\partial^2\varepsilon_{ij}}{\partial x_k \partial x_l} + \frac{\partial^2\varepsilon_{kl}}{\partial x_i \partial x_j} = \frac{\partial^2\varepsilon_{ik}}{\partial x_j \partial x_l} + \frac{\partial^2\varepsilon_{jl}}{\partial x_i \partial x_k} \tag{1.16}$$

The mathematical complexity of this set of equations (Eqs. 1.8–1.16) both for the dynamic but even for the static cases makes exact analytic solutions for elastic problems almost unobtainable. Exceptions are problems that due to their symmetry can be reduced to simpler forms. The most common solvable problems are "two-dimensional" (2D) ones, where the influence of the third dimension is ignored. Two types of such problems are of importance. In the first, we deal with a thin plate, where it is assumed that the thickness is much smaller than the other dimensions and can be ignored (plane stress); and in the second a very thick specimen is considered where the third dimension is ignored (plane strain) under the condition that *no change* of the applied force occurs across the thickness of the plate and the whole system is homogeneous and therefore solutions do not change with the coordinate in this direction.

1.1.2 Energy Considerations and the Griffith Criterion

Fractures occur in solids at much lower stresses than those which can be deduced from simple estimations. For example, if we assume that the solid breaks when the distance between its atomic planes become elongated by, say, 1 / 10 of the equilibrium distance, this would mean that $\varepsilon \sim 1/10$ and $\sigma = E\varepsilon \sim E/10$. Most solids break under loads that

are two or three orders of magnitude lower than this value. This discrepancy was resolved by Griffith (1920). In principle his argument is that the stress is not transferred to the solid homogeneously. Rather, due to the existence of flaws in the body (and almost all solids contain flaws, unless grown in a very special method – controlled whisker procedure), the stress becomes concentrated at the tip of such a flaw. Hence, strains and stresses at this location become much larger than those prevailing in the rest of the material – leading to fracture there. In fact, it is the longest flaw (favorably oriented), which sets the limit for the critical stress, the stress above which fracture would occur, as is shown presently.

Consider (Fig. 1.2), a large plate of thickness b and cross section A, which is operated on by a constant force f or a stress σ_0 ($= f/A$) and in which there exists a flaw (fracture) of length c. The fracture evidently has caused the elastic energy in its vicinity to be relieved. We can estimate the volume wherefrom the elastic energy was relieved to be approximately equal to the half cylinder shown.

This volume is

$$V \sim \frac{1}{2}\pi c^2 b \tag{1.17}$$

And according to Eq. 1.5, the total relieved energy is

$$W_E \sim V\frac{\sigma^2}{2E} = \frac{\pi}{4}\frac{\sigma_0^2}{E}c^2 b \tag{1.18}$$

Therefore, should the fracture propagate by an additional increment Δc, the change in relieved energy would be

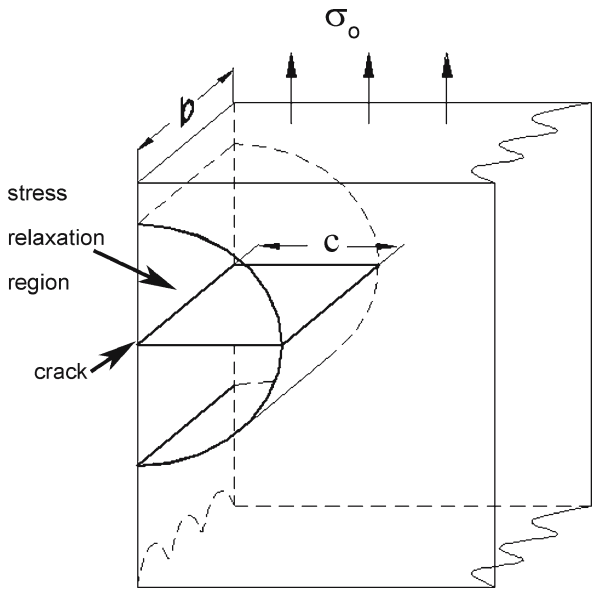

Fig. 1.2.
A through crack in a semi infinite slab and the (schematic) region in which energy is relaxed

$$\Delta W_{\mathrm{E}} \sim \frac{\pi}{2}\frac{b}{E}\sigma_0^2 c\Delta c \tag{1.19}$$

By the way, the energy per unit length $\Delta W_{\mathrm{E}}/\Delta c$ is usually denoted by the (not very fortunate) term "energy release rate" G (in honor of Griffith).

According to Griffith, the energy thus released from the elasticity stored reservoir should go in its entirety (or almost so) to create the areas of the new addition to the fracture surface. If we assume that the energy needed for the creation of a new unit of fracture area, Γ, is a material constant (it is in fact half of the energy needed to break the chemical bonds between the two newly created surfaces), then the energy required for an increment Δc of the fracture is

$$\Delta W_{\mathrm{s}} = 2\Gamma b\Delta c \tag{1.20}$$

The factor of two comes because two new surfaces are created above and below the increment. Energy balance entails that the change in the released increment of elastic energy be equal to the increment of surface energy, i.e.,

$$2\Gamma b\Delta c \sim \frac{\pi}{2}\frac{b}{E}\sigma_0^2 c\Delta c \qquad \text{or} \qquad \frac{\Delta W_{\mathrm{E}}}{\Delta c} = \frac{\Delta W_{\mathrm{s}}}{\Delta c}$$

yielding

$$\sigma_0^2 c \sim \frac{4}{\pi}\Gamma E \tag{1.21}$$

A similar calculation applies for an internal flaw (crack). Assume that this crack is circular of radius c. The volume from which the elastic energy was released is

$$V = \frac{4}{3}\pi c^3$$

and therefore in this case

$$W_{\mathrm{E}} = \frac{4}{3}\pi c^3 \frac{\sigma_0^2}{2E}$$

where σ_0 is the remote stress perpendicular to the flaw. The surface energy needed to create this flaw is $W_{\mathrm{s}} = 2pc2\Gamma$. Griffith's incremental energy balance,

$$\frac{\partial W_{\mathrm{E}}}{\partial c} = \frac{\partial W_{\mathrm{s}}}{\partial c}$$

yields

$$\sigma_0^2 c = 2E\Gamma \tag{1.21'}$$

Although the method used here to obtain Eq. 1.21 or 1.21' is somewhat crude, the result, except perhaps for the coefficient, is accurate. This is Griffith's condition. Let us first calculate the value of σ_0 needed to initiate a crack and compare it to the homogeneous estimate of $E/10$ we had before. The decrease with respect to $E/10$ of σ_0 needed for fracture commencement can be seen as a measure of the enhancement of stress at the crack tip relative to σ_0. From Eq. 1.21,

$$\sigma_0 = \frac{E}{q}; \qquad q \approx \sqrt{\frac{Ec}{\Gamma}} \tag{1.22}$$

Therefore, the magnitude of q is a measure of stress increase (relative to σ_0) at the tip of a flaw of length c.

Let us examine soda lime glass as an example. The relevant constants for glass are $E \sim 6.2 \times 10^{10}$ Newton m^{-2} and $\Gamma \sim 0.54$ Joule m^{-2}, hence for glass $q \sim 3.4 \times 10^5 \sqrt{c}$. This relation is plotted in Fig. 1.3. It is seen that our first estimate of q, $q \sim 10$ is obtained only for flaw lengths of the order of atomic distances, while for usual flaw lengths of the order of 0.1 mm, q is of the order of several thousands.

According to the Griffith criterion, Eq. 1.21, therefore, the important experimental variable "responsible" for crack initiation is the product $\sigma_0^2 c$ of $\sigma_0 \sqrt{c}$ and not σ_0 itself. When this variable reaches a certain threshold, which depends on the specific material and on the geometry of the loading system, fracture should commence. This threshold according to Eq. 1.21 depends on the Young modulus and the surface energy of the fracturing sample. As will be shown next (Sect. 1.3), a more elaborate and accurate treatment of linear elasticity (called linear elastic fracture mechanics (LEFM) an established branch of mechanical engineering nowadays) yields the same result as Eq. 1.21, up to a change of coefficient, for uniaxial constant loading. This LEFM treatment has been used for many years now to achieve solutions for engineering static safety problems and has proven extremely useful for that purpose. Basically, it is an extension of the Griffith approach. As we shall point out, however, this approach, so successful for regular static cracking problems, is inadequate when dealing with the following two important issues:

1. Fracture development under low stresses in very long time periods (the so-called "creep" situation).
2. Dynamic crack propagation.

We dedicate a section for each of these problems.

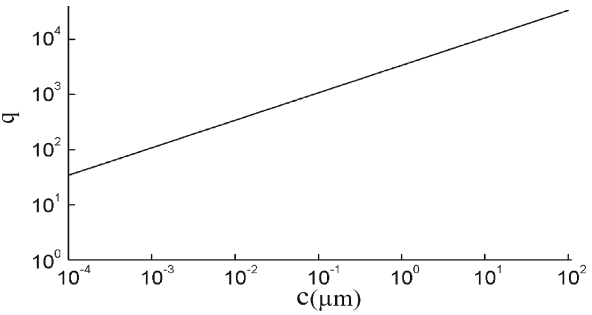

Fig. 1.3.
The amount q by which the stress σ_0, needed to cause fracture, is decreased from E as a function of the Griffith-fracture length c

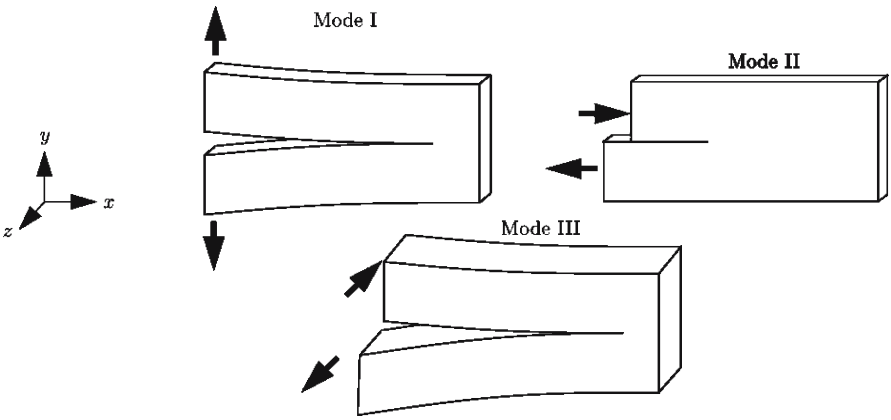

Fig. 1.4. The three fracture modes

1.1.3 Fracture Modes

Cracks can appear in solids under stress only in three different geometrical situations, called modes, or in situations that are combinations of these modes. Figure 1.4 shows these three geometries called mode I, mode II and mode III. Almost all engineering treatments of fracture problems are developed in a mode I geometry, which is the prevalent mode of fracture. The presence of mode II and III in addition to mode I is manifested by changes of crack directions as in the appearance of lancets, striae or plumes, undulations etc. In geological cracks, we discern between "joints" that are created in a mode I geometry and "folds" that are created under the other mode types. In the description of all three modes (Fig. 1.4), the fracture surface is in the x-z-plane and the fracture propagates in the x-direction. In mode I, stress (tension or compression) is applied in the $\pm y$-direction and the displacements $\mathbf{u}$ also occur in the same direction. Modes II and III are shear modes. In mode II, the shearing stress and the displacements are in the same direction ($\pm x$) as that of the crack propagation. Mode III fracture is also called an "antiplane" mode, since stress and displacements occur in the $\pm z$-directions, out of the plane of the fracture and normal to the plane of the specimen.

1.2 Nucleation

1.2.1 General

Let us first define the three different nucleation processes that are used here (see also Sect. 2.2.2 for additional applications of the term "nucleation"):

1. "Flaw nucleation" is the process or processes by which a seed for the subsequent creation of a propagating fracture is created. The seed is usually a flaw in the otherwise "perfect" or homogeneous solid, which facilitates the appearance of a crack in its continuation (see Sect. 1.1.2).

2. "Microcrack nucleation" is the process or processes by which a flaw (which is itself not a microcrack) develops small cracks at the positions of highest stress concentrations such that
   a the combined structure, flaw plus small cracks, can be considered a microcrack for subsequent developments,
   b this combined structure is stable, and
   c it has not reached the critical (Griffith) condition for propagation.
3. "Crack nucleation" is the process or processes by which a *critical crack* (i.e., a crack fulfilling the Griffith criterion for propagation) is created.

Crack nucleation can be "homogeneous", i.e., with no flaws present (a rare occurrence) or "heterogeneous", where a flaw distribution already exists in a solid. Note that in the literature the term "crack nucleation" is used to describe both flaw- and crack-nucleation processes. The terms homogeneous and heterogeneous are also used to describe materials. Thus a homogeneous material is an ideal material, which is made up of the same chemical substance, is devoid of grains and is completely devoid of flaws. The only existing material that is almost completely homogeneous is a glass wisker, i.e., a glass fiber grown under very strict conditions of purity. Since no flaws (or almost no flaws) are created in the production phase, q of Eq. 1.22 is of the order of ten and this material fractures only under very high stresses. Its fracturing is also "homogeneous", namely all parts of it separate at the same time and the material integrates into dust under a large blast. Heterogeneous brittle materials can be divided into three groups according to the degree of severity of the heterogeneity. The least heterogeneous material is regular glass, containing flaws of all kinds (see below). Next in line are rocks or ceramic materials having the same chemical composition. These materials are grainy materials containing grain boundaries and "triple points" as inherent flaws. This group further divides into isotropic (i.e., having the same properties in any direction) and unisotropic. The most heterogeneous (third) group of materials are ceramics or rocks which consist of substances having different chemical compositions. These are usually both grainy and unisotropic. Homogeneous (heterogeneous) nucleation is a nucleation process in a homogeneous (heterogeneous) material.

We use the term "flaw" here as a general term for defect. This is the usual meaning of the term in the fracture literature, while, e.g., in solid state physics the common term is "defect". A flaw can be two-dimensional in the form of a microcrack, or three-dimensional, such as a pore, an inclusion, a vacancy, a dislocation etc. The term "Griffith flaw" is used in the literature generally to describe a flaw in the form of a microcrack (the common form of flaw in glass). A three-dimensional flaw can be transformed to a microcrack by developing actual microcracks at points where high stress concentrations exist (critical or singular points; see below). Note that regular glass, besides Griffith flaws, can contain other flaws (voids etc.) generated during its formation stages or by external environmental degradation. In general, the appearance of flaws in a solid or on its surfaces can be induced by the activity of two mechanisms, "external agents" operation or internal processes. The first mechanism includes surface abrasions and erosion, corrosion by chemical substances, radiation and impact effects, etc. The operation of each agent is subject matter for extensive research. A short review can be found in Lawn (1993, Chap. 9). We shall not consider here the flaws that develop during the production phase and include pores, vacancies, grain boundaries, inclusions etc. (see *ibid*). In this section, we will concentrate on the internal

processes and specifically on microcrack and *crack* nucleations. Note that the use of the term "homogeneous nucleation" in the literature is somewhat controversial. In the words of Frost (2001), "roughly it means the appearance of a crack where there was none present before. But the condition of there being no crack before depends on the precision of our observation." In physics and metallurgy, nucleation means an appearance of a new "phase" in a position "*where absolutely nothing* of the sort existed before." In fracture nomenclature, this term usually means "where absolutely nothing *could be seen (optically)* before." We will have more to say on this subject when discussing thermal nucleation below.

A nucleation of even a microcrack in a perfect (homogeneous) solid would entail stresses of the order of $E/10$ (or $G/10$; Sect. 1.1.2), or corresponding amounts of energy. Following the Griffith model, we look for stress concentration mechanisms that could facilitate this process. In Sect. 1.2.2 we shall review (Frost 2001 and Evans 1974) the possible stress concentration mechanisms capable of reducing the stress (energy) needed for microcrack nucleation, and in Sect. 1.2.3 and 1.2.4 we will present two modern theoretical approaches to crack nucleation. The first one is "thermal nucleation", which has recently been verified experimentally and the second is the so-called "fiber bundle model", which can apparently be used for general grainy materials.

1.2.2
Stress Concentration Avenues to Microcrack Nucleation

The stress concentration mechanisms (see Frost 2001) are elastic stress concentrations resulting from

1. Interior flaws.
2. Elastic anisotropy.
3. Thermal expansion mismatch or thermal expansion coefficient anisotropy, and inelastic mechanisms.
4. Dislocation pile-up.
5. Grain-boundary sliding.

We shall briefly touch upon two of the elastic mechanisms. For the inelastic ones see Frost (2001) and references therein.

1.2.2.1
Elastic Anistropy

We shall treat only heterogeneous anisotropic materials of the second group (Sect. 1.2.1). In heterogeneous materials of the third group (which are made up of grains of *different* substances), there are additional stress concentration possibilities resulting from the mismatch of elastic constants between neighboring grains, which can be treated in a similar way to the one presented here.

Tvergaard and Hutchinson (1988) considered stress concentrations in 2D solids. The treatment was extended to 3D problems by Ghahremani et al. (1990), who treated grains in hexagonal tiling where all boundaries meet at 120° – which is the case we will consider here. Picu and Gupta (1996) extended the treatment to general 2D configurations and Picu (1996, 1997) extended it to several 3D problems.

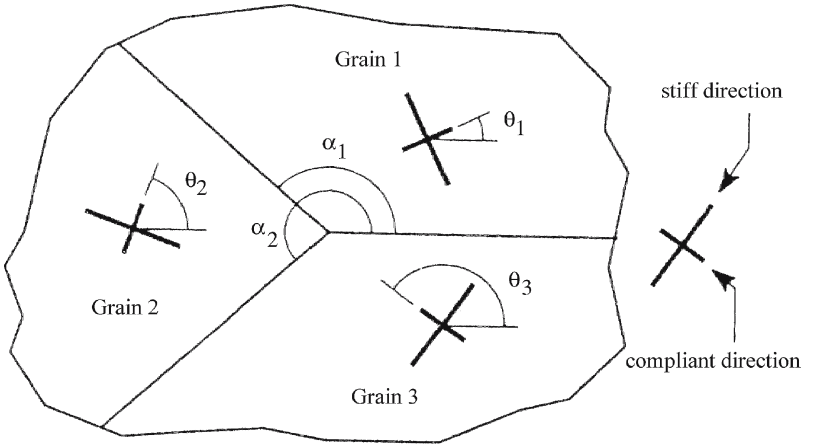

Fig. 1.5. Geometry used for the calculation of stress singularity due to anisotropic elasticity (Frost 2001)

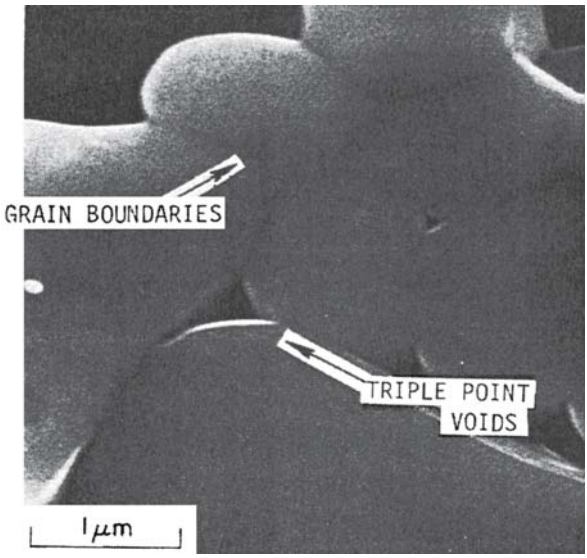

Fig. 1.6.
A scanning electron micrograph of a typical triple point void in sintered Al_2O_3 (Evans 1978)

Each crystalline grain of an anisotropic solid has a "stiff" elastic direction and a "compliant" direction, i.e., the strain in the first direction is smaller than the one in the second direction for the same applied stress. When adjacent to each other, grains can have several orientation angles. Consider Fig. 1.5, which shows a rather simple geometry, in a 2D situation. Even here there are several (five) orientations: α_1, α_2 (here 120° and 240°, respectively) specifying the relative orientations of the grain boundaries and three θ measuring the angles of the stiff directions in each grain. Picu and Gupta (1996) calculated the stress singularity, which arises in such a geometry, in polar coordinates (r, θ) around the triple point (Fig. 1.6):

$$\sigma_{ij}(r,\theta) = kr^{\gamma}\phi_{ij}(\theta) \tag{1.23}$$

where k is a constant, γ is an exponent defining the stress singularity and $\phi_{ij}(\theta)$ is a function of θ only with no singularities. The value of γ is crucial for nucleation. In order to achieve stress concentration, γ has to be negative (in which case there exists a real σ singularity, i.e., $\sigma \to \infty$ for $r \to 0$), and for *crack nucleation* to occur, γ has to be less than –0.3 (Frost and Gupta 1993), since only then a σ singularity that is sufficiently high to overcome atomic cohesion extends beyond atomic dimensions. Picu and Gupta (1996) considered random orientations of the crystal axes for the 120–240° triple junctions and for other symmetric ($\theta_1 = -\theta_3$) situations. Specific problems should be checked there. For example, for ice they have shown that no crack nucleation can occur from elastic anisotropy.

1.2.2.2
Thermal Expansion Mismatch or Anisotropy (Evans 1978)

Evans (1978) calculated the stress concentration, which occurs in polycrystalline (grainy) solids due to the thermal expansion anisotropy. As for the elastic anisotropy case (Sect. 1.2.2.1), thermal expansion singularities were found at grain corners (triple points; Fig. 1.6) and were shown to decrease rapidly with distance from these corners. The maximum stress concentration for defects located on grain boundaries was again found for those defects residing at the triple points. Grain arrays were shown (Fig. 1.7)

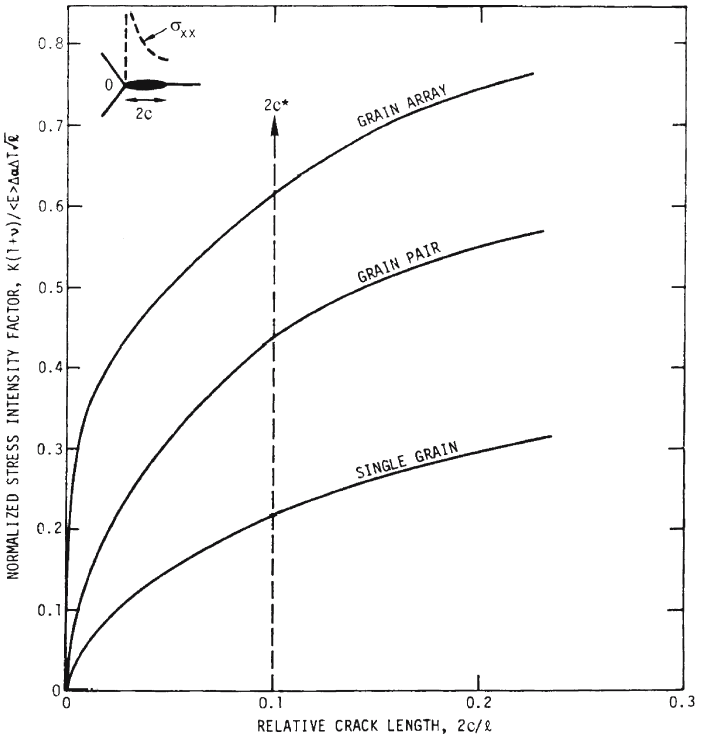

Fig. 1.7. The normalized stress intensity factor plotted as a function of relative crack length for regular hexagonal grains; the single grain solution, as well as the solutions for a grain pair and a grain array are shown (Evans 1978)

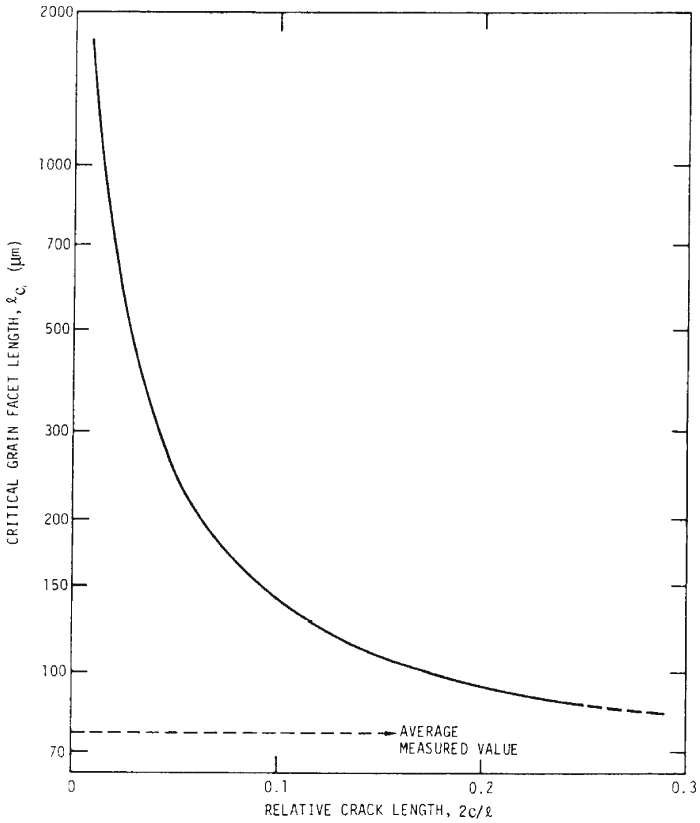

Fig. 1.8. The variation of the predicted critical facet length with the triple point defect size for Al_2O_3. Also shown is the average value obtained experimentally (Evans 1978)

to magnify the stress intensity factor (see Sect. 1.3.3) over that of a single grain by up to ~4. "The incidence of microfracture will thus be strongly dependent on the relative orientation of neighboring grains" (Evans 1978). Stress intensity factor values are crucially dependent on the ratio between the defect (flaw) size (which Evans transforms to an equivalent crack size; Evans 1974) to the size of the grain. Results also yield a critical grain size (facet length) l_c, for inducing microfracture (Fig. 1.8).

1.2.3 Thermal Nucleation

1.2.3.1 *Thermal Fluctuations and Arrhenius Process*

In many areas of physics and chemistry, the probability of crossing an energy barrier is encountered. The theory is usually named after Arrhenius or also by the name "reaction rate". For a theory based on the Fokker-Planck equation, see e.g., Gardiner (1990). A naïve explanation of this approach is as follows. We are dealing with a system (A) that

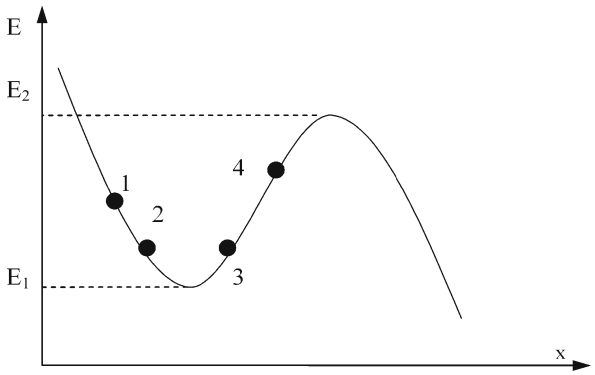

Fig. 1.9.
A schematic "barrier passing". The energy of the system is shown as a function of a parameter x (which can represent different variables, e.g., crack length, stress, strain etc.); x is often called the "reaction parameter"

resides in an equilibrium (minimum energy) situation (Fig. 1.9), at a certain "initial" energy level E_1 and interacts with a big system (such as the atmosphere) called a "thermal bath", which keeps the temperature of A constant. Due to the heat exchange with the bath, the system A constantly changes its energy level around E_1 (say by moving along positions 1, 2, 3, 4, etc.). These changes are called "thermal fluctuations". Now suppose that A has a second equilibrium energy state E_2 ($>E_1$). Note that E_2 of Fig. 1.9 is *not* an equilibrium point, since it is not an energy minimum. If we now start with a large number (an ensemble) of identical systems, each having two energy levels E_1 and E_2, the thermal fluctuations will establish a steady state whereby the ratio of the number of systems residing in E_2 to the number of systems residing in E_1 equals $\exp\{-(E_2 - E_1)/(\mathrm{k}T)\}$, where k is a universal (Boltzmann) constant. This situation is called Maxwell's distribution. On this basis, we assume (to get the Arrhenius process) that the probability of a single system (such as that depicted in Fig. 1.9), having only one equilibrium energy level, E_1, and being in contact with a heat bath that keeps it at a constant temperature T, to reach a higher energy level E_2 ($>E_1$), is proportional to $\exp\{-(E_2 - E_1)/(\mathrm{k}T)\}$. This is evidently an approximation, since E_2 is not an equilibrium state. Thus, according to this theory, the probability of a system overcoming an energy "barrier" of $\Delta E = E_2 - E_1$ (Fig. 1.9), per unit time is

$$\nu = \nu_0 \exp\left(-\frac{\Delta E}{\mathrm{k}T}\right) \tag{1.24}$$

where ν_0 is a "normalization" factor and $\Delta E = E_2 - E_1$. In a more generalized case where pressure or volume changes can occur during the process, ΔE would be replaced by the enthalpy difference of the system between the two states.

1.2.3.2
Fracture and Microfracture Nucleation

Figure 2.1 depicts the pattern observed on a fractured glass sample. Here we relate only to the two smallest forms, i.e., c_i and c_cr. The former is created by the *initial* flaw (or actually the microcrack developed from it), while the latter, c_cr, is the critical fracture length wherefrom the crack starts to propagate (above which the Griffith criterion holds). For a physical understanding consider (Fig. 1.10) the total energy of the system as a function of crack length, c. See also Sect. 2.2.2.1 for characteristic lengths of c_i and c_cr.

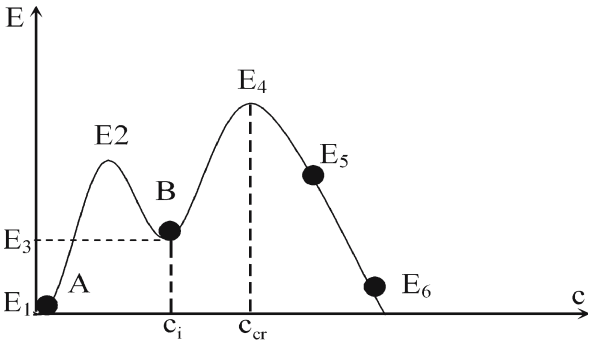

Fig. 1.10.
A schematic representation of the difference between "microfracture nucleation" ($E_1 \rightarrow E_3$ via E_2) and "fracture nucleation" ($E_1 \rightarrow E_4 \rightarrow E_5, E_6$ or $E_3 \rightarrow E_4 \rightarrow E_5, E_6$). *A:* System with no flaws (no microfractures); *B:* System with flaws

As discussed above (Sect. 1.2.1), the term "nucleation" can be used for "microfracture nucleation", i.e., nucleation of a microfracture c_i (around a void, an inclusion or even a small existing microfracture), whose length is smaller than c_{cr}; and it can be used for "fracture nucleation", namely the appearance of the critical crack c_{cr} that causes material failure. While both of these "nucleations" usually proceed in the same manner, i.e., by thermal fluctuations, there is a major difference in their final stability. Microfractures, once nucleated, can remain stable (and do not heal) because they reach a stable or quasi-stable equilibrium, i.e., an energy minimum (or a local minimum) in which the system resides (such as E_3, Fig. 1.10). To remove it from this equilibrium position back to E_1 (to heal the flaw), an energy barrier ($E_2 - E_3$) has to be overcome. In order to have nucleated this flaw, from the equilibrium position E_1, the thermal fluctuations should obviously have taken the system over the barrier $E_2 - E_1$ (and would eventually transfer the system from E_1 to E_3). On the other hand, "crack nucleation" would bring the system from E_1 (if no flaws exist) or from E_3 (in a system with a microcrack) to E_4. Then the system ceases to be stable. It reaches in fact the Griffith criterion, which means that the crack starts propagating indefinitely, thus gaining energy from the field (going to E_5, E_6, etc).

We shall describe only the second procedure, namely the nucleation of a crack leading to eventual rupture. The procedure of "microcrack nucleation" is principally similar. For microcrack nucleation, however, the derivation of the energy barrier ($E_2 - E_1$) from the physical situation is of course different from the one we show here and depends on the existing flaw (see Sect. 1.2.2).

1.2.3.3
Single versus Multiple Crack Nucleation

Two scenarios are conceived in the literature for the fracture process of brittle materials. The first consists of a nucleation and growth of a single critical crack that after reaching the Griffith criterion totally breaks the material. If the rate of stress increase when loading the material is high enough and a critical crack or an effective critical flaw already exists there, then the nucleation part becomes very short. The second scenario (e.g., Spyropoulos et al. 2002), which is assumed to hold in "grainy" materials, i.e., groups 2 and 3 heterogeneous materials (Sect. 1.2.1) and below the critical stress, comprises three to four stages:

1. Nucleation of "many" microcracks under the combined effects of the existing stress and thermal fluctuations.
2. Initial growth of such microcracks.
3. Coalescence of the microcracks into macrocracks.
4. Rupture of the material. In this section we treat the thermal nucleation process, which is related to the first scenario and also briefly the "fiber bundle" model for grainy materials. Other models such as percolation (Hermann and Roux 1990) and self-organized criticality (P. Bak et al. 1987, 1988) will not be touched upon. The models chosen here were those which (recently) have been shown to agree with experiments.

1.2.3.4 *Thermal Crack Nucleation*

For many years, the time to failure of a material under a constant remote stress, σ_0, below that which would cause immediate fracture (Griffith) was calculated by the Zhurkov (1965) or the Mogi (1962) assumption

$$\tau = \tau_0 \mathrm{e}^{-\mathrm{b}\sigma_0}$$

where τ_0 and b are constants. Careful measurements (see below) by Ciliberto and his collaborators have shown that this was not the correct $\tau(\sigma_0)$ relation.

We shall follow an adapted version of the model proposed by Pomeau (1992) for fracture of two- and three-dimensional solids. A similar model was proposed by Golubovic and Feng (1991), and was extended to fractal dimensions by Bonn et al. (1998), who carried out an experiment on polymer gels to verify their theory.

Crack nucleation in 2D and 3D (no flaws – homogeneous nucleation). Nucleation of a critical crack for a material under a constant remote stress, σ_0, i.e., the probability of the appearance of a crack large enough as to fulfill the Griffith criterion, is accomplished by thermal fluctuations, via an Arrhenius-type process (Sect. 1.2.3.1). Assuming there are no initial flaws in the material, the rate of appearance of a critical crack is given by (Pomeau 1992)

$$\nu = \nu_0 \exp\left(-\frac{W}{\mathrm{k}T}\right) \tag{1.25}$$

where ν_0 is a normalizing rate, k is the Boltzmann constant, T is the absolute temperature and W is the "liberated" enthalpy. Here we assume that volume and pressure are unchanged in the process and therefore W becomes the energy barrier needed to be overcome by the process. In a method similar to the one described in Sect. 1.1.2, for a 2D solid, the elastic energy that would be liberated by a fracture of length c is (Fig. 1.11):

$$W_1 \cong -\frac{\sigma_0^2}{2E}\pi c^2 b \tag{1.26}$$

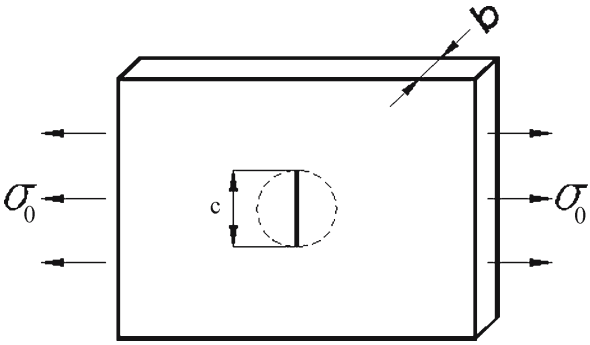

Fig. 1.11.
A schematic "2D" homogeneous nucleation of a crack of length c in an infinite plate under remote tensile stress σ_0

where σ_0 is the remote stress field in the medium, E is the Young modulus and b is the thickness (assumed small with respect to the other dimensions) of the sample. The energy needed to create the two new surfaces is

$$W_2 = 2\Gamma cb \tag{1.27}$$

where Γ is the surface energy. The total energy is therefore

$$W = -\frac{\sigma_0^2}{2E}\pi bc^2 + 2\Gamma bc \tag{1.28}$$

Figure 1.12a depicts W as a function of c. Note that for small c values, W increases linearly with c and then the parabolic part becomes dominant leading to a maximum. This maximum is given by $\partial W / \partial c = 0$, resulting in

$$c_{\max} = \frac{2\Gamma E}{\pi\sigma_0^2}; \qquad W_{\mathrm{m}} = \frac{2\Gamma^2 Eb}{\pi\sigma_0^2} \tag{1.29}$$

Now, if no flaws exist in the material, the critical barrier needed to be overcome by the creation of a critical crack is equal to W_{m}, and hence the rate of nucleation of such flaws is

$$\nu = \nu_0 \exp\left\{-\frac{\sigma_1^2}{\sigma_0^2}\right\} \tag{1.30}$$

where

$$\sigma_1^2 \equiv \frac{2\Gamma^2 Eb}{\pi kT}$$

In three dimensions, the calculation is similar to that appearing in section 1, Eq. 1.23'. The total energy is given (Fig. 1.12b) by

$$W = -\frac{\sigma_0^2}{2E}\frac{4}{3}\pi c^3 + 2\Gamma\pi c^2 \tag{1.31}$$

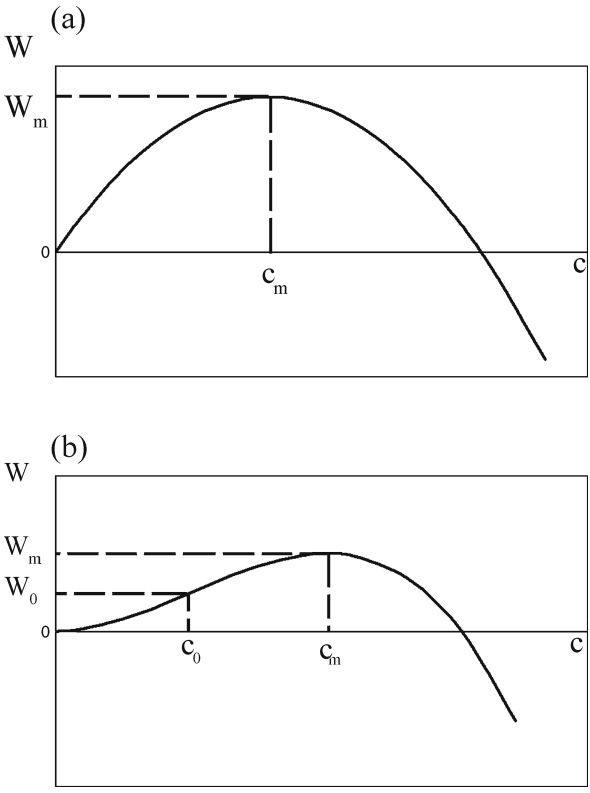

Fig. 1.12.
Total energy (relieved elastic and surface energies) as a function of c. **a** 2D case. **b** 3D case. W_m: Maximum energy occurring at crack length c_m; W_0: Energy for existing crack of length c_0. Note that there should be a dip (energy minimum) at W_0 (not shown)

the maximal energy, which appears for $c_m = 2\Gamma E / \sigma_0^2$, is given by

$$W_m = \frac{8}{3}\pi \frac{\Gamma^3 E^2}{\sigma_0^4} \tag{1.32}$$

and the nucleation rate becomes

$$\nu = \nu_0 \exp\left(-\frac{\sigma_1^4}{\sigma_0^4}\right), \qquad \sigma_1^4 = \frac{8\pi\Gamma^3 E^2}{3kT} \tag{1.33}$$

The way to experimentally verify these results is to measure the time to fracture under a constant stress load that is below the critical stress, i.e., in a creep condition. Thus, in a sequence of papers (Guarino et al. 1999; Scorretti et al. 2001; Ciliberto et al. 2001; Guarino et al. 2002; Politi et al. 2002) Ciliberto and his group performed such measurements on several materials. According to Eq. 1.30 and Eq. 1.33, the times to failure for 2D and 3D materials under a constant σ_0 are given by the reciprocals of the rates, namely,

$$\tau_2 = \tau_{02} \exp\left\{\frac{\sigma_1^2}{\sigma_0^2}\right\} \tag{1.34}$$

and

$$\tau_3 = \tau_{03} \exp\left\{\frac{\sigma_1^4}{\sigma_0^4}\right\} \tag{1.35}$$

respectively. Here τ_{02} and τ_{03} are characteristic times, equal to the $(1/\nu_0)$, for 2D and 3D, respectively. Note that the dependence on σ_0, especially for the 3D case, is very strong: A small change in σ_0 can lead to a large change in τ. Therefore, the measurements must be done very delicately to avoid a situation where the material either breaks immediately or does not break at all (the time to failure is above that of the experiment). Ciliberto's group succeeded in obtaining very accurate measurements and verifying the $\tau(\sigma_0)$ behavior. For example, Fig. 1.13 (adapted from Fig. 4 of Guarino et al. 2002) depicts their results for wood samples (3D). This result, similar results for Perspex by the same group and 2D (Pauchard and Meunier 1993, 1998) and fractal sample (Bonn et al. 1998) time to fracture results, all lead to the same conclusion, namely that the new nucleation theory embodied in Eq. 1.34 and Eq. 1.35 is the correct one. For example, Fig. 1.13 shows the inadequacy of Mogi's (1962) or Zhurkov's (1965) approach and the apparent applicability of Eq. 1.35.

The result of Ciliberto's group did seem to have problems:

1. The distribution of times to failure was not Poissonian as expected.
2. The measured temperature dependence of τ for a linearly increasing load (see below) seemed to yield a temperature of ~3 000 K, while experiments were carried out near room temperature. To explain this discrepancy, they resorted to the "fiber bundle" model (see below), arguing that the spread in fiber strengths could lead to such high effective temperatures.

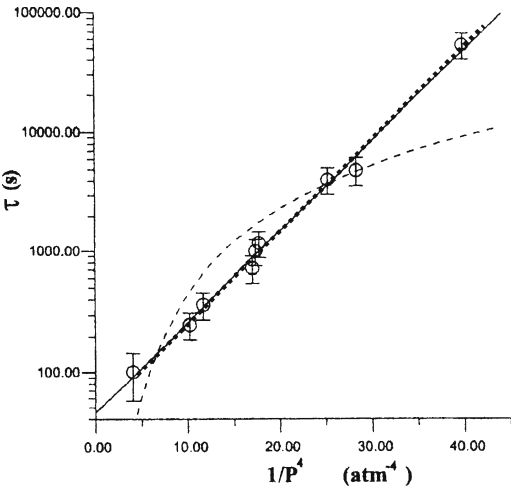

Fig. 1.13. Measurements on wood samples (Guarino et al. 2002). The time τ needed to break the samples under an imposed constant pressure P is here plotted as a function of $1/P^4$ in a semilog scale. The *dashed line* represents the solution proposed by Mogi (1962) ($\tau = ae^{-bP}$). The *continuous line* is the solution proposed by Pomeau for microcrystals ($\tau = \tau_0 \exp[(P_1/P)^4]$, Eq. 1.35 with P instead of σ). In the plot $\tau_0 = 50.5$ s and $P_1 = 0.63$ atm. Every point is the average of ten samples. The *error bar* is the statistical uncertainty. *Dotted line:* Results of our calculation Eq. 1.41 and Eq. 1.42 (with average $c_0 = 1.25 \times 10^{-6}$ cm)

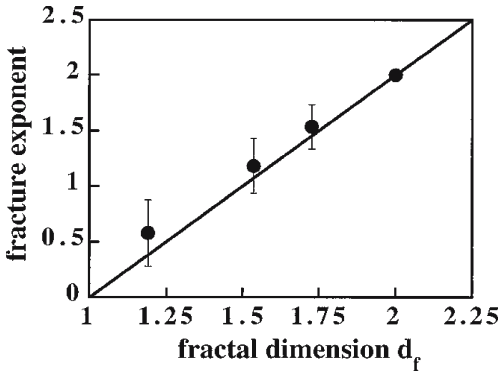

Fig. 1.14.
The absolute value of the measured exponent of activation energy vs. force as a function of the fractal dimension of the gels. The point at $d_f = 2$ is the measurement of Pauchard and Meunier (1993) for a two-dimensional crystal. The line is the prediction from the scaling arguments, Eq. 1.36 (Bonn et al. 1998)

Two-dimensional solids were fractured by Pauchard and Meunier (1993, 1998), and the

$$\exp\left\{\frac{\sigma_1^2}{\sigma_0^2}\right\}$$

relation was shown to hold for the averaged breakage times. As mentioned above, time to failure of polymer gels, whose fractal dimensions were measured by visible light scattering, was measured by Bonn et al. (1998), and the exponent of σ_0 in the delayed time to fracture was shown to agree with these fractal dimensions. Thus, the critical length was predicted to be $c_m = 2(d-1)\Gamma E / d\sigma_0^2$, where d is the fractal dimension of the solid. Hence the energy barrier should be proportional to

$$\frac{\Gamma^d E^{d-1}}{\sigma_0^{2d-2}} \tag{1.36}$$

Figure 1.14 (Fig. 5 of Bonn et al. (1998), adapted) shows the agreement between the (light scattering) measured dimensions, d_f and the dimensions d, obtained from the σ_0 dependence of the delayed times to fracture (derived from Eq. 1.36). These authors also discuss the question of "lattice trapping" (see, e.g., Marder 1996b) and show that the latter cannot be the reason for the delayed fractures since this phenomenon involves delay times that are shorter (or of much lower energy barriers) than those measured.

Thermal nucleation in the presence of flaws (microcracks, heterogeneous nucleation). Thermal nucleation was considered here (Sect. 1.2.3.4) as a process for which the thermal fluctuations were supposed to overcome an energy barrier that started from zero – thus completely disregarding the existing flaw distribution in the material. In this section, we treat nucleation where the stressed sample already contains internal (or surface) flaws, which reduce the energy barrier (Rabinovitch et al. 2004).

The calculation is carried out for the three-dimensional case. Results are easily extended to solids of other dimensions.

It is therefore assumed that at the moment of loading, the sample already possesses a distribution of microcracks each having a different length c_i perpendicular to the

direction of the highest principle stress. Note that a flaw can be looked upon as an "effective microfracture" (Evans 1974) in that the highest stress concentration at a point on its perimeter can be equated to that arising from a 2D microcrack with a (different) effective length. According to Fig. 1.12b, the barrier becomes smaller since the thermal fluctuations need only to augment an existing flaw from c_0, say, to c_m, rather than create a crack of length c_m from the start. The energy barrier now is given by (Fig. 1.12b) $W = W_m - W_0$, where

$$W_0 = -\frac{2}{3}\pi\frac{\sigma_0^2}{E}c_0^3 + 2\pi\Gamma c_0^2 \tag{1.37}$$

The energy barrier, W, is larger than zero for $c_0 < c_m$. The time to fracture under such conditions is therefore

$$\tau = \tau_0 \exp\left[\frac{1}{kT}\left(\frac{\gamma}{\sigma_0^4} + \alpha\sigma_0^2 c_0^3 - \beta c_0^2\right)\right] \tag{1.38}$$

where

$$\alpha = \frac{2\pi}{3E}, \qquad \beta = 2\pi\Gamma \qquad \text{and} \qquad \gamma = \frac{8}{3}\pi\Gamma^3 E^2 \tag{1.39}$$

Clearly, Eq. 1.38 shows that flaws facilitate failure. Thus, denoting by

$$\tau_1 = \tau_0 \exp\left(\frac{\gamma}{\sigma_0^4 kT}\right)$$

(the Pomeau result, Eq. 1.33), Fig. 1.15 depicts the decrease in τ with c_0 ($0 \le c_0 \le c_m$) from τ_1 to τ_0.

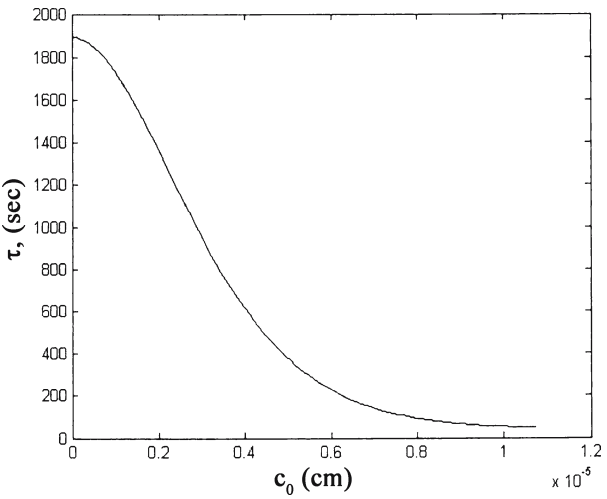

Fig. 1.15.
The lowering of the time to failure for an existing crack of length c_0 in a 3D sample due to the decrease of the energy barrier. The value $c_0 = 0$ is for nucleation where no flaws exist. Here $c_m = 1.3 \times 10^{-5}$ cm, above which $\tau = \tau_0$

Now, the most "important" crack, the one for which the barrier is smallest and hence leads to the shortest time to fracture if augmented, is the crack with the *longest c*. Denoting the length of this crack by c_0, Eq. 1.37 and Eq. 1.38 provide the lowest energy barrier and the shortest (hence the measured) time to failure, respectively.

According to the statistics of extreme values (e.g., Castillo 1988; Kotz and Nadarajah 2000) the longest cracks can have only one of three distributions, Gumbel, Frechet or Weibull. Since the "basin of attraction" of the Gumbel distribution includes the exponential and the Gaussian ones, both of which serve as possible distributions of flaws (Lawn 1993), it is conceivable that the longest flaws here assume the Gumbel distribution. The probability density function of c_0 is therefore assumed (Kotz and Nadarajah 2000) to be

$$p(c_0) = \frac{1}{l}\exp\left(-\frac{c_0 - m}{l}\right)\exp\left(-\mathrm{e}^{-(c_0-m)/l}\right) \tag{1.40}$$

where l and m are parameters.

The following procedure was adopted. For specific chosen values of l and m, a c_0 value is chosen randomly from the $p(c_0)$ distribution. The τ for this c_0 is calculated by Eq. 1.38 for a definite remote stress σ_0 and temperature T. Note that the choice mechanism can generate c_0 values that are already above the Griffith criterion. For these cases, τ is chosen to be τ_0 (see Fig. 1.15). In this way, a histogram of τ for these values of σ_0 and T is obtained, from which the average, $\overline{\tau}$, of τ under these conditions is calculated. Changing σ_0 for the same T, these averages are drawn as a function of σ_0, $\overline{\tau}(\sigma_0)$. This procedure is repeated for different l and m values until the $\overline{\tau}(\sigma_0)$ agrees with the experimental results, at which point the values of l and m are considered to be the correct ones for the flaw distribution. Results are shown in Fig. 1.13 (*dotted line*). It is seen that although $\ln(\tau)$ of Eq. 1.38 is no longer directly proportional to $1/\sigma_0^4$, the changes are minimal and the agreement with experiment is good.

A straightforward understanding of the situation can be obtained by considering $\ln(\tau)$ as a function of $x = 1/\sigma_0^4$. By Eq. 1.38, we obtain

$$\ln\tau = \eta + \frac{1}{\mathrm{k}T}\left(\gamma x + \frac{\alpha c_0^3}{\sqrt{x}}\right) \tag{1.41}$$

where

$$\eta = \tau_0 \exp\left(\frac{-\beta c_0^2}{\mathrm{k}T}\right)$$

Hence $\ln(\tau)$ has a minimum at

$$x_1 = \frac{1}{\tilde{\sigma}^4} = \left(\frac{\alpha}{2\gamma}\right)^{2/3} c_0^2 \tag{1.42}$$

below which it diverges. Therefore, if the stress values used in the experiment are much smaller than $\tilde{\sigma}$, then $\ln(\tau)$ would still follow an almost straight line. For Fig. 1.13, the largest experimental σ or (P) is ~0.7 atm, while for our simulations $\bar{c}_0 = 1.2 \times 10^{-6}$ cm and therefore $\tilde{\sigma} \approx 3.5$ atm.

A second experiment, analyzed, e.g., in Guarino et al. (2002) is where a load, which is linearly increasing with time ($\sigma_0 = A_p t$ for a constant A_p), is applied to different samples until they fail. The breaking times are drawn as a function of A_p in a log-log plot yielding a straight line. In the experiment (Guarino et al. 2002) two temperature values were used, 300 K and 380 K, with almost no difference in the obtained straight lines. On the basis of this invariance, the investigators concluded that there was something amiss and invoked (Politi et al. 2002) fiber bundle theory to explain this apparent difficulty.

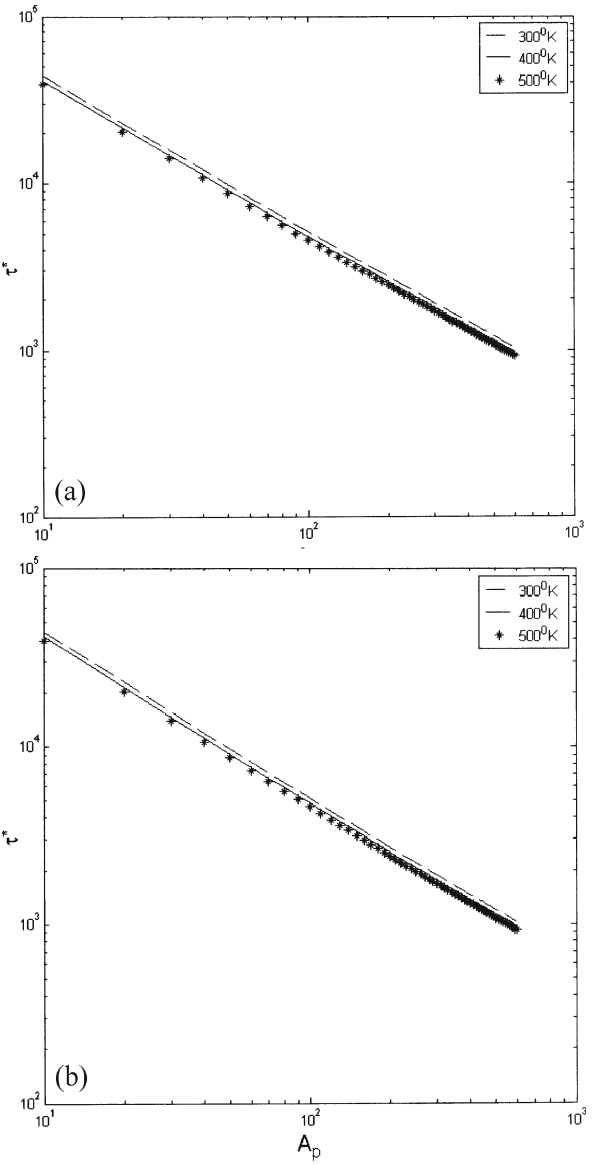

Fig. 1.16.
Time to failure for a linearly increasing stress as a function of stress rate A_p. **a** For $c_0 = 0$ simulating Guarino et al. (2002) results. **b** Averaged times for c_0 chosen according to Eq. 1.40

The difficulty is however only a sham difficulty as can be seen from the following "numerical experiment". First we follow the method used by these authors (Guarino et al. 2002) to treat breaking time problems where the stress changes with time. We regard (Guarino et al. 2002) the variable $1/\tau$ (either of Eq. 1.35 for "no flaw" or of Eq. 1.38 for nucleation under existing flaw distribution) as the "density of damage" per unit time. Breaking is certain to occur after a time τ_1 if

$$\int_0^{\tau_1} \frac{1}{\tau(t)} \mathrm{d}t = 1 \tag{1.43}$$

We now apply Eq. 1.43 to find τ_1 numerically by integrating Eq. 1.35 with $\sigma_0 = A_p t$, or perform a similar calculation using Eq. 1.38 with an appropriate choice process (of c_0) as described before. We obtain (Fig. 1.16) that in both cases *results are almost independent of temperature*. The results of Guarino et al. (2002, Fig. 8) are therefore completely natural and in line with both the "no flaw" and nucleation under existing flaw distribution theories.

We turn now to the time distribution function. Experimental results (Guarino et al. 2002, Fig. 6) show a distribution, which is definitely neither Poissonian (which would have been expected from the Arrhenius approach (e.g., Gardiner 1990)) nor Gaussian. Using Eq. 1.38 and choosing c_0 values randomly according to Eq. 1.39, a series of τ values is thereby generated. In this way, we calculated τ-distribution functions for several temperatures. Distribution results are shown in Fig. 1.17 for different values of temperature. It is seen that

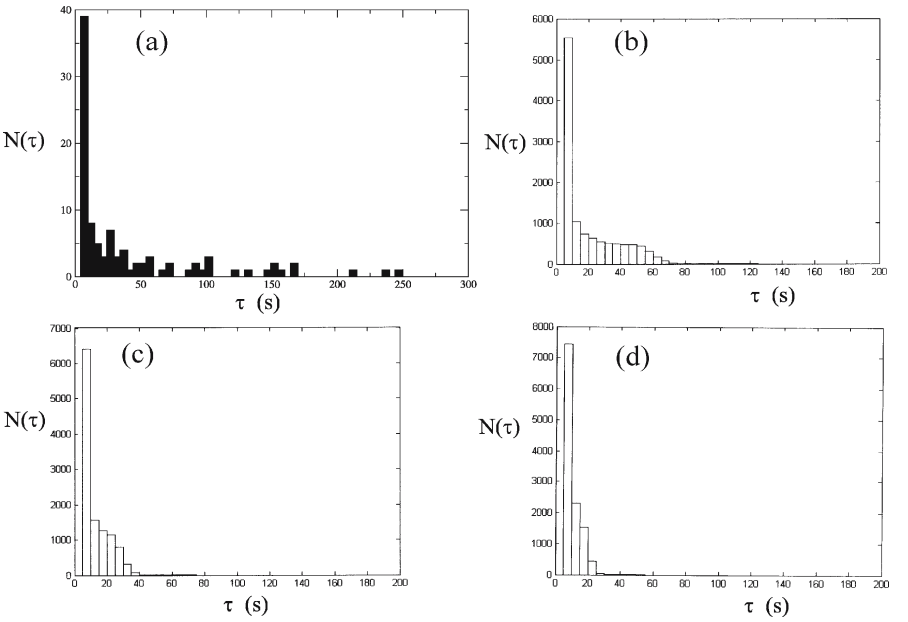

Fig. 1.17. Time distributions for different temperatures. **a** Experimental results (Guarino et al. 2002) $T \approx 300$ K. **b** Results of our calculations (Eqs. 1.38, 1.39 and 1.43) $T = 300$ K. **c** As in **b** but for $T = 400$ K. **d** As in **b** but for $T = 500$ K

1. The distribution function for 300 K is very similar to the experimental results.
2. The change of distribution function with temperature is interesting.

Thus, a relatively small temperature increase causes the "balance" of the distribution to move somewhat towards shorter times, while a large increase (in Fig. 1.17 from 300 K, say, to 500 K) even alters the whole pattern of the distribution, moving it away from a decreasing exponential towards a more "bulky" shape.

It is therefore seen that thermal nucleation is indeed the process behind failure of polycrystalline samples under creep conditions. An improvement of the theory, by the use of nucleation where account is taken of the existing flaw distribution inside the sample, leads

1. To an easier fracture and, more importantly.
2. To an accurate change of lifetime distribution functions with temperature.

1.2.4 Fiber Bundle Model

1.2.4.1 *Introduction*

A brittle heterogeneous solid of the second or third group (Sect. 1.2.1) under an applied stress can break via what we have called the "second scenario" (Sect. 1.2.3.3), namely the appearance of a large number of microcracks. These can either grow or increase in number, leading to their coalescence and eventual failure. In this section, we discuss fiber bundle models which treat the multiple nucleation of microcracks. Such a nucleation is supposed to occur in rock fracture, as is evidenced by the appearance of ever-increasing acoustic emission pulses (see, e.g., Mogi 1962; Hirata et al. 1987; Lockner 1993) and of electromagnetic radiation emissions (see Chap. 5 of this monograph) during such fracture processes. Although the fiber bundle model was developed for and seems most appropriate to describe a solid made up of fibers such as wood or "fibers in matrix" composite materials, it can be shown (Hirata et al. 1987) that results obtained using it agree with "regular" field damage models having nothing whatsoever to do with fibers. The fiber bundle model (FBM) was thus actually used to treat general cases (e.g., Guarino et al. 2002) of fracture. The exact reason for the success of the FBM to describe non-fibrous materials is still unknown. A crude argument might be that most experiments either in tension or compression are conducted under a cylindrical symmetry (uniaxial stress or triaxial stress where the perpendicular axes carry identical loads). For a grainy material, a string of grains parallel to the symmetry axis would constitute a "chain of beads" not unlike a fiber. Moreover, a fracture of a single grain either by a transversal through fracture or a fracture along the grain boundary could be looked upon as a failure of the chain – the fiber.

We shall discuss the FBM only in 1D, namely under the assumption that the lattice-like connection of the fibers is ignored. This restriction is done

1. Since the 1D case can often be analytically or at least asymptotically solved.
2. Since it retains the main features and results of the more complex models.

More realistic models, usually containing entangled numerical calculations, are based on a "chain of bundles" system (see Hidalgo et al. 2002; Gucer and Gurland 1962; Smith and Phoenix 1981; Smith 1982).

Treated here are two cases defined according to how the load is redistributed, following a fiber rupture.

1. The stress is redivided equally among all the remaining fibers (ELS). For this treatment, we will follow mainly the approach of Turcotte et al. (2003).
2. The stress is transferred in decreasing amounts to the "neighbors" of the ruptured fiber (VLS). For this treatment, we will mainly follow the approach of Hidalgo et al. (2002).

Our treatment is meant to be explanatory rather than exhaustive, since other approaches to the unequal redistribution of stress are abundant.

1.2.4.2
Uniform (or Equal) Load Sharing (Turcotte et al. 2003) ELS (Mean-Field Approximation)

Consider (Fig. 1.18) a rod made up of N_0 fibers. Denote by $N(t)$ the number of unbroken fibers at time t. The rate of fibers failure is given by

$$\frac{\mathrm{d}N(t)}{\mathrm{d}t} = -\nu(\sigma_\mathrm{f})N(t) \tag{1.44}$$

where ν is a parameter (called "hazard rate"), which is dependent on the applied fiber stress at time t ("no delay" is usually assumed). If the rod is loaded by a constant force, F_0, the fiber stress in it at time t is

$$\sigma_\mathrm{f}(t) = \frac{F_0}{N(t)s} \tag{1.45}$$

where s is the area of a fiber. This is the uniform load sharing assumption namely that following a failure of a fiber, the load is equally redistributed among the other fibers.

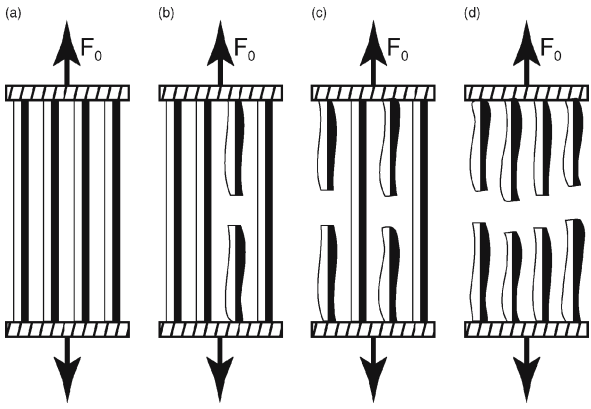

Fig. 1.18. A schematic illustration of the failure of a fiber-bundle with uniform load sharing. **a** Each of the fibers carries one-quarter of the load F_0. **b** One fiber has failed and each remaining fiber carries one-third of the load F_0. **c** Two fibers have failed and each remaining fiber carries one-half of the load F_0. **d** All four fibers have failed and no load is carried (from Turcotte et al. 2003)

In order to complete the presentation of the problem, the functional form of $v(\sigma)$ should be specified. An empirical form for $v(\sigma)$ is

$$v = v_0 \left(\frac{\sigma}{\sigma_0} \right)^{\rho} \tag{1.46}$$

where v_0 is the rate related to the initial stress σ_0 ($= F_0/(N_0 s)$) and ρ is a constant exponent. In order to agree with experimental results, it is shown by Newman and Phoenix (2001) that the range of ρ values is between 2 to 5. Solving Eqs. 1.44–1.46 yields

$$N(t) = N_0 (1 - \rho v_0 t)^{1/\rho} \tag{1.47}$$

The rod fails when $N = 0$. Hence, the time to failure is given by

$$t_f = \frac{1}{\rho v_0} \tag{1.48}$$

Note that this result does not depend on the number of initial fibers but does depend on σ_0. In view of Eq. 1.46, no agreement with Eq. 1.34 or Eq. 1.35 of the thermal nucleation model (Sect. 1.2.3.4) is to be expected. As noted above, Ciliberto et al. (2001) try to build a combined model of thermal nucleation with fiber bundles to explain their experimental results.

A very nice feature of the fiber bundle model is its ability to provide an explanation for the energy emission rate from a fracture either by acoustic emission or by EMR (see Chap. 5). To calculate the rate of say the acoustic emission (ae) in this model, we assume it to be a fraction, η_{ae}, of the total strain energy release rate, $\mathrm{d}W/\mathrm{d}t$:

$$\frac{\mathrm{d}W_{ae}}{\mathrm{d}t} = \eta_{ae} \frac{\mathrm{d}W}{\mathrm{d}t} \tag{1.49}$$

while $\mathrm{d}W/\mathrm{d}t$ is given by

$$\frac{\mathrm{d}W}{\mathrm{d}t} = -w_f \frac{\mathrm{d}N}{\mathrm{d}t} \tag{1.50}$$

where w_f is the stored elastic energy in a fiber at the time of its failure. The latter is evidently given by

$$w_f = \frac{1}{2} \frac{\sigma_{ff}^2}{E} V \tag{1.51}$$

where σ_{ff} is the stress in the fiber at failure, V is the volume of a fiber and E is its Young modulus (assuming they behave elastically until failure). Using Eqs. 1.44–1.51 yields

$$\frac{\mathrm{d}W_{ae}}{\mathrm{d}t} = \eta_{ae} \frac{N_0 V}{2E} v_0 \sigma_0^2 \frac{1}{(1 - t/t_f)^{(\rho+1)/\rho}} \tag{1.52}$$

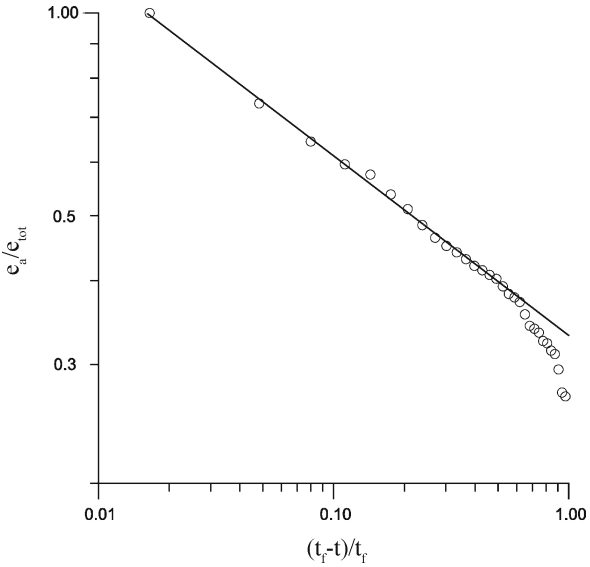

Fig. 1.19.
Cumulative acoustic energy emissions $e_a(t)$ at time t normalized by the total acoustic energy emissions e_{tot} at the time of rupture (t_f) as a function of $1 - t/t_f$. A constant pressure difference was applied at $t = 0$ (Guarino et al. 1999)

A comparison with experiment (e.g., Guarino et al. 2002) of the acoustic energy release as a function of time from failure of chipboard and fiberglass yields an excellent agreement with Eq. 1.52 for $\rho = 3.7$, or $(\rho + 1)/\rho = 0.27$ (Turcotte et al. 2003). Figure 1.19 shows an example of such an agreement for a cumulative acoustic emission as a function of $(1 - t/t_f)$ (Guarino et al. 1998, 1999).

1.2.4.3
Variable Load Sharing (VLS)

The method of stress sharing following a failure of one fiber that is opposite to the one discussed above is called local load sharing (LLS). Already, Coleman (1957) considered the influence of friction among fibers. This friction would tend to concentrate the load in the vicinity of the broken fiber rather than spread it like in the ESL. Here we follow the numerical approach of Hidalgo et al. (2002) (see the list of references there for an accumulation of papers in the area). The model assumes a power law decrease of stress away from the failed fiber. Denoting the stress in fiber i at time t by $\sigma_i(t)$, the additional stress there at time $t + \tau$, $\sigma_i(t + \tau) - \sigma_i(t)$ is obtained by contributions from all failed fibers $B(\tau)$ in the interval τ in the following manner:

$$\sigma_i(t+\tau) - \sigma_i(t) = \sum_{j \in B(\tau)} \sigma_i(t) F(r_{ij}, \gamma) \tag{1.53}$$

where

$$F(r_{ij}, \gamma) = \frac{r_{ij}^{-\gamma}}{\left(\sum_{i \in I} r_{ij}^{-\gamma} \right)} \tag{1.54}$$

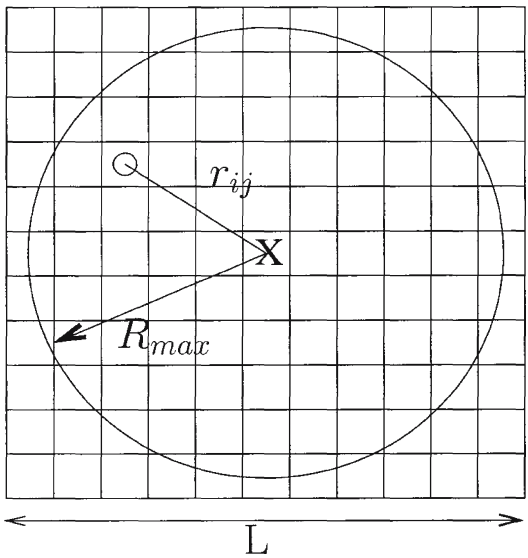

Fig. 1.20.
Illustration of the model construction. X indicates a fiber that is going to break, and ○ is an intact fiber in the square lattice (Hidalgo et al. 2002)

is the normalized contribution fraction from a failed fiber j (at point X in Fig. 1.20) to the fiber i. The sum on i in the normalizing denominator runs over all unfailed fibers at time t, and r_{ij} is the distance from fiber j to fiber i. Hidalgo et al. (2002) have used periodic boundary conditions on an $L \times L$ grid so that the largest value of r used was $(L-1)/\sqrt{2}$. The number of fibers is $N = L^2$. $B(\tau)$, the set of all fibers that break in the increment τ is defined as follows. The system is driven by first applying on it a small value of stress (σ) which is equally distributed among the L^2 fibers. The strengths of the fibers are assumed to be distributed according to a Weibull distribution.

$$P(\sigma_{\text{th}}) = 1 - \exp\left[-\frac{\sigma_{\text{th}}}{\sigma_0}\right]^{\rho} \tag{1.55}$$

where ρ is the so-called Weibull index, which controls the spread in threshold value, and σ_0 is a normalization parameter. Each fiber is ascribed a certain threshold value σ_{th} chosen at random from this distribution. Now the fiber with the lowest value of $(\sigma_{\text{th}} - \sigma/N)$ is sought, and this minimum value is added to all intact fibers. Thus, at least one fiber is going to break and its load is transferred via Eq. 1.53 to the other ones. This may cause more fibers to fail at this stage, defining ultimately the avalanche $B(\tau)$ of all fibers that failed at this stage. When the failures stop, σ is increased again by the same method.

The important parameter is γ (see Eq. 1.53 and Eq. 1.54). It defines the effective range of the influence of one failure. For $\gamma = 0$, the range is infinite and the model is equivalent to the ELS discussed above. For a large γ, this range shrinks and for $\gamma = \infty$ only its nearest neighbors are affected by the failure.

Results of numerical simulations (Monte Carlo type) show some interesting results. Figure 1.21 shows the ultimate strength of the complete bundle as a function of γ for different values of L. Here σ_c is the stress (per fiber) above which all fibers were broken. Three ranges of γ are observed. For $\gamma \leq 2$, the behavior is similar to that of $\gamma = 0$, namely the ELS model. In this range, the ultimate strength depends neither on γ nor on L and can

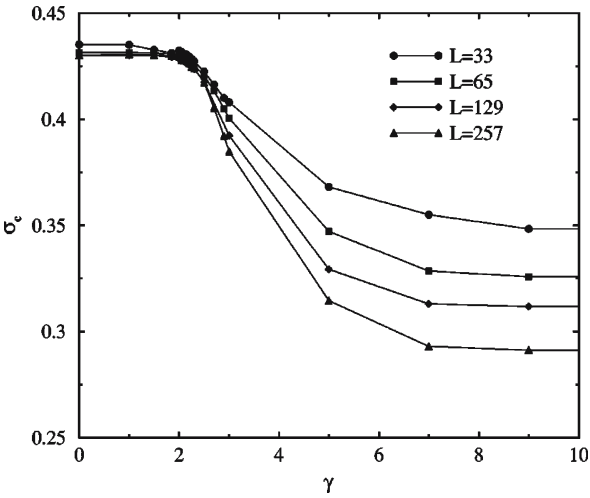

Fig. 1.21.
Ultimate strength of the material for different system sizes as a function of the effective range of interaction γ. A crossover from mean-field to short-range behavior is clearly observed (Hidalgo et al. 2002)

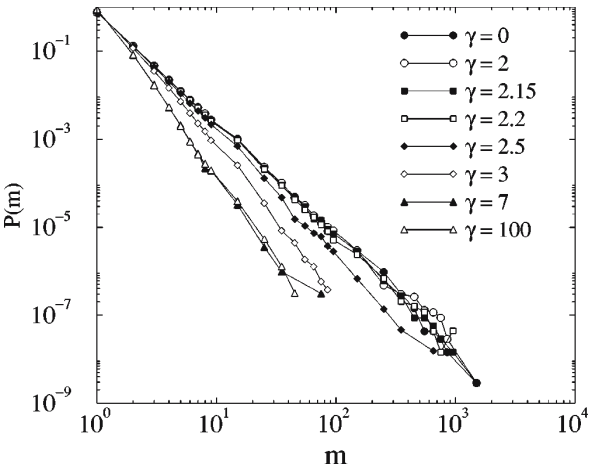

Fig. 1.22.
Avalanche size distributions for different values of the exponent of the stress-transfer function γ ($L = 257$) (Hidalgo et al. 2002)

in fact be calculated exactly. For the Weibull distribution, exact calculation yields $\sigma_c = (\rho e)^{-1/\rho}$. For $\gamma \geq 2$ (local load sharing), σ_c depends on L and, as was shown by Hidalgo et al. (2002), approaches zero for $L \to \infty$ as $\sigma_c(N) \sim 1/\ln N$. This behavior is in line with other short range models (see e.g., Harlow 1985; Kloster et al. 1997). However, for $\gamma \leq 7$, σ_c depends on γ, actually decreasing with increasing γ, while for $\gamma \geq 7$ (extreme local load sharing) σ_c is independent of γ due probably to the discrete nature of the model.

The avalanche size-distribution is shown in Fig. 1.22 for $L = 257$ and different values of γ. For small γ values (mean field approximation or ELS), the distribution can be fitted by a power law.

$$P(m) \sim m^{-5/2} \tag{1.56}$$

A similar result was obtained by exact calculations in this limit (Harlow 1985; Kloster et al. 1997). For a more localized interaction ($\gamma > 2$ say), the causality correlation be-

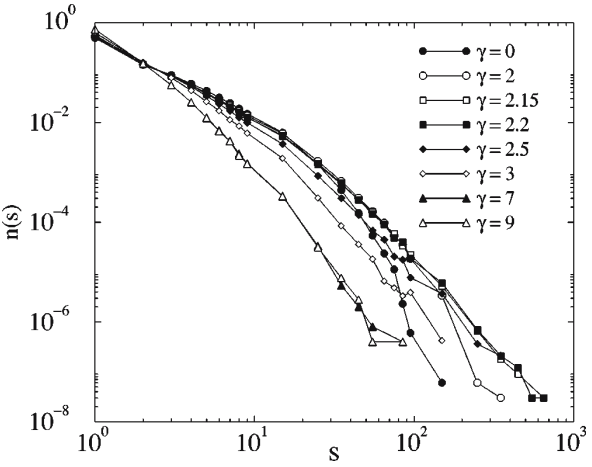

Fig. 1.23.
Cluster size distributions for different values of the stress-transfer function exponent γ. Clearly, two different groups of curves can be distinguished ($L = 257$) (Hidalgo et al. 2002)

tween failing fibers seems to decrease and no relation like Eq. 1.56 can be derived. For small γ values, "any given element could be near to its rupture point regardless of its position in the lattice", while for large γ values "spatial correlation (is) important and concentration of stress take(s) place in the fibers located at the perimeter of an already formed cluster" (Hidalgo et al. 2002) thus reducing the avalanche size.

Figure 1.23 depicts the distribution of cluster sizes, namely the spatially connected (via nearest-neighbors) failed fibers. Shown are clusters just before total failure; the transition from ELS to LLS is obvious. The cluster structure for a complete mean field ($\gamma = 0$) "can be mapped to percolation clusters generated with the probability $0 < P(\sigma_c) < 1$" (*ibid*) except for the exact critical percolation probability, which depends on the Weibull index. For more localized interaction, we approach the "first scenario" (Sect. 1.2.3.3), where a single cluster (crack) is formed leading to complete breakdown. Thus, for large γ values, the total number of clusters decreases.

1.3 Linear Elastic Fracture Mechanics (LEFM)

1.3.1 General

Although the basic physical model (Newton's second law, Hook's law and the boundary conditions which assume that the crack sides are traction free) are simple, the ensuing differential equations (Eq. 1.8–1.16) become mathematically complicated, especially those related to 3D problems. Therefore, most of the theoretical approaches were carried out for 2D problems. Even for 2D, the task of solving these equations is complicated. However, as will be shown, the solution here can be divided into two parts. Firstly, due to the sharpness of the crack tip, the stresses in the immediate neighborhood of the tip turn out to be singular with asymptotic forms (at the tip), which depend only on the mode of loading (of which there are only three; Sect. 1.1.3) and on three related constants (one for each mode). Secondly, the influence of the *external* boundary conditions, i.e., the geometry of the problem and the applied stresses or

strains on the surface of the specimen, is manifested *only* via these constants (called stress intensity factors and denoted by K_I, K_{II} and K_{III}). The energy supplied to the crack tip, which leads to the latter's ability to propagate, is shown to depend only on these stress intensity factors. A balance between this energy and the energy needed to form the new surfaces created by the fracture then yields the extension of the Griffith criterion. Since the surface energy depends on the specific material the specimen is made of, a corresponding material based critical parameter, K_c is defined. Energy balance implies that when K_I say, equals the critical parameter K_{Ic}, fracture becomes possible. Since an absolute majority of fractures actually occur in a mode I situation, the usual result of LEFM is the criterion

$$K_I \geq K_{Ic} \tag{1.57}$$

as a necessary condition of cracking. A second condition, which (together with Eq. 1.57) constitutes a sufficient requirement, is that the equilibrium implied by Eq. 1.21 would not be a stable one (see below). The whole effort of static LEFM is therefore concentrated in calculating K_I for specific geometries and loadings.

1.3.2
Equations of Equilibrium and of Motion

For the sake of completeness, we present here the general equations of motion and equilibrium for a homogeneous solid in the elastic approximation, resulting from Eq. 1.8 in three dimensions. They are written in terms of the displacements **u** in contrast to the presentation in Eqs. 1.8–1.16, which are formulated through stresses (or strains). For actual problems where boundary conditions are usually given in terms of stresses or tractions, the second representation (Eqs. 1.8–1.16) is preferable. Thus, in terms of **u**, the equations become

$$\rho \frac{\partial^2 \mathbf{u}}{\partial t^2} = (\lambda + \mu)\nabla(\nabla \cdot \mathbf{u}) + \mu \nabla^2 \mathbf{u} \qquad \text{(zero body force)} \tag{1.58}$$

or, in terms of the components,

$$\begin{aligned}
\rho \frac{\partial^2 u_x}{\partial t^2} &= (\lambda + \mu)\left[\frac{\partial^2 u_x}{\partial x^2} + \frac{\partial^2 u_y}{\partial x \partial y} + \frac{\partial^2 u_z}{\partial x \partial z}\right] + \mu\left[\frac{\partial^2 u_x}{\partial x^2} + \frac{\partial^2 u_x}{\partial y^2} + \frac{\partial^2 u_x}{\partial z^2}\right] \\
\rho \frac{\partial^2 u_y}{\partial t^2} &= (\lambda + \mu)\left[\frac{\partial^2 u_x}{\partial x \partial y} + \frac{\partial^2 u_y}{\partial y^2} + \frac{\partial^2 u_z}{\partial y \partial z}\right] + \mu\left[\frac{\partial^2 u_y}{\partial x^2} + \frac{\partial^2 u_y}{\partial y^2} + \frac{\partial^2 u_y}{\partial z^2}\right] \\
\rho \frac{\partial^2 u_z}{\partial t^2} &= (\lambda + \mu)\left[\frac{\partial^2 u_x}{\partial x \partial z} + \frac{\partial^2 u_y}{\partial y \partial z} + \frac{\partial^2 u_z}{\partial z^2}\right] + \mu\left[\frac{\partial^2 u_z}{\partial x^2} + \frac{\partial^2 u_z}{\partial y^2} + \frac{\partial^2 u_z}{\partial z^2}\right]
\end{aligned} \tag{1.58'}$$

where ρ is the material density and λ, μ are (see Sect. 1.1.1) the Lamé constants, and it is assumed that body forces are negligible. In the case of equilibrium and static conditions, the left-hand side (or sides) of Eq. 1.58 or 1.58' is zero.

There are several good references in which solutions to Eq. 1.58 are given (e.g., Erdogan 1983; Leibowitz 1968, and see also next section). Several works discuss the steady state solutions while others (see Fineberg and Marder 1999 and references therein) treat the dynamic version. Let us reemphasize that while the steady state (Griffith) results are very useful for basic understanding and for engineering applications, the dynamic solutions are controversial and do not, in general, scrupulously agree with the experimental results (see Sect. 1.4).

Together with Eq. 1.11 and Eq. 1.13, Eq. 1.58 (1.58') constitute a complete set of equations for the linear elastic problem.

1.3.2.1
Antiplane Stress Fracture (Mode III)

A very important 2D case, the equations for which are derived from Eqs. 1.58, is the mode III case. In mathematical terms, this is the simplest case to treat, and can be used as a basis for understanding all types of fracture.

For mode III (see Fig. 1.4), displacements are only in the z-direction; therefore, $u_x = u_y = 0$ and u_z does not depend on z, namely $u_z = u_z(x,y)$. Hence Eqs. 1.58 become

$$\rho \frac{\partial^2 u_z}{\partial t^2} = \mu \left(\frac{\partial^2 u_z}{\partial x^2} + \frac{\partial^2 u_z}{\partial y^2} \right) \tag{1.59}$$

Defining

$$c = \sqrt{\frac{\mu}{\rho}}$$

Eq. 1.59 becomes the so-called "2D wave equation"

$$\frac{1}{c^2} \frac{\partial^2 u_z}{\partial t^2} = \nabla^2 u_z \tag{1.60}$$

where

$$\nabla^2 = \frac{\partial^2}{\partial x^2} + \frac{\partial^2}{\partial y^2}$$

By Eq. 1.11 the only non-zero strain components in this case are

$$\varepsilon_{13} = \frac{1}{2} \frac{\partial u_z}{\partial x} \qquad \text{and} \qquad \varepsilon_{23} = \frac{1}{2} \frac{\partial u_z}{\partial y}$$

leading, by Eq. 1.13, to the only non-zero stress components

$$\sigma_{13} = \mu \frac{\partial u_z}{\partial x} \qquad \text{and} \qquad \sigma_{23} = \mu \frac{\partial u_z}{\partial y}$$

Even in this case, and even for a time-independent solution (where Eq. 1.60 becomes the Laplace equation, $\nabla^2 u_x = 0$), the actual solution may be complicated due to the prevailing boundary conditions.

1.3.3 Two-dimensional (2D) Problems and Stress Intensity Factors

1.3.3.1 *General*

In two dimensions (mode III, Sect. 1.3.2.1, plane stress, plane strain, see above), the equations become much simpler, and it is also easier to understand the problems involved in their solution. We shall treat here only equilibrium problems with no body forces. Extensions to dynamical problems and to problems including body forces can be found in books specializing in those cases (see above and Sect. 1.4). Thus, the 2D equations of equilibrium for stresses in the x- and y-directions stemming from Eq. 1.10 become

$$\begin{cases} \dfrac{\partial \sigma_{xx}}{\partial x} + \dfrac{\partial \sigma_{xy}}{\partial y} = 0 \\ \dfrac{\partial \sigma_{yy}}{\partial y} + \dfrac{\partial \sigma_{xy}}{\partial x} = 0 \end{cases} \tag{1.61}$$

For an elementary derivation of these equations, see e.g., Timoshenko and Goodier (1984) p. 26ff, and for a more mathematical approach see e.g., Landau and Lifshitz (1963) p. 17ff.

It now becomes obvious why the compatibility equations (Eq. 1.16) are needed, since Eq. 1.61 are a set of two equations for three unknowns (σ_{xx}, σ_{yy} and σ_{xy}) and as such are not a complete set. The connections with strains are (Hook's law, Eqs. 1.13 in 2D):

$$\begin{cases} \varepsilon_{xx} = \dfrac{\sigma_{xx} - \nu \sigma_{yy}}{E} \\ \varepsilon_{yy} = \dfrac{\sigma_{yy} - \nu \sigma_{xx}}{E} \\ \varepsilon_{xy} = \dfrac{\sigma_{xy}}{2G} = \dfrac{\sigma_{xy}}{2\mu} \end{cases} \tag{1.62}$$

where $G \equiv \mu$ is the so-called shear modulus. But the three components of strain are obtained from only two displacement components u_x and u_y, which are the basic physical variables (this is actually the reason why Eq. 1.61 consists of only two equations). In 2D, the definition of strains (Eq. 1.11) becomes

$$\varepsilon_{xx} = \frac{\partial u_x}{\partial x}, \qquad \varepsilon_{xy} = \frac{1}{2}\left(\frac{\partial u_x}{\partial y} + \frac{\partial u_y}{\partial x} \right), \qquad \varepsilon_{yy} = \frac{\partial u_y}{\partial y} \tag{1.63}$$

(three components of strain obtained from two displacements). However, Eqs. 1.63 are not independent. For taking the second derivative of the first with respect to *y,* of the second with respect to *x* and *y* and of the third with respect to *x*, we arrive at the "compatibility equations" in 2D

$$\frac{\partial^2 \varepsilon_{xx}}{\partial y^2} + \frac{\partial^2 \varepsilon_{yy}}{\partial x^2} = 2\frac{\partial^2 \varepsilon_{xy}}{\partial x \partial y} \tag{1.64}$$

which can be written (Timoshenko and Goodier 1984) in terms of stresses as

$$\nabla^2(\sigma_x + \sigma_y) = 0 \tag{1.65}$$

where

$$\nabla^2 = \frac{\partial^2}{\partial x^2} + \frac{\partial^2}{\partial y^2}$$

The complete set to be solved for σ is now Eq. 1.61 and Eq. 1.65. We discuss here two types of solutions to this set. One is accomplished by the so-called Airy or stress-function and the second is known as the Westergaard method.

1.3.3.2
Airy-Function (Stress-Function)

A new function Ψ is defined such that the stress components are given by:

$$\sigma_{xx} = \frac{\partial^2 \Psi}{\partial y^2}, \qquad \sigma_{yy} = \frac{\partial^2 \Psi}{\partial x^2}, \qquad \sigma_{xy} = -\frac{\partial^2 \Psi}{\partial x \partial y} \tag{1.66}$$

In this manner, Eqs. 1.61 are immediately fulfilled and in order to fulfill Eq. 1.65, Ψ has to satisfy the following equation:

$$\nabla^4 \Psi = \frac{\partial^4 \Psi}{\partial x^4} + 2\frac{\partial^4 \Psi}{\partial x^2 \partial y^2} + \frac{\partial^4 \Psi}{\partial y^4} = 0 \tag{1.67}$$

To get a solution for a 2D elastic problem, one has to solve Eq. 1.67 with the appropriate boundary conditions. The latter can be given in terms of displacements (u_i), stresses, or tractions (forces, see Eq. 1.7) on the surface of the medium (including the surface of the fracture itself).

1.3.3.3
Westergaard Method (Westergaard 1939)

This method is based on the properties of analytic functions of a complex variable. A variable $z = x + iy$ is defined where x and y are the coordinates of the 2D problem and $i = \sqrt{-1}$. Analytical functions $Z(z)$ are defined as "complex functions of a complex vari-

able which possess a derivative (Z') wherever the function is defined" (Ahlfors 1979). A well-known property of such functions is that their real and imaginary parts are harmonic, i.e., have the properties

$$\frac{\partial \operatorname{Re} Z}{\partial x} = \frac{\partial \operatorname{Im} Z}{\partial y} = \operatorname{Re} Z' , \qquad \frac{\partial \operatorname{Im} Z}{\partial x} = -\frac{\partial \operatorname{Re} Z}{\partial y} = \operatorname{Im} Z' \tag{1.68}$$

and fulfill the Laplace equation

$$\left(\frac{\partial^2}{\partial x^2} + \frac{\partial^2}{\partial y^2}\right)(\operatorname{Re} Z) = \left(\frac{\partial^2}{\partial x^2} + \frac{\partial^2}{\partial y^2}\right)(\operatorname{Im} Z) = 0 \tag{1.69}$$

where ReZ and ImZ are the real and imaginary parts of Z, which can be written as

$$Z = Z(z) = Z(x + iy) = \operatorname{Re} Z + i \operatorname{Im} Z \tag{1.70}$$

Z', $\overline{Z}$ and $\overline{\overline{Z}}$ are defined as the first derivative and the first and second integrals of Z, respectively so that

$$Z' = \frac{\mathrm{d}Z}{\mathrm{d}z} , \qquad Z = \frac{\mathrm{d}\overline{Z}}{\mathrm{d}z} , \qquad \overline{Z} = \frac{\mathrm{d}\overline{\overline{Z}}}{\mathrm{d}z} \tag{1.71}$$

Westergaard then shows that for a restricted group of cases the stress components σ_{ij} can be derived from Z in the form

$$\begin{aligned} \sigma_{xx} &= \operatorname{Re} Z - y \operatorname{Im} Z' \\ \sigma_{yy} &= \operatorname{Re} Z + y \operatorname{Im} Z' \\ \sigma_{xy} &= -y \operatorname{Re} Z' \end{aligned} \tag{1.72}$$

Using Eq. 1.68, it is immediately seen that the stress components defined by Eq. 1.72 fulfill the equilibrium equations (Eq. 1.61) for any analytical function $Z(z)$. The restriction mentioned above is seen from Eqs. 1.72 and amounts to the condition that at $y = 0$, $\sigma_{xx} = \sigma_{yy}$ and $\sigma_{xy} = 0$. The displacements u_x and u_y are given by

$$\begin{aligned} 2\mu u_x &= (1 - 2\nu) \operatorname{Re} \overline{Z} - y \operatorname{Im} Z \\ 2\mu u_y &= 2(1 - \nu) \operatorname{Im} \overline{Z} - y \operatorname{Re} Z \end{aligned} \tag{1.73}$$

where ν is the Poisson ratio, since it can be shown that u_x and u_y of Eq. 1.73 can generate the stress components via Hook's law.

The Westergaard method can be correlated with the Airy or stress function Ψ defined above, for it is easily seen that Ψ can be given by

$$\Psi = \operatorname{Re} \overline{\overline{Z}} + y \operatorname{Im} \overline{Z} \tag{1.74}$$

1.3.3.4
Application to the Internal Crack under Tension

According to Westergaard (1939), if we use for Z the function

$$Z = \frac{\sigma_0}{\sqrt{1 - c^2 / z^2}} \tag{1.75}$$

then Eq. 1.72 and Eq. 1.73 would describe the situation for a crack (of length $2c$) stretching between $x = -c$ and $x = c$ at $y = 0$ in an infinite plane under a remote stress field σ_0 in the y-direction (Fig. 1.24). For $y = 0$ by Eq. 1.72 outside of the crack, the tension is

$$\sigma_{yy} = \frac{\sigma_0}{\sqrt{1 - c^2 / x^2}} \tag{1.76}$$

and inside the length of the crack, by Eq. 1.73, the y displacement is

$$2u_y = \frac{4(1-\nu^2)}{E} \operatorname{Im} \overline{Z} = \frac{4(1-\nu^2)\sigma_0}{E} \sqrt{c^2 - x^2} \tag{1.77}$$

Therefore, the shape of the crack in the vicinity of the tip is parabolic (the complete crack shape is elliptic). At the tips $x = \pm c$, there exists a singularity of σ_{yy}, while u_y is regular.

Irwin (1957) used the solution Eq. 1.75 to calculate the (singular) stress fields near the tip of the crack and to show that these fields can be connected via the energy release rate to the Griffith criterion. Substituting for z near the tip,

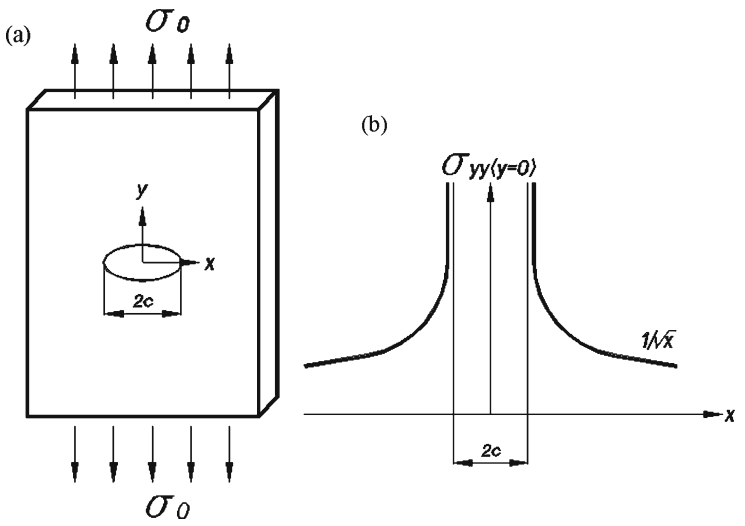

Fig. 1.24. Internal crack (according to Westergaard's paper), which has opened from $z = -c$ to $z = +c$ under the influence of a remote tension σ_0 and the resulting σ_{yy} (at $y = 0$) as a function of x

$$z = c + re^{i\theta} \tag{1.78}$$

where r is the small distance ($r \ll c$) from the tip as an origin

$$r = [(x-c)^2 + y^2]^{1/2} \tag{1.79}$$

and θ is the polar angle, again with the tip as an origin

$$\theta = \arctan\frac{y}{x-c} \tag{1.80}$$

the solution of Eq. 1.75 can be developed in powers of $(r/c)^{1/2}$. The first and dominant term for small r becomes (Irwin 1957)

$$\begin{aligned}\sigma_{xx} &= \frac{K_\mathrm{I}}{\sqrt{2\pi r}}\cos\frac{\theta}{2}\left(1+\sin\frac{\theta}{2}\sin\frac{3\theta}{2}\right)\\ \sigma_{yy} &= \frac{K_\mathrm{I}}{\sqrt{2\pi r}}\cos\frac{\theta}{2}\left(1-\sin\frac{\theta}{2}\sin\frac{3\theta}{2}\right)\end{aligned} \qquad \text{mode I} \tag{1.81}$$

and (see e.g., Lawn 1993)

$$\sigma_{xy} = \frac{K_\mathrm{I}}{\sqrt{2\pi r}}\sin\frac{\theta}{2}\cos\frac{\theta}{2}\cos\frac{3\theta}{2}$$

where $K_\mathrm{I}\,(=\sigma_0\sqrt{\pi c})$ is independent of r and θ and is discussed presently. For mode II, similar calculations lead to a similar result:

$$\begin{aligned}\sigma_{xx} &= -\frac{K_\mathrm{II}}{\sqrt{2\pi r}}\sin\frac{\theta}{2}\left(2+\cos\frac{\theta}{2}\cos\frac{3\theta}{2}\right)\\ \sigma_{yy} &= \frac{K_\mathrm{II}}{\sqrt{2\pi r}}\sin\frac{\theta}{2}\cos\frac{\theta}{2}\cos\frac{3\theta}{2}\\ \sigma_{xy} &= \frac{K_\mathrm{II}}{\sqrt{2\pi r}}\cos\frac{\theta}{2}\left(1-\sin\frac{\theta}{2}\sin\frac{3\theta}{2}\right)\end{aligned} \qquad \text{mode II} \tag{1.82}$$

and for completeness, the mode III result is obtained from Eq. 1.59 above, with the left side equaling zero:

$$\begin{aligned}\sigma_{xx} &= \sigma_{yy} = 0\\ \sigma_{xz} &= -\frac{K_\mathrm{III}}{\sqrt{2\pi r}}\sin\frac{\theta}{2}\\ \sigma_{yz} &= \frac{K_\mathrm{III}}{\sqrt{2\pi r}}\cos\frac{\theta}{2}\end{aligned} \qquad \text{mode III} \tag{1.83}$$

A more elaborate approach for the stress field near the tip of the crack was undertaken by Williams (1957). In his method, the stresses are directly expanded in a series. The leading term agrees with the Westergaard-Irwin results (Eq. 1.81). The other terms in σ come in powers of $r^{1/2}$; thus, the next two terms are a constant (r^0) and a term proportional to $r^{1/2}$. These terms and especially the sign of the constant term are sometimes used for a more elaborate criterion for crack propagation (e.g., Cotterell and Rice 1980).

1.3.3.5
Connection between the Stress Intensity Factors K_I (K_{II}, K_{III}) and the Energy Release Rate

Figure 1.25 shows the (elliptic) crack shape (Eq. 1.77) at its tip (to where the origin of the x-y-coordinate system has been transferred). Irwin (1957) then calculates the energy needed to drive the crack forward, assuming that it can be calculated from the crack vicinity. More comprehensive energy calculations where the energy of the whole medium is accounted for can be found, e.g., in Freund (1972a,b, 1973, 1974). For the static case, however, the outcome of these calculations yields essentially the same results as Irwin's.

Thus, according to Irwin (1957), suppose the crack had moved by a small increment α (see Fig. 1.25). The energy needed to perform this extension is equal to the work needed to close it down, since the theory is linear. Now, the force (per unit area) on the "bulge" for $\theta \cong 0$ and $0 \le x \le \alpha$, $\alpha \ll c$ is, by Eq. 1.81, approximately

$$f = \frac{K_I}{\sqrt{\pi}} \frac{1}{\sqrt{2x}} \beta = \beta f_1(x) \tag{1.84}$$

where β measures the "closure fraction" changing from 0 at the beginning of closure to 1 (end of closure). The y extension u_y for $0 \le x \le \alpha \ll c$ is given by Eq. 1.77 approximately as

$$u_y = \frac{4K_I}{E\sqrt{\pi}} \sqrt{2(\alpha - x)}(1 - \beta) = (1 - \beta) u_y(x) \tag{1.85}$$

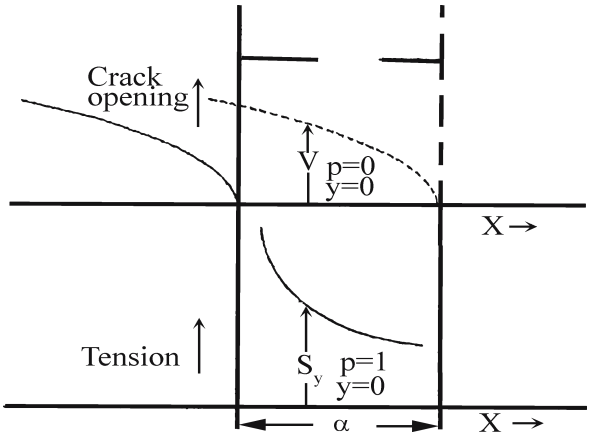

Fig. 1.25.
Irwin's (1957) linear-elastic theory crack opening and stresses near the tip of the crack

The work of closure is therefore

$$W = \int f \, \mathrm{d}u_y = \int_0^1 \beta \mathrm{d}\beta \int_0^\alpha f_1(x) u_y(x) \mathrm{d}x = \frac{2K_\mathrm{I}^2}{E\pi} \int_0^\alpha \left(\frac{\alpha - x}{x} \right)^{1/2} \mathrm{d}x = \frac{\alpha K_\mathrm{I}^2}{E} \tag{1.86}$$

and per unit crack extension, namely the energy release rate is

$$\frac{W}{\alpha} = G = \frac{K_\mathrm{I}^2}{E} \tag{1.87}$$

As stated above, this is a simple mathematical method to obtain the energy derivative with respect to crack length (G).

These results (the set of Eqs. 1.75, 1.77, 1.81–1.83 and 1.87) constitute the basis of the LEFM for the treatment of 2D equilibrium problems. Thus, by a connection with Griffith's criterion, the necessary condition for a flaw to increase in length or for a crack to develop is $G > G_\mathrm{c}$ or $K_\mathrm{I} > K_\mathrm{Ic}$. Here, however, we have also obtained a method of calculating G (or K). For a crack of length $2c$ in an infinite medium (Fig. 1.26a), the above results yield (as in Griffith 1920)

$$K_\mathrm{I} = \sigma_0 \sqrt{\pi c} \tag{1.88}$$

For different geometries, in order to calculate K_I say, the elastic equations should be solved only very near the crack's tip. The value of K_I is then obtained by taking the limit of $\sigma_{yy}\sqrt{2\pi r}$ say as $r \to 0$, for $\theta = 0$. Several methods, both analytical and numerical, were developed for the calculation of K (see e.g., Peterson 1974; Pook 2000; Murakami 1987, 1992, 2001). We present here only a few characteristic results of K_I calculations:

1. Many results are written in the form

$$K = q\sigma\sqrt{\pi c} \tag{1.89}$$

where q is a geometric factor and c is a characteristic crack (or flaw) dimension (explained below). For example, for an edge crack (Fig. 1.26b), $q = 1.12$ and

$$K = 1.12\sigma\sqrt{\pi c} \tag{1.90}$$

2. For an elliptical crack in an infinite plate (Fig. 1.26c) under tensile stress perpendicular to the plane of the crack,

$$K = \frac{M}{Q}\sigma\sqrt{\pi c} \tag{1.91}$$

where Q is the elliptic integral of the second kind:

$$Q = \int_0^{\pi/2} (1 - m^2 \sin^2\theta)^{1/2} \mathrm{d}\theta \,, \qquad m = \sqrt{1 - c^2/a^2} \tag{1.92}$$

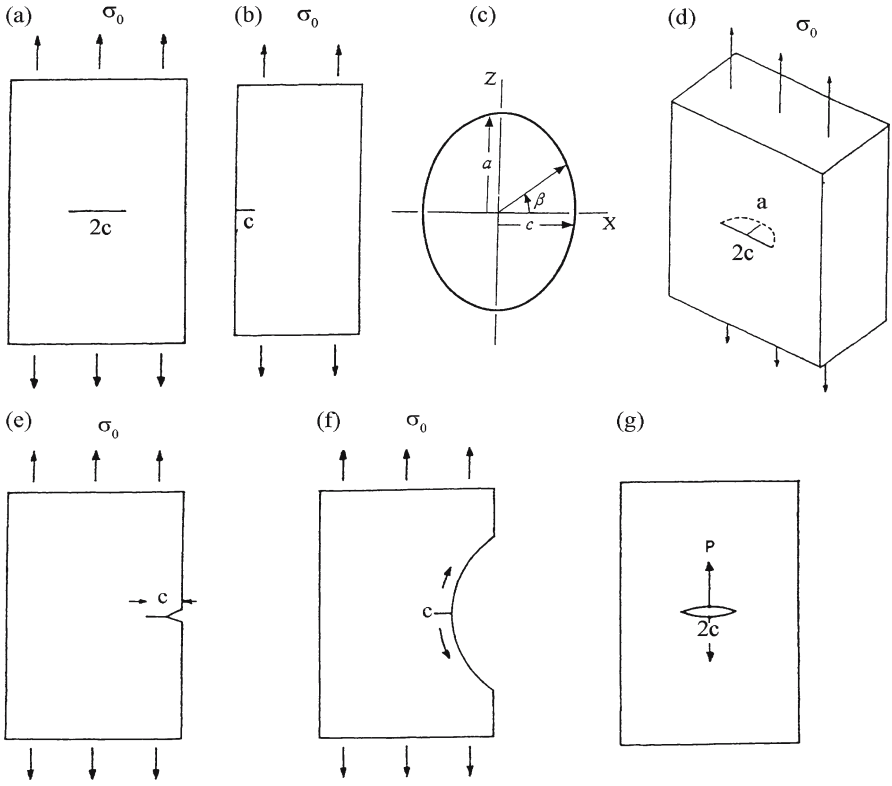

Fig. 1.26. Several cases of K_I values (after Murakami): **a** Internal crack in an infinite plate. **b** Edge crack in an infinite plate. **c** Elliptic crack in the x-z-plane in an infinite body under uniaxial tension σ in the y-direction. **d** Semi elliptical surface crack in a semi infinite body under uniaxial tension σ. **e**, **f** Edge crack in an infinite plate under uniaxial tension: **e** Sharp notch; **f** blunted notch. **g** Two point loads in middle of crack in an infinite plane (Pook 2000)

where a and c are the large and small elliptic radii, and (Rooke and Cartwright 1976)

$$M = [\cos^2\beta + (c/a)^2 \sin^2\beta]^{1/4} \tag{1.93}$$

describes the change of K_I along the ellipse. Note, e.g., that $M = 1$ for $\beta = 0$ (in the direction of c), while $M = \sqrt{c/a}$ (<1) in the direction of a. Here q of Eq. 1.89 is equal to M/Q.

3. For a penny-shaped crack loaded as in No. 2, $a = c$ and

$$K = 2\sigma\sqrt{c/\pi} \tag{1.94}$$

($q = 2/\pi$ in this case).

4. For a semi-elliptic crack at the edge of a semi-infinite plate (Fig. 1.26d) under remote tensile stress,

$$K = 1.12\sigma\frac{\sqrt{\pi\alpha}}{Q} \tag{1.95}$$

and for a semi penny-shaped crack, etc.

$$K = 0.713\sigma\sqrt{\pi c} \tag{1.96}$$

5. The value of c depends on the sharpness of the flaw. For instance, for a sharp groove followed by a crack (Fig. 1.26e), c is the sum of lengths of the groove and the crack, while for a blunt groove (Fig. 1.26f), only the crack length is taken as c.
6. An important case is a crack in an infinite plate operated on by two point loads as in Fig. 1.26g. This case can be used as a basis for K_I calculations using it within a Green's function method, namely considering any load as a superposition of point loads. In this case,

$$K = \frac{P}{b\sqrt{\pi c}} \tag{1.97}$$

where P is the value of the point load and b is the thickness of the plate. Note that here, uncharacteristically, c appears to the power of –½ instead of the usual ½.

1.4 Dynamic Fracture

1.4.1 Mott and Mott-like Approaches

The first attempt to address dynamic fracture was made by Mott (1948). His approach was based only on an energy balance and dimensional considerations. Thus, according to Mott (1948), there are three terms which combine to form the total energy of the system: The kinetic energy T, the liberated elastic (potential) energy U and the dissipative energy S. The only changing variables are the crack length c and its velocity

$$v = \frac{\mathrm{d}c}{\mathrm{d}t} = \dot{c}$$

Therefore by a purely dimensional analysis, the respective energies (for a crack in a slab of constant thickness b under a constant load) should be given by

$$T = \alpha v^2 c^2 b \tag{1.98}$$

$$U = -\beta c^2 b \tag{1.99}$$

$$S = \gamma c b \tag{1.100}$$

where α, β and γ are constants. Note that both T and U are proportional to the volume $c^2 b$ of the material in which elastic energy has been relaxed and which was set in motion by the moving crack with different velocities across it, which are assumed to be proportional to the crack velocity v. The dissipative energy, S, as before, is assumed to be proportional to the newly created area (cb) via a surface energy parameter γ.

The total energy of the system is

$$E_{\text{tot}} = T + P = T + U + S = \alpha v^2 c^2 b - \beta c^2 b + \gamma c b \tag{1.101}$$

where P is the total non-kinetic energy.

Mott then went on to assume that the crack develops under the condition $\partial E_{\text{tot}} / \partial c = 0$, while assuming that $\partial v / \partial c = 0$. This procedure yields

$$v = V\left(1 - \frac{c_0}{c}\right)^{1/2} \tag{1.102}$$

where the final velocity $V = (\beta / \alpha)^{1/2}$, and $c_0 = \gamma / 2\beta$. Since α and β are unknown from first principles, V and c_0 cannot be obtained in this manner from known properties (e.g., sound velocities). But, since for $c = c_0$, $v = 0$, it is assumed that c_0 is the critical microcrack (or effective flaw) length (c_{cr}) (see Sect. 1.2.3.2 and 1.2.3.4). However, a different interpretation of c_0 is presented below in this section.

Mott's assumption that $\partial v / \partial c = 0$ (which is obviously valid only for large values of v approaching the final velocity) has incurred some heavy criticism. Thus, foremost among others, Berry (1960) and Dulaney and Brace (1960) tried to improve on Mott's derivation. To understand their calculations, consider the non-kinetic energy P as a function of c as obtained by Dulaney and Brace (1960) (Fig. 1.27). It is immediately seen that the (static) Griffith criterion for the initiation of a crack, namely $\partial P / \partial c = 0$, occurs at c_0 and that for $c > c_0$ there is an ever-increasing gain of non-kinetic energy for crack elongation. Assuming now that the (dynamic) condition for crack propagation is $E_{\text{tot}} = P_0$, Dulaney and Brace (1960), obtained for the crack velocity

$$v = V\left(1 - \frac{c_0}{c}\right) \tag{1.103}$$

This relation for the crack velocity was deemed to be preferable over Eq. 1.102 (for example Fineberg, Gross, Marder and Swinney (Fineberg et al. 1991) and Marder (1993))

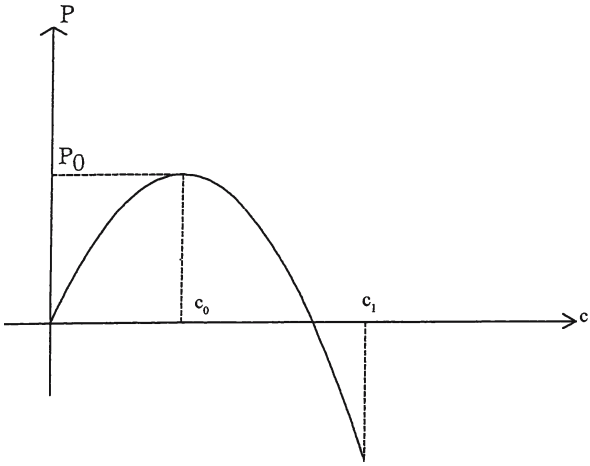

Fig. 1.27. Sum of potential and dissipative energies, P as a function of crack length c; c_0 is the Griffith criterion; c_1 is the beginning of dynamic fracture (Rabinovitch 1994)

although it suffers from two severe drawbacks. Firstly, for velocities that are close to V, even according to Dulaney and Brace (1960), Mott's approximation (Eq. 1.102) should be valid. Secondly, regarding Eq. 1.103 as a differential equation, for $v = \mathrm{d}c/\mathrm{d}t$, it cannot be integrated to obtain $c(t)$ (the improper integral diverges).

We have assumed (Rabinovitch 1994) that the dynamic crack process does not start when the crack length is at c_0. Rather, a delay of fast propagation occurs and the crack's fast movement is initiated only at $c_1 > c_0$. That means that we identify c_0 with c_i (the initial microcrack or effective flaw) and c_1 with c_{cr} (see Sect. 1.2.3.2, 1.2.3.4 and Fig. 2.1). Note however that this assumption entails that for $K_I > K_{Ic}$ ($K_I = K_{Ic}$ occurs at $c_0 = c_i$) the crack propagates with a very low velocity until its length reaches $c_1 = c_{cr}$. While the origin of this delay might be in dispute (for example Schoeck and Pichl 1990; Bernstein and Ness 2003), for our purpose it is the fact that between c_0 and c_1, energy is dissipated into avenues other than the kinetic or potential energies discussed above, which is important. It is therefore assumed that the actual critical length occurs at c_1 ($\geq c_0$), and only for $c > c_1$ can the energy balance à la Mott be performed. Thus, for $c \geq c_1$, the condition E_{tot} = constant with the provision that $v \cong 0$ at $c = c_1$ yields

$$v = V\left(1 - \frac{2c_0}{c} - \frac{k}{c^2}\right)^{1/2} \tag{1.104}$$

where $V = (\beta/\alpha)^{1/2}$, $c_0 = \gamma/2\beta$ as before and

$$k = c_1(c_1 - 2c_0) \tag{1.105}$$

Several points should be noted.

1. Equation 1.104 transfers over to the Mott relation (Eq. 1.102) for large values of c.
2. Very close to c_1, say for $c = c_1 + \varepsilon$ (where ε is a small quantity), the velocity behaves as $\varepsilon^{1/2}$.
3. Equation 1.104 is easily integrated (Gradshteyn and Ryzhik 1980) to yield

$$V(t - t_0) = g(c) + c_0 \ln \frac{g(c) + c - c_0}{c_1 - c_0} \tag{1.106}$$

where $g(c) = (c^2 - 2c_0c + b)^{1/2}$ and t_0 is the time where $c = c_1$. Note that $g(c_1) = 0$ and that, for $t \gg t_0$, $c \approx Vt$.
4. Equation 1.103 is a (non-generic) special case of Eq. 1.104 for $c_1 \to c_0$. In this case, unlike the divergent integral obtained in trying to integrate Eq. 1.103 directly, the limit $c_1 \to c_0$ in Eq. 1.106 is well defined.
5. Since Eq. 1.104 contains three parameters V, c_0 and c_1, which can be adjusted to experimental results, it is not remarkable that such experiments can be approximated quite well by this equation. For example, the results depicted in Fig. 1.31 (see below) by Kobayashi et al. (1974), which were shown by Marder (1993) not to agree with the constant $G(t)$ approach (see below, Sect. 1.4.3), are in a very good agreement with Eq. 1.106 with $V \approx 575$ m s^{-1}, $c_0 \approx 1.33$ cm and $c_1 \approx 3.10$ cm (not shown in Fig. 1.31).

In Sect. 1.4.2 and 1.4.3, we present the linear elastic approach to dynamic fracture.

1.4.2
2D Dynamic Crack

We first consider here the (asymptotic) constant velocity solution. Therefore, starting from Eq. 1.58 we look for solutions that describe crack propagation at a constant velocity of magnitude (v) in the x-direction (Fineberg and Marder 1999, Sect. 2.4). We therefore consider displacements **u,** which have a "wavelike" behavior or, alternatively, where the origin stays at the crack tip, $x = x' - vt$, thus,

$$\frac{\partial}{\partial x'} = \frac{\partial}{\partial x}; \qquad \frac{\partial}{\partial t} = \frac{\partial}{\partial x}\cdot\frac{\partial x}{\partial t} = -v\frac{\partial}{\partial x}; \qquad \frac{\partial^2}{\partial t^2} = v^2\frac{\partial^2}{\partial x^2}$$

and Eq. 1.58 becomes

$$(\lambda+\mu)\nabla(\nabla\cdot\mathbf{u}) + \mu\nabla^2\mathbf{u} = \rho v^2\frac{\partial^2\mathbf{u}}{\partial x^2} \tag{1.107}$$

General solutions can be obtained by defining two auxiliary functions $\Phi(z_\alpha)$ and $\psi(z_\beta)$, where now z_α and z_β depend on the longitudinal and transversal acoustic wave velocities (c_ℓ and c_t respectively, defined in Eq. 1.109)

$$z_\alpha = x + i\alpha y\,, \qquad z_\beta = x + i\beta y \qquad \text{and} \tag{1.108}$$

$$\left.\begin{aligned}\alpha^2 &= 1 - \frac{\rho v^2}{\lambda+2\mu} = 1 - \frac{v^2}{c_\ell^2}\\ \beta^2 &= 1 - \frac{\rho v^2}{\mu} = 1 - \frac{v^2}{c_\mathrm{t}^2}\end{aligned}\right\} \qquad \begin{aligned}c_\ell &= \sqrt{\frac{\lambda+2\mu}{\rho}}\\ c_\mathrm{t} &= \sqrt{\frac{\mu}{\rho}}\end{aligned} \tag{1.109}$$

The displacements are given (as can be checked by inserting Eqs. 1.110 in Eq. 1.107) by

$$\begin{aligned}u_x &= \mathrm{Re}\,\Phi(z_\alpha) - \beta\,\mathrm{Im}\,\psi(z_\beta)\\ u_y &= -\alpha\,\mathrm{Im}\,\Phi(z_\alpha) - \mathrm{Re}\,\psi(z_\beta)\end{aligned} \tag{1.110}$$

The stress fields are given by

$$\begin{aligned}\sigma_{xx} &= \mu(1+2\alpha^2-\beta^2)\,\mathrm{Re}\,\Phi'(z_\alpha) - 2\beta\mu\,\mathrm{Im}\,\psi'(z_\beta)\\ \sigma_{yy} &= -\mu(1+\beta^2)\,\mathrm{Re}\,\Phi'(z_\alpha) + 2\beta\mu\,\mathrm{Im}\,\psi'(z_\beta)\\ \sigma_{xy} &= \mu[2\alpha\,\mathrm{Im}\,\Phi'(z_\alpha) + (\beta^2+1)\,\mathrm{Re}\,\psi'(z_\beta)]\end{aligned} \tag{1.111}$$

where

$$\Phi' = \frac{\partial\Phi(z)}{\partial z} \qquad \text{and} \qquad \psi' = \frac{\mathrm{d}\psi(z)}{\mathrm{d}z}$$

Note that our Φ and ψ are twice the Φ and ψ of Fineberg and Marder (1999).

In order to obtain a solution for a specific problem, "all" that is needed is to find the appropriate Φ and ψ functions. An important example (Fineberg and Marder 1999) is the near-tip behavior of a propagating crack under a mode I loading. Using the static solution (Sect. 1.3.3.4) as a clue and the symmetry properties of the problem, i.e., $u_x(-y) = u_x(y)$ and $u_y(-y) = -u_y(y)$, the appropriate solution is

$$\Phi(z) = \frac{C}{\sqrt{z}}; \qquad \psi(z) = i\frac{D}{\sqrt{z}} \tag{1.112}$$

(where the cuts of the $\sqrt{\ }$ are along the negative x-axis). The boundary condition on the crack surface is that σ_{xy} and σ_{yy} are zero there (relaxed stress). Using these conditions yields

$$\frac{D}{C} = \frac{2\alpha}{\beta^2 + 1} \tag{1.113}$$

As was done for the static case (Sect. 1.3.3.4), near the tip, we can develop the results in powers of $r^{1/2}$, where r is the small distance from the crack tip. We denote

$$\begin{aligned} z_\alpha &= r_\alpha e^{i\theta_\alpha}, \quad \text{so that} \quad r_\alpha = \sqrt{x^2 + \alpha^2 y^2} \quad \text{and} \quad \tan\theta_\alpha = \frac{\alpha y}{x} \\ z_\beta &= r_\beta e^{i\theta_\beta}, \quad \text{so that} \quad r_\beta = \sqrt{x^2 + \beta^2 y^2} \quad \text{and} \quad \tan\theta_\beta = \frac{\beta y}{x} \end{aligned} \tag{1.114}$$

and the leading terms of the stress are again of the order of $r^{-1/2}$. These are (Freund 1990)

$$\begin{aligned} \sigma_{xx} &= \frac{K(t)B}{\sqrt{2\pi r}}\left[-(1 + 2\alpha^2 - \beta^2)\left(\frac{r}{r_\beta}\right)^{1/2}\cos\left(\frac{\theta_\alpha}{2}\right) - \frac{4\alpha\beta}{1+\beta^2}\left(\frac{r}{r_\beta}\right)^{1/2}\cos\left(\frac{\theta_\beta}{2}\right)\right] \\ \sigma_{yy} &= \frac{K(t)B}{\sqrt{2\pi r}}\left[-(1 + \beta^2)\left(\frac{r}{r_\alpha}\right)^{1/2}\cos\left(\frac{\theta_\alpha}{2}\right) + \frac{4\alpha\beta}{1+\beta^2}\left(\frac{r}{r_\beta}\right)^{1/2}\cos\left(\frac{\theta_\beta}{2}\right)\right] \\ \sigma_{xy} &= \frac{2K(t)B\alpha}{\sqrt{2\pi r}}\left[\left(\frac{r}{r_\alpha}\right)^{1/2}\sin\left(\frac{\theta_\alpha}{2}\right) - \left(\frac{r}{r_\beta}\right)^{1/2}\sin\left(\frac{\theta_\beta}{2}\right)\right] \end{aligned} \tag{1.115}$$

where the dynamical stress intensity factor (mode I) is

$$K(t) = \lim_{\substack{x\to 0 \\ y\to 0}} \sqrt{2\pi x}\,\sigma_{yy}(t) \quad \text{and} \tag{1.116}$$

$$B = \frac{1+\beta^2}{4\alpha\beta - (1+\beta^2)^2} \tag{1.117}$$

As is shown presently (Sect. 1.4.3), $K(t)$ is related to the energy flux into the crack tip. Eqations 1.115 can be used to calculate the direction of crack propagation (see e.g., Fineberg and Marder 1999). Alternatively, it can be used (Rabinovitch et al. 1993, see Fig. 2.29) to calculate the direction of secondary cracks that develop ahead of the propagating primary crack. The method used there is as follows. A certain radius $r_0 > 0$ is defined. Eqations 1.115 specify the stress field as a function of $\theta = \text{arctg}(y/x)$. At each θ, the two principal directions and principal stresses (the stress tensor can be digonalized) are calculated. θ_1 is calculated for which the major principal stress σ_1 is maximal and the axis of this principal stress is evaluated. The secondary crack is assumed to originate at (r_0, θ_1) and its direction (α_1) to be perpendicular to the axis thus found. Results (Fig. 1.28) show that both θ_1 and α_1 depend on crack velocity. For low velocities ($v \ll C_\ell$), θ_1 is ~60° and secondary cracks emerge almost parallel to the primary crack, while for higher crack velocities, both θ_1 and α_1 increase in value. The possibility of $\theta_1 > 90°$ is unclear. Experimental results (Rabinovitch et al. 2000a) qualitatively confirm these predictions for low crack velocities.

In addition to Eq. 1.115, the leading terms of the velocity components of the movements near the crack tip are obtained as

$$\frac{\mathrm{d}u_x}{\mathrm{d}t} = \dot{u}_x = -\frac{K(t)Bv}{\sqrt{2\pi r}\mu}\left[\left(\frac{r}{r_\alpha}\right)^{1/2}\cos\left(\frac{\theta_\alpha}{2}\right) - \frac{2\alpha\beta}{1+\beta^2}\left(\frac{r}{r_\beta}\right)^{1/2}\cos\left(\frac{\theta_\beta}{2}\right)\right]$$

$$\frac{\mathrm{d}u_y}{\mathrm{d}t} = \dot{u}_y = -\frac{K(t)Bv}{\sqrt{2\pi r}\mu}\left[\left(\frac{r}{r_\alpha}\right)^{1/2}\sin\left(\frac{\theta_\alpha}{2}\right) - \frac{2}{1+\beta^2}\left(\frac{r}{r_\beta}\right)^{1/2}\sin\left(\frac{\theta_\beta}{2}\right)\right] \tag{1.118}$$

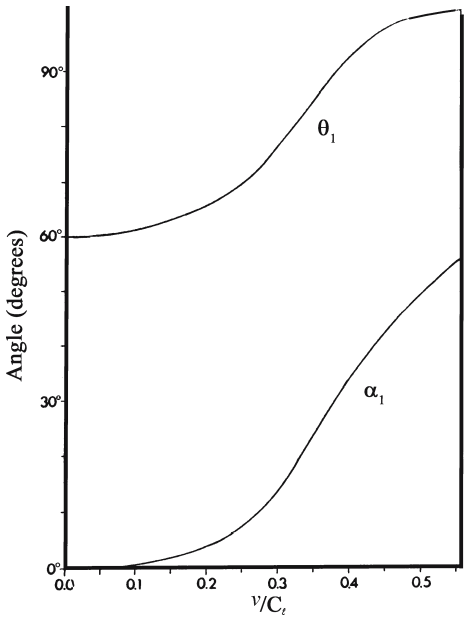

Fig. 1.28.
The angle θ_1 at which σ_1 attains its maximum and the secondary crack direction α_1, vs. normalized crack speed v/C_ℓ (C_ℓ: Longitudinal-wave speed) (Rabinovitch et al. 1993)

Note that unlike the situation in the static case, here $r^{-1/2}$ singularities exist for $\dot{u}_x$ and $\dot{u}_y$ besides those for σ_{ij}. Eqations 1.115 and 1.118 demonstrate that the near-tip LEFM dynamic solutions, like the static case ones, can be divided into two parts: The (r, θ) part that does not and the $K(t)$ part that does depend on the geometry of the sample, the crack length and the remote stresses. It is thus the value of $K(t)$ that should dominate crack extension even for dynamic fracturing.

1.4.3 Energy Calculations

The 3D elastic (potential) energy stored in the sample per unit volume is given by (Eq. 1.5, generalized)

$$e = \frac{1}{2}\sum_{i,j} \varepsilon_{ij}\sigma_{ij} \ , \qquad i,j = 1,2,3 \tag{1.119}$$

In two dimensions, the indices of both ε and σ change only between 1 and 2 (x and y). We denote the indices in the 2D problem by α and β, each of which takes the values 1 and 2. The potential energy (per unit area) in 2D is therefore

$$e = \frac{1}{2}\sum_{\alpha,\beta} \varepsilon_{\alpha\beta}\sigma_{\alpha\beta} \tag{1.120}$$

Using the definition Eq. 1.11 of

$$\varepsilon_{\alpha\beta} \left(= \frac{1}{2}\left(\frac{\partial u_\alpha}{\partial x_\beta} + \frac{\partial y_\beta}{\partial x_a} \right) \right)$$

and the symmetry of σ ($\sigma_{\alpha\beta} = \sigma_{\beta\alpha}$), e can be written as

$$e = \sum_{\alpha,\beta} \frac{\partial u_\alpha}{\partial x_\beta}\sigma_{\alpha\beta} \tag{1.121}$$

The kinetic energy (per unit area in 2D) is given by

$$\tau = \frac{1}{2}\rho\sum_{\alpha}\left(\frac{\mathrm{d}u_\alpha}{\mathrm{d}t}\right)^2 \left(= \frac{1}{2}\rho\left[\left(\frac{\mathrm{d}u_x}{\mathrm{d}t}\right)^2 + \left(\frac{\mathrm{d}u_y}{\mathrm{d}t}\right)^2\right] \right) \tag{1.122}$$

where $\mathrm{d}u_\alpha / \mathrm{d}t$ is the α^{th} component of the velocity and ρ is the material density.

Consider now (e.g., Kanninen and Popelar 1985) the cracked body depicted in Fig. 1.29, where S is its outer boundary on which forces (tractions) $\mathbf{t}$ are applied, $c(t)$ is the crack tip position which changes with time with a velocity $\mathbf{v}$, and Γ^* is a small contour through which the energy flux is delivered to the tip; this Γ^* is eventually reduced to zero, and R is the volume (area in 2D) of the sample.

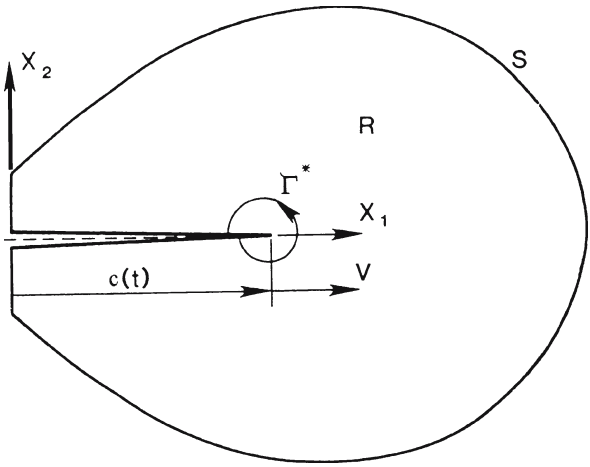

Fig. 1.29.
Dynamic crack propagation in 2D (after Kanninen and Popelar 1985)

Energy balance is enacted as follows. The rate of work, $\dot{P}$, performed by the outer forces (tractions) on S is equal to the rate of the total potential U and kinetic T energy increase in R plus the energy flux Fl into the tip

$$\dot{P} = \dot{U} + \dot{T} + Fl \tag{1.123}$$

where

$$\dot{P} = \int \sum_{\alpha} \dot{u}_{\alpha} t_{\alpha} \mathrm{d}S \tag{1.124}$$

t_α is the α^{th} component of the traction **t**; the total kinetic energy is

$$T = \int \tau \mathrm{d}A = \lim_{\Gamma^* \to 0} \int_R \frac{1}{2} \rho \sum_{\alpha} \left(\frac{\mathrm{d}u_{\alpha}}{\mathrm{d}t} \right)^2 \mathrm{d}A \tag{1.125}$$

and the total potential energy is

$$U = \int e \mathrm{d}A = \lim_{\Gamma^* \to 0} \int_R \sum_{\alpha,\beta} \frac{\partial u_{\alpha}}{\partial x_{\beta}} \sigma_{\alpha\beta} \, \mathrm{d}A \tag{1.126}$$

As always, a dot above a variable means a derivative with respect to time of this variable. We are interested in the flux into the tip, $Fl = \dot{P} - \dot{U} - \dot{T}$. The calculation of the separate terms is quite involved, and only a sketch is given here. A specific complication arises in the calculations due to the fact that the contour Γ^* propagates in time with the crack tip, making R time-dependent. Therefore, for example, $\dot{U}$ includes two terms, one which comes from the rate of change of u_α with time and the other is the contribution from the flux of the density of U through Γ^*.

Consider (Fig. 1.30) a small surface (line in 2D), $\mathrm{d}S = \mathrm{AB}$ which moves with a velocity **v**. All through space (area) there exists a density (an amount per unit volume) of some variable, e.g., energy. In the case of the potential energy, the density is

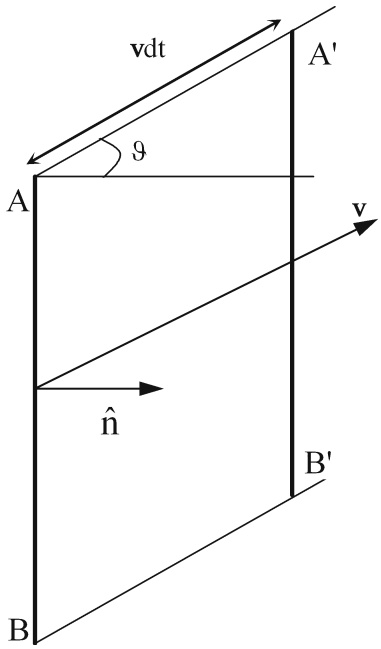

Fig. 1.30.
Schematic representation of an area dS (here the *line AB*) moving through space filled with a density of a specific physical quantity

$$e = \sum_{\alpha,\beta} \frac{\partial u_\alpha}{\partial x_\beta} \sigma_{\alpha\beta}$$

and in the case of the kinetic energy it is

$$\tau = \frac{1}{2} \rho \sum_{\alpha} \left(\frac{\mathrm{d}u_\alpha}{\mathrm{d}t} \right)^2$$

During the time dt, AB has moved by an amount $\mathbf{v}\mathrm{d}t$ to the position A'B'. The area (volume in 3D) traversed by dS is that of the parallelogram ABB'A', namely

$$\mathrm{d}S\, v\, \mathrm{d}t \cos\theta = \mathrm{d}S\, \mathbf{v} \cdot \hat{n}\, \mathrm{d}t$$

where $\hat{n}$ is a unit vector normal to dS. Therefore the amount of energy which passed through dS in the time dt is $e\,\mathrm{d}S\mathbf{v} \cdot \hat{n}\mathrm{d}t$ and the contribution of the movement of dS to the time rate of change of energy, $\Delta\dot{U}$, is

$$\Delta\dot{U} = \sum_{\alpha,\beta} \frac{\partial u_\alpha}{\partial x_\beta} \sigma_{\alpha\beta} \mathrm{d}S \mathbf{v} \cdot \hat{n}$$

Hence, the contribution from the movement of the whole Γ^* is

$$\int_{\Gamma^*} \sum_{\alpha,\beta} \frac{\partial u_\alpha}{\partial x_\beta} \sigma_{\alpha\beta} v_n \mathrm{d}S$$

Therefore,

$$\dot{U} = \lim_{\Gamma^* \to 0} \left[\int_R \sum_{\alpha,\beta} \frac{\partial \dot{u}_\alpha}{\partial x_\beta} \sigma_{\alpha\beta} \mathrm{d}A - \int_{\Gamma^*} \sum_{\alpha,\beta} \frac{\partial u_\alpha}{\partial x_\beta} \sigma_{\alpha\beta} v_n \mathrm{d}S \right] \tag{1.127}$$

where $v_\mathrm{n} = v\cos\theta$ is the component of v normal to Γ^*, θ being the angle between the normal to Γ^* and the **v**-direction. A similar term appears for $\dot{T}$. Hence, as can easily be shown,

$$\begin{aligned} Fl = & \int_S t_\alpha \dot{u}_\alpha \mathrm{d}S + \lim_{\Gamma^* \to 0} \int_{\Gamma^*} \left(\sum_{\alpha,\beta} \frac{\partial u_\alpha}{\partial x_\beta} \sigma_{\alpha\beta} + \frac{1}{2} \rho \sum_\alpha u_\alpha^2 \right) v_\mathrm{n} \mathrm{d}S \\ & - \lim_{\Gamma^* \to 0} \int_R \left(\sigma_{\alpha\beta} \frac{\partial \dot{u}_\alpha}{\partial x_\beta} + \rho \ddot{u}_\alpha \dot{u}_\alpha \right) \mathrm{d}A \end{aligned} \tag{1.128}$$

The next step (e.g., Kanninen and Popelar 1985) is to use the Gauss theorem after inserting the relation

$$\sigma_{\alpha\beta} \frac{\partial \dot{u}_\alpha}{\partial x_\beta} = \frac{\partial}{\partial x_\beta} (\sigma_{\alpha\beta} \dot{u}_\alpha) - \dot{u}_\alpha \frac{\partial}{\partial x_\beta} \sigma_{\alpha\beta} \tag{1.129}$$

After cancellation, this leads to a simpler equation

$$Fl = \lim_{\Gamma^* \to 0} \int_{\Gamma^*} \left[\left(\sum_{\alpha,\beta} \left(\frac{\partial u_\alpha}{\partial x_\beta} \sigma_{\alpha\beta} + \frac{1}{2} \rho \dot{u}_\alpha^2 \right) \right) v_n + t_\alpha \dot{u}_\alpha \right] \mathrm{d}S \tag{1.130}$$

Three remarks are in order.

1. Equation 1.130 means that the flux of energy into the crack tip can be evaluated by using the values of the stress and displacement fields only in the immediate vicinity of the tip.
2. The flux of energy into the tip is given by the sum of fluxes of the kinetic and potential energies into Γ^*, as the tip is propagating, and the rate of work done on Γ^* by the tractions from the exterior of Γ^*.
3. The flux is only obtained in the limit where $\Gamma^* \to 0$. A non-zero different contour around the tip would yield a different value of the right-hand side of Eq. 1.130. An exception to this general state of affairs is the case of a crack moving at a constant velocity, $\mathbf{v} = v_0 \hat{x}$. Here

$$\dot{u}_\alpha = \frac{\partial u_\alpha}{\partial t} = \frac{\partial u_\alpha}{\partial x} \frac{\partial x}{\partial t} = -v_0 \frac{\partial u_\alpha}{\partial x}$$

and Eq. 1.130 becomes

$$Fl = v_0 \int_{\Gamma^*} \left[\left(\sum_{\alpha\beta} \frac{\partial u_\alpha}{\partial x_\beta} \sigma_{\alpha\beta} + \frac{1}{2} \rho v_0^2 \sum_\alpha \left(\frac{\partial u_\alpha}{\partial x} \right)^2 \right) n_x - t_\alpha \frac{\partial u_\alpha}{\partial x} \right] \mathrm{d}S \tag{1.131}$$

For this case (Atkinson and Eshelby 1968), the value of the integral does not depend on the choice of the contour Γ^*, so there is no need to go to the limit $\Gamma^* \to 0$.

Now, to obtain the energy release rate G, recall that G is the rate of change of energy with crack length. Denoting this length by c,

$$G = \frac{\mathrm{d}E_{\mathrm{tot}}}{\mathrm{d}c} = \frac{\mathrm{d}E_{\mathrm{tot}}}{\mathrm{d}t}\left(\frac{\mathrm{d}t}{\mathrm{d}c}\right) = \frac{\mathrm{d}E_{\mathrm{tot}}}{\mathrm{d}t} \cdot \frac{1}{\left(\frac{\mathrm{d}c}{\mathrm{d}t}\right)} = \frac{1}{v_0}\frac{\mathrm{d}E_{\mathrm{tot}}}{\mathrm{d}t} = \frac{1}{v_0} Fl \tag{1.132}$$

Inserting Eqs. 1.115 and 1.118 for $\sigma_{\alpha\beta}$ and $\dot{u}_\alpha$ in Eqs. 1.130 and 1.132 finally yields the result

$$G = \frac{\alpha v^2}{2\mu C_{\mathrm{t}}^2} \frac{K^2(t)}{[4\alpha\beta - (1+\beta^2)^2]} \tag{1.133}$$

where α, β and C_{t} were defined in Eq. 1.109, and v_0 was replaced by v.

Equation 1.133 is sometimes written as

$$G(V) = G(0)g(v) \tag{1.134}$$

where $G(0)$ is the velocity independent energy release rate (e.g., Eq. 1.87) and $g(v)$ (a universal function) contains the v-dependent part of Eq. 1.133. A good approximation for $g(v)$ is (Freund 1972a, see also 1990)

$$g(v) \sim 1 - \frac{v}{C_{\mathrm{R}}} \tag{1.135}$$

where C_{R} is the Rayleigh wave velocity – the velocity of a wave propagating on the surface of the solid.

Equation 1.133 is the dynamic LEFM equivalent of the static case. It describes the driving force for a crack to grow. If the dissipative energy per unit crack length, which is needed for opening bonds, creating secondary damage (e.g., secondary cracks) ahead of the crack tip, etc. is denoted by Γ (which can be velocity dependent), then the condition for crack propagation is

$$G = \Gamma \tag{1.136}$$

Eqations 1.134–1.136 are the ones used to analyze dynamic crack propagation. For example, they imply that when V approaches C_{R}, $G(0)$ should go to infinity to sustain the propagation, namely that C_{R} is the crack's maximal velocity. In experiments conducted on brittle materials under constant load, the crack velocity invariably increases monotonically in time, up to a certain terminal velocity. It can subsequently stay at this velocity, which is then the maximal velocity or it can fluctuate around this terminal velocity (Fineberg and Marder 1999), in which case we define the maximal velocity as the time average of the fluctuations. In the literature, the terms maximal and terminal velocities are therefore usually interchangeable. The energy release rate is proportional to $K^2(t)$. Thus, according to Eq. 1.134, the crack propagates as long as $K(t)$ is larger than

a dynamic critical stress intensity factor called K_{ID}. The latter depends on the material as before but also on the crack velocity (and probably on the temperature). By Eq. 1.133 and Eq. 1.136,

$$K_{ID}(v,T) = \frac{C_t}{v}\sqrt{\frac{2\mu}{\alpha}[4\alpha\beta - (1+\beta^2)^2]\Gamma} \tag{1.137}$$

which is usually called "crack resistance".

If Γ and its dependence on v were known, Eq. 1.136, or alternatively

$$K(t) = K_{ID}(v,T) \tag{1.138}$$

would provide a relation wherefrom the velocity of the propagating crack could be obtained. Therefore, Eqs. 1.134–1.136 or Eq. 1.138 are commonly used by engineers for these calculations. There exist, however, several problems with this approach. As mentioned earlier, the biggest discrepancy with measurement is that the maximal crack velocity is not C_R. Experiments yield values of terminal velocities ranging between ~$0.2C_R$ and $0.7C_R$. But even for small velocities where Eq. 1.136 and Eq. 1.138 are supposed to be a good approximation to the exact situation, there exist several factors (not included in Eq. 1.136 and Eq. 1.138) that influence crack speed. We enumerate here briefly some of these:

1. The rate of loading (Liu et al. 1998; Arakawa and Takahashi 1987).
2. The geometry of the sample (Kobayashi and Mall 1978).
3. The non-uniqueness of the stress intensity factor in defining crack velocities (Dally et al. 1985).
4. Additional effects (Ravi-Chandar and Knauss 1987).

The prevalent measuring methods of dynamic fracture parameters are described, e.g., in Yang and Ravi-Chandar (2001), in Fineberg and Marder (1999) and in Knauss (2000). They include both well-established methods that have been used for a very long time and new developments of the last ten years.

We return now to the question of maximal crack velocity. Table 1.1 (adapted from Fineberg and Marder 1999) shows that for homogeneous brittle materials, the maximal crack speed never exceeds $0.7C_R$. On the other hand, if we assume that $K(t)$ under a constant load σ_0 is proportional to $\sqrt{c(t)}\sigma_0$ (as is the case e.g., for an infinite plate) where $c(t)$ is the instantaneous crack length, Eqs. 1.134–1.136, with the help of Eq. 1.133 yield for a constant Γ

$$q\left(1 - \frac{v}{C_R}\right)c\sigma_0^2 = \Gamma \tag{1.139}$$

Table 1.1.
Maximal crack velocities in some homogeneous brittle materials

Material	v_{max}/C_R
Glass	0.47 – 0.66
PMMA	0.58 – 0.62
Homalite	0.33 – 0.41

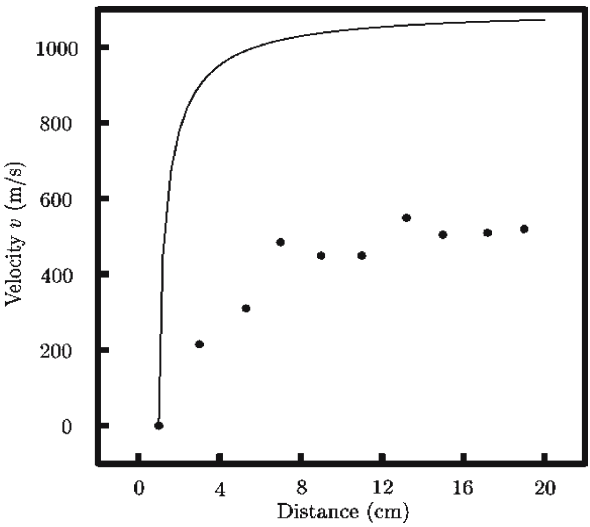

Fig. 1.31.
Data of Kobayashi et al. (1974) in PMMA, showing the discrepancy with linear elastic theory (*full line*)

where q is a constant, or

$$1-\frac{v}{C_R}=\frac{c_0}{c} \tag{1.140}$$

where $c_0 = \Gamma / q\sigma_0^2$ is the length where crack initiation occurred. Equation 1.140 can be used to find the expected LFEM crack velocity

$$v = C_R\left(1-\frac{c_0}{c}\right) \tag{1.141}$$

which is equivalent to Eq. 1.103, with C_R as the terminal velocity. Figure 1.31 shows the experimental results of Kobayashi et al. (1974) mentioned before, together with v according to Eq. 1.141. This figure dramatically emphasizes the discrepancy between the LEFM theory and the experimental results. This discrepancy obviously arises from the processes occurring in the tip vicinity. These concern atomic nonlinear forces, not included in the linear theory (e.g., i–iv above), which lead to instabilities in the crack propagation and to the collapse of the LEFM theory.

Besides our simplistic semiphenomenological approach (see Sect. 1.4.1 and Rabinovitch 1994), there exist at the moment two lines of thought that try to explain these instabilities. They will be denoted by the "velocity threshold" and the "dissipation process" (Sects. 1.4.3.1 and 1.4.3.2, respectively).

1.4.3.1
Velocity Threshold, Microbranching

In a series of careful experiments, conducted mainly on PMMA and Homalite but also on glass samples, J. Fineberg, M. Marder and their group (Fineberg et al. 1991, 1992; Sharon et al. 1995; Sharon and Fineberg 1998, 1999) measured the accurate changes of

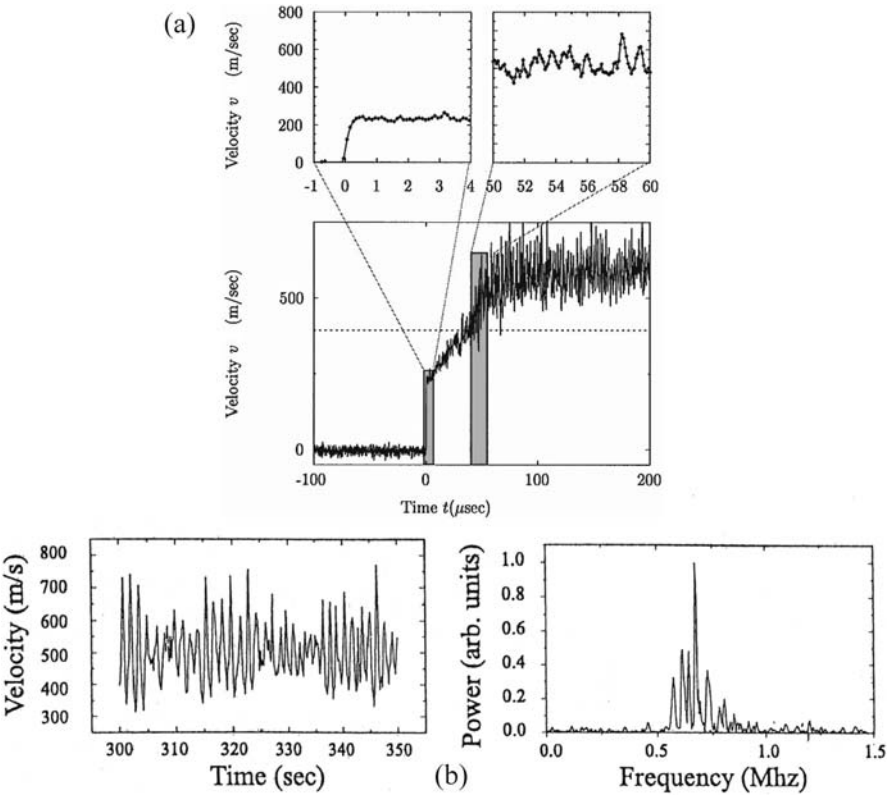

Fig. 1.32. A typical measurement of the velocity of a crack tip in PMMA. **a** as a function of time: After an initial jump to about 150 m s^{-1} the crack accelerates smoothly up to a critical velocity v_c (*dotted line*). Beyond this velocity, strong oscillations in the instantaneous velocity of the crack develop and the mean acceleration of the crack decreases (Fineberg and Marder 1999). **b** The steady-state above v_c and the corresponding power spectrum. Note the existence of a well-defined timescale (from Hauch and Marder 1998)

crack velocities in those materials and the simultaneous appearance of secondary "patterns" around the propagating cracks. It was found that in PMMA at and above a critical crack velocity of $v_c = 0.36C_R$ (which is independent of sample geometry, sample thickness, and the applied stress or acceleration rate of the crack) velocity fluctuations appear (Fig. 1.32) together with microbranching (Fig. 1.33) emanating from the main crack and ending inside the samples. Note that v_c is smaller than the final (or terminal) velocity. They have concluded, therefore, that the fluctuations were due to these microbranching or "branching attempts". They have also identified these microbranching with the "mist" and "hackle" patterns found in brittle materials (Fineberg et al. 1991; Sharon and Fineberg 1996). An additional feature of these velocity measurements in PMMA (not observed in glass) is a velocity jump at the beginning of crack propagation (Fig. 1.34) (see in this connection Rabinovitch and Bahat 1979). In a series of "microscopic" calculations Marder and coworkers (Marder and Gross 1995; Hauch and Marder 1998; Marder and Liu 1993) obtained results that support these experiments. Their models are based on a lattice of points connected by springs whose performance is predetermined. Calculation results show

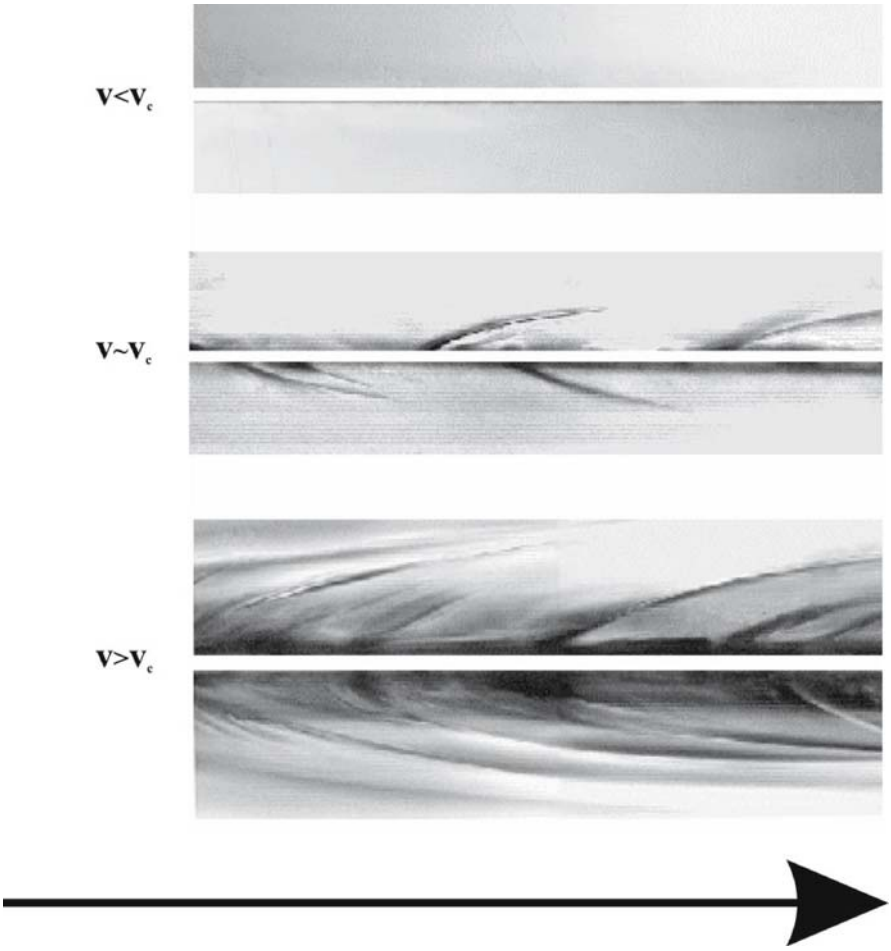

Fig. 1.33. Images of local crack branches in the *x*-*y*-plane in PMMA. The *arrow*, of length 250 μm, indicates the direction of propagation. All figures are to scale with the path of the main crack in white. *Top:* $v < v_c$; *center:* $v = 1.18v_c$; *bottom:* $v = 1.45v_c$ (from Sharon et al. 1995)

1. A velocity "gap" – the initial crack velocity is immediately greater than zero.
2. Instabilities arise whenever the crack velocity exceeds a certain threshold velocity – above which the crack direction bounces and surface roughness is thereby created.

These results agree with some atomistic (e.g., Abraham et al. 1997) and finite element (Xu and Needleman 1994) calculations in the identification of a threshold velocity above which crack direction starts to "wiggle". Such a velocity dependent instability was already predicted by Yoffe (1951), who showed that the stress field around the crack tip was velocity dependent: For small crack velocities, the stress field at the tip perpendicular to r, $\sigma_{\theta\theta}$, had a maximum at the crack propagation direction ($\theta = 0$), while above a certain threshold velocity the maximum was shifted to non-zero θ values (in Yoffe's calculation $\theta = \pm 60°$).

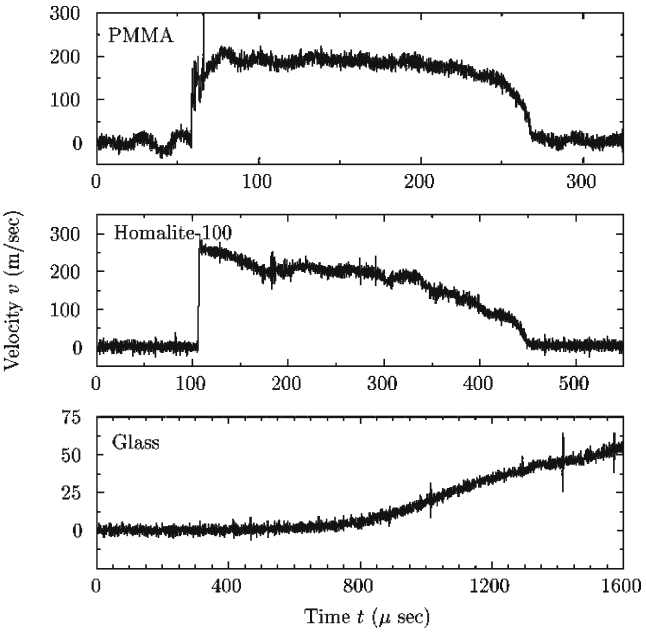

Fig. 1.34. Crack velocity vs. time in geometries designed to produce gradual crack arrest. In PMMA and Homalite, cracks decelerate slowly towards zero velocity on the scale of μs, while in glass, cracks are able to accelerate slowly from zero velocity and travel stably at very low velocities. These data show that jumps in velocity from zero are not intrinsic properties of fracture dynamics in amorphous materials. Data of Hauch and Marder (1998) (from Fineberg and Marder 1999)

1.4.3.2
Dissipation Processes

In this model, instead of crack velocity, the controlling parameter is the energy release rate or the stress intensity factor. However, it is the *static* stress intensity factor and not the *dynamic* one which is experimentally seen to cause the different changes in crack behavior and the corresponding surface patterns (different roughness features). It is assumed that the excess energy released from the elastic field is not "used" solely to increase the kinetic energy of the medium. Rather, it goes into the creation of microcracks or other damage mechanisms ahead of the propagating crack. Several investigators in this school of thought are Kerkhof (1973), Johnson (1992), Ravi-Chandar and Knauss (1984a–d). See also Ravi-Chandar (1998) for a thorough discussion and comparison with the velocity threshold line of thought.

This line of thought is based on the fractographic investigation of fractured surfaces of brittle materials (glass, glass ceramic, ceramics and rocks; see Chap. 2 for a detailed description) in which a universal pattern appears. Figure 2.1b is a representative schematic picture. It is seen that after the crack initiation (at c_i or c_{cr}; see Sect. 1.4.1) in a sequence the following patterns appear: "Mirror", "mist", "hackle" and "bifurcation". The "mirror" is a rather flat surface, reflecting light (hence the name). A careful atomic microscopy measurement, however, shows that "roughness" increases across the whole range of the mirror, although it stays invisible to the naked eye. Crack

velocity increases gradually (Fig. 1.31) across the mirror and usually reaches its terminal value there. The "mist" is a region of numerous secondary fractures, while the "hackle" appears as a set of parabolic (or hyperbolic) secondary markings, the planes of their propagations making acute angles with the primary crack plane. Bifurcations (or branching) and attempted bifurcations appear only *after* the mirror-mist-hackle sequence has occurred (there are however some conflicting observations; Sect. 2.2.3.14) and ultimately induce a splitting of the crack into two or more branches.

The demarcation lines between the different patterns, i.e., the mirror-mist (r_m in Fig. 2.1) mist-hackle (r) and hackle-bifurcation (r_b), are sometimes sharp and sometimes gradual. Many investigators (e.g., Bansal 1977; Johnson and Holloway 1966; Shand 1959) have found that these transition lines can empirically be obtained by relations of the following form:

$$r_i \sigma_0^2 = A_i \tag{1.142}$$

where r_i can assume the values of r_m, r, or r_b; σ_0 is the remote stress in the sample and A_i (= A_m, A, A_b respectively) are material constants. This relation was used, e.g., by Bahat et al. (1982) to evaluate the shape of the mirror boundary when $\sigma_0(\theta)$ changed with the polar angle and by Bahat and Rabinovitch (1988) to evaluate the paleostress in a rock by the shape of its transition line into the hackle zone (mist was barely discernable there).

The empirical result embodied by Eq. 1.142 is very intriguing. It relates the static stress intensity factor (which is proportional to $\sigma_0\sqrt{r_i}$ for an infinite plate) to the transition in crack behavior. This could mean either that dynamic effects, such as the changes of K_I with velocity (see above) do not count, or that all of these transitions occur for the same (or nearly the same) velocity. In either case, Eq. 1.142 seems to indicate that the controlling parameter is K_I, at least for materials other than PMMA, and not the crack velocity.

1.4.4 Fracture Pattern Analysis

A complete understanding of pattern formations on brittle crack surfaces is still missing, although more than a century has passed since they were detected (see Bahat 1991a). The identification of the mist zone as a zone studded by secondary microcracks is perhaps due to Ravi-Chandar and Knauss (1984a–d) and as mentioned above (Sect. 1.4.3.2), the relations (Sect. 1.142) were obtained by many investigators but without a firm theoretical foundation. In a series of papers (Rabinovitch et al. 1994, 2000a,b), we have found some properties of these patterns. These are presently discussed.

Based on the directions of the secondary cracks (Rabinovitch et al. 1993, see Sect. 1.4.2), we have calculated (Rabinovitch et al. 1994) the lengths of these cracks as a function of distance across the mist zone.

This calculation was based on two assumptions:

1. A flaw (or a microcrack), which is found ahead of the propagating crack, starts to grow when the *static* stress intensity factor at its tip becomes equal to K_{Ic}.
2. The primary crack overtakes the secondary crack since the former moves faster, thereby causing the secondary crack to halt.

The outcome was that the lengths of *all* secondary cracks should increase across the mist zone by a common magnifying factor M which itself is growing monotonically as a function of the primary crack length. Although these results agreed quite nicely with the roughness experiment by Ravi-Chandar and Knauss (1984c), this agreement showed only a proportionality correlation. Indeed, a painstaking experiment (Rabinovitch et al. 2000b) showed a rather surprising result. The experiment was conducted on a glass bottle and the lengths of some 12 000 secondary cracks across the mist zone were carefully measured under a microscope. It emerged that

1. The appearance of secondary cracks was abrupt (at the end of the "mirror plane").
2. The length distribution of these cracks consisted of two parts – Gaussian for short lengths (up to ~6 μm) and a negative exponential tail above 6 μm.
3. Length increase across the mist zone did behave like the predicted one with a common increasing magnification M, but only a small fraction (around 9%) of the secondary cracks were really magnified.

These features are not understood as of yet.

A more detailed calculation of the interaction between the primary crack and the secondary cracks in the mist zone was carried out in Rabinovitch et al. 2000a. A penny-shaped flaw (microcrack) was assumed to start its propagation as a secondary crack when the static stress intensity factor at its tip, caused by the primary crack stress field, reached K_{Ic}. It was further assumed that the velocity of the secondary crack increased approximately in an exponential manner, reaching ultimately the "terminal (maximal) velocity" of the material. Each part of the secondary crack overtaken by the primary one ceased to grow, since stress there was relaxed. In this way, the two-dimensional shapes of the secondary cracks could be calculated. Results (Fig. 1.35) showed that these shapes should change along the way from the mirror to the hackle zones from being circular to elliptic and to "teardrop"-like. Since the stress field ahead of the primary crack increases along its way (recall that $K_I \sim \sigma_0\sqrt{2\pi R}$, where R is the primary crack radius), the secondary flaws start to grow as cracks at distances further and further ahead of the primary one. Finally, they acquire such a "forestart" that the primary crack cannot overtake them anymore. This point is assumed mark the beginning of the hackle zone. A secondary crack shape calculation in this zone yields for it a hyperpolic form (Fig. 1.35). Experimental secondary crack shapes (Fig. 1.36) are seen to agree well with the calculated ones.

These results constitute a step in understanding the mirror-mist-hackle-bifurcation sequence of surface patterns.

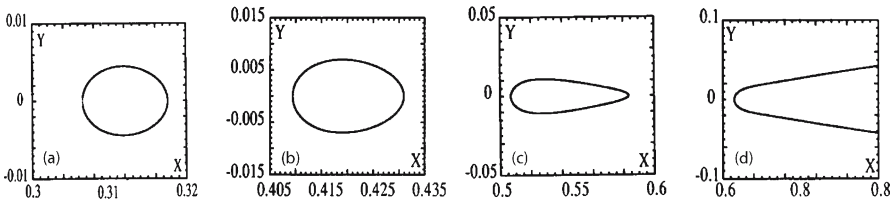

Fig. 1.35. Calculated shapes of "final" secondary cracks in the mist and hackle zones, for different radii R of the primary crack (flaw size $c_0 = 0.002$ mm). x and y scales are in mm. **a** $R = 0.3$ mm, the beginning of the mist zone (*oval*); **b** $R = 0.4$ mm, in the mist zone (*elliptic*); **c** $R = 0.495$ mm, towards the end of the mist zone (*tear drop*); **d** $R = 0.6$ mm, in the hackle zone (*hyperbolic*) (Rabinovitch et al. 2002a)

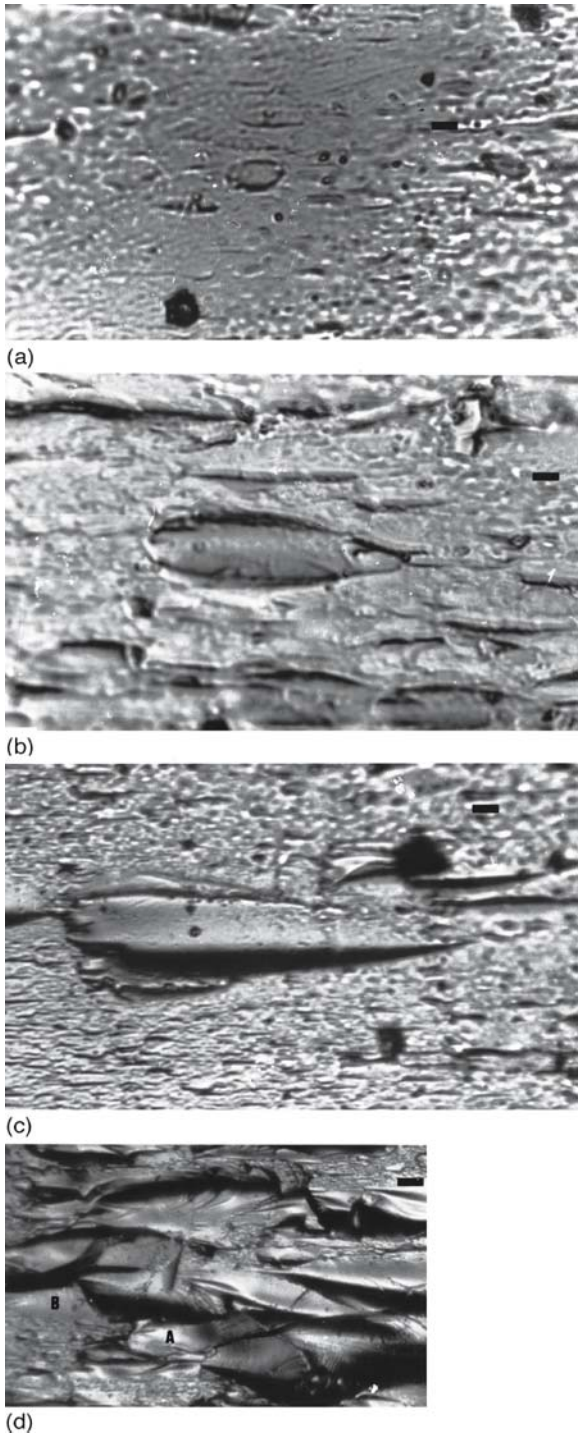

Fig. 1.36.
Experimental results for soda lime fracture. **a** The beginning of the mist zone (*oval*), scale bar 2.5 μm; **b** towards the end of the mist zone (*teardrop*), scale bar 10.0 μm; **c** at the mist hackle transition (*two semiparallel lines*), scale bar 10.0 μm; **d** in the hackle zone (*neighboring hyperbolic forms*, e.g., A and B), scale bar 20.0 μm (Rabinovitch et al. 2000a)

1.5 Subcritical Cracking

1.5.1 General

This section concerns situations for which the Griffith criterion is not fulfilled, i.e., situations where $K < K_c$, hence the name "subcritical". Experimentally this area is divided broadly into two parts called "fatigue" and "creep". The term "fatigue" is nowadays used specifically for a situation where stress (or K) is periodically changed between two values, while the term "creep" is reserved for the description of a gradual rupture under a constant low stress. The fatigue case, which is very important for metallic samples, will not be discussed here except to mention the *empirical*, so-called "Paris law" for the rate of crack length, c, increase with the number of cycles N (Paris and Erdogan 1963)

$$\frac{\mathrm{d}c}{\mathrm{d}N} = C(\Delta K)^p \tag{1.143}$$

where $\Delta K = K_{max} - K_{min}$, K_{max} and K_{min} being the maximum and minimum K values between which the load is cyclically changed and C and p are material constants. Since this relation does not always agree with experiments, more sophisticated relations have appeared (e.g., Suresh 1998).

1.5.2 Creep

This phenomenon of rupture under low stress conditions is also called by many other names, such as corrosion, stress corrosion, corrosion fatigue, static fatigue, etc. It is directly related to the question of flaw and crack nucleation, see Sect. 1.2. Since experiments can only be carried out within a finite temporal span (of a maximum duration of the order of 1 year), geological results can not be directly verified in the laboratory. As we shall show, these results demonstrate an approach to fracture, which is different than the one governing the behavior of shorter times (higher stresses).

The usual accepted result of creep is that of Wiederhorn (1967) or Evans and Johnson (1975). See also Wiederhorn (1978). In this approach, the governing parameter of rupture is again the stress intensity factor K. Results are given in the form of crack velocity vs. K-value. This approach applies to the scenario (see Sect. 1.2.3.3) where a single flaw grows under the external stress field. The whole range of K values ($0 \le K < K_c$) is customarily divided into four parts. In the lowest K region, $K < K_{Isc}$, no crack increase is detected. A controversy exists in the literature whether $K_{Isc} = 0$ or constitutes a real (>0) lower bound. The other three ranges of K (Fig. 4.34) are termed regions I, II and III, respectively. In region I, a very fast increase of fracture velocity with K_I is observed. It is usually empirically described by

$$v = AK_I^n \tag{1.144}$$

where A and n are material constants. A compilation of such constants for rocks can be found in Atkinson (1984) and Atkinson and Meredith (1987a,b). Region II is called the stress corrosion zone, where crack velocity changes slowly with K_I, the change being strongly dependent on the properties of the environment, i.e., temperature, water content of air, material contaminations, etc. Region III is again a transition range (to the supercritical region), where velocity is initially increased very rapidly and eventually saturates to the "final" constant (maximal) velocity of the material.

However, this behavior of crack velocity can not be used for fracture under extremely low stresses. The latter is important especially for geologic situations, where processes occur very slowly and presumably under extremely low stresses (or strains). One of the most important manifestations of such processes is the abundant single layer jointing that has been extensively studied. In the next section we present in detail our contribution to this study and show that the fracture probability under these extreme conditions is not proportional to K_I but rather to σ itself. This result is in line with a recent experiment by Yoon et al. (2000).

1.5.3 The Dependence of Jointing in Rock Layers Solely on Stress

1.5.3.1 *General*

We show that the criterion for fracture for the jointed layers is really based only on the level of stress (σ_0) they have endured during the elapsed geological times. It is therefore conceivable that such a fracture criterion based on σ_0 alone is the prevailing one for extreme below-threshold-extended-time fractures for all brittle materials. This result is shown to be in line with results obtained in current experiments on "lengthy" laboratory creep. Note that we are dealing only with joints that were formed quasi-statically. It is observed that dynamic joints are abundant in granites, whereas quasi-static ones are prevalent in sedimentary rock layers (Bahat et al. 2003). Joint spacing in such layered rocks is considered to be originated by two main processes and possibly by intermediate ones.

The first process envisages the layer denoted by A, as being "sandwiched" by "upper" and "lower" layers, each of which is made of different material than that of A. The neighboring layers, because of their higher compliance, are usually less jointed than A. But they tend to stretch the latter when they themselves are stretched, thus transferring to it the stress field. This process is referred to as the Cox-Hobbs case according to the two authors who analyzed it (Cox 1952; Hobbs 1967). In this process, the three layers are treated as perfectly connected (glued) to each other and the shear stress transferred at the interlayers is transposed into tensile stress in the middle layer. The Cox-Hobbs model can be divided into two parts. The first part, based on Cox (1952), calculates the stress transfer from the outer layers to A, and the second part treats the process of joint "in filling", i.e., the addition of more and more fractures to the layer A as a function of strain (or stress) increase.

The second process by which a layer is stretched and jointed is when it is completely separated from its neighboring layers and is itself pulled upon, either by geologic (tectonic) occurrences or by pore pressure, or both. This process is called the Pollard-Segall (Pollard and Segall 1987) process after the two authors who analyzed it. These two

extreme processes of layer fracturing actually appear in nature, as do intermediate modes in which the "gluing" of the layers is less than absolute and friction exists between layer A and its neighbors, thus transferring to A only part of the stress in them. We emphasize again that we are considering here extremely slow phenomena, which no laboratory measurements can exactly simulate. The experiments that have the closest similarity to them are those related to creep or fatigue (Nomenclature). Although the durations of both experiment types are of course much smaller than geologic ones, we shall use results of creep experiments to glean some information about geologic jointing.

1.5.3.2
The Model by Rives et al. (1992)

We start by analyzing the shapes of the joint spacing distributions obtained experimentally. It such an experiment, a "measuring" line (scan-line) is drawn parallel to the layer; the joints cut it at intersection points; and the distribution of the spacings between these points is analyzed. It was observed that the shape of these distributions is gradually changing with the increase of the density of cracks (number of joints per unit length). The latter is evidently due to the stress magnitude in the layer. The higher this magnitude is, the higher the joint density is and vice versa. The prevailing conjecture regarding this change of shape was that of Rives et al. (1992), who claimed that with increasing joint density the distribution passed from a negative exponential one through a log-normal one to a normal distribution (for very high densities). This conjecture was "supported" by a numerical experiment where a line segment representing the spacing measuring line was cut by randomly applied points (representing the intersection points on the line) with the provision that a new joint could not be closer to an existing one than a certain distance, d. The latter was used as a representative of the "shadow" area, namely, the area around an existing crack where it is highly improbable, due to stress release there, that an additional crack would appear. The interpretation of the numerical experiment apparently showed that the joint spacing distribution actually behaved as predicted. However, Rabinovitch et al. (1999a) considered two difficulties in this interpretation of the numerical experiment. They showed that the numerical result of Rives et al. (1992) did not fit the exact analytical solution of their numerical experiment, which can be obtained from a 1D car parking process model (CPP) (Widom 1966). Moreover, the exact CPP results (Fig. 1.37b,c) are shown not to be compatible with existing joint spacing distribution results, as explained below.

1.5.3.3
The Exact Shadow Model

One of the problems with the CPP model is the analysis of the "shadow". It is not true that a new crack is *completely* prevented from occurring in a close neighborhood of an existing crack (Bai and Pollard 2000a, see below). The probability of such an event is only *decreased* as we approach the existing crack. We denote this probability by $q(x)$, namely, $q(x)\mathrm{d}x$ is the probability that a new crack can appear at a distance between x and $x + \mathrm{d}x$ from an existing crack (examples are shown in Fig. 1.38). Note that for the CPP model $q(x) = 0$ for say $|x| < b, 2b$ denotes the excluded area around an existing crack, while $q(x) = \lambda$ say, for $|x| > b$, where λ measures the crack density as we will show later.

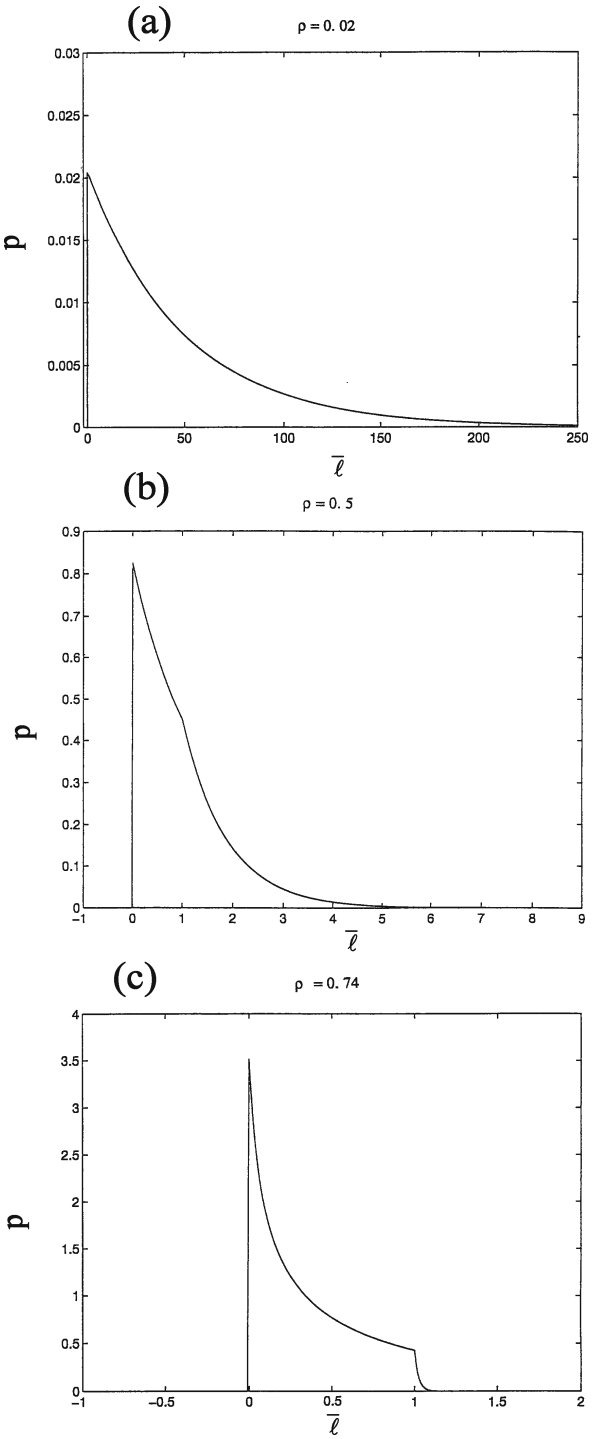

Fig. 1.37.
The calculated probability distribution function p of normalized crack spacing $\bar{\ell}$ obtained under "random sequential addition" of "cracks" onto a scanline (CPP). Three curves are shown for: **a** Very low crack density ($\rho = 0.02$), **b** an intermediate density ($\rho = 0.5$), and, **c** a density very near jamming ($\rho = 0.74$) (Rabinovitch et al. 1999a). Here $\bar{\ell} = (\ell / d) - 1$, where ℓ is the intercrack distance; $\rho = (N / L)d$, where N is the total number of cracks and L is the total length of the scanline. "Jamming" or saturation here means that no additional cracks can be added

We next calculate the joint spacing distribution, which we denote by $p(l)$ (Fig. 1.39), namely $p(l)\mathrm{d}l$ is the probability that the distance between neighboring joints would reside exactly in the interval between the distance l and the distance $l + \mathrm{d}l$ (Rabinovitch and Bahat 1999). The calculation of this distribution is based on the "shadow" probability $q(x)$, in the following way. The probability $p(l)\mathrm{d}l$ is equal to the product of two terms as follows: First, the probability that no fracture has occurred between $x = 0$ and $x = l$, and second, the probability that it actually did occur between $x = l$ and $x = l + \mathrm{d}l$. The second probability is of course $q(l)\mathrm{d}l$, while the first one is somewhat more difficult to obtain. Let us denote this "negative" probability by $y(l)$. We presently show that

$$y(l) = \exp\left[-\int_0^l q(x)\mathrm{d}x\right]$$

Let us divide l into N intervals each of length Δx $(= l/N)$. As mentioned, the probability of an additional fracture appearing in Δx at a distance x from the origin (where a crack resides) is $q(x)\Delta x$. Therefore the opposite probability, namely that no crack appears in Δx is $(1 - q(x)\Delta x)$. Since the occurrence probabilities in all intervals are mutually independent, the ensuing probability that no fracture has appeared in all N intervals is the product, denoted by "Π", of the individual ones, namely

$$y(l) = \prod_{i=1}^{N}[1 - q(x_i)\Delta x] \tag{1.145}$$

Taking the logarithm of both sides we have

$$\ln y(l) = \sum_i \ln[1 - q(x_i)\Delta x] \tag{1.146}$$

where

$$\sum_{i=1}^{N}$$

denotes the sum between $i = 1$ and $i = N$.

Passing to the limit as $\Delta x \to 0$, we get

$$\lim_{\substack{\Delta x \to 0 \\ N \to \infty}} \ln y(l) = -\int_0^l q(x)\mathrm{d}x \tag{1.147}$$

where use has been made of the relation

$$\lim_{\varepsilon \to \infty} \ln|1 - \varepsilon| = -\varepsilon \tag{1.148}$$

And therefore

$$y(l) = \exp\left[-\int_0^l q(x)\mathrm{d}x\right]$$

Hence, the product of probabilities mentioned before yields

$$p(l) = q(l)\exp\left[-\int_0^l q(x)\mathrm{d}x\right] \tag{1.149}$$

Equation 1.149 is an interesting result. It states in fact that to obtain $p(l)$ one has only to know the shadow probability $q(x)$. A nice feature of Eq. 1.149 is that it is normalized for any $q(x)$. This feature is proven as follows. We denote

$$u(l) = \int_0^l q(x)\mathrm{d}x \quad \text{then}$$

$$q(l) = \frac{\mathrm{d}u(l)}{\mathrm{d}l}$$

and

$$\int_0^\infty p(l)\mathrm{d}l = \int_0^\infty \frac{\mathrm{d}u(l)}{\mathrm{d}l}\exp(-u)\mathrm{d}l = \int_0^\infty \exp(-u)\mathrm{d}u = 1 \tag{1.150}$$

In Rabinovitch and Bahat (1999), several possible qualitatively different shadow distributions were considered:

$$q(x) = \begin{cases} \lambda x^\alpha & 0 \le x < \mu \\ \lambda[1-(2\mu - x)^\alpha] & \mu \le x < 2\mu \\ \lambda & 2\mu \le x \end{cases} \tag{1.151}$$

where μ is a parameter measuring the shadow range and α is an exponent defining the qualitatively different distributions.

For each such $q(x)$ (Fig. 1.38), the related $p(l)$ is given in Fig. 1.39. These possibilities of $q(x)$ were applied to several pure experimental distributions ("pure" here means that no addition of distributions from different positions was carried out; each distribution originated from a specific layer which went through the same stress history). The results (Rabinovitch and Bahat 1999) showed that only two types of shadow distributions appeared, one (Eq. 1.151) with $\alpha = 1$ and one with $\alpha = 3$. This fact reminds us of the two main processes mentioned above for layer fracturing, namely the Cox-Hobbs process and the Pollard-Segall process. It was shown (Rabinovitch and Bahat 1999) that in fact, the $\alpha = 1$ distribution was related to rocks for which the Cox-Hobbs process was the preferred jointing method, while the $\alpha = 3$ distribution agreed with the Pollard-Segall one. This result led us to the conclusion that $q(x)$ was proportional to the stress field $\sigma(x)$, where x is the distance from an existing crack. This conclusion is discussed in the remainder of this chapter. First we show the agreement of $\alpha = 1$ and 3 with the two $\sigma(x)$ behaviors; in Sect. 1.5.3.4 we discuss the theoretical implications of this conclusion and show their agreement with a field measurement; while in Sect. 1.5.3.5 a recent creep experiment is shown to lend support to this conclusion.

(*a*) For the Cox-Hobbs case, $\sigma(x)$ is given by

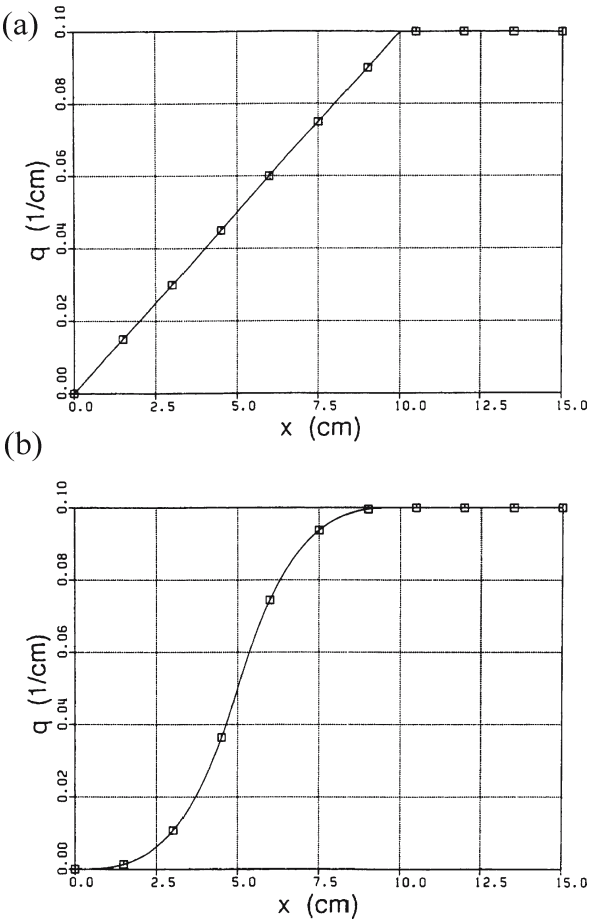

Fig. 1.38.
The complying shadow – the probability $q(x)$ (Eq. 1.151) of a second crack, a distance x away from an existing one, for $\mu = 5$ cm, $\lambda = 0.1$ cm^{-1}, for **a** $\alpha = 1$, and **b** $\alpha = 3$

$$\sigma(x) = \sigma_0 \left[1 - \exp\left(\frac{-x}{\delta} \right) \right] \tag{1.152}$$

where (Cox 1952; Hobbs 1967), $\delta = (d/2)(E/G_N)^{1/2}$, d is the layer thickness, E is its Young modulus, G_N is the shear modulus of the neighboring layers, and σ_0 is the remote stress. For short distances, namely $x \ll \delta$, the exponent can be developed in a Taylor series to yield $\sigma(x) \approx \sigma_0 x/\delta$, which is proportional to x. (*b*) For the Pollard-Segall case, $\sigma(x)$ is given (Pollard and Segall 1987) by

$$\sigma(x) = 8\sigma_0 \left(\frac{x}{\delta} \right)^3 \left[4\left(\frac{x}{d} \right)^2 + 1 \right]^{-3/2} \tag{1.153}$$

and for small values of x, $x \ll d$, $(x/d)^2$ can be neglected with respect to 1 and $\sigma(x) \approx 8\sigma_0 (x/d)^3$ which is proportional to x^3. The powers of x, the α, for the two cases are therefore $\alpha = 1$ and $\alpha = 3$, which are exactly equal to the powers of x in the $q(x)$ relations obtained experimentally.

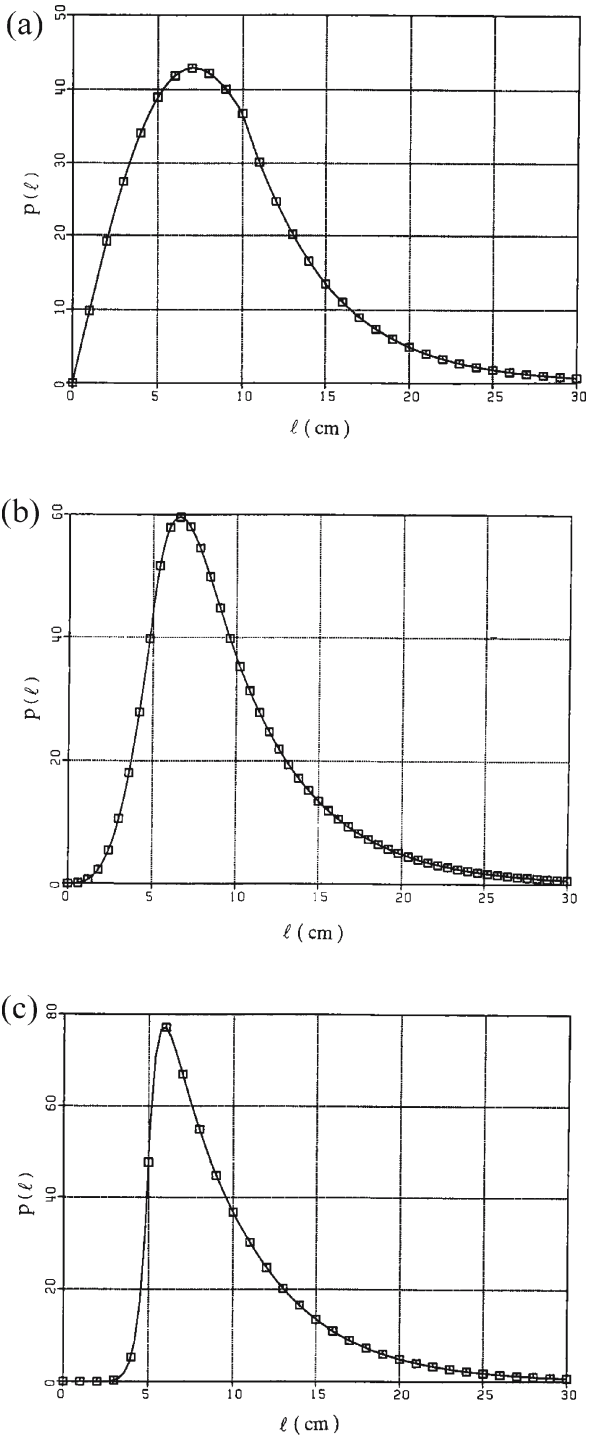

Fig. 1.39.
Simulated fracture spacing distributions, $p(l)$ (Eq. 1.149, 1.150), for $B = 100$, $\mu = 5$ cm, $\lambda = 0.2$ cm^{-1}, for **a** $\alpha = 1$, **b** $\alpha = 3$, and **c** $\alpha = 10$

1.5.3.4 *The Relation between the Shadow and Stress*

Hypothetical K_I dependence. The assumption that $q(x)$, the probability of the appearance of a new crack at a distance x from an already existing one, is proportional to the stress field $\sigma(x)$ itself (and not say, to K_I!) is a very unusual one. To see what happens for "regular" assumptions let us calculate q for a hypothetical case where the Griffith criterion is used, the layer is under a constant stress σ_0 and the flaw length distribution is an inverse exponential. Denoting the flaw length by c, it is thus assumed that $K_I \propto \sigma\sqrt{c}$ and that the flaw length distribution $p(c)$, where $p(c)\mathrm{d}c$ is the probability that the flaw length is between c and $c+\mathrm{d}c$, is given by

$$p(c) = \frac{1}{c_0}\exp\left(-\frac{c}{c_0}\right) \tag{1.154}$$

where c_0 is the average flaw length. The probability that a flaw grows under these stress conditions is the probability that $K_I \geq K_{Ic}$ or that $K_I^2 \geq K_{Ic}^2$. The latter is equivalent to the condition that $\sigma^2 c \geq A$, where $A \propto K_{Ic}^2$. Thus, the probability that a flaw would grow is equal to the probability that $c \geq A/\sigma^2$, or

$$q(x) = \int_{A/\sigma^2}^{\infty} p(c)\mathrm{d}c = \exp\left[-\frac{A}{\sigma^2 c_0^2}\right] \tag{1.155}$$

The ensuing q is evidently not linearly proportional to $\sigma(x)$ and leads to a joint spacing distribution that is not observed experimentally.

Verification of the $q = \gamma\sigma$, Relationship. We establish our proposed relation, $q = \gamma\sigma$, in two ways. In the first one we assume this relation to hold, and calculate the exact $p(l)$ that should arise. This procedure is carried out for the Cox-Hobbs case, and the results are compared with the field data of Becker and Gross (1996) and shown to agree quite well with the experimental distribution obtained there. The second verification of the $q = \gamma\sigma$ relation is derived from a recent extended creep experiment which agrees with this relation for low σ values. The whole procedure will be elaborated here, since several interesting results, besides the verification of the $q(x)$ vs. $\sigma(x)$ relation, were obtained. According to Hobbs (1967), joint spacing should continuously decrease as long as stress (or strain) continues to act on the fractured layer. Experiments, however, display the phenomenon of "saturation", where the density of joints apparently does not grow above a certain critical value. This value is deemed by some investigators (see Bai and Pollard 2000a,b for a review of previous results) to depend on the layer thickness. Bai and Pollard (2000a,b) also challenged the Cox-Hobbs model. This challenge consists of two parts. In the main part, they carry out a finite-element method calculation of a layer containing four joints under strain. In contrast to the Hobbs' assumption that the stress in the layer is always tensile, their numerical simulations indicate that between the inner pair of joints there might appear compressive stresses. The latter are obtained for values of the ratio of inter-fracture spacing to layer thickness that are smaller than a certain threshold, which in turn depends weakly on the elastic parameters of the media and on the overburden stress. Such compressive stresses

would obviously prevent the formation of additional joints in the region where they operate. In the second part of their challenge Bai and Pollard (2000a,b) show that if they extend the basic assumptions of Hobbs to the limit, the results do not fulfill the elasticity theory equations.

We take a different approach and consider Hobbs' (1967) calculation of the stress transfer from the outer layers to A to be a valid *approximation*. As such it does not have to strictly fulfill all the elasticity equations. On the other hand, we develop a different approach to the infilling process than that of Hobbs and show that a modified form of saturation does exist within this approach (see below). This would explain the "closely spaced fractures" for which Bai and Pollard (2000b) invoke an additional mechanism (flaw size, length and position distribution, possible pore pressure).

We now return to our statistical model for the Cox-Hobbs case. Assuming that $q(x) = \gamma\sigma(x)$ where γ is a proportionality constant, we have, by Eq. 1.152.

$$q(x) = \gamma\sigma_0\left[1 - \exp\left(-\frac{x}{\delta}\right)\right] \tag{1.156}$$

By Eq. 1.149 we therefore obtain

$$p(l) = \frac{\eta}{l}[1 - \exp(-z)]\exp[-\eta(z - 1 + e^{-z})] \tag{1.157}$$

where $z = l/\delta$ and $\eta = \gamma\sigma_0\delta$.

Equation 1.157 is the joint spacing distribution for the Cox-Hobbs case, according to our assumption that $q(x)$ is proportional to $\sigma(x)$. Some remarks are in order regarding the different parameters that appear in Eq. 1.157 (or Eq. 1.160, see below):

1. Lengths are always to be measured in dimensions of $\delta = (d/2)(E/G_N)^{1/2}$. The latter has dimensions of length and, in a sense, normalizes bed thicknesses. Normalized spacings $z = l/\delta$ can then be compared between different beds.
2. The proportionality constant $\gamma = q/\sigma$) has dimensions of length · (stress)$^{-1}$ or of (surface tension)$^{-1}$. It can probably be deduced from creep experiments (see below) if the latter can be seen as applicable to geologic processes.
3. The parameter $\eta = \gamma\sigma_0\delta$ is dimensionless. A crude interpretation for it is that it provides the approximate probability that a second crack would appear within a distance δ of an existing fracture. Higher η values therefore imply higher joint densities.
4. The parameter $\gamma\sigma_0 = \eta/\delta$) has dimensions of (length)$^{-1}$. It measures the probability per unit length that a second crack appears a long distance away from an existing fracture. As such it is a direct measure of joint density.

Equations 1.157 (or 1.160) can be viewed as the one and only joint spacing distribution both for low and high densities of joints. It is thus neither a "transition" between exponential, log normal to normal distributions, nor is it the CPP distribution of Fig. 1.37. The exact distribution, Eq. 1.157, is shown in Fig. 1.40 for several joint densities. The latter are represented by the parameter η. Note that the shapes of these distributions could easily mislead one to assume that the formerly mentioned "transitions"

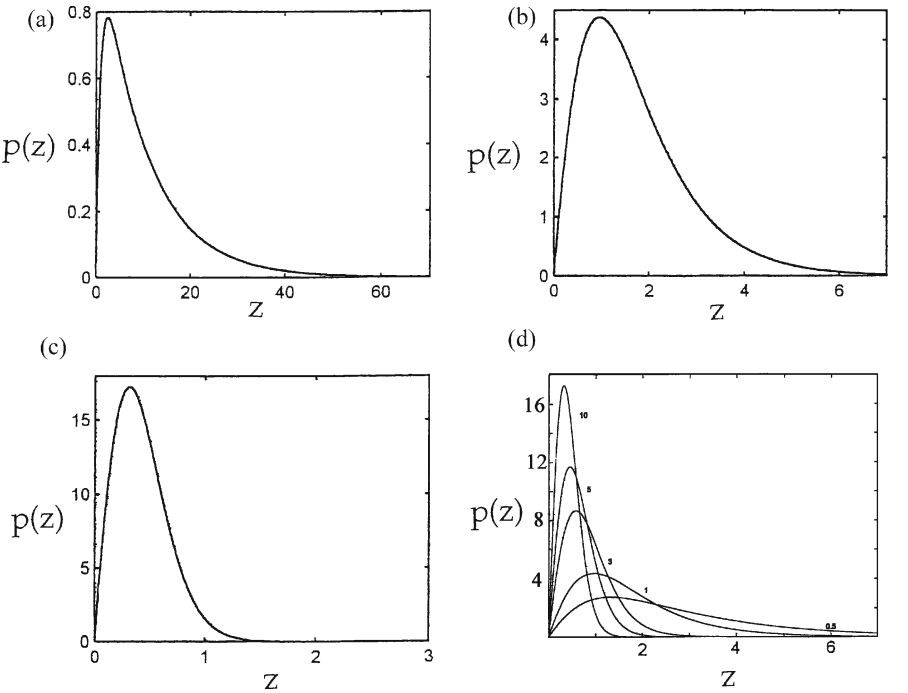

Fig. 1.40. Theoretical spacing distributions, $p(z)$ (arbitrary units) for the Cox-Hobbs case (Eq. 1.157). Lengths z are measured in dimensions of δ: $z = l/\delta$. **a** for $\eta = 0.1$, **b** for $\eta = 1.0$, **c** for $\eta = 10.0$. Note that η is proportional to the remote stress in the layer and to δ. **d** for $\eta = 0.5, 1, 3, 5, 10$; here distributions are shown on the same scale to emphasize the fast change of the peak with η between 0.5 and 3 and the slow change for η between 5 and 10

does occur. Now, before comparing this result to creep measurements, we want to pause a little at this point in order to derive some interesting features of this distribution and discuss the significance of the only two parameters that appear therein, namely δ and η. First, let us remark that since all lengths are scaled by δ, any statistic such as the average or the median should also be proportional to δ. We next discuss the behavior of the distribution median, its peak and the related interesting question of joint "saturation".

We start with the question of what "saturation" is and what is its origin. Saturation arises by the following two opposing influences. On the one hand, a larger stress results in smaller joint spacing. On the other hand, the "shadow" prohibits spacing from going to zero. To better understand this question, consider Eq. 1.157 and Fig. 1.40. It is seen that the distribution becomes more and more concentrated as η (or σ_0) increases. Yet the position of the peak and the mean of the distribution only slightly decrease with η (for high η values), and it seems that they would never become zero. Actually, as σ_0 increases, the *additional* amount of stress needed for the same incremental decrease in spacing greatly increases. To calculate the position of the peak of the distribution as a function of η, we equate to zero the derivative of $p(l)$ with respect to l. This yields $\exp(-z) - \eta(1 - \exp(-z))^2 = 0$ or, denoting $v = \exp(-z)$ and solving for the quadratic equation, we get

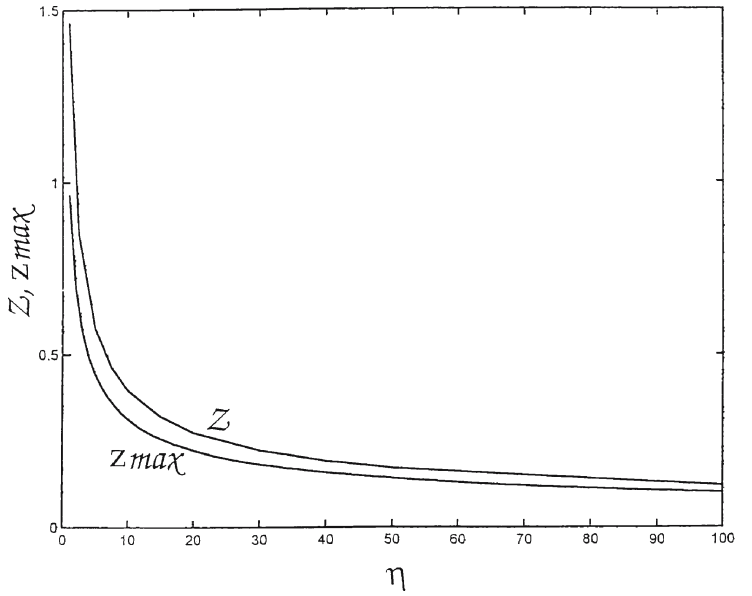

Fig. 1.41. Distribution peaks, z_{max}, and medians Z (both measured in dimensions of δ) as functions of η. Note the fast change of z_{max} and Z values for small η values, where new cracks are relatively easy to form for even a small change of stress; and the very slow (logarithmic) change of these values for larger η (effective saturation) where increasing the crack density becomes harder and harder

$$\nu = 1 + \frac{1}{2\eta} \pm \sqrt{\frac{1}{\eta} + \frac{1}{2\eta^2}} \tag{1.158}$$

hence, the distribution peak is

$$z_{\max} = -\ln\left[1 + \frac{1}{2\eta} - \left(\frac{1}{\eta} + \frac{1}{4\eta^2}\right)^{1/2}\right] \tag{1.159}$$

where only the negative sign was chosen, in order to agree with the fact that $\exp(-z_{max})$ should be less than one. Figure 1.41 shows the change of z_{max} as a function of η. It is seen that although z_{max} tends to zero with η (spacings decrease with stress increase), this tendency is very slow, logarithmic in fact (but not hyperbolic). Therefore, although *no real saturation occurs*, z_{max} presents an "*effective saturation*" behavior, (which is in line with experimental results (quoted by Becker and Gross 1996, Fig. 2) on polystyrene plates and cross-ply glass where the mean fracture spacing was measured as a function of stress (strain) and deemed to be hyperbolic (Rives et al. 1992)). In these experiments, excessive additional stresses are required for the attainment of additional cracks. Note that the change of z_{max} and median values (see below) are gradual and the transition from the range of "easy" crack density increase to the range of "effective saturation" also occurs gradually, (say, in the range $5 < \eta < 15$) rather than through a threshold value of $\eta(\sigma_0)$ (as suggested by Bai and Pollard 2000a).

The median of the distribution $L = \delta Z$ can easily be calculated numerically. Results are shown in Fig. 1.41, where Z is shown as a function of η. It is seen that the behavior of the median is similar to that of the mean, as expected. Since $Z = L / \delta$, which is proportional to L / d, Z is actually proportional to the FSR parameter (Gross 1993) (called by Bai and Pollard the "fracture spacing to layer thickness ratio"). The parameter Z is (within the Cox-Hobbs's model) the "correct" normalized fracture spacing ratio. If Z would have been a constant, then the slope of L as a function of d (more accurately of δ) would have been constant, leading to a constant value of the FSI (Narr and Suppe 1991) which is the slope of the best fit line for points depicting L vs. d for layers of different thicknesses. According to Fig. 1.41, this is not so. The median is proportional to δ only as long as η does not change significantly between different layers. This implies that the straight line obtained for FSI measurements from different layers (Narr and Suppe 1991) is somewhat fortuitous. For an almost "exact" linear dependence, both σ_0 and δ would have to be the same for the different layers, and the spread of layer thickness for the different layers should not be too large and should lie in the larger η ("effective saturation") region.

This study shows that there are only two parameters that can be obtained by the analysis of spacing distributions, i.e., δ and η (or δ and $\gamma\sigma_0$). The value of δ can also be calculated by the layer thickness and the elastic properties of the rock. Therefore, η becomes the most important measurable parameter. Its value

1. Determines the position of the fracture population of a particular layer with respect to effective saturation.
2. On comparing different layers, can provide ratios of remote stresses causing fracture in them. It is seen (Fig. 1.40 and 1.41) that spacing distribution depends on the maximum stress that has acted in the rock layer for a significant period of time.

We now show that the distribution of Eq. 1.157 is indeed compatible with the histograms of joint spacing measured by Becker and Gross (1996, Fig. 9) of the Turonian Gerofit Formation, southern Israel. The comparison is outlined here for their Sect. I, and the results of all sections are given subsequently. Consider the histogram of Sect. I (Fig. 1.42a). The l-axis stretches between zero and 80 cm, in increments of 3 cm. The bars have heights (number of points) as follows (obtained from Becker and Gross 1996, Fig. 9): 1, 4, 9, 14 etc. (since we would like to treat bars with widths of 1 cm each (unit length), each number should actually appear three times with 1 / 3 height). The sum of all spacing is 110. Now, in order that the distribution be normalized (the sum of all bars be equal to one), each number should be divided by $3 \times 110 = 330$. These numbers (* in Fig. 1.42a) are compared to Eq. 1.157 written in the form

$$P(l) = \gamma\sigma_0 \left[1 - \exp\left(-\frac{l}{\delta}\right)\right] \exp\left\{-\gamma\sigma_0 \left[l - \delta\left(1 - \exp\left(-\frac{l}{\delta}\right)\right)\right]\right\} \tag{1.160}$$

in a "least square" fashion (such as "curve fit" in Matlab). Here, the two parameters sought are $\gamma\sigma_0$ and δ. Results for all four sections are shown in Fig. 1.42 and the values of $\gamma\sigma_0$, δ and $\eta = \gamma\sigma_0 \delta$ are summarized in Table 1.2.

As seen, the agreement of the data to Eq. 1.160 is very good, especially the shapes of the distributions. However, the parameters $\gamma\sigma_0$, δ and η of sect. II are seen to be far

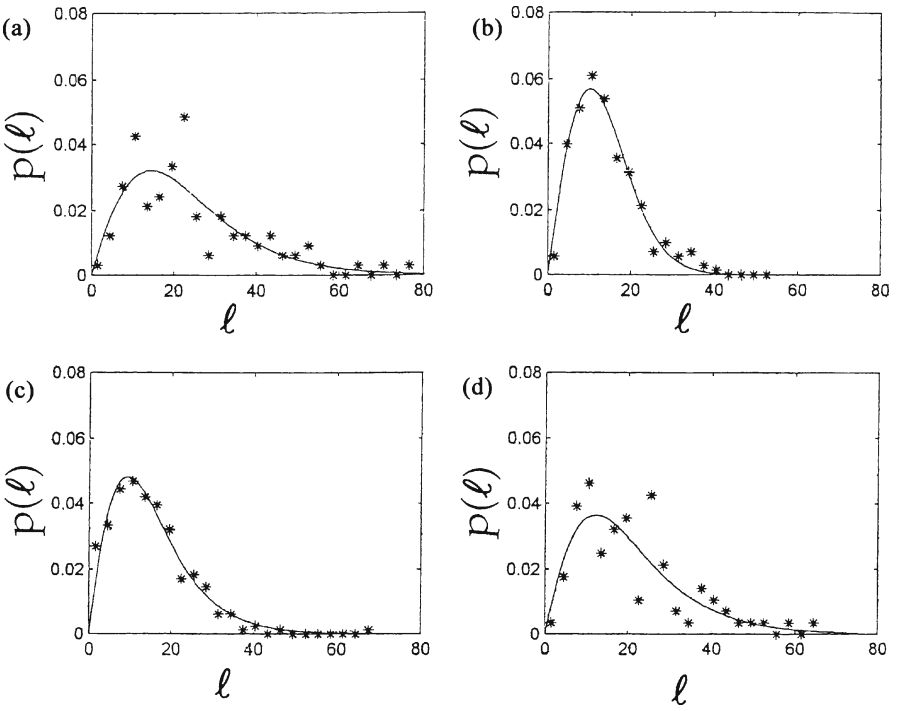

Fig. 1.42. Analysis of results of Becker and Gross (1996) spacing measurements. Sections I–IV are given in **a–d**, respectively. * are measurements and *full lines* are fits (Eq. 1.160). Note that spacing is not normalized to δ (measured in cm) and that $p(l)$ is normalized (see text)

Table 1.2.
Physical parameters of joint spacing (based on data from Becker and Gross 1996)

Section	$\gamma\sigma_o$ (1 cm^{-1})	δ(cm)	η (dimensionless)
I	0.089	19.39	1.725
II	0.637	65.29	41.59
III	0.124	11.37	1.41
IV	0.091	14.15	1.288
IIa	0.276	27.76	6.312

off from all the rest. As discussed by Becker and Gross (1996), this section experienced extreme stress conditions and the data thereof is therefore exceptional. Moreover, these data are composed of several subsections, and such composition is not advisable (see below). Some remarks are in order.

1. The "normalized layer thickness", δ, of sections I, III and IV is ~15.3 ±4 cm and the stress field in sect. III is somewhat higher than these in sect. I and IV (which are rather similar). In order to better understand the results of sect. II, the histogram of sect. IIa was analyzed separately in Fig. 1.43 (the histogram of sect. IIb is dubious since *(a)* this is the section with the largest spread of σ, and *(b)* the number of events does not add up to the quoted 120). As seen from Table 1.2, even sect. IIa

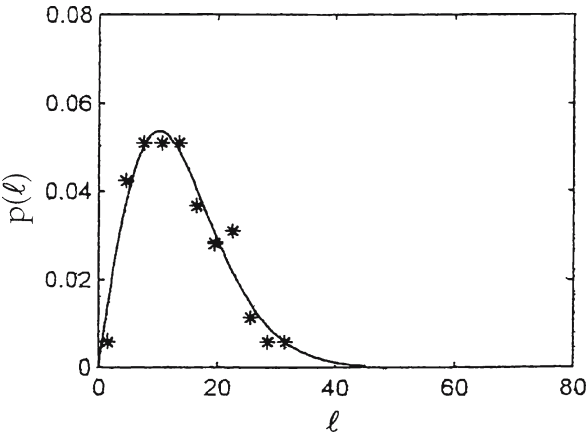

Fig. 1.43.
Section IIa of Becker and Gross (1996). Signs as for Fig. 1.42

shows already much higher parameters than the other three, suggesting unevenness of layer thickness, stresses and/or elastic parameters.

2. As mentioned, Table 1.2 shows that δ for sect. I, III and IV has an average of 15.3 ±4 cm. The latter value could be used as the range of error in the measurement. To check this result, we have calculated δ by its definition $\delta = (d/2)(E/G_N)^{1/2}$. The values of E and G_N for limestone and shale, respectively were taken from Engelder and Peacock (2001) to be 66 ±10 and 6.5 ±0.9, respectively. For a layer thickness of 19 cm (Becker and Gross 1996) the value of δ, calculated by its definition, becomes 29 ±4.2 cm. The discrepancy between $\delta = 15$ cm and $\delta = 29$ cm can be interpreted to represent the deviation of the elastic properties of the rocks in the Gerofit Formation from those borrowed from Engelder and Peacock (2001).
3. It is seen that the only genuine length-normalizing coefficient is δ, being the inherent physical variable of the Cox-Hobbs spacing. Nevertheless, regarding the question of the addition of distributions from different layer positions and different lithologies, it is clear (from Fig. 1.40) that such a procedure is not advisable. For example, an addition of two, even normalized, distributions of types appearing in Fig. 1.40a and 1.40c would create a "distribution" having a fictitious double peak.
4. The values of η obtained for sect. I, III and IV are all around 1.5, placing these sections deep inside the "unsaturated" region in Fig. 1.41. The high η value of sect. II indicates that this section has "suffered" a much higher stress (strain) during its history, bringing it (or at least the IIb part) into the saturated region.
5. A simple test of the self-consistency of the results can be carried out. Consider, e.g., sect. III. A direct measurement from the histogram yields the median to be $L \approx 11.5$ cm. Hence, $Z = L/\delta \approx 11.5/11.37 = 1.01$. By Fig. 1.41, this Z value leads to $\eta \approx 1.7$, which is close to the 1.41 obtained by the least square method.

1.5.3.5
Creep Experiments, a Close Analogy to Slow Geological Fracture

We turn now to creep experiments (see e.g., Poirier 1985). These experiments are usually conducted at high temperatures and low stresses. Due to the limited period of

measurement, however, stresses are usually not as low as those prevailing in geological layers. In creep experiments, the measured quantity is the creep (strain) rate, $\dot{\varepsilon}$, measured by a scanning laser technique. Three stages of creep are usually discerned (primary, secondary and tertiary) by the magnitudes of the respective $\dot{\varepsilon}$. But since in geological processes, the stresses generally involved in single-layer jointing are assumed to be small (see below), we restrict ourselves here to the primary stage. Usually for creep in ceramics, the dependence of creep rate on stress and temperature is represented by the so-called Norton equation:

$$\frac{\partial \varepsilon}{\partial t} = \dot{\varepsilon} = B\sigma^n \exp\left(-\frac{Q}{RT}\right) \tag{1.161}$$

where B is an empirical constant, Q an activation energy and n the stress exponent, which normally ranges between 1 and 2. However, as was pointed out by Yoon et al. (2000) this empirical formula is inadequate to describe low stress creep both in tension and in compression. Although the experiments of Yoon et al. (2000) were carried out only for silicon nitride, we assume that they hold for other ceramic materials as well as for polycrystalline rocks. Their results show that although the creep processes within a material under compression were different from those operating under tension, in both cases the first part of $\dot{\varepsilon}$ (i.e., for small strains, in the "primary" stage) behaved in a similar way with respect to stress: $\dot{\varepsilon}$ was in fact proportional to the stress σ. Note that the obtained behavior for tension was actually

$$\dot{\varepsilon} = a\sigma \exp(\alpha\sigma) \exp\left(-\frac{Q}{RT}\right) \tag{1.162}$$

but for low stresses, $\exp(\alpha\sigma) \approx 1$ and $\dot{\varepsilon}$ is again proportional only to σ.

To recapitulate, according to Yoon et al. (2000) for a brittle material both under tension and under compression, the response in creep is that $\dot{\varepsilon}$, the rate of change of strain, is proportional to the stress σ, when σ is small enough. Since for many joints fracture processes have continued for very long times, it is conceivable that the stresses present were quite small; otherwise, all jointings would have been in the "extreme saturation" state (see above, Sect. 1.5.3.4), which is not the case. We therefore assume that the layer creep rate is given by

$$\dot{\varepsilon} = \sigma a \tag{1.163}$$

where a is a constant. Consider now a layer in which a single joint exists and is under a stress $\sigma(t)$, which is quite small but can change with time. Hence, after eons have passed, the present strain in the layer is given by

$$\varepsilon = \int_0^T \dot{\varepsilon}\,\mathrm{d}t = a\int_0^T \sigma(t) = b\overline{\sigma} \tag{1.164}$$

where $\overline{\sigma}$ is the average stress.

This relation should also be true for each segment Δl around the point x. The strain in the vicinity of x, $\varepsilon(x)$ can be approximated by

$$\varepsilon(x) = \Delta N(x)\frac{\Delta}{\Delta l} \tag{1.165}$$

where $\Delta N(x)$ is the number of fractures in the segment Δl, Δ is the opening of a crack, and it is assumed that the increase in length of the segment is due only to crack openings. Measuring x from an existing joint, $q(x)$ is evidently proportional to $\Delta N(x) / \Delta l$ and hence proportional to $\varepsilon(x)$, which is in turn proportional to $\sigma(x)$.

This argument is obviously somewhat crude, since we have neglected the changes in σ by the newly added joints. If, however, the density of cracks is not very high, this approximation is reasonable.

1.5.3.6 *Summary*

Several important results have been achieved regarding joint spacing.

1. The Rives et al. (1992) conjecture that the joint spacing distribution (JSD) is changing with joint density from negative exponential to log-normal and to normal was shown to be incorrect.
2. The 1D car parking process distribution, which is a derived distribution supposed to simulate the joint spacing one, is shown to be inadequate since it completely ignores the shadow effect.
3. The JSD is shown to be dependent only on $q(x)$, where $q(x)\mathrm{d}x$ is the conditional probability that if a crack exists at $x = 0$, another crack would appear between x and $x + \mathrm{d}x$ away from it.
4. The JSD is exactly calculated from $q(x)$ (Eq. 1.149).
5. An empirical method to analyze experimental joint spacing results is presented. Using the method for several experimental cases revealed that only two processes lead to jointing, the so-called Cox-Hobbs and Pollard-Segall. The method is shown to *possess the ability* to find out which process was operative in a specific layer.
6. A bold assumption is made, partly based on indication from a recent creep experiment under extremely low stress loads, that $q(x)$ is proportional exclusively to the stress level $\sigma(x)$. This assumption is verified by comparing the analytical JSD calculated under this assumption with field data (Becker and Gross 1996). The JSD analytical calculations were carried out only for the Cox-Hobbs case, while the treatment of the Pollard-Segall process is to be carried out in the future.
7. For the Cox-Hobbs case, a complete JSD is obtained, valid both for high joint densities as well as for low ones. Contrasting a recent work by Bai and Pollard (2000a,b), the obtained JSD does not discard Hobbs calculation. It just amends his infilling approach and leads to a new understanding of the saturation phenomenon.
8. Saturation is shown not to be a certain lower level threshold below which joint spacing would never occur. It is rather an infilling process in which joint spacing always decreases when strain (or stress) increases, but when joint spacing is high, the rate of change of spacing with stress is high, while, when it becomes lower, the rate of change decreases logarithmically, i.e., it "costs" higher, and higher stress increments for the same amount of joint spacing decrease. There is a clear distinc-

tion between unsaturated and saturated jointing, although the transition from the first to the second occurs gradually.

9. It is shown that the only two parameters governing the JSD are δ, which is a normalized bed thickness and η, which is proportional to the highest stress level prevailing in the layer. Experimental results can yield only values of these two parameters. The parameter η can be used to compare stress levels at different layers as well as to locate the position of the joint spacing in the measured layer with respect to saturation (that occurs for η values above ~10).

Elements of Fracture Geology

2.1 Introduction

It is often quite a challenge to distinguish between fractures induced in rocks by shear or by tension when examined in micro scales (features that are unseen or almost unseen with the naked eye) or in outcrop scales (between centimeters and tens of meters in size). We take this challenge and concentrate in this chapter on fractures that are predominantly induced by mode I. Thus, fracture geology is limited in the present context to various phenomena of fracture growth, primarily by tension (or extension). This is a constraint that we essentially impose on the other chapters in this book, i.e., Chap. 2 stems from a treatment of principles of fracture physics in Chap. 1 and provides a base for the treatment of fracture provinces on regional scales in Chap. 3 and 4, also concentrating on tensile fracture.

The issues of fracture nucleation and growth in rocks will be raised first, followed by descriptions of fourteen experimental investigations of fractography in technological materials that have bearing on fractography in rocks. The presentation of the data will emphasize the distinction of morphological features in the mirror plane from those in the fringe (Fig. 2.1a–d). Observations on fracture surface morphology from sedimentary rocks as well as from granites will come next. The treatment of two outstanding questions in structural geology and in rock mechanics, namely, conjugate hybrid joints and longitudinal splittings, will end Sect. 2.2. The classification of systematic joints into the burial, syntectonic, uplift and post-uplift four genetic groups (Bahat 1991a) provided reference for subsequent studies on fracture in rocks, for us and for other authors (e.g., Engelder et al. 1993; Ghosh 1993; Bankwitz et al. 1994, 1997). We expand on the nomenclature of uplift and post-uplift joints and introduce the class of "surface joints" in Sect. 2.3. The fascinating multi relationships between primary joints/faults and secondary fractures are far more understood today than one or two decades ago due to recent publications on this issue (Peacock 2001a and references therein). This topic is addressed in Sect. 2.4.

2.2 Fractography and Tectonofractography

2.2.1 Introduction

Fracture initiates at stress concentrators in rocks and in synthetic, brittle and semi-brittle materials (as well as in some non-brittle materials, Bahat 1991a, p. 67). The frac-

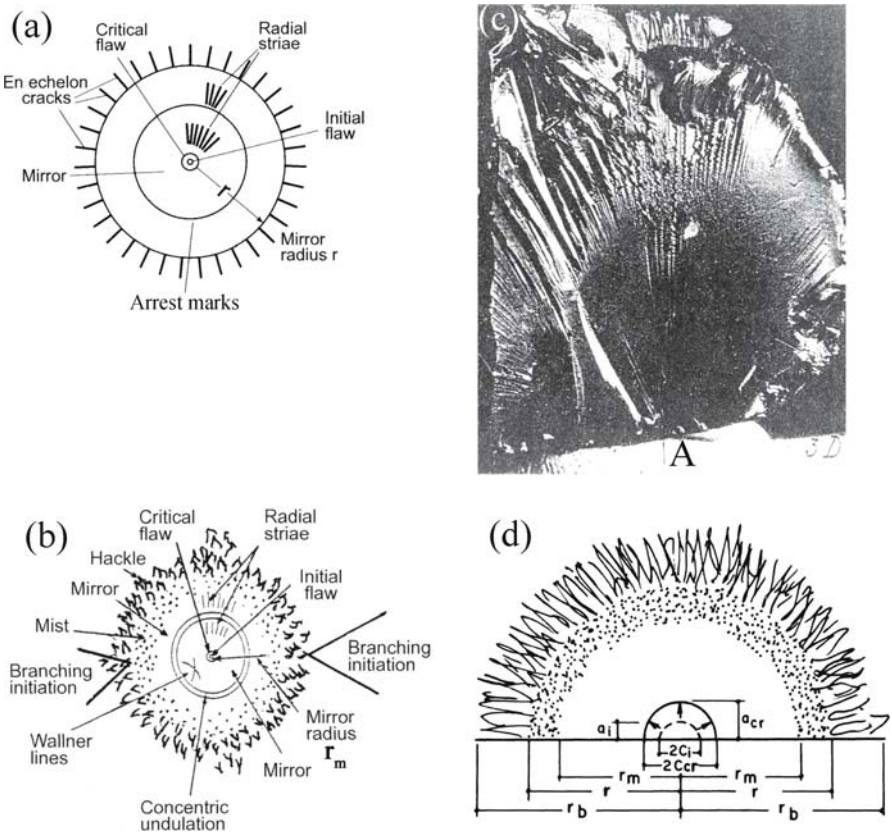

Fig. 2.1. Schematic representation of various fractographic elements on a fracture surface and distinguishing the mirror from the fringe. **a** The mirror radius, r (*arrow*) is measured from the critical flaw to the inner boundary of the *en echelon* fringe. **b** The mirror radius, r_m (*arrow*) is measured from the critical flaw to the inner boundary of the mist. Branching may initiate either from the outer rim of hackles at the right or from the inner rim of hackles, at the left (forming hackle and branching initiation together). **c** A fracture surface in bitumene (from De Freminville 1914). Note a few radial striae within the mirror plane and a multitude of hackles beyond it. Many hackles appear as echelon cracks, extensions of the striae. **d** Schematic fracture surface of brittle materials showing idealized initial flaw length $2c_{ci}$ and depth a_i, critical flaw length $2c_{cr}$ and depth a_{cr}. The three mirror radii, r_m (mirror-mist boundary) r (mist-hackle boundary) and r_b (initiation of microscopic crack branching) are shown as well (modified from Mecholsky and Freiman 1979)

ture then propagates through a great number of disturbances caused by material heterogeneities (e.g., flaws) and inhomogeneous stress fields, emitting sound waves. The sound waves interact with the advancing fracture front, and the results are recorded on the fracture surface by fracture surface morphologies, also termed fracture surface topography, fracture markings, or in short, fractography (e.g., Kerkhof 1973; Hull 1999). Every individual fracture is characterized by its specific fractography. Woodworth (1895, 1896) set the stage for the science of fracture surface morphology by astute observations of the morphology of joints in geologic exposures. He also noted the essential morphologic similarities between fracture markings in glass samples and rock out-

crops. Fractography is that branch of science that analyses fracture surface morphology and related features and their causes and mechanisms in technological materials. Fractography also contributes significantly to the understanding of fracture processes that form joints. The fractographic analysis helps to define on the fracture surface the following (Fig. 2.1a–d):

1. Fracture origin.
2. Properties of the initial flaw and of the critical flaw.
3. Modes and directions of fracture propagation.
4. Stress configurations.
5. Failure types (including, fatigue, brittle, ductile, impact and thermal influences).
6. Fractographic symmetric elements.
7. The distinction between the mirror plane (the parent joint) and the fringe.
8. Estimating the local paleostress.

This analysis establishes whether the surface features reflect a single or multistage fracture process and provides tools for fracture mechanics analysis, fracture toughness properties and related parameters of joints. From all the excellent photographs of mirror planes found in the literature (e.g., Holloway 1986), we select to show the ingenious discovery by De Freminville (1914, Fig. 2.1c). Tectonofractography is a branch of tectonics and tectonophysics, which applies fractographical analysis to rock fractures and to regional fracture systems (joint sets). The objectives of tectonofractography are to determine the fracture paleostress directions and the mechanical conditions involved and identify the tectonic processes that produced the fractures. Both fractography and tectonofractography were discussed extensively in Bahat (1991a). This discussion is expanded in subsequent sections of this volume, while minimizing repetitions from the previous volume to mere essentials.

2.2.2
The Origin: Crack Nucleation via Fractographic Techniques

2.2.2.1
Different Applications of the Term Nucleation

The terms crack (or fracture) origin, crack initiation, nucleation and "Griffith flaws" are often used interchangeably in the literature, relating to vast scale ranges. Lawn (1993, p. 307) distinguishes two ranges of "Griffith flaws" dimensions from which failure of brittle materials initiates. In homogeneous materials like monocrystalline quartz, flaws range from 1 nm (in pristine fibers and whiskers) to 1 μm (in aged, as-handled solids) and usually occur at the surface. In heterogeneous polycrystalline materials like ceramics, flaws range from 1 μm (in high-density, fine grained, polished materials) to 1 mm and above (in refractories and concrete) and occur in both the surface and the bulk. Flaws vary in size, shape and orientation such that the coexistence of more than one flaw type often gives rise to a bimodal or even multimodal flaw population. Lawn (1993, Table 9.1) provides a rather liberal-size classification of "Griffith flaws", inversely correlative to strength. In very strong materials (10 GPa for whiskers) the flaw size is in the nm range, whereas in very weak materials (1 MPa for the Earth's

crust) the flaw size is in the m range. An experimental study of fracture in a transparent glass ceramic reveals two oppositely propagating striae from an origin that cannot be precisely determined in a spot. An area of 1–2 × 1–2 mm is measured instead and termed "nucleation zone", where the bilateral fracture originated (Sect. 2.2.3.7). See a further elaboration on nucleation in micro scales in Sect. 1.2.

Joints. There are earth scientists who search fracture nucleation in the rock microcrack (Simmons et al. 1975) grain size scale (e.g., Segall and Pollard 1983). In the Devonian layered siltstones and shales of the Appalachian Plateau, central New York, and in the Eocene chalks from the Beer Sheva syncline, many joint initiation points are located along bedding boundaries (Bahat and Engelder 1984; Helgeson and Aydin 1991; Lacazette and Engelder 1992; Weinberger 2001a). These initiations occurred at stress concentrators such as free surfaces, fossil inclusions, pyrite concretions, voids, cusps, and burrows along the boundaries. Many other joint initiations in these two provinces occur from stress concentrators within the rock layer, remote from its boundaries (Weinberger 2001a). The exact location of joint nucleation within granite bodies can be fractographically identified on the Borsov joints that formed by slow propagation (Sect. 4.4.2) but not on the Mrákotin joints that formed rapidly (Sect. 4.4.3). On a larger scale, early fan-shaped cracks that were marked by plumes ranging in size from a few meters to tens of meters on surfaces of exfoliation joints interacted with each other and coalesced into composite fractures on vertical cliffs of granitic rocks at Yosemite National Park, California (Sect. 4.5.3.3). The orientation and arrangement of the fans indicate that they initiated in "nucleation zones" at certain heights, from where they propagated upwards and downwards parallel to the cliff of El Capitan monolith.

The treatment of joint initiation has been idealized from a Griffith internal crack model in glass (either elliptic or slit shapes). In moving from a model of a slit (Griffith 1924), the shape of the crack has been thought to be an oblate (Sneddon 1951, p. 486) or a prolate spheroid. The "empty" crack model (that does not have a mass) was modified to one in which fluid pressure is activated from the interior on the crack walls. Secor's theory (1965, 1969) suggests that the growth of an extension fracture at depth in the Earth's crust is a slow process, consisting in detail of numerous short episodes of crack propagation that alternate with longer periods of quiescence. Pore fluids from the surrounding rock percolate into the crack during quiescence and then wedge it open. Secor (1969) considers that the failure criteria for tension fracturing of rocks with internal pore pressure P in plane strain is

$$\sigma_{e3} = -S = -\left[\frac{\pi E \gamma}{2c(1-\nu^2)}\right]^{1/2} \tag{2.1}$$

where σ_{e3} is the least effective principal stress and $-S$ is the tensile strength of the rock (tension considered negative) for the general pore pressure condition $\sigma_{ej} = \sigma_j - P$, (Secor 1969), where c, σ_{ej}, σ_j, γ and ν are the penny-shaped crack radius, the effective principal stress, the principal stress, the fracture surface energy and the Poisson ratio, respectively. Fracture initiates when a fraction of P exceeds σ_3 and becomes effective in wedging open the crack. This will occur when fluid in the crack reaches a "critical volume" (Secor 1969):

$$v_{\text{crit}} = \frac{16}{3}\left[\frac{\pi\gamma(1-\nu^2)}{2E}\right]^{1/2} c^{5/2} \tag{2.2}$$

The cancellation of the traction parallel to the crack is done for convenience. The resemblance of Eq. 2.1 to the known Griffith equation (Eq. 1.21) implies fracture by extension that according to Secor can form joints at considerable depths. Field observations support Secor's model of a fracture process by alternating episodes of crack propagation and periods of quiescence (Bahat and Engelder 1984). A remaining outstanding question, however, is what the range attained by K_I in jointing is. Slow fracture processes in sedimentary rocks cannot be well characterized by K (Sect. 1.5.3), while in granites, in some cases there are indications of jointing under $K_I \geq K_{IC}$ conditions (Chap. 4).

Faults. Segall and Pollard (1983) investigated nucleation and growth of strike slip faults cutting granite. They suggested that faults nucleated on pre-existing joints that acted as weak surfaces capable of accommodating later shear deformations and modeled fault nucleation from sub parallel arrays of joints. Triaxial tests have been used to study the nature of the "damage zone" that propagates ahead of the growing fracture (Hoagland et al. 1973). While the "damage zone" describes a zone at the tip of an existing fracture that consists of multiple cracks oriented with respect to the fracture, "nucleation zone" (see above) relates to an area where fracture nucleation unrelated to an existing fracture occurs. These two terms are occasionally combined. Lockner et al. (1991) and Reches and Lockner (1994) applied triaxial tests to simulate nucleation of faults by the coalescence of axial microcracks into an inclined "process zone" under mixed mode conditions. The latter triaxial experiments were performed on intact granite cylinders 190.5 mm long and 76.2 mm in diameter, and planar quasi-circular "process zones" were suggested to be the nucleation sites. In both the outcrop scale and the triaxial test (Segall and Pollard 1983; Reches and Lockner 1994), the nucleation zones consisted of arrays of cracks, and in the two models, the fault growth continues along the orientation of the array.

Studies of nucleation of earthquakes (e.g., Rice 1979; Rudnicki and Olsson 1998; Gudmundsson and Homberg 1999) are carried out on seismograms (e.g., Umeda 1990; Ellsworth and Beroza 1995). Based on friction parameters, Scholz (1998) distinguishes two regimes, stable and unstable, and suggests that earthquakes can nucleate only in those regions of a fault that lie within the unstable regime. During the inter-seismic period, the fault is loaded by steady slip on the deep, stable portion of the fault. Just before the earthquake, a pre-seismic phase occurs. In this phase, known as nucleation, slip accelerates until instability results in coseismic motions. The nucleation phase is sometimes associated with precursory phenomena, such as foreshocks. A model of earthquake nucleation is considered for the weak crust of California by Bahat et al. (2001a). They suggest that the multi fault rupture pattern in California shows greater resemblance to multi fracture patterns of weak chalk cylinders broken in triaxial tests than to a single process zone in fractured strong granite. The rupture of the chalk cylinders does not start from a localized nucleation; it rather develops from many distinct sites by a coalescence process. Possibly, the nucleation of earthquakes in a weak terrain occurs from many centers rather than a single site.

2.2.2.2
Fractography

We restrict the treatment of crack initiation into a rigid framework, which is limited by visible and measurable fractographic parameters. A key feature is the "critical flaw" (Fig. 2.1a,b), which is measured as $2c_{cr}$ (Fig. 2.1d). When $2c_{cr}$ is attained, crack growth occurs spontaneously, whereas below this length nucleation is unstable and the crack is expected to heal (in glass in vacuum). Thus, the critical flaw is the upper boundary of the crack nucleation stage. The relationship in Fig. 1.12 is analogous to the maximum in free energy plotted against the radius of a nucleated new crystal. Below a "critical radius size" the nucleus tends to be unstable and dissolve, and beyond it crystal growth occurs spontaneously (Carmichael et al. 1974, Fig. 4–14). This analogy should be useful particularly for demonstrating the distinction between rates of nucleation and growth (Bahat 1970).

The "critical flaw" can be identified experimentally, as it grows from the "initial flaw" $2c_i$ (Fig. 2.1d and 2.2), showing that $2c_{cr}$ may reach sizes around 10 mm for an opening mode fracture in glass. It was found (Mecholsky and Freiman 1979) that the ratios of the mirror radii (r_m, r and r_b, Fig. 2.1d) to the critical flaw radius have corresponding constants. However, fracture results obtained by various investigators of glass and ceramics have yielded considerable discrepancies in these ratios, leading to the suggestion that a poor distinction between $2c_i$ and $2c_{cr}$ was possibly an important factor contributing to these discrepancies (Bahat 1991a, p. 109). Fortunately, occasional difficulties in defining the boundaries of $2c_{cr}$ in geological outcrops may be trigonometrically overcome (Fig. 6.18).

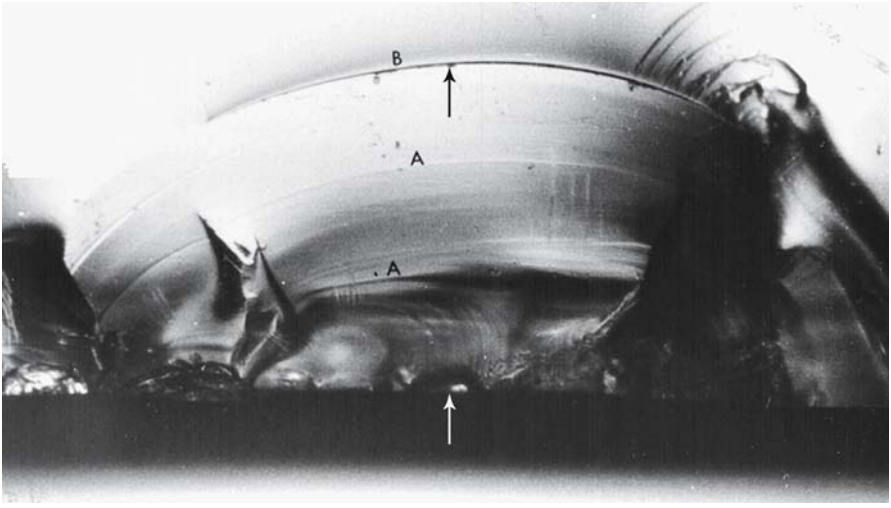

Fig. 2.2. Microphotograph of an initial flaw (*white arrow* pointing upward) growing to concentric ripple marks *A*, and radial scars in glass. These markings reveal that the growth of the initial flaw is controlled by a heterogeneous stress field. Curve *B* marks the transition to the mirror plane at the tip of the critical flaw (*black arrow* pointing downward). Lengths of diameters of initial flaw and critical flaw from ends to ends are 0.9 mm and about 1 cm, respectively (after Bahat et al. 1982)

Thus, in an attempt to provide a common denominator for comparison, where possible, we make the following distinction. The transition from sub-visible defects or singularities (undetected in the optical microscope) to the initial flaw $2c_i$ is at 2 μm (Lawn 1993, p. 13). The initial flaw may reach several mm (Segall and Pollard 1983). Its transition to the critical flaw $2c_{cr}$ varies in the mm range but can reach the cm scale on joints (Bahat and Rabinovitch 1988). These two transitions belong to the nucleation stage, while propagation from $2c_{cr}$ is taken to mark the initial growth (see also Doremus and Johnson 1978; Rabinovitch 1994). Occasionally, initial flaws may deviate from a single plane and can lead to different parts of the flaw acting essentially independently, creating more than one critical crack, such that each one would generate its own part of a mirror plane. The latter effect seems to increase with the decrease of the average angle of the initial flaw relative to the tensile axis (Bahat 1991a, Fig. 2.33d and 2.35c), resulting in the increase of shearing and the reduction of relative tension on the growing crack during the nucleation stage (Fig. 2.2).

2.2.2.3
Fracture Initiation in Stratified Muddy Sediments

In this and in the next section we cite studies by Weinberger (1999, 2001a,b) on fracture initiation in sedimentary rocks. These systematic studies improve our understanding of fracture origin in rocks and help to focus on the difficulties involved in differentiating joint nucleation from joint initial growth.

Persistent desiccation and contraction of muddy sediments give rise to mud cracks. The fracture characteristics of mud cracks were studied in dehydrating mud puddles in the Dead Sea region, Israel (here we cite extensively Weinberger 1999). The mud consists mainly of carbonate and clay particles typically displaying fining upward. There is a distinct surface discontinuity between the upper desiccated layers (that tend to contract and crack) and the uncracked lower ones. This surface is referred to as the bottom of the polygons. Mud cracks with delicate plumes formed several days after a rainstorm and ceased to propagate a few days to weeks after initiation. Several polygons of convenient size and weight (mostly containing a pair of desiccated layers) were then systematically lifted out of the dried puddles and their walls examined under optimal oblique illumination. In this way, the surface morphology of hundreds of mud cracks were studied in precise detail, based on fractographic techniques. The mud cracks form networks of interconnected tension fractures arranged in polygonal patterns. Because tensile stress due to drying declines downward through the sediment, mud cracks have generally been theorized to nucleate near the surface, propagate downwards, and terminate at depth.

Weinberger (1999) found that systematic nucleation at the bottom of the polygons and upward propagation of mud cracks are much more prevalent than previously postulated. The mud-crack initiation points are often located along or near the base of the desiccated sediment, where potential flaws (e.g., long grain boundaries) are more abundant because of the natural fining-upward sorting of grains (Fig. 2.3a). Consequently, these large flaws become critical before small flaws at the top (e.g., short grain boundaries), even though the tensile stress caused by drying declines downwards through the mud (see below). On growing, the cracks predominantly rupture the des-

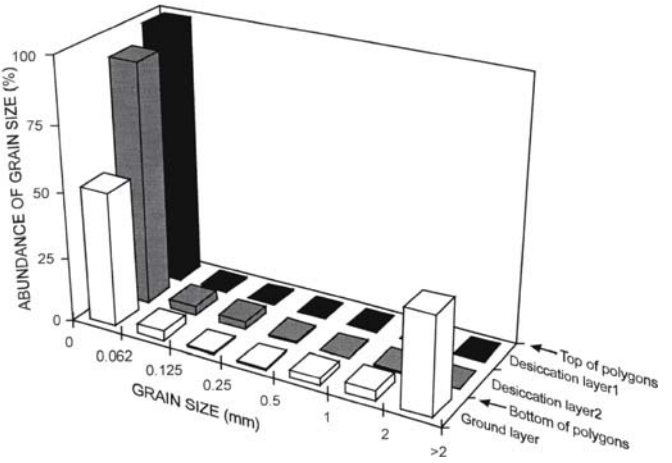

Fig. 2.3. a Grain-size distribution in the studied sediment displaying fining upward (sorting effect) and stratification. This distribution was obtained by gently disintegrating the grain aggregates of each layer and sieving the grains through screens of decreasing mesh size (from Weinberger 1999)

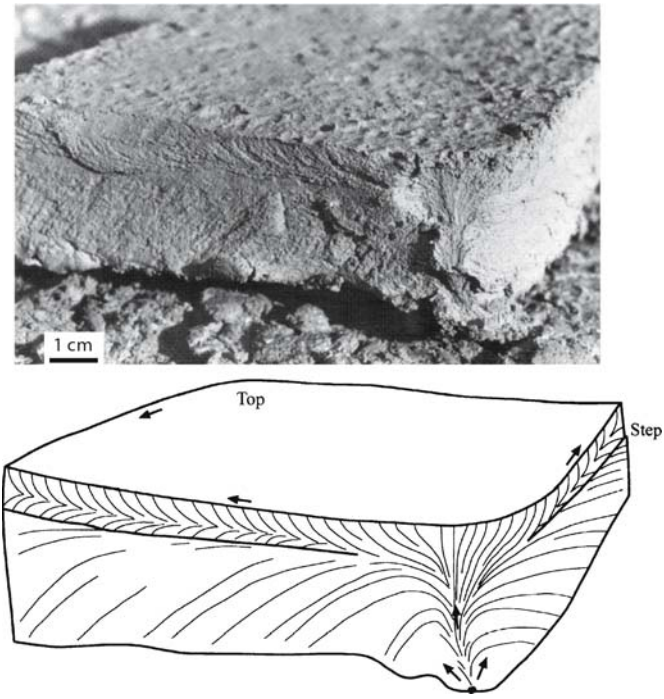

Fig. 2.3. b Oblique view of a polygon, a photograph above and a drawing below, explaining propagation directions by *arrows*. The plume shows that the crack nucleates at depth, ruptures the desiccated layers, and subsequently propagate bi-laterally away from the origin along curved paths. Minor damage caused to the polygon wall during recovery (*left corner* in photograph) is not presented in the surface-morphology drawing. Note in the photograph the dendrite-like plume that is divided into branches that are further sub-divided into minute barbs (from Weinberger 1999)

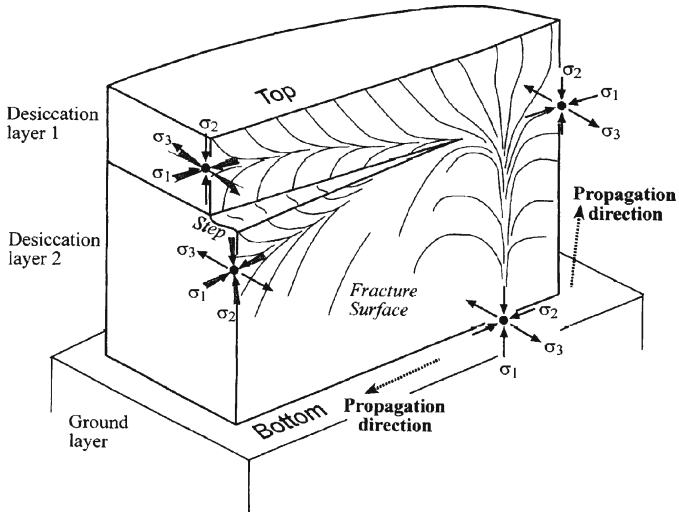

Fig. 2.3. c Schematic illustration of stress distribution throughout a polygon wall. The least compressive principal stress σ_3 is everywhere perpendicular to the crack plane, but the greatest compressive principal stress σ_1 and the intermediate compressive principal stress σ_2 vary in orientation from place to place on that plane. Next to the crack origin, where the crack extends predominantly vertically, σ_1 is vertical and perpendicular to bedding, on account of the weight of the overlying sediment. Away from the crack origin at the region where the crack extends predominantly laterally, the in-plane horizontal stress due to contraction seems to be more significant than the in-plane vertical stress due to the weight of the sediment, and σ_1 and σ_2 switch directions. Plume formation and segmentation along layer boundaries are associated with the indicated rotations of the local principal stresses (from Weinberger 1999)

iccated layers before they significantly extend laterally and sequentially form the polygonal patterns (Fig. 2.3b,c).

Thus, the consistent location of crack origins at the bottom of the polygons strongly suggests that stress concentration due to flaw discontinuities and layer boundaries play a fundamental role during mud-crack nucleation. Consequently, the stress gradient due to drying (possibly related to capillary forces) may be less important for mud-crack nucleation than has been previously postulated. Returning now to the Griffith model, Weinberger explains that mud-crack propagation consumes energy in the form of surface energy for the creation of a new crack surface. This energy comes from the release of elastic strain energy within the drying mud. In this mechanism, the only mechanical energy available to drive a crack is the change in elastic strain energy (Eq. 1.19), which must decrease while the surface energy increases (Eq. 1.20) during crack growth. Adhesive forces along the bottom of the polygons resist the horizontal contraction of the mud. This resistance gives rise to stresses along the bottom and causes the elastic strain energy to be stored. Since crack growth strongly depends on the stored energy, the boundary effect probably plays a key role not only for crack nucleation but also for crack propagation. Hence, Weinberger (1999) describes nucleation and growth processes where actual c_i and c_{cr} (Fig. 2.1) are not identified. It is, however, quite possible that nucleation in the mud took place at sites that ranged between c_i and c_{cr}. Note that the large grains along the bottom of the polygons exceed the size of 0.062 mm (Fig. 2.3a). Thus, his interpretation of both the nucleation and growth processes is quite convincing. See the experiment on profiles of "mud cracks" in Sect. 2.2.3.9.

2.2.2.4
Fracture Initial Growth in Dolomite Layers

Weinberger (2001a) investigates the well-developed surface morphology of joints in the Soreq Formation, Judea Group (Arkin and Hamaoui 1967; Upper Cretaceous, central Israel) that uniquely records the history of fracture initial growth in layered rocks. Weinberger (2001a) uses fractography to elucidate the role of macroscopic flaw distribution in the shape of cavities, on the jointing mechanism in natural conditions, and to examine the effect of bedding interfaces on joint growth and arrangement. The formation of the cavities is related to the dissolution of earlier anhydrite nodules in the dolomite by marine-derived water. The study by Weinberger (2001a) is very detailed and is cited extensively below. We differ from Weinberger in using the term nucleation. For us, joint initiation from $2c_{cr}$ is growth rather than nucleation (as mentioned above). There are cases where a distinction between the nucleation and initial growth stages can be made reasonably well (e.g., Fig. 2.2b), whereas in other instances this distinction is unclear. It could be that nucleation started from certain $2c_i$ sites within the cavities while the anhydrite nodules still resided in them (Weinberger 2001a). It appears more likely however that both nucleation and initial growth occurred from $2c_{cr}$ locations around the peripheries of the cavities after the removal of the anhydrite nodules.

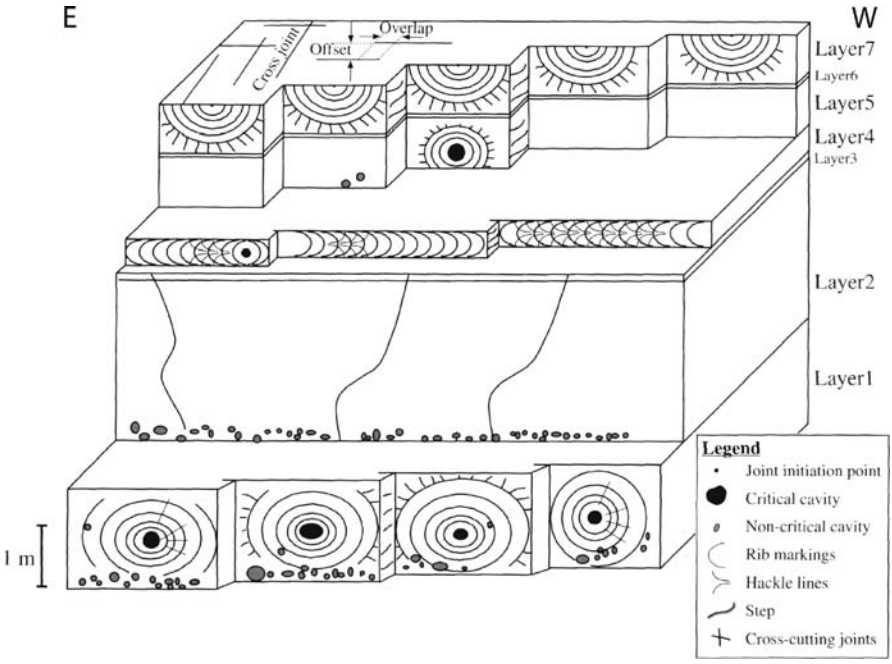

Fig. 2.4. Graphic representation of the outcrop west of Givat Ze'ev, displaying arrays of joints with diagnostic surface morphologies. Joints are selectively confined to certain layers, commonly with a differing fracture surface morphology. Layer 2 and layer 3 are not fractured by a systematic joint set. *Gray ellipses* represent non-critical cavities; *black ellipses* represent critical cavities. Cross-joints and definition of "overlap" and "offset" are indicated at the top of layer 7 (from Weinberger 2001a)

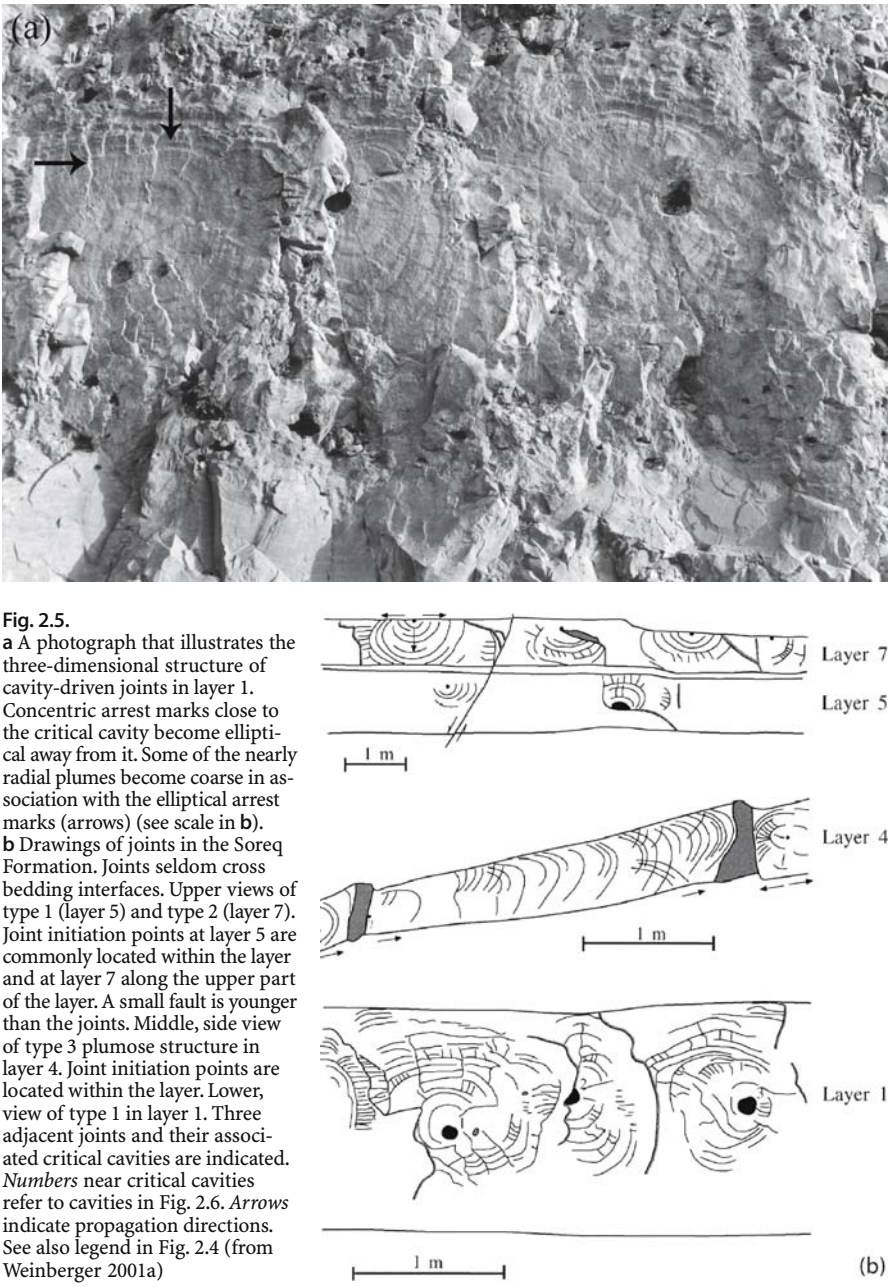

Fig. 2.5.
a A photograph that illustrates the three-dimensional structure of cavity-driven joints in layer 1. Concentric arrest marks close to the critical cavity become elliptical away from it. Some of the nearly radial plumes become coarse in association with the elliptical arrest marks (arrows) (see scale in **b**). **b** Drawings of joints in the Soreq Formation. Joints seldom cross bedding interfaces. Upper views of type 1 (layer 5) and type 2 (layer 7). Joint initiation points at layer 5 are commonly located within the layer and at layer 7 along the upper part of the layer. A small fault is younger than the joints. Middle, side view of type 3 plumose structure in layer 4. Joint initiation points are located within the layer. Lower, view of type 1 in layer 1. Three adjacent joints and their associated critical cavities are indicated. *Numbers* near critical cavities refer to cavities in Fig. 2.6. *Arrows* indicate propagation directions. See also legend in Fig. 2.4 (from Weinberger 2001a)

Cavities associated with joint initial growth in the dolomite layers are termed hereafter "critical cavities" and their respective fractures are termed "cavity-driven joints". A cavity in the present context approximates the "critical flaw" (Fig. 2.1a,b,d): The cavity's horizontal semi-axis, C_h (corresponding to c_{cr}) and vertical semi-axis, C_v (cor-

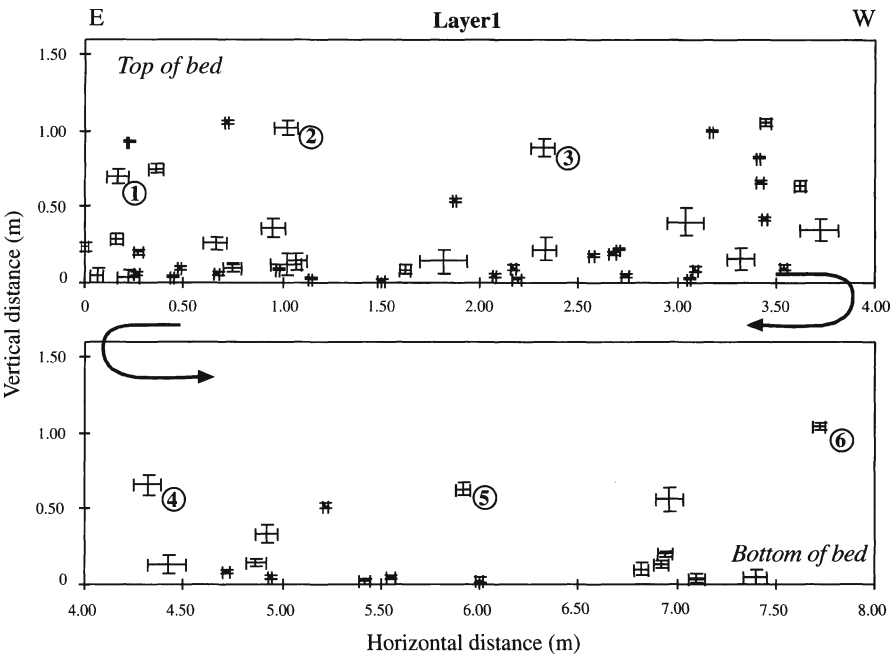

Fig. 2.6. Representative distribution and dimensions of cavities in layer 1 (Fig. 2.4 and 2.5b) along an 8 m E-W traverse. The small steps along the traverse (Fig. 2.4) are not indicated. *Bars* represent the in-plane axes of the ellipsoidal cavities. Cavity centers are located at the intersections of the bars. *Numbers* denote critical cavities that are associated with joint initial growth (from Weinberger 2001a)

responding to a_{cr}) are measured from the center of a cavity to its periphery, defined by the intersection of the respective fracture plane and the cavity rim. The cavity "depth", C_d, is measured from the center of the cavity to its rim normal to the fracture plane. The characteristic size of a cavity, Z, is defined as the mean of C_h and C_v. Fourteen adjacent critical cavities in layer 1, one in layer 5, and five in layer 7 and their associated joints were carefully measured for the analysis (Fig. 2.4–2.5). For comparison, all cavities along an 8 m long traverse in layer 1, including six critical cavities and 58 non-critical cavities, were also studied in detail (Fig. 2.6). An additional interdependent variable, the degree of isolation, can be derived from these measurements. These variables are analyzed below in an attempt to characterize features of flaw criticality.

Shape. Critical cavities are approximately spherical, with $C_h = 45 \pm 20$ mm, $C_v = 43 \pm 20$ mm, $C_d = 45 \pm 23$ mm, and in-plane $C_h / C_v \approx 1$ ratios. Non-critical cavities are also approximately spherical, with $C_h = 35 \pm 27$ mm, $C_v = 30 \pm 23$ mm, and $C_d = 32 \pm 23$ mm (Fig. 2.7a). Noticeably, several eccentric cavities ($C_h / C_v \approx 2$) appearing close to the base of layer 1 are non-critical, e.g., an ellipsoidal cavity at a distance of 4.40 m along the traverse (Fig. 2.6). If a cavity deviates from a perfect sphere, the major semi-axis commonly coincides with C_h. This is particularly the case for critical cavities, where only in one case the difference between C_v and C_h is larger than 3 mm.

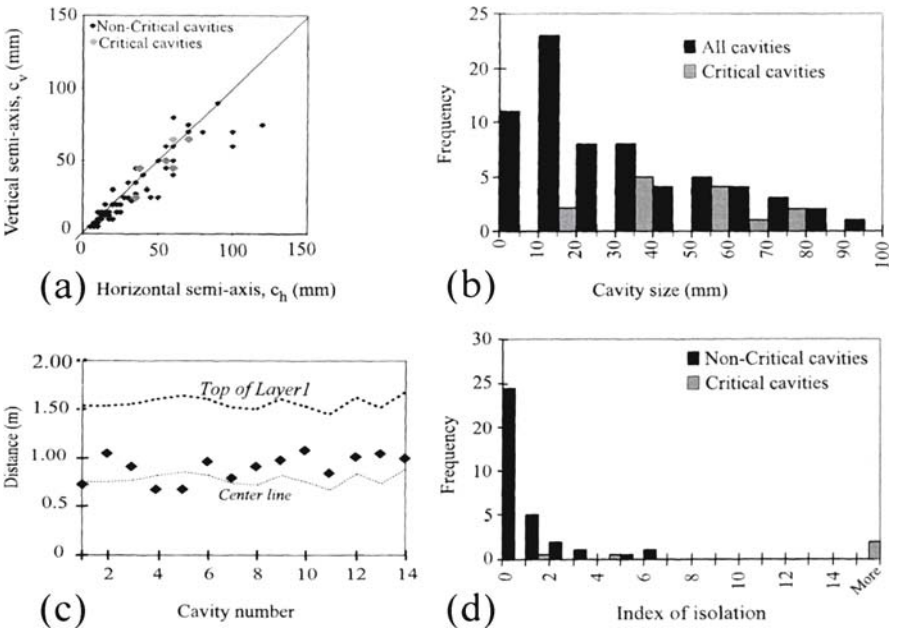

Fig. 2.7. Analysis of cavity shape, size, and distribution in layer 1. **a** In-plane horizontal vs. vertical semi-axes of critical (*gray*) and non-critical (*black*) cavities along an 8 m E-W traverse in layer 1 (Fig. 2.6). **b** Histograms of sizes of critical (*gray*) and non-critical (*black*) cavities in plane 1. **c** Origin location of fourteen cavity-driven joints with respect to the local layer thickness. **d** Histograms of isolation indices of critical (*gray*) and non-critical (*black*) cavities along an 8 m E-W traverse, layer 1 (Fig. 2.6) (from Weinberger 2001a)

Size. The mean characteristic size of all critical cavities ($Z = 44$ mm) is larger than that of non-critical cavities ($Z = 33$ mm). More details are gained from histograms of cavity sizes in layer 1 (Fig. 2.7b). The frequency of critical cavities is different from that of all cavities; relatively small and very large cavities are not associated with joint initiation. Indeed, no critical cavity is among the top five largest and the fifteen smallest cavities.

Location within layer. To test the null hypothesis that cavities (critical and *non*-critical) are randomly distributed with layer 1, the section presented in Fig. 2.6 was divided into 48 area units of 0.5×0.5 m each, and the number of cavities in each unit counted. This procedure provided the observed data for a standard Chi-square test on this cavity population and helped to calculate the expected data based on a Poisson distribution (Davis 1973), with λ equal to the mean size of all cavities. The test concluded that the null hypothesis should be rejected at 95% confidence. Thus, cavity distribution is non-random, reflecting the tendency of cavities to be more abundant toward the layer base. Additionally, of all cavities, critical cavities are generally located closest to the top of the layer. Only 5 out of 58 non-critical cavities are located more closely to the top of the layer than the critical cavities (Fig. 2.6 and 2.7c). In addition, all five are smaller in size than the smallest critical cavity ($C_b = 15$ mm, $C_v = 15$ mm and $C_d = 10$ mm).

Isolation. For each cavity, the distance, *Dj*, was measured from the center of cavity *j* to the center of the in-plane nearest neighbor, and the number of neighbors *Sj* within a radius of 0.5 m around the center of cavity *j* was counted. The dimensionless index of in-plane isolation for cavity *j*, *Ij*, is defined by

$$Ij = \frac{Dj}{Zj} \frac{1}{Sj + 1} \tag{2.3}$$

A high isolation index implies a large distance to the nearest neighbor and a limited number of neighbors. The results indicate that the isolation indices of critical cavities are typically one order of magnitude greater than those of non-critical cavities (Fig. 2.7d), i.e., critical cavities are much more isolated than most of the non-critical cavities. Noticeably, several isolated cavities appearing close to the base of layer 1 are non-critical, e.g., a small cavity at a distance of 6.00 m along the traverse (Fig. 2.6).

Initial growth of joints. Weinberger (2001a) found that the cavity shape plays a minor role in governing the joint initiation points in the Soreq Formation. On the other hand, the cavity size has a noticeable influence on the joint initiation points, because the frequency of critical cavities differs significantly from that of all cavities (Fig. 2.7c) and the mean size of critical cavities is larger than that of non-critical cavities. Noticeably, for two closely located cavities of similar shape, degree of isolation and distance from the layer base, the largest cavity is the one associated with joint initiation (e.g., compare critical cavity 2 and its nearest neighbors to the east at a distance of 0.7 m along the traverse, Fig. 2.6). These observations suggest a cavity size effect, whereby larger cavities preferably fail before smaller ones. This size effect is complicated by post-fracturing dissolution processes that might obliterate the exact cavity size at initiation. Nonetheless, this later dissolution might enlarge all cavities, including the non-critical cavities. Although theoretically the stress concentration factor (SCF-q in Eq. 1.22) of circular hole is 3.0, independent of the size (Lawn 1993, p. 3), actual strength measurements in rock mechanics experiments indicate that sample strength decreases with increasing hole size (Anderson 1995, p. 339). Therefore, the SCF effects of the larger hole act over a wider distance, indicating that the volume over which the stress acts is important for hole failure and rock strength. Other studies have also shown that rock strength decreases with increasing flaw size and flaw density (Wong et al. 1996; Wong and Chau 1998; Bazant and Planas 1998). These size effects, however, are obscured by the fact that they depend on the deformation processes, which in turn depend on the loading conditions (Li et al. 1999). Indeed, in the Soreq Formation, only one critical cavity is among the top five largest cavities, indicating that other factors play a more significant role than the size during jointing.

The distribution of cavities in layer 1 is non-uniform, with cavities clustered toward the layer base. This, in turn, leaves relatively isolated cavities near the middle of the layer, many of which are critical (Fig. 2.6). For two cavities of similar shape, size and distance from the layer base, the more in-plane isolated cavity is the one associated with joint initiation (e.g., compare cavity 6 and non-critical cavity at a distance of 3.45 m along the traverse, Fig. 2.6). The analysis of the stress in the vicinity of a hole in an elastic material indicates that the stress distribution is markedly affected by the hole only within an area of about three radii from the center of the hole (Timoshenko and Goodier 1951). Weinberger (2001a) arrives at the interesting implication that

closely located cavities may inhibit joint initiation because of the stress perturbation induced by adjacent cavities. On the other hand, in more plausible configurations, cavity-driven joints in less dense regions near the middle of the layer might communicate with other cavities, facilitating joint growth caused by stress enhancement.

Three types of ripple marks. Weinberger (2001a) distinguished three types of ripple marks (Fig. 2.5). Type 1 consists of circular-to-elliptical marks and is formed in layers with plentiful cavities. Type 2 consists of semi-circular-to semi-elliptical marks and is formed only in "cavity-free layers". Type 3 consists of marks with approximately similar curvature and is formed in relatively thin layers (<0.4 m).

Summary: Joint growth after initiation from c_i and c_{cr} sites. In summarizing the observations from the study by Weinberger (2001a), the analysis of cavity geometry and distribution reveals that joint initiation at c_{cr} locations is governed by isolated, relatively large cavities, preferably located close to the bedding top and by stress gradients during jointing. In the absence of macroscopic cavities, sites of joint initiation vary in size from c_i to c_{cr} along bedding interfaces (layer boundaries). Consequently, joints typically show several forms of growth, depending on the abundance and spatial distribution of cavities within the layers. In layers with plentiful cavities, joints preferably initiate at critical cavities in the layer interior and propagate vertically upward and downward and horizontally and form circular to elliptical fractures that abruptly end (Fig. 2.4) or more commonly arrest either at layer boundaries or at surfaces of previous joints (Fig. 2.5b). In layers free of cavities, joints commonly nucleate at layer boundaries and propagate downward toward the layer base and adjacent joints (Fig. 2.4, layer 7). Alternatively, they may nucleate at surfaces of previous joints or contacts between joints and layer boundaries (Bahat 1991a, Fig. 4.8).

The various forms of growth in cases where cavities are not apparent are summarized schematically in Fig. 2.8a,b A–H, first defining joint dimensions (Fig. 2.8a). Figure 2.8b A–D show fractographic manifestations of various initiation and growth styles without fringes in single-layer joints. These joints often form fringes along one or two layer boundaries (Fig. 2.8b E, F). Less common are *en echelon* fringes along the distal continuations of joints (Fig. 2.8b G), possibly because the fracture slanting mechanism (Sect. 2.2.5.2) does not promote segmentation there. Very rare are hackle fringes or cuspate hackle fringes (Fig. 2.42) along the distal continuations of single-layer joints in sedimentary rocks (Fig. 2.8b H). In a rare case of a hackle fringe in a sedimentary layer (Fig. 2.30a), the fringe does not occur in a distal position. This general observation, based on thousands of inspections of joint fractographies, provides a strong argument in suggesting that the joints under consideration mostly form under low or very low effective stresses (Sect. 1.5.3).

The division into two forms of fracture growth by Weinberger (2001a) corresponds quite well to an analogous division into two types of fracture growth in technological materials. Breakage in good quality glass bottles most often initiates at the outside wall and propagates inside (towards the center of the bottle), forming semi-circular fracture (Fig. 2.1d), because stress concentrators (e.g., cavities) inside the body are absent. On the other hand, in low-quality materials that contain discontinuities (e.g., cavities/voids), fracture may start from inside the glass body (e.g., Bahat 1991a, Fig. 2.34d) and propagate along directions complying with constraints imposed by the boundary conditions, much as they control fracture in sedimentary layers (Fig. 2.8).

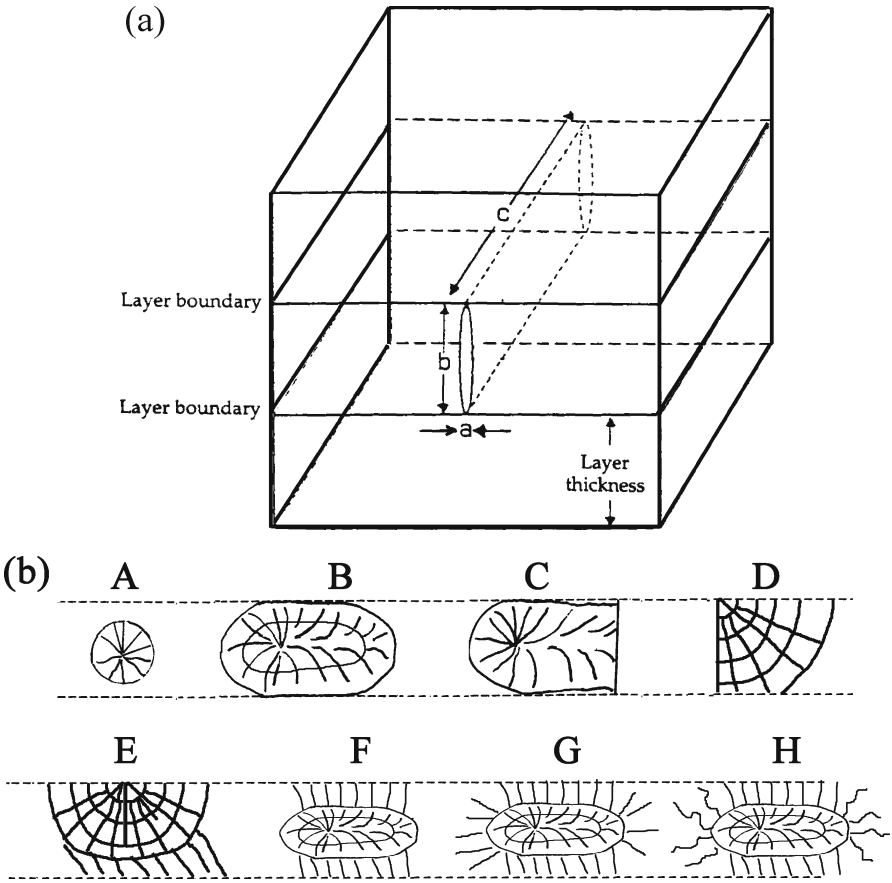

Fig. 2.8. Several styles of joint growth in a rock layer. **a** Definition of thickness, width and length dimensions (*a*–*c*, respectively) of a single-layer joint. **b** Several growth forms of joints, as described by plumes and ripple marks, from left to right: *A*: An initial circular joint; *B*: A full joint growth to an elliptical mirror, limited by the layer boundaries; *C*: An advanced quasi-elliptical joint that arrests along an earlier fracture; *D*: An advanced joint that initiates at a corner formed by a layer boundary and a previous joint; *E*: A semi-elliptical joint initiation at the upper layer boundary and propagation downward creating an *en echelon* fringe; *F*: A full joint growth to an elliptical mirror, forming *en echelon* fringes along the layer boundaries; *G*: A joint like *F* that forms *en echelon* segmentation at its distal ends; *H*: A hypothetical joint *F* that forms hackles at the distal ends (modified after Bahat 1998a and Weinberger 2001a)

2.2.3 Fractographic Experiments

This section brings together a series of fractographic experimental studies (mostly since 1991) that concern fracture areas beyond the critical flaw (Fig. 2.1). The first studies (Sect. 2.2.3.1–2.2.3.7) pertain to fractures that are contained within the boundaries of the mirror plane, while the other studies (Sect. 2.2.3.8–2.2.3.13) relate to fractures that reach the fringe beyond these boundaries. The fractographic results of these studies have implications regarding various tectonofractographic issues, which are discussed in subsequent sections.

2.2.3.1
Experimental Arrest Marks

According to Guin and Wiederhorn (2003), Michalske (1977) carried out on soda lime silicate glass microscope slides the following experiment (Fig. 2.9a–e). First, he propagated a crack in water at a stress intensity factor K_I of 0.375 MPa $m^{1/2}$, which was clearly above the static fatigue limit K_0 (Fig. 4.34). Then, he reduced the applied stress intensity factor to 0.225 MPa $m^{1/2}$, a value clearly below the static fatigue limit, which was inferred from crack growth studies on soda lime silicate glass (Wiederhorn and Bolz 1970). He held the stress intensity for a period of 16 h. Finally, he increased the stress

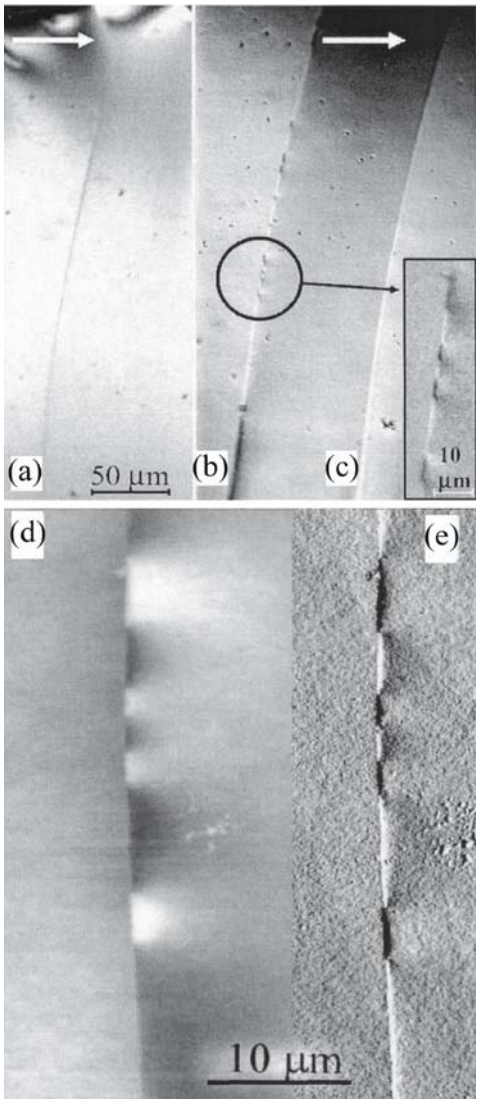

Fig. 2.9.
Optical micrographs obtained by using the height mode, to illustrate the crack deflection along the crack front of crack arrest marks left on fracture surfaces as a consequence of holding the crack for a period of time at a stress-intensity factors that lies below the "fatigue limit". **a** $K_{Ih} = 0.24$ MPa $m^{1/2}$, $t_h = 67$ h, $K_{Ir} = 0.37$ MPa $m^{1/2}$; **b** $K_{Ih} = 0.12$ MPa $m^{1/2}$, $t_h = 48$ h, $K_{Ir} = 0.37$ MPa $m^{1/2}$; **c** $K_{Ih} = 0.12$ MPa $m^{1/2}$, $t_h = 1$ h, $K_{Ir} = 0.35$ MPa $m^{1/2}$, where K_{Ih}, t_h and K_{Ir} are the hold K_I below the static fatigue limit, the hold time and the hold K_I above the static fatigue limit, respectively. The *white arrows* on the figure give the direction of crack propagation. **d** and **e** images by atomic force microscope from the *circled region* of the crack arrest mark shown in **b** using the deflection mode to show the change in slope along the crack front. The crack approaches the arrest mark on a common plane. On *repropagation*, the crack has discontinuously split, some areas along the crack front lying above (*white*) the incoming surface, some areas lying below (*dark gray*) the incoming surface. In **e** the *bright* or *dark hands* indicate a sharp alternate change in crack growth (from Guin and Wiederhorn 2003)

intensity factor to the value used for crack propagation, 0.375 MPa $m^{1/2}$. The time to repropagate the crack was about 2 000 s. Michalske found crack arrest marks on the fracture surface at the site of the arrested cracks that he attributed to restarting crack growth. No such marks were observed for a crack that had its stress intensity factor momentarily reduced and then increased again.

Following up on Michalske's (1977) study and duplicating his experiment, Wiederhorn et al. (2002) and Guin and Wiederhorn (2003) found that the arrest marks appeared not to be the result of blunting, but represented what we term a "split-discontinuity" in the crack surface so that after the hold period below the crack growth threshold, the crack developed waviness that was not there when the crack was arrested (Fig. 2.9b,d,e). By matching both halves of the fracture surface, these authors showed that the split upper and lower surfaces matched across the marks left at the crack front. Within the experimental accuracy of the technique, ±2 nm, crack blunting did not occur. The discovery by Wiederhorn et al. (2002) and Guin and Wiederhorn (2003) of the split-discontinuity shows a subtle but significant mixed mode I and III loading, additional to mode II along arrest marks that form when the crack *restarts* growing (Fig. 2.9e). The implication of this section is discussed in Sect. 2.2.4.2.

2.2.3.2
Experimental Undulations

Richter and Kerkhof (1994) used a method of superposing shock waves or continuous waves onto a static or quasi-static tensile field, causing a crack to propagate in soda lime silicate glass from a starter crack (edge-notched) induced into the glass by thermal or mechanical techniques. This procedure allowed them to create visible, concentric stress wave markings (undulations) on fracture surfaces. The undulations formed in successive positions of crack fronts at definite points in time by applying the stress waves at different modulated frequencies, and this enabled them to calculate the velocity of crack propagation from 10^{-6} m s^{-1} up to the maximum velocity of 1 540 m s^{-1} (Kerkhof 1975). This method has been successfully applied to other materials as well (Richter and Kerkhof 1994).

Figure 2.10 shows a fracture surface of a single edge-notched tensile specimen generated at a stress wave frequency of 5.02 MHz. The fracture surface displays a blunt, starter crack, SC and zones of mist, M, hackle, H, and crack branching, B. The undulations convex in the direction of propagation; they are superimposed by thinner and sharper Wallner lines at different orientations. Also visible are a few straight striae in the mist and hackle zones. In this method, an increase in distances between undulations indi-

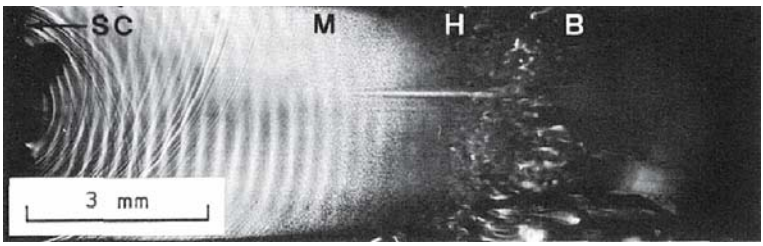

Fig. 2.10. Fracture surface of a single edge-notched tensile specimen showing zones of mist, *M*, hackle, *H*, and crack branching, *B*. Stress wave frequency: 5.02 MHz. *SC* = starter crack (after Kerkhof and Richter 1969)

cates increase in crack velocity. In this example, a relatively high load had to be applied to start propagating the blunt starter crack. Consequently, the crack acceleration was high, leading to wide intervals between the undulations almost throughout the fracture surface, and the maximum crack velocity of 1 540 m s^{-1} was attained. The crack branched beyond the hackle zone after having passing a certain distance at almost a constant crack velocity. After a phase of crack branching, a region of smoother fracture surface occurred.

2.2.3.3
Oscillating Cracks

Yuse and Sano (1993, 1997) applied thermal stress along thin borosilicate cover glasses that varied in size around $100 \times 20 \times 0.1$ mm by heating them to high temperature, T_h (maximum 400 °C), in a hot region. The cover glasses were then moved slowly down into a cold region, T_l (18 °C) at velocity v (maximum 50 mm s^{-1}), while the distance between the upper hot region and the lower cold region was fixed. If v was slow enough, the part of the sample in the hot region was at temperature T_h and the part in the cold region at temperature T_l, imposing a temperature difference $\Delta T \approx T_h - T_l$, and maximum thermal stress between the two regions (Fig. 2.11a). Thus, the control variables of the quasi-static crack propagation were ΔT, v and W, the sample width. Various types of crack patterns were formed by different control parameters. Generally, increasing the values of the control parameters changed the crack morphology from simple to complex, falling into three types with increasing complexity:

1. Straight cracks (Fig. 2.11b).
2. Oscillating cracks (Fig. 2.11c).
3. Branched cracks (Fig. 2.11d,e).

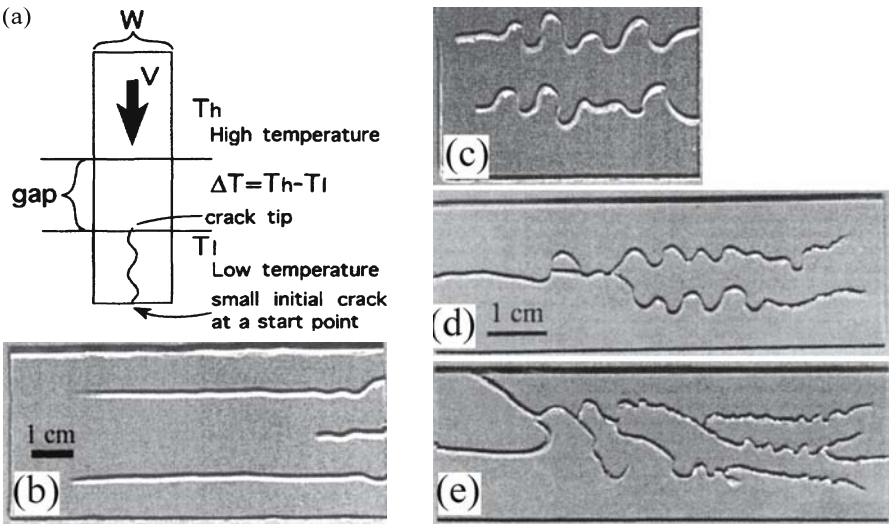

Fig. 2.11. a Configuration of the experiment. A thin sample plate moves slowly across the temperature gradient gap in the direction of the *arrow* with velocity v (after Yuse and Sano 1993). **b–e** Several crack patterns. **b** Straight cracks; **c** two oscillating cracks; **d, e** branched cracks (after Ferney et al. 1999)

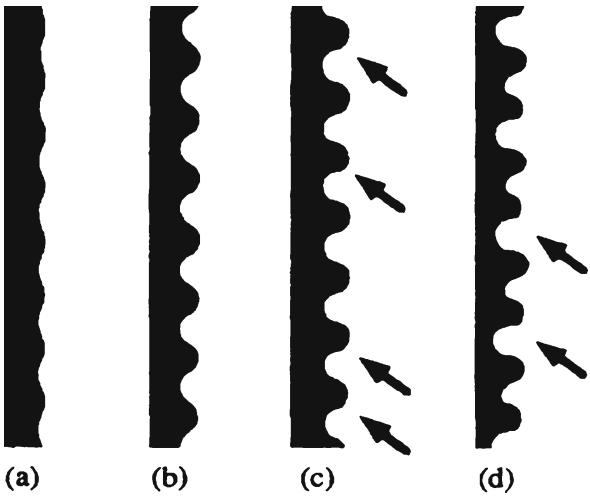

Fig. 2.12.
The morphology of oscillating crack changes from simple to complex with increasing control parameters. *Arrows* show initial cusps. The width is scaled by two (after Yuse and Sano 1993)

We shall concentrate on the oscillating cracks. While both undulations (Sect. 2.2.3.2) and oscillating cracks bend along the crack propagation direction (Fig. 2.11 and 2.12, respectively), undulations appear to superpose as small, secondary bends on primary crack surfaces, while oscillating cracks are larger and exhibit the actual shape of the primary crack. For v and ΔT near the onset of oscillation, the oscillating cracks were almost sinusoidal (Fig. 2.12a). With increasing v or ΔT, the shapes resembled a series of semi-circles (Fig. 2.12b). After that, the crack became asymmetric in the propagation direction. For large v or large ΔT the crack propagated in an almost horizontal direction at a very high speed until it stopped at some distance from the side edge, then grew slowly upward, forming a cusp (Fig. 2.12c). For larger parameters, additional oscillations appear quasi-periodically or double periodically with cusps (Fig. 2.12d).

Yuse and Sano (1997) demonstrate that under severe thermal stresses, cusps replace oscillations within the range where they become asymmetric. Murgatroyd (1942) observed symmetric cusp marks in fractured glass that was caused by a low-energy impact (Bahat 1991a, Fig. 2–20a). He suggested that the crack propagated upward before coming to rest and resumed its course in a slightly downward direction when it recommenced. An asymmetric cusp-like profile was induced in glass by thermal stresses (Bahat 1977). These observations suggest a need to reconcile the occurrences of asymmetric ripple marks and cusps in both slow and fast fracture propagation.

2.2.3.4
The Distinction of Tensile from Shear Fracture Surfaces in Laboratory Tests of Chalk

A full understanding of developments in fracture geology is often hampered by our limited ability to distinguish between "pure" tensile loading (mode I) and processes controlled by shear stresses and mixed mode loading (of modes I, II and III in different combinations), particularly in small sizes (mm–cm). This section relates to this problem. A detailed fractographic technique that was applied on experimentally fractured chalk enabled the establishment of a clear distinction between tensile and shear surfaces (Fig. 2.13–2.17). In their study, Bahat et al. (2001a) tested chalk cylinders

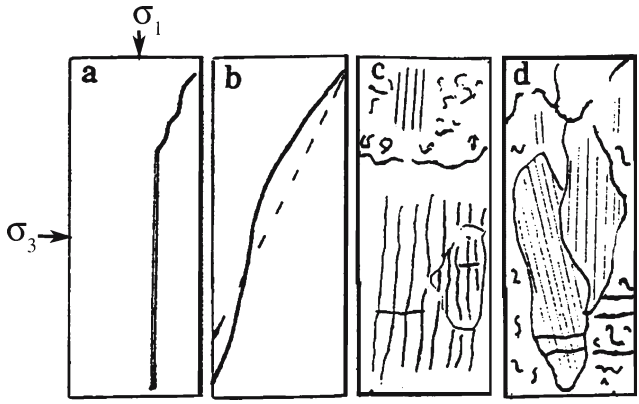

Fig. 2.13. Various types of brittle fracture developed experimentally in chalk. **a**, **b** Profile sections. **a** Longitudinal splitting by uniaxial stress in continuation of initial conic fracture induced by boundary effects at the end of the sample. **b** Shear fracture by a triaxial test, showing formal straight conjugate cut (*dashed line*) and actual curved fracture. **c**, **d** Parallel sections. **c** Derived by uniaxial test, showing a shear surface above, separated by a boundary from a tensile surface subdivided into domains below it. **d** Meso-fracture, cutting throughout the sample, formed by a triaxial test, showing adjacent domains marked by ridges and grooves in different orientations (from Bahat et al. 2001a)

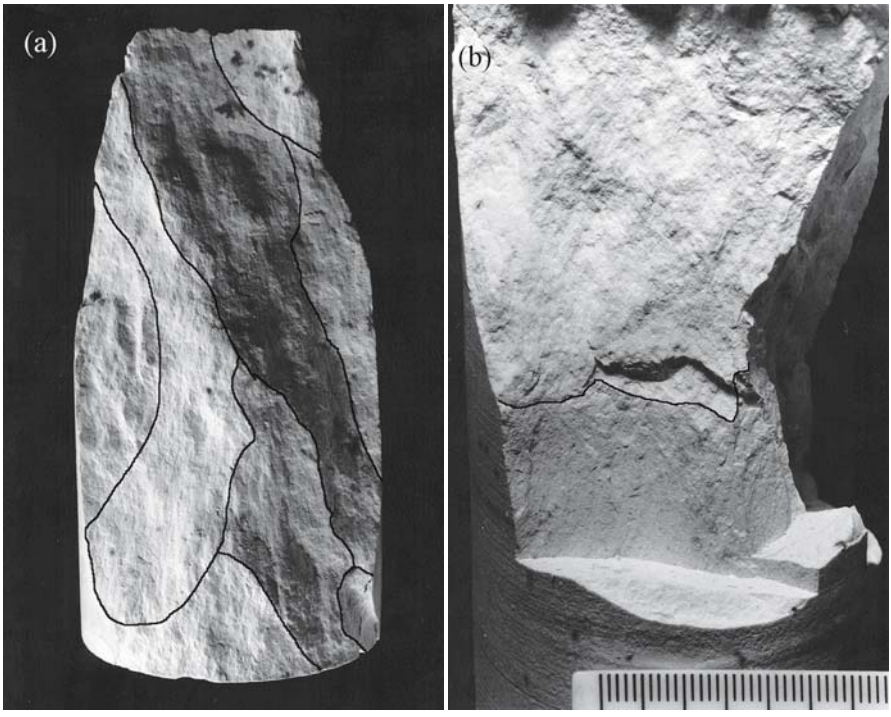

Fig. 2.14. Photographs of fractured chalks under triaxial stresses (cm scale). **a** A shear surface divided into distinct domains in which ridges and grooves slightly change their orientation. **b** A section shows three parts from bottom to top, the original cylinder, a tensile crack (*gray*) and a large shear crack (*white*), respectively. The shear part displays conjugate Lüders' bands (from Bahat et al. 2001a)

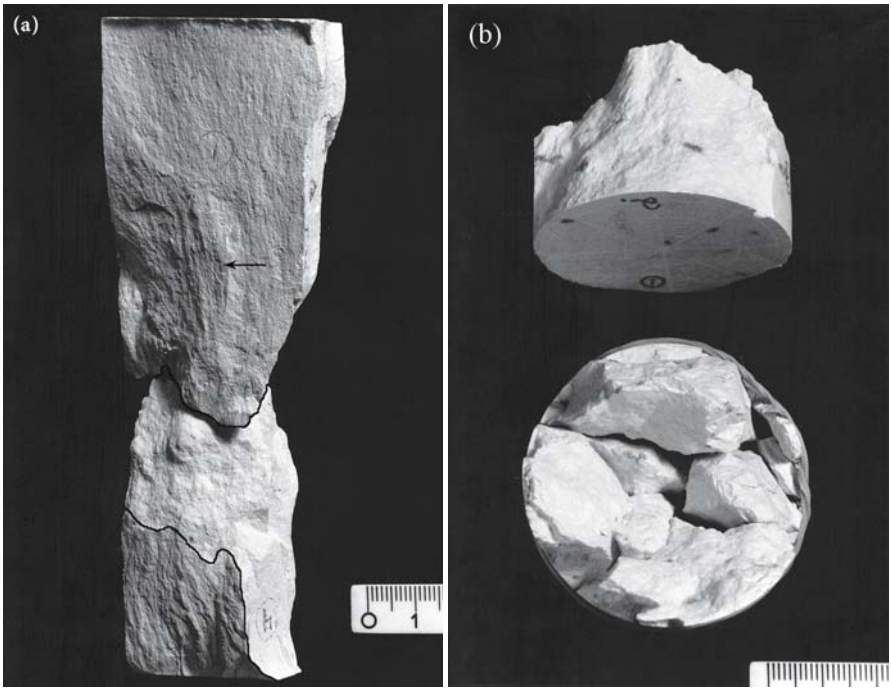

Fig. 2.15. Photographs of fractured chalks under uniaxial stresses (cm scale). **a** A longitudinal split dominated by an axial tensile fracture. The two tensile parts are displaced in order to show a late inclined shear fracture (between upper and lower boundaries) that crossed the split. Sub-axial plumes mark the split. **b** Reconstruction of an original cylinder (at upright position, below) and the quasi-cone (axis parallels to **a**) (from Bahat et al. 2001a)

100 mm long and 52 mm in diameter under both uniaxial and triaxial loading. At the end of this section, we present results of a recent study on the pore radii of this chalk (Rabinovitch et al. 2003a).

Summary of results. The results of the above study are condensed below as follows.

1. The drying and desiccation procedures of the chalk used in the study resulted in high compressive strength results (σ_1–σ_3) ranging from 37.7 MPa to 52.6 MPa.
2. With the exception of a few cylinders that fractured either by a single shear fracture or by strongly dominated longitudinal splittings, most samples under both triaxial and uniaxial loading failed by a combination of shear and tensile fracture (Fig. 2.13–2.15).
3. The authors identified several "key surface morphologies" according to shear and tensile categories (Fig. 2.13). Shear features include a sugary texture, ridges and grooves (RG) and steps (Fig. 2.14). The RG appear on sheared white sugary, ragged surfaces that form curved topographies within boundaries of individual domains (of about 3 to 10 cm^2 in size). RG in neighboring domains may form various angular relationships with the cylindrical axis and are either parallel or sub-parallel to the fracture dip. An individual domain on a shear surface is often subdivided into sub-domains (of about

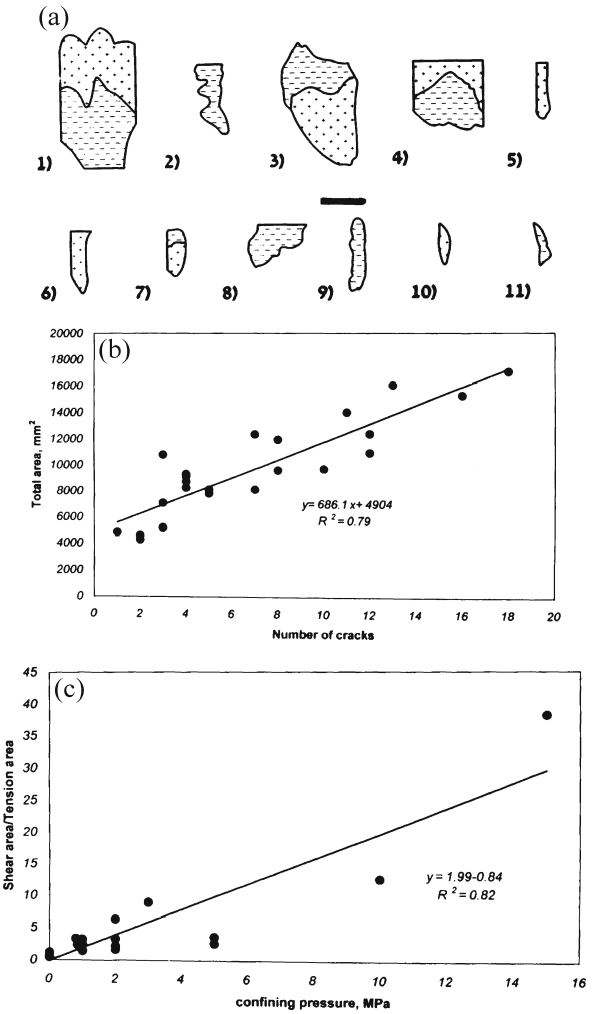

Fig. 2.16.
a A display of half of the total number of fracture surfaces (one of each matching couple) from a sample. Shear surfaces are marked by '–' and tensile surfaces by '+'. *Scale bar* is 4 cm. **b** Relationship between the number of fractures (one from each two matching fractures) and total area of all fractures. **c** Relationship between the ratio of (fractured area by shear) / (fractured area by extension), and lateral compression, σ_3 (from Bahat et al. 2001a)

0.5–1 cm^2 in size) that occur at different topographic elevations. RG maintain the same orientation in passing from sub-domain to sub-domain, indicating the continuity of fracture. A sub-domain consists of a set of microcracks (≤ 0.1–4 mm long) that are aligned along the RG that cross sub-domain boundaries within individual domains. No wing cracks (Sect. 2.4.2) were found on the fracture surfaces.

Tensile features include plumes (or striae) and stairs (Fig. 2.15). The plumes appear as braids on planar tensile surfaces of a matt white-grayish color and on the micro-scale the barbs are sub-parallel to the cylindrical axis. In tensile domains (that are of approximate sizes of shear domains), "stairs" result in a division of large surfaces into smaller planar sub-domains at different elevations, ranging in size from 0.5 cm^2 to 2 cm^2. Sub-domains maintain the general plume orientation within a domain. Domains of all tensile surfaces are planar and smooth, either parallel or sub-parallel to the cylindrical axis.

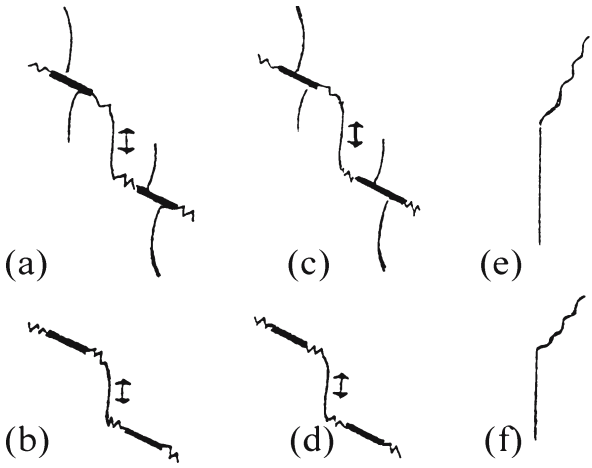

Fig. 2.17.
Schematic summaries of six modes of crack propagation from two experiments on weak rocks. **a**, **b** In uniaxial compression and **c**, **d** in biaxial compression. *Thick inclined lines* are pre-cuts, *zigzag inclined lines* are new shear fractures and *subvertical, slightly curved thin lines* are wing cracks (from Bobet and Einstein 1998, Tables 3 and 4). **e** In uniaxial compression, and **f** in triaxial compression from the present study (without pre-cuts): Shear fractures show ragged profiles and are inclined, and tensile fractures are straight and parallel to σ_1, not showing wing curvature (from Bahat et al. 2001a)

4. Whereas tensile longitudinal splitting (Sect. 2.2.13) can stretch continuously on a parallel tensile plane or on adjacent parallel planes, shear failure into meso-fractures (that divides the cylinder into two pieces) combines a series of distinct domains on separate surfaces that slightly differ in curvature and orientation. Thus, a key feature of single shear fractures (Fig. 2.14a,b) is their strong deviation from planar into concave and convex topographies (Fig. 2.13b). Therefore, surfaces of shear fractures have considerably larger areas than the "nominal" ones, whereas in tensile fractures "actual" and "nominal" surfaces are similar.
5. The reconstruction of the original cylindrical samples was accomplished by assembling the pieces (Fig. 2.15b), which enabled the determination of the fracture sequences that resulted in our experiments by the cross cutting relationships. Four fracture sequences were distinguished:
   a several stages of longitudinal splitting,
   b initial quasi-cone and subsequent longitudinal splitting,
   c longitudinal splitting that initiated from around the sample peripheries and subsequent inclined shear fracture, and
   d longitudinal splitting that initiated from around the sample center and subsequent inclined shear fracture. Generally, the sequence on shear surfaces is incipient shear fracture displayed by RG that occurs before total loss of cohesion, which is then followed by displacement shown by steps.
6. Conic and incomplete "quasi-cones" (Fig. 2.15b) may be obtained under both uniaxial and triaxial tests. The patterns of the tensile fractures often vary with the shape of the quasi-cones from two large matching longitudinal splits to repeated subdivisions into radial longitudinal splitting.
7. The tensile and shear areas that formed were quantified on each fractured sample (Fig. 2.16a). The total fracture area increases with the number of cracks (and fragments) (Fig. 2.16b). The ratio of "fractured area by shear" to "fractured area by tension" tends to increase with confining pressure σ_3 (Fig. 2.16c). Triaxial failures resulted in a few fractures (some 1–12 pieces) and in ratios of total shear area to tensile area >1, while uniaxial failure resulted in many fractures (some seven to eighteen pieces) and in ratios of total shear area to tensile area <1 (Fig. 2.16c).

8. There is a distinct trend of length increase of the longitudinal splits with the decrease of the confining pressure, as shown below by three samples: From 1 cm (when $\sigma_3 = 5$ MPa) through 2 cm (when $\sigma_3 = 2$ MPa) to 4 cm (when $\sigma_3 = 1$ MPa). This correlation shows that tensile longitudinal splitting occurs also under triaxial stresses, where the extent of the tensile fracture is inversely controlled by the confining pressure.
9. Most large fractures are composites of fracture domains. Fractures formed under both uniaxial and triaxial compression show that there is a strong correlation between the orientation of cracks (small fractures) and their mode of propagation: Shear cracks are inclined to σ_1 (Fig. 2.13b), while tensile cracks are parallel or sub-parallel to σ_1 (Fig. 2.13a and 2.17) The transitional angle between the two is $\alpha_c = 8 \pm 2°$. This correlation possibly supports previous suggestions that early microcracks are linked by inclined shear cracks (e.g., Hoek and Bieniawski 1966) rather than by tensile cracks (see implications of this observation in Sect. 2.2.12).
10. The authors correlated variations of the electromagnetic radiation (EMR) with changes of crack sizes in the fractured chalk throughout the investigated stress range (see elaboration in Chap. 5).
11. The multi-fracture complexes exhibited by the chalk samples bear a greater resemblance to surface ruptures that display wide belts of shear zones (associated with earthquakes that occurred in weak crusts) than to single slip surfaces simulated in strong rocks. The possible implication is that fracture in weak crusts is simulated better on weak rocks than on strong ones.

Microcrack populations and orientations. Stress induced microcracks that constitute RG on shear fractures generally are parallel or sub-parallel to the fracture dip, i.e., they may be tilted up to about 10° right or left with respect to the fracture dip (on parallel sections) (Fig. 2.13c–d). Likewise, barbs that constitute plumes on tensile surfaces are sub-parallel to the fracture dip. Whereas microcrack lengths can readily be measured between their tips on RG, barb lengths on tensile surfaces are not clearly defined, because they are continuously connected to form plumes. Microcracks may vary from sub mm to several cm in length, where the upper sizes are limited by the sub-domain and domain boundaries. The cm-long cracks and the microcracks commonly maintain the same sub-axial orientation.

All the meso-fractures that cut through the chalk cylinders (and have surfaces on the order of 50 cm^2 in size) display fracture-composites of domains and sub-domains consisting of microcrack coalescence. These assemblages are more common on the three-dimensional shear fractures (Fig. 2.14a) but also occur on planar tensile surfaces. Note, for example, that even the "uniform" large tensile fracture shown in Fig. 2.15a is divided into a "lower" surface marked by a delicate plume and an "upper" surface (partly shaded) marked by a coarser one (black arrow). Both plumes have the same orientations on the two sub-domains, suggesting that the planar fractures propagated in "sets", much like joint sets in the field.

The large EMR pulse populations at low stresses are obtained from many microcracks. Some of these microcracks possibly reflect dilatancy under both uniaxial and triaxial loadings. Dilatancy is generally understood to occur between one-third and two-thirds of the macroscopic fracture stress and is associated with an opening of mirocracks throughout the sample normal to σ_1 (Brace et al. 1966). Sprunt and Brace

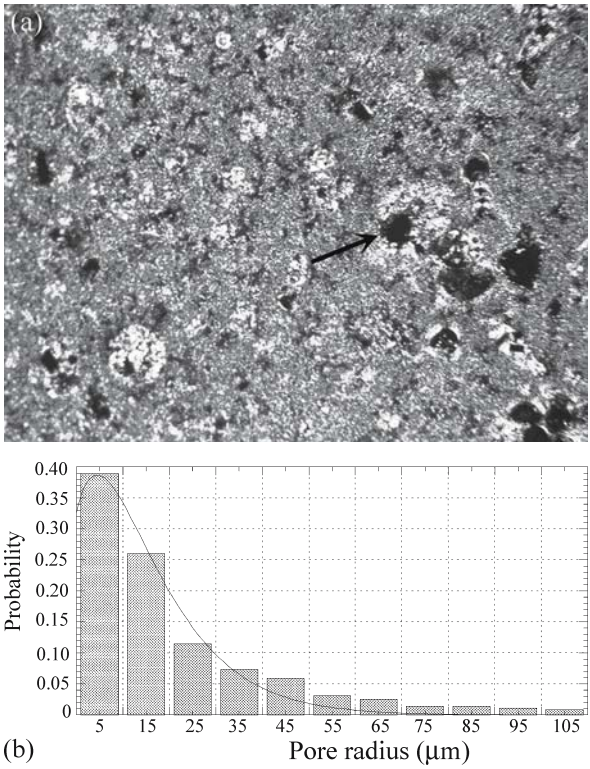

Fig. 2.18.
a Photomicrograph of a Middle Eocene (Horsha Formation) chalk (width of picture is 1.2 mm). *Large white spots* are plankton skeletons, *small white spots* are microsparites, and *gray patches* are micrites (calcite). *Black spots* are pores (the one shown by *arrow* is 84 μm in diameter) and iron oxide grains. **b** Measured pore radii distribution in **a**, fitted to $P'(r) = a^2 r \exp(-ar)$; best fit obtained for $a = 0.105 \pm 0.004\ \mu m^{-1}$ ($R^2 = 0.98$) (**a** and **b** after Rabinovitch et al. 2003a)

(1974) observed that stress-induced microcracks are distinguishable from the initial defects in the rock in their shapes and orientations. The stress-induced microcracks are sharp-ended and elongated sub parallel to σ_1, whereas the initial defects are blunt and are oriented in all directions. Our results show that EMR pulses can be correlated with microcracking throughout most of the stress range, i.e., much earlier than one-third of the peak stress (Chap. 5). This includes pulses at the lower range of σ_1, probably in association with the deformation of "initial defects" (pores). Note that since EMR pulses are created solely by cracks and not by existing defects, this deformation must consist of some cracking. The measured pore radii distribution in the chalk is presented here for reference (Fig. 2.18).

Ridges and grooves and incipient shear before failure. Ridges and grooves (RG) are elongated lineations (slickenlines/slickensides) parallel to the direction of relative slip on fault surfaces. However, their origin is not clear (Davis and Reynolds 1996 p. 277). It is not understood why continuous lineations are longer than the known displacement along faults (Hobbs et al. 1976, p. 303) and how these lineations can be formed when the displacement is negligible (Means 1987). The results obtained by Bahat et al. (2001a) only exacerbate this dilemma. They obtained RG on fractured surfaces that had practically zero displacement. These surfaces did not cut through their respective cylinder peripheries; instead, they were arrested within the cylindrical samples (Fig. 2.14b). The close resemblance of the RG in the latter samples to RG that occur on

surfaces that were relatively displaced (e.g., Bahat et al. 2001a, sample 16) is also intriguing. The only fractographic difference is that steps occur on the fracture surface of sample 16 but not on that of sample 15 in which the cut was arrested within the sample. The implication is that RG develop by the shear process during a decrease in sample cohesion due to microcracking prior to failure. The clear morphology of the plumes in these cases is a compelling indication of the lack of relative displacement on them because such displacements would have erased the delicate plumes.

It is possible therefore to distinguish an incipient shear when some but not total cohesion is lost. This is the time when the grooves and ridges are formed. The displacement that occurs subsequently is recorded by steps that can be assigned to a total loss of cohesion. These observations partly resemble results obtained by Wibberley et al. (2000), who identified an "incipient breakdown zone" at the immediate tip of the micro-fault. This zone consisted of early, long, pervasive tensile micro-cracks, oriented parallel to σ_1 that were later cross-linked by a set of *perpendicular short tensile* microcracks (unlike the results by Bahat et al. 2001a), leading to a subsequent failure.

Inclined shear and axial tensile fractures. The strong correlation between crack orientation and mode of propagation mentioned above relates to both cracks several mm to several cm in length and fractures up to about 10 cm in length. This correlation does not automatically apply to microcracks below 0.1 mm in size, for which Bahat et al. (2001a) did not have accurate fractographic observations. If, however, this correlation could be confirmed for micro-sized cracks, it might have important implications regarding the transition from microcracks to meso-fractures close to the triaxial peak stresses. This would imply that the initial axial tensile fractures (longitudinal splits) were connected by oblique shear microcracks. It would correspond to the observations by Shen et al. (1995) and Bobet and Einstein (1998) on fractures in gypsum, and by us on inclined shear fractures in chalks (Fig. 2.17). Note that Hoek and Bieniawski (1966) also suggest that early microcracks are linked by inclined shear cracks, with the difference that the latter authors assumed the early microcracks to be inclined to σ_1. The "connection" by oblique shear microcracks would differ from the models by Horii and Nemat-Nasser (1985) and by Reches and Lockner (1994), who advocate that such a connection is carried out in granite by tensile microcracks. Additional experiments backed up by close fractographic examination of induced tensile/shear fractures should help to ascertain whether the application of results on microcrack linkage obtained on weak materials (gypsum and chalk) to strong ones (e.g., granite) is justified.

2.2.3.5
Experimental Fracture on Five Sedimentary Rocks

Berea sandstone, Marianna limestone, Hasmark dolomite, Repetto siltstone and Muddy shale have been subjected to triaxial compression tests, measuring the confining pressures, the compressive strength (maximum ordinate of the stress-strain curve) and the dihedral angle 2α (measured relative to the maximum principal stress direction) by Handin et al. (1963). They show that both the compressive strength and dihedral angle results varied considerably in the five tested rocks. Generally, these rocks were weak (not stronger than 6 MPa), and the dihedral angles range was large (ranging

between 0° and 80°) (see Table 2.2). No correlation between the dihedral angle and the confining pressures can be detected for these rocks. We are not aware of significant deviations from the results presented here that have been found for similar rocks by additional investigators (e.g., Friedman and Logan 1973).

2.2.3.6
Experimental Fracture on the Chelmsford Granite

The compressive strength of the Chelmsford granite ranges from 106 MPa to 200 MPa (Peng and Johnson 1972). Peng and Johnson (1972, Fig. 27) observed strong preferred orientation of the growing microcracks under stress along the splits. Characteristically, about 70–80% of the microcracks were oriented within 10° off the maximum principal stress direction σ_1. Some of the microcracks were straight, while others were partly curved. Holzhausen and Johnson (1979) also observed that a characteristic mode of failure for uniformly stressed specimens of Chelmsford granite was evidence of longitudinal splits that were inclined up to about 10° from σ_1. We interpret the straight splits to be essentially extensile (mode I) even if they form small angles 5 ±5° with the load direction (Peng and Johnson 1972, Fig. 18), whereas curved microcracks reflect local growth under shear. This interpretation follows the criteria derived from experimental observations by Bahat et al. (2001a) that shear cracks are inclined (also curved) to σ_1, while tensile cracks are (straight) parallel or sub-parallel to this direction. However, since these criteria concern the behavior of microcracks in a weak rock (chalk), the analogy to a strong rock (granite) should be presently qualified until more evidence becomes available to support it.

2.2.3.7
Experimental Fracture on Glass Ceramic

The fracture properties of glass ceramic induced by compression were investigated by combined electromagnetic radiation (Chap. 5) and fractographic methods (Bahat et al. 2002a). The study of a transparent sample enabled the fractographical elucidation of the sequence of crack nucleation, growth and interaction, and the ultimate longitudinal splitting under the incremental increase of uniaxial stress in five stages. Sample failure by longitudinal split occurred under uniaxial compression of 112 MPa in the fifth stage. A split into two slightly unequal parts (termed larger and smaller) took place along a straight, smooth plane parallel to the sample axis such that different fracture events were identified on the surfaces of the two parts (see more about the sample shape and experimental procedure in Bahat et al. 2002a). Experiments on transparent samples (Germanovich and Dyskin 2000 and references therein, and Sect. 2.4.2.2) were aimed at different objectives.

Striae (plumes) stretch continuously along the fracture surface of the large part almost from end to end of the sample (Fig. 2.19a). They start from an origin that is located about 18 mm from the F end (see below) and 86 mm from the B end, and occur at about mid distance (10 mm) from the two lateral edges of the main fracture. The striae radiate in two directions towards the two ends of the specimen. The bulk of the striae propagate towards the B end such that with the increase of distance from the origin

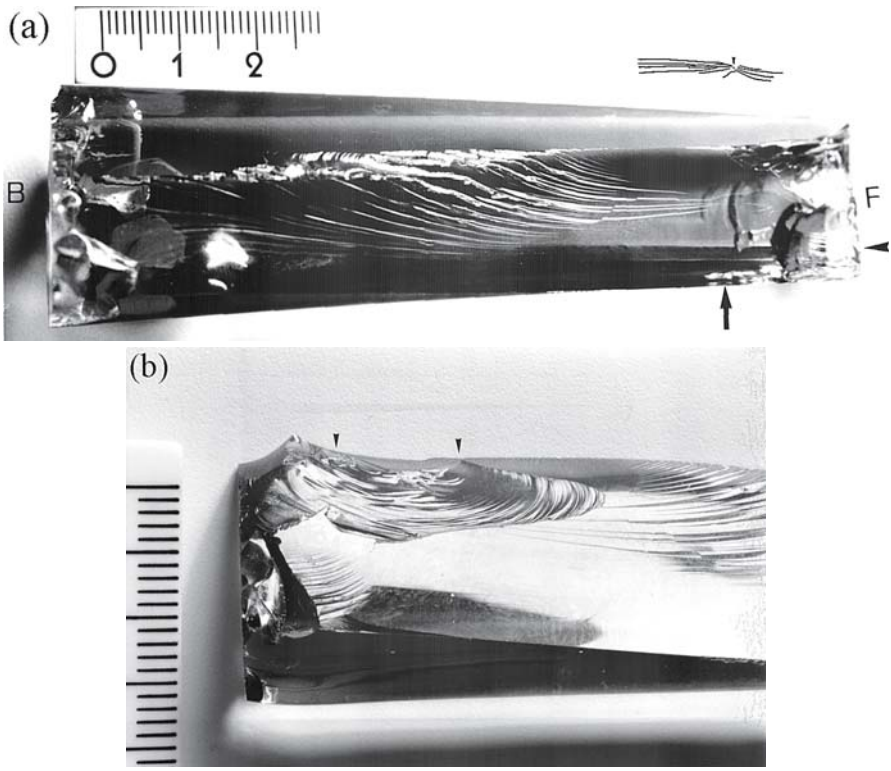

Fig. 2.19. Longitudinal split in a transparent glass ceramic. **a** Striae initiate above *vertical arrow* and propagate bilaterally (see *inset* above photograph) toward *B* and *F* ends of specimen (*horizontal arrow* shows striae at the *F* end) in one part of the split. Striae initiate within the specimen. They propagate along straight trajectories towards the *B* end at first. When gradually growing in size they approach the upper surface of specimen and curve towards that boundary. **b** Two successive cracks that formed after the specimen failure and split formation, when stress has relaxed. Two *arrows* mark the size of the first, successive crack (after Bahat et al. 2002a)

gradual coarsening of the striae morphology occurs. Only three-four short (6–7 mm long) striae propagated towards the F end (inset in Fig. 2.19a). Accordingly, the exact location of the origin, that is, the focus where the radial striae originated, is within an area of 1–2 × 1–2 mm, which we term the "nucleation zone". A microscopic examination indicates that the nucleation zone is not associated with any morphological discontinuities (wing cracks, glass defects etc.). Moreover, the transparency of the sample enables us to verify that no microcracks occur underneath the origin. Various shades in axial and transversal-concentric orientations around the origin are reflections from the outer surface of sample and do not belong to the main fracture surface. Hence, a longitudinal split along almost the entire length of the sample was partly straight and parallel to the compression axis before being deflected by the sample boundaries in the strong glass ceramic material. The second part of the split contains two successive cracks that formed after the specimen failure and split formation, when stress has relaxed, as indicated by the electromagnetic radiation results (Sect. 5.3.4) (Fig. 2.19b).

2.2.3.8
Inducement of En Echelon *Fractures by Mixed Mode I + III in PMMA*

Cooke and Pollard (1996) experimented on rectangular blocks ($15 \times 15 \times 5$ cm, ASTM E399-83) of polymethyl methacrylate (PMMA or Plexiglas), resembling the conceptual fracture mechanics models of mixed mode loading by Lawn (1993, Fig. 2.3) and Broek (1991, Fig. 1.3). They built a system that enabled them to load cracks in mixed mode I + III. Initially, a starter crack was grown from a chevron notch at a rate of about 1 cm in 10 s up to the peak load. Then, when the crack has reached the desired length, the sample was unloaded in order to begin the mixed mode portion of the experiment. They made the distinction that if mixed mode I + II loading is changed abruptly on a quasi-static fracture, the propagation path follows a sharp kink (Erdogan and Sih 1963) (Fig. 2.20a). On the other hand, if the K_{II}/K_I ratio is smoothly changed on a continuously propagating crack, laboratory fractures follow a continuously curving crack path (Cotterell and Rice 1980; Thomas and Pollard 1993) (Fig. 2.20b). A similar relationship between the loading history and the smoothness of the path is expected for mixed mode I + III loading (Fig. 2.20c,d). Cooke and Pollard (1996) considered that fracture propagation paths depend not only on the load ratio applied but also on sample geometry, loading configuration, and interaction among growing fractures.

Cooke and Pollard (1996) found that both the angle of twist ω of the *en echelon* cracks (Fig. 2.21a) and the number of segments formed increase with the increase of the ratio K_{III}/K_I. They however observed that the increase of ω with the ratio K_{III}/K_I falls below theoretical predictions (Cooke and Pollard 1996, Fig. 14). They propose that

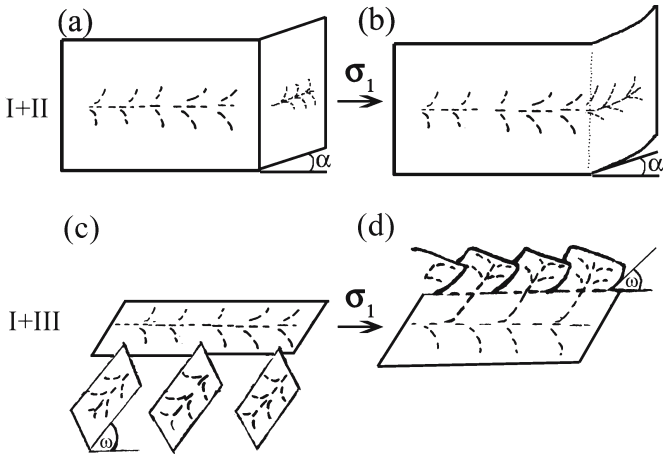

Fig. 2.20. Mixed mode fracture propagation paths for various loadings, when the maximum principal stress σ_1 is horizontal. **a** If a crack is loaded abruptly in mode I + II, a sharp kink is produced, forming the α angle at the distal part of the parent joint; the plume on the parent joint discontinues and a new plume forms on the kink. **b** If mixed mode I + II loading is increased gradually, as the fracture propagates, a path that follows a curve results and the plume on the parent joint continues to the curved kink that forms. **c** An abrupt I + III loading produces twisted echelon segmentation at ω on fringes that form along one or two layer boundaries, the plume on the parent joint discontinues and new plumes form on the fringe. **d** If mixed mode I + III loading is increased gradually, *en echelon* segments that gradually curve result, and the plume on the parent joint continues to the curved segments (modified after Cooke and Pollard 1996)

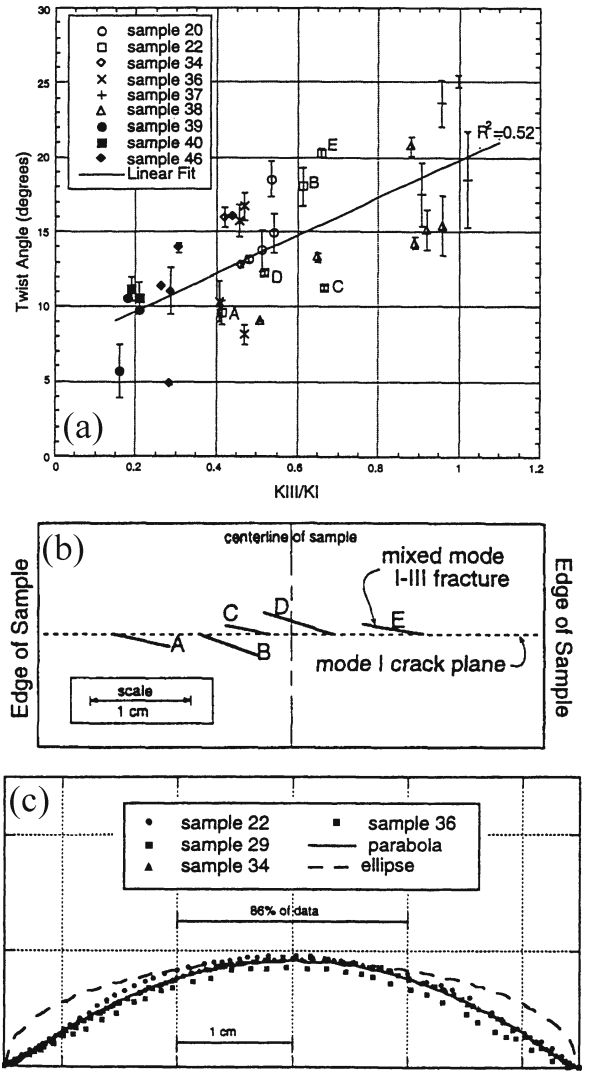

Fig. 2.21.
a Twist angle between parent crack and incipient fracture after break-down vs. stress intensity ratio for nine samples. A linear best fit through all measurements shows a trend of increasing twist angle with K_{III}/K_I. For each sample a similar trend can be observed as K_{III}/K_I varies with echelon fracture location along the breakdown front. Data from sample 22 are labeled with letters corresponding to digitized fractures in Fig. 2.21b and show a trend of increasing twist angle with K_{III}/K_I. **b** Digitized data from an experimental result showing breakdown geometry. Fracture *C* is sandwiched between fractures *B* and *D*. While the overlap with *B* is minor, there is considerable overlap between fractures *C* and *D*. The mechanical interaction between adjacent cracks may act to decrease the angle of twist in experimental and natural mixed mode I + III fractures. **c** Breakdown front shape for four samples compared with half ellipse with major axis of 5.0 cm and half mirror axis of 0.92 cm. The elliptical shape matches best at the center of the sample where most of the data are collected. The difference between the half ellipse approximating the crack front and a best fit through the crack front data is less than 0.1 cm (12%) in the region $-1\text{ cm} < z < 1\text{ cm}$ where 86% of the data are collected (from Cooke and Pollard 1996)

interaction among growing fractures (Fig. 2.21b) may contribute to the discrepancy between theoretically predicted twist angles and those observed in these and other mixed mode I + III experiments. Cooke and Pollard (1996) noted that the majority of the *en echelon* fractures form at the center of the sample where the ellipse best approximates the parabolic breakdown fronts (Fig. 2.21c). Such breakdowns often occur in nature as well (e.g., center of Fig. 2.35c), suggesting that their results are applicable in geological outcrops.

Cooke and Pollard found that the crack front advanced further than expected compared to the trailing edges at the sample sides (Fig. 2.21c). They suggested that when the sample sides are oppositely displaced in a tearing motion by mode III, a component of mode II stress intensity K_{II} is applied to the curved crack front near the sides of

the sample. This is because the direction of shear is not perfectly parallel to the fracture front. Thus, a local mode II is induced in the system loaded by mode III. Similar load superpositions probably occur around the tips of all normal and reverse faults. This experimental finding is supported by a similar study that was carried out on the behavior of the crack front in fractured glass bottles. "Edge effects" caused the mist and hackle zones to advance more at the front center compared to the trailing edges of these zones at their intersection with the bottle's outside surface (Bahat et al. 1982, Fig. 4).

2.2.3.9
Fractography of Tensile Cracks in Starch-Water Mixtures

We briefly cite below a study on desiccation cracks in starch-water mixtures of 50–100 mm in diameter and 2–40 mm in thickness that were investigated by Müller and Dahm (2000) and Müller (2000). Fracture velocities were measured from videos and estimated from photos. Fractures covered the range from spontaneous nucleation, dynamic cracks with velocities of 100–200 mm s^{-1} to quasi-static cracks with velocities of 0.1 mm s^{-1} and less. Plumes that formed on the fracture surface gave the fracture direction (Fig. 2.22a), and their relation to fracture velocity was similar to the relation between seismic rays and seismic wave velocity. A ray-tracing method from seismology was used to calculate plume lines for depth-dependent rupture velocity. Moreover, an inverse method, based on finite difference travel times and conjugate gradients, was developed to invert a set of measured plume directions into a rupture-velocity distribution, which could also depend on the horizontal coordinate on the fracture surface. The main results and conclusions of this study are as follows.

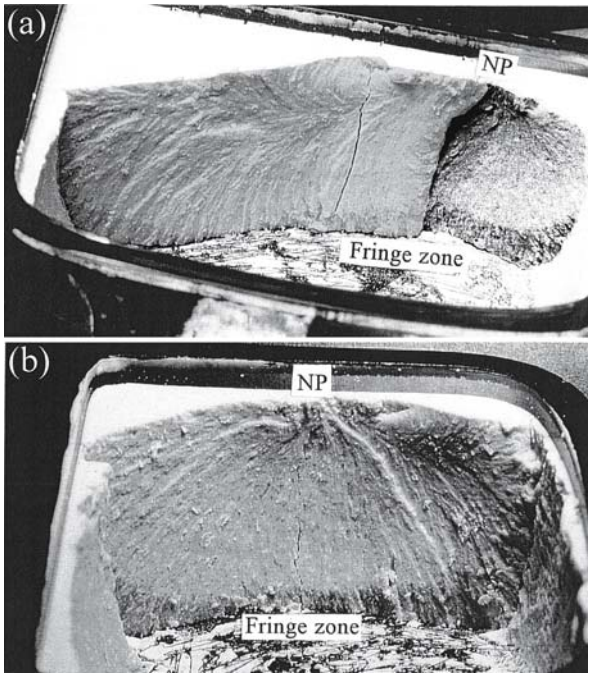

Fig. 2.22.
Fracture surface in starch. **a** A coarse plume propagates on the parent joint from the nucleation point *NP*. A fringe zone shows an angular tilt from the parent joint at the lower right. **b** A coarse fringe zone, where fracture velocity was lowest, formed beyond a mirror boundary. Length (diameter) of specimen is 65 mm (after Müller 2000)

1. Plume lines can successfully be inverted into relative fracture velocity.
2. In thin starch layers (thickness less than 0.2 times the diameter), fracture velocity decreases from top to bottom by a factor of 2–5, following a decrease of tensile stress due to the increase in water concentration.
3. Horizontal variation of fracture velocity reflects horizontal variation of stress, including stress relaxation due to the propagating crack, and ranges from dynamic to quasi-static velocities.
4. In thick starch layers (thickness about 0.5 times diameter), fracture is predominantly quasi-static.
5. Starch cracks sometimes have a fringe zone where topographic amplitudes of the *en echelon* segments are higher and rupture velocities lower than on the main part of the crack (Fig. 2.22b); this probably also applies to joints in rocks and their fringe zones.
6. Starch-water mixtures at rupture have a Poisson ratio close to 0.5. Cracks in starch are closest to subsidence or diagenesis joints in sedimentary racks.

There is some reservation regarding the interpretation of the fringe shown in Fig. 2.22b, because its morphology deviates from the common perfect shingling of *en echelon* segmentation, often seen in nature (e.g., Fig. 2.35). This deviation should possibly be assigned to the material properties and the difficulties involved in its maturing during the fracture process. There is no doubt, however, regarding the distinction between the mirror and the fringe in Fig. 2.22b.

2.2.3.10
Formation of Fringe Cracks in Silicon Single Crystal

Cramer et al., (1999, 2000) conducted dynamic fracture experiments on silicon single crystal plates that were loaded to force a {110} cleavage crack in a <110> direction. The fractographic features that resulted vary with the changes in the average crack velocity v_{av} and the energy release rate G. The fracture surface is smooth and mirror-like at the lowest fracture stress, corresponding to $G = 7$ J m^{-2} (*circles* in Fig. 2.23a). At $G \leq 14$ J m^{-2} and above $v_{av} = 3\,000$ m s$^{-1} = (2/3)v_R$, the Rayleigh wave velocity (triangles in Fig. 2.23a). Atomic Force Microscopy (AFM) reveals that the crack partially deviated from the initial (110) plane and displays hills and valleys extending in the crack propagation direction. Facets appear on {111} planes next to the mirror with further increase in G. The size of the facets increases with increasing G. Instability, exhibited by an abrupt onset of rough hackle zones, starts at $G > 40$ J m^{-2} and at velocities close to V (or v_{ter}), the terminal crack velocity (squares in Fig. 2.23a). The instabilities are manifested by the cracks on the {111} facets to "overgrow" each other, displayed by the simultaneous propagation of two crack fronts and in secondary shear fracture of the material placed between them (Fig. 2.23d).

Thus, there are three modes that show how the excess energy formed with the fracture growth is spent. Initially, the excess energy contributes to the increase in crack velocity. More excess energy results in faceting. Finally, great excess energies lead to path instabilities, resulting in the propagation of multiple cracks. The path instabilities in the silicon plates bear similarities to the bifurcation instability found in PMMA by Sharon and Fineberg (1999). The important difference, however, between the latter

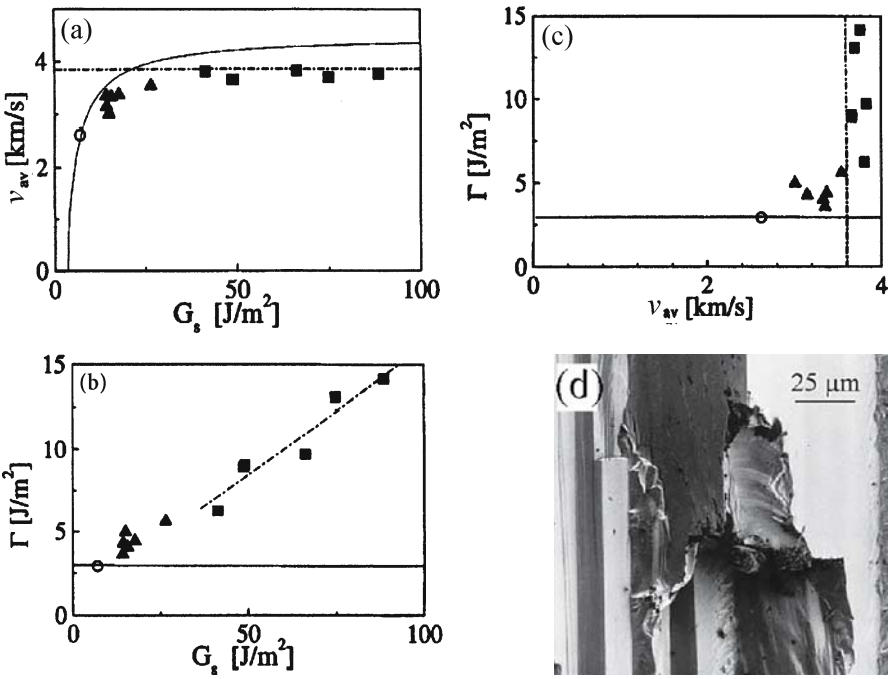

Fig. 2.23. a Dependence of the average fracture velocity v_{av} on the steady state energy release rate G_s. At the lowest G_s (*open circle*) the fracture surface is smooth. A faceted fracture surface is observed at higher G_s (*triangles*). The fracture surface is very rough at the highest G_s (*squares*). The *solid line* follows their Eq. 1, which is given by our Eqs. 1.134–1.136, using $\Gamma = 3$ J m^{-2}. **b** This equation is used to determine Γ as a function of G, and **c** as a function of v_{av}. **d** SEM micrograph, showing smooth *en echelon* segments cleaved from top to bottom at {111} planes (*light*) that are bridged by steps of shear cracks (*dark*) (from Cramer et al. 2000)

and the result by Cramer et al. (2000) (Fig. 2.23d), is that the bifurcation in the isotropic amorphous PMMA occurs along various alternative fracture paths, whereas in the silicon crystal instability develops by tensile cleavage on particular planes that are essentially *en echelon* cracks, which are connected by shear fractures, often termed steps or bridges (Fig. 2.39). Hence, under constraints of anisotropy, *en echelon* segmentation may occur at fracture terminal velocities.

2.2.3.11
Simulation of En Echelon*/Hackle Fringes and Longitudinal Splits in Glass*

A brief description of the investigation. We introduced new loading techniques (Fig. 2.24a–c) in investigating the formation of transitional *en echelon*/hackle fringes and longitudinal splits in soda-lime glass samples. Previous investigators combined sequential loading of mode III after mode I for obtaining *en echelon* fringes (e.g., Sect. 2.2.3.7). In the new experimental setting, a remote uniaxial compression was applied on cylinders (10 cm in length and 3 cm in diameter) that contained pre-cuts along the sample walls. Therefore, the compression was transformed into local mixed mode I + III

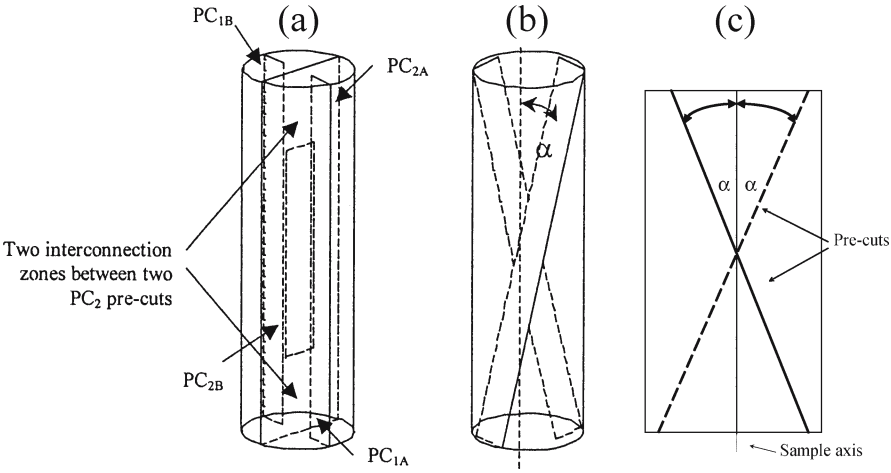

Fig. 2.24. Two pre-cut types. **a** The first type consists of two pairs of pre-cuts (PC_1 and PC_2) parallel to the sample vertical axis. The PC_1 pair is normally oriented to PC_2. PC_{1A} and PC_{1B} are the first and second pre-cuts, respectively, of the first pair PC_1, while PC_{2A} and PC_{2B} are the first and second pre-cuts, respectively, of the second pair PC_2. PC_{2A} and PC_{2B} are interconnected at the top and at the bottom ends of the samples. Depth of the interconnection zones at each end of the sample is 30 mm. **b** The second type consists of two pre-cuts inclined ("X"-wise) to the sample vertical axis. Both pre-cuts create approximately the same inclination angles α to the vertical axis. **c** Measurement of α is carried out between the pre-cut and the vertical axis of the sample

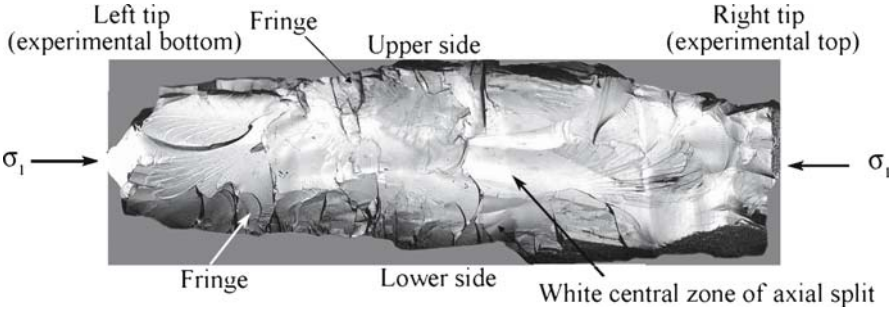

Fig. 2.25. A photograph of a fracture surface of glass that resulted by failure of the second type (135 MPa). Sample length is 100 mm. The sample is rotated 90° clockwise into a horizontal position and *thick arrows* show the direction of the uniaxial compression. Note the plumes that extend close to the two tips in continuation with the axial split at the center

loading, resulting in segmentation into two fringes along the pre-cuts. Subsequently, a longitudinal split of complex fractography formed along the fringes (Fig. 2.25).

Experiment. Two types of crack pre-cut geometries were introduced into the sample walls. The depth of all pre-cuts was 10 mm and aperture 2 mm. The first type consists of two pairs of pre-cuts parallel to the sample vertical axis (Fig. 2.24a, with one pair (PC_1) normally oriented to the other (PC_2)). Two pre-cuts, PC_{2A} and PC_{2B}, of the second pair were also interconnected at the top and bottom ends of the sample. The depth of the interconnection zones was 30 mm at both end parts of the sample. The

second type consists of two pre-cuts inclined (X-wise) to the vertical sample axis (Fig. 2.24b), creating a series of pre-cut angles α, while maintaining about the same α ($\pm 2°$) for the two pre-cuts (Fig. 2.24c). Note that for the first pre-cut type, $\alpha = 0°$. Glass cylinders in the size tested are very strong and generally resisted stresses beyond 200 MPa that we could achieve with our instrument. The introduction of pre-cuts to the samples weakened them. Another method of reducing the effective strength of the material is applied by using truncated elliptic cone shaped samples (Bahat et al. 2002a).

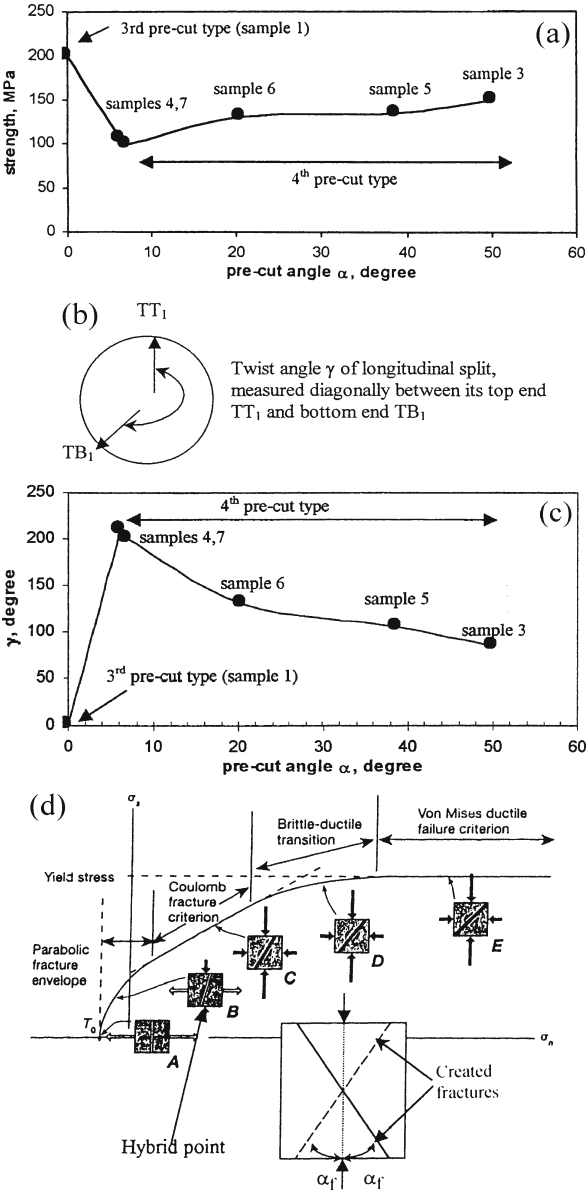

Fig. 2.26.
Fracture parameters of the cylindrical glass. **a** The relation between the pre-cut angle α and sample strength. **b** A look at the sample along the axis. **c** The relation between α and the twist angle of longitudinal splits γ. **d** Schematic picture of a failure envelop, showing an increase stress, corresponding to the increase in the fracture angle α_f created by joints/faults (modified from Twiss and Moores 1992, Fig. 9.9)

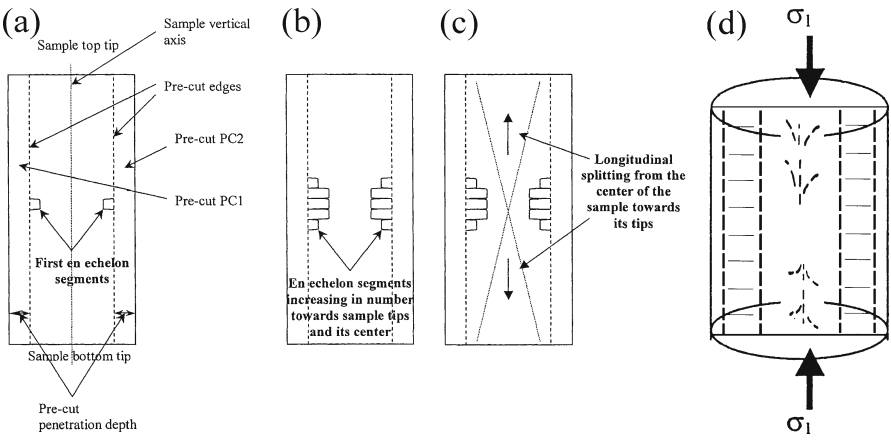

Fig. 2.27. A flat 2D projection of the 3D (twisted splits) surface created during failure of glass samples of the second type. The fracture process consists of three main stages. **a** Nucleation of *en echelon* segmentation at the edges of both pre-cuts at about the middle of sample height. **b** An increase of the *en echelon* dimensions and number, towards the sample center and along both edges of pre-cuts towards sample tips. **c** Propagation of axial splits from *en echelon* fringes (at about the mid sample height) to sample tips (see *arrows*) along the sample vertical axis. **d** Schematic arrangement of three zones, pre-cut, *en echelon* fringe and longitudinal split in the sample

Results. Generally, longitudinal splits do not start from the sample center, because this is a zone of great strength. They often initiate from the sample tip peripheries and propagate axially to the center. Weakening of the sample center can however initiate a longitudinal split there due to local tension induced by buckling (Holzhausen and Johnson 1979) or as in the present study by *en echelon* segmentation. The introduction of the second type of pre-cuts to the samples enables one to study the systematic dependence of strength on α (Fig. 2.26a), showing minimum glass strength at 6.5–7 ±2°, and then a rise in α requires an increase in load. The enlargement of α augments the angle produced between the *en echelon* fringes that form along the pre-cuts in the "X"-wise structure (Fig. 2.26b). The longitudinal splits that form along the fringes interact with each other creating a twist along the cylindrical axis. The twist measured by γ (Fig. 2.26b) increases with α, and the shape of the curve in Fig. 2.26c produces a mirror image of Fig. 2.26a. It is quite intriguing that the minimum and maximum in Fig. 2.26a and c, respectively, are close to the maximum deviation of splits from the sample axis in conventional tests (in granite, Sect. 2.2.3.6, and in chalk, Sect. 2.2.3.4). The fracture sequence is diagrammatically shown in Fig. 2.27a–c.

Discussion. Contrary to previous experiments and many field exposures in sediments that exhibit transitions from parent fractures to fringes, the present study simulates a reverse transition. We demonstrate a transition from fringes to parent fractures by changing local mixed mode I + III to a local single mode I. Monitoring of the electromagnetic radiation (FMR) that was induced by the fractured samples enabled us to determine in real time the sequence of events, the fracture size and the fracture velocities along the various failure stages (Sect. 5.3.4). Very often geological descriptions trail behind descriptions of experimental results. Presently, the fracture sequence described here may be reasoned to be an "unlikely geological process". However, new,

"unexpected" fracture phenomena are repeatedly discovered in granites (Chap. 4), and who knows what else is still concealed from us there? The stress analysis of these unexpected results is currently under investigation.

2.2.3.12 *Hackle Formation in Polymers*

Arakawa and Takahashi (1991) compared fractographic parameters to several mechanical ones in polymers. Fractography was measured by two methods, pit density and surface roughness λ. They scanned the fracture surfaces with a scanning instrument at an interval of 0.5 mm using a needle (10 μm in tip radius) in the direction perpendicular to the direction of crack propagation and defined surface roughness using the term "root mean square roughness" (RMS):

$$\mathrm{RMS} = \left[\frac{1}{L} \int_0^L |f(x)|^2 \, \mathrm{d}x \right]^{1/2} \tag{2.4}$$

where L is the scanned length and $f(x)$ is the roughness height at the point x. Arakawa and Takahashi (1991) found a good correlation between changes in pit density and surface roughness. They employed the shadow optical method of caustics to evaluate K_d and K_c, the dynamic tensile stress intensity factor during crack propagation and the tensile stress intensity factor for the arresting crack, respectively, where a Cranz-Shardin type high speed camera was used. K_d was evaluated by

$$K_d = \frac{2\sqrt{2\pi}}{3Z_0 dc^* \eta^{3/2}} \left(\frac{\phi}{3.17} \right)^{5/2} \tag{2.5}$$

where ϕ is the caustic diameter, Z_0 is a distance between the specimen and the image plane, d is the specimen thickness, c^* is the stress-optical constant for dynamic conditions and η is a convergence factor for incident light rays.

Arakawa and Takahashi (1991) show that the curve linearly correlating crack velocity, v with K_d, may be divided into three regions of different slopes in Hommalite-100 (Fig. 2.28a). There is a gradual increase in K_d with v in the low velocity region A, where λ remained relatively smooth. In region B, there is a rapid increase in K_d along very short intervals of v and a corresponding increase in λ. The curve slope in region C exhibits an additional rapid increase in K_d and an extremely rough surface that reached its peak prior to branching. The latter slope clearly shows that branching did not occur at the peak crack velocity but at the maximum value of K_d, i.e., branching is K_d dependent. The dotted curve connects the peak velocity points, separating the accelerating and decelerating areas in the diagram (see below).

Arakawa and Takahashi (1991) show that maximum λ is best correlated with G_v. The physical meaning of G_v is energy per unit crack width per unit time, and it is considered to relate to the flow rate of energy into the crack tip region. A very good fit among the maxima of the curves of λ, G and G_v occurs for epoxy (araldite D), while it is shown that crack lengths giving peak values of λ and v differ from each other (Fig. 2.28b). A slight discrepancy between crack lengths also seems to exist, giving peak values of λ

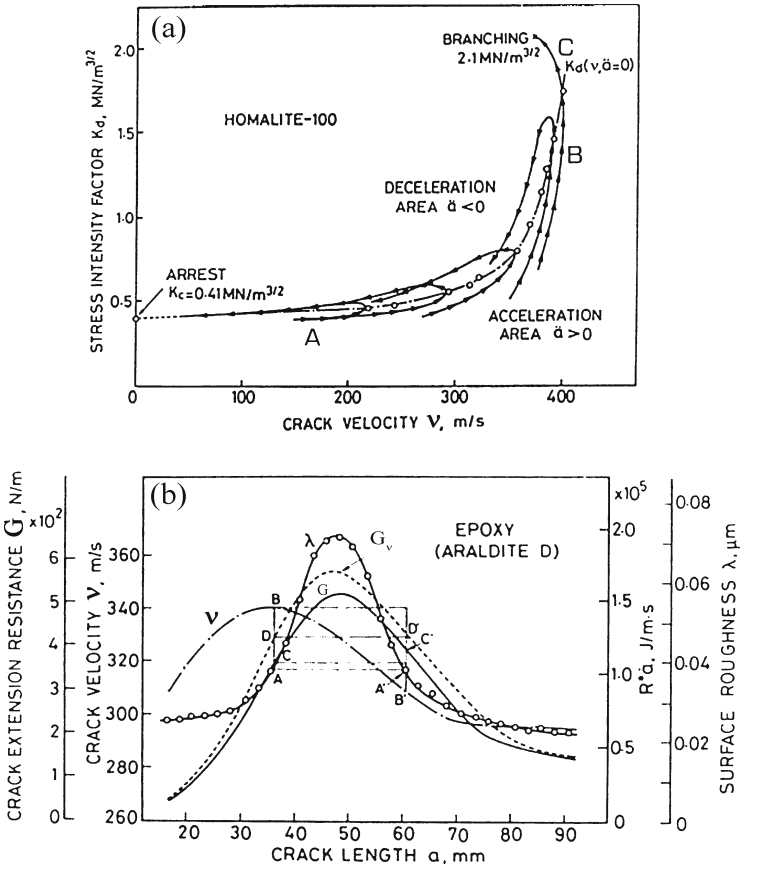

Fig. 2.28. **a** Dependence of stress intensity factor K_d, fracture velocity v and fracture acceleration $\ddot{a}$ in Homalite-100 on fracture length (after Arakawa and Takahashi 1991). **b** Surface roughness λ, specific crack extension resistance G and the product of G_v for epoxy as a function of crack length a (after Arakawa and Takahashi 1991)

and G: For the same λ values indicated by points A and A', the corresponding values of v (at points B and B') or G (at points C and C') slightly differed. On the other hand, a good agreement is shown between crack lengths giving the peak values of λ and G_v, and the values of G_v are almost equal at points D and D', which correspond to points A and A', respectively. These results support the suggestion that λ is dependent on G_v. Hence, the implication is that in the examined polymeric materials, λ behavior (presumably along the traverse through the mirror-mist-hackle-branching, Fig. 2.1) is correlated with G_v, K_d, G, and v in a decreasing order. The results by Arakawa and Takahashi (1991) were confirmed by Arakawa et al. (2000), using different experimental conditions on PMMA. These studies demonstrate that maxima in Fig. 2.28a and b (particularly the latter) show strong fluctuations in the various parameters along the crack length. The *association* of v with the formation of hackle in polymeric materials shows, however, the subordinate *dependence* of this morphology on v. On the other hand, these results indicate the important influence that G_v and K_d have on the formation of hackles.

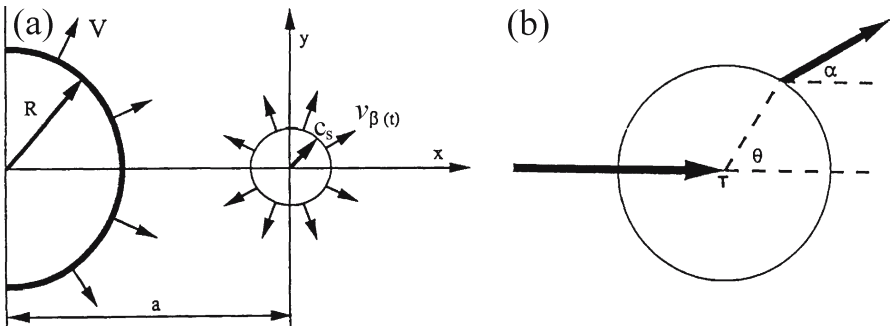

Fig. 2.29. Primary and secondary cracks. **a** A schematic picture of the geometrical setup. A secondary crack of length $2c_s$ at a distance a from the origin of the primary crack of a semicircular radius R starts to grow at velocity $v_{\beta(t)}$ when $t = 0$. **b** Side view of the primary crack, T its tip, while θ and α are the starting growth angle of an existing flaw and the direction of its growth into a secondary crack, respectively (after Rabinovitch et al. 2000a)

2.2.3.13
Hackle Formation in Glass

Previous views about the mist and hackle zones maintain that they are "identical in appearance but different in scale" (e.g., Mecholsky 1991). More recently, however, Rabinovitch et al. (2000a) suggested a fundamental difference between these zones, as explained below. The secondary cracks (SC) start to grow from an existing "Griffith flaw" (Sect. 1.1.2 and 2.2.2) when the critical stress intensity K_{IC} is attained in front of the tip of the primary crack (PC) cutting the glass (Fig. 2.29 and Sect. 1.4.4). The SC move under a changing stress field caused by the PC, whose distance from the SC is continuously changing. Hence the SC start from zero velocity, and asymptotically reach v_t. In the mist zone, the PC overtakes the SC almost instantly after they begin to grow. Therefore, the SC in this zone are short (for details see Rabinovitch et al. 2000b). However, towards the end of the mist zone, the growing SC become longer before the PC overtakes them, and they manage to attain larger sizes and rougher morphologies. Apparently, the transition to the hackle zone is related to the inability of the PC to catch up with the SC. In this case, the SC grow separately compared to those SC that are to a large extent "swallowed up" by the PC and form the mist (Rabinovitch et al. 2000a). Previous authors made the (erroneous) assumption that the SC move from their very incipience, with the same v_{ter} of the PC, resulting in parabolic or hyperbolic shapes throughout. Such shapes actually appear in the hackle zone but not before. Hence, hackle formation is associated with the distinct attainments of v_{ter} by both the primary and the secondary cracks. This *association* however does not imply a *dependence* of hackle formation on v_{ter}. It has been suggested that hackle formation is rather stress intensity dependent (e.g., Bahat et al. 1982). This dependence seems to be more intricate than the latter, as is shown in Sect. 2.2.3.12.

2.2.3.14
The Sequence of Mirror, Mist, Hackle Fringe and Branching on Fracture Surfaces of Glass

It has been accepted by many authors (e.g., Rice 1984, Fig. 1; Hull 1999, Fig. 5.3 and 5.31) that fracture growth from the origin to its termination is in the following "conventional order":

The mirror plane, mist, hackle and branching (branching at the right side of Fig. 2.1b and Fig. 2.10). Branching involves the creation of two secondary fractures, at least one of which is non-coplanar with the primary fracture. Accordingly, a distinction has been made between the radii from the origin to the mist boundary, the hackle boundary and to branching (Fig. 2.1d). This view is quite surprising, considering the existence of many observations that are unlike the conventional order. Rice (1984, Fig. 66b), Ravi-Chandar and Knauss (1984d IV, Fig. 11), Holloway (1986, Fig. 13), Hull (1999, Fig. 5.4) and Bahat et al. (2001b, Fig. 2b) obtained results of a different "fractographic sequence". They show that the mist zone is followed by a transition zone from mist to small hackles, beyond which a drastic change of superposing large hackles on new branches occurs. This indicates simultaneous growths of these two features, i.e., branching occurs before large hackles (branching at the left side of Fig. 2.1b). The same fractographic sequence occurs on joint surfaces in chalks and geological exposures of granites (Fig. 2.30a,b and 2.56). These observations should equate the radii from the origin to the hackle boundary and to branching. What could be the reason for the discrepancy between the "conventional order" and the "fractographic sequence"?

Possibly, the results of repeated four cycles from the mirror plane to branching shown below can be used for explanation. A soda lime silicate glass bottle was fractured by the internal pressure technique (Bahat 1991a, p. 121). The saddle-shaped fragments that characteristically result in such fractures (Fig. 2.30c), which show repeated branching in profile (Fig. 2.30d), were investigated. A saddle-shaped fragment shows the initiation of four cycles from mirror to successive branchings in plan view (Fig. 2.30e). A primary mirror M1 passes on to mist m and then to hackle h, ending in fracture-branching that initiates in the outer boundary of the hackle, at h. The second cycle starts in secondary mirrors that form a shingle-like *en echelon* segmentation M2 that transforms into secondary mist m and hackle h, where a new branching occurs. The third cycle starts by a series of tertiary mirrors M3 in a disturbed shingle-like segmentation. On one mirror, there are undulations that convex in the direction of fracture propagation. The fourth cycle (only part of it has been retrieved) is "disorganized" such that tertiary and quaternary mirrors M4 have no distinct boundaries.

Most intriguing is the change from cycle to cycle when each branching starts with new mirrors. The first branching occurs at the outer boundary of the first hackle (before M2), following the "conventional order". However, the second hackle is already divided into two sub-zones, such that the first one (before M3) belongs to the second cycle, while the second hackle sub-zone rests on the early parts of the third cycle mirrors, M3. The next hackle zone occurs beyond a mist zone at the ends of M3 but also appears to have initiated the fourth cycle, M4. Thus, one observes superposing hackles on the new branch, indicating simultaneous growths of these two features according to the above "fractographic sequence". Hence, both "conventional order" and "fractographic sequence" occur adjacent to each other, forming during the early (second cycle) and late (fourth cycle) stages of the same experiment, respectively, while the fractography of the third cycle, M3, shows a transition between the two.

The occurrence of the "fractographic sequence" in geological exposures (Fig. 2.30a and 2.56) encourages efforts to comprehend the meaning of cycling fractography that may help to improve the understanding of the paleostress conditions leading to dynamic jointing (Sect. 2.4.6.1 and Chap. 4). A possible future discovery of a "conventional order" in geological exposures may add important information for detailed interpretation of the fracture process.

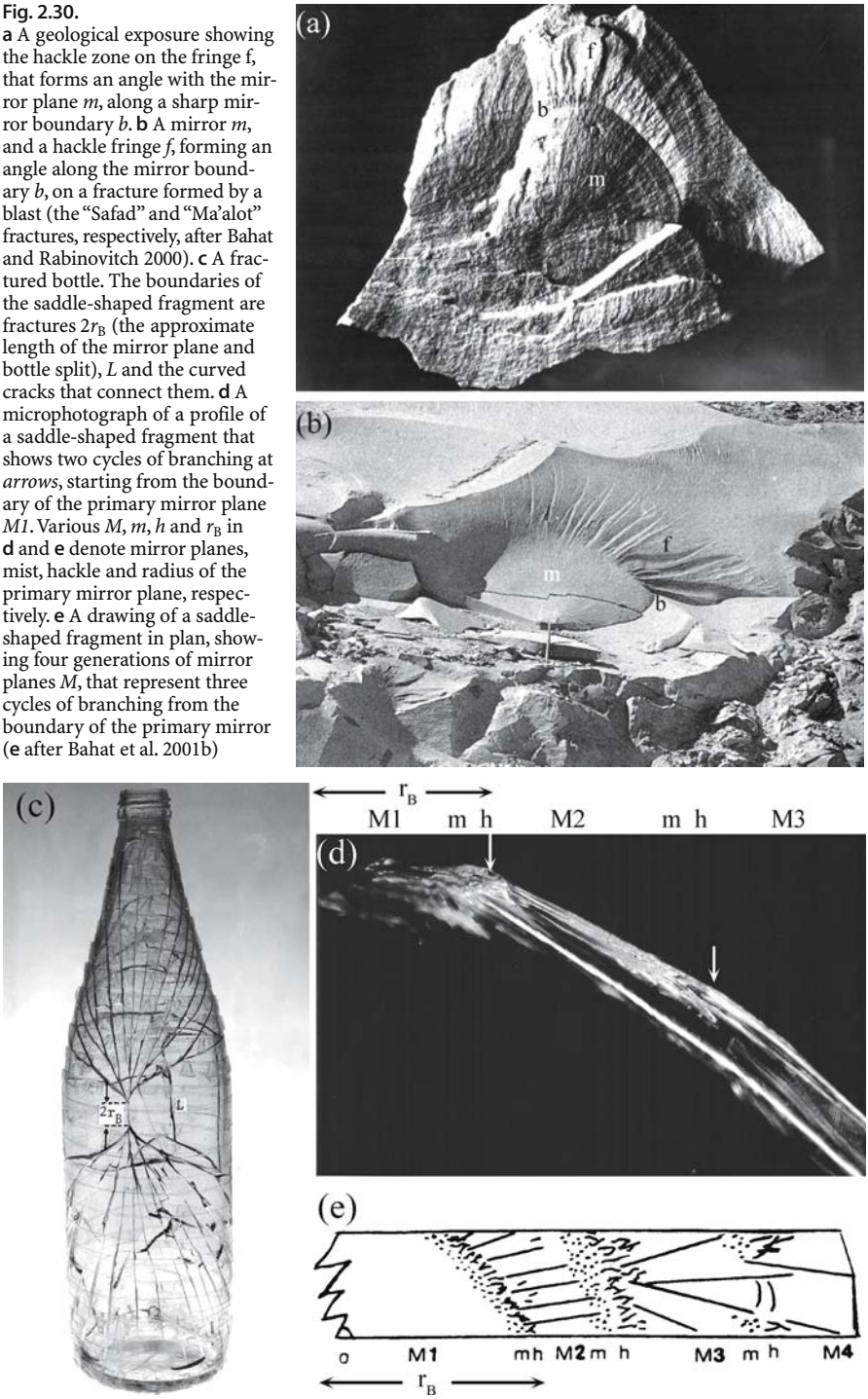

Fig. 2.30.
a A geological exposure showing the hackle zone on the fringe f, that forms an angle with the mirror plane *m*, along a sharp mirror boundary *b*. **b** A mirror *m*, and a hackle fringe *f*, forming an angle along the mirror boundary *b*, on a fracture formed by a blast (the "Safad" and "Ma'alot" fractures, respectively, after Bahat and Rabinovitch 2000). **c** A fractured bottle. The boundaries of the saddle-shaped fragment are fractures $2r_B$ (the approximate length of the mirror plane and bottle split), *L* and the curved cracks that connect them. **d** A microphotograph of a profile of a saddle-shaped fragment that shows two cycles of branching at *arrows*, starting from the boundary of the primary mirror plane *M1*. Various *M*, *m*, *h* and r_B in **d** and **e** denote mirror planes, mist, hackle and radius of the primary mirror plane, respectively. **e** A drawing of a saddle-shaped fragment in plan, showing four generations of mirror planes *M*, that represent three cycles of branching from the boundary of the primary mirror (**e** after Bahat et al. 2001b)

2.2.3.15
Fracture Interaction at Contacts along Layer Boundaries by a Numerical Experiment

The nature of interaction between adjacent fractures has been investigated for decades both in the laboratory and in geological outcrops (e.g., Yokobori et al. 1971; Olson and Pollard 1989, 1991; Bahat 1991a, p. 317). This section relates to fracture interaction with *layer boundaries*, which is fundamental to fracture geology. Furthermore, within layered sedimentary rocks, the termination of fractures at *layer boundaries* can limit vertical flow (particularly in the unsaturated zone, Sect. 6.9) and produce highly tortuous flow paths (e.g., Tsang 1984). In contrast, fractures that propagate straight-through *layer boundaries* (vertically and at various oblique angles) (e.g., Bahat 1991a, Fig. 4.5) provide well-connected pathways for vertical fluid flow (Cooke and Underwood 2001). A potential intermediate case for fluid flow is a fracture that jogs or steps over a few centimeters along successive *layer boundaries* (see the profile in Fig. 2.31). Composite joints, such as those sketched in Fig. 2.31 are believed to form by repeated stepover of a propagating fracture across the *layer boundaries* (Helgeson and Aydin 1991; Cooke and Underwood 2001).

A numerical experiment was carried out by Cooke and Underwood (2001) exploring the influence of *deformation at* contacts along layer boundaries, in the form of local sliding and/or "debonding" and subsequent opening, on the fracture intersection with

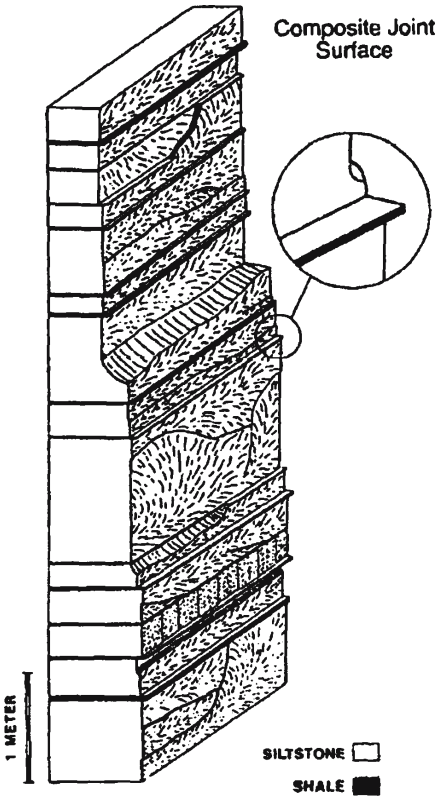

Fig. 2.31.
Sketch of composite joint within interbedded shale and sandstone sequence in New York State. The overall vertical joint trace has a discontinuous nature (after Helgeson and Aydin 1991)

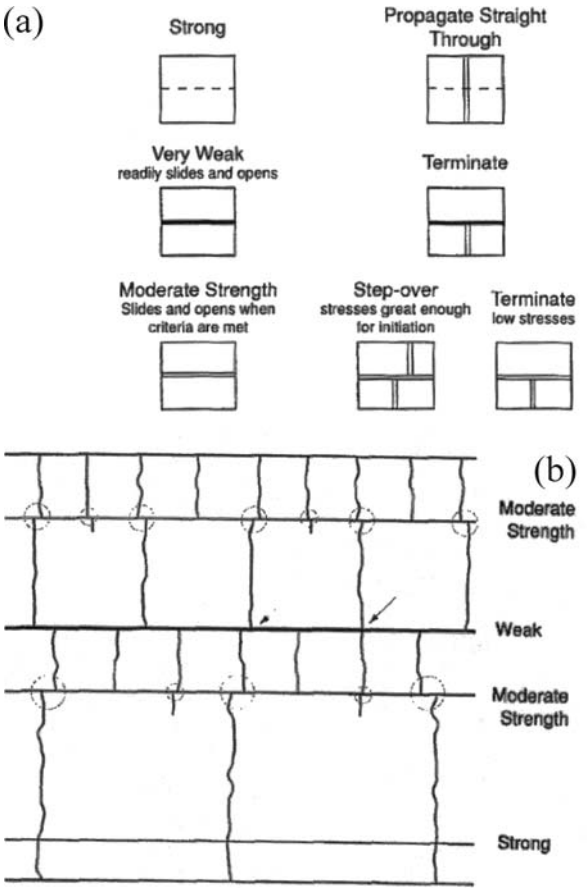

Fig. 2.32.
a Inferred variations in geometry of fracture-bed contact intersection for bedding contacts with different strengths. **b** Hypothetical pattern of fractures within a series of layers separated by different strength interfaces. *Circles* highlight occurrences of step-over fractures due to opening along the moderate-strength interfaces and *circle size* correlates with distance of fracture step-over. The spacing of fractures is approximated from the layer thickness. Apparent step-overs along the weak interface (indicated with *arrows*) result from the coincidental alignment of fractures among layers. The distinction between coincidental alignment and step-over is difficult to assess without characterization of fracture surface textures (i.e., signatures of propagation direction), relative interface strength (to guide probable intersection mechanisms), and consistencies in fracture pattern along bedding contacts (Fig. 2.32a,b from Cooke and Underwood 2001)

layer boundaries (see also Thomas and Pollard 1993). Their conclusions are cited below. Fractures propagating toward *layer boundaries* may either

1. Terminate at the boundary.
2. Propagate straight through the boundary.
3. Step-over to the left or right at the *layer boundaries* (Fig. 2.32a).

Based on the model results, Cooke and Underwood 2001 suggest that local interface opening, rather than sliding, is primarily responsible for the termination and step-over of fractures. Furthermore, the model results suggest that the strength of contacts controls the type of resulting fracture intersection. Fracture termination is favored at very weak contacts, whereas fractures propagate straight through strong contacts (Fig. 2.32b). Most sedimentary contacts will fall between these two end members. Such moderate-strength contacts may develop step-over fractures due to a local opening along the contact, or if the stresses are not great enough to produce new fractures, the parent fracture will terminate at the moderate-strength contact. Fracture termination is more likely un-

der conditions of shallower burial depth, lower effective layer-parallel tension, and fluid-driven propagation, rather than equivalent remote layer-parallel tension. Thicker layers and greater effective layer-parallel tension may produce greater amounts of step-over than thinner layers and more compressive layers. Fractures aligned within several centimeters across a contact may be coincidentally aligned or result in fracture step-over. Careful characterization of the fractures and analysis of the pattern may distinguish whether the fractures are the result of coincidental alignment or fracture step-over.

2.2.4 Joint Mirror Planes

Two end members of mirror planes are characterized in this section, drawing on both laboratory and field observations.

2.2.4.1 *Two Types of Mirror Planes*

We distinguish between two types of fracture mirror planes. One type characterizes fractographies that form dynamically by rapid fracture when high stresses are exerted. This type has been studied for decades in the laboratory on glass, ceramics, metals and polymeric materials (e.g., most of Chap. 2 in Bahat 1991a), and has recently been characterized in outcrops from the South Bohemian Pluton (Chap. 4). The second mirror type characterizes fractographies that form quasi statically by slow fracture when low stresses are exerted. This type is far less known from laboratory investigations than the first type, but it can be identified on innumerable surfaces of systematic joints that cut sedimentary rocks.

The dynamic mirror plane. When fractured primarily by high tensile stress the mirror plane exhibits characteristic morphological features (Fig. 2.1b–d), including the fracture origin at an initial flaw that develops into a larger critical flaw, concentric undulations, striae, Wallner lines, and the mirror boundary. This mirror plane is smooth, and often distinguished as a polished-like surface. Undulations (note below a distinction from ripple marks) develop on this surface by local mixed modes I + II due to stress fields that progressively bend the crack front around the axis normal to the direction of propagation when the two larger principal axes are on the fracture surface. On the other hand, striae form by local mixed modes I + III in a stress field that rotates the fracture front about the axis of the direction of crack propagation (e.g., De Freminville 1914; Smekal 1953). The distance between the origin to the mirror boundary is the mirror radius. Three mirror radii are legitimate, r_m, r and r_b, at the inner boundaries of the mist zone, the hackle zone and branching initiation, respectively (Fig. 2.1a,b,d). In multi-crystal ceramics and rocks, the micro-features of the mist are "camouflaged" by the grain boundaries and only the hackle zone may be recognized. Practically, all the above-mentioned fractographic features are generally restricted to the mirror plane. There is a distinction between primary mirrors that are related to the parent fracture and secondary mirrors that form on subsequent fringes (Fig. 2.30d,e, 4.9c,d and 4.11a–c).

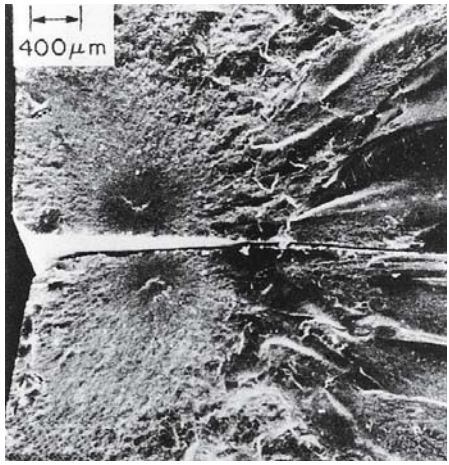

Fig. 2.33a. Two matching halves of a fracture in a ceramic body made of $BaTiO_3$, showing a smooth mirror plane around the fracture origin (*dark gray*), developing towards right into sharp hackle ridges which are termed cuspate-hackles (from Rice RW 1974)

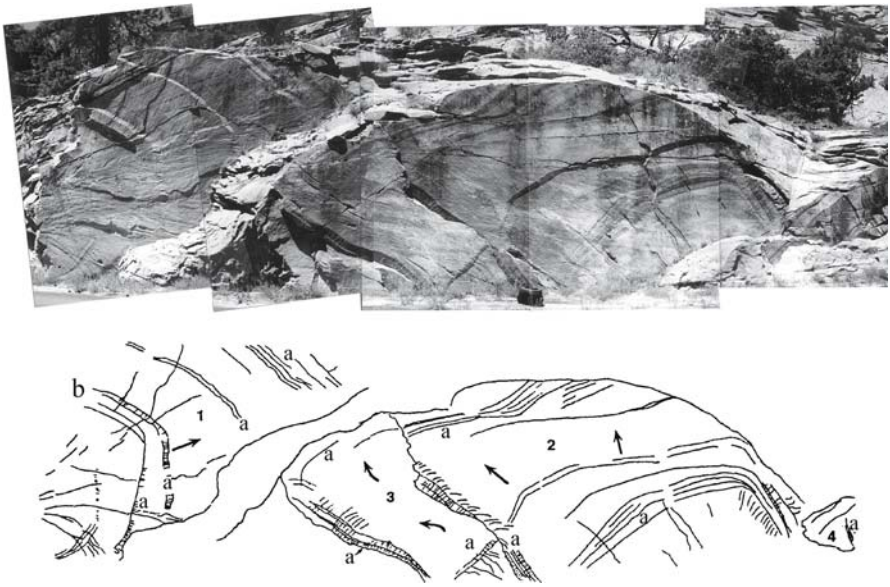

Fig. 2.33b,c. Photograph and drawing of a "wall" consisting of four joints (1–4), that propagate to various directions as shown by *arrows*, arrest marks *a*, occasionally show "box" profiles *b*, and striae *s*, in Zion National Park. A camera bag 38 cm in length is used for scale

The quasi-static mirror plane. When fractured under low stresses, propagation is slow and sub-critical (Sect. 1.5), and a different mirror plane forms. On this mirror, the location of fracture origin can be identified by the convergence of plumes at the center of concentric ripple marks, but the distinction between an initial flaw and the critical flaw is vague. Additional morphological features are arrest marks and the mirror boundary. Experimental sub-critical surfaces are briefly described in Sect. 2.2.3.1. Single-layer joints that cut sedimentary rocks often fall into this category. Quasi-static mirror planes form matte,

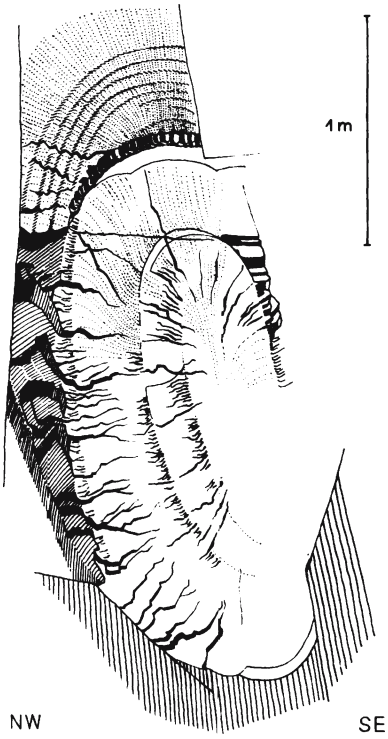

Fig. 2.33d.
An elliptical mirror plane decorated by concentric arrest marks and radial striae in Ordovician pencil slate, Thuringia, Germany. Many short striae superpose the arrest marks, and some striae merge into a single, large stria (from Bankwitz 1965). Recall that those striae are products of mixed modes I and III, and the arrest marks are products of mixed modes I, II and III

Fig. 2.33e.
Photograph of a mirror plane and fringe on an exfoliation joint from Zion National Park. The somewhat hackled *en echelon* segments display different lengths. Note the exact, curved mirror boundary. A page at left is used for scale (after Bahat et al. 1995)

rather than polished-like surfaces. While rapid fracture through grainy ceramic material or rock form transgranular, smooth mirror planes (Fig. 2.33a and 4.11a, respectively), slow, intergranular fractures (Sect. 4.5.2.2) maintain a grainy, matte surface morphology. On such surfaces, arrest marks often replace undulations, plumes replace striae, and minute features including Wallner lines on the mirror plane and mist along the mirror boundary would be unrecognizable. Distinctions between arrest marks and undulations are given below, and distinctions between striae and plumes follow.

2.2.4.2
Fractography on Mirror Planes

We extend below the treatment of fractography on mirror planes from Bahat (1991a) and make some changes along the following lines:

1. Ripple marks on mirror planes.
2. Arrest marks and striae on geological exposures.
3. Undulations on geological exposures.
4. Striae and plumes.

Ripple marks on mirror planes. Ripple marks are systematized on mirror planes according to two categories, type and shape. Two types of ripple marks are distinguished:

1. Arrest marks that signify crack arrest.
2. Undulations that form on the fracture surface while it propagates.

Undulations may form in different fracture velocities, often starting when propagation is slow, and continue at greater velocities (Fig. 2.10), or even maintain slow propagation. Ripple marks occur in various shapes, including curved cross sections (Fig. 2.10), cusps (Fig. 2.12), and angular cross sections that may attain "box" (defined by four kinks) and "semi-box" (defined by three kinks) structures (see below). These distinctions are important for the quantitative interpretation of the mechanism of fracture in geological exposures by using v and K parameters (Sect. 4.8.3).

Arrest marks and striae on geological exposures. The distinction between undulations and arrest marks has been obscured in the past, seriously hindering the application of fractography in engineering materials and structural geology for the interpretation of fracture processes. Particularly, it was impossible to distinguish between ripple marks that formed by rapid fracture (undulations) and ripple marks that reflected slow propagation (arrest marks). Here are a few examples and rules that can help in identifying arrest marks both in experimental specimens and in rock outcrops:

1. Arrest marks may occur in all shapes and sizes, including angular cross sections (Fig. 2.33b,c). Asymmetric cross sections are particularly common.
2. Following the results obtained by Guin and Wiederhorn (2003) (Sect. 2.2.3.1), an arrest mark is associated with an inducement of mixed mode I + III loading at its front (Fig. 2.9), such that striae would be induced on the mirror while *commencing* from this front. Thus, an arrest mark is frequently associated with intense striae morphologies, characterized by either multiple striae that superpose arrest marks or by the increase of the intensity of individual striae, or both (Fig. 2.5a and 2.33b–d).
3. Quite often striae on the mirror plane and particularly in association with arrest marks resemble fringe cracks and may erroneously be interpreted as *en echelon* segments or hackle cracks. The distinction between these two features may be primarily based on two striae types. First, many short striae start when superposing an arrest mark but they fade away after a small distance from it (Fig. 2.33b–d), compared with fringe cracks that maintain their lengths, or even increase it (Fig. 2.34,

2.35, 2.33e). Second, when striae start between arrest marks they merge into a single stria of intense morphology at the arrest mark, compared to *en echelon* segments that maintain their number or hackles that even multiply (Fig. 4.11a). Figure 2.33d shows quite well the two morphological types. Both morphologies signify slow fracture propagation, and an immediate transition from an arrest mark to a hackle fringe that signifies rapid fracture would be an unlikely occurrence (this criterion may be used for examining this theory in future observations).

4. Arrest marks may form in the shape of "box"-shaped structures that superpose mirror planes (Fig. 2.33b,c) or as "semi-box" structures that occur even on fringes (Fig. 2.30a). In the latter case, the right side of the semi-box on the fringe indicates reduction in fracture velocity, compared to its left side, which is marked by hackles that indicate rapid fracture. Note that the striae and the "semi-box" on the fringe are significantly coarser than the striae and undulations on the mirror (see more in Bahat and Rabinovitch 2000).

Finally, many, but not all arrest marks may be recognized. Some more arrest marks that can be identified on rock fractures are presented in Bahat (1991a, Fig. 3.42c, 4.2a,b, 4.4 and 4.11), they all exhibit striae according to the above rules. Occasionally, transitions between areas of multiple striae into mirror areas that are not imprinted by arrest marks and do not contain striae (Fig. 4.36) possibly suggest a reduction in fracture velocity but not quite an arrest.

Undulations on geological exposures. How do undulations differ from arrest marks in geological exposures? Two examples of undulation propagation are described and interpreted below. As mentioned above, when distances between undulations increase, fracture velocities increase (Fig. 2.10). The undulations in Fig. 3.24c display fracture "diffraction" along boundary A, such that they change orientation and trail behind along boundary B. At some stage, however, drag is reduced, resulting in velocity jump (at point C) to conform to a uniform velocity in area D. There is a difference between the shapes of the upper ripple mark and the lower ones at the right side of Fig. 3.24d. The upper one is convex towards the direction of propagation, which is faster midway between the two bounding sub-vertical surfaces, and trailing behind along the surfaces. This is a characteristic feature of undulation propagation on experimental fractures (e.g., Bahat 1991a, Fig. 2.1c). The lower ripple marks are straighter, implying an approach to equal velocity along the fracture front. The ripple marks on the left side of Fig. 3.24d are inclined as they come closer to their arrest at the older horizontal joint, suggesting that these are arrest marks. Note that the undulations are approximately symmetrical and the arrest marks are asymmetric.

Striae and plumes. Striae that form by rapid fracture in glass or glass ceramic penetrate into the material and propagate as sharp, continuous cuts along straight trajectories, unless influenced by boundaries that may deflect them. For instance, there is a change from approximately straight striae within the material in their early part (closer to the F end) and a gradual curving in their continuation towards the B end as they approach the sample upper surface (closer to the viewer, Fig. 2.19a). They may lose some of their sharpness while cutting granular rocks when moving fast (see delicate straight strie and hackle in Fig. 2.30a). They may completely lose their sharpness and sub-divide into dendrite-like plumes, such that every dendrite branch would be further sub-divided into minute barbs (Fig. 2.3b) when propagating slowly (Fig. 2.22). This may explain why the

topography of plumes on mirrors that form dynamically either in the laboratory (Fig. 2.10), by explosives (Fig. 2.30b), or in geological outcrops (Fig. 2.33e, 2.56, 4.11a) is often delicate (or hardly visible), whereas on slowly forming joints, or when they curve (Fig. 4.22), plumes may cover significant areas and attain coarse morphologies (e.g., Fig. 4.7b).

Summary. Two types of mirror planes are distinguished. One type characterizes fractographies that form dynamically by rapid fracture when high stresses are exerted. Such mirror planes are smooth, often distinguished as polished-like surfaces that reflect light. The second mirror type characterizes fractographies that form quasi statically by slow fracture when low effective stresses are exerted. This mirror type characterizes surfaces of many systematic single-layer joints that cut sedimentary rocks; they maintain grainy, matte surface morphologies.

We divide ripple marks in geological exposures into two categories. First, "undulations" generally deviate slightly from symmetrical cross sections (Fig. 3.24c) that signify fracture propagation in various velocities. Second, "arrest marks" often are cut characteristically by striae and deviate considerably from symmetrical shapes, with the occasional tendency to form "box" or "semi-box" cross sections (Fig. 2.33b,c). These marks signify slow propagation down to arrest.

Striae that form by rapid fracture in glass or glass ceramic penetrate into the material and approximate sharp, continuous cuts (Fig. 2.19a). However, when striae propagate slowly in granular rocks, they may completely lose their sharpness and form dendrite-like plumes (Fig. 2.22a, 2.45).

2.2.5 Joint Fringes

2.2.5.1 *Introduction*

We start with a first order distinction between two end member fringe types, *en echelon* fringes (Fig. 2.1a) and hackle fringes (Fig. 2.1b). *En echelon* segmentation from parent fractures generally occurs in reduced velocities (Kulander et al. 1979; Müller and Dahm 2000), standing for the "quasi-static end member", at a velocity of $\leq 10^{-1}$ m s^{-1} (Wiederhorn et al. 1974) in the "fringe spectrum". Hackles form at high velocities (e.g., Kerkhof 1975), representing the "dynamic end member" at a velocity of $\geq 10^{-1}$ m s^{-1} (Wiederhorn et al. 1974). Between these two end members, there are two distinct fringes that bound mirror planes on joint surfaces. One of them consists of somewhat hackled *en echelon* segments (Fig. 2.33e) that display different lengths, resulting in no uniform width of the fringe (Fig. 2.34a). The other one consists of *en echelon* segments of equal lengths that are not hackled (Fig. 2.35a,b), often resulting in a uniform fringe width (Fig. 2.34b).

The need for this distinction has been previously raised, but it has been based on limited data derived from rock exposures in sedimentary rocks (Bahat 1991a, Table 3.3; Bahat 1997). Recent studies on fracture in granites enriched the information on the properties of geological hackle fringes (Chap. 4) so that a sound distinction between the two fringe types becomes possible. Understanding the full mechanical significance of the spectrum between hackle fringes and *en echelon* fringes around mirrors is quite a challenge. This understanding would improve the tectonofractographic understand-

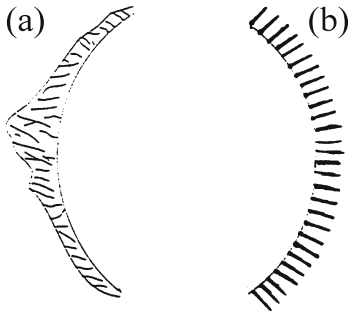

Fig. 2.34.
Diagrams of two types of fringes. **a** A no uniform width of the fringe of hackly *en echelon* segments that have different lengths. **b** A uniform width of the fringe of *en echelon* segments of approximately the same lengths (after Bahat 1998b)

ing of joint formation, including the quantitative estimation of paleostress conditions leading to fracture, as well as applications to other research fields, such as petrology (Chap. 4 and 6). It is appreciated, however, that the above distinction between the two end member fringes is not always simple, and the question whether a particular marking is to be classified as a hackle fringe or *en echelon* fringe may arise in some cases. Occasionally *en echelon* segments and hackle cracks populate the same fringe (Fig. 2.1c). Also, there is an experimental finding of fast propagation of *en echelon* cracks (Sect. 2.2.3.10). Thus, an awareness of occasional difficulties in the distinction between the two end member fringes is required. *En echelon* fringes are better known to geologists than hackle fringes. Also not well known are cuspate hackles, but these form a small subgroup that is not central in this chapter. Accordingly, the next two sections (Sect. 2.2.5.2 and 2.2.5.3) present a recap on *en echelon* fringes and on the sub-group cuspate hackles, respectively (partly from Bahat 1991a, pp. 170–183). The issues of hackle fringes and transitions between the two end member fringes are expanded in Chap. 4.

2.2.5.2
The En Echelon *Fringe*

General. *En echelon* segmentation in non-coplanar planes is ubiquitous on various scales from micrometers to kilometers in geological exposures occurring in different terrains. This implies that breakdowns may be the consequences of various mechanisms (see a comprehensive description of *en echelon* distribution in Pollard et al. 1982). Interaction of non-coplanar cracks was observed by De Freminville (1914) in bitumene. Following that, Preston (1931) modeled the process leading to striae and *en echelon* segmentation in glass. He pioneered the explanation that when a change in the direction of the principal tension occurs, the crack must break down into a number of segments so that each segment readjusts its orientation to maintain normality with respect to the new direction of the principal tension. This mechanism has since been reaffirmed (e.g., Sommer 1969) and was formulated into a sophisticated fracture mechanics theory of mixed mode I + III loading (Lawn and Wilshaw 1975a; Ryan and Sammis 1978; Pollard et al. 1982; Cooke and Pollard 1996; Hull 1999), essentially following the rules leading to the formation of the plumes by the same mixed mode (Fig. 2.20c,d).

Starting with some of the earlier works (e.g., Woodworth 1895, 1896; De Freminville 1914; Murgatroyd 1942; Hodgson 1961a,b; Bankwitz 1965, 1966; Sommer 1969; Kulander et al. 1979; Bahat 1979a, 1986b; Pollard et al. 1982), the study of *en echelon* fringes involved various fracture aspects that have been outlined by Bahat (1991a).

These include fracture geometry, breakdown styles, *en echelon* segments and connecting bridges (or steps), fracture markings on segments, breakdown mechanisms, the different roles of the dilatant *en echelon* cracks vs. their bridges, and the distinction between the influences of remote and local stresses on the evolution of the fringe.

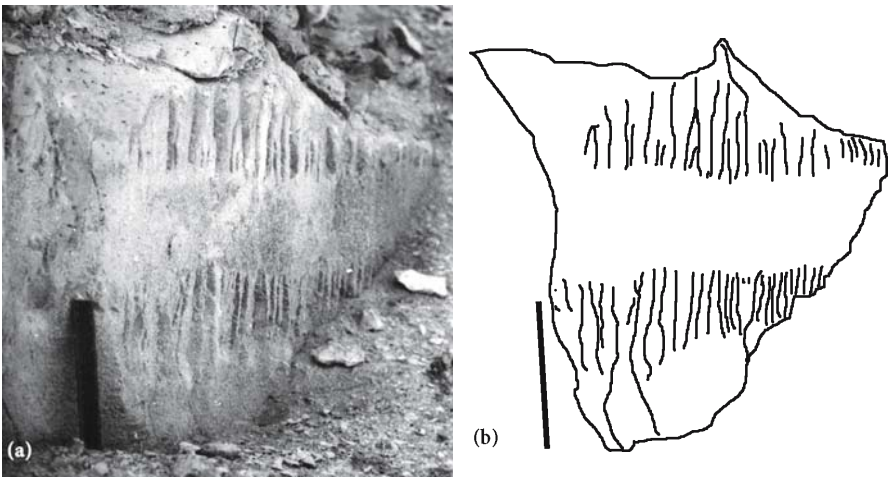

Fig. 2.35a,b. Styles of *en echelon* segmentation. **a** Photograph (from Bahat 1997) and **b** drawing of discontinuous breakdown of *en echelon* fringes both above and below the parent joint. The sense of rotation of the segments in the two fringes is counter clockwise. Note similarity in shape and size of segments in both fringes. *Scale* is 15 cm

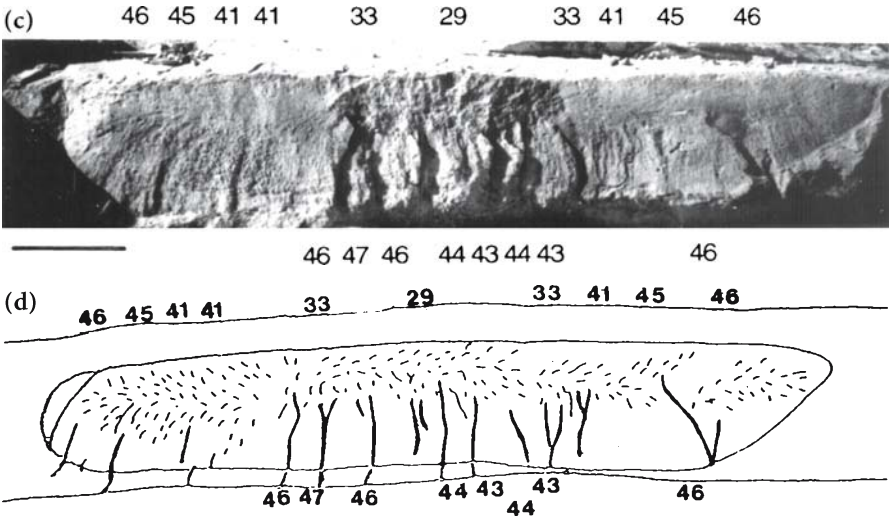

Fig. 2.35c,d. Styles of *en echelon* segmentation. Photograph (**c**) and drawing (**d**) of the curved-joint with an intense discontinuous breakdown into many segments, below the elliptical perimeter of the early "embryonic" joint at center, and a continuous breakdown at the distal sides. The joint undulates along the strike. The *upper numbers* are measured azimuth degrees (from 029° to 046°) on the parent joint. The *lower numbers* are azimuth degrees (from 043° to 047°) on *en echelon* segments. The delicate barbs on the joint surface represent a bilateral plume. *Scale bar* is 50 cm (after Bahat 1997)

Several aspects of *en echelon* segmentation are expanded below, making the distinction that fracture markings on the parent joint record events from the early history of the joint, while fringes reveal processes that were associated with advanced and final stages of fracture.

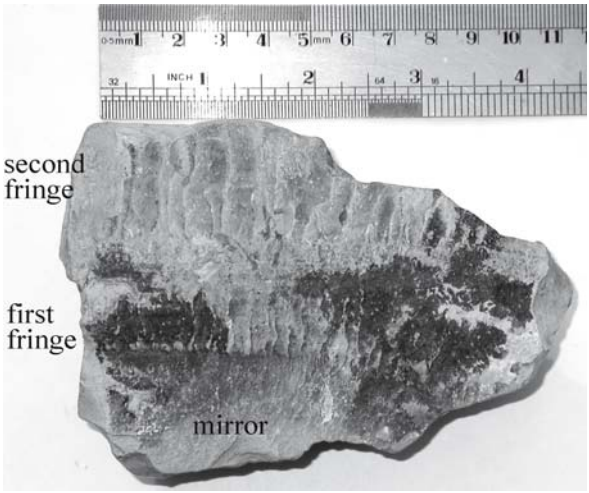

Fig. 2.35e.
Styles of *en echelon* segmentation. "Double fringes" beyond the boundary of the mirror plane on a joint cutting limestone. Note the reverse sense of stepping on the two fringes. The first fringe shows *en echelon* segmentation on which there is an "upstairs climbing" from right to left, while the second fringe shows climbing in the opposite direction, implying change in the stress field between the formation of two fringes (a *non-in situ* Cenomanian sample from Iben-Dib, south Jordan)

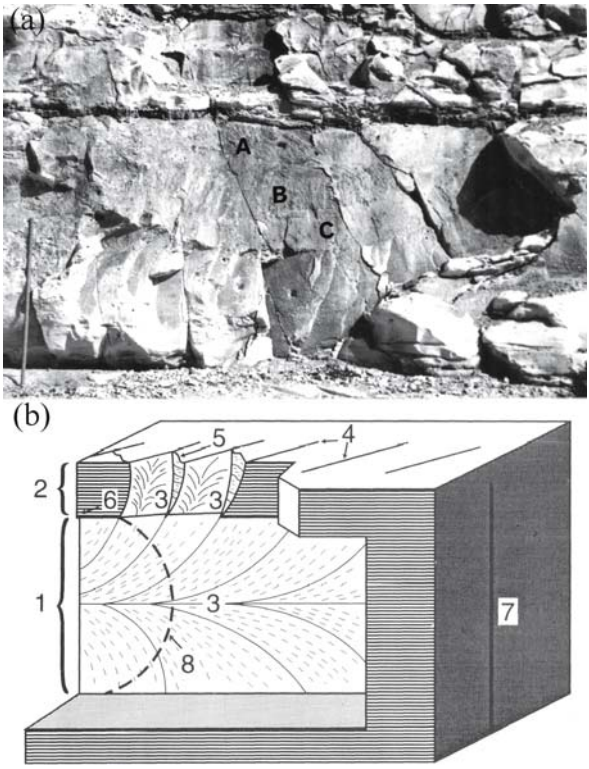

Fig. 2.36.
a A joint from outcrop R showing a division into two parts. An upper semi-ellipse parent joint concave downward is separated by a curved shoulder from a fringe of *en echelon* segments below. There is a (hardly visible) division of the parent joint into three concentric zones (*A*–*C*, see text for more information). Note the steps of different sizes at a discontinuous breakdown along a curved shoulder. *Scale* is 1 m (after Bahat 1997). **b** Schematic block diagram showing primary surface markings of a systematic joint: *1*: Main joint face; *2*: Fringe; *3*: Plumose structures (plumes); *4*: F-joints (b-planes); *5*: Cross-fractures (c-fractures); *6*: Shoulder; *7*: Trace of main joint face. Note that cracks 5 are steps that bridge adjacent *en echelon* cracks in the fringe. Note in **a** and **b** vertical and lateral fracture fronts, respectively (modified by Roberts (1995) from Hodgson (1961a))

Breakdown styles. Two breakdown styles are distinguishable: Discontinuous (Fig. 2.35a and b) and continuous (Fig. 2.35c and d). In layered rocks, the discontinuous breakdown starts along a shoulder at the edge of the parent joint from where the steps start and approach the layer boundary. When the shoulder is straight and parallels the adjacent layer boundary, steps of a given fringe would reach approximately the same maximum size (Fig. 2.35b). However, a discontinuous breakdown with curved shoulders may have steps of different sizes (Fig. 2.36a). Note that in Hodgson's diagram (Fig. 2.36b), *echelons* appear in a discontinuous style and the plumes initiate on them at the fringe of the parent joint (not on the parent joint itself). A discontinuous breakdown is often characterized by a "root zone" (Bankwitz 1966). This zone is a narrow strip of small *en echelon* cracks along the joint shoulder to which larger *en echelon* cracks are added as the fringe develops. The continuous breakdown starts on the joint plane at various distances from the layer boundaries and the steps have no shoulder as a starting line. Such breakdowns often display fringes with steps of quite different shapes and sizes (Fig. 2.35d). On one continuous breakdown, Bankwitz (1966) shows plumes that initiate on the parent joint and continue to propagate along the *en echelon* crack.

Abrupt and gradual loadings. It is inferred from the experimental results by Cooke and Pollard (1996) (present Fig. 2.20c,d) that generally, breakdowns that are manifested by discontinuous *en echelon* segments reflect processes of abrupt twisting. These are associated with abrupt mixed mode I + III loading that occurs between the development of the parent joint and the fringe and produces *en echelon* twisting (e.g., Fig. 2.35a,b). On the other hand, continuous breakdowns are associated with gradual twisting, responding to mixed mode loading as the joint propagates and segmenta-

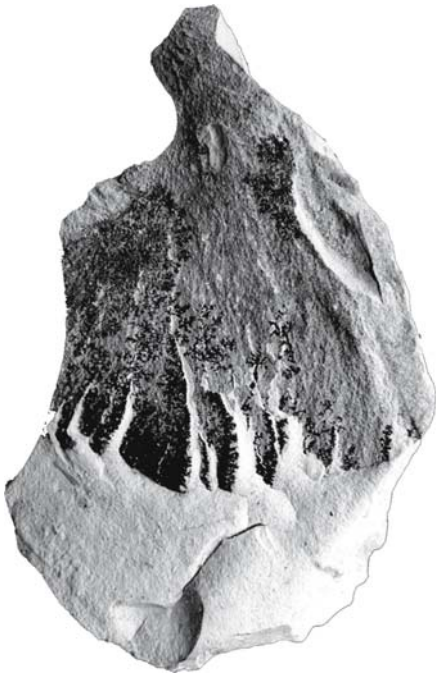

Fig. 2.37.
Mineralization on *en echelon* cracks (*dark color*) but not on the steps that connect them (alternating white fractures) demonstrates two separate phases of failure. The sequence of events in this chalk sample (from the Middle Eocene) was fracture of the parent joint (note delicate plumes), *en echelon* cracking, mineralization of iron oxides that was followed by dendrites of manganese oxides on the parent joint and *en echelon* cracks, and finally, delayed step formation, after flow of solutions had seized (sample length from top to bottom, about 12 cm, after Bahat 1986b)

tion occurs (Fig. 2.35c,d). The gradual mixed mode loading probably does not involve any time-break during the process. It is, however, possible that time breaks do occur during discontinuous processes, but their extents are not known (Fig. 2.35e). Quite possibly the different fracture modes of the *en echelon* cracks and steps that cause propagation vertically downward and laterally, respectively, may be associated with a time interval between them (Fig. 2.37). Two fracture paths are manifested by part D of the composite fracture (Fig. 2.38, see also Fig. 3.40a) along Wadi Secher (Fig. 3.33c). An abrupt clockwise breakdown occurred in part D, striking into a path of twisted segments (azimuths 080–083°). However, as the loading increased while these segments propagated downward beyond the arrest mark, a curved path took over, and a gradual counter clockwise rotation of the segments occurred (into azimuths 072–076°).

In outcrop Y (Fig. 3.33c) continuous and discontinuous breakdowns occur in the same layer (Bahat 1986a). Furthermore, the "curved joint" was first segmented by a discontinuous process underneath the early elliptical fracture on the curved joint, and the second breakdown was continuous along the distal edges (Fig. 2.35c,d). The close proximity of these two breakdown styles suggests that their fracture conditions were not drastically different. The curved joint (Fig. 2.35c,d) and the composite fracture (Fig. 2.38 and 3.40a) demonstrate that the continuous breakdown may have two manifestations. First, a gradual growth of *en echelon* segments from distal locations on the parent joint (Fig. 2.35d) and second, a gradual curving of growing segments (D in Fig. 3.40a). These two fracture manifestations are associated with relatively small twist angles ($0° \leq \omega \leq 11°$). On the other hand, discontinuous breakdowns in the curved joint and in other joints from stations Y and R (Fig. 3.33c, 2.35d, 2.36a) are connected with larger angles ($12° \leq \omega \leq 25°$) (Bahat 1997).

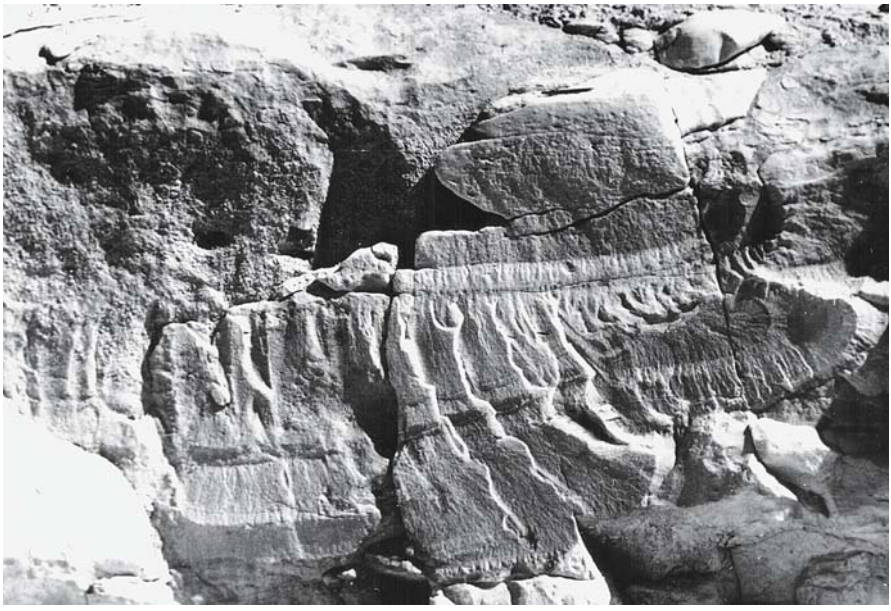

Fig. 2.38. Photograph of a composite fracture from Wadi Secher (see explanation in the text and in Fig. 3.40a) (after Bahat 1997)

Breakdown mechanisms. We discuss below two fracture mechanisms that form *en echelon* fringes by *local* mixed mode loading. The "breakdown" model by Pollard et al. (1982) concentrates on the mixed mode I + III that develops by an abrupt process during the transition from the parent joint to the fringe (Fig. 2.39a–c and 2.40a,b). The "fracture slanting" model (Bahat 1991a, 1997) has some resemblance to the "breakdown" model and supports its basic principles. An alternative model by Ramsay and Lisle (2000) that applies the mixed mode I + III by *remote* extension and shear stresses is presented in Sect. 6.10. See also reservations regarding the "breakdown" model by Lazarus et al. (2001a,b).

Pollard et al. (1982) examined the mechanism of a fracture breakdown into echelon cracks, and this section basically is cited from their work. They use three idealized block diagrams (Fig. 2.39a and 2.40a,b) and show that

$$s = c \sin \omega \tag{2.6a}$$

and

$$m = \frac{W}{2} - k = \frac{W}{2} - c \cos \omega \tag{2.6b}$$

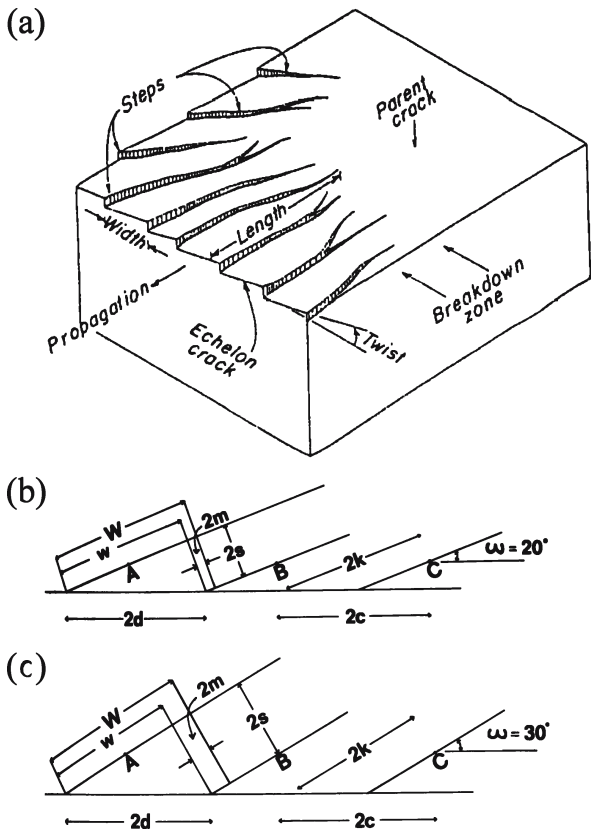

Fig. 2.39.
a Block diagram illustrating the geometry and mutual relations between parent crack and *en echelon* cracks (after Pollard et al. 1982). **b**, **c** Schematic sections of a discontinuous fringe normal to *en echelon* crack lengths. W = crack width, w = part of the width which is not overlapped, 2 m = the overlapped portion of the width, when $W = w + 2$ m; $2s$ step, the normal distance between two adjacent cracks, $2k$ = the distance between centres of two adjacent cracks parallel to cracks, $2c$ = the distance between centers of two adjacent cracks along the shoulder, $2d$ = the distance between initiation points of two adjacent cracks along the shoulder, and the twist angle ω, between the shoulder and *en echelon* cracks. **b** $\omega = 20°$; **c** $\omega = 30°$. A comparison between **b** and **c** shows that overlapping increases with ω. At low ω, $W \cong w$ (after Bahat 1991a)

where ω is the twist angle, $2c$ and $2k$ are different distances between centers, and $2s$ is a step. Pollard et al. (1982) adapt Sommer's (1969) explanation on fracture breakdown, but add the internal pressure P to the normal stress σ_{yy}^{∞} acting on the fracture plane (tensile stress is positive) (Fig. 2.40a,b).

Pollard et al. consider an elastic body subject to remote principal stresses σ_1^{∞} and σ_2^{∞} acting in the y-z-plane, and a fracture of width $2b$ subject to pressure P lying in the x-z-plane with straight tips parallel to z (length and width of parent fracture by Pollard et al. are reversed in the present text, to be consistent with other descriptions). Breakdown into echelon segments is independent of the third remote principal stress, which acts in the propagation direction x. A uniform rotation Ω of the remote stresses about the x-axis introduces a normal stress σ_{yy}^{∞} and a shear stress σ_{yz}^{∞} acting in the fracture

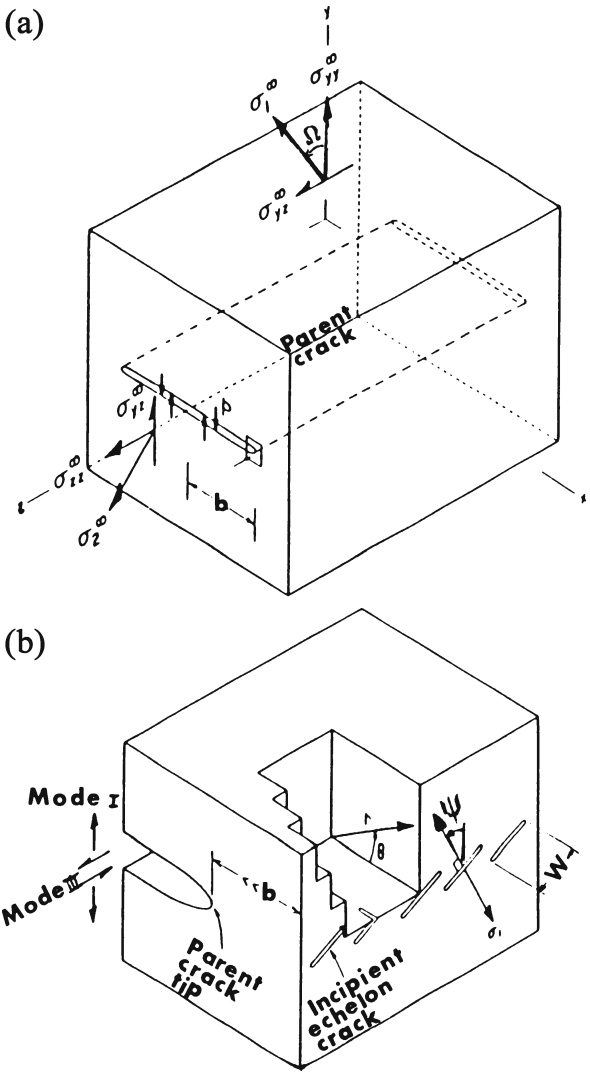

Fig. 2.40.
Block diagrams illustrating relations among applied stresses and cracks. **a** Parent crack of width $2b$ and infinite length in z is loaded by pressure P and remote principal stresses σ_1, σ_2. Rotation Ω of principal stresses about x introduces stresses σ_{yy} and σ_{yz} acting on the crack plane. **b** Small element cut from near parent-crack tip (*small arrowed square* in **a** with incipient echelon cracks of width W whose normal, the maximum local tension σ_1 making angle ψ to the y-axis. Polar coordinates centered at parent-crack tip are r, θ. *Heavy arrows* indicate relative motion of parent crack walls when subject to mode I and mode III deformation (modified after Pollard et al. 1982)

plane. According to Pollard et al., breakdown of the parent fracture depends upon Ω and the applied stress ratio

$$R = \frac{2P + \sigma_1^\infty + \sigma_2^\infty}{\sigma_1^\infty - \sigma_2^\infty}, \qquad P > -\sigma_1^\infty \tag{2.7}$$

The inequality relating P and σ_1^∞ is required for the parent fracture to be open. The numerator in Eq. 2.7 is the difference between the internal pressure and the remote mean stress or pressure, $-(\sigma_1^\infty + \sigma_2^\infty)/2$. The denominator in Eq. 2.7 is the remote maximum shear, $(\sigma_1^\infty - \sigma_2^\infty)/2$.

Near the crack tip the stress field is proportional to the stress intensity factors. Pollard et al. resolve that the remote normal stress and internal pressure contribute to a mode I stress intensity, $K_I = (\sigma_{yy}^\infty + P)(\Pi b)^{1/2}$, and the remote shear stress introduces a mode III stress intensity, $K_{III} = \sigma_{yz}^\infty(\Pi b)^{1/2}$. The tendency for breakdown increases as the ratio of stress intensities K_{III}/K_I differs from zero. Writing σ_{yy}^∞ and σ_{yz}^∞ in terms of Ω and the remote principal stresses by resolving stress in the x-z-plane, Pollard et al. obtain

$$\frac{K_{III}}{K_I} = \frac{\sin 2\Omega}{R + \cos 2\Omega}, \qquad R + \cos 2\Omega > 0 \tag{2.8}$$

Inequality of R and $\cos 2\Omega$ is required for the parent fracture to remain open. For a particular rotation angle, the stress intensity ratio increases as the stress ratio R decreases. For $R \cong 1$, which is reasonably close to the range of R in nature, $K_{III}/K_I \cong \tan\Omega$, and Pollard et al. find that relatively small rotations of the principal stresses could initiate breakdown.

The fracture slanting mechanism. Various fracture properties of both edge and central cracks were investigated in metallic plates as a function of their thickness (Bank-Sills and Schur 1989). It was found that for both geometries, as plate thickness increases the ratio of the critical stress for the slant crack divided by the critical stress for the flat (unslanted) crack increases at failure, and the crack propagation rate for the slant crack is slower than that for the flat crack (Fig. 2.41). Bank-Sills and Schur (1989) observed that for both edge and central slant cracks, the K_{III}/K_I ratio increases as plate thickness de-

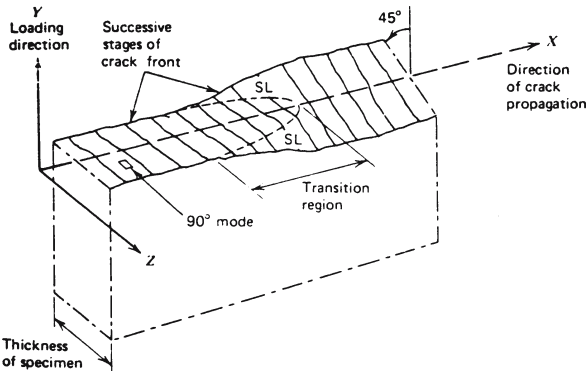

Fig. 2.41. Diagram showing fracture mode transition from flat fracture under plane strain conditions (*left*) to slant fracture under plane stress conditions (*right*) (after Hertzberg 1976)

creases and that the greatest value of this ratio occurs at the plate surface. Furthermore, slant cracks in thinner plates will propagate more rapidly than those in thicker ones. Thus, as thickness increases the tendency for slanting decreases, and the tendency for slanting becomes greater in thinner plates as plane stress conditions are attained.

These experimental results reaffirm previous observations (Hertzberg 1976; Broek 1984) that cracks in tensile fields under fatigue loading propagate out of their plane in thin plates, and they also show that this property is thickness dependent. The tendency for slanting that is associated with the increase in the K_{III}/K_I ratio becomes greater with the decrease in thickness of the plate and from the center of the plate towards its edges. Cooke and Pollard (1996) investigated crack segmentation in PMMA under various K_{III}/K_I conditions. They found that for ω of the *en echelon* cracks and the number of segments formed, both increase with the increase of the ratio K_{III}/K_I (Sect. 2.2.3.8, see also Pollard et al. 1982). Hence, the main resemblance between the "breakdown" and "fracture slanting" models is in the dependence of *en echelon* segmentation on the K_{III}/K_I parameter (Sommer 1969). The fracture slanting model, however, links (and limits) the increase in K_{III}/K_I to plane stress conditions, i.e., to fringes along joints in layered rocks, and it does not apply to *en echelon* segmentation in massive rocks like granite, a limitation not articulated by Pollard et al. 1982. An extension to other quasi-plane stress settings of stratified structures, such as segmentation of large igneous dikes near the ground surface (Anderson 1951) or *en echelon* fracturing on the ground along branches of major strike-slip faults (e.g., Allen et al. 1972), should not be ruled out.

Non fracture slanting mechanisms. Fringes along curved boundaries often exhibit changes in the senses of segment stepping, implying slight deviations from orthogonality of the maximum extensile direction with respect to the parent joint. This mechanism does not operate along straight layer boundaries, but it may operate in connection with *en echelon* segmentation that often occurs on large joints in sandstone at remote locations from straight boundaries (e.g., Fig. 3.23a). Scarcity of hackles on such surfaces seems to suggest sub-critical conditions. Another type of *en echelon* segmentation occurs along fracture fronts when critical stress intensity $K_I \geq K_{Ic}$ and rapid crack propagation conditions are attained (Chap. 4). *En echelon* fringes around exfoliation joints may (Fig. 2.33e, 3.24b and 3.26c) or may not (Fig. 3.24c, 3.25a) attain critical fracture conditions. On fringes along curved surfaces see Sect. 4.5.3.2.

2.2.5.3
The Cuspate Hackle Fringe

Cuspate hackles are distinguishable from *en echelon* and hackle fringes. Cuspate hackles have sharp ridges of approximately constant width that radiate in a fringe around the main fracture. They are common on blasted fracture surfaces (Fig. 2.30b) and rare on joints (Fig. 2.42). The fracture marking from the Charing chalks in Kent, England displays a curious type of fringe. The echelon cracks occur above and below the plume, whereas cuspate hackles continue the trend of the plumes along the distal direction (left side of joint). This is interpreted as greater stress intensity along the lateral fracture propagation as compared to the upward and downward directions. The common occurrence of cuspate hackles in quarries (Bahat 1991a, Fig. 3.60a–c), imply fracture by high energy conditions (fast crack propagation).

Fig. 2.42. Cuspate hackles. A plume developed into right-stepping and left-stepping echelons at the upper and lower parts of the marking, respectively, but transformed laterally towards left into cuspate-hackles, suggesting a lateral cracking under conditions of greater stress intensity. From an Upper Cretaceous chalk in south England (after Bahat 1991a)

The sharp peaks of cuspate hackles are distinct from the flat surfaces of *en echelon* cracks. Crack overlapping, which is a typical feature of *en echelons*, does not occur in cuspate hackles. They have not been identified on fracture surfaces of technical glasses. When they occur on joint surfaces they seem to serve the role of hackles on fracture surfaces of glass. There is a strong resemblance between cuspate hackles on joints and fractures that form by blast to fracture surfaces of some rapidly fractured ceramics (Fig. 2.33a), even if size scales are an order of magnitude different. As mentioned above, hackle fringes are described in Chap. 4.

2.2.6 Mirror Boundaries

We characterized in the preceding sections the properties of the mirror plane and the fringe. Another important parameter is the boundary that separates these two parts of the joint. The importance of finding well-defined critical flaws when coupled with well-defined mirror boundaries provide the necessary conditions for estimating the local tensile paleostress on a joint surface (Bahat and Rabinovitch 1988) (Sect. 6.5). In plutonic rocks, there are occasionally favorite conditions for finding clear mirror boundaries (e.g., Bahat et al. 1999, 2003, see present Chap. 4), no such clarity has been so far obtained in sedimentary rocks. We now consider the criteria for elucidating mirror boundaries of single-layer joints. At least one of the following two criteria must be identified on a joint surface for determining a mirror boundary, while the third and fourth criteria can increase the credibility of the definition:

1. There is a stepwise morphological increase in the size of the cracks across the boundary from plumes on the mirror to fringe cracks (Fig. 2.22b and 2.33a,e). This has to be consistent along at least 50% of the suspected mirror boundary of the investigated joint.
2. The tilt angle ϕ is formed between the imaginary continuation of the mirror plane and the fringe (Bahat and Rabinovitch 2000). This angle is better seen in profile than in plan view (Fig. 4.11c).
3. The ratio of mirror radius (Fig. 2.1d) to the radius of the critical flaw should be 15 ±5 (Bahat and Rabinovitch 1988).
4. Apart from size difference between plumes and fringe cracks, there are occasionally changes in the sense of stepping in the transition from the plume to the *en echelon* segmentation on the fringe (Fig. 3.40b).

2.2.7 Recent Studies on *En Echelon* Fringes from the Beer Sheva Syncline

This section relates to the occurrence of fringes on joint surfaces from sedimentary rocks in the Beer Sheva syncline, based on the study by Bahat (1997) that we cite below. Here we concentrate on fractographic relationships, while the geological implications of this study are presented in Sect. 3.4. The Eocene chalk layers from the Beer Sheva syncline (Fig. 3.33) are only slightly deformed platform cover sediments. Chalk is a weak rock with considerable change in properties when exposed to aqueous solutions. Therefore, fracture may be readily induced in this material, even in very low differential stresses. The focus here is on bed restricted uplift joints (Bahat 1999a). Jointing in Eocene chalks around Beer Sheva is enriched with various phenomena of *en echelon* segmentation that bear relationships to diverse fracture styles and multiple joint systems (Chap. 3).

2.2.7.1 *The Relationship of* En Echelon *Length to Layer Thickness*

Lengths of *en echelon* segments cutting layers of various thicknesses were measured along stations Y, R and Q in Wadi Naim (Fig. 3.33c). In these locations, *en echelon* fringes occur only below the parent joint (Bahat 1986a). The length of the longest segment for each joint was measured from its initiation point to the lower layer boundary. The layer thickness at that location was measured as well (estimated error for both measurements is ±2 cm). Five continuous and fourteen discontinuous segmentations were studied, and the results are summarized in Fig. 2.43. There is a positive linear fit ($R^2 = 0.928$) of the readings for discontinuous segmentation, which is given by $l = 0.270T + 0.829$, where l is segment length and T is bed thickness. R^2 is reduced to 0.836 when one reading ($T = 210$ cm, $l = 55$ cm) is omitted. The readings for the continuous segmentations scatter above the curve. There is no evidence of any layer-parallel slip, along either chalk-chalk or chalk-chert boundaries linked to *en echelon* fringes in the stations investigated in this study. On the other hand, there are many inter-layer radial markings on horizontal layer boundaries that reflect tensile vertical strains perpendicular to layer boundaries in the chalk (Bahat 1991a, p. 298).

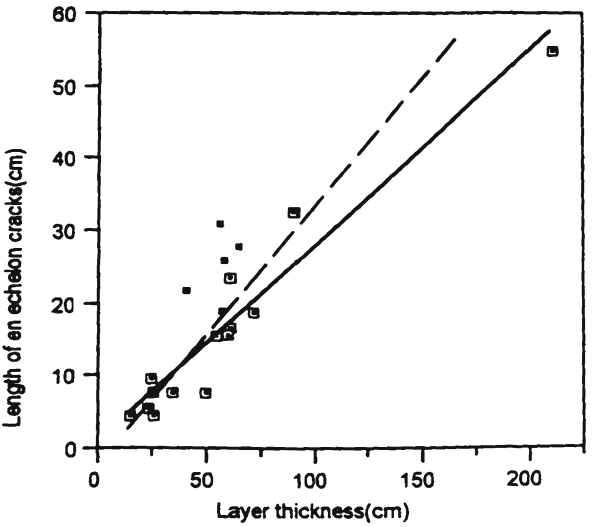

Fig. 2.43.
A plot of layer thickness vs. length of *en echelon* cracks in chalk outcrops along Wadi Naim. The large fourteen *open squares* and the five *solid squares* designate respectively discontinuous and continuous breakdowns. The *solid* and *dashed plots* are the products of 14 and 13 readings of discontinuous breakdowns, respectively. The last reading ($T = 210$ cm, $l = 55$ cm) is omitted from the latter. The former is considered to be a better representation of the results (after Bahat 1997)

2.2.7.2
Similar Fringes below and above the Parent Joint

En echelon segments maintain counter clockwise rotation in fringes close to both the lower and upper boundaries in outcrop X (Fig. 2.35a,b), and the two fringes, above and below the parent joint, have similar geometries and shapes. This coupling implies that *en echelon* segmentation occurred simultaneously in the two fringes. It took place after the end of the required diagenetic process for the equalization of the lithological properties along both the lower and upper layer boundaries. The fractographic features of the joints in outcrop X are quite distinct from the fractographies of all other joints in the investigated area.

2.2.7.3
Opposite Senses of Segment Rotation in a Single Fringe

The observation of the close proximity of both clockwise and counter clockwise rotations of *en echelon* cracks in a single fringe is quite intriguing. Based on experimental results (Cooke and Pollard 1996), it follows that the clockwise twisted segments in fringes reflect right-lateral shear, and the counter clockwise twists disclose left-lateral shear. There is a need to distinguish between two cases of opposite senses of segment rotation in a single fringe: First, in a curved fringe, and second, in a straight fringe.

Opposite senses of segment rotation in curved fringes are quite common in fractured engineering materials and in association with discoid joints. Segment rotation is counter clockwise on the left side of a rounded parent fracture in steel and is clockwise on the right side of the fracture (Fig. 2.44a, after Yukawa et al. 1969). Exactly the same pattern occurs around a discoid joint in the Frauenbach quarzite from the Thuringian Schiefergebirge (Fig. 2.44b, after Bankwitz and Bankwitz 1984). In fact, Bankwitz and Bankwitz (1984, Fig. 2) observed a symmetry that was created by a reverse segmentation. The same segmentation pattern is repeated on the surface of a fractured glass rod that failed under combined operation of modes I and III (Sommer 1969, Fig. 2).

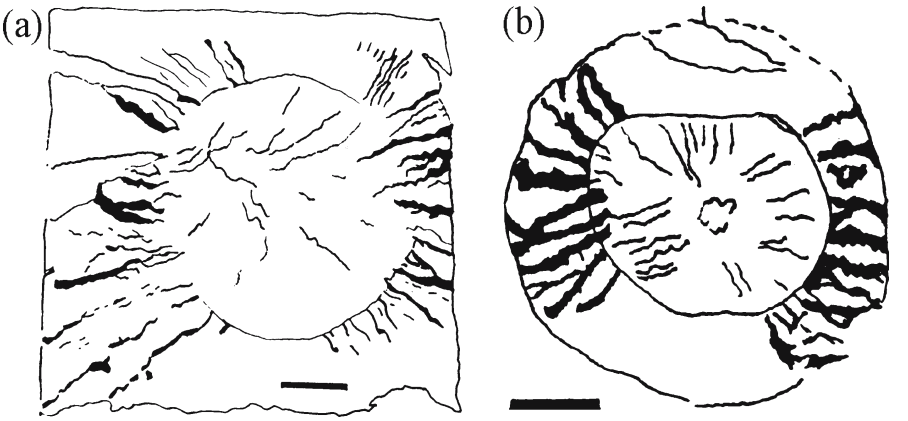

Fig. 2.44. Drawings of fringes around circular parent fractures. **a** Segment rotation is counter clockwise on the left side of a fracture in steel and is clockwise on the right side of the fracture (after Yukawa et al. 1969, Fig. 1). *Scale bar* is 12 mm. **b** A repeated pattern from **a**, around a discoid joint in the Frauenbach quarzite from the Thuringian Schiefergebirge (after Bankwitz and Bankwitz 1984, Fig. 3). *Scale bar* is 5 mm

This fracture pattern is a result of a slight deviation of the tensile axis (by not more than several degrees, Sommer 1969) from normality to the parent fracture. It caused two segmentations advancing in opposite directions, rather than a single propagation that surrounded the entire boundary of the circular parent fracture. The latter propagation would occur under "pure tension", which is probably difficult to achieve, and therefore would be less common. On the discoid from Mt. Carmel (Fig. 3.40c), there is no segment overlapping in certain parts of the concentric fringes. It is assigned to "pure tension", which was applied on the central part of the discoid but not on its right and left parts, suggesting that even locally the stress field was not homogeneous. The "concentric joint" displays opposite senses of segment rotation in a single curved fringe (Fig. 3.40b) induced by a local stress field. A remote deviation of the minimum principal direction would result in similar segment rotations in neighboring joints, typical of many joint fringes along Wadi Naim (Bahat 1986a), which is not the case shown in this outcrop.

2.2.7.4 *Opposite Rotations of* En Echelon *Segments in Fringes below and above the Parent Joint*

Significant dissimilarities in size and shape of different fringes of the same joint should reflect a deviation from simultaneous *en echelon* segmentation. The two fringes in Fig. 2.45 differ in the directions of segment rotation and in segment size and geometry, quite possibly suggesting that the two fringes responded to different loading. It appears that the fracture sequence of this joint was initially:

1. Propagation of the parent joint from left to right, as shown by the plume.
2. Segmentation of the lower fringe in a rational continuation with the plume.
3. Segmentation of the upper fringe follows a change in the loading direction.

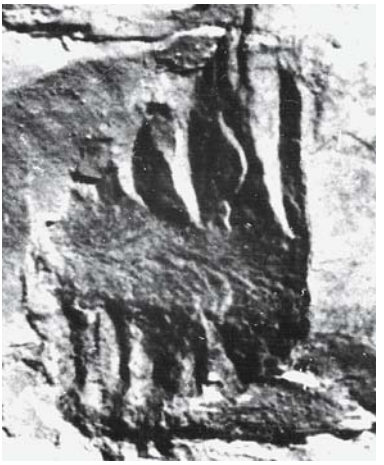

Fig. 2.45.
A fracture cutting Lower Eocene chalk in the Shephela syncline. *En echelon* fringes occur on both the upper and the lower sides of the parent joint. There is a clockwise rotation of the *en echelon* segments with respect to the parent joint in the upper fringe and a counter clockwise rotation in the lower one. However, cracks in the two fringes differ considerably in shape. Length of plume is about 30 cm (after Bahat 1997)

2.2.7.5 *Timing Relationships of Plumes, Arrest Marks and* En Echelon *Segmentation*

The contact relationships of rib marks and barbs, combined with their interactions with crack segmentation, are useful in estimating changes in local stresses and enable the distinction of different stages in the fracture process. The plume on the "curved joint" (Fig. 2.35c) is bilateral, and the segmentation shows a uniform clockwise rotation, which corresponds to one direction of the plume but not to the other. The implication is that breakdown occurred after the completion of the growth of the bilateral joint. Hence, the growth of the curved joint was in several stages:

1. Fracture into an early elliptical joint.
2. Growth along the upper part of the layer into a bilateral joint that curves along the strike.
3. Breakdown of the joint into segments that propagated downward.

Some joint surfaces show divisions into concentric zones that are bounded by arrest marks (Sect. 2.2.4.1). These arrest marks do not only represent the fracture front at "rest" but they also mark the loci of stress redistribution (Murgatroyd 1942). This is revealed by changes in the sense of rotation of overlapping barbs with respect to the *en echelon* segments (Fig. 3.40b) or by changes in the segment azimuths (Fig. 2.38 and 3.40a, part D). Arrest marks (Sect. 2.2.4.1) can be useful in the interpretation of the interrelationships of individual joints associated in a common composite fracture. The series of sub-horizontal arrest marks that continue through parts B, D and E (Fig. 3.40a) suggest an early synchronization of the downward propagation of these parts.

What was the growth rhythm of the various segments along the "curved joint"? There seem to be conflicting observations. On the one hand, the breakdown into segments along the curved joint occurred under various K_{III}/K_I ratio conditions, which may imply that segmentation was not synchronous along the joint, but it occurred at the center before developing at the distal ends. On the other hand, it seems quite likely

that the various segments reached simultaneously the lower part of the joint, as demonstrated by an arrest mark that decorates all the segments at the same height and practically appear to be a monotonous morphological feature. Thus, the possibility of a non synchronous segment initiation but a synchronous completion of segmentation is not ruled out.

2.2.7.6 *The Spreads of Azimuths in Joint Sets versus* En Echelon *Fringes*

The spread of azimuths in individual joints and in joint sets is often greater than the spread of azimuths of the *en echelon* cracks associated with them. One example is shown in Fig. 2.35d. Other joints in outcrop Y show similar patterns. A summary of fracture orientations in outcrop X shows that the mean azimuth of the parent joints is N 03° W with standard deviation ±12° (63 measurements). The corresponding result for the *en echelon* cracks along the fringes of these joints is N 23° W ±6° (91 measurements), i.e., considerably lower spread (Bahat 1986a).

Geologists often appreciate the difficulty in estimating paleostress directions because of the uncertainties involved in determining the spread of the joint population into sets and establishing the average azimuth of a given set. If the spread of azimuths of *en echelon* segments in a set may be considerably smaller than the spread of azimuths of the parent joints associated with that set, it should enable quite readily the distinction between neighboring joint sets and their associated *en echelon* segmentation.

This is well exemplified in Table 2.1. It would be difficult to distinguish between joint sets X and O-Y3 because of the overlapping of ranges of fracture azimuths (350–014° and 012–035°, respectively). It is, however, considerably easier to distinguish these sets on the basis of their segmentation distinct ranges (338–342° and 026–053°, respectively). Hence, the styles of *en echelon* segmentation and rotation can considerably improve the confidence in the division of joints into sets and upgrade the analysis of paleostress directions.

Table 2.1. Orientation of joints and associated *en echelon* segments in the Beer Sheva syncline and corresponding compression

Station	Name of joint or set	Azimuth of joint (°)	Azimuth of segment (°)	Segmentation		Rotation of segment		Corresponding compression
				above joint	below joint	CW	CCW	
1) S	Part D	073	073–083		+	+	+	?
2) Y	The curved joint	029–046	043–047		+	+		Local
3) Y	Set O-Y3	012–035	026–053	+	+		+	Local
4) X	Set X	350–014	338–342	+	+		+	N–S, regional[a]
5) T	Mixed stepping	062–064	047–049 073–080	+ +			+	Local ?

Stations correspond to those in Fig. 3.33c and Bahat (1996a). All results are from vertical outcrops. *Set S* is from unit III and *sets X, Y* and *T* from unit IV. Clockwise is *CW* and counterclockwise is *CCW*.
[a] Southern part of the Dead Sea rift.

2.2.7.7
An Ascending Order of Fracture Morphologies on Joint Surfaces

It is useful to set the various fracture morphologies on joint surfaces in an ascending order of compounded elements. These can be correlated with various stress scenarios, from 1 to 12 (Fig. 2.46). In a crude way, scenarios 1 to 7 represent various manifestations of fracture morphologies that respond to changes in local stresses, whereas scenarios 8 to 12 show fracture morphologies that may help to evaluate changes in directions of remote stresses.

Scenarios 1 to 3 represent unilateral, bilateral and radial modes of joint propagation, respectively. Common to these morphologies is the perpendicularity of the minimum principal stress with respect to the parent joint, with possible slight deviations from it (Bahat 1997). Local constraints dictate the choice among the three, and a prolonged fracture in a thick layer would favor the third one (scenarios 1 and 2 are well known, and scenario 3 is manifested by the parent joint shown in Fig. 2.36a, displaying three concentric plume series.

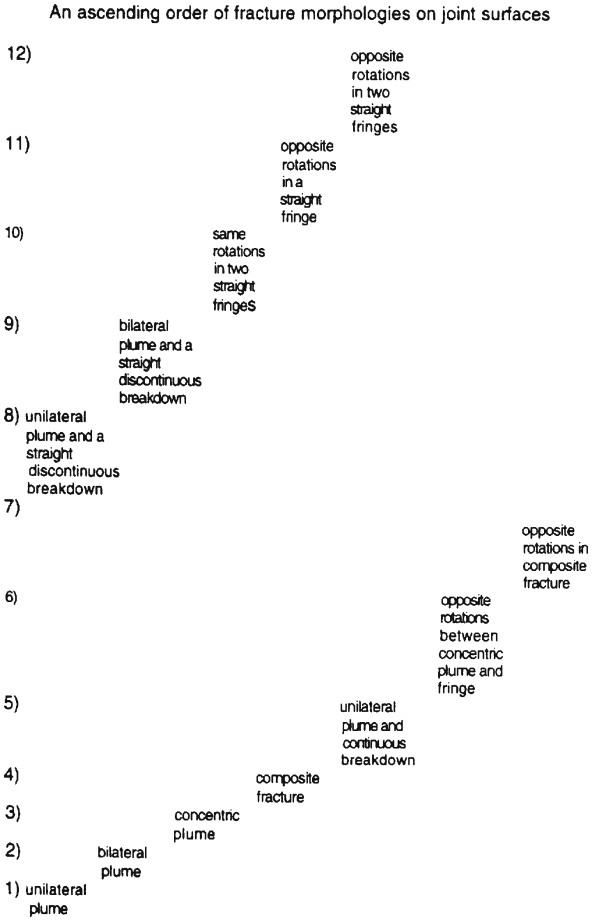

Fig. 2.46. Fracture morphologies on joint surfaces in an ascending order of compounded elements which correlate with twelve stress scenarios; see text for explanation (after Bahat 1997)

Scenario 4 represents a composite fracture that developed by the merging of a series of sub-parallel smaller joints, propagating in the same approximate stress field (Fig. 2.38). Scenario 5 describes the propagation of one part of the composite fracture (Fig. 3.40a, part D), which is the only joint that deflects in response to a slight deviation of the local minimum principal stress from perpendicularity. A deviation of the remote principal stress from perpendicularity to the composite fracture would have resulted in the deflection of additional parts of the composite fracture as well.

Scenario 6 results when the local minimum principal stress tilts somewhat from perpendicularity to the parent joint, so that a left-lateral shear changes to a right-lateral shear (Fig. 2.44a,b). It appears that segmentation without overlapping (Fig. 3.40d) signifies a transitional stage between left-lateral and right-lateral shears. Scenario 7 concerns alternating shears among neighboring joints that constitute a composite fracture. This situation occurs in massive sandstones (Fig. 3.23b,c), but is not known in chalk.

Scenarios 8 and 9 are recognized by the abrupt transitions between the parent joint and the *en echelon* straight fringe. These structures are good candidates for the identification of remote stress directions. Scenario 10 (Fig. 2.35a) may be considered as an "upgrading" of scenarios 8 and 9, also leading to the identification of remote stress directions. Scenarios 11 and 12 are related to opposite segment rotations in straight fringes (Bahat 1997, Fig. 9 and Fig. 2.45, respectively). They also provide indications for the distinction between different remote stress directions.

2.2.7.8
Local Stresses versus Remote Stresses

We summarize below the distinctions between the influences of local and remote stresses on the formation of *en echelon* cracks (Pollard et al. 1982; Bahat 1986a, 1997).

Local stresses. Field observations indicate that much of the interrelationship of the parent joint with the fringe and the behavior of the *en echelon* segments are influenced by local conditions, as itemized below:

1. There is a correlation between the size of *en echelon* cracks formed by the discontinuous breakdown and layer thickness (Fig. 2.43).
2. The various measurements of *en echelon* lengths vs. the layer thickness in the thickness range of 55–65 cm (Fig. 2.43) are all from layer 5 (Bahat 1986a, Fig. 2) and they show both continuous and discontinuous breakdowns that cannot be explained by remote influences.
3. Occasionally, specific timing relationships exist among plumes, the vertical *en echelon* cracks and the horizontal segments of arrest marks. These relationships may occur on surfaces of individual joints or composite joints (Fig. 2.35d and 2.38) but not in association with any of their neighbors along the same layer.
4. The sense of rotation of the segments in the fringe is clockwise, compared to counter clockwise rotation of the barbs on the parent joint (Fig. 3.40b). It seems highly unlikely that these two rotations reflect remote stresses. Quite possibly the counter clockwise rotation of the barbs is in response to local stress.
5. The reverse segment rotation along the fringe of the concentric joint reflects local conditions, rather than two distinct regional loadings.

Remote stresses. In spite of the important influence of local conditions on the behavior of *en echelon* segments, there are certain parameters that can quite clearly be correlated with remote stresses:

1. The decoupling of the fringe from the bilateral plume described above (Fig. 2.35c,d) suggests that these two morphologies were formed in response to distinct stress conditions. Here, the preference of the plumes to propagate bilaterally rather than unilaterally demonstrates a response to local conditions. On the other hand, the azimuth uniformity of the *en echelon* segmentation in the fringe and other fringes of neighboring joints in a set conforms to the influence of a remote stress. The decoupling of a fringe from a unilateral plume is as much an indication that the segmentation in the fringe represents a remote stress (as in the previous case related to the bilateral plume). A good example is provided by Younes and Engelder (1999). The uniformity in the sense of rotation of *en echelon* cracks with respect to their parent joints over great distances is a manifestation of fracture induced by remote stresses.
2. The conformity of clockwise rotation of *en echelon* segments with the NNE joints in station Y, on the one hand, and the strict counter clockwise rotation associated with the N-S joints in outcrop X on the other hand suggest two sets responding to distinct remote stresses (Table 2.1).
3. Specifically, fractures in outcrop X differ from all other fractures in the investigated area by the uniformity of their *en echelon* cracks in terms of their sense of rotation, their size and shape, and in the fringes that occur both below and above the parent joint. This distinct assemblage of properties categorizes a distinct remote stress field.
4. When a set of joints demonstrates a gradual azimuth rotation, the *en echelon* cracks at the fringes of these joints rotate in covariance with the joints (Bahat 1986a).
5. Discontinuous breakdowns are distinct from continuous breakdowns by often having a series of small *en echelon* cracks along the shoulder distributed among the larger *en echelon* cracks. Such series of small cracks have been named the "root zone" (Bankwitz 1966). They generally maintain their azimuths in alignment with their larger neighbor *en echelon* cracks, responding to remote stresses.

Spatial and temporal misalignments. The reader should be aware of differences in terminology. There are investigators that prefer to use different terms in their distinction between the remote and local categories. Younes and Engelder (1999) assert that if an advancing joint enters a volume of rock subject to a stress field misaligned relative to that guiding the parent joint, transverse adjustments in crack propagation due to mixed-mode loading cause the joint to break down into fringe cracks. If the misaligned stress field was present prior to joint propagation, the misalignment is spatial. If the misalignment took place after propagation and arrest of the parent joint, the misalignment is temporal. Due to occasional unclear cases regarding the propagation and arrest of the parent joint, we are not in favor of using this distinction and prefer the terms remote and local according to the description presented above.

2.2.7.9
En Echelon *Segmentation under Constraints*

Dilatational *en echelon* segmentation occurs under favorable conditions for mode III operation, and it is limited when constraints are imposed on this mode. As was mentioned above, *en echelon* segmentation is very common in rocks. It is also frequent in fractured polycrystalline metals (Hertzberg 1976; Tschegg 1983; Broek 1984 and references therein) and in single-crystals (Gilman 1958). On the other hand, *en echelon* segmentation is rare in (non-polymeric) glass, and the widely cited experiment by Sommer (1969) is related to segmentation in glass under fluid pressure.

The explanation to these differences is that defects in the structure continuity, like screw dislocations in single-crystals (Gilman 1958) and inclusions and grain boundaries in steel (Tschegg 1983) and in rocks, promote the development of local, heterogeneous stress fields, resulting in mixed mode loading that induces segmentation. The much smaller population of such discontinuities in non-polymeric glass is possibly the reason for the limitation of *en echelon* cracks in this material. *En echelon* segmentation does occur in polymeric glasses like PMMA (e.g., Cooke and Pollard 1996). However, fracture propagation in this material must involve an early strain and a breakdown of craze fibrils (Maccagno and Knott 1989). The effect of "mode III crack closure" (Tschegg 1983) imposes an important constraint on segmentation. Namely, *en echelon* cracking along layer boundaries would be minimized under compression by the overburden, and therefore, even if found in rocks in considerable depths, an early failure at shallow depths should be suspected. On the other hand, high liquid pressures could overcome the constraint imposed by the lithostatic pressure and induce extensile *en echelon* segmentation at considerable depths, in a similar manner by which they form joints at great depths by mode I (Secor 1965). The latter hypothesis still needs to be verified.

2.2.7.10
The Influence of Ductile Conditions on En Echelon *Segmentation*

We have seen above that mode III loading is a major promoter of *en echelon* segmentation. The plastic zone of mode III loading is several times larger than that for mode I for similar materials and at the same stress intensity values (Tschegg 1983). Thus, segmentation is associated with the increase in the plastic zone. This observation coincides well with the plane strain/plain stress relationship in a plate, showing that the plastic zone gradually increases from the plane strain size in the interior to a plastic zone of a larger size under plane stress at the surface of the plate (Hertzberg 1976; Broek 1984). Analogously in geological terms, conditions along the layer boundaries are more conducive for segmentation than in the layer interior.

2.2.7.11
Limitations and Future Research

The study presented in this section has certain deficiencies that are addressed below. First, most of the information presented here has been gathered by one researcher (the

first author), and some subjective interpretation is perhaps unavoidable. Therefore, the various observations and subsequent rules that were determined in this study should be considered tentative until they are verified in similar sedimentary fracture provinces. Second, the present section essentially relates to a single lithology, chalk. Therefore, some of the relationships that were established here may have to be modified when applied to multi-lithological provinces (such as the Appalachian Plateau). Third, there is a need to further investigate the nature of the continuous breakdown. What causes breakdown to start from the boundary of the parent joint (shoulder in Fig. 2.35a) and when does it to start from within the parent joint (e.g., Fig. 2.35c)? Fourth, alternative theories of fracture mechanisms that exist today regarding the formation of fringes (Sect. 6.10) need to be evaluated, in order to develop a strong framework into which additional field and experimental information would be added and interpreted.

2.2.8
Straight Kinks and Curved Kinks

A kink is generally perceived as a relatively short crack that occurs at the termination of a straight parent fracture that started as a joint. Due to mixed mode I + II loading, kinks deviate from the strike of the parent fracture, pointing towards the continuations of the extensional quadrants (Cotterell and Rice 1980) (Fig. 2.47a). Cruikshank et al. (1991) used a mixed-mode linear elastic fracture mechanics model and applied the maximum circumferential stress criterion (Erdogan and Sih 1963) in order to ac-

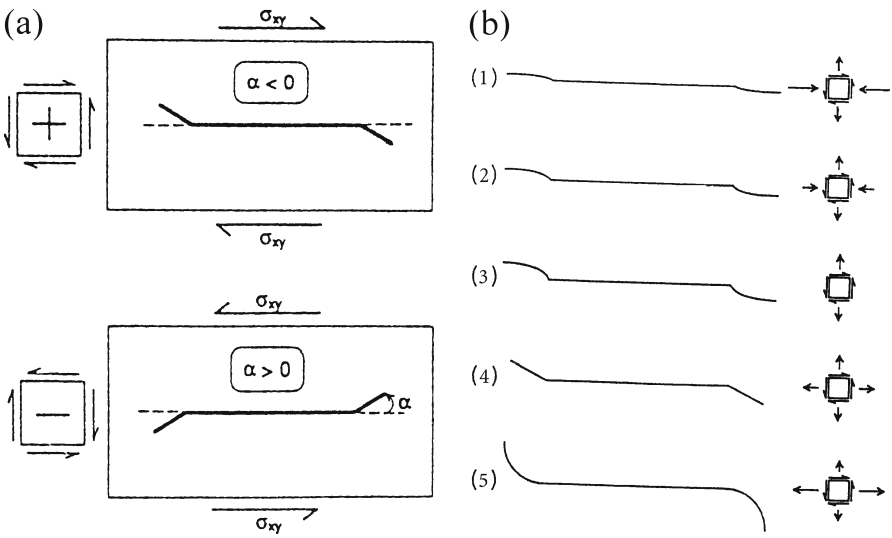

Fig. 2.47. **a** Relations between sense of shear and direction of kinking. For positive, right-lateral shear, the kink angle is negative. For negative, left-lateral shear the kink angle is positive. **b** Examples of idealized tail cracks for various far-field loading conditions. In all cases, pressure within the fracture is adjusted to cause propagation. In *1* and *2*, the stress parallel to the fracture is compressive and in *3* it is zero. Tail cracks kink and then converge. In *4* the stress parallel to the fracture is tensile and equal to that normal to the fracture. The fracture merely kinks. In *5*, the stress parallel to the fracture is a larger tensile stress than that normal to the fracture, and the tail rack diverges (from Cruikshank et al. 1991)

count for the orientation of cracks near the ends of small-displacement faults. They assumed that the faults were subject to uniform driving stresses and that the cracks opened perpendicular to the greatest circumferential stress ($\sigma_{\vartheta\vartheta}$) near the fault tip (see Lawn and Wilshaw 1975a, Fig. 3.4, for general conditions, and present Fig. 1.25 for $\vartheta = 0$). In their model, the sense of kinking indicates the sense of shear during fault-

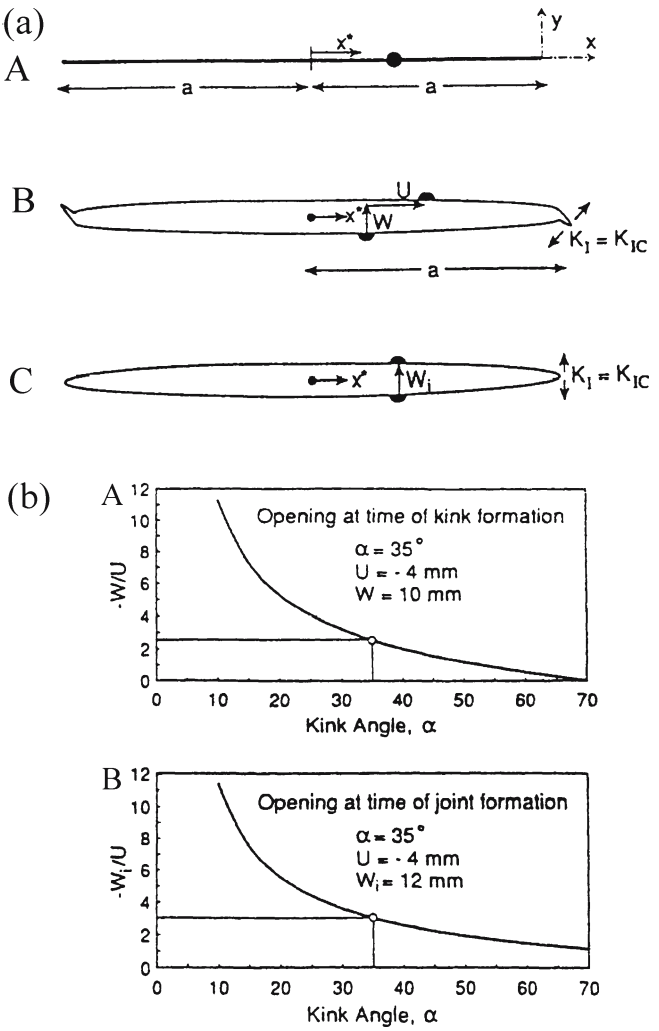

Fig. 2.48. a Definitions of kinematic properties of a crack. *A* Crack length is 2*a*. *y*-coordinate normal to crack, x^*- and *x*-coordinates parallel. *Dot* is a material particle split by the crack. *B* Displacement components, *U* and *W*, of part of a material point along a crack wall relative to the other part of the material point along the opposite crack wall. Mode I stress intensity equal to critical stress intensity for mode I fracturing at the time a kink forms. *C* Displacement in mode I loading at the time the initial fracture formed. Material point split and parts displaced only normally relative to one another. Mode I stress intensity equal to critical stress intensity at the time the fracture stops lengthening. **b** Relations between kink angle α and, *A* ratio of opening, *W*, to slip, *U* along fracture, and *B* relation between kink angle and ratio of initial opening, W_i to subsequent slip, *U*, along fracture (from Cruikshank et al. 1991)

ing: A kink that turns clockwise with respect to the direction of the main joint is a result of right-lateral shear, and a kink that turns counter clockwise is a result of left-lateral shear. Furthermore, the kink angle α, the angle that the secondary fracture forms with the extension of the primary fracture, is related to the ratio of the shear stress responsible for the kinking to the normal stress responsible for the opening of the fault (Fig. 2.47a).

Cruikshank et al. (1991) consider both sharp/straight and curved kinks and show a span of orientations of a straight kink and curved kinks that can be digitally obtained under various loading conditions (Fig. 2.47b). In their model, which limits stresses to principal directions, pressure within the parent fracture is adjusted to cause propagation. Thus, while Cruikshank et al. (1991) concentrate on stress differences (Fig. 2.47b), Cooke and Pollard (1996) study the influence of loading rate on the shape of kinks (Fig. 2.20a,b). Cruikshank et al. (1991) suggest that the amount of opening of a joint at the time it faulted or even at the time the joint itself formed can be estimated by measuring the kink angle and the amount of strike-slip at some point along the faulted joint (Fig. 2.48a,b). They relate the ratio of fault aperture, *W,* to slip, *U,* at the time of faulting to α. For a pure mode I fracture ($W/U = \infty$), $\alpha = 0°$. For a pure mode II fracture ($W/U = 0$), $\alpha = \cos^{-1}(1/3) \approx 70.5°$. For angles between 35° and 55°, they calculated that the ratio of opening to offset at the time of faulting was between 3.02 and 1.70, respectively. These angles hold no matter how large the relative displacements of the fracture walls are, provided they are not zero.

2.2.9 Recent Studies from the Appalachian Plateau

2.2.9.1 *General*

This section relates to the occurrence of fringes and kinks associated with joints in sedimentary rocks from the Appalachian Plateau, based on the study by Younes and Engelder (1999) that we cite below. Here we concentrate on fractographic relationships, while the wide geological implications of their study are cited in Chap. 3. Younes and Engelder (1999) consider three types of fringe cracks in their study area: Gradual *en echelon* fringes (that they term gradual twist hackles), abrupt *en echelon* fringes (that they term abrupt twist hackles), and kinks. A description of these three types with a subsequent discussion is presented below.

2.2.9.2 *Gradual* En Echelon *Fringes*

Gradual *en echelon* fringes occur within the same bed and lithology that hosts the parent joint (Fig. 2.49a,b). The surfaces of the *en echelon* segments occasionally show plumes that indicate an overall vertical propagation direction. Younes and Engelder (1999) observe that this surface morphology is often continuous with that of the parent joint, giving no indication that the parent joint arrested before the gradual *en echelon* fringe propagated. In their model, however, the plumes on the fringe are separated from the plume on the parent joint (Fig. 2.49a), as compared with our model

(Fig. 2.20d) that shows plume continuity. Upon breakdown at the joint tip line (equivalent to the shoulder in Fig. 2.36b), the *en echelon* segments twist away from the parent. The segments realign normal to the local maximum tensile stress, propagating perpendicular (i.e., vertically) to the overall lateral propagation direction of the parent joint. This is clearly seen on the diagram in Fig. 2.49a (not as clear in the photograph of Fig. 2.49b).

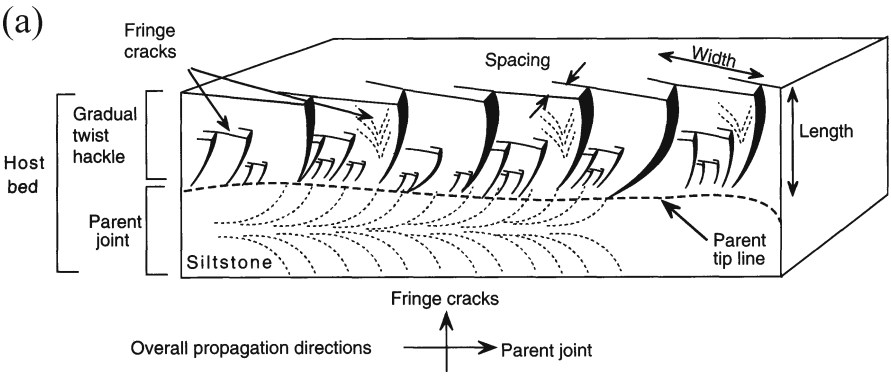

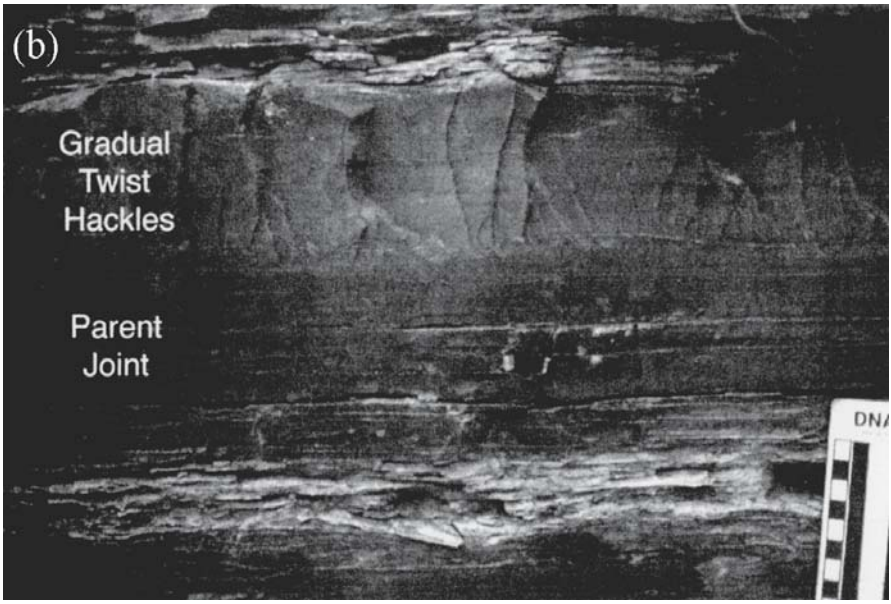

Fig. 2.49a,b. *En echelon* segmentation in the Appalachian Plateau. **a** Schematic of a gradual *en echelon* fringe. The parent joint and *en echelon* fringes are carried within a single host bed. The number of fringe cracks decreases away from the parent joint. The spacing of the cracks changes from small at the tip line of the parent joint to large at the end of the fringe. **b** A photograph of a gradual *en echelon* fringe. A parent joint and an *en echelon* fringe are carried within a single bed of siltstone of the Ithaca Formation at Taughannock Falls State Park, New York. Propagation direction for the *en echelon* fringe is upward. The sense of stress field rotation in this example is clockwise. The *scale* to the lower right is divided into centimeters (from Younes and Engelder 1999, no changes are made in the wording of original figures)

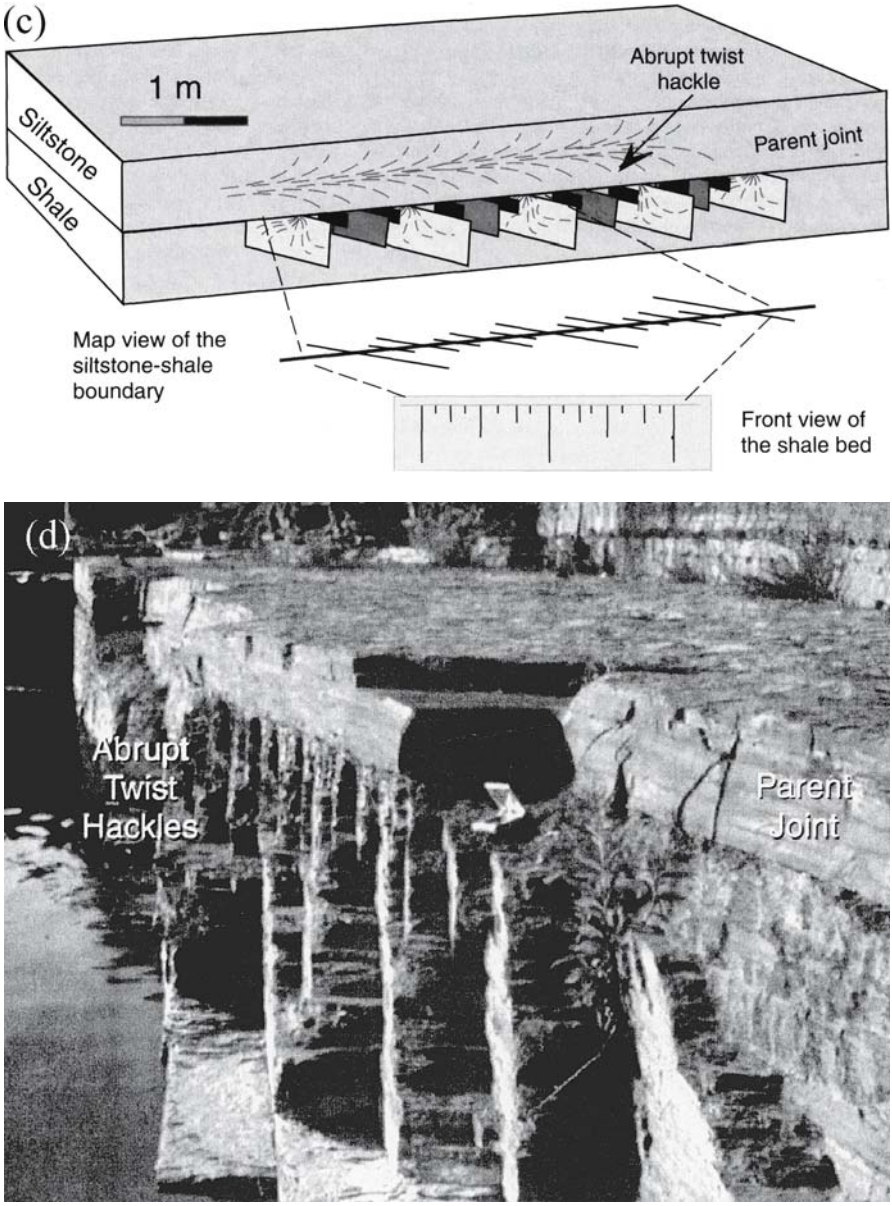

Fig. 2.49c,d. *En echelon* segmentation in the Appalachian Plateau. **c** Schematic of an abrupt *en echelon* fringe. These fringe cracks can propagate downward or upward from a siltstone bed into adjacent bed. They have a characteristic sequence of large and small cracks, indicative of suppressed growth where crack stress shadows limit the growth of some cracks. **d** A Photograph of an abrupt *en echelon* fringe. This set of fringe cracks propagated downward into a thick shale bed from a thinner siltstone bed hosting the parent joint at Taughannock Falls State Park, New York. These rocks are part of the Ithaca Formation. The sense of stress field rotation in this example is clockwise. The *scale* is a geologic compass with an 8-cm base (from Younes and Engelder 1999, no changes are made in the wording of original figures)

2.2.9.3
Abrupt En Echelon *Fringes*

According to Younes and Engelder (1999), abrupt *en echelon* fringes are commonly found in shale and initiate from the tip line of dip joints in siltstone layers that are typically less than 30 cm thick (Fig. 2.49c,d). Because abrupt *en echelon* segments abut the parent joint at a point, they appear in map view to grow across the edge of the parent joint. In contrast with gradual *en echelon* fringes that grow within the same bed as the parent joint, abrupt *en echelon* fringes are separated from parent joints by a layer boundary (Younes and Engelder 1999). These *en echelon* cracks are equally common, propagating upward, downward, or in both directions from siltstone beds.

2.2.9.4
Kinks

According to Younes and Engelder (1999), in the Appalachian detachment sheet kinks occur exclusively in siltstone beds (Fig. 2.50), and no evidence for slip was observed on any parent joint carrying kinks in the detachment sheet. They make the point that kinks occasionally show a surface morphology of plumes that are continuations of the plume morphology from the parent joint. Therefore, they suggest that kinks occur as mode I cracks and the tilt in a crack path is driven by a shear traction superimposed on the parent joint after *arrest*, following a finite amount of mode I propagation (Erdogan and Sih 1963; Cotterell and Rice 1980).

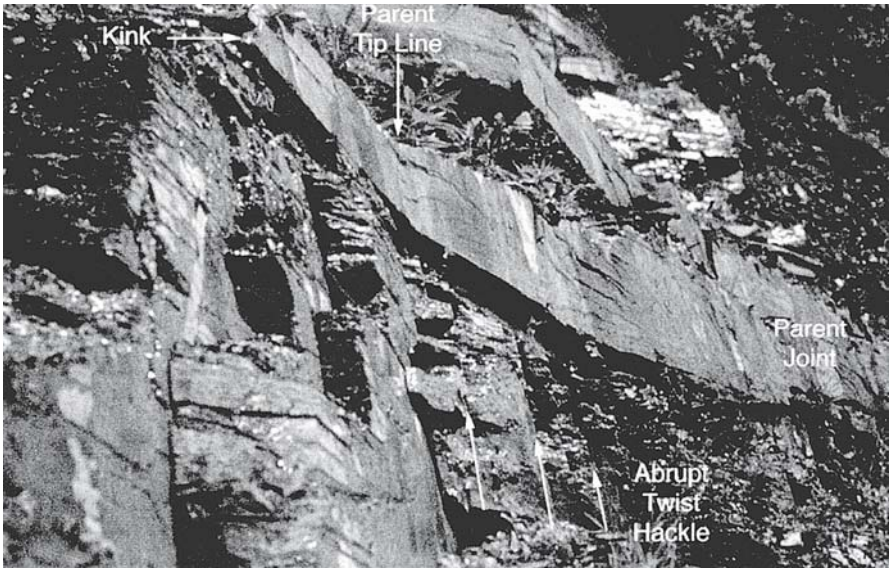

Fig. 2.50. An example of fringe cracks in a siltstone bed of the Ithaca Formation found near Whitney Point, New York. The shale above and below the siltstone bed carried an abrupt *en echelon* fringe. The sense of stress field rotation in this example is counter clockwise, both for the kink and the abrupt *en echelon* fringe. The parent joint is found in a bed roughly 20 cm thick (from Younes and Engelder 1999, no changes are made in the wording of original figures)

2.2.9.5
Tilt and Twist

Younes and Engelder (1999) observe that the angle of twist or tilt of a fringe crack set changes according to the host rock, the type of the fringe crack and the sense of rotation. For simplicity, they use the same angle sign (β) for the twist angle (equivalent to ω in this book), the tilt angle and the kink angle. Younes and Engelder found that the twist angles for clockwise *en echelon* cracks are generally smaller than for counter clockwise *en echelon* cracks. Gradual *en echelon* cracks have small twist angles, with a mode at 3° for clockwise *en echelon* cracks and 6° for counter clockwise *en echelon* cracks. Abrupt

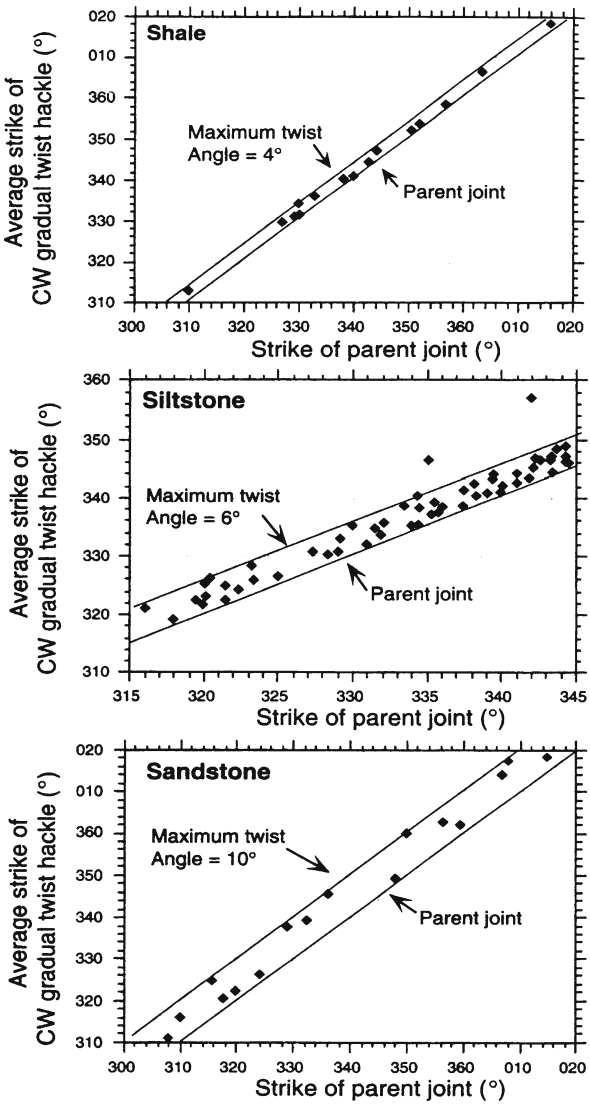

Fig. 2.51.
Change in the angle between parent joint and the clockwise (*CW*) gradual *en echelon* fringes according to lithology. The maximum twist angle increases as the clastic grain size becomes larger (from Younes and Engelder 1999, no changes are made in the wording of original figures)

en echelon cracks have larger twist angles, with a mode at 13° for clockwise *en echelon* cracks, and 22° for counter clockwise *en echelon* cracks. Kinks have tilt angles with a mode of 16° for clockwise *en echelon* cracks and 14° for counter clockwise *en echelon* cracks. The maximum twist angle for gradual *en echelon* cracks varies according to the lithology hosting the parent joint. This is seen in a plot of the strike of fringe cracks vs. the strike of parent joint (Fig. 2.51). In this plot, data for counter clockwise fringe cracks would plot below a line with a slope of one, whereas data for clockwise fringe cracks are plotted above this line. By drawing delimiting envelopes parallel to this line, Younes and Engelder (1999) found the maximum twist angles in coarser beds. For example, *en echelon* cracks in shale layers have a maximum twist angle of 4°, whereas those in sandstone layers reach 10° for *en echelon* cracks with a clockwise twist angle.

2.2.9.6
Discussion on Kinking

While Cruikshank et al. (1991) restrict kinking to faulting on existing joints, Younes and Engelder (1999) consider kinking on joints without slip. The common gradual curving of joints as they approach earlier joints (e.g., Fig. 3.36b) and curved mud cracks that maintain continuous plumes along the strike (Weinberger 2001b, and pers. comm.) imply that curved (gradual) kinking (Fig. 2.20b) is possible. A more difficult issue is whether straight (abrupt) kinks (Cruikshank et al. 1991) exist on joints, i.e., whether kinking occurs in continuation with the propagation of the parent joint (in one event) or after parent joint arrest (in more than one event, Fig. 2.20a). If continuities of plumes are observed on parent joints and straight kinks, single event processes may be suspected. On the other hand, if discontinuities are observed between the plumes on the parent joints and kinks, more than one event should be considered. The latter could be the growth of a kink after a certain time interval following a fracture arrest. A careful inspection of both the continuous and discontinuous plumes should be exercised on suspected straight kinks, because a cutting relationship between two distinct joints of different sets can be mistaken for straight kinking (see Sect. 2.2.10.2 below). It appears to us that presently, no compelling evidence for straight kinking on joints exists, and until such evidence is provided, straight kinking by faulting is the only known mechanism. Finally, the important role of plumes in the interpretation of the genesis of kinks has a certain similarity to their role in the study of pinnate joints (Fig. 2.68d).

2.2.10
On the *En Echelon* Fringe Terminology

2.2.10.1
The Parent Joint is a Part of the Mirror Plane

We note that the gradual *en echelon* fringe type of Younes and Engelder (1999) (Fig. 2.49a,b) resembles the famous diagram of surface markings on a systematic joint by Hodgson (Fig. 2.36b), where an abrupt transition from the parent joint to the fringe occurs along the shoulder. Also, in both diagrams (Fig. 2.36b and 2.49a), new plumes start at the fringes. The gradual *en echelon* fringe of Younes and Engelder (1999) is also similar to the discontinuous fractography (Fig. 2.35a,b), which displays an abrupt transition of

the parent joint to the fringe. The above examples illustrate only part of the confusion regarding joint terminology (see more in Bahat 1991a, Sect. 2.2).

The main deficiency of the existing descriptive schemes of *en echelon* fringe terminology is that actually, they have no compelling limitations. A classification with compelling limitations that would minimize confusions may be achieved by forming a terminology based on superposing crack descriptions on fractographic features that correspond to fracture mechanic rules (Sect. 4.8). We suggest that the key to a comprehensive terminology should be the notion that the parent joint is part of a mirror plane. This relationship will automatically define all the morphological features that reside on the parent joint and on the fringe (Fig. 2.1). This is fairly clear in granites (Chap. 4), but it is occasionally hindered when joints cutting sedimentary rocks are considered, because in the latter rocks the parent joint is often a portion of a mirror plane, which is constrained between layer boundaries and cannot achieve full growth (Bahat 1998a and present Fig. 2.8). This terminology is a part of a wider classification that distinguishes between *en echelon* fringes and hackle fringes (Fig. 2.1, 4.35 and 4.37–4.40).

2.2.10.2
A Fringe of a Parent Joint Can Only Form from "Continuous Material"

The study by Cooke and Underwood (2001) (present Fig. 2.32) seems to justify the reevaluation of previous discussions on three cases of *en echelon* segmentation at different lithological interfaces (Bahat 1997; Younes and Engelder 1999). The first case concerns fracture in Devonian sediments from the Appalachian Plateau (Younes and Engelder 1999) that relates to two joints in siltstone (relatively smooth surfaces) alternating with shale beds (rough surfaces) (Fig. 2.50). While the joint surfaces in the siltstone layers change orientation along the strike (three sectors in the lower layer and two sectors in the upper one) the fracture surfaces in the lower shale bed maintain the same azimuth. We suggest that whereas the sectors of different orientation in the siltstone represent two distinct joint sets, the fractures cutting the shales represent a single, distinct joint set, i.e., the fractures in the shales do not form an "abrupt" *en echelon* fringe to the parent joint in the siltstone. Possibly the set in the shales is Ia and one of the sets in the siltstone is Ib (Engelder and Geiser 1980, the former set is clockwise with respect to the latter). This relationship is repeated in additional outcrops (e.g., Fig. 2.49d). Quite intriguing is the decrease in spacing of the joints in the shales as they approach the lower boundary of the siltstone bed. The reduction in spacing implies an increase in the tensile stress concentration along the boundary between the shales and siltstone. The multiplied tensile stress resulted in a repeated growth of (short) joints in the shales that were added between the earlier long joints of an existing set (Fig. 2.49d and 2.50). Hence, the short joints *are not en echelon segments* in a fringe and are unconnected to remote extension normal to the parent joint in the siltstone, but rather, they relate to the energy released at the contact between the two rocks that affected fracture only in the shales.

The second case is about fracture in chalk adjacent to a fracture in a chert bed (Fig. 2.52a). The interpretation here is the same as for the first case: The short fractures represent a joint set cutting the chalk; they were not formed in a fringe of the

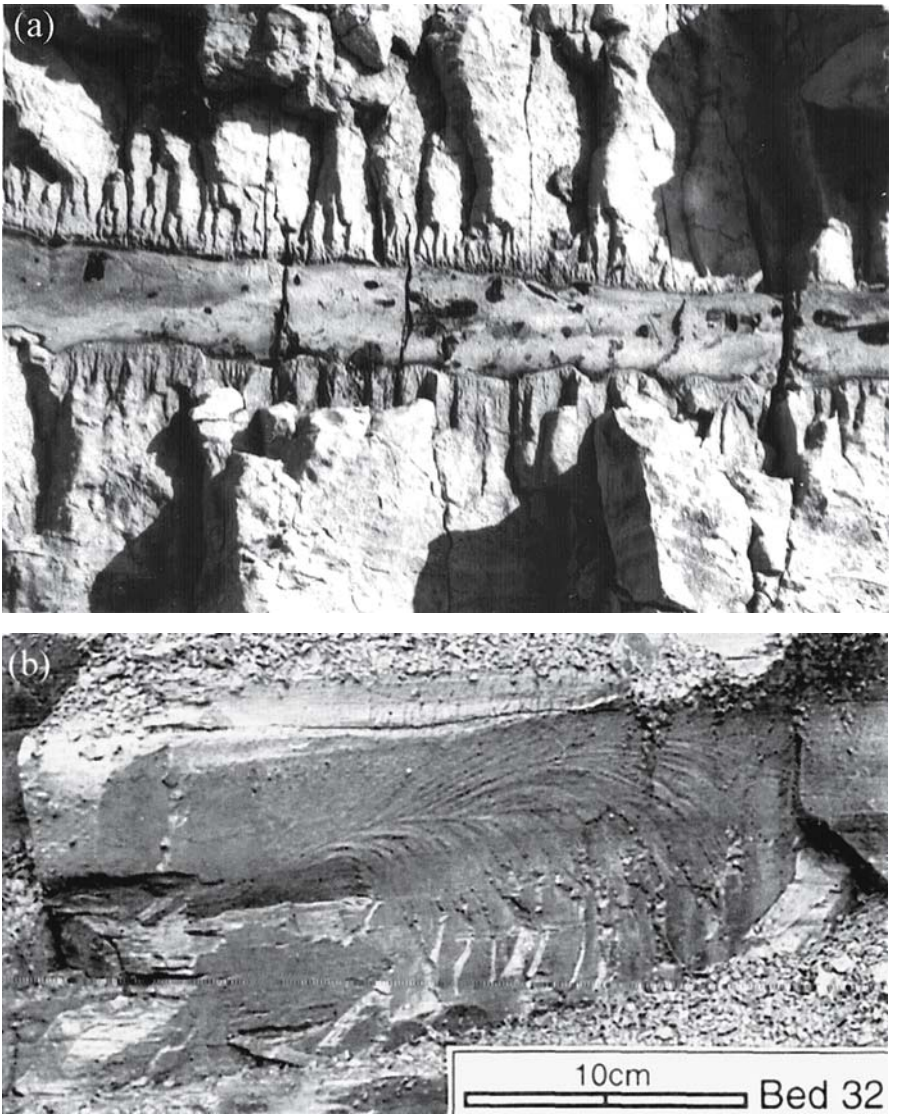

Fig. 2.52. a A sandwich of two chalk layers and a chert bed in the middle from the Mor Formation near Beer Sheva. *En echelon* segmentation occurs in the chalk only along contacts with joints cutting the 15 cm thick chert bed, but not along contacts with unfractured chert nodules (after Bahat 1997). **b** Plumes that developed within the limestone layers appear to have continued, forming a fringe of *en echelon* segments in the interbedded shales underneath the limestone (after Roberts 1995, Fig. 5d)

parent joint in the chert. Quite possibly the interface contacts in the first and second cases were not welded enough to act as a "continuous material", which is a required condition to form a fringe of a parent joint. In these two cases, separate fracture processes took place in the two lithologies.

The third case concerns a study on jointing in interbedded limestones and shales that appear to be welded together (Fig. 2.52b). While plumes developed within the limestone layers, a fringe of *en echelon* segments occurs in the interbedded shales just underneath the limestone in an apparent continuation from the plume in the limestone. However, it appears that both fracture surface morphologies occur on a vertical veneer of secondary mineralization that covers the two lithologies and acts as a "continuous material". Thus, we interpret the sequence under consideration to be: Early vertical fracture through both lithologies, secondary mineralization, and then, late fracture along the contact between the veneer and the early vertical fracture.

Our interpretation of the three cases needs to be verified in additional fracture provinces. Particularly, the first case needs to be carefully examined (we take it as a speculation that could be wrong). If this interpretation is proven correct, it would limit or question the validity of the category of abrupt *en echelon* fringes in the Appalachian Plateau.

2.2.11
Summary of Five Categories of Breakdown Styles

The various extension paths from parent joints by tilt and twist joints to kinks and fringes may be condensed into five categories that reflect different mixed mode loadings and propagation rates. Four categories are summarized in Fig. 2.20a–d. Note that the scheme given in Fig. 2.20c,d concentrates on discontinuous breakdowns that initiate close to the layer boundary (Fig. 2.35a,b), excluding the continuous one that initiates between the layer boundaries (Fig. 2.35c,d). The continuous-gradual style may be considered a variation linked to the gradual, the fourth category, and a full analysis of joint fringes should concern this style as well.

While studying rare hackle fringes in sedimentary rocks, Bahat and Rabinovitch (2000) observed angular relationships that differed from the above four categories. The tilt angle ϕ produced between the mirror plane and the fringe varied from 0° to 30 ±5° along the mirror boundary of a natural joint (Fig. 2.30a), ϕ, of an artificial fracture that formed by blast varied from 30 ±8° to 50 ±8° (Fig. 2.30b). Thus, the tilt angle ϕ appears to be larger on the artificial fracture that was dynamically blasted by high stresses than on the joint surface that was probably created under moderate stress conditions. The fractographic features on the mirrors and fringes of both fractures seem to have been formed discontinuously, suggesting abrupt transitions. Hence, the fractographic relationships in Fig. 2.30a,b suggest a fifth category. This category concerns transitions from the parent fractures to the fringes that are influenced by mixed I + II + III modes. The tilt angle ϕ is induced by mixed I + II modes, and the twist angle ω (although can hardly be measure in the hackle fringes of Fig. 2.30a,b) is formed by mixed I + III modes.

The fifth category is rare in sedimentary rocks but seems to be relatively common in granites. Note that in Fig. 2.30a,b and 2.56a,b, which display semi-circular mirror planes, there are no distinctions between fringes that tilt in the distal direction and perpendicular to it, i.e., normal to the larger or smaller radii of the semi-circular mirror planes. Thus, the fifth category that relates to a rim (consisting of quasi-fringes and quasi-kinks) of secondary cracks that surround the mirror plane is clearly a prod-

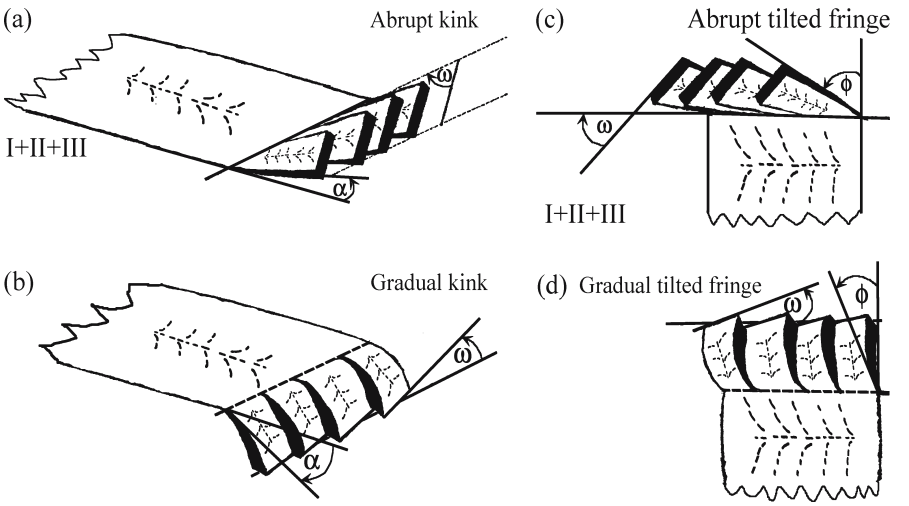

Fig. 2.53. Four styles of breakdown by mixed mode I + II + III. Breakdowns occur in the kink along the distal continuation of the parent joint and in the fringes parallel to layer boundaries in sedimentary rocks. **a** and **b** relate to abrupt and gradual tilted kinks, respectively. The segmented kinks are described by α and ω angular relationships. **c** and **d** relate to abrupt and gradual tilted fringes, described by ϕ and ω angular relationships. ω is formed by the edge of the mirror plane (normal to the main plume) and the segment width, α is formed by the edge of the mirror plane (parallel to the main plume) and the segment length (or its tangent), and ϕ is formed by the edge of the mirror plane (normal to the main plume) and the segment length (or its tangent)

uct manifestation of mixed I + II + III modes. Nevertheless, we generalize and divide this category in our scheme (Fig. 2.53a–d) into four corresponding groups that would also fit hypothetical cases in sedimentary rocks. Groups a and b relate to abrupt and gradual tilted fringes, respectively that form at the distal part of the parent joint; these groups concern segmented kinks that are described by α and ω angular relationships. On the other hand, groups c and d relate to abrupt and gradual tilted fringes, respectively that form along one or two layer boundaries; these groups display ϕ and ω angular relationships. These fractographies are treated in great detail by Bankwitz and Bankwitz (2004) (see more in Sect. 4.4.4).

2.2.12
Recent Studies from the South Bohemian Pluton

2.2.12.1
Introduction to Joints from Two Granitic Quarries

The bulk of the existing knowledge on jointing is related to sedimentary rocks. Most of these joints develop under anisotropic constraints imposed by rock discontinuities such as layer boundaries and fabrics of different origins. In undeformed quasi-isotropic plutonic rocks on the other hand, such discontinuities are rare, and even flow fabrics mostly do not create loss of cohesion in the rock. Therefore, fracture in the latter rocks would be expected to propagate in an unrestricted manner, following fracture

mechanic criteria: Initial elliptical cracks would tend to grow in isotropic materials under tension into larger circular fractures, because the stress intensity factor is greater for the portion of the curve that has a larger radius, resulting in the decrease of ellipticity (Irwin 1962; Roy and Saha 1995).

To our knowledge the granites of the South Bohemian Massif in the Czech Republic exhibit one of the best spectra of joint fractography in the world by showing a great fracto-graphic diversification. Most of these granites had fractured during the late cooling stages of the pluton (Sect. 4.4.5) and were not deformed after solidification (apart from later fracture) before or after their uplifts, at least during the Upper Cenozoic. Therefore, they maintain the original shapes of early fractures from periods before the uplifts. The unfissured properties of these rocks were beneficial during more than a hundred years in the stone industry and construction purposes throughout Europe, leaving behind large quarries, many of which are still active. These quarries display large fractographic features on joints that cut the granites (Bankwitz and Bankwitz 1984). Therefore these granites are most suitable for studying joint fractography in plutonic rocks.

Section 2.2.12.2 presents a description of characteristic fractographic features of the mirror planes and fringes (Fig. 2.1) of ten selected joints from the Borsov granite quarry in the South Bohemian Massif. An additional fractographic treatment that includes geological interpretation of these joints is presented in Chap. 4. Accordingly, the fractographic descriptions are presented in two parts: Photographs are shown in Chap. 2 (Fig. 2.54–2.56) and their corresponding drawings (Fig. 4.6–4.8) and explanation, supplemented by Tables 4.1 and 4.2 are given in Chap. 4. A study on mirror planes and fringes from the Mrákotin granite quarry in this massif is presented in Sect. 4.4.3.1(the deferred treatment of this quarry is done in order to avoid its excessive partition among sections). The Borsov and Mrákotin quarries were chosen from many others in the massif since they best represent fractographic series between end members from "quasi-static" to "dynamic" joints (Sect. 4.9.3.3).

2.2.12.2
Fractography in the Borsov Quarry

Fractographic diversity. In their full exposure, the Borsov joints are divided into four groups:

1. Mirror planes without fringes (J1–J4).
2. Mirrors and simple *en echelon* fringes (J5–J7).
3. Mirrors and non-uniform/complex *en echelon* fringes (J8–J9).
4. A mirror and a hackle fringe (J10). They are briefly itemized below, citing Bahat et al. (2003).

The simplest joint surfaces (J1 and J2) show a superposed single plume on an array of arrest marks (Fig. 2.54a) and a single radial plume (Fig. 2.54b). More complex textures are the series of superposed concentric arrest marks and a radial plume that exhibits considerable changes in barb coarseness (width and height) on J3 (Fig. 2.54c), as well as the outcrop that reveals a set of joints (J4) that exhibit plumes

and arrest marks of different styles and intensities (Fig. 2.54d). These four exposures display incomplete mirrors without fringes (therefore they do not exhibit mirror boundaries).

There are four additional examples of joints that display both mirrors and fringes: First, the heterogeneous combination of arrest marks and plumes with the small fringe on J5 (Fig. 2.55a); second, a series of elliptical arrest marks superposing a multi-texture plume and a triangular fringe on J6 (Fig. 2.55b), and third, a fully developed circular en-echelon fringe of a uniform width on J7 (Fig. 2.55c). The fourth example (J8) consists of a circular mirror boundary with a non-uniform *en echelon* fringe (Fig. 2.55d). Still more complex are the heterogeneous and noncircular mirror boundaries, which are surrounded by complex fringes on the "trefoil joint" (J9) (Fig. 2.56a). The tenth joint, J10, displays a large fringe (relative to the exposed mirror) with transitions from *en echelon* to hackly morphologies (Fig. 2.56b). Fringe morphologies may vary very considerably in comparison to the plumes on the mirrors. Whereas fringe morphologies on J5–J8 (Fig. 2.55a–2.55d, respectively) are generally only slightly stronger than the corresponding plume morphologies, on J9–J10 (Fig. 2.56a–2.56b, respectively) the fringe morphologies are much more pronounced than the corresponding plumes. Finally, note the coarse, cusp nature of some of the arrest marks that decorate some of the "slow joints" (Fig. 2.54c, 2.55a, 2.55b), and lack of coarse ripple marks on the "rapid joints" (Fig. 2.56a–2.56b). A full understanding of this difference requires further studies (Sect. 2.2.4).

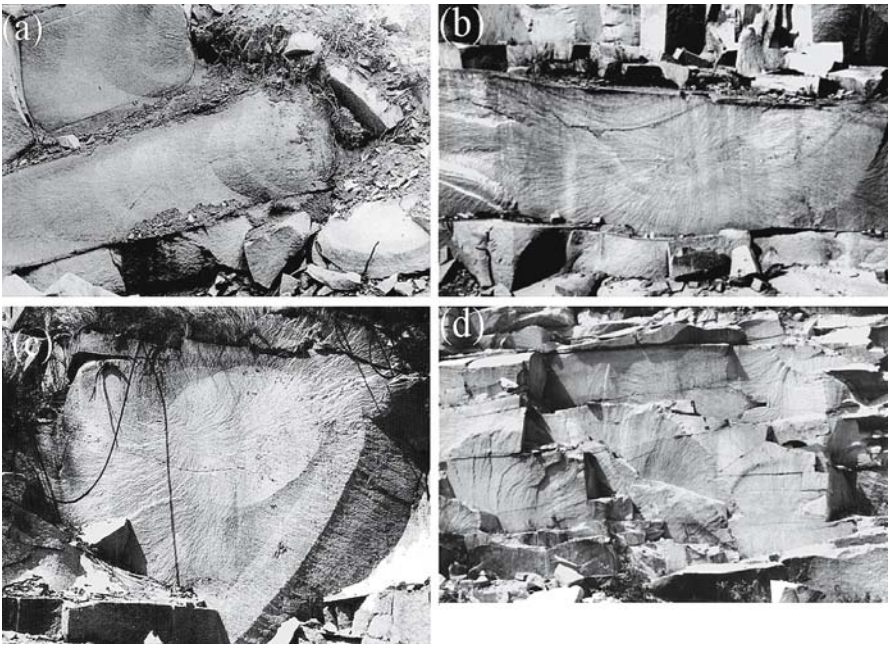

Fig. 2.54. Joints from the Borsov quarry (see corresponding drawings in Fig. 4.6–4.8 for explanation): Mirror planes without fringes. **a** The "multi-arrest mark joint", J1. **b** The "radial plume joint", J2. **c** The "quasi-core joint", J3. **d** The "multi-joint exposure", J4

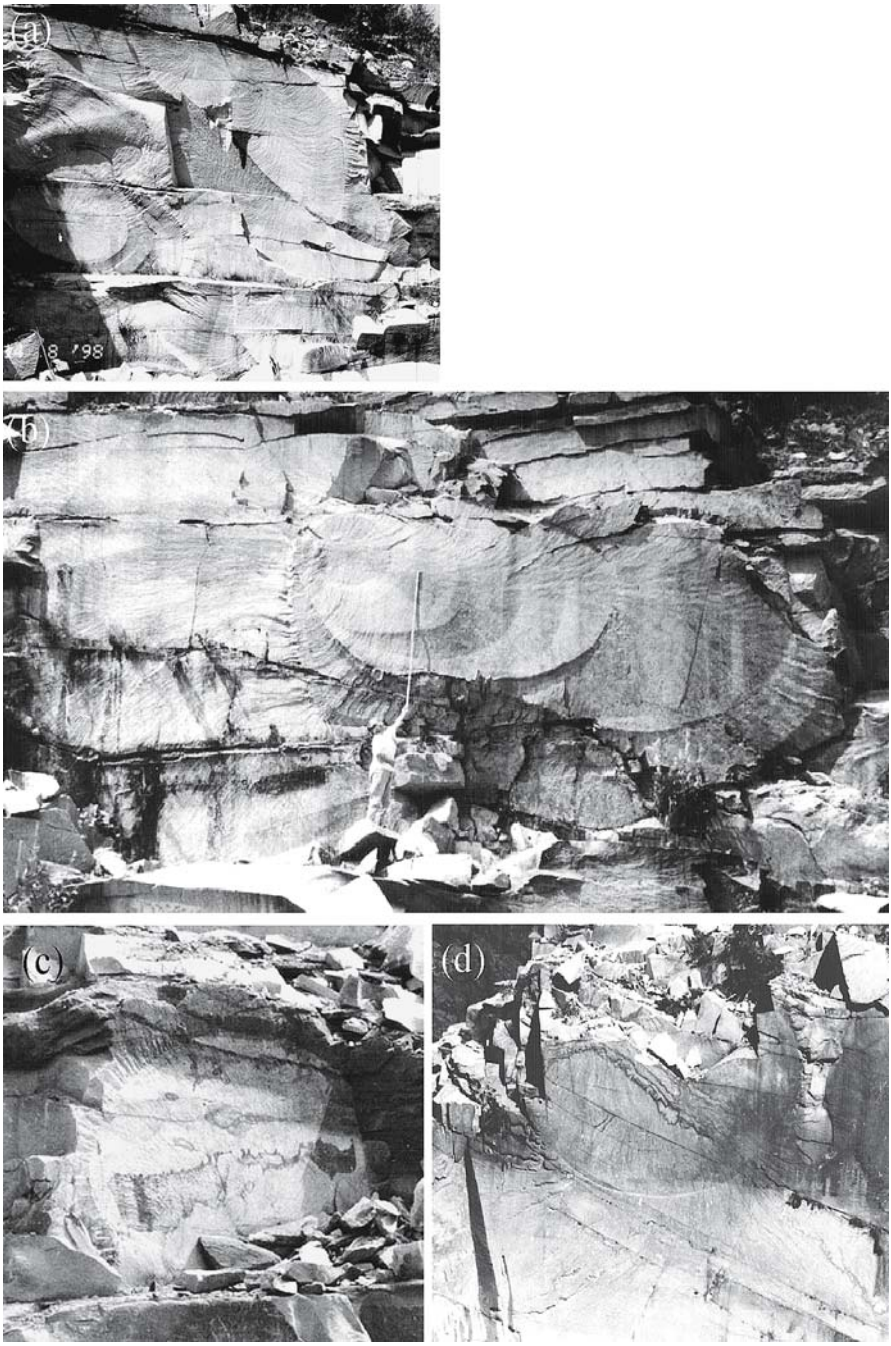

Fig. 2.55. Joints from the Borsov quarry (see corresponding drawings in Fig. 4.6–4.8 for explanation): Mirror planes that contain *en echelon* fringes. **a** "The divided arrest mark joint", J5. **b** The "asymmetric joint", J6. **c** The "uniform fringe joint", J7. **d** The "partly erased joint", J8

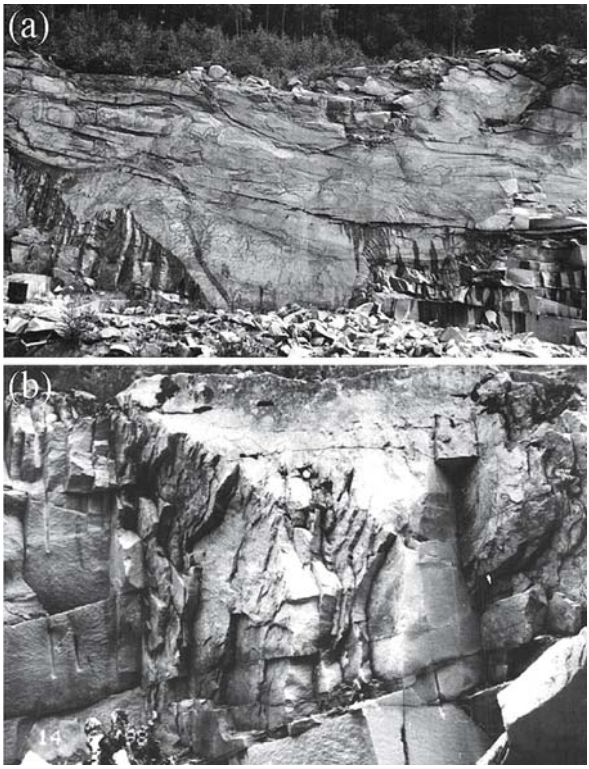

Fig. 2.56.
Joints from the Borsov quarry (see corresponding drawings in Fig. 4.6–4.8 for explanation): Mirror planes with diversified fringes. **a** The "trefoil joint", J9. **b** The "hackled fringe joint", J10

Mirror ellipticities. Practically all the joints at Borsov with exposed boundaries show mirrors that deviate from circularity into various ellipses. Some of these ellipses slightly rotate, i.e., mostly maintaining the large axes of their ellipses at various acute angles with respect to the horizontal orientation. Furthermore, often fracture ellipticity increases (the ratio of long to short axis increases) with joint growth (Table 4.2).

Incremental crack growth displayed by arrest marks. Periodicity and incremental crack growths are common. The arrest marks exhibit two common periodicity styles:

1. Uniform radius of curvature on all arrest marks (J1 in Fig. 2.54a).
2. Concentric growth of arrest marks (J6 in Fig. 2.55b).

Joint J6 displays a new type of incremental fracture of a strict growth of the arrest marks radii along the inclined symmetric axis at a dip of 8°, without propagation along the sub-vertical directions.

Central vs. eccentric fracture origins. Whereas certain joints initiate at the focus of radiating plumes or approximately at the center of the smallest arrest mark (e.g., Fig. 2.54a,b and 2.55b), some other joints initiate close to one side of the elliptic arrest mark (e.g., Fig. 2.54c and 2.55b). It is noticeable that the latter joints that display eccentric origins also show small angle plunge of their symmetry axes.

Variations in plume intensity. The Borsov joints mostly reveal three plume styles (Table 4.1): First, plumes with a uniform intensity, that is, a monotonous barb coarseness (relief); second, plumes that display alternating increases and decreases in their intensities along their imaginary symmetry axis; third, plumes that display an increase in their intensities as they curve away from their symmetry axis.

The first style is represented by J2 (Fig. 2.54b) and J7 (Fig. 2.55a). Whereas the plume of J2 is relatively coarse, that of J7 is weak and is hardly visible. The multi-joint exposure (Fig. 2.54d) displays adjacent joints decorated by plumes of various intensities. However, plumes of individual joints generally maintain uniform barb coarseness. The second style is represented by J3 (Fig. 2.54c), J5 (Fig. 2.55a) and J6 (Fig. 2.55b). On these joints, plumes change their intensities along their lengths at various locations on the mirror. Periodic changes in plume intensity are also known from sedimentary rocks (Fig. 4.36). The large plume of J6 initiates at the edge of the *en echelon* "triangle" fringe (Fig. 2.55b) and propagates horizontally towards the left at much lower intensities than towards the right. A transition of a fringe into a plume on the parent joint is rare, i.e., in all other known descriptions the transition is from plume to fringe. The third style is observed at the lower part of J1 (Fig. 2.54a), on the first and some subsequent elliptical growth stages of J6 (Fig. 2.55b) and on J8 (Fig. 2.55d).

Deviation from orthogonality. Previous studies (e.g., Hodgson 1961a) reported that plumes and ripple marks superpose each other orthogonally at every intersection on a given joint, indicating a simultaneous development of the two features. We found a deviation from the 90° pattern to smaller angles on J6 (see insert to Fig. 4.7b). While plumes generally form by local mixed mode I / III, in the present case the local mixed mode was possibly I / II / III.

2.2.13
Oblique Extension Joints and Longitudinal Splits (or Splittings)

2.2.13.1
Introduction

Conjugate hybrid joint sets. Occurrences of "conjugate hybrid joint sets" that form at small angles (≤45°) in the field have been considered by many investigators (e.g., Muehlberger 1961; Price 1966; Stearns 1968; Ladeira and Price 1981; Etheridge 1983). The same observation was termed differently by various authors, e.g., "oblique extension fracture" (Dennis 1972), "conjugate hybrid joints" (Hancock and Al-Kadhi 1978), "hybrid extension/shear fractures" (Ladeira and Price 1981), "transitional tensile behavior" (Suppe 1985, p. 154), hybrid joints (Bahat 1989), and transitional-tensile fracture (Engelder 1999). According to Hancock (1985), systematic joints can form an angular continuum from a coaxial relationship with the maximum principal compression (0°) to a maximum dihedral angle of c. 45°. Price (1977) and Hancock (1985) interpreted the "hybrid-shear fractures" as belonging to a failure class transitional between extension fractures and Navier-Coulomb shear fractures showing a conjugate set with a dihedral angle greater than 45°. However, explaining the structure of "conjugate hybrid joints" has been an outstanding problem in structural geology. For instance, Engelder (1999) suggests that based on assessments from laboratory (e.g.,

Brace's 1964 tests on a dog-bone-shaped sample), field and petrofabrics (e.g., a fracture system from Price and Cosgrove 1990) and theoretical observations (e.g., Reches and Lockner 1994), the transitional-tensile fracture propagation is unlikely to occur in homogeneous, isotropic rock, and that it is not explained by a parabolic Coulomb-Mohr failure envelope. We examine this suggestion below.

The outstanding question is whether oblique extensile fractures (joints) exist, i.e., whether a parent fracture (a vein) showing shear offset initiated as such within an isotropic, homogeneous rock, and then propagated in its own plane while that plane was subjected to a shear couple as well as an effective crack-normal tension (Engelder 1999). Several observations suggest that under certain conditions such results are possible. The occurrence of straight dilatational *en echelon* cracks at angular relations to the remote compression (Pollard et al. 1982) implies that such a simulation is possible. Willemse and Pollard (1998) observed this in nature and provided an explanation why straight wing cracks (Sect. 2.4.2) are relatively common (Fig. 2.57a). Perhaps another relevant case is bifurcation into two tensile branches that form small angles, bisected by the imaginary continuation of the parent fracture. This is known to occur in various scales, from small size crack bifurcation in glass bottles (Fig. 2.30c) to large ones along faults in California (e.g., faults that branch from bifurcation 6 in Fig. 2.57b are about 500 m long). We are aware that the above three examples can be "excused" on different grounds (mixed mode and pore pressure, the straight wing crack is short, and dynamic fracture, respectively), but they cannot be ignored.

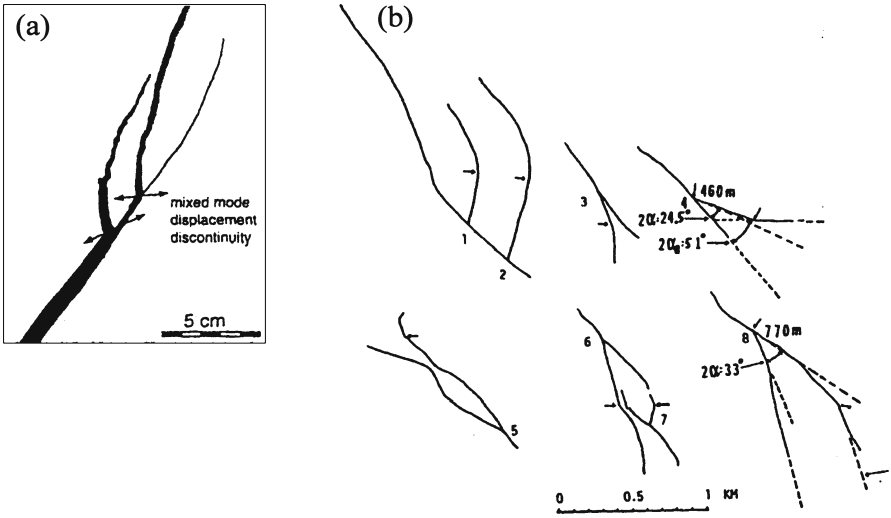

Fig. 2.57. a Wing cracks near tip of a fracture that experienced mixed mode loading i.e., both sliding and opening. Calcite cement (*black*) now fills the flaw and wing crack. Note the sharp angles at which the (*thick*) wing cracks deviate from the parent fracture, the curved shape of the wing cracks, as well as the (*thin*) straight one. Matching up of both surfaces of parent fracture allows determination of the displacement discontinuity as shown. Example from Lower Jurassic limestones between East Quantoxhead and Lilstock, Somerset, England (after Willemse and Pollard 1998). **b** Eight fault terminations by branching (1–8) along segments of the Coyote Creek fault in south California. Branchings 3, 5, 6, 7 and 8 show approximate symmetries between the two branches (forming the angle 2α, that are initially straight, reflecting local tensile stress. Branchings 1, 2 and 4 show deviations from symmetry, implying significant mode II / mode I (modified after Clark 1972 by Bahat 1982)

Let us examine another set of observations. These are related to *en echelon* cracks, which are equivalent to tension gashes and stepping joint segments at parent fracture terminations (Petit and Barquins 1987, 1988; Petit 1988; Price and Cosgrove 1990; Cruikshank et al. 1991) (Fig. 2.58a–d). Petit and Barquins (1987, 1988) induced a wing crack w (that they term branch fracture), and a shear zone of *en echelon* cracks e in PMMA and in sandstone under uniaxial compression, when applied on inclined pre-cuts (Fig. 2.58a,b). The wing crack that showed an opening resulted from local mode I loading below peak stress, and the *en echelon* cracks were induced by local mode II loading under maximal stress conditions. The sandstone revealed cataclastic deformation along the *en echelon* cracks in the shear zone. The wing crack strongly deviated from the direction of the pre-cut, whereas the shear zone was aligned approximately in continuation with it.

The various structures (Fig. 2.58a–d) show that the *en echelon* cracks do not maintain a uniform orientation; instead, they systematically rotate counter clockwise with their distance from the tip of the parent fracture. While in the field where two adjacent parent fractures occur, this rotation could be viewed as a consequence of interaction by the tips of the two fractures (Cruikshank et al. 1991) (Fig. 2.58d), i.e., caused by the interaction of two stress fields. However, this *en echelon* rotation is unrelated to such an interaction in an experiment where only one parent fracture is simulated (Fig. 2.58a,b) and also in the outcrop shown by Fig. 2.58c (assuming an isolated structure), questioning the validity of the interpretation of interaction by the two fractures.

There is a systematic rotation of the *en echelon* cracks towards parallelism to the maximum principal compression (Fig. 2.58a–c), and towards co-axiality with the parent fracture (Fig. 2.58d). Thus, in a given remote stress field, a local predominant mode II close to the tip of the parent fracture gradually changes to a local predominant mode I loading with the distance from the tip reaching the maximum rotation at a *particular distance* from the tip, in a fracture termination zone. This is measurable in Fig. 2.58a–d (see more in Sect. 6.6). Compared with the systems shown in Fig. 2.58a–d, no significant rotation is discerned in the *en echelon* sets that occur beyond the tips of joints along which no strain has occurred (Bahat 1991a, Fig. 4.22). Thus, w and e formed by the same remote stress field (Fig. 2.58a,b) and a reorientation of the remote stress field (Engelder 1999) was not necessary for their creation. They formed by a stable process under conditions of increasing stresses (e.g., Brace and Bombolakis 1963; Jayatilaka and Trustrum 1978). Some of the *en echelon* tensile cracks in the arrays formed oblique to the maximum principal compression in a transient rotation (Fig. 2.58a–c). However, the last *en echelon* crack in the Garden Area (horizontal arrow in Fig. 2.58d) was formed at the end of the transient rotation, possibly suggesting

▶

Fig. 2.58. Rotation of *en echelon* cracks along their arrays, in different systems. **a** Induced wing crack *w* (branch fracture), a shear zone of *en echelon* cracks *e* and *uf* in PMMA under uniaxial compression, when applied on an inclined pre-cut *p* (from Petit and Barquins 1987, 1988). **b** *En echelon* superficial tensile fracture formed from a pre-cut under biaxial loading in a plexiglas plate (after Petit 1988). **c** Rotation of *en echelon* tension gashes at the tip of a tension gash (from Price and Cosgrove 1990). **d** Stepping joint segments (*long*) and echelon cracks (*short*) in the Garden Area, Arches National Park, USA. Two ways that joint segments terminate in the vicinity of neighboring joints. Tips of a segment may simply veer toward a neighbor. Or, beyond the tips of a segment may be "array" of echelon cracks. The segments step right and are twisted a few degrees counter clockwise relative to the trend of the zoned joint, whereas the echelon cracks associated with the segments step left and are twisted a few degrees relative to the trend of the segment. Note that in the sheared stress field shown here, the *en echelon* cracks rotate counter clockwise along their arrays (modified after Cruikshank et al. 1991; see text for explanation)

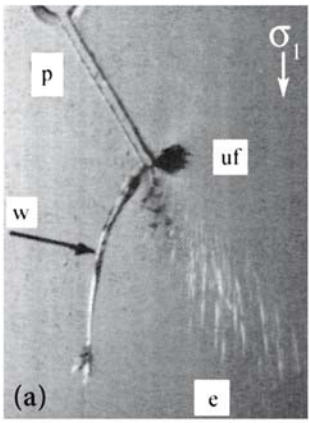
p
σ1
uf
w
(a)
e

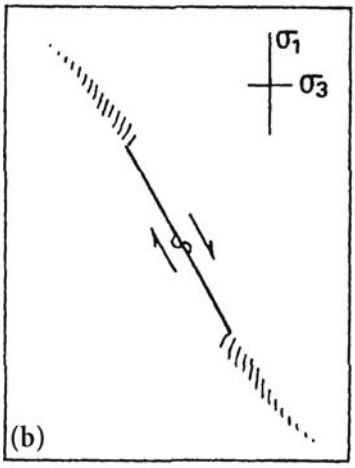
σ1
σ3
(b)

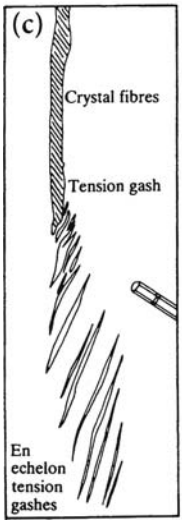
(c)
Crystal fibres
Tension gash
En
echelon
tension
gashes

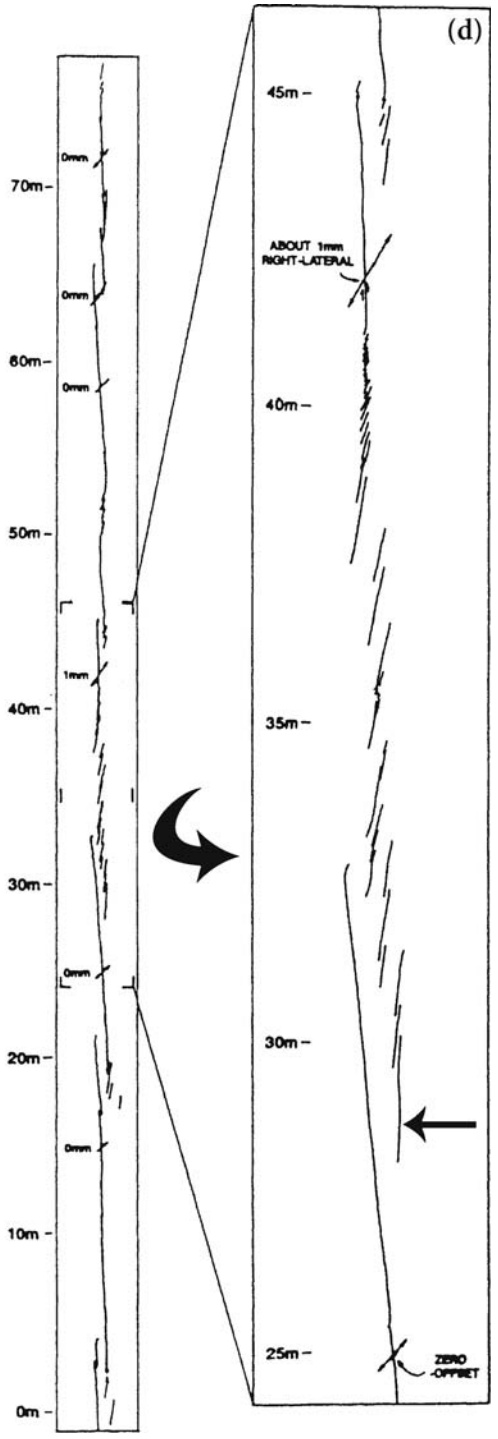
(d)
70m
60m
50m
40m
30m
20m
10m
0m
0mm
1mm
45m
40m
35m
30m
25m
ABOUT 1mm
RIGHT-LATERAL
ZERO
OFFSET

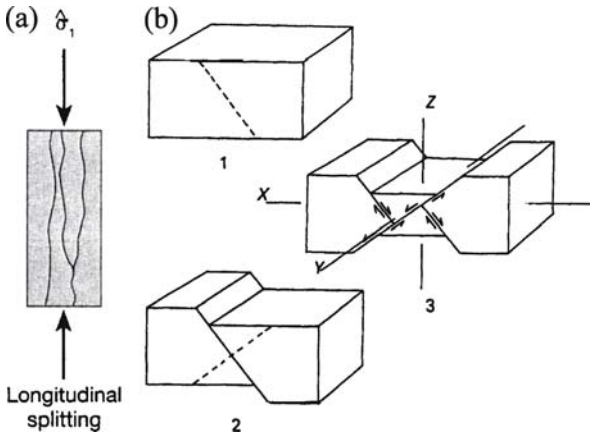

Fig. 2.59.
a Longitudinal splitting along wiggly curves (modified after Twiss and Moores 1992, Fig. 9.2B). **b** A model of a sequential fracture in a conjugate fault set (from Park 1983, Fig. 9.4)

a general condition for forming joints oblique to the maximum principal compression. Hence, oblique extensile fracture is possible.

The problem of oblique extensile joints may be linked with another outstanding enigma: The true nature of the longitudinal splitting. Some authors (e.g., Engelder et al. 1993, p. 46) contemplate the idea that longitudinal splitting is the mechanism leading the formation of regional jointing. At the base of this idea is the rationale that uniaxial compression is coaxial with longitudinal splitting (e.g., Griggs and Handin 1960; Holzhausen and Johnson 1979) and analogically, the maximum horizontal principal stress is coaxial with strikes of individual systematic joints (Engelder and Geiser 1980). It is important to take into account that experimental splitting has been observed by many investigators to be wiggly rather than sharp straight fractures (e.g., Jaeger and Cook 1979, Fig. 4.5.1; Twiss and Moores 1992, Fig. 9.2B; Cosgrove 1995) (Fig. 2.59a). What is the meaning of these deviations from straight fractures? Experimental results obtained from different materials under diverse fracture conditions as well as observations made in geological outcrops are presented in the next sections and compared, seeking to improve the current understanding how oblique extensile joint sets and longitudinal splitting are formed. These sections do not deal with situations of changes in magnitude of initial dihedral angles during fracture growth (e.g., Kalthoff 1973; Ramsay and Lisle 2000, p. 968).

Conjugate vs. contemporaneous, simultaneous and sequential fracture. There is a need to make a few term distinctions. A convenient term in structural geology is contemporaneous. This term is applied when a field relationship reveals that in a given research area, in some locations a joint of set A repeatedly arrests at a joint of set B, suggesting that set A is younger than set B, and in other locations the sequence is reversed. This is taken to indicate with reasonable confidence that the two sets were formed contemporaneously during the same geological period, which could be "short" or "long". Thus, reverse sequences are implied by the term contemporaneous. More challenging is the term simultaneous. It is quite possible to claim that a series of fractures associated with a certain earthquake was formed simultaneously. It is more difficult to prove that a series of joints of a particular (systematic) set was formed together. Probably joints from some sets do not form simultaneously (Bahat 1991a, Fig. 4.8). It is far more difficult to prove that joints of "two conjugate sets" formed

simultaneously. Quite possibly, even two sets that exhibit the closest to ideal field relationships that would justify the term conjugate would be a product of a sequential process. In a way this perplexity resembles uncertainties that are related to conjugate fault sets: Do they really form simultaneously or possibly sequentially (Fig. 2.59b)? We apply here the issue of simultaneously vs. sequentially to two topics, oblique extensile joints and longitudinal splits, and to the problem of two contradicting interpretations regarding the mode of formation of sets 309° and 344° in the Beer Sheva syncline (Sect. 3.4.8 and 6.3.9.1).

2.2.13.2
Fracture Results from Different Sources

This section provides observations from geological outcrops, which are supplemented by experimental results that are presented in Sect. 2.2.3.

Regional joint patterns from chalks in East England. Goodwin (1995) investigated the natural fracture behavior of chalks in south England. He found two sets of regional distribution, striking NW and NE. Both joint sets comprise steep conjugate (ignoring the sequential issue) and vertical joints, everywhere consistent with bedding (Fig. 2.60). In the southern investigated area (Norfolk), traces of the NW set on the vertical NE-NW section typically show conjugate steeply inclined joints that form dihedral angles between 25° and 45°. Vertical joints occur less commonly. In the northern area (south Humberside/north Lincolnshire) by contrast, vertical NE-NW sections across the joint sets show mainly vertical extensional joints with few steeply inclined planes occurring, i.e., the dihedral angle of the Humberside joints <20°. The joints of Norfolk are interpreted by Goodwin (1995) as the conjugate hybrid joints of Hancock (1985, see above). This would include "hybrid joints" that allow for loading of both, shears along, and extension across the plane to take place.

Goodwin (1995) considers two alternative explanations for the differences in size of the dihedral angle in the southern and northern areas. First, the dominance of extensional joints in the north is correlated with "hard" chalk of lower porosity and greater rock strength (dry density 1.78–2.27 g cm^{-3}), compared with the conjugate characteristics in the south that are correlated with "soft" chalk of high porosity and lower rock strength (dry density 1.40–1.72 g cm^{-3}). Second, the above differences reflect a possible northward decrease in differential stress across eastern England. This dilemma was investigated in our laboratory, and the results are in favor of the first explanation (Sect. 6.2.2).

Regional joint patterns from chalks around Beer Sheva, South Israel. Three types of surface markings occur on the single-layer, cross-fold joint surfaces in the Lower Eocene chalks from the Beer Sheva and Shephela synclines in south Israel:

1. Horizontal axial plumes.
2. Circular rib markings.
3. Transitional variations between the two.

The three types may occur together in the same outcrop (Bahat 1991a, Fig. 3.28). About half (56%) of the 225 FSM examined on joints in four outcrops around Beer

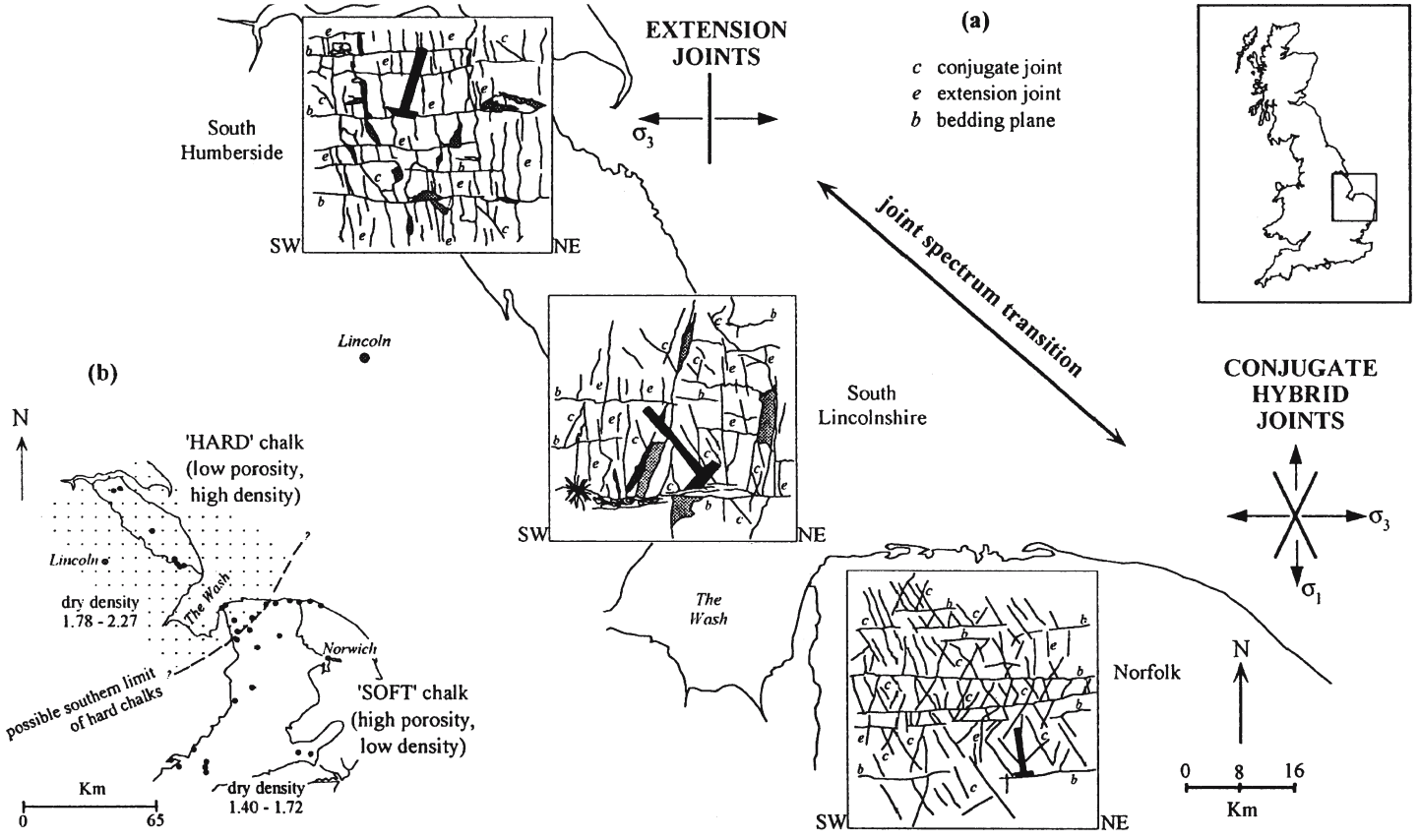

Fig. 2.60. Natural fracture behavior of chalks in south England, see text for explanation (after Goodwin 1995)

Sheva bear circular markings, and these occur on joints of a set of average strike 328° (N 32° W). Sixty five samples (29%) are axial plumes, and these occur on joints belonging to sets of average 309° and 344° strike. Transitional markings make up 12%, and about 3% are other combinations. Joint sets with circular markings and joint sets with plumes occur in separate rock layers, even in the same outcrop.

It was interpreted (Bahat 1987a, 1991a) that possibly the circular markings on the 328° joints have been formed along the direction of the horizontal principal stress, and the axial plumes on sets 309° and 344° were formed on joints at low angles to that principal stress in a conjugate pattern (Stearns 1968). The circular markings developed when the minimum principal stress σ_3 was horizontal and normal to the joint surface, and the maximum horizontal σ_1 equaled the vertical principal stress σ_2, i.e., exerting "pure extension" on the joint. The axial plumes represent the approximate conditions with respect to σ_3 like for the circular markings, when the horizontal principal stress different from the vertical, $\sigma_1 \neq \sigma_2$, exerting some differential stresses on the joints and resulting in superposing a slight shear stress on the joint. The three sets were formed in the Lower Eocene chalks during the burial stage while still immersed in water. Therefore, fracture occurred while the chalk was weak, possibly having the tensile strength of about 0.5 MPa (Bahat 1991a, p. 243). Hence, a dihedral angle of 35° was formed by the strikes of the 309° and 344° sets that resulted from the regional maximum compression in the 328° direction, and the plumes on the surfaces of the former two sets may reflect some mixed mode loading.

2.2.13.3
The Behavior of the Dihedral Angles from Different Sources

Plots of the dihedral angles. The dihedral angles obtained from the different sources presented above are plotted in the range $2\alpha = 0$–$65°$ vs. the compression strength and dry density of the material (Fig. 2.61a and b, respectively, see Fig. 2.24c for the angular geometry). The decrease in 2α with the increase in compressive strength is correlative for various materials. Longitudinal split, probably of an extensile nature, occurs in the range $2\alpha \sim 0$–$20°$ in "strong" glass ceramic, glass and rocks of medium strength. We speculate that in weak rocks, slow (geological rate) fracture may result in extensile fractures that attain 2α values up to 35° by an unclear mechanism. The value of the dihedral angle may stretch up to 65° in "weak" rocks, involving the magnification of the tendency of fracture by mixed modes I + II. There seems to be a general trend of decrease in the dihedral angle with the increase of the dry density of chalks in east England (Fig. 2.61b), resembling the quantitative curve (Fig. 2.61a). However, due to the limited number of points on the latter curve, its value is only qualitative.

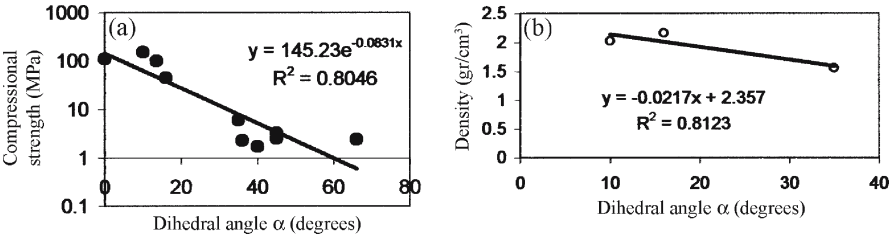

Fig. 2.61. Dihedral angle 2α plot vs. material properties. **a** Compression strength; **b** dry density

The reliability of the results. The comparison of the various dihedral angles obtained from different sources (Table 2.2, Fig. 2.61) needs to be qualified, because the comparison relies on different degrees of certainties regarding the various results. Three reliable results are the ones obtained experimentally on the chalk, glass ceramic and glass (Sect. 2.2.3.4, 2.2.3.7 and 2.2.3.11, respectively), because direct fractographic examinations of their splits clearly suggest that these fractures are essentially extensile. These results suggest that extensile longitudinal split maintains 0° deviation from the compression direction in a strong material (glass ceramic) but may deviate up to $\alpha = 8 \pm 2°$ from this direction in materials of reduced-strength. Included in the latter category are the intensely dried chalk from the Beer Sheva syncline and the glass samples to which pre-cuts were introduced. The results on longitudinal split obtained in fractured Chelmsford granite (Sect. 2.2.3.6) support this suggestion.

Table 2.2. Dependence of the fracture dihedral angle on material/rock properties

No.	Dihedral angle 2α(°)	Compressional strength (MPa)	Dry density for chalk (g cm^{-3})	Material/rock	Source
1	52 – 80 (66)	0.5–4.3 (2.4)		Sandstone Berea weak	Handin et al. 1963
2	20 – 70 (45)	0.4–4.6 (2.5)		Limestone Marianna weak	Handin et al. 1963
3	10 – 80 (45)	0.7–5.9 (3.3)		Dolomite Hasmark weak	Handin et al. 1963
4	0 – 80 (40)	0.3–3.1 (1.7)		Siltstone Repetto weak	Handin et al. 1963
5	0 – 72 (36)	0.4–4.17 (2.3)		Shale Muddy weak	Handin et al. 1963
6	35	6[a]		Chalk Beer Sheva weak	Bahat 1987a, 1989
7	16 ±4	45	2.16	Chalk Beer Sheva medium strength	Bahat et al. 2001a
8	10 ±10[b]	106–200[b]		Granite Chelmsford strong	Peng and Johnson 1972
9	13 – 14 ±2	105–98		Soda lime Glass strong	Section 2.2.3.11
10	0	112		Glass ceramic strong	Bahat et al. 2002a
11	25 – 45	1.40–1.72		Chalk East England	Goodwin 1995
12	0 – 20	1.78–2.27		Chalk East England	Goodwin 1995

[a] This compressional strength is obtained by multiplying the tensile effective fracture stress 0.5 MPa by 12 (Jaeger and Cook 1979).
[b] Interpretation is not clear.
Parenthesis gives mean.

It is not clear how reliable the other results are that are not supported by direct fractographic observations. One is convinced by Goodwin's (1995) results that the stronger chalks in east England have a greater tendency to fracture in extension than the weak ones. The weak chalks (from Norfolk) on the other hand, provide a large range of dihedral angles (25–45°). Fracture at Norfolk probably went far beyond extension, but how dominant the superposed shear mode was in the failure of these chalks is unknown. Muraoka and Kamata (1983) observed that the shear angle ranges between conjugate faults in the Kusu Group were clearly lower in the generally more brittle siltstone (17–45°) than in the sandstone of lower competence (45–69°). Thus, the general trend of the increase of the size of the dihedral angle with the material weakness (incompetence) is also shown for faults.

2.2.13.4
Conjugate Extension Joints and Inclined Longitudinal Splits that Form by Mode I

The results that are summarized in Table 2.2 and ranked in Table 2.3 suggest a new classification that distinguishes four groups. The extension by mode I at $2\alpha = 0°$ for a strong material (item 10 in Table 2.2) is obvious. The interpretation of the results obtained for the materials of reduced strength (items 7 and 9 in Table 2.2, second group in Table 2.3) is that joints may form exclusively by mode I loading, even at small dihedral angles $2\alpha \leq 20°$. This interpretation is supported by the observation made on the tendency of tensile *en echelon* cracks to rotate, so that some of the cracks form oblique to the maximum principal compression under mixed mode I + II loading (Fig. 2.58a–d). With certain qualifications, this interpretation is possibly sustained by fracture in granite (item 8 in Table 2.2). The suggestion given here lacks a statistical support and stays tentative until additional results will confirm it. In the meantime $2\alpha \sim 20°$ will mark the boundary between groups 2 and 3 (Table 2.3). The lack of fractographic criteria to distinguish between these two groups remains a challenge for future research. Finally, the composite failure envelope formally distinguishes between groups 3 and 4 (Fig. 2.26d, B and C, respectively). Additional studies may possibly identify fractographic criteria to distinguish between the latter two groups. The angular boundaries among the four groups are not expected to be "critical angles"; they are likely to be transitional ranges that depend on rock properties (competence/strength) and the rate of applied strain. But the existence of four groups possibly suggests some "spectrum of discontinuities" of dihedral angles, rather than a "continuous spectrum" (Hancock 1986).

Table 2.3. Four fracture groups with varying dihedral angles

Group	Fracture type	Dihedral angle (°)	Loading modes	Offset
1[a]	Axial extension joints	0	Exclusively mode I	None
2[a]	Inclined extension joints	Up to about 20	Exclusively mode I	None
3	Hybrid joints	Up to about 35	Mixed modes I and II[b]	None
4	Conjugate shear fractures	Various dihedral angles, generally >20 (Coulomb fracture criterion)	Mixed modes I and II	Yes

[a] Sets 343° and 350° (Sect. 6.2.2) belong to groups 1 and 2, respectively.
[b] The presence of plumes on the surfaces of hybrid joints testify to lack of offset.

2.2.13.5
The Mechanisms of Plume and Striae Formation on Various Fractured Surfaces

We can now extend the discussion on plume straightness and coarseness (Sect. 2.2.4.2). Striae occur on fractured surfaces from groups 1, 2 and 3 that form under unlike conditions and mechanisms (Tables 2.2 and 2.3). On the extension joints from group 1 (fracture in glass ceramic) the striae are essentially straight, consisting of single fractures, and close to their ends they curve towards one of the sample boundaries and slightly divide into secondary small microcracks (Fig. 2.19a). On the individual surfaces of the fractures from group 2, the micro-plumes are straight (Fig. 2.15a). Straight plumes indicate straight fracture propagation predominantly by mode I that occurred on the relatively small fracture surfaces in the chalk. Almost no plume curving and division into smaller microcracks occurred, because fracture propagation took place on surfaces that were isolated from influences of adjacent sample boundaries. On the other hand, plumes cutting joints from group 3 were strongly affected by layer boundaries, and their division into secondary branches and barbs is quite pronounced (Fig. 2.22a); curving of plumes is more noticeable in thick rock layers.

The plumes in the Lower Eocene chalks (Fig. 2.45) are considerably coarser than the plumes in the Middle Eocene chalks (Fig. 2.35a,c, 2.36a and 2.38). Burial single-layer jointing occurred in the Lower Eocene chalks under increasing overburden stresses, whereas uplift single-layer jointing took place under increasing tensile stresses in the Middle Eocene chalks (Bahat 1999a). These distinct conditions quite possibly resulted in different fracture velocities, which were greater in the chalks of the Middle Eocene than in the chalks of the Lower Eocene for several reasons. First, it is quite likely that fracture velocity will be greater close to the ground surface under tensile conditions, compared to conditions of increasing compression with depth. Second, experiments by Müller and Dahm (2000) (Fig. 2.22) show the correlation of increase in plume coarseness with the reduction in fracture velocity. Third, we use a tentative assumption that still requires confirmation (Sect. 6.3.9.1) according to which the plumes on the conjugate sets 309° and 344° from group 3 were formed under mixed modes I + II, which were associated with the remote compression from 328° compared with the joints cutting the Middle Eocene chalks that do not show a conjugate relationship and appear to have responded to rotating co-axial compression. The possible implication is that while shear modes were minimal on the latter joints, more significant shears were exerted on the conjugate sets 309° and 344°. Possibly, the overburden constraints imposed on the Lower Eocene chalks caused some of mode II to locally transform into mode III (Sect. 2.2.3.8), leading to plume coarsening.

Even more intriguing is the fact that no fringes of *en echelon* segmentation occur on joints cutting Lower Eocene chalks, which are marked by coarse plumes, while fringes of the type shown in Fig. 2.35a are abundant on joints that cut the Middle Eocene chalks, which are marked by delicate plumes. This shows that coarse plumes are not always more likely to transform to *en echelon* segments than delicate ones. This "paradox" supports the suggestion that a time interval may have occurred between the fracture of the parent joint and its fringe of the type shown in Fig. 2.20c, and this could involve significant changes in fracture conditions.

2.2.13.6
Conclusion

1. Our interpretation of the systematic rotation of the *en echelon* cracks towards parallelism to σ_1 (Fig. 2.58a–d) is that in a given remote shear stress field, a local predominance of mode II gradually changes to a local predominant mode I loading. In this setting, a reorientation of the remote stress field is not necessary for creating extensile cracks (mode I) oblique to σ_1 in certain locations. Hence, extensile cracks can form in inclined orientation with respect to σ_1.
2. Based on experimental evidence (Table 2.2), extensile longitudinal splitting can be extended from a dihedral angle of $2\alpha = 0°$ in "strong" materials to $2\alpha \sim 20°$ in materials of "medium strength", supporting the interpretation in conclusion 1.
3. Field evidence possibly suggests that in "weak" materials the dihedral angle of conjugate hybrid joints (mixed modes I + II) may be extended to about 35°.
4. The wiggly longitudinal splits that have been observed by various investigators represent composite fractures consisting of combined extensile and shear growths that interacted with each other.

2.3
On Uplift, Post-Uplift, Neotectonic and Surface Joints

Joints in sedimentary rocks are genetically divided into four groups: Burial, syntectonic, uplift and post-uplift (Bahat 1991a; Engelder et al. 1993; Ghosh 1993; Bankwitz and Bankwitz 1994; Bankwitz and Bankwitz 1997). In this section we refer again to the differences between uplift and post-uplift joint groups and further elaborate on the latter. We briefly discuss the diverse characteristics of "neotectonic joints", "exfoliation joints" (that are distinct from "sheet joints"), "cross joints" and introduce the "surface joints" group.

2.3.1
Neotectonic Joints

2.3.1.1
General

An inventory of neotectonic joint attributes was compiled by Hancock and Engelder (1989) in various terrains containing flat-lying sedimentary sequences in the platform covers of cratons from the Appalachian Plateau, southeast England-northeast France, the Arabian platform, and the Ebro basin in Spain. Systematic neotectonic joints are the youngest tectonic structures in all of these study areas. They are, however, older than superficial non-systematic cross-joints of non-tectonic origin that abut and link them. The next section is a citation from Hancock and Engelder (1989).

2.3.1.2
Fracture Styles of Neotectonic Joint Systems

The geometry of the systematic neotectonic joint systems is characterized by simplicity, irrespective whether they cut previously intact or already fractured rocks

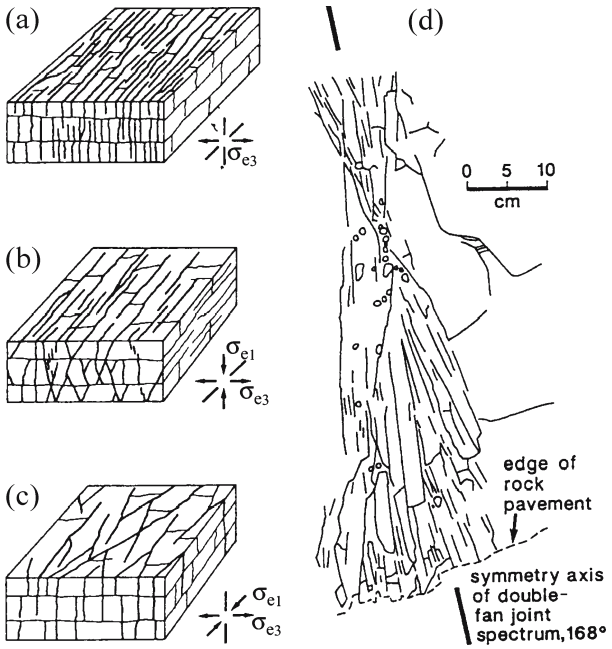

Fig. 2.62. Characteristic neotectonic joint systems. **a** Single set of systematic vertical extension joints linked by non-systematic cross-joints. **b** A spectrum of systematic joints comprising vertical extension fractures and steep conjugate fractures enclosing a range of dihedral angles of less than 45°. Two steep fracture directions are expressed by arrays of *en echelon* vertical joints. Non-systematic joints link systematic joint. **c** A spectrum of systematic joints comprising vertical extension fractures and vertical conjugate fractures (in plan) enclosing a range of dihedral angles of less than 45°. Non-systematic joints link systematic joints; σ_1, maximum effective principal stress; σ_3, minimum effective principal stress. **d** Neotectonic joints cutting horizontal limestones. Line drawing from a photograph, looking down on the double-fan joint spectrum. The symmetry axis of the spectrum trends sub-parallel to the mean strike of all neotectonic joints in the investigated area (after Hancock and Engelder1989)

(Fig. 2.62a). The commonest assemblage comprises vertical joints that are either parallel to each other or dispersed less than 10° about the mean orientation of the set (Fig. 2.62b). Where the vertical set occurs in conjunction with other neotectonic joints, it bisects the acute angle between conjugate sets (Fig. 2.62c). In all the above mentioned four case-study terrains, a less abundant, but nevertheless typical neotectonic joint pattern comprises steep conjugate joints striking parallel to a neighboring single vertical set (Fig. 2.62b). Steep conjugate joints generally enclose dihedral angles (2α) in the range of 10–45°. The latter joint sets appear in some upper but muddier parts of the Devonian succession of western New York State, whereas in the central part of the state, lower silt and shale units are cut by a single set of joints.

Some conjugate joints strike parallel to locally developed late Cenozoic topography. They occur in western New York and postdate systematic cross-fold joint sets (Engelder 1989). Those joints with a dip direction pointing downslope become more prominent in the near surface. This correlation of dip with Cenozoic topography is the strongest evidence supporting a neotectonic age for the east-northeast joints of the Appalachian Plateau.

At a few stations in the Arabian platform and Ebro basin, well-ordered conjugate steep or vertical sets are replaced by a continuum of joint orientations with an angular dispersion of as much as 45° about a symmetry axis that is either vertical or trends parallel to the mean strike of a nearby single joint set (Fig. 2.62d). Hence, Hancock and Engelder (1989) distinguish several fracture styles in the systematic neotectonic joint systems: Vertical single and conjugate sets, steep conjugate sets, conjugate joints which strike parallel to locally developed late Cenozoic topography and joints that their dip orientation is characterized by angular dispersion. In addition to the systematic neotectonic joint systems there are non-systematic fractures, termed "cross joints" (distinct from systematic cross-fold joints) that extend across intervals between earlier systematic joints (Fig. 3.36d) and may be categorized as products of the neotectonic stress field (Engelder and Gross 1993).

2.3.1.3
Neotectonic, Uplift and Post Uplift Joint Systems

According to Hancock and Engelder (1989), burial followed by unloading as a result of denudation and lateral relief consequent of uplift are prerequisites for the formation of shallow neotectonic joints. A major conclusion in their paper is that shallow (at depths of less than 1 km) neotectonic joint systems are the most recent joint system. Therefore, they are of potential value for tracking the orientation of the contemporary stress field even in structurally complex terrains, although there may be a slight misalignment between joint strike and the direction of the maximum horizontal stress. Some regional joints, interpreted as neotectonic, strike parallel to or approximately parallel to the direction of contemporary horizontal maximum compression known from in situ stress measurements or fault plane solutions of earthquakes (Hancock and Engelder 1989; Gross and Engelder 1991). This provides an important motivation for studying neotectonic joints. We argue below that the application of these useful relationships needs to take into consideration a sub-grouping within the broader group of neotectonic joints.

It appears that the "neotectonic joints" (Hancock and Engelder 1989) embrace two distinct categories by Bahat (1988a, 1991a) of shallow fractures (depth down to about 0.5 km) without differentiating between them: The "uplift joints" and the "post uplift joints". The attributes that are common to both, uplift and neotectonic joint systems (in addition to shallow depths) include multilayer and large size characteristics (i.e., larger spacing and apertures than in neighbor joint sets of older generations), significant misalignments between joint strikes, and their occurrence in repeated failure events.

While many attributes are common to both neotectonic joints and uplift joints, post uplift joints seem to be analogous to the conjugate joints that strike parallel to locally developed late Cenozoic topography described by Hancock and Engelder (1989). The latter two are the most recent joint systems. On the other hand, "uplift joints" need not be the most recent joint system. Uplift joints may populate the same outcrop that exhibits "post uplift joints" of a younger generation, and they entirely differ in their strikes (e.g., Bahat 1991a, outcrop 3 in Fig. 5.29). Strike scattering of uplift joints (Bahat 1991a, Fig. 5.28) suggests that while some uplift joints may reflect the contemporary (remote) stress field, others may not. The post uplift joints are geo-morphological products of local stress fields (Bahat et al. 1999) and some of them do not reflect the contemporary stress field. Hence, when neotectonic joints are characterized, their affiliation to either the uplift or post-uplift groups should be considered.

2.3.2
Exfoliation Joints and Sheet Joints

Exfoliation fractures (e.g., Sect. 3.3 and 4.5.3) and sheet fractures (e.g., Twidale et al. 1996) reflect fracture propagation in principal planes normal to the minimum principal stress and form approximately by the same mechanisms. However, they seem to genetically and morphologically represent different categories as will be explained below. Gilbert (1904) believed that sheeting is *older than the topography*. Various authors (e.g., Dale 1923 and Holzhausen 1989) made comments on "generations" of sheet fractures (e.g., preglacial and postglacial). Similarly, Holman (1976) observed hairline cracks, which are evident only where weathering has etched them into relief that commonly subdivide sheets into two to four secondary slabs. Hence, the term sheeting should be applied to horizontal and sub-horizontal fractures that maintain approximately uniform spacing with their neighbor (lower and upper) sheets, but generally increase their spacing with depth. Sheeting does not have to develop parallel to and close to a previous fracture, although sheet fractures often occur in sets. Commensurate with the above, Holzhausen (1989) made the observation that sheet fractures must be products of states of stress that are approximately uniform over distances of at least tens to hundreds of meters in order to explain the regularity and size of the fractures.

Exfoliation joints, on the other hand, are generated by fracture parallel to existing surfaces in all attitudes. They generally develop at short distances from the exposed surface (tens of centimeters), in small spacing, and produce rock slices of both uniform thickness and lenticular shape. In a way, sheeting responds to unloading (before the topography sets in), whereas exfoliation results from loading that takes place following the establishment of the topography. Hence, sheets and exfoliation fractures correspond respectively to uplift and post-uplift fractures. We refrain here from further addressing sheet joints and refer the reader to the literature on this subject (e.g., Johnson 1970). Concentric exfoliation cracks in basalts belong to a different fracture category, which is not treated in this book.

2.3.3
Surface Joints

We introduce a new category of fractures that we term "surface joints". These joints mostly occur in the upper parts of rock outcrops. They may vary in length from several centimeters (Fig. 2.63a) to several meters and can appear in various styles, from straight shapes to twisted forms that transform into non-systematic anastomotic networks (Fig. 2.63b). Occasionally, they occur in chalks of Eocene age in the Beer Sheva region, Israel and are filled with coarse sparitic gypsum. These veins are connected with the loess-soil cover of the Upper Pleistocene, which overlay the chalks, possibly concentrating by roots of sulfate tolerant trees and depositing from groundwater that became over-saturated with $CaSO_4$ (Issar et al. 1988). Particularly characteristic are the sub-horizontal surface joints that occur in "transitional layers" that underlay the upper, eroded soil layer and overlay an uneroded jointed chalk layer (Fig. 2.63a). These surface joints possibly formed perpendicular to tensile stress that was induced by overburden reduction due to the density decrease of the overlying soil, which formed from the eroded chalk (see more in Sect. 6.8).

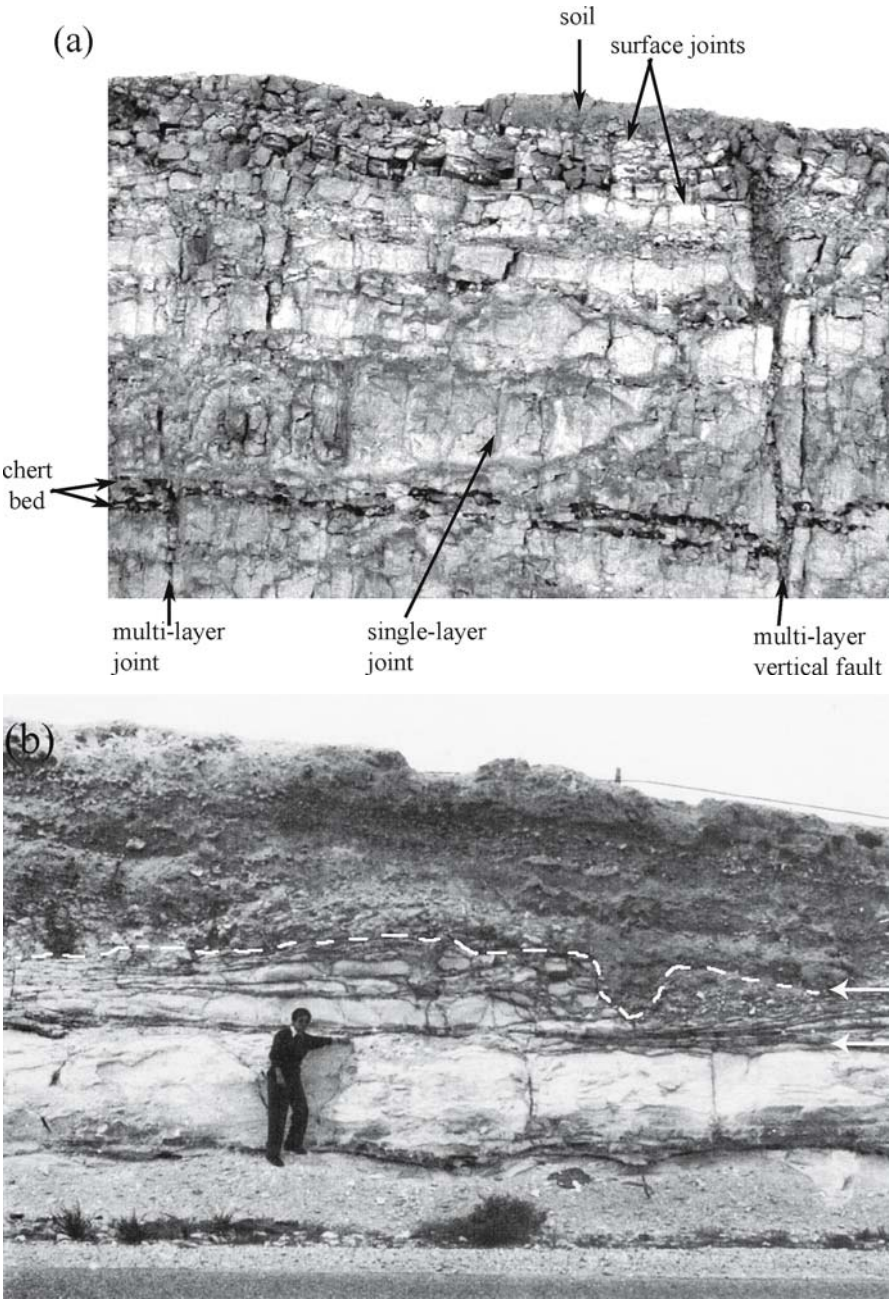

Fig. 2.63. Surface joints. **a** A section that consists of characteristic fracture elements that occur in association with a "transitional layer" of surface joints (bounded by the two *upper arrows*) in Lower Eocene chalks around Beer Sheva, Israel. The thickness of chert bed is 10 cm. **b** The "transitional layer" bounded by the two *arrows*, that underlies the upper, eroded soil layer and overlay an uneroded jointed chalk layer (after Issar et al. 1988)

Surface joints often fill spaces between previous joints and mimic the older joints. Their identification is done by comparing the new, smaller joints that lose some of their straightness and spacing to the larger and straighter, earlier joints that form greater spacing in lower layers where the surface joints do not occur. When they cut rectangular blocks that were formed by orthogonal joints, they further subdivide them to into smaller blocks. Thus, surface joints can be distinguished by their relative irregularities, reduced spacing, non-uniformity in spacing, exaggerated apertures and by their containment of secondary mineralization, erosive rock and soil. These fractures may concentrate along trenches and canals. Although they are essentially non-systematic, they may occasionally appear systematic.

Surface joints have been mistaken for burial joints by some environmental specialists, and this justifies their distinct characterization. The recognition of the importance of surface joints may be critical in planning and evaluation engineering and environmental projects. They are not only a subject of the past; these fractures may develop in the future as well. Joint intensity (fracture area per rock volume) is a basic parameter in geological engineering. The value of this parameter may change substantially between two locations that are only a few meters laterally apart in the same rock layer and differing in depths from the ground surface, along an eroded slope. The engineer may like to consider the minimum depth that a survey trench should reach below the depth of the "transitional layer" for obtaining "clean" information. The hydrologist may be misled by the attitudes and spacing of joints in this zone in predicting the flow properties of water. Finally, surface joints differ from the sub-surface, non-systematic joints that form in association with rockburst in mines (e.g., Jaeger and Cook 1979, p. 505, see also present Chap. 5) and there should not be difficulties in distinguishing between these two fracture groups.

2.4 Primary and Secondary Fractures

2.4.1 Introduction

This section is about secondary fractures that form adjacent to primary fractures when the latter are activated or reactivated by tensile or shear stresses. The geometric relationship of tensile secondary fractures in relation to a primary fracture on a principal plane is relatively simple (the primary fracture is given for simplicity as $2r_B$ in Fig. 2.30c). More complicated is the system of a primary fracture in the shape of a parent joint or a fault in the field, or a pre-cut in the laboratory (Sect. 2.2.3.11) under remote compression at a small angle α to the primary, causing local shear and tensile stresses that result in shear and tensile fracture (Fig. 2.64). In the latter diagram, we show various tensile fracture types, omitting a certain type of joints from a fault termination zone (Fig. 6.19) and shear fractures known from Riedel experiments (e.g., Fig. 2.68). In most cases, these pre-cuts (occasionally also termed slits, out-of-plane fracture, pre-existing crack, plane of weakness, initial crack or initial flaw) are introduced to the material by design (Germanovich and Dyskin 2000). We therefore use the term "pre-cut" in our descriptions. Pre-cuts are distinguished from initial flaws (Sect. 2.2.2.2), which occur as unintentional defects in the material, commonly on sub-

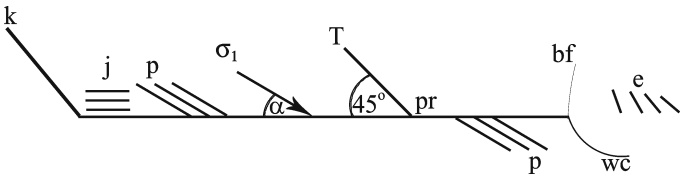

Fig. 2.64. A schematic, idealistic fracture pattern which forms by compression. Compression is applied on the primary fracture or a pre-cut *pr*, at a small angle α. Several types of secondary fractures may form, including, wing cracks *wc*, sets of horsetails (or pinnate joints) *p*, kinks *k* and coplanar joints *j*, at the two extensional quadrants, *and* a tensile fracture *T* that forms at 45° along the primary. In addition, *en echelon* sets *e*, as well as curved branching faults *bf*, may form at the two compression quadrants

millimeter scales. The geometric distinctions and the positioning of the secondary fractures along the primary fracture and next to their tip are described below in relation to the various fracture mechanisms that are involved.

The literature is profuse with terms assigned to secondary fractures by various authors, including wing cracks, curved branches, branch fracture, kinks, curved kinks, pinnate joints, splay cracks, horsetail fractures, bifurcation fractures, overstepping joints, *en echelon* cracks, and more. We concentrate below on several types of secondary fractures, including the wing crack, pinnate joints and horsetail fractures, fracture polarization, termination-zone joints and fracture branching. Additional descriptions of secondary fractures, such as kinks and stepping joints are presented elsewhere in this chapter (Sect. 2.2.8 and 2.2.13).

2.4.2 The Wing Crack Model

2.4.2.1 *Summary of the Conventional Concept*

Different models were proposed to explain the phenomenon of crack growth in compression. We cite below the study by (Germanovich and Dyskin 2000) on this subject. The majority of works relate the crack growth to the action of a stress concentrator situated in the tested sample. The role of such a stress concentrator is frequently played by pre-cuts (Fig. 2.65). The pre-cuts with contacted faces can be considered as the strongest source of the secondary crack growth, and the wing crack geometry has been a convenient modeling tool in describing fracture in compression (Fig. 2.66).

We adhere to the convention of many experimentalists that the pre-cut of length $2c_0$ is inclined with respect to the compression direction at an angle α (Fig. 2.66) (Fairhurst and Cook 1966). One notes, however, that this is the geometry often used for the angle of hade θ, complementary to the dip angle α (e.g., Park 1983, p. 4), a potential source of confusion. A rectilinear pre-cut is opened by a pair of concentrated forces simulating the action of the inclined contact area (Fig. 2.66). The value of these forces (per unit length of the inclined contact area) is assumed to be equal to the horizontal projection of the shear force, *F*, tending to displace the opposite faces of the pre-cut:

$$F = 2c_0(\sigma - q)\beta(\alpha)\,, \qquad \beta(\alpha) = C\sin^2\alpha\cos\alpha \tag{2.9}$$

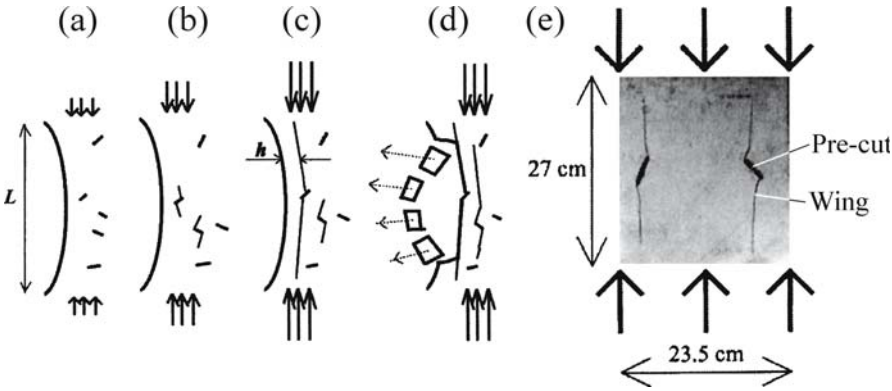

Fig. 2.65. Mechanism of rock fracture near a free surface: **a** Loading begins, **b** crack growth initiates and propagates stably while load is increased, **c** crack starts growing unstably when reaching a critical length ($2l$), while the influence of the free surface is increased, **d** repeated buckling and creating new free surfaces when $L > h$, and **e** growth of initial cracks in the direction of compression in Tennessee Sandstone (after Germanovich and Dyskin 2000)

Fig. 2.66. Wing crack growth under compression (modified from Fairhurst and Cook 1966 by Germanovitch and Dyskin 2000)

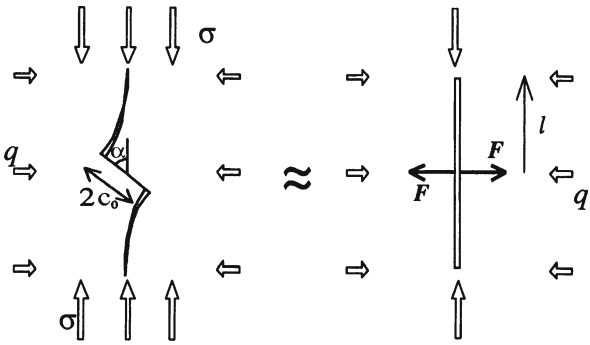

Here σ is the applied compressive stress acting along the free surface, q is the confining pressure and C is a factor accounting for the friction and influence of curvature of the secondary cracks. Using finite clement modeling, Germanovich et al. (1995) calculated C that happened to be of the order of unity. The propagating crack $2l$ is governed by the intensity of the stress concentrations at the crack tip, which is expressed through the stress intensity factor K. As the crack model is symmetrical, only K_I is accounted for (under compressional stress, Fig 2.65a,b).

$$K_I = \frac{F}{(\Pi l)^{1/2}} - q(\Pi l)^{1/2} \tag{2.10}$$

The influence of mode II loading in the case of actual wing crack (Fig. 2.66) is assumed to be suppressed by the compressive stress acting along the crack. Hence, this mode is neglected in the crack growth consideration. The direct numerical modeling reported by Germanovich et al. (1995) confirmed this assumption to a sufficient degree of accuracy.

The conventional criterion of crack growth is

$$K_I = K_{IC} \tag{2.11}$$

where K_{IC} is the rock fracture toughness. It is seen that the crack growth is stable: As the crack elongates, K decreases; hence, greater loads are required to maintain the propagation.

The presence of q significantly reduces K and hence, drastically hampers the crack growth. The influence of the lateral pressure manifests itself in:

1. Reducing the crack opening.
2. Reducing the force, F, by decreasing the shear stress acting on the inclined crack.

The first type of influence is (l / c_0) times stronger than the second one. Since the discussed model accounts for only the main asymptotic term with respect to $l / c_0 \ll 1$, the influence of the lateral pressure on F should be neglected. Therefore, it will be assumed that

$$F = 2\sigma\beta(\alpha)c_0 \tag{2.12}$$

Note application of Fig. 2.65 in Sect. 4.5.3.3.

2.4.2.2 *The Three-Dimensional Wing Crack Model*

According to Germanovich and Dyskin (2000), the above wing crack model represents the experiments and considerations that are essentially 2-D. The real fracture mechanism is, however, 3-D. Numerous experiments on the growth of internal 3-D wing cracks in various transparent and non-transparent brittle materials under uniaxial compression revealed that there is a strong limitation on the extent a single wing crack can grow: Its wings can reach about the size of the pre-cut (Fig. 2.67a), which is insufficient to cause failure. This limitation seems to be universal and independent of the shape and orientation of the pre-cut. Therefore, the actual 3-D crack growth in uniaxial compression differs radically from simple 2-D mechanism crack growth. The main reason for that limitation is in the shape of the wings as they grow, wrapping around the pre-cut.

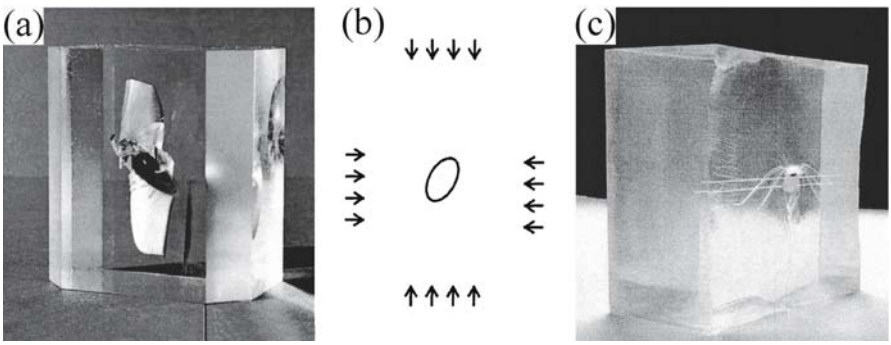

Fig. 2.67. Three-dimensional wing crack growth. **a** A wing crack in PMMA. **b** Schematic diagram of initial flaw in biaxial compression. **c** Extensive wing crack growth in biaxial compression (after Germanovich and Dyskin 2000)

It is this "surrounding" that prevents the wings from extensive growth into plane vertical fractures, such that the ability of the material itself to withstand load gets exhausted for most brittle materials. Accordingly, once the induced stress exceeds the compressive strength of the loaded material, the latter fails in an "inherent mode" regardless of presence or absence of the pre-existing defect. However, under biaxial compression (when one direction is still free of load) an extensive wing crack growth is formed (Fig. 2.67b,c) at a load much below the material inherent strength limit. The reason is that the action of compression in the intermediate principal stress direction prevents wings from wrapping around the pre-cut, enabling them to grow extensively in a plane perpendicular to the unloaded direction.

2.4.3 Pinnate and Horsetail Fractures

There is some uncertainty whether pinnate fractures that form adjacent to faults are shear or tensile structures. Hancock (1972) describes several types of secondary fractures that are associated with shear zones, including veins, arrays of tension gashes in *en echelon* arrangements, Riedel shear structures and pinnate, antithetic conjugate shear fractures at 60°to a fault (Fig. 2.68a,b). There are, on the other hand, descriptions of tensile pinnate fractures (Fig. 2.68c). These tensile sets that form in small angles (<45°) are different from the straight *T* tensile fracture that forms at 45° to the general direction of Riedel shear structure (Fig. 2.68a,b). Hancock et al. (1982) describe an intriguing outcrop (Fig. 2.68d), showing an *en echelon* array of tensile pinnate fractures that are related to a small dextral strike slip fault, where many of the pinnate joints bear plumes with nearly vertical axes aligned perpendicular to the bedding boundary.

The interpretation of the mechanism that created the *en echelon* array of tensile pinnate fractures (Fig. 2.68d) follows from the model depicted in Fig. 2.68a. A primary, remote compression created the stress field of the primary shear couple, which induced the strike slip fault in Fig. 2.68d, i.e., the dextral wrench fault in the latter figure is equivalent to Sc' in the former one. But the plume orientation cannot be explained as a direct consequence of lateral shear by Sc' (that would have formed horizontal plumes); it rather suggests two alternative explanations. First, σ_1'' was vertical (parallel to the plume axes) rather than horizontal. Second, a vertical σ_2'' created the *en echelon* set and plumes. In any event, it is quite clear that the vertical propagation direction of the *en echelon* cracks implies a local stress rotation. While according to the "fracture slanting" model (Sect. 2.2.5.2) the *en echelon* fringe forms by a local rotation of the maximum principal stress from horizontal direction to a vertical one, it appears that in the pinnate joints case presented here, the local stress rotation was driven by mode II exerted by the strike slip fault. The former rotation concerns the creation of a fringe, whereas the latter seems to relate to the entire rock layer, i.e., to what should have been a parent joint if no breakdown had occurred. A mechanical model depicting the difference between the above two systems is a challenge for future studies. Figure 2.68d possibly suggests that vertical plumes on pinnate joints are more common than previously thought: Perhaps they characterize many other conjugate shear zones (e.g., Shainin 1950). If this would be shown, it should support the concept of "tensile pinnate fractures", suggesting that shear pinnate fractures (Fig. 2.68b) are created from joints by a secondary process.

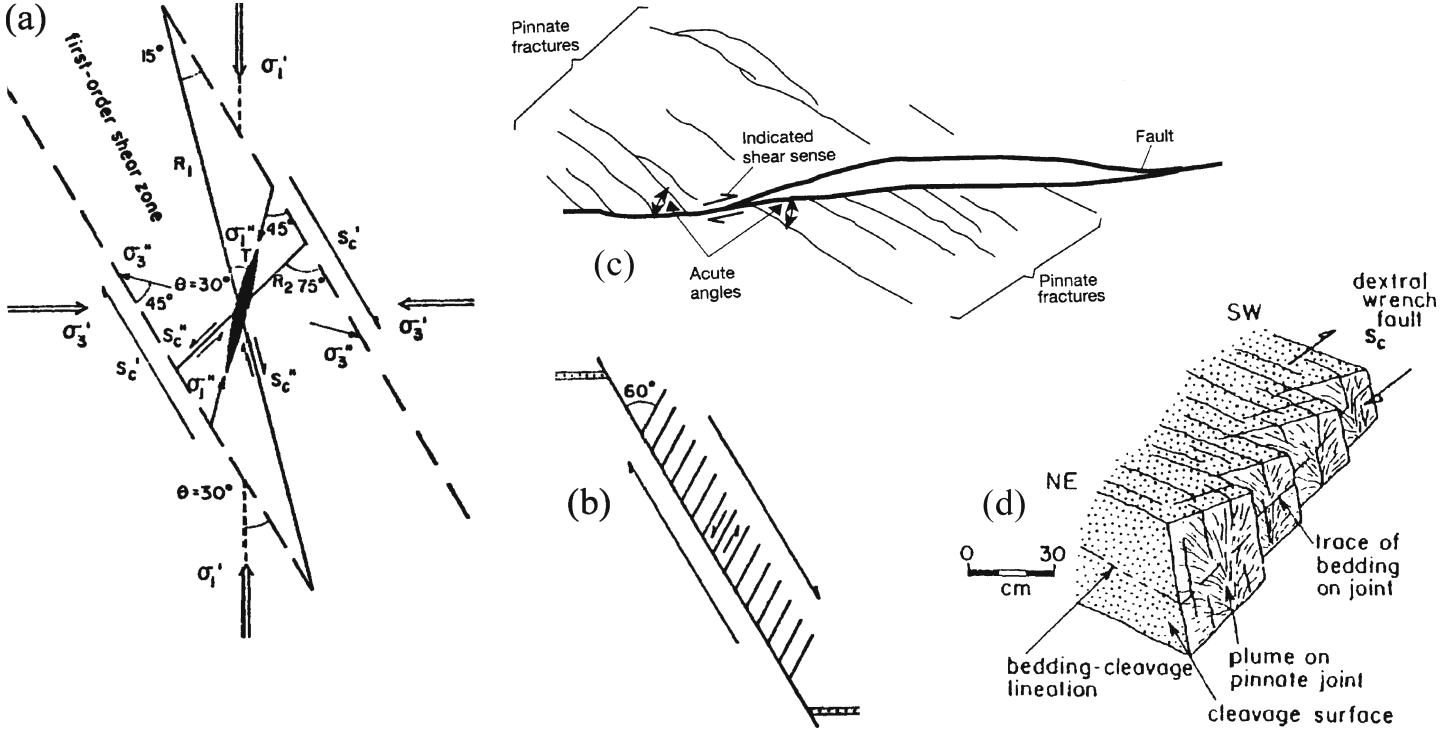

Fig. 2.68 a Conventional interpretation of *en echelon* and pinnate fractures with respect to primary and secondary stresses. *T*: Tension fracture at 45° to an array; R_1 and R_2: Riedel shears at 15° and 75° to an array, *Sc'*: Primary shear couple, *Sc''*: Secondary shear couple which may give rise to third order fractures; σ_1' and σ_3': Primary maximum and minimum principal stresses; σ_1'' and σ_3'': Secondary maximum principal stresses; θ: Angle between shear fracture and σ_1'. **b** Pinnate, antithetic conjugate *shear* fractures at 60° to a fault (modified after Hancock 1972). **c** Pinnate fractures (or feather fractures) along a brittle fault. The acute angle between the fractures and the fault points in the direction of relative motion of the fault block containing the fractures (from Twiss and Moores 1992). **d** Plumes on pinnate joints at St. Ann's Head, Dale, Dyfed southwestern Wales (see text for explanation) (after Hancock et al. 1982)

Horsetail secondary fractures are approximately straight, sub-parallel fractures near the ends of primary fractures that form in response to shearing along primary joints, apparently initiating at roughness elements along the primary fracture, where tension is developed as a result of slip (Cruikshank et al. 1991). Renshaw and Schulson (2001) propose that bending in compression of slender microcolumns that form *between* horsetails could result in instability and localized failure of the structure. It appears from these descriptions that tensile pinnate joints and horsetail fractures relate essentially to the same structure. Thus, we focus here on tensile fracture sets that are confined (but unpolarized, Sect. 2.4.4) to the extensional quadrants and form acute angles with the primary fault (Fig. 2.68c).

Martel (1997) points out that the uniform shear stress along faults applied by Cruikshank et al. (1991) in simulating secondary fracture should result in a single fracture to open precisely at the end of a fault trace. This opening will take place owing to a singular, infinitely strong stress concentration there, and a new, secondary fracture should extend from the fault trace at an angle of about 70° (e.g., Pollard and Segall 1987). According to Martel (1997), this theory encounters two difficulties. First, real materials cannot sustain infinite stress levels. Second, this theory is inconsistent with numerous field observations. Often, multiple secondary horsetails open near, but not precisely at the tip (end) of fault traces (Brace and Bombolakis 1963, Fig. 2). These fractures commonly form behind fault tips. They often have nearly straight traces and intersect at an angle of 50° or less with the fault. Martel (1997) models a small fault along which the shear stress is *non-uniform* when it slips. He postulates a "cohesive zone" where the shear stress is elevated near the fault tip. This zone will help to eliminate the stress singularity and would account for the observed orientation, shape, and distribution of horsetails. Martel's concept is challenging and requires support through future studies.

2.4.4
Fracture Polarization in the Two Extensional Quadrants along the Fault

It has been observed that the occurrence of secondary fracture sets at various acute angles with respect to some primary faults may apparently be polarized in the two extensional quadrants (Sect. 6.7). One set of fractures assumes the form of a joint set that dips approximately in the direction of the primary fault at the upper part of the hanging-wall (Fig. 6.24c). They differ from pinnate fractures and from T fractures that create small angles and 45°, respectively, with the fault (Fig. 2.68a,b). The other set consists of twisted and tilted faults that resemble Riedel shear fractures in the lower part of the foot-wall of a normal fault (1–3 in Fig. 6.24c). Hence, the appearance or absence, the differences in the angular relationships, and the locations of secondary fractures *in* the two extensional quadrants may vary, reflecting subtle differences in the histories and dispositions of the respective stress fields along the fault.

2.4.5
Termination-Zone Joints

Termination-zone joints is the term assigned to a joint set that starts around the tip of a strike slip fault and is associated with the secondary faults that form in its continuation along a termination zone (Sect. 6.6). This set curves in conformity with the primary fault and secondary faults.

2.4.6
Fracture Branching

2.4.6.1
Dynamic Joints

Dynamic jointing can be identified by systematic fracture branching (bifurcation). There is a need to distinguish between systematic and non-systematic branching. Systematic fracture branching implies successive branches that form in a single, *continuous* (rapid) process in which the branches propagate in particular directions, away from the fracture origin (Fig. 2.30c) (see more in Bahat 1991a, p. 112). Systematic dynamic branching joints are very rare in sedimentary rocks, but they are known to have been formed in great depths, probably by extreme fluid pressures in granites (Fig. 2.69a,b, see Chap. 4). Their branching faces one direction, and commonly branching fractures are fairly straight.

Anastomose fracture systems are occasionally wrongly interpreted as bifurcations. Anastomose fractures often form by long, *discontinuous* processes that contain intermittent pauses (e.g., Fig. 3.36f). Numerous repeated "branching" that may be suspected to represent dynamic fracture in such systems is fairly erratic and inconsistent in its directions. This "rebranching" is often the result of adjacent existing fractures that interact due to later stress release processes, rather than a single fracture process. Anastomose fracture systems often display (on both horizontal and vertical outcrops) erosional and colored surfaces recording repeated precipitations from liquid flows, particularly in carbonate rocks.

Fig. 2.69a.
Joint bifurcation by sudden stress release. Lausitz, Cadomian biotite granodiorite, Klosterberg quarry near Bautzen vertical section; s*cale* is 1 m (Fig. 4.3 and Lobst 2001, Fig. A-1)

Fig. 2.69b. Joint bifurcation by sudden stress release. South Bohemian Pluton. The large block at right bifurcates towards left (note optical distortion)

2.4.6.2 *Branching Faults*

Branching faults are secondary fractures, often rectilinear in shape, which propagate unstably from the tip of the primary fracture due to predominant mode I loading, mostly under dynamic conditions. These secondary fractures may be symmetrically displayed at both sides of primary faults in their two termination zones (Fig. 2.57b). It has been suggested that such structures reflect predominant tensile mode even in overridingly shear regimes (Bahat 1982, 1991a). However, deviations from rectilinear to asymmetric "almost straight" or "curved" branching faults may occur when the primary fracture is influenced by significant mode II / mode I ratios. Rectilinear branching faults generally differ from curved splay faults (e.g., Cruikshank et al. 1991, Fig. 12; Twiss and Moores 1992, Fig. 7.10) such that the former type develops unstably whereas the latter may form stably.

Four Fracture Provinces in Sedimentary Rocks

While Chap. 2 is devoted to principles of fracture geology on all scales from laboratory to outcrop (up to 1 km long), the present chapter deals with fracture provinces on regional scales (tens of km in length). An ideal study of a fracture province should present all the province's fracture elements in comprehensive detail: Meso-structures and regional structures complete with their spatial relationships, whether they are interdependent or not. This would throw light on the strain and stress histories of the province, besides providing useful data for applied projects. To date, such ideal studies are practically unavailable; no large fracture province is sufficiently exposed or probed to provide what may be regarded as a full structural picture. Every well-investigated fracture province is "specialized" in certain structural features but nevertheless keeps some of its secrets. The objective of this chapter is, rather than providing a comprehensive review of the literature, to present a brief account on four fracture provinces in sedimentary rocks that display distinct fracture elements that would complement each other. By mentally compounding the characteristics of these separate provinces, a realistic picture may emerge on the nature of large-scale fracture patterns and relationships.

First to be described is a Devonian fracture province of alternating siltstone and shales in the Appalachian Plateau of eastern USA, where the classic work by Sheldon (1912) has demonstrated the concept of regional jointing. This will be followed by a study of the Somerset Buttress anticline in the Jurassic limestone along the Bristol Channel in England, with references to fracturing in some other well-known anticlines. Next we shall bring a description of exfoliation joints that cut Jurassic sandstone at Zion National Park, Utah, in western USA. The fourth region of interest relates to the Eocene chalks around Beer Sheva, southern Israel. A specific discussion is devoted to each province, as well as, a comparative review at the end of this chapter.

3.1
The Devonian Fracture Province of the Appalachian Plateau, New York

3.1.1
General Geology

Engelder and Geiser (1980) mapped 20 000 km^2 of systematic joint sets in the Upper Devonian rocks of the Appalachian Plateau, New York (Fig. 3.1a). In this area, Wedel (1932) mapped very gentle anticlinal folds, with limbs dipping less than one degree and axes whose strikes vary over 30°, from azimuth 090°, in the east to 060° in the west of

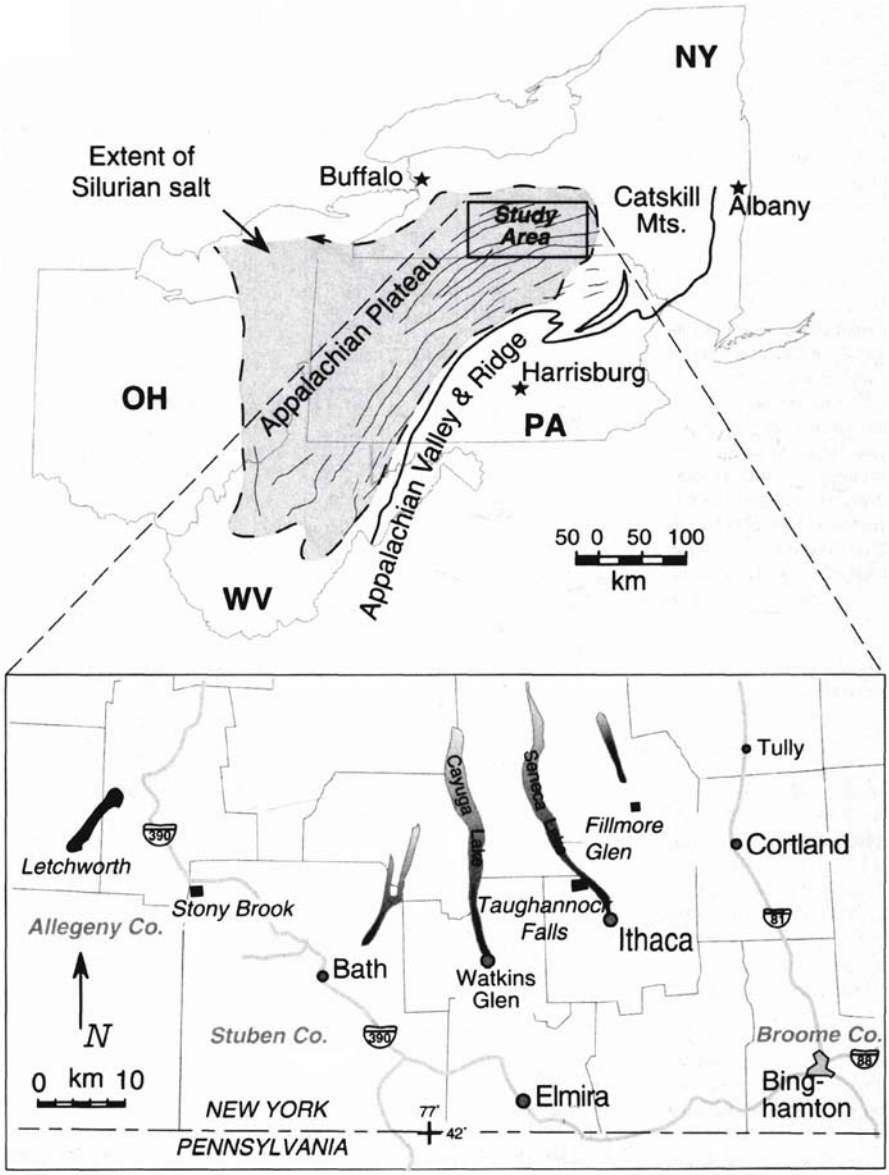

Fig. 3.1a. Geological maps from the Appalachians. Location map of the Finger Lakes district in New York State. The extent of the Silurian salt is *shaded* and *outlined* by *dashes* in the states of New York (*NY*), Pennsylvania (*PA*), Ohio (*OH*), and West Virginia (*WV*) (from Younes and Engelder 1999). *Dark lines* depict the stress trajectories of S_{Hmax} according to the distribution of cross fold joints in the Appalachian Plateau

the region. Engelder and Geiser (1980) discerned two different cross-fold joint sets (or cross-strike sets, approximately perpendicular to the fold axis). These sets preserve their approximate cross-strike position from east to west, with angles between the sets ap-

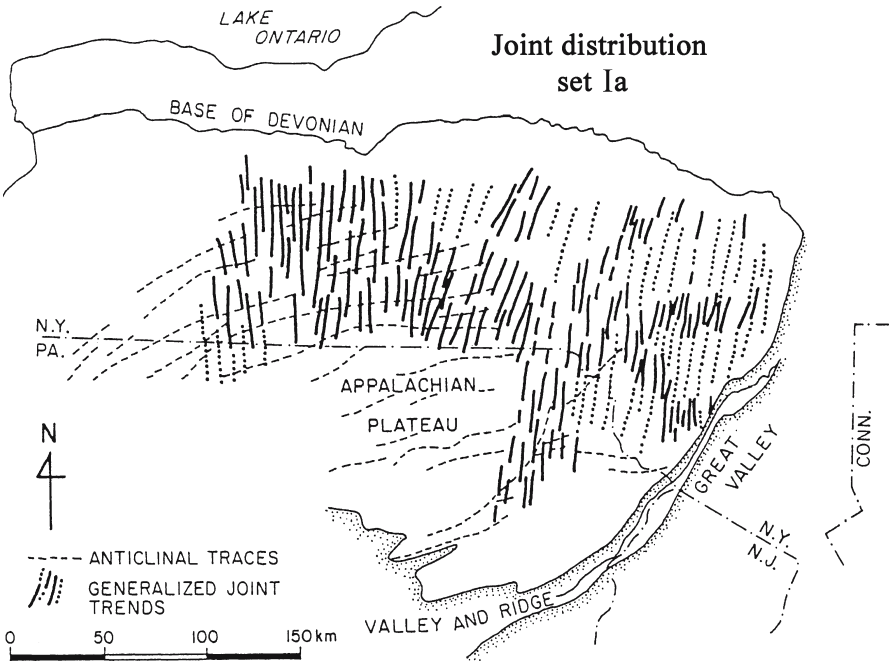

Fig. 3.1b. Geological maps from the Appalachians. Set Ia (from Geiser and Engelder 1983)

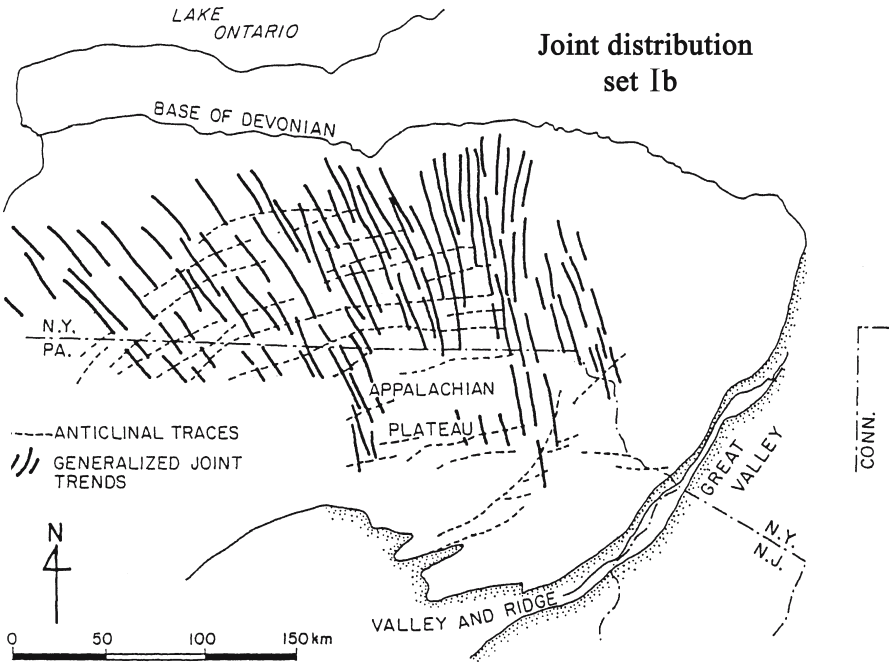

Fig. 3.1c. Geological maps from the Appalachians. Set Ib (from Geiser and Engelder 1983)

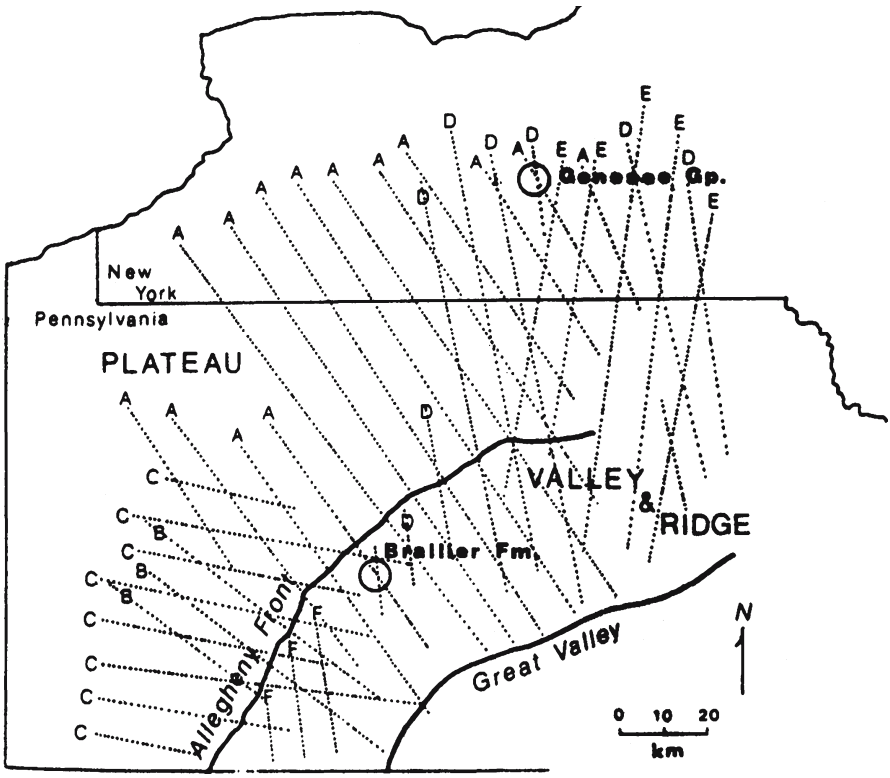

Fig. 3.1d. Geological maps from the Appalachians. Orkan and Voight's (1985) map of the trend lines for regional joint sets within the central Appalachian fold-thrust belt. Sets *A* through *E* are those of Nickelsen and Hough (1967). Regional joint sets are based on the data of Nickelsen and Hough (1967), and Engelder and Geiser (1980) (from Engelder 1993)

proximating 18 ±2° in the east and 30 ±4° in the west. In many outcrops, one joint set parallels the direction of maximum compressive strain (ef) as recorded by fossil distortion (parallel to the bedding). Joints of this set, termed Ia (Fig. 3.1b), are sometime calcite-filled. According to Engelder and Geiser (1980) they are part of joint set I as defined by Parker (1942), of the type called dip joints (i.e., parallel to the dip direction of bedding) by Sheldon (1912) who often found them in more than one orientation. Joints of the other set, termed Ib (Fig. 3.1c), strike at 16–34° counter clockwise from ef and are parallel to eoc, the maximum in situ compressive strain as measured parallel to bedding by overcoring techniques (in the Machias Formation). These correspond to the compressive direction indicated by a penetrative fabric in outcrops in Allegany County (Fig. 3.1b). Sets Ia and Ib are equivalent to the systematic joint sets E and A respectively, described by Nickelsen and Hough (1967) (Fig. 3.1d). In addition, Engelder and Geiser (1980) characterized joint sets II and III. Joints of set II strike sub-parallel to the fold axes. They belong to joint set II of Parker (1942) and were called strike joints by Sheldon (1912). They have the same orientation toward the fold axes as the non-systematic joints described by Nickelsen and Hough (1967). Set III, which belongs to set III of Parker (1942), is not obviously related to either ef, eoc, or to the fold axes.

The above discrimination of joint sets illustrates how complicated the "regional joint pattern" of a given area can be, and how complex the challenge is to try and form a sensible tectonic picture from it. The above references and subsequent studies have made the Appalachian Plateau into a classic arena of fracture studies, where many basic concepts of jointing were first recognized.

A comprehensive updated account of the Devonian Fracture Province of the Appalachian Plateau is presented by Younes and Engelder (1999) and their results and discussion are quoted extensively here. Fringe cracks on joint surfaces and kinks are considered in the context of individual outcrops, in Chap. 2. The application and conclusions obtained from parent joints, fringe cracks and kinks and their relation to the regional tectonics in the eastern United States are given in the present chapter.

Younes and Engelder (1999) document the spatial distribution and nature of joints within the northeastern portion of the Appalachian Plateau detachment sheet (Fig. 3.1a). The area, about 3 000 km^2, includes the Finger Lakes district of New York State, which extends from Broome County to Allegany County (Fig. 3.1a). The detachment sheet in this area consists of clastic sedimentary rocks of the Devonian Catskill Delta, transported from the Acadian highlands to the east (Ettensohn 1985). The delta prograded from east to west, attaining its maximum thickness east of the study area. The delta complex consists of packages grading from black and gray shales through siltstone to sandstone. The clastic Hamilton, Genesee, Sonyea, and West Falls Groups (Fig. 3.2 and 3.3) are separated by three black shale formations: Genesee, Middlesex, and Rhinestreet shales, which reflect anoxic conditions at the time of deposition. The Tully limestone is an important marker bed at the base of the Genesee Group.

The detachment sheet was deformed into a series of low-amplitude folds (mapped in outcrop by Wedel (1932), and in the subsurface by Bradley and Pepper (1938) and Murphy (1981)). Folds of the detachment sheet are broad, persistent, and can be traced farther to the southwest in Pennsylvania and into West Virginia. In the study area, the fold axes trend east-west in the eastern part and northeast-southwest in the western part. The detachment sheet contains layer-parallel shortening structures of Alleghanian age above a decollement within the Silurian Salina salt (Rodgers 1970; Engelder 1979; Murphy 1981). Much of the layer-parallel shortening was accommodated by pressure solution and the formation of solution cleavage (Engelder and Geiser 1979; Geiser and Engelder 1983). The amount of slip on the decollement is as much as 22 km to the north-northwest as estimated at the Allegheny front (Engelder and Engelder 1977). Mapping of the detachment uses strain markers such as deformed fossils and subsurface data (Engelder and Engelder 1977; Engelder 1979; Engelder and Geiser 1980; Beinkafner 1983; Geiser 1988; Hudak 1992). The foreland limit of the detachment sheet and the region of folds in the post-Silurian rocks coincides with the limits of the Silurian salt (Frey 1973).

Joints of Alleghanian age strike approximately normal to the axes of the folds within the detachment sheet (Fig. 3.1b,c) (Parker 1942; Ver Steeg 1942; Nickelsen and Hough 1967; Engelder and Geiser 1980; Geiser and Engelder 1983; Lacazette and Engelder 1992). Note that clockwise rotation from west to east is observed both among individual cross fold and within each set (Fig. 3.1b,c). Multiple sets of cross fold joints are particularly well developed in interlayered siltstone-shale beds, where the earlier dip joints favored siltstone beds. Clear fractographic distinctions can be made among the various cross fold sets (Bahat and Engelder 1984; Bahat 1991a, p. 248), which moreover are occasionally decorated with fringe cracks (Younes and Engelder 1999).

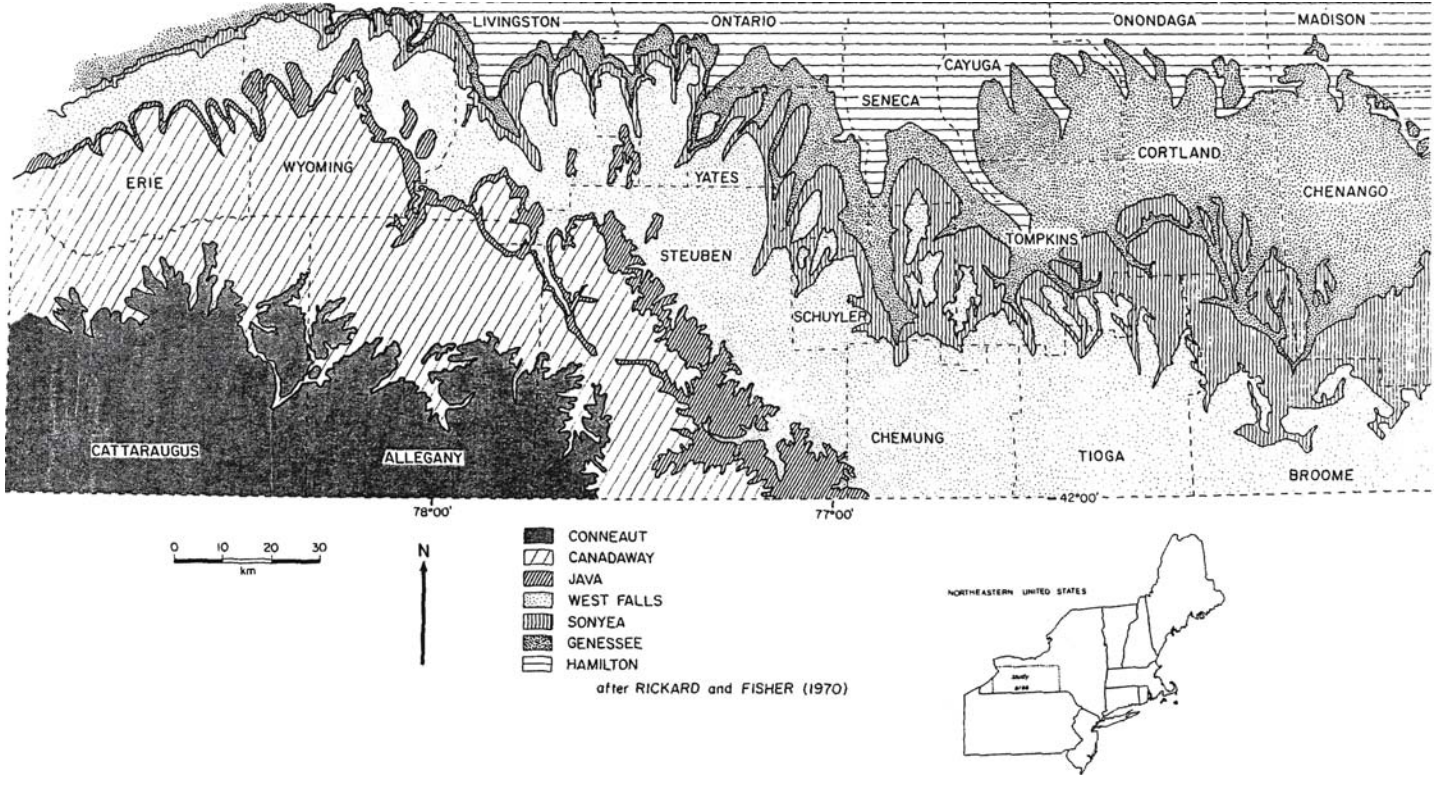

Fig. 3.2. The stratigraphy and geography of the southern tier of New York State (from Engelder and Geiser 1980)

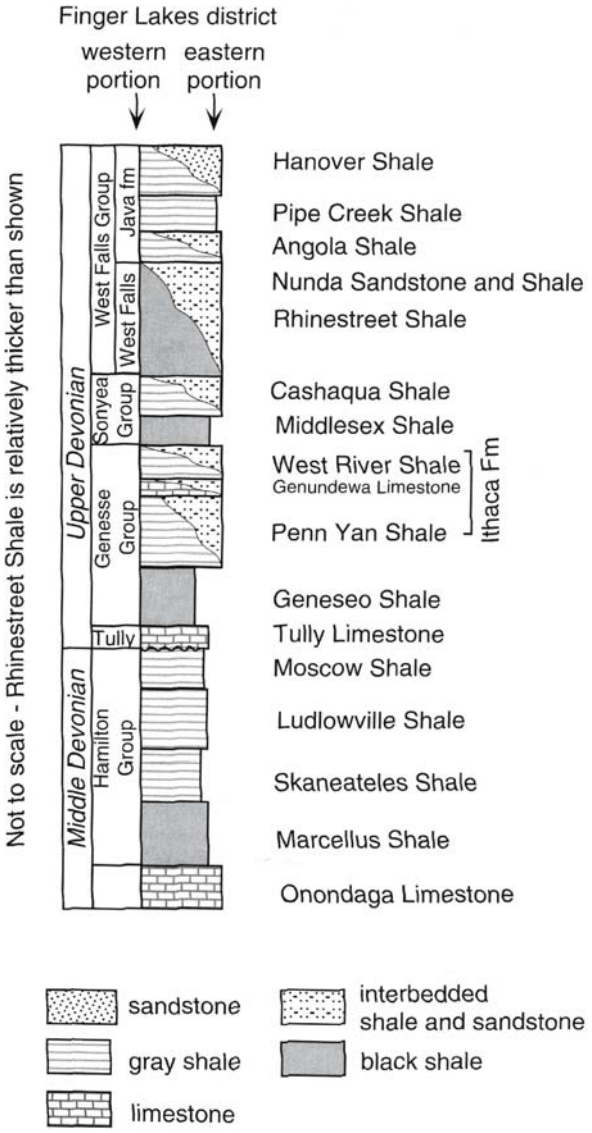

Fig. 3.3.
A simplified stratigraphic column of major rock units in the eastern and western portions of the study area in the Finger Lakes district of New York State (modified from Van Tyne 1983). The facies become progressively coarser to the east as the proximal parts of the Catskil Delta are approached. The unconformity at the base of the Tully limestone extends up to the base of the Cashaqua shale in western New York (from Younes and Engelder 1999)

3.1.2 The Tectonic Problem

Nickelsen (1979), in an analysis of the Bear Valley strip mine in the Appalachian Valley and Ridge recognized a group of structures that testify to a clockwise rotation of maximum horizontal stress (S_{Hmax}) during the Alleghanian orogeny (Younes and Engelder 1999). Engelder and Geiser (1980) also found joint evidence on the Appalachian Plateau of a clockwise rotation of the Alleghanian stress field. Rocks with two distinct cleavages or commonly displaying two dip joint sets led Geiser and Engelder

(1983) to conclude that the Appalachian Plateau was affected by two different tectonic phases: The Lackawanna phase and the Main phase. However, outcrops in the anthracite coal district of the Appalachian Valley and Ridge of Pennsylvania, including the Bear Valley strip mine, indicate that the rotation of the Alleghanian stress field produced structures with a broad range of orientations. From these, Gray and Mitra (1993) concluded that the Alleghanian orogeny was a continuous series of structural events reflecting *a gradual* clockwise rotation in the Alleghanian stress field, not punctuated by two tectonic phases as suggested by Geiser and Engelder (1983). Bahat (1991a, Tables 5.1 and 5.2) and Evans (1994) showed structures in more than two orientations, suggesting that the northeastern portion of the Appalachian Plateau detachment sheet was also deformed by a more continuous clockwise rotation of the Alleghanian stress field. If so, the tectonic evolution of the Appalachian Plateau detachment sheet is consistent with that of the Valley and Ridge. These two conflicting concepts (discrete phases vs. gradual stress rotation) are further discussed in Sect. 6.3.

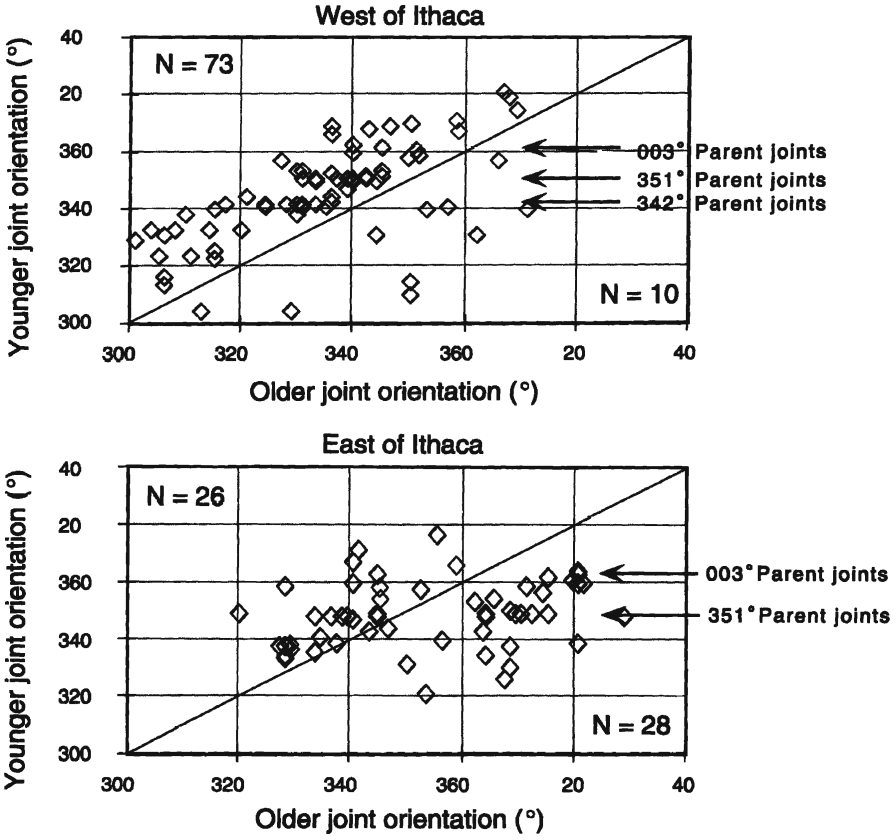

Fig. 3.4. Abutting relationships west and east of Ithaca, New York. The *diamond symbols* above the *straight line* indicate a clockwise abutting relationship, whereas those under the line are counter clockwise rotations. The abutting of joints west of Ithaca is dominated by clockwise rotations, but mixed rotations are found east of Ithaca

3.1.3
Sequence of the Dip Joint Development

Evidence for the timing of joint development is visible throughout the detachment sheet (Younes and Engelder 1999). It consists of curving or kinking of younger joints as they approach the pre-existing joints, or abrupt termination of younger joints against older joints. Unambiguous cases of abutting are less common than mutual cross cutting. Nevertheless, abutments between dip (i.e., parent) joints in the detachment sheet show west-to-east constancy. The later dip joints, particularly in the western part of the study area, strike a few degrees clockwise from earlier dip joints; younger dip joint sets are defined by the horizontal clustering of data in Fig. 3.4. Where present, fringe cracks are always counter clockwise from these parent joints (Fig. 3.5a–c). Clustering is observed in abutting dip joints at strikes 342°, 351°, and 003°, suggesting that younger dip joints have a consistent orientation throughout the region, even though their predecessors show widely varying orientations. The earliest dip joint set, in the range of 320–330°, does not cluster. The same appears to be true for another dip joint set, striking 006° to 021° range in the easternmost part of the study area. These data indicate that joints striking at 342° generally abut joints striking at 320–330°, and 351° joints generally abut 342° joints, and so forth. Nevertheless, an exception to this general rule of clockwise sequence of younger joints is found at the eastern edge of the study area, where 003° joints abut parent joints striking roughly 020°, indicating in this area a counter clockwise rotation of the stress field with time. Thus, the sequence of dip joint

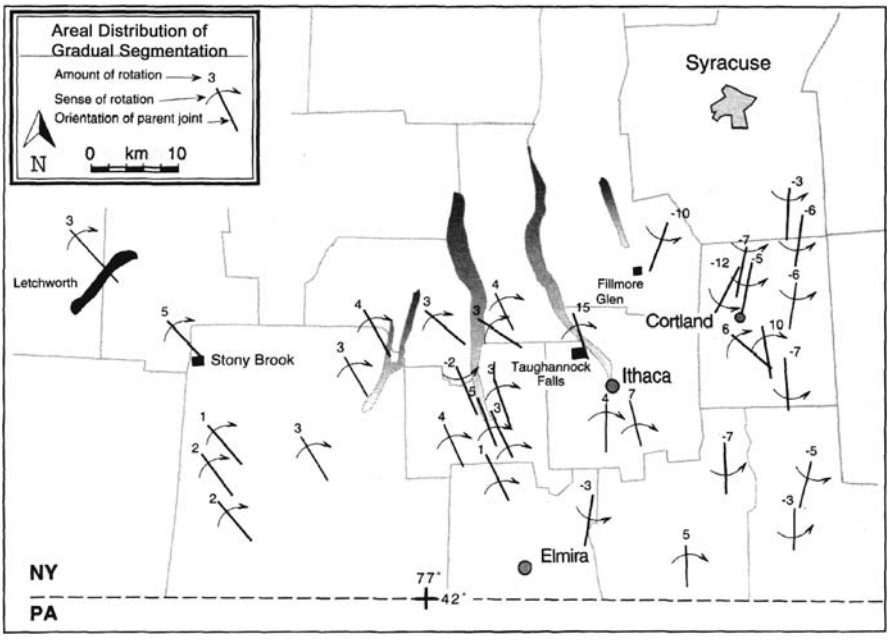

Fig. 3.5a. Arial distribution of gradual segmentation. The amount of rotation shown is the average of all fringe crack sets at every station (modified after Younes and Engelder 1999)

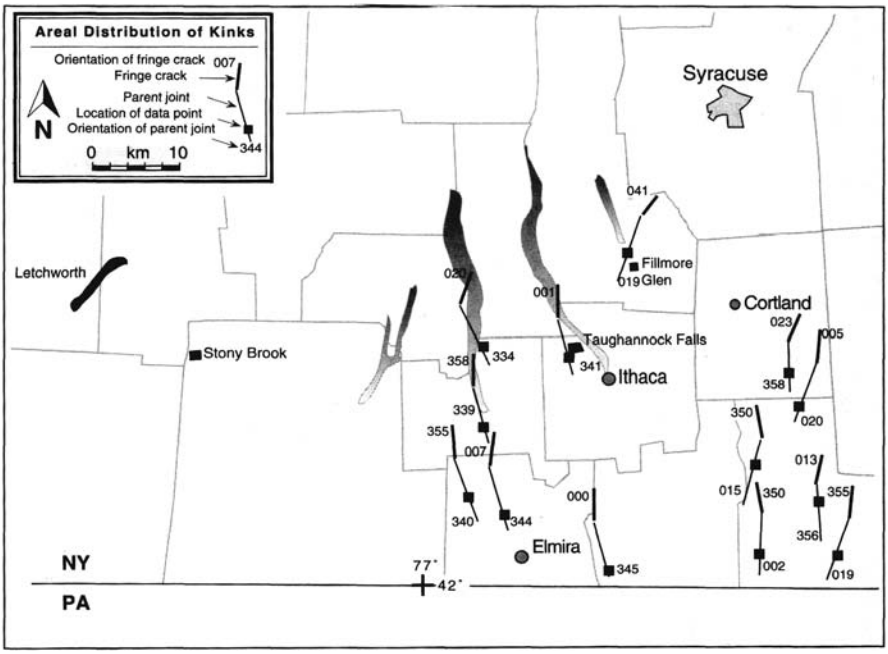

Fig. 3.5b. Arial distribution of kinks (after Younes and Engelder 1999)

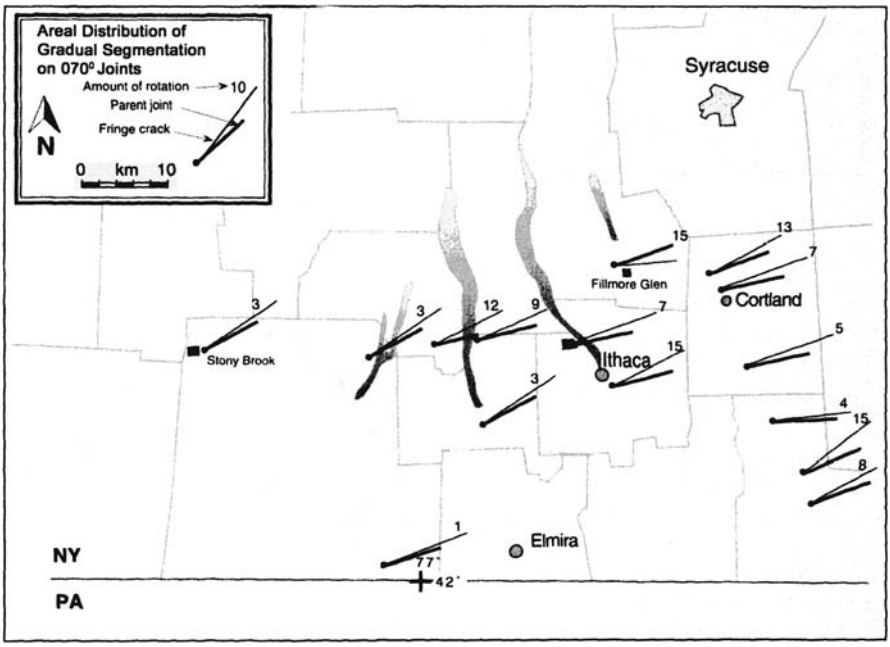

Fig. 3.5c. Arial distribution of of gradual segmentation on 070° joints. The amount of rotation shown is the average of all fringe crack sets at every station (modified after Younes and Engelder 1999)

development in the detachment sheet appears to be as follows (parentheses indicating sets of joints clustered about that orientation):

$$(320^\circ - 330^\circ) \rightarrow \begin{bmatrix} \text{East Ithaca} \\ (006^\circ - 021^\circ) \\ \\ (342^\circ) \\ \text{West Ithaca} \end{bmatrix} \rightarrow (352^\circ) \rightarrow (003^\circ)$$

Other post-Alleghanian joint sets are also found throughout the detachment sheet. One post-Alleghanian 070° set is best developed in black shale below the Rhinestreet Forrmation (Loewy 1995). The 070° joints are cut by Middle Jurassic kimberlite dikes (Kay et al. 1983) in the vicinity of Ithaca, and are therefore older than Middle Jurassic. Another post-Alleghanian 000° set consists of short, curviplanar-to-planar joints that occasionally abut earlier 070° joints. The 000° set striking parallel to the Mesozoic kimberlite dikes (Martens 1924; Parker 1942), is the youngest joint set found by Younes and Engelder (1999).

3.1.4
Progressive Development of the Regional Stress Field

3.1.4.1
Patterns of Parent Joint Sets

Data on the abutting of parent joints of the Appalachian Plateau detachment sheet show that there are at least two joint sets, which according to Engelder and Geiser (1980) extend several hundred kilometers along strike in a fan-shaped pattern. Four development stages are discerned in the pattern of dip joints, as is indicated by both the abutting of parent joints and the rotation angle of fringe cracks. The regional pattern of parent joints is due to the overlapping of joint sets with different strikes and developed from west to east as progresively younger joint sets propagated within a clockwise rotating stress field. Throughout this development, the Alleghanian stress field sweeps through roughly 40 degrees from 320° to 360°. To the southeast in the anthracite region of the Valley and Ridge, the Alleghanian stress field rotated 30 degrees clockwise, from 336° to 006° (Gray and Mitra 1993). Although the stress fields of the Plateau and of the Valley and Ridge differ slightly in magnitude, the correlation is close enough to suggest that both areas underwent similar tectonic development, marked by a clockwise rotation of the horizontal stress field.

3.1.4.2
The Orientation of Fringe Cracks Relative to Their Parent Joints

Fringe cracks occur in most lithologies that are found in the Finger Lakes district of New York State. More than 225 sets of fringe cracks were mapped by Younes and Engelder (1999) in the Finger Lakes district of New York State on the northeastern portion of the Appalachian Plateau detachment sheet. Although there are millions of joints throughout the detachment sheet, joints decorated with fringe cracks are rare,

and within individual outcrops their number varies from one to several dozen. Maps in Fig. 3.5a–c show the orientation and aerial distribution of fringe cracks and their parent joints as expressed by their average strikes. Younes and Engelder (1999) observe that the general orientation of all fringe crack sets throughout the detachment sheet follows the systematic change in fold trend and strike of the parent joints from east to west. In general, and depending on the type of fringe crack, the angle between parent joint and fringe cracks remains about the same across the area. However, there is a pattern to the sense of fringe crack rotation across the region. East of Ithaca, fringe cracks strike counter clockwise from the parent joints, while to the west they strike clockwise from their parents, and both types overlap in the Ithaca area. Because loading conditions and the timing of propagation are different for each fringe crack type, there are characteristic differences in twist and tilt angles (Fig. 2.20). Kinks are concentrated in the eastern half of the study area and tend to strike within a few degrees of 002°, seemingly independent of the parent's orientation.

3.1.4.3
Counter Clockwise Propagation of Fringe Cracks near the Eastern Boundary

According to Younes and Engelder (1999) the abutting geometries of parent joints, coupled with fringe cracks, provide a record of the Alleghanian stress field as it evolved across the Appalachian Plateau detachment sheet. The fidelity of the record of stress field rotation as derived from the abutting geometries and fringe cracks can be evaluated by comparing it with the rotation of the Alleghanian stress field and strain within

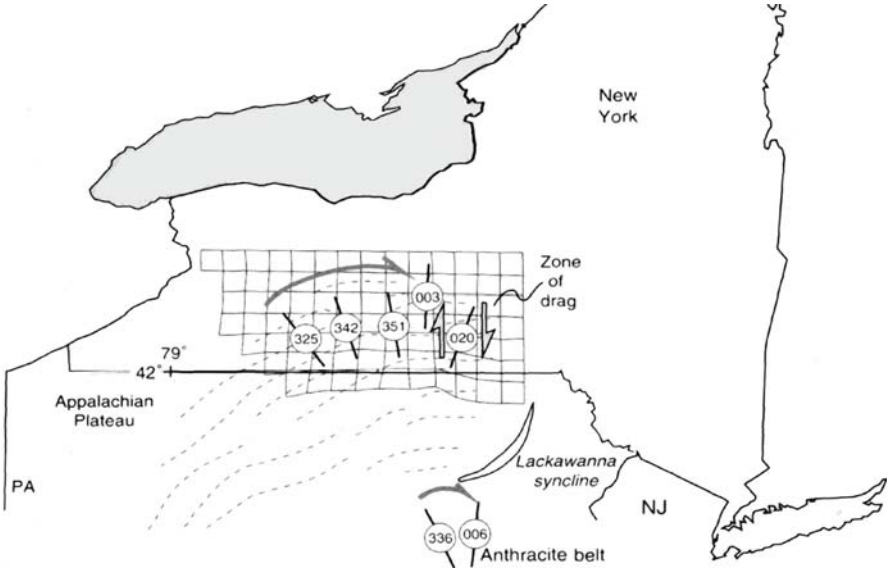

Fig. 3.6. Deformed-state grid given by the displacement field determined from finite strain as indicated by deformed crinoid columnals and from cleavage (adapted from Geiser 1988). *Dashed lines* are traces of the fold axes. The *circled numbers* indicate the trends of joint sets from the Appalachian Plateau (Younes and Engelder 1999), and the direction of the Alleghanian stress field in the anthracite belt of Pennsylvania (Gray and Mitra 1993) (from Younes and Engelder 1999)

the detachment sheet. An isostrain map for layer-parallel shortening of the detachment sheet was constructed by Geiser (1988) from orientation data of cleavage and fossil deformation. Layer-parallel shortening shows a radial fan pattern from west to east (Fig. 3.6). The east-west lines display a uniform spacing (i.e., strain gradient), except east of Ithaca to the eastern part of the study area, where the rectangular grid is distorted and the east-west grid lines are more closely spaced. Greatest grid distortion coincides with the region containing parent joints decorated with fringe cracks, reflecting a counter clockwise rotation on the Alleghanian stress field (Fig. 3.5a). This conformance of fringe cracks to strain distribution provides evidence for constructing the tectonic history of the detachment sheet.

In the eastern part of the study area, evidence is strong for counter clockwise rotation of the stress field after the formation of an initial set of dip joints striking between 006° and 021°. This is indicated by both abutting geometries and fringe cracks. Relative to its orientation farther west (i.e., 342°), the 20° to 30° misalignment of the early stress field to the east is significant. Younes and Engelder (1999) note that this misalignment occurs in the pinchout area of the Silurian salt, which served as a convenient detachment surface. They attribute the misalignment of the stress field to rock drag, produced by the lack of salt detachment east of Ithaca. Drag at the edge of the detachment sheet sets up a local remote stress field, controlling the orientation of early parent joints striking between 006° and 021° (see Geiser 1988). A later stress field producing both the 352° and 003° sets reversed the sense of shear on the parent joints along the eastern boundary of the detachment sheet. This causes the later fringe cracks to form counter clockwise from parent joints.

3.1.5
Tectonic History of the Appalachian Plateau Detachment Sheet

Younes and Engelder (1999) maintain that any tectonic history of the Appalachian Plateau detachment sheet must take into account the following observations:

1. Whenever observed in the same outcrops parent joints in the shale are oriented clockwise relative to parent joints in the siltstone layers.
2. The sequence of formation of parent joints, as indicated by the abutting relationships, shows a clockwise rotation of regional stress from west to east, except in the eastern part of the study area.
3. Fringe cracks on dip joints show a clockwise rotation of the stress field in the west, a counter clockwise rotation in the east, and both kinds of rotation near Ithaca (Fig. 3.5a).
4. The rotation angle for counter clockwise fringe cracks is generally larger than for clockwise fringe cracks.

3.1.5.1
The Proposed Sequence of Stress Directions in the Northeastern Part of the Detachment Sheet

The 320–330° parent joint set. The earliest parent joints in the study area are limited to the western region, the area (Fig. 3.6) that is closest to the extension of the Juniata culmination into the plateau. Joints belonging to this set range over about 10° (320–330°)

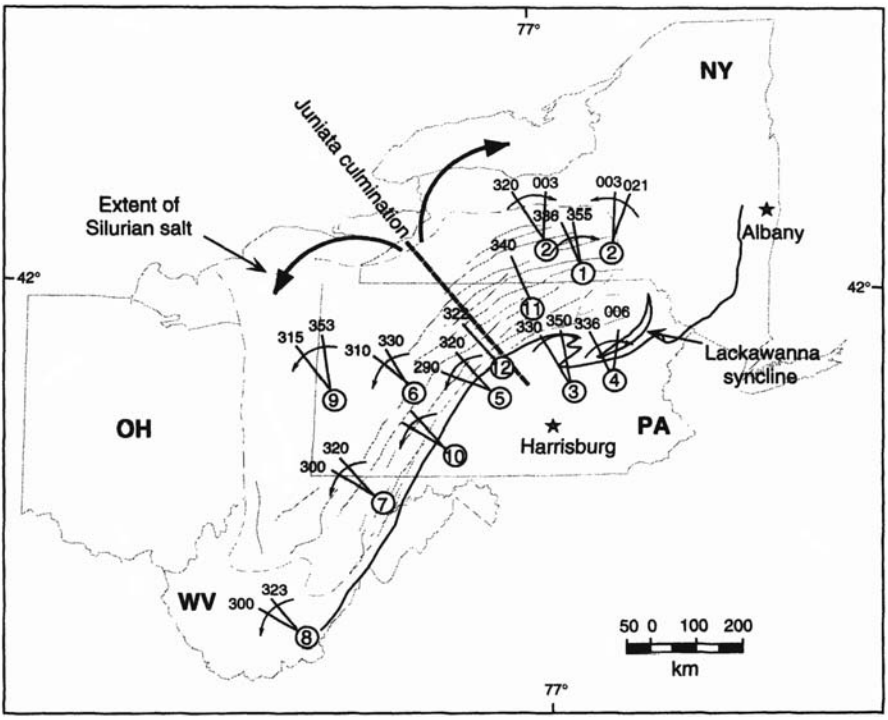

Fig. 3.7. A model for the rotations of the Alleghanian stress field in the Central Appalachian Mountains. The *heavy black line* is the boundary between the Valley and Ridge and Appalachian Plateau. The *short straight segments* indicate the first and last stages of deformation as determined by the following authors indicated by the corresponding number: *1:* Engelder and Geiser (1980); *2:* Younes and Engelder (1999); *3:* Nickelsen (1979); *4:* Gray and Mitra (1993); *5:* Nickelsen (1988); *6:* Nickelsen and Hough (1967); *7:* Dean et al. (1984); *8:* Dean et al. (1988); *9:* Evans (1994); *10:* Nickelsen (1996); *11:* Spiker and Gray (1997); *12:* Nickelsen and Engelder (1989). The *thin arrows* indicate the local sense of rotation, and the *thick arrows* indicate the regional sense of rotation proposed by Younes and Engelder (1999). The *heavy dashed line* marks the location of the Juniata culmination (from Younes and Engelder 1999)

(see explanation below). This same joint set is found west of the Juniata culmination and in the detachment sheet as far south as West Virginia (Fig. 3.7). However, to the west and southwest of the Juniata culmination, the earliest parent joints are characterized by a counter clockwise sequence of development. Zhao and Jacobi (1997) reported that west of the study area, joints striking 322° to 340° predate 312–320° joints and a second group of 280–305° joints. Evans (1994) reported that west of the Juniata culmination, the earliest joint set strikes 350° and is followed by the 320° to 330° joints. In central New York State, the earliest structures include folding (042° fold axes) of the Tully limestone (Younes and Engelder 1995). Because the shortening direction indicated by the deformation of fossils is at a significant clockwise angle with the earliest joints (Engelder and Geiser 1980), these earliest joints apparently predate layer-parallel shortening. The earliest joints in the Valley and Ridge also predate appreciable layer-parallel shortening (Nickelsen 1979). Early joints occur throughout the stratigraphic section near the Juniata culmination, yet farther east they are found only

below the Tully limestone. The orthogonal relationship between the fold axes of the Tully limestone and the early joints suggests synchronous formation of the two features. At this stage, detachment within the salt decollement may have begun but was not well developed. Farther southeast, early fold axes of the Lackawanna syncline (Fig. 3.6) are parallel to those found in the Tully limestone. Thus, we suggest that set 320–330° appears to be of the burial type which forms prior to the onset of intense tectonics (Bahat 1991a, p. 240). The early age of this set fits that of the early fold axes of the Lackawana syncline before the actual detachment. Possibly, the wide range of strike in this set reflects small differential stresses, compared to relatively large differential stresses in the later, syntectonic sets, resulting in narrower strike ranges.

The 342° parent joint set. The propagation of the 342° set marks the initiation of significant detachment along the Salina salt, as indicated by deformed fossils. Clockwise rotation of the stress observed in the early stages of layer-parallel shortening was recorded as cleavage in the Tully limestone. As the amount of layer-parallel shortening increased, the eastern edge of the detachment sheet began to drag where the eastern salt pinch-out prevented easy detachment. As a consequence of this drag, a shear couple developed within the eastern region of the detachment sheet so that the local stress field was rotated considerably clockwise relative to that found in the rest the detachment sheet (more about the association of shear couple and local stress field rotation in Sect. 3.2). Joints in the eastern region propagate in directions ranging from 006° to 021°. During this tectonic stage, folding continued in the section above the Tully limestone. A clockwise stress field rotation east of the Juniata culmination is reflected in the initial development of clockwise fringe cracks in the western region of the study area. The overall uniform strike of set 342° suggests that it is of the syntectonic type.

The 351°parent joint set. A third stage is marked by the propagation of 351° joints. By this stage, parent joints had propagated throughout most of the northern detachment sheet, and drag along the eastern edge of the detachment sheet was at a maximum. At this stage, counter clockwise fringe cracks began to be formed along the eastern edge of the detachment sheet. Kinks equivalent to the 351° parent joints are also found throughout the western parts of the sheet.

The 003° parent joint set. The continuing clockwise rotation of the Alleghanian stress field is next indicated by 003° joints. It is possible that the kinks showing a counter clockwise angle developed during this stage as a result of north-south compression. The general north-south orientation of the kinks (Fig. 3.5b) and their constant angles to the parent joint for both clockwise and counter clockwise sets (Fig. 3.8) indicate that they are related to the same event. This is also supported by the mechanical requirement that kinks will only form after arrest of their parent joints (more in Sect. 2.2.9.6).

The 070° parent joint set. This stage of jointing is best developed in black shales of the Catskill Delta (Loewy 1995) and is the most difficult to date. The 070° joints are a result of tectonic relaxation before abnormal pressure within the delta shales could leak off (McConaughy and Engelder 1999). The 070° set carries fringe cracks that are always rotated counter clockwise (Fig. 3.5c).

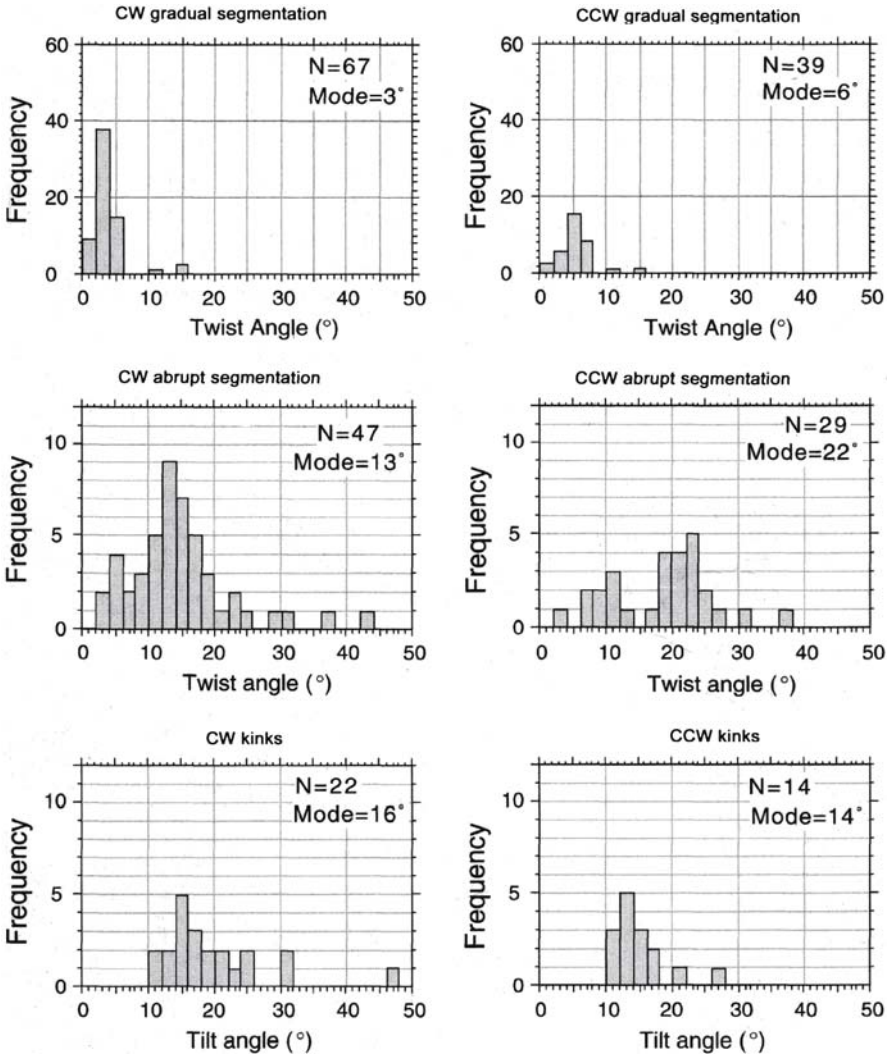

Fig. 3.8. Histograms of the magnitude of clockwise (*CW*) and counter clockwise (*CCW*) rotations for gradual and abrupt fringe cracks and kinks. The number of fringe sets and the statistical mode of orientation are shown inside each histogram. The amount of CCW rotation for fringe cracks is larger than the CW rotation. Kinks have a more consistent orientation (mode is almost the same for CW and CCW rotations) (from Younes and Engelder 1999)

The 000° parent joint set. The propagation of a second north-south joint set is post-Alleghanian. These late joints are parallel to the kimberlite dikes cutting the detachment sheet. These dikes were dated as Early Jurassic, and therefore this set may also be early Mesozoic in age. This later 000° set may be associated with continuing slip on faults of the Clarendon-Linden zone (R. Jacobi 1998, pers. comm. to Younes and Engelder). Joints oriented 003° and 000° are also distinguishable by differences in length and planarity.

3.1.5.2
Tectonics on Either Side of the Juniata Culmination

According to Younes and Engelder (1999), the Juniata culmination correlates with a regional lineament known in central Pennsylvania from surface geology and magnetic and gravity anomalies (Gold and Parizek 1976). The joint propagation sequence around the Juniata culmination indicates that paleostress trajectories rotated away from parallelism with the culmination in opposite directions, leading to a clockwise sequence of structures to the east and north of it and a counter clockwise sequence to the west and south of it (Fig. 3.7 and 3.9) (Younes 1996). As mentioned, the trend of the Juniata culmination is parallel to the oldest joints in the detachment sheet (320–330°).

Nickelsen and Hough (1967) mapped five sets of dip joints in the Pennsylvania portion of the detachment sheet (Fig. 3.1d, sets A–E). Set A, oriented 330°, is parallel to the Juniata culmination and perpendicular to the Lackawanna syncline. It is flanked by joint sets D and E to the northeast, and joint sets B and C to the southwest. Based on the similarities between the joint orientations in central New York State and those in northeastern Pennsylvania, and also on the similarities between those in southeastern Pennsylvania to those in West Virginia (Dean et al. 1984, 1988), Younes and Engelder (1999) relate set D to clockwise stress field rotation in the northeast, and sets B and C to counter clockwise rotation in the southwest. This interpretation agrees with Evans' (1994) analysis of joints west of the culmination. Zhao and Jacobi (1997) reported a clockwise superposition of joints to the east of the Juniata culmination and a counter clockwise superposition of joints west of it.

Exposures of clockwise and counter clockwise fold rotations in the Antes shale of the Sinking Valley fault zone, Pennsylvania, show a transport direction that is compatible with transport parallel to the Juniata culmination (Nickelsen and Engelder 1989). The direction of transport was estimated as 322°, similar to the oldest trends in

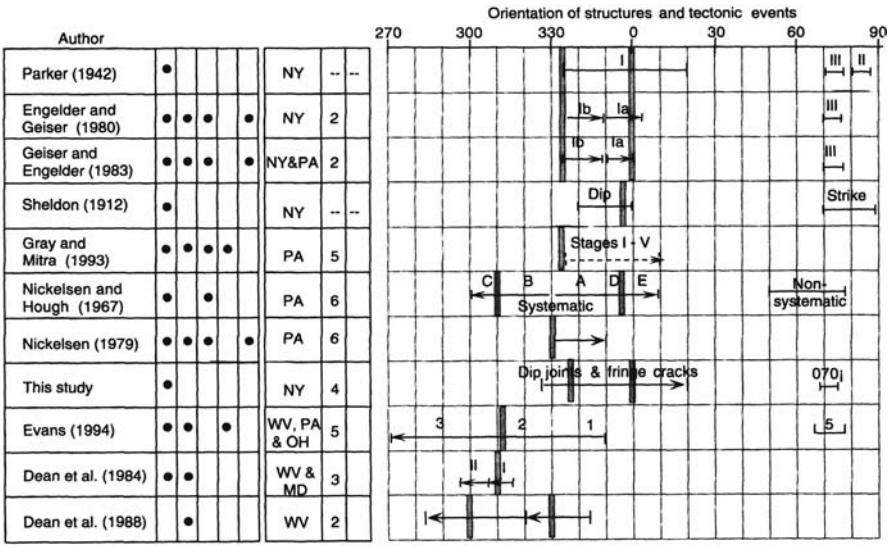

Fig. 3.9. Selected data on the sense of rotation of the regional stress field in the central Appalachian Mountains during the Alleghanian orogeny (from Younes and Engelder 1999)

the study area. Deformation at the Allegheny front near Williamsport, Pennsylvania, shows a single transport direction at 340° (Spiker and Gray 1997). Nickelsen (1988) noted that the Jacks Mountain fault, farther south, is intersected by a series of small wrench faults from which he was able to determine the directions of compression. These directions fall into orientation about 322°, then 335°, and then 312°, which indicates both senses of stress field rotation that might be expected near the culmination. Viewed on a larger scale, the Juniata culmination divides both the Appalachian Plateau and Valley and Ridge into an eastern area of clockwise paleostress rotation and a western area of counter clockwise paleostress rotation (Fig. 3.7).

3.1.6
Three Main Concepts of Regional Cross-Fold Joint Patterns

Based on the previous studies of fracture in the Appalachian Plateau, we distinguish three main concepts relating to regional patterns of cross-fold joints. These concepts apply to the different geometries of joint sets that form during *various time spans*. We distinguish:

1. The "strict orientation pattern" of joint sets (adopted from Nickelsen and Hough 1967) (Fig. 3.10a).
2. The "change in orientation within a joint set" (adopted from Engelder and Geiser 1980) (Fig. 3.10b).
3. The "simultaneous fan-shaped pattern" (adopted from Younes and Engelder 1999) (Fig. 3.10c).

Engelder (1993) notes that Nickelsen and Hough's (1967) outcrop-to-outcrop correlation of joints depends largely on the assumption that the Earth's stress field is "nearly homogeneous", and therefore joints of one set have similar orientations over large regions. If a set of joints at an outcrop differs by, say, 15° from a joint set at other outcrops, then this local suite of joints belongs to a second joint set, regardless of its orientation with respect to local structures. The implication is that joints of one set do not change orientation even as fold axes swing and curve through a mountain range such as the central Appalachian Plateau (superposition of Fig. 3.1d on anticlinal traces of Fig. 3.1c). On a regional scale, the change in strike of fold axes is accommodated by the overlap of joint sets of different orientations.

Engelder (1993) maintains that Nickelsen and Hough (1967) developed their correlation strategy based on the observation that first-order folds in the Pennsylvania Valley and Ridge are kink folds (e.g., Faill 1973) with straight axes. Nickelsen proposed (personal communication to Engelder) that the Valley and Ridge developed as overlapping thrust sheets cored with duplexes moving toward the craton, with straight-axis kink folds delimiting the thrust duplexes. The curvature of the central Appalachian Valley and Ridge is accommodated by abrupt changes in the orientation of first-order folds. Strictly parallel joint sets are a kinematic feature of thrust sheets associated with straight-axis kink folds. Presumably, the motion of various sheets is independent, thereby setting up homogeneous stress fields that produce parallel joint sets, unrelated to others in time and space. If this is indeed the case, then stress trajectories cannot be correlated throughout the whole mountain belt (Engelder 1993).

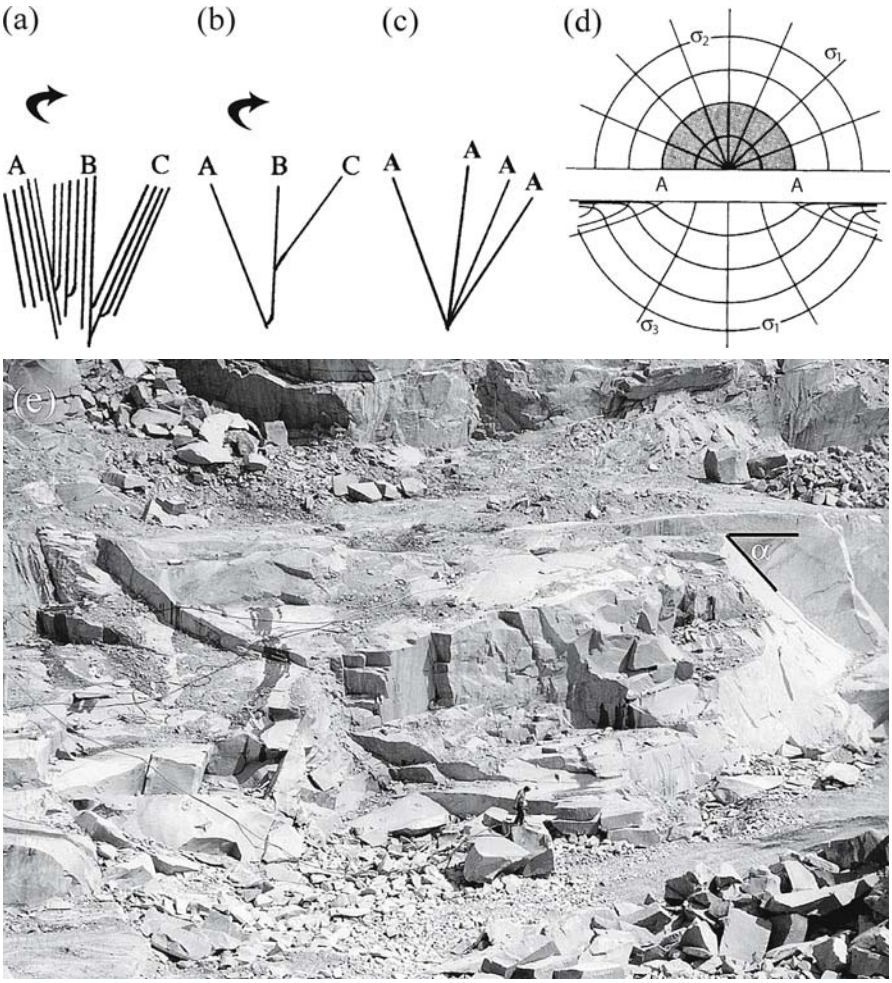

Fig. 3.10. Three concepts of regional cross fold joint formation. **a** Three joint sets (*A*–*C*) form sequentially in a rotational manner (similar to Fig. 3.1d). **b** Joints of a given set rotate sequentially from *A* to *C* (Fig. 3.1b,c). **c** Joints form concurrently in a radial pattern (Fig. 3.12a). **d** Contours of principal stresses strongly deviate from an orthogonal pattern in a Hertzian field induced by indentation. Half-surface view (*top*) and side view (*bottom*) of stress trajectories, plotted for Poisson ratio $u = 0.33$. *AA* denotes diameter of indenter contact (after Lawn and Wilshaw 1975b). **e** Hertzian fracture in granite from the South Bohemian Pluton, showing the cone opening downward (see the α angle), note a person for scale

While remapping cross-fold joints on the Appalachian Plateau, Engelder and Geiser (1980) developed the second concept, using the assumption that joint sets change orientation gradually so as to remain roughly perpendicular to local fold axes. Their analysis implicitly assumes that inhomogeneous stress fields accommodate stress trajectories that curve on a regional scale during an orogenic pulse.

Tracing joint sets in one lithology allows for the possibility that a single joint set can change orientation along with local fold axes (Engelder 1985) (Fig. 3.1b,c). We suggest that in the Appalachian Plateau, the distinction between the first and second

concept is based primarily on criteria of fracture surface morphology: Fractography changes from set to set (Bahat and Engelder 1984), but it remains the same in a given set, even if joints within the set display some change in strike.

While evaluating the concepts that were introduced by Nickelsen and Hough (1967) and by Engelder and Geiser (1980), Younes and Engelder (1999) coined the third concept, the simultaneous fan-shaped pattern. They suggested that if the early joints in the Tully limestone at Taughannock Falls correlate with the 320–330° set found more than 100 km to the west, then the earliest 320–330° set does not fan, but rather is an indication that the same joint set appears in different lithologies in different locations. If, on the other hand, the 342° set in the western part of the study area is simultaneous with the 006° to 021° joint set in the east, then it reveals a fan-shaped pattern. Superimposed on this fanning pattern are two more joint sets, each differing about 10° in strike. Measurements show that individual sets are most recognizable in the abutment of parent dip joints (Fig. 3.4) where later joints cluster at 342°, 351°, and 003°. This joint pattern is consistent with data presented by Nickelsen and Hough (1967), which show how joints of one set cluster about one orientation, not taking part in the fanning pattern.

The first and second concepts require changing stress fields, by rotation mechanisms of S_{Hmax}. The two concepts complement each other in the joint pattern of New York: The various joint sets were formed by the mechanism described in the first concept, showing the rotation from set to set (Fig. 3.1d and 3.10a). The rotation within each set (Fig. 3.1b,c) was effected by the mechanism outlined in the second concept (Fig. 3.10b). Both rotations took place at intermittent time intervals. The third concept, on the other hand, postulates the simultaneous formation of a fan pattern of radial joints over long distances (Fig. 3.10c). We agree with Younes and Engelder (1999) that this concept cannot be rejected, though it would be better supported if fan patterns were found to exist in other fracture provinces. The third concept can be explained by mechanisms that relate to "moderate" heterogeneous stress fields. The radiating joints in Fig. 3.12a seem to be a good example. The formation of conjugate joint patterns may also be connected with simultaneous growth of joints in different directions. For comparison, a "strong" heterogeneous stress field may be induced by Hertzian indentation (Fig. 3.10d). Such extremely heterogeneous stress fields can be postulated for Hertzian fractures (e.g., Fig. 3.10e) found in granites and other magmatic rocks (Bahat 1979c) but rarely for fracturing in sedimentary rocks.

3.2 Fracturing in The Bristol Channel Basin

3.2.1 General Geology and Previous Investigation

The Bristol Channel Basin (BCB) extends on both sides of the Bristol Channel, from west England to South Wales. Unlike jointing in the other three provinces described in this chapter, which affects horizontal or slightly folded layers, joints of the Bristol Channel Basin occur in steeply inclined layers, some dipping more than 30°, due to asymmetric anticlinal folding. Fracturing in this province was described by Rawnsley et al. (1998) who worked on four edge locations of the basin (Fig. 3.11a), and by Engelder and Peacock (2001) who concentrated on the eastern side of the channel (Fig. 3.11b).

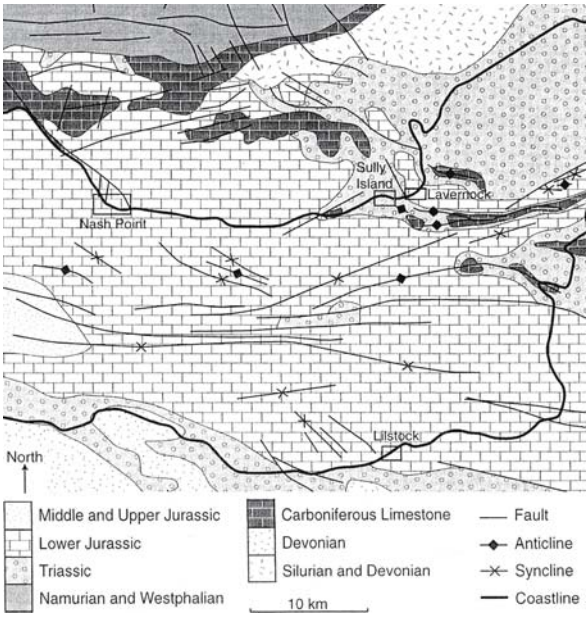

Fig. 3.11a. Map of the Bristol Channel. Map showing the main geological features of the eastern Bristol Channel, with positions of locations studied (modified from Rawnsley et al. 1998, based on the Bristol Geological Survey sheet 51° N–04° W, Bristol Channel)

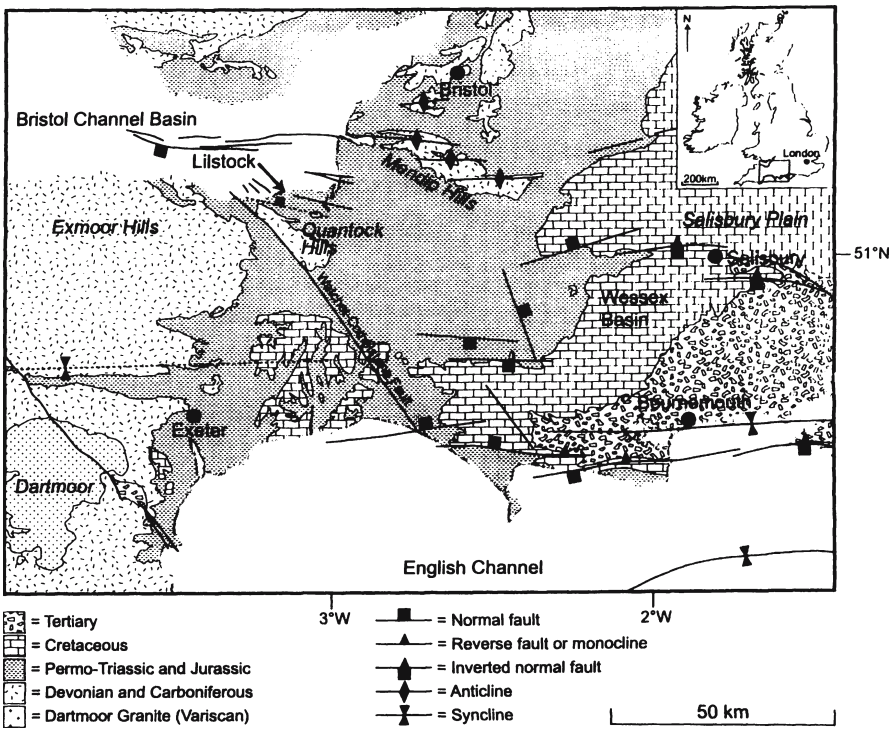

Fig. 3.11b. Map of the Bristol Channel. Geological map of south-western Britain, showing the location of the Bristol Channel basin and Lilstock (from Engelder and Peacock 2001)

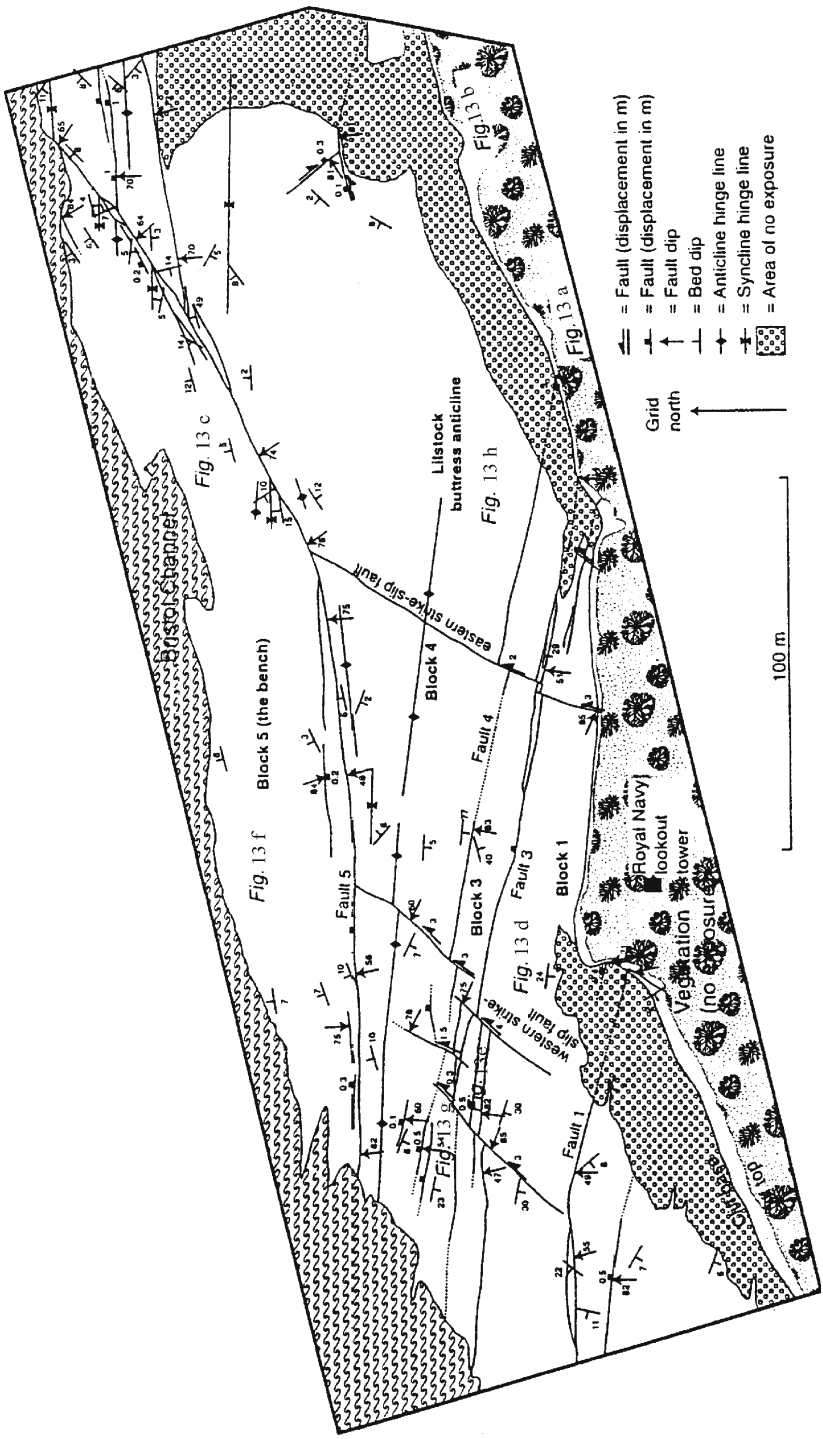

Fig. 3.11c. Map of the Bristol Channel. Geological map of Lilstock Beach (see location in Fig. 3.11a, adaptation from Rawnsley et al. 1998). The locations of photos in Fig. 3.13 are indicated (modified from Engelder and Peacock 2001)

The latter study focuses on the south-dipping beds at Lilstock (Fig. 3.11c), which these authors regard as particularly informative. These two papers, particularly the one by Engelder and Peacock (2001), are quoted extensively in the present section.

The Blue Lias Formation of Lilstock Beach consists of more than 50 limestone beds, 5–40 cm thick (Whittaker and Green 1983), interlayered with shales that range from a few centimeters in thickness to over 300 cm. The order of layers is consistent and can be followed even in separate fault blocks (Engelder and Peacock 2001). According to Rawnsley et al. (1998) (Fig. 3.11a), the BCB is an exhumed E-W-trending Mesozoic basin. Basin formation started as early as the Permian, with N-S extension causing reactivation of south-dipping Variscan thrusts (Van Hoorn 1987; Brooks et al. 1988; Roberts 1989). Extension and subsidence continued through the Triassic and Jurassic. To this stage belong E-W-striking normal faults and calcite veins, which are well exposed on the Somerset coast (Peacock and Sanderson 1991, 1992, 1994). Evidence for Alpine N-S contraction on the Somerset coast includes E-W-striking thrusts and reactivated normal faults (Peacock and Sanderson 1992; Dart et al. 1995) and strike-slip faults which conjugate about N-S (Peacock and Sanderson 1992, 1995). E-W-trending folds are related to wall-rock deformation around the E-W-striking normal faults and were probably tightened during the N-S Alpine compression. NNW-striking faults, e.g., the Sticklepath fault zone, appear to belong to the Variscan phase and may have been active at various times (Holloway and Chadwick 1986; Lake and Karner 1987; Van Hoorn 1987; Roberts 1989). Sinistral displacement occurred on these faults during the early Tertiary, so σ_1 was approximately NW-SE across the BCB at that time (Van Hoorn 1987). Dextral displacement occurred during the late Oligocene to Miocene (Arthur 1989), so σ_1 was approximately N-S across the BCB (Van Hoorn 1987).

Rawnsley et al. (1998) found that the joint patterns at the four edge locations in the BCB all post-date the high-density veins (HDVs) and the faults. The joints appear to have been formed in five main phases:

Phase 1: These are sub-parallel to a regional Alpine compression direction (about 340–350°) and are almost unperturbed by faults. At Nash Point, faulting started to perturb the stress during the development of phase 1 joints, i.e., there is a transition from phase 1 to phase 2 joints. Phase 1 joints were reactivated after phase 3 at Lavernock.

Phase 2: These are joints that were perturbed by faults and by phase 1 joints. The phase 2 joints follow the perturbed stress trajectories and curve from points of stress concentration along fault surfaces, e.g., at fault bends. The transition from non-perturbed (phase 1) to perturbed (phase 2) joints reflects a decrease in the regional compression and an increase in residual tensile stress. Joints of this phase are absent where no faults are present, as at Lavernock.

Phase 3: At Lavernock and Lilstock, phases 1 and 2 seem to have left no traces, and the only joint set found there belongs to phase 3, which is parallel to the 290° striking fold axes. These joints cut the veins that formed during folding and result from the relaxation of the Alpine compressional stresses within the folds. Phase 3 joints typically rotated counter clockwise through time to become parallel to the fold axes, perhaps as a result of diminishing the regional influence. This phase is absent where there are no folds, as at Nash Point.

Phase 4: This phase consists of cross-joints.

Phase 5: This phase consists of polygonal joint patterns. Phases 4 and 5 occur at all the locations studied. They are related to relaxation or contraction of the rock at a late stage. Rawnsley et al. (1998) show that their model applies well to the Liassic exposures around the basin's edge, although different patterns may be found in the unexposed center of the BCB. Such may be the case for a different orientation of joints linked to the regional Alpine compression, which e.g., at Lavernock are 010–020° (Rawnsley et al. (1998, Fig. 7a).

Engelder and Peacock (2001) assume that the present-day lithospheric stress field in the NW European platform has the same orientation as the Alpine stress field of the Miocene (Brereton and Evans 1987; Zoback 1992). Furthermore, the youngest joint set recorded throughout southern England correlates with the contemporary tectonic stress field (Bevan and Hancock 1986; Hancock and Engelder 1989). Hancock and Engelder (1989) argue that exhumation in a late-stage "Alpine" stress field is responsible for these youngest NW-striking joints in northwestern Europe. Thus, the post-Miocene tectonic event caused a clockwise rotation of the European stress field, only to have it return to its "Alpine" orientation, as is testified by the latest jointing in northwestern Europe.

Engelder and Peacock (2001) emphasize that the Alpine deformation, or "Alpine inversion", was accommodated by reverse-reactivation of normal faults, new thrust faults, new strike-slip faults, and by hanging wall buttress anticlines. Beck et al. (1993) define the "buttress effect" as resistance to displacement arising from a space problem; a body of rock can move only if it has somewhere to go. Buttress folds of Eocene to Oligocene age show a parallel geometry that is produced by flexural flow with bed-parallel slip (Nemcok et al. 1995). It should be noted that reverse faulting was more prevalent along the southern margin of the Bristol Channel Basin than on the north margin (Nemcok et al. 1995). Only one case of minor thrust faults associated with folding was found along the north margin in the southern limb of the Trwyn-y-Witch anticline in south Wales (Roberts 1974).

3.2.2 Fracture Description

Following are some fracture descriptions according to Rawnsley et al. (1998), specializing on phenomena that are less common in other provinces, including high-density veins, perturbations of joints near faults, "ladder" patterns and polygonal joints.

High density veins (HDV). Thin, closely-spaced calcite veins appear to be present everywhere in the limestone beds at Lilstock. In the east they mostly strike 270–290°, their common width is about 0.08 mm, and average spacing is less than 10 mm. They are often only visible where differential erosion has enhanced the contrast between the calcite HDVs and the limestone country rock, especially around the edges of joints. In thin sections they can be seen to persist throughout the rock, often forming *en echelon* patterns. HDVs either pass through the fault-related calcite veins or are slightly deviated by them. The HDVs are not perturbed by joints, and some joints may follow HDVs. In the west of the area, the HDVs strike 082–088° and have an average spacing

of about 20 cm. Most of the calcite has been removed, with oxidization fronts about 30 mm wide. In the cliff, the HDVs strike about 110° and dip about 80° more steeply to the north than the bedding. HDVs strike 350–010° at Nash Point, which is the approximate Alpine compression direction. These are followed by 350–010° striking faults. The 010° faults appear to be dextral and the 350° faults appear to be sinistral, so they are conjugate about N-S. Thus, the HDVs represent a pre-joint phase that possibly was associated with faulting that accompanied the Alpine compression.

Converging joints perturbed by the faults. At least three main zones of converging joints occur along the 065° striking section of fault F5 at Lilstock (see also Swaby and Rawnsley 1997, Fig. 6). They are elongated in the 320–360° range. Joint spacing decreases slightly towards the center of the convergence as the joints curve towards the fault (Fig. 3.12a). These converging joints are the longest at Lilstock. For a detailed description, see Rawnsley et al. (1992). According to Engelder and Peacock (2001) the most plausible interpretation of the perturbed joints is that limestone-limestone contact across the fault generated a local stress field during or after the period of high-angle reverse faulting on reactivated normal faults, i.e., joint propagation followed fault initiation but not necessarily total slip. Curved trajectories of phase 2 joints in proximity to phase 1 joints are interpreted by Engelder and Peacock to mean that phase 1 joints were open and also perturbed the stress field during stage 2 joint propagation (Dyer 1988; Rawnsley et al. 1992, 1998).

Ladder joint patterns. "Ladder" patterns occur at Nash Point and at Lilstock. The joint pattern at Nash Point varies across the area. In the east, the main set strikes 155–160°. There is a two-level hierarchy, with 160° joints connected by orthogonal joints to form a "ladder" pattern that crosses layer boundaries. Within these ladders, shorter 160° joints and non-cross-cutting orthogonal joints form a smaller-scale system of ladders (Fig. 3.12b), which mostly do not cross bedding boundaries. Oblique ladders occur at Lilstock over a 095–135° range in all limestone beds within about 30 m of fault F3 (Loosveld and Franssen 1992). They usually rotate counter clockwise with time (i.e., 135° joints are the oldest and 095° joints are the youngest), forming oblique ladders. Left-stepping arrays spaced about 15 m trend 160–170° between two zones of convergent joints. Multidirectional joints also occur between zones of convergent joints and may be formed over extensive areas. Limestones appear to be more jointed than the shales. Joints often pass from the limestones into the shales, suggesting that they initiated in the limestones.

Polygonal joints. These enigmatic joints are found throughout the BCB, typically surrounding blocks. They are believed to indicate horizontally isotropic effective tension. On the other hand, they may represent thermal contraction following uplift, which may also be responsible for non-cross-cutting perpendicular joints between closely-spaced joints. The latest, isotropic joints, are related to biaxial effective tension in the plane of bedding, especially in "shadow zones" between convergence points. Between the convergent zones, an almost isotropic joint pattern was produced by a low horizontal differential stress. Impedance of later joints on earlier joints indicates that the latter were always open. Deciphering the origin of these joints remains a challenge.

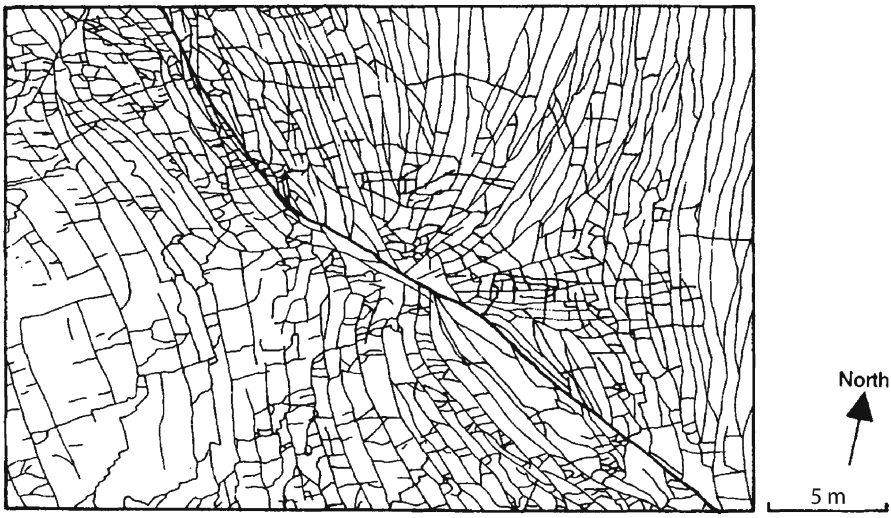

Fig. 3.12a. Line drawing of fracture patterns at Nash Point (see Fig. 3.11a). Perturbations in joints (modified from Rawnsley et al. 1998)

Fig. 3.12b.
Line drawing of fracture patterns at Nash Point (see Fig. 3.11a). Joints displaying a ladder pattern of joints (modified from Rawnsley et al. 1998), note a certain resemblance to cross-joints (Gross 1993)

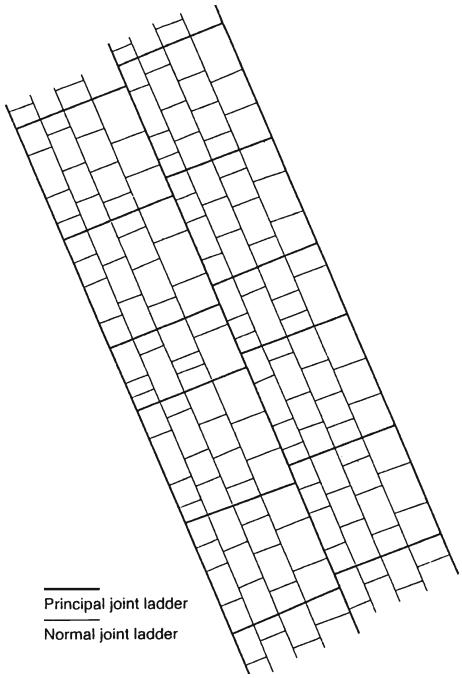

Engelder and Peacock (2001) note that at Lilstock Beach joints within limestone beds are generally contained within these beds and rarely pass into adjacent shales. They also note that patterns of systematic jointing differ from one limestone bed to

the next, which explains the different descriptions of the joint sets at Lilstock Beach in earlier studies. All that can be said about the sequence of jointing at Lilstock Beach is that the joints postdate early normal faulting and vein development. Commonly, joints propagate after normal fault development, as is indicated by abutting and cutting relationships (e.g., Fig. 3.13d,e). Some curving joints radiate from points of stress concentration on faults (e.g., Fig. 3.13c), which are a natural consequence of slip on an irregular fault. These joints could have propagated during a later stage of slip (Engelder and Peacock 2001). By way of comparison, perturbed curving joints that are associated with the Naim fault in the Beer Sheva syncline were formed under a secondary stress field, after cessation of movement along the primary strike-slip fault (Sect. 6.6).

Faults and folds. The structures on Lilstock Beach include a set of four north-dipping, high-angle faults that are offset by later strike-slip faults (Fig. 3.11c). Engelder and Peacock (2001) divided Lilstock Beach using three of these high-angle faults (faults 3, 4, and 5 of Rawnsley et al. 1998) and two strike-slip faults. The area north of fault 5 is called block 5 (or "the bench", in recognition of Loosveld and Franssen's (1992) mapping there). The other three blocks are hanging walls to faults 4, 3 and 1. Engelder and Peacock (2001) refer to the eastern, central, and western portion of each "normal" fault block, depending on outcrop position relative to two prominent strike-slip faults (Fig. 3.11c).

Engelder and Peacock found that separation at any point on the faults can be measured with confidence by juxtaposition of bedding (Fig. 3.11c). Throw on at least one of the high angle faults (fault 4) was reversed during Alpine inversion. Reverse slip may have occurred on the other faults, but the total throw was not reversed. The steep dip of fault 4 and its parallelism with normal faults in the area indicate that it originated as a normal fault, which inversed together with the other reverse faults in the region (e.g., Whittaker and Green 1983; Dart et al. 1995). Net throw (the combination of pre-Alpine normal slip and Alpine reverse slip) on the four faults with throw >2 m is: Fault 1 ~ 18.7 m (normal), fault 2 ~ 8 m (normal), fault 4 ~ 8 m (reverse), and fault 5 ~ 14 m (normal). The outcrop is also cut by numerous high-angle faults with <2 m throw, which mostly exhibit normal slip and are parallel to the strike of bedding. Strike-slip faults displace the high-angle faults and the limbs of the Lilstock buttress anticline. The strike-slip faults are cut off at fault 4 (Fig. 3.11c), indicating that strike-slip faulting and some high-angle faulting may have been contemporaneous (Kelly et al. 1998).

Block 4 consists of a large buttress fold, the Lilstock buttress anticline, with a gently dipping north limb and relatively steep south-dipping beds (Fig. 3.13a,b). The Lilstock buttress anticline originated as a reverse-drag fold (Hamblin 1965) during the Mesozoic normal faulting and was tightened during reverse slip on fault 4. Engelder and Peacock focused their study on joints in the south-dipping limb of this anticline. Beds in the northern half of block 4 dip gently to the north (<5°), whereas beds in the southern half of the outcrop dip to the south, and in places the dip is more than 30°. Along the south side of the Bristol Channel, dips of more than 30° are restricted to the flanks of buttress anticlines. Diagrams of the tight folding typical of buttress folds in the Mesozoic strata of the Somerset coast are presented in Peacock and Sanderson (1992, Fig. 7a) and Dart et al. (1995).

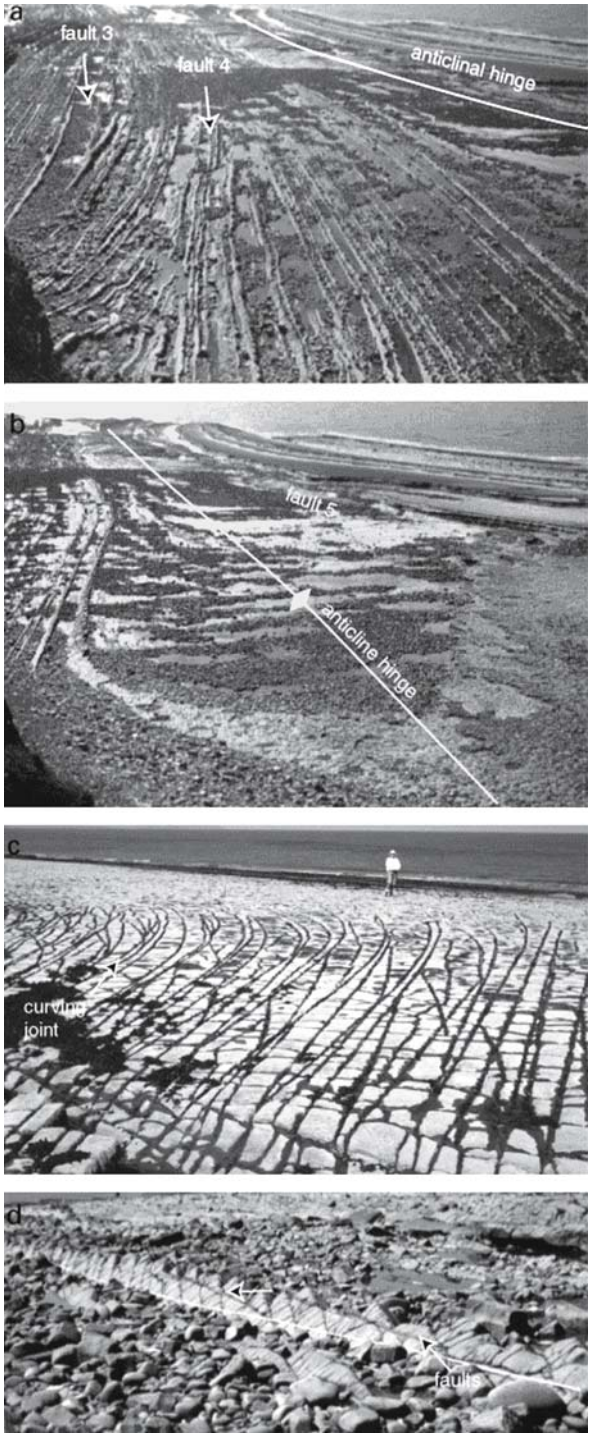

Fig. 3.13a–d. Outcrops from Lilstock. **a** View looking NNW from the eastern cliff along faults 3 and 4 with the hinge of the buttress anticline shown in the background. **b** View looking NNW from the eastern cliff along the hinge of the Lilstock buttress anticline. Bed 0497 is visible in the foreground. A control sample from bed 0497 was taken across the hinge of the anticline and Fig. 3.13h was taken at the point where bed 0497 rolls over into the limb of the anticline. **c** Curving joints in bed 1848 of fault block five. Photographer is standing on fault 5 (location shown in Fig. 3.11c). **d** J2 joints cutting two normal faults within bed 2429 of fault block 1 (from Engelder and Peacock 2001)

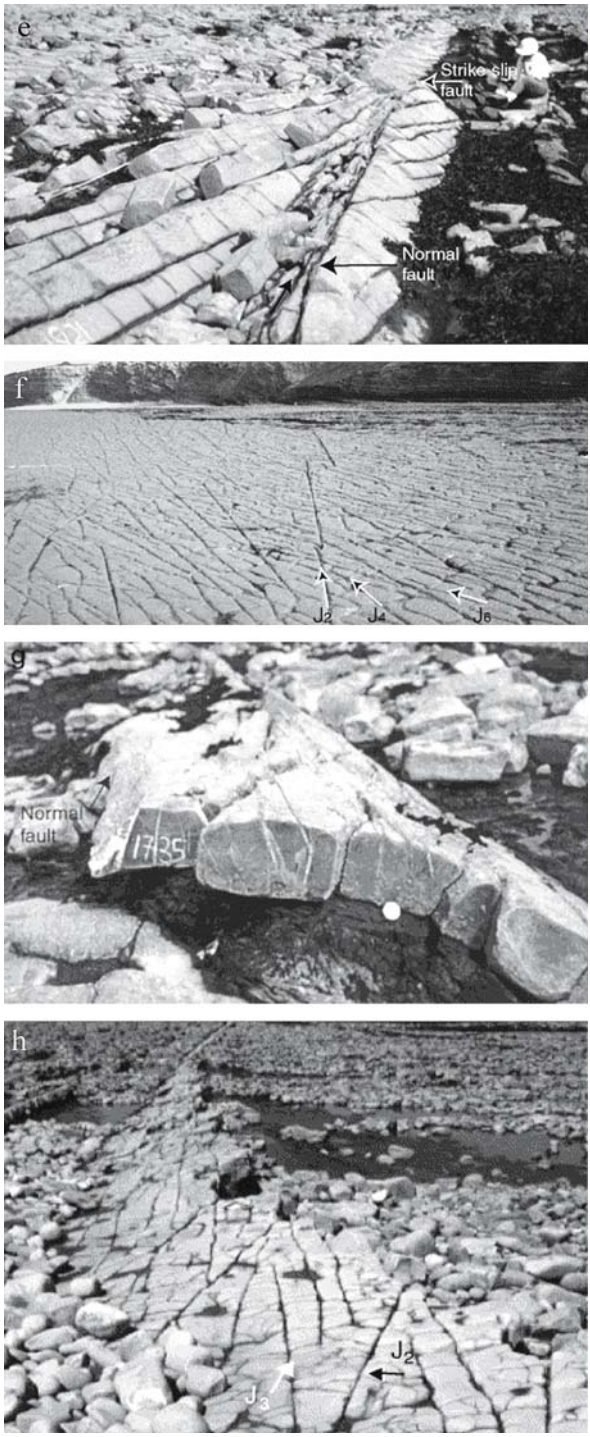

Fig. 3.13e–h.
Outcrops from Lilstock. **e** J3 joints abutting a small (throw <1 m) normal fault in bed 1921 in the western portion of fault block three. A sinistral strike-slip fault offsets bed 1921 (in the foreground) by 2 m. That fault is internal to the western portion of fault block 3. **f** Joint set development within bed 1848 on the bench north of fault 5. Joint set J2 is parallel to the direction of view. Sets J4 and J5 are oriented anticlockwise from set J2, with J6, anticlockwise from J4. The view is looking south-east toward the cliff from where the photographs for Fig. 3.13a,b were taken. View across the bottom of the photograph is about 3 m. **g** J3 joints cutting veins and transecting beds dipping in a relay ramp developed during early extension in the western portion of fault block 3 (coin diameter = 27 mm). **h** The counter clockwise relationship between J2 and J3 in bed 0497 where it rolls over into the south limb of the anticline (from Engelder and Peacock 2001)

3.2.3
Data Collection and Joint Identification

Engelder and Peacock (2001) studied joint development in 25 out of 46 carbonate beds in a 40 m thick Liassic section (British Geological Survey stratigraphic column, Whittaker and Green 1983) (Fig. 3.14). To indicate position in the vertical section, they labeled beds by height (in cm) above an arbitrary datum. For example, bed 1848, 18.48 m above the datum features prominently in the studies of Loosveld and Franssen (1992) and Rawnsley et al. (1998). Engelder and Peacock sampled systematic joints at Lilstock Beach in a volume of Blue Lias measuring 40 m thick by 200 m long (E-W). The repetition of the section by high angle faults permitted sampling up to 50 m along the N-S direction of some beds. Focusing on the effect of Alpine inversion on joint development, they assumed that joints of this stage are likely to be found in the south-dipping limb of the Lilstock buttress anticline in block 4, since the relatively steep dip of these beds indicate they are the most strained rocks at Lilstock Beach. To confirm

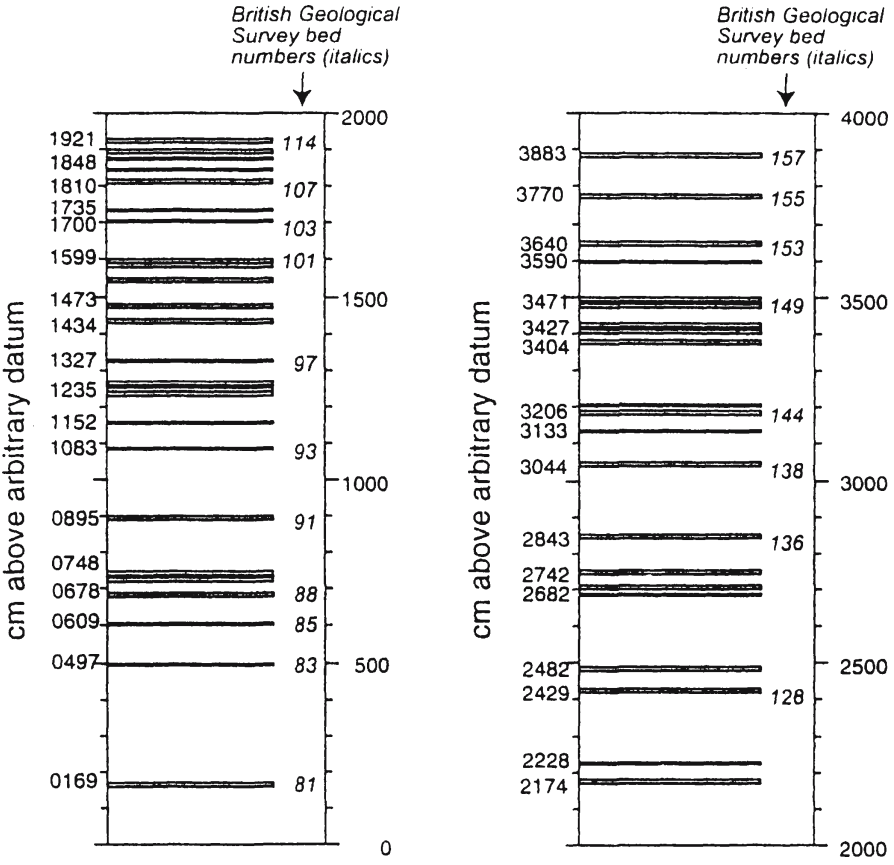

Fig. 3.14. Stratigraphic section at Lilstock Beach showing the position of 46 carbonate beds above an arbitrary datum. The beds are labeled according to their position relative to the datum. The British Geological Survey (Whittaker and Green 1983) designation for each bed is also given (from Engelder and Peacock 2001)

this, they measured the joint patterns on sub-horizontal surfaces in block 5 as well as in the hinge area of the Lilstock buttress anticline of block 4, to serve as control samples. The joint patterns in dipping and sub-horizontal limestone beds were compared. Standard scan line techniques (LaPointe and Hudson 1985) were then used to record the location and orientation of each systematic joint. The joint sets in each bed, based on abutting and orientation characteristics, were then correlated from bed to bed by means of subsequent data reduction. The most subjective assignments concerned curving joints that on the base of orientation might be included in more than one set.

A collection of parallel systematic joints counts as a set (Hodgson 1961b). According to Engelder and Peacock (2001), however, the poles to joints of a systematic set may cluster through several degrees, because individual joints are never perfectly planar and measurements cannot be precise (Fig. 3.15). Therefore, joint sets that differ by less than 10° may have overlapping clusters in a stereographic plot, and not each individual joint can be assigned to a particular set even by post-fieldwork analysis. Hence, Engelder and Peacock rely on field notes, where joints were presorted into sets

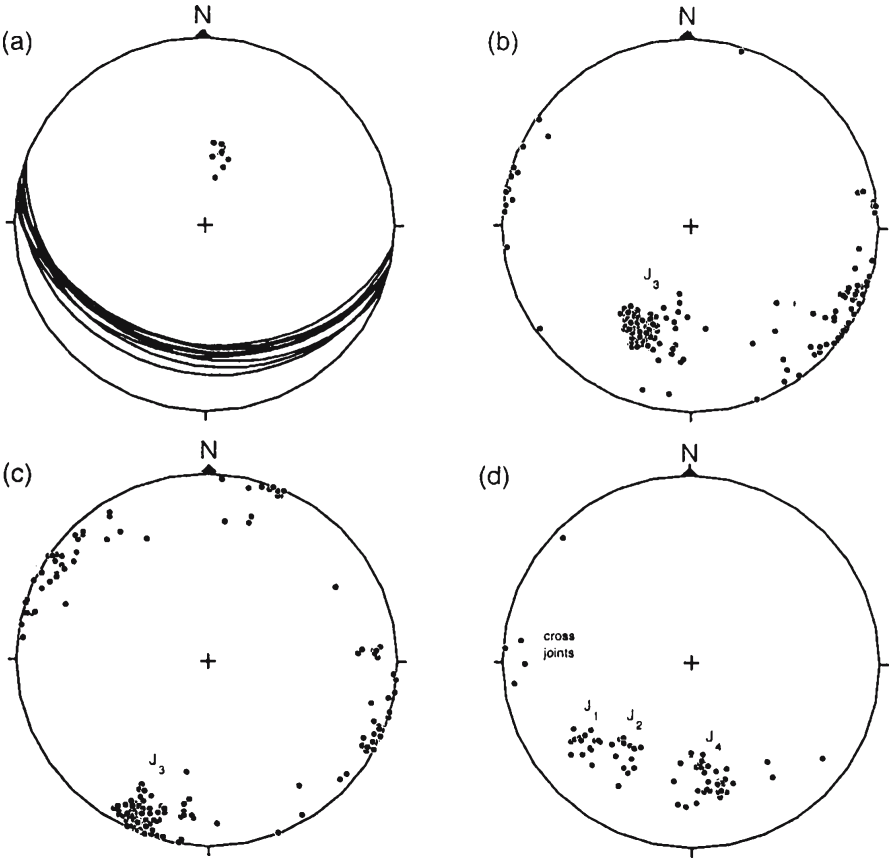

Fig. 3.15. Lower hemisphere stereographic projections for beds and joints in fault block 1. **a** Bedding traces and poles for bed 2429. **b** Present-day poles to joints in bed 2429. **c** Poles to joints in bed 2429 with bed dip removed. **d** Present-day poles to joints in bed 3883 (from Engelder and Peacock 2001)

within each particular bed. The grouping of joints into distinct sets was most difficult where several beds are involved and where joint sets tend to curve, as they do in the south-dipping limbs near the faults of Lilstock Beach. In these cases the control samples (see above) served as a guide. Using this procedure, six joint sets were distinguished, falling in the following ranges: J1, (330–310°), J2 (310–295°), J3 (295–285°), J4 (285–275°), J5 (275–265°), and J6 (<265°)(where 265° is equivalent to 085° in the upper hemisphere). It should be noted that joint distribution in the western part of the BCB differs somewhat from the findings in England. Between Mumbles Head and Rhossilli Bay in south Wales, Roberts (1979) found six sets striking 360°, 340°, 290°, 270°, 240°, and 200°, as perhaps can be expected over such distances and changes in the regional structure. The challenge to the investigator is how to sieve out homogeneous domains from a heterogeneous province for deciphering the tectonic history of the region.

Engelder and Peacock (2001) used a simplified AVTD plot (see Wise and McCrory 1982) for obtaining a qualitative sense of relative joint density by normalizing the data on joint occurrence and comparing joint development in sub horizontal beds with beds that have been tilted by Alpine inversion. This procedure is not given here, and the interested reader is referred to the original paper.

3.2.4
Joint Sets in the Blue Lias

3.2.4.1
Joint Sets in Steeply-Dipping Beds

Joints in the south-dipping limb of the Lilstock buttress anticline dip to the north as expected for beds that dip to the south (Fig. 3.15a–d). These commonly carry more than one joint set, but no beds carry as many sets as found in bed 1848 of fault block 5 (Fig. 3.16a). To correlate joints in the south-dipping limb with the control sample, Engelder and Peacock (2001) rotated joints to their attitude in horizontal bedding. After rotation, the joint-frequency data for steeply-tilted beds were normalized in the same manner as for sub-horizontal beds. The population of joint orientations in the south-dipping beds of Lilstock Beach is indeed different from the population in the sub-horizontal beds. The most prominent joint set in the south-dipping beds, J3, is nearly parallel to the strike of bedding and the hinge of the Lilstock buttress anticline.

3.2.4.2
The Orientations of Joints as Related to Faults

Joints of set J3 (strike 290°) transect the fold and veins in a relay ramp in the western portion of fault block 3 (in bed 1735) (Fig. 3.13g). This relay ramp is evidence that J3 joints post date the early extension of the Bristol Channel. Various relationships between J3 joints and normal faults are observed at Lilstock Beach. For example, some J3 joints cut through incipient high-angle faults without being displaced by them (Fig. 3.13d). Other J3 joints abut high-angle faults without appreciable deflection (Fig. 3.13e). Both types of fault are early calcite-filled normal faults with no evidence of reverse reactivation during Alpine contraction. This is like the relay ramp in bed 1735.

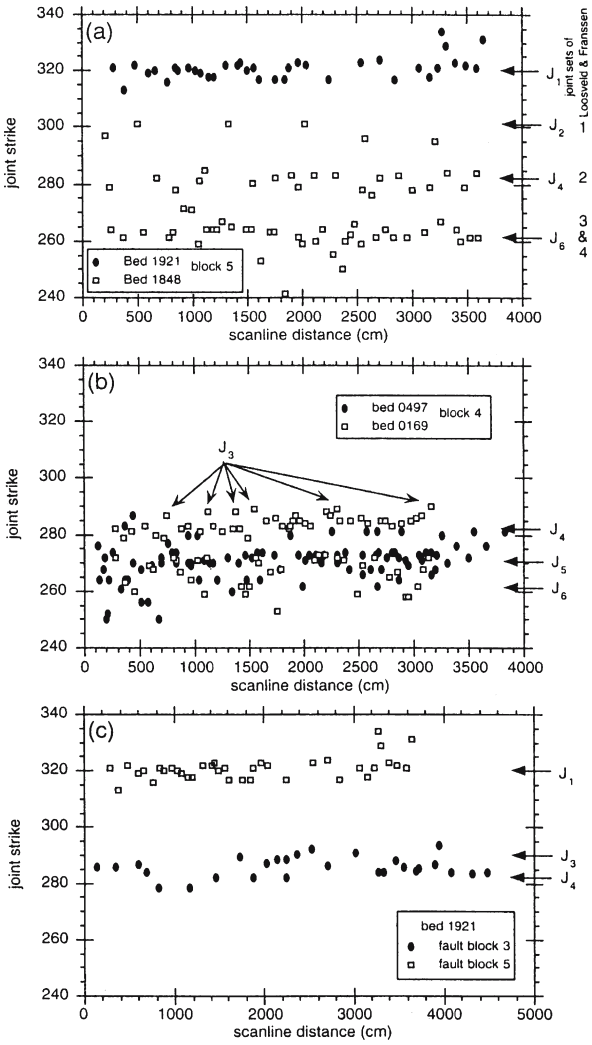

Fig. 3.16.
a Joint strike vs. distance for a scan line corrected to a scan line azimuth of 040° for beds 1848 and 1921 on the bench north of fault 5. **b** Joint strike vs. distance for a scan line azimuth of 044° for beds 0169 and 0497 in eastern fault block 4. **c** Joint strike vs. distance for bed 1921 for a scan line azimuth of 040° for the bench north of fault 5 and 110° in fault block 3 (from Engelder and Peacock 2001)

The orientation of the joint population varies from fault block to fault block. For example, bed 1921 in western block 3 dips up to 43° to the south compared with its slight northward dip in the bench of block 5. Within western block 3, J3 and J4 appear without J1, which is the only set in bed 1921 on the bench (Fig. 3.16c). This example is typical of the difference in joint patterns within the same bed from block to block. Engelder and Peacock (2001) conclude from these frequent differences that jointing took place after beds became isolated within individual fault blocks following at least some fault displacement. The widespread occurrence of systematic joint sets within fault blocks suggests that the internal portions of fault blocks were not affected by stress reorientation during fault slip. They also suggest that, alternatively, these differences mean that different mechanisms operated in the south-dipping limb of the Lilstock buttress anticline and in the sub-horizontal beds.

3.2.4.3
The Sequence of Joint Development

The abutting sequence within sub-horizontal bed 1848 indicates that J2 propagated before J4, which propagated before J6 (Fig. 3.13f). Assuming that joints are created parallel to regional S_{Hmax} directions, this sequence shows the same counter clockwise reorientation of the remote stress field as seen throughout the eastern part of the Bristol Channel (Rawnsley et al. 1998). The same counter clockwise sequence may be traced from the sub horizontal bed 0497, from block 4 into the south-dipping limb of the Lilstock buttress anticline (Fig. 3.13h). This is a rare case of J3 joints abutting joints of J2. Where bed 0497 steepens, J2 is absent and J4 abuts J3. Another case of this counter clockwise joint formation is found in bed 3883, which dips up to 30° in the central and western parts of fault block 1 (Fig. 3.15d). Other beds also show a clear counter clockwise age sequence, although this is found in other joint sets (Table 3.1).

Table 3.1. Joint development: All stations in south limb of buttress anticline

Bed	BGS Beds	Fault block	J1	J2	J3	J4	J5	Sequence[a]
4074	161	1	×					
4005	159	1	×	×				CCW
3883	157	1	×	×			×	CCW
3770	155	1				×		
3590	151	1	×					
3492	149	1	×				×	Separate
3427	147	1	×	×				CCW
3206	144	1				×		
3185	142	3				×		
3133BC	140	1			×		×	Separate
3133A	140	3		×				
3044	138	3			×			
2742D	134	3			×			
2742ABC	134	1			×	×		CCW
2429B	126	4			×		×	CCW
2429AC	126	1		× or	×			Separate
2228	121–123	4		×				
1921A	114	3			×	×		Separate
1848E	109	3		×				
1848CD	109	3			×		×	Separate
1848A	109	4			×		×	CCW
1735C	105	3			×			
1735AB	105	4		×			×	Separate
1700	103	3				×		
1599AB	101	4		×				
1152	95	4					×	
0678	88	4			×		×	Separate
0609	85	4					×	
0497D	83	4				×	×	Separate
0497B	83	4			×		×	CCW

[a] CCW–joints that abut with an counter clockwise sense of development.
Separate–joints that have developed in separate regions of a bed (from Engelder and Peacock 2001).

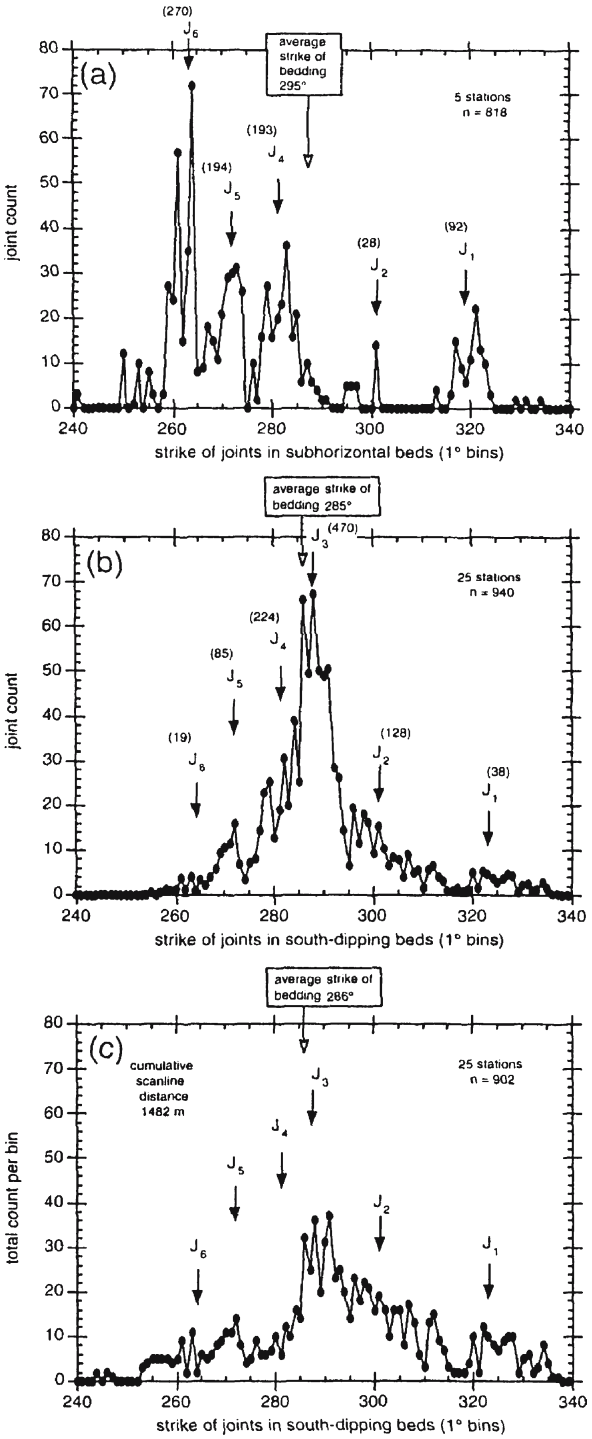

Fig. 3.17.
Joint frequency vs. joint strike. Joint count normalized to a 250 m scan line with the data binned into 1° intervals. **a** Subhorizontal beds in blocks 4 and 5. **b** Dipping beds of the Lilstock buttress anticline, in blocks 1, 3 and 4. **c** Binned data without normalizing joint data for either scan line length or scan line orientation, in blocks 1, 3 and 4 (from Engelder and Peacock 2001)

The counter clockwise age sequence found in south-dipping beds is more clearly observed on sub-horizontal surfaces (Table 3.1). Determination of sequence requires two or more joint sets abutting at a station, but most exposures are too small to display the required joint contacts (e.g., Fig. 3.13d,e,h), although beds may contain two groups of joints with different orientations on different parts of the exposed bedding surface along strike. In such cases, it is difficult to determine whether the groups belong to different sets or whether they belong to a single curving set, as is seen near faults. More than half the samples from the south-dipping beds display only one set (Fig. 3.17), showing no time sequence. As a rule, beds containing J1 or J2 joints lack J3 joints. Where J3 joints are found, they are the oldest joints and strike closest to bedding strike (Table 3.1). Thus, the evidence for the age of J3 relative to J1 and J2 is rather too meager to be definitive.

The distribution of joints in the south-dipping limb of the Lilstock buttress anticline is also correlative to stratigraphic and structural position. J1 and J2 joints (found only in block 1) are high in the section. Sets J3 and J4 are most common in the middle of the section (blocks 3 and 4), with the greatest development of J3 joints near the reverse fault that created the Lilstock buttress anticline. J5 and J6 joints are commonest in the lower parts of the section and nearest the anticline-hinge, where dips are shallow.

3.2.4.4
The Attitude of Joints in Relation to Bedding

Joints in competent beds are typically perpendicular to the bedding (Hancock 1985). However, this is not the case for sets J1 to J5 in the south-dipping beds of the Lilstock buttress anticline. When bedding is restored to the horizontal (e.g., J3 joints in Fig. 3.15c), these joints consistently dip to the north, with their poles plunging south, towards the European Alpine hinterland. The joint-pole plunge angle is used to define the "tilt towards the hinterland" for the joint sets (Fig. 3.18). The tilt increases from 3° for the older J1 joints to 7° for younger J5 joints. J3 joints occur only in the south-dipping limb of the anticline, and are therefore of particular interest for interpreting the geometry and mechanics of fold and joint development; their geometric characteristics are used as a guide in the search for a cause of joint tilt.

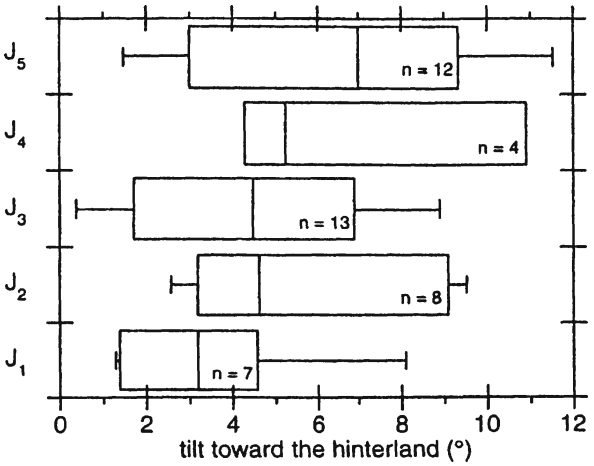

Fig. 3.18.
Box plot for the tilt of the vector mean pole to joints from 44 joint populations in south-dipping beds of the Lilstock buttress anticline. The tilt is measured downward in the direction of the hinterland (i.e., southern Europe) relative to bedding when it is restored to horizontal. The *center line* of each box represents the 50th percentile of the data while the left and right edges of the boxes represent the 25th and 75th percentile of the data, respectively (from Engelder and Peacock 2001)

3.2.5
Stresses in the South-Dipping Limestone Beds during Alpine Inversion

3.2.5.1
J3 Joints in the Lilstock Buttress Anticline

According to Engelder and Peacock (2001), the J3 joints in the south-dipping beds at Lilstock Beach were formed during the development of the Lilstock buttress anticline, reflecting Alpine inversion. They base this conclusion on six observations:

1. J3 joints are rare in the sub-horizontal beds of Lilstock Beach but are the most common set in the steep limb of the Lilstock buttress anticline. The mechanism driving J3 jointing must involve higher strain on the limbs of folds and little strain in the hinge area.
2. J3 joints are most common in the vicinity of fault 4, which was reversed to form the Lilstock buttress anticline. This spatial association suggests that the formation of set J3 with a high-angle reverse fault was synchronous with Alpine inversion.
3. Poles to joints in the southern limb of the Lilstock buttress anticline consistently plunge toward the hinterland, their azimuth parallel to the inferred direction of compression (019°) during Alpine inversion (Kelly et al. 1998). The consistent relation of tilt to bedding suggests that joints developed by shear couple on bedding.
4. The strike of J3 joints is nearly parallel to the strike of beds in the south-dipping limb of the anticline. Strike-parallel joints are commonly associated with outer-arc extension by bending of beds during folding (e.g., Van Hise 1896; Hancock 1985) (Fig. 3.19a), but outer-arc extension by tangential longitudinal strain folding is greater in the hinge area and absent at inflection points in the limbs (Price and Cosgrove 1990).
5. J3 joints cut completely through beds and thus differ from joints that form by outer-arc extension above a neutral fiber (Van Hise 1896).
6. J3 joints are not present in beds with J1 or J2 joints, and vice versa (Table 3.1). Whatever mechanism was responsible for J3, it is clear that they propagated neither in sub-horizontal beds, nor in previously jointed beds.

Alpine inversion was driven by a remote S_{Hmax} directed about 019° (Kelly et al. 1998). This presents a mechanical paradox if J3 joints propagated during parallel folding, because they opened in a direction that nearly coincides with that of S_{Hmax}. If controlled by the remote stress, J3 joints would open in a plane that contains S_{Hmax}. Engelder and Peacock (2001) therefore suggested that the opening must be controlled by a local stress. Accordingly, they sought a set of boundary conditions that generate a local tensile stress on the limestone-shale package when a regional compressive stress is superimposed of the Lilstock buttress anticline.

To understand the tilt of joints in the south-dipping beds of the Lilstock buttress anticline and their ability to open sub-perpendicular to S_{Hmax}, Engelder and Peacock apply a simple finite element model, which involves the development of a shear couple on limestone beds during parallel folding by flexural flow of the shale interlayers. If there indeed is a genetic relationship between the orientation of J3 joints and the shear couple on limestone beds, the model proposes a possible orientation for S_{Hmax} that fits these boundary conditions. To anticipate their result, remote S_{Hmax} controlling J3 joints should be the same direction as the remote S_{Hmax} that caused the conjugate strike-slip faults during Alpine inversion.

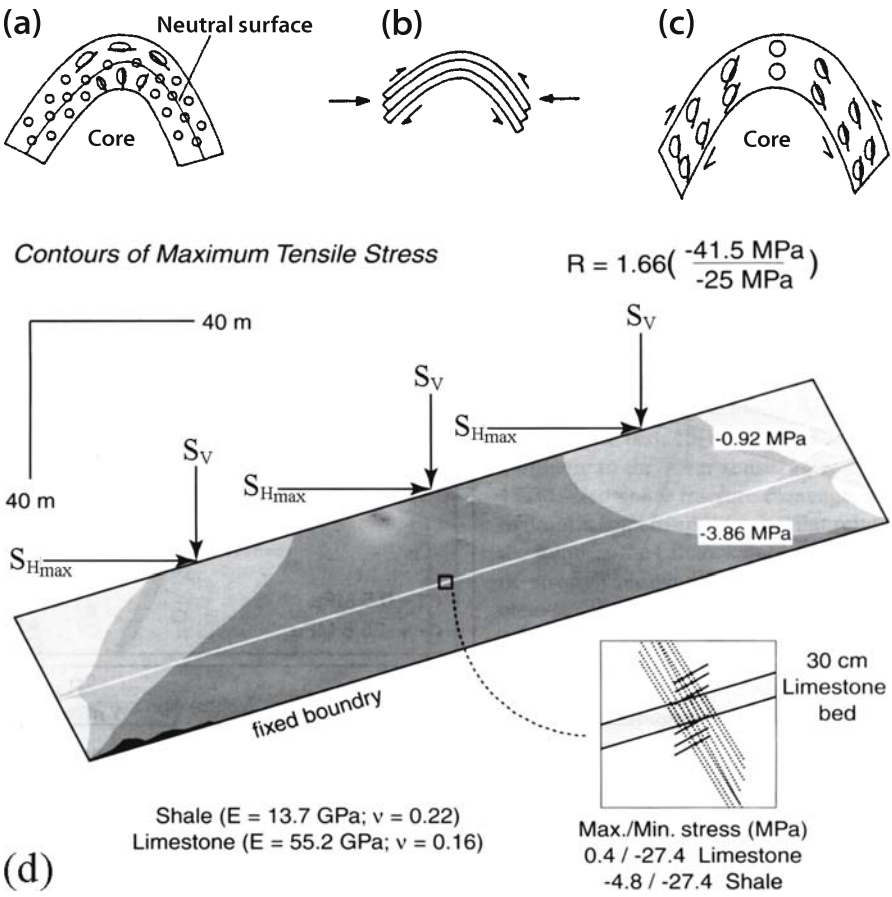

Fig. 3.19. Fold mechanisms. **a** Outer-arc (buckling or tangential longitudinal strain), showing outer-arc stretch, inner-arc contraction and no distortion on limbs. **b** Flexural slip, successive layers are displaced upwards towards the anticline crest with respect to the layer below. Individual layers are unstrained. **c** Flexural flow or flexural shear, showing no shear on hinge and shear within beds on the limbs (Fig. 3.19a–c from Park 1983, p. 72). **d** A three-bed model of the limb of the Lilstock buttress anticline contoured for σ_3 (compressive stress is negative). The top surface is loaded as indicated with the bottom boundary fixed and the left and right boundaries free to shear. The thin middle bed is a 30 cm limestone with elastic properties as indicated. In close-up inset the orientation of the local principal stresses are indicated with $\sigma_1 = -27.4$ MPa and $\sigma_3 = 0.4$ MPa (limestone), and $\sigma_3 = -4.8$ MPa (shale). Tensile stress is indicated by a *solid line* and compressive stress is indicated by a *dashed line* (after Engelder and Peacock 2001)

3.2.5.2
Stress Configuration in Limestone Beds of the Lilstock Buttress Anticline during its Development as a Flexural-Flow Fold

According to Engelder and Peacock (2001), the Lilstock buttress anticline, a sequence of interbedded limestones and shales, should display a significant contrast between the elastic properties of the limestone and shale (e.g., Hatheway and Kiersch 1982).

This lithological pair is commonly associated with flexural slip folding (Fig. 3.19b) in which the more brittle limestone beds slip on ductile shale interlayers (e.g., Ramsay and Huber 1987). Displacement also occurs by layer-parallel shearing of the shale during flexural-flow folding (Fig. 3.19c) (flexural flow is also termed flexural shear, e.g., Twiss and Moores 1992, Fig. 12.7). Often, the shale interlayers are thin as compared to the carbonate beds, but at Lilstock the opposite is the case. Engelder and Peacock suspect that thick shale layers obscure all evidence for slip by simple shear strain within the shale, if present, largely because the shear strain could be relatively small and because such strain markers as stretched ammonites are rare. Nevertheless, the regional S_{Hmax} that tilted the beds of the anticline induced a shear couple in them (assuming for simplicity that S_{Hmax} and S_v are principal stresses). This assumption of a remote horizontal principal stress is supported by horizontal slip on the conjugate strike-slip faults active during Alpine inversion and by slickenside lineation orientations on the inverted normal faults (Kelly et al. 1998).

Engelder and Peacock (2001) mapped the stress fields induced in an elastic medium under loading configurations consistent with a shear couple developed during layer-parallel shear, applying 2D finite element analyses, using the interactive fracture analysis program FRANC (Wawrzynek and Ingraffea 1987). They used a model mesh of quadratic, isoparametric elements (Fig. 3.19d) applying boundary conditions to simulate a three-layer model of a limestone bed of the Blue Lias between two shale layers. Figure 3.19d shows a contour map of the maximum tensile stress (i.e., σ_3 with tensile stress positive) generated in beds dipping at 17° and subject to a stress ratio (i.e., $R = S_{Hmax} / S_v$) of 1.66. Their model has a length to height ratio of 5, which is sufficient to carry end conditions away from the central part of the model, which portrays a 3 m^2, centrally situated square element. The initial versions show that the elastic contrast between the limestone and shale beds leads to a tensile σ_3 within the limestone layers for values of R between one and four and $\nu_{sh} > \nu_{ls}$ (Poisson ratios of shale and limestone, respectively). Tensile stress is generated via the flexural flow as permitted under the tractions specified in Fig. 3.19d. Fixing the ends of the model to prevent layer-parallel shear strain would of course be inconsistent with folding by flexural flow (Price and Cosgrove 1990) and it would not permit the generation of tensile stresses in the stiff beds.

Not only is the local σ_3 tensile in the stiff beds under conditions of flexural-flow folding, but σ_3 cants downward relative to bedding in the direction of the horizontal stress (Fig. 3.19d). When local σ_3 is tensile, joints propagate parallel to local σ_1, which is always compressive in the models (the dashed lines in Fig. 3.19d). Local σ_1 refracts slightly at the boundary between the limestone and the shale beds, becoming steeper in the stiffer limestone bed.

Engelder and Peacock (2001) ran several versions of the model to test the effect of R on the tilt of the local σ_1, and hence the predicted attitude of J3 joints with respect to bedding. As R is increased from 1 to 4, the local σ_1 tilts at an incrementally larger angle toward the foreland in both the shale and the limestone beds. Tensile σ_3 in limestone beds becomes larger (0.5 MPa to 5.2 MPa) as R increases from 1 to 3. At $R \approx 4$, σ_3 in the shale near the limestone bed also becomes tensile. When running the same series of tests for beds dipping at 3°, 5° and 9°, the tilt of the joint plane toward the hinterland (i.e., local σ_1) increases for increasing R, with higher rates of increase

in the more steeply dipping beds. Engelder and Peacock also ran tests (not cited here) to determine the effect of the Poisson ratio on the model. They concluded that ν was smaller in limestones than in shales because more joints would otherwise occur in the shales than in the limestones and because $\nu_{ls} > \nu_{sh}$ is inconsistent with in situ geophysical logging data.

3.2.5.3
Joint Propagation at Depth Not by Means of High Fluid Pressure

Joint development at depth is often attributed to high fluid pressures (Secor 1965; Bahat and Engelder 1984) except in cases of composite layers with different elastic properties (Hobbs 1967; Gross et al. 1995). The above described model for the generation of tensile stresses during flexural flow is a variation on the composite layer model first proposed by Hobbs (1967). An important consequence of the model is that compressive stresses may generate local tensile stresses in the stiff layers of a composite stack where bounding surfaces are subject to shear traction, as would be required for flexural flow folding. This mechanism, acting at depth, can produce jointing also in the absence of high fluid pressure. Engelder and Peacock favor the flexural flow mechanism over hydraulic fracturing because: (1) joints with tilt occur only in dipping rocks of the fold limbs and (2) as predicted by their model, joints are not orthogonal to bedding. Engelder and Peacock's (2001) model for the Lilstock buttress anticline determines that joint (and vein) growth in the limbs of flexural-flow folds should have several distinct characteristics. The joints should extend through the entire bed, should be non-orthogonal to the bedding, and dip toward the anticlinal axial plane, while the poles tilt away from it.

3.2.5.4
Stress Ratio and Frictional Slip

Laboratory values of friction (Zoback and Healy 1984) predict that fault slip occurs when $R = 3$, where R is the ratio of the remote principal compression S_{Hmax} divided by the global vertical stress S_v. Engelder and Peacock (2001) use this stress ratio and the hinterland tilt of joints to predict the dip of bedding at the time of the onset of jointing. Their model predicts that J3 joints with a tilt of about 4° should have propagated by the time beds had been upfolded to have a dip of 3°. If in the course of Alpine inversion faults slipped under low friction, R could have been <3. For example, if $R = 1.33$ due to low-friction faults, a hinterland tilt of 4° could cause jointing in beds dipping as much as 17°. They suggest that the flexural flow model may be applied outside the immediate area of the Lilstock buttress anticline. During the extensional phase of the Bristol Channel tectonics, large blocks throughout the basin were slightly tilted (Dart et al. 1995), entering the Alpine inversion phase when already possessing a modest dip. The model allows tensile stress to be generated at dip angles smaller than 2°, particularly since the Poisson ratio of limestone is lower than that of shale. Many of the jointed strata cropping out on the north and south shores of the Bristol Channel have a gentle dip that would favor joint formation if submitted to inversion tectonics. Joints not orthogonal to the bedding have been recorded at Lavernock Point, South Wales, by Rawnsley et al. (1998).

3.2.6
Conclusions by Engelder and Peacock (2001)

Engelder and Peacock (2001) established the presence of six joint sets in the limestone beds of the Jurassic Blue Lias, numbering them J1 to J6. They all cluster about the axial strike of the 290° striking Lilstock buttress anticline, including J1 (330–310°), J2 (310–295°), J3 (295–285°), J4 (285–275°), J5 (275–265°), and J6 (<265°). In sub-horizontal beds, including those near the hinge surface of the Lilstock buttress anticline, J3 joints are rare. Abutment of joints belonging to J2, J4, J5 and J6 indicates a counter clockwise sequence of development. In the south-dipping beds of the anticline, J3 joints are most frequent in the vicinity of the reverse fault responsible for the anticline. J3 joints are absent where J1 and J2 joints are present and diminish with distance from the anticlinal hinge and higher in the stratigraphic section. J3 joints in the south-dipping beds are not perpendicular to the bedding but have poles that plunge several degrees towards the south when bedding is restored to horizontal.

According to Engelder and Peacock, the mechanism that formed the J3 joints must explain:

1. Their tilt relative to bedding on the steep south flank of the anticline.
2. Their greater frequency in the south-dipping limb as compared to the axial region.

These two characteristics strongly suggest that the J3 joints were formed during folding, but before beds reach their present tilt. These conditions are met in their shear model for interlayered limestone-shale beds during flexural flow folding (Fig. 3.19c), where local tensile stresses are generated within a regional stress field capable of driving inversion tectonics. Such tensile stresses will create through-cutting joints rather than arresting at a neutral surface associated with outer-arc extension (Fig. 3.19a). In this model, joints can open against the direction of the maximum compressive stress under conditions where external tractions are compressive. This indicates that at least some of the joints at Lilstock formed during the main Alpine inversion (cf. Rawnsley et al. 1998). It also shows that joints that are parallel to a fold hinge may form on the limbs during flexural-flow folding and not in the hinge region as a consequence of outer-arc extension during tangential longitudinal strain folding.

3.2.7
Discussion by Engelder and Peacock (2001)

3.2.7.1
The Problem of Delayed Fracture

Both Rawnsley et al. (1998) and Engelder and Peacock (2001) accept that jointing in the Jurassic (Blue Lias) rocks at Lilstock is associated with Late Oligocene to Miocene Alpine compression, i.e., that there was a long time interval between deposition of the limestones and their eventual fracturing. Very often single-layer joints form in sedimentary rocks during their burial stage. There must be a reason why jointing at Lilstock skipped the burial and did not develop during this long time interval. A similar question applies to the "delayed fracturing" in the Middle Eocene chalks of the Beer Sheva

syncline, Israel (Bahat 1999a), where the time interval between deposition and fracturing, all within the Tertiary, was much shorter than at Lilstock Beach. At Lilstock Beach, fracturing began in the syntectonic stage (or during relaxation of tectonic loading). With few notable exceptions (e.g., Becker and Gross 1996; Weinberger 2001a) systematic joints are rare in limestone and dolomite strata in anticlines in Israel (unpublished data by Bahat). What is special about these exceptions, for instance, the Tully limestone (e.g., Younes and Engelder 1999) that contains systematic joints? Why are systematic joints uncommon in the Upper Cretaceous chalks of South England (Bahat 1991a, Sect. 5.3.3), while they are very abundant in Santonian and Eocene chalks in Israel? Research combining limestone petrology and structural geology may shed more light on these questions.

3.2.7.2
Opening of Joints Counter to Remote Compression, and Deviation from Perpendicularity to Layer Boundaries

Engelder and Peacock (2001) found that J3 joints open against the remote compressive S_{Hmax} instead of the expected opening in a plane that contains S_{Hmax}. They consider this to be a "mechanical paradox" and constructed a flexural flow model to explain it. We propose an alternative mechanism of local stress field rotation that would produce fracture patterns similar to those described by Engelder and Peacock.

Previous investigators have also reported on opening of joints against the remote compression. Dieterich and Carter (1969) investigated a numerical model of the stress field in two-dimensional, large-amplitude folding of a viscous layer in a less viscous matrix, using a modification of the finite element method. They found that large magnitudes of σ_1 act parallel to the layer throughout the early stages of folding. With increasing amplitude,

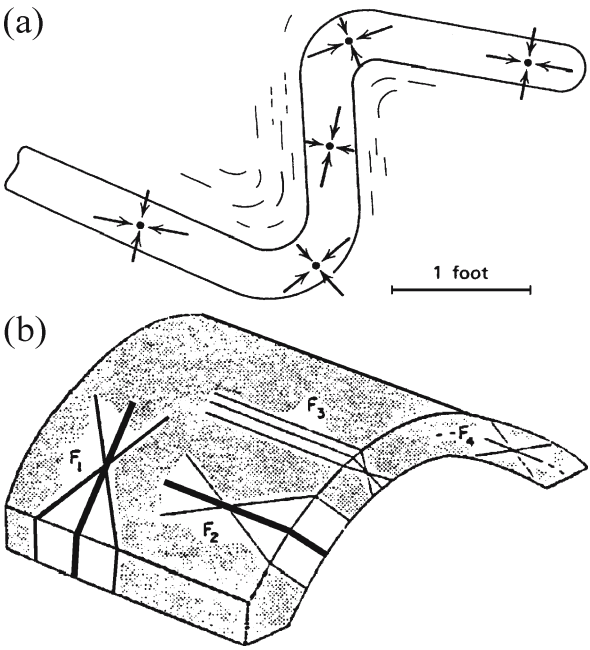

Fig. 3.20.
a A sketch showing geometry of folded quartzite layer. *Dots* indicate locations of specimens used for dynamic analysis of quartz lamellae. *Long arrows* show orientation of σ_1, and *short arrows* show orientation of σ_3 (all principal stresses are compressive and positive) (after Dieterich and Carter 1969). **b** A schematic symmetric fold, showing basic four joint systems, F1–F4. Each system ideally consists of three sets. Fractures from the systems F1 and F2 are more common than others, and in the latter two, the sets co-axial with the principal stresses are more common than the inclined sets

σ_1 decreases in magnitude along the limbs and rotates into increasingly higher inclinations to the layer. In the upper hinge area, σ_1 decays rapidly with increasing amplitude, and the deviatoric stresses parallel to the layer rapidly become low-magnitude tensile stresses. Their analyses generally show that in the limbs of open folds, σ_1 is inclined at low angles to the layer, σ_2 is parallel to the fold axis, and σ_3 is nearly normal to the layer (Fig. 3.20a). Figure 3.20a also implies that the stress axial cross may deviate from orthogonality with respect to the bedding. Thus, the fractures that may develop during the local rotation of the principal stresses need not be normal to the layer boundaries.

According to Dieterich and Carter (1969), similar results were obtained by other studies (Hansen and Borg 1962; Carter and Friedman 1965; Scott et al. 1965), which focused on intragranular flow of calcite and quartz during folding. Burger and Hamill (1976, Fig. 14A) performed petrofabric stress analysis on the Dry Creek Ridge anticline in Montana and also found rotation of principal stress during folding. Initially, the entire multilayer package was subjected to compression with σ_1 parallel to layering and orthogonal to the fold axis. As shortening continued, a neutral surface formed, dividing the hinge and upper limb areas into domains. The compression domain implies σ_1 parallel to layering and orthogonal to the fold axis, and the extension domain implies σ_3 parallel to layering and σ_1 orthogonal to layering.

Reches (1976) identified five joint sets (J1–J5) that cut two asymmetric anticlines in southern Israel, the Hathira and Hazera monoclines. None of the sets display symmetry with the fold axes, and as such they differ from the idealized joint geometry suggested by Stearns (1968) for symmetric folds (Fig. 3.20b). Four sets (J1–J4) are normal to the bedding and are thought to have developed prior to or at the beginning of the folding, and their present orientation reflects their rotation by folding. On the other hand, joint set J5, considered to be related to advanced folding, is inclined to the bedding. Its average strike is 030°, which is sub-parallel to the trend of the monoclines, parallel to the bedding and normal to the axes of the monoclines. The deviation of the five joint sets (J1–J5) of the Lilstock Beach anticline from normality to the bedding resembles that of the J5 joint set from Hathira and Hazera. Tilted joints were observed in the Santonian chalks from the "Arad syncline, Israel. These are apparently related to an intense deformation phase of the chalks (Bahat 1991a, p. 259). It appears that all the above-mentioned tilted sets in both anticlines and synclines were formed during advanced folding, while rotation of the local principal stresses underwent rotation. Hence, the local rotation of the principal stresses during advanced folding in Dieterich and Carter's model and in field observations by others point to an alternative mechanism to the flexure flow model (Fig. 3.19c) proposed by Engelder and Peacock (2001). This mechanism is a more general one and may operate in formations that do not necessarily consist of alternating lithologies (e.g., limestone and shale). It may also explain why there is no actual evidence of slip by simple shear strain, as expected in the flexure flow model within the shales at Lilstock. Finally, Engelder and Peacock (2001) argue that in their model, tensile stresses will drive joints completely through beds, and will not be arrested at a neutral surface in the outer-arc extension model (Fig. 3.19a). Chinnery (1966), on the other hand, maintains that a tensile fracture, once started, could continue to propagate even where entering a region of compression. Thus, the flexure flow model is not the only mechanism to explain the formation of set J3 at Lilstock. For a discussion on fracture in symmetric folds and in slightly folded structures, see Sect. 3.4.

3.3
Post-Uplift Exfoliation Joints and Arch Formation in Sandstone at Zion National Park, Utah, USA

3.3.1
Introduction

3.3.1.1
General

Exfoliation in the massive sandstones of the Colorado Plateau, and at Zion National Park in particular, has drawn the attention of many investigators (e.g., Gregory 1950; Holman 1976). Exfoliation in rocks has been debated since Gilbert (1904) proposed a connection between sheeting and the expansion of the rock body in response to unloading by erosion. Several natural mechanisms have been suggested, including contraction of magma during cooling, regional tectonic stresses and residual stresses, fluctuations of ground and surface temperature and differential weathering (Johnson 1970; Holzhausen 1989).

Various stress conditions have been proposed to explain the formation of exfoliation joints. The stress conditions close to the ground surface, particularly the high compressive stresses that parallel the exfoliation, are of great importance (Dale 1923, p. 34; Holzhausen 1989). Fracturing by residual compressive stresses (Bradley 1963; Holman 1976) develops when critical stress difference occurs between the principal stresses parallel to the surface (e.g., White 1946) and if these are sufficiently high so that additional stress will fracture the rock (Cadman 1969) (for further discussion on exfoliation, see in Holzhausen (1989). Although it is clear that exfoliation in Zion National Park generally parallels earlier fractures, it has been debated whether exfoliation joints curve to remain faithful to the new valley sides, independent of the earlier regional jointing (Bradley 1963), or they rather follow the trends of prominent earlier vertical prominent joints (Gregory 1950).

Sandstone arches in Zion National Park were considered by Gregory (1950) to be primarily the result of erosion. Cruikshank and Aydin (1994) explained the arches of Arches National Park in southeastern Utah as products of localized erosion that occurred at zones of intense fracturing due to shear on existing discontinuities. Robinson (1970) explained the formation of large arches in Zion Canyon by modeling the arch as a plate with a semicircular hole, which is subjected to uniaxial vertical compression. When the rock above the center of the arch is under tension, it would tend to fail along curvilinear stress trajectories.

Apart from scientific interest, exfoliation must be reckoned with in engineering and architecture. Exfoliation results from a rock's tendency to fracture at the appropriate stress, parallel to a previous surface, like cliffs or the topography. It is therefore an important consideration in the construction and maintenance of roads, canals, dams etc. Quarrying and pit mining deal with it daily. Carefully planned excavation, taking account of exfoliation, can overcome some acute safety problems and prevent economic losses (Niles 1871; Cadman 1969; Holzhausen 1989). Knowing a terrain's exfoliation features is essential to hydrological projects of waste disposal and remediation (e.g., Cohen 1993). A distinction is made between the terms "exfoliation" and "sheeting" (see end of chapter). Section 4.5.3 deals with post-uplift exfoliation joints in granites.

3.3.1.2 *Geologic Setting*

Zion National Park, a fracture province marked by a multitude of exfoliation joints and arches, is located in southwestern Utah, between the Hurricane and the Sevier fault zones (Fig. 3.21a). This area occurs within the transitional region between the Colorado Plateau in the east and the Basin and Range province in the west (Grater 1945; Kurie 1966; Stewart and Taylor 1996). Mesozoic rocks of the Colorado Plateau in southern Utah bear structural evidence of three major regional tectonic events (Davis 1999). The first de-

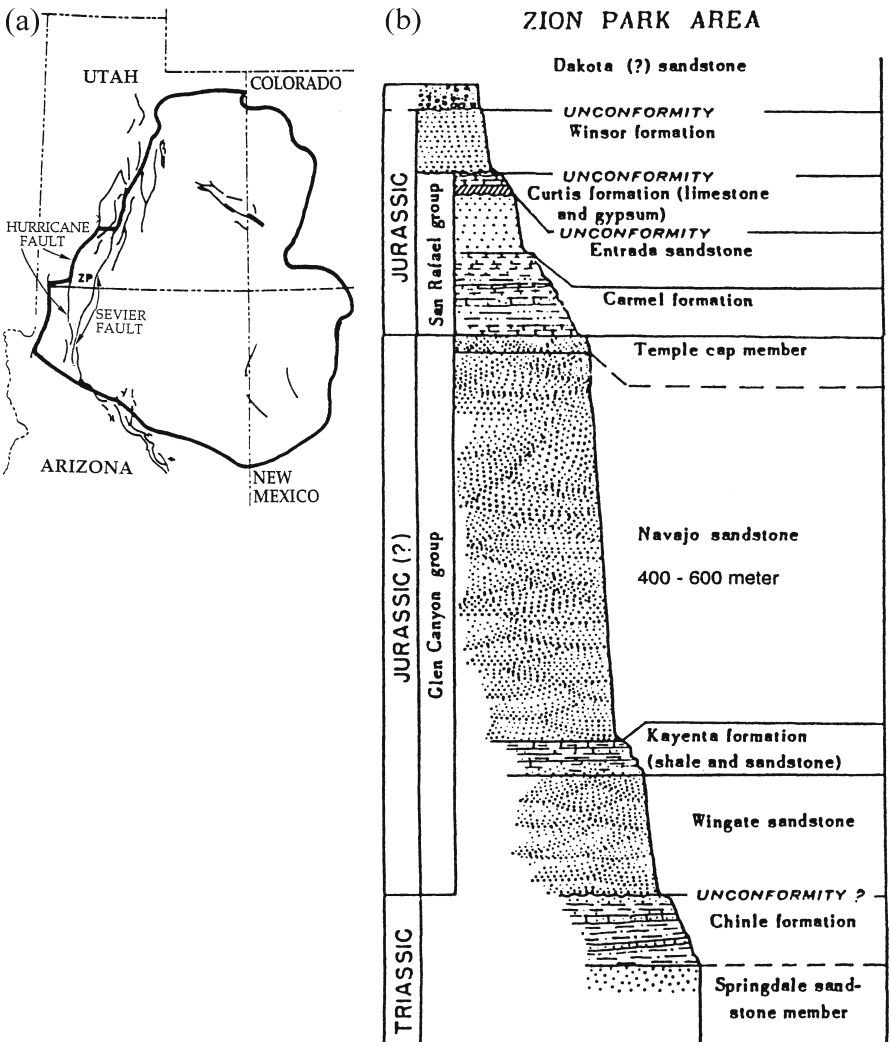

Fig. 3.21. a Simplified structural map of the Colorado Plateau (*thick lines*). *Thin lines* represent major faults; *ZP* designates Zion National Park (modified after Hunt 1956). **b** Stratigraphy of the Navajo sandstone in the Zion National Park area (modified from Gregory 1950)

formation was during the Laramide orogeny, from ca. 90–50 m.y., when an ENE-WSW convergence between the North America plate to the east and the Farallon plate to the west generated horizontal compression that contracted the Colorado Plateau region. The second deformation took place during the Miocene, from ca. 25 to 19 m.y., when the rate of plate-tectonic convergence had slackened from ~100 mm yr^{-1} during the Laramide orogeny to ~50 mm yr^{-1}, and the angle of subduction was becoming steeper. The third deformation was due to the Basin and Range extensional faulting, which began at about 15 m.y. and is still active today. This extension produced three major high-angle normal faults along the southwestern margin of the Colorado Plateau. They are (from west to east): The Hurricane, Sevier and the Paunsagunt faults.

Two regional joint sets striking about NW-SE and NE-SW are known from the Colorado Plateau in northeast Arizona and in southeast Utah (Hodgson 1961b). Three Neogene sets striking 335° (N 25° W), 355° and 030° were identified by Bergerat et al. (1992) in the massive sandstones of the Colorado Plateau. Gregory (1950) observed two series of regional joints striking NNW and ENE in the Zion Park region. No clear correlation can be established between the various joint sets and any of the above major deformations. The present section concentrates on a series of exfoliation joints in the Navajo sandstone associated with the NNW and ENE sets observed by Gregory (1950). The Navajo sandstone is about 400–600 m thick in the park area, and is thought to be of Middle Jurassic age (Fig. 3.21b). The rock is quartz-rich, massive, friable, fine-grained, and equigranular (Grater 1945; Gregory 1950). Various investigators (e.g., Gregory 1950; Bradley 1963) have studied the exfoliation joints in the massive sandstones of the Colorado Plateau and at Zion National Park in particular. Bradley considered the exfoliation to be of Pleistocene age. Based on studies by Bahat et al. (1995, 1999) and Grossenbacher et al. (1996), we characterize below the initiation and growth stages of exfoliation joints in relation to previous regional joints. The role of exfoliation fractures in arch formation is explored, including a mechanical model of arch formation.

3.3.2
Fracture Characteristics at Zion National Park

3.3.2.1
Exfoliation Joints at Zion National Park

Two types of exfoliation joints were discerned at Zion National Park. The first type consists of large fractures that form vertical cliffs. These joints occur mainly along straight tributaries, mostly striking NNW (Fig. 3.22). The tributaries trending NNW are subparallel to each other. Most of them run for 2 000 m or more, and many of them are deep and narrow canyons only tens of meters across with straight walls hundreds of meters high (USGS 1 : 24 000 topographic maps of the Zion Park area, 1980), displaying extensive exfoliation (Fig. 3.23a). Many narrow canyons are elevated from the Virgin River and form large stairs down to the main canyon. They belong to the more generalized regional pattern of prominent fractures that mostly strike NNW or NE at Zion National Park (e.g., Gregory 1950). The second type of exfoliation joints occur in various sizes and orientations that conform to present-day surface morphology (e.g., Fig. 2.33e). Joints of this type occur in various parts of the main canyon as well as along the tributaries.

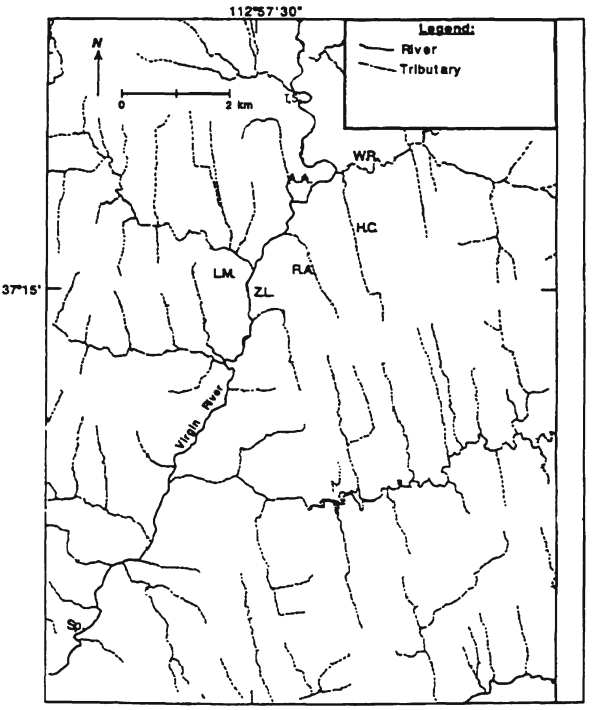

Fig. 3.22a. Tributary map in Zion National Park, Angle Arch, Red Arch, Lady Mountain, Weeping Rock, Hidden Canyon, Springdale and Zion Lodge are designated respectively, by *A.A.*, *R.A.*, *L.M.*, *W.R.*, *H.C.*, *Sp.* and *Z.L. Dashlines* represent tributaries (after Bahat et al. 1995)

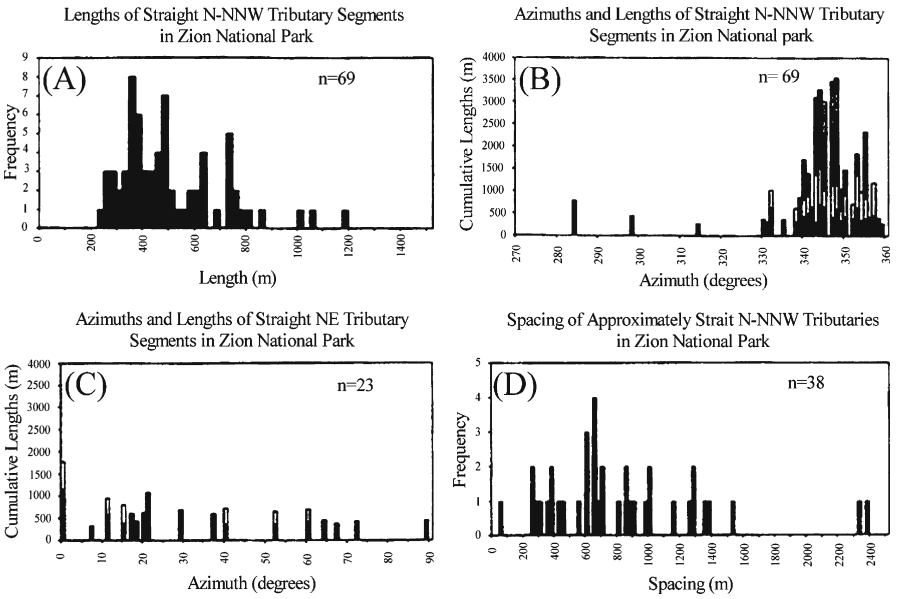

Fig. 3.22b. Histograms of parameters on exfoliation joints along approximately straight tributaries in Zion National Park. *A* Lengths along N-NNW tributaries. *B* Azimuths and cumulative lengths of N-NNW tributaries. *C* Azimuths and cumulative lengths of NE tributaries. *D* Spacing of N-NNW tributaries (after Bahat et al. 1995)

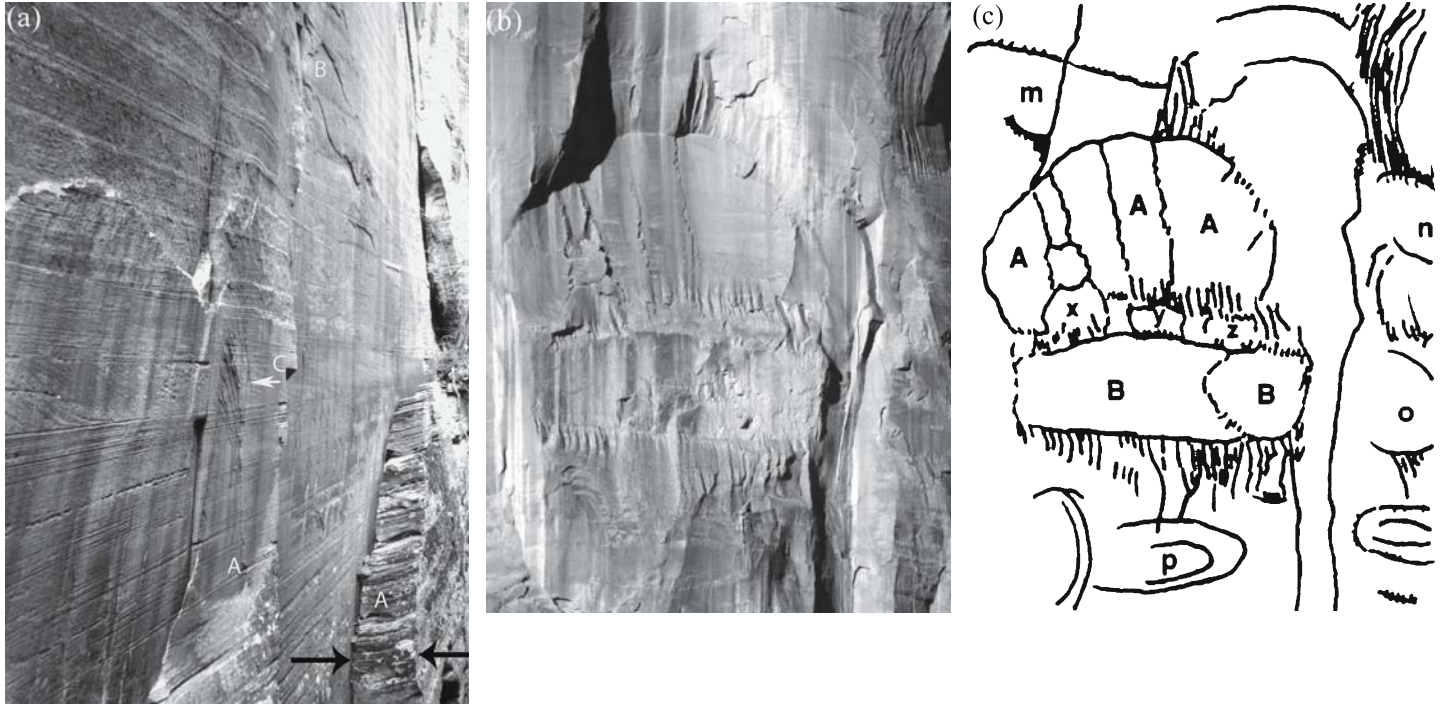

Fig. 3.23. a The lower part of a vertical NNW exfoliation joint in Hidden Canyon, showing two vertical remnants of exfoliated slices (marked *A*), several meters high and up to 1 m thick. Such slices occasionally show *en echelon* relationship. Right-stepping *en echelon* segments cut the exfoliation at upper center (*B*). At the center is another third *en echelon* array (*C*) with inclined stepping, tens of cm long and tens of mm thick, spreading upward from a single center. Note sub-horizontal bedding of the sandstone, which does not interfere with *en echelon* cracks and exfoliation. **b** Interaction of adjacent quasi circular/elliptical cracks of different size that grew independently and impinged on each other on an exfoliated joint. **c** Diagram of **b**. Fracture *A* is ornamented by several long vertical striae that arrest at the *en echelon* fringe below *A*. Fracture *B* is a combination of two smaller fractures and the *en echelon* fringe below *B*. Three smaller fractures, *x*, *y*, *z*, lie along the contact between *A* and *B*. Additional fractures around *A* and *B* are marked by letters *m*–*p*. The height of *ellipse B* is on the order of 4 m (after Bahat et al. 1995)

3.3.2.2
Circular/Elliptical Cracks and Composite Fractures

Joints of the first exfoliation type are often marked by quasi-elliptical or quasi-circular cracks (QCC), which mostly range from one meter to several tens of meters in diameter, occasionally interacting with each other by partial penetration (Fig. 3.23b,c). They grow approximately coplanar to each other and often merge in a variety of styles, producing composite fractures (Bankwitz and Bankwitz 1984; Helgeson and Aydin 1991; Bahat 1991a, p. 268). Some composite fractures form either partial or full ellipses or circles, occasionally rimmed by *en echelon* fringes (Fig. 3.24a,b).

Ripple marks. Ripple marks are of two types: Undulations and arrest marks (Sect. 2.2.4.2). Occasionally, undulations occur on large exfoliation joints unrelated to QCC. A spectacular series of more than forty undulations (Fig. 3.24c) occurs on the western wall of the "Hidden Canyon" (Fig. 3.22a), where they cover a cliff surface tens of meters wide, and about as high. This feature marks the propagation of a large, concentric, single-fracture front that is convex to the north. The undulations show that the joint grew horizontally from south to north. They also show how rock anisotropy influences fracture propagation: The fracture cuts across bedding, but one boundary was resistant, and refracted the fracture front into another direction. Arrest marks propagate in all directions but seem to advance particularly downward (Fig. 3.24d). Arrest marks also occur on fractured side-walls of arches (Fig. 3.24b).

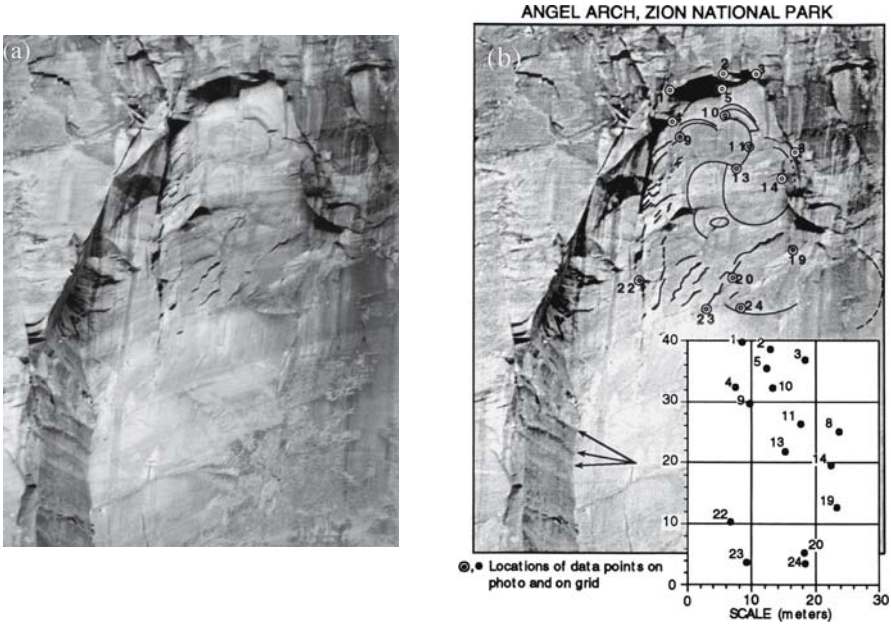

Fig. 3.24a,b. a The Angel Landing Arch. **b** Scaled photograph of the same arch, showing detailed measurements. Many circular/elliptical cracks are surrounded at left by a fringe of *en echelon* radial cracks. Note vertical discontinuity (at left of *points 1* and *4*), and arrest marks on left side-wall (*three arrows*). (after Bahat et al. 1995)

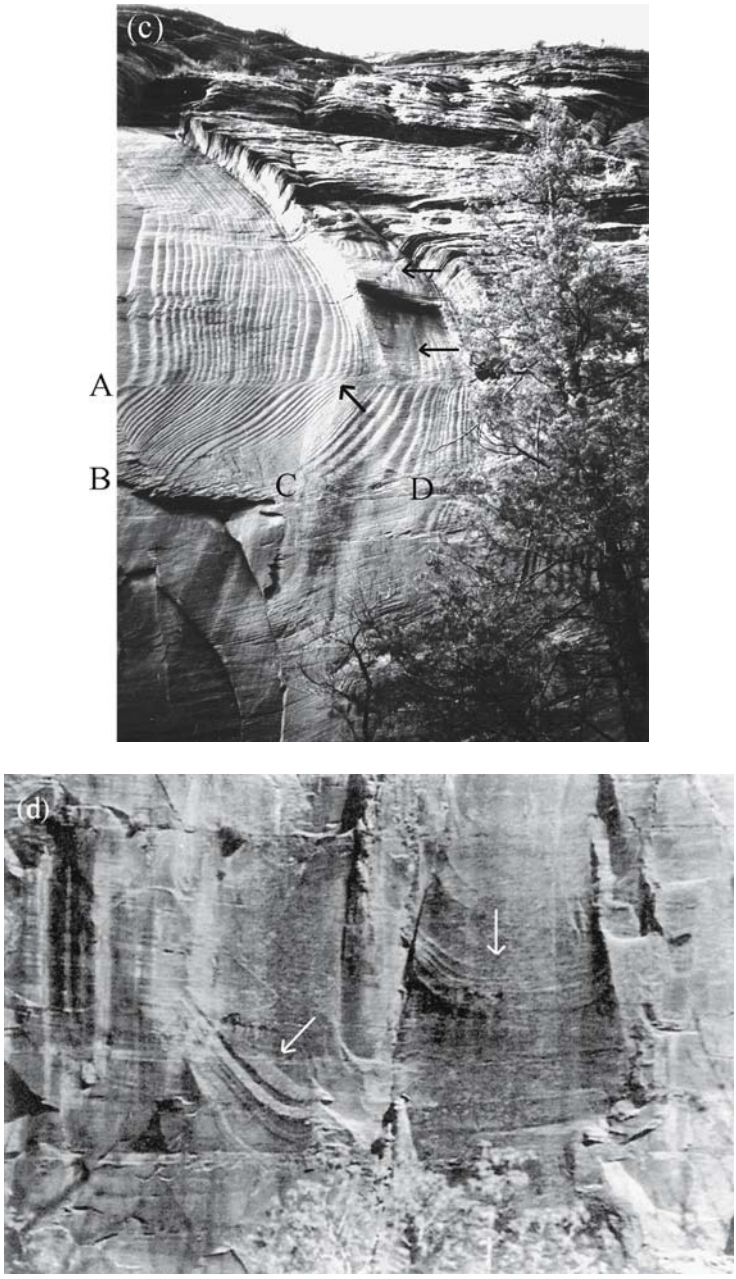

Fig. 3.24c,d. c A central part of a nearly planar, vertical NNW-striking exfoliation joint. Undulations several tens of meter long convex towards right (north). The fracture front is interpreted to have changed its propagation direction at a resistant bedding boundary (*inclined arrow*). The occurrence of two superposing exfoliation joints with similar ripple marks is shown by two sub-horizontal arrows. Letters *A–D* relate to locations of changes in fracture velocity. **d** Different characteristics of ripple marks, undulations – *vertical arrow*, and arrest marks – *inclined arrow* (Sect. 2.2.4.2) (after Bahat et al. 1995)

Radial plumes (striae). Quasi-circular cracks may be decorated by radial striae that indicate the sites of fracture initiation and illustrate the fracture growth mode. Occasionally, radial striae decorate a niche (see below) and constitute the only part remaining of the QCC. Striae are not common. They occasionally occur either as straight individuals, often in radial setting, or as straight strands bent in places (Fig. 3.25a,b).

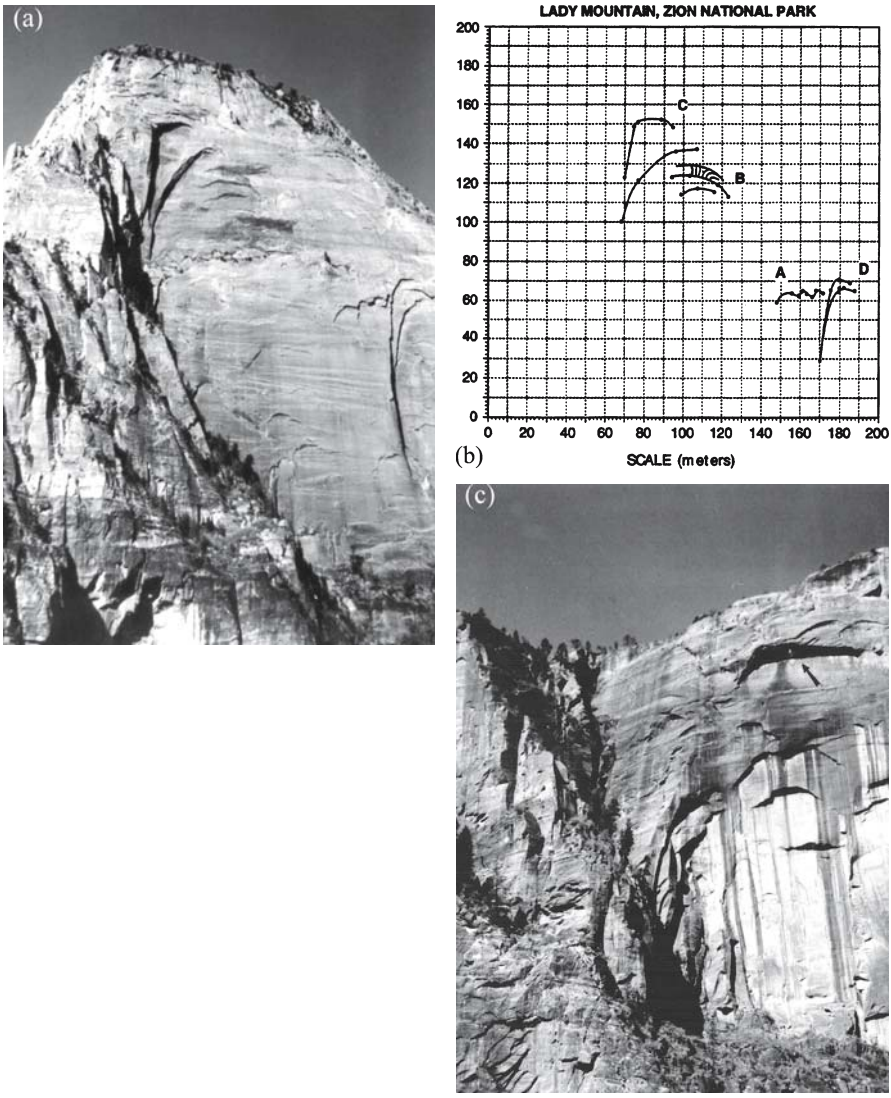

Fig. 3.25. a A series of large *en echelon* cracks on a NE striking cliff at Lady Mountain. Note previous exfoliation slices at left. **b** Scale diagram of **a**, showing crack dimensions. *A* and *B* are series of upward convex niches. Radial striae are marked at *B*. *C* and *D* are two sub-horizontal, straight niches formed by a series of *en echelon* fractures, propagating leftward and producing partial arches. **c** Exfoliations on a cliff, exhibiting a series of small niches (at center), with a large niche or a small arch about 20 m long above (*arrow*). A series of partial arches is seen at lower-center of picture (after Bahat et al. 1995)

3.3.2.3
En Echelon *Cracks, Niches and Arches*

***En echelon* cracks.** Many fractures deviate a few degrees from the cliff plane, and appear as *en echelon* segments, ranging in size from tens of cm to tens of meters. The *en echelon* segments occur in various shapes and orientations. Occasionally three or more *en echelon* sets of different sizes and orientations occur in close proximity (Fig. 3.23a). Other cliffs exhibit large *en echelon* fractures next to niches (Fig. 3.25a,b) or along the mirror boundary (Fig. 3.24a,b).

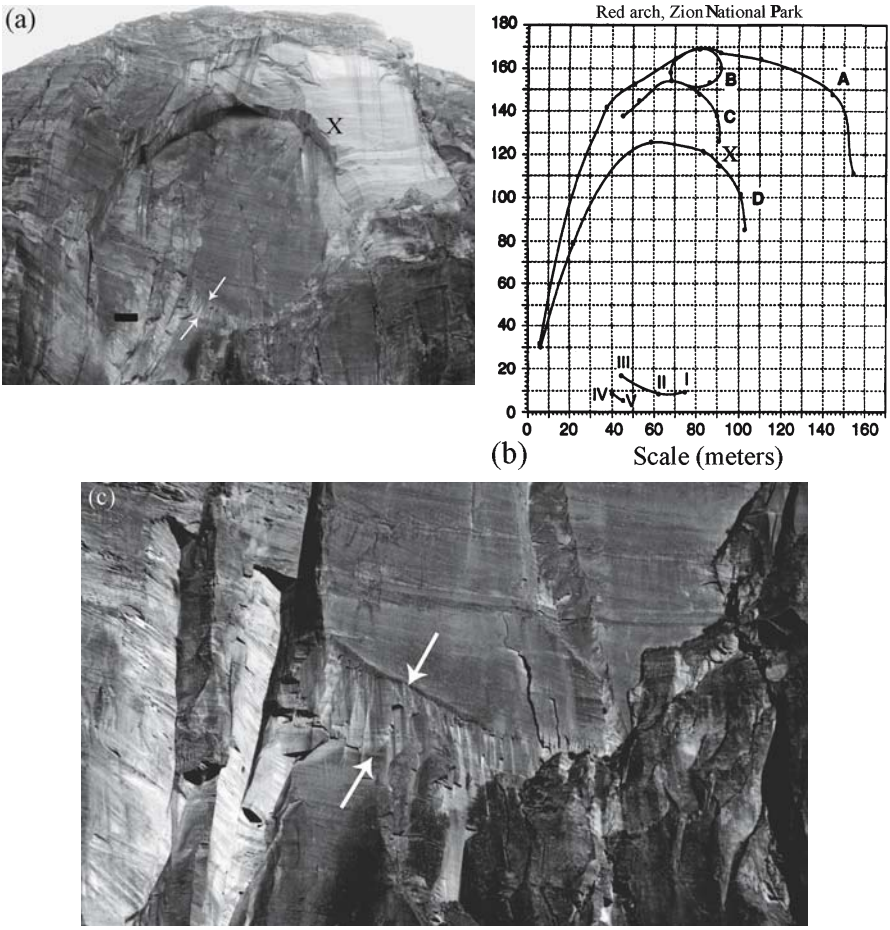

Fig. 3.26. a The Red Arch, showing sharp fracture contours in the upper parts (*x*). Fringe of *en echelon* segments (two *arrows*) marks the lower boundary of the quasi-circular arch and at lower-left side some remnants of exfoliated slices. *Scale bar* is about 15 m. **b** Scale diagram, showing measured dimensions of **a**. *A*, *B* and *C* contours describe earlier large and small "attempts" of arches, while *D* follows the contours of the main, Red Arch quasi-circular contours, surrounding the large, flat back-wall at the center. This back-wall is a mirror plane. Numbers *I*, *II* and *III* mark the upper boundary of the lower fringe of the mirror, and *IV* and *V* occur on the lower boundary of the fringe. *x* in **a** and **b** depict the same spots. **c** The fringe in close-up (after Bahat et al. 1995)

Niches. Occasionally, individual QCCs or composite fractures cut into the rock and deviate several degrees from the cliff face. At these localities, receding bays formed in the cliff are termed niches (Fig. 3.25a–c). The niches commonly appear in crescent shapes that concave downward (distinguished in the outcrop by their shades). Occasionally, they tend to be straight. Sizes vary from several meters to several tens of meters. Two types of niches, A and B, are distinguished. Niches of type A occur close together at about the same topographic elevation (Fig. 3.25b). Type B niches are grouped one above the other. Adjacent niches in an outcrop may show shape and size transitions to "small arches" (Fig. 3.25c). The majority of QCCs, composite fractures, *en echelon* segments and niches occur within the middle third of the cliff face (Fig. 3.24a,b, 3.25a,b, 3.26a,b and 3.27).

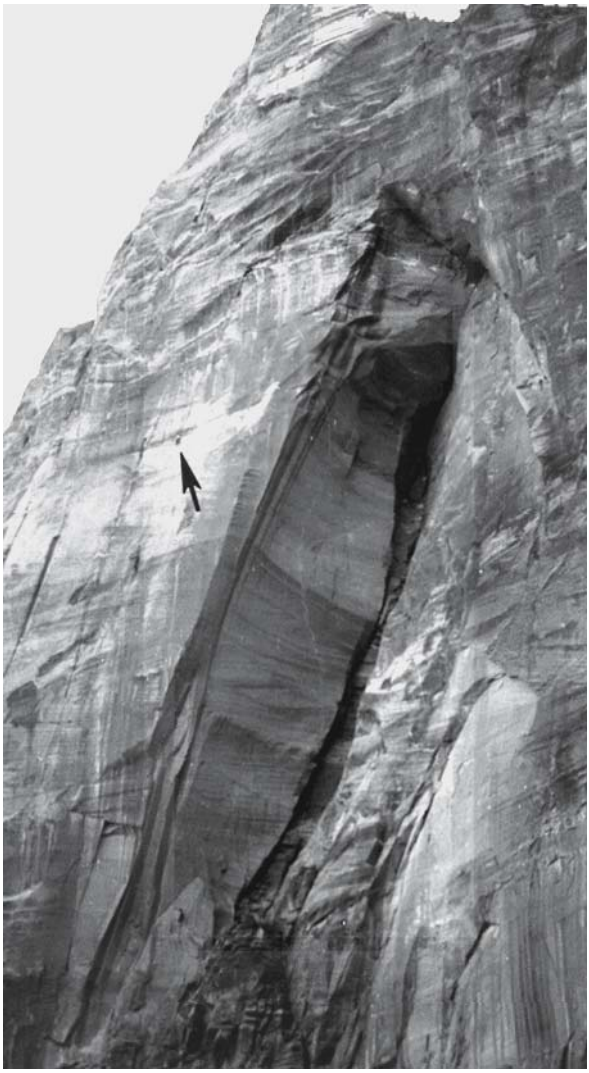

Fig. 3.27.
Side-wall of a partial arch with convex ripple marks indicating downward fracture propagation. The upper mark coincides with a bedding boundary, which influenced its location (below *arrow*). See a rappelling person (*arrow*) for scale (after Bahat et al. 1995)

Arches. Arches are found by the hundred in Zion National Park in a variety of sizes (Table 3.2) and shapes (Fig. 3.26–3.28). Arch sizes range from several meters to many tens of meters. Some are full arches (Fig. 3.26a,b and 3.28a), either symmetric or asymmetric (Fig. 3.28a); others are incomplete arches (Fig. 3.27 and 3.28b). A full arch exhibits a ceiling and two side walls. Height is measured from base to the highest point on the ceiling, and the width is measured between opposite side walls at the base. In some arches, width is larger than the height (Fig. 3.28a), in others this relationship is reversed (Fig. 3.24a,b). Sub-circular arches (Fig. 3.26a) are rare. A partial arch consists of a side wall and a fraction of ceiling (Fig. 3.27 and 3.28). Many ceilings are not fully concave, but partly coincide with straight, sub-horizontal niches or other bedding oriented boundaries (right side of Fig. 3.24a and 3.32b). Occasionally vertical fractures cut ceilings of full arches or form boundaries of partial arches (left side of Fig. 3.24b).

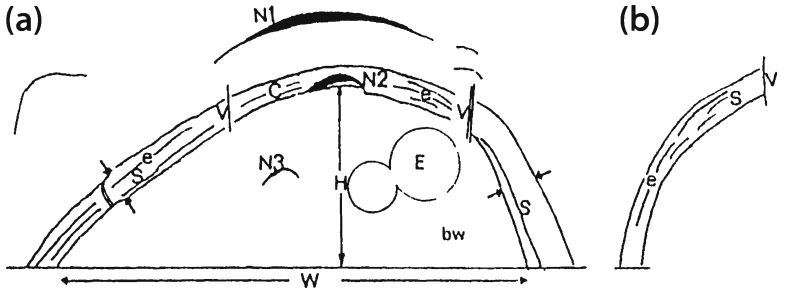

Fig. 3.28. a Diagram showing elements of an asymmetric arch as follows. Side-walls *S*, ceiling *C* of the arch (shown between two *arrows* that indicate thickness on both sides of the arch), the vertical fracture *V* cuts the arch at the ceiling, and exfoliations e divide the rock into slices. The height of the arch *H*, and the width, *W*. *N1*, *N2* and *N3* are niches associated respectively, with external exfoliation, at the ceiling, and cutting the back-wall of the arch. Two QCC, marked *E*, occur on back-wall, *bw*. For simplicity, niches are mostly crescent and not straight. **b** Diagram of a side-wall of a partial arch

Table 3.2. Measured parameters of arches in Zion National Park

Parameter	Angel Landing Arch (Fig. 3.24a,b)	Lady Mountain (Fig. 3.25a,b)	Red Arch (Fig. 3.26a,b)
Strike of exfoliation joint (°)	334	352	042
Dip of exfoliation joint (°)	87 NE	82 NE	67 NW
Arch			
Height (m)	37		56
Width (m)	28		86
Angular partial arch			
Height (m)		50	
Width (m)		20	
Niche			
Height (m)		6	
Width (m)		15	
Elevation of base station (m)[a]	1 467	1 480	1 440
Elevation above sea level (m)[b]	1 504	1 542	1 492

[a] Approximately at the foot of measured cliff (m).
[b] At zero line of grids (from Bahat et al. 1995).

We interpret the external exfoliation above the arch (N1 in Fig. 3.28a) to be a relict of an earlier cliff face. N3 marks the back wall of the arch, which is the youngest, internal exfoliation joint (Bahat et al. 1999) (Fig. 3.26a and 3.28a). Side walls and ceilings of arches penetrate into the cliff, perpendicular to the external and internal exfoliations and connect them. Side walls and ceilings of arches are generally angular toward the external exfoliation, indicating that the side-walls and ceilings were formed by brittle fracture rather than by erosion. Also, concentric arrest marks on side-walls (Fig. 3.24b, 3.27) are interpreted to indicate that the arches were formed as mode I fractures (Bahat 1979a). The lower parts of arches have various shapes. In some arches, the side walls reach close to the ground surface, whereas in others (Fig. 3.26a) they merge into the cliff. The Red Arch is a sub-circular arch, and the lower boundary of the mirror plane (that coincides with the back-wall) is marked by a concave-up *en echelon* fringe (Fig. 3.26a–c). The rock-slice that separates between the external and internal exfoliation joints has remained partly in place, closing the lower left side of the arch.

3.3.3
Fracture Mechanisms at Zion National Park

3.3.3.1
Circularity of QCCs on Principal Planes

When tensile stress operates normal to an elliptical crack, it tends to grow into a circular fracture because the stress intensity K_I is greater at the end of the minor axis of the ellipse. This trend toward greater circularity is apparently the cause of the common occurrence of QCCs and some composite circular fractures (Fig. 3.23c and 3.24). The planarity of both isolated and linked QCCs is consistent with mode I fracturing, with the fracture planes essentially normal to the least compressive stress.

3.3.3.2
Fractography of Exfoliation Joints

The QCCs at Zion National Park resemble the fan-shaped early cracks of the El Capitan granite at Yosemite National Park, which merge into exfoliation joints (Fig. 4.27). The merging fracture styles at the two localities in different rock types is characteristic of post-uplift joints and was first described as such from Eocene rock strata near Beer Sheva (Bahat 1991a, p. 301). The merging style is unknown on surfaces of earlier burial, syntectonic or on uplift regional joints (Bahat et al. 1999). Hence, one good criterion for distinguishing exfoliation joints from other joint types cutting sandstone is their specific fractography of QCC merging (Fig. 3.23b,c and 3.24b).

3.3.3.3
The Growth of Quasi Elliptic Cracks to Composite Exfoliation Fractures

The growth of QCCs into composite exfoliation fractures proceeds through four steps (Fig. 3.29). They begin as QCCs (as shown in Fig. 3.23b,c and upper part of Fig. 3.29a), or as early fans in granodiorite of El Capitan at Yosemite National Park (Fig. 4.27 and

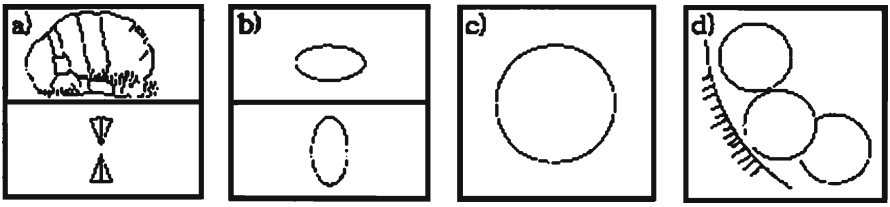

Fig. 3.29a–d. The development of composite fractures from early cracks (see text for explanation)

lower part of Fig. 3.29a). These cracks grow into elliptic fractures, with their long diameter either horizontal or vertical (Fig. 3.29b). The elliptic fracture grows into a circular shape (Fig. 3.29c) by the mechanism described above (Sect. 3.3.3.1). Finally, the fractures grow into a composite exfoliation joint (e.g., Fig. 3.24b and Fig. 3.29d), where they may attain critical conditions (around K_{IC}, Fig. 4.34 and 4.35), leading to the development of an *en echelon* fringe (see lower left side of composite in Fig. 3.26). The latter is also seen at Half Dome at Yosemite National Park (Bahat et al. 1999) (Fig. 6.18).

3.3.3.4
The Evolution of Arches through Niche-Forming Exfoliation

We favor Robinson's (1970) explanation of arch formation by a mechanical process. Figure 3.30 shows the stress trajectories calculated around a circular hole in a plate of elastic rock subjected to uniaxial compression (Means 1979, p. 118). The σ_1 stress trajectories surrounding the hole resemble magnetic force lines around a "circular" magnet or hydraulic streams around a circular obstacle. When a vertical plate with a circular hole is subjected to a biaxial stress with vertical maximum compression σ_1 exerted by the weight of the overlying rock, the resulting strain may lead to an arch. In an isotropic rock, tensile stress will concentrate on point A at the apex of the circular hole, resulting in a vertical fracture normal to the stress trajectories of σ_3 and to the cliff. However, on many full arches (Fig. 3.24) and partial arches (Fig. 3.27) at Zion National Park, vertical fractures (Fig. 3.28a,b) occur at locations like B and C, which are not at the exact apex of a circular hole (Fig. 3.30). Due to the imperfect isotropy of natural rock, arch ceilings are often not rounded at their tops, but are partly shaped by straight niches that follow essentially horizontal sedimentary bedding. Such influence of bedding on fracture growth is seen in many outcrops: Undulations deviate from smooth curvature in Fig. 3.24c, the location of at least one arrest mark coincides with bedding in Fig. 3.27, and niches that follow bedding are shown in Fig. 3.25a. That the modification of arch curvature is caused by unequal strength of the rock is supported by experiment. Robinson (1970) found four values for tensile strength of Navajo sandstone cores determined by uniaxial tension tests. The values found for two cores parallel to the bedding were 3.0 MPa and 1.2 MPa, while values for two cores normal to the bedding were significantly lower, 0.5 MPa and 1.0 MPa. This shows that bedded sandstone is not isotropic. Resistance to fracturing is greater across the bedding than parallel to it.

Arch formation proceeds through several stages of tensile fracture (Fig. 3.31a–d). Vertical fractures (Fig. 3.28a,b) form in zones of tensile stress, which is usually concen-

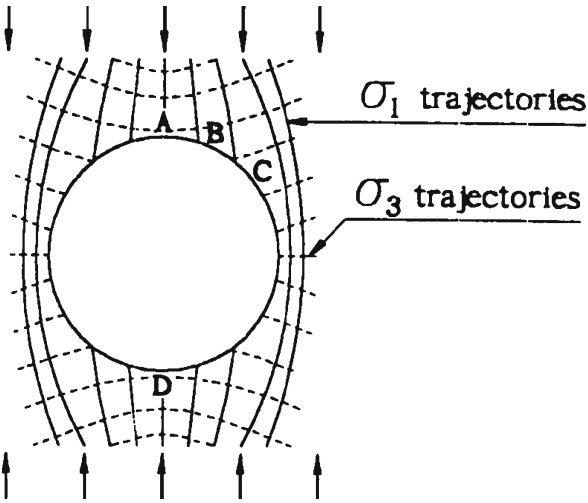

Fig. 3.30.
Stress trajectories near a circular hole in a plate subjected to biaxial compression. *A*, *B* and *C* are possible locations of tensile stress concentration (modified after Means 1987) (see text for explanation)

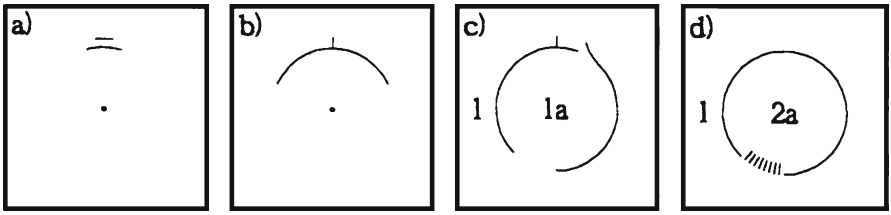

Fig. 3.31. The evolution of an arch from initial niches. **a** Two incipient niches. **b** A vertical fracture forms in the apical part of a growing niche. **c** Vertical fractures grow at the apex and off apex, in analogy to *A* and *B* from Fig. 3.30. **d** The two curves meet and create an arch circle. The area 2*a* can form a mirror, rimmed by a fringe, like the back-wall of the Red Arch

trated at apices of niches or along their sides at their lateral continuations (Fig. 3.31a,b). The vertical fractures propagate downward along the curvilinear stress trajectories σ_1 (Fig. 3.30) almost completely separating area 1a from area 1 on the cliff (Fig. 3.31c). This curvilinearity varies in shape between the quasi-circular geometry of the Red Arch (Fig. 3.26) and the more elongated shape of the Angle Arch (Fig. 3.24), depending on local conditions. Such a fracture would also propagate into the interior of the rock, perpendicular to the cliff surface, even where entering a region of compression (Chinnery 1966). The deeper it propagates into the rock and the more exfoliation joints it traverses, the thicker will become the arch. The thickness of the arch is therefore independent of the depth of the initial niche. Arch thickness is also independent of niche shape, whether semi-circular or straight, because the fracture follows the σ_1 stress trajectories. The ceiling, the side walls and the back wall are fractures, which together with the cliff face separate the arched block from the surrounding sandstone, leading to its collapse by gravity. An arch like the Red Arch (Fig. 3.26a,b) is formed when a rock slice, 2a, is detached from the inner exfoliation and collapses (Fig. 3.31d). This description means that arches may be formed entirely by fracturing, and undercutting by erosion is not required in these cases.

The common occurrence of arches in anisotropic sandstone formations in Zion Canyon and in other provinces (e.g., Fig. 3.32a,b) and their relative rarity in isotropic granitic rocks (Sect. 4.5.3.5) favor the role of rock anisotropy in arch formation by tensile fracturing (Fig. 3.31). Cruikshank and Aydin (1994) explained arch formation in Arches National Park in southeastern Utah by localized erosion along zones of intense shear fracturing. Such fracture zones are not found near arches at Zion Canyon, so that this mechanism probably does not apply to these arches. We did not identify the Zion exfoliation joints and other arch characteristics on the two arches found at Timna in south Israel. These arches are poorly shaped compared with many arches at Zion Canyon, probably because the Timna arches were formed by erosion and not by fracturing.

3.3.3.5
Parallelism between Exfoliation Joints and Previous Regional Joints

The position of the QCCs at Zion Canyon strongly resembles that of the fan-shaped early cracks which appear about halfway up the cliff of El Capitan in Yosemite National Parks (Bahat et al. 1999 and Fig. 4.27). This suggests also similarity in the fracture mechanism. At both localities, earlier cliff-parallel joints provided the free surfaces needed for buckling and longitudinal splitting, which lead to joint exfoliation (Holzhausen and Johnson 1979). Exfoliation at Zion Canyon displays two directions, NW-NNW and NE, occasionally producing square blocks (Fig. 3.32d). These directions correspond to trends of earlier, regional, vertical joints (Hodgson 1961b; Bergerat et al. 1992).

Fig. 3.32a. Arch from thick Paleozoic sandstone, near Petra, south Jordan

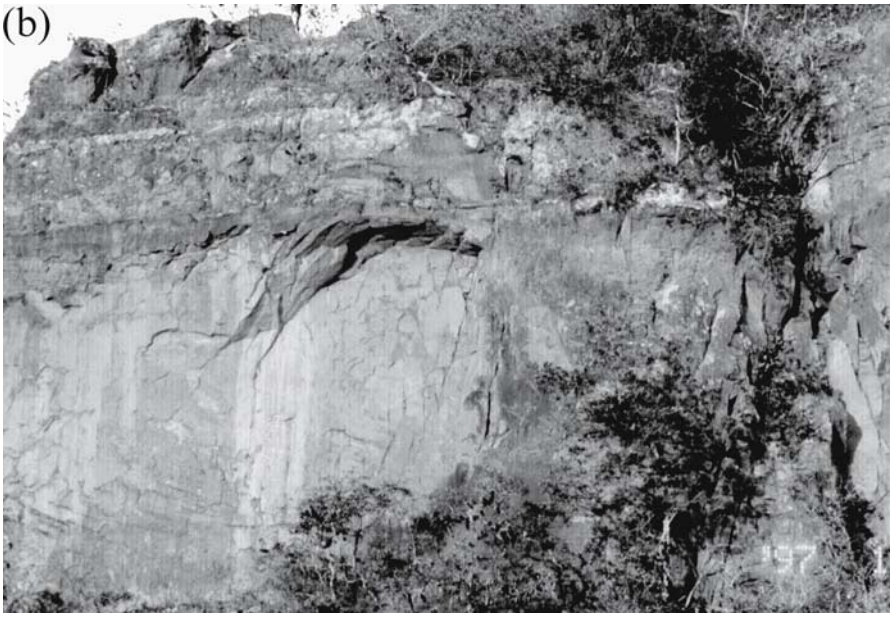

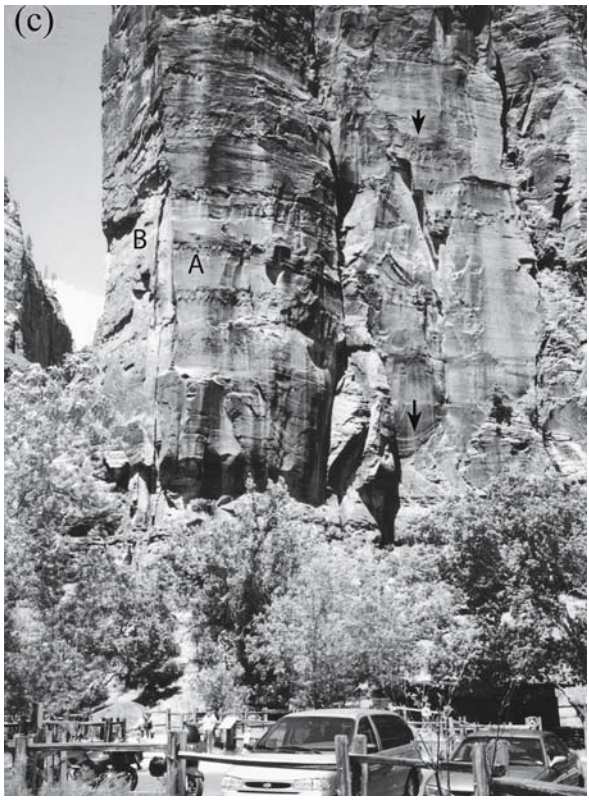

Fig. 3.32b,c.
Arches from: **b** An Arch and niches from thick Jurassic sandstone, in Chapada dos Guimaraes, about 50 km NEE of Cuiaba, central Brazil. Note approximately straight ceilings that conform to bedding; **c** Sub-orthogonal jointing at Zion National Park. The surfaces marked *A* and *B* strike NE-ENE and NNW, respectively. Note arrest marks that convex downward (*arrows*)

3.3.4
Discrimination between Sheeting and Exfoliation

The terms exfoliation (Cadman 1969) and sheeting (Holman 1976; Twidale et al. 1996) have been used interchangeably by many authors. Both sheets and exfoliation fractures reflect fracture propagation in principal planes, normal to the minimum principal stress. However, they belong to genetically and morphologically different categories. Citing Gilbert (1904), who believed that sheeting was older than the topography, we can add that exfoliation follows topography. Therefore, sheeting and exfoliation correspond, respectively, to uplift and post-uplift fractures.

The term sheeting should be applied to series of horizontal and sub-horizontal fractures that maintain approximately uniform spacing but generally with a trend to increase their spacing with depth (Johnson 1970, p. 356). Various authors (including Dale 1923 and Holzhausen 1989) distinguished "generations" of sheet fractures (e.g., preglacial and postglacial). Holman (1976) further distinguished two to four secondary sheets or slabs. Holzhausen (1989) notes that the sheet fractures must be products of states of stress that are approximately uniform over distances of at least tens to hundreds of meters in order to explain the regularity and size of the fractures.

Exfoliation joints, on the other hand, are generated by fracturing parallel to existing surfaces at various orientations, particularly vertical. These joints generally start to develop at a short distance (tens of centimeters), from the exposed surface and form closely spaced sets in small spacing (e.g., Fig. 4.29), producing rock slices that vary from prismatic to lenticular. Thus, whereas sheeting responds to unloading of the overburden, exfoliation results from loading of the overburden.

3.3.5
Summary

The joints at Zion National Park, USA initiated as circular cracks and grew to dimensions as great as several tens of meters. Interaction between these cracks produced composite exfoliation joints tens to hundreds of meters across. Large concentric undulations on some of the large exfoliation fractures indicate a single rather than a composite origin. Generally, exfoliation joints develop parallel and adjacent to joints formed by earlier tectonics. Where the exfoliation joints bend into the cliff, niches are formed, often having crescent shapes that concave downward. Such niches are sites of stress concentration that leads to arch formation. However, the essentially stratified structure of many sandstones causes horizontal extension of the niches, displacing arch formation laterally from the point of stress concentration at the original apex of the niche (Fig. 3.30). Thus, an arch-bounding joint often starts tangent or vertical to a niche and propagates downward, creating a curved surface that approximates the trajectory of σ_1 that is induced by the weight of the overlying rock. The propagating curviplanar fracture also cuts into the rock body, traversing parallel joints that divide the rock into slices parallel to the cliff. Fracture-bounded blocks that detach and fall from the rock body leave an arch-shaped hollow.

3.4 Jointing and Faulting in Eocene Chalk Formations in the Beer Sheva Syncline, Israel

3.4.1 The Beer Sheva Syncline

The Beer Sheva syncline is an asymmetrical fault-fold basin within the Syrian Arc (Krenkel 1924), a sigmoid fold system that stretches from Syria in the north, through Israel to Egypt in the south (Fig. 3.33a). The Beer Sheva syncline, approximately 100 km long, is oriented about 050° (Fig. 3.33b,c). The width of the syncline is not well defined on its western side due to a Cenozoic cover, but is estimated to be about 35 km or less. The structural geology of the Beer Sheva syncline, particularly its northern part, which is rich in Eocene chalk outcrops, was studied by Bahat (1985–2001). Research was also carried out in the Shephela syncline north of Beer Sheva (Fig. 3.33b,c). Fractures, i.e., joints and faults associated with joints, were investigated in two formations: The Mor Formation and the Horsha Formation, lower and lower-middle Eocene, respectively, each of them about 100 m thick. The present account uses data from about one hundred stations (Fig. 3.33d), quoting extensively publications by Bahat.

The Lower (or Early) Eocene Mor Formation, also termed Adulam (Fig. 3.34), is exposed along the peripheries of the syncline. It consists of thin (40 to 90 cm) chalk layers alternating with beds of chert nodules, up to 10 cm thick (Bahat and Grossmann 1988). Two types of joints are common: Single-layer (s.l.) joints and multilayer (m.l.) joints, i.e., that cut through many layers (Bahat 1988a). The cross-fold s.l. joints of set 328° (normal and sub-normal to the synclinal axis) arrest at the boundaries of the chalk layers with chert beds. At one locality, a normal fault that displaces these joints contains in its fracture zone fragments of chert that were broken during early offsetting of the fault, and unfractured nodules that cumulated after fault movement. The solidification of chert (Knauth and Lowe 1978) is associated with the burial phase that includes sedimentation, downwarping and diagenesis, all pre-dating syntectonic deformation and uplift. Chert does not occur in the overlying Middle Eocene strata (Horsha Formation, also termed Maresha). Therefore, both the cross-fold joints and the fault must have evolved before the Middle Eocene, under a tectonic regime that prevailed in the Lower Eocene. The strike-parallel s.l. joints, oriented about 059°, were formed partly intermittently with the cross-fold joints (Bahat 1991a, Fig. 4.8) and partly at a later stage (Gross et al. 1997).

The Horsha Formation, which is exposed at the center of the syncline (Fig. 3.34), differs from the Mor Formation by the absence of chert beds. Single-layer joints in both formations show a general similarity, with several exceptions. Joints of the Horsha Formation vary considerably in orientation, plumes on the joint surface are generally more delicate (Bahat 1987a) and *en echelon* fringes are common (Bahat 1986a). In addition, joints of the Horsha Formation show indications of "delayed fracture" (Bahat 1991a, p. 245, 1997).

The patterns of fold-joint relationships of the Beer Sheva syncline are considerably more diversified than those described in the literature, although they doubtlessly are to be found in other locations also. The detailed planning of environmental engi-

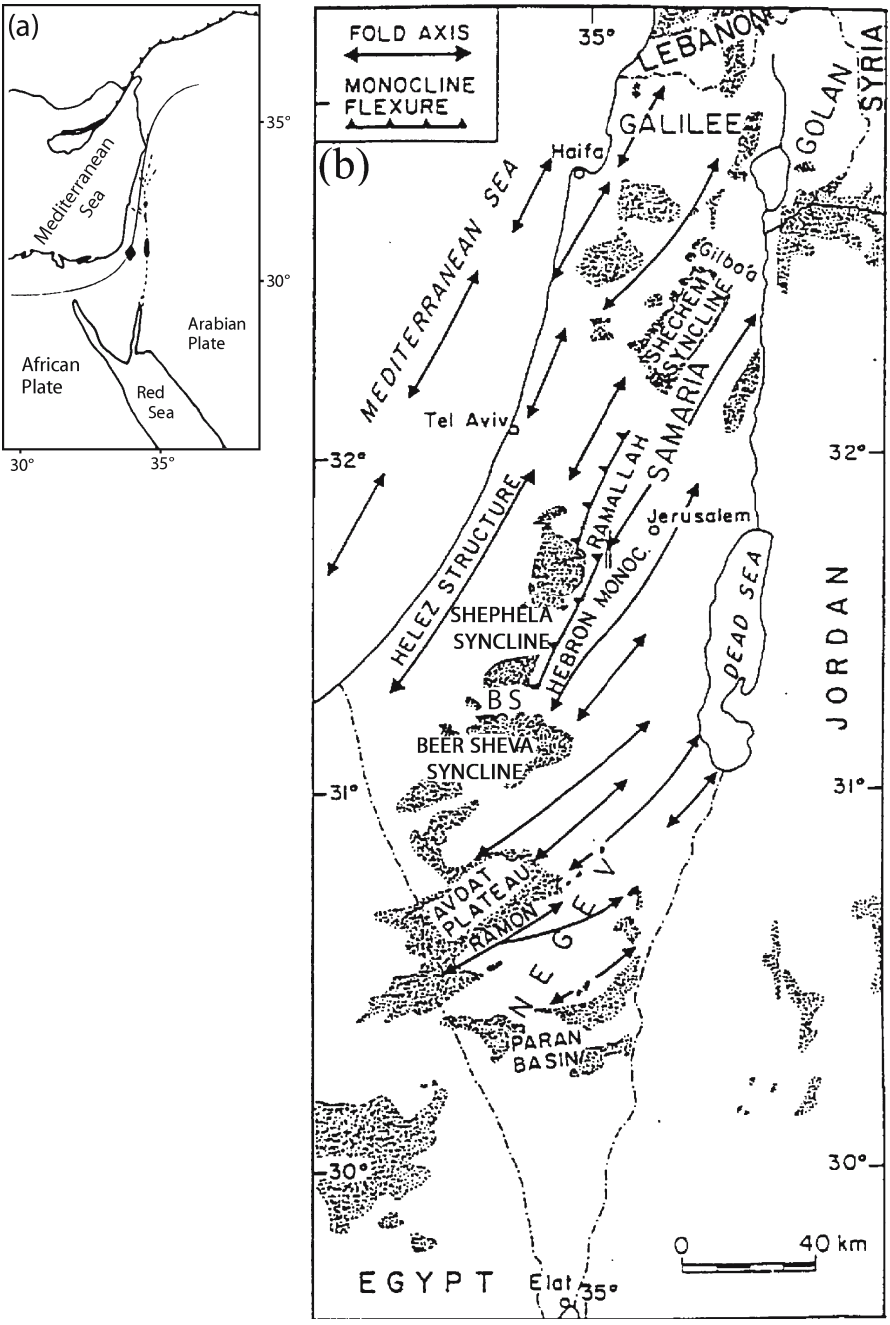

Fig. 3.33a,b. a Location map. The N-S sigmoid trace delineates the Syrian Arc, and the rhomb marks the investigated area in Fig. 3.33b–d. **b** Regional map, showing Eocene outcrops (gray) and major structures of the Syrian Arc system in Israel and adjacent countries. The city of Beer Sheva is marked BS (modified after Buchbinder et al. 1988)

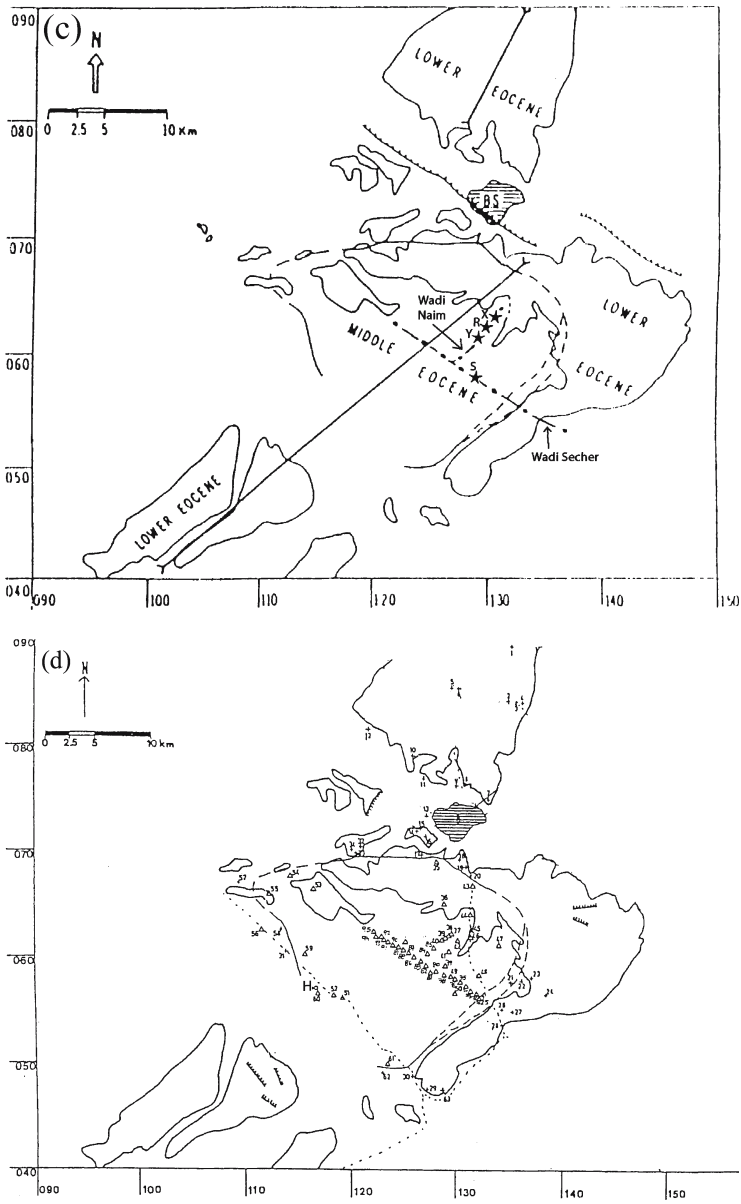

Fig. 3.33c,d. c The city of Beer Sheva (*BS*) is located at the center, between the southern tip of the Shephela syncline in the north and the northern part of the Beer Sheva syncline in the south, axes symbolized by straight lines. *Curved solid lines* are boundaries of exposed Lower Eocene rocks (Mor Formation) after Bentor et al. (1970) and *dashed lines* are approximate boundaries between the Lower and Middle Eocene (Horsha Formation). *Barbed lines* are inferred faults south of Beer Sheva, after Gvirtzman (1969). See references to stations *X*, *Y*, *R* and *S* in the text. **d** Station-map. Stations designated "+" are in the Mor Formation and those marked by "Δ" are in the Horsha Formation. The Δ stations from 70 to 95 are located along Wadi Secher (Fig. 3.37). Stations 37–40 are on outcrops along Wadi Naim. Maps are marked by the Israeli grid (modified after Bahat and Grossmann 1988) (modified after Bahat and Grossmann 1988)

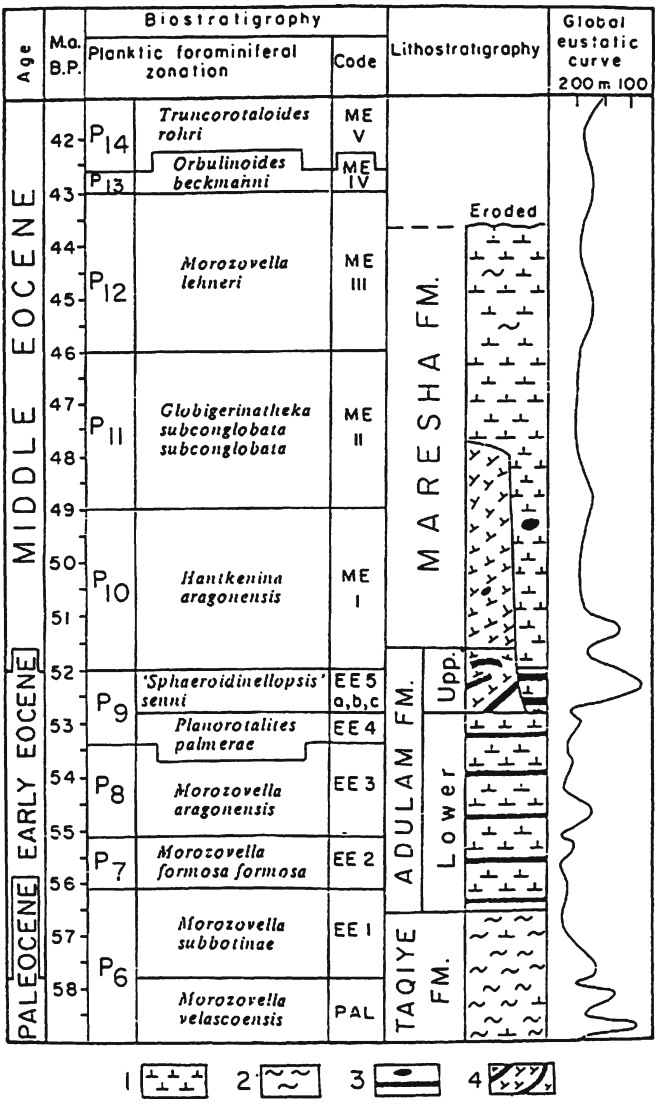

Fig. 3.34. Lithostratigraphy, biostratigraphy, time scale and eustatic sea-level curve of the Early (approximately Lower) to Middle Eocene with reference to the Shephela area. Legend: *1:* Chalk; *2:* Marl; *3:* Chert beds or nodules; *4:* Mass-transported units of chalk and chert (from Buchbinder et al. 1988)

neering projects requires basic data on the whole spectrum of structural relationships. The objective of this section is to synthesize the new results with previous findings and to report on the diversity of fracture in the Beer Sheva syncline. Also, the problems of joint set classification will be considered in some cases, and the various factors that could have contributed to the fracture complexity in this fold will be discussed. The methods of investigation that were applied in the investigation of the syncline are presented in Sect. 6.2, in connection with additional aspects of this topic.

3.4.2
Fractures in the Beer Sheva Syncline

3.4.2.1
General

Folding of the syncline is slight, and joints are mostly vertical or near-vertical. Twenty three fracture sets were distinguished in the Beer Sheva syncline, which are arranged in sixteen groups (Table 3.3). Each group commonly represents a set, except groups 1, 4, 7 and 11 that consist of two or more sets, which have specific genetic affinities. The groups are assembled in four rock units (I–IV in Table 3.3) on the basis of stratigraphy, lithology (Bentor and Vroman 1960; Braun et al. 1977; Buchbinder et al. 1988) and fracture appearance (Fig. 3.35a). The joints in the Mor Formation are represented by unit I, while units II, III and IV represent the joints of the Horsha Formation. Unit II is composed of thick layers (≥5 m), while units I, III and IV are composed of thin layers (≤1 m).

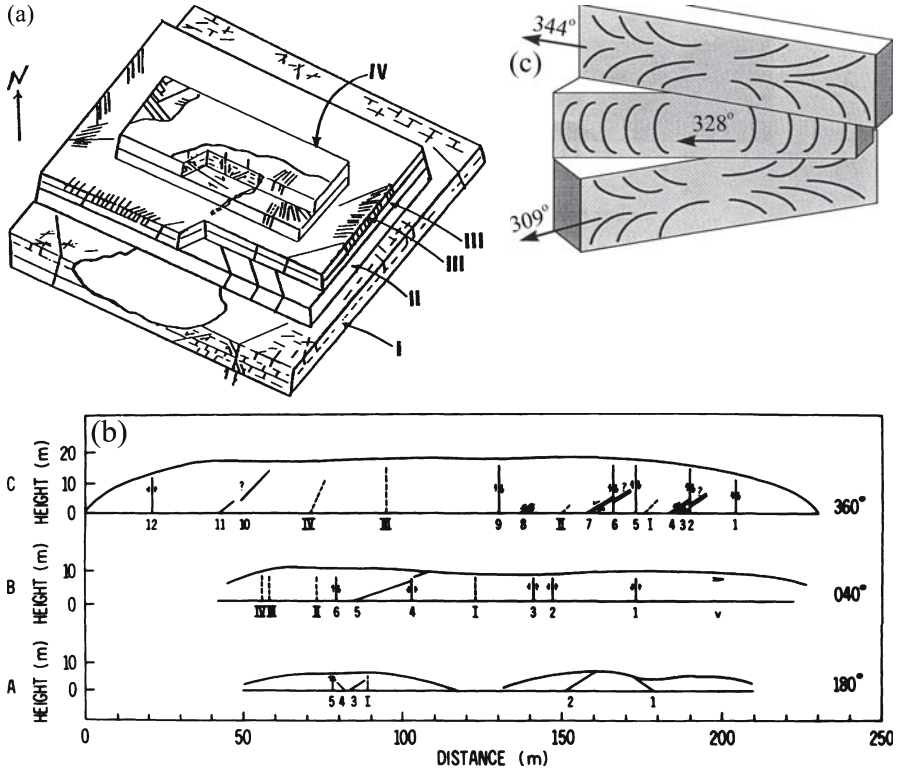

Fig. 3.35. a Diagrammatic (not to scale) illustration of the various fracture elements which are distinguishable in the Mor and Horsha Formations in the Beer Sheva syncline. The diagram consists of four stacked rock units (I–IV), see text for explanation. **b** Three sections from outcrops in unit I showing fracture relationships: Multilayer joints (*dashed lines*), vertical faults (*solid vertical lines*) and normal faults (*inclined lines*); the latter are emphasized where displaced by vertical faults. Numbers at the right indicate strike of outcrops. Stations 20, 63 and 58 (Bahat and Grossmann 1988) are marked by *A*, *B* and *C*, respectively. **c** Diagram of the conjugate three sets from the Mor Formation (see text for explanation)

Table 3.3. Distinct fracture phenomena in Lower and Middle Eocene chalks from the Beer Sheva syncline

Group and set	Eocene period of chalk	Formation and unit	Fracture strike azimuth (°)	Fracture style[a]	Fracture category (location in syncline)	Stress	Source
1a	Lower	Mor (I)	328	s.l.	Burial (distal end)	Regional	a
1b	Lower	Mor (I)	059	s.l.	Burial (distal end)	Regional	a, b
1c	Lower	Mor (I)	309	s.l. hybrid	Burial (distal end)	Regional	a, c
1d	Lower	Mor (I)	344	s.l. hybrid	Burial (distal end)	Regional	a, c
2	Lower	Mor (I)	055	s.l.	Burial (SE flank)	Synclinal	a
3	Lower	Mor (I)	294	Faults	Normal dips < 45° (throughout the fold)	Synclinal	d
4a	Lower	Mor (I)	335	m.l.	Uplift (distal, central)	Regional	a, e, f
4b	Lower	Mor (I)	335 305	Faults	Uplift vertical (distal, central)	Regional	f
5	Lower	Mor[b] (I)		m.l. composite	Post-uplift dips 55°–75° (distal)	Local	f
6	Middle	Early Horsha (II)	336	m.l.	Uplift (distal)	Regional	g
7a?	Middle	Horsha (III)	NE–N	s.l. rotational	Burial?	Synclinal	n.o.
7b?	Middle	Horsha (III)	N–NW	s.l. rotational	Uplift	Synclinal	n.o.
8	Middle	Horsha (III)	055	m.l.	Uplift (transversal)	Regional/synclinal	n.o.

Table 3.3. *Continued*

Group and set	Eocene period of chalk	Formation and unit	Fracture strike azimuth (˚)	Fracture style[a]	Fracture category (location in syncline)	Stress	Source
9	Middle	Horsha (III)	040, 130	Faults	Normal dips > 45˚ < (transversal)	Synclinal/regional	n.o.
10	Middle	Horsha (III)	N–NW	s.l.	Neotectonic[c] (cross joints) (transversal)	Regional/synclinal	i
11a	Middle	Horsha (IV)	318	Fault primary	Strike-slip (axial)	Synclinal	f
11b	Middle	Horsha (IV)		Faults secondary	Strike-slip (axial)	Local	f
11c	Middle	Horsha (IV)	344	s.l.	Confined to faults (axial)	Local	f
12	Middle	Horsha (IV)	012–035	s.l. rotational en echelon single fringe	Uplift (axial)	Synclinal	j, k
13	Middle	Horsha (IV)	062	m.l. rupturing	Syntectyonic-rebound (axial)	Synclinal	f
14	Middle	Horsha (IV)	040–060	m.l. planar	Uplift (axial)	Synclinal/regional	f
15	Middle	Horsha (IV)	358[d]	Faults		Regional	f
16	Middle	Horsha (IV)	350–014	s.l. rotational en echelon two fringes	Uplift (axial)	Regional	j, k

Group 1 consists of *sets 1a–1d*. *Groups 8* and *14* consist of *sets 8* and *14*, respectively. Single-layer joints: *s.l.*; multi-layer joints: *m.l.* Locations in the syncline include: *distal* (northeastern part), *lateral edge* (southeastern part), *central* (close to the centre of the fold), *transversal* (along Wadi Secher that approximately crosses the fold) and *axial* (along Wadi Naim that approximately parallels the synclinal axis). In the *series 1a–d*, *4a–b* and *11a–c* the various individual structures are genetically linked. *Sources: a*: Bahat and Grossmann (1988); *b–g*: Bahat (1989, 1987a, 1985, 1988, 1991a, 1991b); *i*: Engelder and Gross (1993); *j–k*: Bahat (1986, 1997). *n.o.*: (from unpublished report by Bahat and Shavit 1997).

[a] Joints are generally vertical.

[b] Supplemented by data from the Shephela syncline.

[c] Tentative definition based on preliminary studies.

[d] 358˚±10˚ mean of three conjugate faults.

Fractures in the syncline include s.l. joints, m.l. joints and normal faults. Each of these features occurs in several variations with different stratigraphic-structural associations. Some of the s.l. joints are associated with the burial stage, while the m.l. joints are considered to be uplift joints (Bahat 1991a). Other s.l. joints were clearly formed during uplift (Bahat 1999a). Vertical faults occasionally occur in association with m.l. joints, and there are some small strike-slip faults. Wherever two types of fracture strike in different directions, they are assigned to different sets, since their propagation (which is normal to the least principal stress S_{Hmin}) could not be the same for both structures at the same time.

3.4.2.2
Fractures in Unit I (Mor Formation)

Nine joint sets are identified in the Mor Formation (Table 3.3). Those that are associated with the same stress system are grouped together and marked by letters within the group (sets 1a–1d and 4a–4b). Three typical outcrops are shown in Fig. 3.35b.

Group 1. These include s.l. joint sets that are associated with burial. Four sets are identified according to characteristic orientation and appearance (Bahat and Grossmann 1988). Sets 1a and 1b consist of a cross-fold set striking 328°, and approximately orthogonal to it a set striking 059°. Set 328° generally predates set 059°, but there are also indications of reverse order (Bahat 1988a, Fig. 5). These sets are observed particularly in the northeastern distal part of the syncline. In some outcrops, both orthogonal sets are exposed abutting each other, in others only one of the sets is exposed. The orthogonal sets are also concentrated in the southwestern distal part of the Shephela syncline and along the southeast flank of this fold (Bahat and Grossmann 1988). As far as can be seen from exposures, cross-fold joints are rare in the northwestern flank of the Beer Sheva syncline.

Sets 1c and 1d are hybrid s.l. joint sets (Hancock 1985; Bahat 1987a): 1c strikes 309°, and 1d strikes 344°. Both sets occasionally occur in association with set 328° (Fig. 3.35c and 3.36a), but they appear mostly in separate outcrops. The age relation between sets 1a–1b vs. 1c–1d is not clear, although in one outcrop there is evidence that set 328° preceded set 344° (Bahat 1991a, p. 242).

At rare localities, the time sequence of adjacent joints of a given set can be determined based on the curving of joint terminations, where late joints curve toward early joints and arrest at approximately right angles (Bahat 1983; Dyer 1988). In the exposure shown in Fig. 3.36b, joint C postdates joint B, which is younger than joint A. In other exposures, the sequence is more difficult to determine (e.g., Bahat 1988b, Fig. 5; Bahat 1991a, Fig. 3.34).

Group 2. These include joints that are concentrated on the southeastern flank of the Beer Sheva syncline, trending predominantly 055° (Bahat and Grossmann 1988, stations 26, 27, 48, 49 and 50). Cross-fold joints are very rare in these stations. Morphologically, they do not resemble joints from set 1b, but look more like joints of group 7 (Sect. 3.4.2.4). There is a slight, but perhaps significant age difference between the layers that host fracture groups 1 and 2. Both groups belong to the Mor Formation, but in the Beer Sheva syncline the layers that host group 2 occur in an area of a gradual transition to the Horsha Formation along Wadi Secher (Fig. 3.33c) (Bahat and Grossmann 1988, Fig. 3).

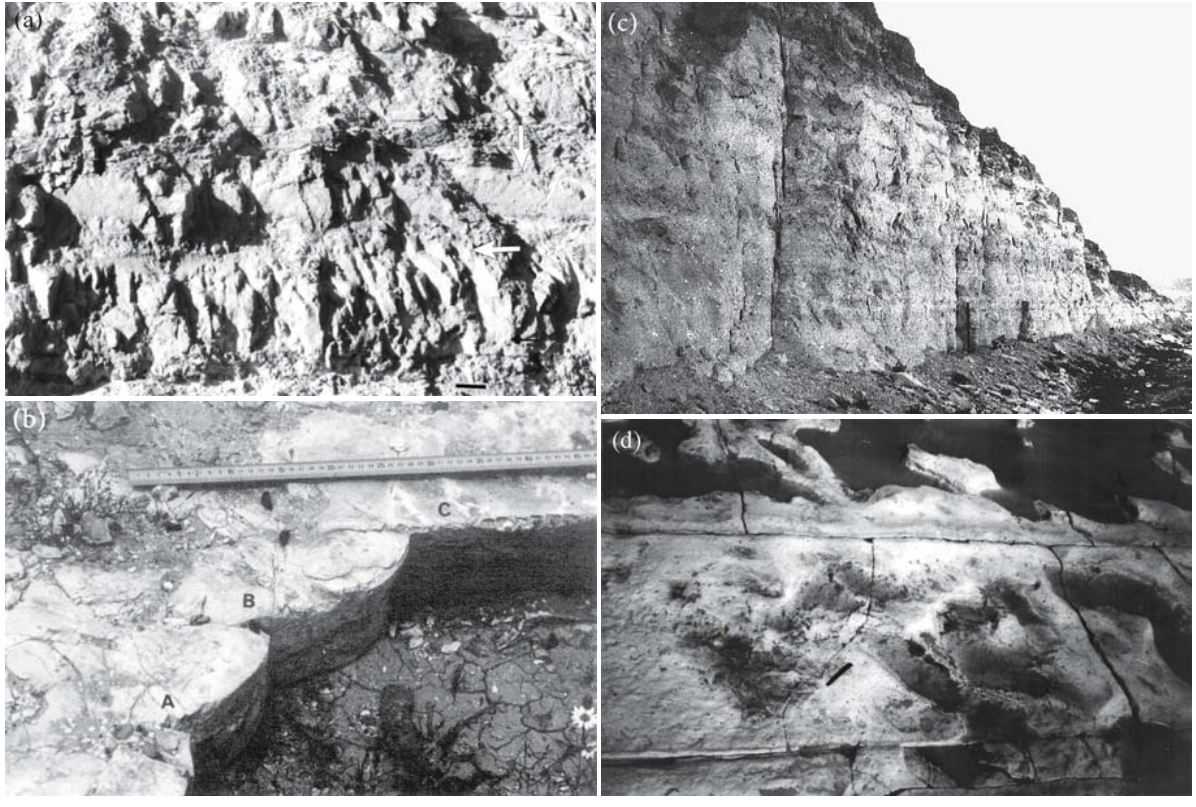

Fig. 3.36a–d. Photographs of outcrops. **a** Joints of sets 328° (marked by *horizontal arrow*) and 309° (marked by *vertical arrow*), cutting the Mor Formation (unit I). *Scale bar* is 25 cm. **b** Joints of set 328° cutting the Mor Formation (unit I), showing the sequence of formation: *A* postdates joint *B*, and *C* is younger than *B*. **c** Multilayer joints cut thick layers in the Horsha Formation (unit II). *Scale* is 90 cm. **d** Cross joint cutting the Horsha Formation (unit III). *Scale bar* is 5 cm

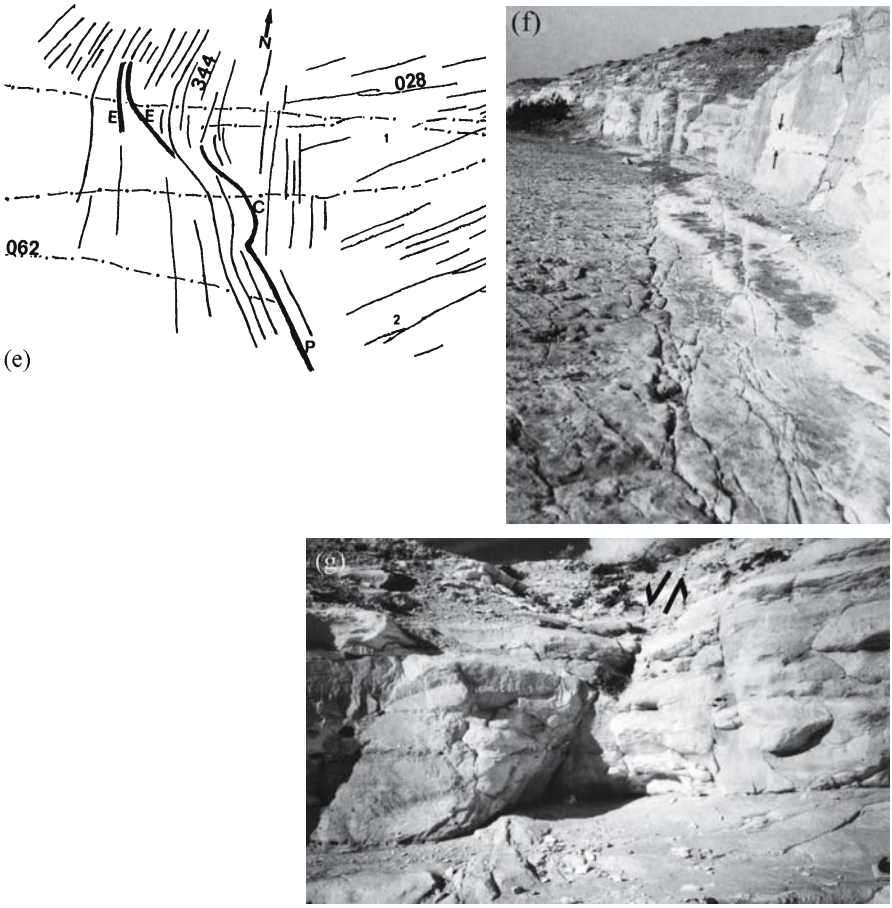

Fig. 3.36e–g. Photographs of outcrops. **e** A syntectonic joint set curves sympathetically with a primary A and secondary faults *B* and *C* in the Horsha Formation (unit IV). **f** Joints from set 062° dissect unit IV along Wadi Naim. They cut the wadi floor anastamotically and become planar m.l. joints as they cut the cliff (unit IV), layer marked by *arrows* is 90 cm thick. **g** Joints of group 12 are displaced by a normal fault from group 15 (unit IV)

Group 3. These include low-angle (dip ≤ 45°) normal faults that strike about 294° and are closely associated with s.l. joint sets 328° and 059° (Bahat 1985; Gross et al. 1997). These faults are thought to be a result of intra-synclinal seismic tremors (Bahat 1985; Buchbinder et al. 1988) (Fig. 3.35bA).

Group 4. This group, trending about 335°, includes vertical m.l. fractures that cut many layers (Bahat 1988a; Bahat 1991a, p. 306). The m.l. fractures are divided into two sets (Fig. 3.35bC). Set 4a consists of non-displacing m.l. joints, occasionally adjacent to vertical faults of set 4b, which developed from the former as a result of changing stress. Set 4b consists of vertical faults, one of which displaces a low-angle normal fault of group 3 (Bahat 1991a, p. 283), suggesting a sequence of (1) early, low-angle normal faults from group 3, (2) set 4a, and (3) set 4b.

Group 5. These include post-uplift joints that occur in the Shephela syncline (Bahat 1991a, Fig. 5.24). They cross the local Lower Eocene chalks at 55° to 75° dip angles and show a relationship to the local topography. The surface morphology of these joints is quite different from burial, syntectonic and uplift joints. They are composite radial fractures, interacting with each other, resembling other post-uplift composite fractures in sandstone and in granite (Bahat et al. 1995, 1999) (Fig. 3.23c and 4.27).

3.4.2.3
Fractures in Unit II (Horsha Formation)

Rocks of this unit are exposed in the northeastern part of the syncline, particularly along the Beer Sheva-Nitsana road (Bahat and Grossmann 1988).

Group 6. Included here are joints oriented 336°, cutting thick chalk layers of about 6–8 m. These joints are flat and smooth, not marked by plumes or *en echelon* fringes, or any other fracture markings. Joint spacing is irregular, varying from 50 cm to 20 m (Fig. 3.36c) (Bahat 1991b). The relation between fracture spacing and bed thickness (e.g., Ladeira and Price 1981) suggest that this set formed after, rather than in the course of sedimentation (Hodgson 1961b). By way of comparison, periodic arrest marks on syntectonic joints in strongly deformed, thick Senonian chalk layers (Bahat 1991a, Fig. 3.22) imply rhythmic fracture propagation, most likely induced by pore pressure (Secor 1969) under intense tectonic strain of the kind that never affected the almost horizontal sediments of the Eocene. These layers never attained over-pressure of fluids during the burial stage, and the m.l. joints of group 6 could develop only after the chalk was sufficiently dewatered and lithified, possibly not before uplift.

3.4.2.4
Fractures in Unit III (Horsha Formation)

Rocks of this unit are exposed along Wadi Secher, which runs down the southeastern flank towards the synclinal center.

Group 7. This group consists of s.l. joints that display strike rotation along Wadi Secher (Fig. 3.33d and 3.37), from about 090° to 020° along its southeastern part, through the 300–360° range along the sector of the wadi that crosses the central part of the syncline further west. Fracture patterns were categorized along Wadi Secher (Fig. 3.37) (with the exception of station 83), according to the "selection method" (Sect. 6.2.1.2). The following features stand out:

1. In the eastern area (stations 71 to 80), most outcrops are dominated by ENE striking joints (050–083°). Further west, the joints strike gradually more to NNE, and there is an increase in the number of N-S and NNW trending joints.
2. Adjacent stations usually have similar joint sets, with subtle transitions. For instance, the major set in the eastern part of station 86B is 060°, and the minor set is 330°; a little further west set 040° becomes dominant, and more to the west set 330° becomes the more important set. In station 86C, set 025° is more important on the eastern side and set 320° is dominant on the western part of the outcrop. However,

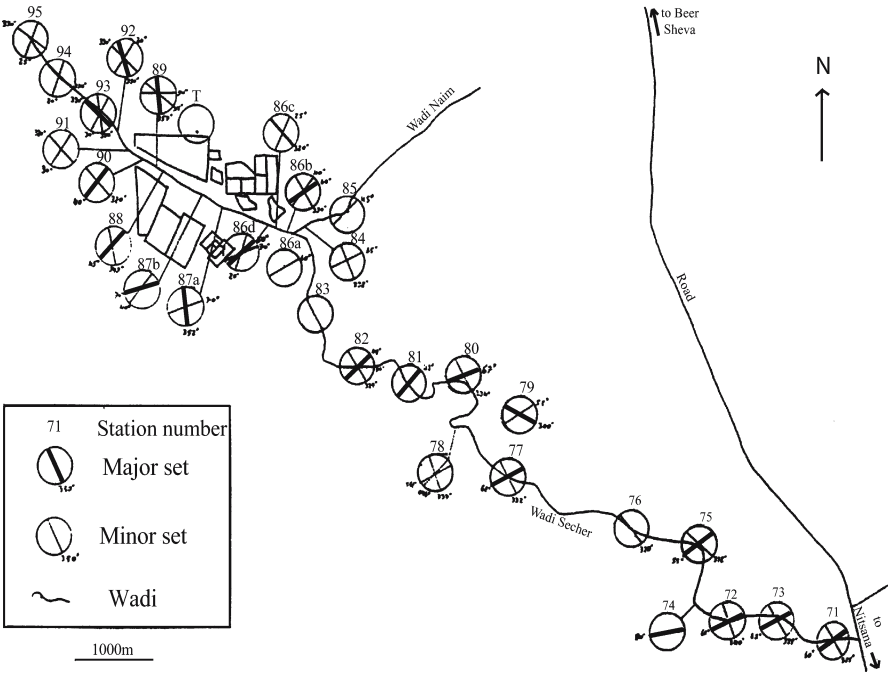

Fig. 3.37. Map-diagram summarizing joint orientations at stations 71–95 along Wadi Secher. *Circles* show the azimuths of sets at each station (with the exception of station 83) (after Bahat and Shavit 1997)

set 060° unexpectedly returns as the dominant set in station 86D, where 020° and 330° are the two minor sets.

3. In spite of the many "unexpected" returns of ENE trending joints, the overall emerging pattern is the increase in importance of NNE and NNW trending joints towards the west.
4. A summary of joint orientation in stations 71–95 (not including station 83) shows the general increase in importance of NNE and N-NNW trending joints relative to ENE trending joints, when moving from east to west along Wadi Secher (Fig. 3.38a–c). Hence, there is a subtle counter clockwise joint rotation in Wadi Secher.

Station 83 (in Fig. 3.37) was studied by the "comprehensive method" (Sect. 6.2.1.2) in greater detail, along a 700 m exposure in Wadi Secher. Joint strikes were measured separately for five "layer groups" (Fig. 3.39a). Average joint orientations in the various layer-groups show distinctive traits (Table 3.4). The combined strikes of s.l. joints from all layer groups of the Horsha Formation at station 83 shows a single maximum at 48 ±16° (F in Table 3.4). Average trends rotate gradually counter clockwise from the older group-layer B through C and D to the younger group-layer E (from 63° through 55° and 51° to 42°, respectively). An exception is the average 42° in layer-group A, which contradicts the trend that was through layer-groups B–E. Joints fringed with *en echelon* segmentation occasionally occur in upper parts of the western cliff of the wadi resemble the *en echelon* fringes that occur in Wadi Naim (see group 12 below).

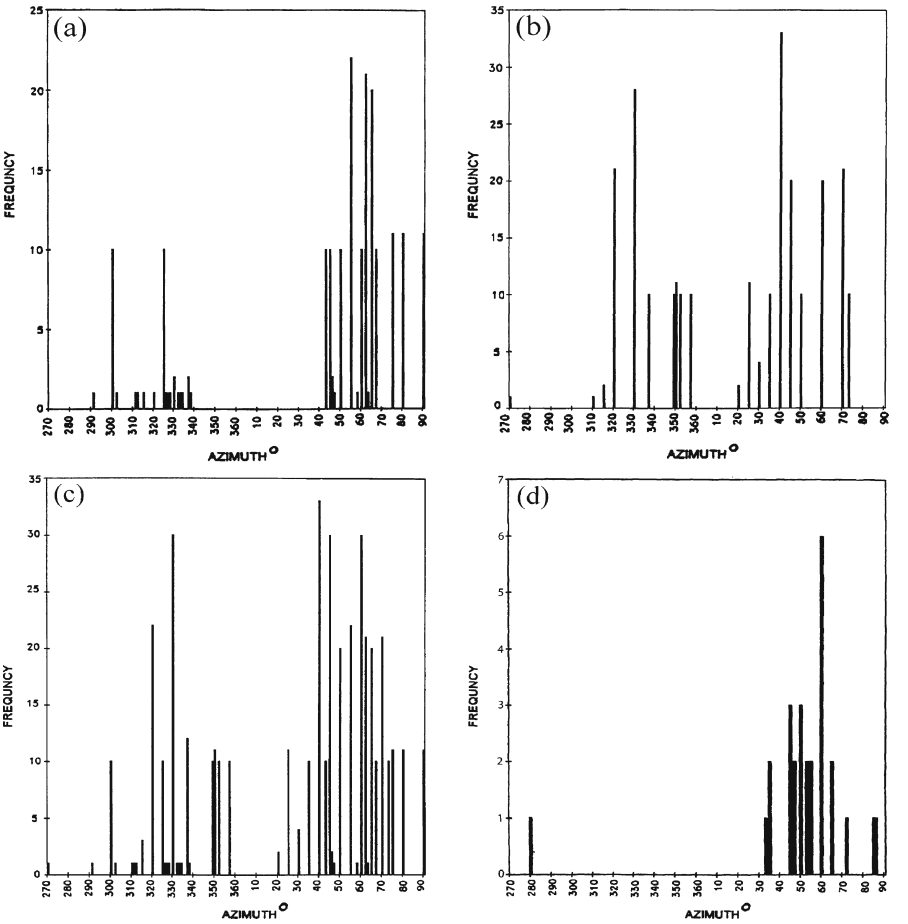

Fig. 3.38. Histograms summarizing data on s.l. joints from all stations in Fig. 3.37, not including station 83. **a** Stations 71 to 86A. **b** Stations 86B to 95. **c** Stations 71 to 95. **d** Multilayer joints in station 83 (after Bahat and Shavit 1997)

Table 3.4.
Strikes and properties of joints trending NE and NW in station 83, Wadi Secher

Layer group	Average of NE joints			Average of NW joints		
A	41.7°	(16.9)	[57]	–	–	–
B	62.7°	(15.0)	[39]	281.3°	(4.8)	[4]
C	55.0°	(7.7)	[244]	–	–	–
D	51.1°	(7.4)	[51]	329.5°	(3.7)	[19]
E	41.9°	(16.1)	[122]	321.1°	(16.5)	[32]
F	47.6°	(15.7)	[670]	318.1°	(17.2)	[85]
G	55.0°	(13.1)	[25]	280°		[1]

( ) and [ ] designate respectively, standard deviation and number of measurements, *A–E* are layer-groups in Fig. 3.39a, *F* is a summary of *A–E*, and *G* is the summary of m.l. joints in station 83 in Fig. 3.37 (after Bahat and Shavit 1997).

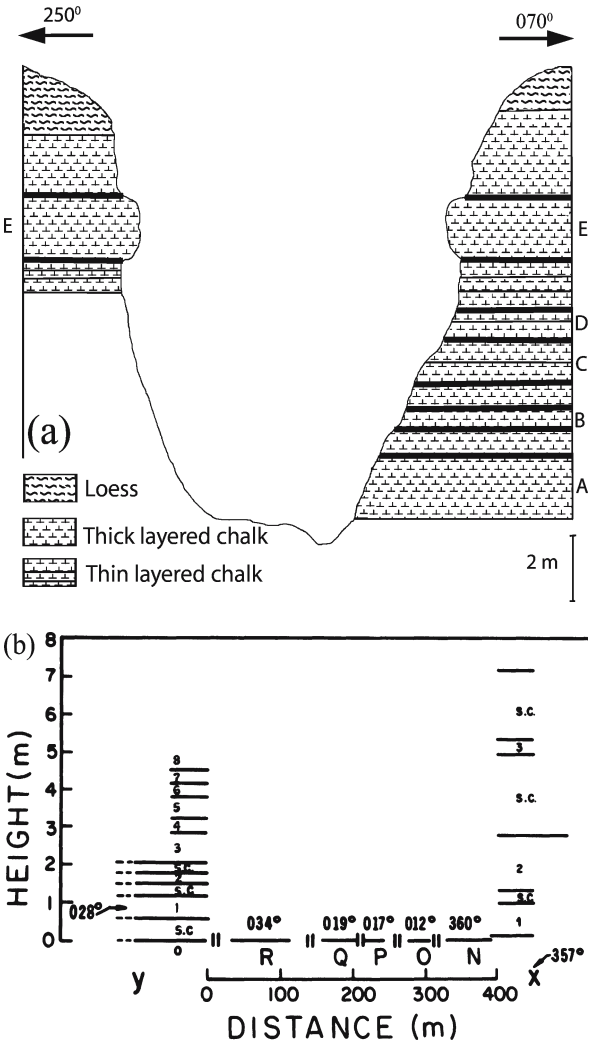

Fig. 3.39.
a Section across Wadi Secher at station 83, showing layer-groups *A* to *E* on the cliffs (note vertical scale) (after Bahat and Shavit 1997). **b** Diagram of outcrops *X* (set 16, Table 3.3) and *Y* (set 12), including floors *N*–*R* between them, showing rotation in mean azimuths of joints from 357° to 034°. Beds of soft chalk (*s.c.*) alternate with hard chalk beds designated by numbers. The two small vertical lines between floors *N* and *Y* represent talus (from Bahat 1986a)

Group 8. Twenty five m.l. joints constitute a set along a 600 m exposure at station 83, with an average trend of 055.0 ±13.1° (Fig. 3.38d). Their average differs by 7.5° from the s.l. average (F in Table 3.4). This relative orientation matching is noticeable, compared with the more pronounced deviations of m.l. azimuths from those of s.l. in the Mor Formation (Bahat 1991a, p. 306). Like m.l. joints in units I and II (Bahat 1991a, Fig. 5.16), group 8 often occurs in fracture zones with closely spaced joints.

The discrimination between s.l. burial joints and m.l. uplift joint in unit I is quite simple due to considerable morphological differences between the two fracture types. On the other hand, the distinction between s.l. and m.l. uplift joints in unit III is not always clear, because in some outcrops there are "transitional" fractures between the s.l. joints of small widths (heights, Fig. 2.8a) and m.l. joints of great widths. Single-

layer joints and "transitional" joints are offset by normal faults, but no contacts between m.l. joints and normal faults were found in unit III. Therefore, it appears that these faults are younger than the s.l. and the "transitional" joints. It is however not clear that the normal faults are younger than the m.l. joints.

Group 9. This group consists of four normal faults, dipping above and below 45°, and striking 052° and 130°, south of station 83. A study of the largest and best exposed fault of this series is discussed in Sect. 6.7).

Group 10. This is a distinct s.l. group which consists of "cross-joints" (as distinguished from "cross-fold joints") that are straight along their central parts, oriented in the N-NW direction, but their tips gradually curve orthogonally towards joints of an earlier set (Fig. 3.36d). Their shape resembles the geometry of curving cross joints whose central straight part parallel to the S_{Hmax} of the neotectonic stress field or its Tertiary predecessor in eastern North America (Engelder and Gross 1993). These cross-joints presumably represent the latest s.l. joints in unit III, in association with uplift and erosion (Hancock and Engelder 1989). There is no indication, however, that these joints are younger than joints of unit IV.

3.4.2.5
Fractures in Unit IV (Horsha Formation)

This unit is exposed in Wadi Naim, along the synclinal axis (Fig. 3.33c,d).

Group 11. Fractures of this group, which cut unit IV, exhibit a unique fault termination zone that consists of three major elements:

1. A primary fault.
2. Secondary faults.
3. A set of fault-associated joints (Fig. 3.36e). A description of group 11 is presented in Sect. 6.6.

Group 12. This group consists of s.l. joints oriented in the 012–035° range, rotating counter clockwise from younger to older layers upstream Wadi Naim (Bahat 1986a, 1999a) (Fig. 3.39b). *En echelon* segmentation occurs intensively along the lower fringe of these joints, and rotates covariantly with the parent joints. Note that *en echelon* fringes are almost exclusive to groups 12 and 16 (see below), and occasionally in group 7 (see above).

Group 13. Joints of set 062° occur in various parts of Wadi Naim, along tens and even hundreds of meters. Unlike the straight m.l. joints of groups 5, 8 and 14, these joints undulate and "branch" from each other anastomotically (viewed in horizontal sections on a platform) (Fig. 3.36f), but on the average strike 062°. They display irregular spacing, and their openings vary from about 1 mm to several centimeters. Intensive irregular cracking occurs at and adjacent to these fractures (as revealed by opening with a chisel, and on vertical exposures). This set was apparently formed by breakage

during an extended buckling-rebound when the compression normal to the syncline axis relaxed (Bahat 1987b), implying an important difference between the genesis of set 062° as compared with the other joint sets (e.g., group 12). Unlike those other sets, which were formed by remote compression co-axial to their strike, set 062° was formed by remote tension. The multilayer joints in general and set 062° in particular are the most important vertical conduits of ground water in the syncline (Sect. 6.9).

Group 14. These m.l. joints strike in the 040–060° range and form remarkably planar cliffs in Wadi Naim, and they are straighter than m.l. joints that cut other units in the syncline. These m.l. joints overprint s.l. joints of group 12 or cut them at small angles (less than 30°). The wadi exposures provide a perfect view of fracture, both at the cliff and in the adjacent floor, revealing all details of the transition from group 13 to group 14. Joints of set 062° significantly change their appearance from an anastomose style when dissecting layers 1–2 in the wadi floor (Fig. 3.39b) to planar joints of group 14 that cut the upper layers of the cliff (Fig. 3.36f) (Bahat 1987b). Hence, following the buckling-rebound that created set 062°, the m.l. joints of group 14 were formed during an advanced uplift process, preserving the same approximate strike for both joint groups. Compared with the profusion of fracture markings on s.l. burial joints cutting Lower Eocene chalks and syntectonic joints cutting Santonian chalks, fracture markings are rare on all m.l. joints. Perhaps it reflects fracture by fluid pressure in the former two cases and tension unrelated to fluid pressure in the latter.

Group 15. These are three neighboring conjugate normal faults (dipping both above and below 45°), striking 358 ±10°. These faults offset s.l. joints from group 12 along Wadi Naim (Fig. 3.36g). There are no contacts between normal faults and m.l. joints from group 14, leaving no clue as to their age relationship (see also Sect. 6.7).

Group 16. This is a 350–014° striking joint set, with *en echelon* fringes both at the top and bottom of the parent joint (Fig. 2.35a) (see group 12 for comparison, and elaboration in Bahat 1986a, 1997).

3.4.3
Fracture Diversity in the Beer Sheva Syncline

The high fracture diversity, allowing the distinction of no less than sixteen groups, may appear bewildering to those not familiar with the Beer Sheva syncline, making one wonder if all the above described twenty three proposed fracture sets in Table 3.3 are really distinct sets, particularly since there are certain proposed sets from different fracture groups that have similar orientations. This issue is addressed below.

3.4.3.1
Strike Superposition of Different Joint Sets

Seven strike superpositions of suspected different joint sets (Table 3.3) are examined for the possibility of genetic linkages, which if found, would reduce the actual number of sets.

Superposition 1. The distinction between s.l. sets 1b and 2 (striking 059° and 055°, respectively) is mostly based on considerable morphological differences. Set 1b characteristically occurs in orthogonal relationship with a cross-fold set 1a, has very small apertures (<0.1 mm) and is confined to the distal end of the syncline. Set 2, on the other hand, does not have an orthogonal counterpart set, has variable openings (apertures up to 10 mm and more) and occurs in the southeastern flank of the syncline. These differences imply different genetic origins for the two sets despite their almost identical orientations: Set 1b is probably an early burial set, whereas set 2 was possibly formed later (Sect. 3.4.2.2).

Superposition 2. Sets 8 and 14 strike about 055°. These m.l. joints are similar in some respects, and they may be genetically related. It is possible that fracturing in these sets took place in different times, or perhaps, fracture occurred in units III and IV at about the same time. There is no compelling evidence either way.

Superposition 3. There is a genetic linkage between joints of sets 4a and 4b trending 335° (Fig. 3.35bC). They are geographically adjacent and possibly the 4b vertical faults developed from the 4a vertical multilayer joints when local stress conditions changed. Thus, they formed in two distinct stress fields (S_{Hmax} parallel and inclined to sets 4a and 4b, respectively) into two fracture sets. Early joints that developed into faults are well known from other fracture provinces (e.g., Segall and Pollard 1983).

Superposition 4. There is no relative age indication for (group) set 6 m.l. joints. Their orientation (336°) suggests genetic association with set 4 m.l. joints that trend in the same direction. This possibility is however challenged by the presence of Upper Pleistocene gypsum mineralization along joints of set 6 (Issar et al. 1988). Some of these gypsum crystals are orthogonal to the jointing, which is not characteristic of set 4. This orthogonality suggests that opening of set 6 joints might be related to the age of mineralization (Ramsay 1980). Thus, in spite of uncertainties of relative age, it appears that set 6 is associated with processes younger than those associated with set 4.

Superposition 5. The strike slip fault (set 11a) preceded the adjacent set 028° that developed during an early stage of the uplift (Bahat 1987b). This fault was formed by horizontal compression along 344°, as evidenced by the orientation of joint set 11c (Fig. 3.36e). The direction of compression is at an approximate 30° angle to the strike of the strike-slip fault. Group 11 is found in a small area only about 16 m long and 7 m wide in Wadi Naim. Thus, a synclinal stress is more likely to be the cause of group 11 formation rather than a regional one.

However, compression from 344° coincides with the strike of set 1d, which occurs in various areas of the syncline and is considered to be a regional direction (Eyal and Reches 1983; Bahat 1999b). Although there is probably no genetic connection between groups 1d and 11, such a connection may still be proven by new findings. A regional compression from 344° could be tectonically effective in the syncline, forming group 11, a short time before the synclinal rebound and stress rotation (Bahat 1999a).

Superposition 6. Joints of set 10 are oriented N-NW and may be suspected to have been produced by the stress field that formed some of the joints of set 7 of a similar trend. However, their distinctive morphologic features, the rotational style of set 7 and the characteristic curvature of set 10 (Fig. 3.36d) all point to different genetic groups.

Superposition 7. Both groups 15 and 16 strike approximately N-S, yet they represent two different mechanisms: One that produced normal faults, and one that that produced joints with two *en echelon* fringes. Nevertheless, their genetic linkage cannot be excluded (Sect. 3.4.6.2).

In summary, we tried to show in the above review how fracturing episodes may be fitted to the documented sets. There is no compelling evidence to rule out genetic linkage between sets 4 and 6, 8 and 14, 1d and 11c, as well as 15 and 16. Combining representative sets from these four couples would reduce the total number of sets in Table 3.3 from 23 to about 19. Yet it is equally likely that superpositions 1, 3 and 6 combine sets of different genetic origin, and mere similarities in strike directions are not a sufficient reason for grouping them together. The great structural diversity in the Beer Sheva syncline may therefore be real.

3.4.3.2
Single-Layer Burial Joints versus Single-Layer Uplift Joints

Burial s.l. joints form early in the history of the rock and typically arrest at layer boundaries. Uplift m.l. joints, on the other hand, develop late in the history of the rock and cross layer boundaries. The discrimination between these two groups is relatively simple, because the m.l. joints, cutting many layers (or thick strata), have wider open-

Table 3.5. Fracture properties of single-layer burial and single-layer uplift joints

	Single-layer burial joints (Mor Formation)	Single-layer uplift joints (Horsha Formation)
1	Orthogonal cross-fold and strike sets	There is no orthogonal jointing
2	There are conjugate joint sets	There are no conjugate joint sets
3	Joints generally are pre-early normal faulting	Joints are post early srike-slip faulting
4	Not contemporaneous with any m.l. set	Contemporaneous with the m.l. 062° set
5	There is no joint rotation	Joint rotation is extensive
6	Older layers fracture first	Younger layers fracture first
7	No fracture interaction among joints	Considerable fracture interaction among joints of set 028°
8	No en echelon segmentation	Fringes of en echelon segmentation associated with NE trending joints
9	Closed joints (aperture <0.1 mm)	Joint opening varies considerably (from 0 to >10 mm)

Sources for data and explanation are given in text.

ings and their spacing is irregular and considerably larger than of the s.l. joints (Fig. 3.36c) (Bahat 1991a; Ghosh 1993, p. 492). Much more difficult is the distinction between burial s.l. joints and uplift s.l. joints, because very often they display similar outcrop features. The distinction is important because it can be useful in deciphering geological processes. Table 3.5 lists nine diagnostic properties of s.l. burial joints and uplift joints in the Mor and Horsha formations (see also Bahat 1999a). One of these properties, the rotation of joint strikes under regional stresses, is treated in Sect. 6.3.

3.4.4 The Structural Interpretation of *En Echelon* Fringes in the Beer Sheva Syncline

En echelon fringes in the Beer Sheva syncline are characterized in terms of style and in terms of paleostress directions (see Sects. 2.2.5 and 2.2.7).

3.4.4.1 *Three Styles of* En Echelon *Segmentation*

Three styles of *en echelon* segmentation can be distinguished in the Beer Sheva syncline. They are represented by set X (unit IV), set O-Y3 (unit IV) and joint S (unit III) (Table 2.1). Set X has *en echelon* fringes both below and above the parent joint (Fig. 2.35a), and in both, segment rotation is counter clockwise, ranging in strike between 338° and 342°. Quite distinct from set X is set O-Y3 in station Y. In this set, a fringe occurs only below the parent joint and segment rotation is clockwise, ranging in strike between 026° and 053° (corresponding to the clockwise rotation of the parent joints). The curved joint in station Y (Fig. 2.35c,d) undulates considerably along the strike but the segmentation is confined to a small azimuth range (043–047°), which is only a limited spread within the range 026° and 053° mentioned above. The concentric joint (Fig. 3.40b) is a subvariation in set O-Y3. Joint S is best represented by part D that strikes 073°, whose general clockwise segment rotation is in the 073–083° range (Fig. 2.38 and 3.40a). However, some counter clockwise segment rotation also is observed on this joint. These three styles differ from the Mt. Carmel style (Fig. 3.40c) (Bahat 1997).

3.4.4.2 *Three Paleostress Directions Set*

Set X consists of joints that strike between 350° and 014° in outcrop X, and seems to reflect a regional N-S post Middle Eocene paleostress. This stress corresponds to the "last phase" N-S regional compression reported by Letouzey and Tremolieres (1980) from southern Israel. Mart and Horowitz (1981, Table I) also described a regional N-S trending joint system along the western shoulder of the Dead Sea rift. Joints from set O-Y3 on the other hand strike over a wide range, from 012° to 035° and are apparently associated with synclinal stresses (Bahat 1997). The joint direction (073°) and *en echelon* characteristics found in part D from station W.S. (Fig. 3.40a) are quite different from X and O-Y3 sets, suggesting three different stress fields.

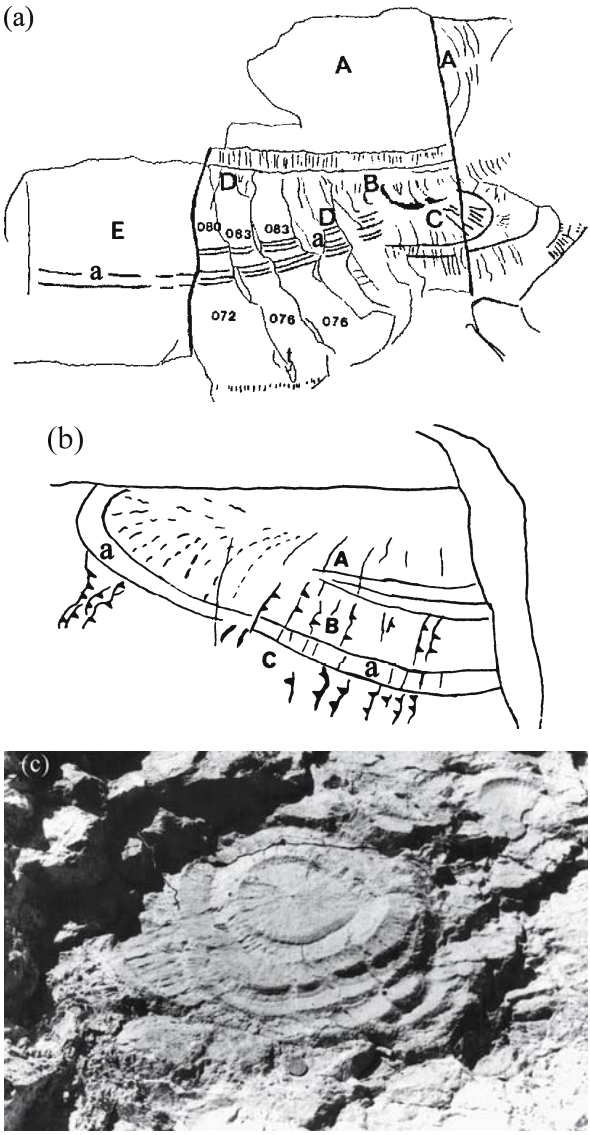

Fig. 3.40.
a Morphological sketch of a composite joint in Wadi Secher (station S in Fig. 3.33c, see Fig. 2.38). The fracture surface is divided into five parts, *A* to *E*. Lower edges of tear surfaces and arrest marks are marked *t* and *a*, respectively. *Numbers* on segments are azimuths (°). Two late fractures are marked by *thick, sub-vertical lines*. *Scale bar* is 15 cm. **b** The "concentric joint". A discontinuous breakdown occurs below the outer arrest mark *a*. The sense of rotation of overlapping barbs is counter clockwise in zones *A* and *B*. Segments at the right side of fringe rotate clockwise with respect to the parent joint (*triangles* along *heavy lines* point to direction of overlapping segments). This rotation conforms to the other rotations in outcrop *Y*. However, segments at the left side of fringe show counter clockwise rotation, which is in conformity with the rotation of overlapping barbs on the joint surface. *Scale bar* is 20 cm. **c** A discoid joint on Cenomanian chalk Mount Carmel, northern Israel cutting. The discoid displays several concentric fringes with a non-uniform breakdown. Segment rotation is counter clockwise on the left side of the discoid and is clockwise on the right side of the joint. There is no overlapping in the upper and lower parts of the discoid (see coin for scale)

3.4.5 Fold-Crossing Joints

3.4.5.1 *General*

The geometric relationships between joints and asymmetric folds are discussed in Sect. 3.2. Quite different are the geometries of joints that develop across symmetric folds (Fig. 3.20b). These have been studied by many investigators (e.g., Price 1966, Fig. 43;

Stearns 1968). De Sitter (1964) demonstrated a 90° rotation of the S_{Hmax} between symmetrical syncline and anticline folds. The rotation occurred due to local tension at the crest of the anticlines and compression at the trough of the synclines, like in a bent beam (outer-arc, Fig. 3.19a) (e.g., Hobbs et al. 1976, Fig. 4.33a; Burger and Hamill (1976); Ghosh 1993, p. 254). All these studies show relatively simple fold-fracture structures, with only a few fracture sets (Fig. 3.41). For instance, Stearns and Friedman (1972) found only five major fracture patterns associated with folds. Ramsay and Huber (1987, p. 655) consider the combination of four sets, two extensile sets (in cross-fold and in strike orientations) and two conjugate sets to be "classical" (which approximates F_1 and F_2 in Fig. 3.20b). When this classical view is "maximized" by additional sets, one obtains all the sets in Fig. 3.20b and 3.41 that still maintain a "simple" fold-joint geometry.

This simplicity often reflects a compromise between deviations in fracture direction that are dictated by local stress field changes around singularities (e.g., Rawnsley et al. 1992) and by the ongoing process of folding (Dieterich and Carter 1969; Burger and Hamill 1976), acting against the tendency of the remote stress to avoid changes by "self-correction". Self-correction, also known as "local symmetry", is a term adapted here from small-scale cracking mechanisms. It is a property that distinguishes between fracture behavior in isotropic and anisotropic materials (Ravi-Chandar and Knauss 1999). While arbitrary loading on a structure could result in a mixed mode loading, a growing crack quickly turns so as to reorient itself into mode I symmetry in isotropic materials. On the other hand, anisotropy forces the crack to grow under mixed mode loading along specific planes in crystals and along faults in earthquakes. Occasionally, however, self-correction into mode I may manifest itself along specific planes in crystals (Cramer et al. 2000 and Fig. 2.23d) as well as along layer boundaries in stratified formations (e.g., Bahat 1991a, Fig. 5.22) and along faults in earthquakes (Bahat 1982). Thus, fold-crossing joints tend toward simplified patterns, due to control by some self-correction mechanism.

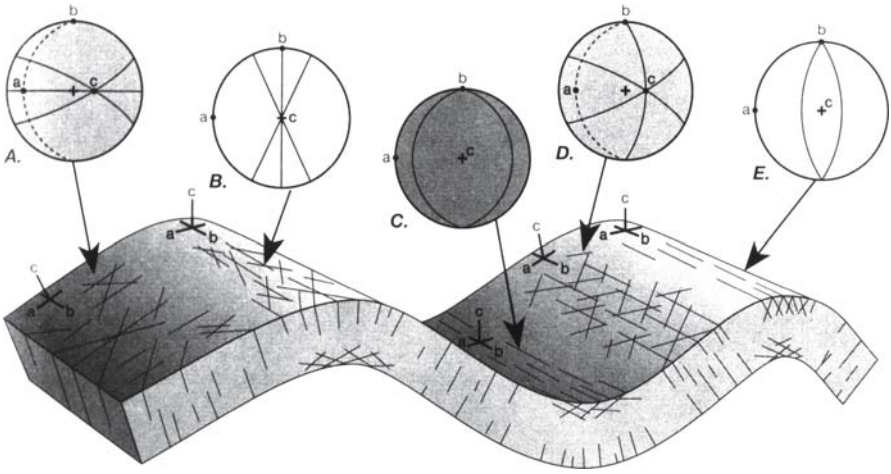

Fig. 3.41. Simple fold-fracture relationship. *a*, *b* and *c* are three tectonic axes. The orientation of *b* is constant, parallel to bedding, while *a* and *c* change their attitudes in different parts of the fold. The stereographic projections show orientations of the coordinate system, of the bedding where it is not horizontal (*dotted great circles*) and of the fractures (*solid great circles*) (from Twiss and Moores 1992)

3.4.5.2 *Fold-Joint Relationships in the Beer Sheva Syncline versus the Simple Fold-Fracture Concept*

Structural features of the Mor and Horsha Formations. We compare the "simple" fold-fracture pattern in Fig. 3.41 to the fracture pattern in the Beer Sheva syncline (Table 3.3, Fig. 3.35a).

1. Outstanding in unit I are two orthogonal sets of s.l. burial joints, trending NW and NE. These are only found in the distal parts of the Beer Sheva and the Shephela synclines. Less common are non-orthogonal s.l. joints, striking NE-ENE. In some outcrops, NNW or WNW joints are added to or occur instead of the more common NW joints. Uplift m.l. joints are often oriented NW-WNW. In one station, a normal fault is displaced along a sheared, vertical m.l. fault (set 4b).
2. NW trending uplift joints cut massive chalks of unit II in the Horsha Formation, above the Mor Formation.
3. In the eastern flank of the Beer Sheva syncline, the most common fractures in unit III are NNE-NE-ENE s.l. joints and m.l. uplift joints trending NE. Further west towards the synclinal center, NW trending s.l. and m.l. joints occur in increasing abundance along Wadi Secher. A series of conjugate, normal faults also occurs along the wadi.
4. An early feature in unit IV is a right-lateral strike slip fault system, striking NNW. A syntectonic, anastomosing joint set sub-parallel to the synclinal axis occurs along Wadi Naim. Almost exclusive to this unit is the abundance of *en echelon* segmentation in NNE-N trending s.l. uplift joints. Single-layer joints reveal a strike rotation. Multilayer joints overprint some of the s.l. joints. A normal fault from a NS striking conjugate set initiates on top of the earlier right-lateral strike-slip fault.

Similarities between the above two patterns. Single-layer joints in unit I and m.l. joints in units II and III generally correspond to the pattern in Fig. 3.41, in the sense that they follow the orientations of elements from groups A and B. Sets 328°, 309° and 344° correspond to the pattern of conjugate hybrid joint structure (Fig. 3.35a), and m.l. joints in unit I partly follow elements from both groups A and B. Similarity also applies to the syntectonic 062° and other m.l. sets in unit IV that fit the extensile direction of group B.

Dissimilarities between the above two patterns. Multilayer joints in unit I occasionally develop in other orientations that differ from the "simple" view (Fig. 3.41) (see Bahat 1991a, p. 306). Neither the post-uplift joints in unit I nor the rotational pattern of s.l. joints in units III and IV have parallels in Fig. 3.41. Groups C and E from Fig. 3.41 are not found in the Beer Sheva syncline. A remarkable difference between the two systems is the considerable vertical continuity of joints as is visible in photographs and diagrams (Price 1966; Stearns 1968; Stearns and Friedman 1972), compared to the short vertical continuity of fractures in the Beer Sheva syncline. With the exception of set 062°, the vertical extent of most fracture groups, including m.l. sets from Table 3.3, is limited to one thick layer (Fig. 3.36c) or to a few tens of thin layers (Bahat 1991a, Fig. 5.16). No m.l. joints have been observed to cross the boundaries between units I–IV, or to reach rocks below the Eocene chalks.

3.4.6
Factors Influencing Fracture Diversity in the Beer Sheva Syncline

The great diversity of fracture structures in the chalks of the Beer Sheva syncline (Table 3.3) points to a considerable diversity of fracture mechanisms. The role of several factors that influenced this diversity is discussed below.

3.4.6.1
The Influence of Paleostress on Fracture Diversity

General. Paleostress is a prime factor in the fracture evolution of the Beer Sheva syncline. Several scales of stress are distinguished. First are the regional stresses of the Mediterranean continental collision area (e.g., Letouzey and Tremolieres 1980) which prevailed from the Upper Cretaceous to the Quaternary. Second are synclinal stresses that originate within the fold and cause structural changes in the syncline (Bahat 1986a). Third, also important, are local stresses that are confined to a particular outcrop (Bahat 1991a, p. 301) or to a particular lithology at a given location (Gross et al. 1997) or to layers of particular thickness (Bahat 1997). In the following discussion, these scales are referred to as regional, synclinal and local.

Regional influences in unit I. The orthogonal sets 328° and 059° (1a and 1b in Table 3.3) cut Lower Eocene chalks and maintain these exact strikes and fracture characteristics in outcrops that are 17 km apart in two distinct folds, the Beer Sheva and the Shephela synclines (Fig. 3.33b,c). The two synclines differ considerably in their orientation (striking about 050° and 028°, respectively). The implication is that sets 328° and 059° were formed in response to large-scale (inter-continental) S_{Hmax} stresses and stress relaxation (Bahat 1989), which were "indifferent" to the already existing shape of the Syrian Arc (e.g., Letouzey and Tremolieres 1980; Zoback 1992; Buchbinder and Zilberman 1997).

In places, the extensile set 328° is associated with conjugate hybrid joint sets (1c and 1d) (Fig. 3.35c and 3.36a), reflecting mixed modes I + II (Sect. 2.2.13). Therefore, sets 1a–d are genetically related to a particular regional stress. Bahat (1999b) suggests an alternative possibility that the three sets 1a, 1c and 1d are genetically unrelated, and that they were formed at different times under different regional stress conditions (Sect. 6.3.9.1, see also Goodwin 1995). According to both models, however, sets 1a–d are products of regional stresses.

Synclinal influences in unit IV. This unit is exposed along the Beer Sheva synclinal axis and consists of Middle Eocene rocks. Sets 12–16 that succeeded group 11 in time, display rock responses to synclinal rebound and uplift. The s.l. joints of set 12 partly interact with joints of set 062° from group 13 that were associated with the synclinal rebound, exhibiting a concurrent relationship (Bahat 1987b). Those s.l. joints of set 12 that show no interaction with set 13 possibly suggest that some of them had developed before set 062°, i.e., before synclinal rebound, and that they continued a prolonged process (Sect. 3.4.6.2 and 3.4.6.3).

Local influences in unit I. The normal faults cutting the Mor Formation (set 3) show evidence of repeated slip, mostly during the Lower Eocene. However, some fracturing can be assigned to local stresses responding to specific lithological conditions (Gross

et al. 1997). Unlike post-uplift joints in sandstone, which tend to follow the orientation of earlier joints (Sect. 3.3), the post-uplift joints of set 5 (Table 3.3) developed in response to local stresses, which show affinity to the erosional morphology of the rock surface (Bahat 1991a, p. 301).

3.4.6.2
Rotations of Synclinal Stresses in Units III and IV

The systematic azimuth rotation of the s.l. joints in Wadi Secher (Fig. 3.37–3.39a and Table 3.4) and in Wadi Naim (Fig. 3.39b) describes fracture sequences, which strongly suggest that these joints were formed by linked mechanism(s), rather than erratically. A mechanism of clockwise stress field rotation was suggested for the formation of the s.l. uplift joints in Wadi Naim (Bahat 1986a, 1999a, present Fig. 3.42a–c). The joints oriented 360° and 012° occur in upper layers, upstream along Wadi Naim, compared to the joints oriented 019° and 028° (wadi slope is exaggerated in Fig. 3.42d). Since the layers are approximately horizontal, the joints oriented 012° fractured earlier than the joints oriented 028°. This sequence is consistent with the propagation of uplift joints. During uplift the stress gradient is such that the least principal stress decreases downward, causing the greatest strain at the surface. Figure 3.42d shows that jointing along Wadi Naim that straddles sub-parallel to the fold large axis occurred in older layers, closer to

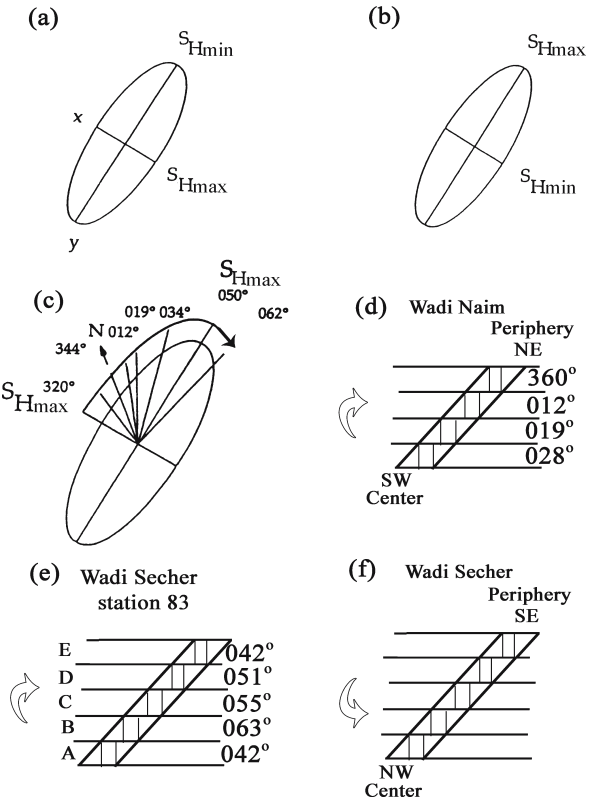

Fig. 3.42. Proposed evolution of fracture in the Beer Sheva syncline under changing synclinal stresses. **a** During buckling, maximum horizontal stress S_{Hmax} parallels the short axis *x* of the syncline, and the minimum horizontal stress S_{Hmin} parallels the long axis *y*. **b** Buckling rebound occurred when the compression along *x* relaxed and became S_{Hmin}, and the compression along *y* became S_{Hmax}. **c** Clockwise paleostress rotation is shown sequentially in Wadi Naim (from Bahat 1999a). **d–f** Diagrammatic wadi section (angle of slope is exaggerated) showing different joint rotation directions (*opened arrows*); see text for explanation

the synclinal periphery, before taking place in younger layers closer to the synclinal center. The detailed results from station 83 in Wadi Secher (Fig. 3.39a and Table 3.4) show that the joints oriented 042° fractured in a younger group-layer (E) before the joints oriented 063° in the older group-layer (B) (Fig. 3.42e), revealing a clockwise joint rotation. Thus, a clockwise joint rotation occurred both in Wadi Secher and in Wadi Naim, implying that jointing along the two wadies probably was associated with the same process of stress field rotation at about the same time. This interpretation does not fit, however, the general fracture pattern from the twenty-eight stations along Wadi Secher (Fig. 3.42f). Here, joints oriented ENE formed earlier in older layers, closer to the synclinal periphery, and a shift towards NNW joint orientation took place later, in younger layers closer to the synclinal center (Fig. 3.37). This shows a counter clockwise rotation (Fig. 3.38a,b and 3.42f), which differs from the clockwise rotation displayed in Fig. 3.42d,e. How can this difference be explained? One possible interpretation is that the s.l. joints in Wadi Secher did not form in a single continuous process. Perhaps, in the southeastern part of the wadi, which is dominated by Lower Eocene chalks (see description of groups 2 and 7 above, Table 3.3), jointing occurred earlier, by a mechanism that differed from the one causing jointing in a later stage, in the Middle Eocene chalks, towards the synclinal center, as shown in station 83. Hence, a unique model of joint rotation in Wadi Secher is uncertain, but this scenario seems to fit the data best.

There are deviations from simple stress rotations, particularly, the "unexpected" departures from the rotation pattern in two scales along Wadi Secher. First, there are repeated azimuth fluctuations in joint rotation along the wadi (Fig. 3.37). Second, the average azimuth of one particular joint set in group-layer A at station 83 is reverse to that of the general rotation in station 83 (Table 3.4). There is also some fluctuation in joint rotation along Wadi Naim: Joints cutting floor R diverge from the general rotation pattern (Fig. 3.39b). These deviations, however, do not invalidate the joint rotation model suggested here; they merely demonstrate the versatility of these processes.

The exclusion of groups 16 and 15, both striking about N-S (Table 3.3) seems inevitable, not least because group 16 is linked with regional stresses (Sect. 3.4.4.1 and 6.3) and group 15 is associated with probably the youngest fracturing along Wadi Naim (Sect. 6.3). The sum of the evidence suggests that sets 15 and 16 were formed after the synclinal stresses had completed their rotation.

3.4.6.3
Additional Factors of Fracture Diversity in the Syncline

The observed fracture diversity in the Beer Sheva syncline is linked to several additional factors:

1. The Beer Sheva fold is a synform.
2. The low strength of chalk.
3. Developments during various stages of burial, unfolding and uplifting.
4. Different lateral position in the fold.

It is often difficult to separate the effect of single factors from the influences of other factors. Accordingly, combined factors are discussed below.

Synforms vs. antiforms and rock strength. Interestingly, systematic joints are rare in Cenomanian chalks, anticlinally folded and uplifted in northern Israel – Mount Carmel and the cliffs of Rosh Hanikra. Particularly intriguing is the absence of m.l. uplift joints comparable to groups 6 or 8 (Table 3.3) from the cliffs of Rosh Hanikra, which extend along hundreds of meters. On the other hand, systematic joints are quite abundant in the synclinal early Senonian (Santonian) and Eocene chalks in Israel. This comparison suggests that joints are abundant in chalks when they are part of synforms but not when they are part of antiforms.

The influence of lithology on jointing is well demonstrated by the profusion of joints in Eocene chalk formations in synclines of south and central Israel, whereas in synclines in northern Israel where the Eocene is dominated by limestone (the Gilboa' and Rosh Pinna synclines, Flexer et al. 1984), jointing is much less developed. It seems that the combination of synform structures with weak rock is particularly conducive to intense and diversified fracturing. The dramatic reduction of strength of wet chalk (Hayati 1975; Bahat et al. 2001a) probably also contributed to differential fracturing, because various fracture episodes are expected to have developed under different degrees of wetness.

The influences of burial, folding, unfolding and uplifting on fracturing in the Beer Sheva syncline. Buchbinder and Zilberman (1997) present a detailed account of the uplifts that affected the eastern Mediterranean margin during the Miocene-Pleistocene. Since Oligocene times, the eastern Mediterranean paleo-shelf (today coinciding with the Judean foothills and extending north-south through the Beer Sheva syncline) has been serially uplifted. Early Miocene, Middle Miocene and Pleistocene uplifts are recognized by sedimentary hiatuses during the periods 25–17 m.y., 14–9 m.y., and 1.5 m.y. to Recent.

The overall character of jointing makes it fairly clear that joints of groups 1 and 3 (Table 3.3) were formed during burial stages (Bahat 1985) and groups 4 and 5 were created during the uplift and post-uplift stages, respectively (Bahat 1991a). Joint rotation in units III and IV is best correlated with unfolding and uplifting that were more influential in the central parts of the syncline, and in various cases specific fracture episodes can be related to particular tectonic phases. Some fracture groups, however, such as 2, 8 and 14, cannot be fixed with certainty in the frame of events (Sect. 3.4.3.1).

Limited sedimentary cover. The young age of the Eocene sediments and the fact that they never were covered by a thick overburden was possibly significant in controlling fracturing processes in the syncline.

3.4.7 Summary

The Beer Sheva syncline is an asymmetric basin in which the sediments are only slightly folded. Nevertheless, the chalky Eocene strata of this syncline display a great diversity of fractures, not visibly related to the basin's asymmetry. The Lower and Middle Eocene chalk formations of the Beer Sheva syncline are divided into four rock units (I–IV), which display considerable differences in fracturing mechanisms. Table 3.3 presents a summary of twenty-three sets in the syncline.

No diversity of joints as rich as in the Beer Sheva syncline has been reported from other folds in rocks of comparable strength.

Different fracture episodes relating to joint sets of similar strikes are presented in "strike-superposition", a method that helps to verify the genetics of sets.

Three scales of paleostresses regimes can be distinguished: Regional (extra-synclinal), synclinal (intra-synclinal) and local (confined to a particular site). The different paleostress scales are most clearly identified in different parts of unit I, particularly in the distal part of the fold, and to a lesser extent in the other units.

Orthogonal sets of single-layer burial joints (328° and 059°) occur in unit I at the northeastern distal part of the syncline which trends about 050°, while the predominant set in the southeastern flank is oriented NE.

Nine criteria of distinction were established between s.l. burial joints in unit I and s.l. uplift joints in unit IV.

Single-layer joints cut units III and IV. Two cases of s.l. joint strike rotation are measured in unit III and one in unit IV. Two measurements, in Wadi Naim and Wadi Secher, show clockwise rotation, and one in Wadi Secher shows a counter clockwise one. These, are best explained by intra-synclinal paleostress rotations: A simultaneous clockwise rotation along Wadi Naim and the younger layers of the Horsha Formation along Wadi Secher. On the other hand, a different, counter clockwise paleostress rotation took place in the older layers of the Horsha Formation and younger layers of the Mor Formation.

Single-layer joints of unit IV, which are the youngest in the syncline, exhibit en echelon segmentation along layer boundaries. Some en echelon segmentation occurs sporadically along boundaries of s.l. joints in unit III, and in one outcrop, in connection with composite fracturing. Styles of en echelon segmentation and particularly their limited spreads of azimuth helped to identify three sets of joints in unit IV. These include, a set produced by a regional N-S post Middle Eocene paleostress, a set with wider azimuth range (012° to 035°) which is connected to stress rotation, and a third set oriented 073°, whose origin is not clear.

Multi-layer uplift joints overprint syntectonic joints (the 062°) in unit IV.

All multi-layer joints cutting units I–IV appear to be related to uplift processes. Their "fine tuning" however is not clear. Strike patterns vary in the four units: A considerable range of strikes in unit I, NNW jointing in unit II, NE jointing in unit III, and joint spreading around NE in unit IV. Joint morphologies vary as well, particularly in unit IV.

The multi-layer joints are the most important vertical conduits of ground water in the syncline (Sect. 6.9).

Compared with the profusion of fracture markings on s.l. burial joints cutting Lower Eocene chalks, and syntectonic joints cutting Santonian chalks, fracture markings are rare on all m.l. joints. Perhaps it reflects fracture by fluid pressure in the former two cases, and tension unrelated to fluid pressure in the latter.

A vertical fault, genetically linked to multi-layer uplift joints, offsets a normal fault in unit I.

In unit I, low angle (dip $\leq 45°$) normal faults interacted with s.l. burial joints. Generally, the interaction took place during the sedimentation stage. High angle (dip $\geq 45°$) normal faults interacted with uplift single-layer joints in unit IV during advanced uplift stages of the syncline.

Unit IV exhibits a unique fault termination zone of a right-lateral strike slip fault. This zone displays primary and secondary faults, and a joint set exclusive to the zone.

Additional factors that contribute to fracture diversity in the Beer Sheva syncline, besides paleostress regimes, include: The synform structure, the low strength of the chalk (especially when wet), and differential developments during stages of burial, unfolding and uplifting.

3.4.8 Open Questions and Future Studies

In spite of detailed studies, many problems relating to fracturing in the Beer Sheva syncline are still unresolved. Following is a brief review of these open questions.

Sets 1a–d are possibly conjugates that formed in one stress field (Bahat 1987a). Alternatively, the three sets 1a, 1c and 1d (Table 3.3) evolved in a process of clockwise stress rotation (Bahat 1999b). Both processes, however, would be caused and sustained by regional stresses (Sect. 6.3.9.1).

If both sets 1d and 11c were formed by regional compression from 344°, future fieldwork may yet discover a genetic relationship between them.

An intriguing issue is fracture by stress relaxation. Currently, it is considered that strike-parallel joints (set 1b) are more widely spaced because they were formed in response to smaller stresses relieved by recurring phases of relaxation, as compared to the cross-fold joints (set 1a) (Bahat 1991a, Table 5.4). The latter were formed by greater, periodically recurring increases in fluid pressures associated with regional stresses.

According to Rawnsley et al. (1998), the joints in the Bristol Channel basin were formed in five main phases, at least partly during relaxation of the Alpine stresses (Sect. 3.2.1). Engelder and Peacock (2001) do not argue against relaxation but assert that the J3 joints in the south-dipping beds of the anticline at Lilstock Beach propagated during folding (before relaxation). Although jointing during stress relaxation has been proposed by various authors (e.g., Price 1974, Bahat 1989) the available arguments are circumstantial and require more compelling geological evidence, though there is experimental evidence of fracturing under this condition (e.g., Sect. 2.2.3.7).

To date, no study has dealt with the connection between "transitional" joints from unit III (group 8) with layer boundaries (Underwood and Cooke 2001 and Sect. 2.2.3.15). Such investigations may help to understand what prevents such joints from becoming m.l. joints.

The unclear genetic relationship between groups 2 and 7 needs to be investigated.

There is currently no proof that s.l. joints from group 10 in unit III are younger than s.l. joints from unit IV.

The structural and genetic relationship of the four adjacent normal faults in Wadi Secher (group 9) needs to be established.

Three adjacent normal faults strike 358 ±10° (group 15). These faults offset s.l. joints from set 12 along Wadi Naim. There are however no contacts between the normal faults and m.l. joints from group 14, leaving their age relationship open.

Field data enabling the timing of groups 8 and 14 are still lacking: Were groups 8 and 14 formed simultaneously, or separately? Were they formed earlier in unit III and later in unit IV, or *vise versa*?

The concept of regional stress meets a difficulty: If the stresses that induced joints were not controlled by the early folding pattern of the Syrian Arc, as suggested above, why are their products (group 1, sets 1a–1d) clearly associated exclusively with the

distal parts of both the Beer Sheva and the Shephela synclines? Should not these sets be uniformly dispersed throughout the two synclines during the Lower Eocene?

More studies are required to explain how lithological differences between chalk and limestone, other than strength (and possibly related to their history of lithification) may influence their modes of fracturing.

The young age of the Eocene sediments and the fact that they never were covered by a thick overburden is most probably significant for the development of fracturing in the syncline, but this topic needs be further investigated.

Finally, a micropaleontological study along Wadi Secher might confirm that unit II is lacking there and establish the rate of joint rotation in station 83.

3.5 Comparison of Unrelated Fracture Provinces

The four different fracture provinces that were selected for presentation in this chapter, the Appalachian Plateau, Bristol Channel, Zion National Park in the Colorado Plateau and the Beer Sheva syncline, do not represent a comprehensive review of the subject. Certainly there are additional such provinces that are worth concentrating on. Nevertheless, even in the present scope it may be instructive to bring up the similarities and differences between these provinces. Soon it will be seen that in spite of being universally subject to the physical laws of rock mechanics and fracture mechanics, the fracture products differ considerably in the four provinces due to the diversity of geological conditions in which they evolved and the unique properties and material individuality of any rock package.

The following topics might be a good basis for inter-regional comparison of jointing.

1. Rock age, lithology and age of fracturing.
2. Genetic classification.
3. Changes in stress fields, structural complexity and overburden.

3.5.1 Rock Age, Lithology and Age of Fracturing

Fracturing took place on the Appalachian Plateau, northeastern United States, in Devonian multi-rock formations of siltstone, shales and limestone. Most foreland fracturing occurred in the Upper Paleozoic during four phases of the Alleghanian orogeny. Later, post-Alleghanian joint sets developed. In the Bristol Channel province, southwestern Britain, Lower Jurassic limestone underwent fracturing during several tectonic stages. The important joint set J3 was formed during the compressional Alpine orogeny that started in the Eocene to Oligocene, and continued through the Late Oligocene to Miocene. In the Beer Sheva province, south Israel, fracturing started during sedimentary burial in the Lower Eocene and continued throughout the Oligocene/Miocene, or later uplift periods, cutting Lower Eocene and Middle Eocene chalks. In the Jurassic sandstone of the Zion province, northwestern U.S., fracturing probably started in the Mesozoic, but main geo-morphological developments occurred at younger Pliocene-Pleistocene ages. In all these events, in unconnected provinces,

different time intervals elapsed between sedimentation and rock fracture, and in each province fracturing took place in different multi-stages, lithologies and stratigraphies. Apparently, the numbers of fracturing styles and packages of fracture-sediment type are limited, but their combinations are numerous.

3.5.2 Genetic Classification

The attempts at genetic classification of joints in the various provinces (i.e., distinguishing between burial, syntectonic, uplift and post-uplift joints) are not simple. Notwithstanding, efforts for obtaining such a classification are justified because they enable one to discriminate between tectonic phases and to establish the actual circumstances of fracturing, such as depths, and sequence of paleostresses.

Fracturing in the Appalachian Plateau probably started in the burial joints of set 320–330° (Younes and Engelder 1999), and these can be linked quite likely to the Ib (325–337°) burial set (Bahat 1991a, p. 251). Fracturing continued with three to four syntectonic stages during the Alleghanian orogeny. Young, post-Alleghanian joints are possibly related to post-uplift events (Hancock and Engelder 1989). In the Bristol Channel province, all jointing seems to be syntectonic (Engelder and Peacock 2001). The Beer Sheva province presents joints of all the four genetic groups, while the magnificent fractures at Zion National Park are mostly post-uplift joints.

3.5.3 Changes in Stress Fields, Structural Complexity and Overburden

Fracture-producing stresses were notably dissimilar in the various provinces. Post-uplift jointing at Zion National Park takes the form of parallel, simple longitudinal splitting (Bahat et al. 1995, 1999), mostly preserving the orientation of older fractures. In this case, maximum compression was vertical, induced by overburden weighing down on present-day plateau rocks consisting of strata that were not folded.

Horizontal compression of the Alleghanian orogeny induced two sequences of rotation (Sect. 3.1) in the Appalachian Plateau, and these were characterized by small differential stresses (6 MPa, Younes and Engelder 1999) and only slight folding. In the Bristol Channel province, joints propagated in response to Cenozoic Alpine compression. This compression also generated the growth of buttress anticlines through the reactivation and reversed pre-Alpine normal faults. The Alpine inversion, which was accompanied by intense deformation, reflects large regional, differential stresses (27.8 MPa in limestone and 32.2 MPa in shale, Engelder and Peacock 2001, Fig. 9). On these buttress anticlines, local stresses were superimposed, forming joints along faults, and other singularities.

In the Beer Sheva syncline, two stress types are distinguished: A regional stress that activated various synclines in the Syrian Arc and affected mainly burial joints, and an intra-synclinal stress, confined to the Beer Sheva syncline that was connected with the formation of syntectonic and uplift joints in the syncline. Young uplift joints superimposed on burial or syntectonic joints are common. Single layer fractures in the slightly folded Eocene chalks were created by very low differential stresses (–0.5 MPa extensile effective stress, Bahat 1989).

When comparing the four provinces, the degree of structural complexity increases from Zion through the Appalachian Plateau, to the Bristol Channel buttress anticline, and finally, the most complex pattern is found in the Beer Sheva syncline. Overburden was thin and fracturing took place close to the ground surface in the canyon at Zion National Park. In the Beer Sheva syncline, overburden was also thin, particularly when fractures developed during and after uplift (possibly tens of meters, probably not more than several hundred meters). The question at what depths fracturing of the various sets occurred, remains partly enigmatic and justifies further research.

Jointing in Granites

Whereas Chap. 3 concerns fracture provinces in sedimentary rocks, Chap. 4 relates to fracture provinces and domains in granites. While a fracture province may concern many plutons that maintain geographic and genetic affinities, a fracture domain often relates to a particular pluton or a pluton-complex in a province. There are many publications on granite that relate to different fracture aspects of the rock (e.g., Johnson 1970; Segall and Pollard 1983). This chapter does not provide a review of the subject; rather it focuses on certain topics. We divide Chap. 4 into two parts. Part 1 (Sect. 4.1–4.6) relates to geological and fractographic aspects of joints; it presents a characterization of joints cutting granites in central Europe and in California, showing the diversity of joint formation in different fracture provinces and domains. The descriptions relate to joints throughout various stages in the granite histories, from fracture during the cooling history of the pluton to fractures that formed after the pluton had arrived at the ground surface. Part 2 (Sect. 4.7–4.10) concerns fracture mechanic aspects of joints, particularly problems of dynamic fracturing by drawing on fractographic properties of joints as follows:

1. Plotting joints on the velocity v vs. stress intensity K curve.
2. Presenting a general discussion of various manifestations of v and K in granites.
3. Calculating the new fracture areas on *en echelon* vs. hackle fringes.
4. Estimating the "index of hackle raggedness" of joints.

We present at the end of this chapter (Sect. 4.11) a description of a method how to drill in situ parts of fractures from the rock.

Part 1

4.1 Background

Bankwitz and Bankwitz (1984, Fig. 8 and 13) describe joints about 40 m long in granite from the South Bohemian Pluton near Mrákotin, west of Telc in the Czech Republic. These joints were considered to be representatives of the uplift stage (Bahat 1991a) because they resembled uplift joints cutting granite in Sinai (Bahat and Rabinovitch 1988). According to the latter authors, the presence of markings on the fractures in those granites was promoted by the rapidity of "late fracture" propagation during the uplift process, despite the coarse textures of the rocks. Recent studies of fracture in the South

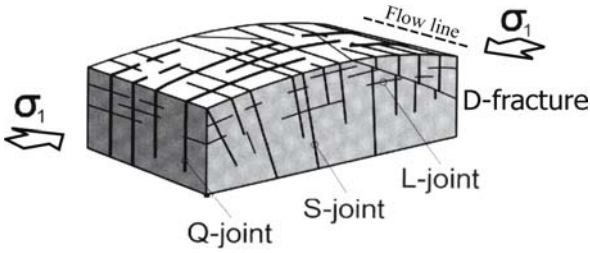

Fig. 4.1.
The Cloos fracture model. Orientation of primary, near vertical Q- and S-joints and oblique faults D, as well as sub-horizontal L-joints with respect to the regional maximum horizontal principal stress σ_1, which is perpendicular to flow lines in the country rock (modified after Müller et al. 2001)

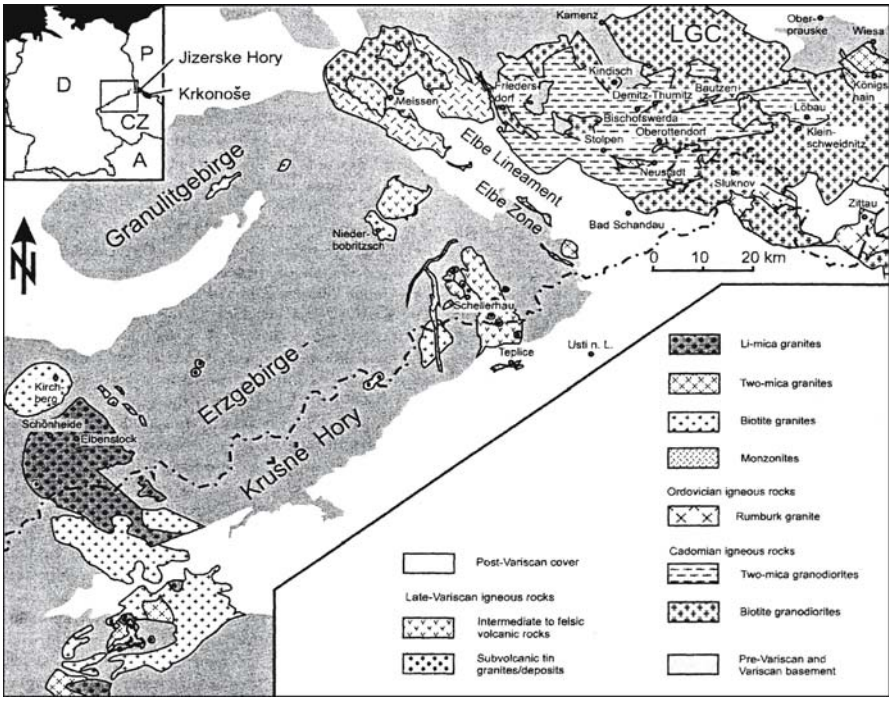

Fig. 4.2a. Distribution of magmatic rocks in the Northern Bohemian Massif including the Lusatian Granodiorite Complex (upper right) and the Erzgebirge (center) (from Müller et al. 2001)

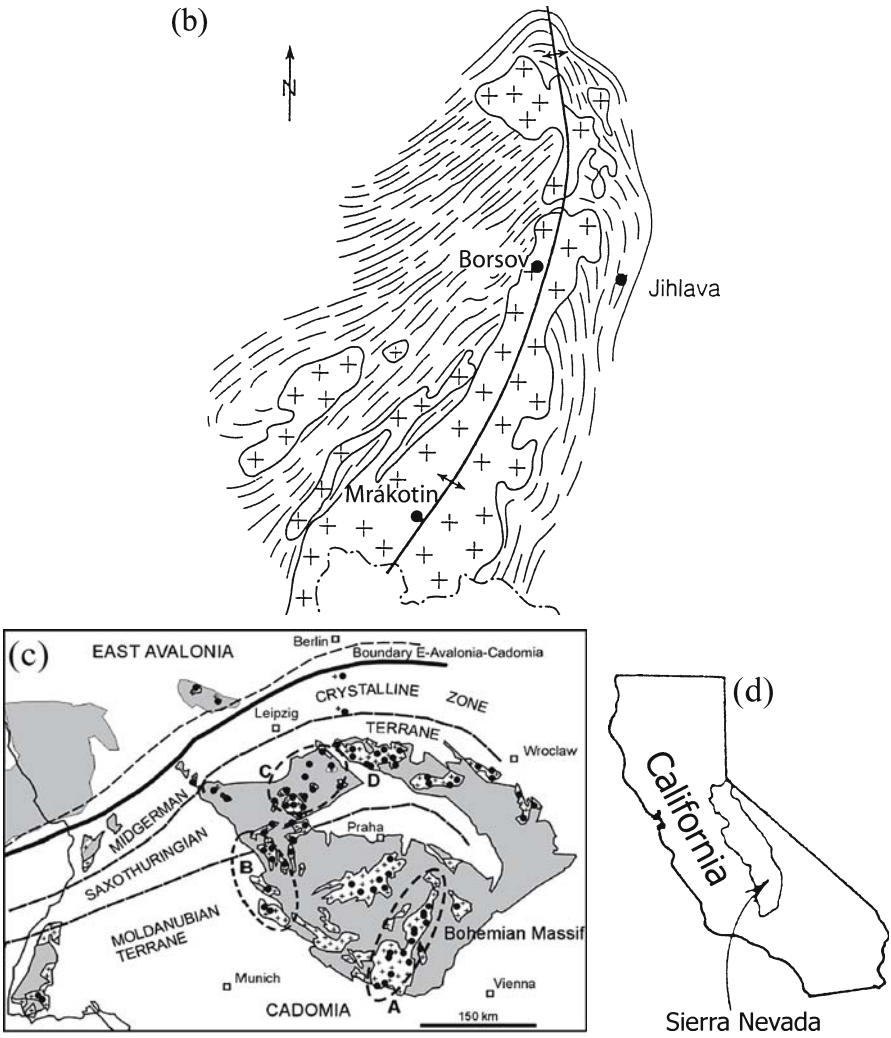

Fig. 4.2b–d. b A simplified geological map of the South Bohemian Pluton (marked +), the axis of major fold the orientation of foliation of gneiss county rock on various sides of the pluton (modified after Benes 1971). **c** Late to post-Variscan granites of the Bohemian Massif: *A:* South Bohemian Pluton; *B:* Oberpfalz plutons; *C:* Erzgebirge plutons; *D:* Lusatian Granite Massif. *Dots* mark localities of investigation by Bankwitz et al. 2004 (from Bankwitz et al. 2004). **d** The Sierra Nevada Batholith from central California (modified after Segall and Pollard 1983)

Bohemian Pluton reveal however that many vertical joints are in fact pre-uplift as will be demonstrated in the following sections. These studies suggest that rapid fracture can occur by "early fracture" in granite while this body still exists at great depths.

We begin by presenting the Cloos (1921, 1922) pioneering model of fracture in granites (Fig. 4.1). The Cloos model provides a sound basis for the classification of fracture in granites and for distinguishing between "early fracture" and "late fracture". A series of recent investigations on fracture in granites from three different provinces, the North

Bohemian Pluton in Germany (Fig. 4.2a), the South Bohemian Pluton in the Czech Republic (Fig. 4.2b), both in central Europe (Fig. 4.2c), and the Sierra Nevada Batholith in central California, USA (Fig. 4.2d) are described. The North Bohemian Pluton is represented by two domains, the Lusatian Granodiorite Complex and the Erzgebirge. The South Bohemian Pluton is portrayed by data gathered particularly in two distinct quarries (Mrákotin and Borsov). The two domains representing the Sierra Nevada Batholith are the Knowles Granodiorite and the pluton complex in Yosemite National Park. Synthesized into these descriptions are several investigations that have not been published before. A section on comparative jointing ends the first part of this chapter.

4.2 The Cloos Model

According to Müller et al. (2001), Cloos (1921, 1922) and his associates investigated the development of fracture in igneous rocks in central Europe, in relation to the mode of emplacement of an intrusive mass. Cooling and hence crystallization, shrinking and degassing of the igneous melt first takes place at the walls and roof of the intrusive mass. Continued movement and intrusion of the still liquid core give rise to stresses in the outer shell of the intrusion.

A system of three main types of "primary fractures" that are orthogonal to each other is recognized and defined by Cloos with respect to flow-lines of oriented crystals, flow-planes and *schlieren*, which develop during the movement of the viscous liquid melt through the process of intrusion. These are Q-joints, ("cross", or "dip fractures"), S-joints ("longitudina1 fractures"), and L-joints ("flat-lying fractures"). A fourth type that forms later than the "primary fractures" is termed "diagonal fractures". The orientation of these fractures with respect to flow-lines is shown in Fig. 4.1.

Q-joints are among the earliest of fractures to develop in the cooling mass. Typically, they form parallel to the main stress direction (σ_1) and perpendicular to the flow lines, i.e., stretching lineation. These fractures are sometimes opened and mineralized (aplite and hydrothermal minerals), and correspond to ac-joints (Fig. 4.1). Q-fractures are less jointed (in terms of divisibility, Müller et al. 2001) than S-joints.

S-joints are oriented perpendicular to the main stress direction (σ_1) and parallel to the flow-lines. The orientation of these fractures is little affected by variations in pitch of the flow-lines. However, variations in trend of the flow-lines are faithfully followed by changes in the strike of the S-joints. S-joints are closed, rarely filled with aplite or "dike" material, and the minerals are usually different from those found in the other kinds of primary fractures.

L-joints tend to develop sub-horizontal near the apex, or dome, of an intrusion or in flat sheets and laccoliths. It is difficult to see how these structures can he interpreted on dynamic grounds. It has, however, been suggested that they form when the center of an intrusion shrinks due to cooling. These structures are also filled with hydrothermal minerals, and have been referred to as primary flat-lying fracture so that they may be distinguished from exfoliation joints that may be much younger.

Diagonal fractures form at 45° or more, to the trend of the flow-lines, resulting from compression normal to, and extension in the azimuthal direction of flow-lines. These fractures are also commonly filled with aplite or hydrothermal minerals. Displacements along the diagonal fractures are clear, indicating that they are shear phenomena.

4.3
Fracture in Granites from the North Bohemian Massif in the Lusatian Granodiorite Complex and the Erzgebirge

Bankwitz and Bankwitz (2004) describe various European granites (mostly Variscan), with a special reference to their age and some fracture properties. This section is mostly cited from Müller et al. (2001). The study areas are the Lusatian Granodiorite Complex (LGC) and the Erzgebirge in SE Germany (Fig. 4.2a), with the main emphasis of the study on the LGC. Kossmat (1927) assigned both the LGC and the neighboring Erzgebirge to the Saxothuringian Zone of the Variscan orogen (Fig. 4.2c).

4.3.1
The Lusatian Granodiorite Complex

4.3.1.1
Geological Background

Based on geological considerations, Watznauer (1954) wrote of a "granite flood", which was assumed to extend from the LGC across the Erzgebirge into Thuringia. In contrast, Suess (1926) proposed to separate the LGC from the Saxothuringian Zone due to the different structure and development of the basement in both domains. Since then, a number of differences and similarities of the crustal structures and their development have been found. The principal difference between the provinces is the main age of intrusion, which is Cadomian (540 to 530 Ma) in the LGC, and late-Variscan (325–318 Ma) in the Erzgebirge (Bankwitz and Bankwitz 2004).

The LGC is separated from the Erzgebirge by the Elbe lineament and by the rock collage of the Elbe Zone (Fig. 4.2a). The LGC is bordered by major faults and over thrusts. The virtually undeformed Cadomian granitoids cover an area of about 2 500 km^2 and constitute a genetically related, mostly peraluminous magmatic suite (Krauss et al. 1992). Most of the contacts of the granodiorites and wall rocks are defined by faults resulting from uplift since the Late Proterozoic (Eidam et al. 1992). The late-Variscan granitoid activity in the LGC is represented by the Stolpen and Konigshain monzogranites, which intruded as stock-like bodies along large deep-seated regional faults (e.g., Hirschmann 1966).

4.3.1.2
The Gravity High of Lusatia

Müller et al. (2001) investigated the gravity field of Lusatia and of the Erzgebirge, using the tomographic method of Linsser-filtering (Linsser 1967; Conrad et al. 1996; Trzebski 1997). The Linsser-filtering provides an alternative technique to the conventional selective gravity field methods since it allows depth selective gravity gradient analyses down to 20 km depth, based on the Bouguer gravity field. Thus revealing information about the three-dimensional extent of steep-dipping (<45°) rock density contrasts in selective depth levels. The LGC and the Erzgebirge are distinguished by the most significant gravity anomalies of the Bohemian Massif: The gravity high of Lusatia and the gravity low of the Erzgebirge. The widespread occurrence of high density rock beneath the LGC is interpreted in terms of the presence

of a large-scale layered gabbroic intrusion ("gabbroic layer", Lindner 1972; Behr et al. 1994) of unknown age associated with a mantle upwelling. This poses the question of whether a gabbro intrusion beneath the LGC could generate around 25 000 km^3 (2 500 $km^2 \times 10$ km thickness) of magma from metagraywacke-metapelitic turbidites (anatexis of late Proterozoic, e.g., Eidam et al. 1992), which are exposed at the NW margin of the LGC.

4.3.1.3 *Results and Discussion*

According to Müller et al. (2001) the strike of the interpolated Q-jointing is harmonic over the whole area of the LGC and forms a sigmoidal pattern (Fig. 4.3a). The general parallelism of the strike of the Q-jointing and the axis of the gravity high is notable. Subsequent to the formation of the LGC, gabbroic magmas mostly used these Q-joints as ascent paths in the western and central part of the LGC (Fig. 4.3b). In the east of the LGC the mafic magmas intruded diagonal joints. The sigmoidal striking of the Q-joints is parallel to the indicators of 5, 7.5 and 10 km depths, which mark the southern boundary of the Lusatian gravity high. The second vertical joint direction, the S-jointing, forms angles between 90° and 60° with the Q-jointing (Fig. 4.3c). Angles of more than 80° between the S- and Q-joints are in accord with Cloos's joint model. The primary orthogonal joint system is overprinted by sets of diagonal joints. This occurs in association with large-scale fault zones at the margin of the LGC. Generally, the primary joint sets Q and S are best preserved in the core zone of the southern part of the gravity high in the area of Bischofswerda and Bautzen (Fig. 4.2a). Thus, it is interpreted by Müller et al. (2001) that since the high density rock beneath the LGC is considered to be a large-scale layered gabbroic intrusion and the pattern of Q- and S-joints fit the high gravity pattern quite well, the updoming of the postulated gabbroic intrusion could have induced these fractures during the solidification of the LGC between 520 and 590 Ma. Lobst (2001) examined field relationships of fractures in the Klosterberg quarry, some 10 km SW of Bautzen, and found that steep E-W oriented joints were older than N-S joints. Apparently, the Klosterberg quarry is located geographically, such that the E-W and N-S joints fit the directions of the Q-joints and S-joints, respectively, in the maps drawn by Müller et al. (2001) (Fig. 4.3). This suggests that the Q-joints were formed before S-joints.

Müller et al. (2001) could not confirm the existence of late-magmatic, flat-lying L-jointing (Fig. 4.1) in the Lusatian granite. On the other hand, they identified a joint set subparallel to the surface topography that was related to late processes of surface exposure of the granite body, which they consider to be an exfoliation set. They observe that the exfoliation is best developed in granites and granodiorites with large joint spacing (>5 m). Such conditions are given in the top area of the Lusatian gravity high between Bautzen, Bischofswerda and Kamenz (Fig. 4.2a). The exfoliation is poor and irregular in regions where joint spacing is <1 m. The distance between the surface parallel joints increases with increasing depth, as observed in other granite quarries (e.g., Johnson 1970, p. 358).

In summary, Müller et al. (2001) show that the primary joint system of the Cadomian Lusatian granodiorite fits the model of updoming by an underneath intrusion: In this case, the presumed gabbroic intrusion at depth. The fractures under investigation formed during the solidification of the LGC between 520 and 590 Ma, such that the Q-joints were formed before S-joints. However, in contrast to the Cloos model it has been found that the formation of sub-horizontal joints in the granite is related to the external process of exfoliation and has no relationship to the primary joint set.

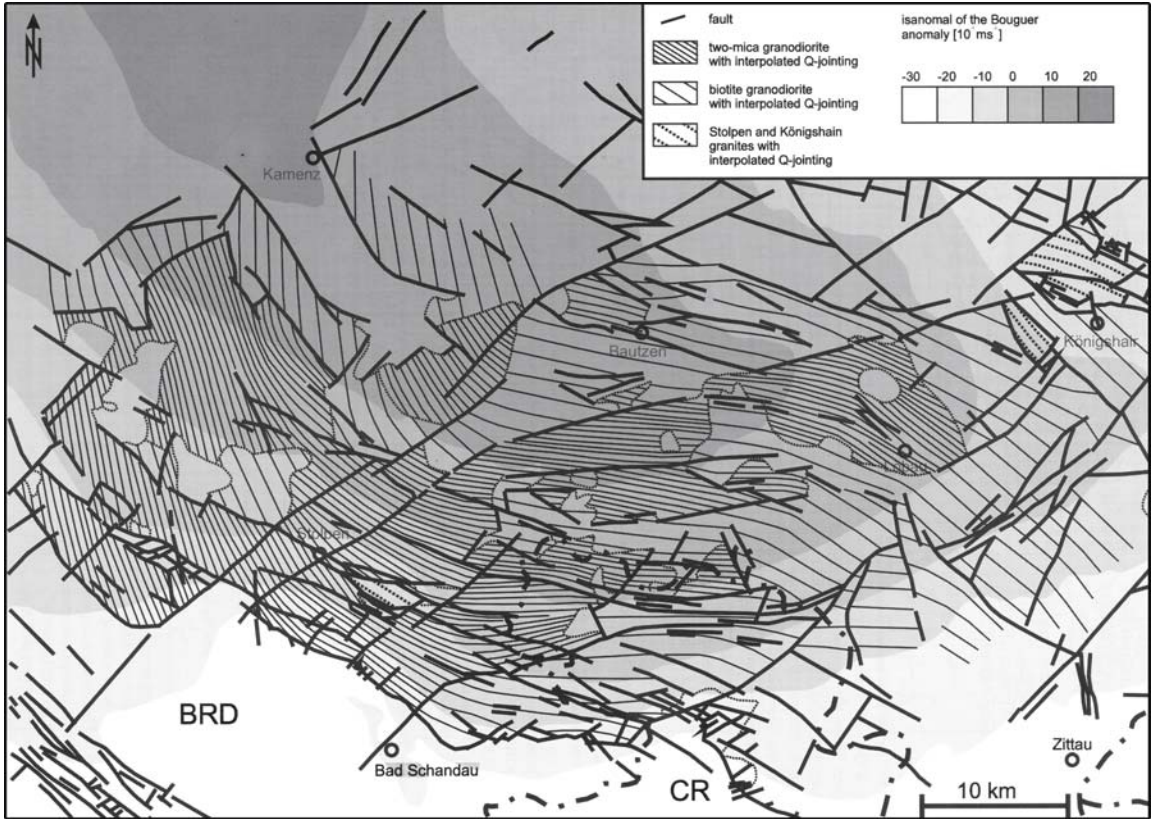

Fig. 4.3a–c. Structural maps of the Lusatian Granodiorite Complex. The maps are underlain by isoanomals of the gravity high of Lusatia with the local maximum NW Kamenz. **a** Main faults (*thick lines*) and interpolated striking Q-joints (*thin lines*) (from Müller et al. 2001)

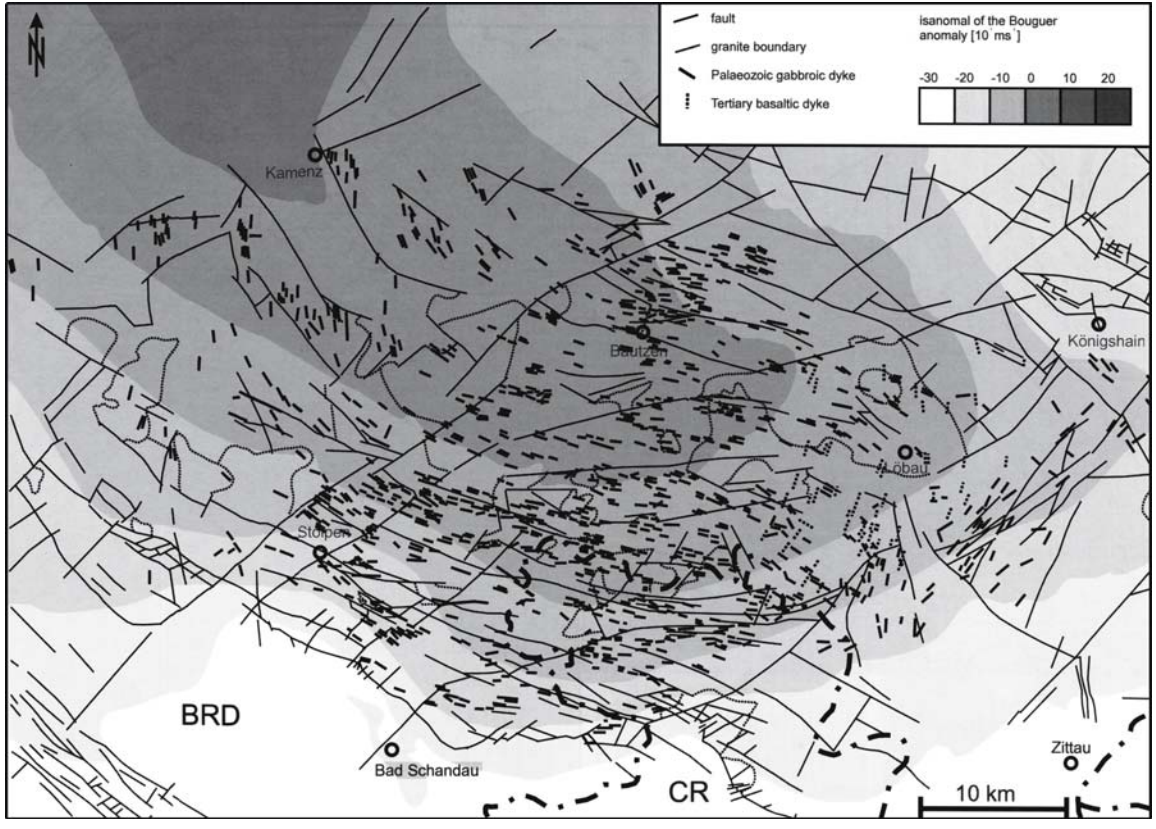

Fig. 4.3b. Structural map of the Lusatian Granodiorite Complex. The map is underlain by isoanomals of the gravity high of Lusatia with the local maximum NW Kamenz. Devonian gabroic dikes used predominantly Q-joints as ascent paths, whereas Tertiary basaltic magmas intruded along N-S to NE-SW trending faults (from Müller et al. 2001)

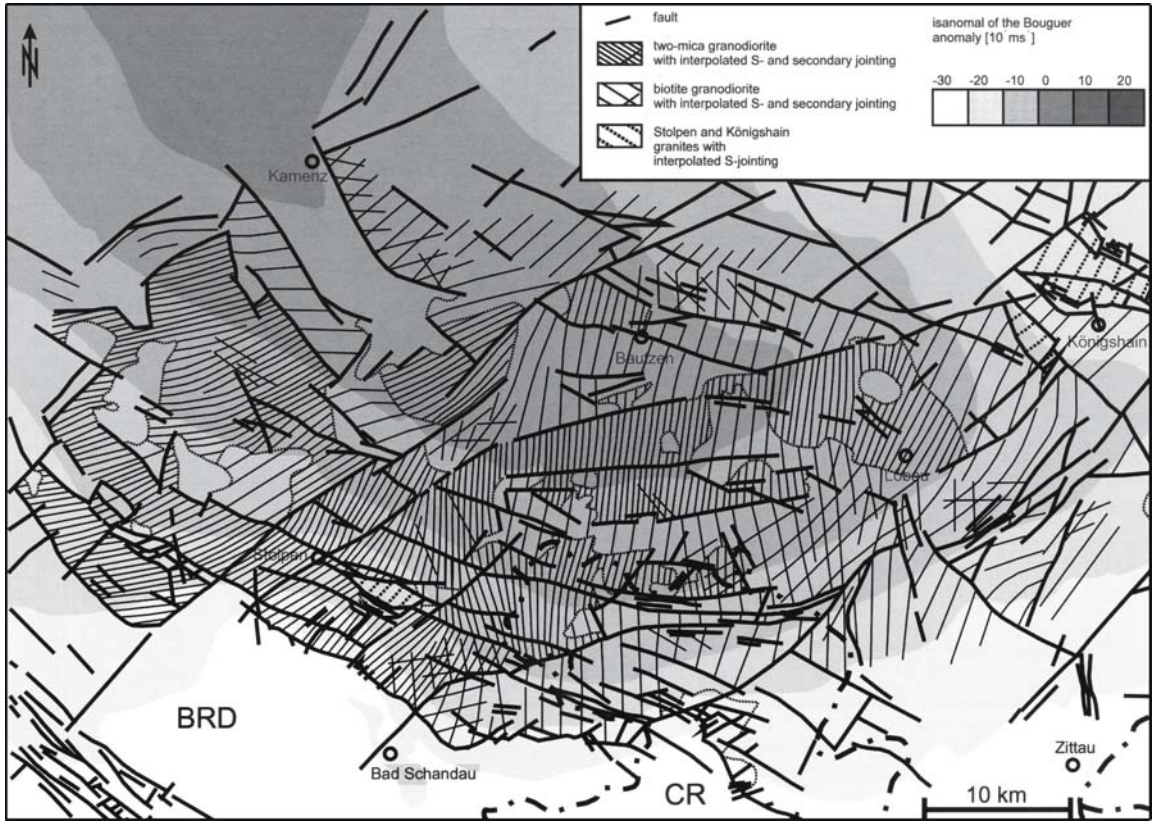

Fig. 4.3c. Structural map of the Lusatian Granodiorite Complex. The map is underlain by isoanomals of the gravity high of Lusatia with the local maximum NW Kamenz. Main faults (*thick lines*) and interpolated striking S-joints (*thin lines*) and additional steep-dipping joints (from Müller et al. 2001)

4.3.2
The Erzgebirge

We consider previous investigations on two plutons in the Erzgebirge, the Niederbobritzsch granite (northeastern Erzgebirge, Fig. 4.2a), studied by Müller et al. (2001) and the Eibenstock granite (southwest Erzgebirge), studied by Bankwitz and Bankwitz 2004).

4.3.2.1
The Niederbobritzsch Granite

According to Müller et al. (2001), the Erzgebirge covers an area of about 6 000 km^2. This area is characterized by Late Carboniferous plutons that intruded Upper Proterozoic to Lower Palaeozoic metamorrphic sequences. The plutons are composed of spatially separated multiphase intrusions with complex textural and field relationships. The granites are traditionally divided into the older (330–320 Ma), and the younger (300–290 Ma) intrusive complexes (Laube 1876; Breiter and Seltmann 1995).

The Bouguer gravity low of the Erzgebirge is the most significant negative gravity anomaly in Central Europe with an extreme of –76 mgal near Karlovy Vary. It extends along the northern margin of the Bohemian terrain and is limited by the Oberpfalz block in the west. The 250-km-long and 40-60-km-wide NNE-SSW striking gravity low continues south of the gravity high of Lusatia to the Jizerské Hory and Krokonose Mountains, where the minimum turns to an E-W direction.

Müller et al. (2001) point out that the NNE-SSW trending joints of the Niederbobritzsch pluton (Fig. 4.4a) are concordant to the ac-plane of the Proterozoic gneisses. These joints are interpreted as Q-joints, because they are opened joints partly filled with quartz. The S-joints strike in the direction of the main stretching axis of the wall rock. Thus, the development of the Q- and S-jointing of the Erzgebirge granites is adapted to the syn-intrusive stress field of the intrusion frame (wall rock), which corresponds to Cloos's joint model. On the other hand, the primary joint sets of the Cadomian granodiorites in the Lusatian Granodiorite Complex reflect the updoming of a postulated gabbroic intrusion, which underlies the granodiorites (as mentioned above).

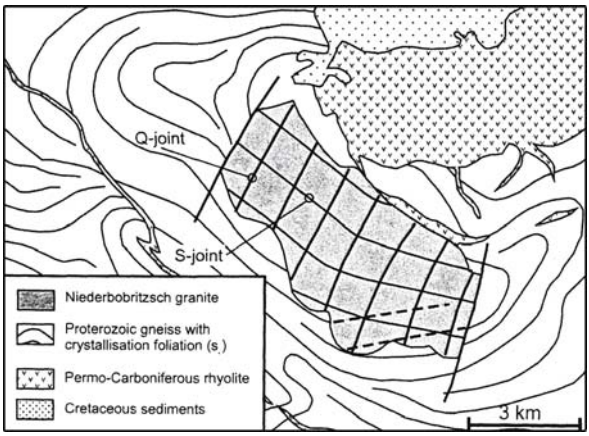

Fig. 4.4a.
The orthogonal Q- and S-jointing of the late-Variscan Niederbobritzsch granite in the eastern Erzgebirge (from Müller et al. 2001)

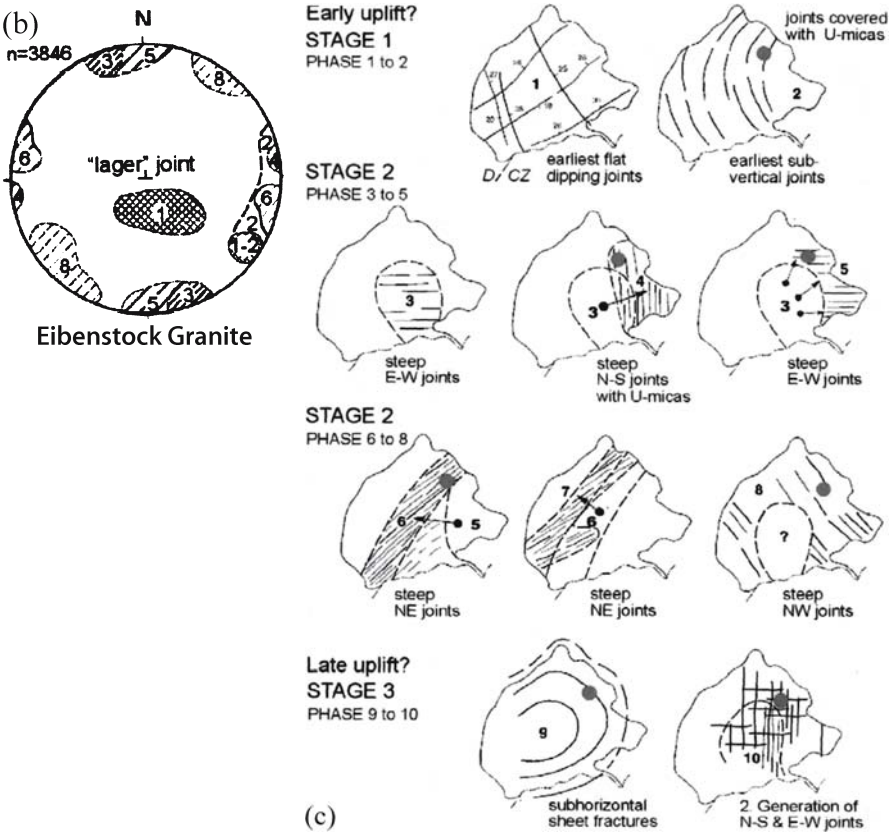

Fig. 4.4b,c. b Synoptic diagram of lower hemisphere stereographic projection of joints in the Eibenstock granite. Numbers *1–8* of maxima indicate the relative sequence of joint formation (from Bankwitz and Bankwitz 1995, 2004). **c** Schematic illustration of the mapped joint sequence in the Eibenstock pluton, see text for explanation (from Bankwitz and Bankwitz 1995, 2004)

4.3.2.2 *The Eibenstock Granite*

The Eibenstock granite is a large laccolithic (exposure of 20×40 km) with complex fracturing. Bankwitz and Bankwitz (1995, 2004) distinguish a series of joint sets in this granite, which they describe in great detail. Jointing started with flat to oblique dipping (18–35°) "lager" joints (Cloos 1921) (Fig. 4.4b,c). The other sets were steeply dipping with the exception of set 9. The first subvertical joints (phase 2) followed the shape of the exposed pluton. The relative timing of the various other sets suggests fracture migration with time, e.g., from phase 3 to phases 4 and 5, and from phase 6 to phases 7 and 8. Sheet fractures formed in stage 3, and finally, a second generation of smaller, N-S and E-W-trending joints was created, terminating at the sheet fractures. A dense deposition of greenish Uranium-micas on joints of sets 2 and 4 helps to distinguish the two generations of orthogonal sets.

4.4
Joints in Granites from the South Bohemian Pluton

This section concentrates on investigations that were carried out in the Borsov and the Mrákotin quarries, citing primarily Bahat et al. (2001a, 2003), Bankwitz and Bankwitz (2004) and Bankwitz et al. (2004).

4.4.1
Geological Setting of the South Bohemian Pluton

The study areas under consideration here are located in the South Bohemian Pluton (SBP) (Fig. 4.2b), which is the northeastern part of the large South Moldanubian Massif that belongs to the internal zone of the Variscan belt of Europe (Fig. 4.2c). The country rock consists predominantly of kyanite-sillimanite bearing gneisses and schists of Late Proterozoic to Early Paleozoic age (Suk 1984; Matte et al. 1990). The metamorphism occurred at 370–350 Ma. The stretching lineation trends NW-SE with indications of a south-eastward shearing (Matte et al. 1990). The SBP intruded the core of an antiform composed of gneisses and schists (Benes 1971). The SBP trends NNE-SSW through the Czech part of the Bohemian Massif. According to Bankwitz et al. (2004),the SBP extends over a distance of 150 km between Havlíckuv Brod in the north and the Danube River,

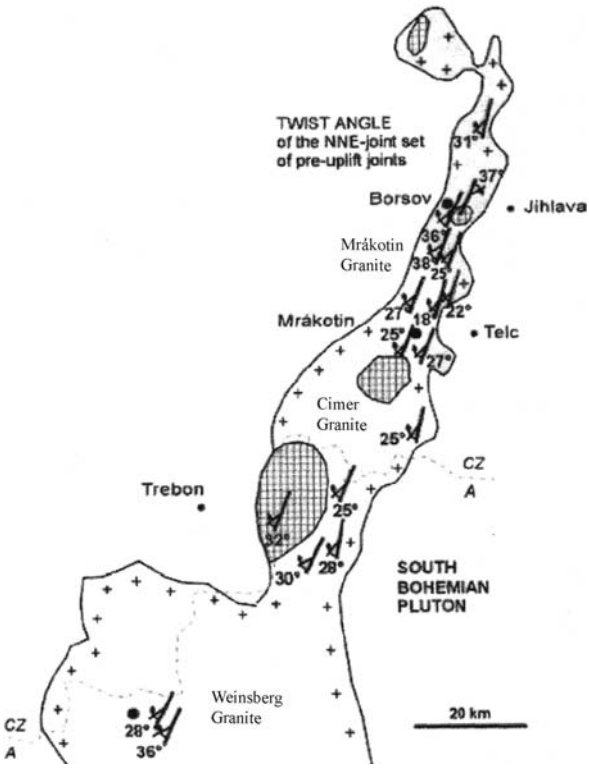

Fig. 4.5.
Geological sketch map of the South Bohemian Pluton, showing the dominant first vertical fracture orientation, set NNE. *Dots:* Locations of investigated fluid inclusions. *Cross hatched areas:* Granite bodies in the axial part of the SBP (modified Breiter 2001 by Bankwitz and Bankwitz 2004)

and further south, recognized from drillings below the Molasse Zone of the Alps (Scharbert 1998). The root zone of the SBP occurs in its southern part between the Danube and the Pfahl faults. The granitoids were emplaced at mid- to upper-crustal levels into hot country rocks (~15–18 to 7–10 km, ~450–650 °C) shortly after the thermal peak of regional metamorphism (Büttner 1997). *P-T*-paths in the country rocks suggest that granite formation, low-*P*/high-*T* metamorphism and extensional thinning were preceded by a phase of intense crustal thickening that occurred during late Palaeozoic continent-continent collision (Gerdes et al. 1998; Matte et al. 1990).

The SBP is a large late-orogenic batholith, which consists of several phases of intrusion with isolated sub-types (e.g., Cimer, Mrákotin, Eisgarn, Weinsberg, Freistadt, Mauthausen types) (Breiter and Koller 1999; Breiter and Sokol 1997; Bankwitz et al. 2004), one of which is the Borsov granite that has a close affinity to granodiorite. Its geochemistry is strongly influenced by the metamorphic country rock. The granitic rocks have developed from a high-*K* peraluminous melt (Breiter and Koller 1999; Matejka and Janousek 1998) with the presence of biotite and biotite-muscovite petrographic manifestations in the rock. According to Matte et al. (1990), the intrusion age is about to 330 Ma. Field contacts in the SBP at the Borsov quarry show that the main fracture systems occur in the following sequence:

1. Early sub-horizontal tension fractures.
2. Vertical or sub-vertical E-W and NNE trending joints.
3. Late, sub-horizontal joints that are represented by the uplift sheeting (e.g., Dennis 1987), cutting the other joints without influencing them, i.e., the joints of the second group had ended their formation before the late joints started.

Both early horizontal and vertical tensile fractures are expected to form in association with the increasing magma pressure in the pluton (Knapp and Norton 1981). This section focuses on the NNE vertical set (Fig. 4.5) due to its particular regional significance, minimizing the treatment of other sets in the pluton.

The South Bohemian Pluton was chosen for investigation for several reasons (Bahat et al. 2003). First, these granites are cut by joints that exhibit a great variety of fracture surface morphologies (displaying most of the features in Fig. 2.1a,b). Second, the fracture morphologies of the joints are usually well preserved, because most of these granites were not deformed in post-Variscan (Late Paleozoic) times. Therefore, the fractures maintained their original shapes from the time before the uplift. Third, the bulk of the existing knowledge on jointing is related to sedimentary rocks, and field observations are normally made along road cuts or natural exposures, which are shallow and seldom allow observations of large joints to their natural ends. These granite rocks have been quarried for more than a hundred years for construction purposes throughout Europe. The large quarries expose large walls required for obtaining good perspective views of large joint fractographic features that granites often exhibit. Fourth, and perhaps most important, the unique exposure of the Borsov granite allows the study of paleo-jointing at the intrusion depth before uplift and erosion. This provides an insight into fracture processes at great depths in the crust. Finally, the SBP is an important part of the Variscan orogen in central Europe and our study may add important information for use in future investigations of the orogen.

It is convenient to distinguish two classes of rock fracture: Those formed by shear stress and those by tensile stress. The vast majority of experimental work in fracture mechanics has concentrated on mode I, tensile fracture propagation (Atkinson 1987). The results of these studies, quite apart from their importance in understanding joint formation, may be applied to a wide spectrum of other geological problems. These include hydrofracturing, microcracks associated with larger structures, tensile fractures of macro and mega-scales (or extensile at great depth), dike formation, magmatic intrusion, boudinage and crevasse penetration (Atkinson 1987). Earthquake studies relate more to mode II shear operations (Scholz 1990), but may have mode I manifestations as well (e.g., Bahat 1982).

4.4.2
Fractographic Versatility on Pre-Uplift Joints in the Borsov Quarry

Existing fractographic studies on fracture in granites generally concern late histories of the granites, following their cooling and uplift (e.g., Holzhausen and Johnson 1979; Bahat et al. 1999), whereas investigations of fractures that formed during the cooling stages (e.g., Knapp and Norton 1981; Lee and Diehl 1989) commonly have not used fractographic techniques. The following sections concern fractures in two outcrops, the Borsov and the Mrákotin quarries from the South Bohemian Pluton in the Czech Republic (Fig. 4.2b), which reveal joints that formed during the early history of the granite.

4.4.2.1
Fractographic Characterization of Ten Joints from the Borsov Quarry

The ten joints with highly diversified fracture surface morphologies (Bahat et al. 2003) are briefly described photographically (Fig. 2.54–2.56), and in their corresponding drawings (Fig. 4.6–4.8). Their properties are summarized in Tables 4.1 and 4.2. The geological interpretation of the fractographies of these joints is presented in Sect. 4.4.5.1, and the fracture mechanic analysis is given in Sect. 4.8.

▶

Fig. 4.6. Drawings of joints from the Borsov quarry (see photographs in Fig. 2.54–2.56, modified from Bahat et al. 2003). Mirror planes that do not contain fringes. **a** The "multi-arrest marks joint", J1. Some fifteen arrest marks superposed by a faint plume. The fracture markings are confined in a "wedge" between two sub-horizontal boundaries, above and below the fracture pattern. Thickness of wedge at the left side is about 90 cm. **b** The "radial plume joint", J2, showing the fracture origin at the center and a radial plume representing the propagation mode. The joint is bounded by two horizontal partings. **c** The "quasi-core joint", joint J3. A mirror plane is decorated by elliptical arrest mark which is partly surrounded by additional partial arrest marks. The origin is situated in an eccentric position with respect to the ellipse, and a continuous plume that starts at the origin propagates in a radial manner to all directions, with various intensities. A symmetric axis passes through regions of greatest intensity plumes. Sub-horizontal fracture *p*, cuts the mirror. **d** The "multi-joint exposure", J4. The plume m1, of the "semi-circular joint" reveals a three-stage concentric growth into a semi-ellipse.The long axis of this semi-ellipse approximately coincides with an horizontal plane p1, that forms its upper boundary. The "circular joint" is characterized by a circular single arrest mark and a faint, single continuous plume, m2, that starts at an eccentric position with respect to the arrest mark and spreads approximately radially. Two upward propagating plumes occur on distinct parallel planes, m3 and m4 at the left side of the "circular joint". Note also the plume m5. Sub horizontal fractures p2 and p3 cut m3 and m2, respectively. However, m4 and m5 seem to truncate against the continuation of p2, suggesting that p2 predates m4 and m5

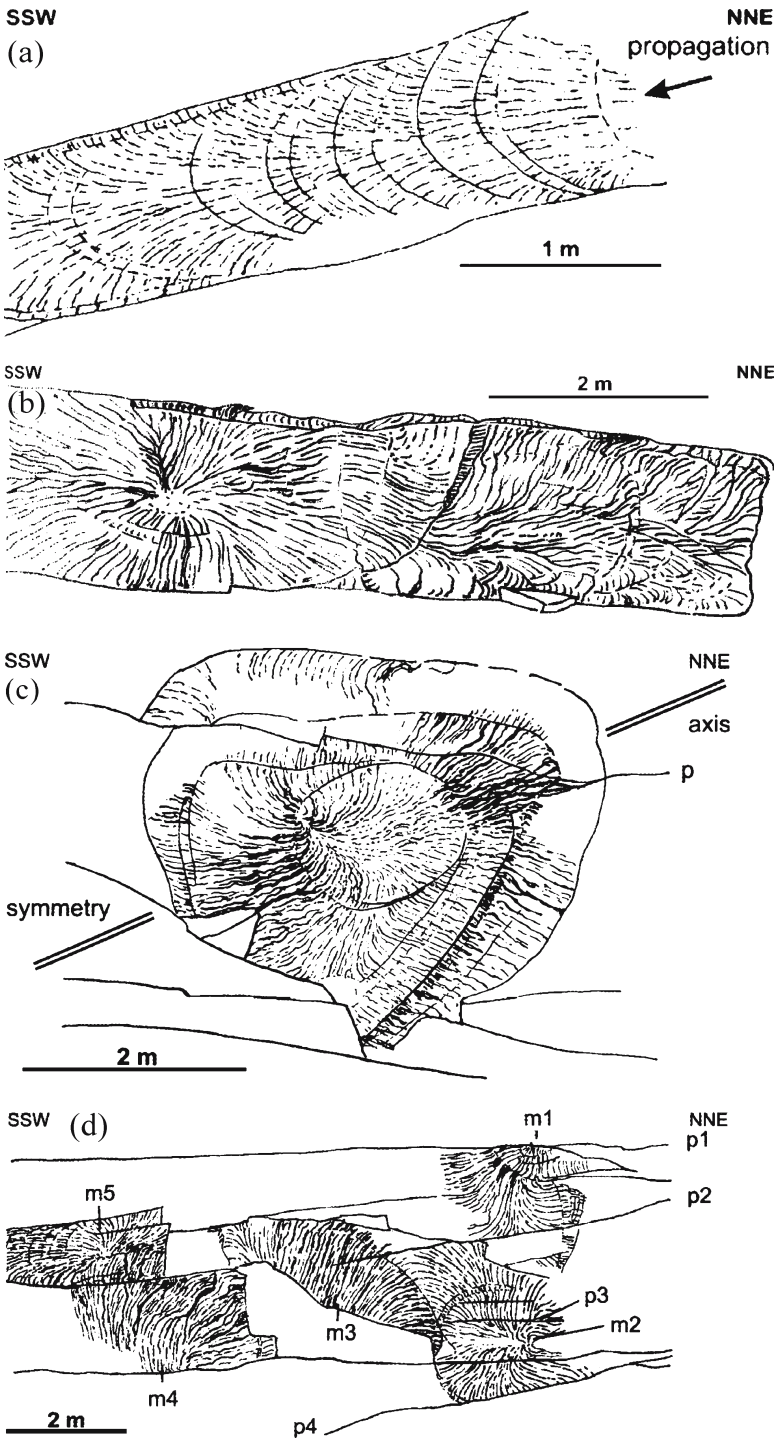
SSW
(a)
NNE
propagation
1 m
SSW
(b)
2 m
NNE
SSW
(c)
NNE
axis
p
symmetry
2 m
SSW
(d)
m1
NNE
p1
m5
p2
p3
m3
m2
m4
2 m
p4

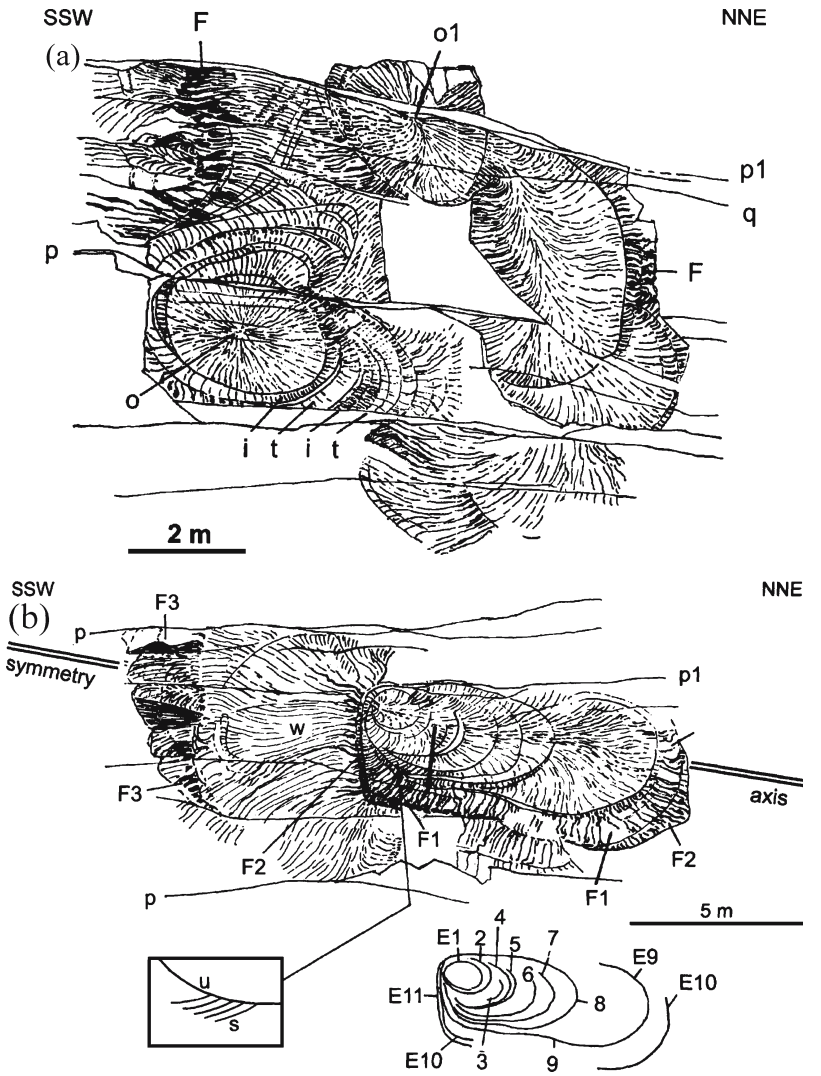

Fig. 4.7a,b. Drawings of joints from the Borsov quarry (see photographs in Fig. 2.54–2.56, modified from Bahat et al. 2003). Mirror planes that contain small *en echelon* fringes. **a** The "divided arrest mark joint", J5 starting at o. A major horizontal parting, p divides the lower semi-circular series of arrest marks from the upper ones of the "divided arrest mark joint". Note a rhythmic increase and decrease in barb-coarseness in certain spacings between the arrest marks, including an inner spacing, *i* which has a greater barb-coarseness than its adjacent outer one, *t*. Another plume started at o1 on parting p1 and was cut by later q. Two plumes terminated in small *en echelon* fringes F. **b** The "asymmetric bilateral joint", J6 displays some ten concentric arrest marks (E1–E10), that propagated from the origin at an eccentric position in ellipse E1 (*inset* at right). The arrest marks are superposed by a continuous plume divided by a symmetry axis. At the left side of the origin there is a large wavy plume, w almost without any arrest marks. A "triangle" fringe of *en echelon* cracks, F1 is separated from w by a "girdle" F2 of short *en echelon* segments. Inset at left shows *en echelon* segmentation, s that initiates from arrest mark u that corresponds to E9. F1 and F2 at the right side are interpreted to be the continuations of F1 and F2 at left. E11 and F3 are additional hypothetical arrest marks and fringe, respectively. J6 is limited by partings p and is cut by a series of sub-horizontal fractures (like p1). Vertical scale at the center is 2 m

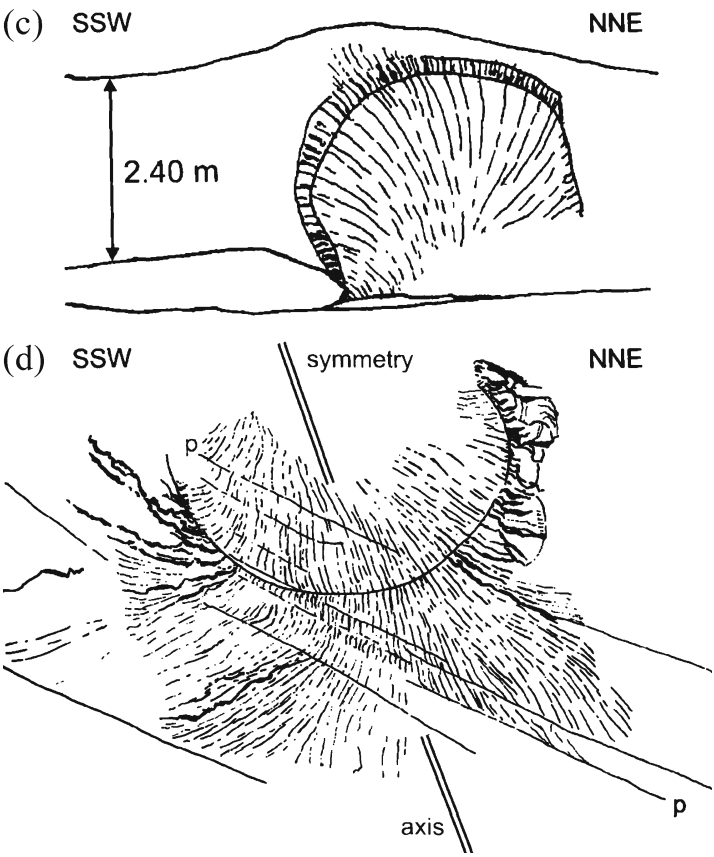

Fig. 4.7c,d. Drawings of joints from the Borsov quarry (see photographs in Fig. 2.54–2.56, modified from Bahat et al. 2003). Mirror planes that contain *en echelon* fringes. **c** The "uniform fringe joint", J7. The boundary between the mirror that is marked by a faint radial plume and the fringe of *en echelon* segments of approximately equal lengths is well defined. **d** The "partly erased joint" J8 shows a mirror that is surrounded by a convex downward circular boundary and a fringe of *en echelon* segments of non uniform sizes. Diameter of the mirror is approximately 10 m

▶

Fig. 4.8. (*see next page*) Drawings of joints from the Borsov quarry (see photographs in Fig. 2.54–2.56, modified from Bahat et al. 2003). Mirror planes with diversified fringes. **a** The "trefoil joint" J9, that forms the shape of a three leaflets flower, showing two types of ripple marks, delicate concentric undulations u (hardly visible), at the mirror center, and two lateral arrest marks a (showing pronounced morphologies), at the left side of mirror. Plumes with a general clockwise, cw stepping are superposed on the latter. The two sides of the mirror contain intensely fractured fringes. The fringe at the left side of the mirror is divided in correspondence with the zigzag of the mirror boundary, into five sectors by the designations *i*, *n*, *t*, *r*, and *m*, where segmentation is counter clockwise, ccw (for details see Bahat et al. 2001). Frame shows location of **b.** **b** The fringe at the right side of the mirror has the shape of a fan which starts at a low side next to the mirror, and opens upward away from the mirror, divided to five distinct sub-fringes. The sense of stepping is not uniform along the various sub-fringes. **c** The "hackled fringe joint" J10, showing a joint on which the fringe is particularly large compared to the mirror size (partly removed), and is heterogeneous with respect to having adjacent hackles and *en echelon* segments. **d** The large diameter in the simplified diagram of (**c**) is about 2 m

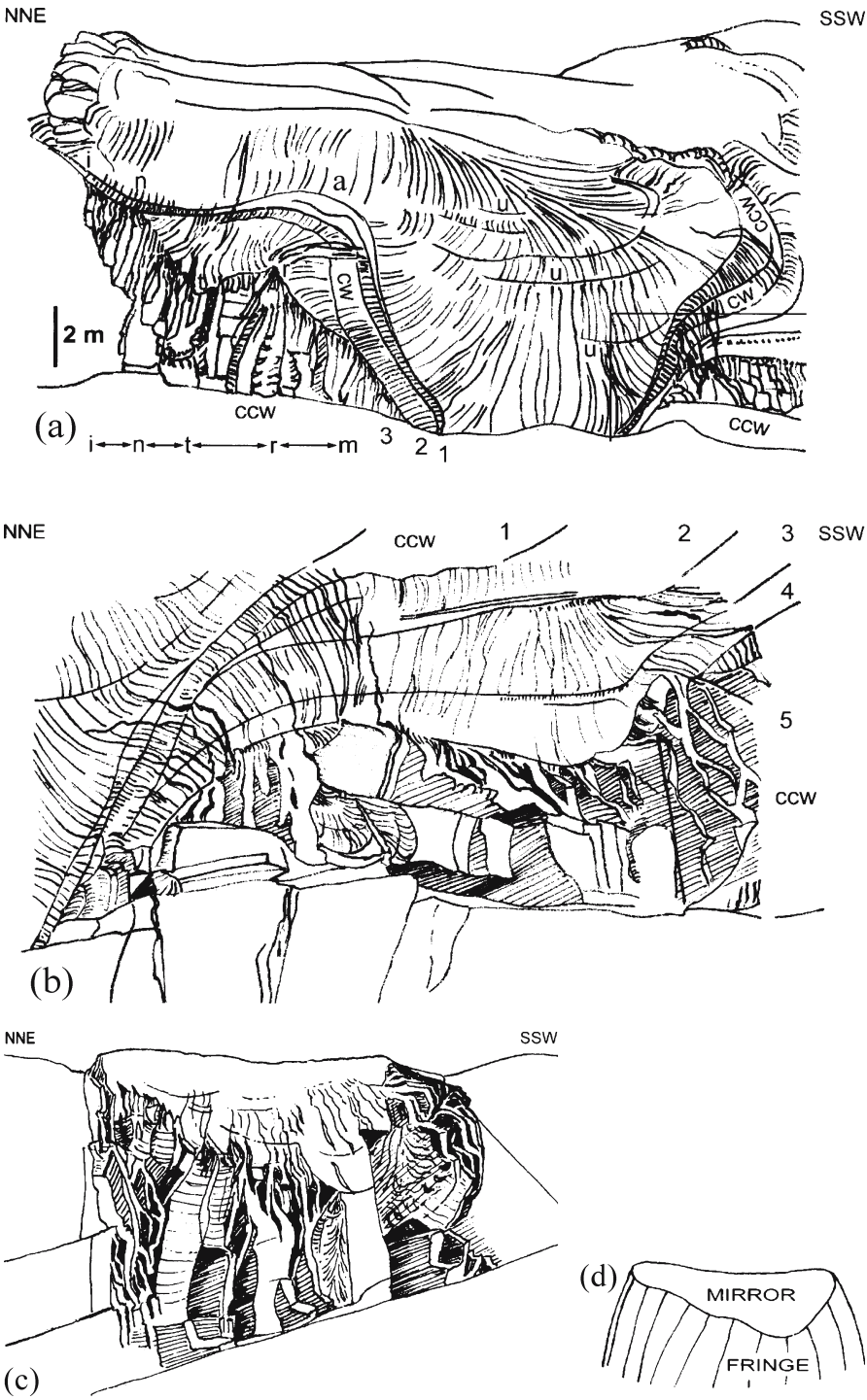
NNE
SSW
a
u
CW
CCW
2 m
(a)
i
n
t
r
m
3
2
1
NNE
CCW
1
2
3
SSW
4
5
CCW
(b)
NNE
SSW
(c)
(d)
MIRROR
FRINGE

Table 4.1. Characteristics of the north-northeast-trending set of joints in the Borsov quarry (example: Ten joints, J1–J10)

Origin point	Mirror shape	No.	Ripple marks		Propagation direction	Superposed features	Fringes	Additional remarks
			Properties	Curvature				
Group 1: Mirrors without fringes								
J1: Multiarrest marks								
At the center of a block between two earlier joints	(Center erased)	15	Increasing width	About half a circle	Laterally, northward	Faint plume on the ripple marks	–	The joint is confined between two flat-lying earlier joints, narrowing northward and connected with a slight decrease of the ripple mark curvature (Fig. 4.6a).
J2: Radial plume joint								
At the center of the mirror	Elliptical	4	Increasing width		Laterally, northward and southward	Coarse plume	–	The joint is confined between two flat-lying earlier systematic joints separated by 186 cm (Fig. 4.6b).
J3: Quasi-core joint								
Excentric, close to the first undulation (left)	Deviation from circularity into an ellipse	4	Some are only partly observable; increasing width	First circle, then ellipse	First oblique to the center (right down) of the ellipse, then radially	Continuous plume; coarse barbs propagating perpendicular to the initial direction	–	One of the postuplift sheeting joints cuts joint J3 horizontally without influencing it. The coarse plume is restricted on the oblique direction (right upward and left downward) in zone of low-ripple mark relief (Fig. 4.6c).
J4: Multi-joint								
a. Semicircular joint								
At the center of the plume	m1: circular	3	Increasing width	Concentric half a circle	Radially	Plume with three-stage growth	–	An earlier horizontal joint forms the upper boundary (p1)
b. Circular joint								
Close to the right side, within the single ripple mark	m2: circular	–	–	–	First laterally southward, then radially	Faint continuous plume	–	Three subhorizontal postuplift joints p2–p4 (sheeting fractures) cut the joint J4 without influencing its pattern.

Table 4.1. *Continued*

Origin point	Mirror shape	No.	Ripple marks		Propagation direction	Superposed features	Fringes	Additional remarks
			Properties	Curvature				
c. Three adjacent joints								
Not completely observable	m3: curved	1			Upward radially	Uniform barbs and coarseness	–	The m3 plane interacts with m2. Great variations in plume morphology: m4 coarser than m2, and both differ from m1. m1 to m5 are not more than 2–5 m apart on three distinct planes that belong to a single set with remarkable variations (Fig. 4.6d).
Not observable	m4	2	Only partly observed		Upward	Plume		
Center	m5	5	Increasing width		Radially	Faint plume		
Group 2: Mirrors with diversity of fringes								
J5: Divided arrest mark joint								
At the center, remote from the adjacent partings	Quasi-circular	11	Increasing; width above p:	Below p: circular; lower right elliptical	Radially; continuations to the upper left and in barb coarseness	Faint radial plume; rhythmic increase (I) and decrease (t)	A small fringe	A horizontal parting (p: emplacement shear band with gneissic fabric) separates the lower quasi-circular arrest mark from the upper asymmetric curved one (Fig. 4.7a).
Neighboring additional joints: Radial plume at the top								
At the center	Circular	3	Increasing width	Quasi-circular	Radially; upper continuation eroded	Faint radial plume; increasing coarseness outside the first arrest mark	Two fringes (F) with en echelon segments at both sides	The radial plume joint interacts with others, e.g., the "divided arrest mark joint" J5, to form a "composite fracture". The subhorizontal parting seems to be younger, without restriction for the upward propagation of the mirror.
J6: Asymmetric bilateral joint								
Close to the left side of the first undulation	Elliptical	10	Increasing width; concentric on a symmetry axis	Circular to elliptical	Laterally, first northward, then southward	Continuous plume northward; wavy plume southward	Three fringes (F1–F3) with sinistral en echelon segments	See explanations in the text (Fig. 4.7b).

Table 4.1. *Continued*

Origin point	Mirror shape	No.	Ripple marks		Propagation direction	Superposed features	Fringes	Additional remarks
			Properties	Curvature				
J7: Uniform frinqe joint								
Near the bottom	Circular	–	–	–	Radially upward	Faint radial plume	One fringe of uniform width, with en echelon segments	All en echelon segments have nearly the same length and twist with respect to the parent joint (Fig. 4.7c).
J8: Partly erased joint								
(Erased)	Circular	–	–	–	Radially downward; upper part unknown (erased)	Radial plume; continues beyond the boundary as plume in the middle part or as coarse relief	One fringe and segments (mainly at both sides) in diversified morphologies	Mirror and fringe are divided by a symmetry axis: the twist of the en echelon segments changes from dextral at the left side to sinistral at the right side of the symmetry axis (Fig. 4.7d).
Group 3: Mirror with complex fringes								
J9: Trefoil joint								
About the center	Elliptical with a large "tongue" downward	5	Increasing width, mainly to the right (southward)	Trefoil-like curved; in the inner part concentric	Radially laterally downward	Faint plume on the mirror and undulations	Three fringes to the left and five subfringes to the right of the tongue are intensely fractured (twist angles). The fringes at both sides differ considerably. Several en echelons and their steps in between are covered with secondary mirrors and fringes, indicating dominant mode I development. For further explanation, see text (Fig. 4.8a,b).
Group 4: Mirror with fringe of en echelon and hackly morphologies								
J10: Hackled fringe joint								
Not observable	Elliptical	–	–	–	Downward	Secondary mirrors with plumes and fringes on a few en echelons	One large fringe compared to the mirror size, with heterogeneous hackles and en echelons. A few are covered by secondary fractographic patterns, comparable to J9. For further explanation, see text (Fig. 4.8c,d).	

Note: The letter *p* is used in figure captions and figures and in this table to designate subhorizontal partings (that are often fractures). For explanations of other letter designations, see figure captions.

Table 4.2. Ellipticities of the north-northeast-trending Borsov joints

Joint		Strike azimuth (°)	Mirror size, L × S (m)	Ellipticities (L / S)			Joint size (L × S): mirror and fringe (m)
No.	Name			Initial mirror	Final mirror	Mirror and fringe	
J1	Multiarrest marks joint	23					
J2	Radial-plume joint	25	1.63 × 1.26				
J3	Quasi-core joint	23	2.60 × 1.90				
J4	Circular joint	~30	2.70 × 2.37	1.14			
J5	Divided arrest mark joint	25	2.61 × 1.90	1.37	1.27	1.67	
J6	Asymmetric bilateral joint	~20	1.40 × 1.10	1.31	2.56	2.29	15.30 × 6.67
J7	Uniform fringe joint	~2	2.90 × 2.60	1.29	1.43	4.29 × 3.00	
J8	Partly erased joint	~25	~6.00 × 5.00	1.20			
J9	Trefoil joint	25					
J10	Hackled fringe joint	~25	2.00 × 0.93	~2.14			

Note: *L* = long axis; *S* = short axis. Initial and final mirrors represent mirrors at their initial and final growth states.

4.4.2.2
The Unique Features of the Mirror Plane, Undulations, Arrest Marks and Fringes of the Trefoil Joint

General. The Trefoil joint is one of the ten Borsov joints described in Tables 4.1 and 4.2 and it displays a unique fracture surface morphology. The mirror plane of this joint deviates considerably from the common circular shape. Part of the mirror boundary extends downward as a "big tongue" beyond the common circular perimeter, and it forms the shape of a three-leaflet flower (Fig. 2.56a and 4.8a). The mirror is marked by two types of ripple marks (Sect. 2.2.4.2). The concentric set of delicate undulations (hardly noticeable on Fig. 2.56a) that imply relatively rapid fracture propagation, differs considerably from the set of lateral arrest marks, which reflect slow fracture propagation (u and a, respectively, in Fig. 4.8a). The arrest lines occur on the left side of the mirror but not at its right side. A faint set of radial striae (a plume) superposes the undulations on the mirror, indicating downward and radial joint propagation. A set of intense striae, emphasize the "semi-box" superpose orthogonally the lateral arrest marks (Sect. 2.2.4.2).

The two sides of the "tongue" contain large fringes that are intensely fractured, and their fracture styles differ considerably from each other. There is a resemblance in shape between the curvatures of the arrest lines and the series of sub-fringes at the right side of the mirror. These sub-fringes show contrasting senses of *en echelon* stepping (see Fig. 2.35e), implying a change of fracture mode under the influences of modified stress fields. The fringe on the left side of the mirror shows a complex fracture (Bahat et al. 2001b) on which we elaborate below. Finally, the mirror is jointed by sub-horizontal parting fractures that generally slope gently from left to right; several of them cut the mirror and the two fringes.

The left fringe. Here we focus on a joint with a particular relationship between a "primary mirror" (the mirror) and a "secondary mirror" that occurs on the fringe. The boundary between the mirror and the fringe is not a continuous curve but a zigzag one (Fig. 4.8a). The fringe is divided into four sectors that generally correspond to the zigzag boundary. These are from left to right, i–n, n–t, t–r, and r–m. We concentrate on the structure in the n–r sector. Two growth styles of *en echelon* segments and steps can be distinguished: First, vertical downward growth of alternating segments and steps from the boundary of the mirror (Fig. 4.9a,b) can be discerned; second, some six segments merge into one step that displays a tensile, secondary mirror plane with semi-circular boundary and a fringe that convex downward in continuation with the lengths of the segments that form the merger (Fig. 4.9c,d). This morphology of a tensile-step differs known fractographies in sedimentary rocks, where mirrors and other tensile fracture markings occur on *en echelon* segments but are absent on steps. Hence, the mirror of the trefoil joint was fractured into a segmented fringe that then continued to fracture into a secondary mirror, which also was fractured into a fringe. We discuss the conditions under which this joint formed in Sect. 4.9.3.1.

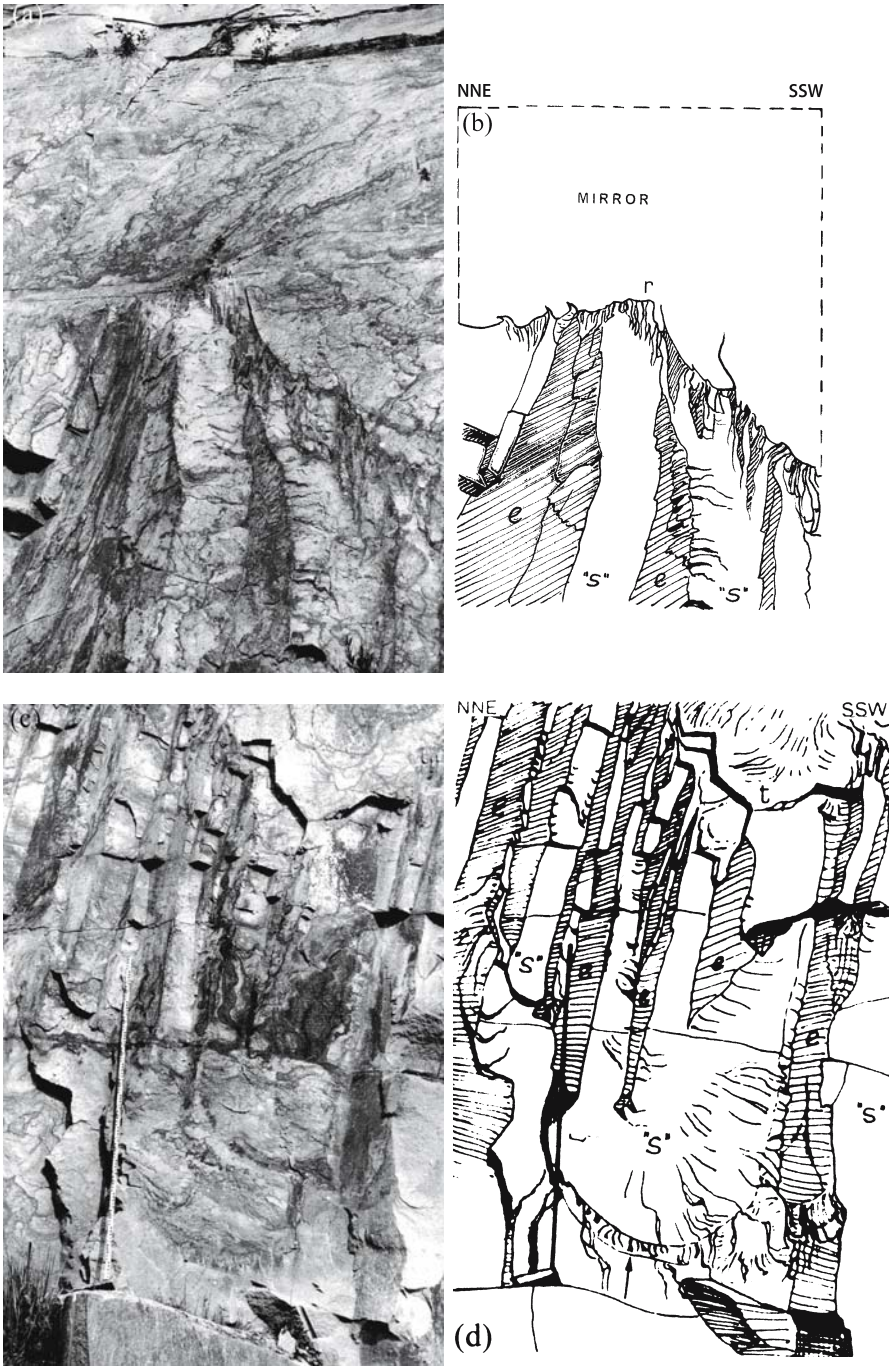

Fig. 4.9. a–d The left fringe of the "trefoil joint", where *e* and "*s*" are *en echelon* segments and steps, respectively (see text for explanation) (after Bahat et al. 2001b)

4.4.3
"Dynamic Joints" in a Fracture Zone from the Mrákotin Quarry

4.4.3.1
Characterization of Mirror Planes and Fringes in the Mrákotin Quarry

According to Bahat et al. (2001c; Bankwitz and Bankwitz 2004), two joint types are distinguished in the Mrákotin quarry (Fig. 4.2b), both of them trend NNE-SSW. First, vertical individual joints that are spaced several meters apart, and second, fracture zones that contain several parallel joints spaced about 5–10 cm (Fig. 4.10a). We concentrate on a set, which is exposed in a fracture zone about 30 m long and about 18 m high. These joints parallel each other on a single wall. The "Mrákotin set" consists of nine distinct neighbor joints, all striking about 025° (Fig. 4.10b,c). Joints A and B occur on one plane, joints C–H form a composite fracture on another plane that is further inside the rock body, and joint I forms a third plane still deeper in the rock. Spacing between the three planes varies from 5 to 20 cm, while joint fringes partly touch neighbor planes. Joints A–H with the exception of C contain mirrors that have one or two hackle-fringes above and below them (Fig. 2.1b). Joint C on the other hand exposes only a fringe at its lower part, which consists of *en echelon* segments (Fig. 2.1a). The mirrors of joints A–H deviate from the conventional penny shape into various ellipticities. The hackles of all fringes have the same sense of stepping in that they show clockwise rotation both above and below the mirrors; that is, they all are arranged such that walking across the hackles is downstairs from left to right (from south to north). Joint I exposes a large faint plume, and its mirror boundaries are not revealed. The nine individual joints are described below from south to north (Tables 4.3 and 4.4).

Joint A. Two large hackle fringes occur above and below the mirror of joint A. Whereas the upper joint boundary is somewhat curved, the lower boundary is fairly straight (Fig. 4.11a–c). Quarrying has removed the southern (left) mirror half and a larger part of the upper fringe so that its length parallel to the joint length is not fully revealed. The length of the lower fringe is 9 m. It becomes gradually wider (the lengths of individual hackles increase) from south (left side of Fig. 4.11a,b) to north (right side of figure) towards the center of the fringe. Hence, maximum width of the fringe occurs at about the middle of its length. There is correspondingly an increase in hackle coarseness in this direction.

In profile, the hackles at the lower fringe show strong deviations from the common uniform "shingle-structure" of *en echelon* fringes. Hackles vary considerably in lengths and show extreme variations in thickness among individuals and along the length of an individual hackle, appearing as wedges (Fig. 4.11c). They are not tabular, but some of them are rather distorted as if responding to a twist mechanism. They have similar strikes, but they differ in their dips. Note that whereas most of the lower hackles dip away from the mirror (towards the left, Fig. 4.11c), some hackles close to the mirror boundary of A dip towards the parent joint (to the right in this figure). Generally, the fringe forms an angle (ϕ) of about 10° with the parent joint. An intriguing feature in this fringe is one hackle, A* that strikes 290° and dips 65° towards NE, i.e., this joint rotates 85° with respect to the strike of A. This hackle has its own mirror and is fringed with a secondary hackle-fringe (Fig. 4.11a–c, Tables 4.3 and 4.4).

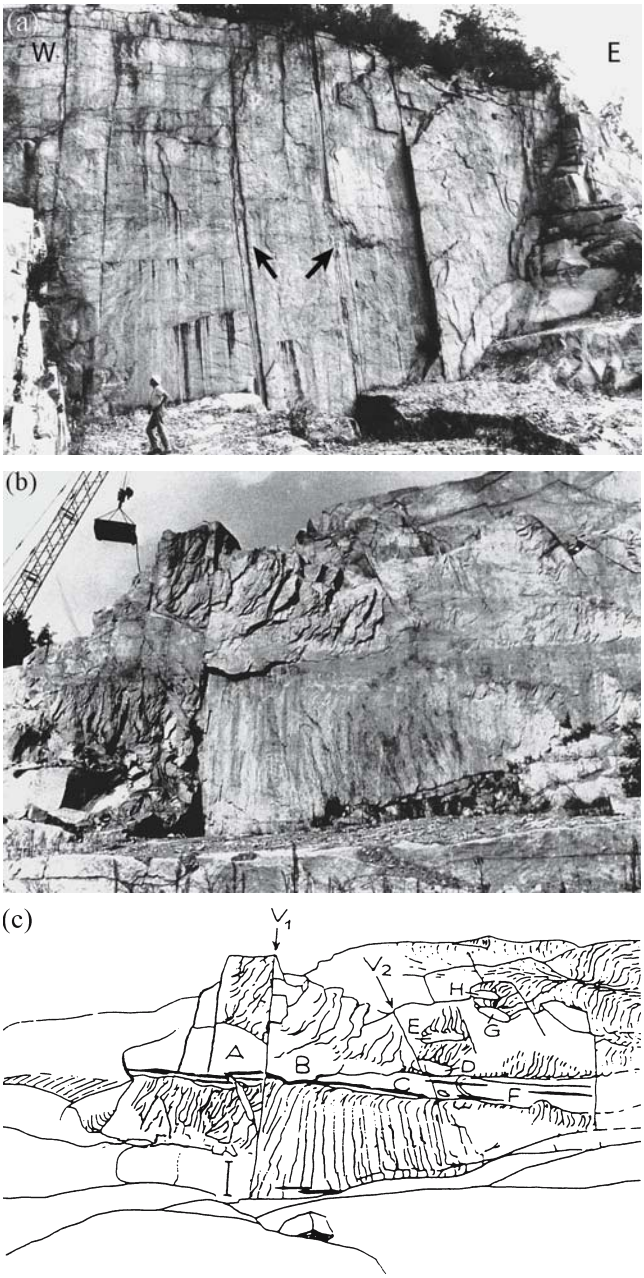

Fig. 4.10. Joints in the Mrákotin quarry. **a** A large joint (18 m high), roughly trending E–W, with vertical traces of approximately NNE trending individual joints and fracture zones (*arrowed*). The latter corresponds to the discussed Mrákotin set in the next figures. (from Bahat et al. 2001c). Photograph (**b**) and drawing (**c**) of the Mrákotin set of nine joints (*A*–*H* and the large plume at the upper right). The sub-vertical fracture *V1* separates joints *A* and *B* and *V2* cuts joint *D*. The fringe of jont *C* is somewhat erroded. Vertical *scale bar* at **c** is 2 m (from Bahat et al. 2002b)

Table 4.3. Characteristics of the 025°-set of joints in Mrákotin (example: Nine joints A–H)

Joint	Max. length (m)	Mirror propagation	Fringe	Boundary	Fringe cracks	Fringe propagation	Hackles and en echelons				Related figures
							Attitude	Strike	Dip	Type	
A	17 17	Laterally Laterally	Upper Lower	Curved Partly straight	Hackles Hackles (twist 25°)	Vertically (tilt 10°)	Hackles vary considerably in length and extremly in thickness (partly appearing as wedges) increasing towards the center of the fringe	Ca. 50°NE	Differing	Not tabular (deviation from common "shingle structure"	4.11
A*	2.7	Oblique			Hackles	Vertically Vertically	Differs from other hackles	290°WNW	65°NE	More tabular	4.11
B		Laterally	Upper		Hackles	Vertically	Similar to joint A fringe, only upper fringe is preserved			More tabular	4.11a; 4.12a
C	13	Laterally	Upper Lower	Covered by B Straight	En echelon segments (twist 20°)	Vertically		Ca. 45°NE		More tabular, but curved	4.12a
D	2.6	Laterally	Only upper Lower mirror boundary interacts with mirror C and F (which are much larger)		Hackles	Vertically	Interacted with the lower fringe of mirror E. This interaction promoted a local enlargement of the upper fringe			Not tabular	4.12a
E	3.4	Laterally	Upper Lower		Hackles	Vertically	Occurs above D				4.12a
F	10	Laterally	Upper Lower	Straight Straight	Hackles Hackles	Vertically Vertically					4.12b,c
G	1.8	Laterally	Upper		Hackles	Vertically	Occurs above joint D and at the right side of H				4.12b,c
H	1.5	Laterally	Upper		Hackles	Vertically	Occurs above joint E				4.10c

A* is one large fringe-hackle of joint A with its own mirror and its own secondary hackle-fringe.

Table 4.4. Fracture parameters of the Mrákotin 025°-joint set

I Joint	II Mirror (m) $L \times W$	III Mirror ratio L / W	IV Lower fringe (m) $L \times W$	V Upper fringe (m) $L \times W$	VI Joint ratio L / W	VII Mean ω echelons/ hackles	VIII Range ω
A	17.0 × 4.0	4.4	16.0 × 4.0	16.0 × 4.0	1.3	26	0–28 ($n = 10$)
A*	2.7 × 0.6	4.5	2.3 × 1.6	2.7 × 1.2	1.3		
B							
C	13.0 × 1.6	8.1	13.0 × 8.0		1.4	20	0–26 ($n = 12$)
D	2.6 × 0.6	4.3		2.6 × 1.0	1.3		
E	3.4 × 1.0	3.4		3.4 × 1.5	1.4		
F	10.0 × 0.5	4.3	10.0 × 4.0	10.4 × 1.0	1.4	25	0–27 ($n = 12$)
G	1.8 × 0.5	3.6		1.8 × 1.8	1.3		
H	1.5 × 0.5	3.3		1.5 × 1.6	1.4		

Explanation: $L \times W$ designates (length × width), i.e. lengths of long and short axes, respectively. L / W designates ratio of long / short axes; ω is the twist angle; A* is a secondary mirror at the fringe of joint A.

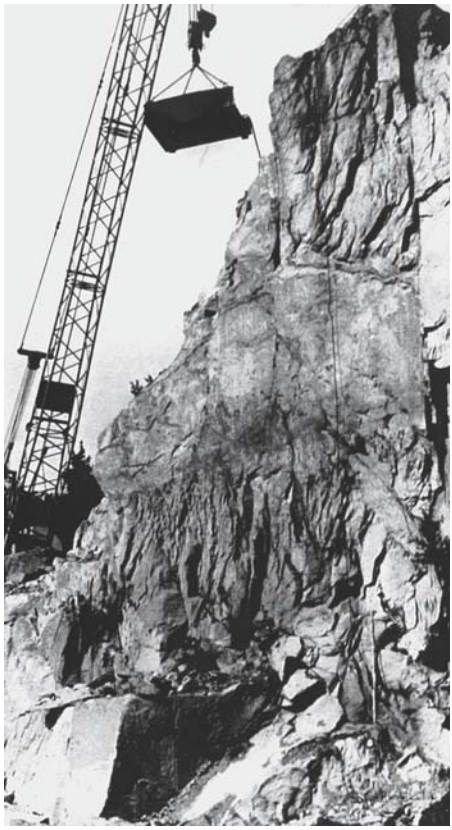

Fig. 4.11a. Joints in the Mrákotin quarry. Photograph of the 025° trending joint *A*. *Vertical ruler* is 2 m (from Bahat et al. 2001c)

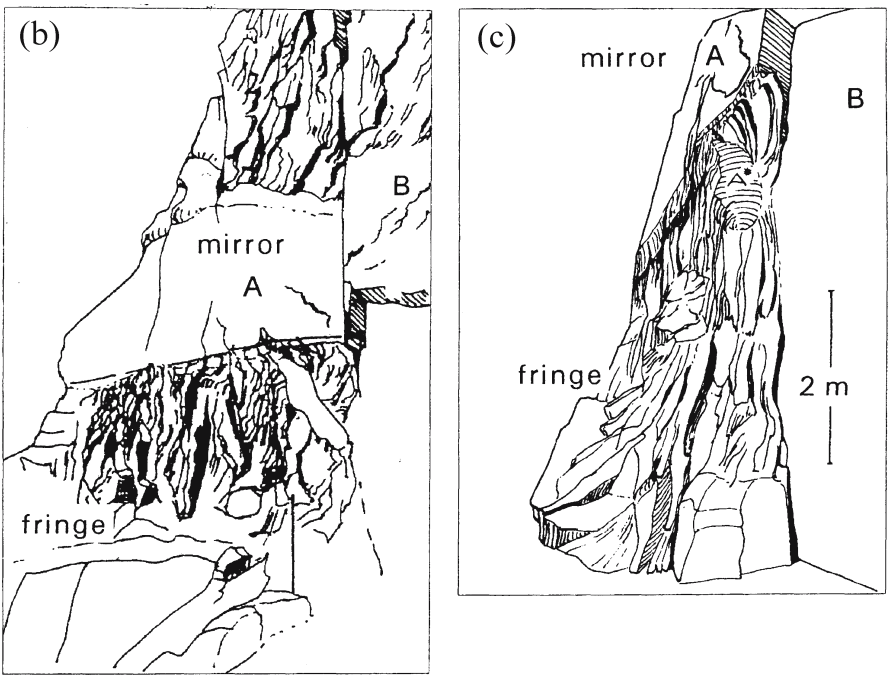

Fig. 4.11b,c. Joints in the Mrákotin quarry. **b** Drawing of the 025° trending joint *A*. *Vertical ruler* is 2 m. **c** Profile drawing of joint *A*, where *A** is possibly an equivalent of *M2* in Fig. 2.30e (after Bahat et al. 2001c)

Joints B–H. Joint B reveals only the upper part of the mirror and the upper fringe. Mirrors A and B are separated by a vertical fracture (V1 in Fig. 4.10c), which had preceded the mirrors because the mirrors and fringes of these joints look as if their shapes were modified along fracture V1 (Bankwitz 1966). This fracture seems to belong to the set that includes the large joint (Fig. 4.10a). The upper part of the parent joint C is partially covered by joint B, but the lower boundary of the mirror of joint C is exposed, and it is approximately straight (Fig. 4.12a). The visible part of joint C has only one fringe, below the mirror, consisting of *en echelon* segmentation. The small mirror D has a fringe only at its upper side. In its lower part, mirror D interacts with mirrors C and F (which are much larger) (Fig. 4.12a–c). Joint E occurs above joint D and has fringes both above and below the mirror. The upper fringe of joint D is relatively large, and it appears that it interacted with the lower fringe of mirror E, penetrating somewhat into the E mirror.

By far the longest mirror in the composite is F (Fig. 4.12b,c). The F-joint seems to have propagated from north to south. There are large fringes above and below the parent joint and both boundaries are fairly straight. The lower fringe is partly erased by the quarrying process. The upper fringe, on the other hand, is well preserved and it has its maximum width at about its mid-length. Joint G is the smallest one; it occurs north of joint E and above the upper fringe of joint F. Joint H is located above joint G and is a little smaller than that joint.

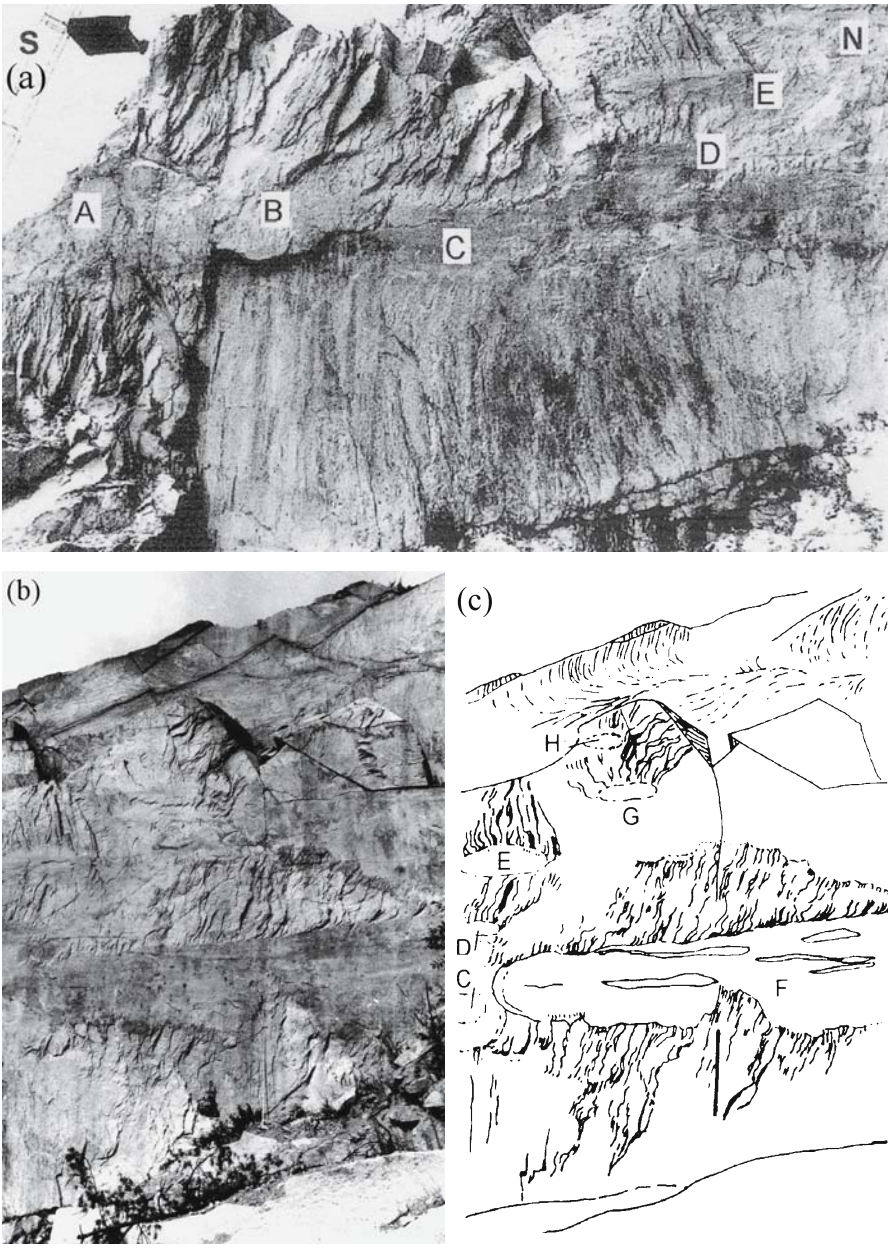

Fig. 4.12. Joints in the Mrákotin quarry. **a** Joints *A–E*. **b** Photograph and **c** drawing of a part of the "composite fracture" wall with joints *C–H*. *Ruler* is 2 m (from Bahat et al. 2001c)

Ellipticity of mirrors and joints. The mirrors of joints D and E are surrounded by curved boundaries. On the other hand, the boundaries of joint A and the lower boundary of joint F approach straightness, and the upper boundary of joint F is straight.

Our measurements of the Mrákotin set (Table 4.4) reveal two features. With the exception of C, for all other joints the ratio of long to short axes is similar for the various elliptical mirrors, ranging from 3.3 to 4.5, independent of elliptical size. However, this ratio is reduced to the range from 1.3 to 1.4 for the full joints (combined mirrors and maximum widths of the fringes for every joint).

Shape of fringes. Joints C and F have only lower fringes, whereas joints D, E, G and H have only upper fringes. The increase in fringe width to a maximum (towards a shape of quasi-triangle) seems to repeat itself in the upper fringes of joints D, E and F, and possibly also in the lower fringes of joints A and F, and the upper fringe of joint B. This characteristic is different from the conventional fringes of uniform width in synthetic materials (e.g., Mecholsky 1991, Fig. 1) and many rocks (e.g., Fig. 2.34b and 2.35a,b).

4.4.4
Twist and Tilt Angles on Joints Cutting Granites in Europe

Two angular relations that fringes form with mirror planes of joints are of particular interest: The twist angle ω and the tilt angle ϕ (Fig. 2.53). The characterization of ω and ϕ may be used in the interpretation of fracture conditions (Cooke and Pollard 1996 and Bahat and Rabinovitch 2000, respectively). Bankwitz and Bankwitz (2004) measured ω and ϕ on joint surfaces that cut various granites in Europe. Their results are summarized in Fig. 4.5, 4.13a,b and 4.14a, providing the first comprehensive account of the tilt angle ϕ in a series of rocks. They illustrate the steady NNE orientation of seventeen pre-uplift joints throughout the SBP and the consistent sense of *en echelon* segmentation with respect to the parent joints, and a large, 16° spread of ω values (between 22° and 38° (Fig. 4.5). Larger joint populations show even greater spreads of ω value, i.e., 40° in the Borsov quarry, and some 35° in the Mrákotin quarry (Fig. 4.13b). Values of ω from the Erzgebirge vary in the 9–22° range (Fig. 4.14a). The spreads of the ϕ values vary considerably from pluton to pluton and the spreads are particularly large in the Borsov quarry (Fig. 4.13a) and in the Erzgebirge (Fig. 4.14a).

Bankwitz and Bankwitz (2004) plotted the logarithmic tilt/twist ratio vs. palaeo-depth of pluton emplacement (Fig. 4.14b). They suggest a correlation in which the shallowest intruded pluton (Eibenstock, Germany) represents the largest ratio range and the deepest pluton (now exposed) is characterized by the smallest ratio range. Apparently, the depth of joints from Borsov is 7.4 km, and the ratio range is very large, while the depth of joints from Weinsberg is 15 km and the ratio range is much smaller, raising the suspicion that in shallow depths fracture conditions are variable, while great depths unify them, and this occurs between 7.4 and 15 km depths. This however does not coincide with the great spread of ϕ values observed in the shallow Erzgebirge (Fig. 4.14a). Quite intriguing is also the low spread of ω on joint surfaces in the Erzgebirge. Perhaps it suggests that fracture took place under relatively uniform stress conditions, which maintained only small variations in the local K_{III}/K_I ratio (Fig. 2.21a). Hence, it appears that generally the spreads of ϕ and ω are quite large (Fig. 4.13a,b) and for no clear reasons. Also noticeable are the ϕ values of some joints that vary very considerably in a given fringe (see gray markings in Fig. 4.13a). This suggests that an interpretation of the petrological conditions (e.g., depth) of these granites during jointing should be carried out with great caution. The great angular ranges found at the Borsov quarry is not surprising in view of the extreme diversified fractography found in this quarry (Fig. 4.6–4.9).

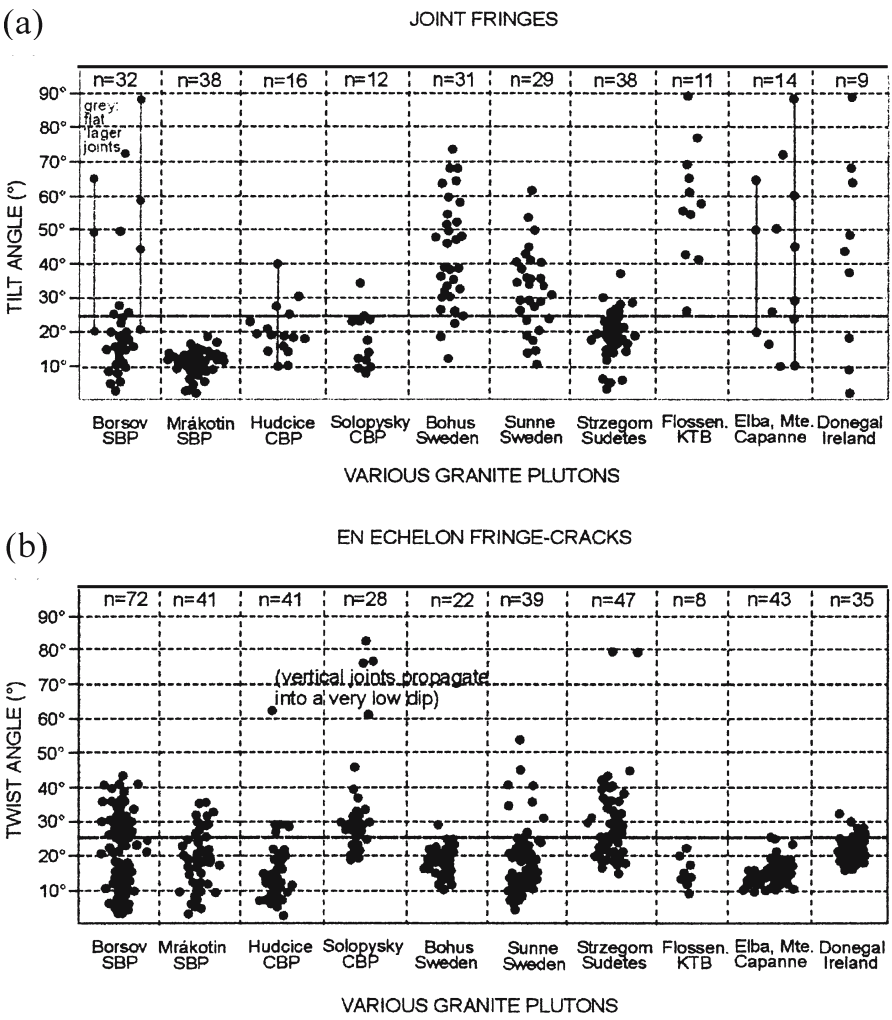

Fig. 4.13. **a** Tilt, ϕ and **b** twist, ω angles on joint surfaces from various plutons in Europe: *SBP:* South Bohemian Pluton; *CBP:* Central Bohemian Pluton. *KTB:* Near the KTB (Continental Super-Deep Borehole); Flossen: Flossenbürg Granite, Bavaria (from Bankwitz and Bankwitz 2004)

4.4.5 Geological Interpretation of the Joint Fractographies in the Borsov and Mrákotin Quarries

While the set described here from Borsov consists of joints that occur in various outcrops within the large quarry, the investigated set from the Mrákotin quarry consists of joints that are displayed on a single wall. The sets from the two quarries display different fractographies, and their respective interpretations focus on different issues complementing each other.

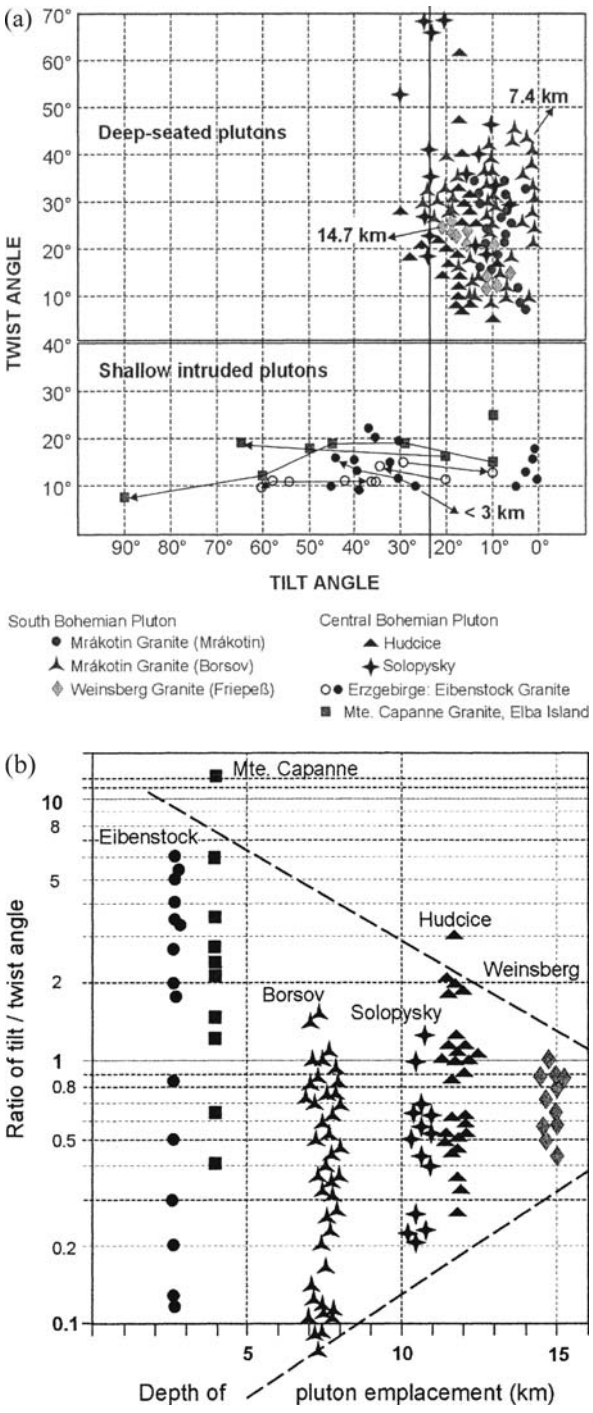

Fig. 4.14.
a Relationship between twist, ω tilt, ϕ angles of early granite joints in different plutons in Europe. **b** The logarithmic ratio of ϕ/ω vs. palaeo-depth of emplacement of the plutons plotted in Fig. 4.14a. The most shallowly intruded pluton (Eibenstock) shows the widest range of ratios; the deepest pluton (Weinsberg, now exposed) is characterized by the smallest range of ratios, between ~0.5 and 1.0. Symbols as in Fig. 4.14a (from Bankwitz and Bankwitz 2004)

4.4.5.1
Geological Interpretation of Joint Fractography in the Borsov Quarry

In this section, we limit our discussion to three aspects of jointing: Fluid-driven fracturing, mirror ellipticities and their unilateral growth, and plutonic vs. sedimentary rock's fractographies.

Fluid-driven fracturing. The Borsov joints cover very wide v and K_I ranges (Fig. 4.35). Particularly intriguing is the question of what could cause these fractures to grow under such extreme different conditions, from sub-critical to post-critical. These conditions could be changes in local stresses due to changes in the magnitude of remote stresses that would alter the component of local normal stress. It appears however that drastic changes in fluid pressures in the granite history could have been the main mechanism leading to joint fracture surface diversification at Borsov. The rhythmic arrest marks (particularly in Fig. 4.6a–c and 4.7a) are linked to the fundamental concept in the Secor theory (1969) of fracturing by pore pressure (Bahat and Engelder 1984). This process involves "fluid-driven fracturing" (Engelder et al. 1993, p. 44) and "rhythms of fluid-pressure build-up and fracture-induced release" Davis and Reynolds 1996, p. 248). Thus, the frequent appearance of numerous arrest marks (Sect. 2.2.4.2) probably indicates fluid-driven fracture processes, at least during the early stages of joint growth at Borsov. This interpretation fits well the presence of biotite and biotite-muscovite petrographic manifestations in the rock.

The elongated axis of the South Bohemian Pluton coincides with the dominant strike direction of the flat dipping main foliation in the neighboring metamorphic country, and structurally coincides with the crest line of the pluton (Benes 1971). This suggests that the shape of the pluton could have controlled significant thermal and fluid-pressure gradients, which in turn influenced the orientation of the joints. It could also influenced one of the regional, horizontal principal stresses in the NNE direction (see below). Such relationships most likely have existed during the late stage of the granite solidification before its uplift. Field contacts at the Borsov quarry support this interpretation: Aplite thin dikes that are associated with two joints seem to register melt fillings along the existing joints, i.e., the NNE joints were available when this late fluid of the granite injected. If aplite represents the fluid that created the joints, this rock should have been associated with all (or most) joints, which is not the case. See an alternative interpretation in Sect. 4.4.6. These joints are less likely to be the result of mechanical stresses induced by thermal gradients during early stages of the cooling process. Such gradients are likely to be influenced by local conditions, causing considerable strike deviations from regional uniform joint patterns. This could not be recognized. It is also unlikely that the NNE fractures are late (Tertiary) uplift joints, mainly because uplift horizontal sheets cut the earlier vertical joints, and the latter do not show fracture morphologies indicating downwards propagation, which characterize uplift joints.

Mirror ellipticities and their unilateral growth. Practically all the joints at Borsov that reveal their boundaries show that their mirrors deviate from circularity into various ellipticities. The incremental crack growth exhibited by J6 shows a pronounced unilateral growth of the radii of arrest marks (Fig. 4.7b), suggesting a general slow fracture growth but a relative faster fracture propagation along the 8° dip of the "mir-

ror symmetry axis" than normal to this direction. Note that the dip of the symmetry axis of J3 is even greater (24°) (Fig. 4.6c); both deviate from either horizontal or vertical directions. Apparently, the same joints that display eccentric origins also show small angle dips of their symmetry axes on the mirror planes. Hence, some earlier fractures that constrain the Borsov joints are not quite horizontal, leading to occasional inclined mirror symmetry axes. The constraints that caused this unilateral growth could be sub-horizontal unisotropies imposed by either petrographic boundaries (Bankwitz and Bankwitz, unpublished), differences between horizontal and vertical compression, or earlier fractures. It appears that constraints by earlier fracture influenced the growth of most Borsov joints as seen on joints J1, J2, J4, J5, J6 and J7.

Plutonic vs. sedimentary rocks. The wide spectrum of fracture surface morphologies displayed by the Borsov joints that reflect different fracture processes in a single set seem to be exclusively associated with jointing in granite during its late solidification stage and do not occur in sedimentary rocks. Fracture markings from a given joint set in sedimentary rocks are commonly limited to simple combinations of one to three features shown in Fig. 2.1a, because they form by a restricted number of fracture mechanisms. Rare complex combinations often reflect special processes. A case in point is displayed by "mark overprinting", where a superposition of a late uplift joint on an early burial (diagenetic) joint shows different fracture surface markings, but these different markings occur along two different sets of joints (Bahat 1991a, p. 288). Unfortunately, only partial mirror boundaries are known from sedimentary rocks, and these are not sufficient for comparison with the present results. The eccentric origins and small dips of the symmetry axes on the mirror planes are rare in sedimentary rocks. In horizontal sedimentary layers, plumes generally are parallel to layer boundaries.

4.4.5.2
Geological Interpretation of Jointing in the Mrákotin Quarry

The joints of the Mrákotin set display composite fractures on three adjacent closely spaced parallel planes in a fracture zone. The joints on each plane interacted intensively with each other such that fringes between mirrors are either missing or increase to large sizes. This interaction resembles the interacting early joints cutting the El Capitan granite at Yosemite National Park (Bahat et al. 1999) (Sect. 4.5.3.3). There are however several important differences between the two interactions.

Dynamic growth. Compared to the El Capitan set that did not develop full mirrors and fringes, the Mrákotin set formed full mirrors and hackle fringes. The hackle fringes imply dynamic growth, i.e., rapid growth of most joints under high stress intensity conditions (Sect. 4.8.4), with the consequence of fracture interaction. Apparently, joints of strongly reduced spacing within fracture zones can be distinctly parametrized from joints in sets that do not occur in fracture zones (Rabinovitch and Bahat 1999). The series of distinct, adjacent joints implies independent fracture nucleation from many sites. The considerable size difference of the mirrors (Table 4.4) suggests that the growth of these joints was strongly affected by local fluid pressure conditions. While most of the Borsov joints (J1–J7) propagated sub-critically during most of their fracture histories (Sect. 4.8.5), most of the Mrákotin joints essentially formed dynamically.

Ratios of long to short axes of joints. The reduction in the ratio of long to short axes of the mirrors from the 3.3 to 4.5 range to the ratio of almost 1 (Table 4.4) for the full joints including fringes is intriguing. The growth towards the ratio 1 is expected from the theory that an ultimate growth of a fracture should follow the trend of decrease in ellipticity (e.g., Irwin 1962; Roy and Saha 1995). The long axes of the elliptical mirrors are horizontal. What stopped the mirrors from growing to a circular (penny) shape? We did not identify early sub-horizontal fractures comparable to those found to have influenced the growth of some of the Borsov joints. The depth of emplacement of the Mrákotin granite was determined by Büttner and Kruhl (1997) to be ~15–18 to 7–10 km (compare to Sect. 4.4.6). Great overburden pressure at these depths may explain what prevented the mirrors from propagating vertically, upward and downward and induced lateral propagation of the mirrors. The question still remains of what has changed when growth occurred beyond the mirror boundaries, and if it was gradual or abrupt. It appears that the change was violent and abrupt, as suggested by the hackles and the quasi-triangle fringe of joint F (Fig. 4.7b). Possibly, the change was caused by a sudden rise in fluid pressure that increased the extensile stress on the joint mirrors, such that the overburden pressure was overcome.

Joints A and C. Joint C differs from all the other fractures in the Mrákotin set in having a fringe consisting of *en echelon* segments, compared to the hackle fringes that characterize the others. Furthermore, joint C is surrounded upward and sidewise by the other joints (Fig. 4.10c and 4.12a). This again implies that the joints did not form by a uniform stress field. It is suggested that fluid pressures were smaller or less effective at the center on joint C and greater around it.

4.4.5.3 *Summary*

This section focuses on the Mrákotin quarry, where a single "vertical wall" exhibits a set of nine joints in a fracture zone. These joints nucleated independently from many sites.

The considerable size difference of the mirrors probably suggests that the growth of these joints was strongly affected by local fluid pressure conditions.

The hackle fringes that characterize these joints imply dynamic growth, i.e., a rapid growth of most joints under high stress intensity conditions, with the consequence of fracture interaction.

For most joints, the ratio of long, sub-horizontal to short axes of the elliptical mirrors ranges from 3.3 to 4.5. However, this ratio is reduced to the range from 1.3 to 1.4 for the full joints (combined mirrors and maximum widths of the fringes for every joint).

The sub-horizontal mirror boundaries of the joints, particularly joint F, imply growth constraints above and below the mirror possibly due to great overburden pressure, which prevented the propagation of the mirror to a circular shape. At some stage the growth was resumed, as demonstrated by the fringes, possibly by a rise in fluid pressure.

It is expected that the fluid pressures that induced fracture in the Mrákotin quarry had to surpass the overburden pressure, and they reached maxima that were greater than the pressures calculated by the fluid inclusion analysis (see below). Possibly, the fluid pressure was smaller or less effective on joint C at the center and greater on the joints around it.

There is a genetic linkage between the joints investigated in the Mrákotin and Borsov quarries. The strike of all mirrors at the Mrákotin quarry is roughly uniformly directed

at NNE, characteristic to the SBP, with the implication that this direction coincides with one of the regional horizontal principal paleostresses (Sect. 4.7, below).

4.4.6 Timing, Depth and Temperature of Joint Formation

This section is cited from Bankwitz et al. 2004, who combined several techniques in studying the timing, temperature and depth of NNE trending joints in the SBP (Fig. 4.5).

Methods. Samples of the Mrákotin granite were taken from fringes of the "Trefoil joint" and the "Bilateral asymmetric joint" that outcrop in the Borsov quarry (Fig. 4.8a and 4.7b, respectively) and from the the Weinsberg granite (Fig. 4.5) at the Friepeß quarry in Austria. The K-Ar method was used on these samples for age determination and for fluid inclusion analysis (applied on muscovites) of the temperature and depth of intrusion of the granites (Scharbert 1998). The latter analysis was also applied on Erzgebirge plutons (Fig. 4.2a).

Temperature and depth of intrusion of the Mrákotin granite and a late dike. According to Bankwitz et al. 2004, the minimum intrusion depth was estimated from the *P-T* conditions of the trapping data of fluid inclusions (Table 4.5), using a lithostatic model with a rock density of 2 600 kg m^{-3}. In the Mrákotin granite, the average temperature of homogenization in the fluid phase of seventeen fluid inclusions is $T = 620$ °C, i.e., the trapping temperature of the inclusions that are under pressure conditions of $P = 1.89$ kbar. Under the assumption of a lithostatic pressure at this crustal level, the depth at the time of inclusion formation of these samples is estimated to be 7.4 km. For the inclusions in the Weinsberg granite, the level of generation was much deeper, at 14.3 km with associated higher temperature and trapping pressure of 3.65 kbar.

Temperature and depth of intrusion of plutons in the Erzgebirge. The heating-quenching microthermometric method was applied by Bankwitz et al. 2004 in the analysis of 1 386 melt inclusions in quartz, apatite and feldspar of several plutons (e.g., Eibenstock, Kirchberg, Bergen and Ehrenfriedersdorf granites) of the Erzgebirge (Fig. 4.2a). According to the deep seismic reflection profile, most of these plutons belong to a shallow granite "sheet" within the upper crust without deep roots (Behr et al. 1994). The estimated trapping pressures of melt inclusions in the various plutons range between 1.1 ±0.1 kbar and 1.0 ±0.1 kbar, and trapping temperatures of 562 ±2 °C to 577 ±7 °C correspond to intrusion levels of about 3 km. Geological evidence for shallow intrusion levels comes from vitreous glass inclusions that occur together with

Table 4.5. Trapping data of fluid inclusions in quartz of a late-granite dike, intersecting the Mrákotin granite (*FK-1*), and in quartz of the Weinsberg granite (*FK-11*). Both granites are granite-types of the South Bohemian Pluton; *n:* Number of determinations

Sample	Salinity (NaCl-equiv. %)	Homogenization temperature (˚C)	*n*	Trapping temperature (˚C)	Trapping pressure (kbar)	Depth (km)
FK-1	5.8 ±0.6	375 ±6	17	620	1.89	7.4
FK-11	13.8 ±0.2	332 ±10	20	662	3.65	14.3

normal crystallized melt inclusions in granitic quartz of several Erzgebirge plutons.. Glass inclusions demonstrate rapid cooling or quenching that is not compatible with a deep intrusion level (Thomas and Klemm 1997). Therefore, the first fractures could be initiated during granite cooling below 560 °C at a depth of about 3 km, where the trapping of the investigated inclusions of the Erzgebirge samples occurred.

Interpretation of timing, depth and temperature of joint formation. Bankwitz et al. 2004 arrived at the following sequence of events. The intrusion age of the Mrákotin granite is 327 ±4 Ma, and cooling took place during the 327–325 Ma interval. According to the cooling age of muscovite extracted from a late-granite dike associated with jointing, fracturing started at 324.9 Ma. After joint initiation cooling of the SBP continued to 320 Ma though, 312 Ma was measured in the southern part of the Cimer granite (Mrákotin granite is the local name of the Cimer granite in the more northern SBP intrusion area). The younger granite Homolka intruded at 320–314 Ma, and then the deep-rooting granite bodies intruded in the axial part of the SBP (the Zvule granite, Breiter 2001). The Mrákotin granite intruded in about 800 °C at a deeper level during 327–328 Ma and exhumed to 7.4 km at 325 Ma. The NNE oriented joints in the Borsov quarry formed at 7.4 km depth in 324.9 Ma by the late-granite dikes that induced natural hydraulic fracturing. The fluid inclusions of the dikes were trapped in 620 °C. The dike then cooled to about 350 °C, given by the cool-

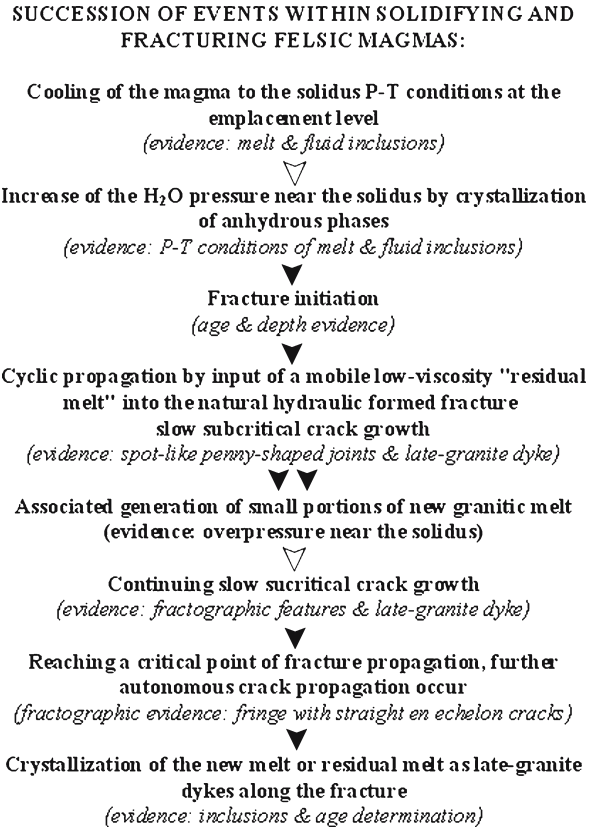

Fig. 4.15.
Model of early deep-seated fracturing in solidifying granite magma of the South Bohemian Pluton, summarized from fractographic investigations on fluid and melt inclusions (from Bankwitz et al. 2004)

ing temperature of the muscovite in the dike in 325 Ma (Scharbert 1998). Finally, most intriguing is the occurrence of NNE oriented joints, presumably of the same set, in plutons that originated in extremely different depths: Joints from Borsov at 7.4 km and joints from Weinsberg (Fig. 4.5) at 15 km.

According to Bankwitz et al. (2004), the sequence of intrusions in the SBP (Table 4.6) combined with the above set of depths and temperature conditions, provide evidence only for weak exhumation during the cooling stage between 327 Ma and 325 Ma. A recognizable exhumation that started at only 310 Ma is known from the Bohemian Massif (west of the SBP where analogous intrusions exist), based on results derived from apatite-fission tracks. This process lasted during the 310–280 Ma period in association with the late-Variscan exhumation (Wagner and Van Den Haute 1992; Menzel and Schröder 1994). The exhumation was not a continuous process. Exhumation of 3.3 km is estimated to have taken place during the first stage (Coyle and Wagner 1995). The second period of exhumation occurred in Lower Triassic and the third in Upper Cretaceous/Tertiary times. Finally, Bankwitz et al. (2004) conclude that the sequence of major events was:

1. Cooling of the Mrákotin granite melt down to the solidus.
2. Injection of residual melt into the solid phase of the Mrákotin granite, thus forming late-granite dikes and creating the NNE-trending hydraulic fractures.

They hypothesize a multi-stage process of repeated cycles of melt generation and fracture (Fig. 4.15), a model that may guide a future stimulating research.

Table 4.6. Succession of early main joints in granites of the SBP

	Early joints	Later joints	
Quarry	**First sets (Ø)**	**Second sets (Ø)**	**Third sets**
Mrakotin granite (SBP-N)			
Boršov	Subhorizontal NNE: 025°/090° + ESE:110° to 120°/090° fringe cracks: 060°/090°	NNE + ESE 042°/040°	ENE ~120°/090° Subhorizontal
Mrákotín	Subhorizontal to W-dip NNE: 025°/085° + ESE:120°/090°		
Rásná	Subhorizontal to W-dip NNE: 010°/090° + ENE:080°/090°	E–W	N–S
Mislotice	NNE	NNW to N–S	
Sumrakov	NNE: 020°/090° + ESE:~115°/090		
Olši	NNE		
Weinsberg granite (SBP-S)			
Friepeß	NNE: 025°/085° fringe cracks: 060°/090°	ESE: ~120°/090°	
Hartelberg	ENE: 080°/080° ESE: 120°/085° NNE: 018°/090° + ESE: 115°/090° Fringe cracks: 060°/090°		
Hartberg	NNE: 010°/090° + ESE: 105°/090°		
Windhaag	NNE: 030°/088° + ESE: 100°/085°		

4.5 Joints in Granites from the Sierra Nevada Batholith in California

4.5.1 Introduction

Bateman and Wahrhaftig (1966) discriminate between several types of joints in the Sierra Nevada (Fig. 4.16a). These include early "cooling", later "steep", presumably near vertical (including vertical), and younger "gently dipping sheeting" as well as "exfoliation joints" that are oriented like the steep joints. They found that generally it is possible to identify two principal groups of steep joints almost at right angles, one group striking NE and the other NW. Bateman and Wahrhaftig (1966) did not distinguish different sets within the groups of steep joints. However, in some places nearly parallel joints cross one another, and where a significant change takes place in the strike of one joint set, the joints of one strike generally interfinger with the joints of another strike; a description that raises suspicion about more than one set (Younes and Engelder 1999 and present Sect. 3.1.2 and 3.1.6). Furthermore, Bateman and Wahrhaftig (1966) note that spacing between joints ranges from less than an inch to hundreds or even thousands of feet. Such changes in spacing often provide guidelines in separating joints into distinct categories and possibly distinct sets (Bahat 1991a, p. 308). Thus, it seems quite possible that the near-vertical joints belong to more than two orthogonal sets.

Bateman and Wahrhaftig (1966) consider that the continuity of joints across boundaries between individual plutons indicates that the joints formed after the consolidation of the entire Sierra Nevada batholith, before the Eocene. The abundance of regional near-vertical joint sets striking N-NW and E-NE that are approximately perpendicular to each other in the Sierra Nevada Batholith was noted by additional others (e.g., Becker 1891; Huber 1987, Fig. 33). Lockwood and Moore (1979) observe that strike-slip microfaults (original joints on which some displacement is measurable) are pervasive throughout the granitic rocks of the eastern Sierra Nevada. Offsets typically range from less than a millimeter to several tens of centimeters, but exceed 100 m in some places. The microfaults are oriented in two nearly vertical conjugate sets: A N-NE striking set showing right lateral offset and an E-NE striking set showing left lateral offset, the latter is more common. They also plotted and measured lineaments (Fig. 4.16b,c) and found that most lineaments visible on aerial photographs are microfaults. The age of this microfaulting is not precisely known. It developed after consolidation of the youngest granitic plutons in the Sierra (79 Ma) and is known to cut a late Miocene volcanic dike in one area. Slickensides along the microfaults are sub-horizontal but show an average plunge of about 3° westward, suggesting that much of the deformation occurred prior to the westward tilting of the Sierran block in late Tertiary time. The direction of maximum horizontal extension strain (determined as the bisector of average microfault trends) changes (rotates) systematically from north to south (WNW at 38.5° N; NW at 36.5° N). A detailed study of microfaults at 37°20' N indicates a maximum extension of 2.3% in a N 61° W direction. These extension directions are remarkably parallel to late Mesozoic to present-day tectonic extension directions in the Basin and Range province. Thus, Lockwood and Moore (1979) differ in the description of fracture from Bateman and Wahrhaftig (1966); they found two major conjugate sets of microfaults, (N-NE and E-NE) rather than two major groups almost at right angles, one set striking NE

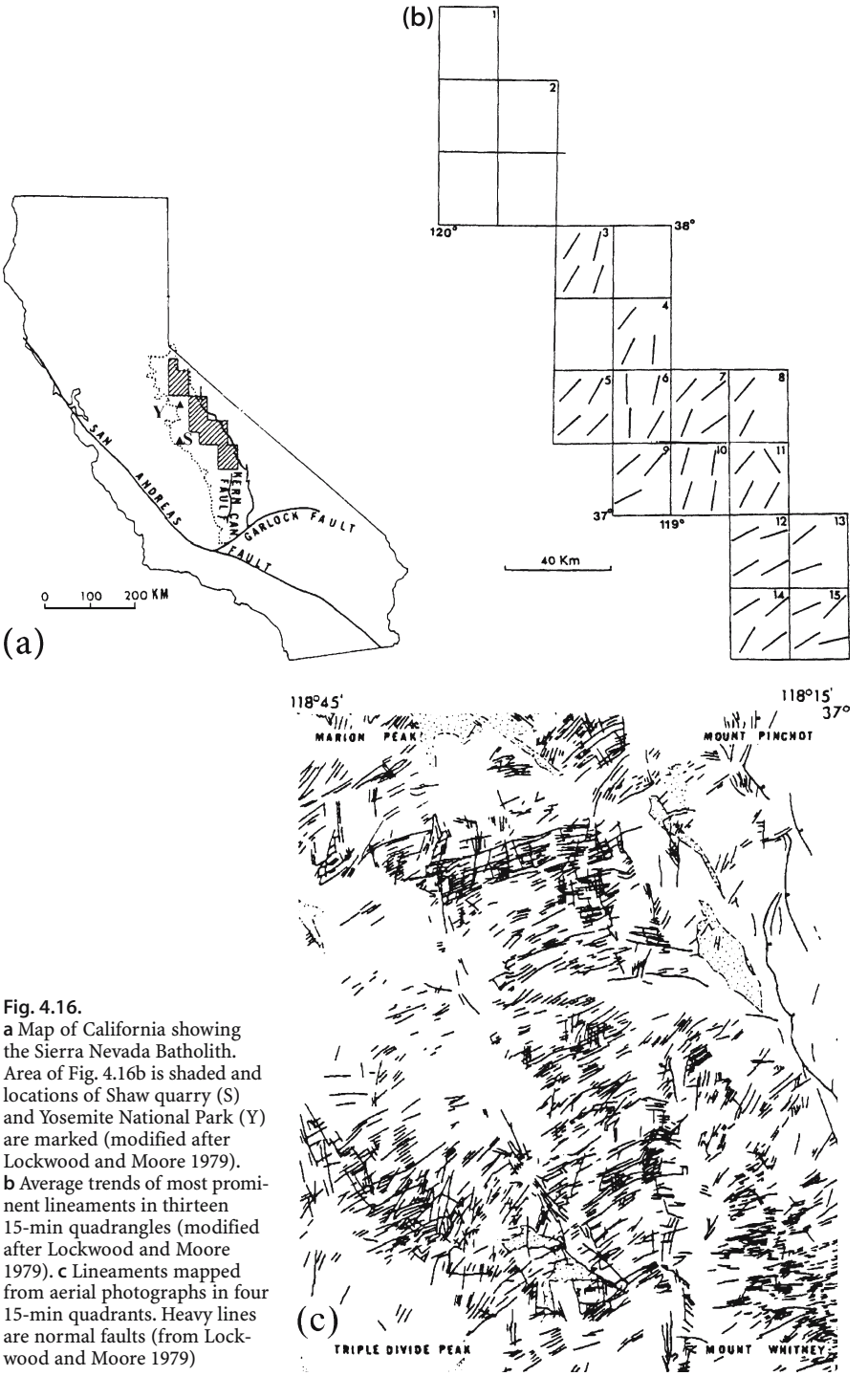

Fig. 4.16.
a Map of California showing the Sierra Nevada Batholith. Area of Fig. 4.16b is shaded and locations of Shaw quarry (S) and Yosemite National Park (Y) are marked (modified after Lockwood and Moore 1979). **b** Average trends of most prominent lineaments in thirteen 15-min quadrangles (modified after Lockwood and Moore 1979). **c** Lineaments mapped from aerial photographs in four 15-min quadrants. Heavy lines are normal faults (from Lockwood and Moore 1979)

and the other NW. However, Lockwood and Moore (1979) agree with the interpretation of Bateman and Wahrhaftig (1966) regarding the "post consolidation" timing of fracture. They conclude that the pattern of microfaulting demonstrates that the (supposedly monolithic) Sierran terrane was affected by the late Cenozoic and possibly earlier regional extension of western North America. Huber (1987) considers that jointing could have occurred during late tectonic events, such as tilting of the Sierra region, 25 to 15 million years ago. Accordingly, these fractures reflect *syntectonic* (possibly *uplift*) processes rather than *cooling* ones.

In contrast to Bateman and Wahrhaftig (1966) and Lockwood and Moore (1979), Balk (1937) and Mayo (1941) consider that the steep orthogonal fracture systems in the Sierra Nevada developed during the emplacement of the plutons, and Segall et al. (1990) suggest that they formed soon after the host pluton was emplaced, between 85 and 79 Ma. Zawislanski (1994) suggests that in the Knowles granodiorite that has been dated as 111 Ma (see below), pegmatites, representing late granite differentiates, may have filled early tension-fractures related to the cooling of the pluton. Thus, it seems justified that the fractures described by Balk (1937), Mayo (1941), Segall et al. (1990) and Zawislanski (1994) be termed *cooling joints*.

Restating the problem, it is possible that different authors may have assigned steep joints to distinct times in relation to the petrological history of the pluton (during emplacement vs. post consolidation of the pluton), and that they consider different fracture systems to represent three or four regional sets rather than two that developed during different geological periods. Alternatively, as inferred from Lockwood and Moore (1979), there was a systematic change in stress direction that resulted in the formation of a series of orthogonal sets of joints and faults (Segall and Pollard 1983), which underwent rotation with time. This problem that confronts the concepts of prolonged paleostress directions vs. rotating paleostresses is analogous to a similar one that relates to the distinction of joint sets in sedimentary rocks (Sect. 6.3).

There are in addition, very young joints that seem to fall into the two categories, termed, "gently dipping sheeting" and "exfoliation joints" (Bateman and Wahrhaftig 1966). Becker (1891) suggests that (presumably the same fractures) are Pliocene in age and Lockwood and Moore (1979) propose that they are post-Pliocene. In summary, there are still many uncertainties about the multi-fracture behavior in the Sierra Nevada Batholith that await further investigation. The present section narrows its interest into only two fracture domains in the Sierra Nevada Batholith, the oblique joints in the Knowles Granodiorite and the exfoliation joints that cut plutons in Yosemite National Park.

4.5.2 Petrographic Study of Two Oblique Joints from the Knowles Granodiorite in Western Sierra Nevada

4.5.2.1 *Previous Studies on the Knowles Granodiorite*

This section relates to the surface properties of two joints from the Knowles granodiorite (Bateman and Sawka 1981). These joints are exposed in the Shaw quarry, next to the Raymond field site (Karasaki et al. 2000), which is located near the edge of

Rte 411, 5 km east of the town of Raymond and 70 km north of Fresno, at the western foothills of the Sierra Nevada Mountains (Fig. 4.16a). The Knowles granodiorite pluton is 15 km by 5 km, elongating in the NS direction and is fine to medium grained, generally not deformed, and has an isotopic age of 111 Ma (Stern et al. 1981; Bateman and Sawka 1981). It intruded the tonalite of Blue Canyon that has been dated at 114 Ma.

Zawislanski (1994) measured 438 fractures in the area around the Shaw quarry and grouped them into four: Two orthogonal, near vertical sets striking at N 30° W and N 60° E and dipping between 75° and 90°, a sub-horizontal set that dips to the west at about 5°, and a less prominent set, termed "oblique", striking at about N 45° E and dipping between 30° to 60° to the NW. He observed that pegmatite dikes are pervasive in the granodiorite. The dikes are oriented in two sets roughly 90° apart, one striking N 35° E, the other striking N 70° W. Dikes in both sets dip between 20° and 60° to the NW and NE. Thus, the orientations of the pegmatite dikes do not coincide with either the near vertical or sub-horizontal fractures, but are similar in orientation to some of the oblique joints. Based on the lack of well-developed chilled margins in the pegmatite dikes, Zawislanski (1994) considers that the dikes were emplaced shortly after the granodiorite emplacement. The dikes are routinely cut by the two near vertical sets, generally with very little to no displacement. Also, the rough coincidence of the NW dipping dikes with oblique joints suggests that the pegmatites may be fillings of early cooling joints. Hence, the sequence that followed the rock emplacement seems to have been oblique joints, pegmatite dikes and near vertical fractures. Zawislanski (1994) also found that sub-horizontal fractures cut the sub-vertical ones. Since the dip of the sub-horizontal fracture roughly coincides with that of the regional slope, he concludes that they are young, unloading fractures.

Zawislanski (1994) also observed that most fractures are very tight and have no significant secondary mineralization, although apertures are often ambiguous in surface exposures due to the tendency of weathering processes to erode and "open" fractures. Displacements on the order of 1 to 2 cm were observed on some sub-horizontal and oblique fractures. However, no measurable displacement was observed on near vertical fractures. Spacing is irregular, with some fractures as closely spaced as a few centimeters (in fracture zones), and some as widely spaced as tens of meters. The average spacing of the near vertical fractures is 0.95 m (standard deviation = 0.85; $n = 85$).

4.5.2.2
Joints C and D in the Knowles Granodiorite from the Shaw Quarry

The fracture classification in granites by Cloos (Fig. 4.1) that divides fractures into near vertical, sub-horizontal and diagonal (oblique) categories provides a good basis for comparison of fractures from different domains and provinces. Most previous efforts of fracture investigation concentrated on the first two categories, almost ignoring the oblique fractures. However, some intriguing observations that were made on diagonal fractures in plutons (e.g., Cloos 1921, 1922; Zawislanski 1994) (Sect. 4.5.2.1) seem to justify their detailed study. Furthermore, near vertical fractures seem to be rare in the Shaw quarry (Fig. 4.17). Accordingly, the present section focuses on two diagonal joints that cut the Knowles granodiorite in the Shaw quarry. Joints C and D that are described in this section differ in their orientations. Joint C strikes 078° (N 78° E) and dips at 42° to the SE and joint D strikes 045° and dips at 36° to the NW

Fig. 4.17. Photographs of a part of the Shaw quarry, showing joint D in three scales. **a** The joint dips from left to right at the lower center of picture and appears to be sub-parallel to several joints above it, that belong to the same set (*D* is about 3 m long). The joints partly show concentric arrangement. An oblique plume (*horizontal arrow*) is seen on a joint from set C. **b** Three drills along joint D from which rock cylinders have been removed. **c** Part of the joint in a close up (note two syringe needles). **d** A large plume (*delicate lines*) is examined by students on a "oblique-concentric joint" in a granite outcrop from the Bohemian Massif

(Fig. 4.17a). The detailed petrography of the fracture apertures of joints C and D is the main subject matter here. In studying the joints, the "epoxy procedure" was applied in order to obtain in-situ samples for preparing thin sections of the fractures (Sect. 4.12).

Microphotography. A series of photo micrographs each covering a square area of 4.5×4.5 cm were taken by both plane light and plane polarized transmitted light from the examined thin sections. These micrographs, partly overlapping each other in order to minimize photograph distortion, were assembled into mosaics covering sections along the joint apertures. A comparison between images obtained by the two lights enables one to distinguish the boundaries of the primary fractures C and D (Fig. 4.18–4.20) and branching of a secondary fracture from joint C (Fig. 4.18a and 4.19c), as well as secondary precipitates, additional very thin cracks, and other common petrographic features.

Distinction between transgranular and intergranular fracture. Both transgranular and intergranular fractures were observed on joints C and D. Several criteria for transgranularity were defined. First, a mineral that shows a uniform extinction at both margins of the joint is more likely to represent a transgranular fracture and is less likely to represent late crystallization of two independent minerals in precisely the same orientation. A further confirmation of transgranularity is obtained when corresponding locations of a certain boundary and/or polysynthetic twins of the mineral

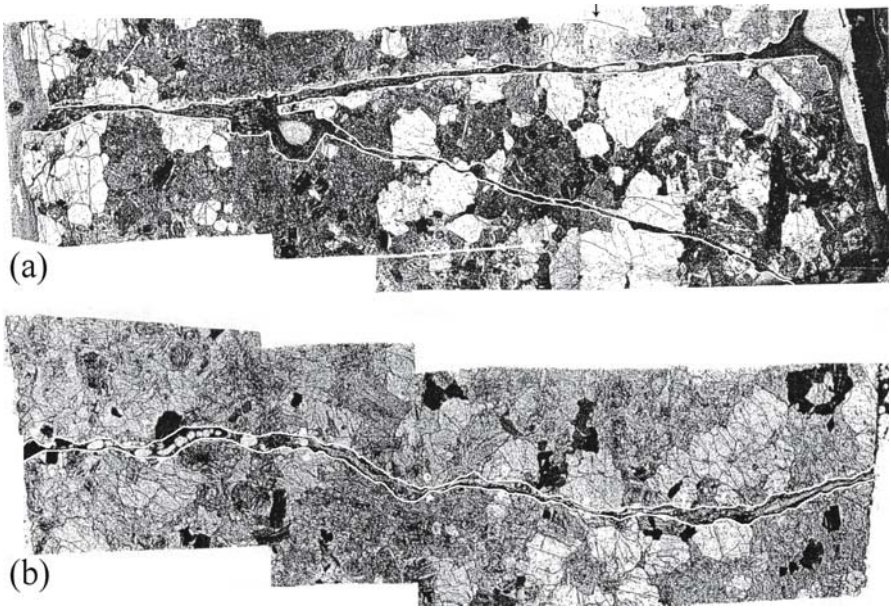

Fig. 4.18. Thin sections of joints C and D constructed by mosaics of micro-graphs. Photographed sections are 4.5 cm long. **a** Joint C, showing straightness of the primary fracture (sub-horizontal) that branches at a large embayment (*dark*) to the secondary fracture, which inclines downward, along a transverse section (parallel to the face of the original rock). **b** Joint D, showing curvatures along a longitudinal section (parallel to the hole formed by drilling). Quartz appears in white and gray, feldspars and muscovite in gray and biotite in black colors

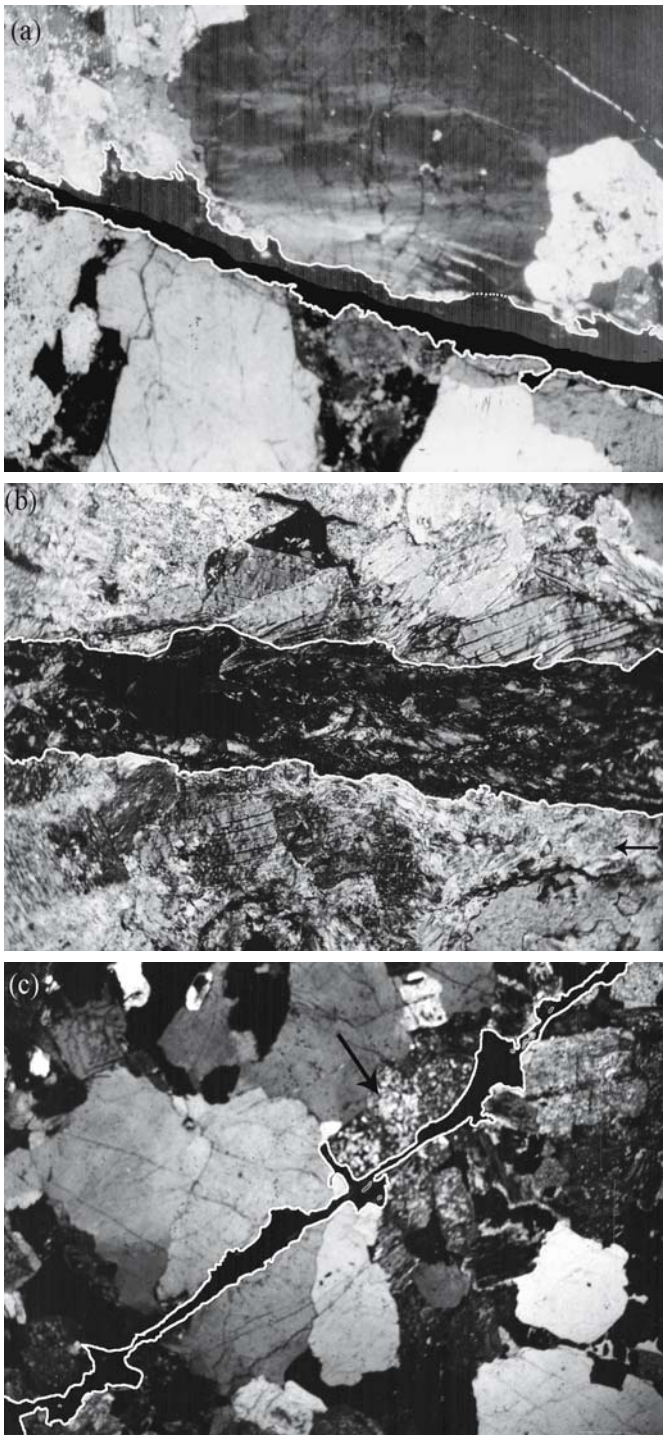

Fig. 4.19.
Profiles of fracture C. **a** Waviness in double refraction occurs on a quartz crystal that is partly cut radially by microcracks. Aperture at center is 0.5 mm (longitudinal section). **b** Inclined crystals of micas along the upper margin of the primary fracture. An angular embayment at lower right of fracture (*arrow*) is filled with unoriented, altered micro muscovite grains. A possible third generation of micro micas, quartz and sericite are scattered along the fracture. Aperture at right is 0.5 mm (transverse section). **c** Transgranular fracture by mode I (without shear displacement) along the branching secondary fracture. Matching is very good in quartz two grains and biotites (scale of several mm) but is poor in the submillimeter scale. Aperture at center, next to the biotites (*arrow*) is 0.1 mm (transverse section)

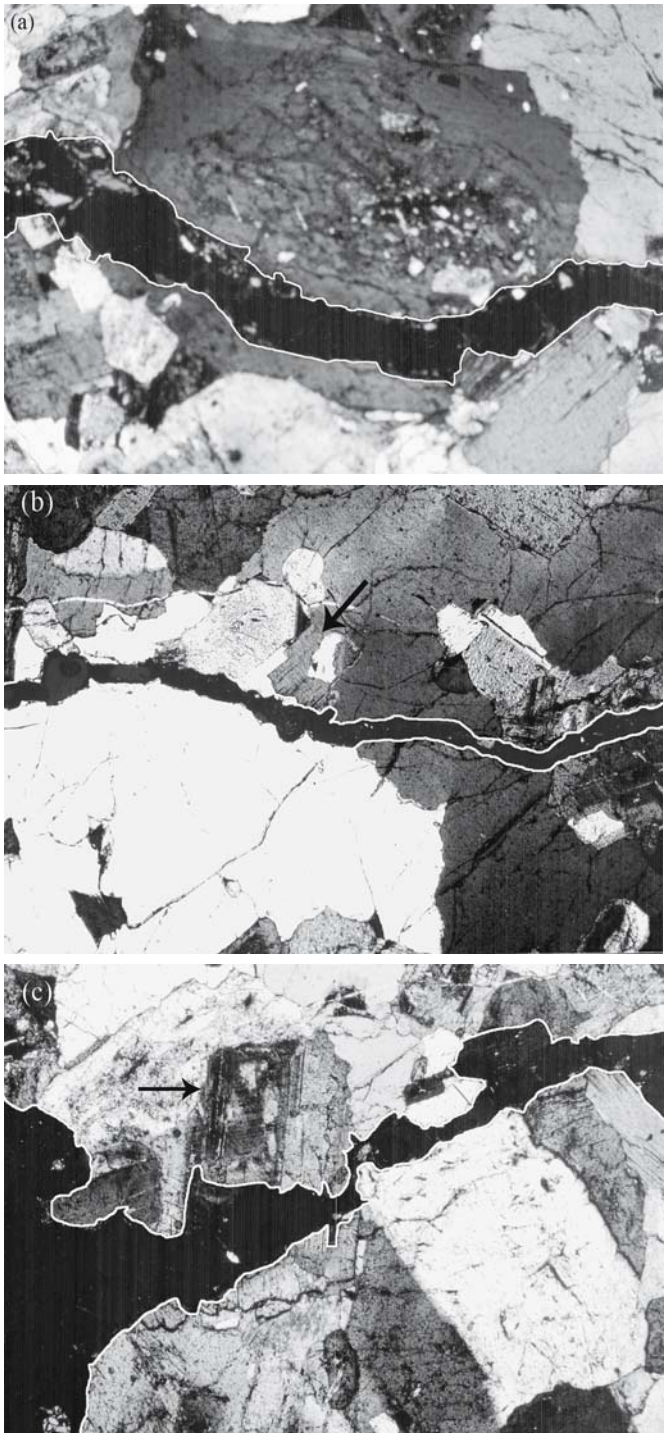

Fig. 4.20.
Profiles of fracture D. **a** A curved transgranular fracture that cuts a K feldspar 5.5 mm long, but propagates around the boundary of a biotite, at lower right (longitudinal section). **b** Two adjacent large quartz crystals at different orientations, appearing as dark and light patches. The dark one is cut by a transgranular fracture. An intergranular fracture propagated along the grain boundaries of medium size plagioclase and biotite at left of center. The length of biotite at center (*arrow*) is 0.8 mm (transverse section). **c** A transgranular fracture through a twinned plagioclase (*arrow*) and K feldspars (light and dark colors), showing considerable variation in aperture and size of mineral fragments along the fracture. The length of twinned plagioclase is 1.6 mm (traverse section). Matching is good in the feldspar scale (several mm) but is poor in the sub-millimeter scale where fragments required to reconstruct the original mineral are missing

can be traced on both sides of fracture (Fig. 4.20b,c). A morphological matching on the sub mm scale, additional to above criteria, provides the highest degree of certainty for transgranularity. Such matchings, however, were rare (see below). Transgranular fracture is a useful tool in determining the extents of opening by mode I vs. shear offsets along the joint walls. When above transgranular criteria are established on a series of different adjacent minerals, their reconstruction to "zero displacement" reveals the extent of opening. A reconstruction that shows deviations from "mode I closing" reveals the extent of shear offset. In contrast to transgranular fracture that cuts through the grain along curved (e.g., Fig. 4.18b and 4.20a) or more often, along straight (e.g., Fig. 4.18a and 4.19c) trajectories, intergranular fracture curves along grain boundaries (Fig. 4.20a). Accordingly, different extinction angles of two grains of the same species on both sides of fracture imply intergranular fracture, particularly when the grain boundaries are not straight.

4.5.2.3 *Results*

Fracture C. The primary fracture C branches out into a secondary one so that it is represented by two fractures (Fig. 4.18a). Both primary and secondary fractures are straight and maintain approximately uniform apertures, ranging from about 0.1 mm to about 0.5 mm, but the joint walls recede considerably from each other into a large embayment at the branching site and in several other locations along the fractures. Fracture is characteristically transgranular, mostly cutting through the larger feldspar and quarts crystals. Occasional intergranular fracture cuts around medium and small size minerals (feldspars, quartz and biotite). There are mineralogical and morphological mismatches along the section shown in Fig. 4.19a, raising the suspicion of a lateral offset along the longitudinal section of primary C. One or two transgranular contacts of quartz grains (arrows in Fig. 4.18a) suggest left lateral offset of about 4 mm. Wave extinction in a quartz crystal, accompanied by local radial microcracks reveal strain in the quartz, possibly caused by an inclined impingement on the primary fracture wall.

The space along the primary fracture is empty in certain locations, but two or possibly three generations of secondary muscovite are aligned in others (Fig. 4.19b). The first generation consists of 0.7 mm long fresh muscovite grains that display high order double refraction colors. Some of them form small angles (0–20°) with respect to the fracture walls. These micas are kinked, reflecting shear strain during their history. The second generation occurs as small altered patches 1–2 mm in size that often fill small embayments along the fracture walls (making it look straighter than it originally was). These muscovites are often altered to sericite, and their double refraction colors are hardly recognizable. The joint space is filled in some locations by late, micro crystals ($\ll$ 1 mm) of mica/sericite and xenomorphic quartz.

Uniform extinction and grain-boundary fit of several minerals along parts of transgranular fracture surfaces of the branching joint testify to an exclusive mode I fracture without any discernable lateral offset (Fig. 4.18a and 4.19c). Matching of the fracture walls along a transgranular fracture in quartz occurs in a scale of several millimeters. However, characteristically, some quartz is missing, thereby negating an unequivocal match at the 0.5 mm scale (left center of figure). A considerably altered grain of biotite 3 mm long is cut by the fracture without lateral displacement (at right side of fracture) (Fig. 4.19c).

Fracture D. Fracture D occurs along a single structure (Fig. 4.18b). The transverse and longitudinal sections reveal curvy fractures to various extents. The longitudinal section exhibits curvatures at two wave lengths. The larger one is about 5 mm (Fig. 4.18b) and the smaller one is about 1 mm (Fig. 4.20a), although there are some straight parts as well. The aperture size deviates considerably from uniformity, between 1.2 mm (Fig. 4.20a,c) down to 0.2 mm (Fig. 4.20b). Fracture is transgranular through the larger crystals of K feldspar (Fig. 4.20a), quartz (Fig. 4.20b) and plagioclase (Fig. 4.20c), along both straight and curved traces. But it is occasionally intergranular around medium- and small-sized minerals (feldspars and biotite) (Fig. 4.20a,b). The transverse section shows a very slight left lateral offset (Fig. 4.20c). Secondary micas are rare along this section, but fragments from broken quartz and feldspars are common along trans-granular parts of the fracture. There is a mismatch on the scale comparable to the joint aperture. No shear offset can be identified in the longitudinal section, and matching improves considerably at 5 mm and above (see good matching in the large K feldspar, in Fig. 4.20a). Thus, the longitudinal and transverse sections both show evidence for just mode I operation, or nearly so.

4.5.2.4
Fracture Behavior in the Two Joints from the Knowles Granodiorite

Comparison with a previous study. Moore and Lockner (1995) investigated the microcrack density (crack length per unit area) in a 19.5 cm-long cylinder of Westerly granite, after inducing a shear fracture by an axial load and 50 MPa confining pressure, at rates less than 10 mm s^{-1}. Their results show that three-quarters of the examined fault length follows intragranular cracks, with only one fourth along grain boundaries. Also, microcrack densities are consistently higher on the dilational side of the shear than on the compressional side. The uneven distribution of microcracks along the "fault" tends to pull the propagating fracture tip towards the dilational side, even though the trend is away from the overall fault strike. As a result, the propagating shear follows the microcrack trend for some distance and then changes direction in order to maintain an overall in-plane propagation path, resulting in a zigzag or saw tooth fracture pattern. Although no systematic investigation of microcrack density was carried out on fractures C and D, an overall impression is that also in the latter fractures, intragranular cracking is more common than intergranular (Fig. 4.18–4.20). However, no distinctions can be made between zones of higher and lower microcrack densities, i.e., no separation between "dilational sides" and "compressional sides" is possible. The waviness along fracture D (Fig. 4.18b) does not resemble the angularity of the zigzag fracture pattern reported by Moore and Lockner (1995, Fig. 14), and fracture C is straight. This comparison possibly suggests that the fracture mechanisms in these two studies were different, shear in the Westerly granite and essentially tensile in the Knowles granodiorite. Nevertheless, in both cases intragranular cracking was dominant.

Fracture sequence. While there seems to have been some shear offset along the primary fracture, no offset is identified in the secondary fracture of joint C. The differences in the modes of displacement between the primary and secondary parts of the joint and lack of muscovite along the secondary fracture suggest that fracture branching occurred after displacement(s) along the primary had taken place. The small angle between the two fractures suggests that a reverse sequence would have caused offsets along the secondary frac-

ture as well. This implies that the geometric splay (Fig. 4.18a) does not reflect a dynamic, single branching of the secondary from the primary in the strict mechanical sense of the term, i.e., the two fractures did not propagate simultaneously under conditions of $K_I > K_{IC}$ (Sect. 4.8.1 and Fig. 2.30c). Thus, a slight opening of the joint enabled the introduction of K-silica rich solutions that produced muscovite, sericite and quartz along the primary joint. Next, a minor shear offset took place along the primary, and then, slightly tilted tensile stress resulted in the formation of the branching fracture.

Straightness characterizes both the primary fracture and the secondary branch of joint C, regardless of the fracture mode, i.e., the offset (s) along the primary that amounted to about 4 mm did not influence the fracture straightness. Quite possibly during the early history of the rock while at depth, lithostatic stresses could have closed the fracture, inducing an impingement of the two fracture walls (Fig. 4.19a), which produced the fragments along the joint, even without lateral offset. This could be an important mechanism contributing to the formation of embayments along the fractures.

The curved part of fracture D reveals a typical transgranular mode I loading (Fig. 4.18b and 4.20a). This precludes the possibility that fracture occurred by curving due to local shears, e.g., due to two approaching non axial fractures from opposite directions (e.g., Yokobori et al. 1971; Acocella et al. 2000). The lack of muscovite flakes along joint D implies that joint C is younger or older than joint D, i.e., joint D formed before the initiation of the hydrothermal activities or after their termination, respectively. However, if analogy is made to the lack of muscovite in the secondary joint C compared to the older, primary C, it appears that joint D is younger than joint C.

It is possible that the relative multitude of joints deviating considerably from verticality in the Shaw quarry may have been the reason for the rarity of vertical or near-vertical fractures in the quarry. A rational for this would be that early oblique fractures released a major amount of stored energy in the rock, minimizing the driving force of subsequent, vertical fracture. This would imply that joints C and D are older than the vertical joints in the area. Such a sequence is supported by the observations made by Zawislanski (1994) in the nearby Raymond field site (Karasaki et al. 2000) that the formation of oblique (diagonal) joints and intrusion of pegmatite dikes preceded the formation of vertical dikes. Thus, further studies are needed to establish whether systematic diagonal fractures have preceded vertical fracture sets in the Sierra Nevada. Finally, some of the oblique straight joints in the Shaw quarry appear to be oblique-concentric joints (Fig. 4.17a), and there is no clear categorization of these fractures. Similar dilemmas occur in other granite provinces as well (Fig. 4.17d), possibly suggesting a distinct class of oblique-concentric joints.

4.5.3
Joint Exfoliation and Arch Formation at Yosemite National Park, California

4.5.3.1
Introduction

The granitic rocks at Yosemite National Park constitute part of the Sierra Nevada batholith (Fig. 4.16a). The "monoliths" El Capitan and Royal Arches are part of the "intrusive suite of Yosemite Valley" (Huber 1987). The El Capitan granite intruded older plutons about 108 million years ago and now makes up the bulk of the western half of the valley area (Fig. 4.21). Huntington (1966) and Huber (1987) found that fracture in

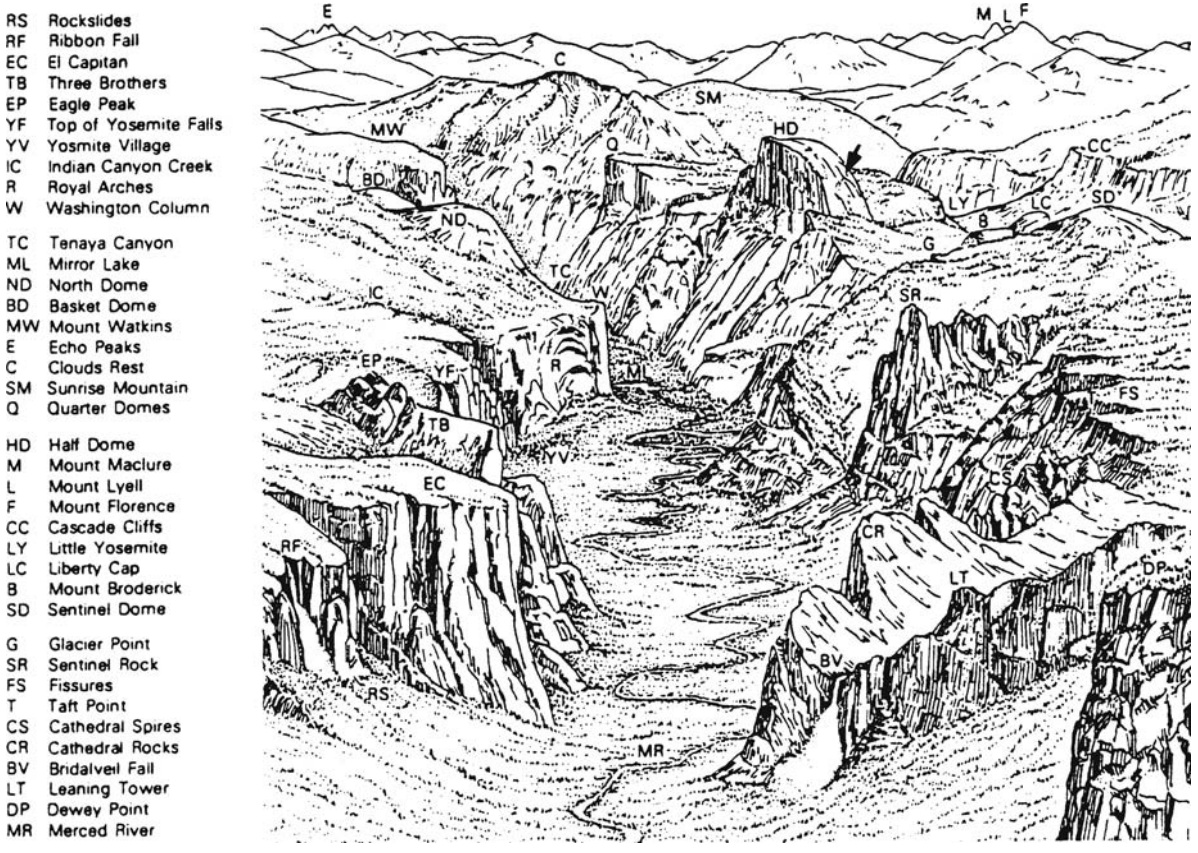

Fig. 4.21. Bird's-eye view of Yosemite Valley, with selected landforms. Note particularly locations of El Capitan, Royal Arches and Half Dome (from Huber 1987, Fig. 18)

the Yosemite Valley varies with the rock. Both composition and texture influence the spacing of joints, such that the finer-grained diorite is the most closely jointed rock and the El Capitan granite is the least fractured (Huber 1987). Huber (1987) suggests that the vertical cliffs of Yosemite may have hidden vertical fractures behind and parallel to the cliff face, i.e., vertical exfoliation possibly takes advantage of free surfaces provided by previous jointing. Important studies on exfoliation in granitic rocks from Yosemite National Park have also been carried out by Cadman (1969) and Holman (1976).

Arches also occur in granitic rocks. However, arches in granites are far less abundant than in sandstone at Zion National Park (Sect. 3.3). Moreover, their occurrence is selective. We divide arches for convenience in this section into "small" and "large" ones. Small arches exclusively develop at the foot of the cliff of El Capitan. Large arches "decorate" selectively one monolith at Yosemite National Park with the majestic "Royal Arches" (Fig. 4.21) but almost no others. Hence, there is some intriguing variability in exfoliation and arch formation in granitic rocks.

Qualitative and quantitative fractographic and electronic surveying methods have been applied in studying exfoliation joints in middle elevations of the cliff of El Capitan and on the cliff of Royal Arches (Bahat et al. 1995, 1999; Grossenbacher et al. 1996), and these are cited here. Characterization of arches at the foot of El Capitan and a comparison of their fracture mechanisms to those that formed arches at Zion National Park are included as well.

4.5.3.2
Joint Exfoliation and Arch Formation at the Foot of El Capitan Cliff

We start in characterizing the exfoliation joints at the foot of El Capitan cliff, by fractographically describing two types of plumes, the "curved-concentric plume" that exhibits some unique features and the "sub vertical" one, which displays rather common features. We then describe the "full arch" and the "series of partial-arches".

a. The curved-concentric plume. This plume occurs on a curved section of the cliff along which there is a gradual strike change of approximately 2–4° (a precise measurement in this location is technically very difficult). The strike change is greater in the upper part of the plume than in the lower one (Fig. 4.22a,b). The curved-concentric plume is divided into three areas (Fig. 4.22b):

1. The plume at the center, p.
2. A series of sub-concentric fractures, cf, at its southwestern side (at left upper part of figure).
3. *En echelon* cracks in a fringe, e, at its northeastern side (at the right side of figure), as itemized below.

▶

Fig. 4.22. a A photograph consisting of a mosaic of five photos and **b** drawing, showing the curved concentric plume on a curved surface (resulting in some optical distortion), at the foot of El Capitan cliff. In the drawing, *p*, *cf*, *e* and *n*, designate the curved-concentric plume, sub-concentric fractures, *en echelon* cracks and niches, respectively. Also, *small B* designates fracture boundaries of the fringe, f, and *z* marks merge zones along the boundary fracture, *BF*. Numbers *1–3* designate the three distinct areas. *Arrows* show directions of fracture propagation. The line *AB* marks a section, which is rotated at 90° in **c**, to show (exaggerated) third dimension of the joint surface

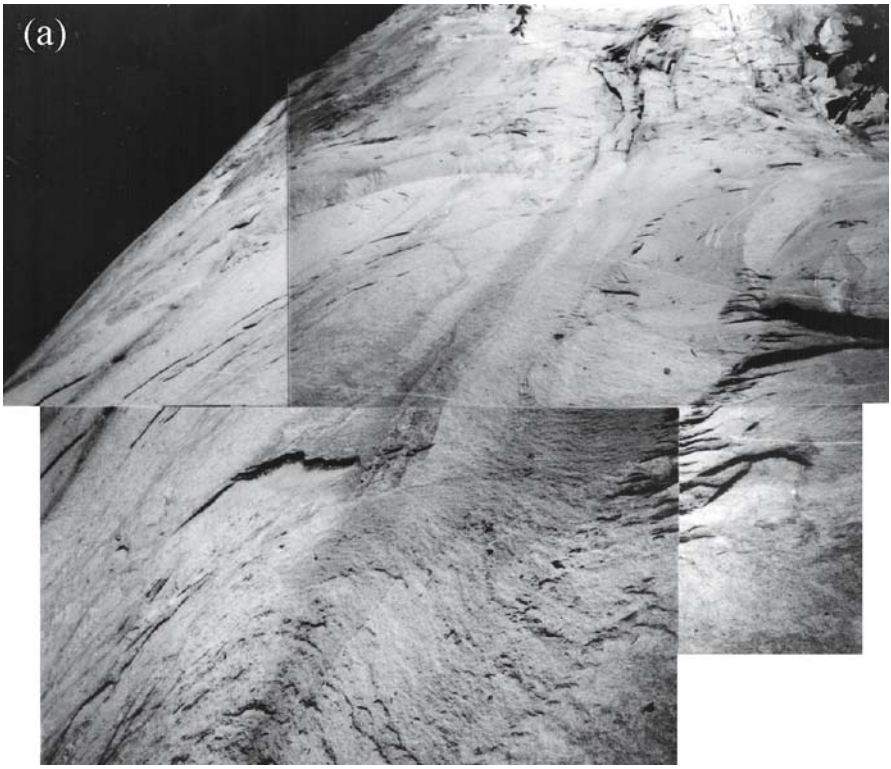
(a)

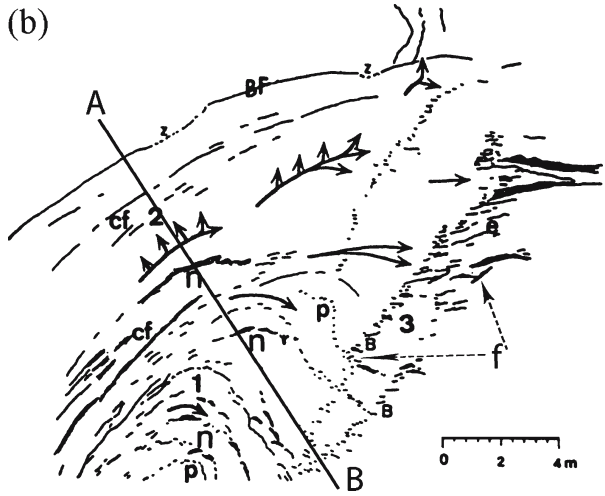
(b)
A
BF
cf
2
n
p
3
B
f
cf
n
1
n
p
B
0
2
4 m

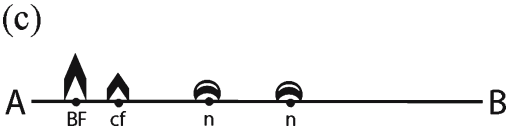
(c)
A
BF
cf
n
n
B

Area 1. The most striking feature in this fracture morphology is the curvature of the plume that propagates upward, and after reaching a peak it bends and the barbs (individual segments of the plume) turn sidewise and then downward, revealing a rotation of the fracture front. The barbs are not uniform in shape along their lengths. As the plume curves, the barbs bend slightly away from the cliff, forming small niches in certain intervals (*n* in Fig. 4.22b,c), as arches of a centimeters or tens of centimeters in size. The bends become particularly prominent at locations of strong surface curvatures, where barbs at higher elevations partly superpose those below them, such that they form a "staircase" climbing up the cliff. There is a gradual increase of the radius of curvature of the plume in higher elevations.

Area 2. The curved-concentric plume becomes coarser, transforming into a series of large niches and concentric fractures at the meter scale (n and cf at the left sides of Fig. 4.22b,c). These fractures cut laterally (asymptotically) into the rock, partially assuming the shape of partial-arches at meter or tens of meter scales. The upper end of this structure consists of three lateral boundary fractures, BF that meet at two "merge zones" (z in Fig. 4.22b) that appear as triangle-like discontinuities along the otherwise continuous curved boundary (Fig. 4.22a).

Area 3. The termination of the concentric plume at its right side is not abrupt; it occurs along two, parallel, straight boundaries (B in Fig. 4.22b) that separate the parent joint from the fringe (Hodgson 1961a). The plumes approach these boundaries suborthogonally, and beyond, *en echelon* cracks, e, maintain the same sense of stepping

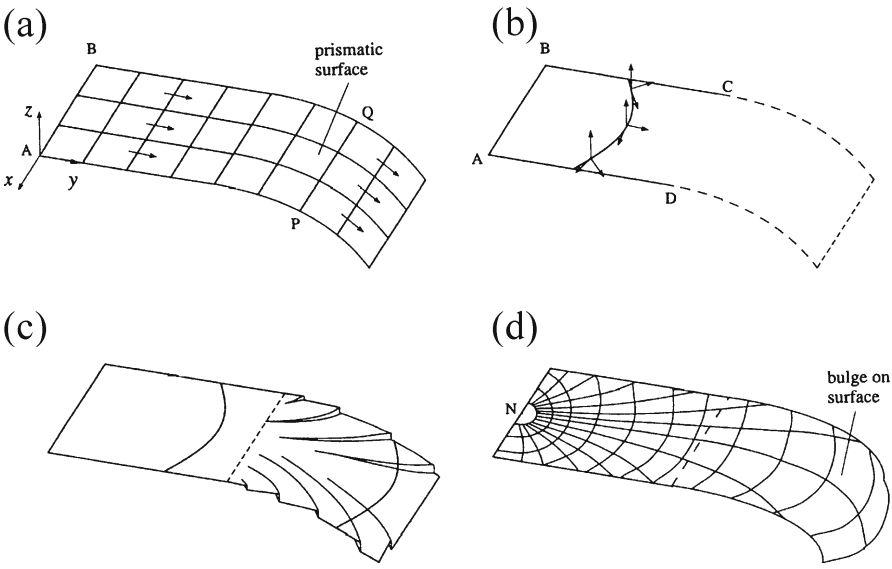

Fig. 4.23. Growth of cracks round by point after bends: **a** Straight-fronted crack moving on a prismatic surface with crack tip parallel to axis of prism. **b** Principal frame fields on a curved crack front. **c** Continued growth of a crack, with a curved front, by twisting into numerous small *en echelon* cracks. **d** Continued growth of a crack with a curved front, by bulging (from Hull 1999)

shown in the plume (the same "staircase" as in area 1). Many *en echelon* cracks are straight and are slightly open. The propagation directions (arrows) are marked in the various transitional parts from area 1 to areas 2 and 3 (Fig. 4.22b).

The fractography displayed by the curved-concentric plume reflects the mechanism of exfoliation around the curved foot of El Capitan (Fig. 4.22a). The mechanism of crack growth into round bends has been investigated by Hull (1999, p. 88) and is cited below. According to Hull (1999, Fig. 3.25), a curved surface is formed by crack tilting (mode II), provided the crack front remains straight and normal to the plane of the specimen. For a variety of reasons, real cracks do not have straight fronts, even in flat plate specimens tested in uniaxial tension. When changes in the local externally applied stress fields cause a crack with a curved front to bend, more complicated crack movements are required. Figure 4.23 is a 3-D representation of the simple case for a straight-fronted crack. The crack front AB is always parallel to the *x*-axis (Fig. 4.23a). A curved surface is formed by tilting about this axis. At any position PQ, the crack tip is always straight and parallel to the *x*-axis. For the realistic case (Fig. 4.23b), the crack front is curved (see ripple marks in Fig. 3.24). Suppose that initially, the crack is in a planar surface and that as it grows the stress fields caused it to bend on a path described by the broken lines. The principal frame fields marked at the tip of the crack show that the crack can continue to propagate in the planar surface without any geometrical constraint. Any stresses that cause the crack to bend, as illustrated, result in local stress fields at the crack tip with a mode III component. This applies to all elements of the crack tip not parallel to the *x*-axis. The crack tip experiences twist forces. However, to maintain a smoothly curving surface, the crack front cannot move by twisting.

There are four possible ways for a crack that is forced to bend to follow the general path marked by the broken lines in Fig. 4.23b. First, the curved crack front straightens and becomes parallel to the *x*-axis. The crack then follows a prismatic surface for continuous tilting at the straight crack tip (Fig. 4.23a). Second, the crack front remains curved and the crack is driven by the stress fields to bend on a path equivalent to the prismatic surface. This inevitably means that the surface cannot remain smooth and continuous. The local mixed I / III stress fields at the crack tip nucleate an array of *en echelon* segments, separated by steps on the fracture surface, parallel to the direction of crack growth (Fig. 4.23c). Third, the crack front remains curved and follows a smooth 3-D double curvature path. This is achieved by the crack front bulging out of the prismatic surface Fig. 4.23d). This diagram shows striae and undulations on the surface with the undulations mapping out the successive positions of the crack tip for a non-twisting crack. Fourth, the crack front moves by a combination of the first three mechanisms, such that the relative contributions depend on the ease of initiating arrays of secondary cracks at the tip of the parent crack.

The propagation of the curved-concentric plume (Fig. 4.22) approximates Hull's (1999) 3-D model (Fig. 4.23). The curved front of the exfoliation joint propagates around the curved surface of the cliff (see the curvilinear shapes of the long arrows in Fig. 4.22b). Breakdowns due to local mixed I / III stress fields occur at the joint tip, initially into delicate plumes, then to coarse plumes and finally, to *en echelon* segmentation. The breakdown of the joint front (Fig. 4.23c) and the bulge (Fig. 4.23d) reflect 3-D dimensions of Hull's model, while the niches of plumes and steps of the *en echelon* segmentation represent the actual 3-D on the cliff (Fig. 4.22a,b).

b. The sub-vertical plume. This plume occurs on a planar section of the cliff on a back wall of a full arch (Fig. 4.24). The convex side of an undulation faces downward, indicating that the plume propagated downward. The plume produces an asymptotic fracture at an angle $\geq 1°$ with the cliff. This undercutting reveals its tensile (Bahat 1979) role in the formation of joint exfoliation.

c. The full arch. A few tens of meters from the curved-concentric plume southwestwards along the cliff, there is a fully developed arch that consists of a ceiling and of two sidewalls (Fig. 3.28 and 4.25). The height of the arch from base to ceiling is about 7 m. At the top of the upper part of the arch is a merge zone of two boundary fractures, which assume the shape of partial-arches. Each partial-arch consists of parts of the ceiling and of a sidewall, such that the concave side of the partial-arch on the right faces towards the left, and on the left the concave side of the partial-arch faces towards the right. Hence, the partial-arches behave independently of each other when forming a full arch.

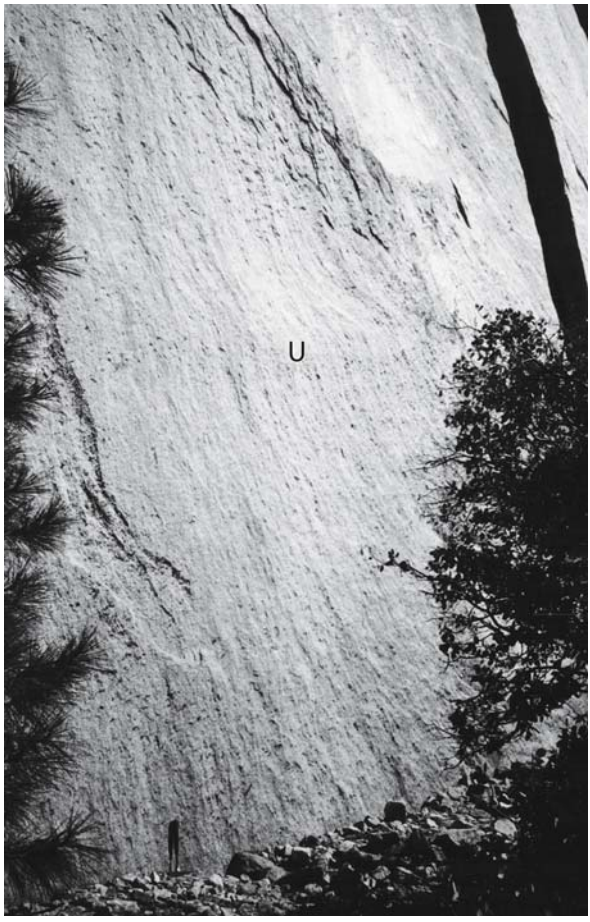

Fig. 4.24.
A coarse, vertical plume undercuts thin slices from the back wall of an arch (at both sides of the plume) at the foot of El Capitan cliff; the sidewall of the arch is shaded at right. The undulation (*u*) maintains orthogonal relation with the plume. Note hammer for scale at lower left

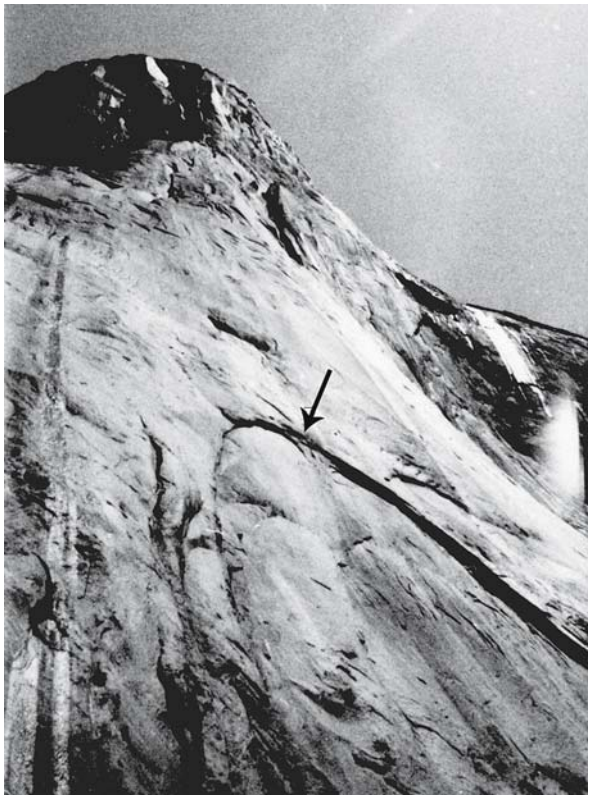

Fig. 4.25.
A full-shape arch at the foot of El Capitan cliff. A little off the top of the arch is a merge zone (*arrowed*) of two partial-arches. Each partial-arch consists of part of the ceiling and a sidewall. Picture is taken looking upward the cliff (note an optical distortion). Size of arch approximates those of the sidewalls in Fig. 4.24 and 4.26

d. The series of partial-arches. There are many partial-arches that do not match with other partial-arches to form full arches. A series of some five individual left partial-arches that are convex in the same direction is shown in Fig. 4.26. Some partial-arches are subdivided into parallel thin slices, about 1 to 10 cm in thickness that form a small angle $\geq 1°$ with the cliff and laterally undercut into the rock. The sidewalls of the various partial-arches resemble the sub-concentric fracture cf (Fig. 4.22a–c).

Discussion and conclusion. The gradual increase in the topographic coarseness from delicate barbs, through small *en echelon* segments into large ones, can be correlated with the local increase of the K_{III}/K_I ratio on the curved section of the cliff. Particularly, large segments occur at the upper part of the fringe (around e in Fig. 4.22a,b). These are also the most twisted and opened cracks, implying the greatest ratio of K_{III}/K_I (Cooke and Pollard 1996). Sommer (1969) observed segmentation in AR glass at as little as 3.3° rotation of the parent fracture from normality to the tensile stress, and this is approximately the change in strike occurring across the areas 1 and 3 (Fig. 4.22b). The joint growth upward and downward (as demonstrated by the curved-concentric plume) along a curved front resulted in plume coarsening and *en echelon* segmentation, following Hull's model (Fig. 4.23c).

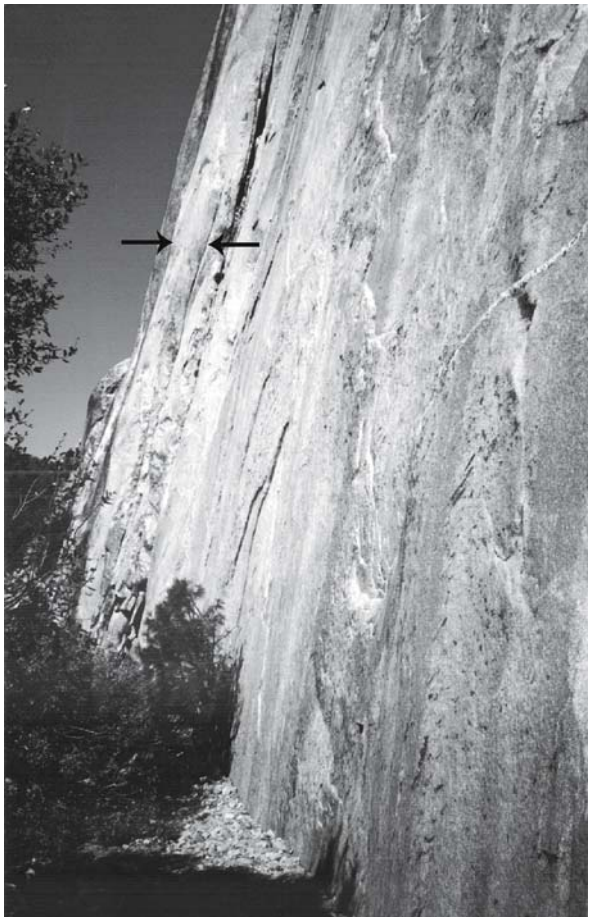

Fig. 4.26.
A series of partial-arches that concave towards right at the foot of El Capitan. Thickness of sidewall (between *arrows*) is about 80 cm

The plume trajectories mark the circular path of the joint front (arrows in Fig. 4.22b). This path differs radically from the unilateral propagation of the vertical plume on the back wall of an arch (Fig. 4.24); both are at approximately the same height on the cliff, only tens of meters away, implying different fracture mechanisms, possibly in different times. It demonstrates the small changes in local stress fields (across tens of meters) within larger stress fields (across hundreds of meters) dominated by remote stresses. There seems to be a gradual structural transition from curved-concentric plumes through niches and sub-concentric fractures into partial-arches. They form sets of various sizes that undercut laterally into the rock, forming small angles of several degrees with the cliff. When matching (left and right) partial-arches merge, full arches develop. A merge often occurs at one (Fig. 4.25) or two zones along the ceiling. Thus, the various fracture features shown in Fig. 4.22, 4.25 and 4.26 provide a complete evolutionary sequence of exfoliation and arch formation at the foot of El Capitan. Note that the mechanisms leading to the formation of the latter arches differ from those that created arches in sandstones (Fig. 3.31).

4.5.3.3
Joint Exfoliation at the Middle Height of El Capitan Cliff

Methods of investigation. Exfoliation surfaces were examined in the middle height of the approximately 1 000 m high granitic cliff of El Capitan (Fig. 4.21), within the frame shown in Fig. 4.27a (this section is cited from Bahat et al. 1999). An electronic total station, which incorporates a laser range-finder, provided the means to survey points and measure angular and size parameters on the cliffs of El Capitan, the Royal Arches and the southwestern side of Half Dome (Sect. 6.5) at Yosemite National Park (see also Grossenbacher et al. 1996). A principal assumption in this technique is that these cliffs are planar, which applies to the investigated exfoliation joints. For the geometries used, a deviation of 3 m from a true planar surface yields an error of at most 1 m in a calculated position on a cliff. With distances measured of about 50–100 m and a distance from base station to cliff of over 300 m, this does not appear to involve significant error, as the relief on the cliff is less than 5 m (as verified by examination of topographic base maps). Taken together, these yield an error of less than 3%, which was deemed acceptable, considering the large distances in the park.

Fractography. Vertical fracture surfaces on the N 32° E oriented exfoliations are marked by tens of early cracks, which are shaped as fans of radial plumes. Each fan is comprised of an origin and radial plumes. In some cases, a single or several concentric ripple marks (Fig. 4.27a,b) form orthogonal relationships with the plumes at their intersections on the fans. Distorted fans manifested by plumes deviating from radial structures are common as well. The size of a fan varies from several meters to several tens of meters. Occasionally, only partially developed radial plumes appear.

These fans cut country-rock and dikes of the Taft Granite (Fig. 4.27b) without apparent change in direction. Early circular cracks resembling in shape and size similar fractures from Zion National Park (Bahat et al. 1995 and present Fig. 3.24b) also occur sporadically on the cliff of El Capitan. The fans are more common than the early circular cracks. Many neighboring fans interacting with each other merge into vertical composite joints, which are several hundreds of meters in size.

The fan population produces a specific fracture pattern at the middle height of the cliff. This pattern is not so clear for fractures A and B (Fig. 4.27c). However, a particular preferred orientation appears for fractures C and D, where fans indicate upward propagation above the approximate height of D (where ripple marks in the fans convex upward), and fans below this height show downward propagation (where ripple marks in the fans convex downward). Hence, fans cutting the granite at El Capitan propagated upward and downward from initiation zones on individual exfoliations. These zones occupy similar heights on the cliff (Fig. 4.27d).

A few exfoliation joints occur parallel to each other on the cliff, such that each two adjacent joints contain a rock "slice" between them. Some of the slices do not maintain a constant thickness, causing deviations from parallelism of the exfoliation joints. Letters A–D represent surviving remnants of distinct exfoliation surfaces, such that D reveals that the previous more external slices (A–C) have been removed at this location (Fig. 4.27c). Exfoliated slices apparently detach selectively from the cliff in a gravity driven process, as revealed by certain undetached parts from the cliff (dash lines in Fig. 4.27c).

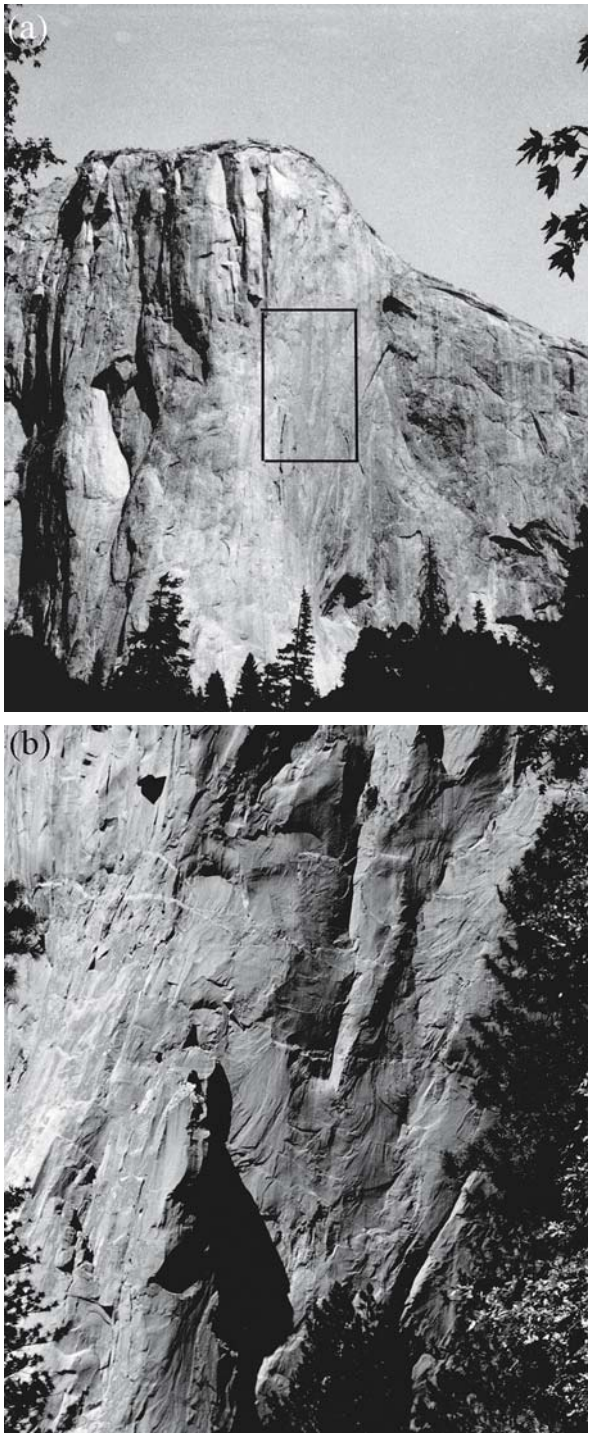

Fig. 4.27a,b.
Exfoliating joints in the El Capitan granite at Yosemite National Park (after Bahat et al. 1999). **a** Photograph of a cliff on El Capitan striking N 32° E, showing the frame which is detailed in **b. b** Photograph of the exfoliated cliff within the frame, showing multiple groups of radial striae. Some groups occur in association with concentric ripple mark, together forming fan-shapes. The cliff is divided by sub-vertical fractures into distinct exfoliations. Fractures cut sub-horizontal dikes of the Taft granite (which have a light color)

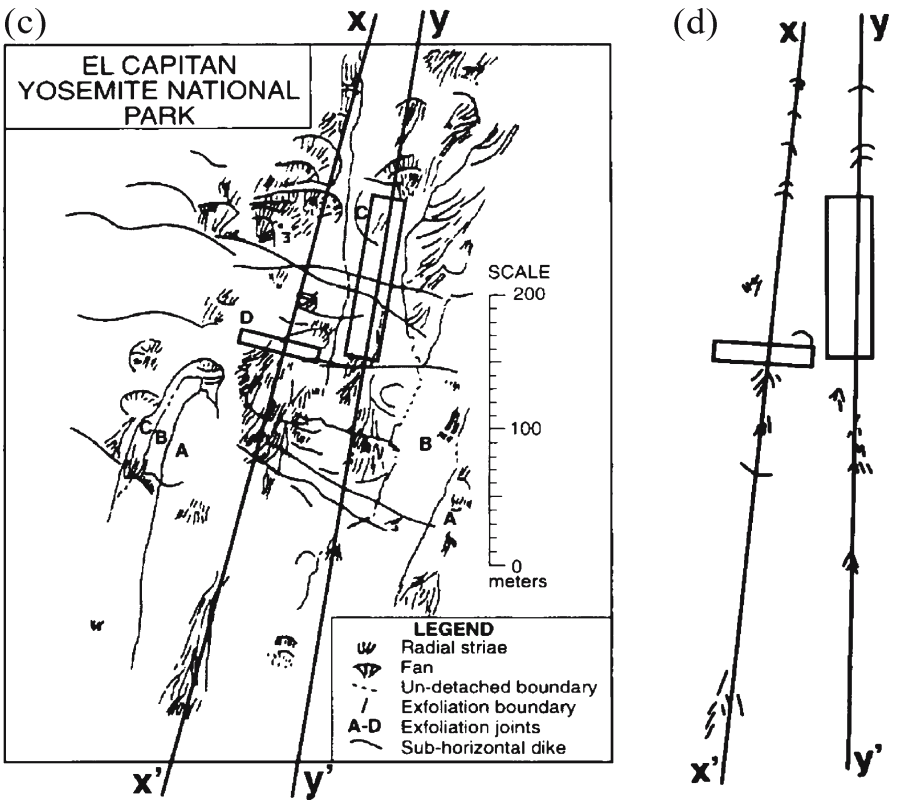

Fig. 4.27c,d. Exfoliating joints in the El Capitan granite at Yosemite National Park (after Bahat et al. 1999). **c** Scaled diagram of **b**, showing exfoliation boundaries between slices belonging to distinct joints *A–D*. *Rectangles* designate initiation zones at which the propagations depart to opposite directions, as shown by traces of convex ripple mark or radial plumes. **d** Traverses *x–x'* and *y–y'* on joints *C* and *D* from **c**, depicting fans. The fans are either radiating barbs or convex ripple marks pointing to the direction of fracture propagation upwards in the upper part of diagram and downwards in the lower one. Rectangles are as in **c**

Mechanism of exfoliation. According to Holzhausen and Johnson (1979) longitudinal splitting occurs parallel or sub-parallel to the direction of loading in uniaxially compressed rock cylinders. Although longitudinal fracture often originates at the ends of the specimens (due to sample end-effects) and propagates toward the center, uniform loading also results in fracture origins within the specimens (Peng 1970). Holz-hausen and Johnson (1979) postulate that an "internal fracture" is formed by the coalescence of earlier axial cracks (analogous to the term composite fracture used in this section), which have created stably under high loads (local compression in Fig. 4.28a,b). An extension of the internal fracture to longitudinal splitting may be caused by buckling of the rock away from this surface. This would happen when the two separated parts of the cylinder bend outward (local tension in Fig. 4.28c). Tension at the tips of the longitudinal split may cause unstable growth to the ends of the specimen. Holzhausen and Johnson (1979) consider several tensile and shear criteria but refrain from advocating one mechanism leading to splitting (Sect. 2.2.3.11 and 2.2.13, see also Fig. 2.65).

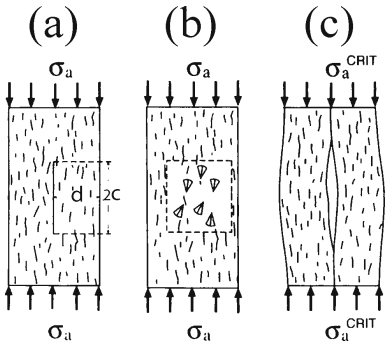

Fig. 4.28.
Schematic representation of how buckling causes longitudinal splitting of cylindrical specimens. **a** Axial cracks coalesce under applied axial stress σ_a to an "internal fracture" of length 2*c* at a distance d from the free surface. **b** The internal fracture shown at 90° position to *a*, exhibiting early cracks in shapes of fans pointing upward and downward, before coalescence. **c** Axial propagation of the internal fracture (in the *a* position) occurs when it buckles outward (from Bahat et al. 1999, modified after Holzhausen and Johnson 1979)

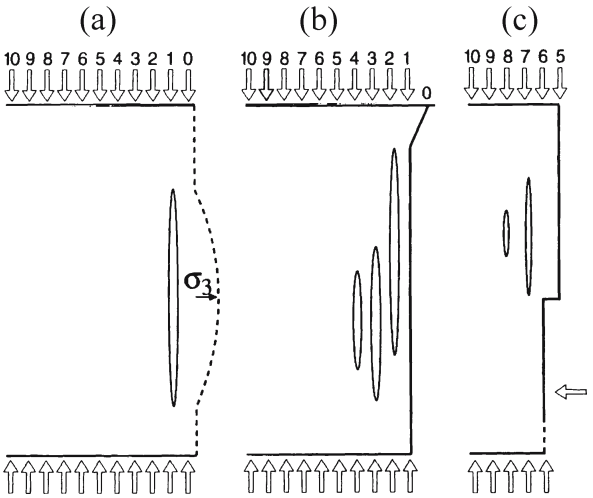

Fig. 4.29.
a A section model showing the profile of joint exfoliation by longitudinal splitting and buckling of the "internal fracture" from Fig. 4.28a. *Vertical arrows* indicate overburden load. Fracture (longitudinal splitting) occurs in association with buckling (an exaggerated buckling is shown by the *dash line*), which develops sub-normal to σ_3 (*horizontal arrow*). **b** An early slice collapsed (at *0*) and washed away, and new exfoliations develop (earlier ones closer to the free surface at *arrow* numbered *1* to *arrow* numbered *10*). **c** A profile of an arch at the lower part of the cliff, which forms when part of the slice collapses (*white arrow*)

The findings in the field are in harmony with various experimental observations made by Holzhausen and Johnson (1979). Coalescence of coplanar fans (Fig. 4.28b–d) that are close to and parallel to free surfaces (the outer surface of the cliff) is the main fracture process in the middle height of El Capitan cliff that leads to exfoliation. Exfoliation developed along principal planes populated by multiple early cracks by a mechanism of longitudinal splitting, which was caused by the overburden load. Splitting occurred upward and downward from an initiation zone at an elevation where the normal resistance to buckling was minimal (Fig. 4.28) next to a free surface in analogy to Fig. 4.29. Fracture propagation on El Capitan cliff was polarized upwards and downwards from this zone. It followed the creation of multi-nucleation sites of independent cracks that had developed into fans and then merged with each other into composite joints (Fig. 4.27c,d).

Considering tension vs. shear mechanisms causing splitting (Holzhausen and Johnson (1979), the fractographic observations suggest the following. First, the ripple marks and plumes on the surfaces of the early joints reflect mode I opening as the predominant mode (Bahat 1979), i.e., on principal planes normal to the minimum principal stress. Second, minor local shear was superposing the tensile mode (Bahat 1987b). Third, significant shear strain can be ruled out because such a process would

have erased the fracture markings, and fourth, the lack of hackle or exfoliation-branching (Fig. 2.1) raises questions about an unstable fracture analogous to that observed experimentally (Holzhausen and Johnson 1979). These observations imply stable joint propagation at the middle height of El Capitan cliff that may be correlated with the compressive state in the uppermost lithosphere. If however buckling is promoted close to the ground surface of the granite, unstable exfoliation may occur (Fig. 2.65).

A formula used by Holzhausen and Johnson (1979) is adapted for the analysis of the critical conditions for buckling:

$$\frac{\sigma_{a,critical}}{\pi^2 \frac{E}{3}} = \left(\frac{d}{2c}\right)^2 \tag{4.1}$$

where $\sigma_{a,critical}$ is the critical axial stress for buckling of a beam with fixed ends, E is Young's modulus, d is the distance between the internal surface (nucleation of the longitudinal split) and the free surface, and $2c$ the internal fracture length (Fig. 4.28). This formula shows that $\sigma_{a,critical}$ increases with d^2. It explains the observations both in granite and in sandstone (Fig. 4.30 and Fig. 3.25c) that vertical dark streaks produced by dripping solutions mark external exfoliations and not internal ones. That is, the earlier longitudinal splits develop close to the free surface at small d values (Fig. 4.29), and then new ones gradually form further inside the rock. Also, Eq. 4.1 implies that rock slices produced between successive exfoliations should be much thinner than the lengths of the associated "internal fractures". This may explain the great ranges of exfoliation spacing depicted in various publications (e.g., Holman 1976, p. 2; Twiss and Moores 1992, Fig. 3.5).

Joints are classified into four fracture categories: Burial, syntectonic, uplift and post-uplift groups. These four groups differ in their various properties, including their fractographies. It turns out that the merger of early circular cracks (Fig. 3.23b,c) and early fans (Fig. 4.27b–d) is common to exfoliation joints in both sandstone and granite. These are characteristic fractographic features exclusive to post-uplift joints, which develop close to a "free boundary" above the ground surface. A similar merger of fans into a larger post-uplift joint has been observed in chalk (Bahat 1991a, p. 301). Mergers of early circular cracks or early fans that occur on post-uplift joints are not known from surfaces of burial and uplift joints, and they are rare on syntectonic joints. As mentioned above, Huber (1987) suggested that the vertical exfoliations possibly took advantage of free surfaces provided by previous jointing. These observations support his suggestion.

4.5.3.4
The Royal Arches

The series of Royal Arches is located between El Capitan and Half Dome in Yosemite Valley (Fig. 4.21) and provides an exceptional occurrence of very large arches (Fig. 4.42a,b). They are considerably larger than arches in Zion National Park (e.g., Fig. 3.24a,b) and are by far larger than arches at the foot of El Capitan. These arches are confined to a single cliff, cutting the entire monolith, in contrast to the division into distinct structures at different heights on El Capitan and the limitation of arches to its lower elevations.

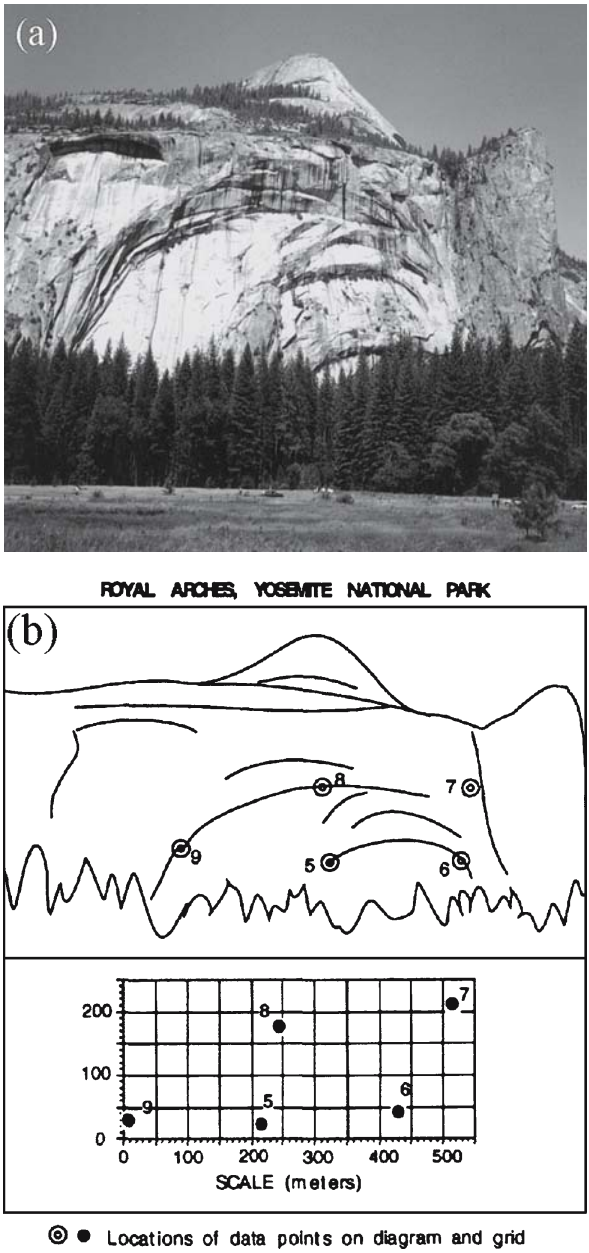

Fig. 4.30.
a Photograph of the Royal Arches. **b** Scale diagram of the Royal Arches showing measured dimensions. There are angular merges of ceilings with the sidewalls at points 5 and 9 and in the upper left arch. Note the division of parallel thick slabs along side-walls and ceilings into series of thin slabs (particularly along arch 7–8–9), often combined with sharp contours that outer surfaces make with sidewalls and ceilings. Note vertical, dark streaks of dripping solutions between 8 and 9

The Royal Arches occur in a concentric structure and show both symmetric and asymmetric features (Fig. 3.28a). The lower and smaller arches tend to be symmetric, whereas the upper and larger arches are asymmetric. The latter arches display angular merges of the ceiling with the sidewalls at one side of the arches (their western

side) and an arcuate continuity of the ceiling with the sidewalls of the arches on the other side (the eastern one). The close association of exfoliation with arch formation observed at the foot of El Capitan is repeated in the Royal Arches. However, the ceilings and sidewalls in the Royal Arches are subdivided by more undercut exfoliation joints (e.g., between points 8 and 9 in Fig. 4.30b).

4.5.3.5
Arch Formation in Granitic Rocks and Sandstones

Structural features common to the various arches. *(a)* Intimate associations of arches with exfoliation joints are almost invariable, suggesting that joint exfoliation is a prerequisite for arch formation. *(b)* Many contacts between the outer surface of cliffs and the ceilings and sidewalls are angular (in some cases close to an angle of 90°), implying a development by fracture, rather than by erosion. *(c)* There are both symmetric and asymmetric arches. *(d)* On many arches, particularly asymmetric ones, there are merge zones of sidewalls and ceilings or matching partial arches, implying that these arches generally form by the connection of distinct structural components. *(e)* Niches occur in multiple sizes at bending barbs on centimeter scale and at sub-concentric fractures on meter scales at the foot of El Capitan (Fig. 4.22). They also appear on large scales of tens of meters on partial-arches and arches in Zion National Park. Niches appear to be initiation sites of many symmetric and asymmetric arches. The shape and symmetry of an arch depends on the number of initial niches and their location along the arch perimeter. A single niche at the highest position of the arch is likely to result in a symmetric arch. On the other hand, niches at positions below the arch summit are likely to produce asymmetric arches.

Structural features that differ in the various arches. *(a)* There are many more arches in sandstone at Zion National Park (Sect. 3.3) than in granitic rocks at Yosemite National Park. *(b)* Arches at the foot of El Capitan differ significantly from the Royal Arches. *(c)* The mechanisms of partial-arch formation at Zion National Park and at the foot of El Capitan are different, as follows: In the sandstone, the ceilings and sidewalls often start tangent or vertical to a niche and propagate downward to yield a curved surface normal to the trajectories of least compressive stress induced by the gravitational load of the overlying rock. This propagating curviplanar fracture often cuts *normally* into the rock body across a series of rock "slices" sandwiched between exfoliation joints that develop parallel to the cliff and to each other. On the other hand, partial arches at the foot of El Capitan are formed by curved-concentric plumes (Fig. 4.22) that undercut laterally and form small angles (1–4°) with the cliff. Correspondingly, arches at Zion National Park are commonly impressively thick, since they consist of many slices of rock, whereas arches at the foot of El Capitan are considerably thinner.

Open questions. The differences in fracture mechanisms suggest that additional to the driving exfoliation, a certain set of conditions needs to be provided for arch formation. The available information does not warrant a speculation on what these combined conditions at each location should be. This leaves several open questions as summarized below.

1. Huntington (1966) observed that for unknown reasons, sheeting developed most abundantly in quartz monzonite and granite, "spottily" in granodiorite, and never in quartz diorite or gabro. That is, arch formation is dependent on the petrography of the rock, which in turn should significantly influence the strength and resistance properties of the rock to fracture. Thus, it is pertinent to enquire how such differences resulted in distinct exfoliation and arch formation on the cliff of El Capitan vs. the Royal Arches.
2. Moreover, there are significant differences in fracture behavior at different heights of El Capitan (Fig. 4.22, 4.24–4.26 vs. Fig. 4.27). These differences cannot merely be assigned to differences in rock properties. We need to determine what the distinct fracture stress conditions were in such cases.
3. Dry conditions probably prevailed during fracture at the middle heights of El Capitan, whereas pore pressure activities quite likely, influenced exfoliation in the sandstone at Zion National Park (Bahat et al. 1995). In view of the multitudes of arches both at Zion National Park and at the Royal Arches, may one assume that fracture conditions (dry vs. wet) have been similar at the two sites?
4. The exfoliations investigated at El Capitan and at Half Dome generally follow the NNE directions of earlier regional fractures in Yosemite National Park (Bahat et al. 1999). The implication is that previous fractures provided free surfaces parallel to which exfoliation occurred in these two sites. This fracture overprinting pattern is repeated at Zion National Park (Bahat et al. 1995). The Royal Arches are approximately E-W and deviate from the regional NNE direction in Yosemite National Park. This could be related to an exfoliation that relates to a different regional-structural setup.

4.6 Fractographies that Pertain to both Quasi-Static and Dynamic Fractures

We start by raising the question of how *en echelon* segments (generally reflecting quasi-static propagation) and hackles (generally reflecting dynamic propagation (Sect. 2.2.5) can occur adjacently on a single fringe (e.g., Fig. 2.1c). The answer is based on the assumption that only "slight deviations" of the direction of the minimum principal compression (or maximum principal tension) from orthogonality to the fracture surface would induce *en echelon* segmentation (Sommer 1969). Accordingly, fringes that form by both quasi-static and dynamic propagations may be influenced by such "slight deviations". Fractures formed quasi-statically when the ratio K_{III}/K_I is high will be dominated by *en echelon* fringes (Fig. 2.1a and 2.35), and these fringes will have the tendency to assume simple, uniform widths (Fig. 2.34b). On the other hand, fractures formed dynamically when K_{III}/K_I is low will be dominated by hackle fringes, on which, however, *en echelon* segmentation in a shingle-like arrangement may be superimposed due to this ratio. Such superposition can explain the frequent occurrence of fringes that show hackles in a shingle-like arrangement (Fig. 4.12b). The latter fringes often exhibit non-uniform widths (Fig. 2.34a and the center of Fig. 4.12b). Hence, it is quite possible that on the fracture surface obtained by De Freminville (1914) (Fig. 2.1c), the two fringe types reflect local slight changes in the extent of normality of the maximum principal tension: The fringe area that displays hackles reflects the "pure" mode I, whereas the fringe area that displays hackles in a shingle-like arrangement reflects a mixed mode I + III loading.

In summary, most fringes from sedimentary rocks suggest quasi-static growth, while rare fringes display cuspate hackles (Bahat 1991a, Fig. 3.41a) or hackles in shingle-like arrangements (e.g., Fig. 2.33e). Note the resemblance between the latter fracture morphology and the fracture surface of a turbine that is interpreted to have initiated in fatigue growth and possibly approached catastrophic fracture when $K_I \sim K_{Ic}$ conditions were attained (Fig. 2.44a) (Bahat 1991a, p. 132). In many outcrops, the distinction between these fringe types would be relatively easy, whereas in others that exhibit transitional fractographies, this distinction is expected to be more problematic. Hackle fringes are far more abundant in granitic rocks than in sedimentary ones, but even in granites hackles often show shingling. Note that in Fig. 4.11 in the lower fringe shingling is almost absent, whereas in the upper fringe shingling is more pronounced.

4.7 Comparative Jointing

4.7.1 Cooling Joints in Granites

4.7.1.1 *Regional Axial Fracture in Two Provinces*

Maps of the two fracture provinces, the Sierra Nevada Batholith (Fig. 4.31) and the South Bohemian Pluton (Fig. 4.32), both show that these are regional, elongated intrusion-complexes consisting of series of large and small discrete plutons that are aligned along the complex axes (Bateman and Wahrhaftig 1966 and Breiter 2001, respectively). According to Breiter (2001), the evolution of the South Bohemian Pluton started with the intrusion of the peraluminous Lasenice granite. Next was the intrusion of high-K peraluminous melt that crystallized as porphyritic Cimer granite in the south and non-porphyritic Mrákotin granite in the north. Further fractionation of the "Cimer melt" produced the Eisgarn granite in the central part of the intrusion-complex. Additional small bodies were then produced by intense fractionation of the "Eisgarn melt" and a still younger magmatic input formed the Zvule, Melechov and Cerinek deep-seated stocks.

A detailed geochemical investigation of the Eisgarn, Zvule and Melechov granites enabled Breiter (2001) to construct the inner structures of these plutons. Breiter (2001) shows that the Eisgarn (Fig. 4.33a), and Melechov (Fig. 4.33b) granites are elongated bodies and their long axes are oriented NNE, whereas the Zvule granite (Fig. 4.33c) has a slight elliptical shape with the longer axis slightly oriented E-W. It has been found that NNE is an important direction of a set of cooling joints along the South Bohemian Pluton (Fig. 4.5). The possible implication of the corresponding direction of the inner structures of the Eisgarn and Melechov granites to the regional direction of the NNE joint set is that there is a genetic connection between the two. Possibly, the cooling joints are aligned in the South Bohemian Pluton along certain discrete plutons as long as they also maintain the regional orientation, i.e., the regional influence is more pronounced than the one exerted by the individual plutons on joint orientation. This interpretation would be challenged if future studies will prove the non-existence of NNE oriented joints in the Zvule granite, which is approximately oriented E-W (Fig. 4.33c).

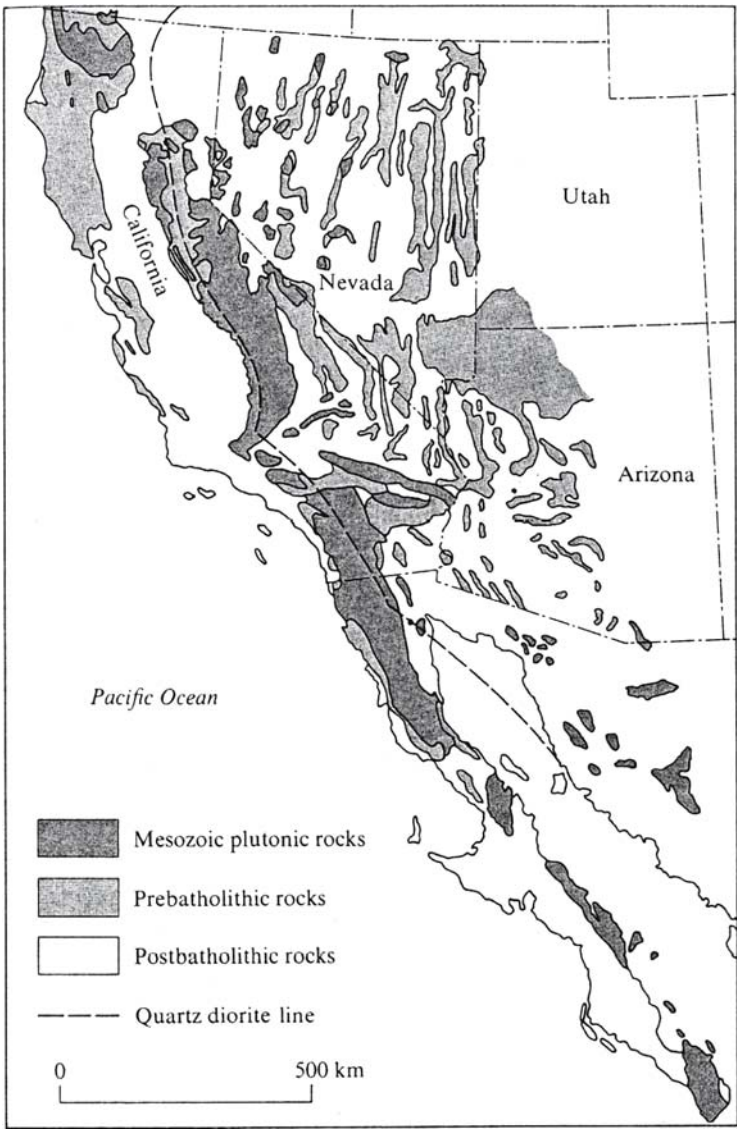

Fig 4.31. The general distribution of Mesozoic plutonic rocks in California and Lower California. The Peninsula Ranges are located in Southern and Lower California. The Sierra Nevada Mountains are in east-central California (modified from Ehlers and Blatt 1982)

To the best of our knowledge, no special treatment of cooling joints exists for the Sierra Nevada Batholith. Furthermore, the classification into distinct genetic groups/stages of joints in granites is challenged by existing investigations. For instance, Davis and Reynolds (1996, p. 265) cite works by Rehrig and Heidrick (1972, 1976) regarding jointing in Late Cretaceous to Eocene plutons in southern Arizona. The latter authors concluded that these plutons were intruded into the upper levels of the crust and as they cooled and congealed,

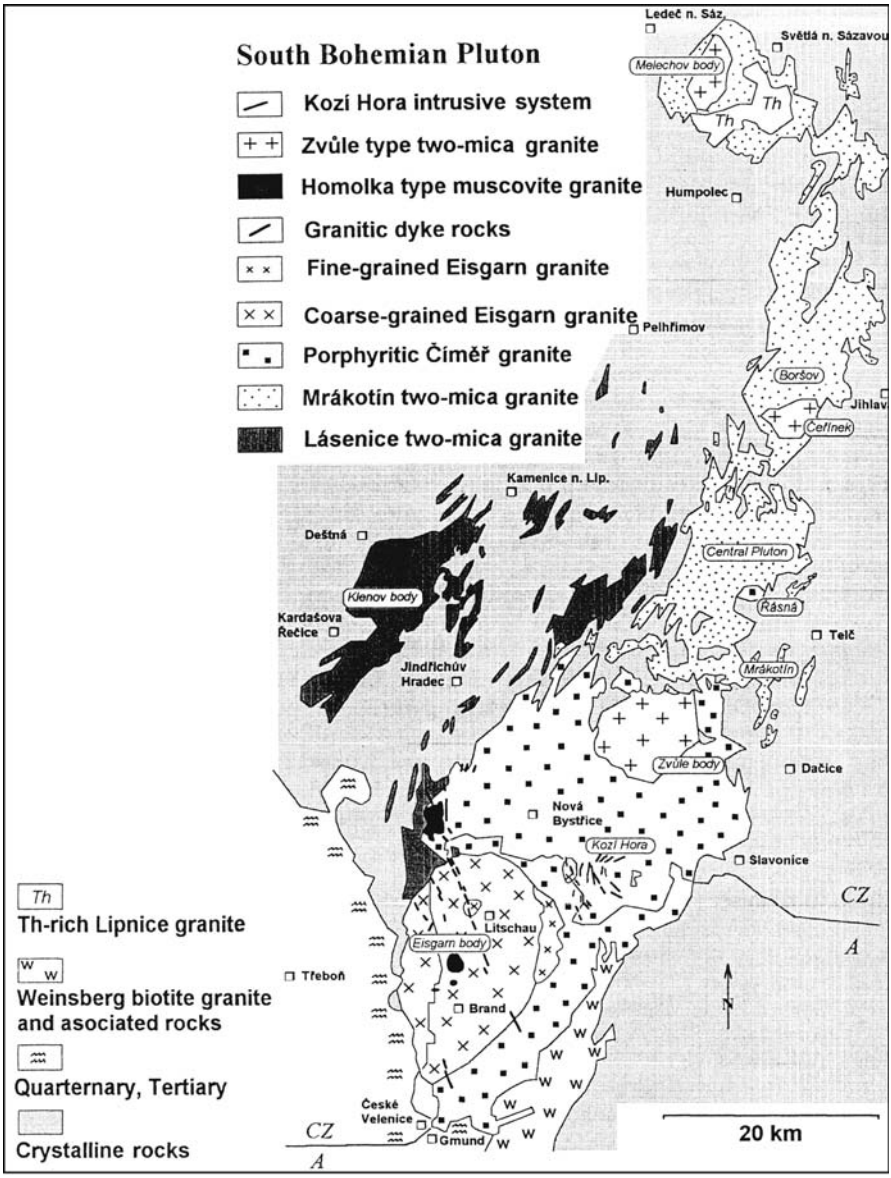

Fig. 4.32. Simplified geological map of the South Bohemian Pluton (after Breiter 2001)

and cracked in directions systematically related to the regional tectonic stress field that existed at the time. Thus, the interpretation seems to be that these joints formed on cooling (like cooling joints) by regional tectonic stress (syntectonic joints) at the upper levels of the crust (as uplift joints?), i.e., this explanation combines three distinct stages and mechanisms in one process. This interpretation may well be legitimate for south Arizona, but it may or may not be applicable to other fracture provinces, like the Sierra Nevada Batholith.

We now return to the debate about the age of the joints in the Sierra Nevada Batholith (Sect. 4.5.1). Suppose some of the joints formed during the emplacement of the plutons (e.g., Balk 1937; Mayo 1941) or soon after it (Segall et al. 1990), so that they might be considered to be cooling joints. According to (Bateman and Wahrhaftig 1966) the granitic rocks of the Sierra Nevada Batholith occupy the axial part of the N 40° W trending, faulted synclinorium, which began to form in Permian or Triassic time in central Sierra Nevada. Intense deformation is manifested by fold axes, steep or vertical beds, cleavage, and lineations that took place, both before and during the magma emplacements. Folds, at least, in the western part of the Ritter Range pendant may be related to the axial region of the synclinorium. Thus, it appears that an early NNW-NW trending structure may have significantly influenced the emplacement of the Ju-

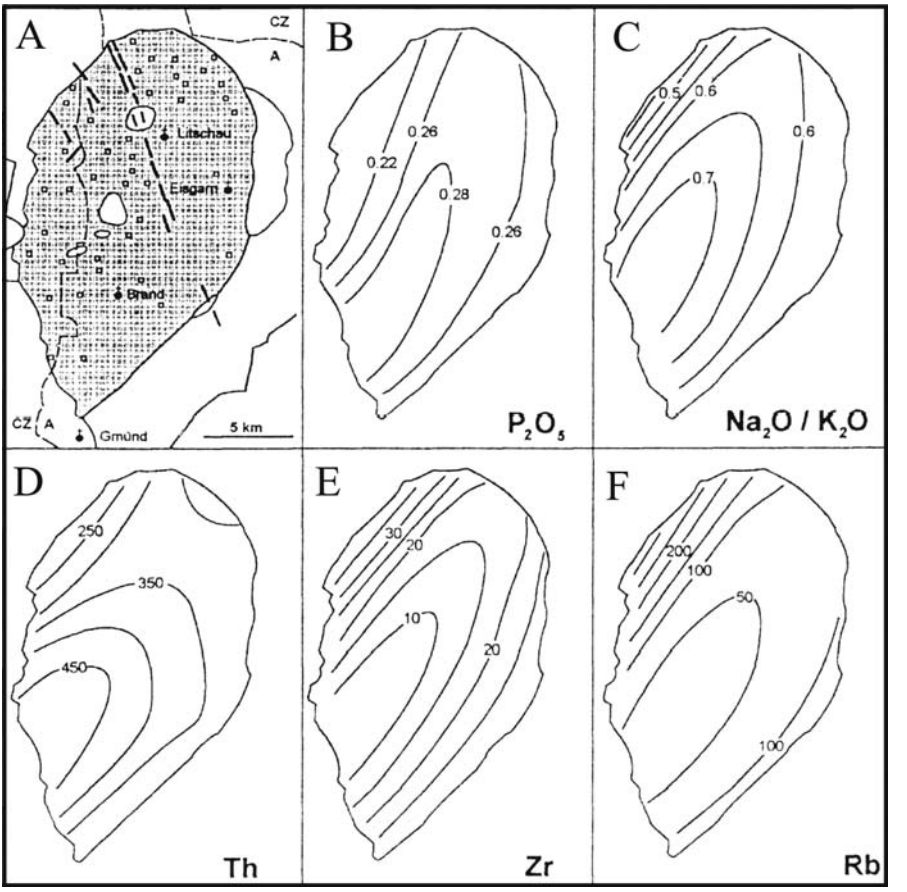

Fig. 4.33a. A detailed geochemical investigation of the Eisgarn, Zvule and Melechov granites by Breiter (2001). An idealized arial distribution of selected elements within the Eisgarn body. The isolines of element contents or ratios were constructed by methods of data interpolation by polynomial regression of third order. *A:* Simplified geological sketch of the interpreted body. The interpreted area is dotted; localization of used samples is expressed by small squares. *B:* Idealized distribution of P_20_5 in wt.%; *C:* Idealized distribution of Na_2O / K_2O-ratio in wt.%; *D:* Idealized distribution of Th in ppm; *E:* Idealized distribution of Zr in ppm; *F:* Idealized distribution of Rb in ppm

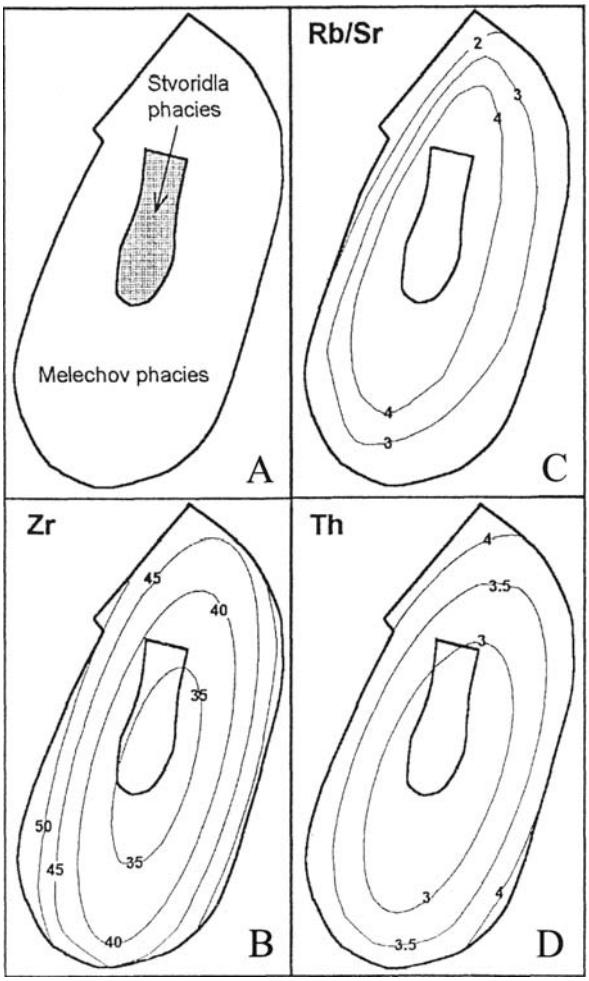

Fig. 4.33b.
Idealized arial distribution of selected elements within the Melechov body. *A:* Simplified geological sketch of the interpreted area; *B:* Idealized distribution of Zr in ppm; *C:* Idealized distribution of Rb / Sr in ppm; *D:* Idealized distribution of Th in ppm (from Breiter 2001)

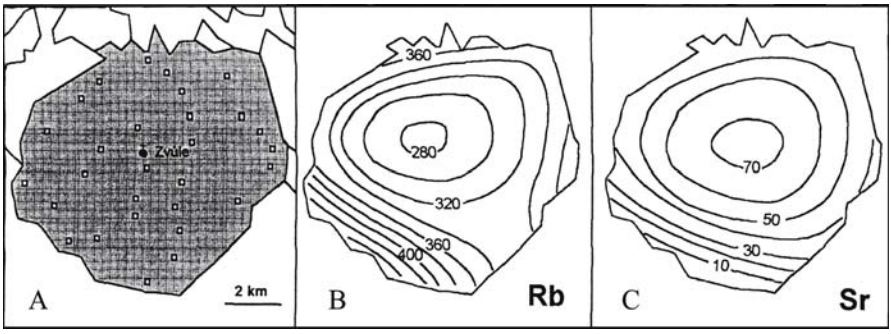

Fig. 4.33c. Idealized distribution of selected elements within the Zvule body. *A:* Simplified geological sketch of the interpreted area. The interpreted area is *dotted*; localization of used samples is expressed by *small squares*. *B:* Idealized distribution of Rb in ppm; *C:* Idealized distribution of Sr in ppm (from Breiter 2001)

rassic granites in central Sierra Nevada. This structure may also have controlled fracturing during cooling of the plutons and possibly also subsequent fractures along this direction. In support of this suggestion, Tobisch et al. (1989, Fig. 7) show a definite NNW-NW trend of a continuous, planar cleavage, predominant throughout the foothills terrain in central Sierra Nevada, where it is heterogeneously developed, occasionally in shear and mylonitic zones in the Upper Jurassic granitoids. Hence, there are similarities in the European and Californian fracture provinces, where in both there are indications that emplacement of granites was influenced by earlier, regional elongated structures, that also controlled later regional jointing.

4.7.2 A Comparison to the Cloos Model

In view of the general NNW-NW orientation of the elongated Sierra Nevada Batholith (Fig. 4.31), the NNW-NW cooling joints in the batholith (Sect. 4.5.1 and 4.5.2.1) seem to have significant similarities to the NNE cooling joints that are oriented along the elongated South Bohemian Pluton which is oriented NNE (Fig. 4.5 and 4.32). It appears that common to these two fracture groups is their fit to the S-joint category in the Cloos model (Fig. 4.1). The NNW-NW fractures developed perpendicular to the main horizontal compression that created the synclinorium and axial structures that subsequently controlled the formation of these fractures in the Sierra Nevada plutons. Furthermore, Lockwood and Moore (1979) found that the direction of maximum horizontal extension strain in the Sierra Nevada Batholith varies between WNW and NW, precisely fitting Cloos's criterion for S-joints, if applied to the fractures in this direction.

Sub-parallelism between fractures and isoanomals of the gravity high of Lusania expressing structural contours of the country rock has convinced Müller et al. (2001) that these fractures are S-joints (Fig. 4.3). The elongated South Bohemian Pluton sub-parallels the earlier structural contours of the country rock (Fig. 4.2b). The similarities in these two sub-parallelisms support the suggestion that the NNE set represents S-joints. It has been suggested that the shape of the South Bohemian Pluton could have controlled significant thermal and fluid-pressure gradients that in turn influenced the orientation of the NNE cooling joints (Bahat et al. 2003). This interpretation would coincide with the Cloos model, if proven in the future that the fluid-pressure gradients were not merely local on the surfaces of the individual joints (Sect. 4.4.5.2), but rather regional, i.e., perpendicular to the whole elongated pluton. The present interpretation relating the two groups of joints to the S-joint category would be challenged if proven that the main horizontal compression was axial during the cooling of the respective plutons, i.e., possibly implying that these fracture groups are Q-joints, which does not seem a likely possibility.

The descriptions of joints C and D (Sect. 4.5.2.2) partly resemble Cloos's "diagonal fractures" (Fig. 4.1). They dip at about 40° and they are partly filled with hydrothermal minerals. However, their strikes are more compatible with that of the Q-joints than with the strike of S-joints (Sect. 4.5.2.2 and Fig. 4.1). Moreover, the present observations suggest that they *predate* the formation of steep joints. If so, they differ from the Cloos model, in which the diagonal fractures are younger than the vertical joints. Furthermore, Cloos's diagonal fractures are clearly faults, whereas fractures C and D (D in particular) seem to fit better the term joints. Perhaps C and D represent a new fracture type that does not appear in the Cloos model?

4.7.3
Joint Genetic Grouping in Sedimentary Rocks and in Granites

The genetic division of systematic joints that occur in sedimentary rocks is into four groups: The burial, syntectonic uplift and post-uplift (Bahat 1991a, pp. 239–322). There are certain indications that the above classification of joints in sedimentary rocks may be partly applicable to joints cutting granite. Bankwitz and Bankwitz (1994, 1997) characterized syntectonic joints in two granite massifs from Europe. Bahat and Rabinovitch (1988) described uplift joints in granite from Sinai, Egypt. Holzhausen (1989) observed fractographic features in sheet joints cutting granite in Massachusetts, and Bahat et al. (1999) described post-uplift joints in granites from California. Thus, there seem to be resemblances in tectonic setting for the last three joint groups (syntectonic, uplift and post-uplift) between granites and sedimentary rocks. On the other hand, there are no corresponding similarities between early joints. The earliest systematic joint sets in sedimentary rocks are burial ones that maintain parallel orientation and approximate uniform dimensions and spacing. Probably the earliest joints in granites form during the cooling process as soon as some critical range of viscosity develops. The cooling of a pluton may be a long, multistage process, consisting of different thermo-mechanical modes. Hence, a correlation between "cooling joints" in granites to burial joints in sedimentary rocks is not possible, and a special genetic classification of cooling joints in plutonic rocks is required.

Part 2

Part 2 concerns fracture mechanic aspects of joints by drawing on fractographic properties of joints as follows:

1. Plotting joints on the velocity v vs. stress intensity K curve (Sect. 1.3–1.5).
2. Presenting a general discussion of various manifestations of v and K in granites.
3. Calculating the new fracture areas on *en echelon* and hackle fringes.
4. Estimating the "index of hackle raggedness" of joints.

4.8 Analysis of Fracture Velocity versus Stress Intensity Factor in the Borsov Joints Based on Fractographic Criteria

This section presents six aspects of the v vs. K_I diagram:

1. Physical meaning.
2. Justification for application to geological fracture.
3. Construction for geological application.
4. General criteria and method of placing the joints on the diagram.
5. Plotting of the Borsov joints on the v vs. K_I diagram.
6. Present limitations of the method.

The basic ideas of this scheme were outlined in Bahat (1991a, p. 234), and these were elaborated in Bahat et al. (2003).

4.8.1 The Velocity versus Stress Intensity Factor Curve

Wiederhorn (1967) and Wiederhorn and Bolz (1970) experimented on glass and showed the dependence of crack velocity v on the applied force and the tensile stress intensity

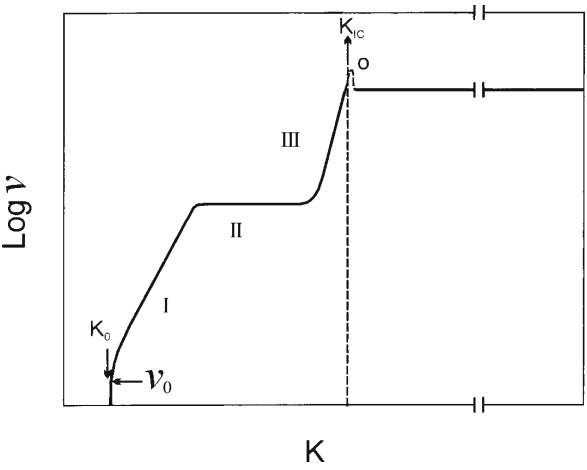

Fig. 4.34. Schematic variation of stress intensity factor K with crack velocity v (modified from Evans 1974). The subcritical curve left of K_{Ic} is divided into three regions I, II and III. K_0 and v_0 are the stress corrosion limit and the crack velocity at this limit (Wiederhorn and Bolz 1970). Supercritical growth occurs mostly along a terminal velocity plateau following a rapid increase in crack velocity at K_{Ic}. A velocity overshoot o, immediately after K_{Ic} and before the plateau has been predicted by Rabinovitch and Bahat (1979)

factor K_I in the sub-critical range (below K_{Ic}, the critical stress intensity factor). Wiederhorn and Bolz (1970) obtained a curve that was characterized by three distinct regions (Fig. 4.34). The slow crack growth in region I is manifested by a linear logarithmic plot. The behavior of region I is attributed to stress corrosion. The rate of crack growth is controlled by the chemical reaction between the reactant (solution) and glass at the crack tip when the system is essentially at equilibrium. Region II is controlled by the rate of reactant transport to the crack tip. In this region V almost does not change and is independent of K_I. In region III crack velocity is quite high; it is insensitive to the reactant and to stress-corrosion. It was also established that regions I–III were sensitive to water environments (vs. vacuum conditions) and were influenced by chemical conditions such as pH. The K_{Ic} line shows that at a critical stage in region III, the crack undergoes a catastrophic growth associated with a sudden jump in V, i.e., at $K_I \geq K_{Ic}$ post-critical crack propagation occurs.

4.8.2
Application of Fractography and Fracture Mechanics to the Study of Joints

Fractographic investigation of joints rests on analogies between the fracture surface morphologies of joints in geological exposures to fractures in glass, ceramics, metals and polymeric materials (e.g., Woodworth 1896; Bankwitz 1965, 1966; Kulander et al. 1979; Bahat 1979a, 1991; Cooke and Pollard 1996). It has been shown that K_{Ic} estimates derived from geological measurements are compatible with existing data from laboratory fracture experiments (Segall and Pollard 1983). Quantitative tectonofractography is a method that was developed to estimate paleostresses from strain measurements on joint surfaces, and this method stems from principles of fracture mechanics (e.g., Bahat 1979a, 1991; Bahat and Rabinovitch 1988; Weinberger 2001a). A strong correlation between the behavior of *en echelon* segmentation in polymethyl methacrylate (PMMA) (by mixed modes I + III) and *en echelon* segmentation in field outcrops was demonstrated by Cooke and Pollard (1996) and Bahat (1997). Sophisticated experimentation by Müller and Dahm (2000) further developed this concept and showed that knowledge of rupture velocities in sedimentary rocks can be gained from experimentation on starch-water mixtures. Particularly important were a series of demonstrations by various investigators (e.g., Atkinson and Meredith 1987a,b) that plots of minerals and rocks on V vs. K_I diagrams greatly resembled analogous plots of glasses. All these (as well as other sources) justify the suggestion by Pollard (2000) that the mode is eminently suitable for the taxonomic classification and description of fractures in the field.

4.8.3
The Velocity versus Stress Intensity Curve for Granite

The curve in Fig. 4.35a is a synthesis of nine elements:

1. The basic concept stems from the sub-critical V vs. K_I curve determined on glasses (Fig. 4.34).
2. Section A–B on the curve corresponds to the sub-critical V vs. K_I curve determined for Westerly granite, under 15 kPa p(H_2O), at 300 °C by Atkinson and Meredith (1987b).
3. From the two hypothetical curves, B–C and B–D, the former assumes the existence of regions I–III and the latter favors the existence of only region III (Fig. 4.35a).

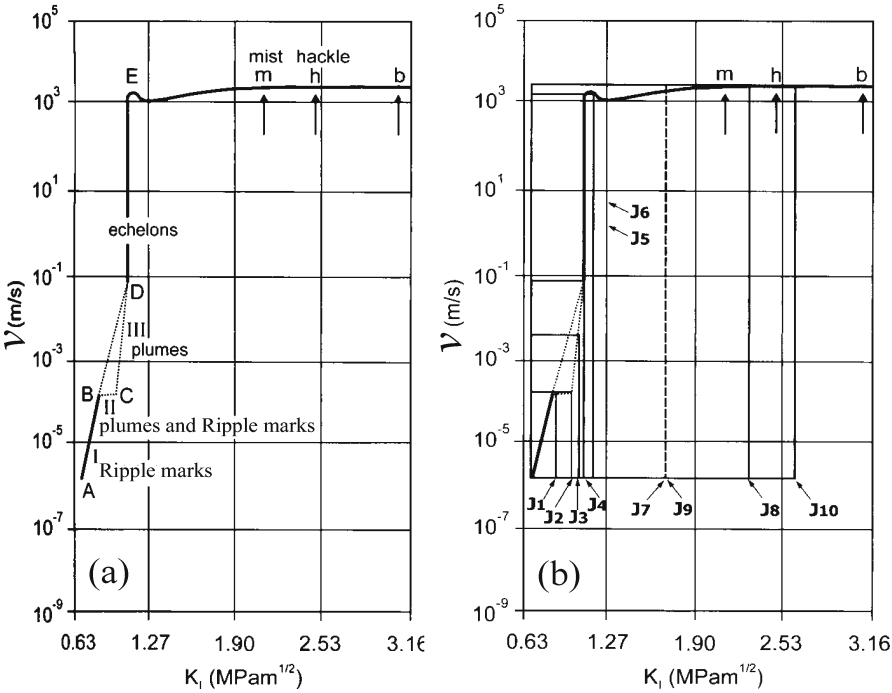

Fig. 4.35. a The V vs. K_I curve for joints in granite from the South Bohemian Pluton, synthesized from laboratory experiments. **b** The estimate of a range of crack velocities for ten joints in granite from the South Bohemian Pluton. For each joint the range of fracture velocity is given in a *rectangular frame* constructed on the curve from Fig. 4.35a, where the vertical right side of each frame gives the maximum fracture velocity that was attained by the joint

4. The position of D approximates $K_{Ic} = 1.09$ MPa $m^{1/2}$ (the K_{Ic} value of Westerly granite at 300 °C, Atkinson and Meredith 1987a).
5. The position of D independently fits well the definition of K_{Ic} at crack velocity of $\geq 10^{-1}$ m s^{-1} (Wiederhorn et al. 1974).
6. A velocity overshoot immediately beyond K_{Ic} at E was mathematically predicted by Rabinovitch and Bahat (1979) and was recently verified experimentally (Cramer et al. 2000, Fig. 1A).
7. Kerkhof (1975) proposed a unified curve for both sub-critical and post-critical conditions (at both sides of K_{Ic}) and suggested that the positions of mist and bifurcation initiations correspond to m and b, respectively. These positions are approximated in the post-critical part of the present curve.
8. We add h (Beauchamp 1996) representing an approximate location for hackle formation between m and b.
9. Finally, the two ends of the curve are at K_0, signifying zero slow crack growth below point A, and at b where the fracture bifurcates along the terminal velocity plateau (Evans and Wiederhorn 1974).

Hence, Fig. 4.35a is essentially based on experimental data from glass but it is constrained by results from granite and the definition of K_{Ic} (elements 2–5).

In further justification of these elements for the construction of Fig. 4.35a, we need to add that the Westerly granite was chosen because of its textural similarity to that of the granite under investigation (fine to slightly medium grain size). Curve A–B was selected because we consider joint fracture under considerable pore pressures at depths of about 10 km, so that assuming 300 °C due to the thermal-gradient seems reasonable. There is no compelling data that indicates which curve, B–C or B–D is more realistic, so we use both. A velocity overshoot immediately beyond K_{Ic} is anticipated to be an inherent property of fracturing in elastic materials following great velocity "jumps" such as the one from D to E. Although a realistic velocity jump is expected to occur along a slope (through a certain range in K_I), a conventional vertical C–D is adapted (Atkinson and Meredith 1987b, Fig. 4,15).

4.8.4
Methodology for Plotting Joints onto Velocity versus Stress Intensity Factor Curve

Various sub critical and post critical growth conditions of joints may be inferred on the v vs. K diagram (Fig. 4.35a) by two fractographic distinctions: First, plumes and ripple marks (see Sect. 2.2.4.2 for definitions) vs. hackle cracks (or hackles) and second, *en echelon* cracks vs. hackles. The first distinction is between characteristic fractographic features below and above K_{Ic} (Fig. 4.34 and 4.35a). Both plumes (striae) on the mirror within the sub critical regime and hackles on the fringe in the post critical regime often occur radially, such that the latter often appear to be in continuation with the former (Fig. 2.30a). However, they can be distinguished quite readily. Whereas striae are delicate and approximate unidimensional textures by their barb lines (Fig. 2.55b and 4.8a), hackles are three-dimensional, coarse complexes consisting of superimposed flakes of material that are separated by microcracks in all orientations. In fringes formed in glass by extremely intense fracture (high K_I values), each flake may display a miniature assemblage of fractographic features shown in Fig. 2.1a. On surfaces cutting granite that represent moderately intense fracture conditions. the differences between plumes and hackles are less discernable than in glass, but they are quite pronounced.

Kerkhof (1975) observed that arrest marks (ripple marks) were induced in plate glass at propagation rates below $v = 4 \times 10^{-5}$ m s^{-1} and $K_I < 0.73$ MPa m$^{1/2}$ that correspond to the range of regions I and II in Fig. 4.35a. Accordingly, we propose that fracture markings in rocks that display arrest marks reflect the range of regions I and II. The frequent occurrence of ripple marks superposed by radial plumes on joint surfaces suggest that the plumes are formed under fracture conditions similar to those that produce ripple marks but under slightly more intense ones, i.e., closer to region II. Fracture experiments on PMMA have shown that circular ripple marks develop before radial plumes on the fracture surface (Bahat 1991a, Fig. 2.50c), i.e., these ripple marks developed at lower K_I values than the plumes. Striae developed on a smooth fracture surface of soda-lime silica glass in water when the velocity of fracture propagation reached about 10^{-2} m s^{-1} at around $K_I = 0.7$–0.8 MPa m$^{1/2}$ (Michalske 1984, Fig. 1). This was above the mid range between the stress corrosion limit, $K_I = 0.3$ MPa m$^{1/2}$, and the fracture toughness $K_{Ic} = 0.9 \pm 0.1$, i.e., striae formed in the range of regions II to III (Fig. 4.35a). We propose that markings like the short rhythmic plumes from the Appalachian Plateau (Fig. 4.36) that show periodic increase of barb intensities reflect the range of regions II to III, whereas long uniform plumes free of arrest lines relate more

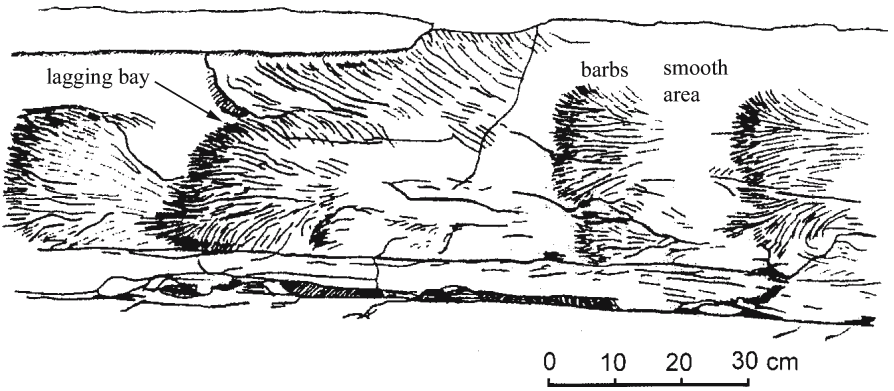

Fig. 4.36. Rhythmic plume growth. Fan perimeters designate loci of arrest marks where barbs reach their maximum intensity and vanish into smooth areas. Barbs then resume their growth as fine lines within the plume that mark the local direction of fracture propagation. The perimeters convex toward the direction of fracture propagation (from right to left) and the barbs may be partly "branched" due to lagging bays (modified after Bahat and Engelder 1984)

to region III (Engelder et al. 1987 and Bahat 1994a, Fig. 3.18). On the other hand, the periodic smooth areas where a new cycle of fracture begins (Fig. 4.36) represent V and K_I conditions within region I and possibly below it.

The second distinction relates to the range of K_I conditions under which *en echelon* cracks develop. This range is unclear because it varies considerably. *En echelon* cracks have been observed in borosilicate glass at very low K_I (Wiederhorn and Johnson 1973 Fig. 5). There are some indications that *en echelon* cracks formed in rocks and rock-like material under low K_I values (Kulander et al. 1979; Bahat 1997; Müller and Dahm 2000). On the other hand, Hertzberg (1976, Fig. 14.9) analyzed the fracture conditions of a turbine rotor made of steel and found that the *en echelon* cracks developed at close to K_{Ic} conditions. This problem is further complicated by the occasional presence of hackle cracks (Fig. 2.1a) and *en echelon* cracks (Fig. 2.1b) at close proximities, suggesting some transitional relationship at the fringe (Bahat 1991a, p. 68). All these support early observations that *en echelon* segmentation depends on the K_I / K_{III} ratio (Sommer 1969). Thus, plotting *en echelon* segmentation (Fig. 2.1b) on the V vs. K curve is still problematic, and a transitional range of some uncertainties may exist up to and around K_{Ic} conditions for *en echelon* cracks (Hertzberg 1976). On the other hand, the situation that concerns hackle cracks (Fig. 2.1a), which are expected to occur above K_{Ic} up to branching, is clearer (e.g., Kerkhof 1975; Rabinovitch et al. 2000a).

4.8.5
Plotting Joints of the Borsov Pluton

It is unrealistic to determine the points of joints J1–J10 (Fig. 4.6–4.8, respectively) along the curve of Fig. 4.35a. A more reasonable approach is to estimate the range of crack velocities for each joint (Bahat et al. 1999), given in rectangular frames, where the vertical right side of each frame gives the maximum fracture velocity that was attained by the respective joint (Fig. 4.35b). It is assumed that joints generally start in low velocities before reaching fast propagation (e.g., Bahat 1991a, p. 58).

We first consider the four joints of group 1 (Fig. 4.6). Based on the criteria in the previous section, the arrest marks superposed by radial plumes on joints J1 and J2 (Fig. 4.6a,b) signify maximum velocities close to region II and region III. There is a considerable variability in the plume intensity of the quasi-core joint, J3 (Fig. 4.6c), implying that fracture stresses, as well as V and K_I were not uniform on the joint surface. The long plumes not associated with arrest marks signify monotonous propagation (approximately constant velocity) that could reach region III. However, the plumes of J3 that are associated with arrest mark seem to signify vacillation between region I and part of region III. These plumes did not develop into fringes. The joints from the multi-joint exposure, J4 (Fig. 4.6d), mostly exhibit fractographies that occur on joints J1–J4, placing them between regions I and III.

The fringes in group 2 display a series of fringes between the two end members shown in Fig. 2.1a,b). The divided arrest mark joint, J5 (Fig. 4.7a) exhibits a small *en echelon* fringe, which may indicate that K_I temporarily reached K_{Ic}, because these fringes resemble the features of the fringe studied by Hertzberg (1976) that formed close to critical conditions (at K_{Ic}). The extended fringe F1 of J6 (Fig. 4.7b) relates to the entire structure consisting of the ten (or eleven?) concentric arrest marks. Accordingly, it appears that both the right side of the joint and the triangle were formed before the propagation of the large wavy plume w from the triangle towards the left. Therefore, the large wavy plume represents an intriguing example of transition from *en echelon* fringe in F1 and F2 to a low intensity plume. We assign to J6 a frame similar to that of J5 (Fig. 4.35a,b).

The *en echelon* segmentation is clearly defined on the fringe of J7 (Fig. 4.7c) and plotting this joint is somewhat problematic, as mentioned above. Prolonged growths under sub-critical conditions, i.e., through regions I–III, may have transformed to the mode of post-critical growth, i.e., possibly beyond K_{Ic} (dashed line in Fig. 4.35b). The extent of this frame is still a topic for future research.

The partly erased joint, J8, shows a well-defined circular mirror boundary, but the fringe is very irregular (Fig. 4.7d). A delicate radial plume reaches the boundary from an inside location of the joint and continues radially downward and sidewise beyond the boundary as irregular *en echelon* segments in diverse morphologies. The *en echelon* segments are delicate in certain areas, while in other locations they assume coarse relieves of hackles. This diversity fits between the two end members shown in Fig. 2.1a,b, suggesting a range in K_I between m and h (Fig. 4.35a,b).

The trefoil joint, J9, has the two most complex fringes on the right and on the left sides of the mirror (Fig. 4.8 and 4.9). However, these fringes fit the pattern of Fig. 2a and resemble the fringes of J7. Therefore their position along the V vs. K_I curve is further left from that of J8 (dash line in Fig. 4.35b). The joint with the hackled-fringe, J10 (Fig. 4.8c), shows features resembling both Fig. 2a and Fig. 2b, but closer to Fig. 2b than to Fig. 2a. We therefore place the right side of the frame further right from h (Fig. 4.35a,b).

4.8.6 Limitations of this Methodology

The curve shape in Fig. 4.34 depends on various parameters, including material properties as well as environmental conditions such as temperature, fluids and pH (e.g., Wiederhorn and Bolz 1970; Guin and Wiederhorn 2003); it is particularly sensitive to stress and stress rate. Therefore, Fig. 4.35a,b may be modified in future research along

the various segments of the curve. Changes may occur along the sub-critical range due to different water/vapor contents, such that various rocks would fit different region II–III relationship. This will come with a deeper understanding of the properties of undulations vs. arrest marks and plumes (striae), i.e., when criteria of distinguishing them on mirrors that form sub-critically from mirrors that form post critically are established (Sect. 2.2.4). Also, plotting of joints in the sub-critical range would be influenced by the dependence of K_I on v that may change along different v ranges (Guin and Wiederhorn 2003). Additionally, the K_{Ic} for granite may change, as K_{Ic} values are refined.

The shape of the post-critical "terminal velocity" segment may vary to fit different dynamic fracture data. Results generally show a strong increase in fracture velocities at the transition from the mirror to the hackle and branching zones (in glass) (Cramer et al. 1999). But velocity fluctuations can also be expected (Sharon and Fineberg 1999). The plot of hackles within a limited range close to h (Fig. 4.35b) would be quite reliable. However, the plot of *en echelon* fringes remains problematic until further information on the dependence of these fringes on K_I (rather than K_I / K_{III}) will become available. Meanwhile, a useful criterion would be (Sect. 2.2.4.2): Faint plumes and lack of arrest marks imply relatively high K_I (Fig. 2.56a), whereas pronounced plumes and arrest marks suggest relatively low K_I (Fig. 2.54a,b). All these may somewhat shift v and K_I values for particular joints, but they would not challenge the principles of the method. Finally, note that while in Fig. 4.34 the curve of terminal velocity is horizontal, it has a slight slope in Fig. 4.35. The actual shape of this curve is still unknown, and it may vary in various materials. Moreover, the exact conditions of tension (or extension) are important. While under pure tension the terminal velocity may be attained rapidly (perhaps on the mirror plane), deviations to bending by slight lateral compression may delay the attainment of terminal velocity (Shand 1954, also Bahat 1991a, Fig. 2.19).

4.9 Velocity and Stress Intensity Manifestations of Fracture Propagation in Granites

The plot in Fig. 4.35b offers a generalized quantitative frame within which various other natural and experimental fractures can be examined; it also demonstrates some of the limitations of this methodology. When using V and K in analyzing the fracture history of joints, one needs to bear in mind several points:

1. Fracture velocity changes all the time, generally by growing up to the terminal velocity, but also up and down.
2. *En echelon* segmentation is a complicated indicator of crack velocity.
3. When quantitative estimate of fracture behavior is impossible (Fig. 4.35b), it is convenient to describe qualitatively the relative increase or reduction in either v or K of specific fracture exposures.
4. There are significant differences in the fitting of curves that correlate v and K with fractographic features (Arakawa and Takahashi 1991; Sect. 2.2.3.12).
5. There are theoretical disagreements regarding the issue of which parameter actually controls dynamic fracture (aspects of fracture velocity in Sect. 1.4, and aspects of stress intensity (Sects. 1.4.3.1 and 1.4.3.2).
6. Both remote and local forces that act on the fracture, influence v and K.

We present below two examples of fracture in granites that touch on these six points. The first relates to fractographic features on the mirror plane of a post-uplift joint from California (after Bahat et al. 1999), while the second concerns the fringes of cooling joints from the Czech Republic (after Bahat et al. 2001a,b, 2003).

4.9.1 Fracture Velocities of Exfoliation Joints Cutting the El Capitan Granite and Comparable Fractures

Fan-like markings on exfoliation surfaces from the middle height of El Capitan are made of radial plumes and concentric ripple marks orthogonal to each other at their intersections, which imply simultaneity (Fig. 4.27). This fracture morphology suggests a sub-critical propagation rate below 4×10^{-5} m s^{-1}, assuming dry conditions, and below 10^{-2} m s^{-1}, if the fracture were immersed in water (Bahat 1991a, p. 234 and present Fig. 4.35). Accordingly, it would take longer than fourteen days to fracture a fan having radial plumes 50 m long in dry conditions, and a fan immersed in water, whose plume is 36 m long would fracture in more than an hour. Due to the uplift of the El Capitan block, the middle height of the cliff is expected to be above the water table. In addition, due to the low porosity of the granite, the above dry conditions are preferred. If however buckling and splitting (Fig. 4.28) would enable water flow into the fracture zone, a more rapid fracture would occur, requiring a much stronger preference of downward fracture propagation compared with an upward propagation, due to the flow of more water towards lower elevations. This is not supported by the fan pattern on the cliff (Fig. 4.27) so that propagation under dry conditions is favored. Olson's (1993) calculations for joints from Sierra Nevada granites (generated by a mechanism other than exfoliation) suggest that fractures of some 10 m long were formed in about three minutes or faster, possibly under conditions approaching critical.

4.9.2 Fracture Velocities Relative to Estimated Paleostress Magnitudes

The calculated tensile paleostresses that initiated joints in granitic rocks under three different geological conditions are presented in Table 4.7. The results compared here were obtained by different procedures. The method applied to the analysis of a fracture on Half Dome (Fig. 6.18) and granite from East Sinai (Bahat and Rabinovitch 1988) is based on measuring fracture markers on surfaces of individual joints. The method used by Segall and Pollard (1983) relies on measurements of extension strain accommodated by the dilation of many joints (and was used for the analysis of fracture in granodiorites from Mt. Givens). Accordingly, these two methods pertain to local and remote stresses, respectively.

Segall and Pollard (1983) assumed quasi-static crack propagation conditions in their analysis of the initial tensile stresses that induced regional joints in the Mt. Givens Granodiorite from the Sierra Nevada. The relatively high fracture stress values resulting in jointing at Mt. Givens (ranging from 1.2 ±1.0 MPa to 26 ±11 MPa) seem to suggest syntectonic fracture (Bahat 1991a). Fracture was enhanced by pore pressure, as testified by mineral fillings (Segall and Pollard 1983), but under considerable depths,

Table 4.7. Tensile paleostress conditions for jointing in granodiorite and in granite

Example			Relative fracture velocities[a]
Post-uplift exfoliation joint in granodiorite from the SW cliff of Half Dome in Yosemite Valley, California			
The stress intensity method Range of fracture stress σ_f		0.01 to 1.48 MPa	Long growth under sub-critical conditions, and short post-critical growth
The surface energy method Range of fracture stress σ_f		0.06 to 0.37 MPa	
Syntectonic joints in granodiorites from Mt Givens (Segall and Pollard 1983)			
	Ward Lake	Florence Lake	Long growth under close to critical conditions, but never reaching them
Initial stress σ_i	≤26 ±11 MPa	10 ±6 MPa	
Initial stress σ_i	≥1.7 ±0.9 MPa	1.2 ±1.0 MPa	
Uplift joint in granite from East Sinai (Bahat and Rabinovitch 1988)			
The stress intensity method Range of fracture stress σ_f		2.9 to 15.8 MPa	Relatively short growth under sub-critical conditions before assuming post-critical growth
The surface energy method Range of fracture stress σ_f		2.4 to 6.0 MPa	

[a] See text for discussion.

that prevented fracture branching (Segall and Pollard 1983). Such conditions would fit sub-critical fracture velocities (Table 4.7). Greater fracture stress results than those mentioned above for the granodiorites were obtained for an uplift joint in granite from Sinai. The latter paleostress results are less, but comparable to those obtained by tensile experiments on granite (from 7 MPa to 18 MPa, Segall and Pollard 1983). Quite possibly, the Sinai joint started to propagate from certain depths below the water table while being exposed to excessive pore pressures that resulted in high fracture stress values.

In summary, fracture velocities may change considerably during the fracture process. A two stage process is assumed for the three granitic rocks:

1. Sub-critical fracture growth, which had occurred before critical conditions were attained.
2. Post-critical fracture velocities that could have initiated under reduced overburden pressures. The difference is in the amount of time needed for fracture growth during the first stage.

The results suggest that the first stage was relatively long for the exfoliation in the cliff of Half Dome, whereas for the joint in East Sinai this stage was relatively short. However, many joints, possibly including the joints from Mt. Givens (Table 4.7) never reach post-critical fracture velocities along their history, mostly because of overburden constraints.

4.9.3
Cycling Fracture

The previous sections relate to the general property of fracture to increase its fracture velocities up to the terminal velocity (Fig. 4.34 or 4.35). Quite common however are alternating changes in fracture velocity (and stress intensity) that are reflected from fractographies, which are displayed on mirror planes (e.g., Fig. 4.7b, 4.36). Rarer and more intriguing are cycles that are exhibited by both mirrors and fringes (e.g., Fig. 4.8a,b). We now interpret the observations from the mirror-left fringe relationship of the trefoil joint (Fig. 4.9c,d) in light of some experimental results.

4.9.3.1
Fracture Velocities During Growth of the Trefoil Joint

Müller and Dahm (2000) formed plumes and fringe zones on surfaces of desiccation tensile cracks that were created by drying starch-water mixtures (Sect. 2.2.3.9). Particularly relevant to the present section were their observations that at transitions from the parent joints to fringes, topographic amplitudes occurred, i.e., enlargements in the crack area, were associated with a reduction in fracture velocities. The latter findings resemble the experimental results obtained by Sharon et al. (1995). They applied tensile stresses perpendicular to a thin plate (0.8 or 3 mm in thickness) made of cast PMMA. These authors found that cracks discontinue their straight propagation and become "unstable" beyond a critical velocity, v_c, of $0.36v_R$, where v_R is the Rayleigh wave speed in the material (the velocity at which a wave moves along a free surface). This transition from quasi-static velocities to dynamic ones involves two coupled phenomena, velocity oscillations and secondary micro-branching from the primary parent crack (Fig. 1.33). Sharon et al. (1995) observed that the increase in new crack area by the formation of the micro-branches was associated with reduction in fracture velocities.

The fractography of the trefoil joint (Fig. 4.9c,d) seems to fit the fracture principles derived by Sharon et al. (1995). The trefoil primary mirror plane and *en echelon* segments (first fringe) are analogous to the primary and secondary (branch) cracks (Sharon et al. 1995), respectively. The trefoil secondary mirror plane and secondary *en echelon* segments reflect the stages of resumption of rapid propagation of the primary crack and subsequent appearance of secondary cracks (Sharon et al. 1995), respectively. The implication is that the remote stress operating on the trefoil joint did not subside (or perhaps was resumed after a quiescent period due to local conditions). Therefore, exerted tension resulted in the creation of a new, secondary mirror that propagated in the same downward direction, as shown by its downward facing convex boundary. The increase in length of the secondary mirror was associated with increasing its fracture velocity in analogy to the above mentioned fracture principles (Sharon et al. 1995). This fracture velocity was reduced again, resulting in the secondary fringe, i.e., the energy dissipation that occurred by creating the new segment surfaces (tensile and shear) was associated with a reduction in fracture velocity, as also observed by Müller and Dahm (2000). Thus, the primary mirror of the trefoil joint was segmented into a fringe that then continued to fracture into a secondary mirror, which also was segmented into a secondary fringe.

4.9.3.2
The Formation of the Trefoil Joint under Mixed Modes Loading

Couplings of velocity decrease with the increase in new fracture surface area were observed both under quasi-static conditions (Müller and Dahm 2000) and through dynamic ranges (Sharon et al. 1995). What are the differences between the two? Sommer (1967, 1969) simulated *en echelon* segmentation on the fracture surfaces of circular glass rods loaded in tension by the superposition of a small amount of torsion, creating conditions of increasing mode III / mode I ratios. On the other hand, high K_I / K_{III} ratio increased crack velocity, leading to crack branching. Bank-Sills and Schur (1989) showed the inherent tendency of increasing mode III / mode I ratios from the center of metallic plates towards their boundaries, and Bahat (1997) reported that the latter tendency occurred also in sub-horizontal chalk beds.

All these experimental and field observations match into the following scenario of the trefoil joint growth. The primary joint propagated down under conditions of increasing K_I magnitudes and very low K_{III} / K_I ratios to the mirror boundary at which an abrupt increase in the mode III / mode I ratio occurred, leading to the breakdown into *en echelon* cracks (Cooke and Pollard 1996). This was linked with energy dissipation on many new crack surfaces and a reduction in crack velocity. The crack speed reduction was probably associated with the "mode III crack closure" effect, which was linked with friction and interlocking interferences along the fracture surfaces (Tschegg 1983). Crack speed reduction can be very substantial under these conditions: *En echelon* cracks have been observed in borosilicate glass after application of stress with an intensity factor less than the fatigue limit at very low crack velocities (Wiederhorn and Johnson 1973, Fig. 5). As mentioned above, recent experiments on rupture velocities in starch show similar results (Müller and Dahm 2000). The second mirror reflects resumed conditions of increasing K_I magnitudes. Hence, the micro-branching processes described by Sharon et al. (1995) relate to crack velocity oscillations under high K_I / K_{III} ratios, whereas the experiments conducted by Müller and Dahm (2000) took place under increasing K_{III} / K_I ratios.

4.9.3.3
Fractographies that Pertain to both Quasi-Static and Dynamic Fractures

How can *en echelon* segments (generally reflecting quasi-static propagation Sect. 4.7.3.1) and hackles (generally reflecting dynamic propagation) occur adjacently on a single fringe? (e.g., Fig. 2.1c). The answer is based on the assumption that even "slight deviations" of the direction of the minimum principal compression (or maximum principal tension) from orthogonality to the fracture surface would induce *en echelon* segmentation (Sommer 1969). Accordingly, fringes formed by both quasi-static and dynamic propagation may be influenced by such "slight deviations". Fractures formed quasi-statically when K_{III} / K_I are high will be dominated by *en echelon* fringes (Fig. 2.1a), and these fringes will have the tendency to assume simple, uniform widths (Fig. 2.34b). On the other hand, fractures formed dynamically when K_{III} / K_I are low will be dominated by hackle fringes, on which however *en echelon* segmentation in a shingle-like arrangement may be superimposed in accordance with this ratio. Such superposition can ex-

plain the frequent occurrence of fringes that show hackles in a shingle-like arrangement (center of Fig. 4.12b). The latter fringes often exhibit non-uniform widths (Fig. 2.34a). Hence, it is quite possible that on the fracture surface obtained by De Freminville (1914) (Fig. 2.1c) the two fringe types reflect local slight changes in the extent of orthogonality of the maximum principal tension: The fringe area that displays hackles reflects "pure" mode I, whereas the fringe area that displays hackles in a shingle-like arrangement reflects mixed mode I + III loading.

In summary, most fringes from sedimentary rocks suggest quasi-static growth, while rare fringes display cuspate hackles (Fig. 2.30a and 2.42) or hackles in shingle-like arrangements (e.g., Fig. 2.33e). Note the resemblance between the latter fracture morphology and the fracture surface of a turbine that is interpreted to have initiated in fatigue growth and possibly approached catastrophic conditions, i.e., under $K_I \sim K_{Ic}$ conditions (Fig. 2.44a) (Bahat 1991a, p. 133). In many outcrops the distinction between these fringe types would be relatively easy, whereas in others that exhibit transitional fractographies, this distinction would be more problematic. Hackle fringes are far more abundant in granites than in sedimentary ones, but even in these rocks hackles often show shingling. Note that in Fig. 4.11a in the lower fringe shingling is almost absent, whereas in the upper fringe shingling is more pronounced.

4.10 New Fracture Area in the *En Echelon* and Hackle Fringes on Joint Surfaces from the Mrákotin Quarry

4.10.1 Fracture Area Increase in the Transition from *En echelon* to Hackle Fringe

A basic physical tendency of a cracked body is to minimize its stored strain energy (Eq. 1.19), which is done by the creation of new crack area (Eq. 1.20). Therefore, measuring changes in crack area is important for the characterization of the fracture process. A comparison of the relative flat areas of the "segments" on the fringe of joint C (Fig. 4.12a and 4.37a) to the extremely wrinkled "flake" surfaces of the hackles on the fringe of joint A (Fig. 4.11a–c and 4.37a,b) intuitively suggests that the overall fracture area of the latter fringe is significantly larger than the former fringe. This intuitive observation regarding the difference in new area in the two fringe types needs to be proven, and meeting this requirement is the main objective of this section, citing Bahat et al. (2002b).

The extent of superposition of two adjacent segments (or flakes) in a fringe is often an enigma. The best way of resolving this question is by removing the upper segment and examining the area underneath the upper segment (Bahat 1986a, Fig. 7). This provides two measurable parts: The revealed area of the upper segment before its removal and the hidden area that belongs to the lower segments. The ratio between the two can then be determined. This determination is however difficult to accomplish because in many outcrops the segments are inaccessible, requiring the pursuit of estimation methods that rely on certain fracture mechanic considerations.

The *en echelon* segments are approximately flat on the fringe of joint C and are not divided into multiple smaller cracks. Therefore, the actual fracture area is given by

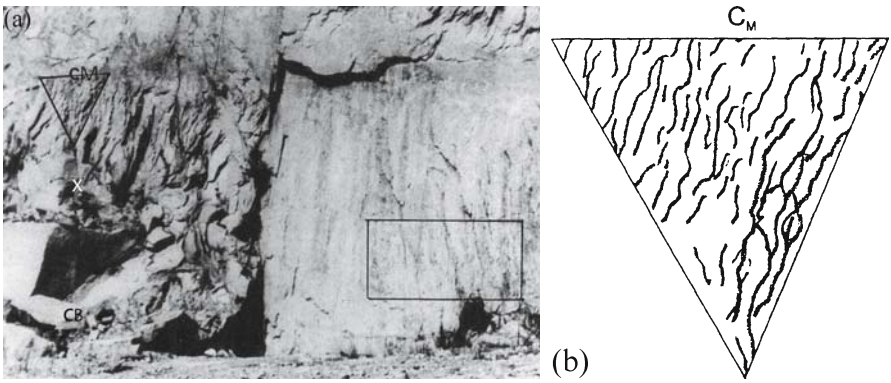

Fig. 4.37. Joints *A* and *C* from the Mrákotin quarry (Fig. 4.10). **a** The "triangle" within the hackle fringe of joint *A* (left), where c_M is on the mirror boundary, and *X* is the most distant point on the lower fringe, at a continuation of the triangle, and *CB* is remote from *x*. The "rectangle" within the *en echelon* fringe of joint *C* (right). **b** An expansion of the triangle, showing the drawn traces of flake boundaries

the sum of the measured, revealed segment areas plus the sum of the estimated underlying, hidden surfaces due to shingling. The number of the hidden parts equals that of the segments, and they are approximately the same for all the observed segments of similar size, which maintain the same twist angle.

The fracture surface is however considerably more complex in the hackle-fringe of joint A. A superposition in an *en echelon* fringe involves the shingling of two adjacent segments, whereas in a hackle-fringe, several (from two to five) small hackle-like flakes often superpose a single "large hackle" (Fig. 4.11a). Furthermore, in this flaky texture, the multi-surfaces that often deviate from planarity overlap each other on a given nominal area such that the actual crack area in the hackle-fringe is a greater sum than the shingling surfaces.

The estimation of the difference between the ratios of the hidden surface area (HA) divided by the revealed surface area (RA) in the two fringes is presented below. We recognize that the difference in the nature of the steps between adjacent segments is different in the two fringes. The step areas are similar for all the adjacent segments in the *en echelon* fringe, whereas in the hackle-fringe, some steps are much larger than others. However, for the sake of simplicity we concentrate on the fracture areas of segments and hackles and do not enter the contribution of the steps and secondary segmentation into our calculation, which are far smaller than the segments. This would reduce the accuracy of our measurements by about 10%.

4.10.2
Estimation of the Fracture Areas in the Fringes of Joints A and C

The *en echelon* fringe on joint C. The exposure of the fringe of joint C is not of a uniform quality throughout its entirety. Therefore we selected a representative area of a rectangle shape for the detailed study. The "rectangle" is 8 m^2 on which 19 ±1 m fracture length of *en echelon* segments were measured (Fig. 4.37a). The rectangle was selected as a representative of the fringe, because:

1. This is a nominal fringe area on which the distribution of fracture length per area is relatively large compared to other fringe areas of this joint.
2. The appearance of fractures is clear, rendering them to be measurable with a reasonable confidence.
3. The rectangle is located at a far end of the fringe, at a relatively long distance from the mirror boundary, such that it fits our "assumption" (see below).

The total fracture area in the rectangle consists of the revealed (nominal) area plus the hidden area. The hidden area between two neighboring segments is not known. In two locations, the maximum superposition at the bottom of the fringe is measured to be (0.2 ±0.1 m) (looking upward towards the mirror). However, this superposition does not necessarily represent the hidden area throughout the various segments, because there is no certainty that the same relative superposition is maintained along the segments. *En echelon* segmentation forms by mixed mode I + III (Sect. 1.1.3). Mode III contributes to tearing the rock in a scissors-like operation. This requires that shingling is zero at the segmentation initiation and the hidden area is increased gradually, stepwise or otherwise. Our "assumption" is that there is a linear increase in the hidden area with distance from the location of superposition initiation (O in Fig. 4.38a).

At the end of the *en echelon* fringe, the average overlap of two adjacent segments (AB) is 0.2 ±0.1 m. Therefore, the angle $\varphi = 1.2 \pm 0.6°$ (Fig. 4.38a, see also difference between l and li). The hidden area (HA_E) is produced by two adjacent segments along the width of the rectangle, and is given by

$$HA_E = S_{ABCD} = S_{ABO} - S_{CDO} = \frac{1}{2}(l^2 - l_i^2)\sin 2\varphi \tag{4.2}$$

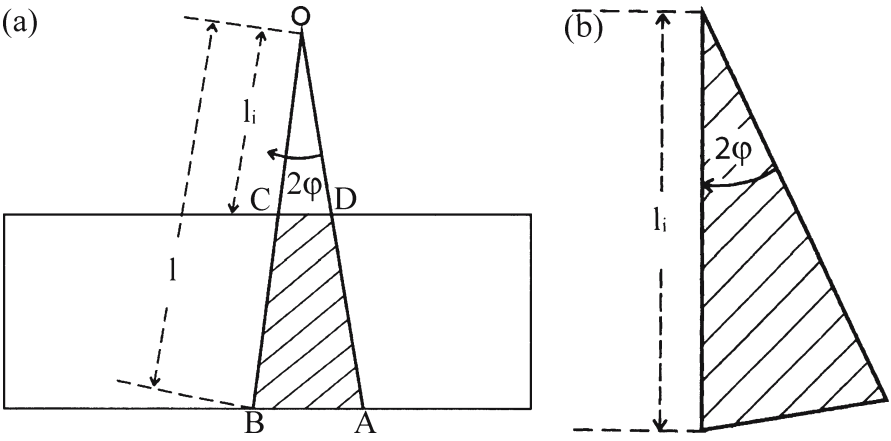

Fig. 4.38. Diagrams for calculating crack areas in fringes. **a** A schematic picture of the overlap development from the location of superposition initiation *O* on the rectangle in Fig. 4.37a. *AB:* The amount of overlap at the end of the rectangle. 2φ is the opening angle of overlap (exaggerated); $l = OB$; $l_1 = OC$; *dashed area*: Overlap inside rectangle; $\varphi = 1.2°$; therefore, $\sin \varphi/2 = 1/2 \times AB/l = 1/2 \times 0.2/4.8 = 0.0208$. **b** Schematic picture of overlap of a single flake. l_i: Length of flake (sub orthogonal to mirror boundary) inside the hackle triangle. *Dashed area* designates overlap = *HPHi*; 2φ is the opening angle (exaggerated). $HPHi = 1/2 l_i \sin 2\varphi$ [area of triangle = 1/2base × height = $1/2(2l_i \sin \varphi(l_i \cos \varphi))$]

Accordingly, $HA_E = 1/2\,(4.8^2 - 2.8^2)\sin 2.4° = 0.32 \pm 0.16$ m^2. The hidden area per 1 meter segment boundary length is therefore 0.16 ± 0.08 m^2 m^{-1}. The revealed area (RA_E) of the rectangle is 8 m^2, and the total segment boundary length in the rectangle is 19 ± 1 m. Hence, the total hidden area is $2 \times 0.16 \times 19 = 6.08$ m^2 ± 3.00 m^2 within the nominal area (the factor of 2 comes from the mirror image to the fracture on its other side that was lost by quarrying) and the ratios of the hidden surface area (HA_E) divided by the revealed surface area (RA_E) is: $u_E = 0.76 \pm 0.4$.

The Hackle fringe on joint A. The "triangle" was selected as a representative of the fringe, because it contains a fairly uniform and clear fracture distribution, rendering them to be measurable with a reasonable confidence. Note that the base of the triangle is on the mirror boundary (Fig. 4.37a). In analyzing the "triangle" we use a similar approach to that applied for the "rectangle" in that we assume that each flake boundary (equivalent to segment boundary) overlaps its neighbor by the same angle as that of the *en echelon* segments, i.e., $\varphi = 1.2 \pm 0.6°$ (Fig. 4.38b). Table 4.8 summarizes the measurements and calculations of the flake boundaries across the triangle (Fig. 4.37b). Fractures (flake boundaries) l_i are measured along their trends sub orthogonal to the mirror boundary. These measurements do not include flake boundaries that curve into orientations that form angles greater than 45° with these trends. Accordingly, the total hidden area is

$$HA_H = \frac{1}{2}\sin 2\varphi \sum_i S_i l_i^2 \tag{4.3}$$

Accordingly, (see Table 4.7 for the calculation of $\sum_i S_i l_i^2$)

$$\frac{1}{2}\sin 2.4° \times 16.92 = 0.35 \text{ m}^2 \pm 0.17 \text{ m}^2$$

The revealed area (RA_H) of the triangle is ~1.86 m^2; hence the ratio of hidden area to the revealed area in the triangle, $u_H = 2HA_H / RA_H = 0.38 \pm 0.2$.

For a fracture growing in tension under a constant load, the energy release rate G is defined as the elastic energy (per unit width) released from the field per unit crack

Table 4.8. Flake boundaries and hidden area in the triangle of joint *A*

Number of cracks n_i	Max. length l_i in Fig. 4.8b (mm)	Flake length l_i real (m)	$n_i l_i$ (m)	$n l_i^2$ (m^2)
18	10	0.142	2.556	0.363
27	20	0.284	7.668	2.178
4	30	0.426	1.704	0.726
3	40	0.568	1.704	0.968
2	50	0.710	1.420	1.008
2	60	0.852	1.704	1.452
3	130	1.846	5.538	10.223
Sum			22.290	16.918

length (Sect. 1.3.3.5). G is usually proportional to $\sigma^2 c$ where σ is the stress field value and c is the crack length: $G = n\sigma^2 c$. On the other hand, by the Griffith criterion, when the crack becomes critical, i.e., for $c = c_{cr}$ (at the critical flaw, Fig. 2.1a), the energy release rate is equal to 2Γ, where Γ is the energy per unit area, $2\Gamma = n\sigma^2 c_{cr}$. Beyond c_{cr}, the excess energy released per unit crack length is therefore $n\sigma^2(c - c_{cr})$. This energy is manifested either as new created area (as in the hackle and bifurcation zones, and to a lesser extent in the mist zone), or as kinetic energy, heat, deformation, radiation, etc.

We assume that the linear relationship between G and c continues throughout the fracture length. Therefore, if the fracture had bifurcated, at say, c_B (an imaginary point that should be further away, beneath point X (Fig. 4.37a), G there would have to be close to twice that of G at c_M (Beauchamp 1995) (to create twice the fracture area, provided that the kinetic energy per unit crack length changes very little at the bifurcation); then we can estimate the maximal additional (hidden) area ratio as a function of crack length, c, to be $\Delta = (c - c_M) / (c_B - c_M)$, where c_M is on the mirror boundary (Fig. 4.37a). In the fringe of joint A, the most distant point, which can be observed on the triangle (point X) is at a distance of 5.20 m from the origin of the crack, and it is clear that no bifurcation has occurred down to this point. Therefore, $\Delta \le (c - c_M) / (X - c_M)$. At the hackle region at the center of the triangle $c \sim 3.06$ m, which limits the hidden area ratio u_H (see below) at this point to be less than $(3.06 - 1.65) / (5.20 - 1.65) = 0.4$.

4.10.3
A Comparison between the Fringes of Joint C and Joint A

The part of the energy release rate, which is used to create the overlapping area is $G - 2\Gamma - qc - p$, where qc is the kinetic energy per unit crack length (q is proportional to v^2, where v is the crack speed). For simplicity, we neglect the plastic energy, p. At c_M, $G(c_M) = 2\gamma + qc_M$. Therefore, for $c_M < c < c_B$ we get that the ratio of the additional area to nominal area is proportional to $c / c_M - 1 = (\eta)$.

In order to compare hidden area ratios between the *en echelon* and the hackle fringes, they should be both at the same scaled distance from the respective crack origins. Since they are situated at different distances, the following procedure is conducted. For the *en echelon* segments in the rectangle, its average distance from the origin is 5.88 m and the distance from the origin to the mirror boundary is $c_M = 0.94$ m; therefore, $\eta_E = 5.88 / 0.94 - 1 = 5.26$. For the hackles in the triangle, a similar calculation yields $\eta_H = 3.06 / 1.65 - 1 = 0.85$. If it is assumed that the hidden area is linear with crack length, the hidden area should be normalized by division by η for an appropriate comparison. We therefore compare the ratio of hidden area to revealed area at the "same distance" for both fringes. For the hackle fringe we have $r_H = u_H / \eta_H = 0.38 / 0.85 = 0.45$, while for the *en echelon* fringe it is $r_E = u_E / \eta_E = 0.76 / 5.26 = 0.14$, which is 3.14 times smaller. In summary, the normalized (real) ratios of hidden area divided by revealed area on the fringes of joints A and C are respectively, $r_H / r_E = 0.44 / 0.14 = 3.14$.

4.10.4
How was Energy Released Differently in the Two Fringes?

It turned out that energy release in the actual formation of new fracture area (per a given nominal fringe area) is substantially greater in the hackle-fringe than in an *en echelon* one.

What is the reason for this? We follow the principle that $G = G_I + G_{II} + G_{III}$ (Lawn 1993, Eq. 2.18) and we neglect G_{II} because of its minor importance in relation to fracture conditions in the two fringes under consideration. The G relationship then becomes

$$G_{IH} = G_{IE} + G_{IIIE} \tag{4.4}$$

That is, the energy release rate by mode I loading in the hackle fringe equals the energy release rate by modes I + III loading in the *en echelon* fringe. How do we explain the reduction of the "effective" G to produce new fracture area in the transition from the hackle fringe to the *en echelon* one?

The state of stress influences the size of the plastic zone, and shear stresses promote the enlargement of this zone (Hahn and Rosenfield 1965). More specifically, the plastic zone associated with the mode III loading is several times larger than that for mode I for similar materials and at the same stress intensity values (Tschegg 1983). Plastic deformation is associated with the loss of considerable energy into heat. The latter energy transition may reach extreme values at rapid fracture velocities (up to 60% or even 90% of G in PMMA and some metals) (Döll 1976), but even at low crack velocities heat losses may be significant under induced plastic conditions. Hence, the transformation of some G_I into G_{III} in the *en echelon* fringe involves an increase in plastic deformation and subsequent heat loss, which is not used in the creation of new fracture surfaces.

4.10.5 Summary

The distinction between fringes of *en echelon* segmentation and hackles on joint surfaces is important because they reflect different fracture conditions. It was found that the normalized (real) ratios of hidden area divided by revealed area on the hackle and *en echelon* fringes of joints A and C are respectively, $r_H = 0.44$ and $r_E = 0.14$, hence, $r_H / r_E = 0.314$. This shows that considerably more new area is formed in hackle zones than in *en echelon* zones per any given nominal area of the fringe. Possibly, the transformation of some G_I to G_{III} in the transition from hackle to *en echelon* fringe involves an increase in heat loss, which is the portion of energy not used in the creation of new fracture surfaces.

4.11 The Index of Hackle Raggedness (*IHR*) on Joint-Fringes of the Mrákotin Joint Set

This section concentrates quantitatively on the fractographic differences between the fringes of joints A, C and F (Sect. 4.4.3), citing Bahat et al. (2004). It has been shown that considerably more new area is formed in hackle sections than in *en echelon* sections per given nominal area of fringe (Sect. 4.9). Since the crack area is a fundamental parameter in fracture physics, we seek to devise a method of correlating changes in crack area by tectonofractographic techniques, i.e., by the characterization of the secondary fracture on joint fringes. The two distinct morphologies manifested by the *en echelon* and hackle fringes (Fig. 2.1) represent contrasted fracture mechanisms,

reflecting different local stress conditions (Sect. 4.8.4). We start dealing with this relationship by formulating a series of criteria for estimating the value of the Index of Hackle Raggedness (*IHR*) on a given fringe, based on geometric distinction of crack features between the hackle and *en echelon* end members in the fringe. We then apply it to joints A, C and F from the Mrákotin set, summarizing the results in Table 4.9.

4.11.1
Criteria of *IHR* and Application to the Mrákotin Joint Set

Before getting into the actual definition and procedure, one has to consider three limitations that qualify the rules. First, there is a need to establish which of the seven key criteria presented below is applicable to a given outcrop. Nature is quite selective in revealing good fracture markings and very often only small parts of the ideal fractography (Fig. 2.1a,b) is exposed. Occasionally, only one fringe is well displayed (the upper or lower). Therefore, in many outcrops only a certain number of these criteria would be useful, according to the quality of the crack exposure. Second, it is required to apply independent estimations of the *IHR*, ranging from 1 to 10 for each of the above criteria. Third, since the *IHR* is new (even for the engineering literature), lack of previous experience justifies at this stage the assumption of equal weight for the various criteria. Therefore, the *IHR* for a given joint will be the mean of *IHR* values from all measurable parameters (criterion 3 is an exception, where the angle of "triangularity" $\sin\alpha$ is converted to *IHR* by multiplication by 10). The total *IHR* error per joint, consisting mainly of measurement errors is thought to be ±0.7.

4.11.1.1
Length Variability

In many fringes *en echelon* segments maintain uniform lengths, if microcracks in root zones (Bankwitz 1966) and elsewhere on the segments are excluded. Hackles on the other hand show great length variability even among neighbor cracks. Hence, increasing deviation of length ratios (of maximum to minimum length in a given fringe) from length uniformity (Fig. 2.34) produces an enlargement of *IHR*. The length ratios of fringe-cracks for joints A, C and F are 6, 1 and 3, corresponding to the respective *IHR*.

4.11.1.2
Rectangularity

En echelon segments approximate rectangular shapes whose aspect ratios can be readily measured. Hackles on the other hand deviate considerably from such shapes. Measurement of the deviations from straight lines (*DSL*) along the rectangle length and width can provide information regarding the departure of the fringe crack from its rectangular shape. We use a set of profiles that resembles the scale of fracture-surface roughness constructed by Barton and Choubey (1977), which shows a gradual *DSL* ranging from 0 to 10 (Fig. 4.39). The *DSL* value is the mean of combined deviations along the length and width of three fringe-cracks, assessed manually. Thus, the *DSL* values of A, C and F are 6.5, 2.5 and 3.5, respectively.

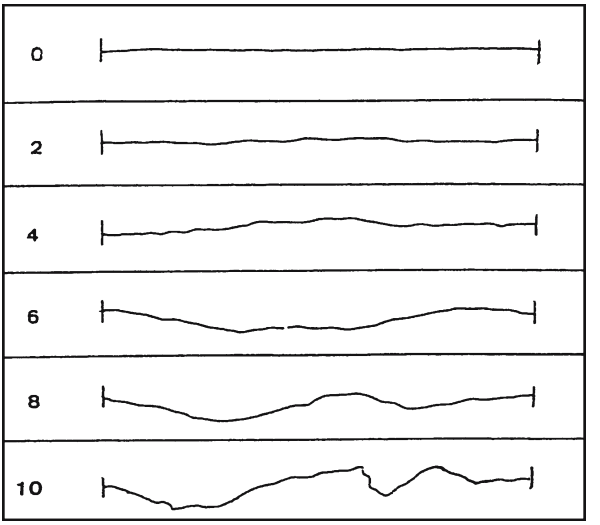

Fig. 4.39.
A set of profiles that show gradual deviations from straight lines on a scale ranging from 0 to 10 (modified from Barton and Choubey 1977)

4.11.1.3
Fringe Width

The tendency of *en echelon* fringes (to be distinguished from individual segments) to maintain uniform widths, compared to non-uniform widths of hackle fringes (Fig. 2.34) has been repeatedly observed (Bahat 1998b). This is also demonstrated by the "quasi-triangular" shapes of the two fringes of joint F (Fig. 4.12c) compared to the approximate parallelism of the mirror and fringe boundaries at the lower side of joint C (Fig. 4.10c). A measure of deviation from a uniform fringe width is given by the angle α that increases with the "triangularity" of the fringe. Unfortunately, this parameter cannot be measured with high confidence for joint A because only certain parts of the fringe lengths of joint A are revealed (sufficient for the study of criteria 1–5 but not for this parameter) so that an appropriate index cannot be established for the latter joint. Accordingly, the $\sin\alpha$ values for joints C and F were estimated to be 0.17 and 0.34 ($\alpha = 10 \pm 2°$ and $20 \pm 2°$), respectively, and the corresponding *IHR* for these joints are 1.7 and 3.4. When clear triangularity is recognized this method would be more reliable than the one given in Sect. 4.11.1.1.

4.11.1.4
Fringe Thickness

En echelon segments have approximately (quasi two-dimensional) planar surfaces and display uniform thickness along their lengths. On the other hand, hackles consist of multi-fracture surfaces superposing each other not uniformly along the crack lengths, often leading to the increase in thickness of individual cracks and in the fringe thickness (*FT*) with distance from the mirror-fringe boundary. Therefore, *FT* is normally maximum at the far end of the fringe and minimum close to the mirror boundary. *FT* is abruptly reduced when fracture branching occurs, but there is not clear evidence that such a process actually took place in this outcrop. The change in *FT* often renders

the hackle-fringe to look quasi three-dimensional (Fig. 4.11c), such that *IHR* increases with the ratio of maximum / minimum *FT*. Changes in thickness were measured on an enlarged profile of a photograph of joint A. These ratios for A and C were found to be 6.5 and 1 ±1, respectively (no measurements for joint F are available).

4.11.1.5 *Fringe Angularity*

There are indications that the angle ϕ that the fringe (as a set of cracks, rather than an individual one) forms with the mirror, increases with the "fracture-dynamics" of the process, i.e., roughly corresponding to the increase in fracture velocity. Bahat and Rabinovitch (2000) found that in the same rock (chalk) the ϕ varies from 0° to 30 ±5° on a natural joint and from 30 ±8° to 50 ±8° on an artificial fracture along a road cut (that was formed by explosion). It is assumed that this relationship may change significantly from rock to rock (see more in Bankwitz and Bankwitz 2004 and Sect. 4.4.4). It was found that $\phi = 5 \pm 2°$ for joint A, while $\phi = 0–1°$ for joint C (it could not be measured for joint F). We therefore assign *IHR* values of 5 and 1 ±1 to joints A and C, respectively.

4.11.1.6 *Crack Dipping*

Deviation of individual fringe-cracks from a uniform dip also increases the *IHR*. Individual *en echelon* segments in a fringe commonly dip in the same direction of the mirror, i.e., the "normal direction", forming zero to small $+\phi$ angles. However, occasionally, different hackle flakes may also dip into the mirror plane, i.e., in the "opposite direction", forming $-\phi$. For determining the *IHR* value we combine the maxima of $+\phi$ with those of $-\phi$ for different cracks on the same fringe to a single angle ϕ_f representing a fringe. Our results show that the ϕ_f values for joints A, C and F are 10 ±5° ($+\phi = 7 \pm 3°$ plus $-\phi = 3 \pm 2°$), ~0.5°and 2–3°, respectively. Accordingly, the corresponding *IHR* are 10, 1 and 2–3.

Table 4.9.
Summary of IHR indices for joints A, C and F

Criterion number	Criterion	A	C	F
1	Length variability	6	1	3
2	Rectangularity	6.5	2.5	3.5
3	Fringe width	n.m.	1.7	3.4
4	Fringe thickness	6.5	0.5	n.m
5	Fringe angularity	5	0.5	n.m
6	Crack dipping	10	0.5	2.5
7	Secondary mirror	n.m.	n.m.	n.m.
Sum		34	6.7	12.4
IHR(mean)		6.8	1.1	3.1

n.m.: not measured.

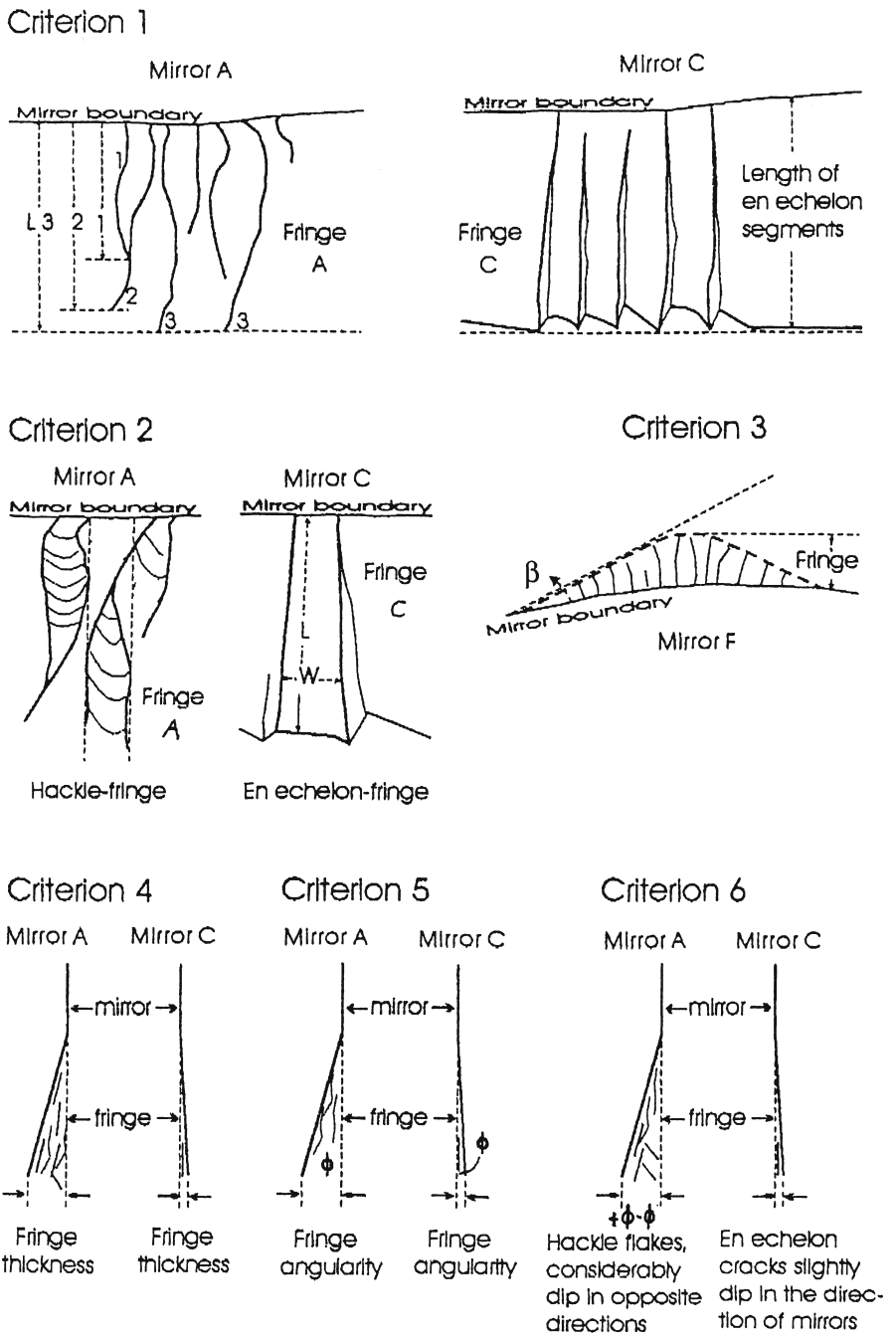

Fig. 4.40. A diagrammatic summary of six criteria for estimating the value of the index of hackle raggedness on joint fringes (see text for explanation)

4.11.1.7
Secondary Mirror

Gross deviations from "normal fringe morphologies" require special attention. They are very rare on *en echelon* fringes and are rare on hackle fringes. Quite intriguing is the rarity of "secondary mirrors" in natural exposures (Fig. 4.11a–c), compared to their frequent appearance in dynamically fractured glass (e.g., Fig. 2.30c). It is presently impossible to construct a scale for secondary mirrors. Quantification of this parameter remains a challenge for future study. Qualitatively, however, this distinction supports the relatively high *IHR* value assigned to joint A that exhibits a secondary mirror.

4.11.2
Discussion

The seven criteria. Criteria 1–6 are summarized diagrammatically in Fig. 4.40. Note that criteria (1–3) relate to changes observed parallel to the mirror, while criteria (4–6) concern parameters perpendicular to the mirror. Criterion 7 requires measurements both parallel and perpendicular to the mirror. We did not use deviations of fringe cracks from a uniform strike as an *IHR* criterion, because we unexpectedly found it not to be diagnostic. The gap between the top value of the scale 10 and the value 6.8 found for joint A probably suggests that joint A was not formed by the most dynamic conditions, and the 10 *IHR* value should be obtained under more extreme dynamic conditions, such as intense fracture of glass would occur in the laboratory (e.g., Fig. 2.30, see also Bahat et al. 1982, Fig. 2).

4.11.3
Summary

A method of quantifying the "spectrum" of secondary fractures on joint fringes ranging from *en echelon* segments to hackle cracks is presented. The method is based on a set of seven criteria that enable one to place every fringe on an "index of hackle raggedness" (*IHR*) along a scale from 0 to 10. This method is applied to the "Mrákotin joint set" from a granite quarry in the Czech Republic part of the South Bohemian Pluton. The results show an *IHR* range between 1.2 ±0.7 and 6.8 ±0.7. The gap that exists between 10, the top value of the scale and 6.8 the maximum obtained value, suggests that the joint for which *IHR* = 6.8 was not formed by the most dynamic conditions, and the 10 *IHR* value should be obtained under more extreme dynamic conditions.

4.12
A Method of Drilling in situ Fracture from the Rock

An important structural problem is the determination of shear offsets along joints, which often are concealed in an outcrop scale, particularly when offsets are limited to short distances (millimeter scale). Thus, transitions from joints to faults are often obscured. This enigmatic situation may be fully or partly resolved by resorting to petrographic methods. A detailed study of millimeter and sub-millimeter scales of past

natural offsets along the fracture requires the assurance that in situ conditions are being maintained in the laboratory.

The objectives in sample preparation are to keep intact both margins of the examined joints following their removal from the outcrop so that the original aperture (or thickness, Fig. 2.8a) would be examined. The sample preparation process consists of several stages:

1. Coat the trace of the fracture with gray epoxy.
2. Inject red epoxy into the aperture to fill the space and stick to the two margins of the fracture.
3. Core drill samples.
4. Vacuum imbed selected samples with blue epoxy.
5. Prepare thin sections.

The "epoxy procedure" consisting of different epoxy colors helps to follow the timing of shear offset in the thin sections.

A 25 gauge 5/8" syringe needle is inserted into the selected fracture (Fig. 4.17c). Then, a Hardman brand double-bubble epoxy is smeared on the front of the fracture. This secures the needle in place, and prevents the forthcoming red epoxy from flowing out of the front of the fracture upon injection. Also, it affixes the two margins of the fracture at the rock surface together to maintain it in the original juxtaposition after sample removal. This epoxy sets in about 5 min.

The next step is to prepare the red epoxy mixture for injection into the fracture. Twenty drops of toluene are mixed into 4 pouches (totaling 8 g) of Hardman epoxy, to which fifteen drops of Morefast brand red epoxy die are added. All of this mixture is stirred for 1.5 min. The epoxy mixture is poured into a 5 cc Luerloc syringe or a 1 cc slip-tip syringe with their plunger removed. The plunger is put back in, and the syringe is then attached to the needle that had previously been imbedded in the rock. The plunger is then depressed, causing the red epoxy to flow into the fracture. Because of the tightness of the aperture, it is impossible in some fractures to obtain penetration of large quantities of injected epoxy. However, even little penetration may occasionally be enough to secure original juxtaposition in a few cylinders. Handling time for the red epoxy mixture is 10–15 minutes, and the setting time, 1 hour.

Electromagnetic Radiation Induced in Fractured Materials

The key to a successful application of electromagnetic radiation (EMR) to rock fracture investigation is a good understanding of the basic physics of EMR emission. Such an understanding is expected to provide useful universal tools or "fingerprints" of the process involved. In this chapter we describe our efforts in the last decade investigating EMR in the radio frequency range (1 kHz to 50 MHz, Fig. 5.1) emitted by fracture. These investigations were conducted in three consecutive principal stages:

1. "Small-scale" laboratory investigations, which consisted of two sub-stages, i.e., quasi-static and dynamic. The aim of this stage was to derive the basic physical principles operating behind EMR emission from microcracking excited by stiff compression and tension and to find the similarities and dissimilarities between EMR emissions from different dynamical and quasi-static cracking.
2. "Medium-scale" pilot investigations carried out both in open quarries during blasting and in underground mines prior to rock bursts and rock and gas outburst. The goal of this stage was to understand the differences in EMR during "low scale" and

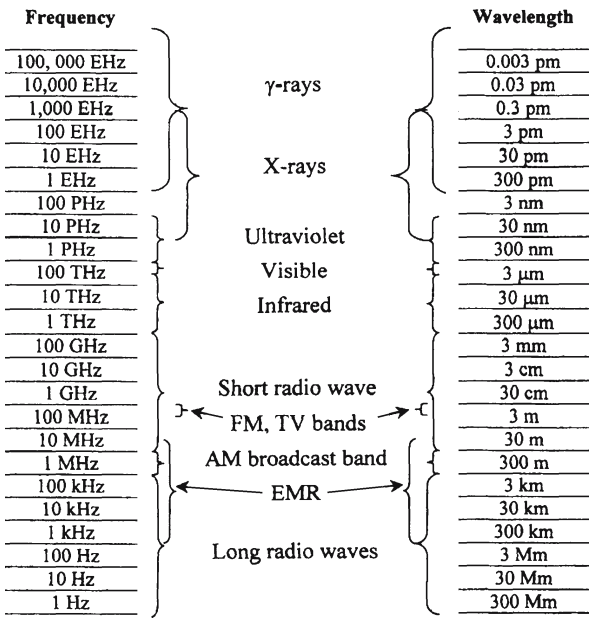

Fig. 5.1. Electromagnetic wave spectrum (E (Exa): 10^{18}, P (Peta): 10^{15}, T (Tera): 10^{12}, G (Giga): 10^{9}, M (Mega): 10^{6}, k (kilo): 10^{3}, c (centi): 10^{-2}, m (milli): 10^{-3}, μ (micro): 10^{-6}, n (nano): 10^{-9}, p (pico): 10^{-12} (Rabinovitch et al. 2000c)

"medium scale" cracking and thereby to pave the way for planning "large-scale" investigations.

3. The "large-scale" stage is meant to study EMR behavior during earthquake nucleation. Since earthquake monitoring and prediction by seismological techniques is "still in its infancy" (Wyss 2001), the possible addition of more sophisticated EMR methods should be welcome. In particular, the EMR method measures micro-cracking, i.e., the initial process in an earthquake, a process occurring much *earlier* than the actual earth movements; the study of which might thus be beneficial for earthquake forecasting.

Accordingly, this chapter *(a)* summarizes our investigations in the small and medium scales, *(b)* reports some improvements suggested thereby for monitoring and prediction in the mining industry and *(c)* points out guidelines for large-scale experiments (earthquake forecasts) based on our acquired theoretical understanding and the "fingerprints" accumulated from tensile and shear experiments.

We hope that this chapter, by describing the current state of the art, could be interesting not only to EMR specialists, but also to rock physicists, geoscientists, and mining engineers who always seek new methods for multi-scale failure investigation.

We begin the chapter with a review of previous EMR investigations (Sect. 5.1), then present our new EMR model (Sect. 5.2) and describe in detail its experimental verification (Sect. 5.3). A comparison of this model with previous ones is presented in Sect. 5.4. Individual EMR pulses and their classifications are given in Sect. 5.5 followed by Sect. 5.6, where influence of the elastic properties of rocks on EMR activity is analyzed. A novel EMR phenomenon, polarization induced in materials during percussion drilling, is examined in Sect. 5.7. EMR effects induced by blasting in open quarries and appearing prior to volcanic eruptions and earthquakes are considered in Sect. 5.8, while universal EMR features are discussed in Sect. 5.9. In Sect. 5.10, which we believe would be interesting mostly for mining engineers, we focus on underground EMR observations prior to rock burst and gas outburst deriving criteria of their forecasting. Finally, a brief summary of the whole chapter is presented.

5.1 History of EMR Research

Emitted EMR from fractures was firstly observed by Stepanov (Urusovskaja 1969). He loaded samples of KCl and detected an appearance of electromagnetic pulses during specimen failure. At that period, the EMR did not gather any implementations, and investigations of this phenomenon were continued basically on samples of alkaline halide crystals (Nabaro 1967; Kornfel'd 1971, 1977; Gol'd et al. 1975; Finkel et al. 1975; Golovin and Shibkov 1986a,b). It was observed that the creation of new microcracks stimulated excitation of EMR (Gol'd et al. 1975; Golovin and Shibkov 1986a,b). These studies were followed by numerous ones that investigated various EMR aspects. The EMR phenomenon was measured for fracture in different materials, including metals and alloys (Misra 1975; Jagasivamani and Iyer 1988), single crystals (Gol'd et al. 1975; Khatiashvili 1984), rocks (Nitsan 1977; Warwick et al. 1982; Ogawa et al. 1985; O'Keefe and Thiel 1995; Rabinovitch et al. 1995, 1996, 1998) and ice (Fifolt et al. 1993; Petrenko 1993).

EMR investigations during rock specimen compression, which in the majority of cases were combined by acoustic emission (AE) measurements (Nitsan 1977; Goncharov

et al. 1980; Warwick et al. 1982; Sobolev et al. 1982; Ogawa et al. 1985; Cress et al. 1987; Yamada et al. 1989; Frid 1990), showed that EMR was indeed detected at the same moment that microcracks were formed. EMR features on different scale levels (earthquake (EQ), rock burst (RB) and rock sample fracture) were studied by Khatiashvili (1984). In all of these cases, EMR anomalies were observed preceding the final rock failure.

According to the theory of material destruction (Zurkov et al. 1969; Regel' et al. 1972; Kuksenko and Mansurov (1986); Kuksenko et al. 1985, 1987; Petrov and Gorobetz 1987; Gueguen and Palciauskas 1994), the process of rock fracturing consists of two stages: The first one consists of an accumulation of microcracks, and the second consists of microcrack clustering and final failure (Sect. 1.2.3.3). Rock destruction processes on all scale levels (from rock samples up to crust fracture) adhere to this "scheme" (Kuksenko et al. 1987; Mansurov 1994). As hypothesized by Gershenzon et al. (1987), EMR is initiated in the first stage, appears before final failure and could be an EQ forecast indicator.

Large-scale EMR studies prior to rock burst (RB) in mines are also registered. Nesbitt and Austin (1988) registered EMR in a gold mine (2.5 km depth). Frid (1997a,b, 2000, 2001) observed EMR anomalies before RBs and gas outbursts. Vozoff and Frid (2001) measured EMR anomalies prior to a roof fall in a coal mine. Sakai et al. (1992); Tomizawa et al. (1994); Tomizawa and Yamada (1995); Rabinovitch et al. (2002a) investigated EMR induced by explosions.

During the seventies and eighties, the interest in EMR emanating from failure of rocks was renewed in connection with the problem of EQ prediction. Numerous investigations (King 1983; Sadovskii et al. 1979; Gokhberg et al. 1979, 1982, 1985; Morgunov 1985; Gokhberg et al. 1986; Gershenzon et al. 1987; Yoshino et al. 1993; Yoshino and Tomizawa 1989), a significant part of which was carried out in Japan and in the former USSR, showed that the magnitude of EMR sharply increased several hours or even days before EQ and quickly decreased at the moment of EQ or directly before it. The magnitude of the detected EMR anomalies was of up to 10–15 dB over the usual noise level. Thus, EMR is associated with fractures on multi-scale lengths and is connected with various applications.

Several atomic-scale models have hitherto been suggested to explain the EMR phenomenon. All of these models were qualitative, and efforts to use EMR quantitatively were unsuccessful, due to the lack of a detailed understanding of the EMR phenomenon (King 1983; Rabinovitch et al. 1998). Until quite recently, the physical mechanism of EMR was unknown (Freund 2000, 2002). An essential requirement for this type of knowledge is a careful laboratory investigation of rock failure. Such an investigation has been carried out by the group of Rabinovitch et al. (1995, 1996, 1998, 1999b, 2000a,b, 2002a,b, 2003a,b).

5.2 Foundations of EMR Model

A general shape of an EMR pulse induced during fracture experiments is shown in Fig. 5.2.

It can be characterized by the following general relationship (Rabinovitch et al. 1998):

$$A = \begin{cases} A_0 \sin(\omega(t-t_0))\left(1-\exp\left(-\dfrac{t-t_0}{\tau}\right)\right), & t < T \\ A_0 \sin(\omega(t-t_0))\exp\left(-\dfrac{t-T}{\tau}\right)\left(1-\exp\left(-\dfrac{T-t_0}{\tau}\right)\right), & t \geq T \end{cases} \tag{5.1}$$

where t is the time, t_0 is the time from the origin up to the pulse beginning and T is the time from the origin up to the EMR pulse envelope maximum. Thus, $T' = T - t_0$ is the time interval to reach pulse maximum; τ is the rise time and the fall time (RFT), which turn out to be the same; A_0 is the pulse amplitude and ω is the frequency. The signal's general shape including its envelope, frequency and duration can be obtained by our basic (see below) theory, while the parameters themselves can be derived by least squares fitting of the experimental results (Rabinovitch et al. 1998, see Fig. 5.16).

Four basic elements of a physical model, which would result in such simple relationships, are (Frid et al. 2003):

1. Time of growth (Rabinovitch et al. 1998): The pulse amplitude, A, increases as long as the crack continues to grow, since new atomic bonds are severed and their contribution is added to the EMR. When the crack halts, as it does if created under a compressive load, the pulse amplitude starts to decay. The time from the start of the pulse up to its maximum, T', is proportional to the number of severed atomic bonds and thus to the crack length ℓ (the crack velocity v_{cr} is almost constant).

$$T' \sim \frac{\ell}{v_{cr}} \tag{5.2}$$

2. Dynamics of growth and decay of the amplitude: In the time increment, dt, 'A' decreases by dissipation (to phonons, see Sect. 5.3.7) to

$$A(t)\left(1-\frac{\mathrm{d}t}{\tau}\right)$$

but it is "replenished" by a term proportional to the number of severed bonds, $\alpha \mathrm{d}x$, where dx is the length increment of the crack in the interval dt (d$x = v_{cr}$dt) and α is a

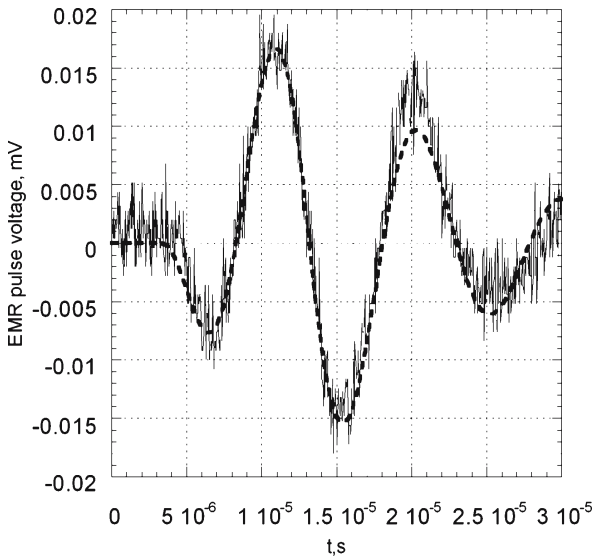

Fig. 5.2. An experimental pulse shape (output voltage against time) and a numerical fit according to Eq. 5.1 (*dashed line*) (Rabinovitch et al. 1998)

coefficient relating the antenna output to dx. α is assumed proportional to the width of the crack, b, (the following calculations assume a constant crack width), to the number of bonds per unit area, to the emittence of a bond, to the solid angle of the crack seen by the antenna and to the latter's conversion factor. It follows that:

$$\frac{\partial A}{\partial t} = -\frac{A}{\tau} + \alpha v_{\mathrm{cr}} \tag{5.3}$$

Hence,

$$A = \alpha v_{\mathrm{cr}} \tau (1 - \mathrm{e}^{-(t-t_0)/\tau}), \qquad t_0 \le t < T\ (= t_0 + T') \tag{5.4}$$

For $t > T$ the crack stops and the amplitude thereafter diminishes resulting in

$$A = A(T)\mathrm{e}^{-(t-T)/\tau}, \qquad t \ge T \tag{5.5}$$

3. Regarding the oscillatory parts of Eq. 5.1, we assume that these EMR waves are created by charge oscillations at both sides of the propagating crack (Fig. 5.3).

   Consider the line of bonds located at the front (tip) of the propagating crack (Fig. 5.3a). These bonds break when the front moves to the next line. Following this

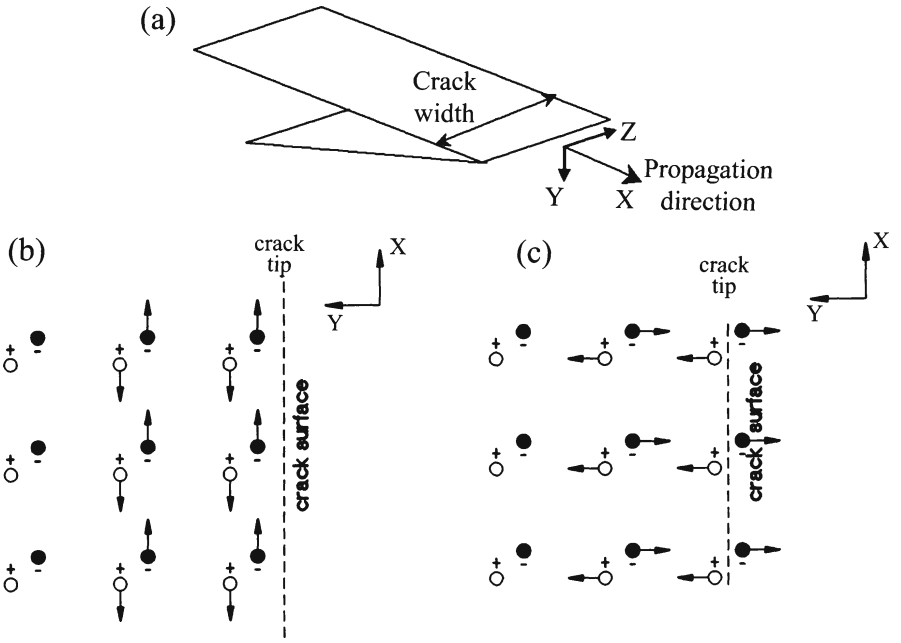

Fig. 5.3. a A schematic picture of crack propagation; **b**, **c** schematic "optical surface wave" at crack surface (a similar wave propagates on the other surface) at a specific time. Crack surface is in the x-z-plane and the crack moves in the x-direction. Note that charge separation can either be longitudinal (**b**) or transverse (**c**) with respect to the surface, with appropriate EMR polarizations. Note also the exponential decay of the wave into the material. Charge separation is oscillatory so that at a later time the dipole directions are reversed (Frid et al. 2003)

break, the atoms on both sides of the bonds are moved to "non equilibrium" positions in relation to their (new) steady state ones and will perform oscillations around them. If each atom (ion) vibrated individually, the situation would resemble the Einstein model of lattice vibrations and the frequency of these oscillations would approach 10^{15} Hz. Since, however, the lines of vibrating atoms move together and are also connected to atoms around them (in the forward direction and also to atoms on their side of the two surfaces newly created by the fracture), the ensuing vibrations are similar to those obtained for the bulk by the Debye model, having much lower frequencies. It is the oscillations stimulated by this process at the new surfaces, which give rise to the EMR, as follows. The positive charges on these surfaces move together in one direction away from the equilibrium plane (one crack side), while the negative charges move in unison in the other direction from the equilibrium plane (the same crack side), and vice versa, retaining an overall charge neutrality throughout. These surface oscillations, similar to "optical" Rayleigh waves, decay exponentially into the bulk (Fig. 5.3b,c) – "surface vibrational optical waves (SVOW)" (e.g., Srivastava 1990), much like "bulk optical (phonon) waves" (e.g., Kittel 1987) observed in vibrating crystals.

4. It has been shown elsewhere (e.g., Srivastava 1990) that surface waves decay in time as a result of an interaction with bulk phonons. We therefore (Rabinovitch et al. 2003a) consider τ to be the relaxation time of such a (Rayleigh-like) surface wave, which interacts with a bulk phonon, leading to the creation of another bulk phonon (a three-phonon process), and use Eq. 13 of King and Sheard 1970) to characterize the process. The rate of occurrence of the process per unit time is given by the golden rule formula (Schiff 1986):

$$P_i^f = \frac{2\pi}{\hbar}\left|\left\langle f\left|H_3\right|i\right\rangle\right|^2 \delta(E_f - E_i)$$

where the initial and the final states are

$$\left|i\right\rangle = \left|n_{\mathrm{R}}, n_{\mathrm{b1}}, n_{\mathrm{b2}}\right\rangle, \left|f\right\rangle = \left|n_{\mathrm{R}} - 1, n_{\mathrm{b1}} - 1, n_{\mathrm{b2}} + 1\right\rangle$$

H_3 is the time dependent anharmonic part of the crystal Hamiltonian, n_{R}, n_{b1} and n_{b2} are the numbers of surface phonons, initial and final bulk phonons, respectively. E_i and E_f are the initial and the final energies of the three-phonon system, so that

$$E_f - E_i = \hbar(\omega_{\mathrm{b2}} - \omega_{\mathrm{R}} - \omega_{\mathrm{b1}})$$

where ω denote the related frequencies. The relaxation time τ, which we identify with the rise and fall time of the EMR pulse, is obtained from the golden rule formula ($1/\tau$ being proportional to the transition probability) using the explicit expression for H_3 (Eq. 6.47 in Srivastava 1990) and the displacement field due to the surface modes written in second quantized notation. Integrating over the states of the initial and final bulk phonons b1 and b2, one obtains (Eq. 8.36, Srivastava 1990)

$$\frac{1}{\tau_{\mathrm{R}}} \propto \frac{\omega_{\mathrm{R}} T^4}{\rho^3 v_{\mathrm{R}}^2} \tag{5.6}$$

where T is the temperature, ρ is the material density, and v_R is the Rayleigh wave velocity. The proportionality coefficient contains data of bulk phonons and of the crystallographic orientation and is considered to be constant for the same material. Note that T is the local temperature at the crack tip. It is much higher than room temperature (Fuller et al. 1975).

In a developing crack, a surface waves propagate along the crack surfaces. Their emitted EMR frequency is the same as that of the oscillating ions of the crack sides (Rabinovitch et al. 1998), ω. Therefore we equate $\omega = \omega_R$.

Several important results can be obtained even from these basic ideas.

1. Equations 5.4 and 5.5 together with oscillations part $\sin \omega(t - t_0)$ immediately lead to the correct empirical shape (5.1).
2. If the half wavelength, $\lambda / 2$, of the surface waves creating the EMR is limited by the crack width b (since at both sides of the crack, atomic movements are restricted), then (Frid et al. 2000; Rabinovitch et al. 2000c)

$$b \approx \frac{\lambda}{2} = \frac{\pi v_R}{\omega} \tag{5.7}$$

3. From Eq. 5.2 and Eq. 5.7,

$$\frac{T'}{\omega} \sim \frac{1}{\pi v_{cr} v_R} S \tag{5.8}$$

where $S = \ell b$ is the crack area. Since T' and ω are measurable quantities (from the pulse shape, using Eq. 5.1), the ratios of the crack surface areas, if not their exact values, can be calculated using Eq. 5.8.
4. Since EMR pulse amplitude A is proportional to α (Eq. 5.4), which was assumed to be proportional to crack width b, it is expected that EMR amplitude should be inversely proportional to the EMR signal frequency $\omega = 2\pi f$.
5. The rise and fall time, τ, is expected to be inversely proportional to the pulse frequency ω (Eq. 5.6).

5.3 EMR Model Verification

5.3.1 Experimental Arrangement

In order to investigate EMR properties through the range of the whole stress strain curve, a triaxial load frame (TerraTek stiff press model FX-S-33090; axial pressure up to 450 MPa; confining pressure up to 70 MPa; stiffness 5×10^9 N m^{-1}) was used (Fig. 5.4).

It is combined with a closed-loop servocontrol (linearity 0.05%), which is used to maintain a constant axial piston rate of displacement. The load was measured with a sensitive load cell (LC-222M, maximum capacity 220 kN, linearity 0.5% full scale). The confining pressure was continually controlled by a clock-type sensor to preserve its

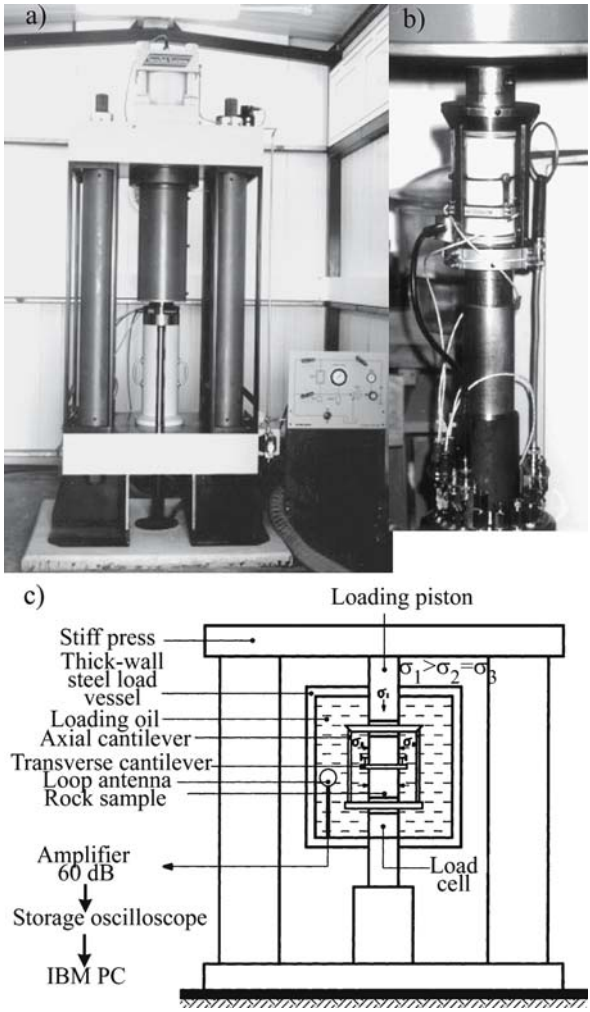

Fig. 5.4.
Compression press: **a** the triaxial load frame, **b** the sample stack, **c** schematic diagram of the EMR experimental arrangement

preset value through volumetric changes of the sample during the loading process. The cantilever set (consisting of axial and lateral detectors; strain range about 10%; linearity 1% full scale) enables us to measure sample strains in three orthogonal directions parallel to the three principal stresses.

A magnetic one-loop antenna (EHFP-30 Near Field Probe set, Electro-Metrics Penril Corporation) 3 cm in diameter was used for the detection of the EMR. It is wound within a balanced Faraday shield, so that its response to external electric fields is negligibly small. A low-noise micro-signal amplifier (Mitek Corporation Ltd, frequency range 10 kHz to 500 MHz, gain 60 ±0.5 dB, noise level 1.4 ±0.1 dB across the entire frequency band) and a Tecktronix TDS 420 digital storage oscilloscope connected by way of a General Purpose Interface bus to an IBM PC completes the detection equipment.

5.3.2 Materials

For our uniaxial and triaxial compression investigation we used the following materials:

1. *Granite.* A large Eilat granite "block" from the Nahal Shelomo area of Sourthen Israel, nearly 3 km from Eilat was used. This granite is gray and consists of K-feldspars (about 40%), quartz (about 35%) albite-oligoclase (about 20%), and biotite (about 3–4%). It is medium to coarse-grained (feldspars and quartz, 2–4 mm; biotite 0.5–1 mm) and non-porphyritic (Bogosh et al. 1997).
2. *Chalk* from the Horsha Formation (Middle Eocene), sampled in the Beer Sheva syncline (Ramat Hovav, about 9 km from Beer Sheva, Israel, Bahat 1991a). Chalk is a pure-white, soft and friable rock consisting of calcitic (nannoplankton) microfossils. The color, purity, texture, cementation and hardness of the rock may vary due to additives such as water, oxides, marl, clay and flint, and by diagenetic and tectonic processes (Mortimore 1990). The strength of chalk under compression depends on the above properties, particularly on the dryness of the sample, and varies from values of ~1 MPa when wet, to some 50 MPa when extremely dry. A strict drying process was therefore applied to the samples, which involved a cycle of heating to 110 °C for 24 hours, and then an immediate transfer to a desiccator to avoid water absorption by the samples. All samples were cut from one chalk layer, with unified co-orientation within the rock, into standard cylinders of 100 mm in length and 53 mm in diameter. The density of all investigated samples was $2.16 \pm 0.01 \times 10^3$ kg m^{-3}. The ends of the samples were scrupulously polished to minimize heterogeneity of the stress field under compression (Jaeger and Cook 1979).

   The endcups had a diameter identical to the samples. To prevent the hydrostatic loading oil from penetrating into the sample pores, all samples were enclosed in plastic jackets (ALPHA FIT-221-3), and the contacts of their ends with the endcups were carefully closed. Each chalk sample was tested axially with a strain rate of 1×10^{-5} s^{-1} and laterally by a different hydrostatic oil pressure. The axial pressure varied from 37 MPa up to 65 MPa and the confining pressure from 0 to 15 MPa.
3. *β-quartz solid solution glass ceramic.* The composition of this material (VISION by Corning) in weight percent is $SiO_2 = 68.8$, $Al_2O_3 = 19.2$, $Li_2O = 2.7$, $MgO = 1.8$, $ZnO = 1.0$, $TiO_2 = 2.7$, $ZnO_2 = 1.8$, plus additional traces (Beall 1989). The glass-ceramic is close to monophase crystals of β-quartz solid solution about 600 Å (60 nm) in diameter and a small amount of zirconium titanate crystals (<100 Å in diameter) which allow efficient light transmission (Beall 1989). The resistance to failure under uniaxial compression of samples, which comply with the standard specification dimensions (106 mm length and 52 mm in diameter), is very high (greater than 450 MPa) and was beyond the load capacities of our press machine. Since our purpose was to overcome the resistance to fracture and to induce controlled cracking (rather than to obtain accurate strength results), we selected a sample geometry that deviates from standard specifications. The best results were obtained for a sample with the following specifications: Length 104 mm and having a frustum shape (the part of a cone left after cutting off a top portion by a plane parallel to the base) and an elliptical cross section, such that the large and small diameters at the base end

are 33 mm and 21 mm, respectively, and the two diameters at the top end of the frustum are respectively 33 mm and 10 mm. The abraded flexural strength of the β-quartz solid solution glass-ceramic is 69.3 MPa (Beall et al. 1967). The axial pressures varied from 0 up to 112 MPa (there was no confining pressure in this case).

4. *Glass.* Cylindrically shaped soda-lime glass samples 10 cm in length and 3 cm in diameter, which were uniaxially loaded. Soda-lime glass is homogeneous and transparent. Its structure consists of glassy matrix consisting of silicon, oxygen and calcium atoms, which are strongly bound, with weakly bound sodium ions. The density of all investigated glass samples was $2.6 \pm 0.01 \times 10^3$ kg m^{-3}.

5.3.3 Amplitude Investigation

The amplitude of the envelope of the EMR pulse (Eq. 5.4) is determined by the following relation:

$$\overline{A} = A_0\left(1 - \exp\left(-\frac{T'}{\tau}\right)\right) \tag{5.9}$$

As we noted above (Eq. 5.7), the frequency of the EMR pulses is inversely proportional to the crack width. EMR pulse amplitude increases as long as new atomic bonds are severed (Rabinovitch et al. 1998, 1999b); hence, this amplitude is related to the crack area, and it is expected that $\overline{A} \propto 1/\omega$ (Rabinovitch et al. 1998, 1999b).

The voltages of the EMR pulses depend on the antenna reaction (antenna efficiency), which changes with frequency. Compensating for this factor, $E = h(\overline{A})$ (E being the field amplitude reaching the antenna), by the appropriate antenna efficiency chart (h-EHFP-

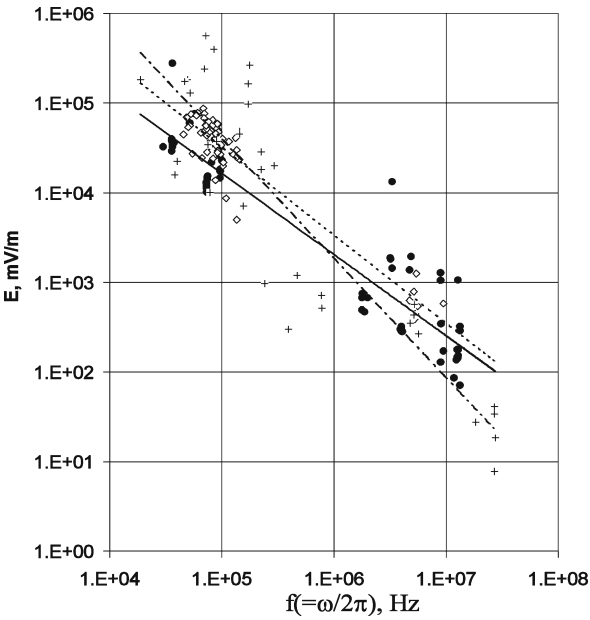

Fig. 5.5. Amplitude-frequency relation of EMR pulses associated with chalk, granite and glass-ceramic compression: Chalk (*filled circles*); granite (*diamonds*); glass-ceramic (*plus signs*); chalk trend line (*unbroken line*); granite trend line (*dashed line*); glass-ceramic trend line (*dashed dotted line*) (Rabinovitch et al. 1999b)

30 Near Field Probe set, Electro-Metrics Penril corporation), we were able to compare the heights of the various EMR signals that have different frequencies.

Figure 5.5 (Rabinovitch et al. 1999b) shows the compensated amplitudes (E) of the electromagnetic field signals induced by the fracture of chalk, granite and glass ceramic samples. Analysis of about 160 pulses shows that the amplitude-frequency ratio of each of the three materials can be fitted by a power-law type relation. Thus, for chalk, the relation is $E \cong 6 \times 10^8 f^{-0.91 \pm 0.04}$ (squared regression coefficient $R^2 = 0.87$), for granite $E \cong 3 \times 10^9 f^{-0.99 \pm 0.04}$ ($R^2 = 0.89$), and for the glass ceramic $E \cong 2 \times 10^{11} f^{-1.32 \pm 0.11}$ ($R^2 = 0.82$).

The exponent of these three relationships is very close to –1, although for the glass ceramic the value is somewhat scattered. EMR pulses induced by chalk and granite fracture could generally be fitted by a single frequency. In contrast, some EMR pulses associated with glass ceramic fracture were "multi-frequent". Therefore the amplitude-frequency ratios of these pulses were corrected in the following way. The contribution of a specific frequency peak of the "fast Fourier transformation" (FFT) to the compensated amplitude was calculated by

$$E(f_i) = \frac{EA_i}{\sum_i A_i}$$

where A_i is the area under the i^{th} peak and E is the measured pulse amplitude. Such a procedure evidently adds errors; it increases the spread of glass ceramic results and could also be the reason for the deviant exponent. If we collect all EMR data on one figure (Fig. 5.6, Rabinovitch et al. 1999b), a single combined relation can be obtained: $E \cong 5 \times 10^9 f^{-1.06 \pm 0.04}$ ($R^2 = 0.84$).

These results imply that the amplitude of the EMR field is indeed inversely proportional to the signal frequency and is hence proportional to the crack width (Rabino-

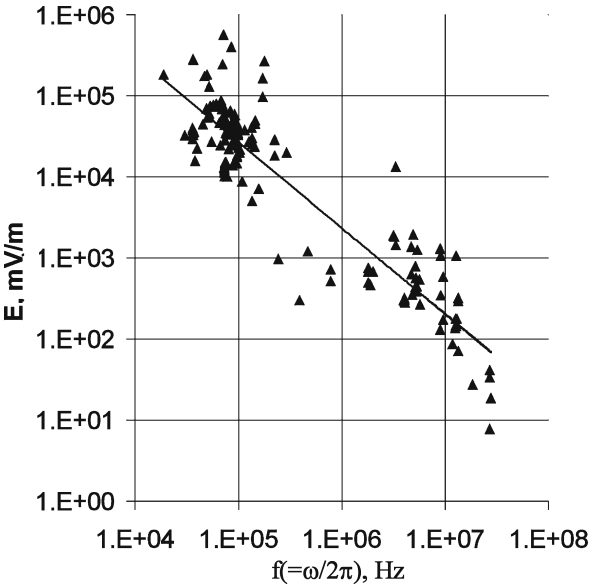

Fig. 5.6. General amplitude-frequency relation of chalk, granite and glass-ceramic samples (Rabinovitch et al. 1999b)

vitch et al. 1998). The final measured amplitude obviously depends also on other parameters such as fracture length, geometry of antenna-fracture orientation, attenuation along the path, etc. These factors constitute the source of the (rather large) vertical spread in the results of Fig. 5.5 and 5.6.

A controversy exists in the literature as to the magnitude of EMR from tensile and shear fracture. While Yamada et al. (1989) maintain that tensile cracking excites more intensive EMR than shear cracking, Petrenko (1993) states that the EMR amplitude is rather much greater for the shear fracture. Here we consider the influence of tensile vs. shear fracture modes on EMR. Since in our model (Sect. 5.2) no distinction is drawn between shear and tensile fracture modes, it is expected that magnitudes of EMR from both would be comparable.

We selected chalk for our study due to its micro-texture and low strength leading to a relatively small number of fragments (between 1 to 18) at failure, which can be analyzed fractographically (Bahat 1991a; Bahat et al. 2001a).

As expected from our previous studies (Bahat 1988c), the fractured surfaces exhibited a useful fractography. Tensile fractures (Fig. 5.7a) were planar and intensely marked by "striae" (plumes) (Bahat 1979a). These surfaces reflected a light grayish color. The shear fractures, on the other hand, had rough morphologies that were marked by white coarse "sugary" textures (Fig. 5.7b). The discrimination between these very distinct surfaces provided us with a fractographic criterion to distinguish between the two modes of

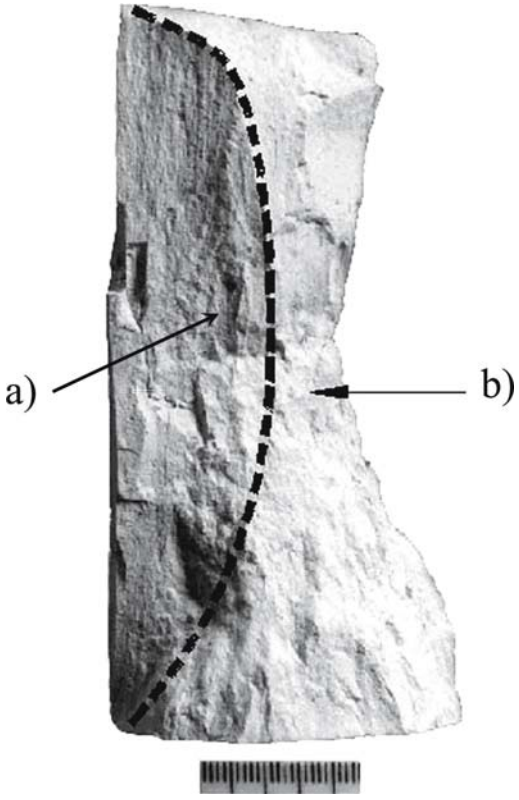

Fig. 5.7.
A photograph of a fractured surface on which the *dashed line* marks the boundary between the tensile part (**a**, showing planarity, gray tint and strong striae) and the shear part (**b**, showing coarse topography, white color and sugary texture). The tensile part (*'a' arrow*) is still covered by a piece of the shear part at the center of the sample. *Scale* in cm (Frid et al. 2000)

fracture and helped us to develop a method for the determination of tensile vs. shear fracture zones.

The area of each fracture was manually measured as the sum of all crack surfaces obtained for each sample for each type (Fig. 5.7, Frid et al. 2000). Measurement errors varied from 3 to 8%. Twenty-three chalk samples were investigated under different loads. The first eleven samples were loaded uniaxially, while the twelve following ones were loaded triaxially. During the triaxial test, the lateral load was changed from 1 to 15 MPa, which caused a monotonous rise of sample strength from 37.7 MPa up to 80.1 MPa. Young moduli for all tested samples ranged from 6.2 up to 11.3 GPa, while the Poisson ratio changed from 0.07 up to 0.37. Since brittle-ductile transformation after the Coloumb-Mohr region diminishes EMR activity (Frid et al. 1999), this region was not treated. Tensile fracture was the preferable mode of failure during uniaxial compression, while the shear mode became significant only during triaxial loading: The "(shear area) / (tension area) ratio" changed from 0.5–0.8 during uniaxial compression to 2–35 during triaxial loading (Bahat et al. 2001a).

We compared the total amplitude (sum of compensated amplitudes) of the EMR pulses from each sample (measured above the sample's elastic limit) with the total respective areas (sums of crack areas of a given sample) of tensile and of shear cracks (Rabinovitch et al. 1999b). Figure 5.8 (Frid et al. 2000) shows a 3D graph of total compensated EMR pulse amplitudes vs. total areas of tensile and shear cracks of all investigated samples. The total EMR amplitude E was fitted by the linear equation: $E = -33.39 + 0.00655\,S_t + 0.00596\,S_s$ (with a squared regression coefficient $R^2 = 0.86$), where S_t and S_s are the total areas of tensile and of shear cracks of a given sample, respectively. The difference between the two coefficients multiplying S_t and S_s is of the order of ±5%, which is rather small and might be attributed to the error in area measurements (3–8%). This result shows that it is only the size of the *entire* area of the crack, irrespective of its mode, which governs the amplitude of the EMR.

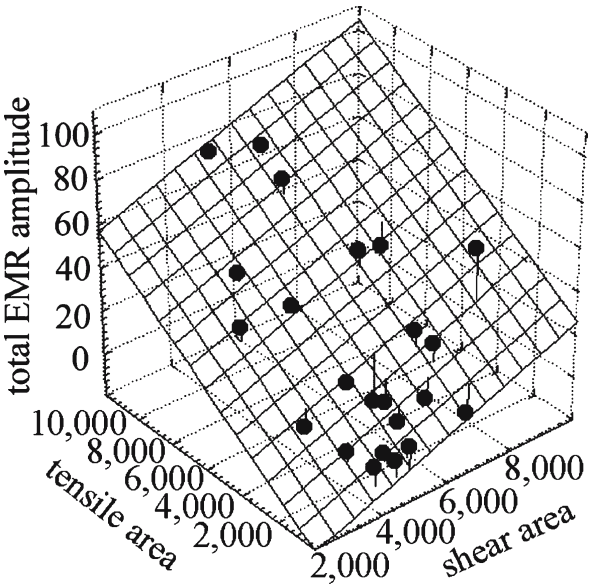

Fig. 5.8.
A 3D experimental graph of total compensated EMR pulse amplitudes (V m^{-1}) vs. total areas (mm^2) of tensile and shear crack areas of all investigated samples and its fit (Frid et al. 2000)

5.3.4
Investigation of the Time up to Envelope Maximum and its Relation with Frequency

To check the validity of Eq. 5.2, two experimental tests were carried out:

1. Mutual measurement of T' and crack lengths (Bahat et al. 2002a) in transparent glass ceramics under compression. A glass ceramic sample was gradually loaded uniaxially. Loading was stopped as soon as EMR pulses were recorded. The sample was removed for a check and then the procedure started afresh. The procedure was repeated five times (five stages-Fig. 5.9). Characteristic pulses of different modes observed during the entire process are presented in Fig. 5.10 and Table 5.1 (Bahat et al. 2002a).

   Figure 5.11 shows an example of an EMR pulse observed during the collapse of a glass ceramics sample with its least square fit to Eq. 5.1. As can be seen, both the accuracy of measurement and that of the parametrization procedure are adequate ($R^2 = 0.96$).

   The results of parametrization of this EMR pulse are marked by arrows in Fig. 5.12, where we summarize our results that pertain to the correlations between T' and crack length. Note that T' values varied between 0.8 and 1.5 μs under low stresses (0.36–1.7 MPa) in association with microcracks of several millimeters in length. T' values of 5–15 μs were associated with stresses of up to 65 MPa and were correlated with cracks of up to several centimeters in length. A value of T' larger than 20 μs occurred under greater stresses (112 MPa) and was correlated with the longitudinal splitting at failure (~10 cm). The correlation between T' and crack length shows a positive trend (Fig. 5.12). A straight line can be drawn through the points representing the stages from 3 to 5 (Fig. 5.9). The dashed line indicates our assertion,

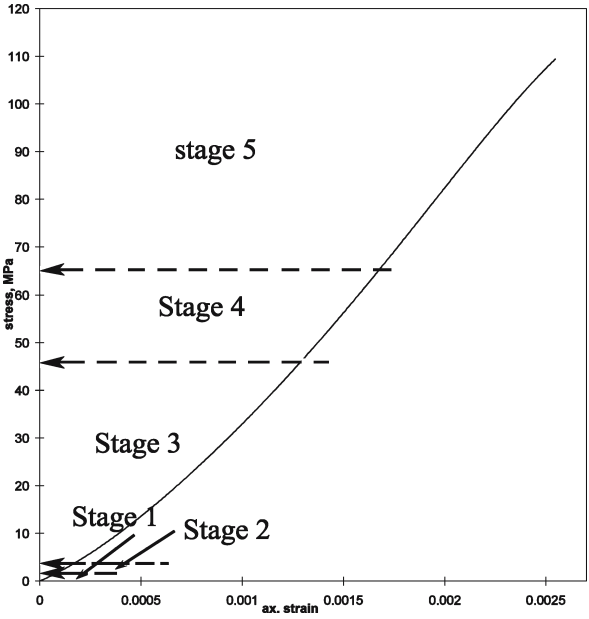

Fig. 5.9.
Stress vs. strain for the fifth stage of the incremental stress increase. *Dashed arrows* indicate stress levels achieved during stages 1–4 (Bahat et al. 2002a)

$T' = 8.15 \times 10^{-7} L$ ($v_{cr} \approx 1\,200$ m s^{-1}), where L is the crack length in mm and T' is in seconds. The R^2 coefficient obtained was 0.73. Considering the small number (five) of points, this coefficient is considered reasonable.

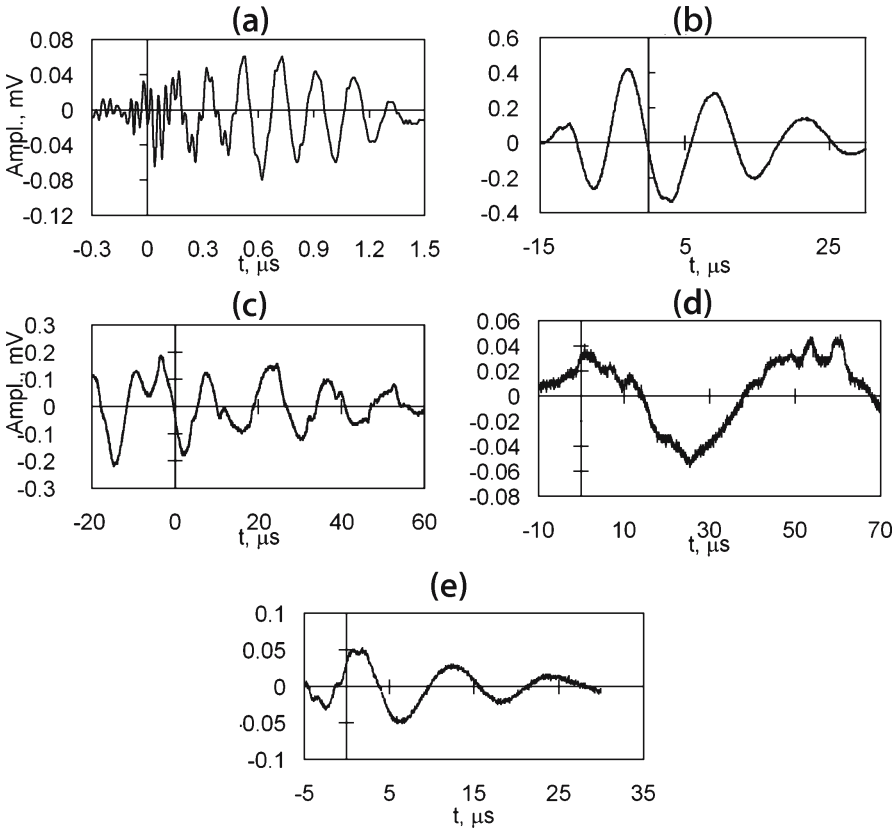

Fig. 5.10 Characteristic pulses of the different modes (Table 5.1). **a** A short pulse (stage 1, pulse 1). **b** A medium, individual pulse (stage 4, pulse 7). **c** A medium, uneven pulse (stage 4, pulse 10). **d** A lengthy pulse (stage 5, pulse 1). **e** A medium, individual pulse (stage 5, pulse 2) (Bahat et al. 2002a)

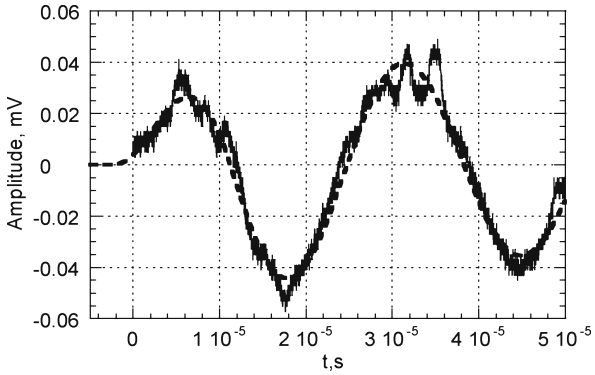

Fig. 5.11. An example of an EMR pulse of the fifth stage with its least square fit to Eq. 5.1 (*dashed line*). Results of fit: $T' = 42 \pm 0.3$ μs, $f = 18.7 \pm 0.012$ kHz, $R^2 = 0.96$ (Bahat et al. 2002a)

Table 5.1. EMR pulse parameters vs. stress and strain in fractured glass-ceramic

Stage	Stress (MPa)	Strain	Pulse number	Frequencies		T' (μs)	Pulse length	Crack size (mm)
1	0.36	0.00042	1	5.2, 27	MHz	0.95	Short	3.5 × 7.5
			2	5.7, 27	MHz	1.5	Short	
2	1.7	0.0011	1	1.2, 5.1, 18.4, 27.5	MHz	0.8	Short	2.0 × 7.0
			2	4.8, 19, 27	MHz	1.5	Short	3.5 × 10
3	47	0.0011	1	49.3, 156	kHz	25	Medium	2 × 5 × 19
4	0.9		1	46.7	kHz	15	Medium	10 × 10
			2	51.8	kHz	15	Medium	
	1.9		3	53, 85	kHz	25	Medium	
	3		4	41, 70, 122	kHz	17	Medium	
	5		5	72	kHz	20	Medium	
	12.5		6	100, 177	kHz	20	Medium	
			7	172	kHz	20	Medium	
	65	0.01850	8	172, 292, 468, 776	kHz	15	Medium	
			9	144, 225	kHz	15	Medium	
			10	75, 144, 225, 780	kHz	15	Medium	
5	112	0.025	1	18.7, 37.9	kHz	42	Lengthy	20 × 100
	<112		2	90	kHz	17	Medium	2.5 × 12
			3	40, 78, 242, 391	kHz	20	Medium	7 × 29

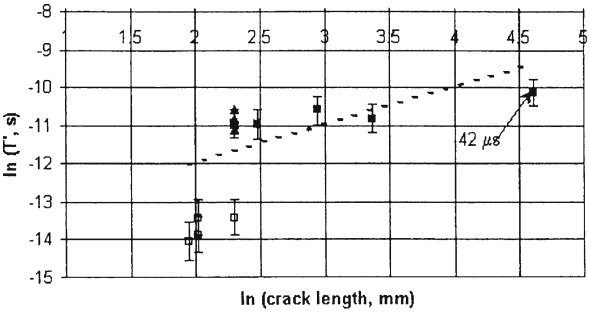

Fig. 5.12. Correlation between T' and crack length. *Open squares* show EMR-fracture data during the first two stages; *closed squares*: Stages 3–5; *closed triangles* show spread of EMR data during the forth stage. *Error bars* here were estimated by the spread of the EMR data of the forth stage of loading to be ~3.5% for ln T' (Bahat et al. 2002a)

Note that the dimensions of the flaky cracks (stages 1 and 2, Fig. 5.9) calculated by EMR parameters (Fig. 5.12) are much less than the measured ones (Table 5.1) and hence deviated from the regression lines in Fig. 5.12. We assume that the initially created cracks during compression were in fact of small dimensions (as measured by the EMR). Eventually these fractures caused flaking off the external surface of the sample of much larger dimensions. The reason that the initial cracks were optically undetected stems from the fact that their apertures, were apparently below the wavelength of light.

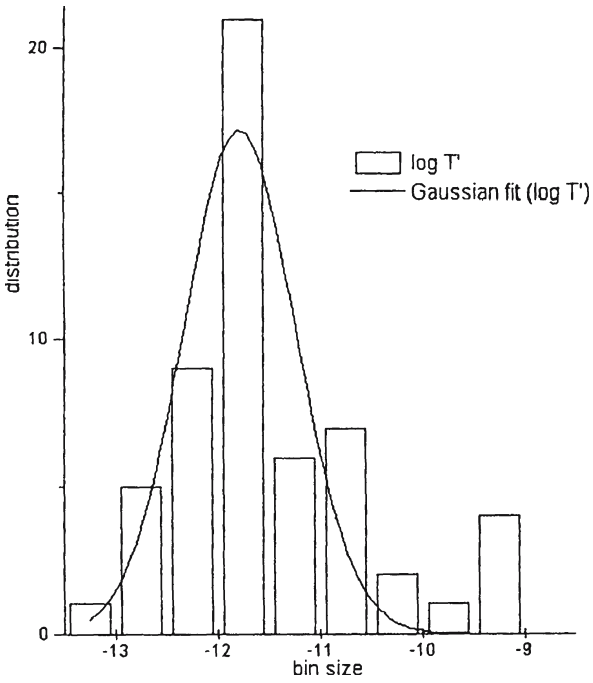

Fig. 5.13.
Histogram of log T' (where T' is the time interval to reach the pulse maximum) and its Gaussian fit Rabinovitch et al. 1998)

2. T' values distribution (Rabinovitch et al. 1998). If we assume that the fracture process develops incrementally and that each new increment is proportional to the existing crack length (as previously observed by Gillespie et al. (1992) and by Cowie and Scholtz (1992a,b), then a log-normal distribution should be expected (Aitchison and Brown 1976). Results show that T' indeed obeys a log-normal distribution (Rabinovitch et al. 1998) (Fig. 5.13).

   Another problem is the possibility of a scaling relation between crack length and width. Walmann et al. (1996) showed that the aperture, u, and the length ℓ of the crack were related by a fractal relation, $u \sim \ell^{\beta}$, where β ranges between 0.5 and 1.

   Although the relation was observed for u and not for crack width, we tried to correlate between T' and ω: $\omega \sim (T')^{-\nu}$, which would have implied a scaling between crack length and width. Results, however, show that the obtained ν is of the order of zero, i.e., crack length is independent of its width, implying that the width is constrained by an auxiliary mechanism, such as grain boundary, intergranular spacing, etc. A similar constraint was already noted (Bahat 1988c) in geological fractures in chalks, where in a given layer of a constant width, there is a wide range of fracture lengths.

5.3.5 Frequency Investigation

Equation 5.7 reveals that for the same crack width, the EMR frequency for stiffer materials would be higher than that for the weaker materials. Indeed, since the Rayleigh wave velocity in a material with a Young modulus E, Poisson ratio μ and density ρ, is given by

$$v_R = \frac{0.87 + 1.12\mu}{1+\mu}\sqrt{\frac{E}{2\rho(1+\mu)}}$$

the ratio of EMR frequencies for two materials is given by

$$\frac{\omega_1}{\omega_2} = \frac{(0.87+1.12\mu_1)}{(0.87+1.12\mu_2)}\frac{(1+\mu_2)}{(1+\mu_1)}\sqrt{\frac{E_1}{E_2}\frac{\rho_2(1+\mu_2)}{\rho_1(1+\mu_1)}}\frac{b_2}{b_1} \tag{5.7'}$$

To check the validity of Eq. 5.7, we compared EMR frequencies and fracture widths for four different materials, the elastic properties of which are shown in Table 5.2 (Frid et al. 2003).

Only during glass uniaxial compression experiments was an exact one-to-one correspondence between the EMR signals and the longitudinal splits causing them obtained. Even during the transparent glass-ceramic experiments not all pairs of EMR signal-fracture (S-F) were perfectly related. In our analysis, we included only those pairs of S-F that could be accurately "linked". During chalk and granite (that are non-transparent materials) experiments, a one-to-one link between EMR signals and fractures was not possible. Moreover, fracture widths and lengths were uncertain since the fracture directions were usually undefined. Hence we included in our analysis only "maximal" fractures, which are, of course, easily discerned, and of those only the ones that had a "stretched shape", where one dimension (considered as length) was significantly larger than the other (considered to be the fracture width). Figure 5.14 (Frid et al. 2003) shows the relation of $\pi v_R / \omega$ (where v_R is calculated by the relation leading to Eq. 5.7') vs. crack widths, b. The slope of this relation is 0.93 ($R^2 = 0.82$), being very close to 1, in agreement with the theoretical prediction (Eq. 5.7 and 5.7').

Table 5.2. Experimental results of material properties

	Young modulus E (GPa)	Poisson ratio μ	Density ρ (kg m^{-3})	Rayleigh wave velocity v_R (m s^{-1})
Glass	45	0.2	2600	2448
Glass ceramics	51.6	0.25	2370	2715
Chalk	8.5	0.16	2604	2377
Granite	44.8	0.32	2160	1178

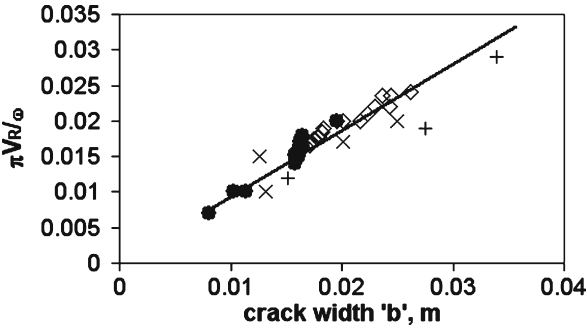

Fig. 5.14. The relation between reciprocal EMR frequency and fracture width for chalk, granite, glass and glass ceramics under compression (• chalk, ◊ granite, + glass ceramic, × glass) (Frid et al. 2003)

5.3.6
T'/ω Investigation (Eq. 5.8)

The T'/ω parameter is directly calculable from the parametrized data, and hence is independent of different auxiliary factors, which can be sources of large fluctuations (errors) if we would like to relate fracture areas to A_0 (Eqs. 5.1 and 5.9).

5.3.6.1
Experimental Procedure and Results

Twenty-four chalk samples were investigated in the conventional compression test (Rabinovitch et al. 2000c). Nine samples were loaded uniaxially and fifteen samples were loaded triaxially. Twenty-one of the twenty-four samples showed a similar EMR behavior, while three (not treated here) behaved differently. Table 5.3 presents rock-mechanics properties of all investigated samples. Figure 5.15 shows a representative normalized stress-strain curve (For the sake of comparison, stress values were normalized by the peak stress value, while the axial strain values were normalized by the axial strain at peak stress) of a chalk sample together with its T'/ω data. The latter was calculated from the EMR data by a least square method as shown in the caption of Fig. 5.16. T'/ω data are shown in Fig. 5.15a in a semi-logarithmic scale and in Fig. 5.15b in a normal scale. As is seen from Fig. 5.15, an increase of stress (strain) is generally followed by an increase of the T'/ω factor, indicating an increase of the area of newly formed cracks. The range of

Table 5.3. Rock-mechanics parameters of investigated chalk samples

Sample number	Confining pressure (MPa)	Strength (MPa)	Differential stress (MPa)	Poisson ratio	Young modulus (GPa)	Shear modulus (GPa)
1	0.00	47.60	47.60	0.21	8.50	3.51
2	0.00	45.20	45.20	0.16	9.00	3.88
3	0.00	50.40	50.40	0.07	9.30	4.35
4	0.00	51.50	51.50	0.15	9.20	4.00
5	0.00	46.20	46.20	0.19	9.70	4.08
6	0.00	41.90	41.90	0.23	7.30	2.97
7	0.00	37.70	37.70	0.14	6.10	2.68
8	1.00	47.60	46.60	0.20	9.30	3.88
9	1.00	39.70	38.70	0.19	7.60	3.19
10	5.00	56.20	51.20	0.15	9.30	4.04
11	10.00	54.20	44.20	0.08	7.70	3.56
12	15.00	65.10	50.10	0.14	9.40	4.12
13	3.00	48.40	45.40	0.20	8.90	3.71
14	0.80	46.00	45.20	0.16	8.70	3.75
15	0.85	47.50	46.65	0.14	9.10	3.99
16	2.00	48.80	46.80	0.13	8.80	3.89
17	2.00	45.80	43.80	0.20	7.70	3.21
18	2.00	47.90	45.90	0.11	8.60	3.87
19	2.00	48.70	46.70	0.19	9.10	3.82
20	5.00	43.50	38.50	0.18	7.80	3.31
21	5.00	44.00	39.00	0.18	7.80	3.31

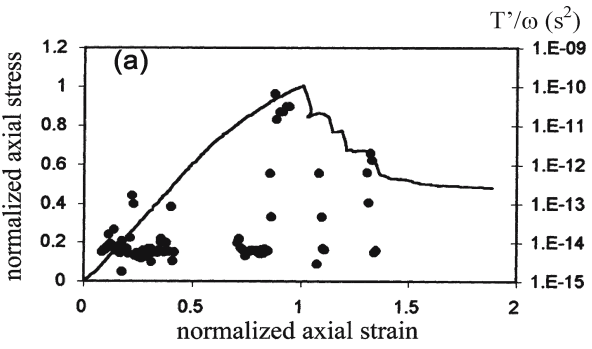

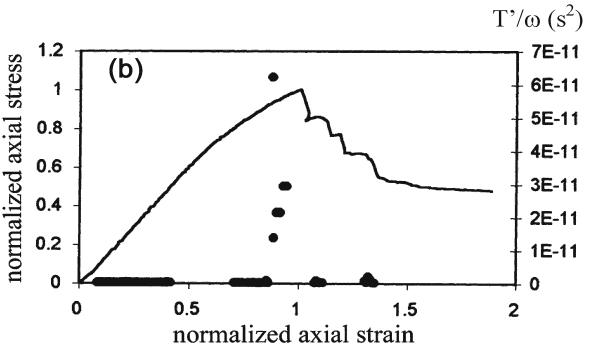

Fig. 5.15.
A representative normalized stress-strain curve of a chalk sample together with its T'/ω data (T'/ω data are shown in a semi-logarithmic scale (**a**), and in a normal scale (**b**)) (Rabinovitch et al. 2000c)

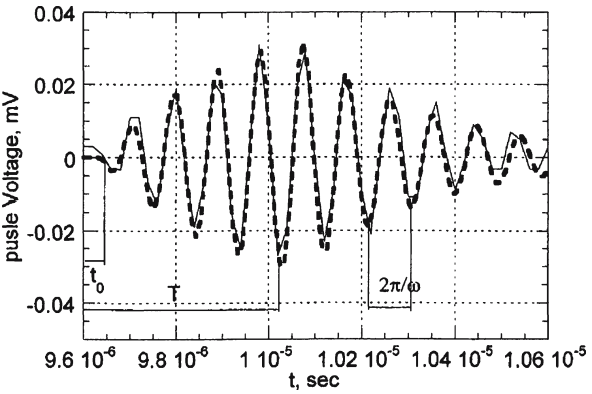

Fig. 5.16.
An experimental EMR pulse and its numerical fit. For this pulse, t_0 is 9.63 μs, T is 10.07 μs. Hence, $T' = T - t_0$ is 0.44 μs. The frequency ω is 6.76×10^7 s^{-1}. Hence, T'/ω is 6.51×10^{-15} (Rabinovitch et al. 2000c)

the value of T'/ω stretches from 10^{-15} to 10^{-10} (s^2) (5 orders of magnitude!). The minimum values of T'/ω were observed at the beginning of the stress-strain curve. Later, the elastic and elastic-plastic zones before the peak of the stress-strain curve, T'/ω values of the order of 10^{-14}–10^{-11} (s^2) were measured, and the T'/ω value jumped to a maximum (of the order of 10^{-10}) in the zone immediately preceding the peak stress. This jump is indicative of the collapse failure. After the peak stress, T'/ω amplitudes (and the corresponding crack areas) decrease back to values of 10^{-14}–10^{-11} (s^2) ("relaxation" region). A similar behavior of T'/ω vs. stress-strain (namely, a gradual increase of T'/ω with stress increase followed by an abrupt jump) was observed during uniaxial compression of glass ceramics (Bahat et al. 2002a), suggesting that such behavior could be of general validity (see below). These

Fig. 5.17.
Fractography: Various fracture types and sizes are shown on specimen No. 1 (Table 5.3). Two large fractures (~4 × 4.5 cm and ~5 × 1.5 cm) are separated by a ridge at the lower part of the picture, whereas the upper part of the picture reveals length variations from 0.1 mm (magnified), through 2–4 mm up to 1–4 cm (cm *scale* at top of picture) (Rabinovitch et al. 2000c, Bahat et al. 2001a)

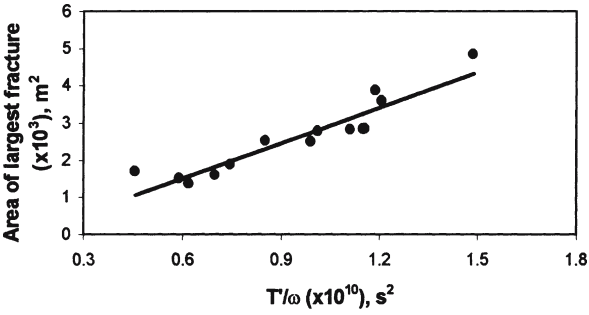

Fig. 5.18.
Experimental largest T'/ω values vs. maximal fracture areas and a linear fit (squared regression coefficient $R^2 = 0.9$) (Bahat et al. 2001a)

results imply that following the early pore-closure zone of the stress-strain curve, microcracking and possibly coalescence occurred, while collapse happened just before peak stress and was followed by smaller relaxation cracking in the post-peak zone.

Fractographic examination of the failed chalk samples revealed fractures ranging in size from 0.1 × 0.1 mm up to about 40 × 50 mm. The failed surface (Fig. 5.17) consists of composites of cracks that vary in size from several mm to several cm. This range of crack areas (10^{-2} mm^2 to ~2 000 mm^2) is in accordance with the variation by 5 orders of magnitude of the T'/ω values mentioned above.

Since a one-to-one correspondence between the EMR pulses and the causative fractures is not possible in the chalk measurement, only the cracks possessing the largest

areas were measured and correlated with the largest T'/ω values (Fig. 5.18, and see also Bahat et al. 2001a). As can be seen, very good agreement exists between Eq. 5.8 and the experimental results both in the range of values and in the correlation of the largest values ($R^2 = 0.9$). In a recent experiment on transparent glass ceramics (Bahat et al. 2002a) and glass (Frid et al. 2003), even a one-to-one correlation was shown to exist between T'/ω and crack area.

The order of magnitude of the velocities in Eq. 5.8 can also be estimated from these measurements. Thus $v \approx [S/(\pi T'/\omega)]^{1/2}$ and, e.g., for the 0.1×0.1 mm case, we have $T'/\omega = 10^{-15}$ s^2 whereupon $v \approx 1.4 \times 10^3$ ms^{-1}. This is of the correct order of magnitude (since the average Rayleigh velocity calculated for chalk (Bahat et al. 2002a), at the known values of its dry density, Young modulus, and Poisson ratio is 1.2×10^3 ms^{-1}).

5.3.7
Decay Time Investigation (Rabinovitch et al. 2003a)

5.3.7.1
Experimental Results and Analysis

We have analyzed EMR pulses of chalk, granite, glass and glass ceramics by fitting them to Eq. 5.1 and deriving their parameters (in particular τ and ω). Figure 5.19a shows the dependence of τ on ω for glass, glass ceramics and granite. The slopes on a logarithmic scale are within -1 ± 0.1, with $R^2 = 0.96$, 0.85 and 0.91, respectively, agreeing with the theoretical prediction (Eq. 5.6). For chalk, however, an "effective" slope of –0.7 is obtained (Fig. 5.19b). It cannot be attributed to the low accuracy of the fitting parameters: The error for τ ranges between 2% and (seldom) 30%, which is quite small in a logarithmic scale, while the error for ω does not exceed a few percent, and is usually only a fraction of a percent. We would like to attribute this "change of slope" to the spread in temperatures of the small cracks there (see below).

The distribution of $(\tau\omega)^{-1/4}$, which according to Eq. 5.6 should be proportional to the absolute temperature for small and large crack widths in granite is shown in Fig. 5.20a and b, respectively. We denote $(\tau\omega)^{-1/4}$ values henceforth as "temperatures". The mean values of the crack "temperatures" in relative units are respectively 0.67 and 0.65 for small and large cracks (in granite), which are considered to be the same within the accuracy for "temperature" values (10%). Similar distributions for chalk are shown in Fig. 5.21a and b. Here, however, the mean values are different, being 0.47 for small crack widths and 0.67 for large ones. As mentioned, the error for ω is not more than a few percent, mostly a fraction of a percent, while for τ it ranges between 2% and 30%. Thus the error of $(\tau\omega)^{-1/4}$ may be estimated as ~10%, yielding "temperatures" of 0.47 ± 0.05 for small cracks and 0.67 ± 0.07 for large cracks.

Figure 5.22 shows the distribution (histogram) of $\log(1/\omega)$ (where $1/\omega$ should be proportional to crack width, Eq. 5.7, for both small and large cracks). We denote by small (large) cracks those cracks that have ω values larger (smaller) than 2×10^7 s^{-1} (e.g., Fig. 5.19). If one assumes the Rayleigh velocity in chalk to be (see above) 1 200 m s^{-1}, then the calculated small crack widths in chalk (by Eq. 5.7) range between 52.5 and 130 μm. For large cracks, the corresponding range is from 130 μm to 1.8 cm.

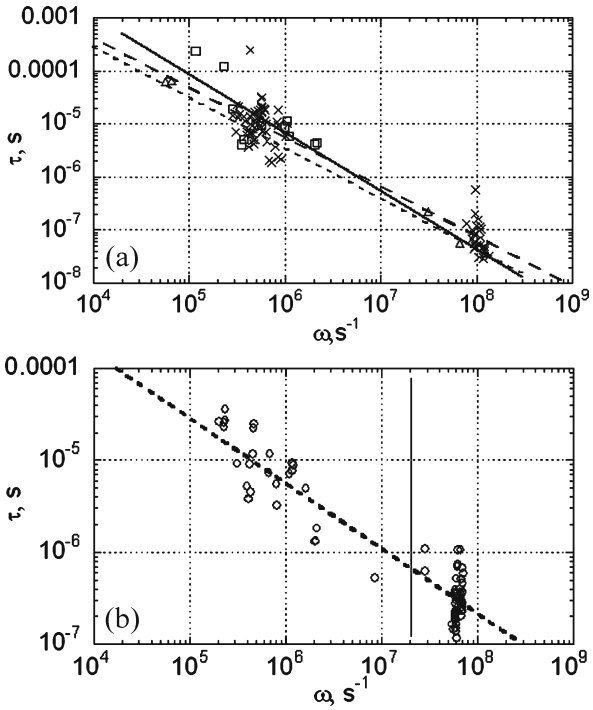

Fig. 5.19.
Rise and fall time τ as a function of frequency ω: The *points* are the experimental results of individual pulses, and the *line* is the power law fitting result: **a** for glass (*triangles*), fitting $\tau = 1.87\omega^{-0.95}$ (*short-dashed line*); for glass ceramics (*squares*), fitting $\tau = 28.1\omega^{-1.1}$ (*solid line*); for granite (×), fitting $\tau = 2.23\omega^{-0.93}$ (*long-dashed line*); **b** for chalk (*circles*), fitting $\tau = 1.87\omega^{-0.7}$ (Rabinovitch et al. 2003a)

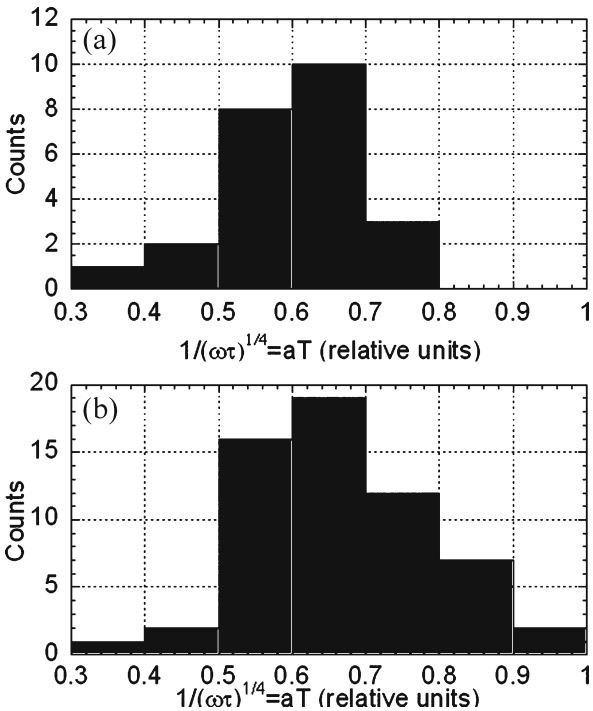

Fig. 5.20.
Frequency counts of "temperatures" $(\omega\tau)^{-1/4}$ for cracks in granite: **a** short cracks; **b** long cracks (Rabinovitch et al. 2003a)

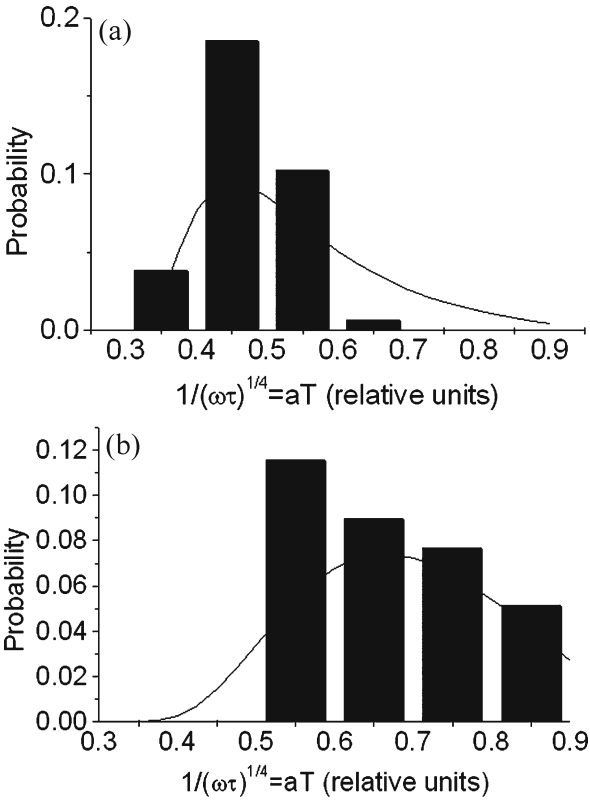

Fig. 5.21.
Frequency counts of "temperatures" $(\omega\tau)^{-1/4}$ for cracks in chalk (*columns*) and calculated (*solid line*) (Rabinovitch et al. 2003a): **a** for short cracks; **b** for long cracks; crack aperture is assumed to behave as $\varepsilon \sim kx^{\alpha}$, where x is the crack half-width (Rabinovitch et al. 2003a)

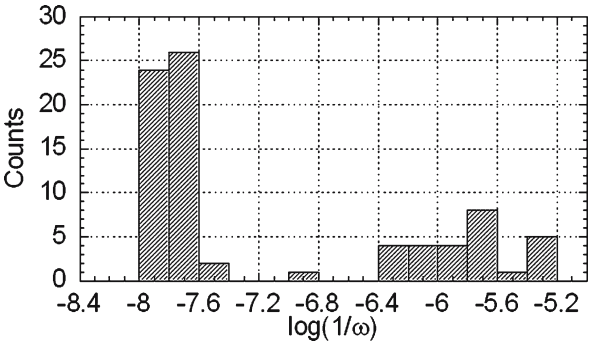

Fig. 5.22.
Frequency counts for $\log(\omega^{-1})$ (ω^{-1} is proportional to crack widths, $b = \pi v_R / \omega$) in chalk fit (Rabinovitch et al. 2003a)

5.3.7.2 *Discussion*

It has been shown that the temperature of dynamically propagating cracks rises (Fuller et al. 1975). The actual temperature rise depends on crack velocity and on material properties (Yatomi 1981). The spread of experimental points in Fig. 5.19 can be attributed to a spread in crack velocities that causes a spread in temperatures. Since we assume that $1/\tau \sim \omega T^4$, the dependence on temperature is very strong. However, cracks

in glass, in glass ceramics (which are not porous) and in granite (the porosity of which is about 5%) lead to almost uniform distribution of crack "temperatures" around their mean (Fig. 5.20, resulting in the almost exact $\omega\tau = \text{const.}$ relation of Fig. 5.19a). In chalk, however, $\omega\tau \neq \text{const.}$ The "temperature distribution" (histograms) for small and large cracks are given in Fig. 5.21a and b. It can be seen that "temperatures" of small cracks are significantly lower than those of large cracks.

We assume that this temperature difference in chalk is due to the interaction between the propagating cracks and the existing material pores. Chalk is the only material of the four analyzed that has large porosity (of about 40%). The pore radii in chalk range (Gueguen and Palciauskas 1994) between 0.05 and 100 μm. The results of our measurements (see Rabinovitch et al. 2003a), together with their exponential fitting, are given in Fig. 2.28b. Note that although the range of observed pore sizes was between 2 μm and 210 μm, their 3D fitting, being exponential, includes all pores, also those of lower sizes. The cracks in chalk encounter one or more pores during their development. Thus crack heat can be partially spent on raising the temperature of the air inside the pores; in addition, air from the pore can enter the crack and expand adiabatically; this process could also lower the latter's temperature. Although all cracks in chalk are cooled down in this way, the temperatures of small-sized cracks are more strongly influenced by these processes than those of large cracks, since the final temperature depends on the ratio between the pore's volume and the volume of the crack. The greater this ratio, the stronger is the temperature decrease. To show the self-consistency of our assumptions, we have theoretically derived the probability distribution of final temperatures (Rabinovitch et al. 2003a). The experimental and the calculated distributions of final "temperatures" for small and large cracks are shown in Fig. 5.21a and b. The agreement is adequate.

5.3.8 Summary of the EMR Model

It is seen that all experiments undertaken to check the validity of the model turned out to yield positive results. Thus,

1. The amplitude $\overline{A}$ was shown to be indeed proportional to $1/\omega$.
2. EMR amplitudes from shear fractures are similar (for similar areas) to those from tensile fractures.
3. T' is proportional to crack length ℓ.
4. The distribution of T' values follows a lognormal curve.
5. No correlation between length and width of cracks is obtained.
6. ω is proportional to $1/b$ and scales with Young modulus.
7. T'/ω is indeed proportional to crack area with the right proportionality constant.
8. τ is proportional $1/\omega$ and reasonable "temperature" distribution can be deduced for porous and non-porous materials.

All of these results support the contention that the model of EMR, although laid out only in a simplistic manner, is the right one. In the next section, we analyze the hitherto existing models of the origin of EMR and show that they all fail to stand experimental or self consistent tests.

5.4
Comparison of the New EMR Model with the Previous Ones

5.4.1
Dislocations and Charged Electrons

Misra (1977) and Misra and Ghosh (1980) suggested that "during non-uniform distribution of dislocations, which occur at the transition stages of elastic-plastic deformations under tension, namely, yield point, end of Luders' strain, and crack propagation, mobile dislocations arrange themselves into some configuration, that is mechanically stable". If, at the halting position of a dislocation, its energy is reduced, the dislocation can become self-trapped. "Conduction electrons (CEs) associated with such a dislocation would be stopped and trapped relative to the positive ions". This CE braking process would be similar to a "Bremsstrahlung" mechanism and would result in the emission of EMR. Misra (1977) further assumed that "during each transition stage (like a yield point and/or fracturing) there must be a re-adjustment of the CE distribution within the microscopic system, and the latter creates an oscillating Hertzian dipole. Thus, the EMR must appear only at transition deformation stages".

In a further analysis Molotskii (1980) pointed out that in the adjustment of the CEs to the slowly moving dislocations, their acquired energy would be of the order of 10^{-11} eV per mean free path, so that the maximum frequency of emitted EMR would be of the order of 10^3 Hz, i.e., significantly lower than the value predicted and measured by Misra. The acceleration of CEs by moving dislocations could not therefore be the cause of the EMR from metals, and Molotskii suggested therefore that the EMR was due to the increase of the total dislocation length and velocity, which occurred at transient deformation stages. Since these dislocations acted as electric dipoles, this mechanism would lead to an accelerated rise in the dipole moment of the material with an accompanying emission of EMR.

Both explanations however relating EMR to dislocation phenomena seem questionable. As is well known the motion of dislocations can be totally neglected in the cracking of brittle materials, and this mechanism therefore cannot explain EMR from glass and other brittle materials (e.g., most geological materials). A typical EMR pulse from the failure of a glass cylinder under uniaxial compression is shown in Fig. 5.23. The shape of EMR signals is found to be invariant for different brittle materials (glass, glass ceramics, granite, rhyolite, limestone, and chalk; Rabinovitch et al. 1995, 1996, 1998, 1999b, 2000a,b, 2002a; Frid et al. 1999, 2000; Bahat et al. 2002a), and even to be inde-

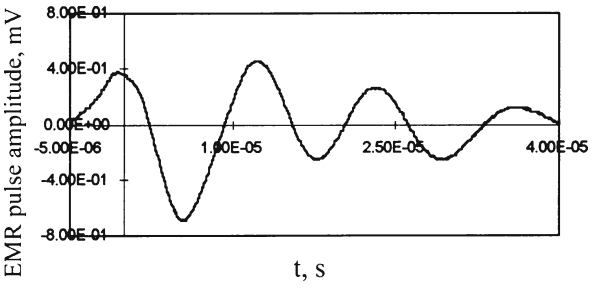

Fig. 5.23.
A typical EMR pulse observed during glass cylinder failure under uniaxial compression (Frid et al. 2003)

pendent of the type of loading (compression, drilling and blasting (Goldbaum et al. 2001; Rabinovitch et al. 2002b) and mining (Vozoff and Frid 2001)).

The basic weakness of the "dislocation movement-hypothesis" was also pointed out by Jagasivamani and Iyer (1988), who showed experimentally that the EMR amplitude even increased with the brittleness of the investigated metals. Indeed, this latter result is in line with our measurements (Frid et al. 1999), which also showed that EMR activity increased with the brittleness of materials and decreased in the case of a transition from a brittle to a ductile behavior.

5.4.2 Discharge

Finkel et al. (1975) demonstrated that the splitting of alkali-halide crystals creates a mosaic of positive and negative charges, which appears on both sides of the fracture as it is formed. Since such charge separation can create an electrostatic field of the order of 10^7 V cm^{-1}, an electric discharge may occur, which was suggested as the origin of EMR (Finkel et al. 1975). However, Miroshnichencko and Kuksenko (1980) and Khatiashvili (1984) have already noted that the spectrum of discharge radiation is known to be of a "white noise" type and to be independent of the mechanical properties of the materials; the observed EMR behaves in an entirely different manner (Miroshnichencko and Kuksenko 1980; Rabinovitch et al. 1998, 1999b; Frid et al. 2000). Our results show that the EMR appears as individual pulses or as clusters of pulses caused by the different (individual or group) fractures (Rabinovitch et al. 1999b, 2000c; Frid et al. 2000). The properties of the pulse are influenced by the dimensions of the fracture (Rabinovitch et al. 1998, 1999b, 2000c; Frid et al. 2000) and by the elastic properties of the materials (Khatiashvili 1984; Frid et al. 1999). Moreover, the high resolution of our experimental system (Rabinovitch et al. 1998) allows us to obtain the exact shapes of the EMR pulses (Figs. 5.2, 5.10, 5.23, 5.24a). These definitely do not behave as "white noise" but rather exhibit a very distinct character (Eq. 5.1). These results confirm those observed by Miroshnichencko and Kuksenko (1980) and Khatiashvili (1984). Note in particular that the EMR spectrum (Fig. 5.24b) is highly localized around a single frequency.

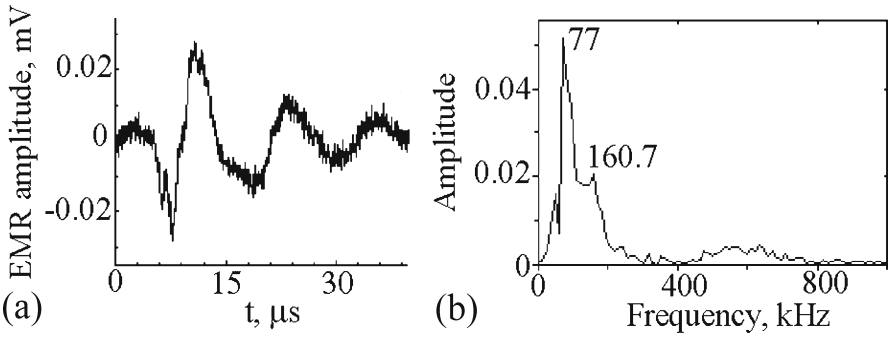

Fig. 5.24. An example of EMR signal **a** excited by fracture of granite in compression and its spectrum **b** (Frid et al. 2003)

5.4.3
Movement of Fracture Tips

EMR is observed (Gershenzon et al. 1985) during the propagation of cracks introduced by cleavage of LiF crystals with a knife. The developing crack (tip) propagates in the direction of indentation. According to their assumption, negative electrical charge moves with the crack tip while positive charge was assumed to accumulate at the region of the indenter-material contact. Dipole radiation should occur from these opposite charges, separated by the length of the crack, by the acceleration of the latter. Based on these assumptions, the power of the emanating EMR was calculated (Gershenzon et al. 1985), further assuming that the charging mechanism arises from moving charged dislocations.

As already pointed out, however, charge transfer by dislocations cannot constitute a general explanation of the origin of EMR. The "movement of fracture tips" explanation is questionable even for a dielectric like LiF, since the velocity of dislocations in alkali halide crystals (Tetelman and McEvly 1967) is *smaller* than the velocity of the crack, implying that charged dislocations cannot be the reason for crack tip charging.

An even stronger adverse argument to this model is that there is no clear reason for any "symmetry breaking", i.e., there is no known mechanism that would select a certain tip (side) to become negative while the other tip (side) becomes positive and not vice versa. In particular for the case discussed by Gershenzon et al. (1985), it is not clear why the crack tip should accumulate negative and not positive charge.

5.4.4
Movements of Fracture Sides (the "Capacitor" Model)

In order to determine whether movement of the crack sides during cracking could cause EMR with the appropriate characteristics, Miroshnichencko and Kuksenko (1980) used the acoustic wave emitted by a fracturing material to drive the plates of a specially built auxiliary-charged capacitor. The EMR from the capacitor was monitored by an antenna. Since the measured signal "shapes" were comparable to those obtained by the "directly" observed EMR, they concluded that the latter was caused by similar movements of the charged sides of the crack.

A decade later, O'Keefe and Thiel (1995) suggested another version of a capacitor model (for EMR from the cracking of compressed ice), in which a charged parallel plate capacitor is created whose plates (crack sides) are being drawn apart. After an initial charge is formed on the crack surfaces, further separation should result in a decrease of capacitance and an increase of the voltage across the crack. A space/time analysis of the emanating radiation can be carried out using the diffusion equation for the electric field in the crack. Although it proved possible to simulate the time decay of the EMR, no oscillatory behavior was predicted. O'Keefe and Thiel (1995) also considered the many routes by which the net charge could be created, i.e., pre-polarization of the material or applied physical gradients due to piezoelectricity or pseudo-piezoelectricity, temperature, deformation, impurity concentration gradient effects, etc. Petrenko

(1993) claimed that the electrification of crack sides could be caused by the surrounding non-homogeneous elastic strains, and Ogawa et al. (1985) assumed that crack side electrification was due to piezoelectrification and to contact (or separating) electrification.

However there are problems with this scenario.

1. In this model the EMR is assumed to be caused by an accelerated dipole created by charged crack sides. This assumption implies that the EMR can arise only from tensile cracks and not from shear ones. In contrast, our measurements of chalk under uniaxial and triaxial compression (Frid et al. 2000) showed that the EMR amplitude is independent of crack mode, tensile or shear and is related only to the entire area of the crack (see Sect. 5.3.3).
2. The capacitor model implies a correspondence between EMR and acoustic emission (AE) signal appearance. However, our own measurements and those of Yamada et al. (1989) show that although there are failure events for which AE and EMR signals are measured together (e.g., Rabinovitch et al. 1995), there do exist events for which AE is detected while EMR is absent and events for which EMR is observed while AE is completely missing. These results therefore disagree with the capacitor model. Note that the last discord between AE and EMR signal appearance is probably due to the difference of mechanisms leading to the two types of radiation and is not yet completely understood.

   In addition, the general no "symmetry breaking" argument mentioned above evidently applies here as well.
3. Even under the assumptions that the two crack sides could be charged in a charge mosaic manner (Finkel et al. 1975), thus retaining an overall charge neutrality and that the EMR was induced by the dipoles consisting of pairs of oppositely charged mosaic "elements" on the two crack sides, the EMR induced by the moving crack would be expected to be very weak due to the cancellation of the radiation originating from mutually oscillating oppositely charged dipoles (random distribution of the mosaic elements).

5.4.5 Summary of the New Model and its Properties

The suggested model of EMR origin can be described as follows: Following the breaking of bonds, the atoms on both sides of the severed bonds are moved to "non equilibrium" positions relative to their steady state ones, and oscillate around them. Lines of oscillating atoms move together, and by being connected to atoms around them (in the forward direction and also atoms on their side of the two surfaces newly created by the fracture), the latter also participate in the movement. The larger the number of cut bonds, the larger is the number of excited atoms, and hence the greater becomes the EMR amplitude. These oscillations behave like surface vibrational optical waves, where positive charges move together in a diametrically opposite phase to the negative ones and decay exponentially into the material like Rayleigh waves. The resulting oscillating electric dipole is the source of the EMR. The pulse amplitude decays by an interaction with bulk phonons.

Our model does not suffer from the defects of the former ones since

1. No dislocations are included in the model, and therefore it can be applied also to brittle and amorphic materials. EMR frequencies obtained experimentally do agree with those of the surface vibrational optical wave (SVOW) model.
2. The spectrum of the SVOW is definitely not of a white noise type. Moreover, it is in line with given in Eq. 5.1 and the measured ones (see, e.g., Fig. 5.24b). In particular the peak frequency depends on crack width according to Eq. 5.7.
3. Note that no symmetry breaking mechanism appears in the SVOW model.
4. Our model is applicable to shear, tensile and even mixed modes of fracture.
5. The exact correlation between AE and EMR predicted by the "capacitor" model is not always found experimentally. No such correlation arises in the SVOW model.
6. Charge neutrality is assured here via a different mechanism ("optical" oscillations). Therefore no cancellation is expected.

5.5 EMR Pulses Induced by Rock Fracture

5.5.1 Previous EMR Pulse Investigations

All previous investigations considered EMR activity (number of EMR pulses) or EMR amplitude (intensity). Several investigators tried to measure EMR signals in different materials: Metals, glasses, ionic crystals and different rocks.

Misra (1975) investigated EMR induced in samples of carbon steel, aluminum, brass, zinc, and lead under tensile loads. The scheme of Misra's experimental arrangement is shown in Fig. 5.25.

Samples were 9 mm in diameter and 160 mm in length. An EMR sensor (a co-axial semi-cylindrically curved foil 27 mm in internal diameter, 50 mm in length and 0.3 mm in thick-

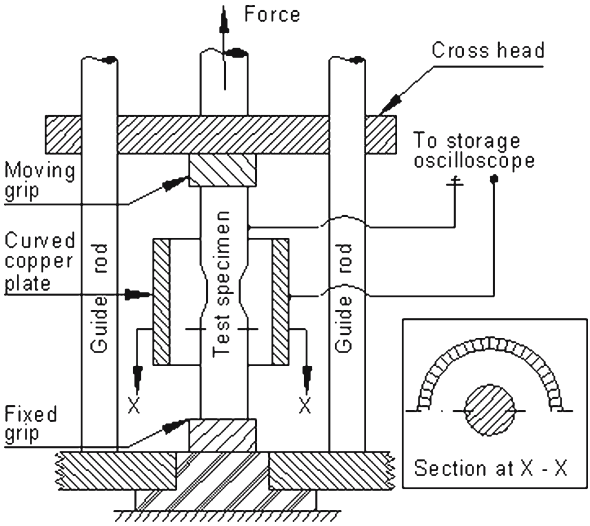

Fig. 5.25. Schematic diagram of the Misra (1975) experimental arrangement

ness) was placed near the fracture zone. EMR signals were passed through an amplifier operating at a frequency of 30 MHz (with a frequency band of 0.7 MHz) and were picked up by a storage oscilloscope. Figure 5.26 shows four examples of EMR signals observed during fracture of samples of carbon steel *(a)*, aluminium *(b)*, brass *(c)*, and zinc *(d)*. EMR signals from different materials were similar in shape but varied in their amplitude.

Jagasivamani and Iyer (1988) also noted that heat-treated high carbon spring steels subjected to tensile loadings emitted EMR during fracture. Figure 5.27 shows an example of EMR bursts measured by Jagasivamani and Iyer (1988).

It was found that the bulk of the EMR energy was in the range of 200 Hz to 10 kHz.

Nitsan (1977) investigated EMR signals induced by the fracture of quatrz-bearing rocks (several different granites, granodiorites, sandstones and quartzites) and single crystals of quartz and tourmaline. Materials were fractured under uniaxial loads between two parallel flat plates or by a small metal ball against a flat surface. The EMR signals were measured by a radio-frequency coil, the effective bandwidth of which was 1–10 MHz. Figure 5.28 shows an example of such EMR pulses observed by Nitsan

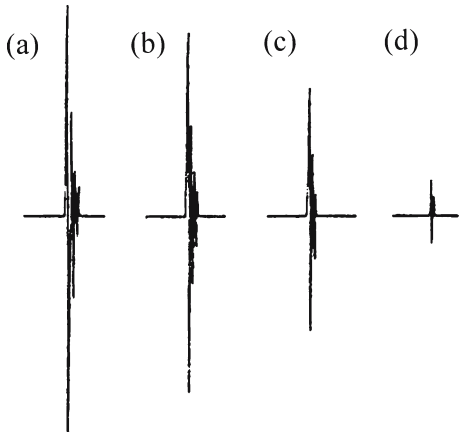

Fig. 5.26.
Four examples of EMR signals observed during fracture of samples of **a** carbon steel, **b** aluminium, **c** brass and **d** zinc (Misra 1975)

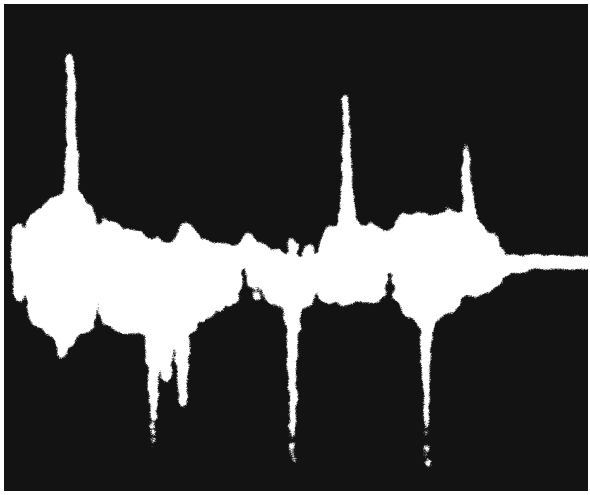

Fig. 5.27.
An example of EMR signals measured by Jagasivamani and Iyer (1988)

(1977). He noted that small cracks induced in quartz and tourmaline crystals were followed by short radio frequency signals with an approximately exponential decay with a time constants of about 10^{-5} s for quartz (Fig. 5.28a) and about half of this time for tourmaline (Fig. 5.28b). Figure 5.28c shows a radio-frequency signal with a more complex shape. This signal was excited by the fracture of a sandstone sample.

Miroshnichencko and Kuksenko (1980) investigated EMR pulses irradiated by ionic crystals, glasses and different rocks during fracture. They detected EMR by an inductance coil of 100 kHz resonance frequency and low Q factor ($Q = 2$). An example of EMR signals induced in diabase is shown in Fig. 5.29.

This signal was induced by a crack of 1 mm in length. Assuming that the creation of the crack took time that was equal to the duration of the first "pulse" namely was 1 μs, Miroshnichencko and Kuksenko (1980) found that the average crack growth velocity was about 1 000 m s^{-1}, which was about one-third of the velocity of sound in this material.

Yamada et al. (1989) observed EMR and acoustic emission during the entire deformation of a rock using a standard uniaxial deformation tests at a constant strain rate of 10^{-6} s^{-1}on cylindrical cores of Indian granites 25 mm in diameter and 62.5 mm in length. In the first experiment, they used five acoustic sensors to detect acoustic emission and one coil antenna to observe EMR. In the second experiment, one acoustic transducer and five coil antennas were used. The EMR antennas consisted of a coil of 20–40 turns of enameled copper wire 0.2 mm in diameter. The coil antennas were tuned in rather narrow bands. Figure 5.30 shows the overall frequency response of the experimental system (Yamada et al. 1989).

An example of Yamada et al. results is shown in Fig. 5.31. They claimed that their EMR signals were associated with cracks of 1–100 μm length. Note that the shape of Yamada et al. (1989) signals is similar to the ones observed by Nitsan (1977) for polycrystaline rocks (Fig. 5.28c).

Ivanov et al. (1990) investigated EMR pulses induced in rock samples from the Konstatinov, Saralin and Tashtagol ore deposits. All samples were investigated under uniaxial compression with different strain rates (10^{-4}–10^{-7} m s^{-1}). The initial signals were detected by a capacitance antenna (copper foil placed at the sample faces), trans-

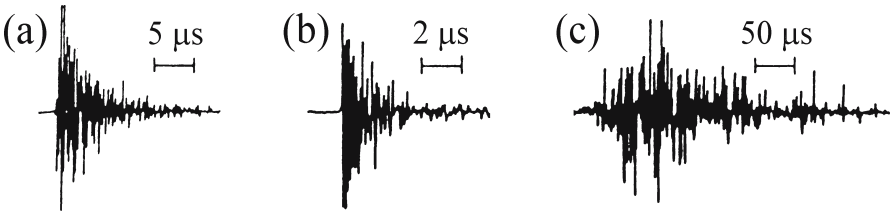

Fig. 5.28. Three examples of EMR pulses observed by the Nitsan (1977): **a** quartz, **b** tourmaline, **c** sandstone

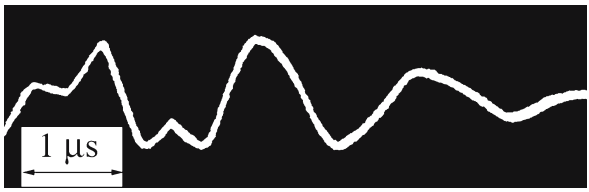

Fig. 5.29. An example of EMR signals induced in diabase (Miroshnichencko and Kuksenko (1980)

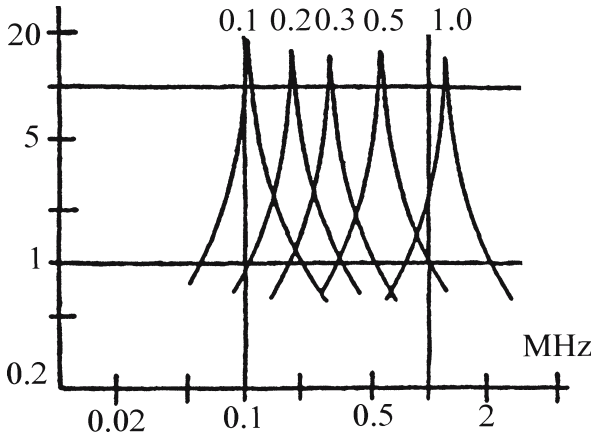

Fig. 5.30.
The overall frequency response of the experimental system (Yamada et al. 1989)

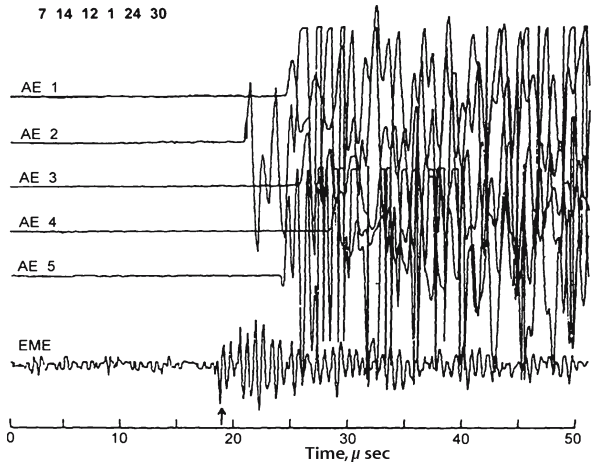

Fig. 5.31.
An example of EMR and AE signals observed by Yamada et al. (1989)

formed by an amplifier and a filter block and stored by a storage oscilloscope, from which screen they were photographed. The filter block consisted of a high frequency filter, which had ten fixed cut-off frequencies: 300 Hz, 1, 3, 10, 30, 100 and 300 kHz, and 1 and 10 MHz. The low-pass filter had seven fixed frequencies: 300 Hz, 1, 3, 10, 30, 100 and 300 kHz. An optimal working frequency band was selected by this filter and henceforth enabled the improvement of the signal / noise ratio. A total of 140 rock samples were studied. Figure 5.32 shows two examples of EMR signals observed by Ivanov et al. (1990).

These authors linked the rise-time of the pulse front with the crack propagation time and the decay time with a charge relaxation process.

Frid (1990) investigated EMR signals during stiff uniaxial compression. He examined rocks from Khibin Deposit (Kola Peninsula), Ural bauxite mines, Shpitzbergen and North Kuzbass coal deposits. EMR was detected by a narrow band resonance antenna (resonance frequency of 100 kHz and a Q factor of 2), passed through a 30 dB narrow band amplifier and stored by a storage oscilloscope, from the screen of which signals were photographed. Figure 5.33 shows an example of an EMR pulse obtained in this investigation.

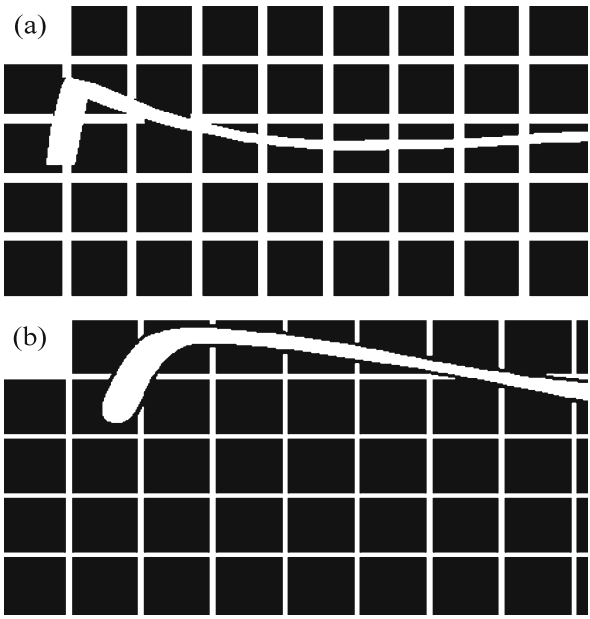

Fig. 5.32.
Two examples of EMR signals observed by Ivanov et al. (1990) induced by gabbrodiorite fracture: **a** horizontal scale 20 μs / division, vertical scale 1 V / division, crack length 2.5 cm; **b** horizontal scale 2 μs / division, vertical scale 20 mV / division, crack length 3.5 mm

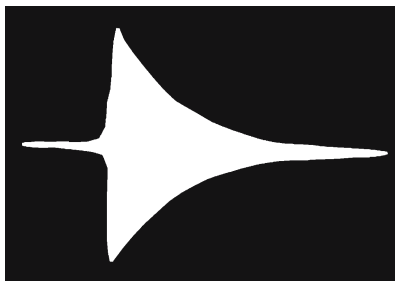

Fig. 5.33.
Typical EMR pulse measured by Frid (1990) during rock fracture

The shapes of signals from all investigated rocks were shown to be similar, whereas amplitudes and decay times were different. Note that the shapes of the EMR signals here are similar to those observed by Nitsan (1977) for a mono-crystalline material (Fig. 5.28a–c).

O'Keefe and Thiel (1995) performed EMR measurements on samples of dimensions $100 \times 100 \times 100$ mm. A schematic illustration of their experimental arrangement is shown in Fig. 5.34. The samples were stressed by uniaxial compression. The signals were detected by a 100 mm dipole antenna placed 100 mm from the sample. The signal was passed through an amplifier (54 dB) and an anti-alias filter (cut-off 160 kHz) and was connected to a PC, where signals were digitized and saved.

The digitization rate was 500 ks s^{-1}. An example of the electric signals observed by O'Keefe and Thiel (1995) is shown in Fig. 5.35.

It is seen that this signal is very similar to those obtained by Ivanov et al. (1990) (Fig. 5.32).

An analysis of all of these results shows that the EMR pulses consist of a rising part and a falling part. The majority of cases also show oscillations under the whole rising and fall-

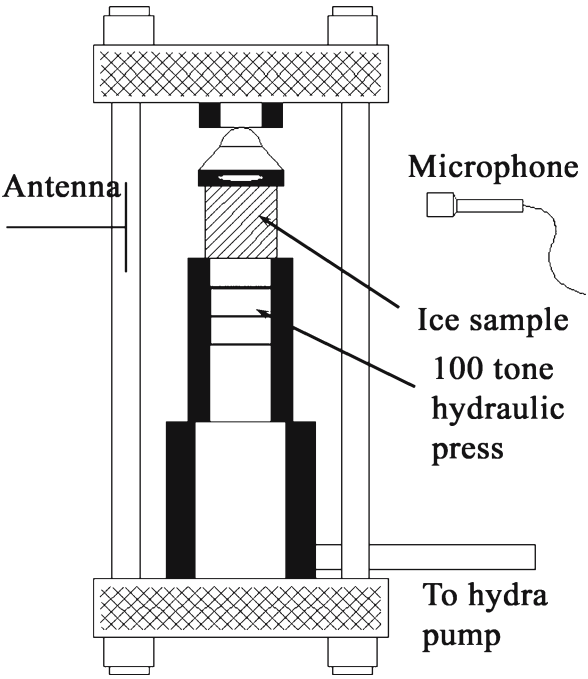

Fig. 5.34.
A schematic experimental arrangement of O'Keefe and Thiel (1995)

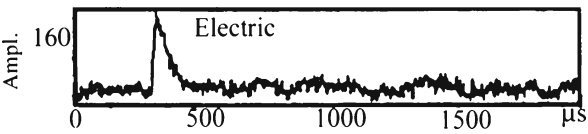

Fig. 5.35.
An example of electric signals observed by O'Keefe and Thiel (1995)

ing envelope. However, these investigations were conducted under different conditions and most of them with the help of a narrow band antenna, which makes a quantitative comparison between them very hard. Moreover, the shape of the signals depends to a large extent on the digitization rate, and the latter must be significantly higher than the 500 ks s^{-1} used, e.g., by O'Keefe and Thiel (1995) in order to obtain an accurate picture.

5.5.2
Our EMR Pulse Classifications

Our investigations (Rabinovitch et al. 1996) showed that

1. EMR pulses appear in two main different forms: "Lengthy" (total duration 30–110 μs and up to 400 μs, e.g., Fig. 5.11) and "short" (0.5–6 μs, e.g., Fig. 5.10a).
2. An analysis of the EMR pulses emanating during uniaxial failure showed that the deformation process can be divided into three zones according to the EMR features (Fig. 5.36, Rabinovitch et al. 1996):
   Zone I: Of individual EMR pulses;
   Zone II: Of EMR pulses with an uneven shape and/or groups of pulses;
   Zone III: Of lengthy EMR pulses.

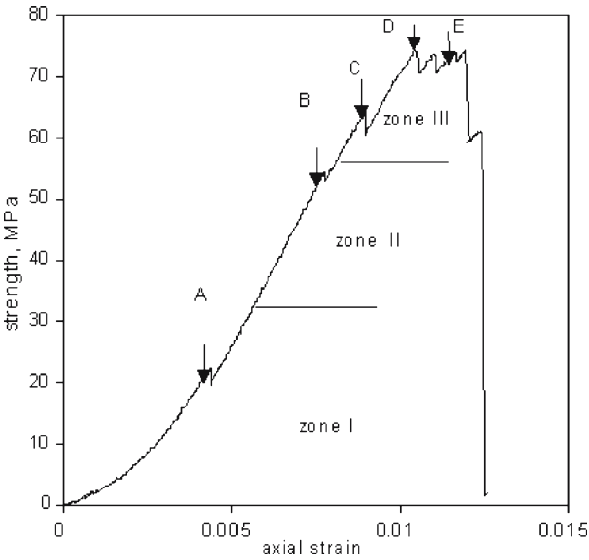

Fig. 5.36.
Stress-strain curve of rhyolite sample. *Arrows* on the graph show moment of EMR pulse excitations. Zone I is defined by individual pulses; zone II is characterized by pulses with uneven shape and/or groups of pulses; zone III shows particularly lengthy pulses (see elaboration of *arrows* (*a*–*e*) significance in Rabinovitch et al. 1996)

3. In the beginning of the deformation individual pulses occurred, while at the upper part of the elastic zone the shape of the EMR events became more complex indicating a superposition of individual pulses (sequences), with internal interpulse spacing of less than 3 μs. The interval between sequences was 40–80 μs.

Lengthy EMR pulses were registered immediately before and at the peak zone.

These results indicate a correlation between the EMR shapes and the failure stages. Thus, individual short pulses (zone I) seem to be correlated with the stage of individual microcrack formation, multi-pulse sequences (zone II) can be correlated with the crack coalescence stage, and the lengthy pulses (zone III) can be correlated with the sample faulting.

5.6 EMR and Material Elasticity

Gol'd et al. (1975) found differences in activity of EMR emanating from different materials in a row of materials investigated under uniaxial compression. Materials were ordered (from "high" to "low") according to the number of EMR signals registered during cracking as follows: Quartz, orthoclase, plagioclase, granites, sandstones, and metamorphosed aleurolites. They noted that a decrease of the number of EMR signals could be due to a decrease of rock/mineral hardness (i.e., elasticity) from quartz via granites to metamorphosed aleurolites. Khatiashvili (1984) investigated EMR induced by splitting of LiF, NaCl, KCL and $CaCO_3$ crystals. He showed that EMR frequency spectra are specific for each crystal (Fig. 5.37a). The spectra differ in the positions and widths of the radiation bands. He also observed that the intensity (amplitude) of the EMR induced by alkali halide crystal failure was proportional to the squares of the elastic moduli and the crack length (Fig. 5.37b). These investigations (Gol'd et al. 1975; Khatiashvili 1984) were carried out only under uniaxial loading.

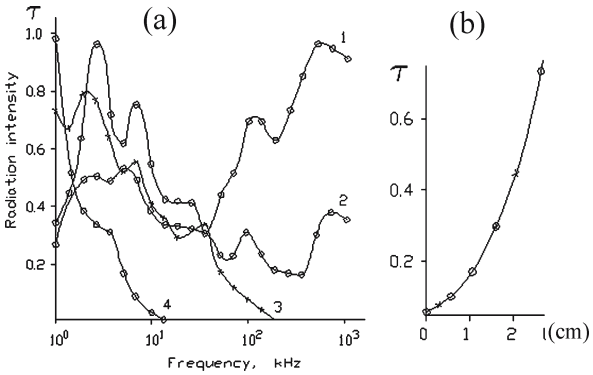

Fig. 5.37.
a EMR spectra from splitting 1-LiF; $0.1I = 1$ mV, 2-NaCl; $0.1I = 80$ μV, 3-KCl; $0.1I = 15$ V, 4-CaCO; $0.1I = 0.1$ mV; **b** EMR intensity as function of fracture length (Khatiashvili 1984)

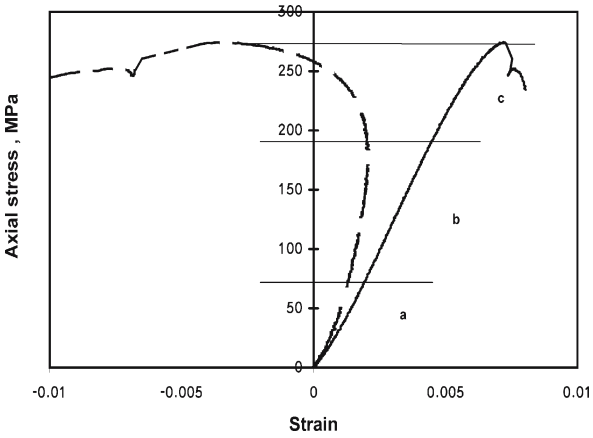

Fig. 5.38.
An example of granite triaxial deformation (confining pressure: 10 MPa); *a* the pore closure region (10 EMR pulses were measured); *b* the elastic region (6 EMR pulses were measured); *c* the nonlinear region before the peak stress (8 EMR pulses were measured); *unbroken line:* Axial strain, *dashed line:* Volumetric strain (Frid et al. 1999)

For our investigations, we used granite samples (see above). Each sample was tested by an axial strain rate of 1×10^{-5} s^{-1} and laterally by different hydrostatic oil pressures. The axial pressure varied from 110 MPa up to 284 MPa and the confining pressure from 0 to 14 MPa.

Figure 5.38 shows an example of a stress-strain curve of a representative granite sample (confining pressure 10 MPa). All rock samples went through the "normal" three deformation stages (Jaeger and Cook 1979) during compression up to the peak stress: *a* the nonlinear region of pore closure (axial strain curve here is slightly bent down, *b* the elastic region (the stress-strain curves are quasi linear), and *c* the nonlinear region before the peak stress.

As seen from the Mohr-Coulomb diagram (Fig. 5.39), the increase of confining pressure from 10 MPa (third circle) to 14 MPa (fifth circle) is not accompanied by an appreciable increase of shear strength (the Mohr-Coulomb envelope becomes much less steep than for smaller confining pressures).

Since, the confining pressure does not cover a wide range of pressures, the ductility stage has not yet been completely reached. However, the failure plane inclination to the axial load axis was measured to be 41 ±1°. Thus, our results are reasonably close to obeying the von Mises ductile failure criteria.

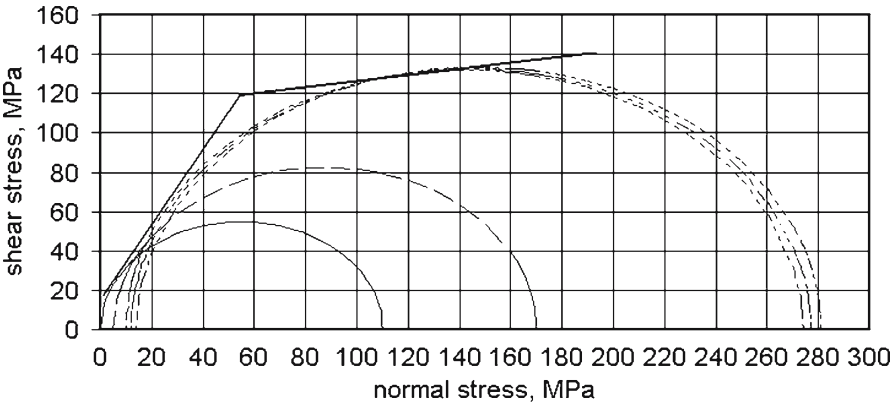

Fig. 5.39. Two stages of the failure envelope (*thick line*) around Mohr circles which represent the different confining pressures, —— uniaxial test, — — — 5 MPa confining pressure, - - - 10 MPa confining pressure, — — — 12 MPa confining pressure, — - - - 14 MPa confining pressure (Frid et al. 1999)

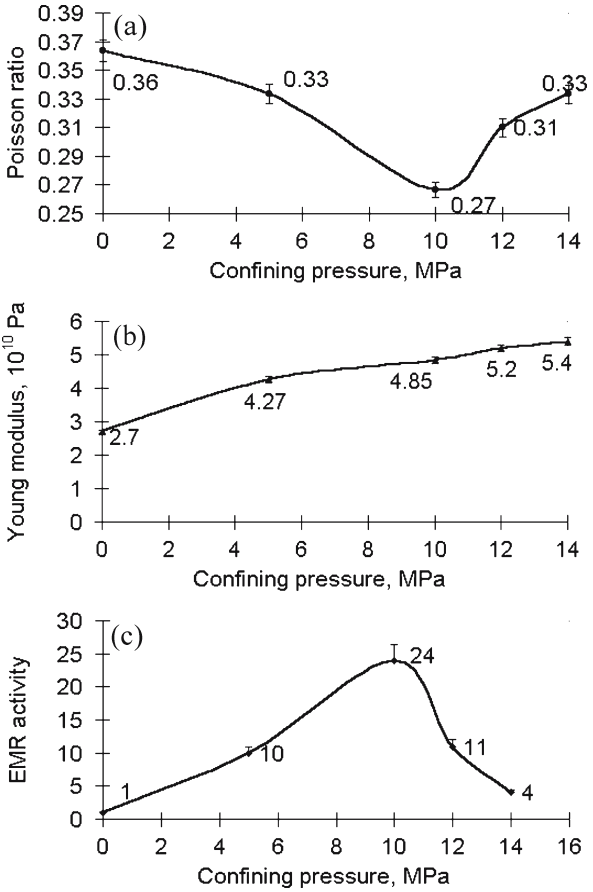

Fig. 5.40. Relationship of the following characteristics with confining pressure: **a** Poisson ratio; **b** Young's modulus; **c** EMR activity. *Error bars* on these figures are determined by the accuracy limits of our rock mechanics equipment; that is ±2% for Poisson ratio and Young's modulus and by the dead time of the storage oscilloscope-IBM PC system (the period it takes for registration, digitizing and memorizing an EMR sequence, during which time the system is shut down. The error in EMR activity is of the order of +2% (Frid et al. 1999)

We denote here the EMR activity as the number of individual EMR pulses emitted during tracing of the entire stress-strain curve. Its value is seen to change with the loading type (Fig. 5.40c), increasing first with the confining pressure and then decreasing again.

We checked the following stress-strain characteristics to investigate possible correlations with EMR activity: Axial strain and its increment; confining pressure; deformation modulus (ratio of axial stress increment to rise of axial strain – the secant modulus) and its absolute value); differential stress; differential volumetric compression work (product of differential stress increment and volumetric strain changes) and its absolute value; elastic strain work (product of average differential stress and elastic volumetric strain changes); elastic volumetric strain (part of volumetric strain that returns to its original value after applied stresses are removed); lateral deformation modulus (ratio of axial deformation increment to rise of lateral deformation – the secant lateral modulus) and its absolute value; maximal stress; Poisson ratio (ratio of lateral elastic deformation to an axial elastic one, measured in the elastic zone of deformation); residual axial strain (remaining axial deformation after removal of external stress); residual strain work (strain work minus elastic work); residual volumetric strain (remaining value of the sum of the three principal strains after removal of external stress) and its absolute value; strain work (product of average differential stress and volumetric strain changes) and its absolute value; volumetric strain (sum of the three principal strains) and its absolute value; Young's modulus (ratio of axial stress increment to rise of elastic axial strain, measured in the elastic zone of deformation).

Note that these stress-strain characteristics can be classified as either "elastic" or "general". For example, the Poisson ratio and the Young modulus are defined here as elastic characteristics and measured in the elastic zone only. Lateral deformation modulus and deformation modulus, on the other hand, are similar in definition to the Poisson ratio and Young modulus, respectively, but they are "general" characteristics: They can change during a loading process.

Our analysis shows that out of all these stress-strain characteristics the Poisson ratio is the *only* one that shows good correlation with EMR activity. The Poisson ratio (Fig. 5.40a) changed from 0.36 (for uniaxial test) via 0.27 for 10 MPa confining pressure to 0.33 for 14 MPa confining pressure. Its squared regression coefficient was –0.93. An increase of the Poisson ratio (Fig. 5.40a) is accompanied by a decrease of EMR activity (Fig. 5.40c) and vice versa. Note that since all samples here are made of the same material (granite), the Poisson ratio varies only with loading conditions, and does not vary with material properties, on the other hand e.g. the Young's modulus (Fig. 5.40b) increases monotonically from 27 GPa to 48.5 GPa with the confining pressure, and therefore it is obvious that its correlation with EMR activity should be poor (the obtained squared regression coefficient was actually 0.18).

The result of a poor correlation between Young's modulus and EMR activity is different from that found previously (Gol'd et al. 1975; Khatiashvili 1984) in which an increase of Young's modulus of a material was associated with an increase in EMR activity. In the previous experiments, however, the correlation between Young's modulus and EMR activity was investigated only under uniaxial compression. Our loading conditions were different. We studied changes of EMR activity during the transition

from tensional fracture (uniaxial test) via brittle shear fracture according to the Coulomb criterion, to shear fracture in the brittle-ductile region under an increase of confining pressure (see, for example, Twiss and Moores 1992, Fig. 9.9). As noted by Jaeger and Cook (1979), Young's modulus increases with the confining pressure, while the Poisson ratio could both decrease and increase. We suggest that our sample deformed with the confining pressure as follows: An increase of the confining pressure from 0 to 10 MPa closed granite microcracks and hence the Poisson ratio was decreased to its intrinsic value of a material devoid of openings. Under a greater confining pressure (12–14 MPa), however, the deformation changed from a brittle to a ductile one causing an increase of Poison ratio. The brittle-ductile transition is confirmed by the large angle (41 ±1°) produced between the axial load and the failure plane and in the insignificant increase of shear strength (Fig. 5.39). Correspondingly during the brittle deformation, EMR activity increased with confining pressure while in the brittle-ductile region EMR activity decreased.

The correlation (or rather anti-correlation) of EMR activity with the Poisson ratio seems plausible. The Poisson ratio measures the compliance of the material in the transverse direction when stressed axially. The lower the Poisson ratio, the harder it is for the material to strain transversally, and hence the higher is the probability of new fractures (especially parallel to the axis) and of the ensuing EMR. On the other hand, the higher the Poisson ratio the easier it is for the material to strain transversally, and accordingly, fewer fractures and lower EMR activity should be expected. The key elastic parameter for EMR characterization during triaxial compression is therefore the Poisson ratio and not the Young's modulus. Note that our results are in line with those of Gol'd et al. (1975) and Khatiashvili (1984) for uniaxial load. Our results, however, being triaxial, do show the correct global parameter to choose. They also indicate that the EMR activity correlates well with the lateral resistance to axial fracture, which is compensated by an increase in the number of new cracks.

5.7 EMR during Percussion Drilling

Recently, Rossmanith et al. (1996, 1997) carried out experimental and numerical investigations in order to understand the mechanism of material damage under percussion drilling. They found that the stress applied during drilling, besides inducing elastic waves emission, also resulted in defect creation: Every time a percussion occurs, existing defects grow, microcracks are formed and propagate, and a "damage zone" around the drilling tip is thus created (Rossmanith et al. 1996, 1997), a zone consisting of a network of many small and a few larger cracks. Another observed defect consists of circumferential cracks around the hole and appears when weak regions exist in the material (Ravishankar and Murthy 2000).

Since fracturing also emits EMR, we discuss here an investigation of the EMR emitted from fractures that develop during percussion drilling.

We used cylindrical samples 100 mm in length and 30 mm in diameter (Fig. 5.41) that were percussion drilled. Drilling was carried out at about the mid length of the cylinder, perpendicular to the cylinder axis. EMR was measured in the frequency range 1 kHz to 50 MHz with 1 μV sensitivity throughout. Radiation was detected by a one-

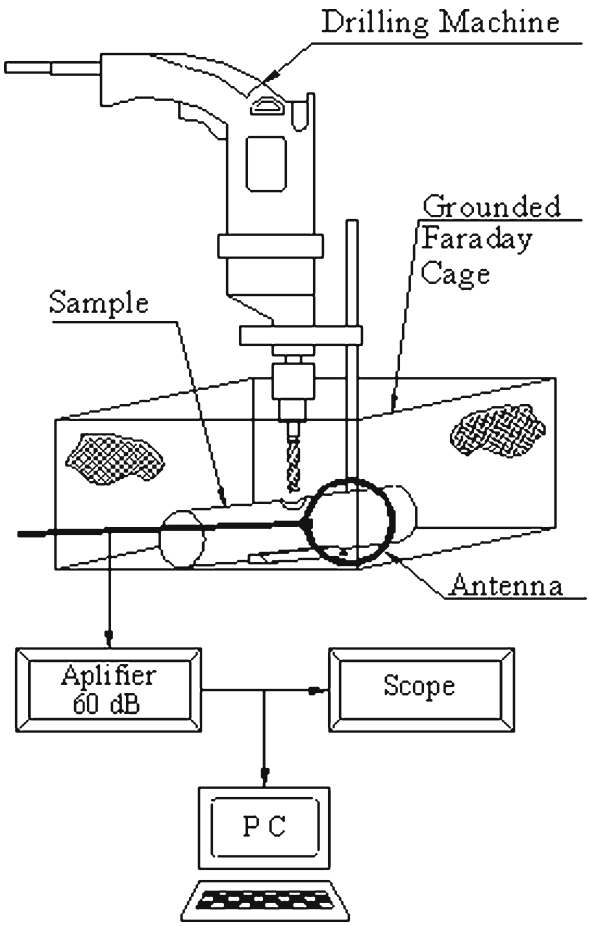

Fig. 5.41.
Schematic diagram of experimental arrangement during drilling (Goldbaum et al. 2001)

loop magnetic antenna 3 cm in diameter, which is electrically "small" and exhibits negligible response to foreign electric fields. The antenna was placed at a distance of 3 cm from the drilling hole. External EMR disturbances were further decreased by the two following methods:

1. The sample together with the antenna were placed in a grounded Faraday cage.
2. The plane of the antenna was aligned perpendicular to the drilling direction, so that the influence of electromagnetic disturbances emitted by the motor of the drilling machine was minimized.

All EMR signals were electrically amplified by 60 dB, digitized and collected at a PC hard disk. The data was analyzed after test completion.

The materials used in the study were chalk from Middle Eocene layers in the Beer Sheva syncline, Eilat granite from the Nahal Shelomo area of southern Israel (Rabinovitch et al. 1999b), Solenhofen limestone from Germany, PMMA and soda-lime glass.

The 700-odd EMR signals measured during percussion drilling of all five materials were classified into four groups:

1. The first group: "Short single pulses" of 0.3–1.5 μs duration.
2. The second group: "Short chain of single pulses" of 2–15 μs duration.
3. The third group: "Extended chain of pulses" of 15–60 μs duration.
4. The fourth group: "Pulses on top of base-line voltage changes" whose duration varies between 10 and 800 μs.

Pulses of the first group (Fig. 5.42a) probably correspond to single cracks and are characterized by a single main frequency ranging between 10 and 25 MHz. It means (Eq. 5.7) that the corresponding cracks are very small, and indeed their T'/ω values (Eq. 5.8) indicate that they range in area from 0.005 mm^2 up to about 0.05 mm^2. Pulses of the second group (Fig. 5.42b) consist of several pulses of the first group type and probably correspond to several overlapping small cracks. Their frequency spectrum is thus a bit more complicated. Pulses of the third group consist of numerous pulses of the first two groups (Fig. 5.42c). Hence, their frequency spectrum shows a broad band (11–23 MHz). These pulses are probably emitted by tiny "powdered" particles fragmented from the walls of the drilled hole, where each particle has its own size and emits its own frequency. Note that like that of the first group, the area of the "powder" particles here ranges from 0.005 mm^2 up to about 0.05 mm^2.

Signals of the fourth group (Fig. 5.42d) (never seen in the compression experiments) show baseline voltage changes with very low frequencies of several kilohertz and in addition contain lengthy groups of the third type. Cracks emitting such radiation should range in area from 1 cm^2 up to 16 cm^2. The additional presence of the third group pulses indicates that "powder" is simultaneously created.

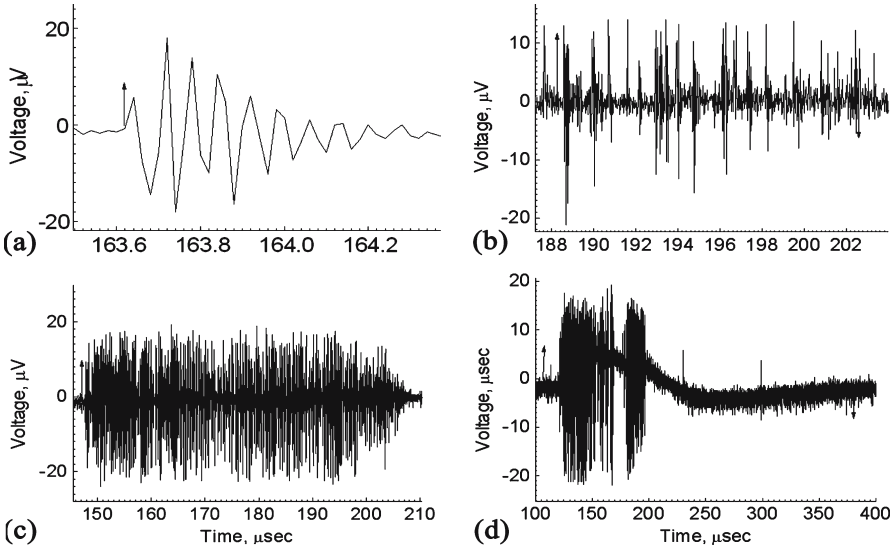

Fig. 5.42. Experimental EMR pulses induced by percussion drilling of the first group (**a**), second group (**b**), third group (**c**) and forth group (**d**) (Goldbaum et al. 2001)

The first three group types have been observed in our compression experiments, where however single pulse frequencies never exceed 10 MHz (Rabinovitch et al. 2000c; Frid et al. 2000).

They provide a new method for a general identification by EMR profile of the wide population of "powdered" and "chipped" particles of various sizes that form by percussion drilling and a one to one identification of all the defects involved in the process. The fourth group is discussed next.

5.7.1 The 4th Group and Polarization

The fourth group includes two different subgroups (4a): "Lengthy forms" (e.g., Fig. 5.42d), whose duration varies between 10 and 800 μs and which show low frequencies (several kilohertz) baseline voltage changes and also contain high frequency third type pulses and (4b): A different type of "Lengthy forms" again decorated by high frequency strings (Fig. 5.42, 5.43).

Here we present the results of investigation of the 4a and 4b signal types (Goldbaum et al. 2001), where the "4" is dropped in following. The samples tested were cylinders of soda-lime glass, 10 cm in length and 3 cm in diameter that were percussion drilled. The experimental arrangement was described in Sect. 5.7.

Signals of groups a and b occurred in 5 glass samples (2, 3, 4, 5, 6). Group 'a' signals are similar to individual EMR pulses (Rabinovitch et al. 1998), but their frequencies are smaller (several kHz). Group 'b' signals (Fig. 5.43) consist of a sharp voltage "jump" (of a duration of ~3% of the whole pulse duration) and range in size between 6 and 12 μV; the high voltage remains more or less constant for a period that varies between 10 and 1 000 μs and is terminated by a rapid falloff (of about the same duration as that of the rise time). Group 'a' signals are frequently followed by group 'b' signals after a time interval of several hundreds of microseconds. This occurrence is denoted by "(a/b) pair". If a 'b' signal has not been detected within this time interval, then an 'a' or a 'b' signal appears after a time period ranging between 0.2 s and 2 s. Sometimes a string of several 'a' signals appears and is followed by a 'b' signal.

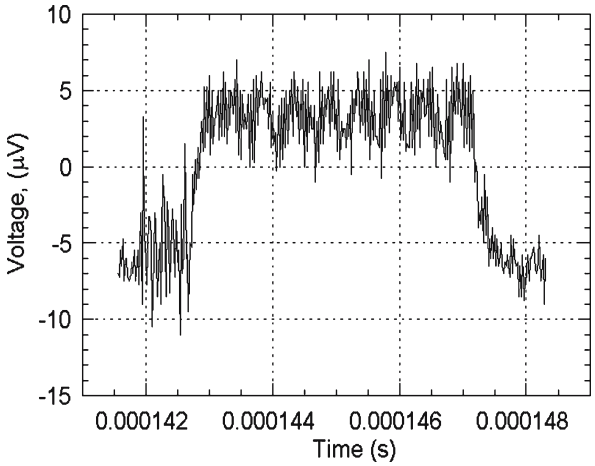

Fig. 5.43. Typical pulse of group 'b' (Rabinovitch et al. 2003b)

5.7.2
Fractographic Examination

Fractographic examination showed that in addition to glass powder and a network of small cracks (Rossmanith et al. 1997), some large "chips" were formed. These are large cracks, which originated at some depth and propagated until reaching the surface of the sample. Their observed fracture areas vary between 1 and 30 cm^2.

As shown in Goldbaum et al. (2001), the 'a' type pulses are excited by the creation of these flakes and the 'b' type pulses are derived from a polarization process, as shown presently.

5.7.3
Brief Theoretical Consideration

The measured quantity in our experiments is the electromotive force in the loop antenna, which is given by

$$V = -\frac{\mathrm{d}\Phi}{\mathrm{d}t}$$

the time derivative of the magnetic flux

$$\Phi = \int B\mathrm{d}S = BS$$

Here B is the magnetic field through the antenna and S is its (constant) area. Since $r/c = 10^{-10}$ s it can be neglected with regard to the apparatus sensitivity (2×10^{-8} s) in comparison and we have (Bleaney and Bleaney 1965):

$$\begin{aligned} B &= \frac{\mu_0 lI \sin\theta}{4\pi r^2} - \frac{\mu_0 l\dot{I} \sin\theta}{4\pi cr} \\ \frac{\mathrm{d}B}{\mathrm{d}t} &= \frac{\mu_0 l\dot{I} \sin\theta}{4\pi r^2} - \frac{\mu_0 l\ddot{I} \sin\theta}{4\pi cr} \end{aligned} \tag{5.10}$$

where μ_0 is the magnetic permeability, c is the speed of light, l is the length of the element in which current is present, r is the distance between the antenna and the current, $I = I(t)$ is the magnitude of the current, the angle θ is that created by the current direction and the radius-vector to the antenna relative to the current, and a dot denotes time differentiation. For EMR, the current is produced by the oscillating surface waves discussed in Sect. 5.2. Since our experiments were carried out in the so-called "short" zone, we can neglect the second terms in (Eqs. 5.10) and write

$$V = -S\frac{\mathrm{d}B}{\mathrm{d}t} = -\frac{S\mu_0 l \sin\theta}{4\pi}\frac{\dot{I}}{r^2} \tag{5.11}$$

Consider now a changing dipole $p(t)$ with a constant length l and changing charge $q(t)$, $p(t) = lq(t)$. The current (Bleaney and Bleaney 1965) is $I = \mathrm{d}q/\mathrm{d}t$, $lI = \mathrm{d}p/\mathrm{d}t$, and

$$l\dot{I} = \frac{\mathrm{d}^2 p}{\mathrm{d}t^2} = \ddot{p} \tag{5.12}$$

Thus, the electromotive force V in the antenna is proportional to the second derivative of the dipole moment:

$$V = -\frac{S\mu_0 \sin\theta}{4\pi r^2}\ddot{p} \tag{5.13}$$

If instead of a dipole moment one considers the sample's polarization P, which is defined as its dipole moment per unit volume, the electromotive force would be proportional to the second derivative of the polarization:

$$V = \frac{-\ddot{P}}{C} \tag{5.14}$$

Here $1/C > 0$ is the proportionality constant. The polarization current is given by the integral of (5.14):

$$\dot{P}(t) = \dot{P}_0 - \int_0^t CV(t')\mathrm{d}t' \tag{5.15}$$

where $\dot{P}_0$ is a constant, and the polarization P is given by the integral of (5.32):

$$P(t) = P_0 + \int_0^t \dot{P}(t')\,\mathrm{d}t' \tag{5.16}$$

5.7.4 Examination of 'b' Type Signals

We assume that the 'b' type signals (Fig. 5.43) originate by a change of material polarization (Eq. 5.14). By Eq. 5.15, the first integral of the signal should be proportional to $\dot{P}$, while the second integral should be proportional to the polarization (P) itself. This sequence is schematically shown in Fig. 5.44. A smoothed 'b'-like signal is shown in Fig. 5.44c, where units of amplitude and the time are evidently different from those of Fig. 5.43, but signal shape is preserved. The first and second integrals appear in Fig. 5.44b and 5.44a, respectively.

Ogawa et al. (1985) measured EMR from impacted materials using an electric sensor. Hence the signals obtained by them (see Fig. 2 and 3 of Ogawa et al. (1985), redrawn here as Fig. 5.45a and b) should be proportional to the depolarization current or to the first derivative of the polarization, and the time derivative of their signal (Fig. 5.45c) should be proportional to $\ddot{P}$.

Comparing the pulse shown in Ogawa et al. (Fig. 3 of Ogawa et al. 1985, redrawn here as Fig. 5.45b) with the integral of a 'b' pulse (Fig. 5.44b), it is clear that they are similar, indicating that both stem from a similar process, namely polarization changes. The shape of the polarization itself can be obtained by the appropriate integrals.

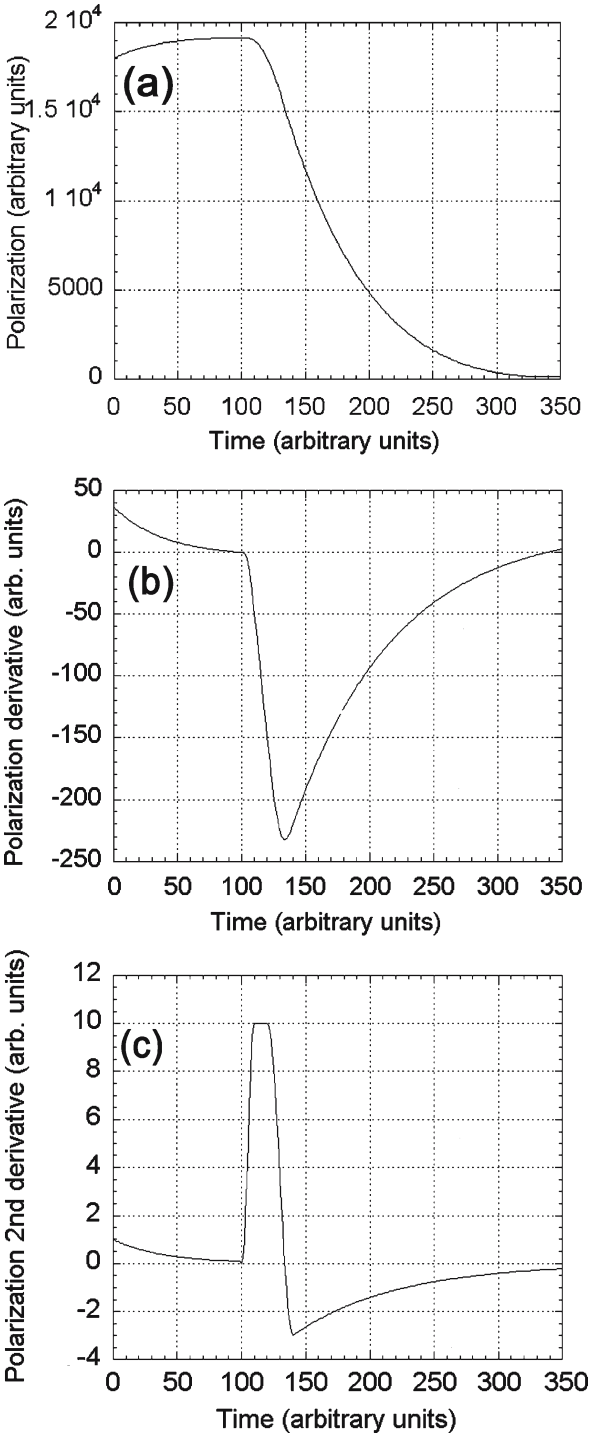

Fig. 5.44.
Schematic polarization accumulation and depolarization process: **a** polarization: *P*. Note: Only the final part of the polarization increase is shown. **b** First derivative of *P*, and **c** second derivative of *P*, as functions of time. Note the negative tail appearing in **c** (Rabinovitch et al. 2003b)

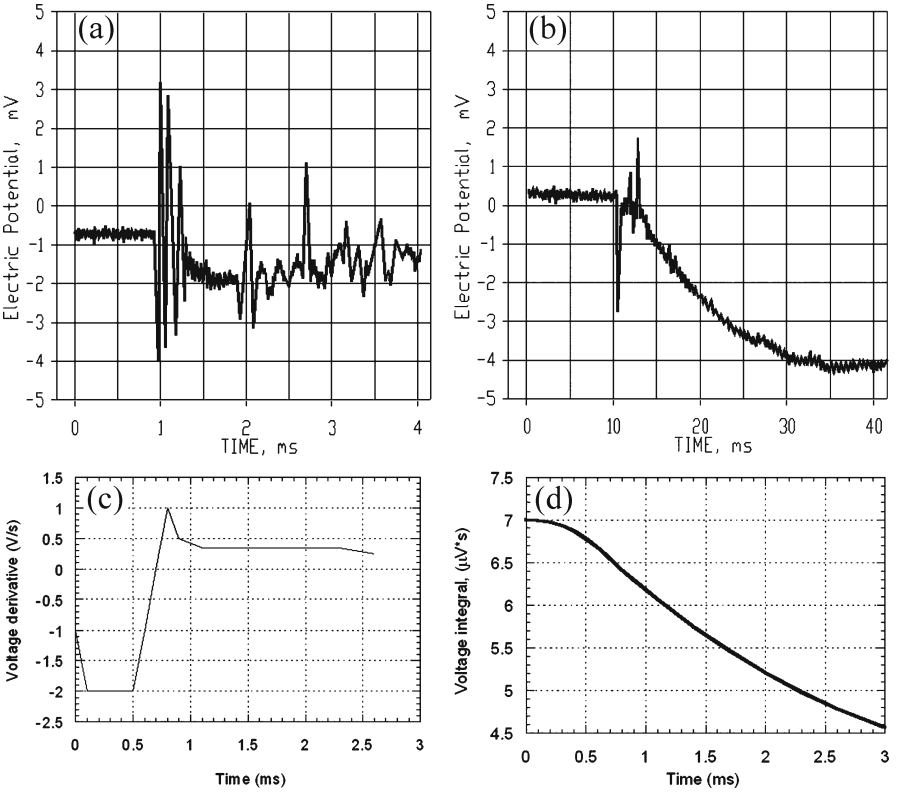

Fig. 5.45. Pulses obtained by Ogawa et al. (1985): **a** their Fig. 2, **b** their Fig. 3, **c** smoothed time derivative of 5.45a, and **d** the integral of 5.45a (Rabinovitch et al. 2003b)

5.7.5 The Polarization Model

The emerging picture of the process is as follows: During drilling a stress-strain field is slowly accumulated in the sample by numerous accumulated impacts (percussions), followed by an increase in polarization (Varotsos et al. 1999) (see Fig. 5.44a) for the final stage of this process). This accumulation of stress and polarization can take place only sufficiently ahead of the drill bit, since the region close to the latter is obviously reached by it, releasing the stress, before the latter grows sufficiently. During polarization increase, $\vec{p}$ is too small to be detected (Fig. 5.44c, the region up to $t = 100$). Note that electric polarization (i.e., the appearance of a dipole moment in a material) can be caused (Khesin et al. 1996, 1997; Rzhevskii and Novik 1978) by four basic processes: Electronic, ionic, dipolar and space charge polarization. Since relaxation times of the first three processes are less than 10^{-6} s and since measured relaxation times for glass polarization are of the order of 10 s (Kuksenko et al. 1990), the process here can only be due to space charge polarization.

Crack development begins when the accumulated stress becomes sufficiently large. Crack propagation (indicated in our measurement by an 'a' signal) is accompanied by stress relaxation, and the latter causes depolarization and an appearance of a 'b' signal.

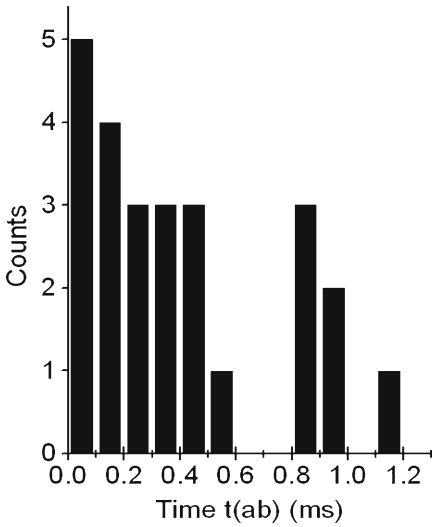

Fig. 5.46.
Distribution histogram of time lags between an 'a' and a following 'b' signal (Rabinovitch et al. 2003b)

Natural polarization relaxation in glass is very slow (see above) and can therefore be neglected. Here however polarization is relaxed by fracturing, and therefore the 'a' signals are followed by the 'b' signals, within a small time interval.

However, polarization does not fall off at once, because not all ions participating in the depolarization current begin their movement at the same moment: An ion begins to move when the acoustic waves excited by fracture reach it.

The time it takes a crack to travel through the entire sample whose size is 10 cm (with a velocity of 300 m s^{-1}, which is low but possible in glass) is 300 μs. We have registered thirty-three couples in which 'a' signals were followed by 'b' ones, and twelve of them have a time lag of less than 300 μs (Fig. 5.46). There are seven couples with a time difference between the 'a' and 'b' pulses of up to 600 μs. These longer times may be due to the fact that not all ions are situated along the way of the propagating crack. Some of them are placed at rather large distances from the crack, so stress relaxation must first reach a definite point on the crack route, and then be transferred by acoustic waves to the distant ions. For larger measured differences, it is assumed that there was an additional signal in between those observed that has not been detected by our equipment possibly because of a very small solid angle at the antenna.

Note that the spread in the histogram (Fig. 5.46) can also be due to another reason. To understand it, let us consider Fig. 5.47a and *b* that schematically show two examples of possible depolarization events. The calculated 'b' signals (second derivatives) (Fig. 5.47c,d) show that the second one (Fig. 5.47d) is shifted by ten time units with respect to the first one (Fig. 5.47c). This means that a negligibly small change in the depolarization shape may cause a significant shift in the 'b' signal origin, and hence to a spread of delay times between the 'a' and the 'b' signals.

Flake cracking induced by the drill bit thus leads to the measurement of a group 'a' and group 'b' signal. When cracking stops, stress relaxation and depolarization current increase also halt. Thus "immediate" depolarization can be incomplete, and some polarization could still remain in the material. The latter continues to decrease rather slowly to zero (Fig. 5.44a). Depolarization current (Fig. 5.44b) generally changes too slowly to

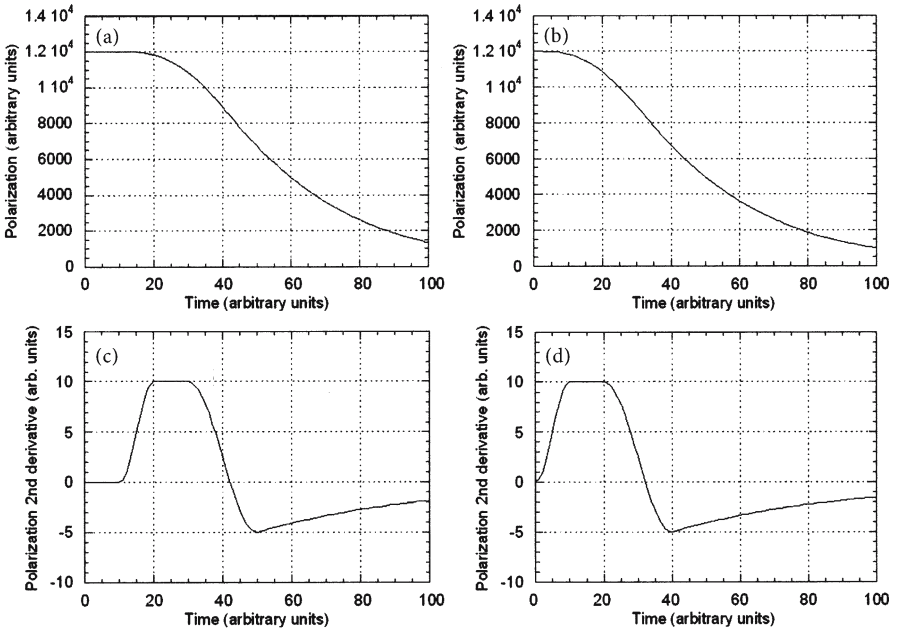

Fig. 5.47. (Schematic) Slight differences in depolarization shapes (**a**, **b**) can cause large shifts in the time lags between the observed signal pair (**c**, **d**) (Rabinovitch et al. 2003b)

give a measurable second derivative (Fig. 5.44c), but in some pulses a "tail" appears (Fig. 5.48a, arrow). Since measurements were carried out only up to 1.3×10^{-3} s, we artificially continued this "tail" (for the specific pulse of Fig. 5.48a) and evaluated its first and second integrals (Fig. 5.48b,c). Note that the derivative of the pulse obtained by Ogawa et al. (1985) (Fig. 5.45c) shows a similar "tail".

The estimated decay (relaxation) time for such a "tail" is several milliseconds, which is much shorter than the ~10 s natural relaxation times observed in glass (Kuksenko et al. 1990). This decay time decrease can be due to material heating. It was shown (Kuksenko et al. 1990) that the EMR pulse decay time decreases significantly with a rise of temperature. Measurements of temperature rise during fracture have been carried out for different materials yielding very high values. For instance, for PMMA the temperature increase was about 500 °C (Swallowe et al. 1986), while for glass it was ~840 °C for a 200 m s^{-1} crack velocity (Li et al. 1988).

Comparison of the general shape and value of the rise-fall times of group 'b' pulses enables us to assume that these pulses are excited by space-charge polarization (Rzhevskii and Novik 1978; Gueguen and Palciauskas 1994). The charge carriers causing polarization are probably the weakly pinned Na^+ ions (Kuksenko et al. 1990) of the glass. Hovestadt (1902) described a change in the position of temperature markers on a thermometer over time. A structural change in a silicate mineral (feldspar) at room temperature was ascribed to a Na^+ displacement under strain (Bahat 1968). These relatively heavy, weakly bound ions (Babcock 1977) can leave their equilibrium positions and move under stress, leading to polarization. When stress is removed or relaxed, these ions return to their equilibrium positions.

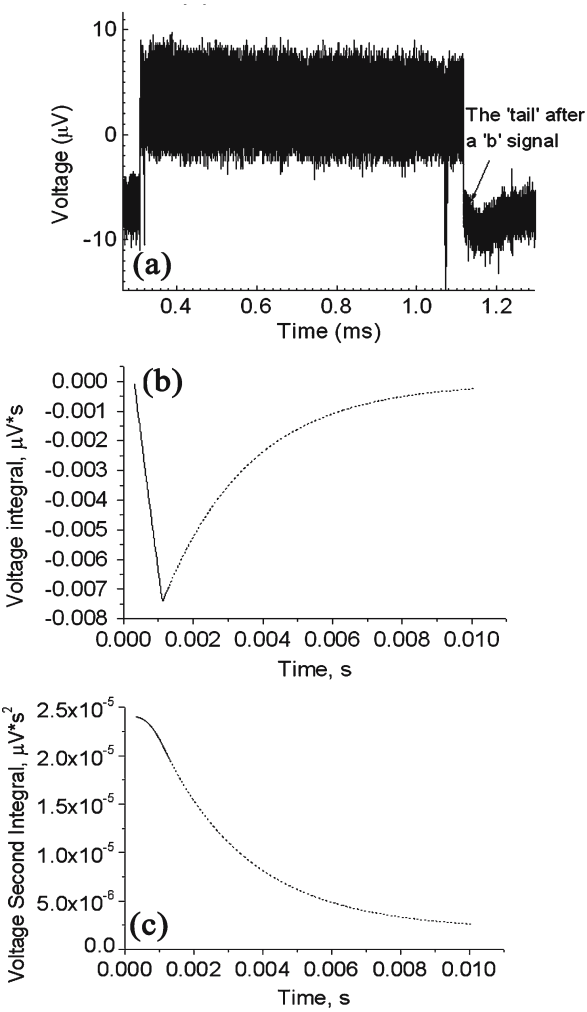

Fig. 5.48.
A 'b' type pulse with a clearly visible "tail" (*arrow*) (**a**), the first integral (**b**) and the second integral (**c**) of the extended pulse (see text) (Rabinovitch et al. 2003b)

One remark is in order. The high frequency "decorations" of both the 'a' and the 'b' signals are evidently due to the powder and small cracks generated by the drill simultaneously with the flaking and depolarization process discussed here.

The flake creation process itself is accompanied by an 'a' pulse, while the depolarization process is accompanied by a 'b' signal. The latter, being fast enough, is registered by our equipment. The flake/depolarization pairs should occur in a cyclic manner, since following depolarization it takes some time for a repolarization process ahead of the drill bit to reoccur. Hence also the emission of 'a'/'b' signals should be cyclic and not continuous. However, since following the first 'a'/'b' pair creation the stress does not fall off to zero, it should take less time for the stress to increase to the critical value than the time to build up the first 'b' pulse. This phenomenon was actually observed as a gradual decrease in the time periods between 'a'/'b' pairs.

5.8
Intermediate- and Large-Scale EMR Detection

5.8.1
Blasting Experiments

5.8.1.1
Experimental Arrangement and Results

Blasting experiments were carried out in Turonian age limestone in an open quarry near the village Omarim, located about 25 km north-east of Beer Sheva (Israel). Two blasts of 5 and 1.4 t of explosive material respectively were performed. In each blast, one slope of the quarry was exploded. The slopes are of a height of about 11 m and of length of about 100 and 20 m, respectively. A magnetic one-loop antenna (Electro-Metrics Penril Corporation) 0.5 m in diameter was used for the detection of the EMR. A low-noise micro-signal amplifier (Mitek Corporation Ltd, frequency range 10 kHz to 500 MHz, gain 60 ±0.5 dB, noise level 1.4 ±0.1 dB throughout) and an analog-to-digital converter connected to a triggered PC completed the detection equipment. We placed our magnetic antenna in front of the blasted slope at a distance of about 100 m from it (Fig. 5.49).

Figure 5.50 shows ~5% (in time) of the EMR-record that was observed during blasting. A detailed analysis of the EMR record shows that the main frequency of the observed pulses lies in the range 2–8 MHz, and that the intervals between individual pulses are of about 1–5 μs (Fig. 5.51). The shapes of individual pulses (Fig. 5.51) that were formed by a digital expansion of Fig. 5.50 are very similar to those observed during compression and drilling (Fig. 5.52a,b). Our analysis shows that it is only the entire durations of the EMR-records that were different. The durations of the EMR records from blasts were similar to those of the explosions themselves ~0.5 s for the more powerful blast (5 t) and ~0.3 s for the second one (1.4 t).

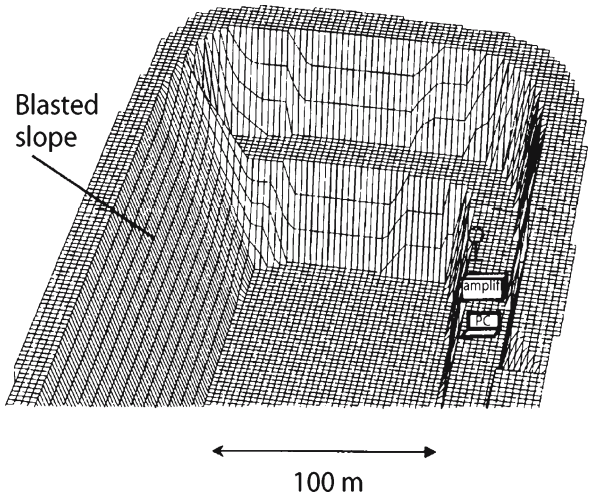

Fig. 5.49.
Schematic diagram of experimental arrangement during blasting

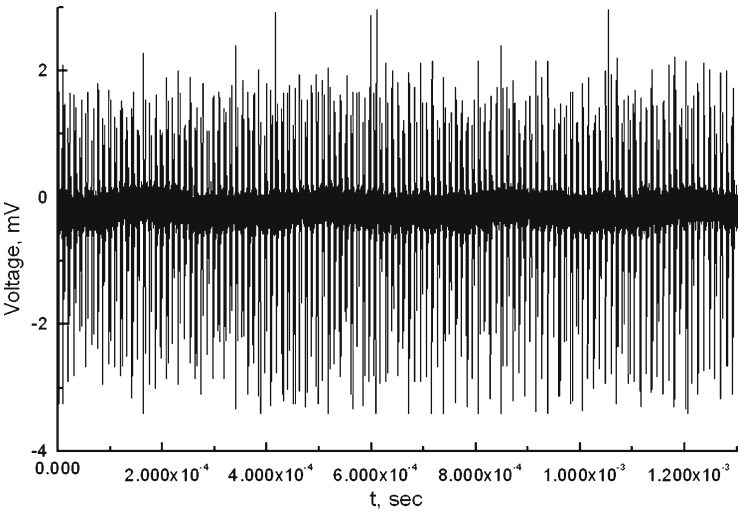

Fig. 5.50. The EMR string induced by blasting (Rabinovitch et al. 2002a)

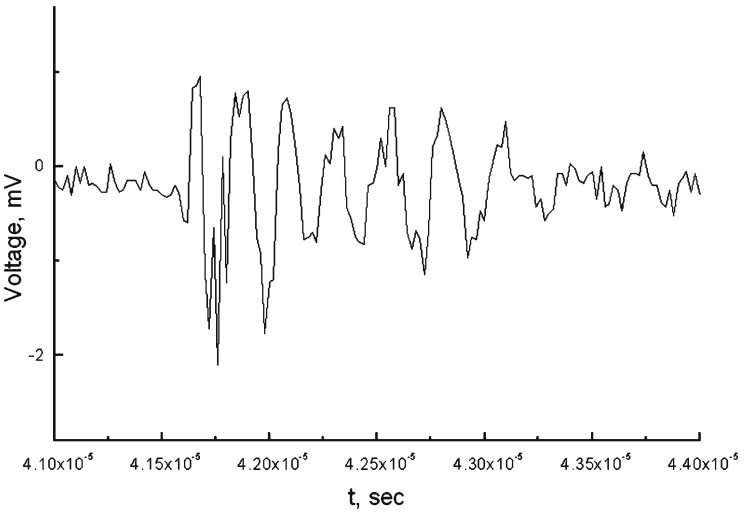

Fig. 5.51. An individual EMR pulse induced by blasting (Rabinovitch et al. 2002a)

5.8.1.2 *Analysis of Results*

As is known (Rossmanith et al. 1997), when stress waves propagate through a brittle material, a population of micro-defects are generated and extended. In drilling and blasting the rock is deformed under dynamic conditions, which create high intensity stress waves. A stress wave of sufficient amplitude (like those created during blasting or drilling) can initiate rock fragmentation at the expense of wave energy (Gueguen and Palciauskas 1994). As is also known (Rabinovitch et al. 1998, 1999b, 2000a, 2000b),

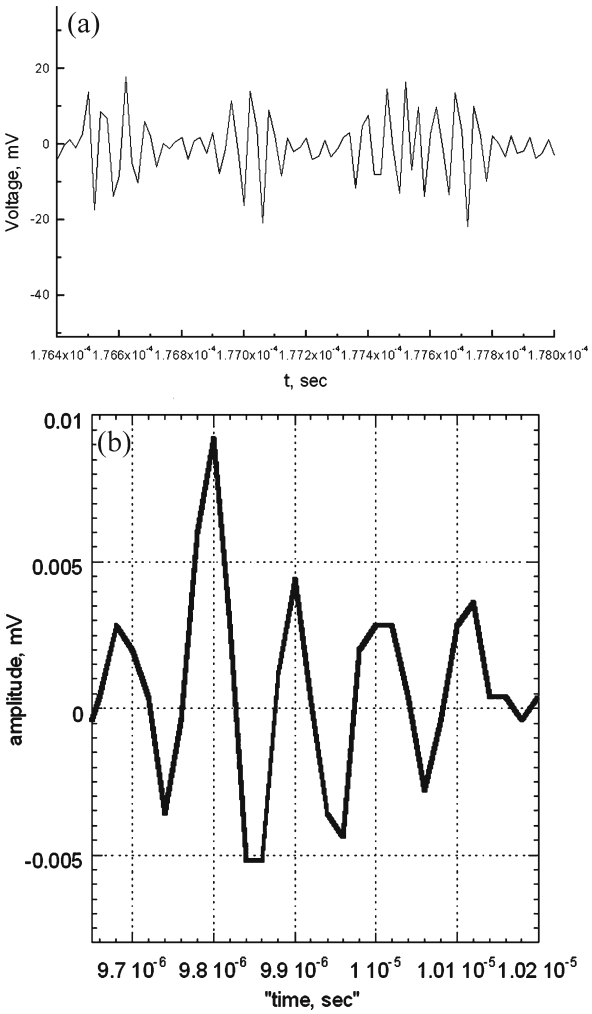

Fig. 5.52.
a Three individual EMR signals from chalk drilling. **b** An experimental EMR pulse induced by chalk compression (Rabinovitch et al. 2002a)

each crack is a source of an individual EMR pulse. Hence, a fragmentation process, such as drilling or blasting, where numerous cracks are created, is an origin of strings of EMR pulses. A larger stress wave energy leads to a larger fragmentation volume in the rock and hence to a larger duration of these strings (and to a larger number of pulses per strings). Therefore EMR pulse strings, which represent a small volume of rock in drilling, are much shorter (2–60 μs) than those induced by blasting (~0.3 and 0.5 s). In comparison, during compression, where these strings stem merely from crack coalescence, the duration of each EMR string never exceeded 30 μs. A zooming in on the EMR strings induced by blasting shows that both the amplitude and the frequency of individual pulses are different from those obtained in drilling and in compression. Nevertheless an overall comparison of EMR signals excited by compression, drilling and blasting shows their basic shape to be invariant to the dynamic/quasi-static loading mode. Note that this basic shape was shown previously to be invariant to the fracture mode

(Rabinovitch et al. 2000c, Sect. 5.2.3). The similarity of shape of single EMR pulses induced by these three processes therefore enables us to analyze the EMR signals induced by drilling and blasting by the same technique we developed earlier for compression (Rabinovitch et al. 2000c, Sect. 5.2). This technique allows us to calculate the dimensions of the crack, which was the source of the measured EMR signal. Our analysis shows that the time from EMR pulse origin up to its envelope maximum T' induced by blasting ranges between 0.01–0.5 μs. The ω value of the signals ranges between 16 and 50×10^6 s^{-1}. Hence their ratio T' / ω will be of about $0.06–1 \times 10^{-14}$ s^2. According to Bahat et al. (2001a), the proportionality coefficient between T' / ω and crack area S is ~3×10^7. Hence, crack areas induced by blasting include a major fraction whose individual areas are estimated to be of about of 0.02–0.3 mm^2. Note that cracks of similar areas are created at the beginning of compression loading (Rabinovitch et al. 2000c, Sect. 5.3.4).

As noted by the Rossmanith et al. (1997), the set of fractures induced by blasting can be divided into three zones: A crush zone (near the borehole) of short uniformly distributed radial cracks; an intermediate zone, where short cracks from the crush zone extend; and an outer zone with long radial cracks. Comparison of crack areas observed during our blasting with this model shows that our EMR signals are induced by the cracks from the two first zones (crush and intermediate) and can indicate the beginning of a dynamic large-scale failure.

5.8.2 EMR Prior to EQ and Volcanic Eruptions

5.8.2.1 *Current State of the Art*

As noted above, during the nineteen seventies and eighties, interest in EMR increased in connection with the problem of earthquake (EQ) prognosis. Several investigators observed the appearance of a disruption of radio communications, atmospheric luminescence and perturbations before EQs (Davis and Baker 1965; Finkelstein and Powell 1970; Drobdev et al. 1978; Galperin et al. 1985; Chmyrev et al. 1986; Kustov and Liperovsky 1988; Bilichenko et al. 1990; Ouellet 1990; Johnston 1991; Derr 1986; Molchanov and Hayakawa 1998a,b; Liu et al. 2000; Lee et al. 2000). Sadovskii et al. (1979) observed an irregularity of EMR before some Karpatian EQs. Gokhberg et al. (1979) investigated EMR prior to an Iranian EQ. This study consisted of EMR registration at frequencies of 25, 385 and 1 630 kHz, for a period starting 55 min before the first EQ shock. EMR perturbations were observed to gradually increase up to the first shock moment. Following this shock, the levels at frequencies of 27 and 1 630 kHz sharply decreased, while those at 385 kHz remained high up to the last "aftershock". These authors proposed that if the EMR sources were deposited in the Earth's crust at the EQ epicenter, the original amplitude of the EMR signal would have to be of the order of hundreds of Volts per meter. Similar works were also conducted in Japan (Gokhberg et al. 1982). EMR was registered at a distance of 250 km from the epicenter of an EQ of magnitude $M = 7$. Since an analysis of "industrial" noise showed its absence at a frequency of 81 kHz, that frequency was chosen for EMR studies. It was shown that 30 min before the EQ, the EMR amplitude rose by up to 15 dB and then sharply decreased at the EQ

moment. EMR intensity (voltage) changes in a tunnel at a depth of about 60 m were also checked. Analysis of diurnal cycles of EMR intensity variations showed that they were significantly disturbed a few days before an EQ. Gokhberg et al. (1986) carried out measurements of EMR features prior to an EQ in Gasli. They found that 2 h 40 min before the EQ ($M = 5$), perturbations above the original noise level were increased by up to 6 dB. Yoshino and Tomizawa (1989) measured EMR (at a frequency of 82 kHz) before a volcanic eruption (VE). The first EMR anomaly was registered two weeks before the VE, and another powerful EMR emission (20 dB higher than the usual noise level) was observed one day prior to the VE. Rikitake (1997), analyzing 60 EQ events measured in Japan, decided that EMR was a "short-term" precursor, with an estimated mean time prior to an EQ of ~6 hours. Nikiforova and Yadakhin (1989) investigated EMR in the Issik-Kul seismic region at a frequency of 15 kHz. They obtained a significant increase of EMR intensity in the immediate zone of active geological faults, and claimed that the EMR sources were of ionosphere origin. On the other hand, Morgunov and Matveyev (1991) conducted an EMR investigation during the Spitak EQ and claimed that EMR could not be explained as an ionosphere disturbance; its origin could only be ascribed to crust destruction. Gershenzon et al. (1987, 1989) and Gokhberg et al. (1982, 1986) proposed that the anomalies of EMR prior to EQ were originated by a mechanic-electric transformation. They noted that before an EQ, a deformation of the Earth's surface took place. Changes in the stress state of surfaces resulted in local destruction, in the formation of micro-fractures and in friction of the nearby rock blocks. Each of these processes could lead to EMR generation. Bella et al. (1992), Morgunov (1985), Morgunov et al. (1988) and Morgunov and Matveyev (1990) also favored the idea that EMR was excited by surface deformation in the vast zone of the EQ vicinity. Gokhberg et al. (1985) noted the following principal features of EMR occurrences:

1. Abnormally high EMR levels, which occur hours or even days before an EQ.
2. The EQ itself takes place during a decrease of this EMR anomaly or immediately after it.
3. The EMR spectrum has a wide frequency range (from several Hz to hundreds kHz).

The third conclusion was also endorsed by Khatiashvili (1984) (who registered EMR in the range of 1–1 000 kHz) and Bella et al. (1992) (who studied EMR in the range of 300 Hz to 300 kHz). It is clear from the above sections that there is no uniquely accepted mechanism regarding the mechanism of EMR prior to an EQ. Parrot et al. (1993), after a detailed consideration of a large number of presently known EMR-EQ investigations, remarked that although the existence of EMR in relation to seismic and/or volcanic activities was clear, EMR selection out of a host of artificial signals remained a significant problem. Nevertheless, investigations of EMR as a precursor to EQ are still in progress (Drakopoulos et al. 1993; Hayakawa et al. 1993; Yepez et al. 1995; Fujinawa and Takahashi 1998) and presently there is an agreement in the literature that EMR might be a prospective forecaster for EQ (King 1983; Mogi 1985; Yoshino et al. 1993). However, as we noted above, all efforts to use EMR for earthquake prediction met with very meager success, due to the lack of a detailed quantitative understanding of the EMR mechanism (King 1983; Rabinovitch et al. 1996).

5.9 Global Features of EMR

5.9.1 EMR versus Gutenberg-Richter Relation

5.9.1.1 *Fractal Nature of Earthquake*

A fundamental observation in seismology is the Gutenberg-Richter law (Gutenberg and Richter 1954):

$$\log(N) = a - bM \tag{5.17}$$

where M is the earthquake magnitude (which is defined as the logarithm of the integral of slip along the fault during an earthquake), N is the number of earthquakes having magnitudes greater than M, and a and b are constants. This power law or fractal distribution is valid both for main events and for aftershocks (Nanjo et al. 1998). It is presently thought that such a distribution can be a fundamental result of "multiple fracturing" (Turcotte 1992), when spontaneously occurring microcracks tend to coalesce, leading, by numerous upscalings, to a catastrophic failure. A similar relation is also observed in laboratory studies of acoustic emission (Lockner et al. 1991; Lockner 1993). It is even true for energy distribution of neutron star-quakes (Jagasivamani and Iyer 1988) (the source of a star-quake is a fracture in its neutron crust, which may release strain energies of up to 10^{46} erg! (Link and Epstein 1996)), which is many orders of magnitude larger than that of an earthquake.

Recently, enough data has been collected to extract statistics on individual systems of earthquake faults (Dahmen et al. 1998), and it was found that the distribution of earthquake magnitudes may vary substantially from one fault system to another and for different Earth regions.

Regarding the exponent 'b' of the power-law distribution, it was previously claimed to be universal and close to 1 (Gutenberg and Richter 1954). In Molchan et al. (1997), the related b-values (for many earthquakes in Italy calculated for the period 1900–1993) are in the range 0.7–1.35. Elgazzar (1998) estimated the b-value to be 0.85 ±0.2. Nanjo et al. (1998) give b to be between 0.5 and 1.5. It has recently been claimed that 'b' fluctuates in time and depends on the earthquake magnitude (Olami et al. 1992; Carlson et al. 1991).

In recent years, numerous investigators tried to explain b theoretically. For example, "self-organized criticality" models were proposed (Bak and Tang 1989; Ito and Matsuzaki 1990; Matsuzaki and Takayasu 1991; Olami et al. 1992) to explain this fractal law as being a result of the extremal nature of the dynamic rules governing the system. There are also other deterministic models (Carlson et al. 1991; Scott 1996) describing earthquake dynamics by the friction and elastic forces acting in the fault zone. For example, the one-dimensional Burridge-Knopoff model (Carlson and Langer 1989) leads to the Gutenberg-Richter law with $b \approx 1$.

Anton (1999) proposed an analytic model based on a relation between stress release rate and kinetic energy loss by seismic waves and noted that the relation $b < 1$ implied that the stress release rate was greater than the loss of kinetic energy by seismic waves.

Gabrielov et al. (2000a,b) developed a "colliding cascades model" consisting of a hierarchical structure. They proposed that an external load applied to the largest block is transferred hierarchically to the smallest components. Fracture processes expand in an inverse manner. The two processes "collide" and interact. On the basis of this model, they argued that the *b*-value should be 0.53 for main earthquakes and 0.69 for aftershocks. Nanjo et al. (1998), Kossobokov et al. (2000), Elgazzar (1998), Anton (1999), and Gabrielov et al. (2000a,b) for the distribution of EQ magnitudes in that the *b* value is of the order of 2/3.

5.9.1.2 *Comparison of Fractal Behavior of EMR and EQ*

As we noted above, amplitude changes of acoustic emission from fractures during laboratory compression tests of brittle materials were considered by Lockner (1993) and Lockner et al. (1991) to be similar to those occurring in EQ. This kind of similarity can also be gleaned from a comparison between energy release during starquakes (Fig. 5.53a, Kossobokov et al. 2000) and our measurements of amplitude of EMR induced by chalk compression failure (Fig. 5.53b). In this section this similarity is investigated, focusing on the possibility of a power law for EMR induced during conventional uniaxial and triaxial fracture.

Figure 5.54 shows the cumulative number (the number of signals having amplitudes larger than *E*) of EMR signals (measured additively from twenty-four chalk samples during uniaxial and triaxial conventional tests) vs. EMR pulse amplitude.

Since the voltage output of the EMR pulses '$\overline{A}$' depends on the antenna reaction (antenna efficiency), which changes with frequency, it was compensated (Sect. 5.3.3). We were thus able to compare heights of EMR signals of different frequencies.

EMR pulse amplitudes *E* changed by 5 orders of magnitude (Fig. 5.54): From 0.001 V m^{-1} to 100 V m^{-1}. The figure consists of four parts. Its main part is consistent with a Gutenberg-Richter type law with a *b*-value of 0.62 ($R^2 = 0.95$).

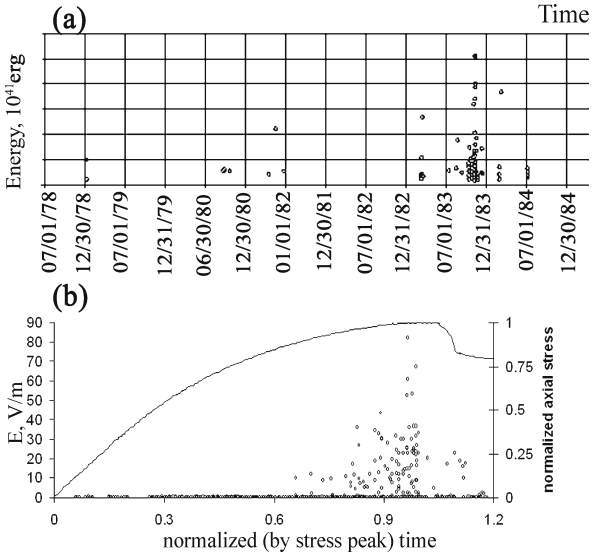

Fig. 5.53.
A qualitative comparison between energy changes during starquakes (**a** after Kossobokov et al. 2000) and **b** amplitude changes of electromagnetic radiation induced by rock compression (Rabinovitch et al. 2002b)

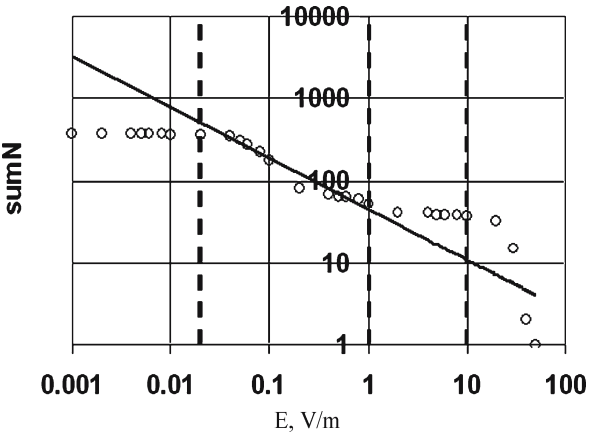

Fig. 5.54.
The number of signals having amplitudes larger than E of EMR signals (measured additively from twenty-four chalk samples during uniaxial and triaxial conventional tests) vs. EMR pulse amplitude (Rabinovitch et al. 2002b)

$$\mathrm{sum}N = 51.44A^{-0.62} \tag{5.18}$$

Note that this b-value is close to 2 / 3 (see above). On both ends of the graph there is a deviation from the Gutenberg-Richter type law. The b-value for the small amplitude range is very low (0.02, $R^2 = 0.76$). This small value might be related to either an incomplete sampling of small events, to noise or to a new physical effect governing the process. In the range of large amplitudes $1 < A < 10$ V m^{-1}, the b-value is also significantly lower (0.08, $R^2 = 0.76$) than in the main part, which might possibly be due to the finite size of the sample. Note that the EMR amplitude in the range of $1 < A < 10$ V m^{-1} is measured when the external stress is higher than the sample's elastic limit (Fig. 5.53b). Figure 5.54 has also a fourth part (A > 10 V m^{-1}) with $b = 2.3$ ($R^2 = 0.77$). This is the range immediately before sample collapse (Fig. 5.53b).

Several investigators have noted this slope change effect for seismic data as values in the smallest and largest ranges in their investigations also deviated from the Gutenberg-Richter type law. For example, Lockner (1993) and Lockner et al. (1991) showed a roll-off in the distribution of AE signals at low amplitudes and explained it as incomplete sampling of small events (Lockner 1993; Lockner et al. 1991). Kossobokov et al. (2000) noted this change of slope effect in the high range of earthquakes and explained it as being due to the maximum energy release being limited by the size of the crust and by the energy density. They also noted that for the largest earthquakes the downward slope may altogether disappear or even turn into an upward slope.

A change of slope effect was also observed by Molchan et al. (1997) for induced seismicity both in the range of small and of large earthquakes.

The decrease of the b-value with stress, as happens here between 1 and 10 V m^{-1} (Fig. 5.54), is also a known effect (e.g., Lockner et al. 1991).

Figure 5.53 exhibits the escalation of the fracture process before collapse. Figure 5.53a (Kossobokov et al. 2000) shows the energy of starquakes vs. time, which occurred at a distance of about 40 000 light years from Earth. Figure 5.53b gives an EMR amplitude-stress-time graph of all chalk samples. Stress values (Fig. 5.53b) were normalized by the peak stress value. Visual comparison indicates that the two graphs are very similar.

5.9.2
Benioff Strain Release

Fracturing processes can be measured either by intensity changes (see, e.g., Fig. 5.54) or by their energy release. The latter is usually represented by the so-called "cumulative Benioff strain release"(Newman et al. 1995; Kossobokov et al. 2000; Gabrielov et al. 2000a,b), which relates the total sum of the square root of the energy released for sequential fracture events to the time prior to the collapse failure. Hence, in addition to the Gutenberg-Richter purely statistical law, the "cumulative Benioff strain release" relation enables us to monitor the continuous development of the upscaling fracture process through time.

The measured EMR amplitude is proportional to the magnetic field intensity (H) reaching the antenna. Since the energy of the electromagnetic field is proportional (Pointing vector) to $|H|^2$, the EMR amplitude is proportional to the square root of the energy. Figure 5.55 shows a bilogarithmic graph of a cumulative amplitude of all EMR signals registered during all samples' compression vs. time before their collapse failure. Since maximal values of EMR amplitude are excited by the samples' collapse failure, their occurrence time was taken as the zero time for each sample.

The graph (Fig. 5.55) shows an almost constant slope in its middle part (about a whole decade). It was fit to a power law ($R^2 = 0.987$ and slope = 1.42) and is seen to be accompanied by some logarithmic-periodic variations. This graph is very similar to the usual "Benioff strain release" ones (e.g., Kossobokov et al. 2000) and the slope of its main part is close to the usual Benioff slope of 1.35 (Newman et al. 1995).

Results obtained here show that both the b value of the Gutenberg-Richter type law and the slope of the Benioff strain release relationship of EMR signals obtained during chalk fracture in the laboratory are similar to those measured in earthquakes and starquakes. The qualitative similarities and even more so the almost exact power laws are striking. The fractal nature of the processes controlling earthquakes and starquakes can therefore be extended to a microscale regime. This "global" nature of multiple fracture effects evidently implies that a basic general process is "acting behind" all these phenomena.

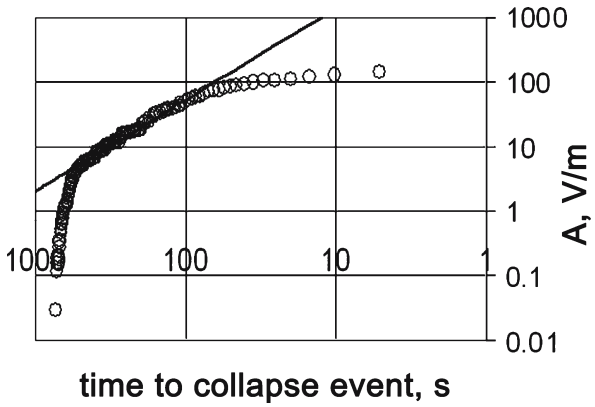

Fig. 5.55.
The "Benioff strain release" relationship of a cumulative amplitude of all EMR signals registered during all samples' compression vs. time before their collapse failure (time goes backwards from the moment of collapse) (Rabinovitch et al. 2002b)

5.10
EMR Induced by Underground Rocks under Stress

5.10.1
General Background

Nesbitt and Austin (1988) registered EMR in a gold mine (2.5 km depth). An EMR signal (1.2 mA m^{-1} amplitude) was generated some seconds prior to the micro seismic event (magnitude of –0.4). Registration of EMR activity in Ural bauxite mines showed (Scitovich and Lazarevich 1985) that its value sharply increased with rock burst (RB) hazard increase. Analogous works in Noril'sk polymetal deposit (Krasnoyarsk region) revealed an increase of EMR amplitude (up to 150–200 mV m^{-1}) and activity in the RB hazardous zones (Red'kin et al. 1985). Markov and Ipatov (1986) investigated EMR activity changes in an apatite underground mine (Khibin deposit, Kola Peninsula) and found out that EMR amplitude in RB hazardous zones was in the range of 8–25 mV m^{-1} and EMR activity there was significantly higher than the regular noise level.

A survey of this general background shows that the EMR investigations in mines are rare and non-systematic. We conducted careful investigations in underground mines in different mining and geological situations associated with an increase of RB and rock-gas outburst hazard. The main aim of these investigations was to correlate between specific EMR patterns and an increase of RB and outburst hazard in underground mines and hence to develop EMR criteria for rock bursts and rock-gas outburst. We hope that a good understanding of these relations would create new avenues for successful "large-scale" EMR investigations of EMR pulses prior to ensuing earthquakes-enabling earthquake monitoring.

5.10.2
EMR in Mines

5.10.2.1
Criterion of Rock-Burst Hazard in Coal Mine and Short Description of the "Gum" Method

RB hazard increases if the load on a given part of a coal seam exceeds some critical level, while the distance from this part to the stress maximum (in the zone of influence of a mine-working) is lower than a critical value (Petukhov and Lin'kov 1983). Note that we use by the term "mine-working" for all underground openings irrespective of their size and purpose. If the potential energy accumulated in the zone of high stress is enough to destroy rocks near a mine-working, RB takes place.

As shown by Petukhov and Lin'kov (1983), the RB safety condition is the following:

$$\begin{cases} P_{\mathrm{n}} < P_{\mathrm{m}} \\ \dfrac{M_{\mathrm{c}}}{E_{\mathrm{r}}} \dfrac{a_{\mathrm{n}}}{h} < 1 \end{cases} \tag{5.19}$$

where P_{n} is the external applied load, P_{m} is the limiting load (strength), M_{c} is the coal drop modulus (descending modulus of the stress-strain curve beyond the peak point under rigid compression, Fig. 5.56), E_{r} is the Young modulus of adjoining rocks, a_{n} is the distance from

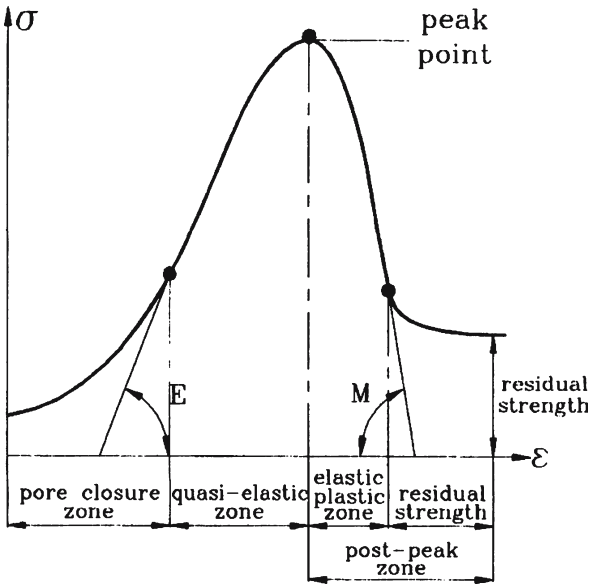

Fig. 5.56.
Typical stress-strain curve during stiff sample compression (Frid 2000)

the mine-working face up to the position where there exists a peak stress, and h is the half thickness of the coal stratum. If coal is under residual strength (non-hazardous condition), both inequalities comply with the following: Load on the given zone is lower than the limiting value (first inequality) and the left side of the second inequality is smaller than 1 (the drop modulus in the residual strength zone is equal to 0).

The RB hazard is usually determined by some standard geomechanical method, e.g., volume measurement of gum (dry coal "powder"), measurement of the diameter of the hole created or the number of disks that are created due to core fracturing as a result of drilling in a highly stressed zone, etc. (Petukhov 1972).

Drilling of a highly stressed coal seam leads to an intensive fracturing process in the zone influenced by the drill hole. The volume of this highly cracked zone depends on the hole diameter, the drilling rate and especially, the stress level. Hence, if the first two parameters remain invariant for a given coal seam, the stress value in the coal seam is responsible for the volume of gum that is recovered from the hole (i.e., from the highly stressed zone drilled by the hole). This method is widely used for RB prediction, although it is time consuming and in some conditions even dangerous.

The normalized ratio, β, of the highly stressed zone (ratio of the non-elastic deformation zone, diameter D, to the hole diameter $d = 0.043$ m, Fig. 5.57, Frid 2001) can be calculated from the following formula (Petukhov 1972) is given by:

$$\beta = -0.5 + \sqrt{0.25 + \frac{3\dfrac{M_0 + M_s}{M_0} n_r - n_r + 2}{n_r - 1}} \tag{5.20}$$

where n_r is the coefficient of coal loosening on the borehole wall that is usually equal to 1.3–1.4, M_0 is the gum volume in the borehole ($M_0 = \Lambda\pi d^2/4$, Λ is the borehole

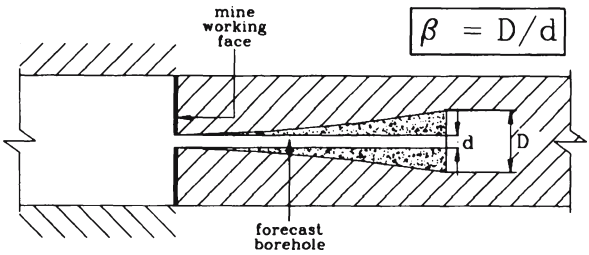

Fig. 5.57.
The zone of non-elastic deformation excited by drilling in the high stressed zone (β is the non-dimensioned diameter of this zone: The ratio of the non-elastic deformation zone diameter D to the hole diameter $d = 0.043$ m) (Frid 2001)

Table 5.4.
Calculation of rock-burst hazardous zone parameters

a' (m)	Gum volume (l m^{-1})	β	$\sigma_{k\gamma H}$ (MPa)	X_m (m)	ξ (m)
4.00	5.00	5.03	54.98	6.35	2.35
5.00	6.00	5.71	58.28	6.98	1.98
6.00	6.50	6.02	59.67	7.43	1.43
7.00	7.50	6.60	62.08	7.96	0.96

length), and M_s is the gum volume induced by drilling in a stressed zone) (Petukhov et al. 1976).

The vertical stress in the coal seam can be determined as follows (Petukhov et al. 1976):

$$\sigma_{k\gamma H} = k_*(1 + 2\ln\beta) \tag{5.21}$$

where k_* is the coal shear strength. Forecast boreholes are usually drilled in successive depths (the length of each beeing 1 m). Hence, we can estimate the vertical stress distribution in the coal seam near the mine-working face.

After the drilling of each interval, the gum volume is measured and if it exceeds a definite limiting value (the experience at the mining works in North Kuzbass shows that the limiting values are 5 to 8 liters per meter at the fourth and the seventh drilling meter from the drift face, respectively, (Table 5.4, Frid 2001)), drilling is stopped, and that part of the mine-working is considered RB hazardous.

As noted by Lockner (1993, 1996), there is a strong parallelism between the well-known Gutenberg-Richter relation for seismic events (from macro (earthquake) to micro (RB)) and power law frequency-magnitude relationship for acoustic emission events. This analogy suggests that micro shocks (high frequency and small magnitude) are precursors of macro failure (large magnitude and small frequency). This is the theoretical basis for RB forecasting by the acoustic emission method (Kuksenko et al. 1982; Mansurov 1994). The EMR frequency range is close enough to the acoustic emission band. Moreover, Gutenberg-Richter type relationships similar to the seismic ones were also observed for EMR (Rabinovitch et al. 2002b, Sect. 5.9.12) Hence, it would be correct to assume that EMR could be useful for RB hazard forecasting along with acoustic emission. Moreover, being non-contact, the EMR method has some advantages over acoustic emission. For example, when a rapid and comprehensive prognosis of a short-term mine-working region (for example, in a drift face) is needed, the roughness of the mine walls becomes a marked problem for the acoustic emission method for rapid data acquisition due to inferior contact between the acoustic emission transducer and the mine wall.

5.10.2.2
EMR Measurements in Coal Mines

EMR pulses excited by rock fracture show up as a "bell-shaped" oscillation characterized by amplitude, a frequency and an individual rise and fall time (Rabinovitch et al. 1995, 1996, Sect. 5.2). As a rule, EMR is measured in mines within the narrow band in the 30–150 kHz range. The middle part of this range (100 kHz) is the most convenient one in coal underground mines (Frid et al. 1992). This range is conditioned both by the industrial electromagnetic noise level in underground mines and the electromagnetic pulses' amplitude. The Electromagnetic pulses' field amplitudes excited by coal failure near the face of a mine-working range are between 5 and 50 μV m^{-1} (Frid et al. 1992) that is at least one order of magnitude larger than mine industrial noise levels. An industrial noise level at the Earth's surface is usually not lower than 5 mV m^{-1}. Hence, an industrial electromagnetic noise in coal mines springs from underground mining machines, but not from the Earth's surface. The daily work cycle of a mine consists of four six-hour shifts: three extraction (mining) ones and one repair shift. The probability to pick up an electromagnetic transient process pulse due to the starting/stopping of electrical mining machines during extraction shifts is large enough, while the electrical noise level during the repair shift is as noted above. Thus, we carried out our measurement during the repair shift. As shown by Frid et al. (1992), EMR registration near a face of coal drift enables us to obtain EMR signals excited by a coal failure up to a depth of 10 m from the drift face. The daily drift moving in North Kuzbass conditions was usually of about 6 m. Hence, a measurement of EMR during the repair shift can characterize at least the daily activity at a coal drift face.

The EMR was measured by a resonance 100 ±1 kHz antenna that was located 1 m from the mine-working face and was connected to a counter. We defined the EMR activity as the number of crossings of the EMR voltage signals (per unit time) through a given voltage level of a special counter (Fig. 5.58, Frid 2001). At all studied points 30 EMR activity readings were taken, each with a duration of 10 s. For simplicity, we named units of EMR activity "pulse per 10 seconds", and they were symbolized by

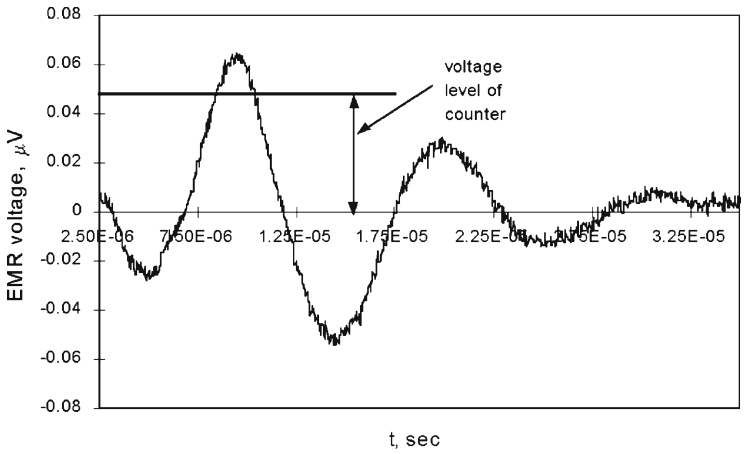

Fig. 5.58. The EMR signal that intersects counter voltage level (Frid 2001)

"pulse/10 s". A complete cycle of EMR measurements at a single drift face is of 5 min duration. This method allowed us to determine a stable mean that characterized EMR activity at a given point.

Our preliminary mine estimation of EMR compatibility conditions showed that choosing the given resonance frequency would allow us to accurately extract the useful signal from the industrial background noise. As is known, the use of the shortest wavelength band of the measuring system is a necessary condition to increase the system's sensitivity. The *Q* factor in our case is 50, resulting in a system sensitivity not lower than 0.1 mV m^{-1}.

5.10.2.3
Mine Investigations prior to Rock Bursts

An increase of RB hazard is usually associated with the existence of pillars, geological faults, sharp changes of inclination angle or thickness of coal seams (Petukhov 1972). We conducted our investigations in coal mines of the North Kuzbass, which exhibited all of these conditions.

An example of EMR registration at the zone of pillar influence is shown in Fig. 5.59 (Frid 1997a) The study was conducted in a mine-working where the influence of pillars was found at a distance of 70 m from the conveyer drift 13. Profiling of the mine-working (in spacing of 10 m) showed an anomalous EMR activity at stressed regions under pillars.

A second example of EMR registration at a zone of pillar influence is shown in Fig. 5.60 (Frid 2001). The EMR sequential measurements (profiling with 3 m spacing) were carried out in an extraction gallery that partly drifted into the zone of pillar influence. As can be seen, EMR activity is anomalous under the pillar (120–140 pulse/10 s). Gum value measurements showed the existence of a RB hazard in this region (gum value was about 7–12 l m^{-1}).

A third example of EMR registration is shown in Fig. 5.61 (Frid 2001). In this case, drift was in a zone of an intensively variable thickness of coal seam and a sharp change-

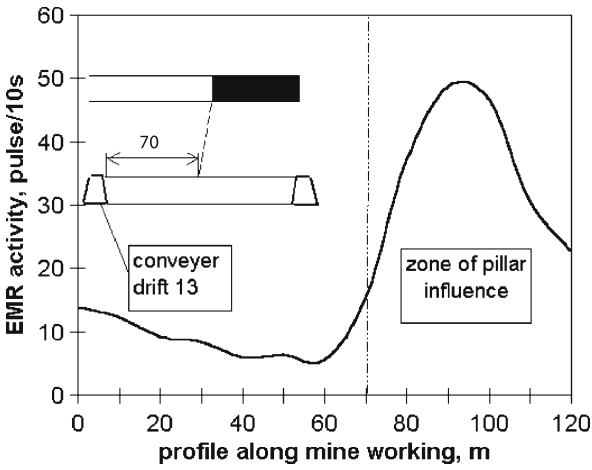

Fig. 5.59. EMR profiling under pillar (Frid 1997a)

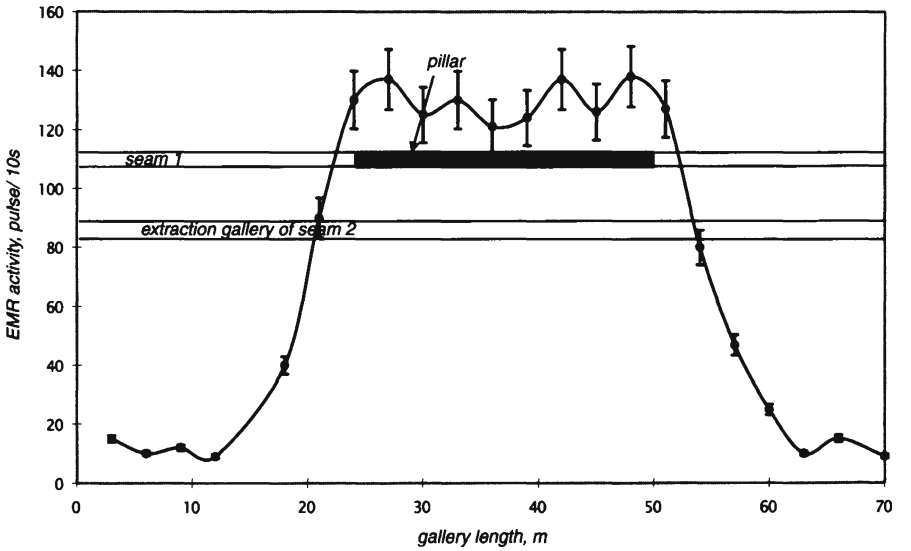

Fig. 5.60. EMR profiling at the zone of pillar influence. The error in EMR activity is of the order of ±7.5% (Frid 2001)

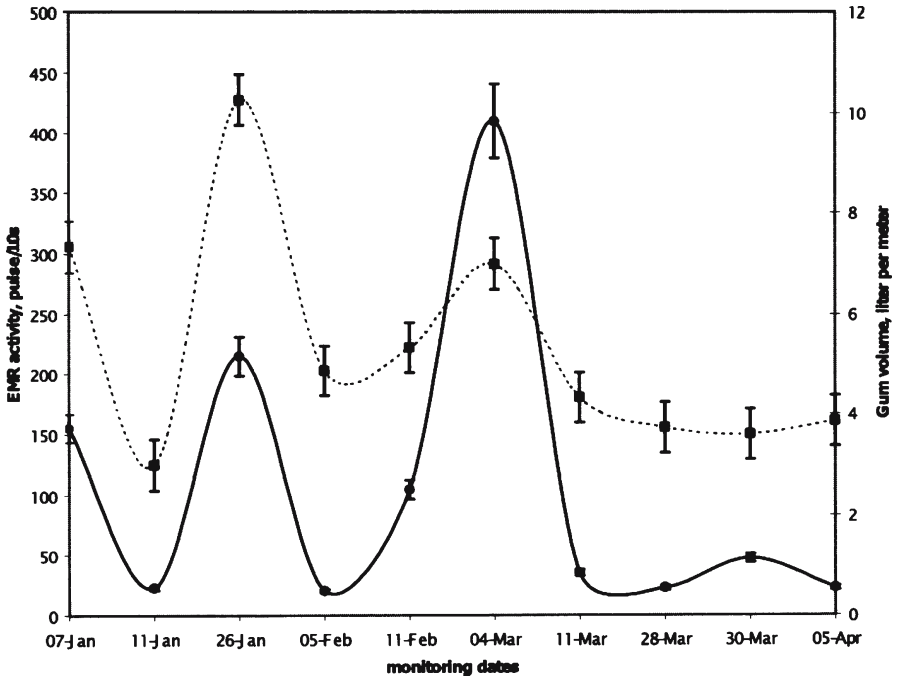

Fig. 5.61. EMR monitoring during drift excavation in an intensively changeable thickness of coal seam. The error in EMR activity is of the order of ±7.5%, while in gum value is of the order of ±0.5 l m^{-1} (Frid 2001)

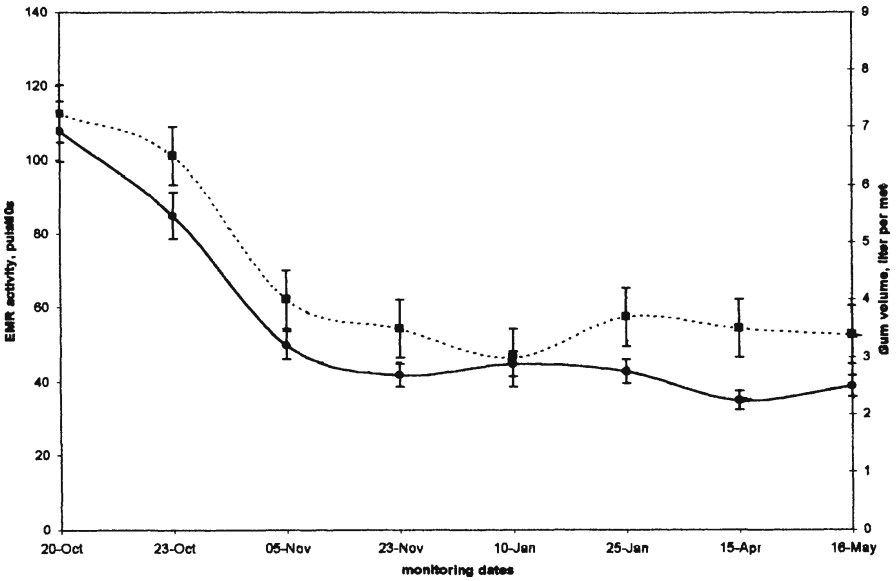

Fig. 5.62. Anomalous EMR activity and gum value in the mine excavation near the uplift. The error in EMR activity is of the order of ±7.5%, while in gum value is of the order of ±0.5 l m^{-1} (Frid 2001)

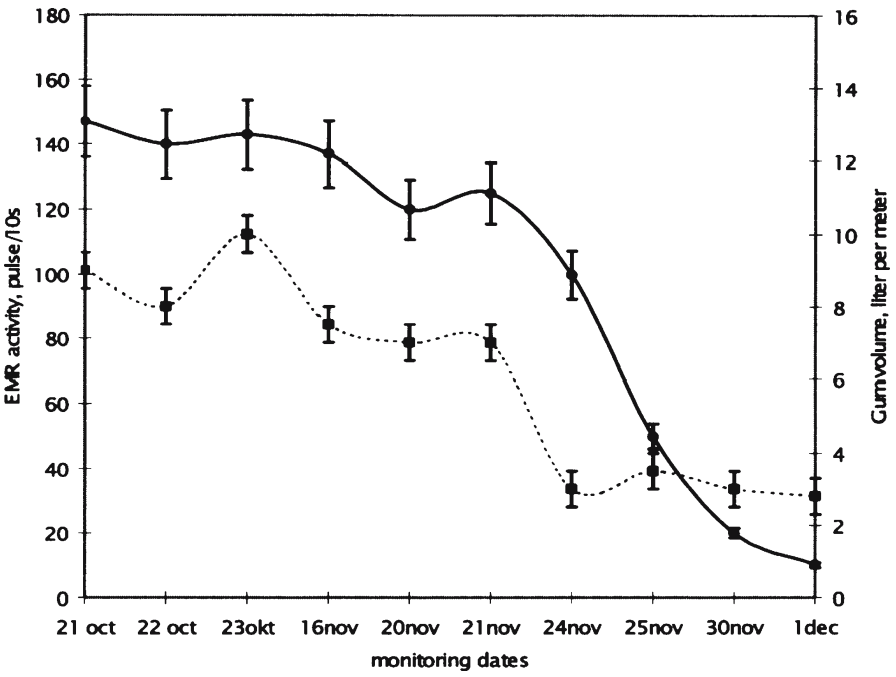

Fig. 5.63. EMR monitoring during pillar unloading. The error in EMR activity is of the order of ±7.5%, while in gum value is of the order of ±0.5 l m^{-1} (Frid 2001)

able inclination angle. The regular thickness of the coal stratum was 1.5–1.7 m. A sharp decrease of the thickness of the coal stratum was associated with a RB hazard increase (a decrease of coal stratum thickness induces a stress maximum nearer to the drift face and hence a RB hazard increase). For example, on 7 and 26 January and on 4 March, the coal stratum thickness decreased to 0.5–0.7 m, with a corresponding gum volume and EMR activity increase of up to 7–10 l m^{-1} and 150–400 pulse/10 s respectively.

Figure 5.62 (Frid 2001) shows an example of an anomalous EMR activity and gum value in a mine excavation that was opened at a distance of 8 m from an uplift with a 2 m amplitude. As the excavation moved away from the uplift, the EMR and the gum monitoring showed gradual decrease. Unloading of RB dangerous rocks near mine-workings is usually performed by the following methods: Hydroprocessing, drilling of boreholes of large diameter and blasting. We carried out EMR activity investigations both before and after these unloading operations. If these operations were successful, i.e., mine-working became safe, EMR activity should have decreased to its usual level.

Figure 5.63 (Frid 2001) shows an example of an EMR registration during pillar unloading. The average level of EMR activity during the period of 21 October to 16 November was 130–150 pulse/10 s. Measurement of the gum volume showed that this pillar was RB hazardous (gum volume was 8–10 l m^{-1}). Unloading was performed by drilling 100 mm diameter holes. The holes enabled us to decrease the pillar brittle response. Drilling began at 17 November. This led to pillar unloading, and both gum volume and EMR activity gradually decreased.

Figure 5.64 (Frid 1997a) shows an example of EMR profiling in a drift that was initially RB dangerous along all of its length after it was unloaded. Unloading was conducted by hydroprocessing that includes the drilling of a borehole of 6 m length at intervals of 30–50 m followed by water pumping into the rock. Hydroprocessing leads to controlled rock cracking and removes the zone of increased stress from the mine-working wall deeper into the rock-mass. Figure 5.64 (Frid 1997a) shows an example of EMR measurement when one part of drift (from 0 to 70 m) was previously hydroprocessed and became safe (gum value was lower than 5.5 l m^{-1}). The average level of EMR activity at this region was not more than 40 pulse/10 s. However, the unprocessed drift zone was very hazardous (gum value of up to 8–9 l m^{-1}), a fact that was reflected by a high level of EMR activity (of up to 250 pulse/10 s).

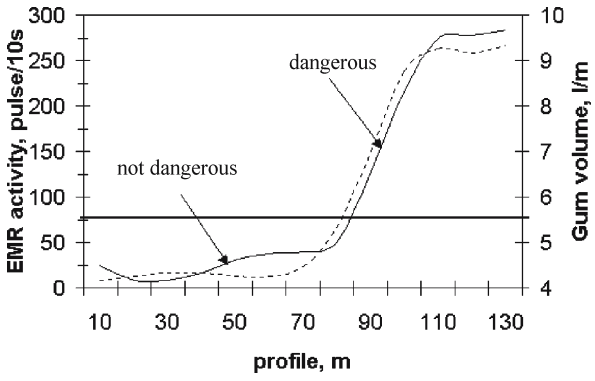

Fig. 5.64.
EMR registration by drift profiling (Frid 1997a)

We carried out EMR investigations in more than 400 different RB situations in underground coal mines (North Kuzbass deposit) (Frid 1990; Frid et al. 1992; Frid 1997a,b). Our investigations showed that an increase of RB hazard, accompanied by an increase of EMR activity, occurred when pillars were found above mine-working, where geological faults existed in the area, and/or where seam thickness sharply diminished (Frid 1997b). These investigations also showed that the highly stressed zone near mine-workings is the source of the EMR (Frid 1990, 1999). An analysis of all the data enabled us to determine the following empirical criterion of RB hazard:

$$N > N_{emp} \tag{5.22}$$

where N is the value of EMR activity registered at a mine-working, and N_{emp} is the limiting value of EMR activity (115–120 pulse/10 s, Frid 1997b). If the value of the EMR activity, N, exceeds N_{emp}, a RB hazard existed.

The amount of time needed to determine the degree of a RB hazard by the EMR and the gum methods at a given point is about 5 and 30 min, respectively. The reduced time is a significant advantage of EMR forecasting. However, the amount of time for data collection to establish an empirical N_{emp} in a specific mine is much longer, even up to several years. The only way to reduce this time is to develop a theoretical model of this criterion. The following section establishes an empirical EMR criterion of RB hazard and compares it with the theoretical criterion.

5.10.2.4
Theoretical EMR Criterion for Rock-Burst Hazard in a Coal Mine

Zone of EMR formation under external stress. Goncharov et al. (1980) carried out an EMR study with a stiff press. They loaded concrete samples of $0.55 \times 0.55 \times 0.65$ m dimensions under compression. The EMR activity was measured with a magnetic antenna that had a resonance frequency of 800 kHz (±1 kHz). The first significant increase of EMR activity occurred at the post-peak zone under a load of 0.95 σ_c, where σ_c is the limit of strength, and a second rise of EMR activity was noted for a load of 0.9 σ_c (in the post-peak zone). Single pulses of EMR accompanied the subsequent decrease of the load until 0.75 σ_c. In the zone of residual strength, EMR activity ceased.

EMR studies with a stiff press were also performed on ores and rocks from the Khibin apatite deposit (Kola Peninsula, Ipatov 1989), on magnetic ores, granites, white marble and coal from Shpitsbergen (Frid 1990). EMR activity was registered with a 100 kHz (±1 kHz) resonance magnetic antenna. The maximum EMR activity was measured in the range of (1.0–0.8) σ_c in the post-peak zone, while in the zone of residual strength EMR activity stopped. Note that wide frequency band EMR measurements (Rabinovitch et al. 2000c) confirmed these results. An analysis showed that the following EMR features were common to all rocks:

1. A sharp increase of EMR activity near the peak stress.
2. An absence of EMR in the zone of residual strength.

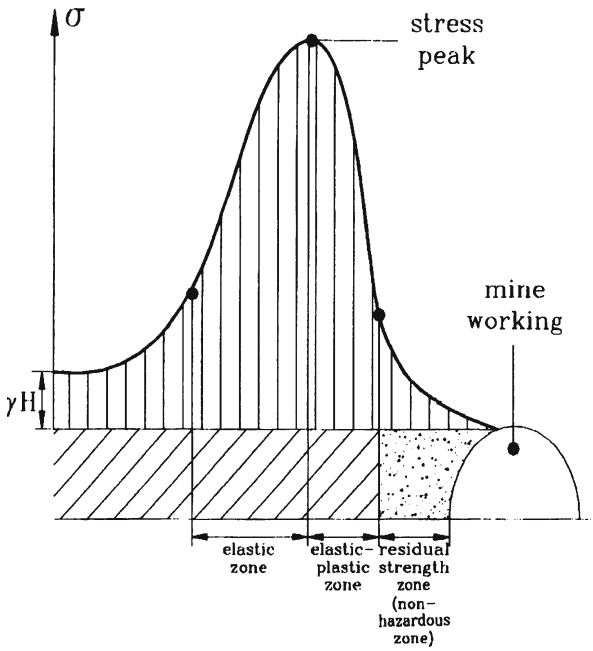

Fig. 5.65.
Typical stress distribution curve in the zone of mine-working influence (Frid 2000)

To check these conclusions in situ we investigated the EMR activity during borehole drilling (hole diameter was 42 mm). Note that the residual strength zone (the last zone during sample deformation on a stiff press, Fig. 5.56) is the nearest zone to the mine-working face (Fig. 5.65).

All holes were drilled at 1 m separation intervals. During all interval drilling, a cumulative value of EMR activity (summarized value of EMR activity per drilling interval) was measured, and after drilling each interval the gum value was measured. Forecast drilling in the mine does not generally achieve stress peak due to instrument "gripping" in a borehole, and stops if gum volume (stress value) becomes higher than a predetermined value. Forecast drilling (in North Kuzbass mines) is generally conducted up to 6 m depth. Figure 5.66 shows two examples of EMR observation during borehole drilling:

1. In the RB hazardous zone (gum value is higher than the limiting value, see below).
2. In the non-hazardous zone (gum value is lower than the limiting value, see below).

As is seen from Fig. 5.66a, gum value increases up to 12 l m^{-1} in the 5^{th} drilling meter. This value is significantly higher than the limiting value (5.5–6 l m^{-1}), and hence the forecast drilling was stopped. It evidently indicates the existence of a RB hazardous zone at the 5^{th} meter depth from the mine-working face. Figure 5.66a shows that when a hole face approaches a stress peak (gum increase above the limiting value), EMR activity sharply increases, and vice versa: If the gum value doesn't change drastically (gum value lower than 5.5–6 l m^{-1} at the 5–6 drilling meter non-hazardous zone, Fig. 5.66b), EMR activity does not essentially increase.

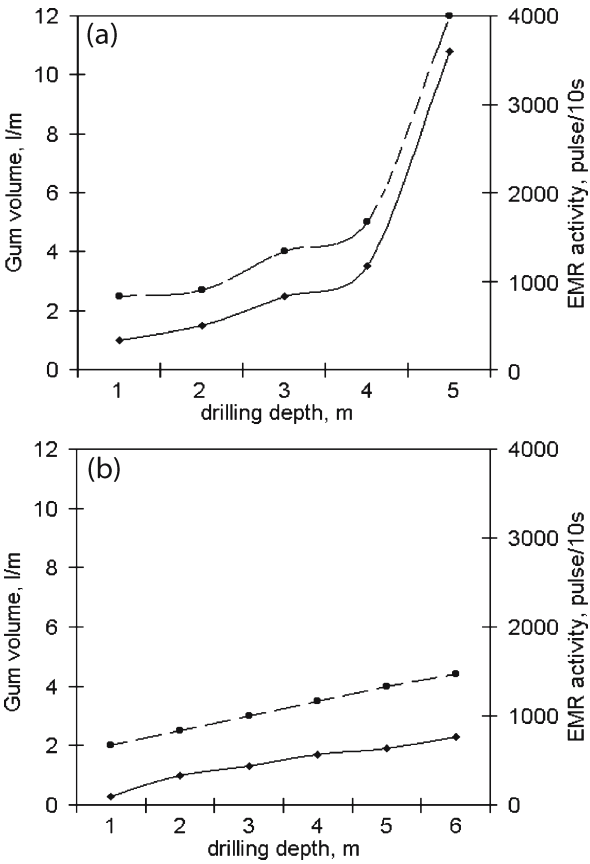

Fig. 5.66.
Two examples of EMR study during forecast drilling: **a** in the rock-burst hazardous zone, and **b** in the non-hazardous zone. *Full-drawn curve* is the Gum value, while the *hatched curve* is the EMR activity (Frid 2000)

The analysis of more than 150 drillings conducted on three different coal stratums (Desyatiy, Koksoviy and Andreevskiy) enables us to summarize some general features of EMR activity associated with borehole drilling:

1. The EMR activity sharply increases if the hole face approaches a zone of highly stressed coal (that is near the stress peak, e.g., Fig. 5.66a).
2. Drilling in a non-hazardous zone does not tangibly affect EMR activity (e.g., Fig. 5.66b).
3. The EMR activity value induced by drilling is lowest nearest to the mine-working face, i.e., in the zone of crushed coal or residual strength (see, e.g., first drilling meter from the mine-working face, in Fig. 5.66).

Calculation of rock-burst hazard zone volume. Drilling for gum volume measurements in a mine is usually conducted up to a depth of increased stress $\sigma_{k\gamma H}$, but stress maximum is usually not measured due to instrument gripping (as a result of the hole squeezing around the drill rods) in the borehole. However, for the theoretical EMR analysis it is important to know the volume of the highly stressed zone, and hence the distance from the mine-working face up to the stress maximum.

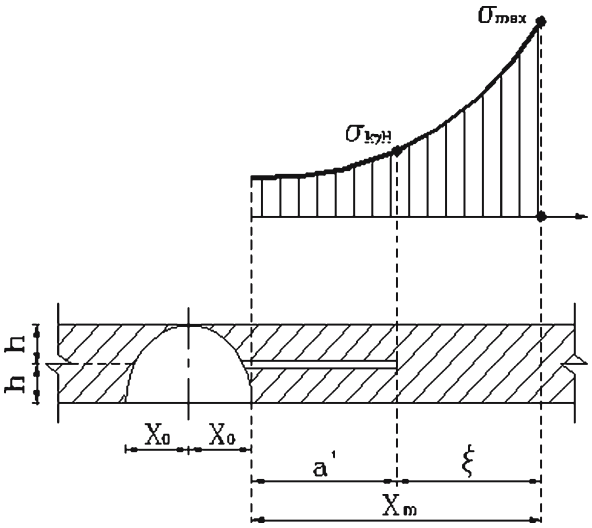

Fig. 5.67.
The vertical stress distribution in the zone of influence of the mine-working (all parameters are discussed in the text) (Frid 2001)

The distance to the stress maximum (Fig. 5.67, Frid 2001) can be estimated as follows (Petukhov et al. 1976):

$$X_{\mathrm{m}} = \frac{1.23X_0}{\left(\dfrac{\sigma_{\mathrm{c}}}{\sigma_{k\gamma H}}\,\dfrac{X_0 + a'}{h}\right)^{2/3}} \tag{5.23}$$

where X_0 is the mine-working half width, a' is the distance from the mine-working face to a boundary of the zone of increased stress ($\sigma_{k\gamma H}$, Fig. 5.67), h is the coal stratum half thickness, and σ_{c} is the coal uniaxial compressive strength (11 MPa; Frid 1990). If we assume that the drift width, $2X_0 = 3$ m (typical for vent and tramming drifts in North Kuzbass mines) and the coal stratum thickness $2h = 2$ m (also a representative value), we can calculate the distance to the stress maximum by Eq. 523. Table 5.4 shows that for all RB hazardous conditions (4–7 m from the mine-working face, Frid 1997a) the stress maximum is about $\xi = 1$ m from the commencement of the stressed zone ($\sigma_{k\gamma H}$ zone, Fig. 5.67).

Let us assume that the RB hazard zone before coal drifting has a parallelepiped form with a width equal to the drift width ($2X_0 = 3$ m), a height equal to the coal stratum thickness ($2h = 2$ m), and a length equal to the distance from the origin of the $\sigma_{k\gamma H}$ stress zone to the stress maximum ($\xi = 1$ m). Hence, the volume of the RB hazard zone would be 6 m^3.

A formation of a 6 m^3 stressed zone cannot be developed instantly. As noted by Kuksenko et al. (1982, 1987), the time to form a highly stressed zone is related to its dimensions. This relation is valid for laboratory fracture experiments, mine pillar loading, RBs and even for earthquakes (Kuksenko et al. 1982; Mansurov 1994) and can be approximated by the following formula:

$$T = 10^{3.75}L \tag{5.24}$$

where T is the time (s) to form the stressed zone, and L is an average dimension of the stressed zone (m).

If the volume of the stressed zone is 6 m^3, its average dimension, L, would be about 2.5 m, and according to Eq. 5.24, the time to develop this zone will be approximately 4 hours.

EMR source size estimation. Assuming that the cracking rate n (number of cracks per unit time) is nearly constant during the whole period of the highly stressed zone formation, then

$$n = \frac{N'}{T} \tag{5.25}$$

where N' is the total number of cracks created in the volume V.

The crack length is associated with the time from the EMR pulse origin up to its envelope maximum (Rabinovitch et al. 1998, 1999b, Eq. 5.2). For 100 kHz pulses (Frid 1997a,b), this time is about $T' = 10–15$ μs (Frid 1990; Rabinovitch et al. 1998).

As noted by Marder (1996a), crack velocity does not exceed the Rayleigh wave velocity v_R. For coal, v_R is of the order of 1 100 m s^{-1} (Frid 1990). Hence, the length of the crack, ℓ, that radiates a 100 kHz EMR pulse would be

$$\ell = v_R T' \tag{5.26}$$

Estimation of EMR activity in the hazardous zone. As follows from the kinetic theory of failure (Zurkov et al. 1969; Regel' et al. 1972; Petrov and Gorobetz 1987), the maximum number of cracks of length ℓ in a volume V is limited by the following relation:

$$N' = \frac{V}{(k\ell)^3} \tag{5.27}$$

where k is about 3, the concentration factor. N' ranges between 45 000 and 170 000 and its average value is 107 500. Hence, the limiting cracking rate (according to Eq. 5.25) will be $n_{lim} = 7.7$ events per second. Hence, a RB hazard situation is predicted when the cracking rate, n, is larger than this limit value:

$$n > n_{lim} \tag{5.28}$$

The final step is to associate this criterion of cracking rate with a specific parameter of the EMR. There are numerous EMR parameters that could be measured in a mine, for example, EMR activity (see Sect. 5.10.2.2), the number of EMR events (often registered as the number of EMR peaks) per unit time, or the energy of EMR pulses per unit time determined, for instance, by the summation of pulse amplitude squared multiplied by pulse duration, per unit time, etc. All of these parameters characterize only the EMR rate (number of EMR events per unit time), and can specify only the cracking rate.

As noted above, the EMR activity is the number of crossings (per unit time) of the EMR signal amplitude a specific voltage level of the counter. The number of crossings formally depends on the EMR amplitude, i.e., the higher the EMR pulse amplitude, the larger is the number of intersections with a defined voltage threshold. However,

our experience shows that the EMR amplitude is relatively stable (5–50 mV m^{-1}) and does not deviate by more than one order of magnitude from its average level. This phenomenon may be explained in the following manner: EMR amplitude is a function of crack area (Rabinovitch et al. 1998, 1999b) and this implies that this amplitude is inversely proportional to the EMR frequency (Rabinovitch et al. 1999b). Hence, if we select a specific frequency range to measure EMR activity (i.e., a definite crack width), we limit the range of EMR amplitudes that will be registered (the EMR amplitude span observed in laboratory conditions by Rabinovitch et al. (1999b) is also not more than one order of magnitude for a given specific frequency).

The amplitude of EMR pulses quickly decreases after 2–3 oscillations (Fig. 5.58, Frid 2001). To differentiate the EMR data from mine industrial noise, we preset the voltage level of our counter to register only the maximal half-wave of the signal (Fig. 5.58). The maximal half-wave therefore intersects a set voltage level twice (Fig. 5.58), and the value of the EMR activity (especially the limiting value) is twice as high as the cracking rate:

$$N_{\text{th}} = 2n_{\text{lim}} = 15.7 \text{ EMR pulses/s (157 EMR pulses/10 s)} \tag{5.29}$$

Hence, the theoretical criterion of RB hazard is the following: A RB hazard situation is predicted if the EMR activity, N, is larger than $N_{\text{th}} = 157$ pulse/10 s:

$$N > N_{\text{th}} \tag{5.30}$$

As seen, the calculated N_{th}=157 pulse/10 s and the empirical N_{emp}=115–120 pulse/10 s criteria (see above following Eq. 5.22) are close enough.

Generalizing formulas (5.22, 5.28–5.30), we can formulate a theoretical EMR criterion via the theoretical value of cracking rate for a given mine situation:

$$N > N_{\text{th}} = kn_{\text{lim}} \tag{5.31}$$

where N is the measured EMR parameter in a mine-working, N_{th} is the theoretical limiting value of this EMR parameter, k is a coefficient that depends on the type of parameter (e.g., k for activity equals 2, but if we measure the number of EMR peaks, $k = 1$), and n_{lim} is the limiting cracking rate.

Our theoretical approach based on a minor number of parameters (limiting value of gum volume, typical mine-working width, coal seam thickness, and coal uniaxial compressive strength) enables us to estimate a value for EMR criterion that must be verified by mine investigations. Its adoption would significantly reduce the time to use the EMR criterion.

5.10.2.5
Precursors to Rock-Gas Outburst

Another dangerous phenomenon in mines is the "rock and gas outburst" in which a burst is assisted by liberated gas (CH_4 in coal mines, N_2 in rock salt mines, etc.). The gas is liberated by the rock fracturing and acts (like pore pressure) to decrease the critical stress level needed for destruction of the mine-working walls (Petukhov and Lin'kov 1983).

At present the standard geo-mechanical method of rock-gas outburst prognosis in coal mines consists of measurement of volumes of gum and gas liberation rate (Petukhov and Lin'kov 1983). Forecast boreholes are usually being drilled at intervals of 1 m. After drilling of each interval, the volume of gum and the quantity of gas liberation are measured. If both of these parameters exceed a definite limiting values, drilling stops, and the given part of the mine-working is considered to be hazardous to rock-gas outburst. An experience of mining works in North Kuzbass shows that a formation of rock-gas outburst hazard zones is reliably fixed at the quantity of gum of more than 5–6 l m^{-1} (liter per meter) and a gas liberation rate value of more than 5 l min^{-1} (liter per minute) at the fourth to sixth intervals (depths) of the forecast borehole (from the fourth to the sixth meter from a mine-working face). This method is widely used, although sometimes bore-holing can itself initiate rock-gas outburst.

EMR observations in coal mines. After registrations of natural EMR activity, the degree of rock-gas outburst hazard at that point of mine-working was detected by the standard method of measurement of the volumes of gum and gas liberation rate.

The first example of the EMR registration is shown in Fig. 5.68 (Frid 1997b). In this case, drift was conducted in a zone of an intensively variable thickness of coal seam and a sharp changeable inclination angle. Figure 5.68 shows that a decrease of seam thickness from 2.6 m (18 April) to 1.1 m (from 17 May up to 30 May) corresponded to rock-gas outburst hazard increase (an increase of gum value of up to 6 l m^{-1} and gas liberation rate quantity of up to 7–12 l min^{-1}) with a simultaneous increase of the natural EMR activity level. A restoration of coal seam thickness to its original value (15 June–29 June) caused a decrease of gum and gas liberation rate parameters to their regular levels and a decrease of EMR activity. An increase of EMR activity was also obtained during a drift conducted through an inclination angle raise (of up to 60°) of the coal seam (5 April, Fig. 5.68).

An example of EMR registration in a zone of geological fault influence is shown in Fig. 5.69 (Frid 1997b). At a distance of 8 m from a geological fault, an anomalous EMR activity was registered (20 October). Controlled boreholing showed that the value of gum was of the order of up to 6 l m^{-1} and the gas liberation rate was of the order of up to 16 l m^{-1}. A further conduction of this drift left the fault influence zone, and EMR activity returned to normal (from 16 May up to 28 October).

EMR monitoring was also conducted in a mine-working where the influence of pillars stretched along 150 m of a drift. Profiling of the mine-working showed an EMR activity at the stressed region under the pillar where the values of gum and gas liberation rate were also irregular: More than 7 l m^{-1} and 8 l min^{-1} respectively.

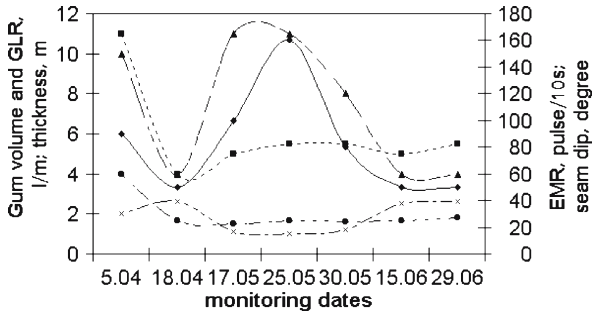

Fig. 5.68.
EMR monitoring in mine-working. Note that *GLR* on this figure is gas liberation rate (■ Gum volume, ▲ GLR, × seam thickness, ● seam dip, ◆ EMR) (Frid 1997b)

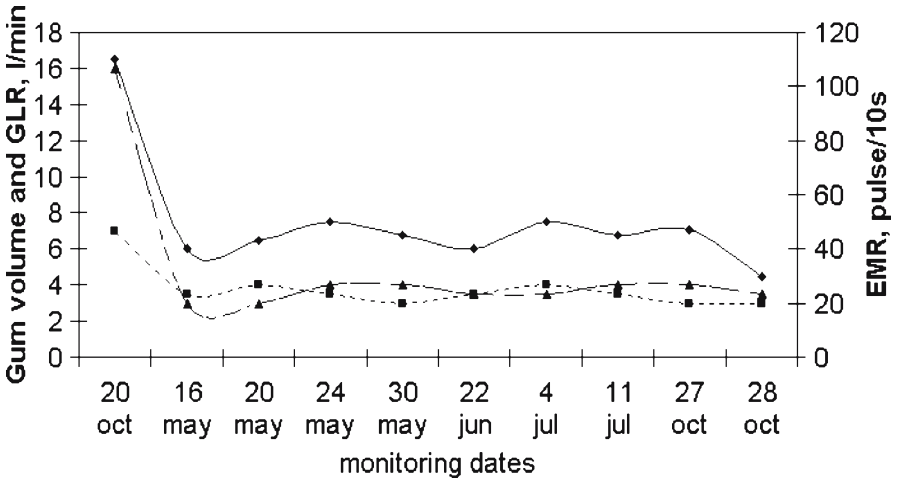

Fig. 5.69. EMR monitoring in drift (■ Gum volume, ▲ GLR, ◆ EMR) (Frid 1997b)

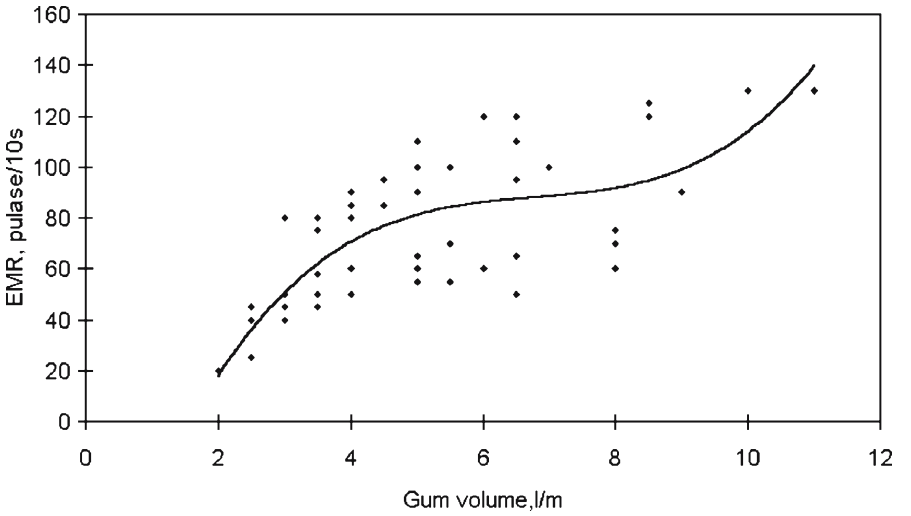

Fig. 5.70. EMR activity vs. Gum volume. Experimental EMR data are marked by ◆ (Frid 1997b)

Electromagnetic radiation forecast criterion. We have conducted more than fifty investigations in rock-gas outburst dangerous and safe mine situations (Frid 1997b). Figure 5.70 depicts a scatter of EMR activity data vs. gum values, while Fig. 5.71 shows EMR activity vs. gas liberation rate values. Significant data dispersion is seen in both cases, yielding regression coefficients in both cases of not more than 0.7. However, both show a monotonic increase of EMR activity with a rise in both gum and gas liberation rate. We hypothesized that the low correlation coefficients imply that the value of EMR activity depends on both parameters together rather than on a single one. To examine this hypothesis, we drew all experimental data (fifty-eight experimental points) in the form of EMR activity vs. both gum volume and gas liberation

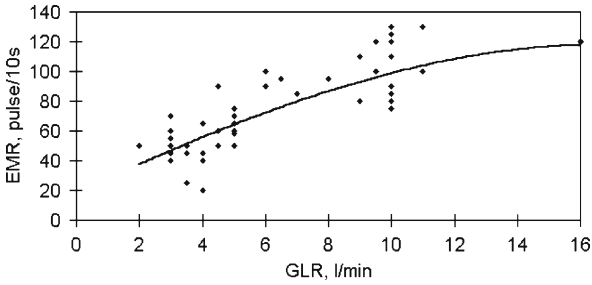

Fig. 5.71. EMR activity vs. gas liberation rate. Experimental EMR data are marked by ◆ (Frid 1997b)

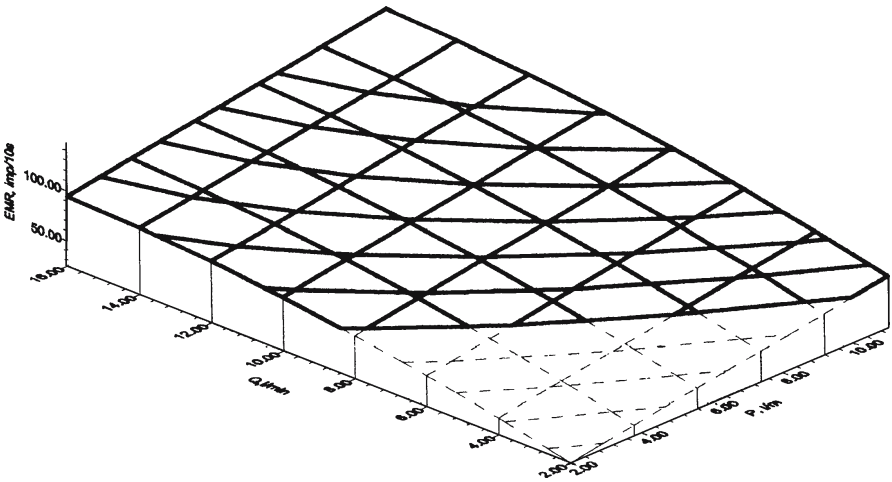

Fig. 5.72. EMR activity surface vs. Gum (P) and gas liberation rate (Q) (Frid 1997b)

rate quantities (Fig. 5.72). A fit of this surface calculated by a least square method is the following:

$$N(P,Q) = -16.1651 + 13.2875Q - 0.361033Q^2 + 6.44858P - 0.227596PQ \qquad (5.32)$$

where N is the EMR activity, while P and Q are gum and gas liberation rate quantities, respectively. A comparison of the experimental and the calculated data in Eq. 5.35 shows a very good correlation (Fig. 5.73). The correlation coefficient is 0.908. Thus, Eq. 5.32 reflects the existence of a relationship between the EMR activity of a coal seam and the gum and gas liberation rate quantities. Hence, an increase of EMR activity can indicate rock-gas outburst hazard development.

We used this equation for an EMR criterion forecast. As was noted above, rock-gas outburst hazard zones are correlated with a quantity of gum of more than 5–6 l m^{-1} and a gas liberation rate of more than 5 l min^{-1}. The related EMR quantity by Eq. 5.32 is 67–73 pulse/10 s. Statistical parameters of gum, gas liberation rate and EMR activity data are shown in Table 5.5. Analysis of this table shows that the EMR criterion yields mean and median values that are very close to the experimental data. We also carried out a correlation analysis of rock-gas outburst hazard estimation by the gum-gas liberation rate method and by the proposed EMR activity criterion. The correlation co-

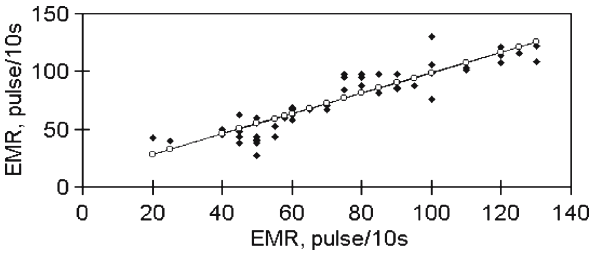

Fig. 5.73. Regression between EMR activity experimental (◆) and calculated data (Frid 1997b)

Table 5.5. Statistical analysis experimental and calculated EMR data

Statistical parameters	Gum (l m^{-1})	GLR (l m^{-1})	EMR (pulse / 10 s)	
			Experimental	Calculated
Mean	4.91	6.43	72.72	74.77
Median	4.00	5.00	70.00	69.66
Minimum	2.00	2.00	20.00	26.95
Maximum	11.00	16.00	130.00	129.71
Count	58.00	58.00	58.00	58.00

efficient is 0.966, indicating a very high forecast probability. Thus, if the EMR activity is higher than 70 pulse/10 s in a zone of a mine-working, this zone should be declared to be rock and gas outburst dangerous.

Equation 5.32 allows us to explain a relationship between the build-up of stress and gas liberation in a mine-working face (and hence, an increase of rock and gas outburst hazard) and the increase of EMR activity. As is seen, EMR activity level is affected by both stress level and gas liberation rate. An increase of stress level near a mine-working causes an intensive fracturing of the extremely stressed coal. This fracturing process is the source of EMR activity increase. Fracturing of the coal seam in a zone of higher stress excites an intensive process of gas liberation and in turn leads to an additional internal (pore pressure like) pressure. This pressure is akin to a tensional stress in the coal mass that enhances a fracturing catastrophe simultaneously leading to a magnified EMR activity.

EMR control of rock-burst and gas-outburst hazard elimination. Both RB and gas outburst hazards in a mine-working face are frequently eliminated by water infusion, the performance of which is usually verified after its completion by the gum method. During infusion, water "impregnates" coal near the mine-working face. If a control hole intersects a water saturated zone, it excites water spouting out. Then gum turns into slime, and it becomes impossible to measure its volume. This situation makes it necessary to drill additional control holes. However, the existence of several control holes (intended to estimate water infusion performance) diminishes the influence of the water infusion itself because the increase of water pressure sometimes causes breaching to a neighboring hole. Hence, we have a vicious cycle: To estimate performance we need a hole, and the holes negatively influence performance. The only way out is to estimate water infusion performance during its execution without drilling holes.

The analyses of safety conditions (see Sect. 5.10.2.1.), EMR features induced by sample compression and associated with borehole drilling (see above), enables us to state two principles of EMR used for water infusion control:

1. RB is impossible if the mine-working face is transferred back to the residual strength.
2. If a material is under residual strength, its loading is not accompanied by EMR excitation.

EMR-water infusion model. As is generally known, rock stress condition may be described by the Coulomb-Mohr envelope (Twiss and Moores 1992). Let us assume that the coal stress condition in the face of a mine-working is described by the Mohr circle (Fig. 5.74, 1, Frid 2000) and by the Coulomb-Mohr envelope below which the material is stable (Fig. 5.74, 1'). A water pressure increase forms a pore pressure, P, that is equivalent to an additive tensional stress. This tensional stress shifts the Mohr circle to the left by P. Hence, a part of the circle will now be above the Mohr-Coulomb envelope (Fig. 5.74, 2), i.e., coal becomes unstable, and will fracture. This fracturing results in an increase of EMR activity. As a result of coal fracturing, its strength decreases. However, if the stress level in a coal stratum is still high, a sharp decrease of water pressure (for example, due to pump stoppage) will excite crack closure and EMR excitation. Hence, a water pressure cycle (both increase and decrease) will affect EMR activity.

Thus, water pressure changes are accompanied by EMR activity up to the transition of coal to its residual strength (Fig. 5.74, 3), and vice versa: An absence of EMR activity variation during water pressure changes during the "loading-unloading" cycle could be a criterion of the water infusion performance or in other words, a check of hazard.

EMR during water infusion in coal mines. EMR measurements during water infusion were carried out on Koksoviy, Andreevsky, and Desyatiy coal stratums in North Kuzbass (Russia) (Frid 2000). Water infusion was conducted in the following manner:

The length of the holes was 6 m and the sealed length was 5–5.5 m (a mining experience in North Kuzbass shows that the existence of a 5–6 m safeguard zone (residual strength zone) in a mine-working face indicates a non-dangerous condition);

Water pressure was increased in steps of 0.2–0.3 γH to provide coal "impregnation" with water, where γ is the rock density (kg m^{-3}) and H is the stratum depth (m).

A new step of water pressure increase took place only after EMR activity stabilization. After reaching 0.8 γH, water pressure was sharply decreased to 0.3 γH; as our experience showed that if the water pressure exceeds a value of 0.8 γH, the probability of the water breaching to the mine-working face becomes very high.

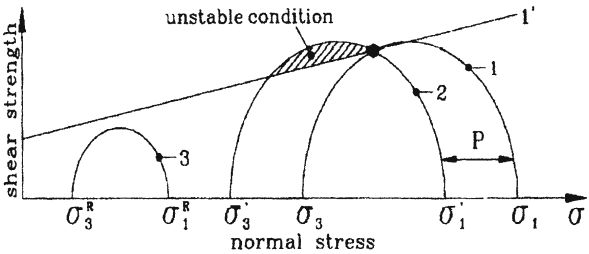

Fig. 5.74.
Mohr-Coulomb failure envelope around Mohr circles which represents the different coal conditions during water infusion (Frid 2000)

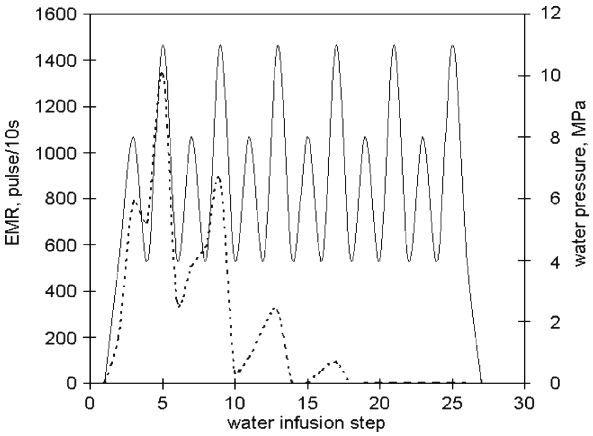

Fig. 5.75.
An example of EMR registration during water infusion. *Full-drawn curve* is the water pressure, while the *hatched curve* is the EMR activity (Frid 2000)

Cycles of pressure increase–decreases were repeated as long as the water pressure changes initiated an EMR activity. When EMR activity induced by water pressure changes ceased, water infusion was terminated.

An example of EMR registration during water infusion is shown in Fig. 5.75. Water infusion was carried out in the drift face of Andreevsky stratum (at 700 m depth, average rock density is about 2×10^3 kg m^{-3}, the step size of water increase is 4 MPa (0.3 γH), and the maximal water pressure value is 11 MPa (maximal water pressure must be less than 0.8 γH, see above). Gum value measured at the drift face was 6 l m^{-1}; hence, a RB hazardous situation existed.

Figure 5.75 shows that an increase of water pressure of up to 4 MPa during the first cycle is associated with EMR activity excitation (of 500 pulse/10 s); an increase of water pressure to 8 MPa initiated an additional increase of EMR activity (to about 800 pulse/10 s). The next decrease of water pressure to 4 MPa caused an insignificant decrease of EMR activity, and a following water pressure increase to 11 MPa resulted in an additional EMR activity jump (to 1 350 pulse/10 s). The next decrease of water pressure to 4 MPa led to a significant decrease of EMR activity, but its level remained high. Therefore, the water pressure rise during the second cycle also induced an increase of EMR activity. After the second cycle of water infusion, EMR activity decreased to 50 pulse/10 s. Drilling of a forecast borehole showed that gum value was about 4.5 l m^{-1}. This value is a little lower than the critical level, although it also shows that the zone of drift influence is still quite stressed. The EMR activity was large up to the third cycle of water infusion, while the fifth and sixth cycles of water infusion were not associated with any EMR appearance. Drilling of a forecast borehole after the sixth cycle of water infusion showed that it was impossible to determine gum value, due to very high coal humidity. However, measurement of natural EMR activity in this zone showed that the average value of natural EMR activity was about 50 pulse/10 s; that is significantly lower than the limiting value of general EMR activity (120 pulse/10 s, Frid 1997a, 2001) and implied that the zone near the mine-working face was safe.

Note that the absence of EMR excitation due to water pressure changes is a qualitative criterion. It does not determine, for example, the number of water pressure cycles still needed for water infusion performance. Our research (more than 70 EMR investigations during water infusion) has shown that the EMR criterion really characterizes water infusion performance.

5.11 Summary

A comprehensive model of EMR emission mechanism from cracks was developed. This model can be described as follows: Following the breaking of bonds, the atoms on both sides of the severed bonds are moved to "non equilibrium" positions relative to their steady state ones and oscillate around them. Lines of oscillating atoms move together and by being connected to atoms around them (in the forward direction and also atoms on their side of the two surfaces newly created by the fracture) the latter also participate in the movement. The ensuing vibrations are similar to those calculated in the Debye model for bulk oscillations. The larger is the number of cut bonds, the larger is the area of excited atoms, and hence the greater becomes the EMR amplitude. These oscillations behave like surface optical waves, where positive charges move together in a diametrically opposite phase to the negative ones and decay exponentially into the material like Rayleigh waves. The resulting oscillating electric dipole is the source of the EMR. The pulse amplitude decays by an interaction with bulk phonons.

The model leads to an invariant EMR 'basic pulse shape' that repeats itself in all examined materials when failed by different testing techniques (including triaxial compression, percussion drilling and large-scale rock explosion). The model enables us to use EMR results for calculating the length, width and area of cracks and to compare them to actual crack sizes measured by fractographic techniques. Thus, a "finger-print" of initial micro-cracking was established. The 'basic shape' appears also in pilot experiments in open quarries during rock explosion.

An overall comparison of EMR signals that were excited by compression, drilling and blasting shows that their basic shape is invariant under both dynamic and quasi-static loadings. The similarity in shape of single EMR pulses, induced by the three processes, therefore indicates that a unified EMR emitting mechanism is operating behind them all and therefore enables us to analyze EMR signals induced by all three processes by the same model.

Moreover, our investigations showed that global relationships (Gutenberg-Richter and Benioff strain release) of EMR signals obtained during rock fracture in the laboratory are similar to those measured in earthquakes.

EMR measurements were conducted in mines. Criteria for rock-bursts and rock-gas outbursts were developed based on results from these measurements and on theoretical models. These criteria are easier and faster to implement than the existing ones, which necessitate drillings and gum and GLR measurements.

Based on these achievements, possible experiments were proposed as guidelines that can lead to earthquake forecasting via EMR detection and monitoring.

Assorted Problems in Fracture Geology

This chapter consists of a variety of basic issues in fracture geology. Section 6.1 explains the importance of studying regional jointing. Section 6.2 outlines some necessary procedures in studying joints, from data collection in field outcrops to joint set discrimination and determination of paleostress directions. Section 6.3 relates to studies of paleostresses in the Israeli Negev and considers regional jointing in the broad context of plate tectonics. Section 6.4 presents a new, perhaps controversial probe into certain properties of joint length. Section 6.5 briefly mentions the method of local paleostress estimation by fractographic techniques. Sections 6.6–6.9 concern four investigations from the Beer Sheva and Shephela synclines. Section 6.6 contains information about a multi-fracture assemblage in a fault termination zone, where a joint set exhibits an intricate pattern of the paleostress trajectories. Section 6.7 describes a variety of fault-joint geometric and genetic relationships across the local stratigraphic column. Section 6.8 explores the formation of "surface joints". Section 6.9 relates to studies on several aspects of fracture hydro-geology. Finally, Section 6.10 presents a new approach to *en echelon* segmentation.

6.1 The Importance of Studying Regional Jointing

Regional vs. local joint distribution. Sections 6.1–6.3 relate to the discrimination of systematic joint populations (Hodgson 1961b) into distinct sets, which is often termed "the study of the regional joint pattern". These joints fall into four groups (burial, syntectonic, uplift and post-uplift) that generally have large, regional spreads and reflect slow, quasi-static fracture (Sect. 1.5), particularly in the early burial stage. They are distinguished from dynamic joints that form rapidly in granites (Sect. 2.4.6.1) and occassionally in connection with earthquakes, and have limited, local distribution. This distinction is an approximation; it is made for convenience and is not always accurate: Some joints may start slowly and reach high velocities (Sect. 4.9) and the identification of dynamic joints is not always simple (Sect. 2.4.6.1).

Definitions and discrimination of joint sets and motivation for their study. There are different definitions for sets. Whereas Twiss and Moores (1992, p. 38) consider that a set consists of joints that have a "similar geometry", for Ghosh (1993, p. 478) this term applies to "an array of parallel joints". It was shown that the task of distinguishing a joint set from others may be simple in some areas (e.g., Gross 1993), but occasionally,

can be quite difficult (e.g., Nickelsen and Hough 1967; Bahat 1991a, p. 251–255; Younes and Engelder 1999). However, a reliable division of joint sets in a fracture province provides the key to identifying directions of paleo-principal directions and supplies a major tool in the investigation of local as well as regional aspects of structural geology. If it is fractographically clear that the joint surface forms normal to the direction of the maximum principal tension or extension (Bahat 1979a), it becomes also clear that a systematic joint set is coaxial with that of the direction of maximum paleocompression (Engelder and Geiser 1980).

The investigation of paleostress directions. It is quite remarkable that similar dilemmas regarding paleostress directions have intrigued investigators of regional fracture in two remote fracture provinces: The Appalachian Plateau in the eastern USA and the Beer Sheva syncline in the Israeli Negev (Chap. 3). This issue is discussed below (Sect. 6.3) by elaborating on results from Israel, with reference to results from the Appalachian Plateau. We note that in the context of identifying directions of paleo principal directions, "cross fold joints" that strike approximately orthogonal to fold axes (Engelder and Geiser 1980) are particularly important in these two provinces and in other investigated areas that exhibit "regional joint patterns".

At the heart of this investigation lies a formidable difficulty: Which methods should one use in discriminating joint sets and what relative weight should be assigned to the results obtained by the various methods? We deal below with this issue in two sections:

1. Qualitative, measurements, classification, plotting and division into sets.
2. Mapping joint distribution.

Experience has shown that the best results derive from a sensible utilization of all qualitative and quantitative methods applicable to a specific research area.

6.2 The Procedures of Studying Systematic Joints

6.2.1 Qualitative, Measurements, Classification, Plotting and Division into Sets

Carrying out the various steps in the procedure of studying joints involves a somewhat complex procedure. The first efforts should be spent on acquiring a general familiarity with the scope of outcrops in the investigated area (e.g., different lithologies and major structures). There seems to be no alternative to a good vehicle and a lot of travelling in the search for appropriate outcrops. Air photographs of various magnifications can help but do not provide reliable substitutes in this pursuit. One starts with a qualitative fracture study. Measurements would be the next step, as a prelude to classification. Classification, plotting and division into sets need to be done in alternating steps when progress of each step is helping to examine the validity of estimations of the preceding ones. A useful procedure of joint investigation is given by Goldstein and Marshak (1988); we try to supplement their manual.

6.2.1.1
Qualitative Description

The qualitative study consists of two parts. The first one involves a general description of the physical features of fracture. These include fracture (three) dimensions, characteristic spacing, straightness vs. curvature, general deviation from verticality, possible orthogonal relationships, anastomotic appearance as well as joint contacts and fracture interaction styles. The second part relates to fractography. Numerous investigators report about the lack of fractographic features in their research areas. However, in many other areas rocks maintain a record of their fracture history by their fracture surface morphology. While the mirror plane (Fig. 2.1) may disclose details of early events, the fringe often tells about late developments of joints. Familiarity with the fractographic descriptions in Chap. 2–4 may help in obtaining this information. First, take photographs of the selected joints (close-ups at various extents), paying particular attention to having the object lighted properly. Photographs taken under different light conditions will show different fractographies of a given fracture surface. It is occasionally advisable to wet the joint surface or increase the light on it. Do not forget to place a scale that does not obscure the features you want to show. Second, make accurate drawings of your selected photographs. Remember that drawing is far from being a trivial undertaking; it is already an important part of the fractographic interpretation. The radial features of the plume will lead to the fracture origin, provide information regarding changes in propagation directions and tell about the sequence of fracture generations when cut by other fractures. The ripple marks will inform something about the growth rhythm of the joint. Perhaps the most difficult task is marking the boundary between the mirror plane and fringe; it can often be quite controversial (Sect. 2.2.6).

6.2.1.2
Measurements

Strike measurements. The number of strike measurements will often be a compromise that takes into account field conditions, joint dips, the objectives of the study, economy of time and method (Goldstein and Marshak 1988). Generally, no dip needs be measured when joints deviate only several degrees from verticality. However, when bedding dip exceeds five degrees, joint strikes may be evaluated only after rotation of bedding to the horizontal position. We describe below several techniques that have been used in studying joints cutting chalk horizontal layers in the Beer Sheva syncline (Chap. 3) that are thought to be adequate.

At least a hundred strike measurements were taken in large outcrops in which thousands of joints were exposed (e.g., stations 2, 3, 4 in Bahat and Grossmann 1988). In such outcrops the "discrimination method" was used, whereby measurements were carried out only on "reliable", original joint surfaces that could be clearly identified by fractographic ornamentation, yielding the accuracy of ±2–3°. This method provided the most trustworthy results. The "comprehensive method" was used in many medium size outcrops in which about a hundred or two hundred joints were exposed, whereby all "reliable", systematic joints were measured (e.g., stations 20 as above, and 83 from present Fig. 3.37). This method provided quite dependable results. Sector intervals of 1°

were used in all the histogram plots, assuming that inaccuracies would balance each other. The "selection method" (Goldstein and Marshak 1988) was used in twenty-nine stations along Wadi Secher (Bahat and Shavit 1997). In this method, we visually scanned each outcrop and selected representatives of the prominent joint sets. We then measured a few tens of joints in each station. This method provided a good "general picture" but its reliability for statistical analysis would be limited. An obvious question that follows this description is: What about taking measurements in rocks where joints are not fractographically decorated, fractures are not quite straight, strike and dip spreadings are significant in suspected individual sets and joint surfaces are weathered and/or splintered (like in many limestones and dolomites throughout Israel and in some chalks in England, Bahat 1991a, Table 5.5)? The answer is yes, take measurements, but be aware of the reduced reliability of the results and stay conservative in data processing and interpretation of the results.

Length measurements. Scaneline (traverse) techniques (e.g., Goldstein and Marshak 1988) are often practiced in studying joint length distribution. We recommend however that a fractographic method should be used where possible. This can be accomplished on vertical exposures along road cuts and wadies. An example is given from Wadi Naim, where the lengths of forty four joints were accurately measured from tip to tip of unilateral and bilateral plumes that mark the joint surfaces along a horizontal 60 cm thick layer (Bahat 1988b). In this method, fracture length is actually measured where the plume tips show the exact ends of the joint (Fig. 6.1). Scaneline techniques are less accurate because they rely on measurements of many fractures even where a large proportion of their traces terminates beyond the boundaries of the typical exposure. This difficulty is overcome by making measurements only at the intersections of the fractures with grids of parallel scanlines without attempting to identify the

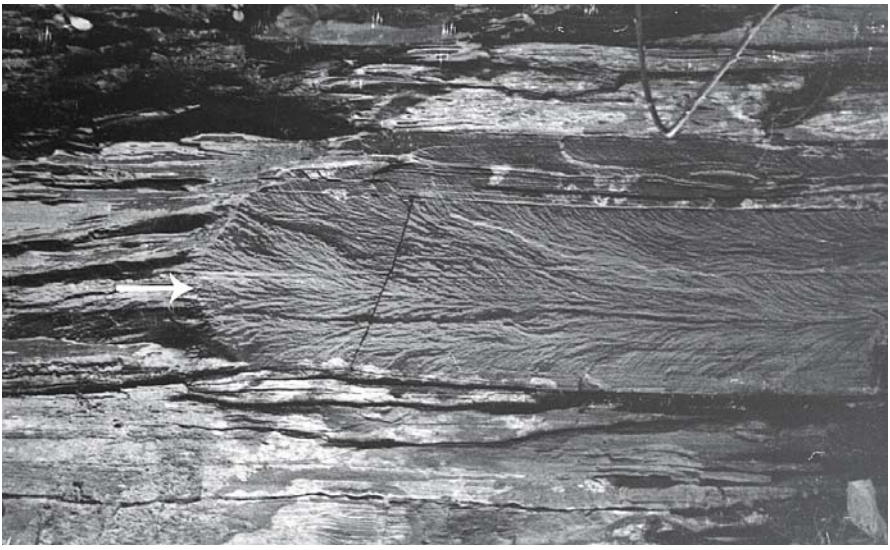

Fig. 6.1. An exact joint tip is shown by the sharp distal boundary (*arrow*) of the plume, for measuring joint lengths. Width of joint is 20 cm

ends of the fracture traces. Fracture trace length is then estimated from the censored data by statistical methods (e.g., Panek 1985).

Additional aspects of joint-set discrimination. There are situations where additional methods are worth considering. "Strike superposition" results are also useful for set discrimination, whereby results obtained in a given area by different investigators (Bahat 1991a, p. 251) or by a given investigator (Sect. 3.4.3.1) are compared. Comparing strikes of *en echelon* segments to strikes of the parent joints (Sect. 2.2.7.6) can also improve the reliability of joint set differentiation. Furthermore, certain joint sets can be identified by particular fracture markings (Fig. 3.36a). Thus, some initial results on the regional joint pattern can be obtained by combined qualitative methods. Often, new research areas require new approaches to the problem. In the Bristol Channel (Sect. 3.2), the regional joint pattern has some unique complications that required the application of sophisticated techniques specially designed for that area (Engelder and Peacock 2001). The study of the gradual development of "surface joints" was carried out by combined photographic and statistical techniques (Sect. 6.8).

A Genetic classification into joint groups. The genetic classification of joints that occur in sedimentary and plutonic rocks is important in fracture analysis, in order to avoid mistakes in the resolution of the regional joint pattern and in the tectonophysics interpretation of the investigated areas (e.g. Sects. 6.9.3 and 4.7.1.1). The genetic classification of joints must be carried out before plotting the results so that joints of different groups should not be plotted unintentionally together. The genetic characterization of various fault-joint types (Sect. 6.7) can also help in understanding the fracture history of investigated areas.

Plotting diagrams. Plotting the sum of measurements following separation into genetic groups is the first step toward interpreting the results. The best way of plotting results for vertical joints (either originally measured as such or after rotation) is by histograms. Bahat (1997) showed that results displayed on a rose diagram may give a different impression from the same results when plotted on a histogram. In extreme cases, while a histogram can show "extra" peaks that possibly suggest a large number of sets, a rose diagram for the same joint population may "hide" an essential peak or two. Thus, there are various degrees of certainty regarding the division into joint sets when all measurements are summarized in histograms or stereographic nets or in both (e.g., Grossmann 1983; Bahat and Grossmann 1988), frequently due to unclear maxima and minima on the plots. Additional statistical techniques are often used in order to increase the credibility of joint set discrimination.

6.2.2
Statistical Analysis in Support of the Division of Joints into Sets

We refer below to two analytical tracks in support of the division of joints into sets; first, methods of separation between two adjacent populations of joint azimuth, and second, by a special reference to joint spacing. Often one selects the technique according to the access to a computer distribution program, and these become more available with time (e.g., Exell, jmp, Rock Works). A few choices are briefly mentioned below.

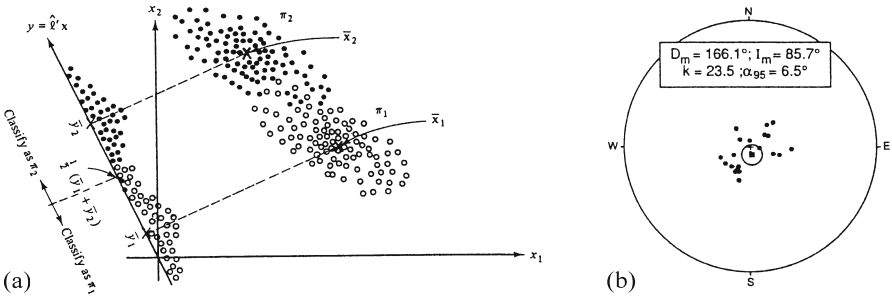

Fig. 6.2. a Fisher's (1938) solution to separate joint populations of two sets when their measurements partly overlap each other is by projecting the sample raw data to improve the definition of the boundary between the two. After rotation of the coordinate system of the original π_1 and π_2 populations, their distinction is significantly improved on the projection (from Johnson and Wichern 1988). **b** Equal-area projection of synthetic directional data that were randomly selected from a Fisherian population with true mean direction $I = +90°$ and precision parameter $k = 20$; individual directions are shown by *black dots*, mean direction is shown by a *solid square* with surrounding α_{95} confidence limit (circle), where D_m, I_m and k are, the calculated mean direction, the calculated mean inclination and the best estimate of k, respectively (from Butler 1992)

Joint set discrimination. A recurrent problem is how to separate two joint populations when measurements of these populations partly overlap each other. Fisher's (1938) solution is by projecting the sample raw data, as illustrated schematically in Fig. 6.2a. This projecting is based on the "Fisher sample linear discrimination function", and the method is explained in textbooks of statistics (e.g., Johnson and Wichern 1988). Smoothing techniques (Wise and McCrory 1982; Goldstein and Marshak 1988) can also help to make peaks stand out more clearly.

Additional contributions which are applicable in the earth sciences stemmed from the need for statistical analysis of paleomagnetism (Fisher 1953; Fisher et al. 1987). Fisher and coworkers developed a method by which each measured direction is given unit weight and is represented by a point on a sphere of unit radius. This method is known as the "Fisher distribution" and occasionally also termed "α_{95}". The confidence limit α_{95} is a measure of the precision at which the true mean direction has been estimated. One is 95% certain that the unknown true mean direction lies within α_{95} of the calculated mean. The inference is that there is a 5% chance that the true mean lies more than α_{95} from the calculated mean (Fig. 6.2b). Thus, the "Fisher distribution" helps to estimate the mean direction of given population. However, this method does not discriminate between populations, i.e., the directions in Fig. 6.2b may represent more than one population, which is disregarded by the small circle of α_{95} confidence limit.

Good computer distribution programs (e.g., jmp) help to calculate many statistical parameters like the arithmetic mean, median, mode, standard deviation, skewness (sk) and kurtosis (ku) (see Nomenclature). In addition, they can divide given collected data of azimuths into sub-populations and offer alternative combinations of sub-populations for comparison. It is up to the researcher to correlate the various combinations with additional qualitative (fracture physical properties and fractography) and quantitative (statistical parameters like kurtosis, spacing and FSR, see below) results in attempting to achieve high resolution in joint set discrimination. Such careful procedures can lead to satisfactory results and improve the credibility of the division into sets, based on the interpretation of histograms.

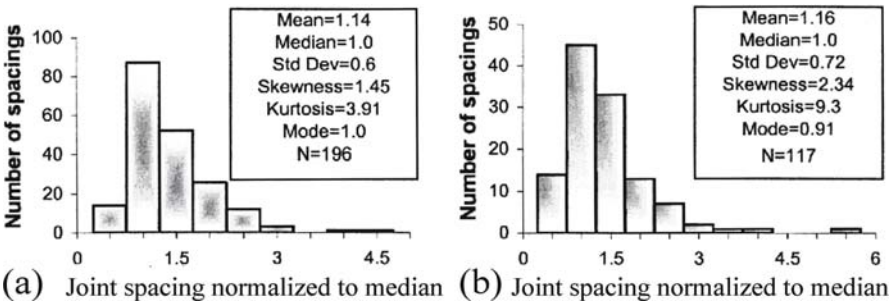

Fig. 6.3. Joint spacing distribution from the Mor Formation. **a** Set 343° (normalized joint spacing histogram of joint set B). **b** Set 350° (normalized joint spacing histogram of joint set C) (from Levi 2003)

Division into joint sets by a special reference to joint spacing. The importance of joint spacing for various geological and other applications is well known (e.g., Price and Cosgrove 1990, p. 54). Spacing is commonly measured between neighboring fractures of the same set along a line orthogonal to the average orientation in the set. We show below how a statistical analysis of joint spacing can improve both, the characterization of joint sets in relation to rock lithologies and the credibility of grouping into sets, citing joint investigation in two quasi-synclines from the south Negev (Levi 2003).

Sets 343° (B) and 350° (C) from the Mor Formation (Fig. 6.3a,b) raise the suspicion of a genetic linkage between the two (Levi 2003 and present Sect. 6.3.6). The high kurtosis value of set 350° suggests the possibility of a connection between the change in joint direction (from 343° to 350°) and differences in mechanical properties of the rocks cut by the two sets, a possibility raised by Goodwin (1995) (see also present Fig. 2.60). Like in the Beer Sheva and the Shephela synclines (Bahat 1987a), the two sets do not mix in the same chalk layer, rather they appear in separate layers (resembling Fig. 3.36a). This enabled the following experiment to be run with a high degree of credibility. Two sets of cylinders were drilled from the corresponding layers and were examined by an ultrasonic method (ASTM: D2845-90) for their wave velocity v_p, Young modulus E, shear modulus G_m and dry density d_d. The results (Fig. 6.4) clearly show a difference between the mechanical properties of the two joint sets. It has therefore been suggested (Levi 2003) that both 343° and 350° sets were formed in one stress field. However, the joints of set 343° formed in co-axial orientation with S_{Hmax} (the maximum horizontal compressive stresses) in the rock of higher density, whereas the joints of set 350° that formed in the rock of lower density deviated from parallelism to S_{Hmax}. This finding corresponds quite well with additional sets of results (Fig. 2.61 and Tables 2.2 and 2.3).

Levi (2003) compares the FSR values (Gross 1993, see Nomenclature) of all the investigated sets discriminated in his study area. The FSR value of set 326° is distinguished among all the other sets in having low values and a very small spread (lower left corner of Fig. 6.5). The other sets have high FSR values that scatter considerably. Levi (2003) considers that these results possibly reflect fracture under different tectonic conditions. Set 326° formed during the burial stage under increasing overburden conditions, resulting in relatively low strains under approximately uniform conditions. On the other hand, the characteristics of the other sets generally fit the criteria of fracture during uplift (Tables 3.3 and 3.5). Single-layer uplift joints form consequent to denudation under conditions of reduced overburden (Bahat 1999a) and are highly

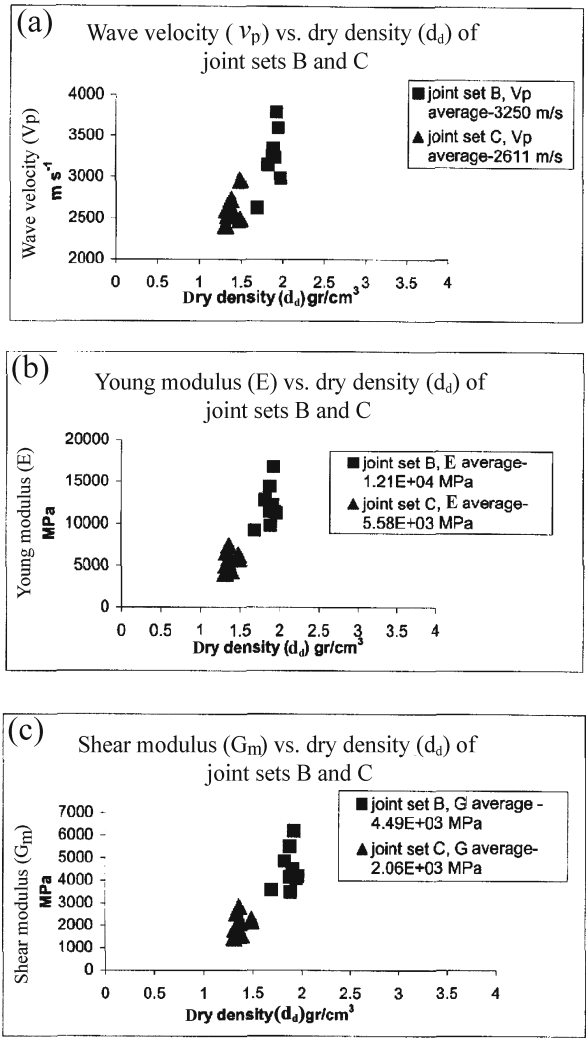

Fig. 6.4.
Plots of elastic properties vs. dry density for sets 343° (B) and 350° (C) from the Mor Formation, when wave velocity is v_p, Young modulus is E, shear modulus is G_m and dry density is d_d (from Levi 2003)

strained, probably in tensile rather than extensile conditions. Such conditions may result in high FSR values (Bai and Pollard 2000a). Fracture of uplift joints occurs in shallow depths, in stress fields that often compromise between regional and local stresses, due to influences from surface conditions (Bahat 1991a, p. 297). Therefore, spread in FSR values (Fig. 6.5) may be expected to characterize uplift joints. Hence, the determination of FSR values and their spread can help in the process of differentiating joint genetic groups.

It was found that the ratio of joint length to joint spacing (L / S) (Bahat 1991a, p. 309) characteristically varies according to joint grouping: Between 2 to 10 in burial joints and in the 20 ≥100 range in syntectonic joints. In uplift joints, L / S values generally range between those of the burial and syntectonic joints. Wu and Pollard (1995) distinguished two kinds of fracture patterns in sedimentary layers and in laboratory speci-

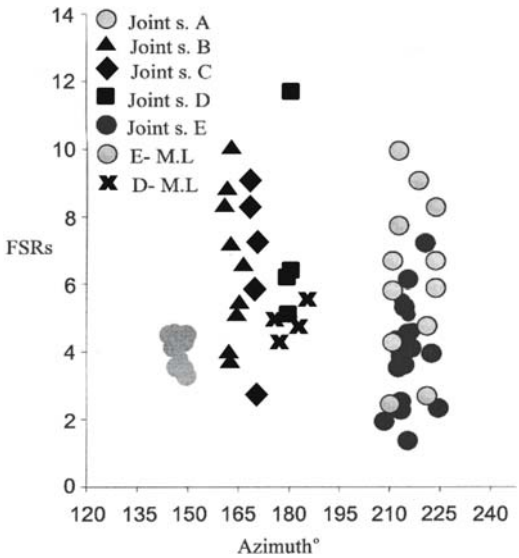

Fig. 6.5.
Spread of FSR values in different joint sets (see text for explanation) (from Levi 2003)

mens. One, termed *poorly-developed*, is characteristic of the early stages in the development of a fracture set when typical fracture lengths are roughly equal to or less than typical spacings, i.e., $L / S \leq 1$. The other, termed *well-developed*, is characteristic of the later stages when fracture lengths are much greater than spacings, i.e., $L / S \gg 1$. Wu and Pollard (1995) suggest that characteristic fracture growths occur under various degrees of strain. Fracture opening occurs during an advanced stage of jointing without significant fracture propagation. As the applied strain increases, the spacing decreases, because existing fractures increase in length and new fractures begin to propagate from flaws. However, when the applied strain reaches a certain limited value, the spacing stops evolving and remains nearly constant as the strain continues to increase. Levi (2003) found that the L / S values for sets 326° and 343° in the Mor Formation are 4.4 and 15.4, respectively, and that these values suggest that set 343° represents a more advanced strain than set 326°. This interpretation corresponds to the distinction made above, based on the FSR criterion. Thus, FSR and L / S are complementary parameters that correlate joint spacing characteristics with strain magnitudes.

6.2.3 Mapping Joint Distribution

Once the classification into joint sets is generally established, maps of joint set distribution can be produced. "Trajectory maps" were successfully produced by Engelder and Geiser (1980) and Geiser and Engelder (1983), showing the regional trajectories of S_{Hmax} inferred by the extrapolation of joint directions of particular sets from station to station (Fig. 3.1b,c). If in addition, one is interested in showing the relative concentration of the various joint sets in particular areas on a structural map, "maps of set distribution" may be used. Such maps may help in the interpretation of the effects of local and regional stress fields (e.g., due to neighboring faults) on the formation of the various sets (Levi 2003, p. 25).

6.3 Paleostresses in the Israeli Negev

We present below two different models regarding mesostructures and paleostresses in the Israeli Negev. One model considers two major stress field regimes that fluctuated through time in Israel (Eyal and Reches 1983; Eyal 1996; Eyal et al. 2001). The other model maintains that the sum of systematic joint sets in the Israeli Negev reflects a system of multi paleostresses (more than two major ones) that generally shows a clockwise rotation with time (Bahat 1997, 1999b). The difference between the two concepts is a reminder of the difficulties involved in interpreting the regional joint distribution in the Appalachian Plateau and the paleostress evolution in that region (Bahat 1991a, p. 251) (Sect. 3.1). A similar dilemma is connected with the interpretation of joint mechanisms in granites (Sect. 4.5.1). Hence, the two concepts represent a basic debate in fracture geology. We present below brief accounts from various studies that relate to this debate and then suggest our interpretation.

6.3.1 Jordan

6.3.1.1 *Clockwise Rotation of Compression in Jordan*

Burdon (1959) suggests three compression phases in Jordan. The first phase 'a' was minor, started in the Maestrichtian and came from southeast, approximately in the 285° direction. These forces were light, and the stresses they induced were relieved by the minor folds seen in the chert beds of the Maestrichtian of the Belqa Series. The second phase 'b' was major, probably in the Lower Miocene, or even a little earlier, approximately in the 322° direction. In north Jordan the Ajlun dome was formed and in the crystalline basement multi fracture systems occurred, including tension fractures in the 322° direction. The third phase 'c' was major. Compression came from the SSE, approximately in the 349° direction and took place in two sub-stages (C1 and C2), which were separated by a comparative quiet stage in the Pleistocene. These two phases were associated with a 107 km displacement along the Dead Sea rift, C1 of 62 km and C2 of 45 km. Salameh and Zacher (1982) measured horizontal stylolites in limestones of the Upper Cretaceous in Jordan. They found two dominant paleostress directions, 310–320° and 350°, which seem to be close to the above phases 'b' and 'c'.

6.3.1.2 *Southwestern Jordan*

Eldeen et al. (2000) present results obtained from kinematic slip data in the eastern margins of the Dead Sea rift in southwest Jordan, and their results are cited below. Stress inversion of fault slip data was performed by using an improved right-dieder method, followed by rotational optimization (Delvaux, TENSOR program). Fault slip data (totaling 2 773 data) include fault planes, slickensides and sense of movements. These results were obtained from rocks ranging in age from Precambrian crystalline basement to Oligocene/Pleistocene sediments and were inverted to determine eighty-eight differ-

ent paleostress tensors. Fault slip data allowed several paleostress tensor groups (stages) from the Precambrian to Post-Pleistocene period to be pointed out and were correlated with the tectonic evolution of the Dead Sea rift. The first two tensor groups were obtained from the Late Proterozoic (between 570 and 560 Ma) dike swarm, and the fault slip data related to the dike emplacement. Both show a transtensional stress regime, the first one (T1) with NE-SW S_{Hmax} corresponding to the major NE-trending dike system, and the second one (T2) with N-S S_{Hmax} corresponding to a minor and later N-S trending dike system.

The other tensors are related to Cretaceous or younger deformation stages, roughly coinciding with the three compression directions observed by Burdon (1959). The oldest stage (T3) has a strike-slip stress regime with E-W S_{Hmax} that affected all Pre-Tertiary series, but not the younger rocks present. The next stage (T4) is also characterized by a strike-slip stress regime, but with NW-SE S_{Hmax}, affecting the Palaeocene-Eocene rocks but not Pleistocene rocks. Eldeen et al. (2000) relate NW-SE trending dykes to the Miocene, including them in stage T4. A transpressional stage (T5), with NNW-SSE to N-S S_{Hmax} affected rocks with an age up to the Pleistocene. In addition, Late Pleistocene extensional stage (T6) with E-W S_{Hmin} (the minimum horizontal compressive stresses) stress regime was evidenced from the fault slip data that affected the Dana Conglomerate. The youngest tensor group obtained from the Dana Conglomerate points to an extensional regime with N-S S_{Hmin} (T7). Eldeen et al. (2000) suggest that the Late Pleistocene-Holocene sinistral strike-slip deformation is still active.

6.3.2 The East Mediterranean

Letouzey and Tremolieres (1980) conducted an extensive investigation of paleostress directions by measuring a large number of tectonic stylolites, joints, shear planes and faults in sedimentary rocks around the Mediterranean Sea. They plotted their results on a series of maps, displaying a complex pattern of paleostress directions that were correlated with different stages of the structural evolution in the region. These tectonic changes were linked to the Europe-African- Arabian indentation in the collision zone since the Upper Cretaceous and closure of the Tethys Ocean (Fig. 6.6a–e). Particularly relevant to the present discussion are the two maps from Turkey (Fig. 6.7a–d) and from Israel (Fig. 6.8). Most intriguing is the great variety of paleostress directions found in south Turkey that were categorized into three phases (we use below only upper semicircle azimuth numbers in describing directions of phases).

Letouzey and Tremolieres (1980) assign to the Late Cretaceous shortening (the "first phase") an early 075° compression direction associated with the Alpine zone that changed to 280° west of the belt of Levantin faults in north Syria (along the continuation of the Dead Sea rift up to south Turkey). The 315° shortening, taken to be the north Arabian average direction, was prominent east of this belt (Fig. 6.7a). Letouzey and Tremolieres (1980) consider that the first phase could correspond to a change in orientation of the stress due to the indentation process or to sinistral rotation of the Anatolian microplate during collision. The 280° corresponds reasonably well to the 290° compression direction found in Israel by them (Fig. 6.8).

The Late Eocene-pre-Middle Oligocene "second phase" is related to a tectonic event well known from the Pontids, Taurus and north Cyprus Mountains. This phase involved

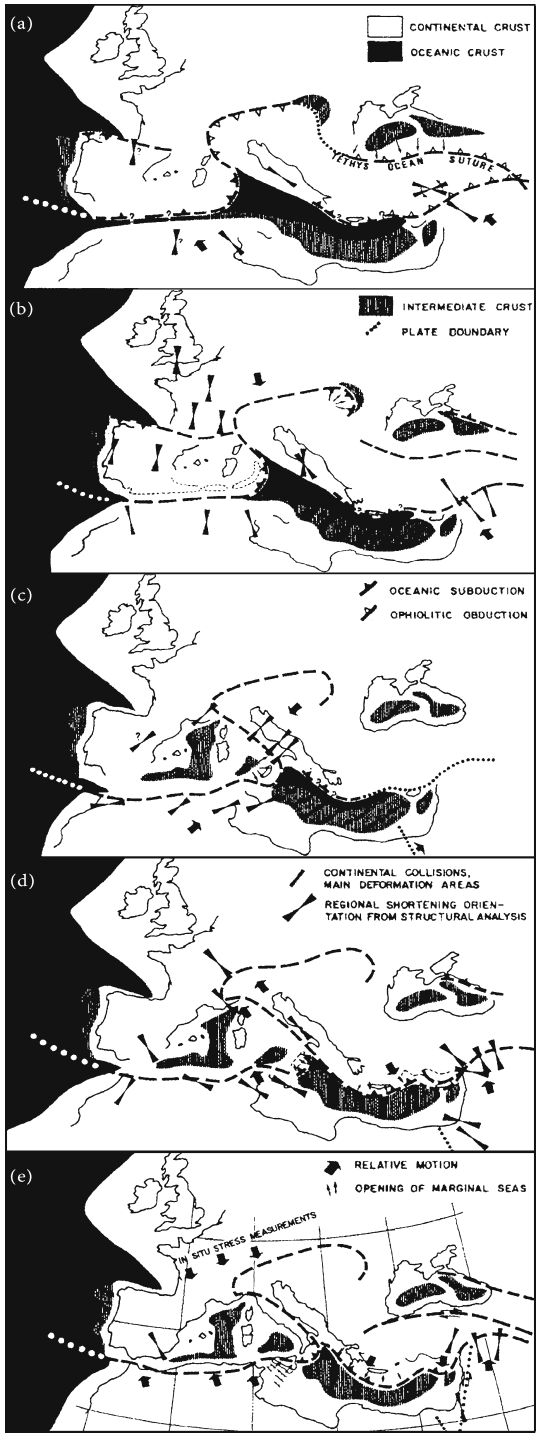

Fig. 6.6.
Sketch of evolution of the Mediterranean basins and paleostress field orientations. On all figures Europe was arbitrarily fixed. Regional paleo-stress orientations are in fossil positions. **a** Late Cretaceous; **b** Eocene; **c** Late Oligocene-Early Miocene; **d** Late Miocene; **e** Plio-Quartenary (from Letouzey and Trémolières 1980, see text for explanation)

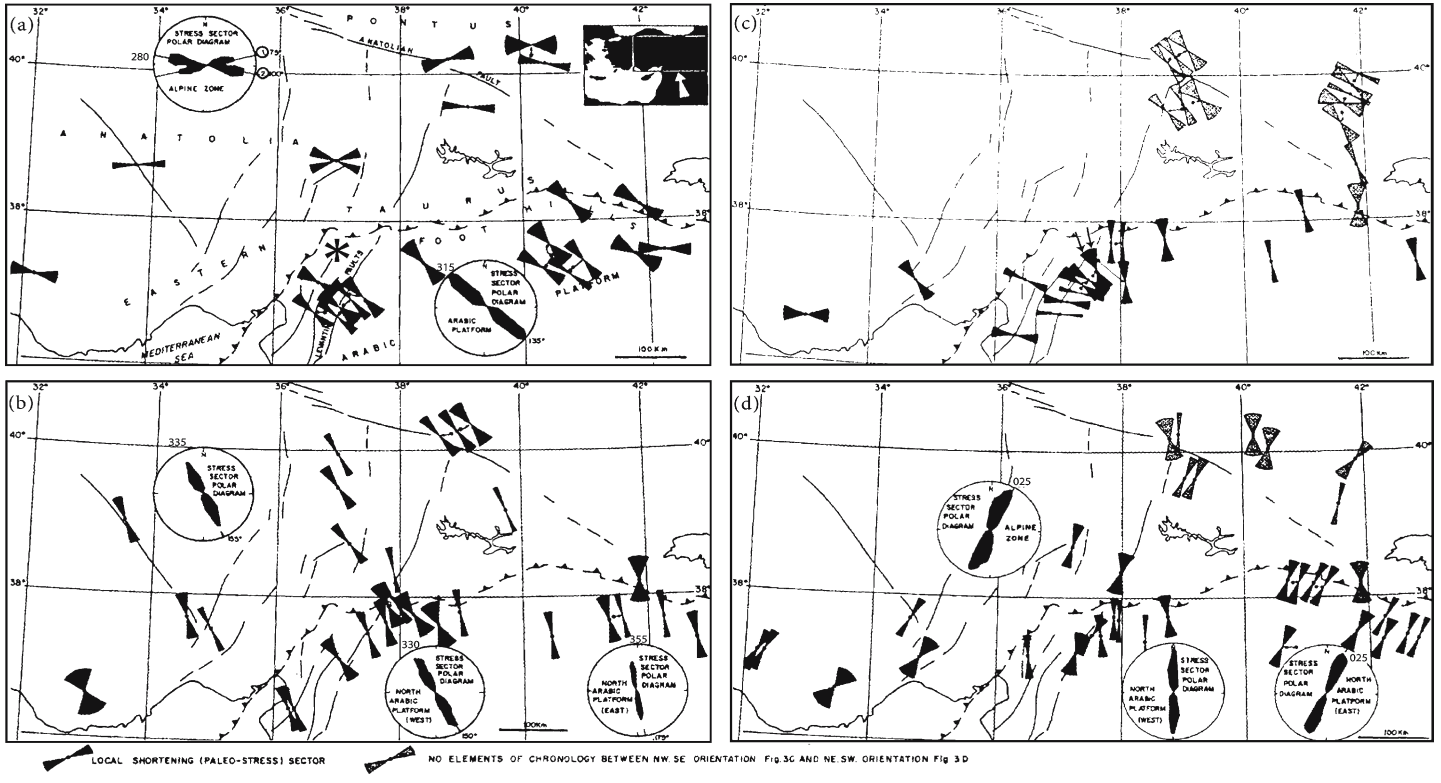

Fig. 6.7. Shortening phases in Eastern Turkey, where circle diagrams give the paleostress directions (PD) discussed in the text. **a** Late Cretaceous phase. At left PD from the Alpine zone, at right PD from the Arabic platform. Note the belt of Levantin faults south of the star (*). **b** Late Eocene-Early Oligocene phase. At lower left PD from the north Arabic platform (west), at lower right PD from the north Arabic platform (east). **c** Late Miocene phase (two small *arrows* show the 343° and 350° shortening directions). **d** Plio-Quaternary phase. At left PD from the Alpine zone. At right PD from the Arabic platform (modified from Letouzey and Tremolieres 1980, see text for explanation)

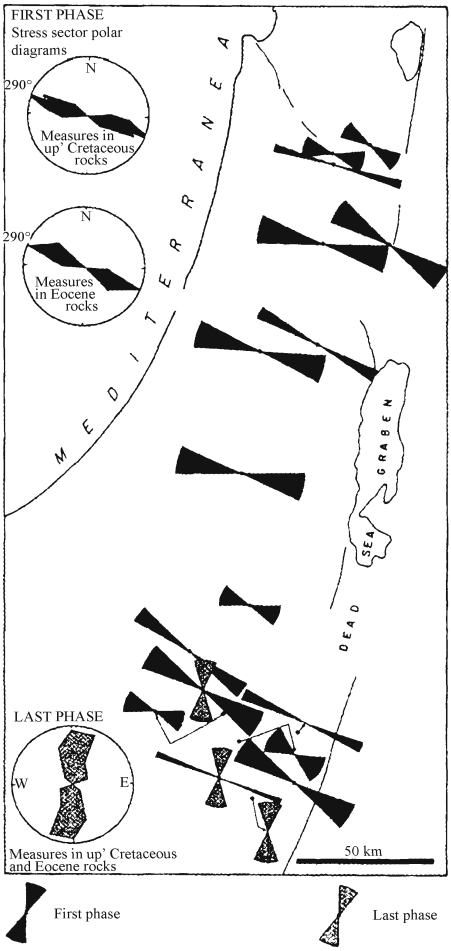

Fig. 6.8.
Measurements of shortening phases in Upper Cretaceous rocks and Eocene rocks from Israel. The first phase (290°) is interpreted to have preceded the last phase (approximately N-S) (from Letouzey and Tremolieres 1980, see text for explanation)

a 25° spatial change in the stress direction observed in the northern part of the Arabian plate, along its collision contact with the Anatolian microplate. The difference is between the 330° direction in the western side and the 355° direction in the eastern side of the northern Arabian plate (Fig. 6.7b).

The tectonics of the Late Miocene (the "third phase") affected all the geological formations that Letouzey and Tremolieres (1980) studied. It was associated with folding, thrusting and breaking of continental blocks and exhibited large changes in orientation of the stress field in different structural areas, showing changes in compression (or partition of) directions between E-W in the western side and 355° in the eastern side of the northern part of the Arabian plate (Fig. 6.7c).

The Plio-Quaternary phase is the continuation of the Late Miocene tectonics in the north of the Arabian platform, including the large strike-slip Levantine and North Anatolian fault systems (Fig. 6.7d). The recorded paleostress compression directions from this tectonics are 025° in the Alpine zone, N-S in the western boundary of the northern Arabian platform, and 025°, east of the boundary of the northern Arabian

platform. The sequence of the latter two directions is not clear, and it is not certain that there was a continuation of the clockwise rotation during this phase. However, Letouzey and Tremolieres (1980) implicitly integrate the influence of the Dead Sea transform into the general pattern of the Europe-African-Arabian collision, not earlier than the Plio-Quaternary (Fig. 6.6e), exhibiting the new plate boundary in the Plio-Quaternary phase.

6.3.3 The Sinai-Israel Sub-Plate

Eyal (1996, Fig. 1) finds that almost all middle Miocene to Recent S_{Hmax} and S_{Hmin} data compiled from the Sinai-Israel sub-plate cluster in two "distinct" orientations. This observation is based on an investigation of both mesostructures (not including joints) and macrostructures (including dikes and focal mechanism data). One S_{Hmax} trend striking 344 ±3° (ninety-eight sites) is consistent with the Dead Sea stress field (DSS), and the second, S_{Hmax} trend striking 282 ±5° (twenty-six sites), is consistent with the Syrian Arc stress field (SAS). These trends correspond to the SAS and DSS by Eyal and Reches (1983) and according to these authors, reflect an "outstanding homogeneity" of the strain in the region. The SAS direction resembles the "first phase" (290°) by Letouzey and Tremolieres (1980) (Fig. 6.8).

6.3.4 Two Synclines in the Northern Negev

Results from the Beer Sheva and Shephela synclines around Beer Sheva enabled Bahat (1997) to show that the regional joint pattern in the Lower Eocene chalks differs significantly from that of the Middle Eocene, indicating heterogeneous strain in Eocene rocks in the area. In addition, the outstanding maxima 334° and 328° shown by Flexer et al. (1984) and by Bahat and Grossmann (1988), respectively (which are based on thousands of measurements in three synclines along the Syrian Arc), strongly point to a NW S_{Hmax}, which is in variance with the 282° SAS direction discussed by Eyal (1996). The maxima 328° and 334° populate the angular zone between the distinct SAS and DSS. In addition, Bahat (1991a, Fig. 5.8) related to an intensely jointed outcrop of Santonian chalk on the rift shoulder east of Arad (next to the Dead Sea) and found that by far the dominant set was oriented about 320°. This direction corresponds far closer to the NW S_{Hmax} than to the DSS. Thus, the combined observations made by Eyal (1996), Flexer et al. (1984) and Bahat and Grossmann (1988) show more than two major paleostress directions (Eyal 1996) since the Upper Cretaceous in Israel.

Combining the above observations with additional results by various authors, Bahat (1999b) suggested an alternative model to the one pertaining to two distinct SAS and DSS stress fields, as follows. A common feature of mesostructures that show WNW-WSW directions of S_{Hmax} is that they generally occur in limestones and dolomites in Cenomanian-Turonian monoclines, whereas those mesostructures that point to NW-NNW S_{Hmax} directions are mainly joints that cut Eocene chalks in synclines. These observations were interpreted according to a "stress rotation" model, which considered an early remote S_{Hmax} that was oriented WSW to WNW during the Cenomanian-Turonian period and was later rotated clockwise to NW-NNW in the Senonian-Eocene.

6.3.5
The Neqarot Syncline in the Central Negev

Eyal et al. (2001) found four joint sets in carbonate beds from upper Turonian rocks within the Neqarot syncline of south-central Israel:

1. A joint set with a mean strike of 160–340° and $\alpha_{95} < 3°$ found in forty beds at thirty-two stations.
2. A joint set with a mean strike of 108–288° and $\alpha_{95} < 5°$ found in twenty-one beds at nineteen stations.
3. A joint set with a mean strike of 036–216° and $\alpha_{95} < 9°$ found in nine beds at eight stations.
4. A joint set with a mean strike of 136–316° and $\alpha_{95} < 6°$ found in six beds at five stations, where α_{95} is the radius of confidence cone of Fisher (1953) vector distribution.

Eyal et al. (2001) also found that the two most prominent joint sets observed in carbonate beds of the Gerofit Formation in Nahal Neqarot (N in Fig. 6.12a) are aligned NNW (340°) and WNW (288°) and are compatible with the DSS and SAS, respectively (Eyal 1996 and Sect. 6.3.3). They found that cross-cutting relations of these joint sets and the other less prominent joint sets imply different timing relationships. In some beds, the WNW set consistently predated the NNW set, whereas in other beds (altogether six stations out of some forty), the NNW set predates the WNW set. Based on these findings Eyal et al. (2001) came up with the following paleostress model. First, these results support the Eyal (1996) model of two major stress field regimes in Israel that fluctuated through time since the middle Miocene, and second, the joint data suggest abrupt changes rather than gradual rotations in stress field orientations. In seeking to establish the validity of the stress model by Eyal et al. (2001), we revisited the Nahal Neqarot outcrop with the objective of examining joint abutting contacts and their sequence as well as their strike spreading and fracture properties. We concentrated on stations that show the succession of DSS compatibles that formed before SAS compatibles as suggested by Eyal et al. (2001, Fig. 2 and Table 1, stations 12, 13, 15, M-4, 26 and 28). New measurements were carried out at specific locations where joints of different sets showed clear contacts (Fig. 6.9a–f), itemizing the results below.

Joints striking 032° arrest at joints that strike 292° in station 28; in these sets spacing is limited to several cm (Fig. 6.9a). In a neighbor outcrop, some 40 m upstream the wadi, a 090° striking joint arresting at a 330° joint and a 297° arresting at a 340° striking joint, forming a 43° angle (Fig. 6.9b). In station 13 we found a 084° joint arresting at a 356° striking joint, creating an 88° angle (Fig. 6.9c). In station M-2 we found in bed 1 a joint striking 286° arresting in joints striking approximately 333° at 47° angle, but the reverse abutting relationship seems to occur as well. While spacing in the former set was some 80 cm, spacing in the latter set was very low, occasionally about 1 cm (Fig. 6.9d). In station M-2, joint strikes in the NNW set range between 325° and 338°. Contacts suggesting the two opposite sequences similar to those shown in station M-2 are repeated in station 15 (Fig. 6.9e). A joint striking 270° abuts two joints that strike 330° and 340° in station 14, forming 60° and 70° angles, respectively (Fig. 6.9f).

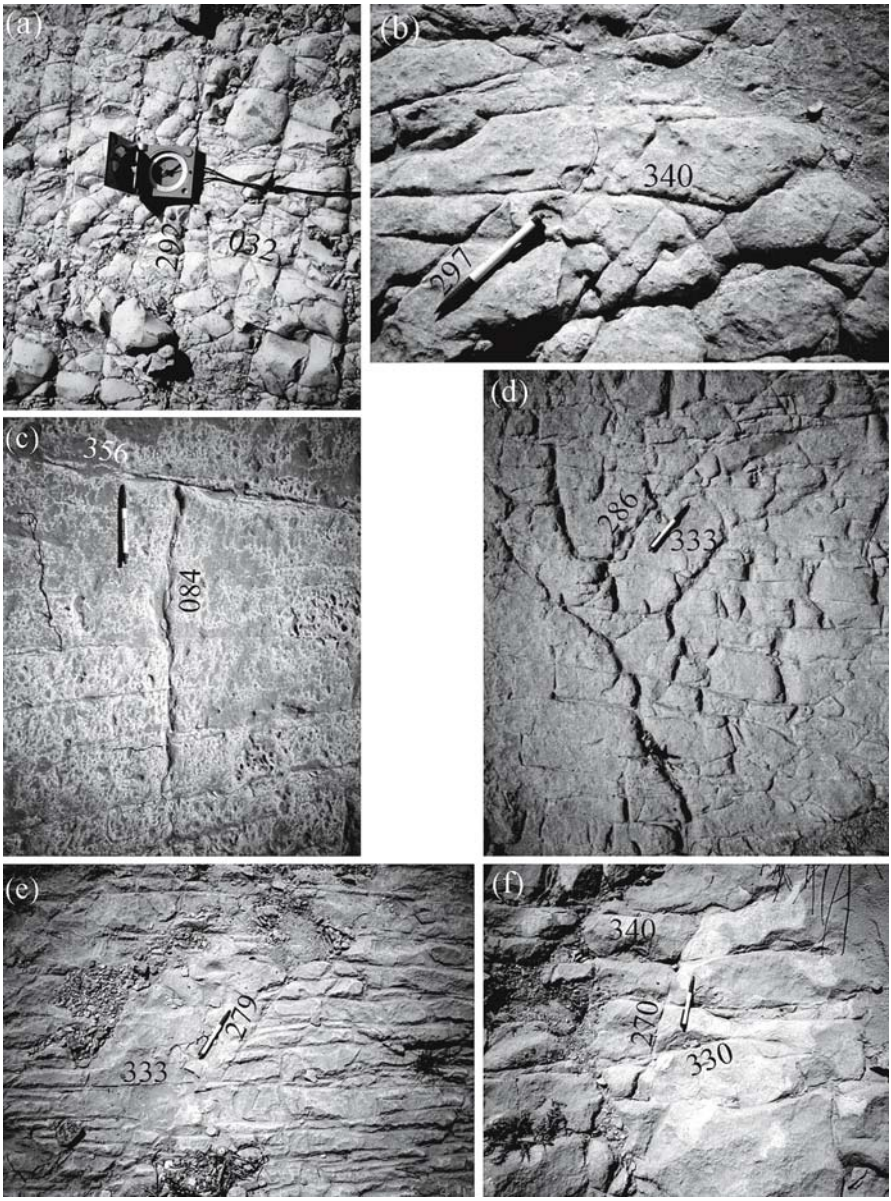

Fig. 6.9. Joint traces in Nahal Neqarot (see text for descriptions). **a** The dominant joint set 292° appears from left to right; **b** A joint oriented 297° parallels to *pen*; **c** A 084° joint arresting at a 356° striking joint; **d** A 286° joint (parallel to *pen*) arrests at joints striking approximately 333°; **e** A contact similar to the one in **d**; **f** A joint striking 090° (parallel to *pen*) abuts two joints that strike 330° and 340°

There are indeed indications in Fig. 6.9a–f that sets grouped in the range 264(084)–297° are younger than sets grouped in the range 330–356° as suggested by Eyal et al. (2001). What remains unclear however is whether this sequence sufficiently justifies the con-

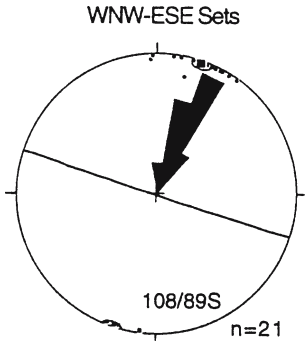

Fig. 6.10.
Summary equal area stereographic projection of the WNW-ESE sets at Nahal Neqarot. Each data point (i.e., pole) is the mean orientation for a single set of systematic joints within an individual bed. The mean orientation for each combined plot is a great circle whose pole is represented by a square. Rose petals indicate the relative frequency of the poles (after Eyal et al. 2001)

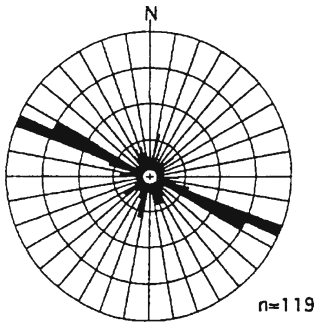

Fig. 6.11.
Rose diagram of joint orientations in the vicinity of a scanline. Sector length is proportional to number of joints (from Becker and Gross 1996)

clusion that these two groups are SAS- and DSS-compatible. The two groups (264–297° and 330–356°) show considerable spreading in Fig. 6.9a–f. Correspondingly, these joints produce a wide range of angles at their contacts (from 43° to 88°). Angular spreading is even greater in Fig. 2 and Table 1 from Eyal et al. (2001), e.g., in station 28, the average of set DSS compatible strikes 328°, which is far from the DSS average. Several joints are oriented reasonably close the specified SAS and DSS directions (282 ±5° and 344 ±3°, respectively, Eyal 1996). These include 286° (Fig. 6.9d), 279° (Fig. 6.9e), 340° (Fig. 6.9b) and 340° (Fig. 6.9f). However, the orientations of most other joints deviate from the specified directions by more than 10°. The strike spread of the WNW set (Fig. 6.9 and 6.10, also Eyal et al. 2001, Table 1) is significantly greater than the strike spread of the SAS compatible set (293 ±3°) obtained by Becker and Gross (1996) (Fig. 6.11). Both data were collected in carbonates of the Turonian Gerofit Formation in the same general area (note the difference in number of measurements in Fig. 6.10 vs. 6.11). This raises the possibility that the WNW oriented joints consist of more than one set. Furthermore, there is a considerable heterogeneity in the physical properties of the joints that represent each of the above two groups (as reflected in Fig. 6.9a–f and other contacts). Particularly, joints of similar trends have considerable spacing differences in different locations in a given outcrop. For instance, in station M-2, joints trending 286° are spaced approximately 80 cm in bed 1 (Fig. 6.9d), while joints trending about 285° have spacing of some 15–20 cm in bed 5, albeit their occurrence in rock layers of a similar thickness (about 40 ±10 cm) and lithology. In addition, the implication that each group is a set, representing a unique paleostress field (Table 1 in Eyal et al. 2001), does not take into account other genetic possibilities: Some of the joints could have been created by influences exerted by the adjacent large Makhtesh Ramon fault (see the neighboring

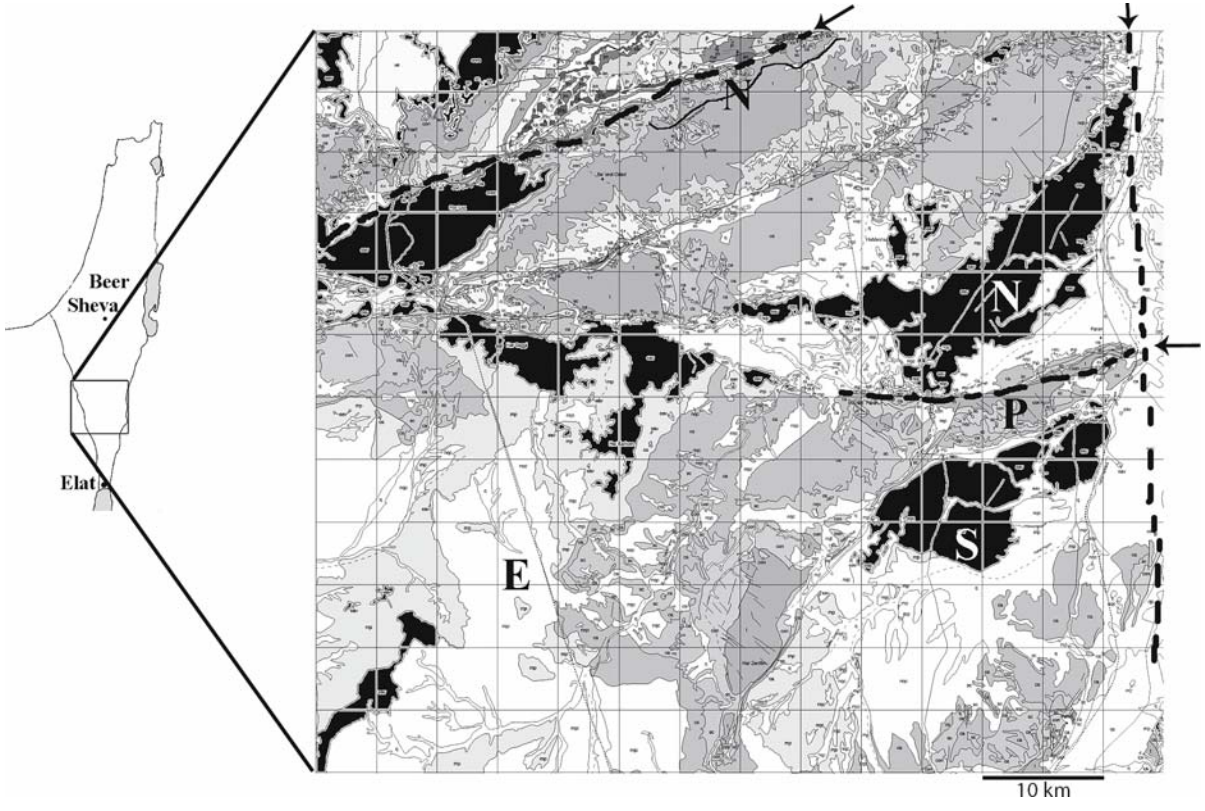

Fig. 6.12a. Geological map of part of southern Israel. The *black areas* marked by *N* and *S* are northern and southern quasi-synclines, separated by the Paaran fault, *P* (*horizontal arrow*). *Vertical* and *inclined arrows* relate to the approximate western boundary of the Dead Sea rift, and the Ramon fault respectively. *E* and *N* neighbor the boundary with Egypt and the Neqarrot outcrop, respectively (from Levi 2003)

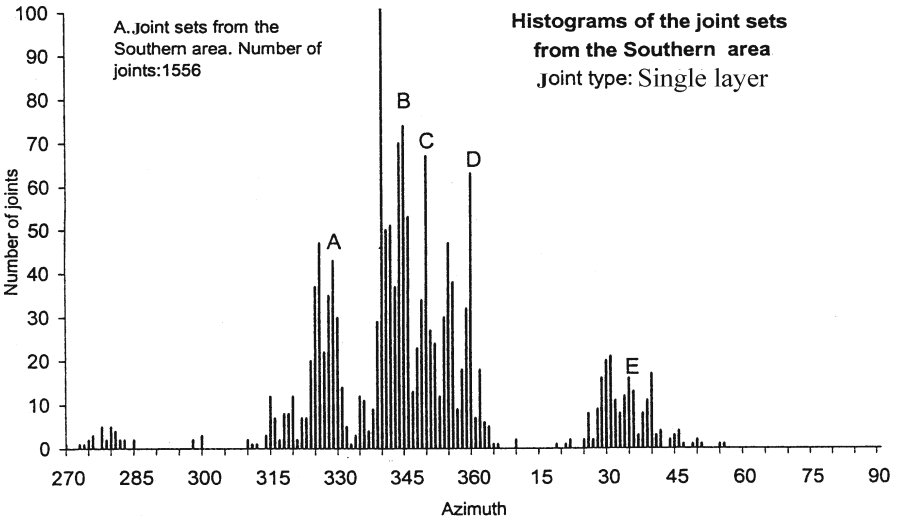

Fig. 6.12b. Histograms of five joint sets (*A–E*) from the quasi-synclinal area south of the Paran fault in Fig. 6.12a (modified from Levi 2003)

Neqarot outcrop N and the Ramon fault, marked by an inclined arrow in Fig. 6.12a), or some of the DSS compatible joints could have been formed by additional stress fields in the area, such as N-S S_{Hmin} (T7, Sect. 6.3.1.2). Finally, Eyal et al. (2001, Table 1) relied on the α_{95} method in their set division, not taking into account the limitations of this method (Sect. 6.2.2). In summary, the repeated observations that sets grouped in the range 264–297° are younger than sets grouped in the range 330–356° support the intriguing sequence suggested by Eyal et al. (2001). However, the strike spreading and other fracture properties stress the possibility that these sets could be associated with more than two unique stress fields.

6.3.6
Two Quasi-Synclines in the South Negev

Five joint sets. Levi (2003) investigated jointing in and around two quasi-synclinal areas (folds that are structurally not well defined), north and south of the Paran fault in south Israel, along the west side of the Dead Sea rift, some 30 km south of the Ramon fault (Fig. 6.12a). His research concentrated on fracture in Santonian and Eocene chalk formations and younger sediments. Based on 2646 strike measurements, he distinguished five single-layer joint sets (A–E): A) 326 ±3°, B) 343 ±2°, C) 350 ±1°, D) 360 ±2°, and E) 033 ±4° (Fig. 6.12b), and two multilayer sets linked to sets D and E. He found that set 326° fractured Eocene Lower Eocene chalks in the burial stage, during rock consolidation. Joint set 343° fractured after set 326°, and Levi (2003) linked it to a clockwise stress rotation during the Miocene. The difference in strike between sets B and C was assigned to lithological differences (Fig. 6.4). Both single-layer and multi layer D and E sets were interpreted to be associated with Pliocene and younger tectonics. However, set D was found to be younger than set E representing a local counter clockwise stress rotation with time.

6.3.7
Summary of Results that Evidence S_{Hmax} Clockwise Rotation

The observations by Eldeen et al. (2000) show evidence for a general clockwise rotation with time of the S_{Hmax} axis from E-W trend in the Cretaceous (their T3), through NW-SE S_{Hmax} that affected the Palaeocene-Eocene rocks (T4) and NNW-SSE to N-S S_{Hmax} affecting rocks with an age up to the Pleistocene (T5). This three-stage (T3–T5) rotation from southwest Jordan fits previous observations quite well. They approximately correspond to the clockwise rotation of the 285°, 322° and 349° compression directions suggested by Burdon (1959) (Sect. 6.3.1.1). Stages T3 and T4 fit the paleo-stress pattern suggested by Bahat (1999b) in the northern and central Negev parts of Israel (WNW-WSW S_{Hmax} in Cenomanian-Turonian monoclines and NW-NNW S_{Hmax} in Eocene chalks from synclines) (Sect. 6.3.4). Clockwise rotation of paleostress S_{Hmax}, was also demonstrated by Levi (2003) in southern Israel (Sect. 6.3.6), with some similarities and a difference compared to the data given by Eldeen et al. (2000). Levi's set A, implying S_{Hmax} 326° in the Lower Eocene and set D, implying S_{Hmax} 360° in Pliocene and younger tectonics correspond well to T4 and T5, respectively. The difference relates to results that concern the Miocene. While set B striking 343 ±2° and set C striking 350 ±1° are connected to the Miocene by Levi (2003), Eldeen et al. (2000) assigned the more westerly direction NW-SE to that period.

The NW-NNW S_{Hmax} (approximately the 326° direction) that correlates with the tectonics that took place during the Eocene (Bahat 1999b; Levi 2003 and possibly Eldeen et al. 2000 as well) matches reasonably well the 330° direction linked with Late Eocene-pre-Middle Oligocene by (Letouzey and Tremolieres 1980) (Sect. 6.3.2, Fig. 6.7b). The compression direction 355° in the eastern side of the northern part of the Arabian plate (Letouzey and Tremolieres 1980) correlates fairly well with Levi's (2003) set C (350 ±1°). Sets B and C are oriented quite close to certain shortening directions measured in the area along the Levantin faults (arrows in Fig. 6.7c). Quite significant are also the similarities of the youngest stress directions. The recorded compression directions by Letouzey and Tremolieres 1980) from the Plio-Quaternary tectonics are N-S in the western side of the northern Arabian plate and 025° from the eastern side of the plate (Fig. 6.7d). Both are almost precisely the same paleostress directions found by Levi (2003) that were implied by sets 360° and 033°, respectively. The N-S compression matches T5 by Eldeen et al. (2000).

In conclusion, the results obtained by Burdon (1959), Letouzey and Tremolieres (1980), Bahat (1999b), Levi (2003) and Eldeen et al. (2000) that were conducted in different areas, i.e., south Turkey as well as south Israel and Jordan, all point to a clockwise rotation of the paleostress field from the Upper Cretaceous to Pleistocene. This rotation possibly started and continued before and beyond these times. Also, with a few exceptions, the linkages of compression directions to specific periods observed by the various authors are fairly close. These correlations support the ideas formulated by Letouzey and Tremolieres (1980), pertaining to the connection between the tectonics along a wide belt east and west of the Dead Sea rift and the Europe-African-Arabian plate collision. These studies particularly demonstrate a linkage between processes that took place in areas from South Turkey and jointing in Israel.

6.3.8
Beyond the Mediterranean Area

6.3.8.1
The Appalachian Plateau

Three cross fold joint sets were distinguished in two outcrops near Watkins Glen in upstate New York (Bahat 1991a, Tables 5.1 and 5.2). This suggested deviation from the previous concept of two major cross fold sets and demonstrated the considerable difficulties that were involved in joint set differentiation. Clearly, any changes in the differentiation of cross fold joint sets would alter the interpretation of both changes in paleostress mechanisms and fracture history in the region. Younes and Engelder (1999) resolved this problem (Sect. 3.1). A review of this subject distinguishes three main concepts of regional cross-fold joint patterns in the Appalachian Plateau (Sect. 3.1.6 and Fig. 3.10a–c). Two of these concepts relate to rotational mechanisms of the horizontal remote compression, and the third one concerns a fan pattern of radial joints that form contemporaneously by a given stress field. The observations from the Appalachian Plateau are combined below with the results from the Israeli Negev in formulating a model of regional jointing.

6.3.8.2
Systematic Jointing and Plate Collision

The lateral movements that took place along the Dead Sea transform ended at the collision front along the Taurus belt in south Turkey. It appears from the above comparison of regional jointing that it is south of this collision front (Fig. 6.6) where strain records from various times tell about the paleostress histories of different regions along the transform, including Israel. Therefore, the sum of systematic joint sets reflecting paleostresses in Israel and its vicinity is best explained via the history of the Europe-African-Arabian collision and closure of the Tethys Ocean zone since the Upper Cretaceous (Letouzey and Tremolieres 1980). A similar explanation of jointing in the Appalachian Plateau can be linked to the closure of the old Atlantic Ocean between the continents of Africa and North America (e.g., Twiss and Moores 1992, Fig. 6.11 and 6.12).

Quite possibly, such correlations may be made in other regions on the glob, where analogous regional closures (e.g., the Canadian Cordillera) can be compared to recorded regional joint patterns in their respective forelands, in accordance with the plate tectonic theory. Ultimately, set directions derived from regional joint measurements in "large forelands" (that formed by regional closures) and in "small forelands" (e.g., Arlegui and Simón 2001) will be linked to a global map of paleostresses analogous to other global stress patterns (Zoback 1989). Such linkages would be particularly relevant to burial and syntectonic joints cutting sedimentary rocks and to lesser extents to uplift and post uplift joints. Repeatedly reactivated burial joints are recognizable even in thrust-and-fold belts (possibly parts of present Fig. 3.1d and Tokarski et al. 1999). Comparing the characteristics of these joints to those associated with forelands would be quite an intriguing project.

A fascinating question is what are the mechanisms of paleostress changes and how fast changes occur by shortening processes. Probably the modes of changes reflect the variable boundary conditions in collision zones that may differ from time to time along each zone. The interaction of two plates (or microplates) involves some rotation at the

contact, but this would be irregular, somewhere between rigid and plastic compliance (Molnar and Tapponier 1975) and occasionally involve back and forth motions. Changes in some strains recording these processes might be gradual, and others will be abrupt. An abrupt change will occur when a previous process ends, enabling the new process to take place. Deformations are observed far away from the collision zone and orientations of paleostresses deduced from structural analyses are surprisingly constant over wide areas on continents (e.g., Sbar and Sykes 1973; Letouzey and Tremolieres 1980). Accordingly, there is justification to look for possible connections between paleostress records in Israel and in the northern part of the Arabian plate in south Turkey.

Is it appropriate to term the sequence described above, from the 326–330° range in the Upper Cretaceous-Eocene through 343° in the Oligocene-Miocene to 360° and 033° in the Plio-Quaternary, to be a clockwise stress rotation? Most probably yes. Was this rotation a gradual progressive process? It probably was not, because it contained deviations from a simple process. Deviations may record local rotations in an opposite direction from the general direction in a region. For instance, while a general clockwise rotation applies to Levi's (2003) joint sets A–E, a local counter clockwise rotation took place between sets D and E (set D was younger than set E) (Sect. 6.3.6). Quite interestingly, gradual paleostress rotations are also recorded on much smaller scales in the Beer Sheva syncline. These rotations were superimposed by deviations from the general trends with back and forth motions (Sect. 3.4, Fig. 3.39b), suggesting diversions from simple, gradual processes.

6.3.9 Open Questions

We consider below several open questions that relate to jointing and paleostresses, including the rotation vs. conjugate concepts, the NNW (approximately 344°) compression, the Zoback (1992) model of global stress in the lithosphere, the timing of strike parallel joints, and the rarity of fracture surface morphology on joints cutting limestone.

6.3.9.1 *The Rotation versus Conjugate Concepts*

The 309° and 344° joint sets were interpreted by Bahat (1987a) to be a conjugate couple associated with the extensile set 328°, which indicated a regional compression, approximately along the bisector of the angle opened between 309° and 344° (sets 1c and 1d in Table 3.3). On the other hand, the idea that the 309° set had been an expression of a "transient stage" of a stress clockwise rotation in the region was entertained as a possible alternative interpretation (Bahat 1999b). This disagreement has been perplexing for some time.

An interpretation that might resolve this disagreement is given below. This explanation stems from results that pertain to the possible existence of extensile fracture at deviating angles from $\alpha = 0$ up to some 10° (Sect. 2.2.13.4). In the process of a clockwise regional rotation of the S_{Hmax} in Israel, from WSW-WNW, say 293° (Becker and Gross 1996) through 309° to 328° and 344° (Bahat 1987a, 1999b), joints in the following orientations were formed sequentially (Fig. 6.13). Set 293° was formed parallel to S_{Hmax}. Set 309° formed during the period of rotation from 293° to 328° (and was

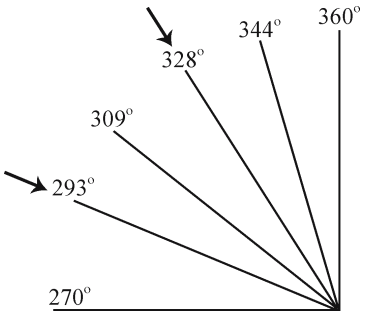

Fig. 6.13.
Formation of a series of joint sets by a hypothetic clockwise stress rotation model. Two *arrows* mark paleostress directions that were coaxial with the joint sets 293° and 328°, while the other sets formed at small angles to rotating horizontal compression

mostly decorated by horizontal plumes). Set 328° was created parallel to S_{Hmax} (and was mostly decorated by concentric rib marks). Set 344° formed during the rotation from 328° to 344° (and was mostly decorated by horizontal plumes). Perhaps fracture of the latter set took place when S_{Hmax} approximated the 330° direction (e.g., the second phase by Letouzey and Tremolieres 1980) or 334° (Flexer et al. 1984). The rate of this rotation is not known, but it is estimated that sets 309° and 328° were created in the Lower Eocene and sets 334° and 344° formed somewhat later. Thus, the similar angular relations between sets 309°and 344° with respect to S_{Hmax} at 328° do not necessarily imply that these three sets formed simultaneously (Fig. 3.10). The speculation depicted in Fig. 6.13 needs to be further investigated in additional fracture provinces before becoming a sound model. The investigation is particularly necessary because this scheme considers creation of joints at small angles with respect to principal stress directions, which is a deviation from the conventional concept of co-axiality of joint formation with respect to the direction of S_{Hmax}.

6.3.9.2
The Significance of FSR Values

It is not really clear what is the genetic significance of the high FSR values and the high scatters of FSR values obtained for set 344° by Levi (2003) (Sect. 6.2.2). One explanation relates them to accumulated strains after repeated stress events (earthquakes) along an extended period of time (Eyal et al. 2001). Levi (2003) shows high FSR values for both B (set 344°) and D (set N–S) (Fig. 6.5). He considers that the latter two sets originated in the early Miocene and Plicetocene, respectively. This raises the question of how the high FSR value could be formed in set D during such a short time, since the Plicetocene, if the mechanism is repeated stresses along an extended period of time (Eyal et al. 2001). In addition, both Eyal et al. (2001) and Levi (2003) found high scatters of FSR values for set 344° (Fig. 6.5), implying that non uniform processes exerted on the rocks and perhaps suggesting more than a single mechanism.

Perhaps an alternative explanation is more plausible (Levi 2003). Set A (326°) formed in the burial stage under increasing overburden conditions, while the rock was not fully solid, and therefore, displayed a fairly uniform FSR distribution. On the other hand, the other sets (B–E) developed during uplift processes (Levi 2003). The uplifts took place under reduced overburden loads and increased tension (Bahat 1999a), so that the rock encountered lower resistance to jointing, with consequent increase of both the FSR values and their scattering.

6.3.9.3
The Global Stress Model

Zoback (1992) presented a model of global stress in the lithosphere consisting of first- and second-order patterns. The first-order midplate stress fields are believed to be largely the result of compressional loads applied at plate boundaries, primarily ridge push and continental collision. These regional uniform stress orientations often extend 20–200 times the approximately 20–25 km thickness of the upper brittle lithosphere. The second-order stresses are local perturbations that are associated with specific geologic or tectonic features, including lithospheric flexure, lateral strength contrasts, as well as lateral density contrasts, which give rise to buoyancy forces. These second-order stress patterns typically have wavelengths ranging from 5 to 10 times the thickness of the brittle upper lithosphere. Often the second-order stress field results in a rotation of the horizontal stresses. The distinction between first- and second-order scales and mechanisms is appealing. Such ideas have been entertained by various investigators in resolving "misalignments" in the field (Currie and Reik 1977).

It appears that on account of great scale differences, there is no clear correlation between the rotation model linked with the continental collisions in the Mediterranean region (Sect. 6.3.2) and the global stress model. The scale of the first-order, which may fit that of the Mediterranean region, does not involve a rotation of the horizontal stresses, and the Mediterranean region is far greater than the scale of the second order. However, a "compromise model", pertaining to a "local perturbation" the size of the Mediterranean region may, with some terminological adaptations, fit the global concept by Zoback (1992)?

6.3.9.4
The Timing of the Strike Parallel Joints

Much emphasis has been placed in previous sections on various aspects of cross fold joint formation. Also important is the relative timing of cross fold and strike parallel joints in a given fold (F_1 and F_2 joints, respectively in Fig. 3.20b) or a slightly folded area, like the Appalachian Plateau or the Beer Sheva syncline. It is generally accepted that F_1 joints form in response to σ_1 compression parallel to layering and normal to the fold axis, during early stages of folding in both (approximately) symmetric (Burger and Hamill 1976) and asymmetric anticlines (Reches 1976). What about the timing of F_2 joints? Burger and Hamill (1976) argue that calcite data that reveal a state of stress associated with the time of F_1 joints formation on the Teton anticline (Friedman and Stearns 1971) contain no evidence for stresses related to F_2 fractures that were also developed. Therefore, it is possible that either the stresses associated with the development of F_2 joints were maintained for too short a time for calcite to undergo appreciable twin gliding or that F_2 fractures formed at very low mean stress. There are, on the other hand, indications of time alternation of F_1 and F_2 joints in the two sets, in slightly folded synclines (Bahat 1991a, Fig. 4.8), and late reoccurrence of F_2 joints when local stresses were resumed (Gross et al. 1997). Many F_2 joints probably formed during relaxation of the remote stress (Price 1974; Bahat 1989, see also Dunne and North 1990). It seems that generally, local principal stress rotation during advanced folding of asymmetric anticlines (Fig. 3.20a) may be sufficient to open joints against the remote compression (i.e., strike parallel

joints). Hence, the timing and sequence of F_2 joints can be quite variable in a fold, and decisions regarding their timing should be taken with great caution until more deterministic criteria become available.

6.3.9.5
Jointing in Limestone

It is our impression that the frequent inferior qualities of joints in limestone, in terms of joint straightness and flatness, azimuth spreading in a given set and rarity of fracture surface morphology, seems to be significant compared with those in chalk. If this impression is sound, it would remain a challenge for combined efforts of experts in structural geology and limestone petrology to resolve this issue.

6.4
Analysis of the "Fat Tail" of Joint Length Distributions

6.4.1
Joint Length Distributions

A "fat tail" is a characteristic of statistical distribution, where the decay of the distribution for "large values" shows a power law behavior and does not conform to either negative exponential or Gaussian forms. Although the statistical "fat tail" data treatment characteristically consists of small populations, these populations are exceptionally important because they are represented by the largest individuals in the system that for certain applications are the dominant ones. For instance, Bahat and Adar (1993) showed that from a series of joint sets around Wadi Naim in the Beer Sheva syncline, Israel, one particular set (that was oriented at azimuth 062°) provided by far the best water flow conditions. This set consisted of the longest fractures in the area, through which most of the water drainage took place (Sect. 6.9). What is the connection between the Naim set 028° (Table 3.5 and Fig. 3.36a,b) and the fat tail (FT) distribution?

We study the fracture length histograms of two joint sets in detail: First, a set cutting Middle Eocene chalks along Wadi Naim in the Beer Sheva syncline, Israel (Fig. 6.14a), and second, a set from Ward lake, California (Fig. 6.14b). We focus on certain characteristics of the longest joints at the "end" of the distribution curve. The joints of the first set that were formed by extension during Tertiary uplifts (Bahat 1999a) are fully revealed along Wadi Naim, showing a bimodal distribution. Bahat (1988b) demonstrated bimodal distributions in additional joint sets, compared to previous suggestions that joint length in rocks had Weibull, normal, or power-law distribution (e.g., Segall and Pollard 1983; Kelner et al. 1999; Zhao et al. 2000 and references therein), and this issue remained an open question until now.

The second distribution (Fig. 6.14b) was considered by Segall and Pollard (1983) to conform to a power-law distribution with powers of ~1.8. The fits of their curve to the actual distribution is not clear. Trying to fit the whole distribution by a power law has two shortcomings:

1. The decrease of frequency for small values of joint lengths is ignored.
2. The bimodal character of the distributions is overlooked.

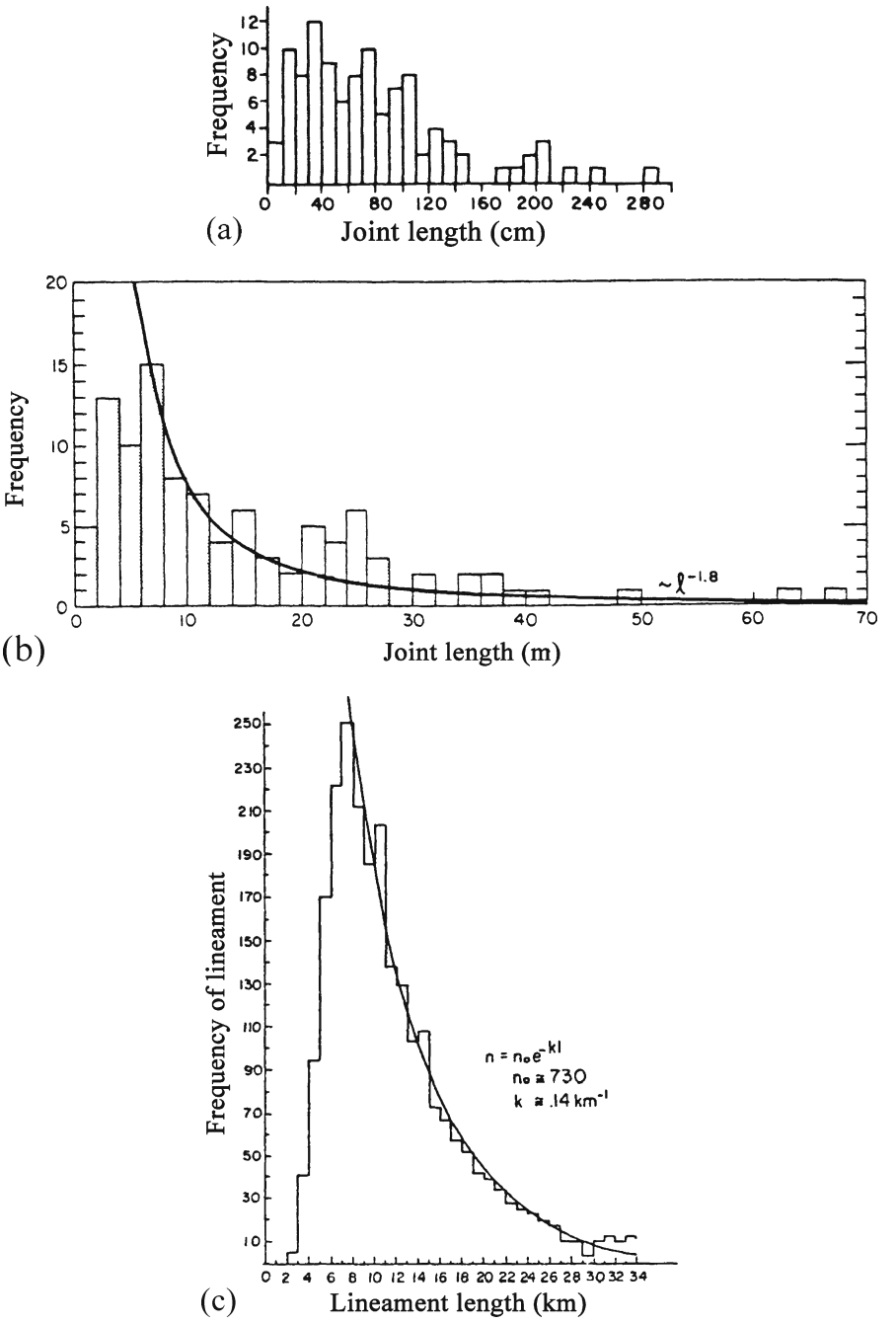

Fig. 6.14. Three histograms of joint lengths (note lithology and scale differences). **a** Set 028° from Middle Eocene chalks (Bahat 1988b); **b** From granodiorite Ward Lake (Segall and Pollard 1983, Fig. 8b). **c** Lineaments (modified from Nur (1982) after Kowalik and Gold (1976))

It is the second problem that is considered here. Apparently, a similar bimodality of fracture length population characterizes findings in much larger scales (Fig. 6.14c). This distribution was considered to be exponentially dependent (Nur 1982). As is presently shown, the second peak of the distribution marks the fat tail, which is indeed given by a power law distribution. The latter, however, has different power values than those used by Segall and Pollard and pertains only to the fat tail and not to the complete joint length distribution.

Drawing for the Wadi Naim set, the cumulative distribution of length, $P(x)$, i.e., the number of all crack lengths larger than or equal to x as a function of the fracture length x, on a log-log plot, one obtains (Fig. 6.15a) a reasonable FT (albeit only for one decade) with a slope of around 2.8. A similar graph (Fig. 6.15b) of the Segall and Pollard (1983) results shows a similar FT behavior with slopes of ~3.3 (for their Fig. 8a results) and ~2.8 (for Fig. 6.14b). Although FT results only continue along a decade or so, they definitely do not conform to exponential or to faster decreases.

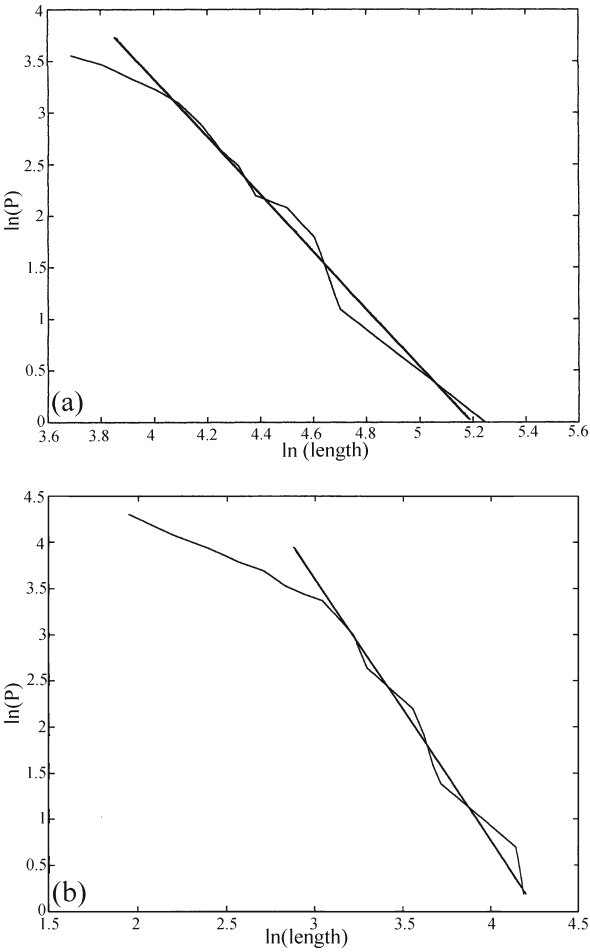

Fig. 6.15.
The cumulative distribution of length, $P(x)$ = number of all crack lengths larger than or equal to x, as a function of the crack length x, on a log-log plot. Straight lines: Linear regression. **a** Results from Wadi Naim (length in cm); **b** results from Ward Lake (length in m)

6.4.2
The "Fat Tail" Phenomenon

There exist many situations that show distributions having FT. These include phenomena in economics (Mandelbrot 1960; Mirowski 1995), physics (Krapivski and Majumdar 2000), earth sciences (Sornette et al. 1996; Caers et al. 1999a,b; Kelly et al. 1994) and are distributed in books and review articles (Arnold 1983; Adler et al. 1998). The connection of FT with fractals has also been extensively discussed (Takayasu 1989). However, the exact origin of the FT behavior is hitherto unknown. Sand dune avalanche distribution was explained by the theory of self organized criticality (Jensen 1998), while some distributions with FT encountered a purely economic model for their origin. None of these models however can be used for the distribution of fracture lengths, which we consider here.

The term FT relates to the following phenomenon. Consider the frequency distribution of lengths of fractures found in a specific rock. The expected behavior of this (or any) distribution is that it should decrease (for large lengths) at least exponentially (say for a Poissonian distribution) or even normally (large numbers rule, Feller 1971, p. 219). There are, however, quite a few distributions for which the frequency, especially for large values (tails) of the measured quantity (large fracture lengths for the example), decreases as some power of this quantity – a FT. It is the purpose of this section to address such a behavior of the distribution of fracture lengths measured in rock layers and to discuss the possible origin of this FT.

6.4.3
The Model

According to Wu and Pollard (1992) (see also Sect. 1.2, second scenario), fractures in a layer develop in two stages. In the first stage, fractures appear at random sites until a certain distribution of spacing saturation (Sect. 1.5) is obtained. In the second stage, almost no new fractures are created but the already existing ones grow in length. We adapt this two-stage model (with some modifications) and treat the second stage here. Consider a fracture of length x. Suppose its closest neighbor is another fracture of length x'. According to Segall and Pollard (1983, Fig. 11) and (Nur 1982), the fracture of length x can (and will) grow if $x > x'$, while the x' crack will not grow. This interaction between x and x' is valid, provided both cracks belong to a set and the spacing between them is less than ~5 times the average inter-crack spacing in the material. Since we treat parallel cracks after they have reached saturation, we adhere to the above assumption: Namely, x grows if larger than x', its nearest neighbor (nn).

The probability that x will grow is therefore

$$\int_0^\infty p(y)\mathrm{d}y \int_0^x \bar{g}(x, y, x')\mathrm{d}x' \tag{6.1}$$

where $p(y)\mathrm{d}y$ is the probability that the nn be at a distance (spacing) of between y and $y + \mathrm{d}y$ from the x fracture, and $\bar{g}$ is the conditional probability that if the fracture is of length x and if its nn is at a distance y from it, than this nn is of length x'. We now as-

sume that $\bar{g}(x, y, x')$ is independent of either x or y. This is a plausible assumption but is not always valid. Under this assumption, $\bar{g}(x, y, x') = g(x')$, the probability that a fracture is of length x'. Note that the integrals on y and on x' of Eq. 6.1 become disconnected and the first integral becomes equal to 1. The probability $g(x)$ evidently depends on time during the process, a dependence suppressed here but to be discussed later on.

Denote by

$$S(x) = \int_0^x g(x')\mathrm{d}x' = 1 - Q(x) \tag{6.2}$$

which under the previous assumption gives the probability that a fracture of length x grows. Note that

$$Q(x) = \int_0^\infty g(x')\mathrm{d}x'$$

Next, we calculate the amount of growth of an x-long fracture. The exact details of this calculation are not of major importance. It is only the scheme that is relevant. Assume that there is a minimal value of extension stress σ_{00} that only when $\sigma > \sigma_{00}$ the fracture can grow. Since the change in crack length Δx is small with respect to the fracture length itself, the criterion $\sigma > \sigma_{00}$ is equivalent to $K_\mathrm{I} > K_{\mathrm{I}0}$ where $K_{\mathrm{I}0}$ is a minimal stress intensity factor below which fractures do not grow at all (K_0 in Fig. 4.34, see also Sect. 1.5). Note that we speak about extreme subcritical conditions in the sense that K_I (and, a fortuori, $K_{\mathrm{I}0}$) are very much smaller than Griffith's K_{Ic}, the value of K_I above which the crack starts to run at great speeds. During a time interval Δt (which can be very long, in a geological process), the stress field has changed. In this interval, there are assumed to have occurred N subintervals, Δt_i, during which σ was larger than σ_{00} and cracks grew.

6.4.4 The Fractal Nature of the Tail

Suppose that the crack growth velocity (v) (Charles 1958, Sect. 1.5) is given by

$$v = \frac{\mathrm{d}x}{\mathrm{d}t} = \mathrm{A}K_\mathrm{I}^\mathrm{n} \tag{6.3}$$

where A and n are constants, and x is the crack length at the time t.

This is the accepted form for the velocity changes during creep for a large series of materials. Note that the most important parameter in Eq. 6.3 is n, which characterizes crack growth for a specific material and can be obtained experimentally from the slope of a $\log v$ vs. $\log K_\mathrm{I}$ plot of actual data. Assuming that the crack growth, Δx_i, during the subinterval Δt_i, is small, namely $\Delta x_\mathrm{i} \ll x$, (Eq. 6.3) can easily be integrated. Since K_I is proportional to $\sigma\sqrt{x}$, we have

$$\Delta x_i \cong b x^{n/2} \int_{\Delta t_i} \sigma^n(t)\mathrm{d}t \tag{6.4}$$

and the total increase in length of a crack of length x during the complete time interval Δt is

$$\Delta x = \sum_{i=1}^{N} \Delta x_i = \mathrm{d}x^{n/2} \Delta t \tag{6.5}$$

where

$$d = b \sum_i \int_{\Delta t_i} \sigma^n(t) \mathrm{d}t$$

The balance equation for the probability (per unit time and per unit length) $g(x, t)$ to find at time t (measured along the process) a crack of length x, is as follows:

$$g(x, t + \Delta t) = g(x, t)[1 - \beta S(x, t)] + g(x - \Delta x, t)\beta S(x - \Delta x, t) \tag{6.6}$$

Here, the first term on the right denotes the probability that the crack had already the length x at time t and stayed at this length, while the second term describes the probability that the crack had a length $x - \Delta x$ at time t, where Δx is given by Eq. 6.5 and was able to grow. This probability is proportional to S at that time. From Eq. 6.6 one gets,

$$\frac{\partial g}{\partial t} = -\beta \frac{\mathrm{d}x}{\mathrm{d}t} \frac{\partial}{\partial x}(gS) \tag{6.7}$$

Since by Eq. 6.2,

$$g = \frac{\partial S}{\partial x}$$

and using Eq. 6.5 the following nonlinear partial differential equation is obtained for S:

$$\frac{\partial^2}{\partial x \partial t} S = -\gamma x^{n/2} \left[\left(\frac{\partial S}{\partial x} \right)^2 + S \frac{\partial^2 S}{\partial x^2} \right] \tag{6.8}$$

A separation of variables $S = X(x)T(t)$ then yields

$$-\frac{T'}{T^2} = \frac{\gamma x^{n/2}(X'^2 + XX'')}{X'} = u = \text{const.} \tag{6.9}$$

where γ is a constant and prime denotes a derivative with respect to the corresponding variable. The time-dependent part is therefore

$$T(t) = [\mathrm{a} - u(t - t_0)]^{-1} \tag{6.10}$$

where t_0 is the initial time and $a = 1 / T(t = 0)$. Equation 6.10 is evidently valid as long as $t < t_1$, where $t_1 - t_0 = a / u$. For "short" times $(t - t_0) \ll a / u$, T increases linearly with time: $T \cong 1 / a + (t - t_0)\, u / a$. This linear increase is in agreement with Wu and Pollard (1992, Fig. 6c). The fractal nature of the tail of the distribution is obtained from the x–dependent part $X(x)$. Assuming $X(x) = \eta x^{\mathrm{m}}$, where η is a constant, Eq. 6.9 can be fulfilled only if

$$n = 2(-m + 1) \tag{6.11}$$

A solution of Eq. 6.8 is therefore

$$S(x,t) = \int_0^x g(x',t)\mathrm{d}x' = \frac{Kx^m}{a - u(t - t_0)} \tag{6.12}$$

or, for "short" times, choosing $t_0 = 0$ as the starting time,

$$S(x,t) = (c_1 + c_2 t)x^m \tag{6.13}$$

hence

$$g(x,t) = (c_1' + c_2' t)x^{m-1} \tag{6.14}$$

Equations 6.11–6.14 establish for this model the "power" character of the distribution $g(x)$. Note that this character stems from the nonlinearity of Eq. 6.7, whose origin is the interdependence of growth of one fracture on its neighbors. Another contributing factor is the Charles "subcritical" fracture velocity-K_I dependence, Eq. 6.3.

6.4.5 Discussion and Conclusion

So far the final bimodal distribution (Fig. 6.14a–c) was considered. Here we explain the process of its creation, starting from a "one peak" distribution. We consider a simple example as follows. Assume that the normalized joint length distribution function *at the time of saturation* is of the form shown in Fig. 6.16a and expressed as

$$g(x) = \left(\frac{2x}{l_0^2}\right)\exp\left\{\frac{-x^2}{l_0^2}\right\} \tag{6.15}$$

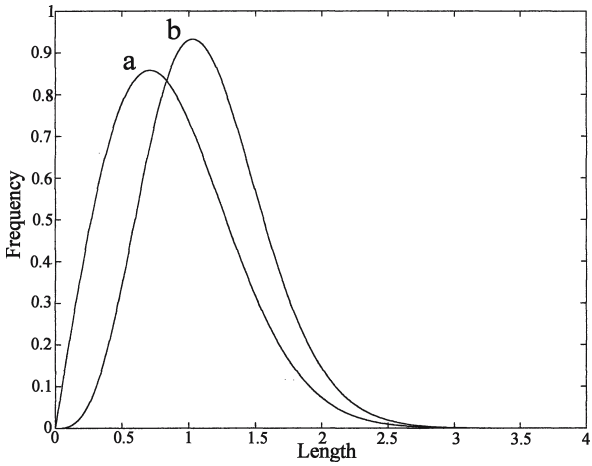

Fig. 6.16.
a The crack length distribution example of Eq. 6.15 with $l_0 = 1$.
b The probability per unit length that a crack of length x and with the distribution of Eq. 6.15 would grow (Eq. 6.16) with $\Delta y = l_0 = 1$

Here l_0 is a scaling length. Note that the maximum of this distribution lies at

$$\frac{l_0}{\sqrt{2}}$$

The probability p that a fracture of length between y and $y + \Delta y$ grows is the product of the probability that the fracture be of such a length, i.e., $g(y)\Delta y$ and the probability that its neigbours are shorter than y, namely,

$$S(y) = \int_0^y g(x)\mathrm{d}x$$

For the distribution of Eq. 6.15,

$$S(y) = 1 - \exp\left\{-\frac{y^2}{l_0^2}\right\}$$

and therefore,

$$p = \left(\frac{2y\Delta y}{l_0^2}\right)\exp\left\{-\frac{y^2}{l_0^2}\right\}\left[1 - \exp\left\{-\frac{y^2}{l_0^2}\right\}\right] \tag{6.16}$$

This relation is depicted in Fig. 6.16b. It is easy to calculate (numerically) that the maximum of p occurs at $y \sim 1.03\, l_0$. Fractures of this length have the highest probability to grow. One therefore expects that with time, a *decrease* of population (dip) would occur in the vicinity of this length and an *increase* of population would appear beyond this point leading to a bimodal distribution (Fig. 6.17), which eventually assumes the slope of Eq. 6.14. Note that for the distribution of Eq. 6.15 the ratio be-

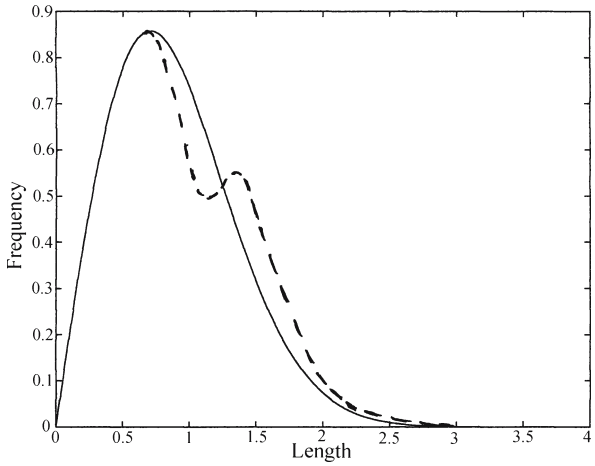

Fig. 6.17.
Full line: The crack length distribution example of Eq. 6.15 with $l_0 = 1$. *Dashed line:* Schematic bimodal distribution obtained after length increase beyond saturation, according to the present model (see Fig. 6.16 and text)

tween the position of population dip ($1.03\,l_0$) and the position of the first maximum ($0.707\,l_0$) is 1.46. This ratio is characteristic of the specific joint length distribution and is not general.

Returning now to the field results, firstly it is clear that a power of –2.8 for $P(x)$ implies a power of $m = -3.8$ for $g(x)$ (Eq. 6.14). Hence, for the results of Segall and Pollard (1983), as well as for the results of Bahat (1988b), n of Eq. 6.3 is ~9.6, by Eq. 6.11. It is definitely within the lower range of n values obtained for rocks (Atkinson 1987, Table 11.6). Let us stress that this is an indirect method to obtain the characteristic creep value of n for these rocks. Since geological creep conditions cannot be reproduced in the laboratory, this is apparently the only method hitherto known to obtain these values.

Note also that the values of n obtained in this method for chalk and for granite are very similar in spite of rock differences. It might be argued that for such prolonged creep processes, n values are smaller than those obtained in the laboratory (Atkinson 1987), and probably these values are within the same range for different rocks. This general result should be tested for other bimodal crack length distributions.

In summary, the present section provides a new interpretation of the profile of joint length distributions. Here, two sets of fracture length measurements are discussed. It is shown that both show a FT behavior with a similar power. Next, a model based on creep growth of cracks is developed to account for the FT behavior and simultaneously explains the appearance of the bimodal behavior of the distribution. We hypothesize that this model should be applicable to additional joint length distributions.

6.5 Estimation of Paleo Fracture-Stress

The methods of paleo-fracture stress estimation on joint surfaces were summarized (Bahat and Rabinovitch 1988; Bahat 1991a, p. 229 and reference therein), and generalized for outcrops that do not display the fracture origin (Bahat et al. 1999). Weinberger (2001a) applied the method for estimating the paleostresses on joints from certain dolomite layers of the Judea Group in central Israel. When the fracture origin is unknown, the mirror radius (Fig. 2.1a,b) cannot be measured directly and needs be calculated. The location of the fracture origin of the joint that is represented by the relict fringe of *en echelon* cracks is uncertain (Fig. 6.18a) so that the mirror radius, r is determined trigonometrically (Fig. 6.18c). The measured distances are given by $2y$ between the two tips of the visible fringe and by x (Fig. 6.18c). Other relationships are $z / \sin\alpha = 2r$, where α is the angle produced by $2y$ and z; $z^2 = x^2 + y^2$ and $r = x^2 + y^2 / 2x$. For the derivation of r, two distances were determined at random locations along the fringe boundary (Fig. 6.18a), resulting in two r values differing 8% from each other, suggesting the error range in measurement. The error in r determination related to distance measurement and to a slight ellipticity deviation of the mirror from circularity is estimated as 15% (see detailed calculations in the above mentioned references). In these calculations, the local paleo-fracture stress is obtained, i.e., the stress applied on the entire joint surface. It is assumed that the stress is unchanged throughout the fracture process. This stress differs from both the (regional) remote stress and the magnified stress acting at the tip of the joint.

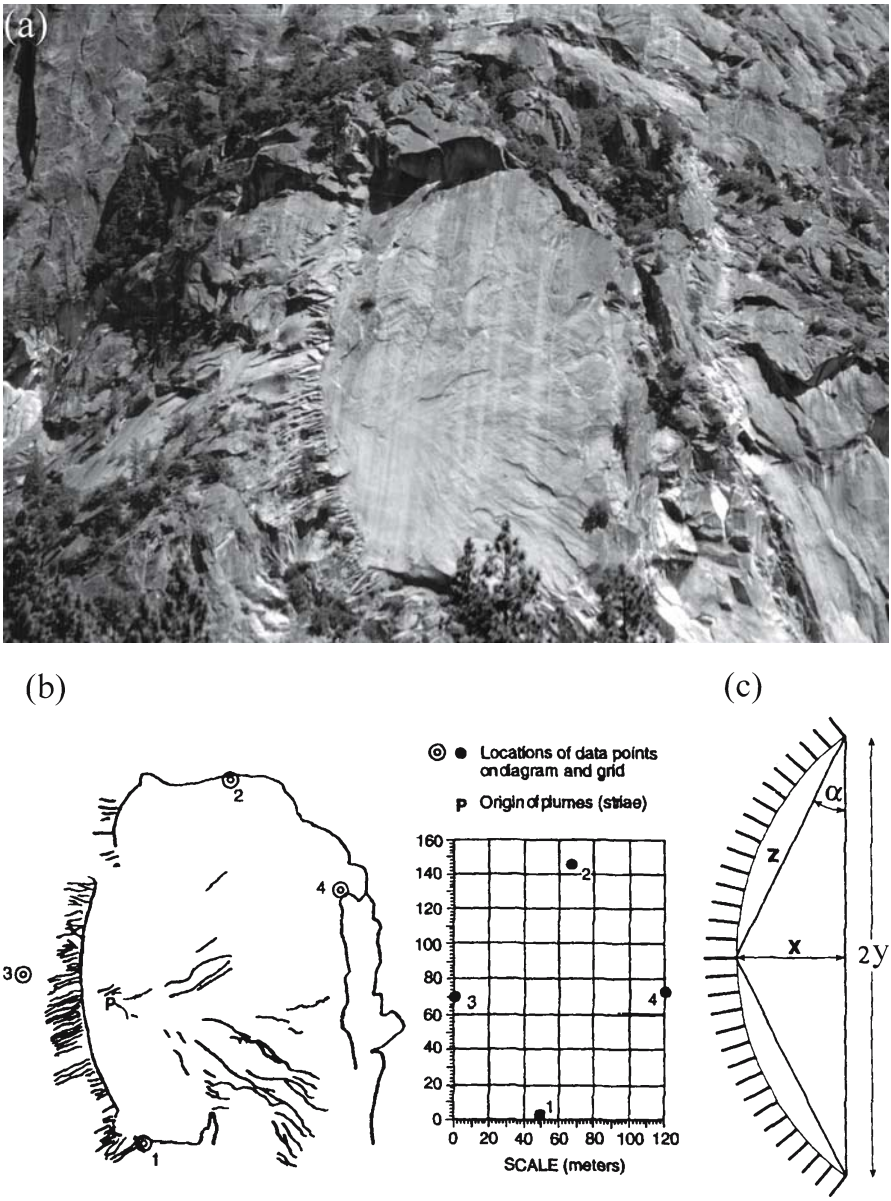

Fig. 6.18. The calculation of mirror radius when it is unmeasurable on the outcrop, applied on exfoliation joints striking N 27° E and dipping 42° NW on the southwestern side of Half Dome at Yosemite National Park. **a** Photograph of a curved fringe of *en echelon* cracks at left representing a remnant of an exfoliation joint (whose origin has been at the right side of the outcrop) on a slice that has been removed. **b** Scaled diagram and grid of **a.** The removal of the external slice exposed the surface of a second exfoliation joint whose origin is identified at *P* by the meeting area of radial barbs of a large plume. **c** Diagram showing the curved inner boundary of the fringe of *en echelon* cracks and the angle α between $2y$ and z (from Bahat et al. 1999)

6.6 Fracture Variability in a Fault Termination Zone

6.6.1 Introduction

A fault termination zone is a segment boundary, often related to earthquake dynamics (Schwartz and Sibson 1989), and is a potential major component in seismic activities (Aki 1979; King 1986). The maximum displacement in the middle of a strike-slip fault transforms into other manifestations of strain around the tip of the fault where the slip approaches zero (e.g. Muraoka and Kamata 1983). Chinnery (1966) shows that following this transformation, new regions develop around the tip of the fault in which the maximum shear stress, instead of being reduced, it may increase considerably. Changes lead to a complex geometry in the fault termination zone, including jogs, secondary faults, folds and rotation of fracture components (e.g. Trudgill and Cartwright 1994). A left-stepping bend with right-lateral shear produce contractional (anti-dilational) jogs, whereas stepping and lateral shear of the same sense produce extensional jogs. Contractional jogs may control rupture initiation and may impede fault growth (Sibson 1985; Scholz 1990, p. 155). Hence, the special conditions that develop in the fault termination zone may create both stabilities and instabilities, and understanding fault termination zones provides a key insight into rupture reoccurrence, fault growth, and growth impedance.

Detailed field characterizations of fault termination zones are rare, mostly because full exposures of such terminations are uncommon (e.g. Cruikshank et al. 1991; Bayasgalan et al. 1999 and references therein). This section concerns a detailed study of a termination zone of a contractional jog, characterized in chalk, which is a weak rock and its failure has resulted in a unique combination of a primary fault and eight secondary structures. The relative ages and interactions of joints and faults are often enigmatic. Previous analyses of curved joints near faults were presented by Rawnsley et al. (1992) in a scale of tens of meters, and by Castaing et al. (1996, Fig. 6) in scales of hundreds of meters. Castaing et al. (1996) observed that joints are both earlier and possibly contemporaneous with the faults. The present section contains a detailed account of relative ages of various components of a strike-slip fault system and a joint set on a small scale (length of 10–20 m in plan). This exposure may provide a template for terminations of larger strike-slip faults.

6.6.2 Description of the Fault Termination Zone

The fault termination zone is confined to a single layer (layer 1 in Fig. 3.39b and 6.19). The map of this zone (Fig. 6.20) is a product of a mosaic of forty overlapping photographs. The pictures were taken at 1 m height at an angle of 90° to the outcrop face. The resolution of the map is ≤10 cm. Details of fracture relationships are supplemented by photographs (Fig. 6.21a–f). The fault termination zone consists of eight fracture elements:

1. A straight fault and a gouge zone (Pr in Fig. 6.19, 6.20 and 6.21a).
2. A curved secondary fault S1.
3. Two left-stepping, secondary faults, S2 and S3.

4. A bulge caused by a local uplift in the northeastern area that surrounds the tip of Pr.
5. A set of curvilinear joints that vary in orientation sympathetically with the faults.
6. Cataclastic fault rock along certain parts of the faults.
7. Transverse cracks perpendicular to Pr in the bulged area.
8. *En echelon* cracks cutting the curved fault.

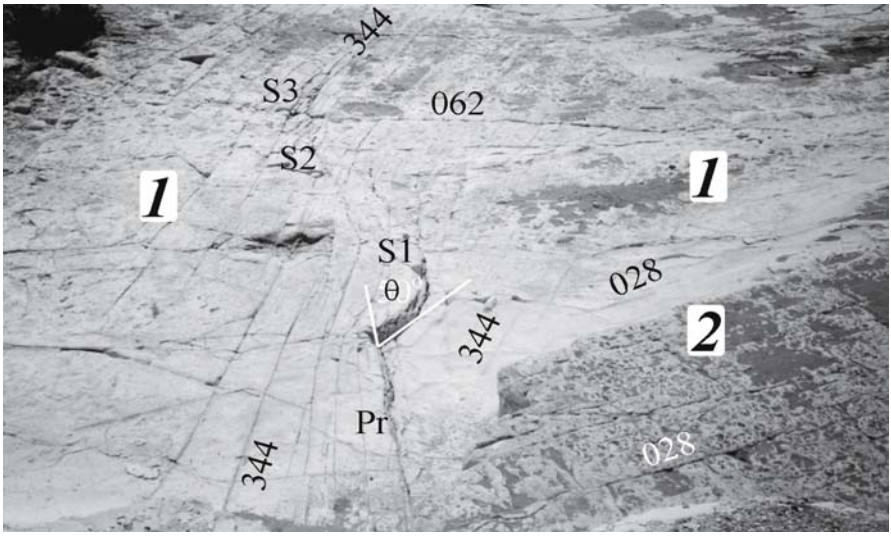

Fig. 6.19. A general view of the fault termination zone. The primary fault *Pr* (is 3.75 m long), the three secondary faults *S1*, *S2* and *S3*, set 344°, layers 1 and 2, joint set 028° in layers 1 and 2, and set set 062°: θ is the branching angle of *S1* from *Pr*

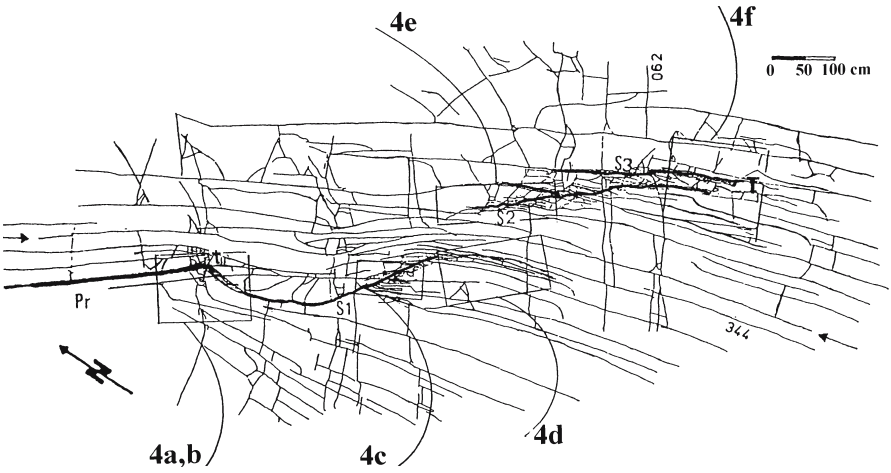

Fig. 6.20. A map of various components of the fault termination zone in layer 1: Curvilinear joint set 344°, the primary fault Pr, traverse cracks t, three segments (*S1*–*S3*) of the secondary faults and the termination at *T*. A single joint that crosses the termination zone is highlighted by two *lateral arrows*. The fault traces are slightly emphasized by rock splintering. The dominant joint set *344°* crossed by younger joint set *062°*. Note *frames* (4a–f) of Fig. 6.21a–f on map. Frames for Fig. 6.21a and b almost coincide

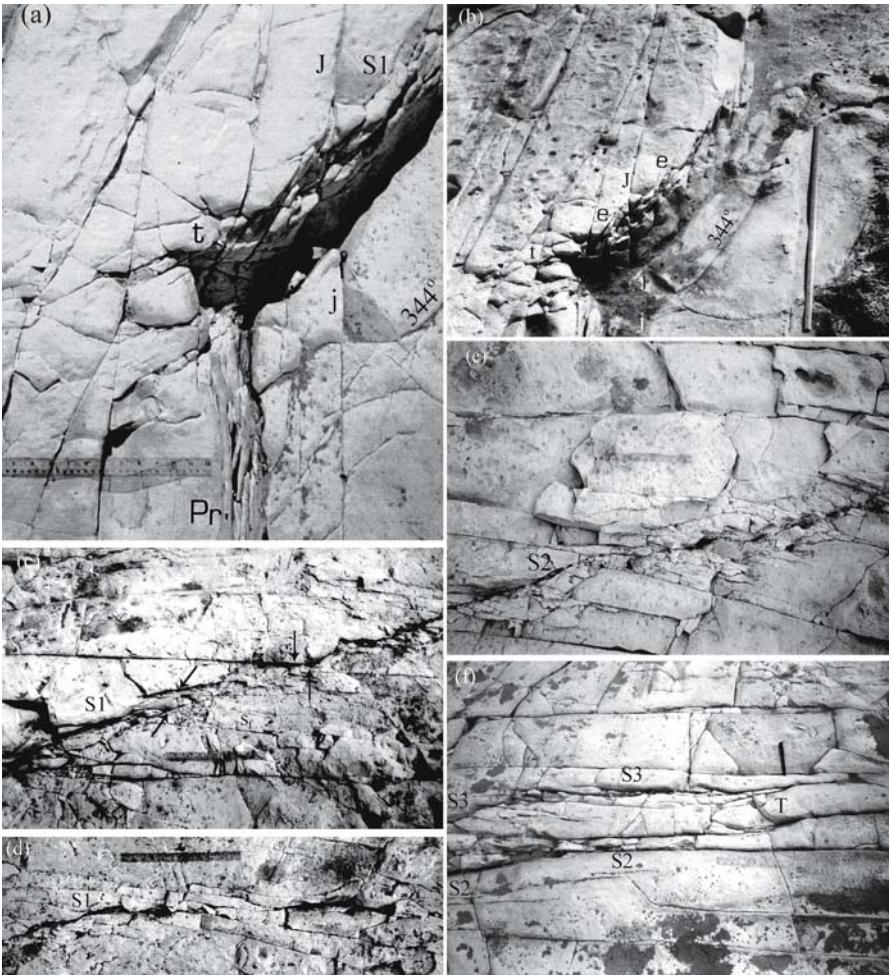

Fig. 6.21. Close-up photographs of parts of the fault termination zone. **a**, **b** The end of primary fault *Pr*, the curved fault S1 and a gap (*black shadow*) at the contact area between the two. The shear zone along the primary fault is populated by shear fractures (on the right side of 30 cm scale). Joints of set 344° are parallel to the primary fault. At the right side of the primary fault is a straight joint j that sub parallels to the joint J. At right-center of picture is a medium-sized joint trending approximately 344° and curves towards joint j. Transverse cracks *t* sub orthogonal to set 344° around the contact area of *Pr* with *S1*. Photographs **a** and **b** were taken from different angles. *S1* starts at the end of *Pr* where the maximum uplift of 18 cm (in shadow) occurs. *S1* is cut by two *en echelon* crack sets e (some of them sub parallel to the meter scale). Joint *j* next to *Pr* differs from Joint *J* next to *S1*. Transverse cracks *t* occur at left side of end of primary fault. **c** Two manifestations of cataclastic fault rock along the second part of *S1* (diagonal in picture). Rock fragmentation occurs between walls of a fault zone (between *inclined short arrows*) and many short joints (S_f) occur at right of fault but do not cross it. Right-lateral 2.5 cm displacement of an early straight, long joint along the fault (*vertical arrows*). An earlier fault would have prevented the long joint from crossing the fault zone. 30 cm *scale* parallels the 344° joints. **d** The curved fault *S1* terminates at an early joint where slight rock fragmentation ends (below 30 cm *scale*). **e** The initial part of the first of two left-stepping faults *S2*. Note intense rock mosaics of short joints and rock fragmentation along the fault. *Scale* is 30 cm. **f** A *pen* (13.5 cm long) points to the fault termination location *T* (see Fig. 6.20). *S2* and *S3* approach this location from left to right along joints. They bound a stretch of gradually reduced width with loss of cataclastic fault rock and increased joint spacing. At the right of *pen* jointing of set 344° initiates a "normal" distribution

The primary fault (Pr) and the gouge zone. This is a straight, vertical fault, which strikes 318° along 3.75 m. The extent of the fault continuation into the cliff is unknown (Fig. 6.19); it curves along the strike before entering into the cliff. There is a gouge zone along Pr that reaches the width of 7 cm at its tip (Fig. 6.21a). The gouge zone is sheared, resulting in slightly curved left-stepping R-shears resembling the right-lateral shear zones obtained experimentally by Bartlett et al. (1981, Fig. 6).

The fault S1: Its gap with Pr and the bulge. The curved fault S1 is vertical. It forms a sickle-like fracture in combination with the primary fault, such that S1 appears to be right stepping with respect to Pr, in a left-stepping system (see S2, S3 and Fig. 6.23 below). The northeastern fault wall (Fig. 6.20) is folded upward, bulging along the end of Pr and the beginning of S1 such that there is a gradual increase of vertical offset in layer 1 from 0 to 18 cm along the two faults, producing a crest at the contact area between them (at the Pr-S1 contact in Fig. 6.22). This crest is restricted to the "uplifted side" (note that layer 1 is higher on the left side of Pr than on its right side (Fig. 6.19)), as distinguished from the "lowered side" of the fault (in the southwestern side of the sickle-like fracture). Thus, bulging on one side of the fault introduced a distinction between uplifted and lowered sides along Pr and S1 and also along S2 and S3 (Fig. 6.22). The angle at branching initiation of S1 from Pr, θ, is 50 ±5° (Fig. 6.19).

There is a gap between the fault walls that continues laterally along S1 until it gradually dies out (Fig. 6.21a,b). There are some remnants of secondary material in this area (gouge?), suggesting that much more of it had filled the gap before being washed away. The gap is irregular and difficult to reconstruct to its original condition. This reconstruction may be achieved in two alternative ways. A good fit is obtained when the down thrown side is brought in contact with Pr by laterally overlapping the shear zone. This would close S1 and would leave about 0.5 cm right lateral displacement along Pr. On the other hand, a left lateral slip of 2.5 cm of the down thrown side along the gouge would also close S1 quite well. Both reconstructions would indicate an original right lateral displacement along Pr and S1.

S1 is divided into three parts that expose different styles of interaction with the joints of set 344° (see below). The first part, the one closer to the tip of Pr is 2.9 m long along its curved contour and has a smooth surface. Joints of set 344° seem to arrest at the first part of S1. Joint j (at the lower part of Fig. 6.21a) is straight while joint J at the upper part of the figure wiggles somewhat, and they do not appear to have been a single joint before separation by the fault. The second part of S1 is 2.4 m long and partially appears as a fault zone containing cataclastic fault rock (Fig. 6.21c) that becomes less abundant towards its end (Fig. 6.21d). A joint of set 344° appears to be right-laterally displaced 2.5 cm along the second part of S1. This joint is straight on both sides of the fault and does not show any interaction with the fault that would indicate any "aware-

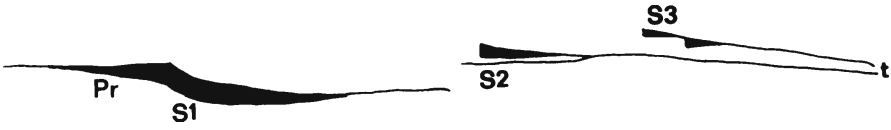

Fig. 6.22. A simplified perspective of fault termination zone. The vertical displacements along *Pr*, *S1*, *S2* and *S3* are shown by *black areas*. Note bending along *Pr* and *S1* and rhythmic maxima for the various faults

ness" of the fault presence (Fig. 6.21c). Thus, the fracture contacts reveal that the first part of S1 preceded the jointing next to it, while jointing occurred before the second part of S1, implying intermittent growth of either faulting or jointing there. There are in addition short joints (see below) that arrest at the second part of S1 (Fig. 6.21c). Along its third part, which is about 35 cm long, S1 makes a slight right turn towards its end, cutting a few medium-sized joints (see below) before coinciding with the direction of one of the joints (Fig. 6.21d). Cataclastic fault rock is minimal along the third part of the curved fault.

Two left-stepping faults. Two left-stepping faults (S2 and S3 in Fig. 6.19 and 6.20) occur near the curved fault. S2 starts about 4 m and 0.5 m from the closest points of Pr and S1, respectively. S2 is slightly concave toward the southwest. It overlaps about 0.7 m with the curved fault. At 2.15 m distance from its northwestern end, the fault splays with a branch about 1.30 long at a 20° angle. S2 crosses joints of set 344° near its early part (Fig. 6.21e), and then it coincides with a joint. The splay of this fault also coincides with a joint. S3 is almost straight, overlaps S2 and runs entirely along a joint. The distance between S2 and S3 varies from about 40 cm at their northwestern ends to about 30 cm at their southeastern termination.

The two left-stepping faults terminate in close proximity to each other (Fig. 6.21f, at T). The intensity of cataclastic fault rock declines to almost zero beyond T. The number of joints diminishes from some ten before T to three beyond this termination. Also, the opening along the fractures reduced at T from 1–2 cm to 1 mm or less.

The folding to bulges along S2 and S3 have maxima (11 cm and 8.5 cm, respectively) at the northeastern up-thrown part of each fault, and they vanish along the vertical fault planes towards the southwestern ends (Fig. 6.22). S2 and S3 differ significantly in orientation from S1. Whereas S1 strongly deviates from the direction of the primary fault Pr, S2 and S3 start to propagate along strikes, approximately in continuation with Pr (Fig. 6.20 and 6.21). While fault S1 terminates with only little cataclastic deformation along a joint of set 344°, fault S2 initiates with abundant cataclastic fault rock (Fig. 6.21e).

The joint set 344°. This set displays a strong curvilinearity along which growth occurred in several stages (generations). The joint set is spatially restricted to layer 1 in a 7 m wide area around the faults. The area is bounded by talus along the northeastern side and by a joint set oriented 028° along its southwestern side (at the right of Fig. 6.19 and 6.20). The joints of set 344° change strike in "four zones" of the termination zone as follows. The joints are approximately straight and parallel to Pr along the fault. Beyond the tip of Pr the joints curve sympathetically with respect to the secondary faults, S1, S2 and S3, forming the "curvilinear zone". On the southeastern side, beyond the final fault termination (T in Fig. 6.21f) and throughout the sourthwestern "lowered side" of the fault all joints are straight with uniform 344° orientation.

A joint oriented 344° in the "lowered side" curves and "hooks" into a straight joint that parallels to the primary fault (Fig. 6.21a), suggesting a fracture sequence between the joints, because the former joint "knew" about the existence of the straight joint. At least one joint approximately follows the shape of S1: First, the concavity of S1 towards northeast and then, its concavity towards southwest, towards the termination of S1.

(Fig. 6.19 and 6.20). Some joints however are crossed by the secondary faults at acute angles ~40° or at smaller angles ~5–15°. Individual joints of set 344° may be up to 10 m long with only very little interaction with each other. Hence, although these joints curve and vary in orientation, they are termed set 344°.

We divide the joints of set 344° into three groups according to their lengths. The "long", "medium-sized" and "short" fractures are up to 10 m, 4 m and 1 m long, respectively. The long and medium-sized joints are parallel to each other. Near S1 and along S2 and S3, medium-sized joints fill gaps between long joints (Fig. 6.20), reducing spacing to about 2 cm. However, further away from the faults S2 and S3, towards the southeast end of the outcrop where long joints are oriented 344°, their spacing becomes larger and ranges from 10 to 25 cm, not having the medium-sized joints among them. Thus, the medium-sized joints appear to postdate the long joints.

The long and medium-sized joints cut by S1 are distinguished from the short joints not cut by S1 (Fig. 6.21c). The medium-sized joints appear to be quasi-systematic (straight and parallel to each other), whereas the short joints are non-systematic and somewhat distorted. Joints of set 344° are generally quite closed (an aperture of about 0.1 mm or less). However, some of them widen their apertures up to about 1 cm along the second part of S1, and particularly, along the stretch between S2 and S3.

Cataclastic fault rocks. In certain locations, the country rock is intensely ruptured into fragments that range in size from several millimeters to several centimeters. The "mosaic style" occurs along the second part of S1 (Fig. 6.21c), where rock fragmentation occurs between two walls of a fault zone. A mosaic is also spatially associated with short joints that either start or arrest at the southwestern side of the fault zone, on which perpendicular younger cracks may arrest, creating a rock mosaic of square and angular splinters. This style is also in association with S2, but the mosaic next to S2 (Fig. 6.21e) is more intensely populated. Mosaics extend up to 30 cm from a fault, mostly occurring along the concave side of the faults (Fig. 6.21e), where the secondary faults cross the 344° joints, particularly where joint spacing is small. Fragmentation also occurs as rock splintering not associated with rock mosaics. They are particularly found between S2 and S3. This splintering also extends to distances of up to about 12 cm across the two sides of the faults.

Transverse cracks perpendicular to Pr in the bulged area. The bulged area close to the tip of Pr is intensely fractured by transverse cracks. The cracks are short (about 12 cm), trending approximately orthogonal to the primary fault (t in Fig. 6.20 and 6.21a), and generally arrest at joints of set 344°. The transverse cracks cut part of the gouge along the primary fault (they are not visible in Fig. 6.21a).

***En echelon* cracks.** Two sets of *en echelon* cracks cut the bulged area of the first part of S1 at its continuation from the tip of Pr (e in Fig. 6.21b). Their azimuths are 330° and 350°, and their crack length averages are about 22 cm and 14 cm, respectively. Cracks of set 350° generally arrest at cracks of set 330°, implying that set 330° generally was older. Rock splintering associated with these cracks is not as intense and irregular as the cataclastic fault rock along the second part of S1 and the left-stepping faults.

Table 6.1. Ratios of fracture parameters in the fault termination zone

Fracture parameter	Ratio
1. [Length (max) S1] / [length (straight) S1]	455 / 435 = 1.05
2. [Length (straight) S1] / [length (straight) S2]	435 / 470 = 0.93
3. [Length (straight) S1] / [distance between edge of Pr to start of S2]	435 / 350 = 1.24
4. [Length (max) S1] / [vertical offset (max) of S1]	455 / 18 = 25.3

S1, and *S2* are the curved fault and the first of the two left-stepping faults, respectively. The terms *max* and *straight* designate the full curved length of a fault, and the length of a fault ignoring the curvature, respectively. Ratios are obtained by division of parameters given in centimeters.

6.6.3 Fracture Parametrization in the Fault Termination Zone

Ratios of fracture parameters. Assuming similarity of strike-slip faults in various scales and therefore similarity of their termination zones, ratios of fracture parameters are possibly more important than absolute values. Some ratios of fracture parameters are summarized in Table 6.1. It turns out that the "straight" lengths of S1 and S2 (ignoring curvature along the fault) and the distance from the tip of Pr to the initiation of S2 (Fig. 6.20) are about the same.

Fracture sequence in the fault termination zone. The great versatility of fracture styles and their clear exposure enables one to decipher the sequence of most fracture processes in the fault termination zone (Table 6.2). The right-lateral offset along Pr resulted in creating a wing crack (the first part of S1) and a gap at the contact area between Pr and S1. More than a single offset along Pr (repeated S2 and S3 faults and e cracks) resulted in the deformation in the termination zone. Bulging in the area close to the tip of Pr has resulted in transverse cracks oriented 025° (characteristic to crests of outer arcs, Fig. 3.19a). These cracks arrest at the 344° joints that parallel to Pr in the "uplifted side" of the fault, suggesting that maximum bulging occurred after the formation of 344° joints. On the other hand, joints of set 344° seem to arrest at the first part of S1, suggesting that the first part of S1 preceded the joints. Also, in the "lowered side" a joint oriented 344° curves and "hooks" into a straight joint that parallels Pr, suggesting a time interval between these joints. Assuming that the straight parallel joints on both sides of Pr were formed approximately simultaneously, it should follow that the lateral component of deformation creating S1 preceded the vertical offset associated with the bulging. That is, when the lateral offset(s) was exhausted, further stress release resulted in vertical stresses producing the bulging.

The onset of cataclastic deformation along the second part of S1 suggests a change in mode of fracture at the transition from the first part of S1. This change is not surprising, considering the change in orientation along S1 with respect to the 344° azimuth, which is taken to be the σ_1 trajectory of the stress field that created Pr (Fig. 6.20). In analogy to previous observations (e.g., Brace and Bombolakis 1963; Jayatilaka and Trustrum 1978), the second part of S1 was formed by a stable process under conditions of increasing stresses. This part of S1 postdated a 344° joint (Fig. 6.21c). The implication is that the second part of S1 developed discontinuously (incrementally) with

Table 6.2. Sequence of fracture episodes of joints and faults in the fault termination zone

Episode No.	Joints/cracks	Faults	Uncertainties
1	–	Offset along Pr	
2	–	First part of S1	
3	Parallel to Pr	–	
4	–	Vertical displacement along Pr and S1	
5	Long (up to about 10 m long) curvilinear and 344 oriented	–	
6	–	Transverse cracks near tip of Pr	
7	Medium (up to about 4 m long)	–	?
8	–	Second part of S1 and rock splintering along S1	
9	Short (up to about 1 m)	–	?
10	Cross (one cm) in mosaics	–	
11	–	Third part of S1 and rock splintering along S1	
12	Short (up to about 1 m)	S2 and rock splintering along S2	?
13	Cross (one cm) in mosaics	–	
14	–	S3 and rock splintering along S3	
15	Short (up to about 1 m)	–	?
16	–	Rock splintering between S2 and S3	

Pr, *S1*, *S2* and *S3* are, the primary fault, the curved fault, first of the two left-stepping faults and second of the left-stepping faults, respectively. Uncertainties in time relationship of joints and faults are marked by *?* and are discussed in text.

respect to the first part of S1. The curved fault S1 terminates with only little cataclastic deformation along a joint of set 344° (Fig. 6.21d), whereas the initiation of S2 is associated with intense cataclastic deformation (Fig. 6.21e). This suggests that an early episode of secondary faulting ended with the termination of S1, but the creation of S2 manifests a new fracture episode that occurred when high stresses were attained.

Many short joints arrest at S2. Since S2 postdated S1, the joints that interact with S2 quite likely postdated those that are associated with S1. Spacing of set 344° in various areas adjacent to the secondary faults is reduced down to about 2 cm. The reduced spacing reflects multi-stage jointing of medium-sized and short joints: Late joints fractured between and parallel to previously long joints. It has been observed in many outcrops of syntectonic joints (joints associated with intense deformation) cutting chalks that these fractures generally form by more than a single failure event (Bahat 1991a, p. 282).

Generally, cataclastic fault rock is thought to form concurrently with faulting. However, it should not be ruled out that the mosaics that occur close to one boundary of a second fault (center of Fig. 6.21c) could also reflect post fault energy release. The question marks in Table 6.2 indicate that certain parts of the fracture sequence are not certain. Episode 7 is marked by '?', because only one medium-sized joint is cut by the second part of S1. The reason for marking '?' in relation to episodes 9, 12 and 15 is that short joints may be contemporaneous with the adjacent faults but could also be post faulting.

Two gap types. The gap continuation along the first part of S1 (Fig. 6.21a,b) is a result of a mode I fracture. Closing the gap into its original condition before faulting by a left lateral slip of the down thrown side along the gouge would create an appearance of a continuation of j- and J-joints across S1 and may suggest that the joint predated S1. On the other hand, closing the gap by contacting sidewise the down thrown side with Pr (overlapping across the shear zone) may result in an offset of joints j and J across S1. This would fit the model of joint j arresting at the earlier S1, becoming the favored explanation, implying that the shear zone developed only after the separation of the two walls of Pr.

It may be speculated that the growth of some primary faults and their termination zones to large (continental) strike-slip faults can be explained by a stepwise process. This takes place by reoccurring bridging of the gaps between the tip of the primary fault and the initiation of the first or second *en echelon* faults (Pr, S2 and S3, respectively, in Fig. 6.20). Such a process might shift the location of maximum stress intensity from the tip of Pr to the termination of S2 and/or S3 (point T) before the next earthquake would take place.

Models of termination zones and experimental results. There is an important difference between two existing models of termination zones. In one model of a right lateral offset, all secondary faults maintain left-stepping configuration, splaying towards one side of the continuation of the primary fault (Fig. 6.23a) (Hobbs et al. 1976, Fig. 7.18d and Twiss and Moores 1992, Fig. 7.7). Chinnery (1966) suggests two possible theoretical combinations of straight primary and curved secondary faults. One of them consists of a sickle-like structure that resembles the present combination

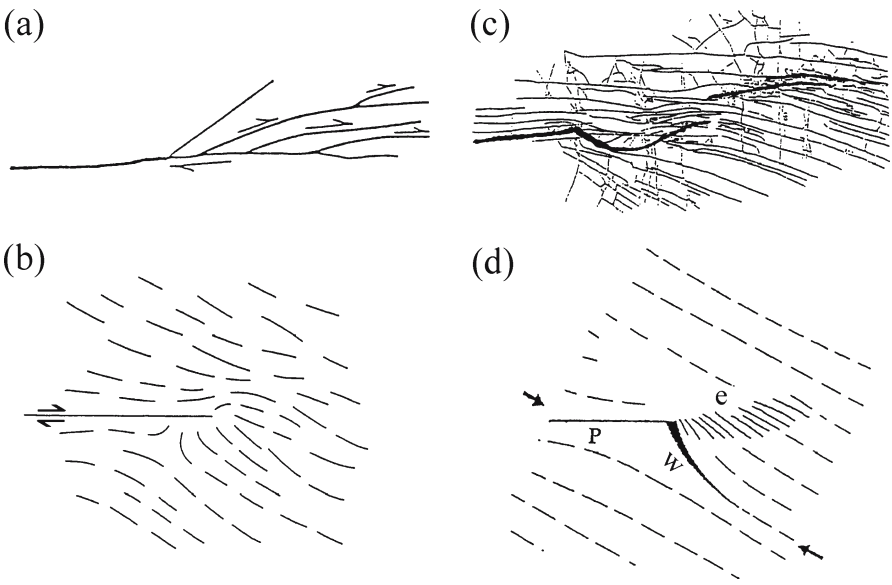

Fig. 6.23. Comparison of previous models of fault termination zones to the present observations for right lateral strike-slip faults. **a** Splay faults branching from primary fault near its terminus (modified after Hobbs et al. 1976). **b** Trajectories of maximum principal stress direction shown by *dashed lines* at the termination zone of a strike-slip fault (from Means 1979, after Chinnery 1966). **c** Miniature of fault pattern from present map in Fig. 6.20. **d** Compression applied at a small angle to primary fault *P*, resulting in secondary fractures *w* and *e* (see text for explanation) (modified after Petit and Barquins (1987, 1988)

of Pr and S1: The trajectories of the maximum principal stress at the termination zone of a strike-slip fault (Means 1979) resemble the contours of the present joint set 344° (Fig. 6.23b and c, respectively). In the latter, the curved fault S1 appears to be the result of right stepping, apparently in conflict with the requirement of an exclusive left-stepping arrangement of the first model (Fig. 6.23a).

Petit and Barquins (1987, 1988) demonstrate experimental results obtained from PMMA and sandstone under uniaxial compression, which strongly resemble the fracture geometry in the termination zone (Fig. 6.23d, see also Fig. 2.58a). In their experiments, the "sickle" formed by Pr and S1 and the secondary fault S2 are represented by P, w and e, respectively. The location and the angular relationship with respect to the primary fault Pr suggest that S2 and S3 are analogous to the "shear zone" e that Petit and Barquins (1987, 1988) produced under maximal stress conditions. They also found that the wing crack resulted from mode I operation, which shows opening, and the shear zone resulted from mode II loading (see Sect. 2.2.13). Also relevant is the experiment by Petit and Barquins (1987, 1988) on sandstone that revealed cataclastic deformation along the *en echelon* cracks at e, resembling the cataclastics found along S2 and S3. There is an additional resemblance between these experimental results and the fault termination zone, in that w deviates from the direction of P, and e strikes approximately in continuation with P (Fig. 6.23d).

Bulging and vertical offset. Spatial constraints cause shear stresses around the tip of the primary fault that are partly released by lateral displacement and partly by vertical offset. The area in the termination zone may be divided into compressional and tensional regimes. In a contractional jog, a vertical upthrow along one side of the fault would occur in the compressional regime and a downthrow would occur in the tensional one (Chinnery and Petrak 1968). Accordingly, bulging along the primary and secondary faults is exhibited in the upthrown block (Fig. 6.19) as expected. The rhythmic maxima in the vertical displacements along S1, S2 and S3 imply that these bulges occurred concurrently with each individual fault. A single vertical displacement at a later time would be expected to have been monotonous with a gradual change from maximum to minimum throughout the termination zone rather than a rhythmic one. This rhythmic mechanism supports the suggestion of an incremental growth of the secondary faults (Table 6.2).

6.6.4 Open Questions

The student may like to ask several questions that need to be further explored:

1. How do existing left-stepping configurations (Fig. 6.23a) reconcile with the field and experimental data shown in Fig. 6.23c,d?
2. How similar or different to this fault termination zone are termination zones of other contractional jogs?
3. To what extent fault termination zones change with size?
4. Set 344° was induced by a perturbation at the tip of the fault (rather than along it, Fig. 3.12a). There is a need to characterize the secondary stress field that formed around the tip of the primary fault and induced the three secondary fractures (far away from the Pr tip).

6.7 Fault-Joint Relationships in the Beer Sheva Syncline, Israel

6.7.1 Introduction

This section relates to eight distinct fault-joint systems in the Beer Sheva syncline from south Israel that differ from each other in their genetic affiliation and their geometric and age relationships, citing Bahat (2000, 2004).

6.7.1.1 *Joints and Fault Classifications*

Joints are the most ubiquitous structures in sedimentary rocks. This is because joints may be formed under small differential stresses, and therefore most environments are conducive to their development, both systematically and non systematically (Hodgson 1961b). Nelson (1979), Engelder (1985) and Bahat (1991a) proposed genetic classifications of joints. According to the latter classification, joints may be divided into four groups: Burial, syntectonic, uplift and post uplift. These can be distinguished in the field by both geometric and fractographic criteria. The four groups reflect four characteristic stages in basin evolution.

The last fifty years of fault investigation enjoyed the benefit of the pioneering classification of faults into three classes by Anderson (1951). The great power of Anderson's grouping stemmed from its simplicity. It helped to demonstrate the dependence of the three main fault types on systematic changes in the stress field that also reflected on the most likely tectonic conditions. However, fault classification cannot be applied to timing of basin histories. On the other hand, extended research on the temporal relationship between fault-joint relationships (FJR) (e.g., Sterns 1968; Pohn 1981; Cruikshank et al. 1991; Gross 1995; Martel 1997; Kattenhorn et al. 2000; Wilkins et al. 2001; Eyal et al. 2001) has accumulated a vast amount of knowledge that can be used in refining the fracture histories of basins. The work by Peacock (2001a) is a recent summary of some key observations related to this topic.

6.7.1.2 *The Importance of Temporal Fault-Joint Relationships*

The temporal fault-joint relationships are important for a variety of reasons that are specified below.

1. Sequences between faults and joints may help to decipher the tectonic history of the region (including earthquakes), and temporal relationships.
2. They also provide information on the stress history of the region.
3. Faults may affect later joint development and joints may transform to faults (Segall and Pollard 1983), and these processes are mechanically intriguing.
4. Distinct joint/fault genetics may be linked with different fracture parameters (aperture, length, spacing, interaction, etc.).

5. Fluid flow (water, hydrocarbon liquids and gas) depends on fault-joint relationships and their fracture parameters. For instance (Bahat 1991a, p. 239).
   a Burial pre-fault joints may be closed due to their development in a process of increasing lithostatic pressure;
   b Some syntectonic, syn-fault joints may be sealed into veins, while others strongly enhance water flow, like the strike parallel joints (062°) in the Beer Sheva syncline;
   c Uplift joints that form after burial-normal faults are opened fractures.

Unlike many other folds that exhibit relatively uniform structures, the Beer Sheva Eocene syncline is divided into four distinct stratigraphic units that display different fracture characteristics and store a record of many (more than twenty) different fracture episodes since the Lower Eocene (Sect. 3.4). One manifestation of this multi-fracture complex is the occurrence of at least eight distinct FJRs. Various aspects of FJRs in this syncline were introduced in previous publications, including pre and post-fault burial joints, syn-fault syntectonic joints and post-fault uplift joints that partly transform into faults (e.g., Bahat 1991a, pp. 241, 275 and 282; 1998a, 1999a; Gross et al. 1997). A synthesis of the previous observations constitutes the major part of this section, with the objective of demonstrating the extent to which the estimation of timing of fracture development, relative to the structural history of a syncline can be achieved. Price's (1974) model of fracture in basins is adapted here in analyzing fracture in the Beer Sheva syncline, as in previous publications (e.g., Bahat 1989). A distinction is made in the following description of the various FJR types between the "primary faults" and the various joints (or faults in one case) that are associated with them, which are collectively termed "secondary fractures". This distinction is not relevant to type 8 (see below).

6.7.2 Eight Types of Fault-Joint Relationships

Eight FJR types of fault-joint relationships from the Beer Sheva syncline (Fig. 3.33b) are characterized below. Table 6.3 summarizes FJR that take into account different parameters:

1. Temporal relationships.
2. Geometric contacts.
3. Tectonic setting.
4. Stresses.
5. Fracture system.

Six types relate to normal faults, one type concerns the terminal zone of a strike-slip fault and the eighth type is about vertical faults.

Type 1 joints occur in the Mor Formation of the Lower Eocene and is associated with a normal fault from the burial stage of the syncline (Bahat 1985). The fault strikes ~292° and dips ~45° N, cutting alternating chalk layers (about 90 cm thick) with chert beds (about 10 cm thick) (Fig. 6.24a,b), while the chalk is dissected by two orthogonal, vertical, single-layer joint sets oriented 328° and 059°. Joints of the cross-fold set 328° arrest at the boundary of the chalk layers with chert beds. The fault that dis-

Table 6.3. Eight types of fault-joint relationships (FJR) in the Beer Sheva syncline, Israel

FJR type[a]	Temporal relationship of joints	Joint attitude in relation to the fault one	Tectonic setting	Joint formation by stresses remote/local	Fracture system
1 (n)	Pre-fault	Different, independent	Burial, early	Remote	Closed, non-interacting joints, regular spacing (Fig. 6.24b)
2 (n)	Post-fault	Different, independent	Burial, early	Remote/local	Closed, non-interacting joints, decreased spacing (Gross et al. 1997)
3 (n)	Syn-fault	Correlative, dependent	Syntectonic early uplift	Local	Local fracture multiplication (in sector I, Fig. 6.24c and 6.25)
4 (n)	Syn-fault	Correlative, dependent	Syntectonic early uplift	Local/remote	Local twisted secondary faults (in sector III, Fig. 6.24c and 6.25)
5 (s)	Post-fault	Secondary Stress field	Syntectonic early uplift	Local	Non-interacting joints, variable spacing along primary and secondary faults (Fig. 6.20)
6 (n)	Pre-fault	Different, independent	Late uplift	Remote	Regular joint spacing (Fig. 3.36g)
7 (n)	Syn-fault	Correlative, dependent	Late uplift	Remote	Decreased joint spacing (Fig. 6.24d)
8 (v)	Transitional	Parallel	Uplift	Remote/local	Deep penetrating, creating vertical joints and faults (Fig. 3.35b)

[a] Normal fault (*n*), strike slip fault (*s*), vertical fault (*v*).

places these joints contains in its fracture zone fragments of chert that had been broken during early offsets of the fault and unfractured nodules that precipitated after the cessation of the fault activities. The precipitation of chert is associated with the diagenetic (burial) stage of the chalk (Knauth and Lowe 1978). Chert does not occur in the overlying Middle Eocene (Horsha Formation). Therefore, both the cross-fold joints and the normal fault occurred before the sedimentation of the Middle Eocene, i.e., they were formed during the burial stage by a process controlled by the tectonic regime that prevailed in the Lower Eocene (Gross et al. 1997). The joint orientations are unrelated to the fault attitude, requiring that the remote stresses had to change from the conditions under which the joints were formed to new conditions that induced the fault. Hence, during the burial stage of the syncline, differential stresses gradually increased, such that the formation of the cross-fold joints and some strike-parallel joints preceded the creation of the fault (Bahat 1985, 1991b; Gross et al. 1997). Generally, joint orientation and spacing is almost the same around the fault.

Type 2 relates to the same fault that is shown in Fig. 6.24a,b but it concerns a local spacing reduction in the hanging wall compared to the uniform spacing elsewhere around the fault. Gross et al. (1997) found that due to dragging of one of the chert beds, an unrelieved strain remained stored in the hanging-wall from the early stages of the fault slip. This unrelieved strain was subsequently released in the form of ~055° oriented joints. Hence, the fracture sequence during the burial stage was early cross-fold and strike-parallel orthogonal joint sets, normal faulting and subsequently some additional fold strike-parallel joints in the hanging wall.

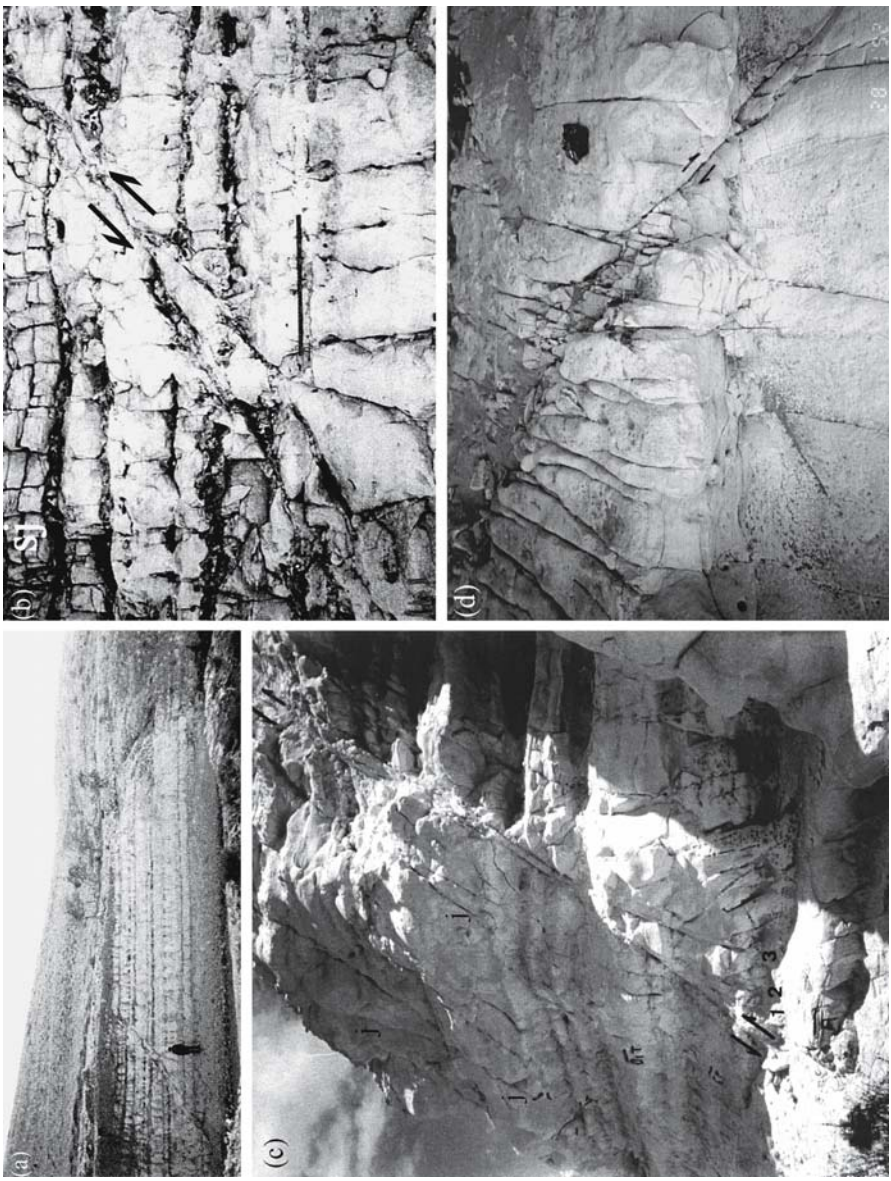

Fig. 6.24.
Structural relationships of faults and associated joints from the Beer Sheva syncline. **a** Two conjugate faults. **b** An enlargement of the fault dipping towards left, to which types 1 and 2 relate. The faults cross vertical single-layer joints in Lower Eocene chalks near Beer Sheva. The two orthogonal joint sets and the faults strike in three distinct directions. Thus, joints and faults were formed in different remote stress fields (after Bahat 1985). **c** Types 3 and 4. Type 3 is represented by inclined joints that parallel the dip of a normal fault in Wadi Secher at the upper hanging wall (marked j). Type 4 is shown as inclined secondary faults (f1–f3, marked 1–3, respectively) at various acute angles to the primary fault in the lower footwall. **d** Type 7. Spacing of the vertical joint set decreases considerably as the joints come closer to the normal fault, which is a characteristic feature of syntectonic joints. Therefore, the primary fault and joints developed in the same remote stress field. The *black rectangle* is 10 cm long

Two more joint spacing peculiarities were observed in the same outcrop (Bahat 1991a, p. 255). First, joint spacing is wider in thinner chalk beds, i.e., the layer thickness-joint spacing plot shows a negative slope for both cross-fold joints and strike joints, which is in contrast to most observations by other investigators that show positive plots (e.g., Price and Cosgrove 1990, p. 54). An exceptional finding of a negative slope was also made by Eyal et al. (2001) in the chalky limestone beds Nahal Neqarot in southern Israel. Second, for a given layer thickness, joint spacing is a little wider in the strike-parallel joints (oriented 055°) than in the cross-fold joints (oriented 326°). An explanation for these two observations requires further studies. It is possible that spacing is wider in the strike-parallel joints because their formation was associated with stress relaxation, compared to the cross-fold joints that reflected regional stresses (Bahat 1989).

Types 3 and 4 joints outcrop along Wadi Secher (Fig. 3.33c) and occur in the Middle Eocene chalks of the syncline. The joints of Type 3 are inclined and are approximately parallel to the Secher fault dip (Fig. 6.24c). Fracture distribution around the fault is explained by Fig. 6.25a–e. The remote stresses (σ_1^{∞}, σ_2^{∞}, σ_3^{∞}) have induced the normal fault that dips towards left (Fig. 6.25a). A new, local stress field (σ_1, σ_2, σ_3 in the shape of a stress ellipsoid) was created by the slip (or slips) along the fault (Chinnery 1966). A damage volume was formed along the fault by its initial formation and by its subsequent slips. The damage volume is the rock volume that contains secondary structures (mostly fractures) that are confined to the fault, and it approximates the shape of an ellipsoid (Fig. 6.25b). Two orthogonal planes can schematically describe the distribu-

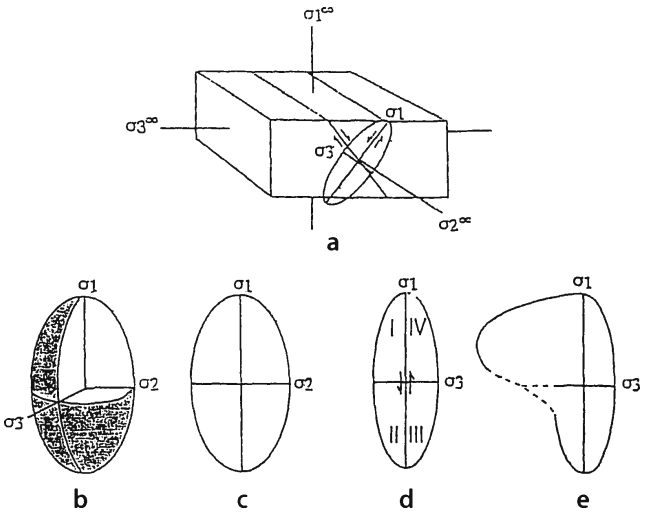

Fig. 6.25. Diagram of primary normal fault and secondary fractures in three dimensions. **a** The normal plane (*ellipse*) that describes the arrangement of local principal stresses is superposed on one of two conjugate faults in a rectangular block that describes the remote principal stresses. Orientations of remote and local principal stresses differ significantly. These figures contain geometric elements from Means (1979) and Park (1983) (see explanation to types 3 and 4). **b** Stress ellipsoid in perspective, showing its two principal planes, the fault plane σ_1–σ_2, which is termed the "parallel plane" with its elliptical tip line boundary, and the "normal plane" σ_1–σ_3. **c** The "parallel plane" that contains the fault plane with its elliptical tip line boundary. **d** The "normal plane" is divided into four sectors *I*–*IV*. **e** The approximate shape of sector *I* in the normal plane of the Secher fault A

tion of secondary fractures in a damage volume. The tip line forms an elliptical line (Walsh and Watterson 1988; Knott et al. 1996) that marks the loci on the fault plane (approximately the "parallel plane") along which displacement has decreased to zero (Muraoka and Kamata 1983; Walsh and Watterson 1988) (Fig. 6.25c). The "normal plane" is orthogonal to the parallel plane and is divided into four sectors (I–IV) by the trace of the fault and the tip line (Fig. 6.25d). For normal faults the extensional sectors I and III are widest (where rock is weak) and narrowest in the contractional sectors II and IV (where rock is strong) (e.g., Knott et al. 1996).

The direction of maximum shear stress in the initial field of remote stress ($\sigma_1^\infty, \sigma_2^\infty, \sigma_3^\infty$) is transformed to the direction of σ_1 (Fig. 6.23b) in a simple 45° rotation exercise (Means 1979, problem 12.4) during the formation of the local stress field. This explains how the local minimum principal stress (σ_3) was normal to the fault plane, creating type 3 joints (Fig. 6.24c). Some twelve joints of type 3 are spatially confined to sector I in the damage volume of the Secher fault (one or two joints occur in sector IV as well). Unexpectedly, the width of sector I of the Secher fault was found to be about 60% of the length of the fault, implying a strong deviation of the normal plane from an elliptical shape (Fig. 6.25e). Accordingly, the schematic shape of the damage volume (shown two dimensionally in Fig. 6.25d) is modified to a more realistic "quasi-ellipsoid damage volume" (Fig. 6.25e). Type 3 joints resemble the (unspecified) fractures that are parallel to the dip of the normal fault from the known results described by Stearns (1968) (the fractures dipping towards left in Fig. 6.26). They also resemble the FJR of large strike-slip faults in which joints cut parallel to the dip and strike of the primary fault close to the fault termination zone (Chinnery 1966, Fig. 5).

Type 4 joints consist of a series of three fractures (f_1–f_3) that formed in sector III of the normal Secher fault (Fig. 6.24c and 6.25d). Fractures f_1 and f_3 exhibit changes in orientation relative to that of the fault. The fault strikes 040° and dips 51° to NW, f_1 strikes 035° and dips 68° to NW, f_2 strikes 038° and dips 69° to NW and f_3 strikes 088° and dips 85° to NW. The changes reflect combined strike twist and dip tilting from an attitude relatively close to that of the fault to an almost vertical fracture that totally divorced from the trend of the fault. This reflects a response to local perturbed stresses

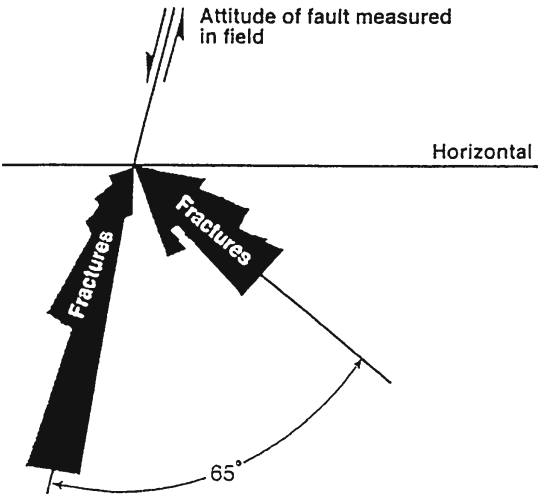

Fig. 6.26.
Rose diagram showing the distribution of dips of two sets of fractures (unspecified) associated with a normal fault (after Stearns 1968, and Twiss and Moores 1992)

along the fault (Rawnsley et al. 1992) that were effective in initiating fractures f_1–f_3, combined with a gradual increase of the influence of the remote stresses with distance of the fractures from the fault (up to about 3.5 m). There is some shear displacement along these fractures, which distinguishes them from the joints of the other types. Type 4 resembles the fracture set that occurs at a large angle (>45° but <90°) relative to the fault in the Stearns model (dipping to the right in Fig. 6.26). However, in the latter the angles created between the fault and joints are larger than in type 4 (see more about the model depicted in Fig. 6.25 in the discussion section). Type 4, like type 3 is thought to be genetically related to displacements along the fault, in association with an early uplift stage in the Beer Sheva syncline (see below).

Type 5 joints occur at a fault termination zone (Sect. 6.6), cutting a Middle Eocene chalk layer during the uplift stage. The termination zone consists of a primary fault, secondary faults, and a joint set in Wadi Naim (Fig. 6.19 and 6.20). The primary fault is a vertical right-lateral strike-slip fault, striking 318°. A set of three partly curved secondary faults initiate at the tip of the primary fault, and a joint set striking 344° curves sympathetically with the primary and secondary faults in a close proximity with the faults. Therefore, the 344° striking joints are considered to be genetically associated with the faults, and they are termed syntectonic joints. The 028° striking joint set is ubiquitous in Wadi Naim. However, where these joints approach the termination zone they arrest or interact (hooking style) with the 344° striking joint set, but they never penetrate to the termination zone. Therefore, the 028° striking joint set postdated the above three structures in the same chalk layer, i.e., they are younger than type 5 FJR joints. Thus, sets 344° and 028° belong to two separate fracture events: An early and an advanced one during the uplift process (Bahat 1999a).

Type 6 joints are cut by the Naim normal fault A (Fig. 3.36g). There are no visible differences in the behavior (spacing) of the joints from both sides of the fault. The strike of this set forms an angle larger than 45° with the strike of the fault. Unlike the system described by Kattenhorn et al. (2000) there are no genetic relations between the fault and joints. These are single-layer uplift joints that were associated with the advanced uplift in the syncline, but they had been preceded by the earlier 344° uplift set (type 5). Therefore, the fault of type 6 was associated with an advanced uplift stage of the syncline.

Type 7 joints are adjacent to Naim normal fault B that occurs some 125 m west of Naim fault A. The joints show significant decrease in spacing close to the lower part of fault B (Fig. 6.24d), and as such they comply with a basic criterion of syntectonic joints (Bahat 1991a, p. 279). Compared to types 1 and 6, which reflect joints and faults that formed by different stress fields, type 7 represents an assemblage of joints that were formed in the same local stress field as the fault. Thus, even if the faults from types 6 and 7 cut the same chalk layers and appear to belong to the same fault system, these two types seem to show different FJR manifestations. Whereas the fault of type 6 is associated with joints that formed before faulting, the fault of type 7 created a local stress field that formed syntectonic joints adjacent to it.

Type 8 joints occur in the Lower Eocene chalks around Beer Sheva in the form of vertical multilayer joints that often traverse the entire exposed outcrops; they may run alongside or across burial normal faults from type 1 (Fig. 3.35b). Often multilayer joints are associated with vertical multilayer faults in irregular 5–20 m spacing. These vertical fractures are considered to have been formed after the burial stage during a single or multi uplift episodes of the area (Fig. 5.15 in Bahat 1991a).

6.7.3 Discussion

6.7.3.1 *Genetic Relationships and Relative Ages of Fractures*

Types 1, 2 and 8 occur in Lower Eocene chalks. While types 1 and 2 are products of the burial stage, type 8 formed much later by uplift (Bahat 1985, 1991a). The primary faults of types 3, 4, 5 and 7 were created by remote stresses, but their secondary fractures resulted from local stresses that were associated with slip (or slips) along the respective faults, i.e., the primary fault and secondary fractures of these types are genetically related. On the other hand, type 6 concerns a fault and neighbor joints that were genetically unrelated, because they were formed by two distinct remote stresses. The genetically unrelated style of type 6 resembles that of type 1 from the Lower Eocene, whereas the genetically related style of types 3, 4, 5 and 7 resembles that of type 2. Hence, the joints of types 1 and 6 are pre-fault secondary fractures, whereas the joints of types 2, 3, 4, 5 and 7 are both post and syn-fault fractures.

These genetic relationships can help in working out the relative ages of types 3–7. The secondary fractures associated with types 3 and 4 formed in pristine chalks and predated the regional joints along Wadi Secher. On the other hand, types 6 and 7 occurred in chalk layers that had already been jointed in previous fracture episodes. The five FJR types 3 to 7 occur in Middle Eocene chalks and originated during uplift processes that took place in the syncline (Bahat 1999a). Also, types 3 and 4 are associated with the Secher fault as they cut older chalk layers at the flank of the fold (Wadi Secher, Fig. 3.33c), while types 5–7 are exposed in younger layers closer to the synclinal center (along Wadi Naim). Therefore, types 3 and 4 preceded types 6 and 7. Types 3 and 4 belong to an early uplift stage, whereas types 6 and 7 are correlated with an advanced uplift. Since type 7 joints are younger than type 6 joints, they may be categorized as late uplift products.

There are limitations in estimating the relative ages of certain FJRs. Type 5 preceded types 6 and 7, but no correlation can be made regarding the relative ages of types 3–4 and type 5 because they occur in remote locations and lack cutting relationships. Also, no comparison is possible regarding the timing of types 5–7 and type 8. It may however be suggested that the multilayer fracture of type 8 were products of stronger tensile stresses than types 5–7 (Bahat 1991a).

6.7.3.2 *Limitations of the Model Depicted in Figure 6.25*

The set of joints of type 3 formed in a principal plane sub-parallel to the plane of the primary fault (Fig. 6.24c) and the model in Fig. 6.25 explains how this was possible. This model is simple for normal faults that dip 45° or close to it, because for such faults the direction of maximum shear stress in the initial field of remote stress is easily transformed to the direction of σ_1 in the local stress field (Fig. 6.25a). The validity of this model would be verified if type 3 joints were exactly parallel primary faults in other fracture provinces. For normal faults whose dips deviate from 45°, additional studies will show the required changes and expected spreads in orientation of the secondary fractures of type 3. Perhaps the relatively large dip spread of the set that resembles type 3 joints in Fig. 6.26 is a good realistic example.

6.7.3.3
Speculation on Future Implications

Fractures in the Beer Sheva syncline display two FJR systems that are linked to burial, whereas six others relate to various syntectonic/uplift categories. Joint sets within these systems are categorized into pre-, syn- and post-fault associations. Early and late events that relate to pre-faulting and post-faulting, respectively can be distinguished in the burial system. In the uplift category, syn-fault early uplift and post-fault early uplift events can be distinguished from pre-fault and syn-fault late uplift events. Future studies may possibly show fuller ranges of FJR than the one described in the Beer Sheva syncline. These would include pre, syn and post fault joints in the three categories, burial, syntectonic and uplift and to lesser extents in the post-uplift category. Complex FJR structures in association with combined structures like burial-syntectonic or syntectonic-uplift can also be expected.

6.8
The Path from Geological Joints to Soil through a Transitional Layer of Surface Joints

This section concentrates on a "transitional layer" that lies above the uneroded chalk layers of the Mor Formation and below the soil cover that lies at the top of many outcrops around Beer Sheva, in south Israel (Sect. 3.4). The transitional layer reveals various extents of erosion in different locations and is characterized by an abundance of "surface joints" that were added to the earlier single-layer joints, which formed in the chalk of the Mor Formation (Fig. 2.63a) during the Lower Eocene (Bahat 1985). The surface joints may interest soil specialists, hydrologists and environmentalists, because they represent an important stage in the transition of rock to soil. In addition, these joints add significantly to the fracture population in the transitional layer and therefore increase the penetration of running water to the ground. An outcrop that shows the succession of several chalk layers, the transitional layer and the soil cover (Fig. 6.27a,b) was selected in the Shephela syncline (Fig. 3.33b) for detailed investigation, as described below.

6.8.1
Methods

For fracture analysis in Fig. 6.27b, photographs using Kodak Gold 200ASA film were taken, digitalized using an Epson Perfection 1600 scanner and panoramas built up using the photomerge utility of Adobe Photoshop Elements. These were entered into ImageJ (Rasband 2003). The scale was calibrated using a stick of known length (130 cm) that had been included in the photographs for this purpose. A grid 200×200 cm was then overlain on the pictures and then returned to Photoshop. Individual layers were divided into quadrants of 200 cm long. The photographs were again saved and re-entered into ImageJ. Using a Wacom graphics pad and pen, the vertical and horizontal fractures of each quadrant were outlined and measured separately using the software measuring utility. The area of each quadrant and the distance of the middle of the quadrant from the surface were similarly obtained. The results were recorded in Microsoft Excel and the total length of fractures was divided by the area to give fracture intensity (fracture length, given in cm, per unit area, given in m^2).

Fig. 6.27a. An outcrop that consists of six rock layers which are overlaid by a soil bed. **a** The examined outcrop, showing the frame which is detailed in **b**, where all fractures are traced

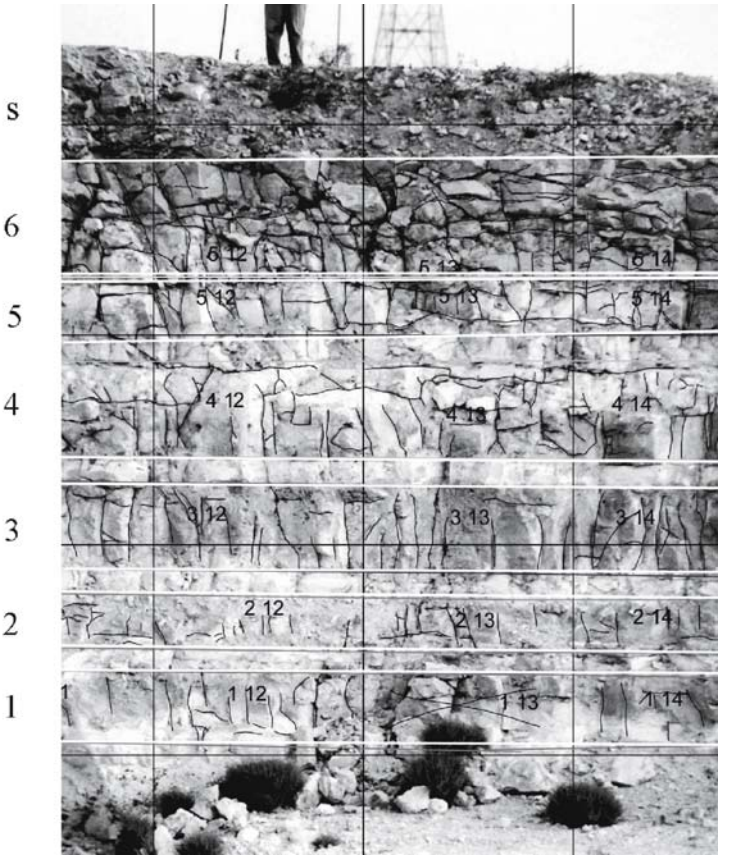

Fig. 6.27b. An outcrop that consists of six rock layers which are overlaid by a soil bed. Frame with traced fractures. *Numbers* are marked on each quadrant. The first digit marks the layer number and the other two relate to sequential quadrants to which the outcrop is divided

6.8.2 Results

Figure 6.27a shows a panorama of the examined outcrop, which is marked by a frame. All the fractures that are confined to individual chalk layers and the transitional layer are traced within the frame (Fig. 6.27b), revealing two distinct major fracture groups: Vertical and sub-vertical (VSV) joints and horizontal and sub-horizontal (HSH) joints. Figure 6.28a–c show plots of fracture intensity (cm m^{-2}) per quadrant vs. distance from the surface, i.e., every point on the graph represents a quadrant average. The curve that connects the averages of fracture intensities of the vertical fractures (VFI) undulates throughout the six layers (Fig. 6.28a), suggesting that vertical fractures were not significantly affected by the process leading to the development of the "transitional layer". On the other hand, a gradual, strong increase in fracture intensity of the horizontal fractures (HFI) is seen in layers 3–6 (Fig. 6.28b): From the average 122 cm m^{-2} (60.5 standard deviation) to

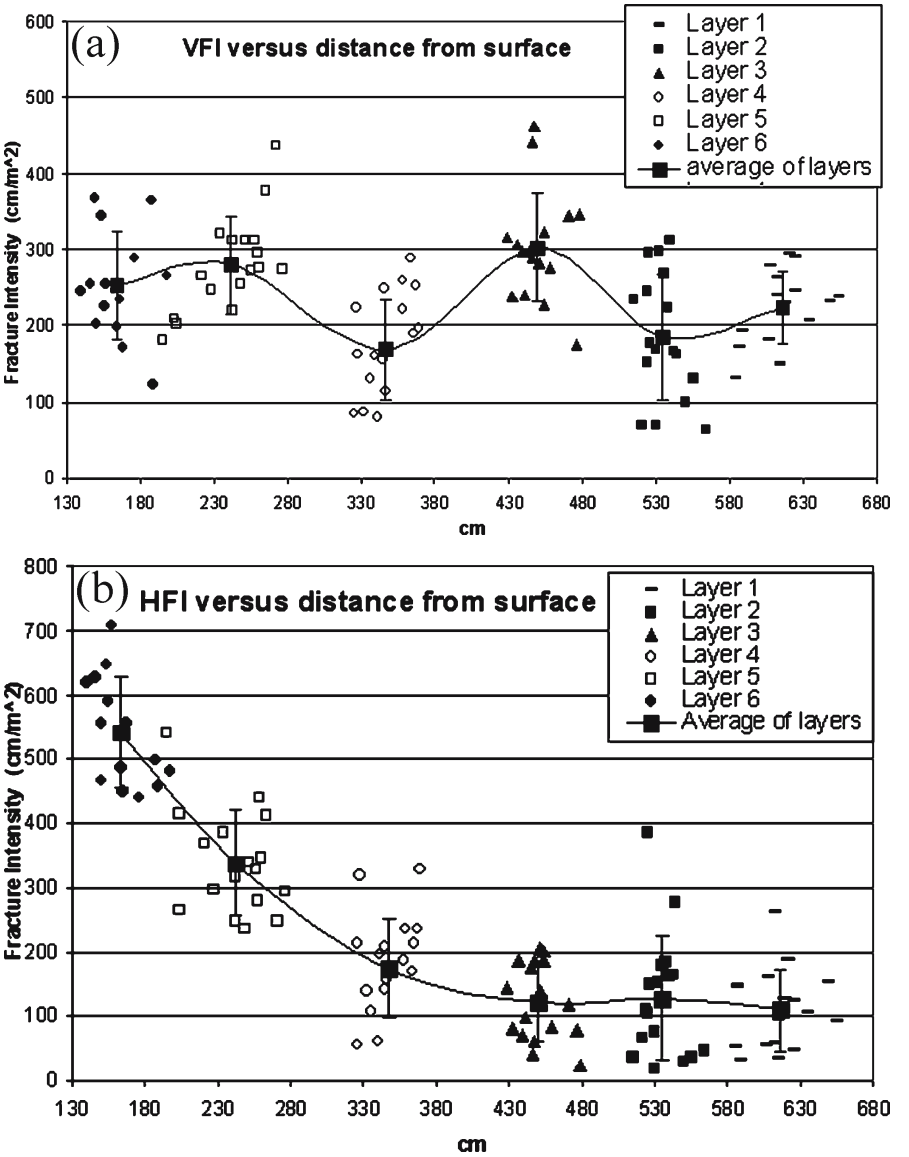

Fig. 6.28. Fracture parameters of single-layer fractures vs. vertical distance from the surface above the soil bed. **a** Fracture intensity of vertical joints. **b** Fracture intensity of horizontal joints

541 cm m^{-2} (85.5 standard deviation). The latter curve suggests that only the two upper chalk layers (4–5) were somewhat affected by the process leading to the development of the "transitional layer" in layer 6. Hence, the curve in Fig. 6.28b provides a "fracture profile" that characterizes the transition from rock (chalk) to soil in this outcrop (Fig. 6.27a).

6.8.3 Discussion

The increase of the population of the horizontal fractures in layers 4–6 and particularly in layer 6 suggests that fracture was induced by a stress field in which the minimum principal stress was vertical. This stress field was created by the reduction of the compression exerted by the weight of the overburden. The distinct, very strong concentration of HSH in layer 6, i.e., closest to the soil surface, implies that the change in stress field is much younger (Pleistocene or younger) than the latest uplift processes in the region (Sect. 3.4). Three mechanisms seem to be relevant here. First, the gradual transition of the upper rock layer into soil reduced the density of the latter, which resulted in some decrease in the vertical compression on layer 6, leading to the development of a vertical tension, much as it follows uplift and denudation processes in larger dimensions. The decrease in the vertical compression was strong in the transitional layer, moderate in layers 4 and 5, and practically absent in deeper layers. Second, what is particularly striking is that the transitional layer is almost exclusively limited to layer 6. This is such a common feature in all the outcrops of the region that it is inconceivable that the "right" amount of overburden was removed to produce cracking only in this layer. Thus, there must be some additional factor acting locally in the transitional layer. Haiaty (1975) shows that the tensile strength of the Eocene (Yoqneam) chalk drops dramatically from 4.3–27.5 kg cm^{-2} in the dry zone to 2.3–8.5 kg cm^{-2} in the water saturated zone. More recently Bahat et al. (2001a) showed that even a small amount of water markedly reduces the (compression) strength of chalk. Thus the exclusive contact of layer 6 with the water saturated loess soil was sufficient to critically reduce the rock strength, causing fracture. Third, rhythmic changes in temperature were particularly effective in the transitional layer: Diurnal/nocturnal variation of temperature does not occur deeper than 30 cm in these rocks (commun. from Howard C. B. on unpublished work). Perhaps a combination of these three mechanisms explains the formation of the surface joints.

6.9 Hydro-Geological Research in the Beer Sheva Syncline

6.9.1 Introduction

The well-exposed outcrops in the Negev desert enabled detailed studies to be carried out on fracture-geology in the Beer Sheva syncline (Sect. 3.4). This syncline also provides good grounds for hydro-geological investigation. Most of this investigation is concentrated in a relatively small area of some 25 km^2 in the center of the syncline around the large Ramat Hovav complex of chemical industry and the National Site for Treatment and Isolation of Hazardous Waste (Fig. 6.29). According to Nativ et al. (1995), the aridity of the area (180 mm yr^{-1} rainfall) and the low-permeability chalk matrix (~2 millidarcy; Dagan 1977a,b) were considered a natural barrier to potential groundwater contamination resulting from the industrial activities. However, the high concentrations of heavy metals and organic pollutants found in the local groundwater (Nativ and Nissim 1992) invalidated the concept of a natural barrier to contaminant migration across the vadose zone. These observations as well as others, such as seasonal fluctuations in groundwater lev-

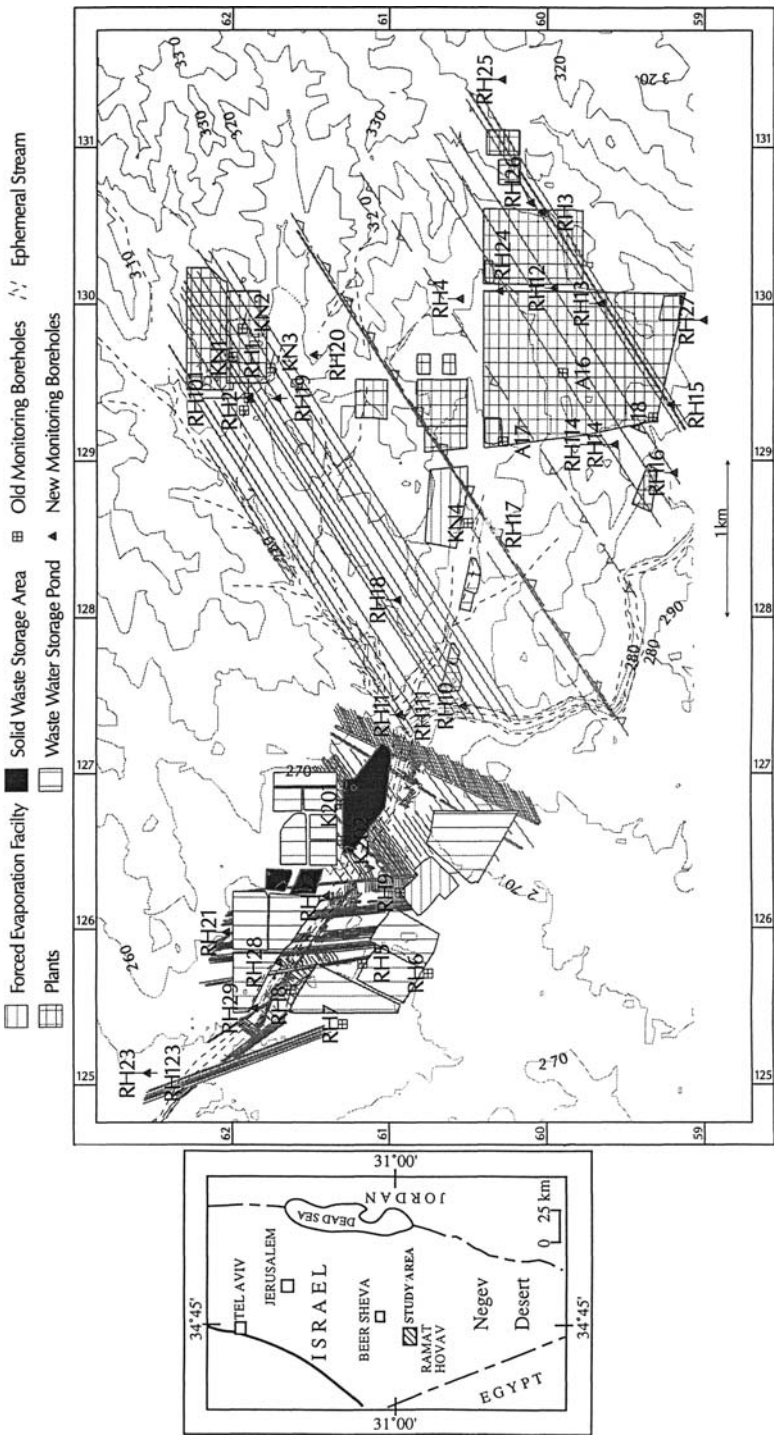

Fig. 6.29. Location map for the chemical industrial complex, facilities, ephemeral streams and observation holes. Old wells are represented by *squares* and new wells are represented by *triangles*. *Contours* describe topography and their interval is in meters. *Straight lines* are inferred fractures interpolated between measurement points along the ephemeral streams and man-made cuts. The trace of Wadi Secher is marked by *double dashed line*. *A*, *B* and *C* are locations of water level mounds (from Nativ et al. 1999)

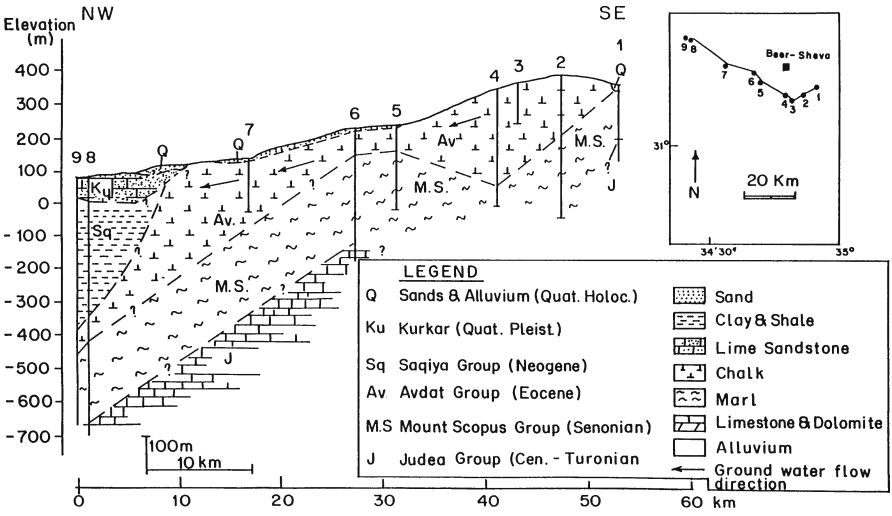

Fig. 6.30. Schematic geological cross section for the northern Negev Desert (from Nativ et al. 1999)

els, water table responses to flood events, the occurrence of tritium in the groundwater, as well as the behavior of additional chemical and isotopic tracers (Nativ and Nissim 1992), indicate that the groundwater is rapidly affected by on-surface activities, and infiltrating water and contaminants bypass the low-permeability chalk matrix via preferential flow paths. Nativ and Nissim (1992) suggested that the numerous fractures crossing the chalk matrix (Bahat 1988a) serve as preferential flow paths for contaminant migration from land surface to groundwater (Dahan et al. 1999) (Fig. 6.29). Although the Eocene (also termed Avdat) chalk is not a major water source (groundwater is brackish), the hydrological relationships between the chalk and the adjacent aquifers could result in the contamination of fresh groundwater (Fig. 6.30). The underlying Judea aquifer in the Cenomanian rocks provides over 30×10^6 m^3 of water annually to the city of Beer Sheva and its vicinity. Kronfeld et al. (1993) have documented leakage between adjacent aquifers(as a result of excessive pumping). This section presents a brief account of recent hydro-geological studies in Ramat Hovav.

6.9.2
Summary of the Results

Selected summaries are grouped into fluid flow and transport sections, ending with a section on open questions that stresses the awaiting challenges.

6.9.2.1
Fluid Flow through Fractures Intersecting Chalk

Preferred flow directions. A regional hydrogeological investigation of the flow pattern in the Eocene chalk formations in the area indicates a general subsurface flow in the 270° direction in the upper eastern basin following the topographic inclination (Nativ and Nissim 1992). However, toward the lower part (further west) of the

Beer Sheva syncline the groundwater flow is directed to the northwest (310°). Rophe et al. (1992) measured water levels in three observed wells in Ramat Hovav. The best fit with the obtained data indicates that the maximum hydraulic conductivity lies at an azimuth of 238° in which direction the IG (imaginary gradients) is minimal. Rophe et al. (1992) hypothesized the existence of a major set of fractures at this azimuth. Apparently, the 238° azimuth corresponds quite well to the direction of set 062° (242°), which consists of long and deep penetrating fractures in the syncline (Bahat and Adar 1993, present Fig. 6.29 and group 13 in Sect. 3.4.2.5). This finding has recently been confirmed by many hydraulic conductivity measurements (Nativ et al. 2003).

Water recharge and percolation through fractures. Four dry-drilling holes were bored by Nativ et al. (1995) through the vadose zone. Core and auger samples, collected at 30- to 50-cm intervals, were used for chemical and isotopic analyses, enabling the construction of the following:

1. A tritium profile to estimate the rate of water flow through the unsaturated zone.
2. Oxygen-18 and deuterium profiles to assess the evaporation of water at land surface before percolation and in the upper part of the vadose zone after infiltration.
3. Chloride and bromide profiles as tracers for inert solutes and pollutants.

The tritium and bromide profiles showed the rate of infiltration through the unsaturated matrix to be very slow (1.6–11 cm yr^{-1}). A conceptual model was proposed in which a small portion of the rainwater percolates downward through the matrix, while a larger percentage of the percolating water moves through preferential pathways in fractures. The water flowing through the fractures penetrates the matrix across the fracture walls where it increases the tritium concentrations, depletes the stable isotopic composition, and dilutes the salt concentrations. The observed rapid downward migration of tritium and heavy metals through the profuse fractures makes the chalk inefficient as a hydrologic barrier.

Hydraulic properties of fractures in chalk. One of the challenges of monitoring network design in a fractured rock setting is the heterogeneity of the rocks. Nativ et al. (1999) summarize the activities and problems associated with the monitoring of contaminated groundwater in porous, low-permeable fractured chalk in Ramat Hovav (Fig. 6.29). The fracture systems and their hydraulic properties were characterized by Nativ et al. (2003) to estimate contaminant release from Ramat Hovav. These included identification of the prevailing directions of fracture systems in outcrops, in cores retrieved from inclined coreholes, in coreholes using video logs, and in trenches. The orientation and inclination of these fracture systems were determined, and evidence of groundwater flow on the fracture surfaces was described and ranked. Their hydraulic conductivity was determined through slug and pumping tests performed at discrete intervals. Temperature, electrical conductivity, caliper, gamma and heat-pulse logs were conducted in the same coreholes. The results from the logs, tests, and core descriptions were compared to identify reliable and cost-effective tools for investigating the hydraulic characteristics of fracture systems. Nativ et al. (2003) concluded that in the study area:

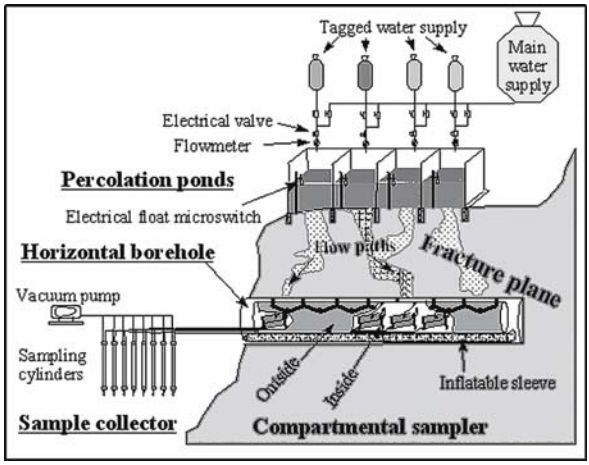

Fig. 6.31a.
Schematic cross section of the field setup used to determine solute and particle flux through a single natural fracture (after Dahan et al. 1998 and Weisbrod et al. 2000a)

1. Fracture mapping in outcrops and coreholes (including downhole video and caliper logs) must be supplemented by hydraulic testing of the mapped fracture sets in the coreholes.
2. Inclined coreholes provide information regarding the orientation of the hydraulically active fracture systems that cannot be obtained from vertical boreholes.
3. Hydraulic testing of unpacked holes provides a reasonable estimate of the maxtmum hydraulic conductivity.
4. The hydraulic conductivity distribution with depth is log normal and all significant ground water flow takes place within the upper 25 m.

Percolation experiments in natural discrete fractures. The mechanisms controlling fluid flow through fractures intersecting chalk in the vadose zone were studied by Dahan et al. (2000) through water percolation experiments (Fig. 6.31a) in natural discrete fractures and by close examination of the inner structure of fracture voids. The percolation experiments showed that the flow is focused in dissolution channels along the fracture plane and that fluxes and flow trajectories within that net vary in both time and space. The locations of the dissolution channels, the main potential flow paths within the fracture plane, were generally associated with fracture intersections. The flow through these channels was governed primarily by the mineralogical composition of the filling material and the inner structure of the fracture voids. Salt dissolution, solid-particle migration and clay swelling were found to be the predominant processes controlling flow through the dissolution channels. These physical changes in the structure of the filling material in the dissolution channels accounted for the observed unstable flow behavior. The results suggest that models aimed at simulating water percolation through fractures in unsaturated chalk should consider the mapping of fracture intersections in addition to the commonly used mapping of fracture lineaments. Moreover, the detailed characterization of fracture apertures may not be the key parameter determining fracture flow, because in such formations the flow is controlled primarily by filling material. These materials undergo significant physical variations during wetting and drying cycles (Weisbrod et al. 1999).

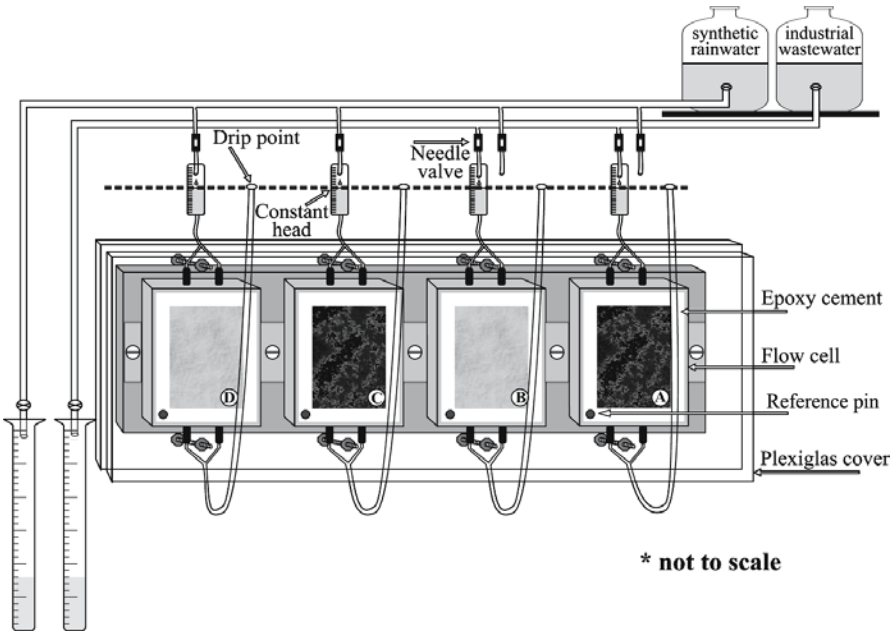

Fig. 6.31b. Schematic description of experimental setup. The solutions were drained from the dripping point into the gradual cylinders and then to the four flow cells (from Weisbrod et al. 2000b)

6.9.2.2
Transport of Solutes and Particles

Groundwater salinity. The processes affecting salinization of precipitation, surface water, vadose water and groundwater in the chalk aquitard were studied by Nativ et al. (1997a,b). Observations spanning eighteen years included the collection of rainfall at three rain sampling stations, flood water at six flood stations, vadose water from four coreholes penetrating chalk formations, and groundwater from sixteen monitoring wells tapping the chalk aquitard. Dissolved carbonate dust and evaporation of the falling raindrops result in $Ca(HCO_3)_2$ facies and increased ion concentration of the rainwater with respect to inland, more humid regions. Based on isotopic compositions, the exposure of flood water to evaporation during flood events is minimal. The observed $Ca(HCO_3)_2$ facies and salt enrichment by a factor of three to five in the flood water with respect to precipitation, results primarily from interactions of the flood water with the chalk and limestone bedrock, including ion exchange on Na- and K-bearing minerals and the dissolution of calcite, gypsum and halite. The presence of these salts at and near land surface results from the complete evaporation of rainwater in land surface depression storage areas following most rain events. Water percolation and salt dissolution account for the NaCl facies of vadose water and the variable rates of isotopic depletion and salt dilution observed in the underlying heterogeneous groundwater in the saturated zone. Although the variable mixing with low-saline, isotopically depleted water percolating from the fractures accounts for the depleted isotopic composition of the groundwater, its relatively low solute content cannot modify the groundwater NaCl

facies. Consequently, only groundwater salinity in the chalk is reduced by the preferentially flowing water, but the $Ca(HCO_3)_2$ facies prevailing in the rainwater and flood water disappears, and the NaCl imprint from the vadose zone prevails.

Fracture surface erosion. Two coated and two uncoated slices from the fracture surface of an unsaturated chalk core were exposed by Weisbrod et al. (1999) to short flow events (twenty-four, eight, and nine hours) of industrial wastewater and/or synthetic rainwater, followed by long drying periods (weeks) (Fig. 6.31b). The topography of the fracture surface was shown to be unstable due to the detachment of colloidal and large-sized particles during the first three to seven hours of flow. Following rainwater flow, erosion was more pronounced on the coated than on the uncoated surface (mean erosion of 0.313 and 0.134 mm, respectively) (Fig. 6.32). Interaction with industrial wastewater generated a skin of organic matter and gypsum that collapsed following contact with rainwater, leading to a deeper erosion of the uncoated surface than of the coated one (1.238 and 0.549 mm on the average, respectively). Erosion of the fracture surface was measured using a laser-scanning system and was calculated from high-resolution topographical maps (elevation $z \leq \pm 0.01$ mm) generated by Geographic Information System (GIS, ARCInfo) prior to and following the flow experiments. The

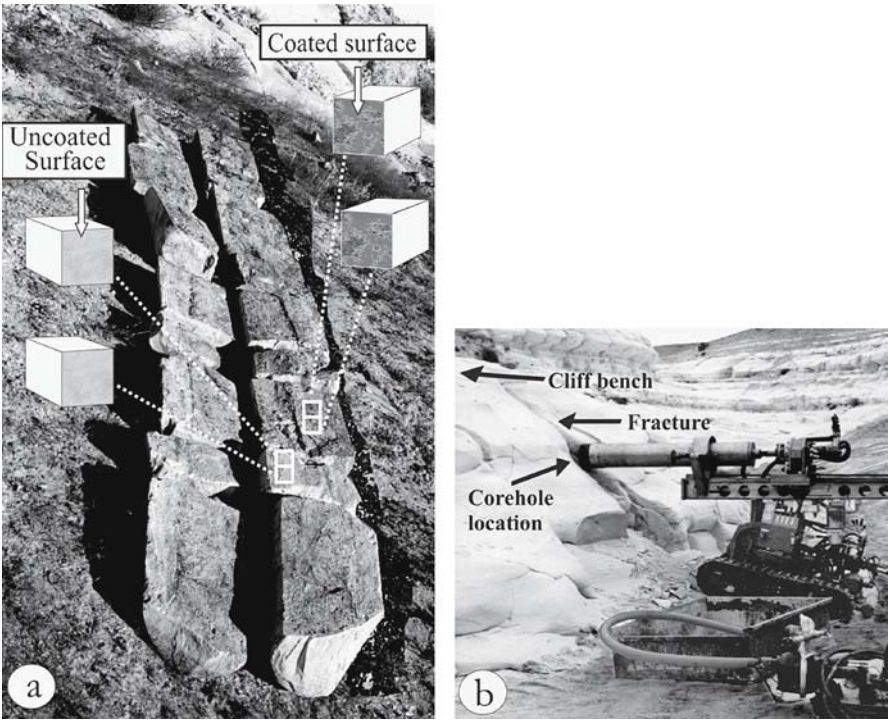

Fig. 6.32. a The naturally fractured core used for the experiments (5 m long, 25 cm diameter) showing the sampling location where two slices were sawed out from the coated areas (by surface weathering and precipitates of secondary mineralization) and two from the uncoated areas. The area of each slice was 42–50 cm^2, with a thickness of 4.5 cm. **b** The drilling site and drilling machine of the horizontal corehole from which the core was retrieved (from Weisbrod et al. 1999)

mean thickness of the eroded surface was found to be strongly correlated with the calculated total accumulated mass of particles and soluble salts released from the fracture surface. This relationship can be used to evaluate fracture surface erosion in large field and laboratory experiments.

Flow experiments on fracture surface properties. The surface topography of a natural fracture intersecting a chalk formation was mapped by Weisbrod et al. (2000b) (see also Weisbrod et al. 1998), using the aforementioned high-resolution laser-scanning device, and its roughness was evaluated using five different criteria. Two coated and two uncoated slices (Fig. 6.32) of the natural fracture surface were encased in flow cells and exposed to short (twenty-four and eight hours) interactions with percolating synthetic rainwater and industrial wastewater, followed by long drying periods (weeks) (Fig. 6.31b). These flow experiments simulated the intermittent infiltration of surface runoff and industrial effluents typical of the study area and resulted in erosion of the fracture surfaces and modification of their roughness. The temporal variations in surface roughness were evaluated using commonly used criteria. The surfaces coated by secondary mineralization (Avigur and Bahat 1990; Weisbrod et al. 1999) were significantly rougher, had greater relief, more heterogeneous topography, and a larger surface area than the uncoated surfaces (matrix mineralogy). The observations suggest that coating and fast weathering (caused by intermittent flow events) significantly change roughness, surface area, relief, and the heterogeneity of a fracture surface. These in turn may affect the spatial distribution of flow paths across that fracture surface.

Particle detachment and transport from fractures. A series of field and laboratory experiments were conducted by Dahan et al. 1999 and Weisbrod et al. 1999), respectively, to study the mechanisms of particle detachment and transport from fractures in vadose chalk. Experiments of intermittent flow events along fracture surfaces were carried out in the laboratory. In the field (Fig. 6.31a), water was percolated from land surface via a discrete fracture into a compartmental sampler installed inside a horizontal corehole located below the surface. The mass, size distribution and composition of the particles drained with the water from the fracture voids were examined along with flow rates and salt dissolution. Two boreholes penetrating the underlying saturated zone were sampled and analyzed for colloidal concentration and composition. The results of these experiments summarized by Weisbrod et al. (2002) suggest that:

1. Particle detachment causes flow-rate variability in the unsaturated fracture.
2. The mechanisms of particle detachment and salt dissolution within the fracture are linked.
3. Although most of the detached particles are large and likely to accumulate inside fractures, some colloidal particles also eroded from the fracture void and are likely to be transported to the groundwater.

Most of the detached particles had a mean diameter of >2 μm, while the mobile colloidal phase in the groundwater had a mean diameter of ~1 μm.

6.9.3
Open Questions Related to Water Flow in Heterogeneous Fracture Systems

The aforementioned summaries of recent studies from Ramat Hovav reveal a commendable progress in understanding water conduct (i.e., water flow and solute and particle transport) in the chalk aquitard. We return now to the work by Nativ et al. (2003) and take the risk of extrapolating it into six major challenges that are still awaiting the investigators in this area. The first challenge is differentiating the contributions of local geological structures to water conduct. The second is "getting the general picture" on water conduct by synthesizing these contributions. The third is minimizing the gaps along the interface between this "general picture" and adapted or newly devised conceptual and network fracture models on liquid flow (e.g., Nelson 1987; Berkowitz et al. 1988; Odling et al. 1999; Bonnet et al. 2001; Connoly and Cosgrove 1999). Contribution in this direction has been made by Berkowitz et al. (2001). The fourth is characterizing the differences between quasi-static and dynamic systems (such as intermittent changes in the apertures of joints) and applying them to new conceptual models. The fifth is devising engineering methods for eliminating water pollution, locally and regionally, and monitoring their execution. Finally, the sixth is comparing the Ramat Hovav system to other systems and models (e.g. Long et al. 1996).

We limit our comments to addressing the first challenge. This would involve differentiating the water conduct when flowing through different structures, as demonstrated by the two examples below. First, it is generally accepted that the major conduits in the area are the NE-ENE uplift multilayer joints (Fig. 6.29). It should be noticed, however, that the NE-ENE uplift fracture category consists of a series of fracture sets that formed in different geological associations when cutting Lower and Middle Eocene chalks (Table 3.3), and correspondingly, would have different drainage properties (including different affinities to coating and uncoating properties that were demonstrated above). Second, while many joints and faults provide poor drainage systems to water flow due to secondary minerals that often form along them (e.g., Avigur and Bahat 1990; Dahan et al. 1999), many other faults enhance rock permeability and water flow (e.g., Witherspoon and Newman 1967; Birkeland and Larson 1978). Quite important is the observation that liquid drainage may be considerably improved along fracture intersections (e.g., Hsieh et al. 1985; Dahan et al. 2000). The Beer Sheva syncline is profused with faults (Nativ et al. 2003) and joints (Sect. 3.4). Furthermore, there are numerous intersections and many styles of contact between faults and joints in the syncline (Sect. 6.7), and these should contribute significantly to the "general picture" of water conduct (see also Bahat 2004).

Finally, the investigation in Ramat Hovav involved recently an international participation of teams from Ben Gurion University of the Negev, The Hebrew University of Jerusalem (Israel), Bonn University, The University Of Karlsruhe (Germany), Penn State University, The University of California (Berkeley, USA), The Geological Survey of Denmark and Greenland (GEUS), The British Geological Survey (BGS) and The Volcani Research Center (Bet Dagan, Israel). These teams issued a series of annual reports (2000–2003), which were partly covered under the name FRACFLOW, a project promoted by the European Commission (see also Bloomfield 1999). These reports concerned various aspects of water flow through fractured rocks and contamination (note particularly Adar and Nativ 2003).

6.10
A New Fringe Characterization and Analysis

The mechanism of *en echelon* segmentation by local stress rotation (Fig. 2.40) via the fracture slanting model (Sect. 2.2.5.2) is workable (see also Preston's (1931) model in Bahat 1991a, Fig. 2.5). However, some people still debate the exact gear that drives the local stress rotation (e.g., Lazarus 2001a,b). Ramsay and Lisle (2000) suggest a new mechanism, which differs from the model by Pollard et al. (1982) by exposing the rock to superposing *remote* shear stress on normal stress rather than *local* shear stress superposing on normal stress. The model by Ramsay and Lisle (2000, p. 948) is cited below with minor modifications, presenting one of their solutions (Fig. 6.33a–d).

When the *en echelon* segments have the same sense on either side of the parent joint (Fig. 6.33b), the situation is such that the layer boundaries are subjected to a shear strain (shear plane parallel to the bed boundaries, shear direction oblique to the main central fracture, and similar shear sense on both boundaries). The fracture tip propagates from its point of origin in such a way that the incremental fracture surface is oriented perpendicular to the maximum deviatoric tensile stress direction (and maxi-

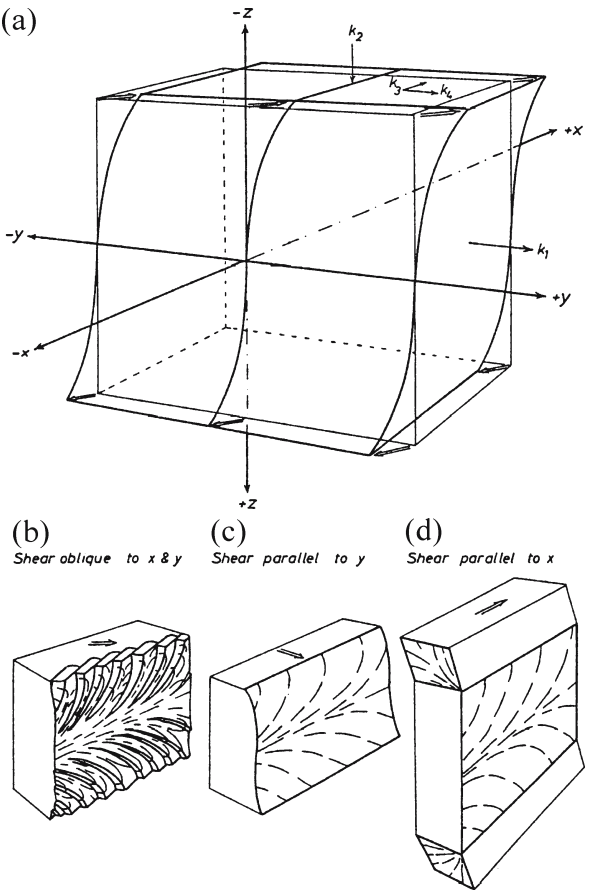

Fig. 6.33.
Three-dimensional block model of *en echelon* segmentation, combining layer parallel extension, layer normal shortening with layer boundary shear. **a** The various *k*-parameters, see text for their significance. **b**, **c** and **d** show the predicted joint surface patterns arising with differing types of boundary shear (from Ramsay and Lisle 2000)

mum extensive elastic strain) that are normal to the parent joint. The layer is oriented parallel to the *x*-*y*-plane, with boundaries at $z = \pm 1.0$ (Fig. 6.33a). It has been subjected throughout to a uniform stretch parallel to the *y*-direction of k_1 and a uniform shortening in *z* of k_2, with no change in the *x*-direction (plane strain for this deformation component). The layer has then been displaced by a shear displacement with shear plane *xy*, with vector components at each level of k_3 parallel to *x* and k_4 parallel to *y* and which vary in shear intensity (γ) with distance from the central plane (i.e., with *z*) according to $\gamma = az^3$.

The odd power of *z* accords with the observation of shear sense symmetry based on similar *en echelon* symmetry on either side of the parent fracture. In this model, k_1, k_2, k_3, k_4 and a are all constant terms chosen to suit individual problems: k_1 and k_2 are paired parameters which describe the background bed-parallel, bed-perpendicular strains (and which include volume change $\Delta_v = 1 - k_1 k_2$): k_3, k_4 and *a* define the value of the shear at $z = \pm 1$ ($\gamma = a(k_1^2 + k_2^2)^{1/2}$), and orientation ($\alpha$) of the shear direction from the *x*-axis ($\tan \alpha = k_4 / k_3$). The equations which define the displacement of any point with initial coordinates (x, y, z) and final coordinates (x', y', z') are:

$$\begin{aligned} x' &= x + ak_3k_2^3z^3 \\ y' &= k_1y + ak_4k_2^3z^3 \\ z' &= k_2z \end{aligned} \tag{6.17}$$

The displacement gradient matrix is (from Eq. 36.62 by Ramsay and Lisle 2000):

$$M = \begin{vmatrix} 1 & 0 & 3ak_3k_2^3z^2 \\ 0 & k_1 & 3ak_4k_2^3z^2 \\ 0 & 0 & k_2 \end{vmatrix} \tag{6.18}$$

We cite Ramsay and Lisle's (2000) solution for shear at 45° to the *x*-(and *y*-)axis, for the parameters $k_1 = 1.10$, $k_2 = 0.90$, $k_3 = k_4 = -0.10$, $a = 1.00$, as applied to the fracture in Fig. 6.33b. These parameters give small strains with an increase in volume ($\Delta_v = +0.01$) and Ramsay and Lisle (2000) consider that they are compatible with an uplift type of overall displacement and with small shear strains along the boundary of the layer ($\gamma = \pm 0.14$ at $z = \pm 1.0$). The values and orientations of the principal strains are set out in Table 6.4.

The special interest in these data is the systematic change in the plane normal to the greatest extension as one moves from the central line of the layer, because this plane would be the one that would guide the orientation of the frontal fracture propagation plane. In the center of the layer the extension fracture would propagate parallel to the *xz*-surface of the coordinate system (strike 0, dip vertical), but as it propagates towards edge of the layer the fracture systematically changes both its strike and dip through the values, 0/1 to E, 179/5 to E, 175/10 to E, 166/18 to E, and 156/25 to E. This orientation change is exactly that which one observes in the *en echelon* segments in joint fringes (Fig. 6.33b). The stresses at the tips of the *en echelon* segments will be changed from that of the general situation, and there will be a strong tendency for interlinking of the tips of one segment with the surface of the next segment by a step (bridge) (Fig. 2.39).

Table 6.4.
The values and orientations of the principal strains

z	$1 + e_1$	$1 + e_2$	$1 + e_3$
0.0	1.10 0/270	1.00 0/000	0.90 90/090
±0.2	1.10 1/270	1.00 2/180	0.90 87/025
±0.4	1.10 5/269	1.00 9/178	0.90 80/026
±0.6	1.11 10/265	1.01 16/172	0.88 71/027
±0.8	1.13 18/256	1.03 17/161	0.85 64/029
±1.0	1.17 25/246	1.04 14/149	0.81 61/032

See text for explanation (from Ramsay and Lisle 2000).

Although the values of the strains used in this example are perhaps a little large for elastic deformations, the orientation changes depend almost entirely upon the proportional values of the pairs of constants governing the relative values of the bulk distortion and the shear components, so the conclusions as to the main features of the geometry are valid for a large range of parameters. Finally, the program of Appendix 36.B TWISTHACKLES.BAS (given in Ramsay and Lisle 2000) enables the constant parameters to be varied as one wishes to explore the properties of different models.

Nomenclature

Physical Terms

Creep. A slow incremental crack increase under a constant or slowly varying load that is below that of the the Griffith criterion.

Critical dynamic stress intensity factor K_{ID}. The value that if the stress intensity factor is larger than it, dynamic (fast) fracturing would continue. K_{ID} is usually larger than K_{IC} (see Eq. 1.137).

Critical or post critical conditions. Are associated with crack growth at $K_I = K_{IC}$.

Critical stress intensity factor. A material-dependent property K_{IC}. When $K_I = K_{IC}$, the Griffith criterion is fulfilled and fracturing can commence.

Effective saturation. An assumption that beyond a certain value, crack density increases very slowly (logarithmically) with load increase.

Fatigue. Material failure by cracking under periodic or repeated stresses.

Flaws. General name for small heterogeneities in rocks (fossils, concretions, pores) that may initiate crack growth.

Griffith criterion. A necessary condition for fracturing of materials: The stress intensity factor K_I, becomes equal to the critical stress intensity factor K_{IC}.

Griffith flaws. Flaws in brittle material (glass) that have an effective length of ≈2 μm (Lawn 1993, p. 13), while in rocks they may range up to lengths of grain boundaries.

Linear elastic fracture mechanics (LEFM). The framework theory for linearly calculating stress fields in different configurations and deducing K_I values. Very valuable for static fracture problems, but fails for dynamic or extremely slow fracturing.

Saturation of crack spacing. An assumption that the crack spacing (No. of cracks per unit length) is limited. Once the spacing reaches this value, no increase is possible under any load.

Stable crack growth. Occurs under loads in which K_I decreases with the increase in crack length, and the crack arrests when the load is removed (also termed 'controlled').

Stress concentration. A situation where near to an abrupt geometrical change in the material, such as a flaw, crack, pore, vacancy, etc., a local increase of stress occurs in the stress field.

Sress intensity factor K_I. A measure of the ratio of the maximal stress concentration near a flaw to the nominal stress. In an infinite plate under remote tension, σ_0, having a sharp flaw of length c, expressed as $K_I = \sigma_0(\pi c)^{1/2}$.

Sub-critical conditions. Are associated with crack growth below the critical stress intensity factor K_{IC}.

Time to failure. The time interval from the minute of application of a load, smaller than that needed for instantaneous fracture, until the sample breaks.

Unstable crack growth. Occurs 'catastrophically' at $K_I = K_{IC}$ even when unloaded (also termed 'uncontrolled').

***v* vs. K_I diagrams.** Correlate the changes in the instantaneous crack velocity v with values of the instantaneous tensile stress intensity factor K_I.

Nomenclature of Main Fractographic Features

Arrest marks. Ripple marks that form on the fracture surface and signify slow crack propagation down to arrest, or crack restarting growing.

Barbs. See plumes.

Dynamic mirror plane. Forms when fractured primarily by high tensile stresses; it propagates rapidly and exhibits characteristic morphological features.

***En echelon*-fringe.** A fringe populated by *en echelon* cracks.

***En echelon* segmentation.** Cracks that systematically relate to each other in a 'shingle-like' arrangement and are confined to the fringe.

Fractography. The branch of science that analyses fracture surface morphology and related features and their causes, as well as mechanisms, in technological materials.

Fringe. A zone that surrounds the mirror plane and contains cracks that display rough morphologies.

Hackle cracks. A series of cracks that relate to each other three dimensionally in various directions and are confined to the fringe.

Hackle-fringe. A fringe populated by hackle cracks.

Mirror boundary. A narrow morphological rim separating the mirror from the fringe.

Mirror plane. The crack surface that contains the initial flaw, the critical flaw, the striae (plume) and the ripple marks.

Oscillating cracks. Bends of the mirror plane around the axis normal to the direction of crack propagation.

Plumes. Form by slow fracture on the mirror plane due to stress fields which rotate the fracture front about the axis of the direction of crack propagation, and often are identified by their dendrite-like morphologies consisting of many splayed barbs.

Quasi-static mirror plane. Forms when fractured under low stresses; it propagates subcritically and exhibits characteristic morphological features.

Ripple marks. Form on the mirror plane due to stress fields that intermittently bend the crack front around the axis normal to the direction of propagation, when both axes are on the fracture surface. Two types of ripple marks occur, undulations and arrest marks.

Striae. Form by rapid fracture on the mirror plane due to stress fields which rotate the fracture front about the axis of the direction of crack propagation, and often are identified by sharp, continuous cuts in the material (glass or rock).

Undulations. Ripple marks that form on the fracture surface and signify crack propagation in various velocities.

Nomenclature of Joints

Burial joints, or subsidence joints. Form during the sedimentation and diagenetic processes, and often are single-layer joints. They may form in great depths.

Cooling joints. Form during various cooling stages of the pluton (or volcanic rock).

Crack. In the present text is almost synonymous with fracture. It is generally applied to small fractures. These are general terms, regardless of loading mode.

Cross-fold joints. Form sub-orthogonal to fold axes.

Cross-joints. A set of younger, nonsystematic joints that arrest at earlier, systematic, single-layer joints, seen in plan view (Gross 1993).

Dihedral angle. Produced between two genetically linked fractures or fracture sets (joints or faults) that maintain a conjugate relationship.

Fault. Of a primary nature, that originated by slip(s), which resulted in lost cohesion in the rock. Of a secondary nature, that formed by slip(s) on an existing joint.

Fractography. Fracture markings that describe the surface morphology that forms essentially by an opening mode. Every such surface (joint) has a unique fractography.

Group. This term is occasionally applied (rather than set or system) when fracture affinities are debatable.

Joint. A surface on which the rock has lost cohesion and does not show a discernible lateral slip.

Joint set. Consists of a series of joints of similar strikes that exhibit similar fracture surface morphologies (if present). This similarity often reflects on the same fracture conditions, even if in different fracture episodes.

Joint system. Consists of various joint sets that probably are genetically linked.

Multi-layer joints. Cut many layers, often dissecting the entire outcrop. They are widely and irregularly spaced.

Orthogonal joint sets. Form perpendicular to each other (in a map), but may deviate up to 10° from this relationship.

Post uplift joints. Post uplift fractures that form in association with erosion.

Single-layer joints. Cut vertically individual layers (or less commonly, two layers) but arrest at the layer boundaries. They maintain small, regular spacing.

Strike joints, or strike-parallel joints. Form sub-parallel to fold axes.

Surface joints. Recent fractures that are confined to the upper layer, below the soil cover.

Syntectonic joints. Form during intense deformation, occasionally associated with faulting. They may form in great depths.

Tectonofractography. The application of joint fractography to the interpretation of tectonophysical processes.

Uplift joints. Form during uplift. They can be both single-layer and multi-layer fractures and form in shallow depths.

Selected Supplementary Parameters

Skewness. The degree of asymmetry, or departure from symmetry, of a distribution. If the frequency curve of a distribution has a longer "tail" to the right of the central maximum than to the left, the distribution is said to be skewed to the right or to have positive skewness. If the reverse is true, it is said to be skewed to the left or to have negative skewness (Spiegel 1961).

Kurtosis. The degree of peakedness (between high and flat-topped peaks) of a distribution, usually taken relative to a normal distribution (Spiegel 1961).

Statistics of extremes. The statistics of the largest (or smallest) members of a population, e.g., the severest earthquakes, the highest waves, etc.

FSI. The fracture spacing index, defined as the slope of the best-fit line when joint spacing is plotted versus layer thickness (Narr and Suppe 1991).

FSR. The fracture spacing ratio defined as the layer thickness divided by the median joint spacing for an individual bed (Gross 1993).

L / S. The ratio of joint length to joint spacing (Bahat 1991a, p. 309; Wu and Pollard 1995).

References

Abraham FF, Brodbeck D, Ridge WE, Xu X (1997) A molecular dynamics investigation of rapid fracture mechanics. J Mech Phys Solids 45:1595–1619

Abraham FF, Walkup R, Gao HJ, Duchaineau M, De la Rubia TD, Seager M (2002) Simulating materials failure by using up to one billion atoms and the world's fastest computer: Brittle fracture. Proceedings of the National Academy of Sciences of the United States of America 99:5777–5782

Acocella V, Gudmundsson A, Funiciello R (2000) Interaction and linkage of extension fractures and normal faults: Examples from the rift zone of Iceland. J Struct Geol 22:1233–1246

Adar E, Nativ R (2003) Contaminant transport, monitoring and remediation strategies in fractured chalk in the northern Negev. Annual Report for the year 2002, submitted to the Ramat Hovav Industrial Council

Adler RJ, Feldman RE, Taqqu MS (1998) A practical guide to heavy tails, statistical techniques and applications. Birkhauser, Boston

Ahlfors LV (1979) Complex analysis, 3rd edn. McGraw Hill Book Co, Aucland

Aitchison J, Brown JAC (1976) The lognormal distribution. Cambridge University Press, Cambridge

Aki K (1979) Geometric features of a fault zone related to the nucleation and termination of a earthquake rupture. U.S. Geological Survey Open-File Report 89–315, pp 1–9

Allen CR, Castle RO, Clark MM, Grantz AA, Sharp RV, Theodore TG, Wolfe EW, Young TL (1972) Map showing surface ruptures created at the time of and after the Borrego Mountain Earthquake of April 9, 1968 (GMT). U.S. Geological Survey, Professional Paper 78, Plate 1

Anderson EM (1951) The dynamics of faulting, 2nd edn. Oliver & Boyd, Edinburgh

Anderson TL (1995) Fracture mechanics: Fundamentals and applications. CRC Press, London

Anton L (1999) Simple equation for earthquake distribution. Phys Rev E 59(6):7213–7215

Arakawa K, Takahashi K (1987) Dependence of crack acceleration of the dynamic stress intensity factor in polymers. Exp Mech 27:195–200

Arakawa K, Takahashi K (1991) Relationships between fracture parameters and fracture surface roughness of brittle polymers. Int J Fracture 48:103–114

Arakawa K, Mada T, Takahashi K (2000) Correlations among dynamic stress intensity factor, crack velocity and acceleration in brittle fracture. Int J Fracture 105:311–320

Arkin Y, Hamaoui M (1967) The Judea Group (Upper Cretaceous) in central and southrn Israel. Isr Geol Surv Bull 42

Arlegui L, Simón JL (2001) Geometry and distribution of regional joint sets in a non-homogeneous stress field: Case study in the Ebro basin (Spain). J Struct Geol 23:297–313

Arnold BC (1983) Pareto distributions. International Co-operative publishing house, Fairland, Maryland, USA

Arthur MJ (1989) The Cenozoic evolution of the Lundy pull-apart basin into the Lundy rhomb horst. Geol Mag 126:187–198

Ashcroft NW, Mermin ND (1981) Solid state physics. CBS Publishing, Tokio, pp 398

Atkinson BK (1984) Subcritical crack growth in geological materials. J Geophys Res 89:4077–4114

Atkinson BK (1987) Introduction to fracture mechanics and its geophysical applications. In: Atkinson BK (ed) Fracture mechanics of rocks. Academic Press, pp 1–26

Atkinson C, Eshelby JD (1968) The flow of energy into the tip of a moving crack. Int J Fracture Mech 4:3–8

Atkinson BK, Meredith PG (1987a) The theory of subcritical crack growth with applications to the minerals and rocks. In: Atkinson BK (ed) Fracture mechanics of rock. Academic Press, London, pp 111–166

Atkinson BK, Meredith PG (1987b) Experimental fracture mechanics data for rocks and minerals. In: Atkinson BK (ed) Fracture mechanics of rock. Academic Press, London, pp 477–525

Avigour A, Bahat D (1990) Chemical weathering of fractured Eocene chalks in the Negev, Israel. Chem Geol 89:149–156
Babcock CL (1977) Silicate glass technology methods. John Wiley & Sons Ltd., New York
Bahat D (1968) Structural changes at room temperature of heated anorthoclases. Can Mineral 9:531–538
Bahat D (1970) Kinetic study on the hexacelsian-celsian phase transformation. J Mater Sci 5:805–810
Bahat D (1977) Thermally-induced wavy Hertzian fracture. J Am Ceram Soc 60:118–120
Bahat D (1979a) Theoretical considerations on mechanical parameters of joint surfaces based on studies on ceramics. Geol Mag 11:81–92
Bahat D (1979b) On the African rift system, theoretical and experimental study. Earth Planet Sc Lett 45:445–452
Bahat D (1979c) Interpretation on the basis of Hertzian theory of a spiral carbonatite structure at Homa Mountain, Kenya. Tectonophysics 60:235–246
Bahat D (1982) Extensional aspects of earthquake induced ruptures determined by an analysis of fracture bifurcation. Tectonophysics 83:163–183
Bahat D (1983) New aspects of rhomb structures. J Struct Geol 5:591–601
Bahat D (1985) Low angle normal faults in Lower Eocene chalks near Beer-Sheva, Israel. J Struct Geol 7:613–620
Bahat D (1986a) Joints and en echelon cracks in Middle Eocene chalks near Beer-Sheva, Israel. J Struct Geol 8:181–190
Bahat D (1986b) Criteria for the differentiation of en echelons and hackles in fractured rocks. Tectonophysics 121:197–206
Bahat D (1987a) Correlation between styles of fracture markings and orientation of cross-fold joints. Tectonophysics 136:323–333
Bahat D (1987b) Jointing and fracture interactions in Middle Eocene chalks near Beer-Sheva, Israel. Tectonophysics 136:299–321
Bahat D (1988a) Early single-layer and late multi-layer joints in the Lower Eocene chalks near Beer-Sheva, Israel. Annal-Tecton 2:3–11
Bahat D (1988b) Fractographic determination of joint length distribution in chalk. Rock Mech Rock Eng 21:79–94
Bahat D (1988c) Fractographic determination of joint length distribution in chalk. Rock Mech Rock Engin 21:79–94
Bahat D (1989) Fracture stresses at shallow depths during burial. Tectonophysics 169:59–65
Bahat D (1991a) Tectonofractography. Springer-Verlag, Heidelberg
Bahat D (1991b) Plane stress and plane strain fracture in Eocene chalks around Beer-Sheva. Tectonophysics 196:61–67
Bahat D (1997) Mechanisms of dilatant en echelon crack formation in jointed layered chalks. J Struct Geol 19:1375–1392
Bahat D (1998a) Four joint genetic groups and their distinct characteristics. In: Rossmanith HP (ed) Mechanics of jointed and faulted rock, MJFR-3, Vienna, Austria. Balkema, Rotterdam, pp 211–216
Bahat D (1998b) Quantitative tectonofractography – an appraisal. In: Rossmanith HP (ed) Mechanics of jointed and faulted rock, MJFR-3, Vienna, Austria. Balkema, Rotterdam, pp 59–67
Bahat D (1998c) On joints and paleostress associated with folds along the Syrian Arc in the Negev. Israel J Earth Sci 48:29–36
Bahat D (1999a) Single-layer burial joints vs. single-layer uplift joints in Eocene chalk from the Beer-Sheva syncline in Israel. J Struct Geol 21:293–303
Bahat D (1999b) On paleostresses associated with the Syrian Arc in Israel. Isr J Earth Sci 48:29–36
Bahat D (2000) The quasi-ellipsoid damage zone of faults and five types of fault-joint relationship in the Beer Sheva syncline, Israel. IX Congresso Geologico Chileno, pp 749–753
Bahat D (2004) Eight distinct fault-joint geometric/genetic relationships in the Beer Sheva syncline, Israel. In: Cosgrov JW, Engelder T (eds) The initiation, propagation and arrest of joints and other fractures. Spec Publ Geol Soc London (in press)
Bahat D, Adar EM (1993) Comment on "Analysis of subsurface flow and formation anisotropy in a fractured aquitard using transient water level data" by Rophe B, Berkowitz B, Magaritz M, Ronen D. Water Resour Res 29:4171–4173
Bahat D, Engelder T (1984) Surface morphology on cross fold joints of the Appalachian Plateau, New York and Pennsylvania. Tectonophysics 104:299–313
Bahat D, Grossmann HNF (1988) Regional jointing and paleostresses in Eocene chalks around Beer-Sheva. Israel J Earth Sci 37:1–11
Bahat D, Rabinovitch A (1988) Paleostress determination in a rock by a fractographic method. J Struct Geol 10:193–199
Bahat D, Rabinovitch A (2000) New fractographic aspets of natural and artificial fractures in chalks, from the Upper Galilee, Israel, and experimental fracture in Perspex. J Struct Geol 22:1427–1435

Bahat D, Shavit R (1997) Fracture in the Beer-Sheva Syncline (Ramat Hovav). Unpublished report submitted to the Ramat Hovav Industrial Municipality
Bahat D, Leonard G, Rabinovitch A (1982) Analysis of symmetric fracture mirrors in glass bottles. Int J Fracture 18:29–38
Bahat D, Grossenbacher K, Karasaki K (1995) Investigation of exfoliation joints in Navajo Sandstone at the Zion National Park and in granite at the Yosemite National Park by tectonofractographic techniques. LBL-36971; UC-400, 67 pp
Bahat D, Grossenbacher K, Karasaki K (1999) Mechanism of exfoliation joint formation in granitic rocks at Yosemite National Park. J Struct Geol 21:85–96
Bahat D, Rabinovitch A, Frid V (2001a) Fracture characterization of chalk in uniaxial and triaxial tests by rock mechanics, fractographic and electromagnetic radiation methods. J Struct Geol 23:1531–1547
Bahat D, Bankwitz P, Bankwitz E (2001b) Joint formation in granite plutons: En echelon-hackle series on mirror fringes (Example: South Bohemian Pluton, Czech Republic). Zeitschrift der deutschen geologischen Gesellschaft 152:593–609
Bahat D, Bankwitz P, Bankwitz E (2001c) Changes of crack velocities at the transition from the parent joint through the en echelon fringe to a secondary mirror plane. J Struct Geol 23:1215–1221
Bahat D, Frid V, Rabinovitch A, Palchik V (2002a) Exploration via electromagnetic radiation and fractographic methods of fracture properties induced by compression in glass-ceramic. Int J Fracture 116:179–194
Bahat D, Bankwitz P, Bankwitz E, Rabinovitch E (2002b) Comparison of the new fracture areas created by the formation of en echelon and hackle fringes on joint surfaces. Z Geol Wissenschaft 30:1–12
Bahat D, Bankwitz P, Bankwitz E (2003) Preuplift joints in granites: Evidence for subcritical and postcritical fracture growth. Geol Soc Am Bull 115:148–165
Bahat D, Bankwitz P, Bankwitz E (2004) Title?. In: Cosgrov JW, Engelder T (eds) The initiation, propagation and arrest of joints and other fractures. Spec Publ Geol Soc London (in press)
Bai TX, Pollard DD (2000a) Fracture spacing in layered rocks: A new explanation based on the stress transition. J Struct Geol 22:43–57
Bai TX, Pollard DD (2000b) Closely spaced fractures in layered rocks: Initiation mechanism and propagation kinematics. J Struct Geol 22:1409–1425
Bak P, Tang C (1989) Earthquakes as a self-organized criticality. J Geophys Res 94:15635–15637
Bak P, Tang C, Wiesenfield K (1987) Self-organized criticality – An explanation of 1/f noise. Phys Rev Lett 59:381–384
Bak P, Tang C, Wiesenfield K (1988) Self-organized criticality. Phys Rev A 38:364–374
Balk R (1937) Structural behavior of igneous rocks. Geological Society of America Memoir
Bank-Sills L, Schur D (1989) On the influence of crack plane orientation in fatigue crack propagation and catastrophic failure. American Society for Testing and Materials, Standard Technical Publication 1020:497–513
Bankwitz P (1965) Über Klüfte I. Beobachtungen im Thüringischen Schiefergebirge. Geologie 14:241–253
Bankwitz P (1966) Über Klüfte II. Die Bildung der Kluftoberfläche und eine Systematik ihrer Strukturen. Geologie 15:896–941
Bankwitz P, Bankwitz E (1984) Die Symmetrie von Kluftoberflächen und ihre Nutzung für eine Paläospannungsanalyse. Z Geol Wissenschaft 12:305–334
Bankwitz P, Bankwitz E (1994) Event related jointing in rocks on Bornholm Island (Denmark). Z Geol Wissenschaft 22:97–114
Bankwitz P, Bankwitz E (1995) Aspekte der Entwicklung von Klüften in postkinematischen Graniten des Erzgebirges (speziell Eibenstocker Massiv). Z Geol Wissenschaft 23:777–793
Bankwitz P, Bankwitz E (1997) Fractographic features on joints in KTB drill cores as indicators of the contemporary stress orientation. Geol Rundsch 86:S34–S44
Bankwitz P, Bankwitz E (2004) The relationship of tilt and twist of fringe-cracks in granite plutons. In: Cosgrov JW, Engelder T (eds) The initiation, propagation and arrest of joints and other fractures. Spec Publ Geol Soc London (*in press*)
Bankwitz P, Bankwitz E (1994) Event related jointing in rocks on Bornholm usland (Denmark). Z Geol Wiss 22:97–114
Bankwitz P, Bankwitz E (1997) Fractographic features on joints in KTB drill cores as indicators of the contemporary stress orientation. Geol Rundsch 86 Suppl:S34-S44
Bankwitz P, Bankwitz E, Thomas R, Wemmer K, Kämpf H (2004) Age and depth evidence for pre-exhumation joints in granite plutons: Fracturing during the early cooling stage of felsic rock. In: Cosgrov JW, Engelder T (eds) The initiation, propagation and arrest of joints and other fractures. Spec Publ Geol Soc London (*in press*)
Bansal GK (1977) On fracture mirror formation in glass and polycrystalline ceramics. Phil Mag 35: 935–944

Bartlett WL, Friedman M, Logan MJ (1981) Experimental folding and faulting of rocks under confining pressure, Part IX. Wrench faults in limestone layers. Tectonophysics 79:255–277
Barton NR, Choubey V (1977) The shear strength of rock joints in theory and practice. Rock Mech 10:1–54
Bateman PC, Sawka WN (1981) Raymond Quadrangle, Madera and Mariposa counties, California; analytic data. U.S. Geological Survey Professional Paper 16:107–172
Bateman PC, Wahrhaftig C (1966) Geology of northern California. Bulletin – California, Division of Mines and Geology, pp 107–172
Bayasgalan A, Jackson J, Ritz JF, Carretier S (1999) Field examples of strike-slip fault terminations in Mongolia and their tectonic significance. Tectonics 18:394–411
Bazant ZP, Planas J (1998) Fracture and size effect in concrete and other quasi-brittle materials. CRC Press, Boca Raton
Beall GH (1989) Design of glass-ceramics. Rev Solid State Sci 3:333–354
Beall GH, Karstetter BR, Rittler HL (1967) Crystallization and chemical strengthening of stuffed quartz glass-ceramics. J Am Ceram Soc 50:99–108
Beauchamp EK (1995) Crack front stability and hackle formation in high velocity glass fracture. J Am Ceram Soc 78:689–697
Beauchamp EK (1996) Mechanics for hackle formation and crack branching. In: Varner JR, Frechette VD, Quinn GD (eds) Fractography of glasses and ceramics III. The American Ceramic Society, Ceramic Transactions 64:409–446
Beck ME, Rojas C, Cembrano J (1993) On the nature of buttressing in margin-parallel strike-slip fault system. Geology 126:755–758
Becker GF (1891) The structure of a portion of the Sierra Nevada of California. Geol Soc Am Bull 2:49–74
Becker A, Gross MR (1996) Mechanism for joint saturation in mechanically layered rocks: An example from southern Israel. Tectonophysics 257:223–237
Behr H-J, Dürbaum H-J, Bankwitz P, DEKORP Research Group (B) (1994) Crustal structure of the Saxothuringian Zone: Results of the deep seismic profile MVE-90 (East). Z Geol Wissenschaft 22:647–769
Beinkafner KJ (1983) Terminal expression of decollement in Chautauqua County, Now York. Northeastern Geology 5:160–171
Bella F, Bjadji PF, Della Monica J, Zilpimiani DO, Manguladze PV (1992) Observations of natural electromagnertic radiation during earthquakes of central Italy. Izv-Phys Solid Earth 28:88–94
Benes K (1971) Structure of plutonic bodies in the Bohemian Massif. Upper Mantle Project (UMP), Final Report Geology, Praha, pp 111–119
Bentor YK, Vroman A (1960) The geological map of Israel, scale 1 : 250 000, sheet 16, Mt. Sodom, 2nd edn, with explanatory notes. Government Printer, Jerusalem
Bentor YK, Vroman A, Zak A (1970) Geological map of Israel, 1:250 000. Survey of Israel
Bergerat F, Bouroz-Weil C, Angelier J (1992) Palaeostresses inferred from macrofractures, Colorado Plateau, Western USA. Tectonophysics 206:219–243
Berkowitz B, Bear J, Braester C (1988) Continuum models for contaminant transport in fractured porous formations. Water Resour Res 24:1225–1236
Berkowitz B, Nativ R, Adar E (2001) Evaluation of conceptual and quantitative models of fluid flow and chemical transport in fractured media. In: Panel on Conceptual Models of Flow and Transport in the Fractured Vadose Zone, U.S. National Committee for Rock Mechanics, Board on Earth Sciences and Resources, National Research Council (eds) Conceptual models of flow and transport in the fractured vadose zone. National Academy Press, Washington, pp 115–147
Bernstein N, Ness DW (2003) Lattice trapping barriers to brittle fracture. Phys Rev Lett 91:025501–1–4
Berry JP (1960) Some kinetic considerations of the Griffith criterion for fracture I. Equations of motion at constant force. J Mech Phys Solids 8:194–206
Bevan TG, Hancock PL (1986) A late Cenozoic regional mesofracture system in southern England and northern France. Journal of the Geological Society London 143:355–362
Bilichenko SV, Iljin FS, Kim EF (1990) ULF response of the ionosphere for earthquake preparation processes. Dokl Akad Nauk SSSR+ 311:1077–1080
Birkeland PW, Larson EE (1978) Putnam's Geology, 3rd ed. Oxford Univ Press New York
Bleaney BI, Bleaney B (1965) Electricity and magnetism. Oxford University Press, London
Bloomfield JP (1999) Fracflow-geological state-of-the art review. British Geol. Surv., Natural Envir. Res. Coun., Technical Report WD/99/13, 45 pp
Bobet A, Einstein HH (1998) Fracture coalescence in rock-type materials under uniaxial and biaxial compression. Int J Rock Mech Min 35:863–888
Bogosh R, Bourne J, Shirav M, Harnois L (1997) Petrochemistry of a Late Precambrian granitiferous granite, pegmatite and aplite, southern Israel. Mineral Mag 61:111–122

Bonn D, Kellay H, Prochnow M, Ben-Djemiaa K, Mounier J (1998) Delayed fracture of an inhomogeneous soft solid. Science 280:265–267
Bonnet E, Bour O, Odling NE, Davy P, Main I, Cowie P, Berkowitz B (2001) Scaling of fracture system in geological media. Rev Geophys 39:347–383
Brace WF (1964) Brittle fracture of rocks. In: Judd WR (ed) State of stress in the earth's crust. Elsevier, New York, pp 111–180
Brace WF, Bombolakis EG (1963) A note on brittle crack growth in compression. J Geophys Res 68: 3709–3713
Brace WF, Paulding JBW, Scholz C (1966) Dilatancy of the fracture of crystalline rocks. J Geophys Res 71:939–953
Bradley WC (1963) Large-scale exfoliation in massive sandstones of the Colorado Plateau. Geol Soc Am Bull 74:519–528
Bradley WH, Pepper JF (1938) Structure and gas possibilities of the Oriskany Sandstone in Steuben, Yates, and parts of the adjacent counties. New York Geological Survey Bulletin 899-A
Braun M, Flexer A, Lasman N (1977) Geological report – Ramat-Hovav underground oil storage project. Geoprospect LTD
Breiter K (2001) South Bohemian pluton. Overview. Exkursionsführer und Veröffentlichungen der GGW, Berlin, 212:130–140
Breiter K, Koller F (1999) Two-mica granites in the central part of the South Bohemian Pluton. Abhandlungen der Geologischen Bundesanstalt Wien 56:201–212
Breiter K, Seltmann R (1995) Ore mineralizations of the Krušné Hory Mts. (Erzgebirge). Third Biennial SGA Meeting, Excursion Guide, pp 1–200, Czech Geological Survey, Prague
Breiter K, Sokol A (1997) Chemistry of the Bohemian granitoids: Geotectonic and metallogenetic implications. Sbornik geologickych ved, 31, Praha, pp 75–96
Brereton NR, Evans CJ (1987) Rock stress orientations in the United Kingdom from borehole breakouts. Report of the Regional Geophysics research Group, British Geological Survey, no. R6 87/14
Broek D (1984) Elementary engineering fracture mechanics, 3rd edition. Martinus Nijhoff Publishers, Boston, p 469
Broek D (1991) Elementary engineering fracture mechanics. Kluwer Academic Publisher, Dordrecht
Brooks M, Trayner PM, Trimble TJ (1988) Mesozoic reactivation of Variscan thrusting in the Bristol Channel area, UK. J Geol Soc London 145:439–444
Buchbinder B, Zilberman E (1997) Sequence stratigraphy of Miocene-Pliocene carbonate-siliciclastic shelf deposits in the eastern Mediterranean margin (Israel): Effects of eustasy and tectonics. Sedimentary Geology 112:7–32
Buchbinder B, Benjamini C, Mimran Y, Gvirtzman G (1988) Mass transport in Eocene pelagic chalk on the northwestern edge of the Arabian platform, Shefela area, Israel. Sedimentology 35:257–274
Burdon D (1959) Handbook of the geology of Jordan. Benham & Co, Colchester
Burger HR, Hamill MN (1976) Petrofabric stress analysis of the Dry Creek Ridge anticline, Montana. Geol Soc Am Bull 87:555–566
Butler RF (1992) Paleomagnetism: Magnetic domains to geologic terranes. Blackwell Scientific Publications, Oxford, 319 p
Büttner S (1997) Die spätvariszische Krustenentwicklung in der südlichen Böhmischen Masse: Metamorphose, Krustenkinematik und Plutonismus. Frankfurter Geowissenschaftliche Arbeiten, A 16
Büttner S, Kruhl JH (1997) The evolution of the late-Variscan high-T/low-P region: The south-eastern margin of the Bohemian Massif. Geol Rundsch 86:21–38
Cadman J (1969) The origin of exfoliation joints in granitic rocks. Unpublished Ph.D. thesis. University of California, Berkeley, USA
Caers J, Beirlant J, Maes MA (1999a) Statistics for modeling heavy tailed distributions in geology. Part I. Methology. Geology 31:391–410
Caers J, Beirlant J, Maes MA (1999b) Statistics for modeling heavy tailed distributions in geology. Part II. Application. Geology 31:411–434
Carlson J, Langer J (1989) Mechanical model of an earthquake fault. Phys Rev A 40:6470–6484
Carlson J, Langer J, Shaw B, Tang C (1991) Intrinsic-properties of a Burridge-Knopoff model of an earthquake fault. Phys Rev A 44(2):884–897
Carmichael ISE, Turner FJ, Verhoogen J (1974) Igneous petrology. Mc-Graw Hill Book Company, New York, p 739
Carter NL, Friedman M (1965) Dynamic analysis of deformed quartz and calcite from dry Creek Ridge Anticline Montana. Am J Sci 263:747–785
Castaing C, Halawani MA, Gervais F, Chilès JP, Genter A, Bourgine B, Ouillon G, Brosse JM, Martin P, Genna A, Janjou D (1996) Scaling relationships in intraplate fracture systems related to Red Sea rifting. Tectonophysics 261:291–314
Castillo E (1988) Extreme value theory in engineering. Academic Press, Boston

Charles RJ (1958) Dynamic fatigue of glass. J Appl Phys 29:1657–1662
Chinnery MA (1966) Secondary faulting I. Theoretical aspects. Can J Earth Sci 3:163–174
Chinnery MA, Petrak JA (1968) Dislocation fault model with a variable discontinuity. Tectonophysics 5:513
Chmyrev VM, Isaev VN, Bilichenko SV (1986) Electric fields and hydromagnetic waves in the ionosphere above an earthquake center. Geomagn Aeronomy+ 26:1020–1022
Ciliberto S, Guarino A, Scorretti R (2001) The effect of disorder on the fracture nucleation process. Physica D 158:83–104
Clark MM (1972) Surface rupture along the Coyote Creek fault. US Geol Surv Prof Pap 787:190–207
Cloos H (1921) Der Mechanismus tiefvulkanischer Vorgänge. Friedrich Vieweg, Braunschweig
Cloos H (1922) Über Ausbau und Anwendung der granit-tektonischen Methode. Abh Preuss Geol Landesanstalt 89:1–18
Cohen AJB (1993) Hydrogeologic characterization of a fractured granitic rock aquifer, Raymond, California. Lawrence Berkeley Laboratory – 34838, UC-400
Coleman BD (1957) Time dependence of mechanical breakdown in bundles of fibers. I. constant total load. J Appl Phys 28:1058–1067
Connoly P, Cosgrove J (1999) Prediction of fracture-induced permeability and fluid flow in the crust using experimental stress data. AAPG Bull 83:757–777
Conrad W, Behr HJ, Trzebski R (1996) Die LINSSER-Filterung des Schwerefeldes der Süddeutschen Grossscholle und ihre Interpretation. Z Geol Wissenschaft 21:21–40
Cooke ML, Pollard DD (1996) Fracture propagation paths under mixed mode loading within rectangular blocks of polymethyl metha-crylate. J Geophys Res 101:3387–3400
Cooke ML, Underwood CA (2001) Fracture termination and step-over at bedding interfaces due to frictional slip and interface opening. J Struct Geol 23:223–238
Cosgrove JW (1995) The expression of hydraulic fracturing in rocks and sediments. In: Ameen MS (ed) Fractography: Fracture topography as a tool in fracture mechanics and stress analysis. Geological Society Special Publication 92:187–196
Cotterell B, Rice JR (1980) Slightly curved or kinked cracks. Int J Fracture 16:155–169
Cowie PA, Scholtz CH (1992a) Displacement-length scaling relationship for faults: Data synthesis and discussion. J Struct Geol 14:1149–1156
Cowie PA, Scholtz CH (1992b) Growth of faults by the accumulation of seismic slip. J Geophys Res 97:11085–11095
Cox HL (1952) The elasticity and strength of paper and other fibrous materials. Brit J Appl Phys 3:72–79
Coyle DA, Wagner GA (1995) Spaltspuren – Ein Beitrag zur postvariszischen Tektonik und Abtragung des KTB-Umfelds. Geowissenschaften 13:142–146
Cramer T, Wanner A, Gumbsch P (1999) Dynamic failure of glass and single-crystalline silicon. Z Metallkd 90:675–686
Cramer T, Wanner A, Gumbsch P (2000) Energy dissipation and path instabilities in dynamic fracture of silicon single crystals. Phys Rev Lett 85:788–791
Cress GO, Brady BT, Rowell GA (1987) Sources of electromagnetic radiation from fracture of rock samples in the laboratory. Geophys Res Lett 14(4):331–334
Cruikshank KM, Aydin A (1994) Role of fracture localization in arch formation, Arches National Park, Utah. Geol Soc Am Bull 106:876–891
Cruikshank KM, Zhao G, Johnson AM (1991) Analysis of minor fractures associated with joints and faulted joints. J Struct Geol 13:865–886
Currie JB, Reik GA (1977) A method of distinguishing regional directions of jointing and of identifying joint sets associated with individual geologic structures. Can J Earth Sci 14:1211–1228
Dagan G (1977a) Hydrological analysis of BS3, BS4, TH4 and TH5 exploratory wells data. Petrol Ser Ltd, Tel Aviv
Dagan G (1977b) Hydrological analysis of BS5 and BS10 exploratory wells data and summary of hydrological results for Ramat Hovav Area. Petrol Ser Ltd, Tel Aviv
Dahan O, Nativ R, Adar EM, Berkowitz B (1998) A measurement system to determine water flux and solute transport trough fractures in the unsaturated zone. Ground Water 36:444–448
Dahan O, Nativ R, Adar EM, Berkowitz B, Ronen Z (1999) Field observation of flow in a fracture intersecting unsaturated chalk. Water Resour Res 35:3315–3326
Dahan O, Nativ R, Adar EM, Berkowitz B, Weisbrod N (2000) On fracture structure and preferential flow in unsaturated chalk. Ground Water 38:444–451
Dahmen K, Ertas D, Ben-Zion Y (1998) Gutenberg-Richter and characteristic eathquake behaviour is simple mean-field modes of heterrogeneous faults. Phys Rev E 58(2):1494
Dale TN (1923) The commercial granites of New England. U.S. Geological Survey Bulletin 738
Dally JW, Fourney WL, Irwin GR (1985) On the uniqueness of the stress intensity factor-crack velocity relationship. Int J Fracture 27:159–168

Dart CJ, McClay K, Hollings (1995) 3D analysis of inverted extensional fault systems, southern Bristol Channel Basin, UK. In: Buchanan JG, Buchanan PG (eds) Basin inversion. Geological Society Special Publication 88:393–413
Davis JC (1973) Statistical and data analysis in geology. John Wiley & Sons Ltd., New York
Davis GH (1999) Structural geology of the Colorado Plateau region of southern Utah, with special emphasis on deformation bands. Geol Soc Am, special paper 342
Davis K, Baker DM (1965) Ionospheric effects observed around the time of the Alaskan earthquake of 28 March 1964. J Geophys Res 70:2251–2253
Davis GH, Reynolds SJ (1996) Structural geology of rocks and regions. John Wiley & Sons Ltd., New York
De Freminville MCh (1914) Recherches sur la fragilité –l'éclatement. Rev Metall-Paris 11:971–1056
De Sitter LU (1964) Structural geology. McGraw Hill, New York
Dean S, Baranoski M, Bertoli L, Kribbs G, Stephan T, Kulander B, Sochman D, Mumpower D (1984) Regional fracture analysis in western Valley and Ridge and adjoining plateau' West Virginia and Maryland. AAPG Bull 67:448
Dean SL, Kulander BR, Skinner JM (1988) Structural evolution of the Alleghanian orogeny in southeastern West Virginia. Geol Soc Am Bull 100:299–310
Dennis JG (1972) Structural geology. The Ronald Press Company, New York, p 532
Dennis JG (1987) Structural geology: An introduction. Wm C Brown Publishers, Dubuque
Derr JS (1986) Luminous phenomena and their relationship to rock fracture. Nature 321:470–471
Dieterich JH, Carter N (1969) Stress history of folding. Am J Sci 267:129–154
Döll W (1976) Application of an energy-balance and an energy method to dynamic crack-propagation. Int J Fracture 12:595–605
Doremus RH, Johnson WA (1978) Depths of fracture-initiating flows and initial stages of crack propagation in glass. J Mater Sci 13:855–858
Drakopoulos J, Stavrakakis GN, Latoussakis J (1993) Evaluation and interpretation of thirteen official-telegrams for the period September 10, 1986 to April 28, 1988. Tectonophysics 224(1–3):223–236
Drobdev VI, Krasnov VM, Salihov RM (1978) About ionospheric perturbation associated with earthquake and explosions. Izvestia Vysshih Uchebnih Zavedeniy 21:1862–1978 (*in Russian*)
Dulaney EN, Brace WF (1960) Velocity behavior of a growing crack. J Appl Phys 31:2233–2236
Dunne WM, North CP (1990) Orthogonal fracture systems at the limits of thrusting: an example from southwestern Wales. J Struct Geol 12:207–215
Dyer R (1988) Using joint interactions to estimate paleostress ratios. J Struct Geol 10:685–699
Ehlers EG, Blatt H (1982) Petrology: igneous, sedimentary and metamorphic. WH Freeman and Company, San Francisco, 732 pp
Eidam J, Hammer J, Korich D, Krauss M (1992) Zur Abgrenzung altersverschiedener Granitoide innerhalb des Lausitzer Granodiorit-Massivs. Z Geol Wissenschaft 20:289–293
Eldeen ZU, Delvaux D, Jacobs P (2000) Tectonic and paleostress evolution in the Wadi Araba segment of the Dead Sea rift, SW Jordan. The first Stephan Müller Conference of European Geological Society (EGS). From Continental Breakup to Collision. Israel, Dead Sea. Abstract
Elgazzar AS (1998) An inhomogeneous self-organized critical model for earthquakes. Physica A 251:303
Ellsworth WL, Beroza GC (1995) Seismic evidence for a seismic nucleation phase. Science 268:581–858
Engelder T (1979a) Mechanisms for strain within the Upper Devonian clastic sequence of the Appalachian Plateau, western New York. Am J Sci 279:527–542
Engelder T (1979b) Nature of deformation within the outer limits of the Central Appalachian foreland fold and thrust belt in New York State. Tectonophysics 55:289–310
Engelder T (1985) Loading paths to joint propagation during cycle: An example of the Appalachian Plateau, USA. J Struct Geol 7:459–476
Engelder T (1989) The analysis of pinnate joints in the Mount Desert Island granite: Implications for post-intrusion kinematics in the coastal volcanic belt, Maine. Geology 17:564–567
Engelder T (1993) Stress regimes in the lithosphere. Princeton University Press, Princeton, N.J., 457 pp
Engelder T (1999) Transitional-tensile fracture propagation: A status report. J Struct Geol 21:1049–1055
Engelder T, Engelder R (1977) Fossil distortion and decollement tectonics of Appalachian Plateau. Geology 5:547–460
Engelder T, Geiser P (1979) The relationship between pencil cleavage and lateral shortening within the Devonian section of the Appalachian Plateau, New York. Geology 7:460–464
Engelder T, Geiser P (1980) On the use of regional joint sets as trajectories of paleostress fields during the development of the Appalachian Plateau, New York. J Geophys Res 85:6319–6341
Engelder T, Gross MR (1993) Curving cross joints and the lithospheric stress-field in eastern North-America. Geology 21:817–820
Engelder T, Peacock DCP (2001) Joint development normal to regional compression during flexural-flow folding: The Lilstock buttress anticline, Somerset, England. J Struct Geol 23:259–277

Engelder T, Geiser P, Bahat D (1987) Alleghanian deformation within shales and siltstones of the Upper Devonian Appalachian Basin Finger Lakes district, New York. Geol Soc Am Continental Filed Guide, Northeastern Section, pp 113–118
Engelder T, Fischer MP, Gross MR (1993) Geological aspects of fracture mechanics: A short course manual notes. Geological Society of America Annual Meeting, Boston
Erdogan F (1983) Stress intensity factors. J Appl Mech-T ASME 50:992–1002
Erdogan F, Sih GC (1963) On the crack extension plates under plane loading and transverse shear. J Basic Eng-T ASME 85:519–527
Etheridge MA (1983) Differential stress magnitudes during regional deformation and metamorphism: Upper bound imposed by tensile fracturing. Geology 11:231–234
Ettensohn FR (1985) The Catskill Delta complex and the Acadian orogeny: A model. In: Woodrow DL, Sevon WD (eds) The Catskill Delta. Geological Society of America Special Paper 201:39–49
Evans AG (1974) Role of inclusions in fracture of ceramic materials. J Mater Sci 9:1145–1152
Evans AG (1978) Microfracture from thermal expansion anisotropy – I. Single phase system. Acta Metall 26:1845–1853
Evans MA (1994) Joints and decollement zones in Middle Devonian shales: Evidence for multiple deformation events in the central Appalachian Plateau. Geol Soc Am Bull 106:447–460
Evans AG, Johnson H (1975) The fracture stress and its dependence on slow crack growth. J Mater Sci 10:214–222
Evans AG, Wiederhorn SM (1974) Proof testing of ceramic materials – An analytical basis for failure prediction. Int J Fracture 10:379–392
Eyal Y (1996) Stress field fluctuations along the Dead Sea rift since the Middle Miocene. Tectonophysics 15:157–170
Eyal Y, Reches Z (1983) Tectonic analysis of the Dead Sea rift region since the Late Cretaceous based on mesostructures. Tectonophysics 2:167–185
Eyal Y, Gross MR, Engelder T, Becker A (2001) Joint development during fluctuation of the regional stress field in southern Israel. J Struct Geol 23:279–298
Fabrocini A, Fantoni S, Eckhard K (eds) (2002) Introduction to modern methods of quantum many body theory and their applications. World Scientific
Faill RT (1973) Kink-band folding, Valley and Ridge-Province, Pennsylvania. Geol Soc Am Bull 84:1289–1213
Fairhurst C, Cook NGW (1966) The phenomenon of rock splitting parallel to the direction of maximum compression in the neighborhood of a surface. In: Proceedings of the 1st Congress International Society for Rock Mechanics, Lisbon, pp 687–692
Feller W (1971) An introduction to probability theory and its applications. John Wiley, New York
Ferney BD, DeVary MR, Hsia KJ (1999) Oscillatory crack growth in glass. Scripta Materialia 41:275–281
Fifolt DA, Petrenko VF, Schulson EM (1993) Preliminary study of electromagnetic radiation from cracks in ice. Phil Mag B 67(3):289–299
Fineberg J, Marder M (1999) Instability in dynamic fracture. Phys Rep 313:1–108
Fineberg J, Gross SP, Marder M, Swinney HL (1991) Instability in dynamic fracture. Phys Rev Lett 67:457–460
Fineberg J, Gross SP, Marder M, Swinney HL (1992) Instability in the propagation of fast cracks. Phys Rev B 45:5146–5154
Finkel VM, Golovin YI, Sereda VE (1975) Electrical effects accompaying fracture of LiF crystals and problem of rock control. Sov Phys Sol-State 17(3):492–495
Finkelstein D, Powell J (1970) Earthquake lighting. Nature 228:759–760
Fisher RA (1938) The statistical utilization of multiple measurements. Ann Eugenic 8:376–386
Fisher RA (1953) Dispersion on a sphere. P Roy Soc Lond A Mat 217:295–305
Fisher NI, Lewis T, Embleton BJJ (1987) Statistical analysis of spherical data. Cambridge, London
Flexer A, Diamant E, Polishook B, Livnat A (1984) Relation of joints in the 'Avedat group (Eocene) to the tectonic pattern of Israel. Israel J Earth Sci 33:12–25
Freund LB (1972a) Crack propagation in an elastic solid subjected to general loading – I. Constant rate of extension. J Mech Phys Solids 20:129–140
Freund LB (1972b) Crack propagation in an elastic solid subjected to general loading – II. Non uniform rate of extension. J Mech Phys Solids 20:141–152
Freund LB (1973) Crack propagation in an elastic solid subjected to general loading – III. Stress wave loading J Mech Phys Solids 21:47–61
Freund LB (1974) Crack propagation in an elastic solid subjected to general loading – IV. Obliquely incident stress pulse J Mech Phys Solids 22:137–146
Freund LB (1990) Dynamic fracture mechanics. Cambridge Univ Press
Freund F (2000) Time resolve study of charge generation and propagation in igneous rocks. Geophys Res Lett 105(5):11001–11019
Freund F (2002) Charge generation and propagation in igneous rocks. J Geodyn 33(4–5):543–570

Frey MG (1973) Influence of Salina salt on structure in the New York – Pennsylvania part of the Appalachian Plateau. AAPG Bull 57:1027–1037
Frid V (1990) Rockburst hazard forecast of coal seams by theirs electromagnetic radiation. Ph.D. thesis, The state research institute of mining geomechanics and mine surveying (VNIMI), St. Petersburg (*in Russian*)
Frid V (1997a) Rock-burst hazard forecast by electromagnetic radiation excited by rock fracture. Rock Mech Rock Eng 30(4):229–236
Frid V (1997b) Electromagnetic radiation method for rock and gas outburst forecast. J Appl Geophys 38:97–104
Frid V (2000) Electromagnetic radiation method water-infusion control in rockburst-prone strata. J Appl Geophys 43:5–13
Frid V (2001) Calculation of electromagnetic radiation criterion for rockburst hazard forecast in coal mines. Pure Appl Geophys 158:931–944
Frid V, Shabarov A, Proskurjakov V (1992) Formation of electromagnetic radiation in coal stratum. J Min Sci+ 28(2):139–145
Frid V, Rabinovitch A, Bahat D (1999) Electromagnetic radiation associated with induced triaxial fracture in granite. Phil Mag Lett 79:79–84
Frid V, Bahat D, Goldbaum J, Rabinovitch A (2000) Experimental and theoretical investigation of electromagnetic radiation induced by rock fracture. Israel J Earth Sci 49:9–19
Frid V, Rabinovitch A, Bahat D (2003) Fracture induced electromagnetic radiation. J Phys D Appl Phys 36:1620–1628
Friedman M, Logan JM (1973) Lüders bands in experimentally deformed sandstone and limestone. Geol Soc Am Bull 84:1465–1476
Friedman M, Stearns DW (1971) Relations between stresses inferred from calcite twin lamellae and macrofractures, Teton Anticline, Montana. Geol Soc Am Bull 82:3151–3162
Frost HJ (2001) Mechanisms of crack nucleation in ice. Eng Fract Mech 68:1823–1837
Frost HJ, Gupta V (1993) Crack nucleation mechanisms and fracture toughness measurements in freshwater ice. In: Proceedings of the AMD Symposium on Ice Mechanics held at the Joint SES-ASC-ASME Conference in Virginia (1993), June 6–9, AMD-Vol. 163, ASME, New York, p 235
Fujinawa Y, Takahashi K (1998) Electromagnetic radiations associated with major earthquakes. Phys Earth Planet In 105(3–4):249–259
Fuller KNG, Fox PG, Field JE (1975) Temperature rise at tip of fast-moving cracks in glassy polymers. P Roy Soc Lond A Mat 341:537–550
Gabrielov A, Keilis-Borok V, Zaliapin I, Newman WI (2000a) Critical transitions in colliding cascades. Phys Rev E 62(1):237–249
Gabrielov A, Zaliapin I, Newman WI, Keilis-Borok VI (2000b) Colliding cascades model for earthquake prediction. Geophys J Int 143:427–437
Galperin YI, Jorjro NV, Kavrazhkin RA, et al. (1985) VLF and ELF effects in the upper ionospheric caused by large-scaled acoustic waves in the lower ionosphere observed from Aurol-3 satellite. In: Results of the ARCARD-3 Project, Cepadues, Toulouse, pp 661–664
Gardiner CW (1990) Handbook of stochastic methods for physics, chemistry and natural sciences, 2nd edn. Springer-Verlag, Berlin
Geiser PA (1988) The role of kinematics in the construction and analysis of geological cross section in deformed terranes. In: Mitra G, Wojtal G (eds) Geometries and mechanisms of thrusting. Geological Society of America Special Paper 222:47–76
Geiser P, Engelder T (1983) The distribution of layer parallel shortening fabrics in the Appalachian foreland of New York and Pennsylvania – Evidence for 2 non-coaxial phases of the Alleghanian Orogeny. Geol Soc Am Mem 158:161–175
Gerdes A, Wörner G, Finger F (1998) Late-orogenic magmatism in the southern Bohemian Massif – Geochemical and isotopic constraints on possible sources and magma evolution. Acta Universitatis Carolinae Geologica Praha 42:41–45
Germanovich LN, Dyskin AV (2000) Fracture mechanisms and instability of openings in compression. Int J Rock Mech Min 37:263–284
Germanovich LN, Ring LM, Carter BJ, Ingraffea AR, Dyskin AV, Ustinov KB (1995) Simulation of crack growth and interaction in compression. Proc Inter Cong Rock Mech Balkema, Rotterdam, Brookfield, pp 1:219–226
Gershenzon N, Zilpimiani D, Maguladze P (1985) Electromagnetic radiation from crack tip during ionic crystals fracture. Dokl Akad Nauk SSSR+ 248:1077–1081
Gershenzon N, Gokhberg M, Morgunov V (1987) Sources of electromagnetic emissions preceding seismic events. Izv-Phys Solid Earth 23(2):96–101
Gershenzon N, Gokhberg M, Karakin A (1989) Modeling the connection between earthquake preparation process and crystal electromagnetic emission. Phys Earth Planet In 57(1–2):129–138

Ghahremani F, Hutchinson JW, Tvergaard V (1990) Three-dimensional effects in microcrack nucleation in brittle polycrystals. J Am Ceram Soc 73:1548–1554
Ghosh SK (1993) Structural geology: Fundamentals and modern developments. Pergamon Press, Oxford
Gilbert GK (1904) Domes and dome structures of the High Sierra. Geol Soc Am Bull 15:29–36
Gillespie P, Walsh JJ, Watterson J (1992) Limitations of displacement and dimension data for single faults and the consequences for data analysis and interpretation. J Struct Geol 14:1157–1172
Gilman JJ (1958) Creation cleavage steps by dislocation. Trans Metall Soc AIME 212:310–315
Gokhberg M, Morgunov V, Aronov E (1979) High frequency electromagnetic radiation during seismic activity. Dokl Akad Nauk SSSR+ 248:1077–1081
Gokhberg M, Yoshino T, Morgunov V (1982) Results of recording operative electromagnetic Earthquake precursor in Japan. Izv-Phys Solid Eart+ 18(2):144–146
Gokhberg M, Gufel'd I, Gershenzon N (1985) Electromagnetic effects during rupture of the Earth's crust. Izv-Phys Solid Eart+ 21:52–62
Gokhberg M, Morgunov V, Matveyev V (1986) On the observation of anomalous electromagnetic emission in the epicentral zone of an Earthquake. Izv-Phys Solid Eart+ 22(8):676–678
Gol'd RM, Markov G, Mogila PG (1975) Pulsed electromagnetic radiation of minerals and rocks subjected to mechanical loading. Izv-Phys Solid Eart+ 7:109–111
Gold DP, Parizek RR (1976) Field guide to lineamer and fractures in central Pennsylvania. International Conference on New Basement Tectonics, 2nd edn. Newark University of Delaware
Goldbaum J, Frid V, Rabinovitch A, Bahat D (2001) Electromagnetic radiation induced by percussion drilling. Int J Fracture 111:L15-L20
Goldstein A, Marshak S (1988) Analysis of fracture array geometry. In: Marshak S, Mitra G (eds) Basic methods of structural geology. Prentice Hall, Englewood Cliffs, NJ, pp 249–267
Golovin Y, Shibkov A (1986a) Dynamics of dislocation pile-ups and pulsed polarization of LiF single crystals in the case of single slip. Sov Phys Sol-State 28(9):1625–1626
Golovin Y, Shibkov A (1986b) Fast electrical processes and dynamics of dislocations in plastically deformed alkali halide crystals. Sov Phys Sol-State 28(11):1965–1968
Golubovic L, Feng S (1991) Rate of microcrack nucleation. Phys Rev A 43:5223–5227
Goncharov A, Korjakov VP, Kuznetzov VM (1980) Acoustic emission and electromagnetic radiation during uniaxial compression. Dokl Akad Nauk SSSR+ 255(4):821–824
Goodwin AM (1995) Spatial change in joint geometry in the Chalk of eastern England. In: Ameen MS (ed) Fractography: Fracture topography as a tool in fracture mechanics and stress analysis. Geological Society Special Publication 92:197–213
Gradshteyn IS, Ryzhik IM (1980) Table of integrals, series and products, fourth edn. Academic Press, New York, pp 80ff
Grater RK (1945) Landslide in Zion Canyon, Zion National Park, Utah. J Geol 53:116–124
Gray M, Mitra G (1993) Migration of deformation fronts during progressive deformation – Evidence from detailed structural studies in the Pennsylvania anthracite region, USA. J Struct Geol 15(3–5): 435–459
Gregory HE (1950) Geology and geography of the Zion National Park region Utah and Arizona. Geol Surv Prof Paper 220
Griffith AA (1920) The phenomena of rupture and flow in solids. Philos T Roy Soc A 221:163–198
Griffith AA (1924) The theory of rupture. Proceedings of the First International Conference of Applied Mechanics, Delft, pp 55–63
Griggs DT, Handin J (1960) Observations on fracture and hypothesis of earthquakes. In: Griggs DT, Handin J (eds) Rock deformation. Geol Soc Am Mem 79:347–364
Gross MR (1993) The origin and spacing of cross joints: Examples from the Monterey Formation, Santa Barbara coastline, California. J Struct Geol 15:737–751
Gross MR (1995) Fracture partitioning: Failure mode as a function of lithology in the Monterey Formation of coastal California. GSA Bull 107: 779–792
Gross MR, Engelder T (1991) A case for neotectonic joints along the Niagara Escarpment. Tectonophysics 10:631–641
Gross MR, Fischer MP, Engelder T, Greenfield RJ (1995) Factors controlling joints spacing in interbedded sedimentary rocks: Integrating numerical models with field observations from the Monterey Formation, USA. In: Ameen MS (ed) Fractography: Fracture topography as a tool in fracture mechanics and stress analysis. Geological Society (London) Special Publication 92, pp 215–233
Gross MR, Bahat D, Becker A (1997) Relations between jointing and faulting based on fracture-spacing ratios and fault-slip profiles: A new method to estimate strain in layered rocks. Geology 25:887–890
Grossenbacher K, Bahat D, Karasaki K (1996) Triangulator: Excel spreadsheets for converting relative bearings to XYZ coordinates, with applications to scaling photographs and orienting surfaces. Comput Geosci 22:1053–1059

Grossmann NF (1983) A numerical method for the definition of discontinuity sets. Proc. 5th Congress International Society for Rock Mechanics, Melbourne, Balkema, 1:B17–B21
Guarino A, Garcimartin A, Ciliberto S (1998) An experimental test of the critical behavior of fracture precursor. Eur Phys J B 6:13–24
Guarino A, Ciliberto S, Garcimartin A (1999) Failure time and microcrack nucleation. Europhys Lett 47:456–461
Guarino A, Ciliberto S, Garcimartin A, Zei M, Scorretti R (2002) Failure time and critical behaviour of fracture precursors in heterogeneous materials. Eur Phys J B26:141–151
Gucer DE, Gurland J (1962) Comparison of statistics of two fracture models. J Mech Phys Solids 10:365–373
Gudmundsson A, Homberg C (1999) Evolution of stress fields and faulting in seismic zones. Pure Appl Geophys 154:257–280
Gueguen Y, Palciauskas V (1994) Introduction to the physics of rocks. Princeton University Press, Princeton
Guin JP, Wiederhorn SM (2003) Crack growth threshold in soda lime silicate glass: Role of hold-time. J Non-Cryst Solids 316:12–20
Gutenberg B, Richter CF (1954) Seismicity of the Earth and associated phenomena. Princeton University Press, Princeton
Gvirtzman G (1969) The Saqiye Group (late Eocene to early Pleistocene) in the coastal plain and Hashephela regions. Geol Surv Isr Bull 51(2)
Hahn GT, Rosenfield AR (1965) Local yielding and extension of a crack under plane stress. Acta Metall 13:293–306
Hamblin WK (1965) Origin of Òreverse dragÓ on the downthrow side of normal faults. Geol Soc Am Bull 76:1145–1164
Hancock PL (1972) The analysis of en-echelon veins. Geol Mag 3:269–276
Hancock PL (1985) Brittle microtectonics: Principles and practice. J Struct Geol 7:437–457
Hancock PL (1986) Joint spectra. In: Nichol I, Nesbitt RW (eds) Geology in the real world – the Kingsley Dunham volume. Institution of Mining and Metallurgy, London, pp 155–164
Hancock PL, Al-Kadhi A (1978) Analysis of mesoscopic fractures in the Dhurma-Nisah segment of the central Arabian Graben system. J Geol Soc 135:339–347
Hancock PL, Engelder T (1989) Neotectonic joints. Geol Soc Am Bull 101:1197–1208
Hancock PL, Dunne WM, Tringham ME (1982) Variscan structures in south-west Dyfed. In: Bassett MG (ed) Excursion-guide on geological excursions in Dyfed, South-west Wales 12:215–248
Handin J, Hager RV Jr, Friedman M, Feather JN (1963) Experimental deformation of sedimentary rocks under confining pressure: Pore pressure tests. AAPG Bull 47:717–755
Hansen EC, Borg IY (1962) The dynamic significance of deformation lamellae in quartz of a calcite-cemented sandstone. Am J Sci 260:321–336
Harlow DG (1985) The pure flaw model for chopped fiber composites. P Roy Soc Lond A Mat397:211–232
Hatheway AW, Kiersch GA (1982) Engineering properties of rock. In: Carmichael RC (ed) Handbook of physical properties or rock. CRC Press Inc, Boca Raton, Florida, pp 289–311
Hauch JA, Marder MP (1998) Energy balance in dynamic fracture, investigated by a potential drop technique. Int J Fracture 90:133–151
Hayakawa M, Tomizawa I, Ohta K (1993) Direction finding of precursory radio emissions associated with earthquakes: a proposal. Phys Earth Planet In 77:127–135
Hayati G (1975) The engineering geology of some chalks in Israel. Ph.D. Thesis, Technion, Israel Inst of Technol, (*in Hebrew*)
Helgeson DE, Aydin A (1991) Characteristics of joint propagation across layer interfaces in sedimentary rocks. J Struct Geol 13:897–911
Hermann HJ, Roux S (eds) (1990) Statistical models for the fracture of disordered media. North Holland, Amsterdam
Hertzberg RW (1976) Deformation and fracture mechanics of engineering materials. John Wiley & Sons Ltd., New York, p 605
Hidalgo RC, Moreno Y, Kun F, Herrmann HJ (2002) Fracture model with variable range of interaction. Phys Rev E 65:046148–1–8
Hirata T, Satoh T, Ito K (1987) Fractal structure of spatial distribution of microfracturing in rock. Geophys J Roy Astr S 90:369–374
Hirschmann G (1966) Assyntische und variszische Baueinheiten im Grundgebirge der Oberlausitz. Freiberger Forschungsh C 212:1–146
Hoagland RG, Hahn GT, Rosenfield AR (1973) Influence of microstructure on fracture propagation in rock. Rock Mech 5:77–106
Hobbs DW (1967) The formation of tension joints in sedimentary rocks: An explanation. Geol Mag 104:550–556

Hobbs BE, Means WD, Williams PF (1976) An outline of structured geology. John Wiley & Sons Ltd., New York, p 571
Hodgson RA (1961a) Classification of structures on joint surfaces. Am J Sci 259:493–502
Hodgson RA (1961b) Regional study of jointing in comb ridge-Navajo Mountain area, Arizona and Utah. AAPG Bull 45:1–38
Hoek E, Bieniawski ZT (1966) Fracture propagation mechanism in hard rock. C R Congr Soc Int Mec Roches 3:243–249
Holloway DG (1986) The fracture behaviour of glass. Glass Technol 27:120–133
Holloway S, Chadwick RA (1986) The Sticklepath-Lustleigh fault zone: Tertiary sinistral reactivation of a Variscan dextral strike slip fault. J Geol Soc London 143:452–477
Holman WR (1976) The origin of sheeting joints. A hypothesis. Unpublished Ph.D. thesis. University of California, Los Angeles, USA
Holzhausen GR (1989) Origin of sheet fracture, 1. Morphology and boundary conditions. Eng Geol 27:225–278
Holzhausen GR, Johnson AM (1979) Analyses of longitudinal splitting of uniaxially compressed rock cilinders. Int J Rock Mech Min 16:163–177
Horii H, Nemat-Nasser S (1985) Compression-induced microcrack growth in brittle solids: Axial splitting and shear failure. J Geophys Res 90:3105–3125
Hovestadt M (1902) Jena glass and its scientific and industrial applications. Macmillan & Co, London
Hsieh PA, Newman SP, Stiles GK, Simpson ES (1985) Field determination of the three-dimensional hydraulic conductivity tensor of anisotropic media. 2. Methodology and application to fractured rocks. Water Resour Res 21:1667–1676
Huber NK (1987) The geologic story of Yosemite National Park. U.S. Geological Survey Bulletin 1595
Hudak P (1992) Terminal decollement in the Appalachian plateau of northwestern PA. Northeastern Geology 1:108–112
Hull D (1999) Fractography: Observing, measuring, and interpreting fracture surface topology. Cambridge University Press, Cambridge
Hunt CB (1956) Cenozoic geology of the Colorado Plateau. U.S. Geological Survey Professional Papers 279, 99 pp
Huntington HE (1966) The Yosemite story. Doubleday & Company, New York
Ipatov Y (1989) Fundamentals of electromagnetic radiation method for rockburst forecast on Khibin apatite mines, Ph.D. thesis, The State Research Institute of Mining Geomechanics and Mine Surveying (VNIMI), St. Petersburg (*in Russian*)
Irwin GR (1957) Analysis of stresses and strains near the end of a crack traversing a plate. J Appl Mech-T ASME 24:361–364
Irwin GR (1962) Crack-extension force for a part-through crack in a plate. J Appl Mech-T ASME 29: 651–654
Issar A, Bahat D, Wakshal E (1988) Occurrence of secondary gypsum veins in joints in chalks in the Negev, Israel. Catena 15:241–247
Ito K, Matsuzaki M (1990) Earthqaukes as self-organized critical phenomena. J Geophys Res 95: 6853–6860
Ivanov VV, Pimonov AG, Yegorov PV, Kolpakova LA (1990) Determination of the constants of termofluctuational equations for strength and crack parameters from electromagnetic pulse emissions of rocks. Izv-Phys Solid Earth 26(7):597–601
Jaeger JC, Cook NGW (1979) Fundamentals of rock mechanics. Chapman and Hall, London, pp 593
Jagasivamani V, Iyer KJL (1988) Electromagnetic emission during the fracture of heat-treated spring steel. Mater Lett 6(11–12):418–422
Jayatilaka A de S, Trustrum K (1978) Fracture of brittle materials in uniaxial compression. J Mater Sci 13:455–457
Jensen HJ (1998) Self-organized criticality. Cambridge Univ Press, Cambridge
Johnson RM (1970) Physical processes in geology. Freeman and Company, San Francisco
Johnson E (1992) Process region changes from rapidly propagating cracks. Int J Fracture 55:47–63
Johnson JW, Holloway DG (1966) On the shape and size of the fracture zones on glass fracture surfaces. Phil Mag 14:731–743
Johnson RA, Wichern DW (1988) Applied multivariate statistical analysis. Prentice Hall, Engelwood Cliffs, New York
Johnston AC (1991) Light from seismic waves. Nature 354:361
Kalthoff JF (1973) On the propagation direction of bifurcated cracks. In: Sih GC (ed) Dynamic crack propagation. Noordhoff, Leyden, pp 449–458
Kanninen MF, Popelar CH (1985) Advanced fracture mechanics. Oxford University Press, New York
Karasaki K, Freifeld B, Cohen A, Grossenbacher K, Cook P, Vasco D (2000) A multidisciplinary fractured rock characterization study at Raymond field site, Raymond, CA. J Hydrol 236:17–34

Kattenhorn SA, Aydin A, Pollard DD (2000) Joints at high angles to normal fault strike: An explanation using 3-D numerical models of fault-perturbed stress fields. J Struct Geol 22:1–23
Kay SM, Snedden WT, Foster BP, Kay RW (1983) Upper mantleand crustal fragments in the Ithaca Kimberlites. J Geol 91:277–290
Kelly PM, Leach CA, Pawlings RD (1994) Acoustic, emission studies of fatigue loaded SiC platelet-reinforced Y-TZP. J Mater Sci Lett 13:211–212
Kelly PG, Sanderson DJ, Peacock DCP (1998) Linkage and evolution of conjugate strike-slip fault zones in limestones of Somerset and Northumbria. J Struct Geol 20:1477–1493
Kelner S, Bouchon M, Coutant O (1999) Characterization of fractures in shallow granite from the modelling of the anisotropy and attenuation of seismic waves. B Seismol Soc Am 89:706–717
Kerkhof F (1973) Wave fractographic investigation of brittle fracture dynamics. In: Sih GC (ed) Dynamic crack propagation. Noordhoff, Int Pub Leyden, pp 3–35
Kerkhof F (1975) Bruchmechanische Analyse von Schadensfällen an Gläsern. Glastech Ber-Glass 48:112–124
Kerkhof F, Richter H (1969) Investigation of the influence of water vapour on crack velocities in glass by ultrasonic fractography. Proc. 2nd Intern. Conference on Fracture, Brighton 40:463–473
Khatiashvili N (1984) The electromagnetic effect accompanying the fracturing of alkaline halide crystals and rocks. Izv-Phys Solid Eart+ 20:656–661
Khesin B, Alexeyev V, Eppelbaum L (1996) Interpretation of geophysical fields in complicated environments. Kluwer Academic Publishers, London
Khesin B, Alexeyev V, Eppelbaum L (1997) Rapid methods for interpretation of induced polarization anomalies. J Appl Geophys 37:117–130
King CY (1983) Electromagnetic emissions before earthquakes. Nature 301:377
King GCP (1986) Speculation on the geometry of the initiation and termination process of earthquake rupture and its relation to morphology and geological structure. Pure Appl Geophys 124: 567–585
King PJ, Sheard FW (1970) Unharmonic attenuation of surface waves on crystals at low temperatures. P Roy Soc Lond A Mat 320:175–179
Kittel C (1987) Quantum theory of solids. John Wiley & Sons Ltd., New York
Kloster M, Hansen A, Hemmer PC (1997) Burst avalanches in solvable models of fibrous materials. Phys Rev E 56:2615–2625
Knapp RB, Norton D (1981) Preliminary numerical analysis of crystallization and stress evolution in cooling pluton environments. Am J Sci 281:35–68
Knauss WG (2000) Prospectives in experimental solid mechanics. Int J Solids Struct 37:251–266
Knauth LP, Lowe DR (1978) Oxygen isotope geochemistry of cherts from Onverwacht group (3.4 billion years), Transvaal, South-Africa, with implications for secular variations in isotopic composition of cherts. Earth Planet Sc Lett 41:209–222
Knott SD, Beach A, Brockbank PJ, Brown JL, McCallum JE, Welbon AI (1996) Spatial and mechanical controls on normal fault populations. J Struct Geol 18:356–372
Kobayashi AS, Mall S (1978) Dynamic fracture toughness of Homalite-100. Exp Mech 18:11–18
Kobayashi A, Ohtani N, Sato T (1974) Phenomenological aspects of viscoelastic crack propagation. J Appl Polym Sci 18:1625–1638
Kornfel'd MI (1971) Electrical charges on the surface of alkaline-halide crystals. Sov Phys Sol-State 13(2):381–385
Kornfel'd MI (1977) Mechanism of electrification of cleaved crystals. Sov Phys Sol-State 19(4):648–649
Kronfeld J, Rosenthal R, Weinberger G, Flexer A, Berkowitz B 1993. The interaction of two major old water bodies and its implication for the exploitation of groundwater in the multiple aquifer system in the central and northern Negev. Journal of Hydrology 143: 169-190
Kossmat F (1927) Gliederung des varistischen Gebirgsbaues. Abh Sächs Geol Landesamt 1:1–39
Kossobokov VG, Keilis-Borok VI, Cheng B (2000) Similarities of multiple fracturing on a neutron star and on the Earth. Phys Rev E 61(4):3529–3533
Kotz S, Nadarajah S (2000) Extreme value distributions theory and applications. Imperial College Press, London
Kowalik WS, Gold DP (1976) The use of Landsat-1 imagery in mapping lineaments in Pennsylvania. Proc. 1st Int. Conf. on the New Basement Tectonics. Utah Geol Soc, pp 236–249
Krapivsky PL, Majumdar SN (2000) Traveling waves, front selection and exact nontrivial exponents in a random fragmentation problem. Phys Rev Lett 85:5492–5495
Krauss M, Eidam J, Hammer J, Korich D (1992) Die cadomisch-variszische Entwicklung des Lausitzer Granodiorit-Komplexes. Zbl Geol Paläontol Teil I 1/2:71–85
Krenkel E (1924) Der Syrische Bogen. Centrail Mineral 9:274–281, 10301–10313
Kuksenko VS, Mansurov VA (1986) Fracture localization in rocks at different scale levels. Physical-technical Problems of Economical Resources Mining 3:49–55

Kuksenko VS, Lyashkov AI, Mirzoev KM (1982) Connection between the sizes of cracks generated under loading and duration of elastic energy emission. Dokl Akad Nauk SSSR 246(4):846–848
Kuksenko VS, Manzikov V, Mansurov VA (1985) Regularities in the development of microfocal rupture. Izv-Phys Solid Earth 21(7):553–556
Kuksenko VS, Ingevatkin IE, Mahgikov BC (1987) Physical and methodical foundations of rockburst forecast. Physical-technical Problems of Economical Material Mining 1:9–21
Kuksenko VS, Kilkeev RS, Lyashkov AI (1990) Electrification of quartz glass by mechanical loading. Sov Phys Sol-State 32(8):1320–1322
Kulander BR, Barton CC, Dean SC (1979) The application of fractography to core and outcrop fracture investigations. Report to U.S. D.O.E. Morgantown Energy Technology Center, METC SP-79/3
Kurie AE (1966) Recurrent structural disturbance of Colorado Plateau margin near Zion National Park Utah. Geol Soc Am Bull 77:867
Kustov VA, Liperovsky T (1988) About perturbation in ionospheric F-region begore strong earthquake. Izv-Phys Solid Eart+ 4:12–20
Lacazette A, Engelder T (1992) Fluid-driven cyclic propagation of a joint in the Ithace siltstone, Appalachian Basin, New York. In: Evans B, Wong TF (eds) Fault mechanics and transport properties of rocks. Academic Press Ltd, London, pp 297–324
Ladeira FL, Price NJ (1981) Relationship between fracture spacing and bed thickness. J Struct Geol 3:179–183
Lake SD, Karner GD (1987) The structure and evolution of the Wessex Basin, southern England – an example of inversion tectonics. Tectonophysics 137:347
Landau LD, Lifshitz EM (1963) Theory of elasticity. Pergamon Press, London
LaPointe PR, Hudson JA (1985) Characterization and interpretation of rock mass joint patterns. Geological Society of America Special Paper 199
Laube GC (1876) Geologie des böhmischen Erzgebirges I. Archiv f Naturwiss Landesdurchforsch, pp 1–208
Lawn BR (1993) Fracture of brittle solids, 2nd edn. Cambridge Solid State Science Series, Cambridge University Press, Cambridge
Lawn BR, Wilshaw TR (1975a) Fracture of brittle solids. Cambridge University Press, London, pp 1–204
Lawn BR,Wilshaw TR (1975b) Review indentation fracture: Principles and applications. J Mater Sci 10:1045–1081
Lazarus V, Leblond JB, Mouchrif SE (2001a) Crack front rotation and segmentation in mixed mode I + III or I + II + III. Part I: Calculation of stress intensity factors. J Mech Phys Solids 49:1399–1420
Lazarus V, Leblond JB, Mouchrif SE (2001b) Crack front rotation and segmentation in mixed mode I + III or I + II + III. Part II: Comparison with experiments. J Mech Phys Solids 49:1421–1443
Lee FT, Diehl SF (1989) Geologic and geomechanical properties of the Mount Valdo granite, Maine. Maine Geological Survey, vol 2, pp 187–200
Lee CC, Liu JY, Pan CJ (2000) The height of sporadic-E layer simultaneously observed by the VHF radar and ionosondes in Chung-Li. Geophys Res Lett 27:641–644
Letouzey J, Tremolieres P (1980) Paleo-stress fields around the Mediterranean derived from microtectonics: Comparison with plate tectonic data. Rock Mech 9:173–192
Levi T (2003) Joint sets as a tool for analyses the tectonic deformation in the central Arava western margins. Ms Sc Thesis, Ben Gurion University, Israel (*in Hebrew*)
Li Z, Yang J, Lee H (1988) Temperature-fields near a running crack tip. Engng Fracture Mech 30:791–799
Li L, Aubertin M, Simon R (1999) Multiaxial failure criterion with time and size effects for intact rocks. In: Amadei B, Kranz RL, Scott GA, Smeallie PH (eds) Rock mechanics for industry. Balkema, Rotterdam, pp 653–659
Lindner H (1972) Ergebnisse der Gravimetermessungen im Bereich des Lausitzer Massivs und seiner Randgebiete. Geologie 21:927
Link B, Epstein RI (1996) Thermally driven neutron star glitches. Astrophys J 457:844–854
Linsser H (1967) Investigation of tectonics by gravity detailing. Geophys Prosp XV/3:480–515
Liu C, Knauss WG, Rosakis AJ (1998) Loading rates and the dynamic initiation toughness in brittle solids. Int J Fracture 90:103–118
Liu JY, Chu YH, Chen MQ (2000) Modeling and ground observations of the ionosphere related to the COSMIC project. Terr Atmos Ocean Sci 11:349–364
Lobst R (2001) Der Intrusionsverband cadomischer Granodiorite am Klosterberg bei Demitz-Thumitz. Exkursionsführer und Veröffentlichungen der GGW 212:67–69
Lockner DA (1993) The role of acoustic emission in the study of rock fracture. Int J Rock Mech Min 7:883–889
Lockner DA (1996) Brittle fracture as an analog to earthquakes: Can acoustic emission be used to develop a viable prediction strategy. J Acoustic Emission 14(3–4):S88–S101

Lockner DA, Byerlee JD, Kuksenko V, Ponomarev A, Sidorin A (1991) Quasi-static fault growth and shear fracture energy in granite. Nature 350:39–42
Lockwood JP, Moore JG (1979) Regional deformation of the Sierra Nevada, California, on conjugate microfault sets. J Geophys Res 84:6041–6049
Loewy S (1995) The post-Alleghanian tectonic history of the Appalachian Basin based on joint patterns in Devonian black shales. University Park, Pennsylvania, Pennsylvania State University, (*Master's thesis*)
Long JCS, et al. (1996) Rock fractures and fluid flow: Contemporary understanding and applications. Commission on Geosciences, Environment and Resources (CGER), The National Academies Press, 551 pp
Loosveld RJH, Franssen RCMW (1992) Extensional vs. shear fractures: Implications for reservoir characterization. Society of Petroleum Engineers 25017:23–30
Maccagno TM, Knott JF (1989) The fracture behaviour of PMMA in mixed modes I and II. Eng Fract Mech 34:65–86
Mandelbrot B (1960) The Pareto-Levy law and the distribution of income. Int Econ Rev 1:79–106
Mansurov VA (1994) Acoustic emission from failing rock behavior. Rock Mech Rock Eng 27(3):173–182
Marder M (1993) Simple models of rapid fracture. Physica D 66:125–134
Marder M (1996a) Energetic developments in fracture. Nature 381:275–276
Marder M (1996b) Statistical mechanics of cracks. Phys Rev E 54:3442–3454
Marder M, Gross SP (1995) Origin of crack tip instabilities. J Mech Phys Solids 43:1–48
Marder M, Liu XM (1993) Instability in lattice fracture. Phys Rev Lett 71:2417–2420
Markov GA, Ipatov Y (1986) Method of electromagnetic radiation for rockburst forecast on apatite mines. Eng Geol 3:54–57 (*in Russian*)
Mart Y, Horowitz A (1981) The tectonics of the Timna region in Southern Israel and the evolution of the Dead-Sea Rift. Tectonophysics 79:165–199
Martel SJ (1997) Effects of cohesive zones on small faults and implications for secondary fracturing and fault trace geometry. J Struct Geol 19:835–847
Martens JH (1924) Igneous rocks of Ithaca, New York and vicinity. Geol Soc Am Bull 3:305–320
Matejka D, Janousek K (1998) Whole-rock geochemistry and petrogenesis of granites from the northern part of the Moldanubian batholith (Czeck Republic). Acta Universitatis Carolinae Geologica 42:73–79
Matsuzaki M, Takayasu H (1991) Fractal features of the earthquake phenomenon and a simple mechanical model. J Geophys Res 96:19925–19931
Matte PH, Maluski H, Rajlich P, Franke W (1990) Terrane boundaries in the Bohemian Massif: Result of large-scale Variscan shearing. Tectonophysics 177:151–170
Mayo EB (1941) Deformation in the interval Mt. Lyell–Mt. Whitney, California. Geol Soc Am Bull 94:563–575
McConaughy DT, Engelder T (1999) Joint interaction with embedded concretions: Joint loading configurations inferred from propagation paths. J Struct Geol 21:1637–1652
Means WD (1987) A newly recognized type of slickensise striation. J Struct Geol 9:585–590
Means WD (1979) Stress and strain. Springer-Verlag, Heidelberg
Means WD (1987) A newly recognized type of slickenside striation. J Struct Geol 9:585–590
Mecholsky JJ (1991) Quantitative fractography: An assessment. In: Frechette VD, Varner JR (eds) Fractography of glasses and ceramics II. Ceramic Transactions 17:413–451
Mecholsky JJ, Freiman SW (1979) Determination of fracture mechanics parameters through fractographic analysis of ceramics. In: Freiman SW (ed) Fracture mechanics applied to brittle materials. ASTM Spec Tech Pub 678:136–150
Menzel D, Schröder B (1994) Geologische Kriterien zur Unterbau-Exhumierung im Naab-Gebirge. KTB Report 94–3:179–184
Michalske TA (1977) The stress corrosion limit: Its measurement and implications. In: Bradt RC, Evans AG, Hasselman DPH, Lange FF (eds) Fracture mechanics of ceramics: Surface flaws, statistics, and microcracking, vol 5. Plenum Press, New York, p 277
Michalske TA (1984) Fractography of slow fracture in glass. In: Mecholsky JJ Jr, Powell SR Jr (eds) Fractography of ceramic and metal failures. Philadelphia, American Society for Testing and Materials Special Technical Publication 827:121–136
Miroshnichencko M, Kuksenko V (1980) Emission of electromagnetic pulses during nucleation of cracks in solid insulators. Sov Phys-Solid State 22(5):895–896
Mirowski P (1995) Mandelbrot's economics after a quarter century. Fractals 3:581–600
Misra A (1975) Electromagnetic effects at metallic fracture. Nature 254:133–134
Misra A (1977) Physical model for the stress-induced electromagnetic effect in metals. Appl Phys 16:195–199
Misra A, Ghosh S (1980) Electromagnetic radiation characteristics during fatigue propagation and failure. Appl Phys 23:387–390

Mogi K (1962) Study of elastic shocks caused by the fracture of heterogeneous materials and its relation to earthquake phenomena. B Earthq Res I Tokyo 40:125–173
Mogi K (1985) Earthquake prediction. Academic Press, Tokyo
Molchan G, Kronrod T, Panza G (1997) Multiscale seismicity medel for seismic risk. Bull Seismol Soc Am 87:1220–1229
Molchanov OA, Hayakawa M (1998a) Subionospheric VLF perturbations possibly related to earthquakes. J Geophys Res 103(A8):17489–17504
Molchanov OA, Hayakawa M (1998b) On the generation mechanism of ULF seismogenic electromagnetic emissions. Phys Earth Planet In 105:201–210
Molnar P, Tapponier P (1975) Cenozoic tectonics of Asia: Effects of a continental collision. Science 189:419–426
Molotskii MI (1980) Dislocation mechanism for Misra effect. Sov Tekh Phys Lett 6(1):22–23
Moore DE, Lockner DA (1995) The role of microcracking in shear-fracture propagation in granite. J Struct Geol 17:95–114
Morgunov V (1985) Electromagnetic emission during seismic activity. Izv-Phys Solid Earth 21(3): 220–226
Morgunov V, Matveyev V (1990) Electromagnetic emission in aftershocks of Spitak earthquake. Izv-Phys Solid Earth 26:457–461
Morgunov V, Matveyev V (1991) Electric and electromagnetic effects in the epicentral zone of Spitak aftershocks. Izv-Phys Solid Earth 27:1002–1005
Morgunov V, Gerasimovich E, Matveyev V (1988) Deformation of the Earth surface and anomalous electromagnetic emission. Izv-Phys Solid Earth 24:924–929
Mortimore RN (1990) Chalk or chalks. Proc Intern Chalk Symp, Brighton Politechnic, Thomas Telford, pp 15–45
Mott NF (1948) Fracture of metals: Theoretical considerations. Engineering-London 165:16–18
Muehlberger WR (1961) Conjugate joint sets of small dihedral angle. J Geol 69:211–219
Müller A (2000) Cathodolumuniscence and characterization of defect structures in quartz with applications to the study of granitic rocks. Thesis, University Göttingen, pp 1–229, *http://webdoc.sub.gwdg.de/diss/2001/mueller/index.html*
Müller G, Dahm T (2000) Fracture morphology of tensile cracks and rupture velocity. J Geophys Res 105:723–738
Müller A, MŸller B, Behr HJ (2001) Structural constants in granitic rocks of the Lusatian Granodiorite Complex and the Erzgebirge, Germany – in commemoration of Hans Cloos. Z Geol Wissenschaft 29:521–544
Murakami Y (ed) (1987) Stress intensity factors handbook, vol 1, 2. The Society of Materials Sci, Japan, Pergamon Press, Oxford
Murakami Y (ed) (1992) Stress intensity factors handbook, vol 3. The Society of Materials Sci, Japan, Pergamon Press, Oxford
Murakami Y (ed) (2001) Stress intensity factors handbook, vol 4, 5. The Society of Materials Sci, Japan, Pergamon Press, Oxford
Muraoka H, Kamata H (1983) Displacement distribution along minor fault traces. J Struct Geol 5:483–495
Murgatroyd JB (1942) The significance of surface marks on fractured glass. J Soc Glass Technol 26: 155–171
Murphy PJ (1981) Detachment structures in south central NY. Northeastern Geology 3:105–116
Nabaro B (1967) Theory of crystal dislocations. Oxford University Press, Oxford
Nanjo K, Nagahawa H, Satomura M (1998) Rates of aftershocks decay and the fractal structure of active fault systems. Tectonophysics 287:173–186
Narr W, Suppe J (1991) Joint spacing in sedimentary rocks. J Struct Geol 13:1037–1047
Nativ R, Nissim I (1992) Characterization of a desert aquitard – hydrologic and hydrochemical considerations. Ground Water 30:598–606
Nativ R, Adar E, Dahan O, Geyh M (1995) Water recharge and solute transport through the vadose zone of fractured chalk under desert conditions. Water Resour Res 31:253–261
Nativ R, Adar E, Dahan O, Nissim I (1997a) Water salinization in arid regions – Observations from the Negev desert, Israel. J Hydrol 196:271–296
Nativ R, Halleran A, Hunley A (1997b) Evidence for ground-water circulation in the brine-filled aquitard, Oak Ridge, Tennessee. Ground Water 35:647–659
Nativ R, Adar EM, Becker A (1999) Designing a monitoring network for contaminated ground water in fractured chalk. Ground Water 37:38–47
Nativ R, Adar E, Assaf L, Nygaard E (2003) Characterization of the hydraulic properties of fractures in chalk. Ground Water 41:532–543
Nelson RA (1979) Natural fracture systems: Description and classification. Bull Amer Assoc Petrol Geolog 63:2214–2221

Nelson RA (1987) Fracture reservoirs: Turning knowledge into practice. J Petrol Technol 16470:407–414
Nemcok M, Bayer R, Miliorizos M (1995) Structural analysis of the inverted Bristol Channel Basin: Implications for the geometry and timing of fracture porosity. In: Buchanan JG, Buchanan PG (eds) Basin inversion. Geological Society Special Publication 88:355–392
Nesbitt AC, Austin BA (1988) The emission and propagation of electromagnetic energy from stressed quartzite rock underground. The Trans of the SA Inst of Electr Eng 79:53–57
Newman WI, Phoenix SL (2001) Time dependent fiber bundles with local load-sharing. Phys Rev E 63:0215071–19
Newman WI, Turtcotte DL, Gabrielov AM (1995) Log-periodic behavior of a hierarchical failure model with applications to precursory seismic activation. Phys Rev E 52(5):4827–4835
Nickelsen RP (1979) Sequence of structural stages of the Allegheny orogeny at the Bear Valley strip mine, Shamokin, Pennsylvania. Am J Sci 279:225–271
Nickelsen RP (1988) Structural evolution of folded thrusts and duplexes on a first-order anticlinorium in the Valley and Ridge Province of Pennsylvania. In: Mitra G, Wojtal S (eds) Geometries and mechanics of thrusting with special reference to the Appalachians. Geological Society of America Special Paper 222:89–106
Nickelsen RP (1996) Alleghanian sequential deformationon on the SW limb of the Pennsylvania Salient in Fulton and Franklin Counties, south-central Pennsylvania: Pennsylvania Geology Survey. Annual field conference of Pennsylvania geologists, 61st, guidebook, pp 1–9
Nickelsen RP, Engelder T (1989) Fold-thrust geometries of the Juniata culmination, Central Appalachians of Pennsylvania. In: Engelder T (ed) Structures of the Appalachian foreland fold-thrust belt. International Geological Congress, 28th, Fild Trip Guidebook T166
Nickelsen RP, Hough ND (1967) Jointing in the Appalachian Plateau of Pennsylvania. Geol Soc Am Bull 78:609–630
Nikiforova NN, Yadakhin TN (1989) Studies of electromagnetic emission of tectonic origin in the Kirghiz SSR. Phys Earth Planet In 57:68–74
Niles WH (1871) Peculiar phenomena observed in quarrying. Proc Boston Soc Nat Hist vol 14
Nitsan V (1977) Electromagnetic emission accompanying fracture of quartz-bearing rocks. Geophys Res Lett 4(8):33–336
Nur A (1982) The origin of tensile fracture lineaments. J Struct Geol 4:31–40
O'Keefe SG, Thiel DV (1995) A mechanism for the production of electromagnetic radiation during fracture of brittle materials. Phys Earth Planet In 89:127–135
Odling NE, Gillespie P, Bourgine B, Castaing C, Chils J-P, Christensen NP, Fillion E, Genter A, Olsen C, Thrane L, Trice R, Aarseth E, Walsh JJ, Watterson J (1999) Variations in fracture system geometry and their implications for fluid flow in fractured hydrocarbon reservoirs. Petrol Geosci 5:373–384
Ogawa T, Oike K, Miura T (1985) Electromagnetic radiation from rocks. J Geophys Res 90(d4): 6245–6249
Olami Z, Feder HJS, Christensen A (1992) Self-organized criticality in a continuous, non-conservative cellurar automaton modeling earthquakes. Phys Rev Lett 68:1244–1247
Olson JE (1993) Joint pattern development: Efects of subcritical crack growth and mechanical crack interaction. J Geophys Res 98:12251–12265
Olson JE, Pollard DD (1989) Inferring paleostress from natural fracture patterns: A new method. Geology 17:345–348
Olson JE, Pollard DD (1991) The initiation and growth of en-echelon veins. J Struct Geol 13:595–608
Orkan N, Voight B (1985) Regional joint evolution in the Valley and Ridge Province of Pennsylvania in relation to the Alleghany Orogeny: Guidebook for the 50th annual field conference of Pennsylvania geologists. Bureau of Topography and Geological Survey, Harrisburg, Pa, pp 144-164
Ouellet M (1990) Earthquake lights and seismicity. Nature 348:492
Panek LA (1985) Estimating fracture trace length from censored measurements on multiple scanlines. Proceedings of the International Symposium on Fundamentals of Rock Joints, Björkliden, pp 13–23
Paris P, Erdogan F (1963) A critical analysis of crack propagation laws. J Basic Eng-T ASME 85:528–534
Park RG (1983) Foundations of structural geology. Chapman and Hall, New York, p 135
Parker JM (1942) Regional systematic jointing in slightly deformed sedimentary rock. Geol Soc Am Bull 53:381–408
Parrot M, Achache J, Berthelier J, Blanc E (1993) High frequency electromagnetic effects. Phys Earth Planet In 77:65–81
Pauchard L, Meunier J (1993) Instantaneous and time-lag breaking of a two-dimensional solid rod under a bending stress. Phys Rev Lett 70:3565–3568
Pauchard L, Meunier J (1998) Experimental study of the breakage of a two-dimensional crystal. Phil Mag B78:221–224
Peacock DCP (2001a) The temporal relationship between joints and faults. J Struct Geol 23:329–341

Peacock DCP (2001b) Are the lower planes of double seismic zones caused by serpentine dehydration in subducting oceanic mantle? Geology 29:299–302
Peacock DCP, Sanderson DJ (1991) Displacements, segment linkage and relay ramps in normal-fault zones. J Struct Geol 13:721
Peacock DCP, Sanderson DJ (1992) Effects of layering and anisotropy on fault geometry. J Geol Soc London 149:793–802
Peacock DCP, Sanderson DJ (1994) Geometry and development of relay ramps in normal-fault systems. AAPG Bull 78:147–165
Peacock DCP, Sanderson DJ (1995) Strike-slip relay ramps. J Struct Geol 17:1351–1360
Peng S (1970) Fracture and failure of Chelmford Granite. Ph.D. thesis, Stanford University, Stanford, USA
Peng S, Johnson AM (1972) Crack growth and faulting in cylindrical specimens of Chelmsford Granite. Int J Rock Mech Min 9:37–86
Peterson RE (1974) Stress concentration factors. John Wiley & Sons Ltd., New York
Petit J-P (1988) Normal stress dependent rupture morphology in direct shear tests on sandstone with applications to some natural fault surface features. Int J Rock Mech Min 25:411–419
Petit J-P, Barquins M (1987) Formation de fissures en milier confine dans le PMMA (polymetachrylate de methyle): modele analogique de formation de structures tectoniques cassantes. C R Acad Sci Paris 305:55–60
Petit J-P, Barquins M (1988) Can natural faults propagate under mode II conditions? Tectonophysics 7:1243–1256
Petrenko VF (1993) On the nature of electrical polarization of materilas caused by cracks. Application to ice electromagnetic radiation. Philos Mag B 67(3):301–315
Petrov VA, Gorobetz LZ (1987) Size effect of the concentration threshold of destruction. Izv-Phys Solid Eart+ 23(1):75–77
Petukhov IM (1972) Rockbursts on coal mines. Nedra, Moscow
Petukhov IM, Lin'kov LM (1983) Mechanics of rock bursts and outbursts. Nedra, Moscow
Petukhov IM, Lin'kov LM, Sidorov VS (1976) Theory of protective stratums. Nedra, Moscow
Picu RC (1996) Singularities of an interface crack impinging on a triple grain junction. Int J Solids Struct 33:1563–1573
Picu RC (1997) Three-dimensional stress concentration at grain triple junctions in columnar ice. Phil Mag Lett 76:159–166
Picu RC, Gupta V (1996) Singularities at grain triple junctions in two-dimensional polycrystals with cubic and orthorhombic grains. J Appl Mech-T ASME 63:295–300
Pohn HA (1981) Joint spacing as a method of locating faults. GLGYB 9:258–261
Poirier JP (1985) Creep of crystals. Cambridge University Press, Cambridge, UK
Politi A, Ciliberto S, Scorretti R (2002) Failure time in the fiber-bundle model with thermal noise and disorder. Phys Rev E 66:026171–026176
Pollard DD (2000) Strain and stress: Discussion. J Struct Geol 22:1359–1367
Pollard DD, Segall P (1987) Theoretical displacements and stresses near fractures in rock: With applications to faults, joints, veins, dikes, and solution surfaces. In: Atkinson BK (ed) Fracture mechanics of rock. Academic Press, London, pp 277–349
Pollard DD, Segall P, Delaney PT (1982) Formation and interpretation of dilatant echelon cracks. Geol Soc Am Bull 93:1291–1303
Pomeau Y (1992) Brisure spontanée de cristaux bidimensionnels courbés. C R Acad Sci Paris, t314, Série II, pp 553–556
Pook LP (2000) Linear elastic fracture mechanics for engineering: Theory and applications. WIT Press, Southampton, Boston
Preston FW (1931) The propagation of fissures in glass and other bodies with special reference to the split-wave front. J Am Ceram Soc 14:419–427
Price NJ (1966) Fault and joint development in brittle and semi-brittle rock. Pergamon Press, New York, pp 110–161
Price NJ (1974) The development of stress systems and fracture patterns in undeformed sediments. Int Soc Rock Mech Cngr Proc pp 487–496
Price NJ (1977) Aspects of gravity tectonics and the development of listric faults. J Geol Soc London 133:311–327
Price NJ, Cosgrove JW (1990) Analysis of geological structures. Cambridge University Press, Cambridge, England
Rabinovitch A (1994) On the Mott derivation of crack velocity. Phil Mag Lett 70:231–233
Rabinovitch A, Bahat D (1979) Catastrophe theory: A technique for crack propagation analysis. J Appl Phys 50:321–334
Rabinovitch A, Bahat D (1999) Model of joint spacing distribution based on shadow compliance. J Geophys Res 104:4877–4886

Rabinovitch A, Belizovsky G, Bahat D (1993) On the direction of secondary cracks in brittle fracture. Int J Fracture 63:R25–R30
Rabinovitch A, Belizovsky G, Bahat D (1994) Length distribution of secondary cracks in brittle materials. Phil Mag Lett 70:277–288
Rabinovitch A, Bahat D, Frid V (1995) Comparison of electromagnetic radiation and acoustic emission in granite fracturing. Int J Fracture 71(2):R33–R41
Rabinovitch A, Bahat D, Frid V (1996) Emission of electromagnetic radiation by rock fracturing. Z Geol Wissenschaft 24(3–4):361–368
Rabinovitch A, Frid V, Bahat D (1998) Parametrization of electromagnetic radiation pulses obtained by triaxial fracture in granite samples. Phil Mag Lett 77(5):289–293
Rabinovitch A, Bahat D, Melamed Z (1999a) A note on joint spacing. Rock Mech Rock Eng 32:71–75
Rabinovitch A, Frid V, Bahat D (1999b) A note on the amplitude – frequency relation of electromagnetic radiation pulses induced by material failure. Phil Mag Lett 79:195–200
Rabinovitch A, Belizovsky G, Bahat D (2000a) Origin of mist and hackle patterns in brittle fracture, Phys Rev B 61:14968–14974
Rabinovitch A, Zlotnikov R, Bahat D (2000b) Flaw length distribution measurement in brittle materials. J Appl Phys 87:7720–7725
Rabinovitch A, Frid V, Bahat D, Goldbaum J (2000c) Fracture area calculation from electromagnetic radiation and its use in chalk failure analysis. Int J Rock Mech Min 37:1149–1154
Rabinovitch A, Bahat D, Frid V (2002a) Similarity and dissimilarity of electromagnetic radiation from carbonate rocks under compression, drilling and blasting. Int J Rock Mech Min 39(1):125–129
Rabinovitch A, Frid V, Bahat D (2002b) Gutenberg-Richter type relation for laboratory fracture induced electromagnetic radiation. Physical Review E 65:011401–011404
Rabinovitch A, Frid V, Bahat D, Goldbaum J (2003a) Decay mechanism of the fracture induced electromagnetic pulses. J Appl Phys 93(9):5085–5090
Rabinovitch A, Frid V, Goldbaum J, Bahat D (2003b) Polarization-depolarization process in glass during percussion drilling. Phil Mag 83(25):2929–2940
Ramsay JG (1980) Crack-seal mechanism of rock deformation. Nature 284(5752):135–139
Ramsay JG, Huber MI (1987) The techniques of modern structural geology, vol 2: Folds and fractures. Academic Press, London
Ramsay JG, Lisle R (2000) The techniques of modern structural geology, vol 3: Applications of continuum mechanics in structural geology. Academic Press, New York
Rasband W (2003) Image J 1.30V. National Institutes of Health, USA
Ravi-Chandar K (1998) Dynamic fracture of nominally brittle materials. Int J Fracture 90:83–102
Ravi-Chandar K, Knauss WG (1984a) An experimental investigation into dynamic fracture – I. Crack initiation and crack arrest. Int J Fracture 25:247–262
Ravi-Chandar K, Knauss WG (1984b) An experimental investigation into dynamic fracture – II. Microstructural aspects. Int J Fracture 26:65–80
Ravi-Chandar K, Knauss WG (1984c) An experimental investigation into dynamic fracture – III. Steady state crack propagation and crack branching. Int J Fracture 26:141–154
Ravi-Chandar K, Knauss WG (1984d) An experimental investigation into dynamic fracture – IV. On the interaction of stress waves with propagating cracks. Int J Fracture 26:189–200
Ravi-Chandar K, Knauss WG (1987) On the acceleration of the transient stress field near the tip of a crack. J Appl Mech-T ASME 54:72–78
Ravi-Chandar K, Knauss W (1999) Processes controlling fast fracture of brittle solids. Comput Sci Eng 1999 Sept/Oct:24–31
Ravishankar SR, Murthy CRL (2000) Characteristics of AE signals obtained during drilling composite laminates. NDT&E International 33:341–348
Rawnsley KD, Rives T, Petit JP, Hencher SR, Lumsden AC (1992) Joint development in perturbed stress fields near faults. J Struct Geol 14:939–951
Rawnsley KD, Peacock DCP, Rives T, Petit JP (1998) Joints in the Mesozoic sediments around the Bristol Channel Basin. J Struct Geol 20:1641–1661
Reches Z (1976) Analysis of joints in 2 monoclines in Israel. Geol Soc Am Bull 87:1654–1662
Reches Z, Lockner DA (1994) Nucleation and growth of faults in brittle rocks. J Geophys Res 99: 18159–18173
Red'kin V, Kuprijanov AS, Bufalov VV (1985) Geophysical devices for distance rock burst control. In: Smirnov V (ed) Geophysical methods of stress and deformation control. Novosibirsk, pp 81–82 (*in Russian*)
Regel' VR, Slutsker AI, Tomashevskii EE (1972) The kinetic nature of the strength solids. Sov Phys Uspekhi 1:45–65
Rehrig WA, Heidrick TL (1972) Regional fracturing in Laramide stocks of Arizona and its relationship to porphyry copper mineralization. Econ Geol 67:198–213

Rehrig WA, Heidrick TL (1976) Regional tectonic stress during the Laramide and late Tertiary intrusive periods, Basin and Range Province, Arizona. Arizona Geological Digest 10:205–228
Renshaw CE, Schulson EM (2001) Universal behavior in compressive failure of brittle materials. Nature 412:897–900
Rice RW (1974) Fracture topography of ceramics. In: Frechette VD, La Course WC, Burdick VL (eds) Surfaces and interfaces of glass and ceramics. Plenum Publishing Corpration, New York, pp 439–472
Rice JR (1979) Theory of precursory processes in the inception of earthquake rupture. Gerl Beitr Geophys 88:91–127
Rice RW (1984) Ceramic fracture features, observations, mechanisms and uses. In: Mecholsky JJ, Powell SR (eds) Fractography of ceramic and metal failures. ASTM, Philadelphia, pp 1–51
Richter HG, Kerkhof F (1994) Stress wave fractography. In: Bradt RC, Tressler RE (eds) Fractography of glass. Olenum Press, New York pp 75–109
Rikitake TJ (1997) Nature of electromagnetic radiation precursory to an earthquake. J Geomagn Geoelectr 49:1153–1163
Rives T, Razack M, Petit JP, Rawnsley KD (1992) Joint spacing: Analogue and numerical simulations. J Struct Geol 14:925–937
Roberts JC (1974) Jointing and minor tectonics of the vale of Glamorgan between Ogmore-by-Sea and Lavernock Point, South Wales. Geol J 9:97–114
Roberts JC (1979) Jointing and minor tectonics of the South Gower Peninsula between Mumbles Head and Rhossilli Bay, South Wales. Geol J 14:1–14
Roberts DG (1989) Basin inversion in and around the British Isles. In: Cooper MA, Williams GD (eds) Inversion tectonics. Spec Publ Geol Soc London 44:131–150
Roberts JC (1995) Fracture surface markings in Liassic limestone at Lavernock Point, South Wales In: Ameen MS (ed) Fractography: Fracture topography as a tool in fracture mechanics and stress analysis. Geological Society (London) Special Publication 92:175–186
Robinson ES (1970) Mechanical disintegration of the Navajo Sandstone in Zion Canyon, Utah. Geol Soc Am Bull 81:2799–2806
Rodgers J (1970) The tectonics of the Appalachians. Wiley Interscience, New York
Rophe B, Berkowitz B, Magaritz M, Ronen D (1992) Analysis of subsurface flow and anisotropy in a fractured aquitard using transient water level data. Water Resour Res 28:199–207
Rossmanith HP, Knasmillner RE, Daehnke A, Mishnaevsky L (1996) Wave propagation, damage evolution and dynamic fracture extension. 1. Percussion drilling. Mater Sci+ 32:350–358
Rossmanith HP, Daehnke A, Knasmillner RE, Kouzniak N, Ohtsu M, Uenishi K (1997) Fracture mechanics applications to drilling and blasting. Fatigue Fract Eng M 20:1617–1636
Roy A, Saha TK (1995) Interaction of a penny-shaped crack with an elliptic crack. Int J Fracture 73:51–65
Rudnicki JW, Olsson WA (1998) Reexamination of fault angles predicted by shear localization theory. Int J Rock Mech Min 35: Paper No 88
Ryan MP, Sammis CG (1978) Cyclic fracture mechanisms in cooling basalt. Geol Soc Am Bull 89: 1295–1308
Rzhevskii VV, Novik GY (1978) Foundations of rock physics. Nedra, Moscow
Sadovskii MA, Sobolev GA, Migunov NI (1979) Changes of natural radiowaves radiation during Karpatian earthquake. Dokl Akad Nauk SSSR+ 244(2):316–319
Sakai H, Oda H, Nakayama T, Doi H (1992) Electromagnetic changes at explosion seismic experiment. J Phys Earth 40:447–458
Salameh E, Zacher W (1982) Horizontal stylolites and paleostress in Jordan. Neues Jahrb Geol P M 8:509–512
Sbar ML, Sykes LR (1973) Contemporary compressive stress and seismicity in eastern North America: An example of intra-plate tectonics. Geol Soc Am Bull 84:1861–1882
Scharbert S (1998) Some geochronological data from the South Bohemian Pluton in Austria: A critical review. Acta Universitatis Carolinae Geologica Praha 42:114–118
Schiff LI (1986) Quantum mechanics. McGraw Hills, London
Schoeck G, Pichl W (1990) Bond trapping of cracks. Phys Stat Solidi 118:109–115
Scholz CH (1990) The mechanics of earthquakes and faulting. Cambridge, Cambridge University Press
Scholz CH (1998) Earthquakes and friction laws. Nature 391:37–42
Schwartz DP, Sibson RH (1989) Fault segmentation and controls of rupture initiation and termination. U.S. Geological Survey Open File Report 89–13
Scitovich VP, Lazarevich LM (1985) Estimation of stress condition of rock massive by EMR. In: Smirnov V (ed) Geophysical methods of stress and deformation control. Novosibirsk, pp 65–66 (*in Russian*)
Scorretti R, Ciliberto S, Guarino A (2001) Disorder enhances the effects of thermal noise in the fiber bundle model. Europhys Lett 55:626–632
Scott DR (1996) Seismicity and stress rotation in a granular model of the brittle crust. Nature 381:592–595

Scott WH, Hansen EC, Twiss RJ (1965) Stress analysis of quartz deformation lamellae in a minor fold. Am J Sci 263:729–746
Secor DT Jr (1965) Role of fluid pressure in jointing. Am J Sci 263:633–646
Secor DT Jr (1969) Mechanics of natural extension fracturing at depth in the Earth's crust. In: Research in tectonics. Geol Surv Canada Paper 3–47
Segall P, Pollard DD (1983) Joint formation in granitic rock of the Sierra Nevada. Geol Soc Am Bull 94:563–575
Segall P, McKee EH, Martel SJ, Turrin BD (1990) Late Cretaceous age of fractures in the Sierra Nevada Batholith, California. Geology 18:1248–1251
Shainin VE (1950) Conjugate sets of en echelon tension fractures in the Athens limestone at Riverton, Virginia. Geol Soc Am Bull 61:509–517
Shand Shand EB (1954) Experimental study of fracture of glass: 2 Experimental data. J Am Ceram Soc 37:559–572
Shand EB (1959) Breaking stress of glass determined from dimensions of fracture mirrors. J Am Ceram Soc 42:474–477
Sharon E, Finberg J (1996) Microbranching instability and the dynamic fracture of brittle materials. Phys Rev B 54:7128–7139
Sharon E, Fineberg J (1998) Universal features of the micro-branching instability in dynamic fracture. Phil Mag B78:243–251
Sharon E, Fineberg J (1999) Confirming the continuum theory of dynamic brittle fracture for fast cracks. Nature 397:333–335
Sharon E, Gross SP, Fineberg J (1995) Local crack branching as a mechanism for instability in dynamic fracture. Phys Rev Lett 74:5096–5099
Sheldon P (1912) Some observations and experiments on joint planes. J Geol 20:164–183
Shen B, Stephensson O, Einstein HH, Ghahreman B (1995) Coalescence of fractures under shear stresses in experiments. J Geophys Res 100:5975–5990
Sibson RH (1985) Stopping of earthquake ruptures at dilatational jogs. Nature 316:248–251
Simmons G, Todd T, Baldridge WS (1975) Toward a quantitative relationship between elastic properties and cracks in low porosity rocks. Am J Sci 275:318
Smekal A (1953) Zum Bruchvorgang bei sprödem Stoffverhalten unter ein- und mehrachsigen Beanspruchungen. Oesterr Ing-Arch 7:49–70
Smith RL (1982) The asymptotic-distribution of the strength of a series-parallel system with equal load-sharing. J Appl Probab 10:137–171
Smith RL, Phoenix SL (1981) Asymptotic distributions for the failure of fibrous materials under series-parallel structure and equal load-sharing. J Appl Mech-T ASME 48:75–82
Sneddon IN (1951) Fourier transforms. McGraw Hill Company Inc., New York, p 542
Sobolev GA, Semerchan AA, Salov BG (1982) Precursors of the destruction of large rock sample. Izv-Phys Solid Eart+ 18(8):572–580
Sommer E (1967) Das Bruchverhalten von Rundstäben aus Glas im Manteldruckversuch mit Überlagerter Zugspannung. Glastech Ber-Glass 40:304–307
Sommer E (1969) Formation of fracture "lances" in glass. Eng Fract Mech 1:539–546
Sornette D, Knopoff L, Kagan YY, Vanneste C (1996) Rank-ordering statistics of extreme events: Application to the distribution of large earthquakes. J Geophys Res 101:13883–13893
Spiegel MR (1961) Statistics. McGraw-Hill Book Company, N.Y., 359 pp
Spiker EC, Gray M (1997) A study of progressive deformation at the Allegheny Front, Lycoming County, Pennsylvania. Geological Society of America Abstracts with Programs, vol 29, no 1
Sprunt ES, Brace WF (1974) Direct observations of microcavities in crystalline rocks. Int J Rock Mech Min 11:139–150
Spyropoulos C, Scholz CH, Shaw BE (2002) Transition regimes for growing crack populations. Phys Rev E 65:0561051–05610510
Srivastava GP (1990) The physics of phonons. Adam Hilger, Bristol
Stearns DW (1968) Certain aspects of fracture in naturally deformed rocks. In: Riecker RE (ed) Rock mechanics seminar, vol 1. Special rept., Terrestrial Sciences Lab Air Force, Cambridge Research Labs, Bedford, Mass, pp 27–116
Stearns DW, Friedman M (1972) Reservoirs in fractured rock. In: King RE (ed) Stratigraphic oil and gas fields. AAPG M Em 16:82–106
Stearns DW (1968) Certain aspects of fracture in naturally deformed rocks. In: Riecker RE (ed) Rock mechanics seminar, vol. 1, special rept. Terrestrial Sciences Lab Air Force, Cambridge Research Labs, Bedford, Mass, pp 27–116
Stern TW, Bateman PC, Morgan BA, Newell MF, Peck DL (1981) Isotopic U-Pb ages of zircon from the granitoids of the central Sierra Nevada, California. U.S. Geological Survey Professional Paper 17 pp

Stewart ME, Taylor WJ (1996) Structural analysis and fault segment boundary identification along the Hurricane fault in southwestern Utah. J Struct Geol 18:1017–1029
Suess FE (1926) Intrusionstektonik und Wandertektonik im variszischen Grundgebirge. Gebrüder Borntraeger, Leipzig, 268 pp
Suk M (1984) Geological history of the territory of Czech Socialist Republic. Geological Survey, Prague
Suppe J (1985) Principles of structural geology. Prentice-Hall, Englewood Cliffs, NJ
Suresh S (1998) Fatigue of materials, 2nd edn. Cambridge University Press, Cambridge
Swaby PA, Rawnsley KD (1997) An interative #D fracture modeling environment. Soc Petroleum Eng 9:88–92
Swallowe GM, Field JE, Horn LA (1986) Measurements of transient high-temperatures during the deformation of polymers. J Mater Sci 21:4089–4096
Takayasu H (1989) Fractals in the physical sciences. John Wiley & Sons Ltd., New York
Tetelman AS, McEvly AJ (1967) Fracture of structural materials. John Willey & Sons Ltd., New York
Thomas R, Klemm W (1997) Microthermometric study of silicate melt inclusions in Variscan granites from SE Germany. J Petrology 38:1753–1765
Thomas AL, Pollard DD (1993) The geometry of echelon fractures in rock: Implications from laboratory and numerical experiments. J Struct Geol 15:323–334
Timoshenko SP, Goodier JN (1951) Theory of elasticity. McGraw-Hill, New York
Timoshenko SP, Goodier JN (1984) Theory of elasticity, 3rd edn. McGraw-Hill Int Book Co, Auckland
Tobisch OT, Paterson SR, Saleeby JB, Geary EE (1989) Nature and timing of deformation in the Foothills terrane, central Sierra Nevada, California: Its bearing on orogenesis. Geol Soc Am Bull 101:401–413
Tokarski AK, Zuchiewicz W, Swierczewska A (1999) The influence of early joints on structural development of thrust-and-fold belts: A case study from the Outer Carpathians (Poland). Geol Carpath 50:178–180
Tomizawa I, Yamada I (1995) Generation mechanism of electric impulses observed in explosion seismic experiments. J Geomagn Geoelectr 47:313–324
Tomizawa I, Hakayawa M, Yoshino T (1994) Observation of ELF/VLF electromagnetic variations associated with seismic experimental explosion. In: Hayakawa M, Fujinawa Y (eds) Electromagnetic phenomena related to earthquake prediction. Terra Scientific Publishing Company, Tokyo, pp 337–347
Trudgill B, Cartwright J (1994) Relay-ramp forms and normal-fault linkages, Canyonlands National Park. Utah Bull Geol Soc Am 106:1143–1157
Trzebski R (1997) Morphogenesis, tectonic setting and intrusion dynamics of the late-Variscan granites at the northwest-margin of the Bohemian Massif. Göttinger Arb Geol Paläont 69:1–66
Tsang YW (1984) The effect of tortuosity on fluid-flow through a single fracture. Water Resour Res 20:1209–1215
Tschegg EK (1983) Mode 3 and mode 1 fatigue crack propagation behaviour under tortional loading. J Mater Sci 18:1604–1614
Turcotte DL (1992) Fractals and chaos in geology and geophysics. Cambridge University Press, Cambridge
Turcotte DL, Newman WI, Shcherbakov R (2003) Micro and microscopic models of rock fracture. Geophys J Int 152:718–728
Tvergaard V, Hutchinson JW (1988) Microcracking in ceramics induced by thermal expansion or elastic anisotropy. J Am Ceram Soc 71:157–166
Twidale CR, Vidal Romani JR, Campbell EM, Centeno JD (1996) Sheet fractures: Response to erosional offloading or to tectonic stress? Z Geomorph 106:1–24
Twiss RJ, Moores EM (1992) Structural geology. Freeman & Company, New York
Umeda Y (1990) High-amplitude seismic-waves radiated from the bright spot of an earthquake. Tectonophysics 175:81–92
Urusovskaja AA (1969) Electric effects associated with plastic deformation of ionic crystals. Sov Phys Uspekhi 11:631–643
Van Hise CR (1896) Principles of North-American Pre-Cambrian geology: U.S. geology. U.S. Geological Survey 16th Annual Report, pp 581–874
Van Tyne A (1983) Natural gas potential of the Devonian black shales of New York. NoE Geol 5:209–216
Varotsos P, Sarlis, N, Lazaridou M (1999) Interconnection of defect parameters and stress-induced electric signals in ionic crystals. Phys Rev B 59:24–27
Ver Steeg K (1942) Jointing in the coal beds of Ohio. Econ Geol 37:530–509
Vozoff K, Frid V (2001) Electromagnetic emissions monitoring to warn of wind blasts and gas outs. Results of ACARP Project at Moonee Colliery: C9005. In: Symposium on Geological Hazards, Rafferety's Resort Newcastle, 15–16 November 2001
Wagner GA, Van Den Haute P (1992) Fission track dating. Enke-Verlag, Stuttgart
Walmann T, Malthe-Sorenssen A, Feder J, Jossang T, Meakin P, Hardy HH (1996) Scaling relations for the lengths and widths of fractures. Phys Rev Lett 77:5393–5396

Walsh JJ, Watterson J (1988) Analysis of the relationship between displacements and dimensions of faults. J Struct Geol 10:239–247
Warwick JW, Stoker C, Meyer TR (1982) Radio emission associated with rock failure: Possible application to the great Chilean earthquake of May 22, 1960. J Geophys Res 87(b4):2851–2859
Watznauer A (1954) Die erzgebirgischen Granitintrusionen. Geologie 3:688–706
Wawrzynek PA, Ingraffea AR (1987) Interactive finite element analysis of fracture processes: An integrated approach. Theor Appl Fract Mec 8:137–150
Wedel AA (1932) Geological structures of the Devonian strata of southcentral New York, New York State. Mus Bull 294:74
Weinberger R (1999) Initiation and growth of cracks during desiccation of stratified muddy sediments. J Struct Geol 21:379–386
Weinberger R (2001a) Joint nucleations in layered rocks with non-uniform distribution of cavities. J Struct Geol 23:1241–1254
Weinberger R (2001b) Evolution of polygonal patterns in stratified mud during desiccation: The role of flaw distribution and layer boundaries. Geol Soc Am Bull 113:20–31
Weisbrod N, Nativ R, Ronen D, Adar E (1998) On the variability of fracture surfaces in unsaturated chalk. Water Resour Res 34:1881–1887
Weisbrod N, Nativ R, Adar E, Ronen D (1999) Impact of intermittent rainwater and wastewater flow on coated and uncoated fractures in chalk. Water Resour Res 35:3211–3222
Weisbrod N, Nativ R, Adar E, Ronen D (2000a) Salt accumulation and flushing in unsaturated fractures in an arid invironment. Ground Water 38:452–461
Weisbrod N, Nativ R, Adar E, Ronen D, Ben-Nun A (2000b) Impact of coating and weathering on the properties of chalk fracture. Geophys Res Lett 105:27853–27864
Weisbrod N, Dahan O, Adar EM (2002) Particle transport in unsaturated fractured chalk under arid conditions. J Contam Hydrol 56:117–136
Westergaard HM (1939) Bearing pressure and cracks. Trans Am Soc Mech Eng 61A:49–53
White WS (1946) Rock-bursts in the granite quarries at Bare, Vermont. U.S. Geological Survey, Circular 13
Whittaker A, Green GW (1983) Geology of the country around Weston-super-Mare. Memoir of the Geological Survey of Great Britain. Sheet 279 and parts of 263 and 295
Wibberley CAJ, Petit JP, Rives T (2000) Micromechanics of shear rupture and the control of normal stress. J Struct Geol 22:411–427
Widom B (1966) Random sequential addition of hard spheres to a volume. J Chem Phys 44:3888
Wiederhorn SM (1967) Influence of water vapor on crack propagation in soda-lime glass. J Am Ceram Soc 50:407–414
Wiederhorn SM (1978) Mechanisms of subcritical crack growth in glass. In: Bradt RC, Hasselman DPH, Lange FF (eds) Fracture mechanics of ceramics, vol 4. Plenum, New York, pp 549–580
Wiederhorn SM, Bolz LH (1970) Stress corrosion and static fatigue of glass. J Am Ceram Soc 53:543–548
Wiederhorn SM, Johnson H (1973) Effect of electrolyte PH on crack propagation in glass. J Am Ceram Soc 56:192–197
Wiederhorn SM, Johnson H, Diness AM, Heuer AH (1974) Fracture of glass in vacuum. J Am Ceram Soc 57:336–341
Wiederhorn SM, Dretzke A, Rodel J (2002) Crack growth in soda-lime-silicate glass near the static fatigue limit. J Am Ceram Soc 85:2287–2292
Wilkins SJ, Michael RG, Wacker M, Eyal Y, Engelder T (2001) Faulted joints: Kinematics, displacement-length scaling relations and criteria for their identification. J Struct Geol 23:315–327
Willemse EJM, Pollard DD (1998) On the orientation and patterns of wing cracks and solution surfaces at the tips of a sliding flaw or fault. J Geophys Res 103B:2427–2438
Williams ML (1957) On the stress distribution at the base of a stationary crack. J Appl Mech-T ASME 24:109–114
Wise DU, McCrory TA (1982) A new method of fracture analysis: Azimuth versus traverse distance plots. Geol Soc Am Bull 93:889–897
Witherspoon PA, Newman SP (1967) Evaluating a slightly permeable caprock in aquifer gas storage. I. Caprock of infinite thickness. J Petrol Technol 19:949
Wong RHC, Chau KT (1998) Peak strength of replicated and real rocks containing cracks. Key Eng Mat 145–149:953–958
Wong RHC, Chau KT, Wang P (1996) Microcracking and grain size effect in Yuen Kong marbles. Int J Rock Mech Min 33:479–485
Woodworth JB (1895) Some features of joints. Science 2:903–904
Woodworth JB (1896) On the fracture system of joints, with remarks on certain great fractures. Boston Society Natural History Proceedings 27:63–184
Wu H, Pollard DD (1992) Propagation of a set of opening-mode fractures in layered brittle materials under uniaxial strain cycles. J Geophys Res 97:3381–3396

Wu H, Pollard DD (1995) An experimental study of relationship between joint spacing and layer thickness. J Struct Geol 17:887–905
Wyss M (2001) Why is earthquake prediction research not progressing faster? Tectonophysics 338: 217–223
Xu XP, Needleman A (1994) Numerical simulations of fast crack growth in brittle solids. J Mech Phys Solids 42:1397–1434
Yamada I, Masuda K, Mizutani H (1989) Electromagnetic and acoustic emission associated with rock fracture. Phys Earth Planet In 57:157–168
Yang B, Ravi-Chandar K (2001) Crack path instabilities in a quenched glass plate. J Mech Phys Solids 49:91–130
Yatomi C (1981) The effect of surface-energy on temperature rise around a fast running crack. Eng Fract Mech 14:759–762
Yepez E, Angulobrown F, Peralta J (1995) Electric field pastterns as seismic precursors. Geophys Res Lett 22(22):3087–3090
Yoffe EH (1951) The moving Griffith crack. Phil Mag 42:739–750
Yokobori T, Uozomi M, Ichikawa M (1971) Interaction between non-coplanar parallel straggered elastic cracks. Rep Res Inst Strength and Fract of Mater 7:25–47
Yoon KJ, Wiederhorn SM, Luecke WE (2000) Comparison of tensile and compressive creep behavior in silicon nitride. J Am Ceram Soc 85:2017–2022
Yoshino T, Tomizawa I (1989) Observation of low-frequency electromagnetic emissions as precursors to the volcanic eruption at Mt. Mihara during November, 1986. Phys Earth Planet In 57:32–39
Yoshino T, Tomizawa I, Sugimoto T (1993) Results of statistical analysis of low-frequency seismogenic EM emissions as precursors to earthquakes and volcanic eruptions. Phys Earth Planet In 77:21–31
Younes AL (1996) Tectonic implications from joints and fold history in the Appalachian Plateau, central New York. Geological Society of America Abstracts with Programs, vol 28, no 3, A-111
Younes AI, Engelder T (1995) Paleostress rotation as indicated by joints within the Appalachian Plateau: Clockwise, counterclockwise, or both? American Geological Society, Abstracts of the Annual Meeting, Session 135
Younes AI, Engelder T (1999) Fringe cracks: Key structures for the interpretation of the progressive Alleghanian deformation of the Appalachian Plateau. Geol Soc Am Bull 111:219–239
Yukawa S, Timo DP, Rubio A (1969) Fracture design practices for rotating equipment. In: Liebowitz H (ed) Fracture. Academic Press, New York, pp 65–157
Yuse A, Sano M (1993) Transition between crack patterns in quenched glass plates. Nature 362:329–331
Yuse A, Sano M (1997) Instabilities of quasi-static crack patterns in quenched glass plates. Physica D 108:365–378
Zawislanski P (1994) Surface fracture distribution at Raymond field site, Raymond, California, Lawrence Berkeley National Laboratory Report, LBNL-42675
Zhao M, Jacobi RD (1997) Formation of regional cross-fold joints in the northern Appalachian Plateau. J Struct Geol 19:817–834
Zhao YX, Gao Q, Wang JN (2000) The evolution of short fatigue crack lengths and crack density: Two approaches. Fatigue Fract Eng M 23:929–941
Zhurkov SN (1965) Kinetic concept of the strength of solids. Int J Fracture Mech 1:311–323
Zoback ML (1989) Global patterns of tectonic stress. Nature 34:291–298
Zoback ML (1992) First- and second-order patterns of stress in the lithosphere: The world stress map project. J Geophys Res 97:11703–11728
Zoback MD, Healy JH (1984) Friction, faulting, and in situ stress. Ann Geophys 2:689–698
Zurkov SN, Kuksenko VS, Slutsker AI (1969) Formation of submicroscopic cracks in polimers under load. Sov Phys Sol-State 11(2):238–245

Subject Index

C

D

E

F

G

Q

R

S

T